ISBN: 978-4-909106094 C3051

SEE-MIE 2022 Proceedings

EDITED BY
Zakaria Hossain

November 10-12, 2022
Yokkaichi Mie Japan

SEE 2022, MIE, JAPAN
STRUCTURE, ENGINEERING AND ENVIRONMENT

PROCEEDINGS OF EIGHTH INTERNATIONAL CONFERENCE – SEE 2022
STRUCTURE, ENGINEERING & ENVIRONMENT MIE, JAPAN 10-12 NOVEMBER, 2022

Structure, Engineering and Environment

Edited by

Prof. Zakaria Hossain
Graduate School of Bioresources
Mie University, Japan

THE GEOMATE INTERNATIONAL SOCIETY

Published by:
The GEOMATE International Society
Tsu city, Mie, Japan
E-mail: society@geomate.org
http://www.geomate.org/

ISBN Number: 978-4-909106094 C3051

Table of Contents

Preface

On behalf of the SEE 2022 Organizing Committee, it is our great pleasure to welcome you to the Eighth International Conference on Structure, Engineering & Environment, held at Miyako Hotel Yokkaichi, Mie, Japan organized in conjunction with Mie University Research Center for Environmental Load Reduction, The GEOMATE International Society, Useful Plant Spread Society, Glorious International, AOI Engineering, HOJUN, JCK, CosmoWinds and Beppu Construction, Japan.

The conference covers three major themes with many specific themes including:

Advances in Building Structure
Advances in Infrastructures
Advances in Civil Engineering
Advances in Structural Engineering
Advances in Geological Engineering
Advances in Geometics Engineering
Advances in Chemical Engineering
Advances in Environmental Engineering
Advances in Geotechnical Engineering
Advances in Architectural Engineering
Advances in Industrial Engineering
Advances in Manufacturing Engineering
Advances in Materials Engineering
Advances in Mechanical Engineering
Advances in Petroleum Engineering
Advances in Process Engineering
Advances in Environmental Technology
Advances in Geophysics
Advances in Hydrology
Advances in Recycle Solid Wastes
Advances in Use of reclaimed Waters
Advances in Water Distribution
Advances in Water Treatment
Advances in Irrigation and Drainage
Advances in Farm Structures

Even with the COVID-19, this year we have received many submissions from different countries all over the world including Australia, Czech Republic, . The technical papers were selected from the vast number of contributions submitted after a review of the abstracts. The final papers in the proceedings have been peer reviewed rigorously and revised as necessary by the authors. It relies on the solid cooperation of numerous people to organize a conference of this size. Hence, we appreciate everyone who support as well as participate in the joint conferences.

Last but not least, we would like to express our gratitude to all the authors, session chairs, reviewers, participants, institutions and companies for their contribution to SEE 2022. We hope you enjoy the conference onsite and ZOOM online and find this experience inspiring and helpful in your professional field. We look forward to seeing you at our upcoming conference next year.

Best regards,

Prof. Dr. Zakaria Hossain, Chairman

Organization

Scientific Committees:

Honorary Chairman: Dr. Sohji Inoue, E/Prof. Mie University, Japan
Conference Chairman: Dr. Zakaria Hossain, Prof. Mie University, Japan

Conference Organizing Committee:

Dr. Zakaria Hossain, Prof. Mie University, Japan (Chair)
Dr. Satoshi Kaneco, Prof., Mie University, Japan (Co-Chair)
Dr. Sohji Inoue, E/Prof. Mie University, Japan (Co-Chair)
Dr. Toshinori Sakai, Prof. Mie University, Japan (Co-Chair)
Dr. Takamitsu Kajisa, E/Prof. Mie University, Japan (Co-Chair)
Dr. Masaaki Kondo, A/Prof. Mie University, Japan (Co-Chair)

National & International Advisory Committee:

Dr. Fumio Tatsuoka, E/Prof., Tokyo University of Science, Japan
Dr. Junichiro Takeuchi, Prof., Kyoto University, Japan
Dr. Kingshuk Roy, Prof., Nihon University, Japan
Dr. Sai Vanapalli, Prof., University of Ottawa, Canada
Dr. Musharraf Zaman, Prof. Univ. of Oklahama, USA
Dr. Rafiqul Tarefder, Prof. University of New Mexico, USA
Dr. M. Bouassida, Prof., National Sch. of Engg. of Tunis
Dr. L.R. Austriaco, E/Prof., Angles Univ. Found., Philippines
Dr. M. Ibn Ibrahimy, Prof., Int. Islamic Univ., Malaysia
Dr. Mohammad Shariful Islam, Prof., BUET, Bangladesh.
Dr. Bujang B.K. Huat, Prof., Univ. Putra Malaysia
Dr. Nemy Banthia, Prof., UBC, Canada
Dr. Ian Jefferson, Prof., Univ. of Birmingham, UK
Dr. John Bolander, Prof., Univ. of California, USA
Dr. Shamsul Chowdhury, Prof., Roosevelt Univ., USA
Dr. Isabel Pinto, Prof., University of Coimbra, Portugal
Dr. Mark Jaksa, E/Prof., University of Adelaide, Australia
Dr. Jim Shiau, A/Prof., USQ, Australia
Dr. Hj. Ramli Bin Hj. Nazir, A/Prof., UTM, Malaysia
Dr. H.M. Shahin, Prof., Islamic University of Technology, Bangladesh
Dr. Md. Ariful Islam, A/Prof. Ohio State University, USA
Dr. Md. Nurul Amin, Prof. Dhaka University, Bangladesh
Dr. Chan Chee-Ming, Prof. Universiti Tun Hussein Onn Malaysia
Dr. Ahmed H. A. Dabwan, A/Prof. TATI Univ. College, Malaysia

International Technical Program Committee:

Prof. Adolf Heinrich Horn, Geological Institute - Federa University of Minas Gerais, Brazil
Prof. Bang-Fuh Chen, National Sun Yat-sen University, Taiwan
Prof. Bindeshwar Singh, Kamla Nehru Institute of Technology, India
Prof. Catherine Mulligan, Concordia Institute of Water, Energy and Sustainable Systems, Canada
Prof. Chi-Min Liu Chienkuo Technology University, Taiwan
Prof. Daffalla Rabih, Kenana Sugar Company, Sudan
Prof. Essaid Bilal, Ecole Nationale Superieure Des Mines De Saint Etienne, France
Prof. Hakan Caliskan, Usak University, Faculty of Engineering, Turkey
Prof. Ibrahim Maiyza, National Institute of Oceanography & Fisheries, Egypt
Prof. Loc Nguyen, Sunflower Soft Company, Vietnam
Prof. Marilia Hagen, Indiana University, United States
Prof. Md Najib bin Ibrahim, Universiti Teknologi MARA, Malaysia
Prof. Md. Abdul Baset Mia, BSMR Agri. Univ., Bangladesh
Prof. Mihaela Popescu, University of Craiova, Romania
Prof. Mohamed Abdou, Faculty of Education Department of Mathematics, Egypt
Prof. Mohamed Tahiri, Présidnce de l'Université Hassan II de Casablanca, Morocco
Prof. Nazar Oukaili, University of Baghdad, Iraq
Prof. Radim Cajka, Technical University Ostrava, Faculty of Civil Engineering, Czech Republic
Prof. Rajaraman Jambunathan, AMET University, India
Prof. Saad Farhan Ibrahim Alabdullah, University of Almustansiriyah, Iraq
Prof. Salem Alsanusi, Benghazi, Libya
Prof. Sudhir Kumar Das, Retired Senior Project Manager of Indian Railways, India
Prof. Zachary Senwo, Alabama A&M University, United States
Prof. Imed Jabri, University of Tunis, Tunisia
A/Prof. Bindeshwar Singh Kamla Nehru Institute of Technology, India
A/Prof. Hasi Rani Barai, Yeungnam University, South Korea
A/Prof. Jamaluddin Mahmud, Universiti Teknologi MARA, Malaysia
A/Prof. Mohamed Ramadan, University of Hail, Saudi Arabia
A/Prof. Najam Hasan, Dhofar University, Oman
A/Prof. Nosina Krishna Chaitanya, Jawaharlal Nehru Technological University, India
A/Prof. Nurbek Saparkhojayev, Almaty Management University, Kazakhstan
A/Prof. Pandian Vasant, Universiti Teknologi Petronas, Malaysia
A/Prof. Teodor Lucian Grigorie, University of Craiova, Romania
A/Prof. Zawawi Daud, Universiti Tun Hussein Onn Malaysia
A/Prof. Abdull Halim Abdul, OIl and Gas department, Malaysia
A/Prof. Baoping Cai, China University of Petroleum, China
A/Prof. Dariusz Jakóbczak, Koszalin University of Technology, Poland
A/Prof. Edgar Allan Mendoza, University of the Philippines
A/Prof. Lakhveer Singh, Universiti Malaysia Pahang (UMP) Malaysia, Malaysia
A/Prof. Lidia Sas Paszt, Research Institute of Pomology, Poland
A/Prof. Mahmood Barbooti, University of Yechnology, Iraq
A/Prof. Majid Mirzaei, Universiti Tunku Abdul Rahman, Malaysia
A/Prof. Najeh Lakhoua, University of Carthage, Tunisia
A/Prof. Ryan Joseph Calinao, Lyceum of the Philippines University-Laguna
A/Prof. Sarawut Thepanondh, Mahidol University, Thailand
A/Prof. Yasir Al Hussein, Jerash University, Faculty of Engineering, Jordan
A/Prof. Grigorie Teodor Lucian, University of Craiova, Romania
A/Prof. Hêriş Golpîra, Islamic Azad University, Sanandaj, Iran
A/Prof. Muhammad Aslam, King Abdulaziz University, Saudi Arabia
A/Prof. Tomasz Plech, Medical University of Lublin, Poland
A/Prof. Fellah Mamoun, Abbes laghrour University, Algeria
A/Prof. R. S. Ajin, GeoVin Solutions Pvt. Ltd., India
A/Prof. Roman Szewczyk, Industrial Research Institute for Automation and Measurements, Poland

Dr. Abolghasem Akbari, University Malaysia Pahang, Malaysia
Dr. Ahmad Safuan A Rashid, Universiti Teknologi Malaysia, Malaysia
Dr. Akinola Johnson Olarewaju, Federal Polytechnic Ilaro, Ogun State, Nigeria
Dr. Alexandre Costa, Federal University of the valleys of Jequitinhonha and Mucuri, Brazil
Dr. Angelo Gallone, Scotland's Rural College (SRUC), United Kingdom
Dr. Azizul Azhar Ramli, Universiti Tun Hussein Onn Malaysia
Dr. Bashir Dar, University of Kashmir Delina Baramulla J&K India, India
Dr. Bassam Abdellatif, National Authority for Remote Sensing and Space Sciences, Egypt
Dr. Binh Phu Nguyen, National University of Singapore, Singapore
Dr. Cazacu Gabriela, S.C. Geotech Dobrogea, Romania
Dr. Chengen Yang, Intel Corporation, United States
Dr. Dayang Norulfairuz Abang Zaidel, Universiti Teknologi Malaysia
Dr. Evgeni Starikov, KIT, Karlsruhe, Germany; Chalmers, Gothenburg Sweden, Germany
Dr. Fatma Khanchel, University of Tunis El Manar, Tunisia
Dr. Hamidreza Khataee, Griffith University, Australia
Dr. Hêriş Golpîra, Islamic Azad University, Iran
Dr. Iskhaq Iskandar, Dept. Physics, University of Sriwijaya, Indonesia
Dr. Jingwei Zhao, University of Wollongong, Australia
Dr. Jitendra Agrawal, Rajiv Gandhi Proudyogiki Vishwavidyalaya, India
Dr. Liza Patacsil, Malayan Colleges Laguna, Philippines
Dr. Mohamed Amine, Ferrag Guelma University, Algeria
Dr. Mohd Afendi Rojan, Universiti Malaysia Perlis, Malaysia
Dr. Mohd Altaf, University of Kashmir Delina Baramulla J&K India, India
Dr. Mohd Hairy Ibrahim, Sultan Idris Education University, Malaysia
Dr. Mostafa Khater, Egypt - El Sharqia - Zagazig, Egypt
Dr. Najam Hasan, Dhofar University, Oman
Dr. Namir Alkawaaz, University of Almustansiriyah, Iraq
Dr. Nashrul Fazli Mohd Nasir, Universiti Malaysia Perlis, Malaysia
Dr. NaufaL Mansor Kampus Uniciti Alam, Universiti Malaysia Perlis (UniMAP), Malaysia
Dr. Obed Majeed Ali, Northern Technical University, Iraq
Dr. Piyapong Janmaimool, King Mongkhut' University of Technology, Thailand
Dr. Po-Sheng Chiu, National Cheng Kung University, Taiwan
Dr. Prabu Mohandas, Adhiyamaan College of Engineering, India
Dr. Raman Kumar, D A V Institute of Engineering and Technology, India
Dr. Riccardo Colella, University of Salento, Italy
Dr. Rolando Javellonar, Romblon State University, Philippines
Dr. Shikha Agrawal, Rajeev Gandhi Technical University, India
Dr. Stefania Tomasiello CORISA, University of Salerno, Italy
Dr. Sumiyyah Sabar, Universiti Sains Malaysia, Malaysia
Dr. Suphaphat Kwonpongsagoon, Mahidol University, Thailand
Dr. Wei Hong Tan, Universiti Malaysia Perlis, Malaysia
Dr. Yoshiro Fujii, Shin Kobe Dental Clinic, Japan
Dr. Yuk Feng Huang, Universiti Tunku Abdul Rahman (UTAR), Malaysia
Dr. Zongyan Zhou, Monsh University, Australia
Dr. Purnanand Savoikar, Goa Engineering College, India
Dr. Ahmed Toaha Mobashsher, University of Queensland, Australia
Dr. Chupong Pakpum, Maejo University
Dr. Emanuele Quaranta, Politecnico di Torino, Italy
Dr. Jiangling Yin, Apple Inc., Cupertino, CA, United States
Dr. Khor Shing Fhan, Universiti Malaysia Perlis, Malaysia
Dr. Mario Chauca, Ricardo Palma University, Peru
Dr. Santosh Gaikwad, Model College, Ghansawangi, India
Dr. Tse Guan Tan, Universiti Malaysia Kelantan
Dr. Vikas Panthi, National Institute of Technology, India
Dr. Watoo Phrompittayarat, Naresuan University, Thailand

Dr. Hamidreza Namazi, Nanyang Technological University, Singapore
Dr. Parichat Phumkhachorn, Ubon Ratchathani University, Thailand
Dr. Subhasis Roy, University of Calcutta, India

Conference Correspondence:

Prof. Dr. Zakaria Hossain (Director)
Dept. of Environmental Science and Technology, Mie University, Japan
Mr. Alex Otieno Owino (Secretary)
Dept. of Environmental Science and Technology, Mie University, Japan
E-mail: conference@geomate.org
Tel & Fax: +81-59-231-9578

Editorial and Executive Committee:

Prof. Dr. Zakaria Hossain
Engr. Alex Otieno Owino
Engr. Md. Aminul Islam

Keynote Papers

8th Int. Conf. on Structure, Engineering & Environment (SEE), Mie, Japan, Nov.10-12, 2022, ISBN: 978-4-909106094 C3051

EFFECTIVENESS OF BRYOPHYTES AND CICADA SHELLS AS A BIO-INDEX FOR HEAVY METAL CONTAMINATION OF RIVER WATER AND SOIL

Hiroyuki Ii[1]
[1]Faculty of Systems Engineering, Wakayama University, Japan

ABSTRACT

Metal concentrations of sampled bryophytes varied widely and increased depending on the metal contamination conditions. The highest values in bryophytes were several 10,000 ppm for Cu and Zn, 100,000 ppm for Pb, several 1,000 for As and a few 100 ppm for W. Bryophytes are therefore considered to be an effective index of Cu, Zn, Pb, As, and W contaminations. However, the heavy metal concentration in bryophytes at a W mine was low and the heavy metal concentration in other plants showed a higher concentration than that of bryophytes. The presence of W is thought to be the cause of the decrease in the heavy metal concentrations in bryophytes. The other possibility is that only bryophytes with a low copper concentration can grow. The highest Zn concentrations in a cruciferous species reached several 10,000 ppm among sampled plants. The Cu and Zn concentrations in both cicada shells and adult cicadas were not always high at metal mines. Therefore, Cu and Zn concentrations of cicada shells were not effective as a Cu and Zn contamination index. Pb and As concentrations in cicada shells at Pb and As mines were higher than those for non-Pb and non-As contaminated areas and were higher than those in cicada adults. Therefore, cicadas were thought to release Pb and As into their shells during molting and maintain high concentrations of Pb and As in their cicada shells. Pb and As concentrations in cicada shells were thought to be an effective contamination index.

Keywords: Cicada shells, Bryophyte, Heavy metals, Bio-index, Metal contamination

INTRODUCTION

Metal concentrations in river water and soil were measured to investigate the influence of heavy metals on local plants, insects and animals. Generally, metal concentrations in river water is very low. Moreover, they are changeable depending on the change of flow rate. Heavy metals in soil contain both soluble and insoluble metals, but living organisms use only soluble metals. Not all heavy metals in the soil are used by living organisms. Therefore metal concentrations in river water and soil were not always useful as an index of the influence of heavy metals on life. Then, in this study, bryophytes and cicada shells were proposed as a new index for gauging metal contamination. Bryophytes are easily found around rivers and cicada shells are easy to sample without digging and both contain long term information and bryophytes and cicadas absorbed metal into living body.

Bryophytes were the first green plants to colonize the terrestrial environment [1], and as such had to evolve mechanisms to cope with the much greater amounts of heavy metals present on land than in the water [2]. The absence of a root system indicates the ability of these plants to absorb heavy metals over their entire surface [2], [3]. The lack of the cuticle layer, which makes their cell walls easily accessible for metal ions [4], [5], pronounced ion-exchange properties [6] and a large surface-to-weight ratio also significantly contribute to this ability [7].

Advantages of bryophyte-performed monitoring, compared to conventional measurements, are cost-effectiveness and easier sampling that results in a much higher sampling density and a larger number of sites that can be included in the survey [3], [8]. Due to the great capacity of bryophytes to absorb and retain heavy metals in high concentrations, it is also easier to perform chemical analysis and there are fewer contamination problems [9].

The heavy metal concentration in river insect larvae was found to decrease with weight. In identical river conditions the heavy metal concentrations in different insects, weighing the same as the larvae, were the same. Therefore, bio-concentrations in small herbivorous insect larvae to large carnivorous insect larvae was not found [10]. Heavy metals in river insect larvae was thought to be released with the shells of river insect larvae. Although it is difficult to sample shells of river insect larvae because the molting of aquatic insects is carried out in water, it is easy to sample cicada shells found on trees. Metal concentrations in cicada shells show a positive correlation with soil metal concentrations [11]. Comparing metal

concentrations in cicada shells and cicada bodies, Al, Fe, and Pb were enriched in cicada shells and Cu and Zn were enriched in cicada bodies [12]. Thus, cicada shells are thought to be useful as a bio-index for metal contamination. The purpose of this study is therefore to clarify the effectiveness and character of bryophytes and cicada shells as a bio-index for heavy metal contamination of rivers and soils in comparison with plants at the same sampling points and cicada adults.

METHOD

Bryophytes and some kinds of plants (ferns, cruciferae, pines, Boenninghausenia albiflora, alders, rushs, laurels, and fruit plants) and cicada shells and adults were sampled at metal contaminated and metal non-contaminated areas. Metal contaminated areas were metal mine dumps and the ruins of old factories. Metal mines were Ikuno (Cu, Pb, As, Zn and W), Waidani (Cu, Pb, Zn and As), Tada (Cu, Pb and Zn), Rendaiji (Cu, Pb and Zn), Kiwada (Cu, As and W), Kaneuchi (Cu, As and W), Nishinomaki (As), Dundas (Cu, Pb, Zn and As), Naganobori (Cu and As), Iwami (Pb, Zn), Ningyotouge (U), Nyu (Hg) [13], [14]. Nishikino is the ruin of a wire factory. Bryophytes in non-contaminated areas were sampled at the river sides of the Yoshi and Tenjin rivers (Okayama and Tottori prefecture) and a small river on the Izumi and Kongo mountains.

The cicada shells and cicada adults sampled were black cicadas, large brown cicadas, evening cicadas, *Oncotympana maculaticollis* and *Platypleura kaempferi* and *Terpnosia nigricosta* (sampled at only Kusatsu). They were sampled on trees located at metal contaminated areas (trees were on the metal mine dump) and non-contaminated areas. Non-contaminated areas were city parks in Osaka, Wakayama and Tokyo, Serpentinite Hill (Ryumon, Kamogawa (Mineoka), Nakase and Ogose, basalt lava (Fujinomiya) and a hot spring area (Kusatsu).

In the laboratory, the sampled bryophytes, plants and cicada adults and shells were first rinsed with ultra pure water and then desiccated by a dryer. After drying, they were dissolved with concentrated nitric acid and filtered with a membrane filter with a 0.45 micrometer pore size. After filtering, the W, Cu, Pb, Zn and As concentrations in plants and cicada were measured by ICP-OES (AMETEK, Inc., SPECTRO ARCOS) in the laboratory at Wakayama University. The actual detection limit of ICP-OES is 0.001ppm for W, Cu, Pb, Zn and As. Plants, excluding bryophytes, were divided into leaves, stems and roots and each part was separately analyzed.

RESULTS

Bryophyte

Firstly, Cu, Pb, Zn, As and W concentrations of bryophytes were measured by studying the differences of metal concentrations in bryophytes between metal contaminated and non-contaminated areas. Bryophytes in Ikuno, Waidani, Tada, Rendaiji, Kiwada, Kaneuchi, Nishinomaki and Dundasu mines were sampled as metal contaminated areas. Yoshi River (Okayama prefecture) - Tenjin River (Tottori prefecture) and Izumi Mountain (Wakayama and Osaka prefecture) - Kongo Mountain (Osaka and Nara prefecture) areas were non-contaminated areas.

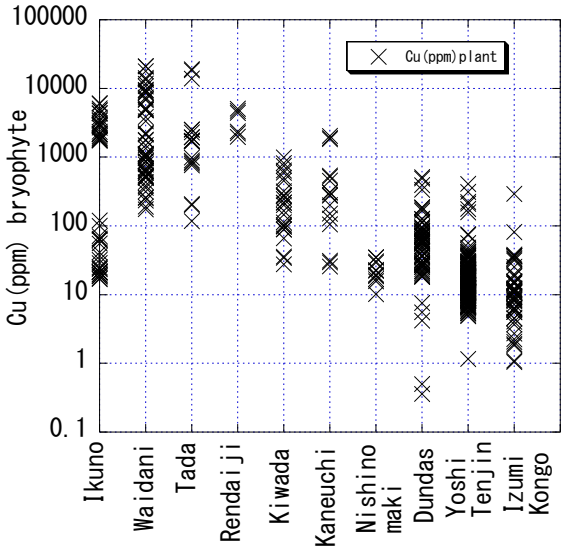

Fig. 1 Cu concentrations of bryophyte for metal contaminated and non-contaminated areas.

Figure 1 shows Cu concentrations in bryophytes for metal contaminated and non-contaminated areas and their variations were several 0.1 ppm to several 10,000 ppm. Except for Nishinomaki mine, mainly Cu ore was produced at the mines and their Cu concentrations were over 100 times higher than those for non-contaminated areas, mainly several to several tens ppm. Cu concentration at the Nishinomaki mine was the same as those at the non-contaminated area. Even at the same mine, Cu concentrations varied with sampling points. Under the same non-contaminated conditions, those sampled at Yoshii - Tenjin River area were higher than those sampled at Izumi - Kongo area. The Cu concentration in bryophytes varied widely by location and particular sampling points. The highest Cu concentration of bryophytes reached over 10,000 ppm at Waidani and Tada mines and these values were also recorded by past studies [10], [11], [15], [16], [17], [18], [19]. Therefore, the Cu concentrations in bryophytes was very sensitive to

metal contaminated conditions. However, Cu concentrations for Ikuno, Kiwada and Kaneuchi mines accompanied with W mineral were not much higher than those for non- contaminated areas.

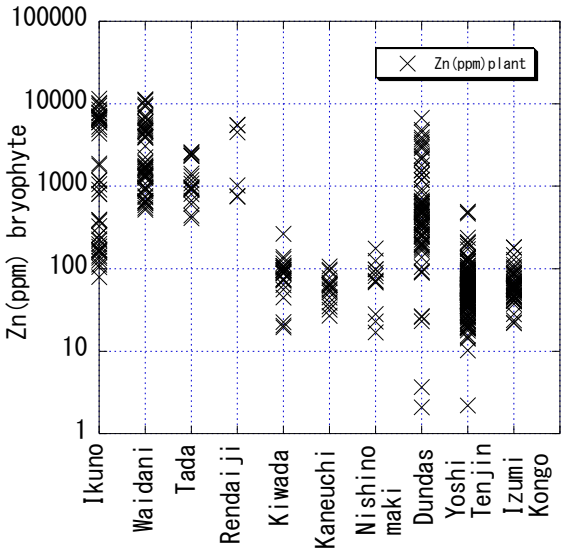

Fig. 2 Zn concentrations of bryophyte for metal contaminated and non-contaminated area.

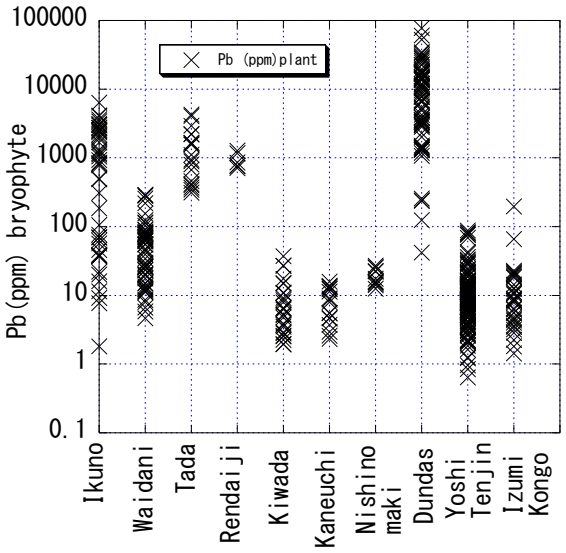

Fig. 3 Pb concentrations of bryophyte for metal contaminated and non-contaminated areas.

Figure 2 shows Zn concentrations in bryophytes for metal contaminated and non-contaminated areas and the variation was several ppm to a few 10,000 ppm. Except Nishinomaki, Kiwada and Kaneuchi mines, Zn concentrations in bryophytes at Zn mines were 10 to 100 times higher than those for non-contaminated areas whose concentrations were mainly several 10 to several 100 ppm. Zn. Bryophytes sampled at metal non-contaminated areas were the same as those at the Nishinomaki, Kiwada and Kaneuchi mines. Even at the same mine, Zn concentrations varied with sampling points. However under the same non-contaminated conditions, Zn concentration variations between the Yoshii - Tenjin River area and the Izumi - Kongo area were small. Zn concentrations in bryophytes varied widely by location at particular sampling points. The highest Zn concentrations in bryophytes reached10,000 ppm at the Waidani and Ikuno mines and these values were the largest values compared with past studies [11], [15], [16], [17], [18], [19]. Therefore, the Zn concentration in bryophytes was very sensitive to the level of metal contamination.

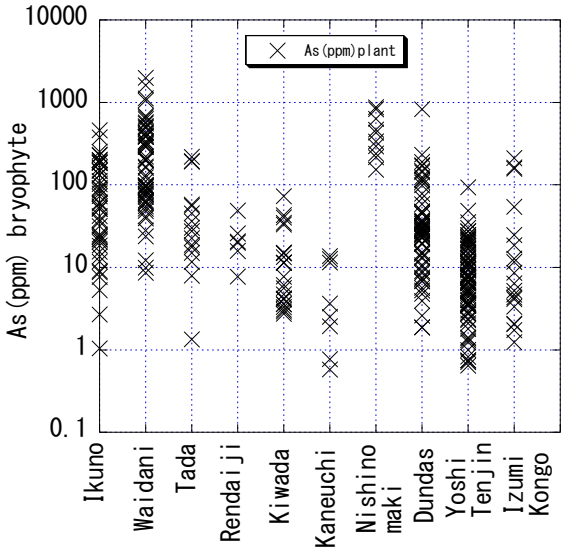

Fig. 4 As concentrations of bryophyte for metal contaminated and non-contaminated areas.

Figure 3 shows Pb concentrations in bryophytes for metal contaminated and non-contaminated areas and their variation was from several 0.1 ppm to about 100,000 ppm. The exceptions being Nishinomaki, Kiwada and Kaneuchi mines where Pb concentrations in bryophytes at Pb mines were from 10 to 1000 times higher than those for non-contaminated areas whose concentrations were mainly several to several 10 ppm. Pb in bryophytes sampled at metal non-contaminated areas were the same as those at the Nishinomaki, Kiwada and Kaneuchi mines. Even at the same mine, Pb concentrations varied by sampling points. Pb concentrations in bryophytes varied widely by location and particular sampling points. The highest Pb concentrations in bryophytes reached several 10,000 ppm at the Dundas mine and these values were the largest values compared with past studies [10], [15], [16], [17], [18], [19]. Therefore, the Pb concentrations in bryophytes were very sensitive to the metal contaminated conditions.

Figure 4 shows As concentrations in bryophytes

for metal contaminated and non-contaminated areas and their variation was from several 0.1 ppm to several 1,000 ppm. Bryophyte As concentrations at Nishinomaki, Ikuno, Dundas and Waidani mines where As ore mineral was extracted were over 100 ppm, 10 to 100 times higher than those for non-contaminated areas. As minerals, Realgar AsS and orpiment As2S3 were found at the Nishinomaki mine. The maximum As concentration in bryophytes reached several 1,000 ppm at the Waidani mine and these values were the largest values compared with past studies [10], [11], [15], [16], [17], [18], [19]. Therefore, As concentrations in the bryophytes were sensitive to the metal contamination condition.

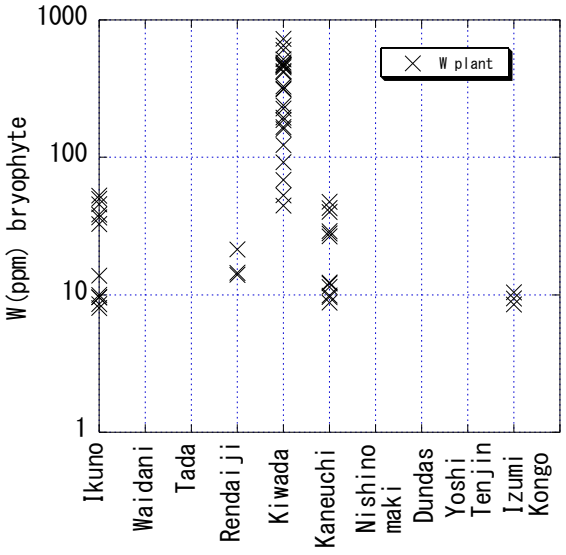

Fig. 5 W concentrations of bryophyte for metal contaminated and non-contaminated areas.

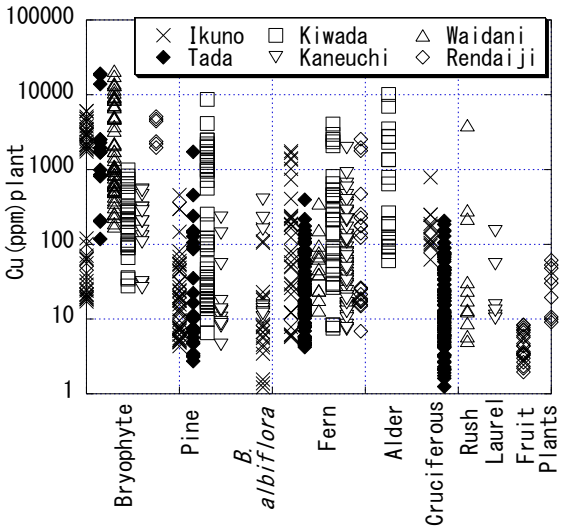

Fig. 6 Cu concentrations of plants for metal mines.

Figure 5 shows the W concentrations in bryophytes for metal contaminated and non-contaminated areas and their variations which were from several ppm to a few 100 ppm. W concentrations in most of the samples were very low and undetectable. However, W concentrations at the Kiwada mine was 100 to 1000 ppm, 10 to 100 times higher than the non-contaminated areas. The sampling points at the Kiwada mine were the stored ore composed of mixed sands and stones with a W content of of about 10%. The plants in this area had grown naturally for over 10 years. At the Ikuno and Kaneuchi mines, W minerals were found but the W concentrations were not extremely high, 10 to 100 ppm. The maximum W concentration in the bryophytes reached several 100 ppm at Kiwada mine. Therefore, the W concentrations in the bryophytes was sensitive to the metal contaminated condition.

Plants

Next, Cu, Pb, Zn, As and W concentrations of the bryophytes and plants were measured to study the difference in metal concentrations between bryophytes and plants for Ikuno, Waidani, Tada, Rendaiji, Kiwada, and Kaneuchi mines. Figure 6 shows Cu concentrations in bryophytes and plants for metal contaminated areas. Cu concentrations in bryophytes were not always the highest value of all plants for each metal contaminated area. For the Kiwada mine, Cu concentrations in alders had the highest values even though their Cu concentrations varied. It's root concentrations were high. Cu concentrations in bryophytes at the Tada, Waidani and Rendaiji mines were the highest values compared to other plants. Cu concentrations in bryophytes at the Kaneuchi and Ikuno mines were almost the same as those of ferns. Kiwada mine was a W mine and plants and bryophytes were sampled on the W ore sediments. Ikuno and Kaneuchi mines produced W ore accompanied with Cu ore. Tada, Waidani and Rendaiji mines did not produce W minerals. When accompanied with W minerals, Cu concentrations in bryophytes at mines were lowered. Therefore, the W mineral was thought to be important for Cu concentrations in bryophytes.

Figure 7 shows Zn concentrations in bryophytes and plants for metal contaminated areas. The highest Zn concentrations were in cruciferous plants at the Tada and Ikuno mines. They were several 10,000 ppm, and the highest of the sampled plants as well as the ferns at the Tada mine. The highest bryophyte Zn concentrations at the Ikuno and Waidani mines reached 10,000 ppm. Therefore, the Zn concentrations in bryophytes were not always the highest values among the plants for each metal contaminated area. However, the Zn concentrations in pines and other plants were lower than those of the bryophytes. For the Kiwada mine, the highest Zn values in the bryophytes, pines, ferns and alders increased from several 100 ppm to 1,000 ppm in that

order. Zn concentrations in the bryophytes for the Kiwada mine was almost the same as non-Zn contaminated areas. When accompanied with W minerals, Zn concentrations in bryophytes at mines were lowered. Therefore, the W mineral was thought to be important for Zn concentrations in bryophytes.

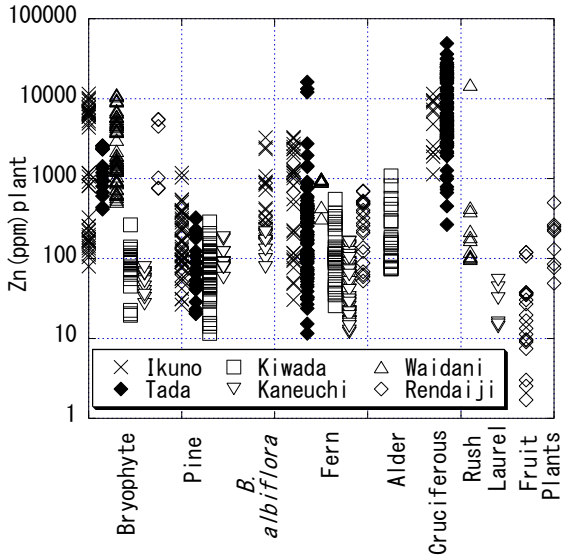

Fig. 7 Zn concentrations of plants for metal mines.

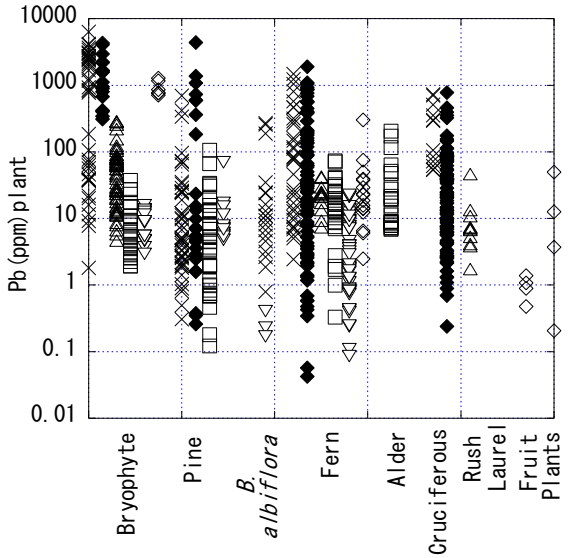

Fig. 8 Pb concentrations of plants for metal mines

Figure 8 shows Pb concentrations in bryophytes and plants at metal contaminated areas. Pb concentrations in bryophytes were always the highest value among plants in each of the metal contaminated areas except for the Kiwada and Kaneuchi mines. The highest Pb concentrations in bryophytes reached several 1,000 ppm. Pb concentrations in pine roots, ferns and cruciferous plants were over 1,000 ppm, although Pb concentrations in pines, ferns and cruciferous plants were variable. The highest Pb concentrations were, several 100 ppm, in the alders, ferns and pines at the Kiawada mine which were higher than the several 10 ppm, in the bryophytes at the Kiwada mine. The highest Pb concentrations in pines and ferns at Kaneuchi were several 10 ppm, almost the same as those in the bryophytes at Kaneuchi. Without the W mineral, the highest Pb concentrations in bryophytes reached several 1,000 ppm. When accompanied with W minerals, Pb concentrations in bryophytes at mines were low. Therefore, the W minerals are thought to be important for Pb concentrations in bryophytes. Without W, the bryophytes' Pb concentrations reached the higher values.

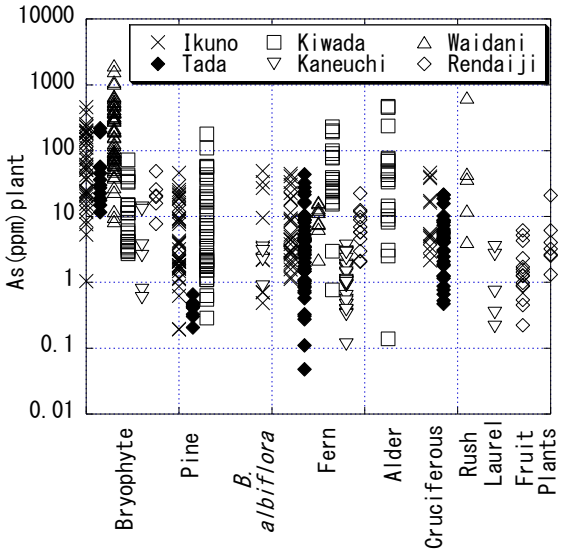

Fig. 9 As concentrations of f plants for metal mines.

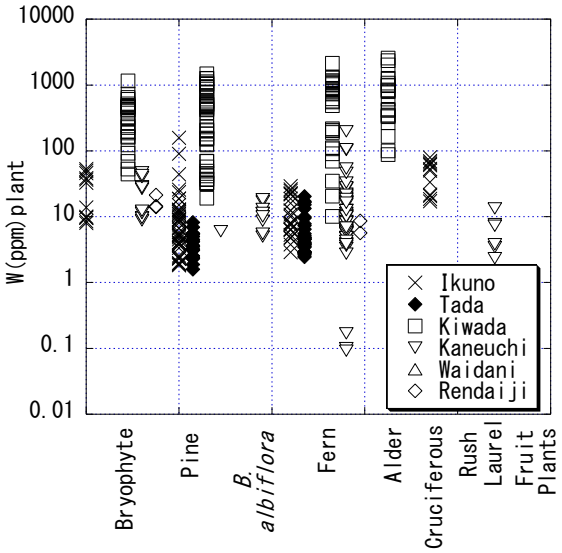

Fig. 10 W concentrations of f plants for metal mines.

Figure 9 shows As concentrations in bryophytes and plants for metal contaminated areas. As concentrations in bryophytes were always the

highest values among plants for each of the metal contaminated areas except for the Kiwada W mine. The highest As concentrations in bryophytes reached a few 1,000 ppm. The highest As concentrations in pine roots, ferns and alders were over 100 ppm, although the As concentrations were variable. The highest As concentrations, were several 100 ppm,in alders, ferns and pines at the Kiawada mine which were higher than the several 10 ppm, in the bryophytes at the Kiwada mine. Without a lot of W minerals, the highest As concentrations in the bryophytes reached a few 1,000 ppm. When accompanied with a lot of W minerals, As concentrations in bryophytes at the mines was low. Therefore, W minerals were thought to be important for As concentrations in bryophytes.

Figure 10 shows W concentrations in bryophytes and plants for metal contaminated areas. W concentrations in bryophytes were not always the highest values among plants for each of the metal contaminated areas. For the Kiwada mine, the highest values in bryophytes, pines, ferns and alders increased from 1,000 ppm to several 1,000 ppm in that order. The maximum W concentrations in bryophytes, pines, ferns and alders in the Kiwada mine were more than 10 to 100 times higher than those in the Ikuno and Kaneuchi mines and the W concentrations in plants depended on the W concentrations in the soil.

Cicada shells and adults

Cu, Pb, Zn, As and W concentrations in cicada shells and adults were measured by studying the difference in metal concentrations in cicada shells and cicada adults comparing metal contaminated and non-contaminated areas.

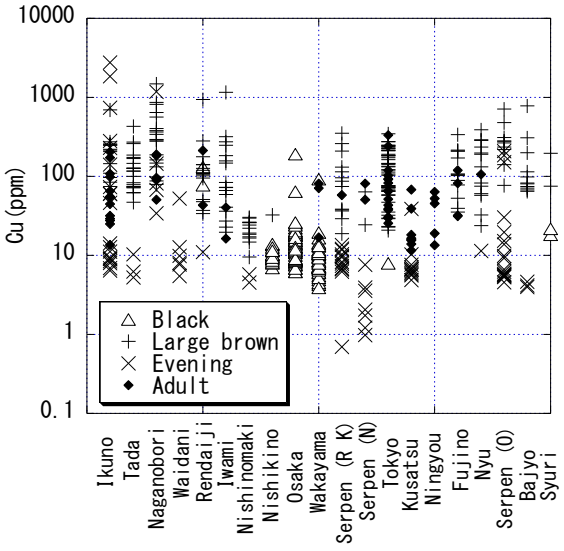

Fig. 11 Cu concentrations of cicada shell and cicada adult.

Figure 11 shows Cu concentrations of cicada shells and cicada adults which were very variable. From several 0.1 ppm to several 1,000 ppm for cicada shells and from several 10 ppm to over 300 ppm for cicada adults. The mark of "Large brown" showed large brown cicadas and *Oncotympana maculaticollis* as well as the following figures. They were the same sizes. The mark of "Evening" showed evening cicadas, *Platypleura kaempferi* and *Terpnosia nigricosta* (sampled at only Kusatsu) as well as the following figures. They were the same sizes. Black cicadas (the mark of Black) were sampled in city parks and ruins in various cities in West Japan. Their shell Cu concentrations were mainly several to several 10 ppm and lower than those of the other cicada shells. Cu shell concentrations of large brown cicadas and *Oncotympana maculaticollis* were from 10 to several 1,000 ppm and higher than those of other cicada shells. Cu shell concentrations of large brown cicadas and *Oncotympana maculaticollis* for Cu non-contaminated areas, serpentinite, Tokyo parks, and Fujinomiya (Basalt flow) were almost the same as the Cu mining areas (Ikuno, Tada, Naganobori, Rendaiji, and Iwami mines). Cu shell concentrations of the evening cicada and *Platypleura kaempferi* were very variable, from several to several 1,000 ppm. Their Cu concentrations at Cu mines (Ikuno, Tada, Naganobori, Rendaiji, and Iwami mines) were not higher than those at Cu non-producing. Therefore, the Cu concentrations in cicada shells at Cu metal mines were not always high.

The Cu concentration variations in cicada adults was very narrow relative to those of cicada shells when comparing Cu concentrations in cicada adults between Ikuno mine and Tokyo parks. Both variations were almost the same. Therefore, the Cu concentrations in cicada shells for Cu metal mines were not always high when comparing Cu concentrations between cicada shells and cicada adults at the same points and these results were consistent with past results [12]. Therefore, cicadas did not selectively release Cu into their shells during molting.

Figure 12 shows Zn concentrations of cicada shells and cicada adults. The concentrations were from several ppm to 10,000 ppm for cicada shells and from 50 ppm to 1,200 ppm for cicada adults.

Zn concentrations in black cicada shells were from 10 to several 1,000 ppm, not lower than those of the other cicada shells and had a very wide variation unlike the Cu results. Zn shell concentrations in large brown cicadas and *Oncotympana maculaticollis* were from several 100 ppm and lower than those of the other cicada shells even for Zn mines such as Ikuno, Tada, Rendaiji and Iwami. Zn concentrations in the shells of large brown cicadas and *Oncotympana maculaticollis* at Zn metal mines were not always high relative to

those for non-Zn contaminated areas, serpentinite, Tokyo parks, and Fujinomiya (Basalt flow).

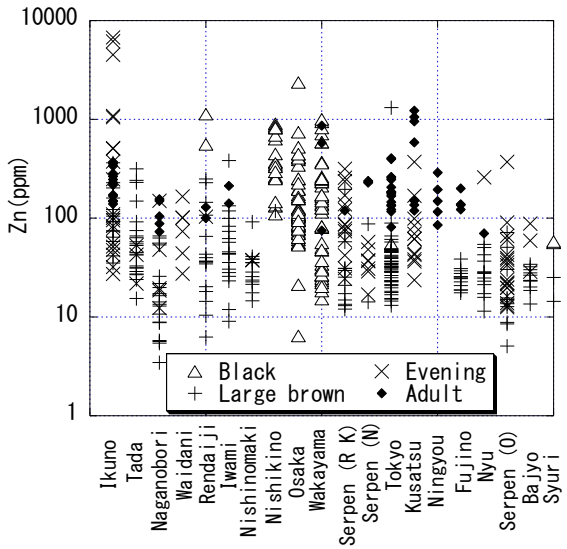

Fig. 12 Zn concentrations of cicada shell and cicada adult.

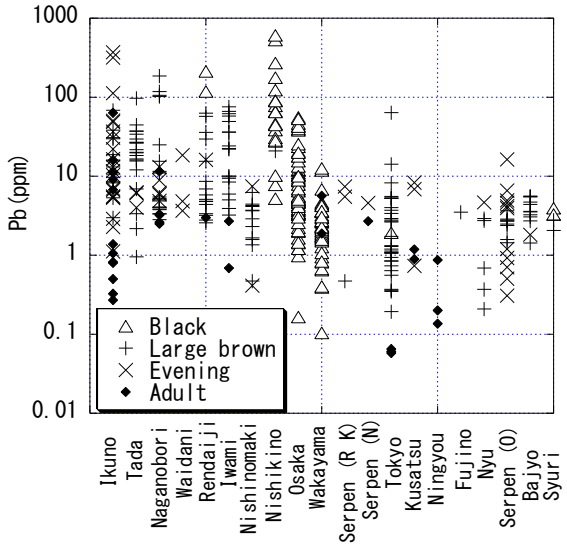

Fig. 13 Pb concentrations of cicada shell and cicada adult

Zn concentrations in the shells of evening cicadas and *Platypleura kaempferi* were very variable, from several 10s to several 1,000 ppm and higher than those in large brown cicadas and *Oncotympana maculaticollis*. The Zn concentrations at Zn mining areas (Ikuno, Tada and Waidani mines) were not higher than those at non-Zn mining areas. Therefore, Zn concentrations in cicada shells for Zn metal mining areas were not always high.

The Zn concentration variations in cicada adults were very narrow relative to those of cicada shells. When comparing the Zn concentrations in cicada adults between the Ikuno mine and Tokyo parks, the variations were almost the same. Therefore, the Zn concentrations in cicada adults for Zn metal mines were not always high when comparing Zn concentrations between cicada shells and cicada adults at the same points, Ikuno mine, Kusatsu hot spring and Tokyo parks. Both Zn cicada adult concentrations were higher than those of cicada shells and these results were consistent with past results [12]. Therefore, the cicadas selectively kept Zn in their bodies during molting.

Figure 13 shows Pb concentrations in cicada shells and cicada adults The concentrations were from 0.1 ppm to several 100 ppm for cicada shells and from several 0.01 ppm to several 10 ppm for cicada adults.

Pb concentrations in black cicada shells had a wide variation, from 0.1 to several 100 ppm. However, these values were divided into three types. At Nishikinohama (ruins of wire factory), they were several ppm to several 100 ppm. At Osaka parks, they were from 1 to several 10 ppm. At Wakayama parks, they were from several 0.1 to 10 ppm. The differences were thought to depend on contamination because Osaka parks in the city were more polluted by air than Wakayama and the wire factory previously used Pb.

Pb concentrations in the shells of large brown cicadas and *Oncotympana maculaticollis* were from several ppm to several 100 ppm for Pb mines such as the Ikuno, Tada, Naganobori, Rendaiji and Iwami mines and from several 0.1 ppm to less than 10 ppm for non-Pb contaminated areas such as serpentinite. Similarly, Pb concentrations in the shells of evening cicadas and *Platypleura kaempferi* were from several ppm to several 100 ppm for Pb mines such as the Ikuno, Tada, Naganobor, and Waidani mines and from several 0.1 ppm to less than 10 ppm for non-Pb contaminated areas such as serpentinite. Therefore, Pb concentrations in cicada shells at Pb mines were higher than those for non-Pb contaminated areas.

The high Pb concentrations in cicada adults sampled at Pb mines were higher than those at non-Pb contaminated areas although they had wide variations. When comparing the Pb concentrations in cicada shells and adults, the Pb concentrations in cicada shells were higher than those in cicada adults even though both concentrations had wide variations. As a result, these results were consistent with past results [12]. Therefore, cicadas were thought to release Pb into their shells during molting and keep high Pb concentrations in their shells in Pb contaminated areas. Pb concentrations in cicada shells was thought to be contamination index.

Figure 14 shows As concentrations in cicada shells and cicada adults and their concentrations were from 0.1 ppm to several 1,000 ppm for cicada shells and several 0.1 ppm to several ppm for cicada adults.

Generally, As concentrations in black cicada shells had a wide variation, from 0.1 to10 ppm. As The concentrations in the shells of large brown cicadas, *Oncotympana maculaticollis.* evening cicadas and *Platypleura kaempferi* at the Ikuno, Naganobori, Nishinomaki and Bajyo mines and serpentinite (Nakase mine), of As minerals were higher than those of non-As contaminated areas (mines without As mineral and serpentinite (R, K, O). Therefore, As concentrations in cicada shells at As mines were higher than those for non-As contaminated areas.

The As concentrations in cicada adults were from several 0.1 to several 1 ppm at the Ikuno mine The As produced was almost the same as other areas. Therefore, As concentrations in cicada adults for As contaminated areas was not always high. When comparing the As concentrations in cicada shells and adults, the As concentrations in cicada shells were over 10 times, higher than those of cicada adults and in particular, for the Ikuno mine and Tokyo parks

Therefore, cicadas were thought to release As into their shells during molting and keep a high As concentration in their shells. As concentration in cicada shells was thought to be contamination index.

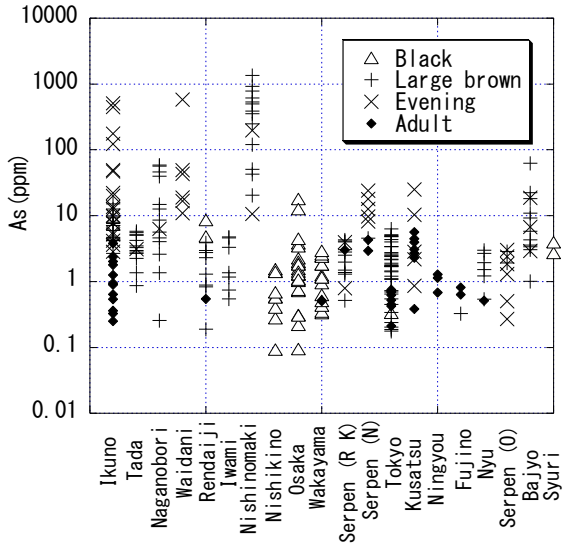

Figure 1 4 As concentrations of cicada shell and cicada adult

CONCLUSIONS

In this study, effective indicators of metal contamination need a wide variation of metal concentrations depending on the contamination. Therefore, metal concentrations in bryophytes, plants, cicada shells and cicada adults sampled at metal-contaminated and non-contaminated areas were measured.

The metal concentrations in bryophytes varied from several 0.1 ppm to several 10,000 ppm for Cu, from several ppm to a few 10,000 ppm for Zn, from several 0.1 ppm to about 100,000 ppm for Pb, from several 0.1 ppm to several 1,000 ppm for As and from several ppm to a few 100 ppm for W and increased depending on the metal contamination conditions. Therefore, it is considered to be effective as an index of Cu, Zn, Pb, As, and W contaminations. However, the Zn concentrations in bryophytes was not always the highest among the plants in each of the metal-contaminated areas. The highest Zn concentrations in a kind of cruciferous plants were several 10,000 ppm, which was the highest among the sampled plants. In addition, where there is a large amount of W, such as the Kiwada W mine, the heavy metal concentrations in bryophytes were not high, and the heavy metal concentrations in other plants showed a higher concentration than that of the bryophytes. At the W mine, the alders had the highest Cu, Zn, Pb, and As concentrations. The presence of W is thought to be the cause of the decrease in the heavy metal concentration in bryophytes, which prevents the adsorption of metals into the cell walls of the bryophytes. The other possibility is that only bryophytes with a low metal concentration were growing.

The metal concentrations in cicada shells from black cicadas, large brown cicadas, *Oncotympana maculaticollis*, evening cicadas and *Platypleura kaempferi* varied from several 0.1 ppm to several 1,000 ppm for Cu, and several ppm to 10,000 ppm for Zn. The metal concentration variations in cicada adults was from several 10 ppm to 300 ppm for Cu, and 50 ppm to 1,200 ppm for Zn. The Cu and Zn concentrations in both cicada shells and adults were not always high for the metal mines and cicada shell concentrations were not always higher than those of cicada adults. Therefore, the cicadas did not selectively release Cu and Zn into their shells during molting and as a result the Cu and Zn concentrations in cicada shells sampled from Cu metal mines (Cu and Zn contaminated areas) were not always high. As a result, it is unsuitable for a Cu and Zn contamination index.

The metal concentrations in cicada shells and cicada adults were from 0.1 ppm to several 100 ppm and from several 0.01 ppm to several 10 ppm for Pb and from 0.1 ppm to several 1,000 ppm and from several 0.1 ppm to several ppm for As. Pb and As concentrations in cicada shells at Pb and As mines were higher than those for non-Pb As contaminated areas. Pb and As concentrations in cicada shells were higher than those of cicada adults. Therefore, cicadas were thought to release Pb and As into their shells during molting and keep Pb and As high concentration in cicada shells in Pb and As contaminated areas. Pb and As concentrations in cicada shells were thought to be a good contamination index

REFERENCES

[1] Nickrent D. L., Parkinso, C. L., Palmer J. D., and Duff R. J., Multigene phylogeny of land plants with special reference to bryophytes and the earliest land plants. Molecular Biology and Evolution, Vol. 17, 2000, pp. 1885-1895.

[2] Degola F., De Benedictis M., Petraglia A., Massimi A., Fattorini L., Sorbo S., Basile A., and di Toppi L. S., A Cd/Fe/Zn-responsive phytochelatin synthase is constitutively present in the ancient liverwort Lunularia cruciata (L.) Dumort. Plant and Cell Physiology, Vol. 55, 2014, pp. 1884-1891.

[3] Berg T. and Steinnes E., Use of mosses (*Hylocomium splendens* and *Pleuroziumschreberi*) as biomonitors of heavy metal deposition: from relative to absolute deposition values. Environmental Pollution Vol. 98, 1997, pp. 61-71.

[4] Choudhury S. and Panda S. K., Toxic effects, oxidative stress and ultrastructural changes in moss *Taxithelium nepalense* (Schwaegr.) Broth. under chromium and lead phytotoxicity. Water, Air, Soil Pollution, Vol. 167, 2005, pp. 73-90.

[5] Koz B. and Cevik U., Lead adsorption capacity of some moss species used for heavy metal analysis. Ecological Indicators, Vol. 36, 2014, pp. 491-494.

[6] Little P. and Martin M. H., Biological monitoring of heavy metal pollution. Environmental Pollution, Vol. 6, 1974, pp. 1-19.

[7] Sun S. Q., He M., Cao, T., Zhang Y. C. and Han W., Response mechanisms of antioxidants in bryophyte (*Hypnum plumaeforme*) under the stress of single or combined Pb and/or Ni. Environmental Monitoring ad Assessment, Vol. 149, 2009, pp. 291-302.

[8] Schröder W., Holy M., Pesch, R., Harmens H., Ilyin I., Steinnes E., Alber R., Aleksiayenak Y., Blum O., Coşkun M. and Dam M., Are cadmium, lead and mercury concentrations in mosses across Europe primarily determined by atmospheric deposition of these metals? Journal of Soils and Sediments, Vol. 10, 2010, pp. 1572-1584.

[9] Berg T., Røyset O. and Steinnes E., Moss (*Hylocomium splendens*) used as biomonitor of atmospheric trace element deposition: estimation of uptake efficiencies. Atmospheric Environment, Vol. 29, 1995, pp. 353-360.

[10] Ii H. and Nishida A., Effectiveness of Using River Insect Larvae as an Index of Cu, Zn and As Contaminations in Rivers, Japan, International Journal of GEOMATE, Vol. 12, No.33, 2017, pp. 153-159.

[11] Ii H., Effectiveness of using cicada shell and river bryophyte as an index of available Cu, Zn, Pb, As, Ni and Cr contamination, in Proc. 4th Int. Conf. on SEE, 2018, pp. 914-919.

[12] Robinson Jr. G.R., Sibrell P.L., Boughton C.J. and Yang L.H., Influence of soil chemistry on metal and bioessential element concentrations in nymphal and adult periodical cicadas (Magicicada spp.), Science of the Total Environment, Vol. 374, 2007, pp. 367-378.

[13] Exploration Working Group of Japan Mining Industry Association, Overview of Japanese deposits, Volume1, Japan Mining Industry Association, 1965, pp. 1-581. In Japanese.

[14] Exploration Working Group of Japan Mining Industry Association, Overview of Japanese deposits, Volume2, Japan Mining Industry Association, 1968, pp. 1-941. In Japanese.

[15] Ii H., Konno H., Yamashita Y., Uno J., Shimogaki H., Ikeda S. and Nishimura T., Arsenic concentration and stable isotopic ratios of oxygen and hydrogen for groundwater and river water around the Midoro and Shidenhigashi tunnels in Gose city, Nara, central, Japan, in Proc. 7th Int. Conf. on GEOMATE, 2017, pp. 684-689.

[16] Ii H. and Yamashita M., Mapping stable isotopic ratios of stream water and Cu, Zn, Pb and As concentrations of Bryophyte along streams in the east of Okayama and Tottori prefectures, Japan, in Proc. 4th Int. Conf. on SEE, 2018, pp. 925-930.

[17] Kubohara T. and Ii H., Cu Co and Ni Contamination Index for River Using River Insects and River Plants, International Journal of GEOMATE, Vol.11, Issue 26, 2016, pp.2651-2658.

[18] Kubohara T. and Ii H., Evaluation of Metal Contamination for River using Bryophyte in the Kinokawa River Catchment, International Journal of GEOMATE, Vol.12, Issue 37, 2017, pp.135-142.

[19] Kubohara T. and Ii H., Zn and Fe Contamination Index for River using River Insects and Water Plants in The Kinokawa River Catchment, International Journal of GEOMATE, Vol.19, Issue 75, 2020, pp.76-83.

8th Int. Conf. on Structure, Engineering & Environment (SEE), Mie, Japan, Nov.10-12, 2022, ISBN: 978-4-909106094 C3051

CURRENT CHALLENGES IN GEOLOGICAL STORAGE OF CARBON DIOXIDE

John Victor Smith[1]
[1]Faculty of Engineering, RMIT University, Australia

ABSTRACT

The storage of carbon dioxide in secure underground sites has been identified as an important contributor to preventing climate change impacts of excessive CO_2 in the atmosphere. Significant quantities of carbon dioxide must be collected and stored for this technology to make the required contribution to climate change abatement. The quality of the storage must be validated by a range of techniques to ensure that the CO_2 is stored safely without the risk of excessive leakage. The carbon dioxide can be stored as a gas, supercritical fluid or a solid by mineralization. Trapping gas or supercritical fluid requires a setting similar to the natural trapping of gases in sub-surface sedimentary rock reservoirs. Mineralization most commonly occurs in the form of carbonate minerals. The most advanced high-volume projects focus on the trapping of supercritical fluids. Smaller scale project have achieved some success in mineralization within basalt lavas. Other potential geological settings are reviewed.

Keywords: CO_2 Sequestration, Geological Storage, Saline Aquifers, Carbonate Mineralization

INTRODUCTION

International studies of pathways to moderating climate change recognize the need for reduction in atmospheric carbon dioxide (CO_2) by use of geological storage [1]. The most advanced methods of geological storage of CO_2 are those that build on knowledge and technology of the oil and gas industries. In particular, the injection of supercritical CO_2 into sedimentary rock reservoirs has been demonstrated as a feasible technology [2]. The injection of dissolved gas into reactive rocks such as basalt has also been demonstrated as a feasible technology, albeit at a smaller scale [2].

Biological and soil-based sequestration is acknowledged as a significant technology [3] but is not addressed in this paper.

In this paper, challenges and opportunities for geological storage of CO_2 are reviewed. In particular, the need for greater application of knowledge of the permeability and reactivity of a range of geological settings is addressed. The primary challenge recognized is the need for large volume storage.

DEEP STORAGE

The transition to supercritical CO_2 with pressure means that efficient storage can be achieved at depths where pressure is sufficient to maintain the supercritical condition.

As supercritical CO_2 is injected into an aquifer flow initial follows Darcy's Law. However, Darcy flow soon gives way to Invasion Percolation flow behavior. Invasion Percolation flow is dominated by capillary and buoyancy effects. The unit-less Capillary Number can be used to define the transition of the flow mechanisms [4].

Depleted Reservoirs

The most direct experience of geological storage of CO_2 comes from injection into productive reservoirs for the purpose of enhancing oil and gas recovery. These reservoirs may become suitable places for storage of CO_2. However, the presence of numerous production wells in some such fields may make the seal integrity problematic [2].

Saline Aquifers

Most deep aquifers are typically saturated with saline water. Such aquifers have generally not been drilled extensively and can provide large potential storage volumes.

The Sleipner project has used a deep saline aquifer below the previously productive oil and gas fields in the North Sea to store large volumes of CO_2 [5]. Such offshore basins represent very extensive potential reservoirs for future CO_2 storage [6].

Onshore basins also include many potential saline aquifers. Large CO_2 storage projects such as In Salah in Algeria [7] and Aquistore in Canada [8] have used such onshore basins.

Non-Sandstone Aquifers

The potential for storage sites is greatly increased if aquifers other than sandstones can be found to have adequate permeability. One such example is at the CO_2 injection site at Tomakomai, Hokkaido,

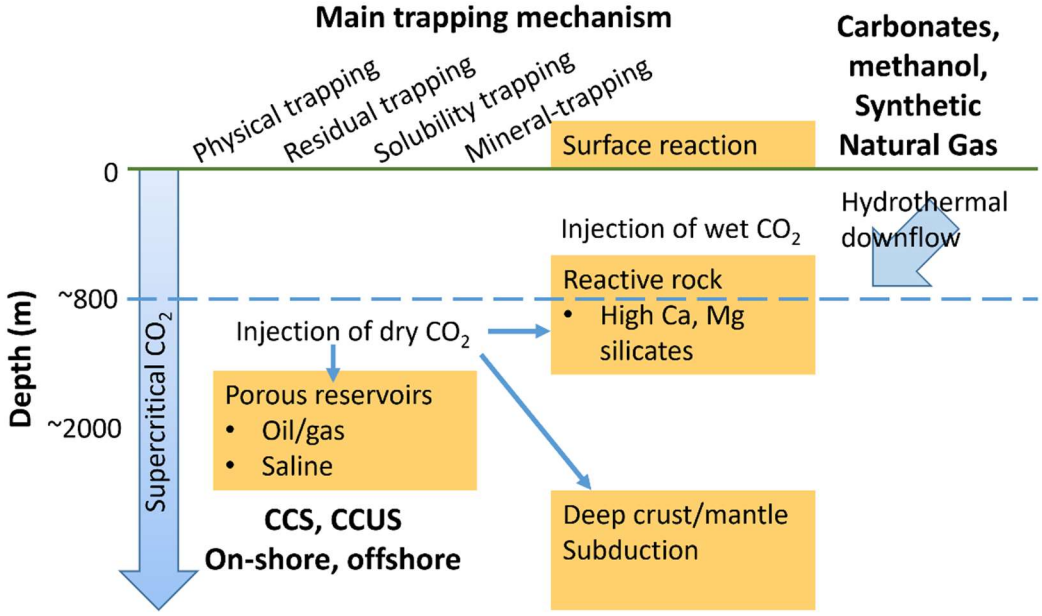

Fig.1 Conceptual summary of some methods of carbon dioxide trapping relative to depth

Japan.

The Tomakomai trial CO_2 injection site targeted a sandstone aquifer and a volcanic unit [9]. The volcanic unit being the Takinoue Formation which consists of a lower mudstone and upper volcano-clastic members. During investigation, the volcano-clastic rocks were considered to have potential as a reservoir. The upper Takinoue Formation is divided into two parts, an upper part dominated by tuff and a lower part dominated by lava and breccia. According to the data used at the assessment stage of the project, the lava and breccia tended to have higher permeability than the tuff. Seismic data also supported the potential for coarse volcanic sediments to have high porosity and permeability. A structural trap was also present in the form of an anticline. The overlying thick mudstones of the Fureoi and Biratori-Karumai Formations were considered to have potential to form a good cap rock [9].

However, low injectivity was achieved in the Takinoue Formation compared to the Moebetsu Formation sandstones which were the main reservoir targeted in the trial [10]

Gas Injectivity

The Aquistore project in Canada showed a general increase in well injectivity performance with time. These injectivity observations and operational data were collected from two highly instrumented injection and observation wells specifically drilled for CO_2 storage at Aquistore [11]. The injection location typically experience complex stress conditions that can overcome the tensile strength of the host rock leading to temperature-induced pore deformation, tensile micro-cracks, and/or mobilising of pre-existing critically stressed fractures.

The stress-dependent changes in effective permeability in the injection region are speculated to enhance CO_2 injectivity performance. However, the temperature-induced stresses could also create new, localized, flow pathways through low-permeability non-reservoir formations, including caprock units.

The overall pore pressure distribution in an aquifer has the potential to re-activate faults which would become evident as seismic activity. It is noted that although this has occurred at some projects no induced seismicity has been detected at the Aquistore project [8].

Understanding the complex thermal and stress phenomena in a reservoir injected with CO_2 is essential for successful long-term containment and conformance of the host aquifers and sealing units [11]. Other processes at the injection point include CO_2-brine chemical interaction such as salt precipitation which can locally impede injectivity [12, 13].

It has been proposed that CO_2 plumes can potentially be used as a recirculated geothermal fluid with a syphon effect [14,15].

OPPORTUNITIES FOR MINERALIZATION

Many of the existing projects intend to store CO_2 by trapping the gas within pore space. Some mineralization may incidentally occur. Other projects are focusing on the potential to form minerals with CO_2 as a form of storage. There are also significant new technologies developing to utilize CO_2 in manufacturing which will not be reviewed here.

Near Surface

The process of weathering of rocks generally consumes CO_2. More specifically, a number of projects are investigating the use of mine tailings as an opportunity to store CO_2. Mine tailings are typically fine-grained and some have significant alkalinity to react with CO_2 [16,17]. Another project is applying carbonate mineralization with CO_2 to the problem of dealing with asbestos minerals that are present in some mine waste dumps and tailings [18].

Shallow Underground

The Carbfix project in Iceland is a well known site where carbonate mineralization is the main focus as a carbon storage mechanism [19]. The CO_2 is typically not in a supercritical state as the depth of injection is down to about 750 m. The gas is mixed with and/or dissolved in water which is understood to enhance the mineralization process. The abundance of calcium in basalt promotes the formation of calcium carbonate (calcite).

Studies on the natural carbonate mineralization systems in the basalt have also contributed to understanding of the mechanism [20].

Deep Underground

Other projects have targeted gaseous storage and mineralization with supercritical injection of CO_2 into basalt [21]. In the Columbia River basalts brecciated zones between lava flows at depths between 800-900m were injected with supercritical CO_2 [22].

Approximately 1000 tonnes of CO_2 were injected over a 25-day period in July to August of 2013. Testing two years later identified free phase supercritical CO_2 fluid in the vicinity of the injection site. Carbonate mineral (ankerite, a mixed Ca-Mg-Fe carbonate) nodules were also recovered from the core sampling and could be directly linked to the injected CO_2 through analysis of isotopes [22].

It is notable that in saline aquifers natural carbonate minerals can also be found forming. For example, siderite (Fe carbonate) has been recorded in aquifers related to the Gorgon CO_2 storage project in Australia [23].

Reactive Rocks

Oceanic Crust

As pointed out by the proponents of the Carbfix project, Iceland is a location where oceanic crust is present above sea-level [19]. They emphasize that the entire oceanic crust is basaltic rock with CO_2 mineralization potential. As will be discussed below there are many other geological environments with potentially reactive rocks.

Fig.2 Natural mineral infilling in a fracture in basalt (photograph by author)

Ultramafic Rocks

Basalt is known as a ‘mafic’ igneous rock due to containing mainly silicate minerals with a high proportion of Mg, Fe and Ca. Such minerals include olivine, pyroxenes and plagioclase. These minerals have the greatest potential to fix CO_2 as carbonate minerals because they have a high molar proportion of divalent cations and they react relatively rapidly to form carbonate minerals [24].

Ultramafic rocks contain even higher proportions of Mg and as such are also potential opportunities for reactions with CO_2 [24]. Ultramafic rocks are present in many locations around the world.

Intrusive Mafic (and Ultramafic) Rocks

An interesting occurrence of mafic (and ultramafic) rocks is as intrusions into sedimentary strata. This is of interest as the sedimentary layers may represent reservoirs and caprocks augmented by the presence of reactive mafic rocks.

Many onshore and offshore basins contain mafic intrusions within their strata. For example, the passive margin sedimentary sequences of the Otway Basin of Victoria, Australia have been trialed for CO_2 storage. The strata have also been found to contain mafic intrusions that were initially indentified due to the doming of strata in their vicinity [25].

The Sydney Basin in New South Wales, Australia was intruded by mafic magmas within the sedimentary strata. One such intrusion is the Prospect Intrusion which is approximately 100 m thick with the mafic rock dolerite in the upper half and the ultramafic rock picrite making up the lower half. Picrite formed by the gravity-driven accumulation of olivine crystals during cooling [26].

The intrusion is exposed at the surface and is not a high potential CO_2 storage location itself but understanding of its geology is a natural laboratory for understanding permeability and reactivity in such rocks. The intrusion has a significant amount of calcite formed by reaction of the mafic rocks with CO_2. Two groups of calcite have been identified as early high temperature calcites related to magmatism and later low temperature calcites related to circulation of water from the surrounding strata.

Isotopic analysis indicates that the later calcite crystallized at between 51–73ºC, which is consistent with the temperature of water circulating from the surrounding sedimentary layers. These carbonate minerals deposited in the vesicles and fractures within the intrusion and were derived from later, cooler fluids with significant meteoric (near-surface) input.

The Prospect Intrusion was emplaced at the boundary of the highly permeable Hawkesbury Sandstone and the overlying low permeability Ashfield Shale. A CO_2-rich fluid derived from marine porewater in the Ashfield Shale may have contributed to the formation of the later carbonates. The Ashfield Shale has a low permeability implying that the composition of its porewater at the time of emplacement of the Prospect Intrusion (ca 180 Ma) would have been similar to the composition it had at the time of sedimentation [26].

Another intrusion in the Sydney Basin is the Coonemia Complex which has similar proportions to the Prospect Intrusion. Isotopic studies of the Coonemia Complex show that the mafic rocks underwent carbonate alteration at periphery as reactions occurred with the pore water of surrounding sedimentary rocks [27].

Greenstones

Greenstone is the name mainly applied to rocks which were formerly basalts and were metamorphosed during continental collisions and other related tectonic events. The greenstone rocks typically retain their high levels of calcium and magnesium although some mineral reactions have typically occurred.

Much of Western Australia has greenstone as the dominant rock type. Also, Victoria, Australia was thought to have small amounts of greenstone but recent studies of the deep crust have found that large zones of greenstone are present [28].

Volcanicalstic Rocks

Volcaniclastic (or volcanoclastic) rocks are formed by a combination of volcanic and sedimentary processes. The resulting materials can be mafic in composition and be permeable. The material produced is often chemically immature and even felsic (opposite composition to mafic) materials can react to form carbonate minerals during alteration and may therefore have potential as storage sites [29].

Carbonate Sequences

Intuitively, carbonate rocks themselves, for example limestones, seem least likely to be reactive to CO_2. However, a study of injectivity of water and CO_2 found that the acidity of the solution produced complex dissolution and re-precipitation processes that led to a net gain of carbonate mineralization [30].

Seals

As CO_2 is dominated by buoyancy within the saline host waters a seal or caprock must be present to prevent leakage of the gas. As with oil and gas reservoirs, the seal is typically a low permeability fine-grained rock such as a shale (Fig. 3).

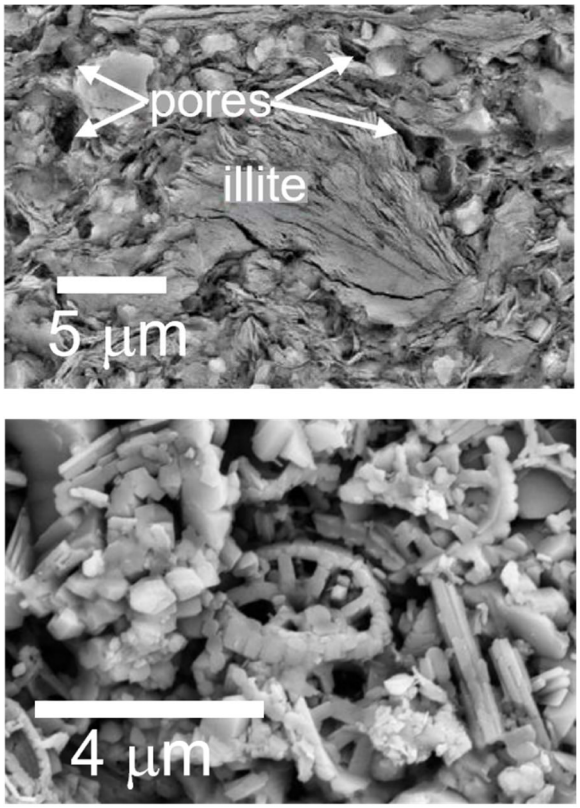

Fig.3 Porosity in mudrocks related to composition. Upper) terrestrial argillaceous rock (Ashfield Shale) [31]. Lower) Carbonate argillaceous rock [32]

The efficacy of fine-grained rocks in trapping supercritical CO_2 is under intensive laboratory experimentation and field trials. Fine-grained rocks have a porosity and permeability that may be affected by CO_2 [30]. This is especially problematic where the fine-grained rock has a significant component of carbonates that may be dissolved in the acidic CO_2-rich conditions [31].

DISCUSSION

When considering the future of geological storage of CO_2 all parts of the geological cycle should be considered (Fig. 4). Sedimentary, igneous and metamorphic rocks all have potential to have permeability to transmit and store gas. All rock types have potential to contain reactive minerals that can contribute to mineralization of the CO_2.

Finding favorable combinations of these features at appropriate depths and with sufficient volumes for storage is challenging but literally represents a world of opportunities.

Geology also provides many natural analogues for CO_2 storage and mineralization that can be interpreted from the natural rock record.

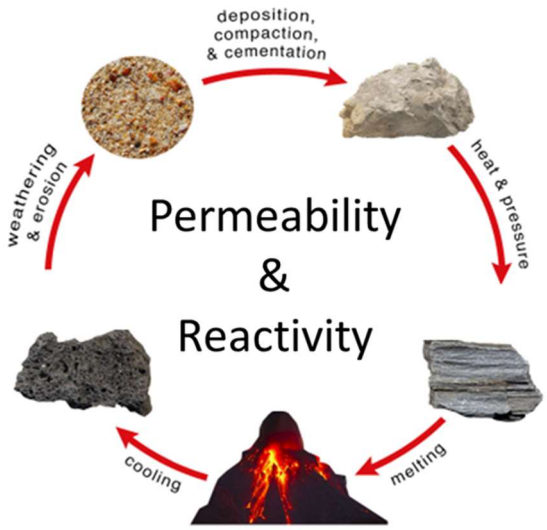

Fig.4 Suitable conditions of permeability and reactivity to CO_2 can occur throughout the geological cycle

CONCLUSIONS

The critical challenge for geological storage of CO_2 is to store large volumes of carbon so that a significant impact on atmospheric carbon can be achieved. This challenge can best be achieved by continuing with development of storage in large, deep offshore and onshore saline reservoirs. Continued experimentation with deep and shallow reactive rocks is also needed. High calcium and magnesium silicate rocks are abundant in the Earth's crust and where suitable permeability conditions exist – forming a considerable volume of mineralized carbon could be achieved.

Locating high volume reservoirs with an enhanced reactivity behavior such as sandstones with high calcium/magnesium content should also be a high priority.

ACKNOWLEDGMENTS

Discussions on carbon sequestration with colleagues at RMIT University and CMW Geosciences are acknowledged.

REFERENCES

[1] IPCC, 2022: Climate Change 2022: Impacts, Adaptation, and Vulnerability. Contribution of Working Group II to the Sixth Assessment Report of the Intergovernmental Panel on Climate Change. Cambridge University Press.

[2] Kelemen P., Benson S.M., Pilorgé H., Psarras P., and Wilcox J., An Overview of the Status and Challenges of CO_2 Storage in Minerals and Geological Formations. Frontiers in Climate, Vol. 15, 2019, pp. 1-9.

[3] Min K., Berhe A.A., Khoi C.M., van Asperen H., Gillabel, J., and Six J., Differential Effects of Wetting and Drying on Soil CO_2 Concentration and Flux in Near-Surface vs. Deep Soil Layers. Biogeochemistry, Vol. 148, Issue 3, 2020, pp. 255-269.

[4] Pruess K., and Garcia J., Multiphase Flow Dynamics During CO2 Disposal into Saline Aquifers. Environmental Geology, Vol. 42, Issue 2, 2002, pp. 282-295.

[5] Furre A.K., Eiken O., Alnes H., Vevatne J.N. and Kiær A.F., 20 Years of Monitoring CO2-Injection at Sleipner. Energy Procedia, Vol. 114, 2017, pp.3916-3926.

[6] Ringrose P.S., and Meckel T.A., Maturing Global CO2 Storage Resources on Offshore Continental Margins. Scientific Reports, Vol. 9, Issue 1, 2019, pp. 1-10.

[7] Ringrose P.S., Mathieson A.S, Wright I.W., Selama F., Hansen O., Bissell R., Saoula N., and Midgley J., The In Salah CO2 Storage Project: Lessons Learned And Knowledge Transfer. Energy Procedia, Vol. 37, 2013, pp.6226-36.

[8] Shokri A.R., Hau K.P., Saar M.O., White D., Nickel E., Siddiqi G. and Chalaturnyk R., Modeling CO2 Circulation Test for Sustainable Geothermal Power Generation at the Aquistore CO2 Storage Site, Saskatchewan, Canada. In 2nd Geoscience and Engineering in Energy Transition Conference, Vol. 1, 2021, pp. 1-5.

[9] Matsuura T., Mikami J., Ito D., Kamon M., Maeda T., Tomita S., Inamori T., Aoki N., Katoh A., Akaku K., and Kuroki S., Reservoir Evaluation for the T1 Member of the Takinoue Formation at

Tomakomai Candidate Site for CCS Demonstration Project in Japan. Energy Procedia, Vol. 37, 2013, pp. 4982-4989.
[10] Sawada Y., Tanaka J., Suzuki C., Tanase D., and Tanaka Y., Tomakomai CCS Demonstration Project of Japan, CO2 Injection in Progress. Energy Procedia. Vol. 154, 2018, pp. 3-8.
[11] Birkholzer J.T., Oldenburg C.M. and Zhou Q., CO2 migration and pressure evolution in deep saline aquifers. International Journal of Greenhouse Gas Control, Vol. 40, 2015, pp.203-220.
[12] Pruess K. and Müller N., Formation Dry-Out from CO2 Injection into Saline Aquifers: 1. Effects of Solids Precipitation and their Mitigation. Water Resources Research, Vol. 45, Issue 3, 2009, pp. 1-11.
[13] Falcon-Suarez I.H., Livo K., Callow B., Marin-Moreno H., Prasad M., and Best A.I., Geophysical Early Warning of Salt Precipitation During Geological Carbon Sequestration. Scientific Reports, Vol. 10, Issue 1, 2020, pp. 1-4.
[14] Atrens A.D., Gurgenci H., and Rudolph V., CO2 Thermosiphon for Competitive Geothermal Power Generation. Energy and Fuels, Vol. 23, Issue 1, 2009, pp. 553-7.
[15] Randolph J.B., and Saar M.O., Combining Geothermal Energy Capture with Geologic Carbon Dioxide Sequestration. Geophysical Research Letters, Vol. 38, Issue 10, 2011, pp. 1-7.
[16] Wilson S.A., Raudsepp M., and Dipple G.M., Quantifying Carbon Fixation in Trace Minerals from Processed Kimberlite. Applied Geochemistry, Vol. 24, Issue 12, 2009, pp. 2312-2331.
[17] Mervine E.M., Wilson S.A., Power I.M., Dipple G.M., Turvey C.C., Hamilton J.L., Vanderzee S., Raudsepp M., Southam C., Matter J.M., and Kelemen P.B. ,Potential for Offsetting Diamond Mine Carbon Emissions Through Mineral Carbonation of Processed Kimberlite. Mineralogy and Petrology, Vol. 112, Issue 2, 2018, pp. 755-765.
[18] Hamilton J.L., Wilson S.A., Turvey C.C., Morgan B., Tait A.W., McCutcheon J., Fallon S.J., and Southam G., Carbon Accounting of Mined Landscapes, and Deployment of a Geochemical Treatment System for Enhanced Weathering at Woodsreef Chrysotile Mine, NSW, Australia. Journal of Geochemical Exploration. Vol. 220, 2021, PP. 1-14.
[19] Gislason S.R., Wolff-Boenisch D., Stefansson A., Oelkers E.H., Gunnlaugsson E., Sigurdardottir H., Sigfusson B., Broecker W.S., Matter J.M., Stute M., and Axelsson G., Mineral Sequestration of Carbon Dioxide in Basalt. International Journal of Greenhouse Gas Control, Vol. 4, Issue 3, 2010, pp. 537-545.
[20] Olsson J., Stipp S.L., Makovicky E., and Gislason S.R., Metal Scavenging by Calcium Carbonate at the Eyjafjallajökull Volcano. Chemical Geology, Vol. 384, 2014, pp. 135-148.
[21] McGrail B.P., Schaef H.T., Spane F.A., Cliff J.B., Qafoku O., Horner J.A., Thompson C.J., Owen A.T., and Sullivan C.E., Field Validation of Supercritical CO2 Reactivity with Basalts. Environmental Science and Technology Letters, Vol. 4, Issue 1, 2017, pp. 6-10.
[22] White S.K., Spane F.A., Schaef H.T., Miller Q.R., White M.D., Horner J.A., and McGrail B.P., Quantification of CO2 Mineralization at the Wallula Basalt Pilot Project. Environmental Science and Technology, Vol. 54, Issue 22, 2020, pp. 14609-14616.
[23] Tenthorey E., Boreham C.J., Hortle A.L., Underschultz J.R., and Golding S.D., Importance of Mineral Sequestration During CO2 Gas Migration. Energy Procedia, Vol. 4, 2011, pp. 5074-5078.
[24] Kelemen P., Benson S.M., Pilorgé H., Psarras P., and Wilcox J., An Overview of the Status and Challenges of CO2 Storage in Minerals and Geological Formations. Frontiers in Climate, Vol. 1, Issue 9, 2019, pp. 1-20.
[25] Niyazi Y., Warne M., and Ierodiaconou D., Post-Rift Magmatism and Hydrothermal Activity in the Central Offshore Otway Basin. Marine Geology, Vol. 438, 2021. pp. 1-25.
[26] Williams M.L., Carr P.F., Isotope systematics of secondary minerals from the Prospect Intrusion, New South Wales. Australian Journal of Earth Sciences. 2005 Dec 1;52(6):799-806.
[27] Carr P.F., The Coonemia Complex: A Differentiated Shoshonitic Intrusion, Southern Sydney Basin, Australia. South African Journal of Geology. Vol. 97, Issue 4, 1994, pp. 486-495.
[28] Bowman N.H., Van Otterloo J., Cairns C.P., Taylor D.H., and Cas R.A., Complex Evolution of Volcanic Arcs. Journal of Volcanology and Geothermal Research, Vol. 373, 2019 pp. 120-132.
[29] Zhu S., Yue H., Zhu X., Sun S., Wei W., Liu X., and Jia Y., Dolomitization of Felsic Volcaniclastic Rocks in Continental Strata. Sedimentary Geology, Vol. 353, 2017, pp. 13-27.
[30] de Dios J.C., Le Gallo Y. and Marín J.A., Innovative CO2 injection strategies in carbonates and advanced modeling. Fluids, Vol. 4, Issue 1, 2019, pp. 1-25.
[31] Ou K., Pineda J.A., Liu X., and Sheng D., Osmotic Effects on the Microstructure of Ashfield Shale. Japanese Geotechnical Society Special Publication, Vol. 7, Issue 2, 2019, pp. 669-674.
[32] Nole M., Daigle H., Milliken K.L., and Prodanović M., A Method for Estimating Microporosity of Fine-Grained Sediments and Sedimentary Rocks. Sedimentology. Vol. 63, Issue 6, 2016, pp. 1507-1521.

8th Int. Conf. on Structure, Engineering & Environment (SEE), Mie, Japan, Nov.10-12, 2022, ISBN: 978-4-909106094 C3051

DEVELOPMENT OF A NEW VIBRATION ACTUATOR FOR INSPECTION OF LARGE IRON STRUCTURES

Hiroyuki Yaguchi
Faculty of Engineering, Tohoku Gakuin University, Japan

ABSTRACT

In general, vibrations generated by machines are generally considered harmful. Research to reduce these vibrations is still being actively conducted. On the other hand, research has been conducted on the effective use of mechanical vibration. However, there are only a few examples of practical applications, such as ultrasonic motors, vibration conveyors and vibration power generation. The author has devised a propulsion module using an original magnetic circuit. By combining this propulsion module with mechanical vibration, an actuator with a new operating principle was invented. In the present study, four types of vibration actuators with a new operating principle proposed by the authors are shown. The vibration type actuator can be driven directly without any additional device. The developed actuators are smaller and lighter than existing robots, and have many advantages such as propulsive force per own weight, movement efficiency, and scalability. In recent years, the inspection and maintenance of social infrastructure such as large bridges and tanks has become a very important issue. One of these actuator systems can be equipped with an automatic tapping device to realize the inspection of large steel complex structures. The four vibration type actuators introduced in this paper are compact, lightweight, and have good controllability, so they can also be used as driving sources for robots. Moreover, since these actuators have high output per unit volume, they are useful in various industrial fields as new devices.

Keywords: actuator, mechanical vibration, system, electromagnetic force, inspection, complex iron structure

INTRODUCTION

In recent years, many large structures have been constructed in every country due to economic development. Infrastructures built 50 years ago do not have well-developed earthquake resistance standards. Within 20 years, it is expected that more than 50 % of Japan's social infrastructure will be more than 50 years old.

For this reason, they may collapse in the event of a large-scale disaster. However, due to the location of the site, it is very difficult to inspect large steel structures such as large bridges and storage tanks. For this reason, various inspection robots have been developed to ensure the safety of workers and to reduce costs. In particular, there is a high demand for inspection at the cable joint of a cable-stayed bridge having a height of a main tower over 200 m.

Numerous robots have been proposed for structural inspection. Adhesion methods for wall surface movement include the following proposed techniques: mimicking of a living leech [1], roller structure with a belt and suction cups [2], van der Waals forces [3], negative pressure produced by a pump [4], adhesive materials [5], and a claw gripper [6]. Multiple actuators are always mounted on the drive unit of these robots. Additionally, these methods involve complicated mechanisms and require the adhered device to have a relatively large weight. Recently, robots that apply drone technology [7, 8] have been developed. However, drone inspection technology has not advanced because it requires skill in investigations due to the effects of strong winds and thunderstorms.

In general, vibrations generated by machines are generally considered harmful. Research to reduce these vibrations is still being actively conducted. On the other hand, research has been conducted on the effective use of mechanical vibration. However, there are only a few examples of practical applications, such as ultrasonic motors, vibration conveyors and vibration power generation. The author has devised a propulsion module using an original magnetic circuit [9]. By combining this propulsion module with mechanical vibration, an actuator with a new operating principle was invented. As a result of them, the author proposed an actuator capable of movement on a magnetic substance by combining electromagnetic force and mechanical vibration. [10 - 12]. The results demonstrate that the actuator can move stably in slide-on-ceiling and wall-climbing plane motions.

In this paper, in addition to the actuators shown above, four vibration actuator systems capable of movement by a new principle were introduced.

1) Vibration actuator combining electromagnetic force and mechanical vibration.
2) Vibration actuator using the phase difference of vibration.
3) Rotary type vibration actuator system.
4) Vibration actuator system combining flexible material and magnetic wheel.

As previously mentioned, the inspection and maintenance of social infrastructure such as large bridges and tanks has become a very important issue. These actuators have been shown to be applicable for inspection of social infrastructure.

OUTLINE OF COMBINING ELECTROMAGNETIC FORCE AND MECHANICAL VIBRATION

An actuator capable of movement on an iron structure by combining electromagnetic force and mechanical vibration has been proposed [10 - 12].

Fig. 1 shows a diagram of the vibration actuator capable of movement on a magnetic substance. The vibration actuator consists of a permanent magnet, a translational spring, an electromagnet, an acrylic

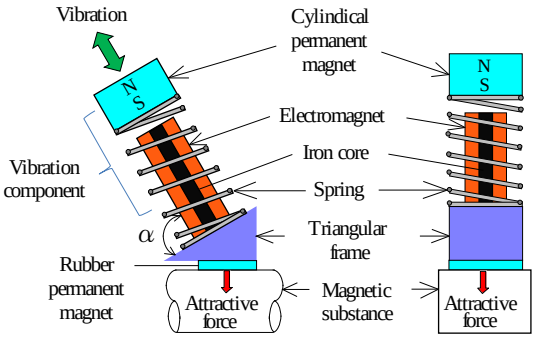

Fig. 1. Structure of the vibration actuator.

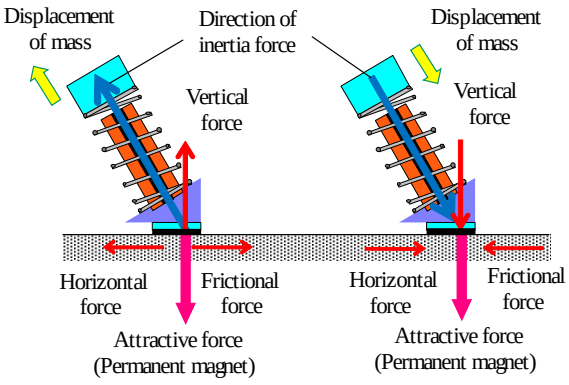

(a) Sliding (b) No sliding

Fig. 2. Principle of locomotion.

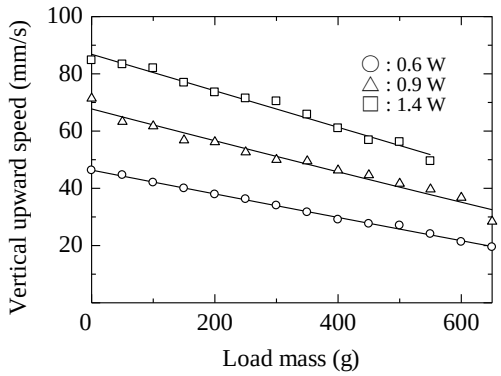

Fig. 3. Relationship between load mass and vertical upward speed for single actuator.

frame of triangle shape, a permanent magnet attached to the bottom of the frame and a natural rubber sheet. The permanent magnet, which is the mass of the vibration component is cylindrical NdFeB and is magnetized in the axial direction. This magnet is 15 mm in diameter and 6 mm in height. The surface magnetic flux density measured using a tesla meter was 380 mT. The translational spring was a stainless steel compression coil type having an outer diameter of 14 mm, a free length of 30 mm, and a spring constant k of 4,812 N/m. The electromagnet was inserted in the translational spring. This electromagnet consists of an iron core having a diameter of 5 mm and a length of 25 mm with 1000 turns of 0.2-mm-diameter copper wire.

The permanent magnet attached to the bottom of the frame has a diameter of 12 mm, and a thickness of 5 mm. The average surface magnetic flux density was 383 mT. The natural rubber sheet with a thickness of 1 mm was attached to this permanent magnet for the purpose of increasing the frictional force. The vibration component was inclined at angle α from the horizontal plane. The vibration actuator has a height of 42 mm, a width of 15 mm, and a total mass of 30 g.

The angle α of the vibration component was set to 60 degrees based on the results obtained in a previous study [10]. The attractive force generated by the permanent magnet attached at the support part acts on the vibration actuator when it is placed on a magnetic substance, as shown in Fig. 2(a), (b). The frictional force between the rubber sheet and the magnetic substance alternates periodically during one cycle of vibration. Because the horizontal component of the inertial force exceeds the frictional force, the vibration actuator is propelled by the difference between the frictional forces in the forward and backward directions acting on the

rubber sheet in the support [10-12].

In the experiment, an iron rail with a width of 50 mm, a thickness of 50 m, and a length of 1,000 mm was used as the target magnetic structure. The vibration component was driven at a resonance frequency of 106 Hz using a signal generator and an amplifier. The attractive force F between the actuator unit and the iron rail was 8 N. The coefficient of friction between the iron rail and the natural rubber as measured in the experiment was 0.67.

Fig. 3 shows the relationship between the load mass and the vertical upward speed of the actuator when the input power was 0.6, 0.9, and 1.4 W. In this figure, the actuator can move upward at a speed of 24.1 mm/s even with a load mass of 650 g.

This vibration actuator has a very simple structure and can generate propulsion about 21 times its own weight. However, the movement direction is limited to only one direction movement from the principle of operation.

PRINCIPLE OF OPERATION FOR VIBRATION ACTUATOR USING PHASE DIFFERNCE

To solve the problem described above, a new vibration actuator that extends the principle of operation invented [13] by the authors was proposed. New principle of operation for the actuator capable of reciprocating movement by controlling the phase of two vibration components has been considered. As shown in Fig. 4, when two vibration components A and B are arranged orthogonally, the movement direction of the new vibration actuator can be changed by controlling the phase of the vibration in each component. The cases of displacement in the horizontal and vertical directions are referred to as the vibration components A and B, respectively. The displacement coordinates x and y of each of the vibration components A and B are determined as shown in Fig. 4.

When the vibration actuator is set on a magnetic substance, the frame of this actuator is held by the main and sub rubber permanent magnets with the attractive force of F_m and F_s. Due to this reaction, the vibration component can be displaced. It was assumed that the vibration components A and B were vibrating at the angular frequency ω. The period of the vibration component in this case is τ,

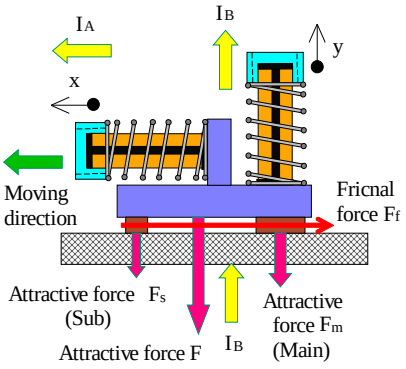

(a) Sliding

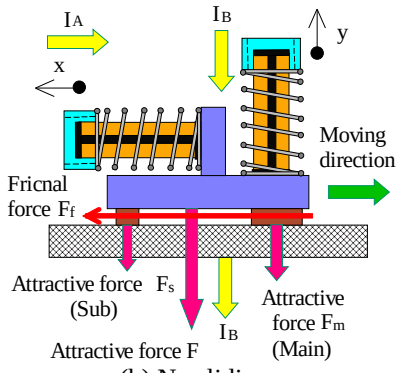

(b) No sliding

Fig. 4. Principle of reversible motion (In-phase).

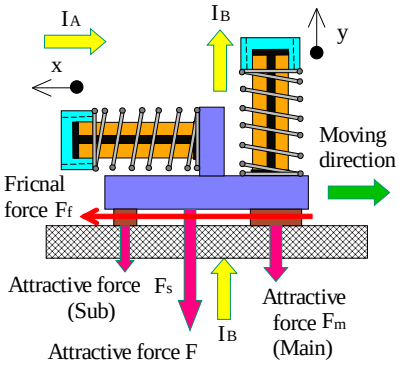

(a) Sliding

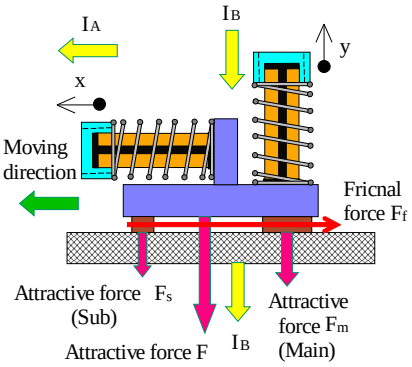

(b) No sliding

Fig. 5. Principle of reversible motion (Out-of-phase).

respectively.

First, as shown in the Fig. 4(a), consider a case where the phase difference between the vibration components A and B is 0 degree (in-phase). Focusing on one cycle ($\tau = 2\pi/\omega$) in the vibration component B, the holding force F and the frictional force F_f of the support part for the actuator change periodically as shown in Equation (1) due to the inertial force I_B by the permanent magnet of the vibration component B.

$$F = F_m + F_s - I_B \sin \omega \tau \ (0 < \tau < \pi/\omega) \ , \ F_f = \mu F \quad \text{---------- (1)}$$

where, t is time, and μ is the friction coefficient. When the component A is displaced in the +x direction in the same phase while the vibration component B is displaced in the +y direction, the vibration actuator easily slides in the +x direction. As shown in equation (2), when the inertia force I_A of the permanent magnet in the vibration component A exceeds the friction force F_f, the actuator can move in the +x direction.

$$I_A > F_f \quad (2)$$

On the other hand, as shown in Fig. 4(b), when the vibration component B is displaced in the -y direction, the holding force F and the frictional force F_f increase as shown in Equation (3) due to the inertial force IB by the permanent magnet.

$$F = F_m + F_s + I_B \sin \omega\tau \ (\pi/\omega < \tau < 2\pi/\omega) \ , \ F_f = \mu F \quad \text{---------- (3)}$$

Even if the component A is displaced in the -y direction in opposite phase, the inertia force I_A cannot exceed the friction force F_f. Therefore, the actuator cannot move as shown in Equation (4).

$$I_A < F_f \quad (4)$$

The actuator can move in one direction by changing the frictional force of the rubber permanent magnet attached to the frame.

Fig. 5 shows a case where the phase difference between the vibration components A and B is 180 degrees (opposite phase). The actuator can move in the -x direction according to the principle of movement by the frictional force and the inertial force described above. Accordingly, the present actuator can change the movement direction between forward and backward by controlling the phase of the two vibration components. For the vibration component, a smaller spring and permanent magnet were used than in Chapter 1, and the propulsion characteristics were measured.

The load mass was attached to the frame of the actuator using a string. The tilt angle of the iron rail was set to 90 degrees. Figs 6 and 7 show the

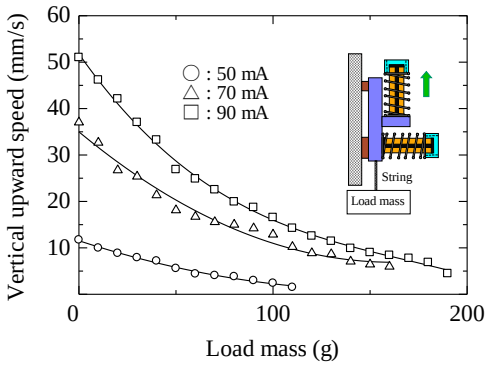

Fig. 6. Relationship between load mass and vertical upward speed (Direction A).

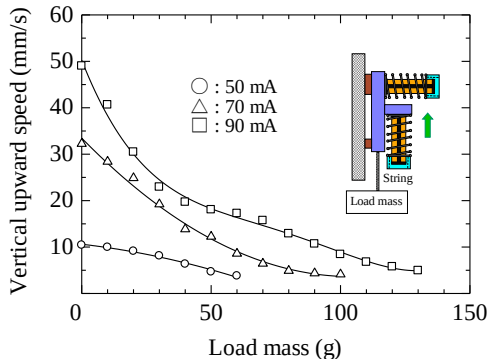

Fig. 7. Relationship between load mass and vertical upward speed (Direction B).

relationship between the load mass mounted on the actuator and the vertical upward speed when the actuator moves forward and backward direction. The input current to the electromagnet in each vibration component was changed from 50 mA to 110 mA in three types. As shown in the figure, the maximum pulling force of the actuator in the case of forward movement is 1.9 N, while that in the case of backward movement is only 1.3 N. As described above, this is because the attractive force of the sub rubber permanent magnet has an effect. The presence of the attractive force asymmetric with respect to the vibration component B degrades the movement characteristics of the actuator. However, the sub rubber permanent magnet is needed to drive the actuator straight. However, this actuator cannot move on steel structures with small rust and unevenness.

OUTLINE OF WHEEL TYPE ACTUATOR

In order to solve the above problems, a rotary movement type actuator has been developed [14, 15].

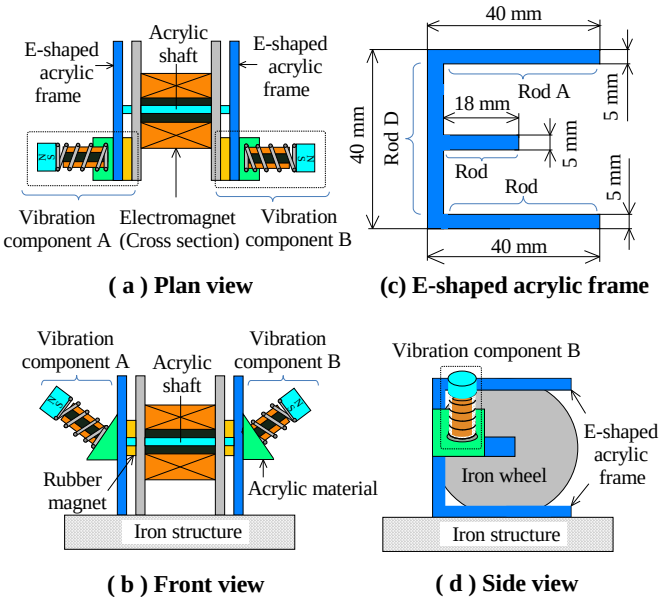

Fig. 8. Structure of the magnetic wheel actuator.

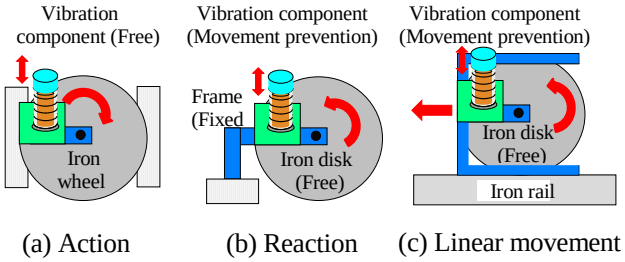

Fig. 9. Principle of locomotion.

By extending the principle of locomotion, as shown in Fig. 8, a new type of a magnetic wheel actuator is suggested. The magnetic wheel actuator consists of two vibration components (labeled A and B), two E-shaped acrylic frames with four rods (labeled A, B, C, and D), an electromagnet, an acrylic shaft, and two iron disks. The vibration component was a smaller spring and permanent magnet than in Chapter 1. The two iron disks are rotated using the reaction force generated by the vibration component as described below. Since the frictional force between the iron disk and the rubber magnet can be maintained constant, the frictional force during the rotational movement of the wheel actuator on the structure does not change. The dimensions of the E-shaped frame in this figure correspond to those of an iron disk of 40 mm in diameter. The thickness of this E-shaped frame is 3 mm.

The principle of operation of this rotary actuator will be discussed. As shown in Fig. 9, when the vibration component is placed on an iron structure, the component can vibrate due to the attractive force

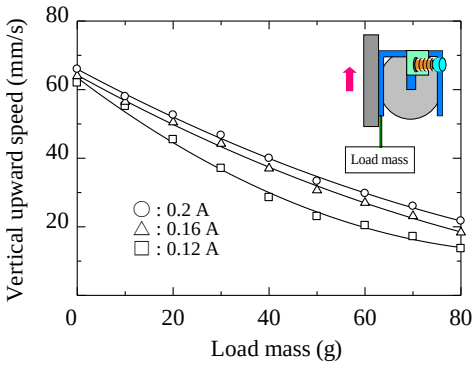

Fig. 10. Relationship between load mass and vertical upward speed.

of the rubber magnet. The vibration component moves as a result of the vertical and horizontal components of the forces generated by the vibration component attached at an angle of 60°. When the vibration component is placed on a fixed iron disk, as shown in Fig. 9(a), the component moves in the direction in which the vibration component is tilted. When a supported state is imposed in order to prevent the motion of the vibration component, the iron disk rotates as a result of the reaction force of the component, as shown in Fig. 9(b). By inserting the vibration component into the E-shaped acrylic frame in such a way that the component is attracted to the iron disk, it is possible to rotate the disk while preventing the movement of the vibration component. When the two vibration components (A and B) are driven at the same frequency and the same amplitude, the wheel actuator can move linearly.

Fig. 10 shows the relationship between the load mass and the vertical upward speed for the input power of 0.37 W for each vibration component. Here, the DC input current into the electromagnet of the magnetic wheel was changed to 0.12 A, 0.16 A, and 0.2 A. As shown in the figure, the maximum pulling force of this magnetic wheel actuator is 0.8 N. However, this rotary actuator is not capable of traveling on a stepped surface. Also, an inspection device cannot be mounted.

VIBRATION ACTUATOR SYSTEM CAPABLE OF MOVEMENT OVER A STEP

Finally, a new vibration actuator system was developed [16] capable of movement with the inspection device on a complex steel structure with steps of 25 mm in height. This new vibration actuator system has a flexible frame capable of deformation over uneven parts of the structure surface. Silicone rubber was used for the flexible

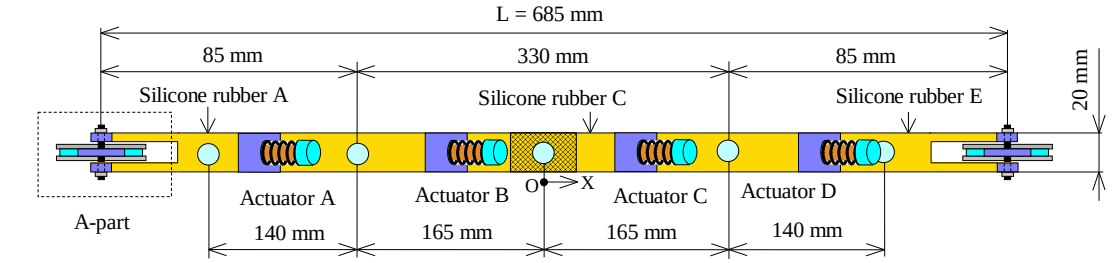

(a) Plan view

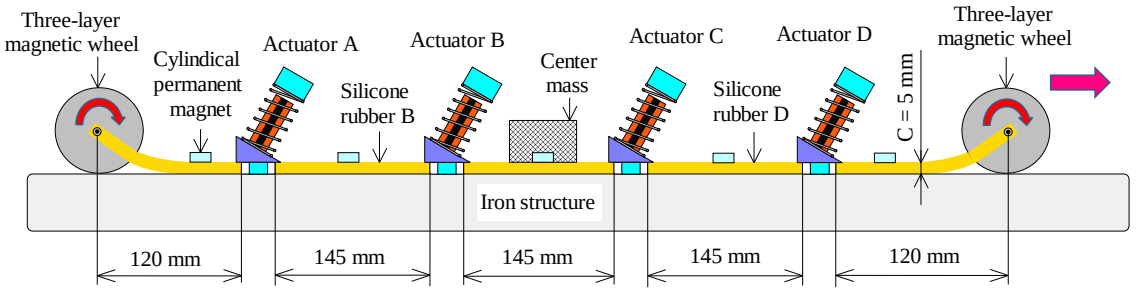

(b) Front view

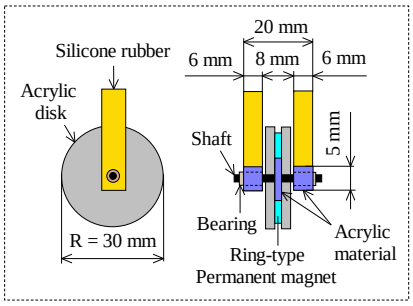

(c) Details of Area A in (a)

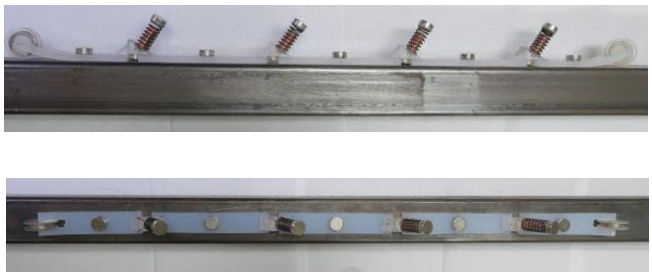

(d) Photograph of actuator system

Fig. 11. Vibration actuator system capable of movement over a step.

frame, and the attractive force was generated by multiple permanent magnets.

Fig. 11 shows a vibration actuator system in which four actuators (A, B, C, D) capable of movement are connected by a flexible silicone rubber frame. The silicone rubber is divided into five segments. The lengths of silicone rubber segments A, B, C, D, and E and are L_1, L_2, L_3, L_4, and L_5, respectively. A magnetic wheel is attached to opposite ends of silicone rubber segments A and E. By attaching a magnetic wheel to the tip of the actuator system, it is possible to exert an appropriate attractive force on the iron structure and provide a guide for movement over a step. The magnetic wheel has a three-layer structure in which a ring-type permanent magnet is sandwiched between two acrylic disks having outer diameters of 30 mm and a thickness of 2 mm. In addition, auxiliary permanent magnets are placed at distances x_1, x_2, x_3, x_4, and x_5 from the origin O to adhere to an iron structure during movement over a stepped surface.

The longitudinal stiffness of the silicone rubber connecting the four actuators has a significant effect on the traction and movement over a step. Furthermore, the attractive force exerted by the magnetic wheel also affects the movement over the step. Because there are countless combinations of parameter for designing the actuator system, the following four criteria were introduced:

1) The total length of the actuator system is approximately 700 mm to allow portability.
2) Considering long cable traction over 200 m, the traction force for the actuator system is more than 15 N (load mass of 1,500 g).
3) In the future, an automatic tapping device mass weighing 260 g can be installed in the center of the actuator system.

4) The height of the step over which the actuator system can move does not exceed 25 mm in the vertical plane.

Preliminary experiments were conducted to satisfy the above design criteria. By trial and error, the dimensions of the silicone rubber material were determined. All silicone rubber segments A, B, C, D, and E had a thickness of 5 mm. In addition, the width B and length L of the silicone rubber were set to B = 20 mm and L_1 = 120 mm, L_2 = 140 mm, L_3 = 140 mm, L_4 = 140 mm, and L_4 = 120 mm. As the auxiliary attractive force, cylindrical permanent magnets were arranged at x_1 = 0 mm, x_2 = 165 mm, x_3 = 305 mm, x_4 = -165 mm and x_5 = -305 mm in segments A, B, C, D, and E. Cylindrical permanent magnets with an outer diameter of 15 mm and a thickness of 6 mm were attached at these positions. The attractive force on the iron rail for this magnet was 1.8 N. The vibration components described in Chapter 1 were used.

The ring-shaped permanent magnet for the magnetic wheels had an outer diameter of 16.5 mm, an inner diameter of 8.5 mm, a thickness of 4 mm, and a magnetic flux density of 356 mT. A three-layered wheel with a shaft with an outer diameter of 1 mm in the center was attached to the silicone rubber via bearings. The attractive force for the magnetic wheel was 0.9 N.

The overall length of the actuator system was 715 mm, and the distance between the magnetic wheels was L = 685 mm. The width, height, and total mass of the actuator system were 20 mm, 42 mm, and 250 g, respectively. In this system, the attractive force F for each vibration actuator was set to 11 N. Fig. 11(d) shows photographs of the vibration actuator system.

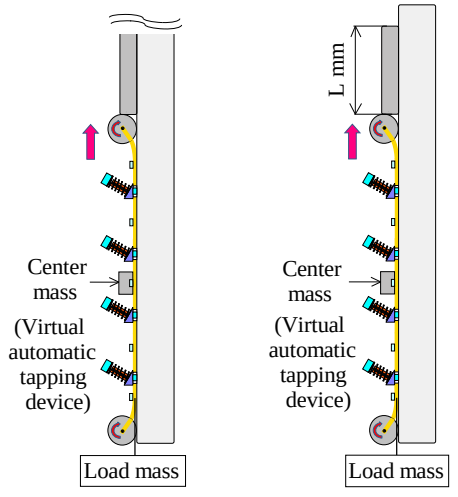

(a) Single infinite step (b) Two steps

Fig. 12. Two step patterns for vertical iron structure.

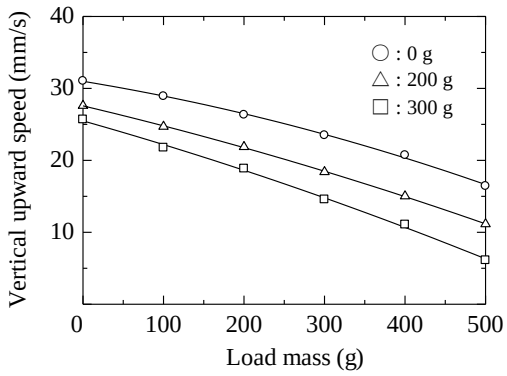

Fig. 13. Relationship between load mass and vertical upward speed for single infinite step.

The locomotion characteristics of the vibration actuator system for two step patterns were measured. First, as shown in Fig. 12(a), an iron structure having a single step with an infinite length was examined. In these experiments, the measurement distance was set to 750 mm. The power input to each actuator was 1 W.

Fig. 13 shows the relationship between the load mass of the actuator system and the vertical upward speed for a single step with a height of 25 mm by varying for central masses of 0, 200, 300, 400, and 500 g. It was found that even with a central mass of 300 g, a traction force of 5 N (load mass of 500 g) was generated. However, the speed was only 6 mm/s.

Next, the speed of the actuator system for the two-step case shown in Fig. 12(b) was measured. Even for a central mass of 300 g, the system could move over the vertical surface while generating a traction force of 5 N.

CONCLUSIONS

In the present study, four types of vibration actuators with a new operating principle proposed by the authors are shown and their movement characteristics were introduced. Each actuator has its own characteristics and can be used according to the case of application. All vibration actuators can be driven directly without any additional device. These developed actuators are smaller and lighter than existing robots, and have many advantages such as propulsive force per own weight, movement efficiency, and scalability.

In particular, in the vibration actuator system combining flexible material and magnetic wheel, the

experimental result of the actual prototype demonstrates that the maximum efficiency of the vibration actuator was 25.2 %, and the maximum pulling power was 6.5 N. Therefore, this actuator system has the potential for inspection of large social infrastructures. In recent years, the inspection and maintenance of social infrastructure such as large bridges and tanks has become a very important issue. This actuator system can be equipped with an automatic tapping device, which might allow it to inspect large iron complex structures.

However, this actuator system cannot switch its direction of movement. To solve this problem, it is necessary to change the actuator to a structure that uses a vibration phase difference, as previously proposed by the author. It is necessary to put the research results to practical use and contribute to society.

REFERENCES

[1] Kanada A., Giardina F., HowisonT.,Mashimo T. and Iida F., "Reachability Improvement of a Climbing Robot based on Large Deformations induced by Tri-Tube Soft Actuators, Soft Robotics Vol. 6, No. 4(2019)

[2] Ge D., Ren C., Ma S. and Matsuno T., Guide Rail Design for a Passive Suction Cup based Wall-Climbing Robot, in Proc. 2016 IEEE/RSJ International Conference on Intelligent Robots and Systems (IROS2016), pp. 5776-5781, 2016.

[3] Kim S., M. Spenko, S. Trujillo, B. Heyneman, V. Mattoli and M. R. Cutkosky, "Whole body adhesion hierarchical directional and distributed control of adhesive forces for a climbing robot", IEEE International Conference on Robotics and Automation, (2007).

[4] Subramanyam A., Mallikarjuna Y., Suneel S.and Bhargava K. L., " Design and Development of a Climbing Robot for Several Applications", International Journal of Advanced Computer Technology, Vol. 3, No. 3, pp. 15-23 (2011).

[5] Unver O. and Sitti M., " Tankbot: A Miniature, Peeling Based Climber on Rough and Smooth Surfaces", in Proc., IEEE International Conference on Robotics and Automation, pp. 2282-2287 (2009).

[6] Provancher W., Ensen-Segal S. and Fehlberg M., " ROCR: An Energy-Efficient Dynamic Wall-Climbing Robot", IEEE Transaction on Mechatronics, Vol. 16, No. 5, pp. 897-906 (2011).

[7] N. Mahamud, G. Muhammad Shahriar, H. U. Khan, S. Sharmin and N. J. Lisa, " ALW drone: A new design and efficient approach", in Proc., IEEE 19th International Conference on Computer and Information Technology (ICCIT), DOI:10.1109/ICCITECHN.2016.7860244 , pp. 474-479 (2017).

[8] M.Morita, H. Kinjo, S. Sato, T. Sulyyon and T. Anezaki, " Autonomous flight drone for infrastructure (transmission line) inspection", in Proc., IEEE International Conference on Intelligent Informatics and Biomedical Sciences (ICIIBMS), pp. 198-201, DOI: 10.1109/ICIIBMS.2017.8279692 (2017).

[9] Yaguchi H. and Izumikawa T., " Wireless In-Piping Actuator Capable of High-Speed Locomotion by a New Motion Principle, IEEE/ASME Transactions on Mechatronics, Vol. 18, No. 4, pp. 1367 - 1376 (2013).

[10] Yaguchi H. and Sakuma S., " A Novel Magnetic Actuator Capable of Free Movement on a Magnetic Substance", IEEE Transactions on Magnetics, Vol. 51, No. 11, DOI:10.1109/TMAG.2015.2443061 (2015).

[11] Yaguchi H. and Sakuma S., " Characteristic Improvement of a Magnetic Actuator Capable of Movement on a Magnetic Substance", IEEE Transactions on Magnetics, Vol. 52, No. 7, DOI: 10.1109/TMAG.2016.2533433 (2016).

[12] Yaguchi H., and Sakuma S., Vibration Actuator Capable of Movement on Magnetic Substance Based on New Motion Principle, Journal of Vibroengineering, Vol. 19, Issue 3, pp. 1494 -1508 (2017).

[13] Yaguchi H., A new type of electromagnetically propelled vibration actuator for appearance inspection of iron structure, International Journal of GEOMATE, Vol. 20, No. 77, pp. 69 - 76 (2021).

[14] Yaguchi H., Kimura I., and Sakuma S., A Novel Actuator System Combining Mechanical Vibration and Magnetic Wheels Capable of Rotational Motion Using Shape Memory Coils, Actuator, Vol. 8, No. 1, pp. 1 - 12 (2019).

[15] Yaguchi H., and Itoh Y., Vibration actuator system with small-scale size capable of visual inspection of large complex iron structures, Applied Sciences, Vol. 11, No. 16, pp. 1 - 16 (2021).

[16] Yaguchi H., and Itoh Y., Vibration actuator system for internal inspection of large complex iron structures, International Journal of GEOMATE, Vol. 22, No. 89, pp. 9 - 15 (2022).

Technical Papers

Structures

8th Int. Conf. on Structure, Engineering & Environment (SEE), Mie, Japan, Nov.10-12, 2022, ISBN: 978-4-909106094 C3051

TORSIONAL BEHAVIOR OF SPANDREL REINFORCED CONCRETE BEAMS

Noor Ayaad[1] and Nazar Oukaili[2]
[1] Department of Civil Engineering Department, University of Baghdad, Baghdad 10070, Iraq.
[2] Department of Civil Engineering Department, University of Baghdad, Baghdad 10070, Iraq.

ABSTRACT

Spandrel beams are typically subjected to a series of vertical eccentric loadings when used in parking structures or the abutments of bridges. Embedded Through-Section (ETS) method is a recently developed method to increase the shear capacity of reinforced concrete using steel reinforcing rods. This study presents an experimental program conducted on spandrel beam systems to gain a deeper understanding considering different parameters including the aspect ratio of the section (i.e., height/thickness) and the strengthening type (i.e., the effectiveness of the ETS method). This study focuses on the test results including the ultimate shear-torsion capacity, cracking load, load-twisting, and load-deflection responses. The outcomes had shown the superior performance of the ETS method, increase in torsion capacity was 45% compared to the control spandrel beams (i.e., unstrengthened). These results also indicate that using embedded steel rods showed improvement in restricting the deflections and rotation of spandrel beams due to increasing spandrel stiffness. The skewed failure plane for the strengthened spandrel beams was slowly reaching the upper surface of the web which was attributed to the prop effect provided by embedded steel rods.

Keywords: L-Shaped Spandrel Beam, Torsional Equilibrium, Shear Effects, Rotation, ETS Method

INTRODUCTION

The L-shaped spandrel reinforced concrete beams are structural members that are subjected to a series of discrete loads eccentric to the shear center of the beam.These loads cause vertical displacement, significant lateral displacement, and rotation. The maximum internal torsion and shear effects occur in the end regions of the specimen. In many cases, a continuous ledge runs along the bottom edge on one side of the beam, resulting in what is known as an L-shaped spandrel beam. The spandrel beams are subjected to high shear, torsion, and bending moments consequently resulting in deformations in the vertical plane and out plane accompanied by flexural and shear cracks [1,2]. These loads with respect to the unsymmetrical L-shaped spandrel cross-section cause vertical in addition to significant lateral displacements and rotation. The ends of these spandrel beams are also connected to the columns to prevent out-of-plane rotation about the longitudinal axis. In addition, the deck sections are often connected to the spandrel web inner face at discrete locations, providing lateral restraint along the span. The maximum torsional and shear effects occur in the end regions. Point loads from the deck sections locate along the ledge, column reactions appear at each end, and lateral restrain forces from the spandrel deck connection distribute along the inner face of the web [3,4].

The required reinforcement for spandrel members, as required by international codes [5,6] is generally designed according to a general procedure originally proposed by Zia and McGee [7].

Though several studies on the spandrel reinforced concrete beams have been performed in past decades, studies on spandrel beams strengthening were loaded under two stages are exceptional. In terms of the influence of the ETS method on the torsional behavior of spandrel beams, no studies have been conducted yet with many unanswered questions. Therefore, the objective of this research study is to investigate the effect of the efficiency of embedded steel rods installed through the web of spandrel beams to improve the torsional behavior of L-shaped reinforced concrete spandrel beams loaded in two stages under static loads.

EXPERIMENTAL PROGRAM

Four simply supported L-shaped RC beams were cast and tested under two stages of loadings. The ledge mid-span was loaded under an eccentric one-point load to study various limit state behaviors. Two spandrel beams were tested as control specimens without strengthening, while the others were retrofitted with the embedded through-section (ETS) method using steel rods.

Test Matrix and Reinforcement Details

In this experimental study, two aspect ratios were investigated 4.3 and 3. The aspect ratio of the

spandrel beam is defined as the ratio of the web height to web thickness (h/t). All spandrel beams have a span of 1500 mm, with a ledge cross-section of (250 x 200) mm. Whereas the ledge was cut back for 150 mm on either end of the spandrel beam to simulate an idealistic field conditions detail that allows the typical web to be connected to supporting columns. The geometry of the slender and compact spandrel beams had web sections of (650 x 150) and (450 x 150) mm, respectively. Each side of the web was provided with two holes over the web's cross-sectional width to achieve connection with the vertical rigid frame assembly with high-strength threaded rods, as idealistic field conditions. Table 1 summarizes the details of the tested spandrel beams.

Table 1 Properties of spandrel beams

Spandrels ID	Aspect ratio	Strengthening status	Cylinder concrete strength, (MPa)
SB1-US-S	4.3	Unstrengthen	43.20
SB1-ES-S	4.3	Strengthened	44.66
SB2-US-S	3.0	Unstrengthen	45.00
SB2-ES-S	3.0	Strengthened	45.47

All spandrel beams in his study were fabricated according to international codes [5,6]. Conventional deformed steel reinforcement was used to resist the bending, shear, and torsion combination that was induced in each spandrel. According to the assumptions of the mentioned codes the outer branches of closed vertical stirrups are resisting torsion stress and acting as a hanger for the ledge. Thus, all spandrel beams were designed to resist shear-torsion distress, and twist loadings. In this present study, to assure end-region failures, additional flexural and ledge reinforcement was provided. Also, the ledge punching shear (localized failures) must be considered and prevented to transfer the load from the ledge to the spandrel web by using extra reinforcement. All spandrel beams had one configuration of shear and torsion reinforcement which was available in the frontal and back web faces. Figure 1 shows the concrete geometry and dimensions while Fig. 2 shows the reinforcement configurations used for test spandrel beams.

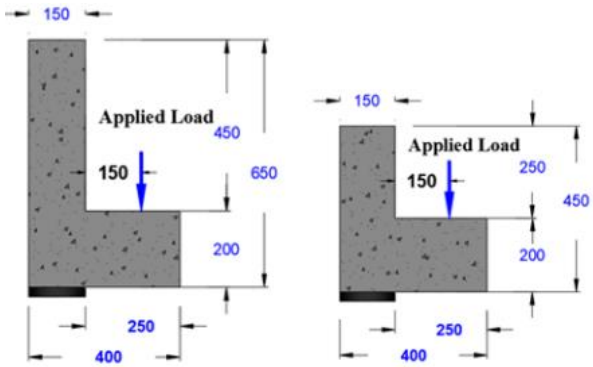

Fig. 1 Geometry and dimensions for tested spandrels. (all dimensions are in mm)

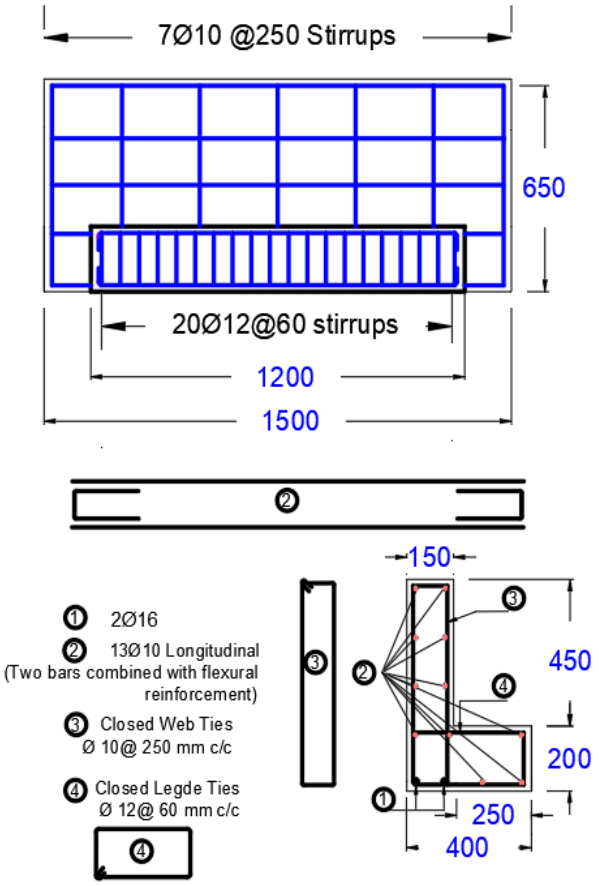

Fig. 2 Reinforcement details for tested spandrels. (all dimensions are in mm)

Material Properties

The properties of hardened concrete were based on the average strength of three samples for each spandrel beam. Concrete standard samples were prepared and tested to determine the compressive strength of concrete.

Three standard cylinders of (150 × 300) mm were tested in conformity with (ASTM C39-17) and three standard cubes of size (150 mm × 150 mm × 150) mm were tested to determine the compressive strength of concrete. Table 2 summarizes the compressive strength of concrete. Three samples of each steel bar with 0.5 m length with a diameter of Ø 10 mm, Ø12, and Ø 16 mm were tested. The ASTM A615 was used to evaluate the yield tensile strength

and ultimate tensile strength of steel bars. The results of the reinforcing steel bar are listed in Table 3.

Table 2 Compressive strength of concrete

Spandrels ID	Properties		
	f_{cu} *, (MPa)	f'_c **, (MPa)	$\frac{f'_c}{f_{cu}}$
SB1-US-S	53.60	43.20	0.80
SB2-US-S	57.00	45.00	0.79
SB1-ES-S	57.13	44.66	0.78
SB2-ES-S	54.50	45.47	0.83

*Compressive strength of the cube
**Compressive strength of the cylinder

Table 3 Mechanical properties of steel reinforcement

Nominal diameter, (mm)	f_y, (MPa)	f_u, (MPa)	Elongation, (%)
Ø 10	575.00	670.67	9.34
Ø 12	605.05	698.00	9.42
Ø 16	612.67	707.00	11.18

Setup and Instrumentation

The same loading rig was used to test both slender and compact spandrel beams which applied a single point load at the mid-span section of the ledge at a distance of 150 mm from the frontal face of the web. To record the applied load at the spandrel beam, a 1000-kN capacity of load cell was used. All spandrel beams were tested in a simply supported scheme at the ends over an effective span of 1300 mm and were rested on thick steel plates with dimensions of (100 x 150) mm, centered relative to the spandrel web, through which the vertical components of reactions were transferred. Two load cells were used with a capacity of 500-kN to determine the vertical component of the reaction, one for each end located at the center of the web. Two main features of these load cells, are mainly, monitoring and recording the reaction value at the site of influence. All spandrel beams were supported laterally by restraining the web at both ends. The vertical rigid assembly was used to restrain the movement of the test specimen and to provide torsional restraint at the web ends. To capture the lateral forces at the web ends, other load cells were connected at the top of the web's frontal face and the bottom of the web's back face. Furthermore, linear variable displacement transducers (LVDT) were used for recording vertical deflections and lateral displacements at various locations. The electrical resistance pre-wired strain gauges were used to measure strains in concrete and steel reinforcement. All instrumentation was linked to a computerized (NI) data acquisition system to capture data automatically. Figure 3 shows a profile of the test setup while the plate of the completed test setups is shown in Fig. 4.

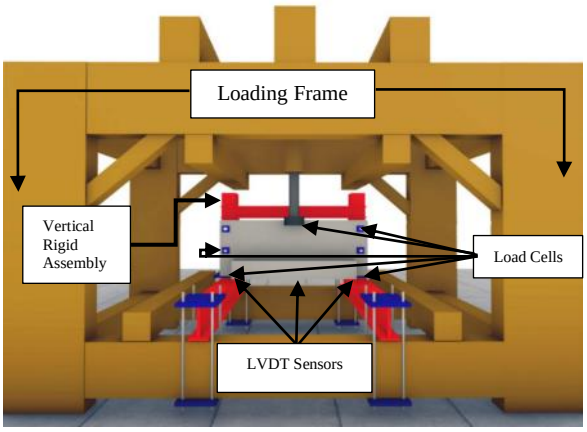

Fig. 3 Profile of the test setup.

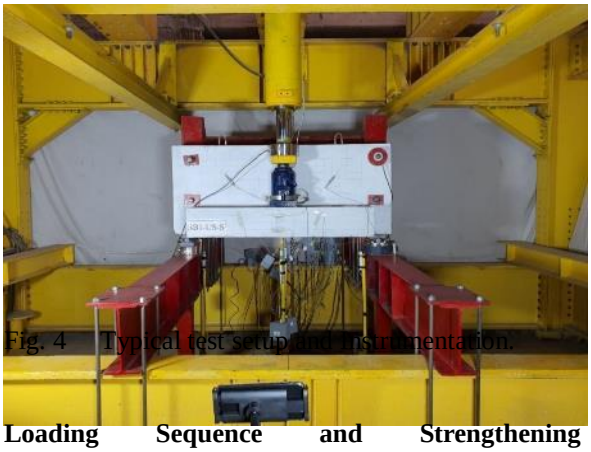

Fig. 4 Typical test setup and instrumentation.

Loading Sequence and Strengthening Implementation

The control specimen (unstrengthened) was exposed to two stages of monotonic static loading. In stage 1, the load was applied up to the level corresponding to 60% of yielding stress in the vertical steel stirrup at the web mid-span section followed by an unloading process up to zero level. In stage 2, the test specimen was reloaded up to the failure level in multi-steps.

At every loading step, the corresponding linear and rotational displacement were recorded and the developed cracks were traced. The testing procedure of the strengthened spandrel beams was the same as for the control specimen during stages 1 and 2 except that, before starting the reloading stage, the spandrel beam was strengthened using (ETS) method by steel

reinforcing rods which were installed through the centerline of the web's cross-sectional width. One strain gauge was used to measure steel rod strain (SG-2). After completing the steel rod installation, the spandrel beam was reloaded in steps to failure. Figure 5 illustrates the loading sequence for a typical test. Fig. 6 shows the preparation of the steel rods.

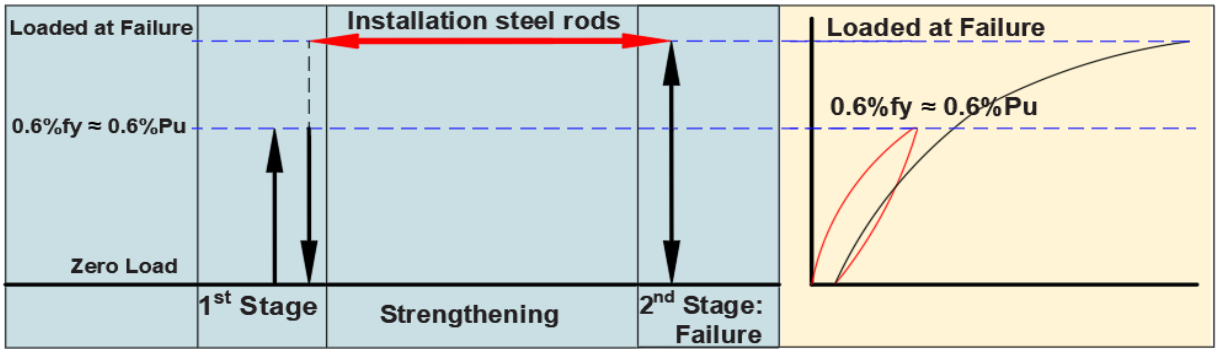

Fig. 5 Typical loading sequence.

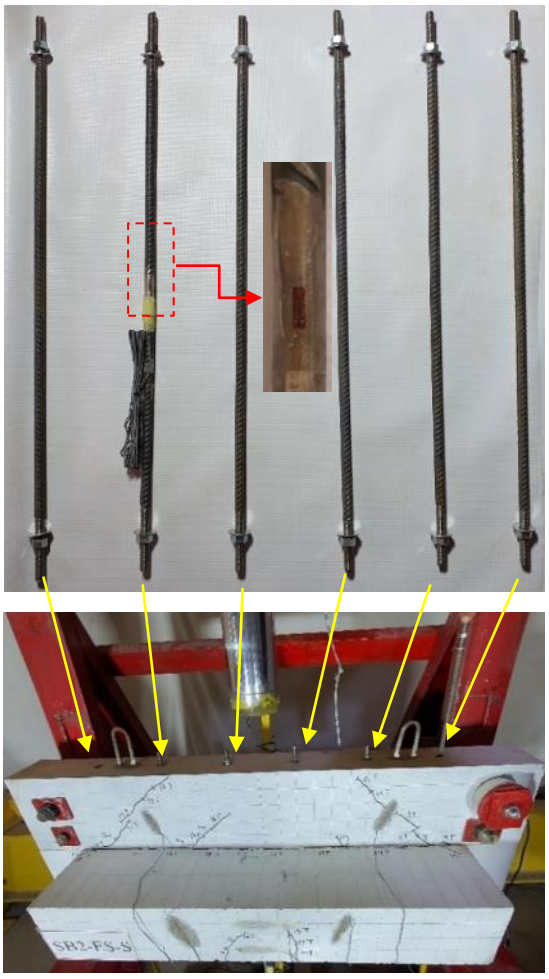

Fig. 6 Preparation of the steel reinforcing rods.

EXPERIMENTAL RESULTS AND DISCUSSION

Cracking Pattern and Failure Modes

At stage (1) of loading, all the tested spandrel beams showed cracks in various directions. Generally, light deviant cracks have occurred on the web's frontal face (inner) of the spandrel beam while minimal flexural cracking appeared on the web's back (outer) face near the mid-span section. Several of these cracks were closed during unloading. Also, at stage (2) of loading, the cracking propagation was investigated when the load reached to failure level. The cracking pattern for all tested spandrel beams was similar. This cracking pattern appeared when a spandrel beam was exposed to the combination of shear and torsion stresses. In the web's frontal face of the spandrel beam, it is substantial to detect that the shear and torsional stresses act in the same direction which led to creating a high conventional diagonal tension in the end regions of the web. Diagonal cracks on this face were initiated from the outer corners of the ledge and propagated upward with an initial angle of nearly 45 degrees. Moving away from the web ends to the mid-span section, the crack's angle progressively dropped and the crack changed its direction that became parallel to the intersection line between the web and the ledge. Also, there was inclined severe cracking at 45 degrees on the web's frontal face adjacent to the support, resulting from the out-of-plane bending induced by the end lateral couple force needed to prevent the spandrel from turning toward the applied load in response to eccentric vertical load.

In the web's back face (outer) of the spandrel beam, the diagonal tension was reduced and could even be reversed to that on the frontal face depending on the values of the shear and torsional stresses. Spread some vertical flexural cracks during loading upward from the soffit of the ledge around the region of the mid-span section. These cracks were wrapped under the soffit of the web also linked to the flexural cracks on the web's back face. Between the ends of the spandrel beam and the mid-span section, many tilted cracks were noticed, due to the shear effect in these

regions. Increasing the applied load to higher levels, the symptoms of severe spiral cracking would become prominent in all spandrel beams' end regions of the web's faces accompanied by face-shell concrete spalling as their surfaces warp and deform under the effects of torsion stress, see Fig. 7. All four spandrel beams elucidated the same failure mode including moderate diagonal cracking on the web's frontal face and moderate flexural cracking on the web's back face at the first stage. While, at the failure stage, the spandrel's failure modes began to vary depending on the availability of the ETS steel rods.

As was expected, localized failures did not occur during the testing of all spandrel beams. The control spandrels failed along a skew-diagonal crack growing upward from the bottom corners of the web and showed inclusive diagonal cracking on their inner faces along with inclusive flexural cracking on their outer faces with virtually identical modes at end regions. The skew-crack plane intersected the bottom edge of control spandrel beams and intersected the top edge of that spandrels. At the failure stage, the observed failure mechanism for the strengthened spandrel beams (SB1-ES-S and SB2-ES-S) the skewed failure plane slowly reached the top surface of the web that reflected the torsion effect. The crack width depends on the implementation of the strengthening system. It was observed that the strengthened spandrel beams (SB1-ES-S) and (SB2-ES-S) had minimal crack width across the top edge of the web in comparison to the control spandrel beams (SB1-US-S) and (SB2-US-S), even though the strengthened spandrels were subjected to higher applied loading, see Fig. 7

Load-Deflection Response and Degrees of Rotation

The vertical deflection and the horizontal displacement were measured at the mid-span section. At loading stage (1), the deformational behavior of all spandrel beams was almost correspondent. It was observed that during loading, the spandrel beam rotated toward the applied load achieving at mid-span section a bottom surface outward movement (i.e., away from the applied load) and a top surface inward movement (i.e., toward the applied load), more so the bottom surface moved more than the top surface. The contribution of steel rods gave the superior torsional load with the presence of transverse steel reinforcement in the strengthened spandrel beams when using the ETS method. Further, the embedded steel rods method has proven to be an effective way to improve the shear and torsion capacities of spandrel beams even in the presence of a limited amount of internal transverse steel reinforcement of the web. Figure 8 shows the load-vertical mid-span deflection curve, whereas the profile of deflected shape at the mid-span section is plotted in Fig. 9. The values of rotation degrees for all tested spandrel beams are shown in a bar chart in Fig. 10. In comparison to control spandrel beams, the strengthened spandrel beams showed stiffer behavior attributed to the implementation of embedded steel rods which achieved an effective restrainer to the increased deflection. Thus, the maximum rotation values of spandrel beams (SB1-US-S) and (SB2-US-S) were exceeding the rotation values of strengthened spandrels (SB1-ES-S) and (SB2-ES-S), see Table 4. ETS steel rods that were inserted inside the web section led to reducing the angle of rotation in the strengthened spandrels due to the increase of the restraining effect induced by the embedded steel rods installed in the structural member. This is due to the propped concrete core of the specimen where the rods were embedded, although the strengthened spandrels afforded a higher load.

Strain of Reinforcing Steel and ETS steel rods

The strain gauges were glued on transverse steel reinforcement and embedded steel rods to monitor the strain readings and elucidate the load-strain response during loading for each specimen. A strain gauge (SG-1) was positioned on the vertical leg of the transverse reinforcement of the web, whilst the strain gauge (SG-2) was placed on the embedded steel rods, see Fig. 5. As mentioned before, the tested spandrel beams were first exposed to incremental concentrated load up to the load that attained a strain in the web's vertical steel stirrup at the mid-span section of 1725×10^{-6} (i.e., a strain corresponding to 60% f_y of the bar of 10 mm diameter). At this stage, all spandrel beams showed an identical linear elastic behavior with various slopes, see Fig. 11.

Whereas, after cracking and increasing torsional load, the slope of these curves incrementally dropped with different slope changes depending on the level of deterioration that affected the tested specimen (i.e., the aspect ratio and the availability of the strengthening system). The spandrel beams were unloaded in one step. Otherwise, at the unloading stage, the strain (SG-1) is incrementally decreased where the residual value ranged between (503 - 630) $\times 10^{-6}$ (i.e., 30% of the yielding strain). Thus, all specimens passed over the yielding strain of 2875×10^{-6}at the failure stage. It is important to observe that the strain value in embedded steel rods (SG-2) achieved (1066×10^{-6}) at failure load. The strain in the transverse steel was significantly greater in specimens with no embedded rod. The load-strain relationships in embedded steel rods were illustrated in Fig. 12.

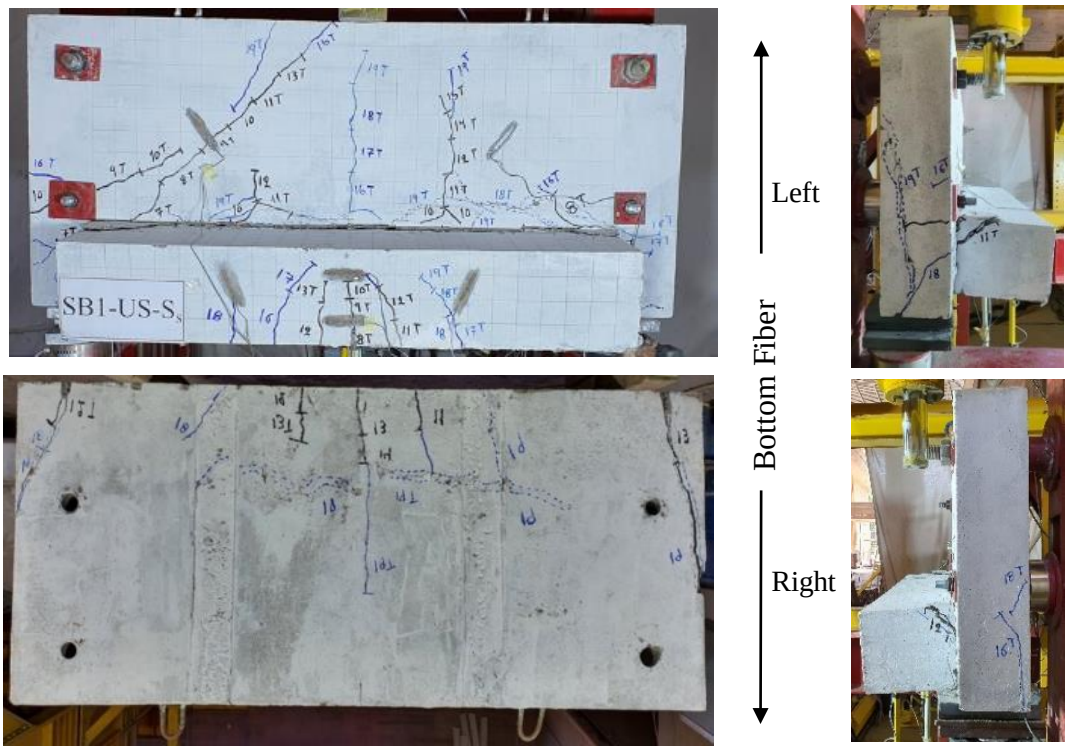

Fig. 7 Cracking pattern and failure mechanism of spandrel beams.

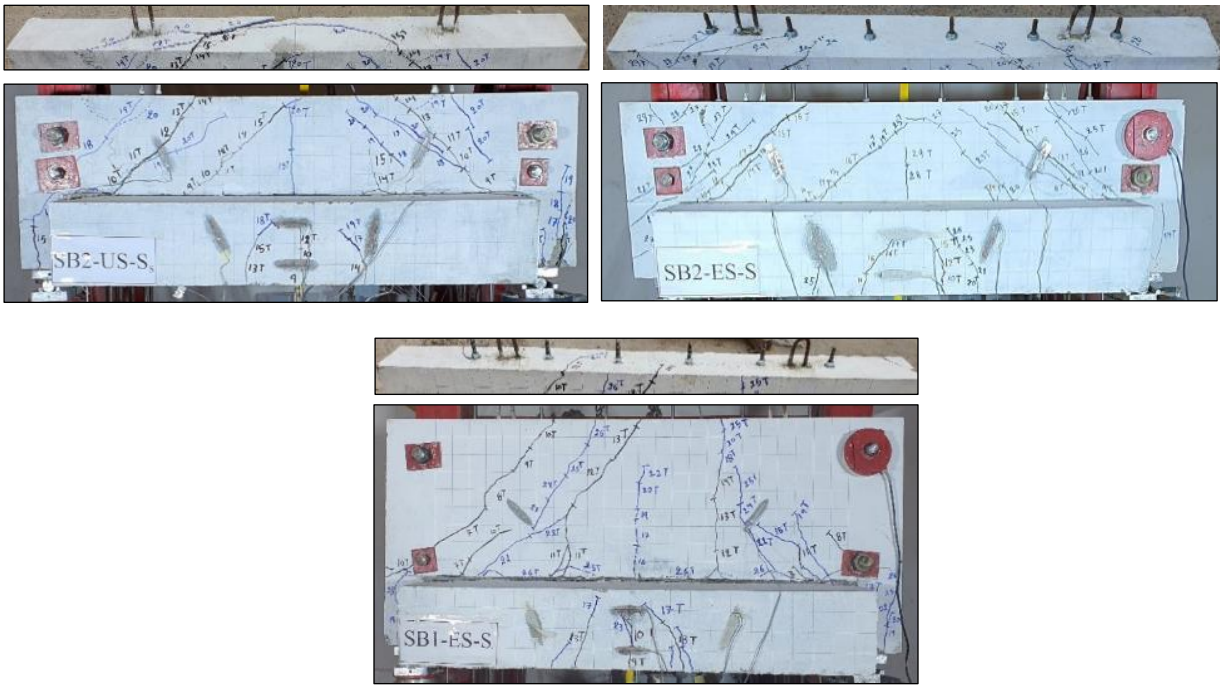

Fig. 7 Continued.

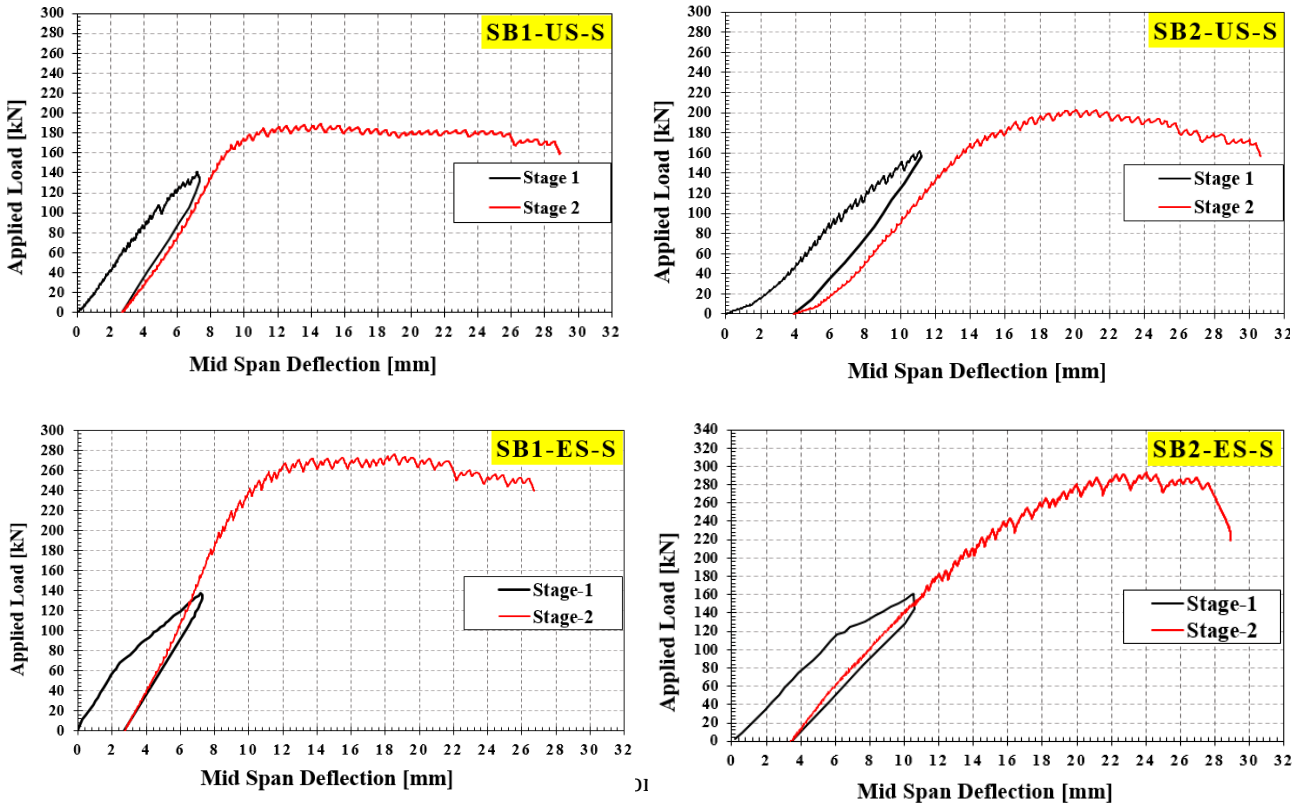

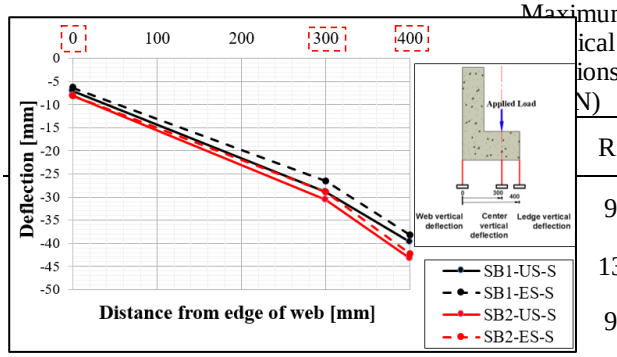

				Maximum lateral reactions, (kN)			Mid-span vertical deflection, (mm)	Rotation, (deg.)
				Right	Bottom left	Top right		
SB1-US-S	290.0	45	139.7	93.8	34.2	33.4	28.90	1.50°
SB1-ES-S	290.0	45	139.7	131.2	47.0	42.5	26.70	1.35°
SB2-US-S	290.0	45	139.7	99.3	85.6	79.9	30.61	4.40°
SB2-ES-S	290.0	45	139.7	142.0	130.4	124.5	28.90	3.90°

Table 4 Test results of load and deflection at failure

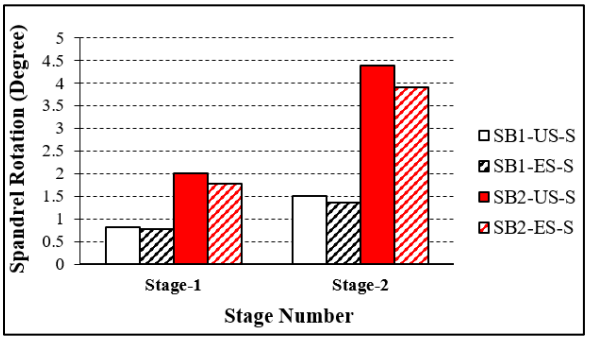

Fig. 9 The profile of deflected shape at mid-span

Fig.10 A bar chart of the values of rotation degrees for all tested spandrel beams. section.

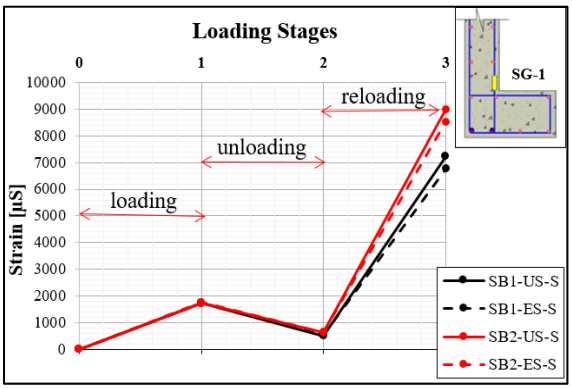

Fig. 11 The strain profile in transverse steel.

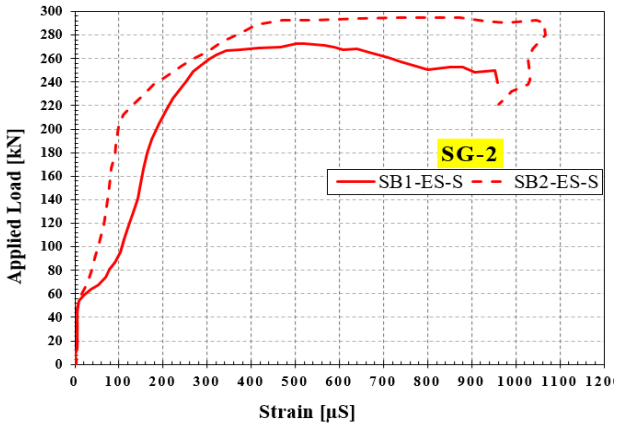

Fig. 12 The load-strain relationships in ETS steel rod.

CONCLUSIONS

Depending on the results of this study, the main conclusions are summarized as follows:

1. At stage (1) of loading, the diagonal shear cracks on the end regions of the web's frontal face appeared and initiated from the outer corners of the ledge and extended up with an initial angle of about 45°. During increasing applied load, the failure mechanism (i.e., skewed failure plane) for the strengthened spandrel beams was delayed reaching the upper surface of the web which was attributed to the prop effect provided by embedded steel rods.

2. The increase in crack width depends on the implementation of the strengthening scheme. It was observed that the strengthened spandrel beams (SB1-ES-S) and (SB2-CES-S) had minimal crack width across the upper surface of the web that reflected the torsion effect in comparison to the control spandrel beams (SB1-US-S) and (SB2-US-S), even though the strengthened spandrels were subjected to higher applied loading.

3. Using the ETS method is efficient in providing additional torsional capacity. The contribution of steel rods gave the superior torsional load with the presence of transverse steel reinforcement in the strengthened spandrel beams. In this experimental test, the embedded (SB1-ES-S) and (SB2-ES-S) spandrel beams increased the torsional capacity by 45%, relative to the control specimen. These results confirmed that the performance of strengthening specimens was satisfactory and will increase the torsional strength of RC spandrel beams.

4. The outcomes indicate that using embedded steel rods showed moderate improvement in controlling the deflections and rotation angle of spandrel beams. The reduction in rotation degree of the spandrel (SB1-ES-S) when compared to the control spandrel beam (SB1-US-S) was 10%, while the reduction in (SB2-ES-S) was about 11.4% when compared to its counterpart spandrel beam (SB2-US-S). This moderate improvement is attributed to the strengthened spandrel beams afforded a higher load.

REFERENCES

[1] Lucier G., Walter C.A., Rizkalla S., Zia P., and Klein G., Development of a Rational Design Methodology for Precast Slender Spandrel Beams: Part 1, Experimental Results., PCI Journal, Vol.56, Issue 2, 2011, pp.88-112.

[2] Alla O.K., and Rizkalla S., Design and Behavior of Ledges for Short Span L-Shaped Spandrel Beams. A thesis requirement for the degree of Master of Science, North Carolina State University, 2015

[3] Walter C.A., Rizkalla S., Behavior of Slender Precast L-Shaped Spandrel Beams, A thesis requirement for the degree of Master of Science, North Carolina State University, 2008

[4] Lucier G.,Walter C., Rizkalla S., Zia P., and Klein G., Development of a Rational Design Methodology for Precast Slender Spandrel Beams. Technical report no. IS-09-10. Constructed Facilities Laboratory, North Carolina State University, Raleigh, NC.2012

[5] ACI Committee 318 Building code requirements for structural concrete, (ACI 318-19) and commentary (318R-19). American Concrete Institute, Farmington Hills, Michigan. USA. 2019

[6] PCI Industry Handbook Committee. PCI Design Handbook: Precast and Prestressed Concrete. MNL-120. 8th ed. Chicago, IL: PCI. 2017

[7] Zia P.,and McGee D., Prestressed Concrete under Torsion Shear and Bending. Journal of the American Concrete Institute, vol.73, Issue 1, 1976, pp.26-32.

8th Int. Conf. on Structure, Engineering & Environment (SEE), Mie, Japan, Nov.10-12, 2022, ISBN: 978-4-909106094 C3051

EXPERIMENTAL STUDY ON SEISMIC SHEAR DEFORMATION OF BOX TUNNEL FOCUSING ON STIFFNESS RATIO AND FRICTION BEHAVIOR

Takafumi Shimada[1], Hidetoshi Nishioka[2] and Takahiro Furukawa[3]
[1,2,3] Faculty of Science and Engineering, Chuo University, Japan

ABSTRACT

In the design of cut and cover box tunnels, the interaction between the structure (box) and surrounding ground must be properly evaluated. In particular, when it comes to determining the strain transmissibility during earthquakes (shear strain of the box/shear strain of the ground), the shear modulus ratio of the surrounding ground to the box is a key parameter; however, the effect of ground nonlinearity on this relationship has not yet been elucidated. The interaction forces between a box and the surrounding ground can be roughly divided into the shear force along the box surface and the normal force. Considering the frictional and sliding motion is especially important when evaluating the shear force. In this study, we conducted model experiments in a small shear soil tank containing stacked aluminum rods, which were used to simulate ground nonlinearity, with the stiffness of the box and friction coefficient used as parameters. The experiments showed that the smaller the shear modulus of the box was with respect to the ground, the greater the effect of frictional motion on the box surface.

Keywords: Box tunnels, Seismic shear deformation, Shear soil tank test, aluminum rods model ground, FE analysis

INTRODUCTION

The interaction between the structure and surrounding ground must be properly evaluated during the seismic design because underground structures, such as cut and cover box tunnels, are surrounded by ground. In general, seismic motions that should be considered in seismic design are those caused by inertial forces or shear deformation of the surround-ding ground. As most underground structures have a relatively large inner space, the influence of inertia forces is small, while the influence of ground displacement is dominant. The interaction force that deforms the box during ground displacement is considered highly dependent on the shear modulus ratio G_g/G_s, which is the ratio of the ground stiffness G_g (i.e., the shear modulus of the ground) to the box stiffness G_s (i.e., the shear modulus of the cut and cover tunnel frame). The interaction forces can be roughly divided into the shear force along the peripheral surface of the box and the normal force on the peripheral surface of the box. When evaluating the shear force, frictional motion (the presence or absence of sliding) should be considered.

In previous research, we conducted simple shear tests on a model where the ground comprised stacked aluminum rods, with boxes of different shear modulus embedded to investigate the effect of the shear modulus ratio on the interaction forces [1]. However, in this study, we did not fully investigate the frictional motion of the peripheral surface of the box. Therefore, in the present study, we conducted experiments using three different model boxes with different box stiffness values G_s, with and without friction reduction on the surface of the box (which was used as a parameter), to investigate the frictional motion of the box (in particular the presence or absence of sliding).

OUTLINE OF EXPERIMENT

Model Ground and Test Apparatus

The model ground was constructed by piling up a mixture of 150 mm long aluminum rods of three different diameters (1.5 mm, 2 mm, and 3 mm) in a weight ratio of 1:1:1. We iteratively piled the aluminum rods to a depth of 20 mm and then compacted them using a small vibrator and a 200 mm × 150 mm plate, preparing a model ground with a unit weight of 21.0 kN/m^3.

Figure 1 shows the test apparatus used in the experiments. The shear soil tank has pin hinges at the top and bottom of the left- and right-side walls to allow for simple shear deformation. We capped the model ground constructed in the soil tank with a lid, applied an overburden pressure w to it, and used a jack to apply a horizontal load to the soil tank itself to induce a simple shear deformation in the model ground.

The overburden pressure was set to w = 3.07 kN/m^2, corresponding to a vertical stress σ_v of 4.8 kN/m^2 at the top surface of the model box. Note that the inner surface of the soil tank and the underside of

the top lid were in direct contact with the aluminum frame and aluminum rods.

We installed model boxes with a width and height of 40 mm at the center of the model ground and generated simple shear deformations within the model ground to simulate the behavior of the box during an earthquake. In the experiment, we directly measured the load of the jack used to deform the soil tank and the displacement of the side walls, and then used image analysis to calculate the shear strains on the model box and ground.

Model Boxes

The three model boxes used in this study were made of materials with different box stiffnesses G_s, which are listed in Table 1. The friction conditions were set as experimental parameters and are shown in Table 2. Under Case F1, the friction is cut using a Teflon sheet. Under Case F2, the friction is not cut, and the coefficient of friction is 0.85.

To simulate the burial of the model boxes, we arranged three blocks with a width of 40 mm, height of 40 mm, and depth of 30 mm at equal intervals in the depth direction and embedded them in the model ground. Note that the box stiffness G_s shown in Table 1 is the entire shear modulus of the model box, averaged in the horizontal depth direction.

RESULTS OF EXPERIMENTS

Characteristics of the Model Ground

A total of six boxes were tested twice using three values of box stiffness G_s (90, 199, and 453) and two types of skin friction conditions (F1 and F2). Figure 2 shows the relationship between the experimentally obtained model ground shear stress τ and soil tank shear strain γ_{gf}, and Fig. 3 shows the relationship between the ground stiffness G_g and soil tank shear strain γ_{gf}. The shear stress τ was determined by dividing the jack load by the contact area of the lid, and the soil tank shear strain γ_{gf} was determined by the amount of angular change in the side wall. The ground stiffness G_g was obtained as the secant modulus by dividing the shear stress τ by the shear strain γ_{gf} of the soil tank at that time.

Figures 2 and 3 clearly show that the model ground exhibits nonlinearity at the microstrain level. The ground stiffness G_g varied with the soil tank shear strain γ_{gf} and was obtained by averaging the values at three strain levels, as outlined in Table 3.

Relationship Between the Shear Strain of the Model Box and Surrounding Ground

Figure 4 shows the relationship between the experimentally obtained shear strain of the box γ_s and

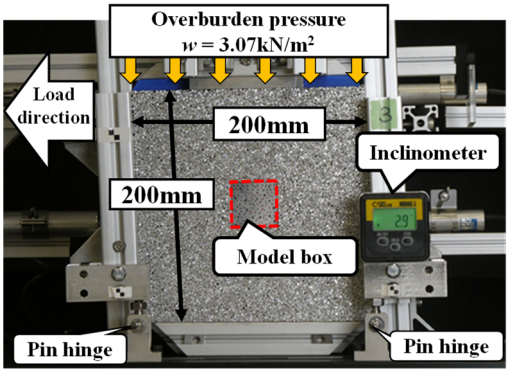

Fig. 1 External view of test apparatus.

Table 1 Box stiffness G_s of model boxes used in the experiment

Case Name	Case1	Case2	Case3
G_s (kN/m²)	90	199	453

Table 2 Friction conditions

	Friction conditions
F1	With friction cut by Teflon sheet
F2	Without friction cut

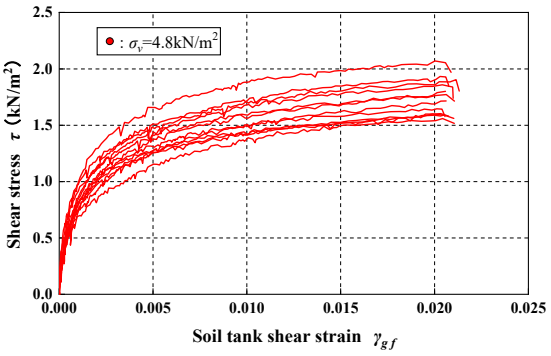

Fig. 2 Relationship between shear stress τ and soil tank shear strain γ_{gf}.

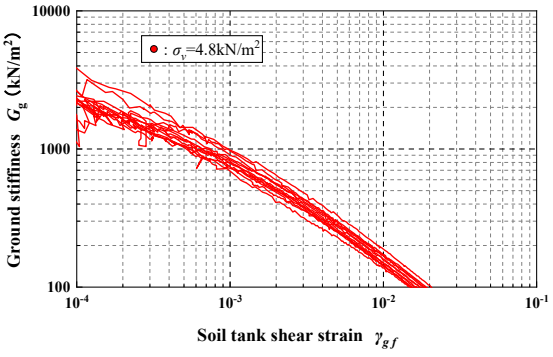

Fig. 3 Relationship between ground stiffness G_g and soil tank shear strain γ_{gf}.

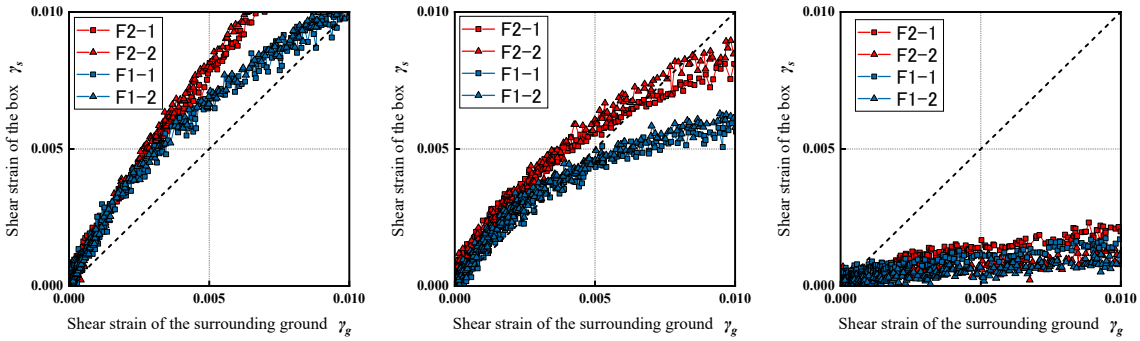

(a) (b) (c)

Fig. 4 Relationship between shear strain of the box γ_s and of the surrounding ground γ_g: (a) case 1 G_s = 90 kN/m^2; (b) Case 2 G_s = 199 kN/m^2; (c) Case 3 G_s = 453 kN/m^2.

of the surrounding ground γ_g. Note that Fig. 4 is organized according to the experimental cases detailed in Table 1. To calculate the shear strains, we used image analysis to find the vertex displacement in a rectangular area (about 120 × 120 mm) around the model box and the surrounding ground and then calculated the strains by assuming that each region was a constant strain element [1].

Figure 4 shows that as the box stiffness G_s increases, the box strain γ_s decrease, confirming the same pattern observed in our previous study [1]. The relationship between the shear strain of the box γ_s and of the surrounding ground γ_g was different with and without friction reduction after γ_g = 0.005 in Case 1 and γ_g = 0.0025 in Case 2. In Case 3, where the box stiffness G_s was large, there was no clear difference between the cases with and without friction reduction.

These tendencies indicate that the sliding motion on the surface reduces the strain on the box, and the reduction of friction can be expected to improve the seismic resistance; however, the smaller the box stiffness, the greater the effect, and the greater the box stiffness, the smaller the anticipated effect.

FE ANALYSIS

Overview of Analysis

Our experiments revealed that the relationship between the shear strain of the box γ_s and of the ground γ_g of the ground changed depending on the friction reduction conditions of Case 1 and Case 2. To reproduce this tendency in an analytical study, we conducted a two-dimensional finite element analysis.

The analytical model used in the FE analysis is depicted in Fig. 5. In the FE analysis, we modeled both the box and the ground as square 2 × 2 mm plane strain elements, with the box positioned in the center of the ground. A joint element was also provided between the box and ground elements to account for the effects of sliding and separation.

The load conditions in the analysis were

Table 3 Box stiffness G_s of model boxes used in the experiment

Soil tank shear strain γ_{gf}	0.001	0.005	0.01
G_g average value (kN/m^2)	797.2	272.1	155.6

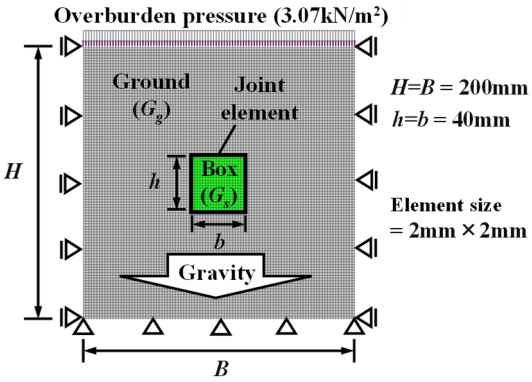

(a)

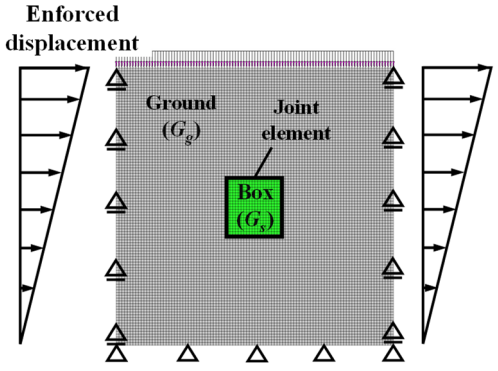

(b)

Fig. 5 Diagram of the analytical model and conditions used for the FE analysis: (a) initial step; (b) Enforced displacement step.

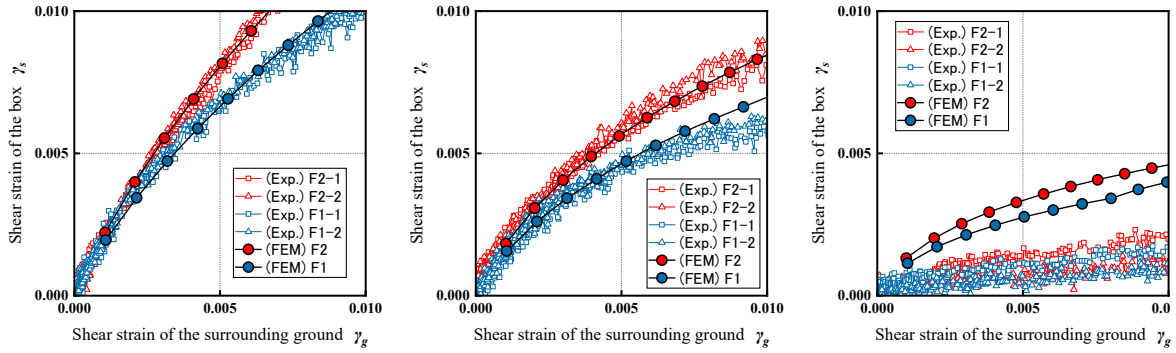

(a) (b) (c)

Fig. 6 Comparison of the relationship between the shear strain of the box γ_s and of the ground γ_g obtained by either experiments or by FE analysis: (a) case 1 G_s = 90 kN/m^2; (b) Case 2 G_s = 199 kN/m^2; (c) Case 3 G_s = 453 kN/m^2.

implemented as follows. After applying the gravity and the overburden pressure in the initial step, we subjected the ground to rightward enforced displacement to simulate a linear tilt on both sides of the soil tank to induce simple shear deformation of the model ground. The boundary conditions were set as fixed to the bottom and horizontally fixed to the sides for the initial step before being fixed to the bottom and vertically fixed to the sides during the enforced displacement loading.

We used the same values of box stiffness G_s in the FE analysis as used in the experiments, as detailed in Table 1. To express the characteristic that the ground stiffness G_g decreases with an increase in the shear strain γ_{gf} of the soil tank, we used

$$G_g = 6.32 \times \gamma_{gf}^{-0.702} \quad (1)$$

to set the equivalent linear stiffness according to the soil tank shear strain γ_{gf}. Note that Eq. (1) is an approximation of the relationship between the ground stiffness G_g and the soil tank shear strain γ_{gf} shown in Table 3.

The Poisson's ratio ν of the ground was set as ν = 0.3 based on a previous analytical study of aluminum rods model ground [2]. And for the box, ν = 0.499 because the model material used in the experiment was a dense rubbery material and was considered incompressible. The unit weight of the box was set to a value based on the specific gravity of the materials used in the experiment, while the unit weight of the ground was set to a value based on the unit weight of the model ground. The boundary between the box and the ground was a joint element that models Coulomb's friction law. The friction coefficient μ was set to μ = 0 (an extremely small value in the analysis) for Case F1 (with friction cut by the Teflon sheet) and μ = 0.85 for Case F2.

Analysis Results

Figure 6 shows the relationship between the shear strain of the box γ_s and of the ground γ_g obtained from the 2D FE analysis, along with the corresponding results obtained from the experiments.

The experimental results, including the effects of cutting the friction, were accurately reproduced by the analysis for Cases 1 and 2. However, while the analysis reproduced the small effect of the presence or absence of the friction cut for Case 3, the results do not quantitatively match, possibly because the equivalent linear model does not reproduce the smaller shear strain of the box in the experiment due to the pre-dominant rotation of its bottom caused by the nonlinear behavior of the ground near the bottom.

CONCLUSIONS

In this study, we conducted model experiments and an FE analysis with three different model boxes of different box stiffness values G_s, both with and without friction reduction on the surface of the box. Our experimental and analytical investigations confirmed that cutting friction as a seismic countermeasure was effective when the box stiffness was small but not when the box stiffness was large.

REFERENCES

[1] Shimada T., Nishino F. and Nishioka H., Experimental Study on the Effect of Nonlinearity of Ground on Shear Strain Ratio in Cut and Cover Tunnel During the Earthquake, Journal of Japan Society of Civil Engineers, Ser. A1 (Structural Engineering & Earthquake Engineering (SE/EE)), 2022. “In press, in Japanese”

[2] Akagi H., Sato K. and Kiriyama T., Numerical Study on Load-settlement Relationships of Shallow Foundation Under Extremely Low Confining Pressure, Proceedings 6th International Conference on Particle-Based Methods - Fundamentals and Applications, Barcelona, Spain, 2019.

8th Int. Conf. on Structure, Engineering & Environment (SEE), Mie, Japan, Nov.10-12, 2022, ISBN: 978-4-909106094 C3051

GLOBAL DAMAGED INDEX ASSESMENT OF DYNAMIC LOADS BASED UPON ARTIFICIAL NEURAL NETWORKS

Widya Apriani[1], Reni Suryanita[2] and Hendri Rahmat[3]
[1,3] Civil Engineering, Lancang Kuning University, Indonesia
[2]Civil Engineering Department, Faculty of Engineering University of Riau

ABSTRACT

Disasters due to the collapse of bridge structures that cannot be predicted in advance require enormous rehabilitation costs. This is caused by a decrease in ability or damage that cannot be identified earlier (early warning). The difficulty of directly predicting the condition of the bridge structure is caused by the limitations of the test equipment and the testing environment conditions. Structural Health Monitoring (SHM) is an effort to identify damage, including determining the event, location and severity of each damage. This study aims to evaluate the Damage Index condition of the bridge structure due to the dynamic load of the bridge so that it can be used for planning maintenance of rational and economical structures. The study centered on various dynamic loads from the analysis of Steel Arch bridges. The damage detection approach is based on Artificial Neural Networks (ANN) with the help of the MATLAB computer program. In this study, the Global damage index uses the parameters of acceleration, velocity, displacement, and stiffness reduction. The newly proposed damage expression combines the top three influential engineering determining parameters (EDPs). In this study, ANN method requires structural dynamic response statistics as a damage index for SHM so that it can predict the health condition of bridge structures quickly. Then, verification is carried out using the finite element method program. The results are A comparison between the proposed GDI with Park- Ang GDI. The Proposed Damage Estimation method produces a relative index that is 20% higher than that of Park-Ang. The R-value for training and testing of ANN ranges from 97.2% to 97.6%, which shows that the ANN predictions for displacement, velocity, and center span acceleration of the bridge structure can represent 97.2% to 97.6% of all data. This shows that the level of accuracy of the target value with the predicted value of ANN is very good.

Keywords: Artificial neural network, Steel arch bridge, Bridge condition, Global damage index

INTRODUCTION

Bridge structure has a risk of susceptibility to damage and decreased strength during its service life due to various factors, with earthquakes being one of the most severe. The structure needs to be monitored with a Structural Health Monitoring System tool to prevent the danger of structural failure due to disasters occurring (Mardiyono et al., 2012), resulting in the loss of property and many lives (Hait et al., 2019). In this study, the case study is the Siak III Bridge, which was built in 2011. This type of bridge is a curved steel frame that has a length of 120 meters, a height of 11 meters and a width of 11 meters, the type of girder is a steel structure (Muslikah, 2011). This bridge is not equipped with a bridge SHM tool. This bridge is located in Indonesia, where the country is known as the ring of fire for earthquakes with moderate to high earthquake risk levels (You et al., 2014).

To predict the condition of the bridge, there are several methods that can be applied, among then are field visualization (Park et al., 2001) and numerical prediction (Apriani & Lubis, 2019). However, to date, procedures that require data and time as well as high accuracy are needed. Damage assessment procedures using the Damage Index (DI) on bridges can be applied (Park et al., 2001). DI is generally defined as the ratio of the initial resistance capacity to the reduced resistance capacity of a structure. Comprehensive reviews have been done with well-narrated damage assessment structures for the determination of the local Damage Index and GDI for buildings (Kurniawandy & Nakazawa, 2019) and bridges (Suryanita & Adnan, 2013). Park-Ang DI for the MDOF system has introduced the Damage Index method (Hait et al., 2019). From the literature review, the building DI was evaluated using the maximum deformation and cyclic loading as described in the Park-Ang method. It is stated that the deviation value in a four-storey building can be predicted, but it is difficult to apply if the number of floors of the building increases, because it requires accurate calculations and requires a large amount of time. For large-scale investigations, this method is difficult to apply. In this study, the method proposed to assess the damage is the Global Damage Index (GDI) method with the Proposed Damage Estimation Procedure approach. This method combines many engineering determining parameters (EDP), such as acceleration, velocity, and maximum displacement. The EDP was combined into an equation by multivariable

regression (MVR) analysis . A correlation has been established between the Park-Ang GDI and EDP by MVR analysis. The application of this method to a multi-storey building structure shows satisfactory results. Therefore, this study will apply the GDI method as the proposed damage estimation procedure.

METHODOLOGY

This research consists of the stages of diagnosis, analysis, and verification. The diagnosis begans with a numerical analysis model and experimental bridge girder. This phase was done by entering data input into the finite element program to then be used as input data on artificial neural networks with the help of a computer program called MATLAB. The designed bridge girder was subjected to NLTHA analysis under real earthquake ground floor motion to reveal true elastoplastic behavior. Adopting the Park-Ang method assumes that all members are corrupted and all DI members are estimated to determine global damage. It is, therefore, very important to know the level of vulnerability that reflects the actual condition of the building after an earthquake. In this study, a new damage expression is proposed to combine the top three influential EDPs as an option to estimate structural DI. The diagnosis phase was carried out by comparing the results obtained from ANN analysis with the finite element method program (SAP, 2000). Furthermore, testing is done to reflect the actual conditions as a basis for condition assessment (Asmarani et al., 2020). Based on the simulation carried out, the total weight of the passing vehicle was generated based on the recorded dynamic response. Artificial neural network planning is carried out with the stages of training and evaluation stages and preparing the data beforehand.

Ground Motion Selection

The time historical ground motion of an earthquake provides an overview of the intensity, a measure related to a certain level of disaster, namely the return period, which will describe the magnitude, distance to the epicenter, site conditions, and several parameters that determine the characteristics of the ground motion characteristics (Wahyudi, 2017). It is necessary to pay attention to the selection of records with the appropriate magnitude because this has a very large influence on the frequency content and duration of ground motion. A means of selecting and scaling the time history record of real earthquake accelerograms to match the response spectrum of the design earthquake acceleration according to Seismic Code Indonesia (SNI 1726-2012) has been carried out covering the period range period 0.05 until 4.0 seconds. Then, the response spectrum analysis is applied to the adjusted accelerogram and a response spectrum graph is generated that closely follows the design response spectrum as the target.

Indent are two ways to modify a time history record to fit the design response spectrum, namely: (a) scaling in the time domain, and (b) scaling in the frequency domain. The scaling procedure in the time domain is carried out to obtain the minimum difference squares between the ground motion response spectrum and the target spectrum (minimum least squares method), namely:

$$[difference] = \int_{T_B}^{T_A} \left[\alpha S_a^{actual}(T) - S_a^{target}(T)\right]^2 DT \quad (1)$$

Where the actual Sa is an actual earthquake acceleration response spectrum. Sa target are the target earthquake acceleration response spectrum. α is a scale factor. T are oscillator period. TB is lower boundary period of scaling. TA is upper limit period of scale. By differentiating equation (1) once against α and then equating it to 0 (zero), a scale factor will be obtained:

$$\boldsymbol{\alpha} = \frac{\sum_{T=T_B}^{T_A} (S_a^{actual} - S_a^{target})^2}{\sum_{T=T_B}^{T_A} (S_a^{actual})^2} \quad (2)$$

The results shown in fig. 1 are the results of modifying a time history record to fit the design response spectrum from Imperial Valley earthquake data to Pekanbaru-Indonesia response spectrum data.

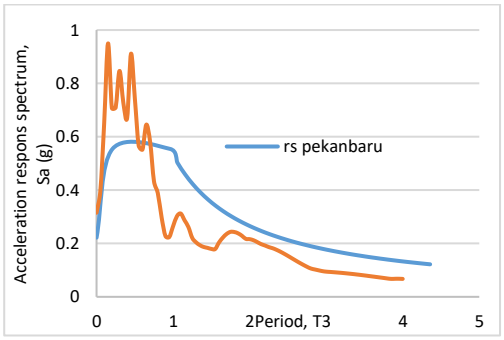

Fig. 1 Acceleration Response Spectrum adjusted for location at Pekanbaru, Indonesia.

So that the earthquake accelerogram response spectrum is obtained which is adjusted for the following Pekanbaru city:

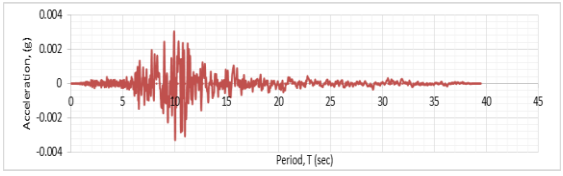

Fig. 2 Earthquake accelerograms adapted for the

city of Pekanbaru

Model Selection

The model used is a steel arch bridge with a length of 168 m. Bridge structure elements consist of arch rib frame (1200x800 x 24mm), hanger (100 mm, fy is 490MPa), tie beam (600x600x24mm), concrete floor beam (400x400 mm). Type of structure is JIS G 3106 SM YB, stress yield (fy) is 295 MPa, modulus of elasticity existing condition is 200,000 MPa, and specific gravity is 78.5 kN/m^3.

Table 1 Damage scenarios of steel Hollow Beam

Damage Case	Stiffness reduction, SR (%)	Young Modulus (MPa)
1	10	180000
2	20	160000
3	30	140000
4	40	120000

The equipment needed in this research is supported by the Engineering Laboratory of the University of Riau, including LVDT. To measure the vibration, the LVDT sensor is installed on the bridge girder. Furthermore, the resulting dynamic response data is recorded with a data acquisition unit (Data Acquisition Device). The data are stored for later processing with calibration result data. Calibration is done using acceleration data. The following are the results of modifying a time history record to fit the design response spectrum from Imperial Valley earthquake data to Pekanbaru response spectrum data.

Experimental Procedure: Analyzed Similitude Girder

The girder element in this case study has a large dimension and cannot be tested in a laboratory. Therefore, modeling is made using the similitude method, namely scaling the dimensions of the model dimensions, loading, and material parameters to be smaller. Experimental models using the LVDT tool were used to obtain estimates of lateral deflection and lateral strain due to loading. The similitude girder results were further validated by the results with the use of the LUSAS program (Tan et al., 2017). The results show the maximum load that can cause the girder to melt, which is the reference in the deflection analysis in FEM and ANN. Bridge girder number 11 is modeled to be a simple supported I beam using an analyzed similitude girder with a scale ratio of 1: 5. The LVDT tool is attached to both sides of the end of the girder. The planned load is in stages from 10 to 60 kN. The load is applied through the loading plate as pressure on the beam, as shown in Figures 3.

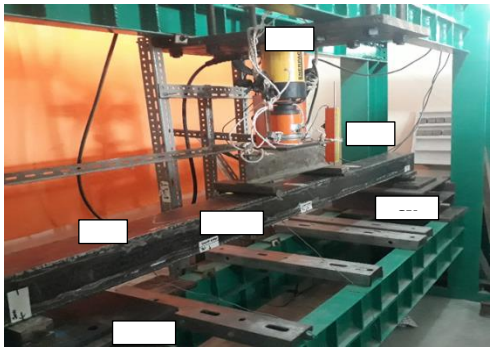

Fig 3 Schematic diagram of the laboratory girder of arch bridge model.

Existing DI of Structure

A method for estimating DI is based on several responses, such as ductility, displacement, joint rotation and no. of the inelastic loop. Among them, Park-Ang DI, a significant and well-known method, was adopted in this study. The formula for determing DI as proposed by Park and Ang is given in Eq. (3)

$$\boldsymbol{DI} = \left(\frac{\boldsymbol{\delta_M}}{\boldsymbol{\delta_u}} + \frac{\boldsymbol{\beta}}{\boldsymbol{Q_y \delta_u}} \int \boldsymbol{dE}\right) \qquad (3)$$

When Damage Index is equal to 0, it indicates no breakdown, DI indicates total damage or collapse, δM is maximum deformation under earthquake, δu is highest deformation under monotonic loading, Qy is calculated yield strength, dE is incremental absorbing hysteretic energy and β is a non-negative parameter.

This is complicated, because you have to enter the parameters one by one for each girder. Furthermore, the parameters of acceleration, velocity, and maximum displacement on each girder are also input to the GDI calculation of the Proposed Damage Estimation Procedure method, which is more complete and faster in analyzing.

Proposed Damage Estimation Procedure (EDPs)

The proposed damage procedure is a combination of parameters that most influence the occurrence of global damage. This is under the corresponding Eq. (2). The EDP was combined into equations by multivariable regression (MVR) analysis. A correlation has been formed between Park-Ang GDI and EDP by MVR analysis and the DI expression is mentioned in Eq (2). This concept applies nine factors, namely acceleration direction x, y and z (%), velocity direction x, y, and z, as well as displacement direction x, y, and z for four planned stiffness reductions, namely 20%, 30%, and 40 %. The parameter coefficient is determined by the MVR analysis. The parameters are a combination of nine effect EDPs and estimates 21 data points from the simulation considered by the model. Given the maximum value of the parameter, GDI is estimated

from a structure directly using Eq. (2).

GDI = -0,0102 X1+ 0,0045 X2 + 0,00162 X3 + 0,3897 X4 + 0,01808 X5 + 0,04159 X6 + 0,02328 X7 - 0,0035 X8 - 0,00339 X9 (4)

Predictive Model Based on ANN

On the other hand, to predict GDI, the ANN model was used based on the damage model. The summary of the proposed method can be expressed by several parameters, such as acceleration, velocity, and displacement. In Park-Ang DI, only deformation and dissipating hysterical energies are considered. Artificial neural networks (ANN) are derivatives of the biological nervous system. This method has reliability if used to complement the Structural Health Monitoring System (SHMS). With ANN, predictions of structural health conditions can be done quickly, because, in the process, ANN mimics the workings of the human brain.

The backpropagation algorithm belongs to the restricted learning class, where the learning algorithm is trained on the examples of desired behavior. In a multi-layer backpropagation network, the output from one layer becomes input to the next layer. The steps below are for predictive model based on ANN.

Step 1: Initialize the weights to initialize a small random value.

Step 2: A set of training is chosen randomly and put into a neural network. For each pair of training, steps 3-8 are repeated.

Step 3: The first layer receives the input signal hi and sends this to the adjacent layer (hidden unit). Each hidden unit (zj, j = 1, ...) adds the weighted input signal as:

Step 4: Each output unit (yk, k = 1, ..., n) sums the weighted input signal as:

$$(y_{in})_k = (w_o)_k + \sum_{j=1}^{m} z(w_j)_k \quad (5)$$

And apply the activation function to calculate the output signal, $yk = \theta\ (yin\ k)$.

Step 5: Each unit of output (yk, k = 1, ..., n) receives a target pattern that matches the input training pattern, calculates the error information term

$$\delta_k = (d_k - y_k)\theta(y_{in})_k \quad (6)$$

Calculate a weighted correction term (used to update wjk later)

$$\Delta wjk = \alpha\delta kzj \quad (7)$$

$$\Delta w0k = \alpha\delta k \quad (8)$$

Step 6: Each hidden unit (zj, j = 1, ...) adds the delta input and multiplies it by the derivative of the activation function to calculate the error information,

$$(\delta in)\ j = \sum_{i=1}^{n} \delta_k w_{jk} \quad (9)$$

$$\delta \mathrm{j} = (\delta in)\ \theta(z_{in})_j \quad (10)$$

$$\Delta wij = \alpha\delta jxj \quad (11)$$

$$\Delta w0j = \alpha\delta j \quad (12)$$

ANN modeling was executed using MATLAB (2013a). Sharing training data and testing the ANN model was carried out according to Shahin et al. (2004). The ANN model is trained by 70% data and tested by 30% data. Statistically, the obtained training statistical parameters and test data. In this approach, backpropagation has been adopted. The neural architecture of the network model is optimized by the nine numbers of neurons in the hidden layer of the Internet by trial and error. The ANN model performance is reported in terms of two statistical parameters: mean squared error and the linear correlation coefficient (R). Levenberg-Marquardt optimization and weight backpropagation bias function were used to better generalize to training data.

Data inputted by ANN consist of nine input layers and nine neurons. which are displacement, velocity and acceleration. The sum of iteration done is 1000 times and the correlation coefficient value approaches one.

The verification phase is done by comparing the results obtained from ANN analysis with the finite element method program. Based on the bridge detail survey data in the form of bridge structure dimensions and, material characteristics, a bridge structure model can be using the finite element method. The bridge structure model is made by adjusting the calibration results and bridge load stress results of the bridge structure, then loading simulation that can respond in the form of strain due to vehicles that cross over the bridge. Based on the simulations that have been carried out, the total weight of the vehicle passing is based on the dynamic response that has been recorded.

RESULT AND DISCUSSION

Table 2. shows the difference in displacement test results in the similitude mode test and compared with the results of the LUSAS analysis on bridge girder number 11. The results show that the increased load results in greater deflection. Displacement in experimental testing showed a greater result of 0.55% compared to using LUSAS. The first melting condition occurred at a load of 50 KN with a deflection of 11.92 kN. The difference between the maximum deflection results from the analysis of the similitude and LUSAS methods at 50 kN loading was 3.404 mm. Loads above 50 kN show a more gentle graph, meaning that, during this time, the girder elements have begun to experience strain hardening. The maximum load value is used as a reference for making stiffness reduction (RI) simulations for ANN analysis with a maximum of 50% with a range of 20%, 30%, 40%, 50 and 60%.

Table 2 Results of Flexural Structure Laboratory Testing with LVDT 1 and LVDT 2

Load (kN)	Displacement 0,25 L (mm) (LVDT 1)		Displacement 0,25 L(mm) (LVDT 2)	
	Lusas	Experimental	Lusas	Experimental
10	1.015	1.78	1.528	2.26
20	2.031	3.32	3.056	4.3
30	3.046	4.82	4.585	6.46
40	4.061	6.48	6.113	8.88
50	5.076	8.48	7.642	11.92 (yield)
60	6.49	11.56	9.9	16.66

From Fig. 4 it can be seen that the deflection in the middle of the span on the graph coincides between the results obtained from the LUSAS program (65.14 mm) and experimental results (65.88 mm). At lines above 50 KN, melting begins with a deflection value of 11.92 mm

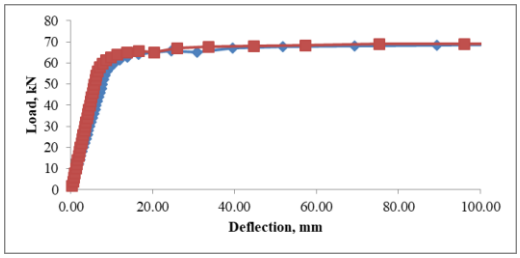

Fig. 4 Deflection in LUSAS and experimental

Therefore, the reduction in stiffness is limited to 50 KN. There is a good agreement between the predicted values and the experimental data. The testing of girders has been analyzed with the help of the SAP 2000 and LUSAS programs. Based on the results of laboratory tests, the maximum deformation and cyclic loading are input to the DI calculation of the Park-Ang method.

A comparison between the proposed GDI with Park- Ang GDI has been plotted in Fig. 5. Comparison between the Park-Ang Damage Index and the Proposed Damage Estimation Procedure are made to the maximum load value, which is used as a reference for making a stiffness reduction (RI) simulation, which is a maximum of 50%.

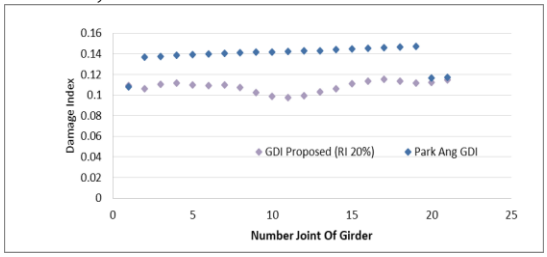

Fig.5 Compared Global Damage Index and Park-Ang Damage Index

The Proposed Damage Estimation Procedure method produces a 20% higher relative index compared to Park-Ang. The Park-Ang method only uses the maximum deformation parameter and cyclic loading as the main parameters. Meanwhile, the proposed GDI uses more complex determining parameters (EDP), such as acceleration, velocity, and maximum displacement.

ANN is performed after data input in the form of GDI values is obtained. The trial process was carried out approximately 150 times on the variation of ANN training parameters; the best training results were obtained with the number of iterations of 50000 epochs, a learning rate coefficient of 0.05, a range of normalization of maximum to minimum variables of 0 - 0.5, and one hidden layer with the number of neurons as many as 10 neurons.

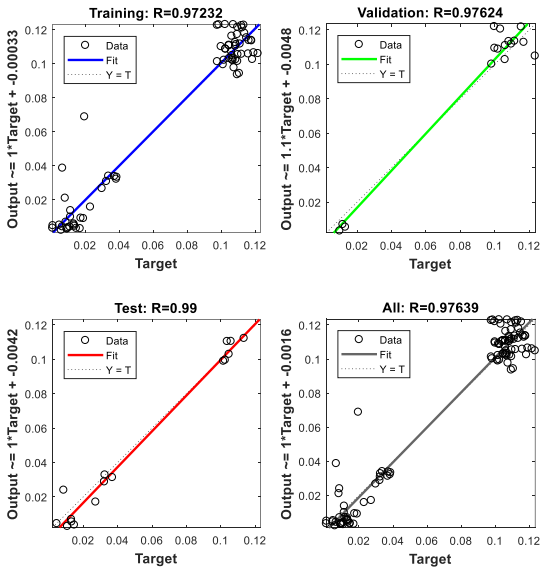

Fig. 6 Coefisien of determination (*R*)

To determine the accuracy of the target value with the ANN prediction value, the coefficient of determination (R) is shown in Fig.6. If R is 1, then the ANN prediction results for the target are considered accurate and the predicted results are close to the real one. Calculation of R for displacement, velocity, and the acceleration for the X, Y, and Z directions are shown in Table 5 and Table 6. Based on the two tables, for the results of training and testing, the R values were obtained ranging from 97.2% to 97.6%. From this value, it can be concluded that the ANN prediction for displacement, velocity, and middle spans of the bridge structure girder can represent 93.0% to 97.2% of all data. This shows that the level of accuracy of the target value with the ANN prediction value is very good.

The iteration process is carried out until the ANN error rate is smaller than the desired error rate limit (MSE). However, the iteration process can also stop if there are too many iterations and the error rate does not show a decreasing pattern. In addition to calculating the MSE value, the coefficient of

determination (R) is also calculated to determine the accuracy of the ANN prediction results. If the R-value gets closer to 1, this indicates that the ANN prediction results are getting closer to the real one (target).

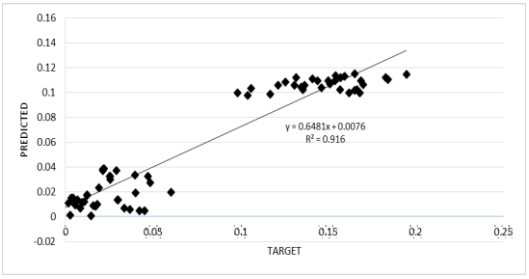

Fig. 7 Plot damage indexed prediction vs. target

The comparison between the predicted severity and target data for the test data set is shown in Figure 10. Based on Figure 10, the ANN that has been trained has been able to predict the Global Damage Index very well. This is indicated by the sufficient proximity of the distribution of the target and predicted points to the diagonal line. ANN succeeded in predicting the severity of the damage for the test equipment which was close to the actual output. The results also look quite reasonable and the test set error has very similar characteristics without over-fitting.

CONCLUSION

A comparison of the two methods of Park Ang and Pusposed has been carried out on the case study of the bridge box girder in this paper. ANN is used to evaluate the accuracy of the analysis. Based on the findings of this study the following conclusions were drawn.

1. A comparison between the proposed GDI Park – Ang GDI has been analyzed. The Proposed Damage Estimation Procedure method produces a relative index that is 20% higher than that of Park Ang. The Park Ang method only uses the maximum deformation parameter and cyclic loading as the main parameters. Meanwhile, the proposed GDI uses more complex determining parameters (EDP) such as acceleration, velocity, and maximum displacement. Artificial Neural Networks model based on acceleration, velocity, and displacements data domain indicated that all MSE models have the same trend after 50000 iterations.
2. The R-value for training and testing of ANN ranges from 97.2% to 97.6% which shows that the ANN predictions for displacement, velocity, and center span acceleration of the bridge structure can represent 97.2% to 97.6% of all data. This shows that the level of accuracy of the target value with the predicted value of ANN is very good.

ACKNOWLEDGMENTS

Gratitude to the Ministry of Research, Technology and Higher Education of Indonesia Grant for Higher Education Cooperation Year 2019–2020, Ministry of Public Works and Public Housing Indonesia and Civil Engineering Study Program at Lancang Kuning University.

REFERENCES

[1] Hait, P., Sil, A., & Choudhury, S. (2019). Overview of damage assessment of structures. *Current Science*, *117*(1), 64–70. https://doi.org/10.18520/cs/v117/i1/64-70

[2] Kurniawandy, A., & Nakazawa, S. (2019). Seismic performance evaluation of existing building using Seismic Index method. *MATEC Web of Conferences*, *276*, 01015.

[3] Neves, A. C., González, I., Leander, J., & Karoumi, R. (2017a). Structural health monitoring of bridges: a model-free ANN-based approach to damage detection. *Journal of Civil Structural Health Monitoring*, *7*(5), 689–702. https://doi.org/10.1007/s13349-017-0252-5

[4] Tan, Z. X., Thambiratnam, D. P., Chan, T. H. T., & Abdul Razak, H. (2017). Detecting damage in steel beams using modal strain energy based damage index and Artificial Neural Network. *Engineering Failure Analysis*, *79*(January), 253–262. https://doi.org/10.1016/j.engfailanal.2017.04.035

[5] Widya Apriani, Fadrizal Lubis, R. S. and Y. F. (2019). Proceedings of AICCE'19: The Evaluation of Changes in Camber Position to Deflection of Arch Steel Bridge in Extreme Loads. In I. Marco di Prisco, Politecnico di Milano, Milano (Ed.), *Proceedings of AICCE'19 : The Evaluation of Changes in Camber Position to Deflection of Arch Steel Bridge in Extreme Loads* (pp. 843–853). Springer. https://link.springer.com/chapter/10.1007/978-3-030-32816-0_62

8th Int. Conf. on Structure, Engineering & Environment (SEE), Mie, Japan, Nov.10-12, 2022, ISBN: 978-4-909106094 C3051

STRUCTURAL DESIGN OF SEISMIC ISOLATION FOR TEMPLE AND SHRINE

Yasuhide Mochida[1], Kengo Wada[1]
[1]Ritsumeikan University, Japan [2]Graduate School of Science and Engineering, Ritsumeikan University, Japan

ABSTRACT

Seismic isolation is known as effective for saving traditional architecture. However, there are only a few existing seismic wooden buildings, because traditional building has great variability of material and structural characteristics. Thus, I suggest new type of design flow for temple and shrine, which consider this dispersion. This flow consists of three stages: seismic diagnosis for original building, seismic diagnosis for seismic isolated building and force test. Considering scattering, force test plays a very important role. Then, I evaluate the usefulness of the flow by virtual building. As a result of the evaluation, it becomes clear that by fitting the interlayer deformation angle of seismic isolated building in maximum elastic deformation angle of original building, force test is possible. Through this test, I can obtain "true restoring force characteristics of original building", which solves these problems. Lastly, I notice that by using this data, design flow is useful for designing Seismic Isolation Retrofit of temple and shrine.

Keywords: Seismic isolation retrofit, force test, Restoring force, Seismic diagnosis

INTRODUCTION

Given the damage to traditional wooden buildings caused by earthquakes, it is important to improve the durability of traditional wooden buildings. To improve durability, seismic isolation retrofitting of traditional wooden buildings is being promoted. However, the number of seismic retrofits of existing traditional wooden buildings is very small. The reason for this is the large variation in the material and structural properties of wooden buildings themselves. In other words, there is a gap between the average estimated performance and the actual value of the building. For this reason, it is considered most effective to directly understand the characteristics of a building in the field by means of microtremor measurements and vibration tests. To date, studies have been conducted to estimate vibration characteristics by collecting various types of measurement data, and to evaluate the resilience characteristics of each structural element by creating a frame model of the entire building. In this study, first, existing examples will be surveyed and analyzed to clarify the construction method of seismic isolation work. After that, we will show the problems that variations in the structural performance of traditional wooden buildings themselves pose to seismic isolation retrofit design, and propose a design flow, which we hope will contribute to the maintenance and preservation of traditional wooden buildings as well as to the seismic isolation retrofit of traditional wooden buildings with high reliability.

OVERVIEW OF SEISMIC ISOLATION RETROFIT CONSTRUCTION

Table 1 shows a list of seismic isolation retrofit construction of wooden structures. The buildings are

Table 1: List of Wooden Seismic Isolation Retrofit Construction

CLASS	A	B	C	D	E	F	G
NAME	Houtoku Ninomiya Shrine worship hall	Yutenji Main Hall	Yotensa Jizo Hall	Hongwanji Obihiro Betsuin Main Hall	Main hall of temple H, Ota-ku, Tokyo	Eiheiji Nagoya Betsuin	Nishi Arai Daishonin Temple
LOCATION	Jonai, Odawara City, Kanagawa Prefecture	Nakameguro, Meguro-ku, Tokyo	Nakameguro, Meguro-ku, Tokyo	Obihiro City, Hokkaido	Ota-ku, Tokyo	Higashi Ku, Nagoya City, Aichi Pref.	Nishi Arai, Adachi-ku, Tokyo
TYPE OF WORKS	Seismic retrofit	Seismic retrofit	Seismic retrofit	Seismic retrofit	Seismic retrofit	new construction	Seismic retrofit
COMPLETION	1894	1860	1718	1929	1612	1953	826年(1971年
CONSTRUCTION PEROID	January 1998～ December 1999	November 2009～ April 2010	January 2014～ August 2015	October 1996～ November 1997	April 2009～ March 2010	February2014～ March2016	April 2008～ October 2008
BUILDING AREA	176	379	74	947	159	436	1624
FLOOR SPACE	176	379	74	947	159	702	2330
NUMBER OF STAIRS	0－1－0	0－1－0	0－1－0	0－1－0	0－1－0	1－1－0	0－2－0
HEIGHT	13.08	11	15	25.45	9.5	17.06	27
STRUCTURE	W+RC(Base)	W+RC(Base)	W+RC(Base)	W+RC(Base)	W+S(Floor)	W+RC(Floor)	RC
SEISMIC ISOLATOR	Laminated rubber : 600φ2 units, 550φ2 units, 350φ1 unit, Viscous damper:2 units	Rolling Bearing:52 units, laminated rubber :10 units, Oil damper:8 units	Viscous damper :4 units, Oil damper:2units	Laminated rubber :450φ20 units, 500φ6 units	Torerubber:5 units,Viscous dampe :58 units, ResinWind-resistant restraining device :2 units	Laminated rubber:4 units、 Viscous dampe:21 units、 Oil damper:4 units	High Damping Laminated Rubber :32 units, Viscous damper :7 units, Oil damper:8 units

classified as temples and shrines and were completed between the 1600s and 1900s. The seismic isolation retrofit work was done between 1996 and 2015. The buildings are all one-story, and the seismic isolation method is the foundation seismic isolation method. The basic construction process is to temporarily receive and dismantle the wooden frame or to construct the foundation slab with towing. In principle, this method does not damage the appearance of the existing building, improves its seismic resistance, and maintains its cultural value. Here, one newly constructed wooden seismically isolated building of a temple and shrine and one reinforced concrete seismically isolated retrofit building were used for comparison.

EXISTING BUILDING DESCRIPTION

Yutenji Main Hall and Shoin

Since this building consists of the main hall, the shoin and the butsuri-den, the renovation was divided into two phases, from the shoin to the main hall. Fig. 1 shows the layout of the seismic isolation system. The seismic isolators consisted of 52 units of linear rolling bearings, 10 units of laminated rubber reinforcing materials, and 8 units of oil dampers. The seismic isolators were installed between the newly constructed RC base and the RC foundation slab. The newly constructed RC foundation supports the upper wooden structure. Fig. 2 shows a cross-section of the seismic isolation layer.

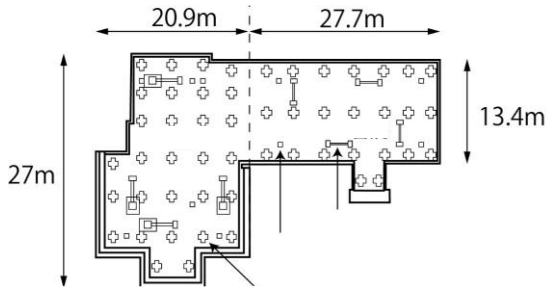

Fig. 1 Layout of seismic isolation system

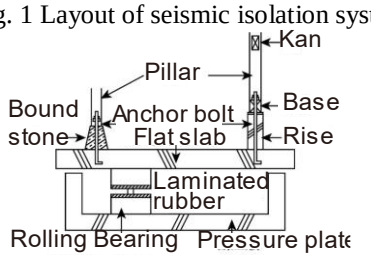

Fig.2 Cross section of seismic isolation layer

Yutenji Jizo Hall

The ground where the Jizo Hall originally stood was excavated and seismic isolators were installed. For the towing work to the original location, the Jizo Hall was raised 50 cm, the floating pillar was fixed between steel frames from both sides, the steel frames were placed on rails, and the Jizo Hall was moved 30 m. The Jizo Hall was then towed to the original location.

Houtoku Ninomiya Shrine Worship Hall

Fig. 3 shows the arrangement of the seismic isolation devices. Five laminated rubber bearings and two adhesive dampers were used for the seismic isolators. The overall construction process was as follows: (1) Once the wooden worship hall was dismantled, a solid foundation was installed on the site. (2) A seismic isolation layer was installed on top of the solid foundation. (3) RC lattice beam foundation is installed on top. (4) Rebuild the wooden portion.

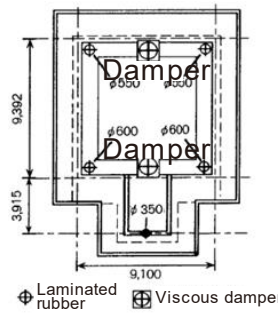

Fig. 3 Layout of seismic isolation layer

Honganji Obihiro Betsuin Main Hall

The seismic isolators used were 26 laminated rubber bearings with lead plugs. The building is supported on direct foundations, but for the renovation, one of the existing foundations was removed and a new deep pile foundation was built on it, and the seismic isolators were installed. The construction procedure was as follows (1) Remove the existing wooden floor and construct a temporary foundation. (2) Construction of reinforced foundation beams on both sides of the existing foundation beams. (3) Remove the existing foundation at the location where the seismic isolation device was to be installed. (4) Deep foundation piles, new foundation, and seismic isolation components were installed at the same location. (5) Remove the remaining existing foundations and temporary foundations. (6) Construct a RC first floor slab on top of the steel floor assembly.

Branch temple of Ikegami Honmonji

Fig. 4 shows the layout of the seismic isolation layers. The building was constructed using the "column leg anchorage" method, in which the seismic isolation devices were directly attached to the column legs. The seismic isolators consisted of 58 units of sliding

bearings and 5 units of laminated rubber reinforcing materials. In addition to the seismic isolators, a wind restraint system was also installed as a countermeasure against wind storms. The construction procedures were in the following order: (1) reinforcement of the shed roof, (2) fixing of the column legs, (3) jack-up, (4) pile press-in, (5) solid foundation driving, (6) installation of the equipment, (7) jack-down, and (8) exterior work such as seismic isolation clearances.

Eiheiji Nagoya Betsuin

This building is a newly constructed seismic isolation. It is a temple building with one basement floor and one ground floor, with an eave height of 10.5 m. The seismic isolation system consists of 20 elastic sliding bearings, four natural rubber laminated bearings and four oil dampers. The seismic isolators used were 20 elastic sliding bearings, 4 natural rubber laminated bearings, and 4 oil dampers. The arrangement of the seismic isolators is shown in Fig. 5. The clearance between the main body and the outer basement wall was set at 600 mm because of relative displacement during earthquakes.

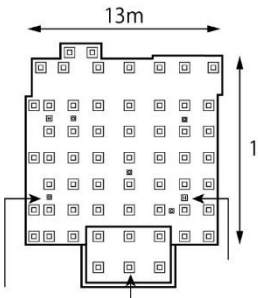

Fig.4 Layout

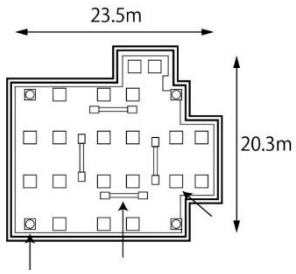

Fig.5 Layout

Nishiarai Daishi Soji Temple

The building is a "mid-level seismic isolation building" with seismic isolators placed at the tops of the first floor columns; because the first floor is seismically isolated, the RC walls under the front staircase and at the rear of the building were removed and replaced with drywall. The seismic isolation system consisted of 7 elastic sliding bearings, 32 laminated rubbers, and 8 oil dampers. The construction procedure was as follows: 1) Temporarily support the superstructure with jacks; 2) Cut the columns; 3) Install the seismic isolation bearings, preload jacks and preload cases underneath; and 4) Place concrete for the lower part of the bearings.

CONSIDERATION OF SEISMIC ISOLATION CONSTRUCTION

Seismic isolation systems for wooden seismic isolation retrofits are often based on sliding supports, restoring rubber, and oil dampers. In addition, the general construction procedure is as follows: temporary bearing jack-up → ground excavation → seismic isolation layer construction → jack-down. Most of the seismic isolation layer construction uses RC foundation slab and RC base of the first floor. The main reason for this is the effective seismic use of the RC foundation for the purpose of weight reduction of the lightweight wooden frame for long-period construction and to establish a rigid floor assumption for the first floor.

PROBLEMS IN SEISMIC ISOLATION

Constant microtremor measurements are used to determine the vibration characteristics of traditional wooden buildings. The natural period of a steel-frame building is proportional to its height, as stipulated in the second bulletins of the 1980 Construction Notice No. 1793, but for a traditional wooden building, as shown in Fig. 6, there is a range between 0.4 and 0.6 seconds for a building 7 m high, for example.

In addition, in structurally evaluating wooden buildings, it is often assumed that the horizontal structural surfaces are rigid. However, most traditional wooden buildings have flexible floors. In a flexible floor, each vertical structural plane behaves non-uniformly depending on the stiffness, bearing capacity, and arrangement of the vertical structure. Since it is difficult to calculate this, the assumption of a rigid floor is often used in the design of seismically isolated buildings.

In addition, as shown in Fig. 7, the natural period varies due to the sliding of the column legs.

Generally, the resilience of traditional wooden buildings is evaluated on a street-by-street basis using the deformation increment method. However, as

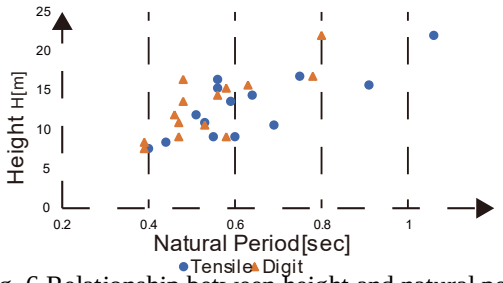

Fig. 6 Relationship between height and natural period

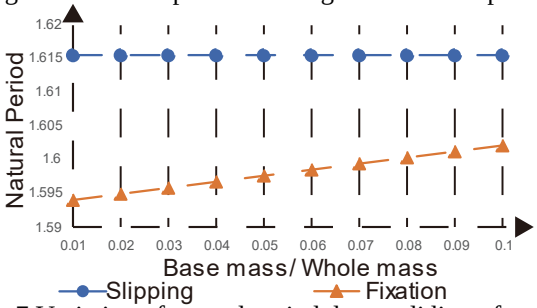

Fig. 7 Variation of natural period due to sliding of column legs

shown in Fig. 8, the effect of the PΔ effect due to vertical loading is expected to cause variation in the restoring force.

SOLUTIONS TO PROBLEMS IN SEISMIC ISOLATION

For the eigenvalue evaluation, the eigenperiod under low strain can be obtained by measuring the constant microtremors in the field survey.

The rigid-bed assumption can be established by placing a concrete slab between the seismic isolation layer and the upper building when the building is seismically isolated. To prevent the column legs from slipping, the foundation stones are fixed with concrete, and horizontal movement is restrained by passing transverse members between the columns and anchor bolts.

To obtain the building-derived resilience, it is proposed to conduct on-site static loading tests. Slowly apply positive and negative forces to the actual building up to an arbitrary angle of inter-story deformation, measure the maximum load at each measurement point as shown in Fig. 9, and create a deformation angle-restoring force envelope. Since it is not possible to measure beyond the elastic range of the building as a problem of the test, seismic diagnosis of the existing building and calculation of the seismic response after base isolation on the safe side without considering variations are conducted in advance to confirm that the maximum elastic deformation angle of the building does not exceed the maximum response deformation angle after base isolation. Then, the required restoring force can be obtained without damaging the building by applying force up to the maximum deformation angle after seismic isolation.

TRADITIONAL WOODEN SEISMIC ISOLATION RETROFIT DESIGN FLOW

Fig.10 shows the flow. To accurately determine the response of existing buildings, the stiffness of a one-mass model is determined by calculating backwards from the natural period obtained from constant microtremor measurements. In the seismic diagnosis, the response to level 1: rare seismic motion and level 2: extremely rare seismic motion is examined based on seismic response calculations to determine the need for base isolation and to determine the maximum elastic deformation angle of the building. If necessary, a seismic isolation method is developed. In the seismic isolation layer setting, the seismic isolation device and slab are selected. Based on this, the seismic response of the upper building and the two-mass system is calculated to determine the seismic isolation effect. In addition to Level 1 and Level 2 ground motions, Level 3 ground motions are

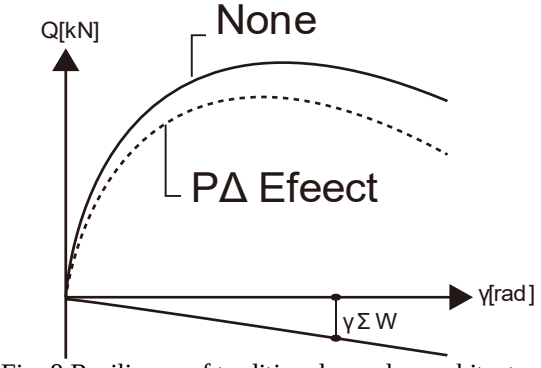

Fig. 8 Resilience of traditional wooden architecture

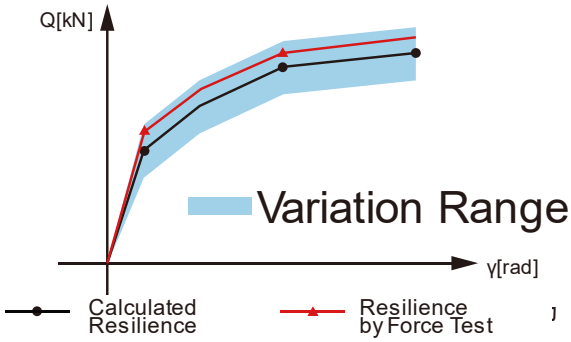

Fig.9 Creation of restoring force by force testing

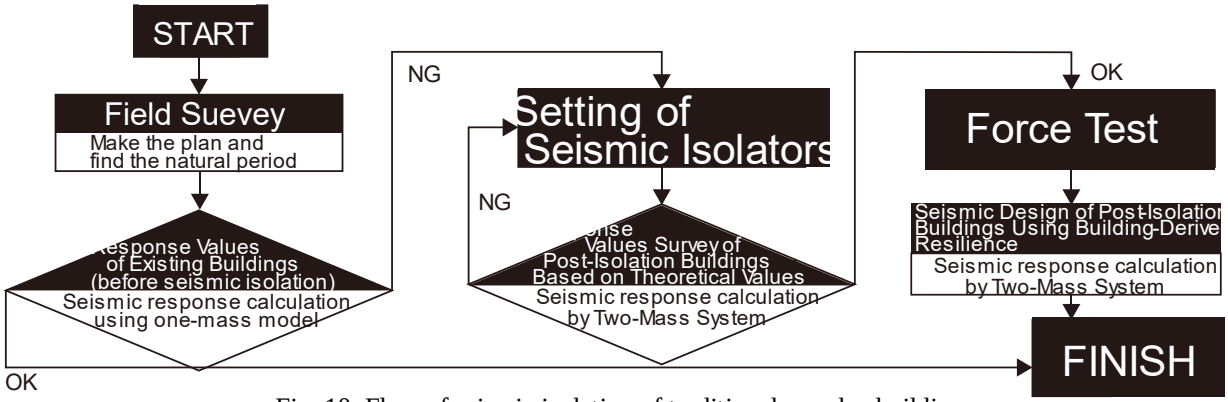

Fig. 10. Flow of seismic isolation of traditional wooden buildings

set for verification of the margin. If the seismic response does not satisfy the judgment, the seismic isolation layer is set up again. If the judgment is satisfied, confirm that the maximum response deformation angle of the upper building after base isolation is within the maximum deformation angle of the elastic range of the existing building, and conduct a force test. After obtaining the true restoring force of the existing building through the force test, perform the seismic response calculation again using a two-mass system. Confirm that the response value satisfies the judgment and complete the design.

VERIFICATION OF DESIGN METHOD

Overview of the building for verification

The virtual temple model prepared for validation was reduced to a one-mass system and is shown in Fig.11 and Table 2.

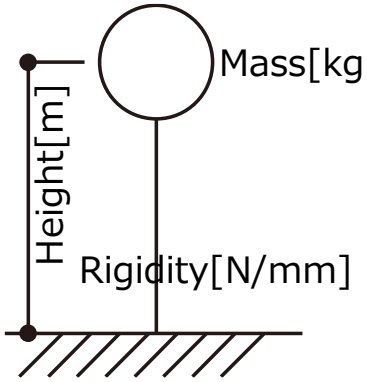

Fig. 11 1-mass point system model

Table 2: Building Characteristics

Building Overview		Single-story wooden house
Dimensions	Tensile Spacing × Girder Length	10.8[m] × 10.8[m]
Height	H[m]	7
Mass	M[kg]	27232
Rigidity	K[N/mm]	stepwise

Response values of existing buildings (before seismic isolation)

Table 3: Response values of existing buildings (before seismic isolation)

RESPONSE VALUE		BCJ-L1	BCJ-L2
1	Shearing Force	62.8	-
2	Acceleration	232.6	-
3	Deformation Angle	1/267	-
TARGET VALUE		≦1/120	≦1/25
JUDGEMENT		OK	NG
Maximum Angle		1/60	

The response values to level 1.2 earthquake motion were investigated by seismic response calculations. As shown in Table 3, it was found that seismic isolation was necessary. The maximum elastic deformation angle was 1/60.

Setting of seismic isolators

The seismic isolation layer was a combination of laminated rubber and sliding bearings as shown in Fig. 12. A two-mass system model of the seismic isolation layer (seismic isolator + concrete slab) and the upper building was used for the model.

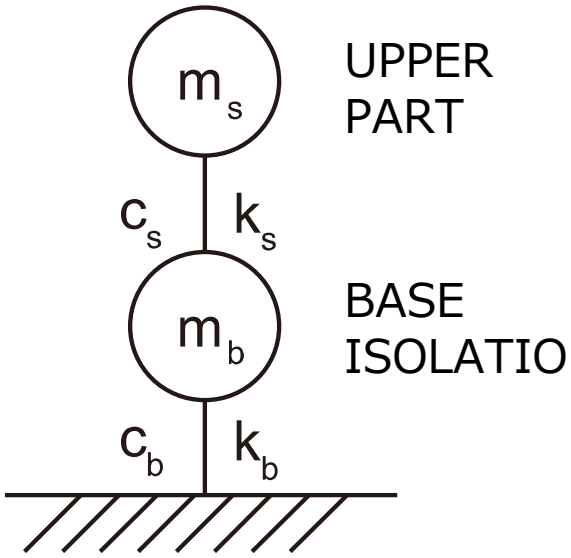

Fig. 12. Model of post-seismic isolation building

Response values survey of post-isolation buildings based on theoretical values

The results in Table 4 show that the building after seismic isolation satisfies the determination. Since the building can be subjected to forces up to the maximum building elastic deformation angle (1/60), it can be concluded that force tests can be performed.

Table 4. Response values of buildings after seismic isolation (theoretical values)

	RESPONSE VALUE		BCJ-L1	BCJ-L2	BCJ-L3
UPPER PART	1	Shearing Force	17.4	27.8	29.4
	2	Acceleration	64.4	103	108.9
	3	Deformation Angle	1/285	1/156	1/50
BASE ISOLATION	1	Shearing Force	117.4	180.5	-
	2	Acceleration	25.2	389	-
	Skewness[%]		50	100	150
TARGET VALUE	Deformation Angle		1/250	1/150	1/50
	Acceleration		250	300	-
	Skewness[%]		50	100	150
JUDGEMENT			OK	OK	NG

Seismic design of post-isolation buildings using building-derived resilience

Table 5 shows the results of the seismic response calculations using the restoring forces assumed in the force tests. As a result, a larger response value was predicted, but the target value was sufficiently met.

Table 5. Response values of buildings after seismic isolation (original building values)

	RESPONSE VALUE		BCJ-L1	BCJ-L2	BCJ-L3
UPPER PART	1	Shearing Force	11.1	60.2	-
	2	Acceleration	41.1	223	-
	3	Deformation Angle	1/296	1/164	-
BASE ISOLATION	1	Shearing Force	117.4	180.5	-
	2	Acceleration	25.2	389	-
	Skewness[%]		50	100	150
TARGET VALUE	Deformation Angle		1/250	1/150	1/50
	Acceleration		250	300	-
	Skewness[%]		50	100	150
JUDGEMENT			OK	OK	NG

CONCLUSIONS

In this study, seismic isolation retrofit construction for existing traditional wooden buildings was first investigated and the construction method was analyzed. As a result, it was found that the construction procedure of the RC base increases the weight of the lightweight wood structure and lengthens the natural period, and that the rigid floor is effective in making the horizontal structure of a traditional wooden building, which generally has a flexible floor, behave in a constant manner.

A seismic isolation retrofit design flow was then proposed, and the validity of the flow was verified using a concrete building. In the flow, in order to obtain accurate response values for a pre-isolation building with seismic retrofit, a response calculation based on theoretical values was performed in advance, a static force test was conducted on the building based on the obtained response values to obtain the restoring force derived from the building, and the post-isolation seismic response calculation was conducted again using these values. The design method was proposed to obtain accurate response values derived from the building by conducting static force tests on the building based on the response values obtained after the post-isolation calculations. The verification showed that the actual response values were predicted to be slightly larger than the theoretical values calculated, indicating the validity of using the building-derived values, even when considering the safety side.

REFERENCES

[1] Japan Institute of Building and Structural Engineers, *ISCA Edition Design of Wooden Building Structures (2nd ed.)*, Japan, 2021

[2] Yoshihiro Yamazaki, Hiroyasu Sakata, *Simple Evaluation and Control Methods for Dynamic Properties of One-Layer Wooden Structures with Soft Floors*, Japan, 2018

[3] Editorial Committee of Design Manual for Wooden Buildings Using Traditional Construction Method, *Wooden Seismic Design Method for Traditional Construction*, Japan, 2019

[4] Architectural Institute of Japan, *Seismic Isolation Structure Design Guideline*, Japan, 2013

8th Int. Conf. on Structure, Engineering & Environment (SEE), Mie, Japan, Nov.10-12, 2022, ISBN: 978-4-909106094 C3051

STRESS ANALYSIS OF VALLEY FILLS CONSIDERING RAINFALL INFILTRATION CONDITIONS

Daiki Yamashita[1] and Shin-ichi Kanazawa[2]
[1]Environmental Science and Technology, Master's Program Graduate School of Science and Technology Niigata University, Japan;
[2] Civil Engineering Program, Faculty of Engineering, Niigata University, Japan

ABSTRACT

In recent years, many cases of collapse and damage of soil structures have been reported worldwide due to the sudden increase in heavy rainfall due to climate change. However, analysis of the factors that lead to the fracture of these structure and the fracture mechanisms have not been fully investigated. Therefore, numerical analysis is attracting attention as a way to better understand the behavior of ground under various construction and rainfall conditions to ensure the ultra-long-term safety of soil structures and to extend their life. Under these circumstances, we performed in this study a construction analysis of valley fills by using three types of materials (sand, silt-mixed sand, and sand-mixed silt) and rainfall analysis under multiple conditions and intensities. From the analysis results, we conclude that the weakening of valley fills can be roughly divided into three patterns according to the relationship between the flow rate due to rainfall and the infiltration rate of the embankment material.

Keywords: Valley fills, Finite element analysis, Rainfall analysis

1. INTRODUCTION

In recent years, many cases of collapse and damage to soil structures have been reported due to the increase in sudden heavy rains due to climate change, such as guerrilla rainstorms and typhoons. The danger of sediment-related disasters increasingly plague us every year. Even in the last few years, major disasters are still fresh in our memory, such as the flooding and collapse of river embankments caused by the typhoon in East Japan in the first year of Reiwa and the landslide that occurred in Izusan district, Atami City, Shizuoka Prefecture, in the third year of Reiwa. In addition, the typhoon in East Japan in the first year of Reiwa broke 140 embankments nationwide. These disasters are becoming a familiar problem in our daily lives.

At origination, soil structures are managed by compaction at the time of construction to improve deformation characteristics due to rainfall infiltration. However, to date, the factors and mechanisms that lead to the fracture of soil structures have not been fully elucidated. Because of this, soil structures have generally been constructed based on a specification design that lacks consideration of long-term safety; although, in recent years, the introduction of performance design has progressed in this regard. Under these circumstances in recent years numerical analysis has been given particular importance in the field of geotechnical engineering as a method for ensuring safety and examining the required performance of both design methods. Furthermore, the frequent damage to soil structures described above makes it urgent to understand the behavior of ground under various construction and rainfall conditions to ensure the safety of soil structures. Against this background, this study will analyze the construction of valley-filled embankment using three types of materials (sand, silt-mixed sand, and sand-mixed silt) and rainfall analysis under multiple conditions and intensities. Based on the results, we analytically examine the changes in ground behavior when fill materials and rainfall conditions change.

2. AIR-DISSOLVED UNSATURATED SOIL / WATER / AIR COUPLED FINITE ANALYSIS

In this study, we use the air-dissolved unsaturated soil / water / air coupled finite analysis code "DACSAR-MP" [1]. The unsaturated soil elasto-plastic composition model, water retention curve model, and finite element formulation in this analysis code are as shown below.

2.1 The unsaturated soil elasto-plastic composition model

So far, several unsaturated soil composition models have been proposed, but the elasto-plastic composition model of unsaturated soil proposed by Ohno et al. [2] is used in this analysis code. Ohno et al. [2] propose a model in which the effective saturation is used as a state agent to express the rigidity, with reference to the model given the definition of effective stress considering the water content of Karube et al. [3]. The effective stress is

given by the following equations, Equation (1) shows the effective stress, Equation (2) shows the basic stress tensor and attractive stress, and Equation (3) shows the attractive force.

$$\boldsymbol{\sigma}' = \boldsymbol{\sigma}^N + p_s \mathbf{1} \tag{1}$$

$$\boldsymbol{\sigma}^N = \boldsymbol{\sigma} - p_a \mathbf{1}, \ \ p_s = sS_e \tag{2}$$

$$s = p_a - p_w, \ \ S_e = \frac{S_r - S_{rc}}{1 - S_{rc}} \tag{3}$$

Here, $\boldsymbol{\sigma}'$ is the effective stress tensor; $\boldsymbol{\sigma}^N$ is the base stress tensor; $\boldsymbol{\sigma}$ is the total stress tensor; $\mathbf{1}$ is the second order unit tensor; p_a is the pore air pressure; p_s is the suction stress; s is the suction; p_w is the pore water pressure; S_e is the effective degree of saturation; and S_{rc} is the degree of saturation at $s \to \infty$.

Furthermore, in this study, the EC model of Ohno et al. [4], who has no singular point (Ex: Pre-consolidation stress at saturation) on the yield surface, was incorporated into the analysis code in order to avoid shifting to a singular point that cannot be differentiated in numerical calculation. The EC model is an elasto-plastic composition model that expresses the soil's contractility characteristics as an exponential function, and Ohno et al. [4] derived the yield function of unsaturated soil as follows.

$$f\left(\boldsymbol{\sigma}', \zeta, \varepsilon_v^p\right) = MD \ln \frac{p'}{\zeta p'_{sat}} + \frac{MD}{n_E}\left(\frac{q}{Mp'}\right)^{n_E} - \varepsilon_v^p = 0 \tag{4}$$

Here, p'_{sat} is the yield stress at saturation; p' is mean effective principal stress; q is axial stress; M is the q/p' in the limit state; D is the dilatancy coefficient; ε_v^p is the plastic volume strain; and n_E is the shape parameter.

In addition, the increase in consolidation yield stress due to desaturation is expressed in the form of ζ times the consolidation yield stress p'_{sat} in the saturated state. ζ is a function of the effective saturation and can be expressed as the following equation.

$$\zeta = \exp\left[(1 - S_e)^b \ln a\right] \tag{5}$$

Here, b is parameter to adjust the spacing of the isosaturation lines on plane $e - \ln p'$; a is parameter that determines the multiplication factor of the consolidation yield stress when the increase in rigidity due to desaturation is maximum. In particular, a is often treated as a fitting parameter.

Substituting $n_E = 1.0$ into Equation (4) gives the following equation.

$$f\left(\boldsymbol{\sigma}', \zeta, \varepsilon_v^p\right) = MD \ln \frac{p'}{\zeta p'_{sat}} + D\eta - \varepsilon_v^p = 0 \quad \left(\eta = \frac{q}{p'}\right) \tag{6}$$

From Equations (3) and (5), it is shown that Equation (6) is the original Cam-Clay model [5] because it is $\zeta = 1$ in the saturated state ($S_e = 1$).

Fig.1 shows a conceptual diagram of the yield surface of unsaturated soil shown by the S_e - Hardening model [2], and Fig.2 shows the yield surface of the EC model proposed by Ohno et al. [4]. This shows that the larger n_E is, the more the singular point is eliminated and it becomes differentiable, and in the case of $n_E = 2.0$, it is similar to the modified Cam-Clay model [6]. In this analysis code, it is used as an isotropic model.

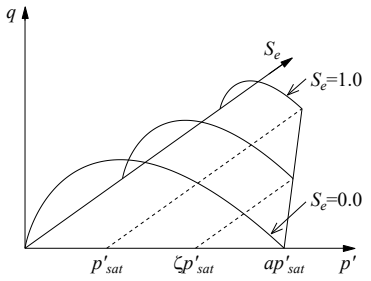

Fig. 1 Conceptual diagram of the yield surface of unsaturated soil

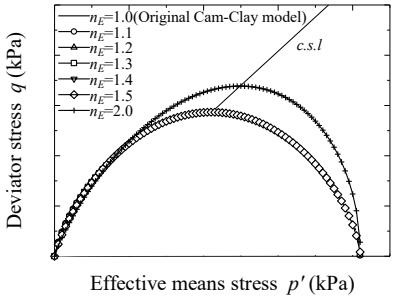

Fig. 2 Yield surface of EC model

2.2 Moisture characteristic curve model

It is widely known that the water retention curve (suction-saturation relationship) that influences the mechanical behavior of unsaturated soil differs between dehydration and water absorption. In other words, the water characteristic curve showing the suction-saturation relationship is not unique, and there are innumerable scanning curves depending on the water retention state during dehydration or water absorption. Therefore, Kawai et al. [7] proposed a water characteristic curve model capable of expressing hysteresis by utilizing the fact that these scanning curves have similar shapes during dehydration and water absorption. In addition to the model capable of hysteresis expression, this analysis code uses the logistic curve equation as shown in Fig.3. Here, the figure is "(1) dehydration curve" and "(2) water absorption curve" drawn on the dehydration side and the water absorption side from an arbitrary suction-saturation state, which was proposed by Sugii and Uno [8].

Here, the dehydration curve that passes through an

arbitrary suction-saturation degree (s_1, S_{r1}) converges to the limit water content ratio w_C at $s \to \infty$, and if the influence of the gap is ignored, the saturation degree that converges at $s \to \infty$ is $S_{rc} = G_s w_c / e$. Here, G_s is soil particle specific density; e is void ratio. Using S_{rf}^* obtained in this way, the dehydration curve is expressed by the following equation.

$$S_r = \frac{S_{rf}^* - S_{rc}}{1 + \exp\left(A^D + B^D \log_e s_1\right)} + S_{rc} \tag{7}$$

Here, S_e is the effective degree of saturation; S_r is the degree of saturation; s is the suction; S_{rc} is the degree of saturation at $s \to \infty$; S_{rf} is the degree of saturation in $s = 0$; A, B are fitting parameters of moisture characteristics (subscript D indicates dehydration).

Next, the water absorption curve that passes through an arbitrary suction-saturation degree (s_1 , S_{r1}) has a non-constant convergence saturation at $s \to \infty$, so unlike the dehydration curve, two parameters S_{ra} and S_{rf} must be determined. In other words, it is sufficient to find S_{ra}^* that satisfies the following equation.

$$\frac{S_{r1} - S_{ra}}{S_{rf}\left(S_{ra}^*\right) - S_{ra}^*} = \frac{1}{1 + \exp\left(A^W + B^W \log_e s_1\right)} \tag{8}$$

As a result, the dehydration curve and water absorption curve at any suction-saturation degree can be obtained. Here, the subscript W indicates the water absorption.

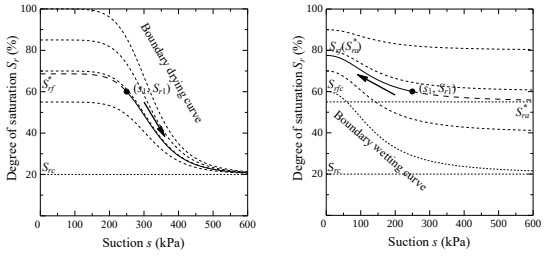

(1) Dehydration curve (2) Water absorption curve

Fig. 3 Moisture characteristic curve model

2.3 Finite element formulation

The governing equation in the unsaturated soil / water / air coupled problem consists of balanced ceremony, effective stress formula, unsaturated elasto-plastic constitutive equation, conformity expression, Darcy's rule, air Darcy's rule, continuous conditional expression, and continuous conditional expression considering gas phase, and is given by the following equations.

・Balanced ceremony

$$\mathrm{div}\boldsymbol{\sigma}^T + \rho\mathbf{g} = 0, \quad \boldsymbol{\sigma} = \boldsymbol{\sigma}^T \tag{9}$$

・Effective stress formula

$$\boldsymbol{\sigma}' = \boldsymbol{\sigma}^N + p_S\mathbf{1}, \quad \boldsymbol{\sigma}^N = \boldsymbol{\sigma} - p_a\mathbf{1} \tag{10}$$

・Unsaturated elasto-plastic constitutive equation

$$\dot{\boldsymbol{\sigma}}' = \mathbf{D} : \dot{\boldsymbol{\varepsilon}} - \mathbf{C}^S \dot{S}_e \tag{11}$$

・Conformity expression

$$\boldsymbol{\varepsilon} = -\frac{1}{2}\left(\nabla\mathbf{u}\right)^S \tag{12}$$

・Darcy's rule

$$\tilde{\boldsymbol{v}} = -\mathbf{k} \cdot \mathrm{grad}h \tag{13}$$

・Air Darcy's rule

$$\tilde{\boldsymbol{v}}_a = -\mathbf{k}_a \cdot \mathrm{grad}p_a \tag{14}$$

・Continuous conditional expression

$$n\dot{S}_r - S_r\dot{\varepsilon}_V + \mathrm{div}\tilde{\boldsymbol{v}} = 0 \tag{15}$$

・Continuous conditional expression considering gas phase

$$(1 - S_r)\dot{\varepsilon}_V + n\dot{S}_r - n(1 - S_r)\frac{\dot{p}_a}{K_a} - \mathrm{div}\tilde{\boldsymbol{v}}_a = 0 \tag{16}$$

Here, assuming that the saturation is a function that can be expressed only by suction, the following equation is obtained.

$$\dot{S}_r = \frac{dS_r}{ds}\dot{s} = -\frac{dS_r}{ds}\dot{p}_W \tag{17}$$

In addition, the increment of suction stress in Equation (10) is calculated by the following equation.

$$\begin{aligned}\dot{p}_S &= \frac{\dot{S}_r}{1 - S_{rc}}s + \frac{S_r - S_{rc}}{1 - S_{rc}}\dot{s} \\ &= \frac{1}{1 - S_{rc}}\left(\frac{dS_r}{ds}s + S_r - S_{rc}\right)\dot{s}\end{aligned} \tag{18}$$

However, S_{rc} is considered to be the saturation degree indicated by the adsorbed aqueous phase, and is a material constant.

Here, $\boldsymbol{\sigma}'$ is the effective stress tensor; $\boldsymbol{\sigma}^N$ is the base stress tensor; $\boldsymbol{\sigma}$ is the total stress tensor; p_s is the suction stress; p_a is the pore air pressure; $\mathbf{D}$ is the elastic stiffness tensor; $\boldsymbol{\varepsilon}$ is the strain tensor; $\mathbf{C}^S$ is the coefficient tensor; S_e is the effective degree of saturation; $\mathbf{u}$ is the displacement vector; $\tilde{v}$ is the flow velocity vector of interstitial water; $\mathbf{k}$ is the permeability coefficient tensor; h is the all head; S_r is the degree of saturation; ε_V is the volumetric strain; n is the porosity; K_a is the air pressure; $\tilde{v}_a$ is the flow velocity vector of interstitial air; and the

superscript S indicates the symmetric part of the tensor in ( ).

By weakly formalizing the above governing equation, discretizing it spatially and temporally, and solving it under the conditions of initial value and boundary value, the solutions of unknowns $\left\{ {}_{\Delta}\mathbf{u}^{N} \right\}$, $\left\{ {}_{\Delta}\mathbf{h}^{N}\Big|_{t=t+\Delta t} \right\}$, and $\left\{ {}_{\Delta}\mathbf{p_a}^{N}\Big|_{t=t+\Delta t} \right\}$ can be obtained.

Here, ${}_{\Delta}\mathbf{u}^{N}$ is the amount of change in node displacement; ${}_{\Delta}\mathbf{h}^{N}$ is the amount of change in total head in minute time Δt ; ${}_{\Delta}\mathbf{p_a}^{N}$ is the amount of change in air pressure in a minute time Δt .

3. ANALYSIS MODEL DETERMINATION AND CONSTRUCTION METHOD

3.1 About the analysis model

In this study, we perform construction-rainfall analysis for valley fills. There are various standards and formats for the valley fills, but in this study, the analysis model shown in Fig.4 is used as the finite analysis model. The size of the valley fills structure is a trapezoid with an upper side of 18m, a lower side of 10m, and a height of 3m. The foundation ground is set to surround the embankment, with a total length of 3.6m and width of 20m. The embankment is composed of a total of 400 meshes, 10 in the vertical direction and 40 in the horizontal direction. The displacement boundary, head boundary, and air boundary are as follows.

＜The displacement boundary＞
・Lower side, right left side, upper side (foundation part): x, y-axis fixed
・Upper side (embankment part): freedom

＜The head boundary＞
・Lower side: drainage conditions
・ Top side, right and left sides: non-drainage conditions

＜The air boundary＞
・Upper side: exhaust conditions
・Lower side, right left side : non-exhaust conditions

In addition, the road earthwork-embankment guideline [9] states that the embankment material should be easy to use in construction, maintain the safety of the embankment, and not cause harmful deformation. With this guideline, structures are constructed using a wide range of materials, as shown in Table 1. Therefore, in this study, we will perform construction-rainfall analysis considering three types of materials that imitate "sand", "sand-mixed silt", and "silt-mixed sand". Each material parameter and moisture characteristic curve are shown in Table 2 and Fig.6. These parameters were determined with reference to the research results by Honda, Iizuka, Ohno, Kawai and Wang [10]. The parameters shown below are for use in the embankment. When these materials are used for the foundation, the permeability coefficient was lowered by 2 orders to make the foundation less permeable than the embankment portion of the model.

Regarding the material parameters, λ is the expansion index; κ is the compression index; M is the limit state parameter; m is the unsaturated permeability coefficient of Mualem [11]; n is the E_c model parameter; n_E is the enlargement ratio of yield surface; e_0 is the initial void ratio; ν is the Poisson's ratio; k_x is the permeability coefficient in the x-axis direction [m/day]; k_y is the permeability coefficient in the y-axis direction [m/day]; S_{r0} is the critical saturation; and G_s is the soil particle density.

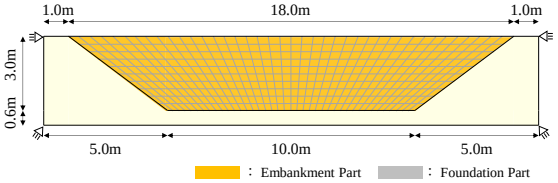

Fig. 4 Finite element analysis model

Fig. 5 Various boundary conditions

Table 2 Material parameters

M	m	n
1.33	0.80	1.0
n_E	e_0	ν
1.3	1.2	0.33
S_{r0}	S_{r-0}	G_S
0.15	0.50	2.7

Common to all materials

λ		
Sand	Silt-sand	Sand-silt
0.10	0.12	0.18
κ		
Sand	Silt-sand	Sand-silt
0.010	0.012	0.018
k_x , k_y [m/day]		
Sand	Silt-sand	Sand-silt
8.7	0.87	0.087

Different materials

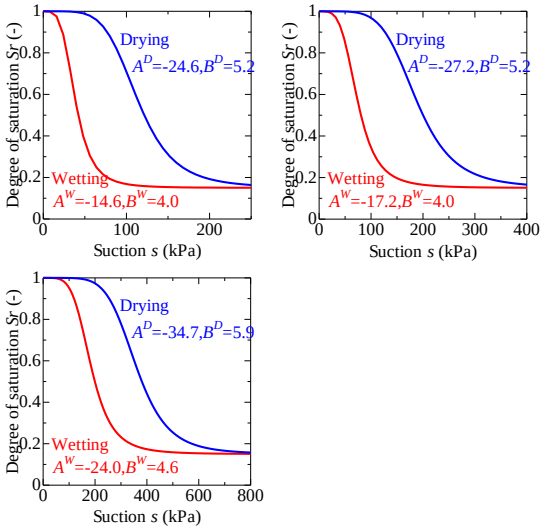

Fig. 6 Moisture characteristic curve (upper left: sand, upper right: sand-mixed silt, lower left: silt-mixed sand)

3.2 Construction analysis

3.2.1 Construction method

In this study, after performing the construction analysis of the valley fills under the above-mentioned conditions, the rainfall analysis was performed by giving the upper surface of the embankment a flow rate similar to rainfall. However, there are few existing examples of numerical analysis of valley fills by construction method. Therefore, the construction analysis was performed by each of the following four construction methods, and the construction method to use for the analysis was determined from the results.

The four different construction methods are as follows.

① The foundation and embankment portions of the structure are generated all at once.
② After generating the foundation, the embankment is generated all at once.
③ After generating the foundation, the embankment is divided into 10 layers for every 30cm of layer thickness.
④ After generating the foundation, the embankment is generated with a layer thickness of 30cm compacted with 300kPa (repeated for a total of 10 layers).

After the construction was complete, a flow rate equivalent to a rainfall intensity of 100mm/hour was given to the upper surface of the embankment until the total flow rate reached 200mm. The ground behavior of each case was compared. In this investigation, the analysis model and various boundary conditions are as described in the previous section, and the material used is "sand".

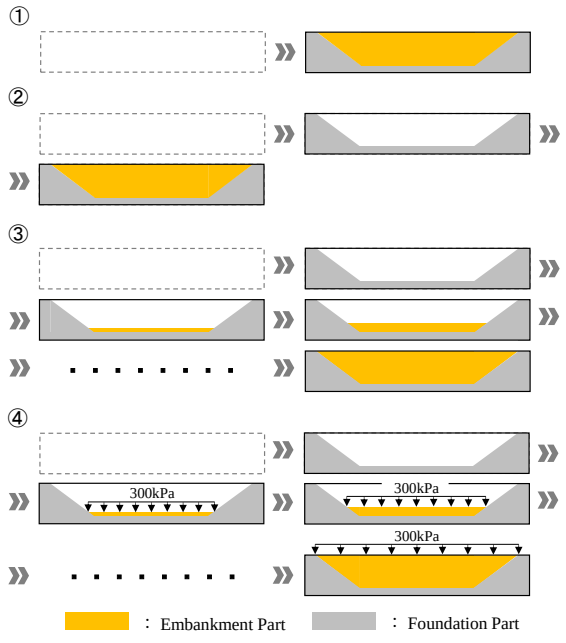

Fig. 7 How to construct valley fills

3.2.2 Construction analysis results

Fig.8 shows the analysis results of the various construction methods described in the previous section. The results show effective mean stress p', degree of saturation S_r, void ratio e, shear strain ε_s, and suction S in each construction method, and only the left half of the model is shown.

From the above analysis results, effective mean stress p', degree of saturation S_r, void ratio e, shear strain ε_s, and suction S demonstrate the following tendencies in all construction methods, and no significant difference in ground behavior depending on the construction method was observed.

・Effective mean stress p'
Stress decreases in the upper part of the embankment and near the boundary between the embankment and the foundation.

・Degree of saturation S_r
Degree of saturation increases near the upper surface of the embankment.

・Shear strain ε_s
Shear strain occurs along the boundary between the embankment and the foundation.

・Suction S
Suction disappears near the upper surface of the embankment.

For the void ratio e, the results show a decrease at the boundary between the embankment and the foundation for all construction methods. However, in the construction methods ③ and ④, in which the embankment is divided into layers, the range in which the void ratio decreases is wide. Furthermore, in construction method ③, an increase in the void ratio

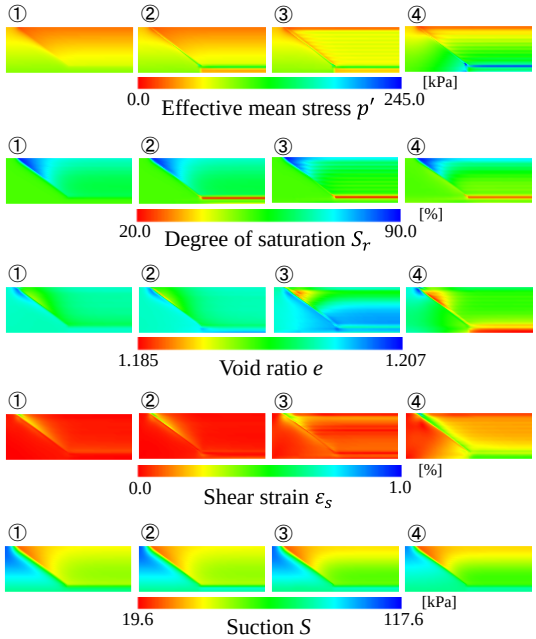

Fig. 8 Construction analysis results

between the bottom of the embankment and the foundation also occurs. This was contrary to what was expected from the results of change in saturation, as it is uncommon for the porosity ratio at the bottom of the embankment to rise, that is, for the volume to expand before rainfall has penetrated to the bottom.

Based on the above results, construction method①, where "the foundation and embankment are generated all at once", was adopted for this study.

4. CONSTRUCTION / RAINFALL ANALYSIS CONSIDERING VARIOUS MATERIALS

4.1 Construction / rainfall analysis conditions

To clarify the changes to the in-ground behavior of the valley fills by material type and rainfall intensity, construction and rainfall analysis were performed in this study using the combinations shown in Table 3. The analysis model and construction method used were as described in the previous section. In addition, for rainfall analysis, rainfall was applied only to the upper surface of the embankment after the valley fills was constructed. Regarding the rainfall intensity, two patterns were applied: 10mm/hour, which is defined as slightly heavy rain, and 100mm/hour, which is defined as heavy rain [12].

Furthermore, in order to investigate how the behavior of the ground changes due to actual heavy rainfall, rainfall analysis was performed with reference to the rainfall data of the East Japan Typhoon in the first year of Reiwa [13].

Table 3 Analysis pattern

	100mm/hour	10mm/hour	2019 Typhoon No.19
Sand	Pattern 1	Pattern 4	Pattern 7
Silt-mixed sand	Pattern 2	Pattern 5	-
Sand-mixed Silt	Pattern 3	Pattern 6	-

Embankment material Rainfall

4.2 Construction / rainfall analysis results

4.2.1 Analysis results focusing on materials

Fig. 9 shows the results of construction and rainfall analysis of various materials at a rainfall intensity of 10mm/hour. The results show effective mean stress p', degree of saturation S_r, void ratio e, shear strain ε_s, and suction S in each construction method, and only the left half of the model is shown. The duration of rainfall was 20 hours, and the total rainfall was 200mm.

First, we examine effective mean stress p' and compare each stress distribution. The results confirmed that the more permeable the material, the lower the effective mean stress across a wide area of the embankment. This is thought to be due to the disappearance of suction and the increase in pore water pressure due to rainfall. It was also confirmed that the stress value near the boundary between the

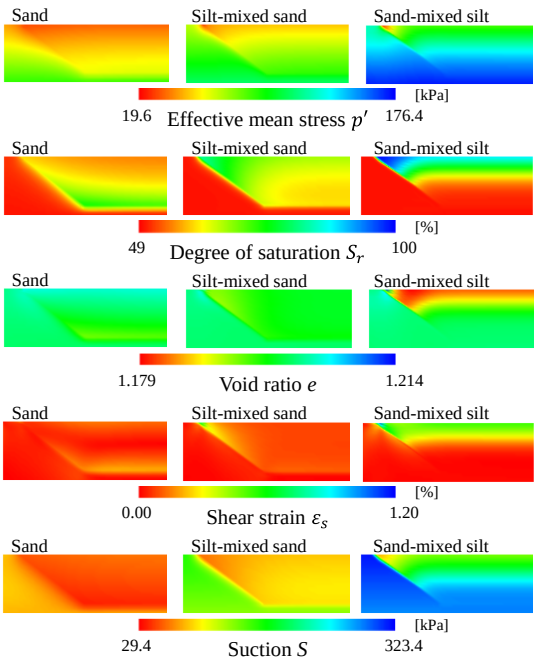

Fig. 9 Analysis results focusing on materials

embankment and the foundation decreased regardless of material.

Next, we examine degree of saturation S_r and compare each distribution. The results confirm that the poorer the permeability of the material, the more the saturation inside the embankment progresses. In addition, the more impervious the material, the more rainfall permeates the upper surface of the embankment. Therefore, impervious material cannot allow rainfall to penetrate the inside of the embankment. On the other hand, these results confirmed that rainfall penetrated to the bottom of the embankment with materials having good permeability, such as sand, and the characteristics of rainfall penetration for each embankment material could be reproduced.

Finally, we compare each distribution of shear strain ε_s. These results confirmed that, as with the distribution of the degree of saturation, larger shear strain occurred in materials with poorer permeability. Examining the location of shear strain reveals that a large value was generated where saturation had progressed into all the embankment material. However, the maximum shear strain in this analysis was about 1.20%, suggesting that the embankment was weakened, but likely not to the point leading to fracture.

The above results confirm that when focusing on material type, materials with poor permeability promote saturation on the upper surface of the embankment and structures built with these materials may weaken with rainfall.

4.2.2 Analysis results focusing on rainfall intensity

Fig. 10 shows the analysis results of construction

method by each rainfall intensity in the material "sand". The results show effective mean stress p', degree of saturation S_r, void ratio e, shear strain ε_s, and suction S for each construction method. Only the left half of the model is shown in the figure. The duration of rainfall was 2 hours at a rainfall intensity of 100m/hour and 20 hours at a rainfall intensity of 10mm/hour. The total rainfall was 200mm.

First, we examine effective mean stress p' and compare both stress distributions. The results confirm that the stress value decreased as rainfall intensity increased. As mentioned above, this is thought to be due to the disappearance of suction and the increase in pore water pressure due to rainfall.

Next, we look at the degree of saturation S_r and compare both distributions. These results confirm that saturation progresses as rainfall intensity increases. In addition, saturation progresses only to the top edge of the embankment at a rainfall intensity of 100mm/hour; whereas, saturation progresses to the bottom of the embankment at a rainfall intensity of 10mm/hour. It is probable that rapid rainfall with a rainfall intensity of 100mm/hour did not allow the rainfall to penetrate into the embankment. On the other hand, at a rainfall intensity of 10mm/hour, there was sufficient margin for rainfall penetration, so rainfall likely penetrated to the bottom of the embankment and saturation progressed.

Finally, we compare both distributions of shear strain ε_s. The shear strain results confirm that there was no large difference in the shear strain values between the two rainfall intensities, but there was a large difference in the location of where the shear strain occurred. Similar to the above discussion of saturation, the shear strain values tended to increase at the areas where saturation progressed. Shear strain was confirmed near the boundary between the embankment and the foundation at a rainfall intensity of 100mm/hour, and at the bottom of the embankment at a rainfall intensity of 10mm/hour. Here, the maximum value of shear strain was about 0.4%. As mentioned above, this does not lead to the destruction of the embankment, but it does suggest that progressive weakening may occur at the affected sites.

The above analysis results confirm that the area of valley fills weakening differs depending on the difference in rainfall intensity.

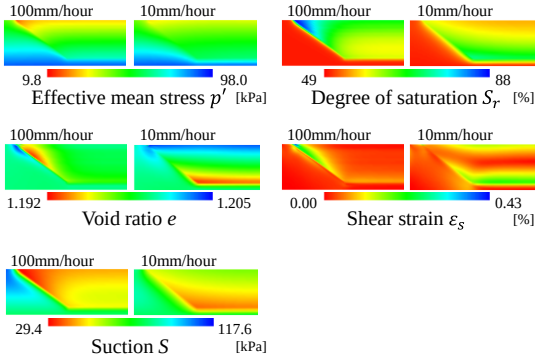

Fig. 10 Analysis results by rainfall intensity

4.2.3 Rainfall analysis results simulating full-scale heavy rainfall

In this study, rainfall analysis using actual heavy rainfall data was carried out, and changes in ground behavior over time were also be investigated. In this analysis, we analyzed the rainfall with reference to the rainfall data from the typhoon in East Japan in the first year of Reiwa. The data used is the maximum 24-hour rainfall during the East Japan typhoon in the first year of Reiwa at the meteorological observation point in Mitsumine, Chichibu City, Saitama Prefecture. The total rainfall is 561.5mm/hour.

Fig. 12 shows the time course of each parameter for the study elements of the embankment in the rainfall analysis. The study elements are as described in Fig.11.

As a general feature, analysis results confirmed that the effective mean stress decreased, the degree of saturation increased, the void ratio decreased, shear strain was present, and suction disappeared in the entire embankment. This indicates that the stress decreases with volume compression, and, considering the $e - \ln p'$ relation, it demonstrated that there is a tendency for weakening throughout the embankment. This was particularly remarkable in No.181, an element at the bottom of the embankment. Furthermore, from around 10 hours, when the rainfall

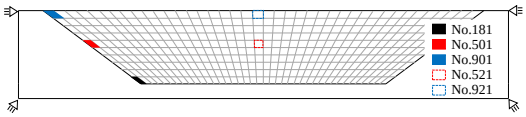

Fig. 11 The study elements

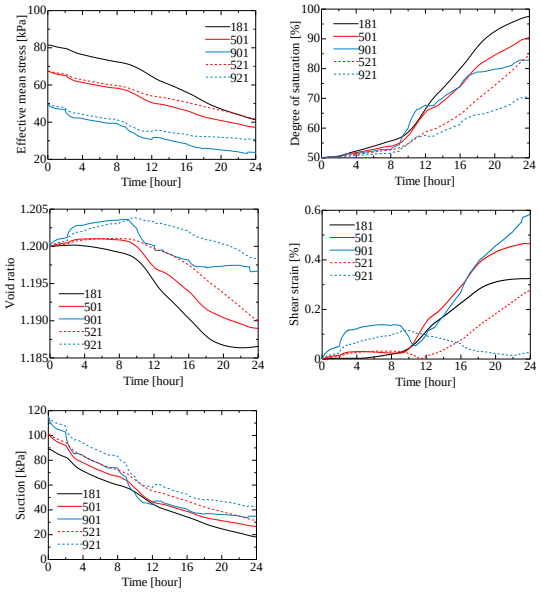

Fig. 12 Changes over time for each parameter for each element

intensity became high, a remarkable increase in the degree of saturation and a decrease in the void ratio were confirmed in No. 901, the upper surface element of the embankment. This suggests that there is a tendency for weakening near this element. Comparing the behaviors of the elements at the same depth (No.901-No.921, No.501-No.521) confirmed that the elements at the end of the embankment had a significant increase in the degree of saturation and a higher occurrence of shear strain compared to the elements at the center of the embankment.
The above suggests that as a result of the actual-scale heavy rainfall, the valley fills tend to weaken in the vicinity of the boundary between the embankment and the foundation.

5. SUMARRY

In this study, we performed construction and rainfall analysis focusing on soil materials and rainfall intensity of valley fills using unsaturated soil / water / air coupled finite element analysis. As a result, it was possible to analytically express the changes in the behavior of the ground depending on the material and rainfall. In all cases, the results suggest weakening of the ground due to rainfall. The analysis results in the previous chapter clarified that the tendency of weakening, based on rainfall amount and embankment permeability, exhibits the following three patterns.

(1) Rainfall > Permeability (Penetration rate)

Although rainfall permeates the lower layer, not all rainfall permeates, and it becomes saturated from the upper layer, which tends to weaken accordingly. At this point, the degree of saturation progresses along the boundary between the embankment and the foundation.

(2) Rainfall < Permeability (Penetration rate)

The valley fills become saturated from the lower layer (bottom) of the embankment and tends to weaken accordingly. At this point, the degree of saturation progresses along the boundary between the embankment and the foundation.

(3) Rainfall << Permeability (Penetration rate)

Only the upper layer tends to saturate without penetrating from the upper layer to the lower layer of the embankment. At this point, the degree of saturation progresses quickly near the boundary between the embankment and the foundation, weakening the structure and leading to its destruction.

Because the purpose of this study is to follow the changes in the ground behavior of the valley fills, measures such as drainage layers were not expressed. In addition, the maximum rainfall duration was 24 hours, and it was not possible to analytically examine long-term changes to ground behavior. Therefore, in the future, we would like to run analysis assuming long-term rainfall and the change in the behavior in the ground when measures such as drainage layers are implemented.

6. REFERENCES

[1] Kanazawa S., Toyoshima K., Kawai K., Tachibana S. and Iizuka A.: Analysis of mechanical behavior of compacted soil with F.E. method, journal of JSCE, No.68 (2), pp.291-298, 2012.

[2] Ohno S., Kawai K. and Tachibana S.: Elasto-plastic constitutive model for unsaturated soil applied effective degree of saturation as a parameter expressing stiffness, journal of JSCE, Vol.63/No.4, pp.1132-1141, 2007.

[3] Karube D., Kato S., Hamada K. and Honda M.: The relationship between the mechanical behavior and the state of porewater in unsaturated soil, journal of JSCE, No.535/III-34, pp.83-92, 1996.

[4] Ohno S., Iizuka A. and Ohta H., Two categories of new constitutive model derived from non-linear description of soil contractancy, Journal of applied mechanics, pp. 407-414, 2006.

[5] Schofield, A and Wroth, P.: Critical State Soil Mechanics, McGraw-Hill, pp. 1-310, 1968.

[6] Roscoe, K. H and Burland, J. B.: On the Generalised Stress-Strain Behavior of Wet Clay, Engineering Plasticity eds. J. Heyman and F. A. Leckie, Cambridge University Press, pp.535-609, 1968.

[7] Kawai K., Wang W. and Iizuka A.: The expression of hysteresis appearing on water characteristic curves and the change of stresses in unsaturated soils, Journal of applied mechanics, Vol.5, pp.777-784, 2002.

[8] Sugii T. and Uno T.: Modeling the New Moisture Characteristic Curve, Journal of JSCE, pp.130-131, 1995.

[9] Japan road association: Road earthwork-embankment work guidelines, MARUZEN publishing, 2010.

[10] Honda M., Iizuka A., Ohno S., Kawai K. and Wang W.: A study of the evaluation method for deformation characteristic of compacted soil, journal of JSCE, No806/III-73, 33-44, 2005.12.

[11] Mualem, Y.: A new model for predicting the hydraulic conductivity of unsaturated porous media, Water Resources Research, Vol.12, No.3, pp.514-522, 1976.

[12] Japan Meteorological Agency:

[13] Cabinet office, Government of Japan: About the damage situation related to Typhoon No. 19 etc. in the first year of Reiwa, p1, 2020.

8th Int. Conf. on Structure, Engineering & Environment (SEE), Mie, Japan, Nov.10-12, 2022, ISBN: 978-4-909106094 C3051

ANALYTICAL STUDY OF THE STRENGTH CHARACTERISTICS OF COMPACTED SOIL

Kazuki Naito[1] and Shin-ichi Kanazawa[2]
[1] Environmental Science and Technology, Master's Program Graduate School of Science and Technology Niigata University, Japan;
[2] Civil Engineering Program, Faculty of Engineering, Niigata University, Japan

ABSTRACT

In recent years, many cases of river embankment and levee collapse due to sudden torrential rains or earthquakes have been reported. The mechanism of the strength development of compacted soil in the field has not been fully elucidated, and it is important to clarify compaction and collapse mechanisms based on the mechanics of unsaturated soil to establish a quality evaluation method. Therefore, in this study, compaction behavior considering soil material was analyzed using the coupled soil/water/air finite element analysis program (DACSAR-MP). Subsequently, the obtained compaction specimens of silt-mixed sand were subjected to flooding analysis and constant volume shear analysis to determine their strength properties.

Keywords: Compaction curve, Unsaturated soils, Water characteristic curve

INTRODUCTION

Many cases of riverbank and embankment failure have been reported in recent years due to sudden heavy rains, typhoon torrential rains, and earthquakes. To date, the mechanisms of the strength development of compacted soil in the field and its relationship with the strength of the soil have not been fully elucidated. Current construction guidelines do not prepare mangers for the maintenance of embankments subjected to recent torrential rains and earthquakes. To establish a quality evaluation method for embankment structures that considers performance design, it is important to clarify the relationship between compaction mechanisms and the strength of embankment structures based on unsaturated soil mechanics and the mechanism leading to collapse, and to propose an index for evaluating compacted soil.

In this study, the coupled soil/water/air finite element analysis program (DACSAR-MP) [1][2] is used to analytically explain the mechanical interpretation of compaction behavior considering differences in soil materials. The strength properties of the compaction specimens were then determined by performing water immersion and shear analyses.

ANALYSIS METHOD

In this study, we use the air-dissolved unsaturated soil / water / air coupled finite analysis code "DACSAR-MP" [1][2]. The unsaturated soil elastic-plastic composition model, the water retention curve model, and the finite element formulation in this analysis code are described below.

The Unsaturated Soil Elastic-plastic Composition Model

So far, several unsaturated soil composition models have been proposed, but the elastic-plastic composition model of unsaturated soil proposed by Ohno et al [3] is used in this analysis code. Ohno et al [3] propose a model in which the effective saturation is used as a state agent to express the rigidity, with reference to the model given the definition of effective stress considering the water content of Karube et al [4]. The effective stress is given by the following equations, Equation (1) shows the effective stress, Equation (2) shows the basic stress tensor and attractive stress, and Equation (3) shows the attractive force.

$$\boldsymbol{\sigma}' = \boldsymbol{\sigma}^N + p_s \mathbf{1} \tag{1}$$

$$\boldsymbol{\sigma}^N = \boldsymbol{\sigma} - p_a \mathbf{1}, \quad p_s = sS_e \tag{2}$$

$$s = p_a - p_w, \quad S_e = \frac{S_r - S_{rc}}{1 - S_{rc}} \tag{3}$$

Here, $\boldsymbol{\sigma}'$ is the effective stress tensor; $\boldsymbol{\sigma}^N$ is the base stress tensor; $\boldsymbol{\sigma}$ is the total stress tensor; $\mathbf{1}$ is the second order unit tensor; p_a is the pore air pressure; p_s is the suction stress; s is the suction; p_w is the pore water pressure; S_e is the effective degree of saturation; and S_{rc} is the degree of saturation at $s \to \infty$.

Furthermore, in this study, the EC model of Ohno et al [5], which has no singular point on the yield surface (e.g., pre-consolidation stress at saturation), was incorporated into the analysis code to avoid

shifting to a singular point that cannot be differentiated in numerical calculation. The EC model is an elastic-plastic composition model that expresses the soil's contractility characteristics as an exponential function. Ohno et al [5] derived the yield function of unsaturated soil as follows.

$$f\left(\boldsymbol{\sigma}', \zeta, \varepsilon_v^p\right) = MD \ln \frac{p'}{\zeta p'_{sat}} + \frac{MD}{n_E}\left(\frac{q}{Mp'}\right)^{n_E} - \varepsilon_v^p = 0 \qquad (4)$$

Here, p'_{sat} is the yield stress at saturation; p' is mean effective principal stress; q is axial stress; M is q/p' in the limit state; D is the dilatancy coefficient; ε_v^p is the plastic volume strain; and n_E is the shape parameter.

In addition, the increase in consolidation yield stress due to desaturation is expressed in the form of ζ times the consolidation yield stress p'_{sat} in the saturated state. ζ is a function of the effective saturation and can be expressed as the following equation.

$$\zeta = \exp\left[(1-S_e)^b \ln a\right] \qquad (5)$$

Where, b is parameter to adjust the spacing of the is saturation lines on plane $e - \ln p'$, and a is a parameter that determines the multiplication factor of the consolidation yield stress when the increase in rigidity due to desaturation is maximum. In particular, a is often treated as a fitting parameter.

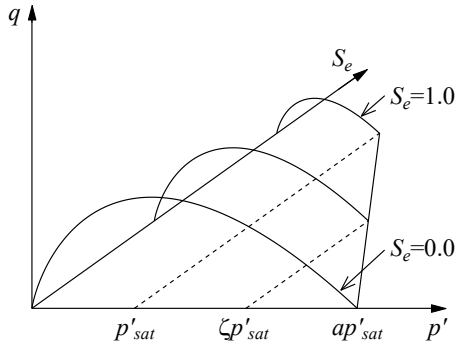

Fig.1 Conceptual diagram of the yield surface of unsaturated soil

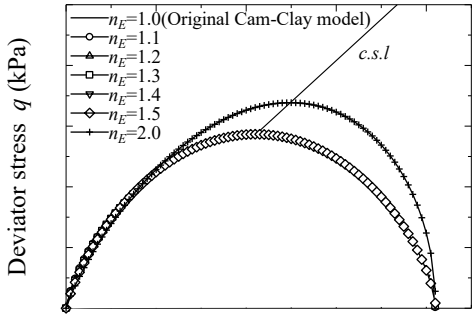

Fig.2 Yield surface of the EC model

Substituting $n_E = 1.0$ into Equation (4) gives the following equation.

$$f\left(\boldsymbol{\sigma}', \zeta, \varepsilon_v^p\right) = MD \ln \frac{p'}{\zeta p'_{sat}} + D\eta - \varepsilon_v^p = 0 \quad \left(\eta = \frac{q}{p'}\right) \qquad (6)$$

From Equations (3) and (5), it is shown that Equation (6) is the original Cam-Clay model [6] because it holds $\zeta = 1$ in the saturated state ($S_e = 1$).

Figure 1 shows a conceptual diagram of the yield surface of unsaturated soil shown by the S_e - Hardening model, and Fig.2 shows the yield surface of the EC model proposed by Ohno et al [4]. This shows that the larger n_E is, the more the singular point is eliminated and becomes differentiable. In the case of $n_E = 2.0$, this is similar to the modified Cam-Clay model [7]. In this analysis code, the EC model is used as an isotropic model.

Moisture Characteristic Curve Model

It is widely known that the water retention curve (suction-saturation relationship) that influences the mechanical behavior of unsaturated soil differs between dehydration and water absorption. In other words, the water characteristic curve showing the suction-saturation relationship is not unique, and there are innumerable scanning curves depending on the water retention state during dehydration or water absorption. Therefore, Kawai et al [8] proposed a water characteristic curve model capable of expressing hysteresis by utilizing the fact that these scanning curves have similar shapes during dehydration and water absorption. In addition to using a model capable of hysteresis expression, this analysis code uses the logistic curve equation as shown in the Fig.3. In this figure, "(1) dehydration curve" and "(2) water absorption curve" are drawn on the dehydration side and the water absorption side from an arbitrary suction-saturation state, as proposed by Sugii and Uno [9].

In the model shown in Fig.3, the dehydration curve that passes through an arbitrary suction-saturation degree (s_1 , S_{r1}) converges to the limit water content ratio w_C at $s \to \infty$, and if the influence of the gap is ignored, the saturation degree that converges at $s \to \infty$ is $S_{rc} = G_s w_c / e$; where, G_s is soil particle

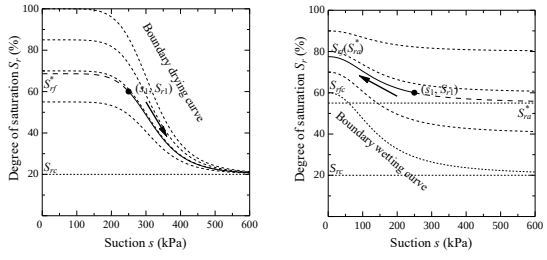

(1) Dehydration curve (2) Water absorption curve

Fig.3 Moisture characteristic curve model

specific density and e is void ratio. Using S_{rf}^{*} obtained in this way, the dehydration curve can be expressed by the following equation.

$$S_r = \frac{S_{rf}^{*} - S_{rc}}{1+\exp\left(A^D + B^D \log_e s_1\right)} + S_{rc} \tag{7}$$

Where, S_e is the effective degree of saturation; S_r is the degree of saturation; s is the suction; S_{rc} is the degree of saturation at $s \to \infty$; S_{rf} is the degree of saturation in $s = 0$; and A, B are fitting parameters of moisture characteristics (subscript D indicates dehydration).

The water absorption curve that passes through an arbitrary suction-saturation degree (s_1 , S_{r1}) has a non-constant convergence saturation at $s \to \infty$, so unlike the dehydration curve, two parameters S_{ra} and S_{rf} must be determined. In other words, it is sufficient to find S_{ra}^{*} that satisfies the following equation:

$$\frac{S_{r1} - S_{ra}}{S_{rf}\left(S_{ra}^{*}\right) - S_{ra}^{*}} = \frac{1}{1+\exp\left(A^W + B^W \log_e s_1\right)} \tag{8}$$

This yields the dehydration curve and the water absorption curve at an arbitrary suction-saturation level. The subscript W denotes the water-absorption curve.

Formulation of The Finite Element Method

The governing equation in the unsaturated soil/water /air coupled problem consists of a balanced ceremony, an effective stress formula, an unsaturated elastic-plastic constitutive equation, a conformity expression, Darcy's rule, air Darcy's rule, a continuous conditional expression, and a continuous conditional expression considering gas phase, and is given by the following equations.

・Balanced ceremony

$$\mathrm{div}\boldsymbol{\sigma}^T + \rho\mathbf{g} = 0, \quad \boldsymbol{\sigma} = \boldsymbol{\sigma}^T \tag{9}$$

・Effective stress formula

$$\boldsymbol{\sigma}' = \boldsymbol{\sigma}^N + p_s\mathbf{1}, \quad \boldsymbol{\sigma}^N = \boldsymbol{\sigma} - p_a\mathbf{1} \tag{10}$$

・Unsaturated elastic-plastic constitutive equation

$$\dot{\boldsymbol{\sigma}}' = \mathbf{D} : \dot{\boldsymbol{\varepsilon}} - \mathbf{C}^S \dot{S}_e \tag{11}$$

・Conformity expression

$$\boldsymbol{\varepsilon} = -\frac{1}{2}\left(\nabla\mathbf{u}\right)^S \tag{12}$$

・Darcy's rule

$$\tilde{\boldsymbol{v}} = -\mathbf{k} \cdot \mathrm{grad}h \tag{13}$$

・Air Darcy's rule

$$\tilde{\boldsymbol{v}}_a = -\mathbf{k}_a \cdot \mathrm{grad}p_a \tag{14}$$

・Continuous conditional expression

$$n\dot{S}_r - S_r\dot{\varepsilon}_v + \mathrm{div}\tilde{\mathbf{v}} = 0 \tag{15}$$

・Continuous conditional expression considering gas phase

$$(1-S_r)\dot{\varepsilon}_v + n\dot{S}_r - n(1-S_r)\frac{\dot{p}_a}{K_a} - \mathrm{div}\tilde{\mathbf{v}}_a = 0 \tag{16}$$

Where, assuming that saturation is a function that can be expressed only by suction, the following equation is obtained.

$$\dot{S}_r = \frac{dS_r}{ds}\dot{s} = -\frac{dS_r}{ds}\dot{p}_w \tag{17}$$

In addition, the increment of suction stress in Equation (10) is calculated by the following equation.

$$\begin{aligned} \dot{p}_s &= \frac{\dot{S}_r}{1-S_{rc}}s + \frac{S_r - S_{rc}}{1-S_{rc}}\dot{s} \\ &= \frac{1}{1-S_{rc}}\left(\frac{dS_r}{ds}s + S_r - S_{rc}\right)\dot{s} \end{aligned} \tag{18}$$

Furthermore, S_{rc} is the saturation degree indicated by the adsorbed aqueous phase and is a material constant.

Here, $\boldsymbol{\sigma}'$ is the effective stress tensor; $\boldsymbol{\sigma}^N$ is the base stress tensor; $\boldsymbol{\sigma}$ is the total stress tensor; p_s is the suction stress; p_a is the pore air pressure; $\mathbf{D}$ is the elastic stiffness tensor; $\boldsymbol{\varepsilon}$ is the strain tensor; $\mathbf{C}^S$ is the coefficient tensor; S_e is the effective degree of saturation; $\mathbf{u}$ is the displacement vector; $\tilde{v}$ is the flow velocity vector of interstitial water; $\mathbf{k}$ is the permeability coefficient tensor; h is the all head; S_r is the degree of saturation; ε_v is the volumetric strain; n is the porosity; K_a is the air pressure; $\tilde{\boldsymbol{v}}_a$ is the flow velocity vector of interstitial air; and the superscript S indicates the symmetric part of the tensor in ( ).

COMPACTION BEHAVIOR CONSIDERING SOIL MATERIAL

Analysis Conditions

In this study, the coupled soil/water/air finite element analysis program (DACSAR-MP) was used to analyze static compaction tests considering material properties.

As shown in Fig.4, a specimen of 5 cm in length and 5 cm in width was assumed for the analysis domain. To make it easier to see the flow of water, the specimen was made slightly smaller than a normal specimen. This specimen was divided into 10 elements.

[Boundary conditions**]**

<The displacement boundary>

・Lower side: x, y-axis fixed
Right left side: x-axis fixed

<The air boundary>

・Upper side: exhaust conditions
・Lower side, right left side: non-exhaust conditions

<The head boundary>

・Totally undrained

The third level headings

[Initial conditions**]**

・Initial moisture content: w=6%~32% (1%~2% increments)
・Loading load: 100 kPa to 100 kPa increments
・Loading time: 50 min
・Unloading time: 5 min

The material constants used in the analysis are shown in Table 1 for the three cases of clay, silt-mixed sand, and sand, respectively. The moisture property curves are shown in Fig. 5.

Here, regarding the material parameters, λ is the expansion index; κ is the compression index; M is the limit state parameter; ν is the Poisson's ratio; $\boldsymbol{k_a}$ is permeability [m/day]; $\boldsymbol{k_w}$ is saturated hydraulic conductivity [m/day]; G_s is the soil particle density; m is the unsaturated permeability coefficient of Mualem [10]; a is a magnification parameter of consolidation yield stress by unsaturation; n is the

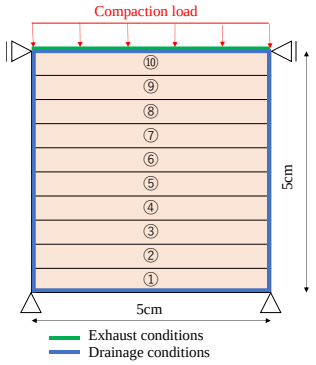

Fig.4 Finite element analysis model

Table 1. Material parameters (first row: clay, second row: silt-mixed sand, third row: sand)

λ	κ	M	ν'	K_a(m/min)	K_w (m/min)	G_s	m
0.19	0.019	1.33	0.33	6.0×10^{-9}	6.0×10^{-7}	2.70	0.8
a	n	e_0	γ_t	S_{r0}	n_E	m(subloading surface)	P'_{sat}
10.0	1.0	0.9	1.5	0.15	1.3	10	15.0

λ	κ	M	ν	K_a(m/min)	K_w (m/min)	G_s	m
0.11	0.011	1.33	0.33	6.0×10^{-3}	6.0×10^{-3}	2.70	0.6
a	n	e_0	γ_t	S_{r0}	n_E	m(subloading surface)	P'_{sat}
5.0	1.0	0.8	1.8	0.15	1.3	10	8.0

λ	κ	M	ν'	K_a(m/min)	K_w (m/min)	G_s	m
0.14	0.016	1.33	0.33	6.0×10^{-4}	6.0×10^{-4}	2.70	0.8
a	n	e_0	γ_t	S_{r0}	n_E	m(subloading surface)	P'_{sat}
10.0	1.0	0.9	1.709	0.15	1.3	10	8.0

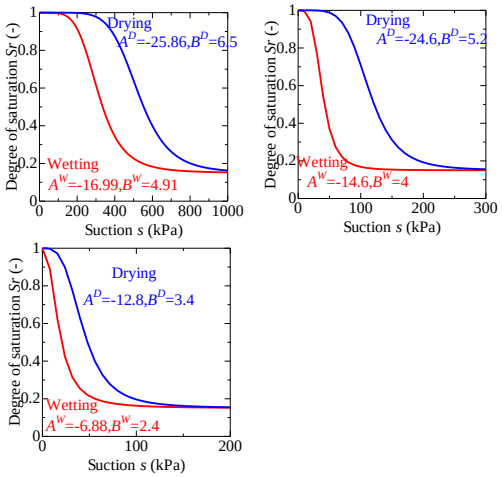

Fig.5 Water retention curve (upper left: clay, upper right: silt-mixed sand, lower left: sand)

$\boldsymbol{E_c}$ model parameter; $\boldsymbol{e_0}$ is the initial void ratio; $\boldsymbol{\gamma_t}$ is wet unit volume weight; $\boldsymbol{S_{r0}}$ is the critical saturation; $\boldsymbol{n_E}$ is the enlargement ratio of yield surface; m is the subloading surface parameter; and $\boldsymbol{p'_{sat}}$ is consolidation yield stress due to unsaturation.

Analysis Results and Discussion

Figure 6 shows the compaction curves for each material obtained from the displacement of the contact point of the uppermost element in the analysis domain shown in Fig. 4. The analysis was terminated at the load at which the pore pressure turned positive and the compacted soil was confirmed to be in a leaky condition (1100 kPa for clay, 700 kPa for silt mixed sand, and 700 kPa for sand). As similarly demonstrated by Kawai et al, all of the compaction curves obtained were convex upward along the zero-air gap curve from the elastic region to the plastic

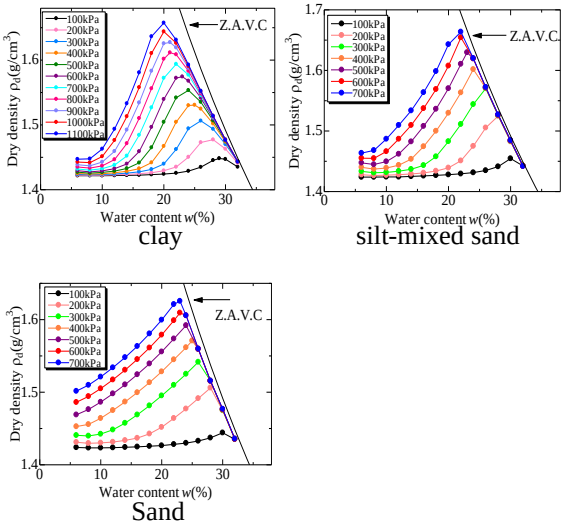

Fig.6 Compaction curves

region as the water content increased from low to high, in line with the laboratory test results. Furthermore,

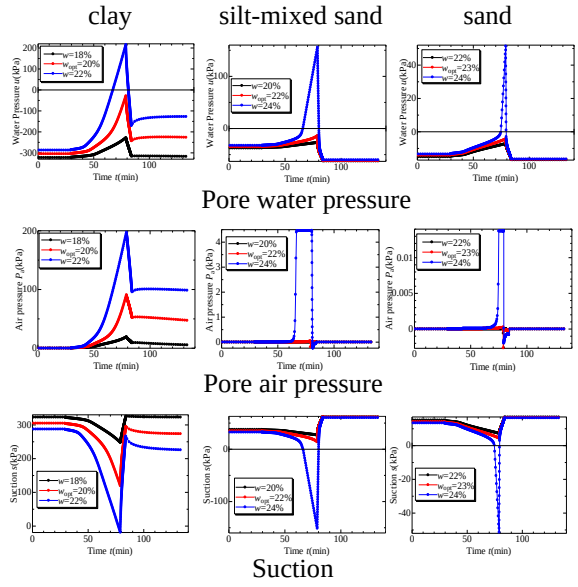

Fig. 7 Chronological change for each parameter

by using a subloading surface model, a smooth compaction curve could be expressed.

Using the quantities obtained from the compaction curves, a mechanical interpretation of the compaction mechanism was attempted. Figure 7 shows the results of various characteristics for each material at 1000 kPa for clay and 600 kPa for silt-mixed sand and sand. The obtained optimum moisture content ratio was compared with the results at 2% before and after the optimum moisture content ratio was reached. The dry side, the optimum moisture content ratio, and the wet side are black, red, and blue lines, respectively.

First, we examine the change in pore water pressure over time. For each material, the pore water pressure remained negative at the optimum water content and at relatively drier water contents. On the other hand, the pore water pressure turned to positive pressure at the relatively wetter side of the optimum water content ratio. Pore water pressure turned positive at the optimum water content ratio when the load was 1100 kPa for clay and 700 kPa for silt-mixed sand and sand. The fact that the pore water pressure turned positive indicates that the compacted soil was in a leaky state; the boundary conditions for compaction were not satisfied; and the compaction effect was not achieved.

Next, we examine the change in pore air pressure over time. The pore air pressure of clay remained high after unloading, while that of silt-mixed sand and sand showed almost no change from pre-loading conditions. This indicates that the effect of pore pressure is not caused by suction in silt-mixed sand and sand. In the case of clay, the air inside the soil is not fully released due to the characteristics of the material, indicating that the compaction effect is not sufficiently effective.

Finally, we examine the change in suction over time. The suction expression at unloading was significantly different between the relatively drier side and the wetter side of the optimum moisture content ratio. On the wetter side, the change in suction during unloading was large, and suction dropped to a negative value. This phenomenon occurred even at the optimum water content ratio, at 700 kPa for silt-mixed sand and sand. In the case of clay, pore air pressure also plays a role in suction development, so suction was positive even at a loading of 1100 kPa. However, the pore water pressure also turned positive, indicating that the compaction effect was not achieved.

In the compaction curves shown in Fig.6, the optimum water content ratio did not change at 1000 kPa and 1100 kPa for cohesive soil and at 600 kPa and 700 kPa for silt-mixed sand and sand. The fact that the optimum water content ratio did not change even when the load was increased indicates that the compaction effect was not obtained.

The suction effect (pore pressure) results and the compaction curves show that water leaked during compaction at 1100 kPa for clay and at 700 kPa for silt-mixed sand and sand, and that there was no change in optimum water content. This suggests that the specimens were over-compacted as they approached the saturated state from the unsaturated state, even though the compaction curve could still be drawn. Therefore, the analysis shows that the maximum compaction load that can achieve the best compaction effect is 1000 kPa for cohesive soils and 600 kPa for silt-mixed sand and sand.

INUNDATION ANALYSIS

To understand the collapse phenomenon associated with water absorption in unsaturated soils, this study performed a flooding analysis and compared the results after inundation with the initial water content ratio (initial saturation) as an internal condition to understand the soil's mechanical behavior.

Analysis Method

The maximum compaction load of 600 kPa for the silt-mixed sand obtained from the compaction analysis was used to represent the flooding collapse of the specimen by increasing the water head from the bottom surface after compaction. The optimum moisture content and maximum dry density of the specimens were 22% and 1.65 g/cm3, respectively. The initial water content ratios were 8%, 20%, 22%, 24%, and 32%.

Analysis Method

The results of the analysis are shown below. First, we examine changes from different initial water content ratios. Figure 8 shows the mean effective stress *p'*, void ratio *e*, and degree of saturation S_r, respectively.

The results of the mean effective stress p' illustrate that for all initial water content ratios, the values are lower after inundation than after compaction, indicating that strength is reduced due to water immersion.

The void ratio e indicates that at low initial water content, the void ratio is smaller than after compaction, indicating compressive behavior. At the optimum water content, the void ratio did not change much. Swelling behavior was predominant at high water content.

In addition, examining the degree of saturation, Sr, confirms that at higher water contents, i.e., water contents that show swelling behavior, transitions from an unsaturated to saturated state during compaction indicate that the initial degree of saturation influences the deformation after compaction.

These results indicate that the responses to the water table are divided into two groups: one on the compaction side and the other on the swelling side, depending on the initial water content (initial saturation) during the rise of the water table. In the case of low water content, the behavior is mainly compressive, and the pore ratio decreases despite the lower effective stress. This indicates the occurrence of internal fractures(collapses) peculiar to unsaturation.

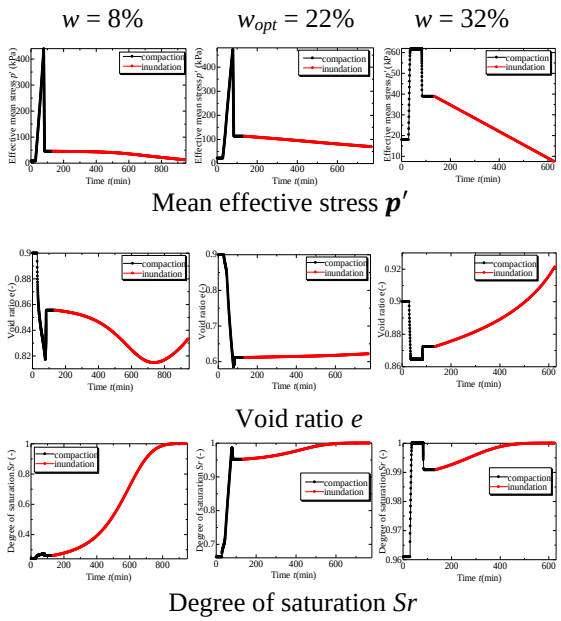

Fig. 8 Chronological change for each parameter

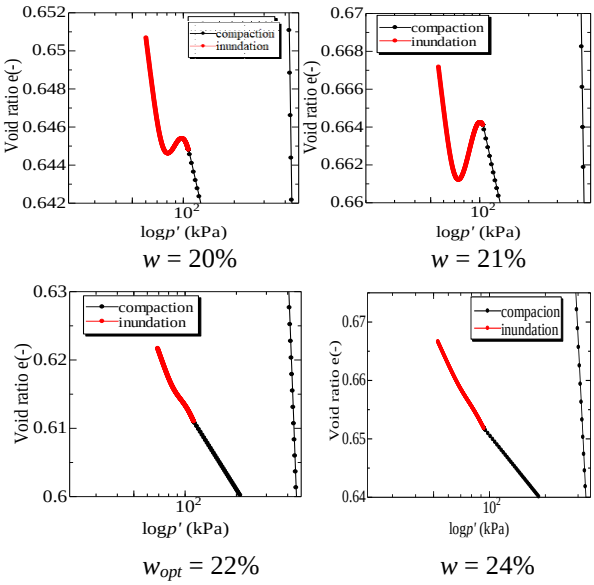

Fig. 9 *e*-log*p'* curve (Enlarged view)

Collapse Threshold

From these results, it is necessary to determine the specific threshold at which collapses are likely to occur. A comparison of the change in void ratio near the optimum water content ratio was observed in the water immersed portion of the *e*-log*p'* curve.

Figure 9 shows that the smallest change in void ratio after compaction and inundation occurred at a water content of 20%. The changes after compaction at the optimum water content ratio and on the wetter side of optimum were larger than those on the drier side. These results indicates that the strength against water immersion is slightly higher on the drier side of optimum than at the optimum water content.

CONSTANT VOLUME SHEAR ANALYSIS

In addition to inundation as an external factor, it is also important to understand strength properties due to shear for the stability analysis of unsaturated soils. In the case of unsaturated soil, the influence of other factors, such as the magnitude of suction in the soil, exhaust and drainage conditions, and other characteristics, are considered. In this study, compaction was considered as an unsaturated exhaust and undrained compressive deformation, and constant volume shear was applied to a specimen of silt-mixed sand under undrained conditions to analytically investigate strength properties.

Analysis Method

The material parameters, moisture property curves, and analysis domain used were the same as in the previous section, using silt-mixed sand. After compaction, the specimens were subjected to constant volume shear by applying strain until failure.

Analysis Results

Figure 10 shows the stress paths in the compaction and shear processes. The black line represents the behavior due to compaction and the red line represents the behavior due to shear. It can be seen analytically that the compaction causes the yield surface to expand, and the shear process causes it to hit the limit state line, leading to failure. Figure 11 shows the maximum shear strength at each water content ratio. Here, it can be seen that the shear strength increases gradually from the low water content ratio toward the optimum water content ratio, but decreases abruptly when the optimum water content ratio is exceeded. Since there is no significant difference in suction change before and after the optimum moisture content ratio, it is necessary to investigate this factor in the future. However, in the present analysis, the strength was shown to be dangerous because it resulted in a significant decrease in strength on the wet side above the optimum moisture content ratio.

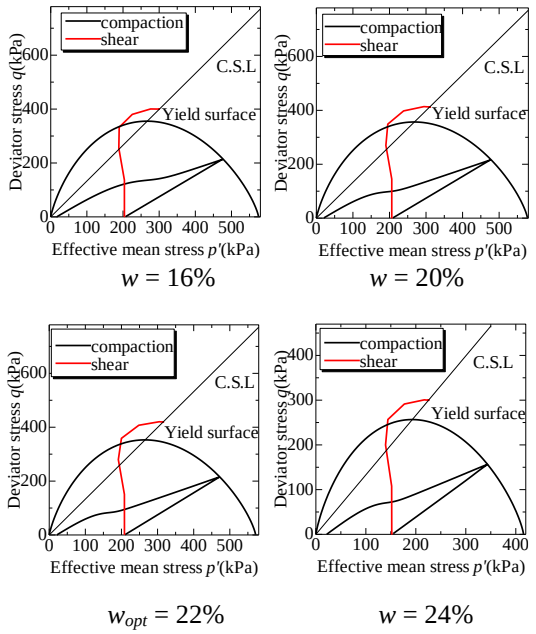

Fig. 10 Stress path

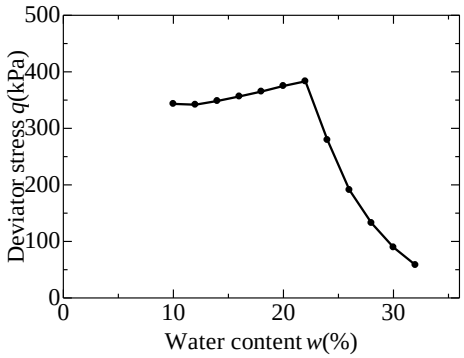

Fig. 11 Relation between water content and shear strength

CONCLUSION

- soil/water/air coupled finite element analysis program was used to draw compaction curves that more closely resemble actual conditions.
- The loading of 1100 kPa for clay and 700 kPa for silt mixed sand and sand, in relation to suction, pore water pressure, and the compaction curves drawn, indicated that it was over compaction . Although previous studies have shown this in soil/water coupled analysis, the present soil/water/air coupled analysis and the consideration of air dissolved in the soil/water/air coupled analysis confirm the over compaction.
- The collapses associated with flooding are greatly affected by the initial water content (initial saturation). At low water content ratios, the soil exhibits compressive behavior with negligible volume change, beyond which the soil begins to swell.
- The threshold of collapses was determined, and the highest strength was obtained at the optimum moisture content or slightly drier side of the optimum moisture content. Although the D values control is defined as 90% or more of the optimum moisture content, the results indicate that construction on the dry side is safer against flooding due to rainfall and flooding.
- Constant volume shear was expressed analytically to understand the strength properties.

In summary, the present study showed that construction on the dry side is the safer side and exhibits more strength in construction using D values in the field.

REFERENCES

[1] Kanazawa S., Toyoshima K., Kawai K.,

Tachibana S. and Iizuka A.: Analysis of mechanical behavior of compacted soil with F.E. method, journal of JSCE, No.68 (2), pp.291-298, 2012.

[2] Kawai K., Shibata M., Kanazawa S.: Simulations of static compaction with unsaturated soil/water coupled F.E. code, journal of JSCE, No,12, pp.429-436, 2009.

[3] Ohno S., Kawai K. and Tachibana S.: Elastic-plastic constitutive model for unsaturated soil applied effective degree of saturation as a parameter expressing stiffness, journal of JSCE, Vol.63/No.4, pp.1132-1141, 2007.

[4] Karube D., Kato S., Hamada K. and Honda M.: The relationship between the mechanical behavior and the state of porewater in unsaturated soil, journal of JSCE, No.535/III-34, pp.83-92, 1996.

[5] Ohno S., Iizuka A. and Ohta H., Two categories of new constitutive model derived from non-linear description of soil contractancy, Journal of applied mechanics, pp. 407-414, 2006.

[6] Schofield, A and Wroth, P. : Critical State Soil Mechanics, McGraw-Hill, pp. 1-310, 1968.

[7] Roscoe, K. H and Burland, J. B.: On the Generalised Stress-Strain Behavior of Wet Clay, Engineering Plasticity eds. J. Heyman and F. A. Leckie, Cambridge University Press, pp.535-609, 1968.

[8] Kawai K., Wang W. and Iizuka A.: The expression of hysteresis appearing on water characteristic curves and the change of stresses in unsaturated soils, Journal of applied mechanics, Vol.5, pp.777-784, 2002.

[9] Sugii T. and Uno T.: Modeling the New Moisture Characteristic Curve, Journal of JSCE, pp.130-131, 1995.

[10] Awal A.S.M.A, Hosseini H. and Hossain M.Z., Strength, Modulus of Elasticity and Shrinkage Behaviour of Concrete Containing Waste Carpet Fiber, International Journal of GEOMATE, Vol. 9, Issue 17, 2015, pp. 1441-1446.

[11] Mualem, Y.: A new model for predicting the hydraulic conductivity of unsaturated porous media, Water Resources Research, Vol.12, No.3, pp.514-522, 1976.

8th Int. Conf. on Structure, Engineering & Environment (SEE), Mie, Japan, Nov.10-12, 2022, ISBN: 978-4-909106094 C3051

CORROSION BEHAVIOR ANALYSIS OF SELF-COMPACTING CONCRETE USING IMPRESSED CURRENT AND RAPID CHLORIDE PENETRATION TEST

Stephen John C. Clemente[1] and Jason Maximino C. Ongpeng[2]
[1]Asst. Professor, FEU Institute of Technology, Philippines; [2] De La Salle University, Philippines

ABSTRACT

Corrosion is the leading reason for reinforced concrete structures reduced service life. Structures such as ports and harbors and bridges and other offshore and near shore are prone to chloride-induced corrosion. This research evaluates the use of self-compacting concrete (SCC) as an alternative concrete for such structures. In theory, SCC reduced water content, and high cement and powder content will help protect the reinforcement from chloride intrusion because of its lower porosity and the alkalinity that the cement provided. Sixteen different mixtures of SCCs were mixed and tested for rheology, compressive strength, rapid chloride ion penetration test (RCPT), and impressed current (IC). Water content is the significant factor that affects both RCPT and IC. The segregation of SCC when too much water-cement ratio is combined with a high amount of superplasticizer resulted in high level of corrosion in the reinforcement. The formation of cracks accelerates the corrosion due to the increased flow of current in the IC set-up. The impressed current technique is the suggested method for determining the corrosion resistance of concrete since it simulated the similar effect of corrosion to concrete which is cracking. It also stimulates the effect of rust on the flow of current. A rapid chloride penetration test is a good indicator of the durability of concrete but may be insignificant for predicting the corrosion level of reinforcement for SCC. Segregation negatively affects the total charge passed in the impressed current and the corrosion level of the rebar.

Keywords: Self-Compacting Concrete, Corrosion, Impressed Current, Rapid Chloride Penetration, Segregation

1. INTRODUCTION

Self-compacting concrete is one of the new types of concrete that has high workability as compared to conventional concrete. SCC constituents are similar to normal concrete except for the addition of chemical admixtures such as superplasticizer (SP) for improving the flowability and viscosity agent for controlling the segregation. SCC can be utilized for most concrete structures that have formworks. It is best used for structures with high-density reinforcement such as ports, buildings, and bridges since it can easily penetrate and flow freely through the tight spacing of reinforcement.

Corrosion is one of the problems for reinforced concrete structures especially for those exposed to high chloride environments such as near shore and offshore structures. Since the concrete has porosity, the reinforcement inside which is commonly made of steel is prone to corrosion. When the steel is converted to rust which is commonly 3-6 times the original volume of steel [1], this will induce stress on the concrete. Stress will cause cracking and eventually spalling of the concrete cover. Cracks and spalling will eventually cause acceleration of corrosion since the reinforcement will not have any protection [2][3].

Different mixtures of SCC particularly different amounts of cement, water, and SP will yield different rheological properties, compressive strength, and pore structure of the hardened concrete. Similar to normal concrete, SCC is prone to segregation because of the presence of a superplasticizer [4]. SP should be checked for compatibility with the cement and other constituents of the concrete. Most SPs brand indicates the limit for the dosage of SP to ensure that bleeding and segregation are prevented.

This research explored the use of self-compacting concrete for marine structures using rapid chloride ion penetration and impressed current technique for accelerated corrosion. Different mixtures of SCC with varying amounts of cement, water, and superplasticizer were tested for rheology, 28th-day rapid chloride ion penetration, and corrosion test. Linear regression analysis was performed to determine the effect of materials constituents on the RCPT and corrosion level of rebar. Segregation resistance of the SCC was also tested and correlated to the total charge passed in the impressed current and the corrosion level of the rebar.

2. METHODOLOGY

2.1 Design Mix of Self-Compacting Concrete

The table below shows the different design mixes of SCC. Cement was varied between 430 to 500 kg/m^3. Water was varied between 210 to 250 liters/

m^3 and superplasticizer content was between 1% to 1.8% by weight of cement. The gravel and sand were fixed at 780kg/m^3 and 830 kg/m^3 respectively. The researchers used a central composite design for the design mix of SCC. Plus sign (+) or capital (A) indicates the highest amount or dosage of the constituents, while the negative sign (-) or small (a) indicated the lowest amount or dosage. Zero (0) indicated the middle amount or dosage. The researcher used 3/8 inches as the maximum size for coarse aggregates and river sand. For the cement, this research used Type 1 cement and a polycarboxylate ether type for SP conforming to ASTM C494 Type G.

Table 1 Design Mix of SCC

	Cement (kg)	Water (L)	SP (%)
Max	500	250	1.8
Ave.	465	230	1.4
Min	430	210	1

2.2 Rheological Test

Rheological tests were performed to check the workability of the concrete. The researchers follow the standard of EFNARC with regard to the performance of these tests. Four different criteria were considered such as flowability, viscosity, passing ability, and segregation resistance. Table 2 shows the rheological tests needed for each criterion including the equipment used and the passing level for each test.

Table 2 Rheological Tests [5]

Criteria	Rheological Test	Equipment	Passing
Slump Flow	Slump Flow	Slump Cone	550mm
Viscosity	T500	Slump Cone	-
Passing Ability	L-Box	L-Box	0.8
Segregation	Segregation	GTM Screen	20%

2.3 Rapid Chloride Ion Penetration Test

A rapid chloride ion penetration test was used to check the durability as well as the porosity of the different design mixes of SCC. The researchers follow the standard of ASTM C1202, Standard Test Method for Electrical Indication of Concrete's Ability to Resist Chloride Ion Penetration. Using a 100mm diameter by 50mm sample cast from the different design mix of SCC. The samples were coated at the side using marine epoxy to ensure that there is no leakage (See Figure 1). The samples were put in a dry vacuum for 3 hours and then 1 hour for saturated vacuum and allowed to be soaked for 18 hours ± 2 hours. After soaking, the samples were inserted into the cells, the right-side cell is positively charged and filled with 0.3N of NaOH solution, meanwhile, the left side has a negative charge with a 3% NaCl solution (See Figure). The cells were connected in a 60Volts potential for 6 hours while the reading was taken every half hour. The total charge passed was computed in Coulombs (C).

(a)

(b)

(a) Fig. 1 RCPT Samples with Marine Epoxy on Side
(b) Fig. 2 RCPT Set-Up

2.4 Impressed Current Technique

To accelerate the corrosion of the reinforcement, the impressed current technique was used. This technique accelerates corrosion by increasing the rate of chloride ions flowing with the help of a power source.

This research used a 100mm cube sample with a 20mm diameter rebar at the center. The rebar is attached negative charge of a 3V adaptor and a copper plate on the positive charge side. The samples were soaked in a 5% NaCl solution as shown in Figure 3.

3. RESULTS AND DISCUSSION

3.1 Compressive Strength Rheological Properties

As shown in Table 3 are the results of rheological tests results and the compressive strength test result. Since the researchers used a high amount of cement and sand (830kg/m^3), many of the design mixes yield low flowability and passing ability. SCC with a higher amount of fine materials (sand and cement) will have higher viscosity [5]. Only mixtures 1, 5, 8, 10, 12, and 14 passes all requirements for rheology.

Table 3. Rheological and Compressive Strength

Mix No.	SF (mm)	T50 (sec)	L-Box	GTM (%)	fc' (Mpa)
SCC1	610	1	0.95	0.3	42.35
SCC2	470	8	0.12	0.21	41.83
SCC3	460	5	0.33	0.29	35.75
SCC4	540	6	0.29	0.75	34.17
SCC5	650	2	0.85	1.7	27.98
SCC6	540	2	0.63	5.72	17.77
SCC7	300	DNR	0	0.2	47.71
SCC8	630	2	0.8	3.09	26.76
SCC9	560	3	0.75	0.62	33.81
SCC10	630	2	0.8	0.77	31.18

SCC11	575	3	0.57	1.69	41.54
SCC12	565	3	0.84	0.74	36.5
SCC13	540	2.5	0.72	0.47	31.84
SCC14	720	1	1	10.02	41.57
SCC15	665	1	0.67	9.78	22.33
SCC16	470	7	0.41	0.23	32.45

Note: DNR- did not reach (since the slump flow is less than 500mm, t50 test cannot be performed).

3.2 Rapid Chloride Ion Penetration Results

All 16 mixes of SCC were tested in RCPT, mixtures 1, 8, 9, 10, 11, 13, 15, and 16 yield a high chloride permeability which is >4000. This is due to the high water-cement ratio of these samples which is >0.50. Other mixtures yield moderate chloride permeability (between 2000-4000) which is typical for concrete with a water-cement ratio between 0.40 to 0.50 [6].

Table 4. RCPT Result

No.	Design	Total Charge (Actual)	Total Charge (Estimate)
SCC1	++-	4400	4394.17
SCC2	+−+	3378	3372.15
SCC3	−−−	3902	3895.14
SCC4	−−+	3648	3643.05
SCC5	A00	3803	3797.34
SCC6	a00	3983	3975.05
SCC7	+−−	3770	3762.56
SCC8	0A0	4788	4778.18
SCC9	000	4925	4924.39
SCC10	−+−	5628	5622.69
SCC11	00A	4163	4159.25
SCC12	000	3557	3555.35
SCC13	00a	4323	4317.58
SCC14	+++	3922	3919.35
SCC15	−++	4238	4237.28
SCC16	0a0	4046	4040.92

Shown in Figure 4 SCC mix number 10 yields the highest current flowing for the whole duration of the test. This mixture has high water content with the lowest cement and SP.

Although other mixtures with high water content yield lower flow of current, it can be observed that these mixtures yield high segregation of about 10.02% for SCC14 and 9.78% for SCC15 have the two lowest currents flowing among all mixture with (+ or A) levels of water content. The segregation or bleeding is due to the high amount of water and superplasticizer.

During the experimentation, the researchers noticed a little bleeding of water on these mixes due to the high SP content of 1.8% by weight of cement. This bleeding may contribute to the loss of water in the mixture during casting and may contribute to a denser concrete. The height of the specimen used for RCPT which is 50mm may play a big role in diffusing the negative effect of bleeding and segregation in the specimen used for RCPT. Several researchers explored this but there are still no established guidelines about this phenomenon.

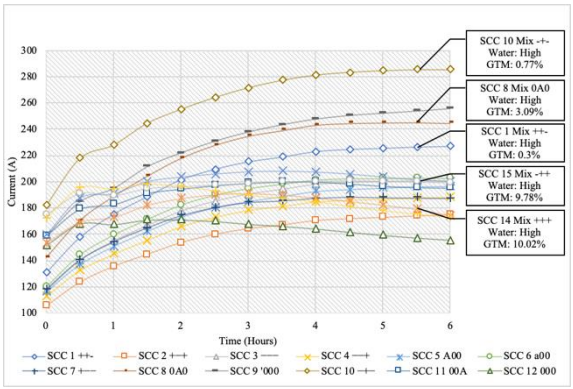

Fig. 4 RCPT Graph

3.2.1 Correlation of RCPT and Material Constituents

Simple regression analysis is performed to analyze the effect of each constituent on the total charge passed in Coulombs. As shown in Table 5A, the linear model derived has an R-squared value of 0.6026.

Table 5A. Regression Analysis for RCPT (Regression Statistics)

Regression Statistics	Value
Multiple R	0.7763
R Square	0.6026
Adjusted R Square	0.5032
Standard Error	403.1950
Observations	16

Although water is the only significant factor with a P-value of less than 0.05, cement and SP may still be considered substantial factors with P-values of 0.12 and 0.06 respectively. Only water yields a positive coefficient, meaning increasing its amount will result in increased charge passed (Coulombs) [7]. For the SP, a higher amount of SP will result in a lower charge passed, this result may provide evidence that a certain range of bleeding in concrete may result in a denser concrete which resulted in high compressive strength and lower charge passed referring to SCC14.

Table 5B. Regression Analysis (Coeff and P-Values)

	Coeff	S. Error	t Stat	P-value
Intercept	3048.27	2286.64	1.33	0.21
Cement	-6.07	3.64	-1.67	0.12
Water	21.16	6.38	3.32	0.01

SP	-668.50	318.75	-2.10	0.06

The researchers considered a linear correlation between the water-cement ratio and the total charge passed in RCPT. Although considered as a moderate correlation having an R^2 value of 0.432 as shown in Figure 5, the model suggests that a higher water-cement ratio of SCC will yield to higher charge passed which is an indication of higher porosity in the concrete [8].

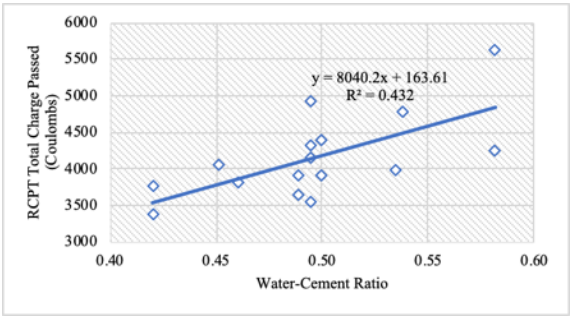

Fig. 5 Correlation Between W/C and RCPT

3.3 Impressed Current

3.3.1 Comparison of Corrosion Level

Shown in Figure 5 is the corrosion level of each sample exposed in impressed current for 5 days and 10 days. Some samples more than doubled after their corrosion level considering 5 days to 10 days of exposure due to the presence of cracks and eradication of the passive layer that protects the reinforcement.

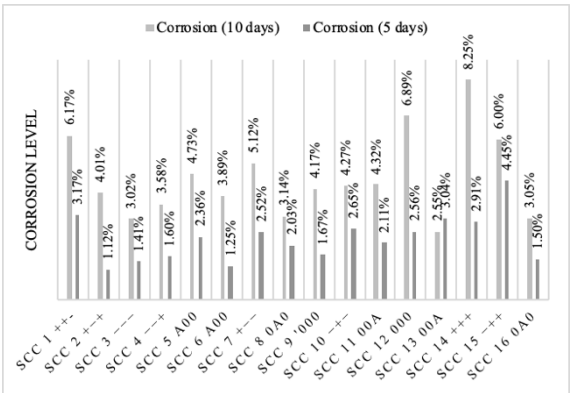

Fig. 6 Corrosion Level

3.3.2 Influence of Material Constituents and Cracks on Impressed Current

SCC 7 shows a hairline crack before reaching the 5th day on impressed current. This is due to the very high current density of around 1.59mA/cm^2 for SCC7. SCC14 which yields the 4th most corrosion level among 16 mixes exposed to 5 days of impressed current is due to the uneven surface due to high segregation (See Figure 7). Bleeding and segregation also cause diluted cement paste and decrease the transport resistance of the concrete [9].

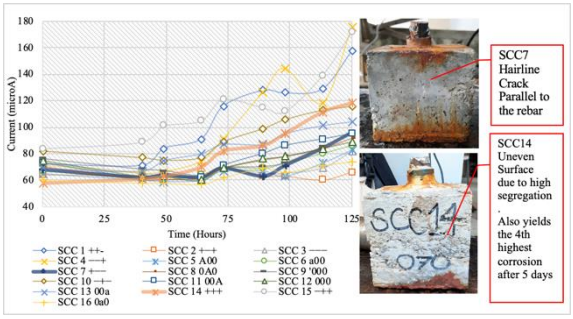

Fig. 7 Impressed Current (5 days)

SCC 7 which ranks 5th for the highest corrosion level out of 16 samples shows a crack parallel to the length of the rebar. The crack started at around 90 hours as shown in Figure 7, the current started to pick up due to the direct path of the current. SCC14 shows a severe crack at the edge and the bottom part which resulted in a big chunk of reinforcement corroded at the bottom part. This crack is directly towards the reinforcement that resulted in a high flow of current. Due to the presence of rust on the surface of reinforcement and sometimes filling in the voids and cracks, it can alter the flow of current since rust is a poor conductor of electricity [10][11].

Also shown on the graph, the current goes up and down over time. This is due to the change in the resistance of concrete, and the presence of cracks and rust.

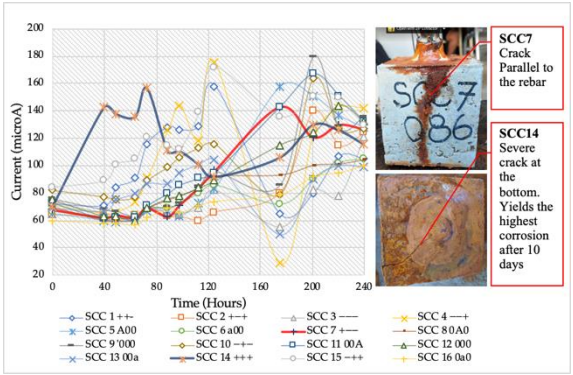

Fig. 8 Impressed Current (10 days)

A simple regression analysis was conducted to analyze the relationship between the cement, water, and SP content of SCC to the corrosion level of the rebar. As shown in table 6, an R2 value of 0.44 was derived from the regression model that indicated a moderated correlation.

3.3.3 Regression Analysis Corrosion Level

Table 6. Regression Analysis for Corrosion Level (Regression Statistics)

Regression Statistics	Value
Multiple R	0.6674
R Square	0.4454
Adjusted R Square	0.3068
Standard Error	0.0130
Observations	16

Table 7 shows the derived linear regression model. Water content is the only significant factor with P-values of 0.05. All coefficients were positive as shown in the table. A higher dosage of SP will be induced bleeding, but in this experiment, the dosage of SP is limited to 1.8% by weight of cement which is below the recommended 2% by the manufacturer. The segregation was also within the allowed range of below 20%. SP-induced bleeding for samples with a high amount of cement as observed from SCC14 may result in high compressive strength but the segregation of coarse aggregates at the bottom contributed to the pore structure of the concrete, thus increasing the corrosion on the reinforcement [12].

Table 7. Regression Analysis for Impressed Current (Coefficients and P-Values)

	Coeff	S.Error	t Stat	P-value
Intercept	-0.1759	0.0739	-2.38	0.03
Cement	0.0002	0.0001	1.82	0.09
Water	0.0005	0.0002	2.20	0.05
SP	0.0126	0.0103	1.22	0.25

3.4 Correlation Analysis Between Corrosion Level and Total Charge Passed (RCPT and Impressed Current)

The total charge passed is calculated using the area generated by the current flowing (y-axis) and time in seconds (x-axis). As shown in Figure 9, a moderate correlation with an R2 value of 0.48 was observed between the total charge passed and corrosion level. In this experiment, the voltage of the power source is set as a constant. The rate of electron flowing in the circuit (power source→copper →NaCl solution→porous structure of concrete→steel reinforcement→power source) serves as the resistance of concrete.

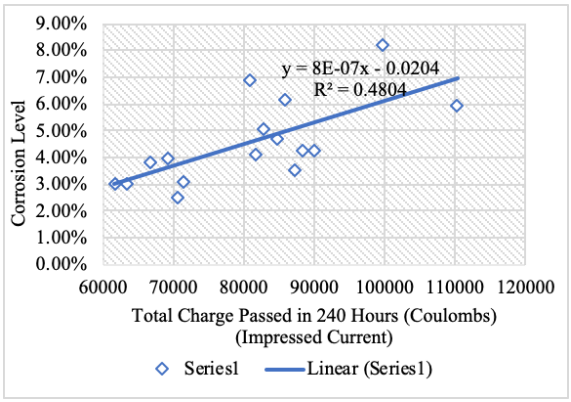

Fig. 9 Impressed Current (10 days)

The result of the RCPT has no significant correlation to the total charge passed in the impressed current with an R^2 value of 0.0206. The RCPT test results only characterized the concrete's pore structure and can be used as a durability indicator. The corrosion of reinforcement inside the concrete is affected by other factors such as the passive layer of protection, cracks, temperature, etc.

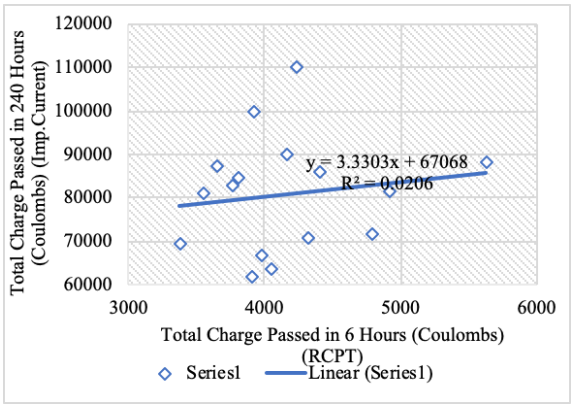

Fig. 10 Impressed Current (10 days)

3.5 Effect of Segregation on Corrosion and Total Charge Passed.

As shown in Figure 11, the model suggests that higher segregation in SCC resulted in to increase in the total charge passed in the impressed current set-up and also yields higher corrosion levels in the reinforcement with R squared of 0.5539 and 0.2877 respectively.

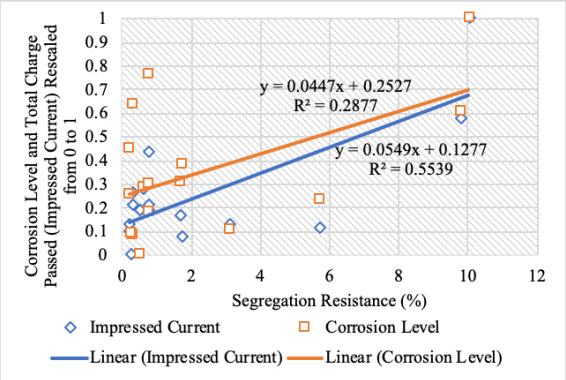

Fig. 11 Effect of Segregation on Corrosion

4. CONCLUSION

Water is the only significant factor with P-value less than 0.05 for both the RCPT test and impressed current (corrosion level). The water-cement ratio is the leading factor in the porosity of the SCC and increases the total charge passing in the specimen for the RCPT test.

The crack in SCC7 increases the flow of current in the circuit. This is the reason for the high corrosion level of the reinforcement in that specimen. SCC14 has the highest segregation of 10.02% and the concrete shows inconsistencies on the surface due to bleeding. Segregation at the bottom of the specimen increases the potential for chloride intrusion due to the pore structure created by the capillary action at the coarse aggregates.

RCPT is not a good indicator for SCC in predicting its corrosion resistance. This is due to the other factors present that affect the rate of corrosion such as cracks and the formation of rust. The impressed current technique performed in this experiment can be a standard for testing the corrosion resistance of concrete as protection for the reinforcement. It will capture most of the factors such as the materials constituents, cracks, porosity, and temperature.

ACKNOWLEDGMENTS

The researchers want to give thanks to the whole project team for doing the experiments, Engr. Jaysoon Macmac, Engr. John Bryan Tiu, Engr. Angelou Faye Nuñez, Engr. Rafael Reymundo, Engr. Hannah Lou Argota and Engr. Angel Rose Macapanas. Special thanks to the Department of Science and Technology Philippine Council for Industry, Energy, and Emerging Technology Research and Development for the funding of the project.

REFERENCES

[1] Smith, J. L., & Virmani, Y. P. (2000). Materials and methods for corrosion control of reinforced and prestressed concrete structures in new construction (No. FHWA-RD-00-081). United States. Federal Highway Administration.

[2] Concha N, Oreta AW. A model for time-to- cracking of concrete due to chloride induced corrosion using artificial neural network. InIOP Conference Series: Materials Science and Engineering 2018 Oct (Vol. 431, No. 7, p.072009). IOP Publishing.

[3] Ghanooni-Bagha, M., Shayanfar, M. A., Shirzadi-Javid, A. A., & Ziaadiny, H. (2016). Corrosion-induced reduction in compressive strength of self-compacting concretes containing mineral admixtures. *Construction and Building Materials*, *113*, 221-228.

[4] Clemente, S. J. C. (2015). Artificial neural network modeling of rheological parameters and compressive strength of self-compacting concrete with zeolite mineral as a partial replacement for cement.

[5] EFNARC, F. (2002). Specification and guidelines for self-compacting concrete. *European federation of specialist construction chemicals and concrete systems*.

[6] Shi, C. (2004). Effect of mixing proportions of concrete on its electrical conductivity and the rapid chloride permeability test (ASTM C1202 or ASSHTO T277) results. *Cement and concrete research*, *34*(3), 537-545.

[7] Yang, C. C., & Chiang, C. T. (2005). On the relationship between pore structure and charge passed from RCPT in mineral-free cement-based materials. *Materials chemistry and physics*, *93*(1), 202-207.

[8] Ghafoori, N., Najimi, M., Sobhani, J., & Aqel, M. A. (2013). Predicting rapid chloride permeability of self-consolidating concrete: a comparative study on statistical and neural network models. *Construction and Building Materials*, *44*, 381-390.

[9] Safiuddin, M., West, J. S., & Soudki, K. A. (2008). Durability performance of self-consolidating concrete. *Journal of Applied Sciences Research*, *4*(12), 1834-1840.

[10] Concha, N. C., & Oreta, A. W. C. (2021). Investigation of the effects of corrosion on bond strength of steel in concrete using neural network. *Computers and Concrete*, *28*(1), 77-91.

[11] Yoo, D. Y., Gim, J. Y., & Chun, B. (2020). Effects of rust layer and corrosion degree on the pullout behavior of steel fibers from ultra-high-performance concrete. *Journal of Materials Research and Technology*, *9*(3), 3632-3648.

[12] Gao, X., Zhang, J., & Su, Y. (2019). Influence of vibration-induced segregation on mechanical property and chloride ion permeability of concrete with variable rheological performance. *Construction and Building Materials*, *194*, 32-41.

8th Int. Conf. on Structure, Engineering & Environment (SEE), Mie, Japan, Nov.10-12, 2022, ISBN: 978-4-909106094 C3051

DAMAGE AND SUBMERGED PROBABILITY EVALUATION OF FLOATING OFFSHORE WIND TURBINES UNDER WIND AND WAVE ACTIONS

Ken-ichi Fujita[1], Harumi Yashiro[2]
[1] Faculty of Engineering, Nagasaki Institute of Applied Science, Japan;
[2] School of Systems Engineering, National Defense Academy of Japan, Japan

ABSTRACT

This study presents an evaluation method of damage probability of floating typed offshore wind turbines under wind and wave actions, in addition to submerged probability of blades of the turbines by the inclination of the turbines by the actions. The response of the structure for wind is evaluated by a static analysis, on the other hand, wave response analysis of the structure is evaluated by using a stationary random vibration theory and a wet-mode superposition method. The random variable of the responses is expressed by linear combination of the results of response analyses of the structure. The damage probability of the structure is evaluated by using a reliability evaluation method of structures. Whereas, the submerged probability of blades in the roll motion of the structure is evaluated by using the results of the response analysis. In the evaluation of the submerged probability, relation between the stability of the floating base and the inclined moment by wind is used. The dynamic behavior of the floating wind turbine is analyzed by taking account of a sea water-structure interaction. The sea water region is modeled by boundary element (BE) and the floating wind turbine is modeled by finite element (FE). Numerical examples present the damage probability and the submerged probability of large and small scaled floating wind turbines for wind and wave actions.

Keywords: Floating offshore wind turbine, Damage probability, Submerged probability, Reliability, Stationary random vibration

INTRODUCTION

To promote of utilization of the wind energy is one of the global goal toward to realization of the decarbonized society and the carbon neutrality. Installation of the wind turbines in the sea area compared with that of on land has several advantage as follows; no restrictions of scale of wind turbines, stably utilization of the wind on the sea and extremely small of the effect of vibration hazard and noise caused by the rotation of the wind turbine. Moreover, installation at the deep ocean can be available by selecting the floating type.

In planning and design of floating wind turbines, selection of structural type, evaluations of the motion and the structural strength are important because the structures are always oscillating and moving by wind and wave actions. The dynamic behavior of the floating wind turbines for wind and wave have been investigated in many studies [1]-[6]. Moreover, from a view point of long-term operation, dynamic behavior of floating wind turbine considered partially damage of structural element have been studied [7]-[8]. However, studies on structural risk for wind and wave of offshore wind turbines have not seen, such as a seismic risk evaluation for on structures on land. The structural risk evaluation of the wind turbine can be considered to be necessary from a view point of long-term operation.

In this study, to develop a structural risk evaluation method for wind and wave actions of the wind turbines. an evaluation method of damage probability of the floating wind turbines and submerged probability of blades are presented. The wind and irregular wave response analyses of the floating wind turbine are carried out to evaluate the both probabilities. The wind response is evaluated by using a static analysis. On the other hand, the irregular wave response is evaluated by using a stationary random vibration theory and a wet-mode superposition method [9]. The random variable of the responses is expressed by linear combination. In the response analysis, a coupled model of boundary element (BE) and finite element (FE) is used. The sea water region is modeled by BE. The offshore wind turbine is modeled by FE. In addition, the floating base and the tower are discretized by using Mindlin's plate elements and beam elements, respectively. Moreover, the damage probability and the submerged probability of large and small scaled floating wind turbines for wind and wave actions are evaluated.

ANALYTICAL MODEL AND CONDITIONS

The floating wind turbine in this study is shown in Fig.1. The global coordinate system *x-y-z* is used. The

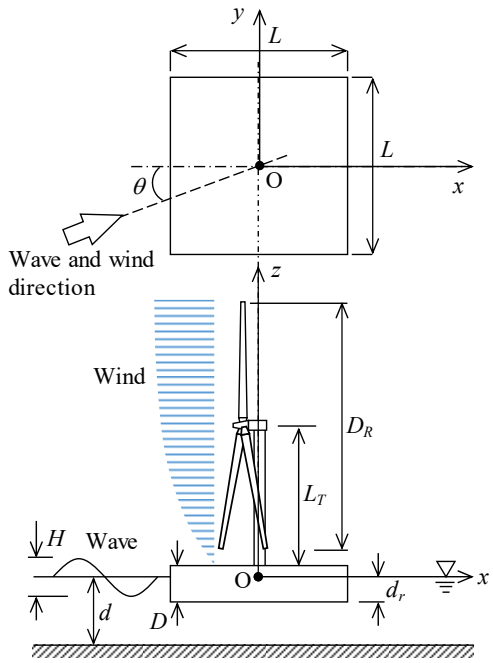

Fig.1 Geometric parameters of a floating offshore wind turbine

origin is placed on the still water surface. The floating base has a square plane and the base has no moorings. The tower has cylindrical cross section and uniform outer diameter. In this figure, L, D and d_r are the length, depth and draft of the floating base, respectively, L_T is the length of the tower, D_R is the diameter of the rotor, d is the depth of sea water, H is the wave height and θ is the incident angle of wind and wave.

The analytical conditions used in this study are as follows:

1) The motion of the floating wind turbines is governed by a linear random vibration theory.
2) The sea water is inviscid, incompressible and irrotational.
3) The irregular wave is followed to an ergodic process with mean value zero.
4) The strength and response of the floating wind turbines follows normal distribution.
5) The wind and wave are incident from the same direction.
6) The wind load is not acted on the floating base.

RESPONSE EVALUATION OF FLOATING WIND TURBINES

The wind response of the floating wind turbine is evaluated by a linear static analysis. The irregular wave response is evaluated by using a stationary random vibration theory. Sea water-structure interaction is considered in the wave response analysis.

Wind Response

The wind load acting on the floating wind turbine is evaluated statically. The equation of equilibrium of the floating wind turbine for wind load is given by

$$([K_S]+[K_W])\{U\}=\{F_W\} \tag{1}$$

where $[K_S](NP\text{x}NP)$ the stiffness matrix of the wind turbine, $[K_W](NP\text{x}NP)$ is the hydrostatic stiffness matrix, $\{U\}(NP\text{x}1)$ is the displacement vector of the floating wind turbine, $\{F_W\}(NP\text{x}1)$ is the wind load vector and NP is the total number of degrees-of-freedom of the floating wind turbine.

The wind pressure, P_W, acting on the wind turbine and the wind speed, V_z, at a height of z above the sea surface are given by the following equations, respectively.

$$P_W(z)=\rho_A V_z^2 C_d/2 \tag{2}$$

$$V_z/V_0=(z/z_0)^{1/n} \tag{3}$$

where ρ_A is the mass density of air, C_d is the drag coefficient, V_0 is the mean velocity at a reference height z_0, $1/n$ is the exponential of the power row. In this study, ρ_A=1.22kg/m^3, C_d=0.7 and n=7 are used.

Irregular Wave Response

Irregular wave and wave spectrum

The profile of incident irregular wave profile of h can be expressed by sum of a large number of wave components.

$$h=\sum_{j=1}^{\infty}\sqrt{2S_\eta(\omega_j)\Delta\omega}\cdot\exp[-i\{\omega_j t-k_j(x\cos\theta+y\sin\theta)+\varepsilon_j\}] \tag{4}$$

where i is the imaginary unit, t is the time, ω_j, k_j and ε_j are the circular frequency, wave number and phase of j-th wave, respectively, and $\Delta\omega=\omega_{j+1}-\omega_{j-1}$. $S_\eta(\omega)$ is Pierson-Moskovitz wave spectrum given by a mean wind speed V_0 at 19.5m height above the sea surface.

$$S_\eta(\omega)=\alpha(g^2/\omega^5)\exp\{-\beta(g/\omega V_0)^4\} \tag{5}$$

where α=8.10x10^{-3}, β=0.74 and g is the gravitational acceleration.

Stationary random vibration

The equation of motion of the floating wind turbine taking account of the sea water-structure

interaction is given by the following equation:

$$([M_S]+[M_W])\{\ddot{U}\}+([C_S]+[C_W])\{\dot{U}\} +([K_S]+[K_W])\{U\}=\{F_{WE}\} \quad (6)$$

where $[M_S](NP\text{x}NP)$ and $[C_S](NP\text{x}NP)$ are the mass and damping matrices of the floating wind turbine, respectively, $[M_W](NP\text{x}NP)$ and $[C_W](NP\text{x}NP)$ are the added mass and radiation wave damping matrices, respectively, $\{F_{EW}\}$ is the wave exciting force and $\cdot = \partial / \partial t$. $[M_W]$, $[C_W]$ and $\{F_{EW}\}$ can be evaluated by BE.

The displacement vector, $\{U\}$, can be given by multiplying wet-mode shape matrix $[\varphi](NP\text{x}NM)$ obtained by eigenvalue analysis of Eq. (6) and generalized coordinate vector $\{q\}(NM\text{x}1)$. In addition, NM is the number of mode superposition.

$$\{U\}=[\varphi]\{q\} \quad (7)$$

The generalized coordinate vector, $\{q\}$, is obtained from the following equation:

$$\{q\}=[H(i\omega)]\{Q(i\omega)\} \quad (8)$$

where $\{Q(i\omega)\}(NM\text{x}1)$ is the generalized force vector and $[H(i\omega)](NM\text{x}NM)$ is the frequency response function given by the following equation:

$$[H(i\omega)]=(-\omega^2[M]+i\omega[C]+[K])^{-1} \quad (9)$$

where $[M](NM\text{x}NM)$, $[C](NM\text{x}NM)$ and $[K](NM\text{x}NM)$ are the generalized mass, damping and stiffness matrices, respectively.

The variance of the floating wind turbine can be evaluated by integrating the cross power spectrum density function obtained from Fourier transform of autocorrelation function of the response over the entire circular frequency region.

The variance, U_j^2 (j=1,2, ⋯ ,NP), of the displacement response is obtained from the following equation:

$$U_j^2=\int_0^\infty S_{Ujj}(\omega)d\omega \quad (10)$$

where $S_{Ujj}(\omega)$ is the diagonal component of the cross-spectral density function matrix, $[S_U(\omega)](NP\text{x}NP)$, expressed by the following equation:

$$[S_U(\omega)]=E[\{U(i\omega)\}\{U^*(i\omega)\}^T] =[\varphi][H(i\omega)][S_{F\varphi}(\omega)][H^*(i\omega)]^T[\varphi]^T \quad (11)$$

where $E[\ ]$ is the expected value, * is the complex conjugate, $\{U(i\omega)\}(NP\text{x}1)$ is Fourier transform of $\{U\}$ and $[S_{F\varphi}(\omega)](NM\text{x}NM)$ is the cross-spectra density function of the generalized force expressed by the following equation.

$$[S_{F\varphi}(\omega)]=E[\{Q(i\omega)\}\{Q^*(i\omega)\}^T] \quad (12)$$

The variance of the internal force of the floating wind turbine can be evaluated by the same method.

DAMAGE PROBABILITY EVALUATION OF WIND TURBINES

The damage probability of the wind turbine for wind and wave is evaluated by using probability density functions of yield strength and internal force. The functions can be obtained from random variables of the yield strength and the internal force.

The damage mode considered in this study is a combined stress of compressive force and bending moment at the base of the tower. A performance function, Z, with respect to the damage by the combined stress can be defined as

$$Z=1-(S_C/R_C+S_B/R_B) \quad (13)$$

where S_C and S_B are the random variations of the compressive force and the bending moment at the base of the tower occurred by wind and wave actions, respectively, and R_C and R_B are the random variations of the buckling strength and the yield bending strength of the tower, respectively.

S_C and S_B can be expressed by linear combination of static and dynamic analyses results. R_C and R_B are evaluated by using a statistical data on yield strength of steel. The damage occurs when Z in Eq. (13) becomes less than zero. The damage probability is evaluated by using an Advanced First-Order Second-Moment (AFOSM).

SUBMERGED PROBABILITY EVALUATION OF BLADES

Submerge of the blade is assumed to be occurred in the roll motion (incident direction θ=90deg) of the floating wind turbine. The submerged probability in this study is defined as the probability that the edge of the blade is on a circular arc of a fan-shaped of underwater part as shown in Fig.2. In this figure, θ_B is the angle between the blades, θ_C is the central angle of the fan-shaped and R_x is the roll angle in the motion of the floating wind turbine.

The submerged probability, p_{WC}, of the blade in this study can be expressed by the following equation:

$$p_{WC}=\theta_C/\theta_B \quad (14)$$

The roll angle, θ_C, can be evaluated by sum of the roll angles for wind and wave. The mean value, R_{xw}, of

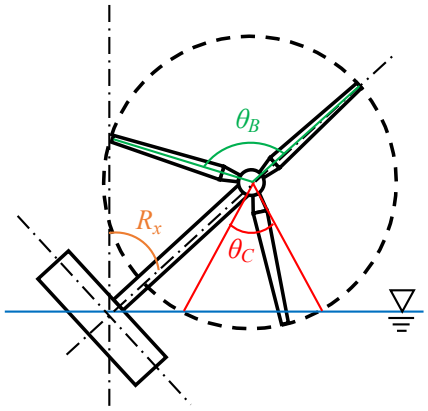

Fig.2 Definition of R_x, θ_B, θ_C in evaluation of submerged probability

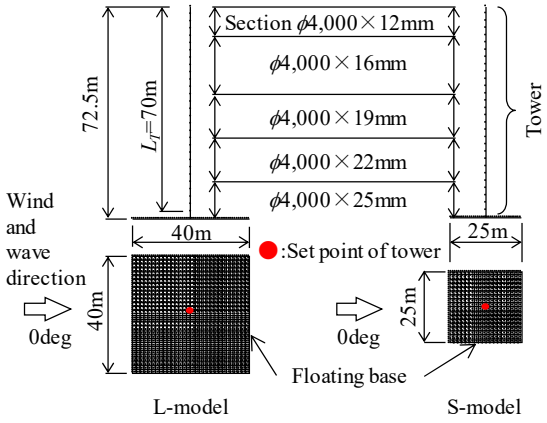

Fig.3 Mesh discretization of analysis model

the roll angle by wave can be described by using the standard deviation, σ_θ, of the roll. The probability density function of the envelope of the wave response in time domain assumed to be follow Rayleigh distribution.

$$R_{xw} = 1.253\sigma_\theta \tag{15}$$

EVALUATION RESULTS AND DISCUSSION

Analytical Model

The damage probability of tower and the submerged probability of blade are evaluated by using the proposed method. The target model is 3MW wind turbine set on two-types floating base (L-model and S-model) of different scales. The discretization of analytical models and the specifications of the floating wind turbine are shown in Fig.3 and Table 1, respectively. In the analysis, blades, hub and nacelle of the wind turbine are modeled as one concentrated-mass. The wind speeds, V_z, at height of the hub above still sea surface (H_T=71.25m) are 10, 15, 20 and 25m/s for operation and 30, 40, 50 and 60m/s for non-operation. Projected areas of the rotor in operation

Table 1 Specification of analytical model

Item	Symbol (Unit)	L-model	S-model
Length of floating base	L (m)	40	25
Depth of floating base	D (m)	5	5
Draft of floating base	d_r (m)	3.75	3.75
Young's modulus	E_p (N/m^2)	5.789×10^9	5.926×10^9
Poisson's ratio	ν_p (–)	0.3	0.3
Total mass of overall structure	m_S (kg)	6.151×10^6	2.402×10^6
Tower length (above deck)	L_T (m)	70	
Mass of tower	m_T (kg)	128×10^3	
Mass of nacel, hub and blades	m_B (kg)	160×10^3	
Young's modulus of wind turbine	E (N/m^2)	2.058×10^{11}	
Poisson's ratio of wind turbine	ν (–)	0.3	
Mass density of tower	ρ_T (kg/m^3)	7850	
Depth of sea water	d (m)	50	
Mass density of sea water	ρ_W (kg/m^3)	1025	

Table 2 Mean and standard deviation of yield strength

Steel grade	Mean (N/mm^2)	Standard deviation (N/mm^2)
SM490	361.865	34.421

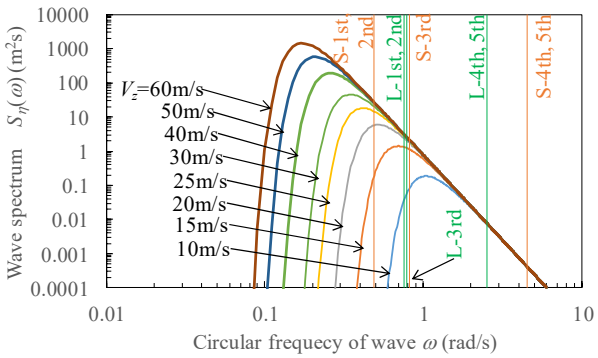

Fig.4 Pierson-Moskowitz wave spectrum

and non-operation are shown in Table 1. The wind and wave directions are zero degrees for the damage evaluation and 90 degrees for the submerged evaluation, respectively.

The mean value and standard deviation of SM490 class steel used to the tower is shown in Table 2. The wave spectrum used in this study are shown in Fig.4. In this figure, natural circular frequency up to the fifth mode by sea water-structure coupled free vibration analysis of models is plotted by straight lines.

Response Analysis Results

The bending moment distributions in wind on the center line in the both models are shown in Fig.5. The maximum bending moment occurs at the base of the tower. The difference of the bending moment distribution and magnitude between the both models cannot be seen. The magnitude of the bending moment in the operation is larger because the

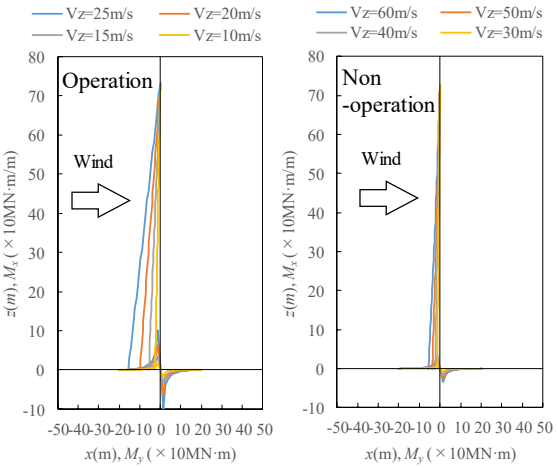

(a) L-model

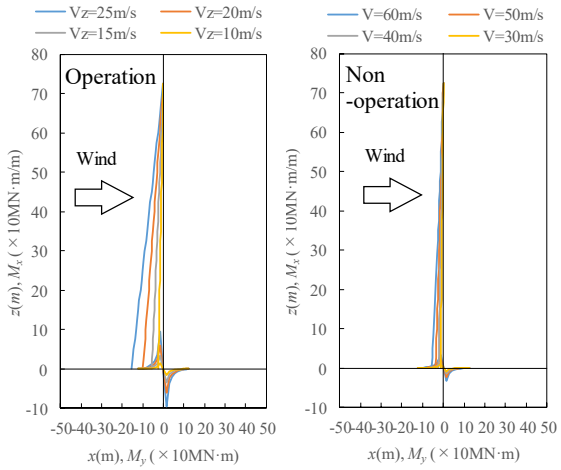

(b) S-model

Fig.5 Bending moment distribution in wind

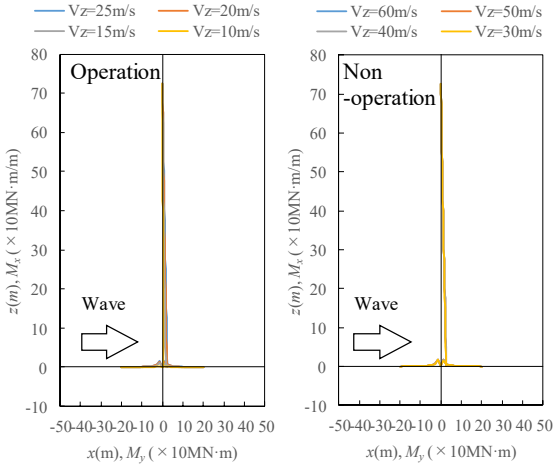

(a) L-model

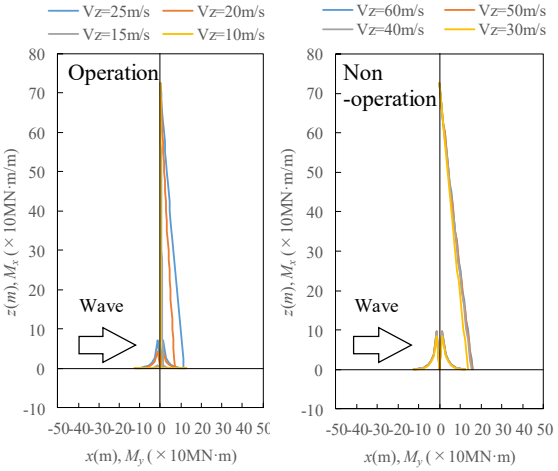

(b) S-model

Fig.6 Standard deviation of bending moment distribution in irregular wave

projection area of rotor in the operation is large.

The standard deviations of the bending moment distributions in irregular wave of the models are shown in Fig.6. The bending moment in S-model becomes larger than that of L-model because of large motions induced on S-model. In the non-operation, the difference of the bending moment in the irregular wave is small because the pitch motion in long wavelength becomes small for small scaled floating structures.

Damage Probability of Wind Turbine

In evaluation of the damage probability of the tower, the random variable of the internal force can be evaluated by linear combination of the results of response analysis for wind and wave. The mean value and the standard deviation can be evaluated by the internal force obtained by the wind response and irregular response analyses, respectively. The mean value and the standard deviation of the strength can be evaluated by using the cross-sectional performance of the tower and the random variables of steel shown in Table 2. The random variables of strengths are shown in Table 3.

The damage probability at the base of the tower of the both models for several wind speeds is shown in Fig.7. The probabilities between L-model and S-model have difference value though the specifications of the tower are same. The difference of the probability depends on the size of the floating base. The probability becomes high for the both models in the operation because of large projection area for wind. The probability of the tower on S-model in the non-operation becomes high because the pitch motion in relatively small scaled floating structures tends to be excited easily by wind and wave.

Submerged Probability of Blades

The submerged probability is evaluated by using

Table 3 Mean and standard deviation of allowable yield strength

Strength	Mean	Standard deviation
Buckling R_C	4.535×10MN	0.431×10MN
Bending R_B	11.157×10MN·m	1.061×10MN·m

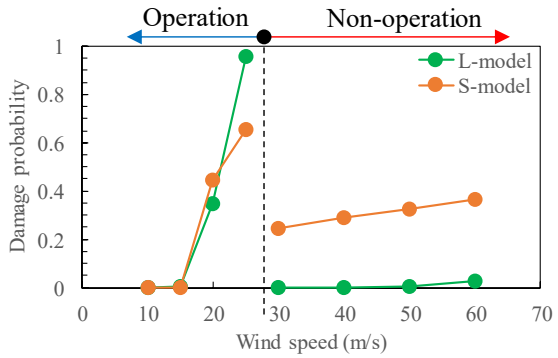

Fig.7 Damage probability at base of tower

the roll angle obtained from the response analysis results. The probability of the both models in the non-operation is shown in Fig.8.

The probability of S-model becomes large with increasing of wind speed. However, the probability of L-model is extremely small. It can be considered that the roll motion in large scaled floating structures tends to be not excited by wind and wave.

CONCLUSIONS

An evaluation method of the damage and the submerged probabilities of the floating wind turbine for wind and wave are proposed. The summary of this study can be drawn as follows.

1) The damage probability of the floating wind turbine in operation depends on the size of the projection area for wind. On the other hand, the probability in non-operation depends on the scale of the floating base.
2) The submerged probability of blade depends on the scale of the floating base. For small floating base, the probability becomes high with increasing of wind speeds.
3) Bending moment occurred in wind tower is dominated by magnitude of the roll and pitch motions of the floating wind turbine.

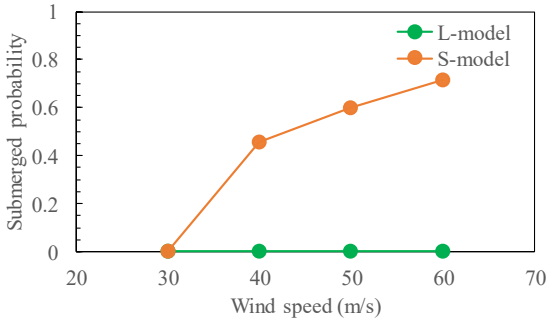

Fig.8 Submerged probability of blades

REFERENCES

[1] Phuc P.V. and Ishihara T., A Study on the Dynamic Response of a Floating Offshore Wind Turbine System Part 2: Numerical Simulation, Proceedings of 12th International Conference on Wind Engineering, 2007.
[2] Hu C., Sueyoshi M., Liu C. and Liu Y., Hydrodynamic Analysis of a Semi-Submersible-Type Floating Wind Turbine, Journal of Ocean and Wind Energy, Vol.1, No.4, 2011, pp.202-208.
[3] Myhr A. and Nygaard T.A., Comparison of Experimental Results and Computations for Tension-Leg-Buoy Offshore Wind Turbines, Journal of Ocean and Wind Energy, Vol.2, No.1, 2015, pp.12-20.
[4] Wehmeyer C. and Rasmussen J.H., Mooring Response of a Floating Offshore Wind Turbine in Nonlinear Irregular Waves, Journal of Ocean and Wind Energy, Vol.2, No.1, 2015, pp.37-44.
[5] Mantadakis N., Loukogeorgaki E. and Karimirad M., Accounting for Hydroelasticity in the Analysis of Offshore Wind Turbine Spar-Type Platforms, International Journal of Offshore and Polar Engineering, Vol.31, No. 1, 2021, pp.121-128.
[6] Suzuki H., Xiong J., do Carmo L.H.S., Vieira D.P., de Mello P.C., Malta E.B., Simos A.N., Hirabayashi S. and Gonçavelos R.T., Elastic Response of a Light-Weight Floating Support Structure of FOWT with Guywire Supported Tower, Journal of Marine Science and Technology, Vol.24, 2019, pp.1015-1028.
[7] Bae Y.H. and Kim M.H., The Dynamic Coupling Effects of a MUFOWAT (Multiple Unit Floating Offshore Wind Turbine) with Partially Broken Blade, Journal of Ocean and Wind Energy, Vol.2, No.2, 2015, pp.89-97.
[8] Karimirad M. and Michailides., Fault Condition effects on the Dynamic Response of V-Shaped Offshore Wind Turbine, Journal of Marine Science and Technology, Vol.24, 2019, pp.34-45.
[9] Hamamoto T. and Fujita K., Wet-Mode Superposition for Evaluating the Hydroelastic Response of Floating Structures with Arbitrary Shape, Proceedings of the 12th International Offshore and Polar Engineering Conference, 2002, pp.290-297.

8th Int. Conf. on Structure, Engineering & Environment (SEE), Mie, Japan, Nov.10-12, 2022, ISBN: 978-4-909106094 C3051

RESILIENCE ASSESSMENT OF A FIVE-STOREY SOCIALIZED HOUSING USING THE REDI RATING SYSTEM

John Pol A. Aguilar[1], Wilfed A. Chan[2], Ted Marius U. Delos Reyes[3], *Richard M. De Jesus[4], *Rodolfo P. Mendoza Jr.[5] and *Kenneth Roi P. Toral[6]
[1,2,3,4,5,6]Faculty of Engineering, De La Salle University (Manila), Philippines

ABSTRACT

Socialized housing is a government-backed initiative to provide affordable housing for the marginalized sector. Due to their low-cost nature, its structural integrity is often compromised under natural disasters. Currently, socialized housing in the Philippines is built using the code-based design (CBD) philosophy, where life safety is the priority regardless of the damage the building will sustain. Therefore, frequent shaking experienced by the country often leads to irreversible building damage and costly repairs. Resilience-based design (RBD) extends beyond life-safety by considering the repair consequences under a site-specific, design-level shaking. This study utilizes the REDi framework to determine the resilience level of the structure, in conjunction with the software SeismoStruct for structural analysis and PACT for loss estimation. As a case study, the standard, five-storey, low-rise socialized housing structure in the Philippines were evaluated for their seismic resilience using the REDi methodology. The study found that the Philippine low-rise socialized housing structure is not seismically resilient.

Keywords: Earthquake; Resilience; Infill wall; Sandwich panel; Philippine socialized housing

INTRODUCTION

The Philippines is along the pacific ring of fire and is frequented by strong earthquakes for the past decade causing severe infrastructure damage and high casualties. Residential structures are found to be the most susceptible to damage, especially those that are not designed to withstand earthquakes [1]. Socialized housing is a kind of residential structure that are awarded to the poorest of the poor which are less capable in mitigating seismic risks. As such, natural disasters often result to an increase in poverty, higher casualties, and a higher amount of destroyed dwellings in this sector [2].

Fig. 1 NHA Low-rise Socialized Housing Structure.

Caloocan City has the highest share of socialized housing units in the Philippines and all of which are classified as a five-storey low-rise building [3]. The standard design of such structures by the National Housing Authority (NHA) is analyzed in this study where it follows the provisions stated in the National Structural Code of the Philippines. The code-based design lacks the consideration for building protection and recovery which is addressed in a resilience-based design (RBD) philosophy.

The REDi Rating System that was developed by Arup is a tiered ranking approach resilience evaluation that classifies the seismic resilience of a structure into three levels of increasing resilience – Silver, Gold, and Platinum. The framework is divided into four resilience categories: Organizational Resilience, Building Resilience, Ambient Resilience, and Loss Assessment. The first three categories evaluate the seismic resilience of the building, the contingency measures within the facility in case of disasters, and the impact of the environment and adjacent structure on the building's vulnerability to earthquakes. The Loss Assessment can be further subdivided into the Direct Financial Loss Assessment for the probable financial losses with a design level earthquake, and the Downtime Assessment which evaluates the period where the building would be unusable due to repairs, utility disruption and delays.

This study aimed to identify the seismic resilience, calculate the expected financial loss, repair time, injuries, casualties, and estimate the re-occupancy and recovery times of the existing standard five-storey low-rise socialized housing in the Philippines based on the REDi Framework.

RESEARCH SIGNIFICANCE

This study can serve as a basis for the improvement of the housing facility and community measures to be used on similar projects in the future. In the societal level, this provides confidence that the local infrastructures can secure public investments and serve the general public's interest of providing safe and equitable homes for the poor. The ninth Sustainable Development Goal (SDG) created by the United Nations is also addressed which advocates the creation of resilient infrastructures, promotes sustainable industrialization, and fosters innovation [4].

METHODOLOGY

As a case study, a five-storey socialized housing building located in Caloocan City, Philippines is used. The components of the REDi Rating Assessment are discussed in the following chapters.

Organizational Resilience

Qualified professionals were interviewed to assess the level of contingency planning set in place for the building occupants. The interviewees were the contractor of the socialized housing project and the senior engineer for NHA – Caloocan District Office which were both knowledgeable with the operations and protocols employed within the building. A site investigation was done to verify that the results of the interview were accurate and were implemented within the actual building. The investigation verifies whether the facilities within the building are still usable and are in good condition, the placement of emergency kits within the building, presence of non-structural component within that may injure the occupants, and presence of safe egress space. Evaluating possible areas of congestion were identified in the investigation through the number of occupants per room.

Building Resilience

The structure was modelled using an inelastic force-based frame element with plastic hinges using SeismoStruct. Mander et al. [5] concrete and Menegotto-Pinto [6] steel model was used to define the material properties. Non-linear static pushover analysis was conducted to determine the structure's drift capacity while an Eigenvalue analysis is done to calculate the building weight and fundamental period. A site-specific response spectrum based on the 50-year return period, Design Level Earthquake (DLE) are required as input to SeismoStruct, which is developed from the geotechnical data and seismicity maps for the site. Component damages are assessed from the average damage states for beam-column joints, masonry wall, stairs, lighting, and distribution panel derived from the PACT loss assessment, which is formulated in Chapter 3.4.

Ambient Resilience

Hazard maps were used to identify the possible earthquake-induced hazards that may affect the building's seismic performance which were obtained through Hazard Hunter and the Metro Manila Hazard Susceptibility Map provided by the Philippine Institute of Volcanology and Seismology.

Professional interview with the NHA representative and building contractor was done to inquire for the proximity of surrounding buildings and non-building installations. Seismic hazards in Caloocan City were analyzed before assessing the resiliency of the building against such natural hazards. The design specifically studies the possible tsunami and liquefaction hazards of the building which either have a higher ground level for the possibility of a tsunami or a deeper foundation that reaches the bedrock for those that are susceptible to liquefaction. In the interview, it was asked if the design was adequate and complies with standard protocols in mitigating damage due to said hazards.

Direct Financial Loss Assessment

The building information model using the Performance Assessment Calculation Tool (PACT) is defined to calculate the expected repair costs, repair time, injuries and fatalities for the structure under a design level earthquake. This utilizes the Monte Carlo simulation account for uncertainties in the structural model and its seismic response.

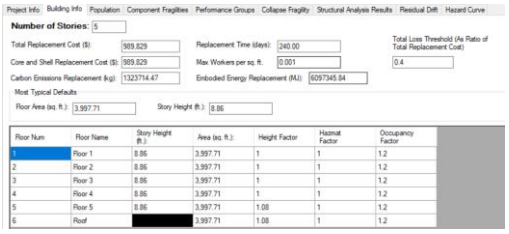

Fig. 2 PACT Building Information Tab

The structure is composed of five stories, with a floor area of 3,997.71 sf and a story height of 8.86 ft. The total replacement cost is USD 959,099.73 while the estimated replacement time is around 240 days. The Multi-Residential population model used has a peak of 3.1 occupants per 100 sf is used.

Component fragility functions defines the probable repair costs and time for each sequential damage state of each damageable component. Repair cost and time data for common building components in the Philippines are used in this study

[7]. Components are classified as either drift- or acceleration-sensitive, and fragility quantities per floor are obtained from the structural plans.

Fragility curves, which models the probability of collapse at different values of the spectral acceleration, are derived from the pushover curves and generated using SPO2FRAG [8]. This is a MATLAB-based tool that predicts the Incremental Dynamic Analysis (IDA) results for an equivalent single degree-of-freedom (SDOF) system using the structure's pushover and Eigenvalue properties.

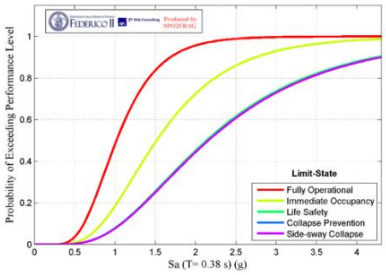

Fig. 3 Structural Fragility Curve.

Lastly, the story drift ratio and peak floor acceleration at each floor, when subjected to pushover loading at the DLE shaking intensity, are defined. The structural analysis calculations follow the Intensity-based Assessment: Simplified Analysis procedure of FEMA P-58 [9].

Downtime Assessment

Weighted average damage states and the corresponding repair classes were determined using PACT's pre-defined fragility database. For a socialized housing structure, the priority recovery state is re-occupancy and functional recovery. Re-occupancy indicates that heavy damage that poses a risk to life-safety had occurred to the structural or non-structural building components. Functional recovery indicates damage occurred on the non-structural components only. Although it does not pose a life-safety risk, repair is still required.

The downtime assessment consists of three downtime sources: due to repair, due to delay, and, due to utility disruption. Downtime due to repairs constitutes the actual repair time of damaged components, which is dependent on the repair sequence and schedule. Initially, the structural and non-structural repair times were obtained. The number of workers and repair time distribution per floor was calculated based on the floor area and repair sequence.

Downtime due to delays constitutes the delays in the initiation or completion of repairs. Professional interviews were conducted to determine the impeding curve per impeding factor. Given this, the median delays were determined based on the framework by Almufti and Willford [10]. Three delay paths were determined in which the longest governed this downtime source.

Downtime due to utility disruption constitutes the restoration of electrical, water, and natural gas systems. In determining the disruption time of electrical systems, the REDi methodology suggests the use of achieving 50% recovery in the disruption curve. For water and natural gas systems, the peak ground velocity (PGV) and dominant seismic wave (i.e., either R or S-waves) for Metro Manila was used [11]. This was used to calculate the repair rate (in repairs/km) which was then used to determine the disruption times from the disruption curves.

The total downtime was plotted on a Gantt chart to visualize the downtime schedule for a specific recovery state.

RESULTS AND DISCUSSION

The final rating for each resilience categories were determined by the lowest rating across all the criteria under each resilience category. For organizational resilience, as shown in Table 1, it was rated silver due to the lack of earthquake preparedness, low-use fixtures, back-up power, and security systems installations as required by FEMA.

For building resilience, Table 2 shows that the final rating is not resilient. This is due to the residual drift in a certain floor exceeding the maximum permissible drift of 0.5%, when subjected to seismic loads in the X-direction.

For ambient resilience, the governing rating is gold, as shown in Table 3, due to the insufficient visual and geotechnical tests conducted as compared to the prescribed rapid visual screening scoring methodology by FEMA 154.

The loss estimates from PACT will be discussed below. The median repair cost for the socialized housing structure under a DLE is USD 42,988. Fig. 4 shows that the highest share in repair costs is due to damage in the beam-column joints, at 60.89% of the total repair costs, and is concentrated at the ground floor only. Masonry walls account for the second highest repair cost among building components, at 38.05% of the total cost. Repair cost for other components is significantly lower than the repair cost for the frame joints and masonry walls.

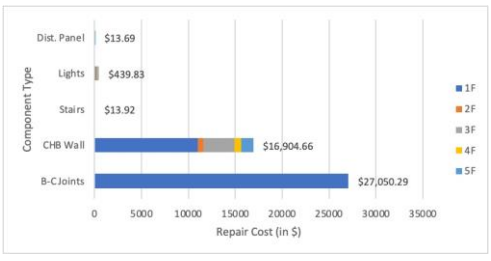

Fig. 4 Repair Cost Distribution per Component.

Table 1 REDi Assessment for Organizational Resilience

Resilience Criteria	Rating	Remarks
Resilience Workshop	P	Meetings about structural integrity and insurances were done. Earthquake drills and safety protocols were conducted.
Back-up Utility Lines	G	Back-up power were only for Sewage Treatment Plants (STPs).
Low-use Fixtures	G	No low-flow faucets and bulbs being used were CFL.
Security	S	No CCTVs nor alarm systems in the building only guards.
Long-lead Time Items	P	STP generator sets can be replaced within 2 weeks to 1 month, and circuit breakers and panels within 1 month.
Food and Water	S	No readily available supply on site.
Preparedness Training	G	Does not conduct earthquake drills, but first aid kits are present.

Table 2 REDI Assessment for Building Resilience

Resilience Criteria	Rating	Remarks
Design Level Earthquake	P	Response spectra is based on DLE (50 YRP from site PSHA).
Code Minimum Requirements	P	Structural design is compliant with NSCP 2010. Structure passed the ASCE 41-17 code check for shear and chord rotation.
Design Demands	P	Response spectra for pushover analysis is based on the DLE.
Minimize Structural Damage	S	Average DS for beam-column joints is more than 1 (DS=2.68).
Minimize Residual Drift	NR	Residual drift at the 4th floor (along X-axis) is more than 0.5% (Δ=1.03%).
Minimize Non-structural Damage	P	Average DS for all non-structural components are less than 1. Maximum average DS at stairs (DS=0.94).
Equipment Functionality	S	Replacement time for the distribution panel is less than 6 months. Panel's shake table qualification cannot be verified.
Protect Facades	S	Average DS for masonry wall is more than 1 (DS=2.00).
Anchor Heavy Building Contents	P	Distribution panels, transformers, and fire control systems are anchored to the wall. Compliant with FEMA-E-74 standards.
Stairs	P	Average DS for stairs is less than 1 (DS=0.94).
Simulation Model	P	SeismoStruct model is 3D. Analysis follows the performance-based requirements of FEMA P-58 and ASCE 41-17.
Structural Peer Review	P	Structural engineers and consultants conduct peer reviews during the planning phase.
Installation of Non-structural components	P	General contractor inspects the compliance of completed works with drawings and technical specifications required by the client.

Table 3 REDI Assessment for Ambient Resilience

Resilience Criteria	Rating	Remarks
Design for Liquefaction	P	Safe from liquefaction hazard.
High Liquefaction Hazard	P	Not susceptible to liquefaction.
Other Ground Failures	P	Nearest dam is approximately 7.5 km away. Safe from Landslides and Ground Rupture. Low flood susceptibility.
High Tsunami Hazard	P	Not within inundation area. Less than 0.5 meters flood height.
Assessment of Surrounding Building	G	Initial visual and geotechnical test before construction was done but not based on the Rapid Visual Screening of FEMA.
High Hazard from Surrounding Building	G	No readily available supply on site.

Table 4 REDI Assessment for Loss Assessment and REDi Baseline Criteria Objectives

Resilience Criteria	Rating	Remarks
Re-occupancy	NR	Re-occupancy of the building would take 247.460 days.
Functional Recovery	NR	Functional Recovery of the building would take 247.521 days.
Direct Financial Loss	G	The scenario expected loss due to repairs would be 4.63% of the total building value.
Occupant Safety	NR	Injuries are about 8 persons while fatalities are about 3 persons.
Utility Disruption	G	Disrupted utility can be restored within 1 month (21 days).

Considering a parallel schedule where repairs can start simultaneously at all floors, Fig. 5 shows that the median repair time at the ground floor governs and is equal to 96.94 days. Masonry walls and beam-column joints account for majority of the repair time across all floors, at 60.86% and 36.73% of the total repair time, respectively.

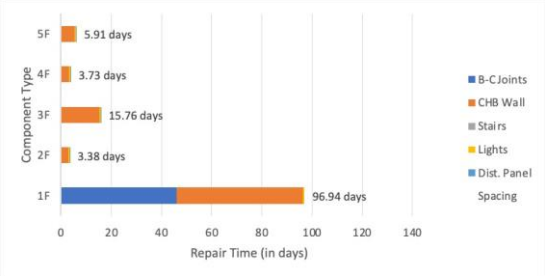

Fig. 5 Repair Time Distribution per Component.

Lastly, the expected number of injuries in the building under DLE is equal to 2.27 persons, while the number of casualties is 7.73 persons.

Table 5 Average Damage State and Repair Class

Component Type	Average Damage State	Repair Class
Beam-Column Joint	2.5745 2.7849	3
Masonry Wall	2.0000	3
Stairs	0.9330	1
Pendant Lighting	0.4956	3
Panel Box	0.0180	2

Table 5 displays the repair average damage states and repair classes of the building components of the socialized housing. The structural and lighting component resulted to repair class 3. This indicated that these are the components which needs to be repaired to achieve a re-occupancy recovery state. The panel box falls under repair class 2. Repair of this component is required to achieve functional recovery. Lastly, the stairs must undergo repair to achieve full recovery despite only obtaining minimal damage.

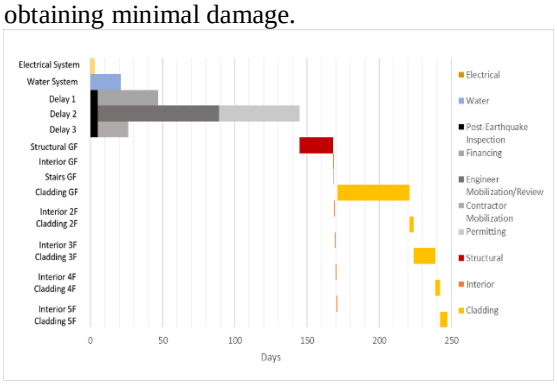

Fig. 6 Total Downtime for Re-occupancy.

Figure 6 illustrates the total downtime sequence to achieve re-occupancy. Downtime due to utility disruption and due to delays can be seen to occur simultaneously. With this, the latter governs the initial downtime sequence. Particularly, the second delay path of post-earthquake inspection, engineer mobilization/review, and permitting resulted to the largest delay source, accounting for 145 days. The downtime due to repair follows. Based on the repair schedule, the repair downtime resulted to 102.46 days. The cladding repair sequence or repair of concrete hollow block (CHB) of this downtime source was discovered to be the largest among all building components. This indicates that the wall component requires the greatest amount of repair time. The total downtime for re-occupancy is 247.460 days (8 months).

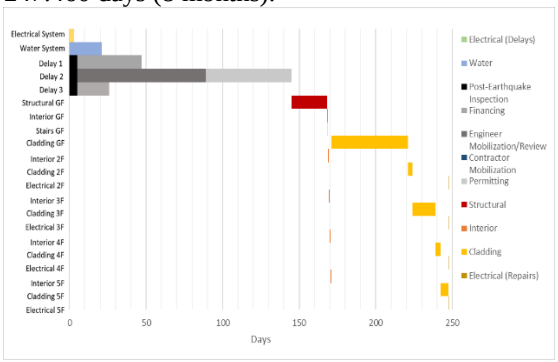

Fig. 7 Total Downtime for Functional Recovery.

Figure 7 illustrates the total downtime to achieve functional recovery. As mentioned previously, in order to achieve functional recovery, building components with repair class 2 must also be considered. With this, the difference between the downtime for re-occupancy and functional recovery is the electrical repair sequence only. Downtime due to utility disruption and due to delays are similar with the re-occupancy schedule. The total downtime for functional recovery is 247.521 days (8 months).

Table 4 shows a final rating of not resilient for loss assessment and REDi baseline resilience objectives. Both re-occupancy and functional recovery exceeded the silver rating minimum by 65 days. In the criteria of occupant safety, it was also deemed not resilient since both physical injuries and fatalities will likely occur.

CONCLUSIONS

Infrastructure damage and structural collapse due to seismic events are prevalent in the Philippines. Numerous design paradigms in building construction has paved the way for different results and improvements in the structural life and design. In this study, it focused on the resilience-based design. This design paradigm focuses on the ability of a community to reduce the probability of structural failure and consequences. In addition to this, the level of damage associated with the repair time has also been considered especially in terms of how long it would take the building to perform its original function or purpose.

With the use of the REDi Rating System, the standard five-storey low-rise socialized housing in the Philippines was assessed using a design level earthquake in terms of organizational resilience, building resilience, ambient resilience, and loss assessment. It was therefore concluded that the building was deemed not resilient based on the REDi Framework. The building failed to achieve a resilient rating in terms of building resilience and loss assessment, particularly on the downtime assessment and occupant safety criteria.

ACKNOWLEDGMENTS

The researchers would like to extend their gratitude to the building contractor, E.M. Cuerpo Inc., and the National Housing Authority Caloocan District Office for providing their time and expertise, which are vital to the completion of this research endeavor.

REFERENCES

[1] Garciano, L., & Taclibon, P. (2013). The October 15, 2013 Bohol Island, Philippines earthquake and its damaging effects: An investigative report. Japan Society of Civil Engineers.

[2] Jia, H., Chen, F., Pan, D., & Zhang, C. (2018, December 10). The Impact of Earthquake on Poverty: Learning from the 12 May 2008 Wenchuan Earthquake.

[3] Dungca, J., & Macaraeg, C. (2016). Development of a Reference for Seismic Amplification: The Case of Metro Manila. 19th Congress of International Association for Bridge and Structural Engineering. Stockholm, Sweden.

[4] United Nations. (2015). Sustainable Development Goals. Retrieved from https://www.undp.org/sustainable-development-goals#industry-innovation-and-infrastructure

[5] Mander, J., Priestley, M., & Park, R. (1988). Theoretical stress-strain model for confined concrete. Journal of Structural Engineering, 30, 1804-1826.

[6] Menegotto, M., & Pinto, P. (1973). Method of analysis for cyclically loaded R.C. plane frames including changes in geometry and non-elastic behaviour of elements under combined normal force and bending. Symposium on the Resistance and Ultimate Deformability of Structures Acted on by Well Defined Repeated Loads, 15-22.

[7] Ausan, R., Cabatit, K., Quiaem, M., & De Jesus, R. (2019). Resiliency of a Four-storey Standard School Building Using the REDi Framework. International Journal of GEOMATE, 7.

[8] Baltzopoulos G., Baraschino R., Iervolino I., Vamvatsikos D. (2017) SPO2FRAG: Software for seismic fragility assessment based on static pushover. Bulletin of Earthquake Engineering.

[9] Applied Technology Council. (2017). FEMA P-58: Seismic Performance Assessment of Buildings. U.S. Department of Homeland Security, Federal Emergency Management Agency, Washington D.C.

[10] Almufti, I., & Willford, M. (2013). REDi™ Rating System: Resilience-based Earthquake Design Initiative for the Next Generation of Buildings

[11] Torregosa, R., Sugito, M., & Nojima, N. (2001). Strong Motion Simulation for the Philippines Based on Seismic Hazard Assessment. Journal of Natural Disaster Science, 33-51

8th Int. Conf. on Structure, Engineering & Environment (SEE), Mie, Japan, Nov.10-12, 2022, ISBN: 978-4-909106094 C3051

THE EFFECT OF TSUNAMI LOAD ON PRAYOGA FOREIGN LANGUAGE COLLEGE IN PADANG CITY, INDONESIA

Fauzan[1], Ferdy Muhammad Ikhwan[1], Dyan Adhitya Nugraha M[1] and Zev Al Jauhari[2]
[1]Engineering Faculty, Andalas University, Indonesia
[2]Department of Civil Engineering, Bengkalis Polythecnic, Indonesia

ABSTRACT

Padang as the capital city of West Sumatra is located on coastal areas and has a high level of tsunami disaster vulnerability (High Risk Zone). Therefore, public buildings in Padang city must have certain technical engineering so as to reduce the risk of structural failure. One of the public buildings that needs to be considered as an educational facility in Padang city is the Prayoga Foreign Language College (STBA) building. Based on the results of an evaluation conducted by the Andalas University assessment team, the Prayoga STBA building was designed without taking into account the tsunami loads. Therefore, it is necessary to re-analyze the building by taking into account the tsunami loads. In this study, the building was analyzed using ETABS v.18.1.1 software with reference to current Indonesian building standards such as SNI 2847:2019 for building structural concrete requirements, SNI 1726:2019 for earthquake resistance building design, SNI 1727:2020 for minimum design load for buildings, and international standard of FEMA P646-2019 for tsunami loads calculation. The results of the analysis show that the building is able to withstand the earthquake load, but the capacity of the building is insufficient when the tsunami loads are applied to the structure. The beams and columns on the 1st and 2nd floors do not have strong enough capacity to resist the tsunami loads, so there is a possibility of structural failure. The effect of tsunami loads on the internal forces and other structural responses of the building is also discussed in this paper.

Keywords: Tsunami, Evaluation, capacity, ETABS

INTRODUCTION

Prayoga Foreign Languages College (STBA Prayoga) building is one of the private colleges located on Padang city. STBA Prayoga is a development of the Prayoga Foreign Language Academy (ABA) which is under the auspices of the Prayoga Foundation. Indonesia, especially the Padang city, is an area with an earthquake-prone category [1]. The Padang city itself has been recorded to have occurred several large earthquakes, one of which was the Padang earthquake on September 30, 2009 [2], [3]. View of the STBA Prayoga Padang building is shown in Fig. 1.

Fig. 1 STBA Prayoga Building in Padang city.

The STBA Prayoga building is close to the beach which is very vulnerable and will have a very impact if there is a tsunami hit Padang city. Therefore, it is necessary to know whether the STBA Prayoga building can withstand the combined earthquake and tsunami loads, as well as the impact that occurred due to the tsunami loads. Previously, the STBA Prayoga building had been evaluated by the Andalas University (UNAND) assessment team using the previous building codes. Based on previous evaluation data by UNAND assessment team, this building was designed without taking into account the tsunami loads. Therefore, a structural evaluation of the building using the current Indonesian building codes and international code of FEMA for tsunami vertical evacuation structure should be carried out by taking into account the tsunami loads. This study foccused on the investigation of tsunami loads effect on the STBA Prayoga building.

ANALYSIS AND DISCUSSION

The Location of STBA Prayoga Building

Based on the data observed using Google Maps, the location of the STBA Prayoga Building on Veteran Street, No. 8, West Padang is 450.23m distance from the shoreline. The location of the building is also around urban areas, offices and residential areas [4].

The Level of Tsunami Vulnerability

The STBA Prayoga building is located on the red zone (high-risk zone) of the tsunami [1] and the area with a tsunami inundation depth of 5 m [5].

Building Data

STBA Prayoga Building is the five-story building made of reinforced concrete structures with size 48m length and 12m width. The yield strength of steel (fy) was 240 MPa and 400 MPa for plain and deformed reinforcements, respectively, while the compressive strength of the concrete (fc') was 24.5 MPa. The dimensions of the structural elements are:

1. Beam: B1, G1 (35 x 75cm), B2, G2 (35 x 50cm), B3 (20 x 30 cm), CG1, G3, G4 and G5 (20 x 75cm)
2. Column: K1, K2, K3 (65 x 65 cm) and K4(40 x 40 cm).

The Modelling of Building Structure

Structural analysis of the STBA Prayoga Building was carried out using ETABS software. The columns and beams of the building structure are modeled as frames, the floor plates are modeled as slab elements, and the structural walls are modeled as wall elements [6]. The 3D modeling of the building structure was carried out in accordance with the existing condition of the current STBA Prayoga Building, as shown Fig. 2.

Fig. 2 3D structural modeling of STBA Prayoga.

Loading Analysis

Dead load

Dead loads are obtained from the self-weight of building materials and building components [7]. The dead load on the building was calculated using the Indonesian Standards Building, SNI 1727:2020 [7]. The dead loads that work on the STBA Prayoga Building are:

1. The self-weight of structural elements was calculated directly by the structure analysis program ETABS.
2. Super imposed dead load was calculated based on SNI 1727:2020, as shown in Table 1.

Table 1 Dead load on the STBA Prayoga building

Material type	Load value
Plaster	42 kg/m^2
BV plafond	20 kg/m^2
BV ceramics	48 kg/m^2
BV wall	250 kg/m^2

Live load

Based on article 4.3.1 of SNI 1727:2020, explaining the living load used for building planning must use a maximum living load [7]. Table 2 shows the live loads on the STBA Prayoga Building.

Table 2 The live loads of the STBA Prayoga building

Room type	Load value
Classrooms	1.92 kN/m^2
1st floor corridor	4.79 kN/m^2
Corridor above the 1st floor	3.83 kN/m^2

Earthquake load

The spectrum response is used as an analysis of dynamic earthquake loads. The spectrum response earthquake load is calculated based on SNI 1726:2019 using the 2019 Indonesian Earthquake Hazard Map [8]. Therefore, the design spectral acceleration parameter values for medium soil, the value of spectral design SD1 and SDS are 1.0g and 0.68g, respectively. Figure 3 shows the spectrum response of STBA Prayoga in Padang City with medium soil conditions.

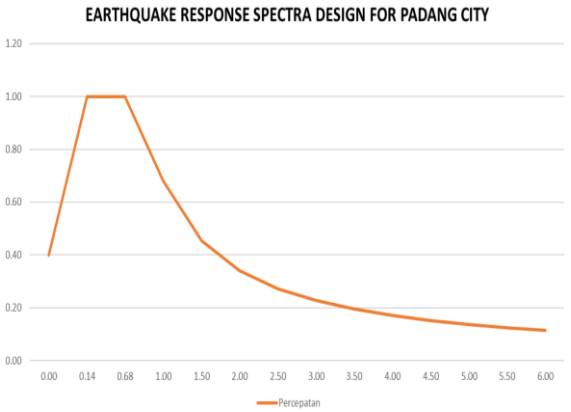

Fig. 3 The graph of spectrum response in Padang City.

The spectrum response data are inputted into the structural modeling, then scale factor calculations are performed on ETABS using Eq. (1):

$$SF = G.I/R \quad (1)$$

Where, G is acceleration of gravity, I is building priority factor and R is response modification coefficient.

Tsunami loads

Article 8.8 of FEMA P-646 2019 explains the calculated loads as follows:

1. Hydrostatic force
Hydrostatic force is the horizontal force that caused by the water pressure against to a surface. The amount of this force depends on the depth of water [9]. Hydrostatic force can be calculated by the Eq. (2).

$$Fh = 0{,}5\ \rho_S\ g\ b\ h_{max}{}^2 \quad (2)$$

Where ρ_S is tsunami volume weight, g is acceleration of gravity, b is width that accept the pressure and h_{max} is maximum of water height above the wall base.

2. Buoyant force
The buoyant forces on a structure subject to partial or total submergence will act vertically through the center of mass of the displaced volume [9]. The buoyant force on the structure can be calculated by the Eq. (3).

$$Fb = \rho_S\ g\ V \quad (3)$$

Where V is the volume of water below the maximum inundation.

3.Hydrodynamic force
Hydrodynamic force is a combination of horizontal forces caused by the compressive force of moving water and the friction caused by the flow around the structure [9]. Hydrodynamic force can be calculated by the Eq. (4).

$$Fh_d = 0{,}5\ \rho_S\ cd\ b\ (hu^2)_{max} \quad (4)$$

Where cd is the drag coefficient, h is the depth of flow and u is the flow velocity.

4.Surge force (impulse force)
Surge forces are caused by the leading edge of a surge of water impinging on a structure and by the water wave that comes suddenly. Surge force of the building is 1.5 times the hydrodynamic force [9].

5.Debris load
Debris impact is caused by a buildup of debris that assumed by additional hydrodynamic force and depends on the thickness of the layer of debris. To calculate the debris force, use the Eq. (5).

$$F_{dm} = 0{,}5\ \rho_S\ cd\ Bd\ (hu^2)_{max} \quad (5)$$

6.Impact load
Impact loads are those that result from debris such as driftwood, small boats, portions of house, or any object transported by floodwaters, striking against buildings and structures [9]. As an approach, this value is calculated by the following Eq. (6).

$$F_i = 1{,}3\ u_{max}\ \sqrt{k + md(1+c)} \quad (6)$$

Where u_{max} is maximum flow, the volume of water below the maximum inundation.

7.Extra gravity load
Due to the high depreciation rate of water is rapid, it is likely that there will plenty of water suspended in the floor, causing the addition of a significant gravitational force on the floor [9]. Potential extra load of gravity per unit area can be calculated by the Eq. (7).

$$F_i = \rho S\ x\ g\ x\ hr \quad (7)$$

Where hr is hmax - 1st floor height.

8.Uplift forces on elevated floors
Uplift hydrodynamic force is given on the top floor of the tsunami inundation affected [9]. This load can be calculated by the Eq. (8).

$$F_u = 0{,}5\ C_u\ \rho_S\ Af\ Uv^2 \quad (8)$$

Where C_u is uplift coefficient, Af is tsunami inundation area and Uv is hydrodynamic uplift force. The calculation results of tsunami loads are given in Table 3.

Table 3 The tsunami loads of the STBA Prayoga building

Load type	Load value
Hydrostatic forces	329.946 kN
Buoyant forces	17.266 kN/m^2
Hydrodynamic forces	84.077 kN
Surge forces	126.116 kN
Floating debris impact forces	447.815 kN
Debris load	517.398 kN
Extra gravity load	15.107 kN/m^2
Uplift forces on elevated floors	8.41x10^{-6} kN/m^2

Load Combination

The load combination refers to SNI 1726-2019 for the combination of loading due to the earthquake, and

FEMA P646-2019 for the combination of loading due to the tsunami loads [8], [9]. The load combination for this analysis is as follows:

1. 1.4 DL
2. 1.2 DL + 1.6 LL+ 0.5 R
3. 1.2 DL + 1.0 LL ± 1.0 EQx ± 0.3 EQy
4. 1.2 DL + 1.0 LL ± 0.3 EQx ± 1.0 EQy
5. 0.9 DL ± 1.0 EQx ± 0.3 EQy
6. 0.9 DL ± 0.3 EQx ± 1.0 EQy
7. 1.2 DL + 0.25 LL + 1 (FB+FU) + 1 Lref
8. 1.2 DL + 0.25 LL + 1 (FH+FHD) + 1 Lref
9. 1.2 DL + 0.25 LL + 1 (FI+FHD) + 1 Lref
10. 0.9 DL + 1 (FB+FU)
11. 0.9 DL + 1 (FH+FHD)
12. 0.9 DL + 1 (FI+FHD)

Inter Story Drift

Based on SNI 1726:2019, the inter story drift (Δ) must be calculated as using the following Eq. (8) [8].

$$\delta = \frac{Cd_{\delta x}}{Ie} \leq 0{,}010\ h_{sx} \quad (8)$$

From Eq. (8), the inter story drift can be obtained. Tables 4 and 5 show the inter story results in X and Y direction with and without tsunami loads.

Table 4 Inter Story drift in X-direction

Story	Displacement - X		Limit (mm)	Increased ratio (%)	Check $\Delta_{limit}>\Delta x$
	With tsunami loads (mm)	Without tsunami loads (mm)			
5	4.671	4.697	35	0.55	OK
4	7.715	7.803	35	1.14	OK
3	10.362	10.828	35	4.49	OK
2	13.416	14.777	35	10.14	OK
1	1.793	1.984	42	10.63	OK

Table 5 Inter story drift in Y-direction

Story	Displacement - Y		Limit (mm)	Increased ratio (%)	Check $\Delta_{limit}>\Delta x$
	With tsunami loads (mm)	Without tsunami loads (mm)			
5	2.574	2.585	35	0.43	OK
4	4.411	4.429	35	0.42	OK
3	4.217	4.231	35	0.35	OK
2	3.843	3.920	35	2.00	OK
1	0.532	0.554	42	4.14	OK

It can be seen from Tables 4 and 5 that the inter story drift of the building in X and Y direction is still at the permissible range of story drift as required in Indonesian building codes. The increase of the inter story drift in the X-direction that occurs due to the impact of the tsunami load is more than the increase of the inter story drift in the Y-direction, because the direction of the tsunami comes parallel to the Y-direction so that it has more impact on the X-direction.

CROSS-SECTIONAL CAPACITY OF THE STRUCTURE

Column Capacity

For determining the capacity of the column to withstand the working loads, it can be seen from the column interaction diagram and shear capacity [10], [11]. The calculation results of the interaction diagram and shear capacity due to tsunami loads [12] – [15] will be explained below.

First floor column P-M interaction diagram

Figure 4 shows the P-M interaction diagram obtained from structural analysis results with and without tsunami loads, respectively.

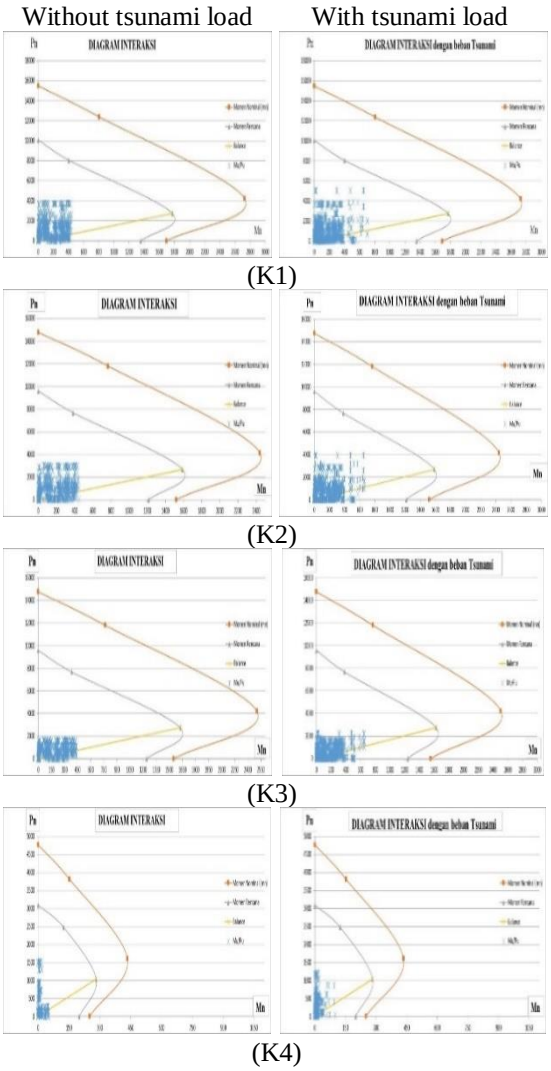

Fig. 4 First floor column P-M interaction diagram.

It can be seen from Fig. 4 that the increase in internal force marked in blue is quite significant, the bending capacity of the columns are able to withstand the working loads, including tsunami loads.

Shear capacity of columns

The shear capacity of the building columns is shown in Table 6.

Table 6 Shear capacity columns with and without tsunami loads

Story	Column type	ΦVn (kN)	Without tsunami loads		With tsunami loads		Increased ratio (%)
			Vu (kN)	Check	Vu (kN)	Check	
1	K1	475.29	404.24	OK	690.94	Not OK	71
	K2	475.29	363.14	OK	517.06	Not OK	42
	K3	493.68	275.13	OK	460.75	OK	68
	K4	168.61	60.45	OK	123.54	OK	104
2	K1	475.29	282.48	OK	430.54	OK	52
	K2	475.29	196.31	OK	407.14	OK	107
	K3	493.68	176.24	OK	398.85	OK	126
	K4	168.61	64.65	OK	245.64	Not OK	279
3	K1	475.29	357.82	OK	362.53	OK	1
	K2	475.29	216.65	OK	221.49	OK	2
	K3	493.68	171.19	OK	171.19	OK	0
	K4	168.61	27.93	OK	42.51	OK	52

Based on the results of the shear capacity of the columns in Table 6, it can be seen that the shear capacity of the building without tsunami load is able to withstand the working loads, while the shear capacity of the building with tsunami loads shows that the 1st and 3rd floor columns is not able to withstand the shear force. The increase in shear force that occurs due to tsunami loads is quite significant, especially for the 1st and 2nd floors with a maximum increase on the 2nd floor of 279.9%.

Beam Capacity

Flexural capacity of beams

The results of the calculation and comparison of the flexural capacity of beams with and without tsunami loads are shown in Table 7 [10], [11].

From Table 7, it can be seen that the beam flexural capacity increases significantly on the 2nd floor beam. The highest increase of beam flexural capacity occurred on the B2 beam on 2nd floor, which is 230.54%.

Shear capacity of beams

The results of the calculation and comparison of the shear capacity of beams with and without tsunami loads is shown in Table 8.

Table 7 Beam flexure capacity at 1st floor and 2nd floor with and without tsunami

Story	Beam type	Location	ØMn (kNm)	Without tsunami load		With tsunami load		Increased ratio (%)
				Mu (kNm)	Check	Mu (kNm)	Check	
1	B3	At support	40.24	16.86	OK	27.78	OK	65
		At field	40.24	7.27	OK	13.39	OK	84
	G1	At support	276.22	263.80	OK	288.51	Not OK	9
		At field	276.22	111.55	OK	111.16	OK	0
	G2	At support	196.35	138.28	OK	146.37	OK	6
		At field	196.35	102.26	OK	144.47	OK	41
	G3	At support	371.97	314.58	OK	385.95	Not OK	23
		At field	371.97	125.33	OK	182.83	OK	46
	G4	At support	441.73	396.54	OK	469.11	Not OK	18
		At field	576.62	210.53	OK	286.77	OK	36
	G5	At support	267.76	253.33	OK	347.05	Not OK	37
		At field	267.76	108.41	OK	168.73	OK	55
2	B1	At support	150.42	39.21	OK	58.08	OK	48
		At field	198.79	2.54	OK	2.67	OK	5
	B2	At support	78.94	37.79	OK	81.19	Not OK	114
		At field	78.94	12.21	OK	40.35	OK	230
	B3	At support	67.76	24.56	OK	24.28	Oke	0
		At field	67.76	9.85	OK	10.57	Oke	7
	CG1	At support	509.95	478.08	OK	973.87	Not OK	104
		At field	371.97	289.05	OK	572.62	Not OK	98
	G1	At support	340.86	248.84	OK	538.81	Not OK	117
		At field	209.81	189.35	OK	209.97	Not OK	11
	G2	At support	165.84	142.04	OK	139.77	OK	0
		At field	196.35	57.20	OK	56.33	OK	0
	G3	At support	509.95	489.28	OK	507.43	OK	3
		At field	300.66	231.65	OK	228.99	OK	0
	G4	At support	641.75	578.07	OK	743.51	Not OK	29
		At field	371.97	246.39	OK	243.67	OK	0
	G5	At support	441.73	415.96	OK	405.45	OK	0
		At field	300.66	221.34	OK	212.58	OK	0

Based on Table 8, it is seen that two beam elements are not able to resist the shear force that works when tsunami loads were applied on the building.

The increase that occurred in the shear force of the beams was not as large as the increase in the columns, but the increase was still quite significant according to Table 8, in which the increase that occurred did not exceed 100%.

The checks of mass participation, P-delta and structural irregularities in the STBA Prayoga Padang Building have all met the requirements in SNI 1726-2019 and FEMA P646 [9]. Based on the structural response results, the STBA Prayoga Padang building is strong enough to withstand the earthquake load, but not strong enough in resisting the applied tsunami loads. The influence of the tsunami loads on the STBA Prayoga Padang building is significant enough so that the columns and beams of the 1st and 2nd floors of the building have the possibility of damage or collapse [12] – [14].

Table 8 Beam shear capacity with and without tsunami

Story	Beam type	Location	ØVn (kN)	Without tsunami load		With tsunami load		Increased ratio (%)
				Vu (kN)	Check	Vu (kN)	Check	
1	B3	At support	75.79	11.49	OK	19.23	OK	67
		At field	66.74	16.26	OK	16.26	OK	0
	G1	At support	474.32	194.24	OK	215.85	OK	11
		At field	329.56	184.27	OK	206.25	OK	11
	G2	At support	525.15	109.09	OK	171.12	OK	56
		At field	525.15	149.18	OK	149.18	OK	0
	G3	At support	661.23	187.81	OK	196.64	OK	4
		At field	661.23	194.93	OK	194.94	OK	0
	G4	At support	661.23	232.41	OK	325.21	OK	39
		At field	516.71	233.87	OK	233.87	OK	0
	G5	At support	661.23	137.64	OK	171.64	OK	24
		At field	516.71	138.04	OK	138.04	OK	0
2	B1	At support	442.15	54.13	OK	122.21	OK	125
		At field	313.47	53.65	OK	145.01	OK	170
	B2	At support	176.81	54.13	OK	82.54	OK	52
		At field	166.85	53.65	OK	115.02	OK	114
	B3	At support	87.85	15.04	OK	15.28	OK	1
		At field	78.20	20.76	OK	24.51	OK	18
	CG1	At support	366.42	222.03	OK	465.37	Not OK	109
		At field	366.42	6.90	OK	6.90	OK	0
	G1	At support	586.91	208.42	OK	492.07	OK	136
		At field	385.85	195.13	OK	441.75	Not OK	126
	G2	At support	403.50	131.03	OK	131.13	OK	0
		At field	403.50	151.14	OK	178.11	OK	17
	G3	At support	661.23	230.66	OK	364.03	OK	57
		At field	516.71	237.71	OK	381.99	OK	60
	G4	At support	661.23	290.35	OK	477.64	OK	64
		At field	661.23	294.41	OK	489.92	OK	66
	G5	At support	661.23	164.49	OK	225.88	OK	37
		At field	516.71	180.51	OK	240.35	OK	33

CONCLUSION

Based on the results of the analysis that has been carried out, the following conclusions can be drawn:

1. The addition of the tsunami load on the STBA Prayoga Padang building increase the P-delta value by 0.5%-10% in the X direction and 4% - 4% in the Y direction, while the increase in inter story drift in X-direction is 0.5% - 10%, and Y-direction is 0.4%-4%.
2. For the internal force that occurs in the column, the maximum increase occurred in the 1st floor and 2nd floor columns, which is 67.296% for the axial force, 279.960% for the shear force, and 469.308% for the moment, while there is no significant increase for the 3rd floor column and above.
3. A significant increase occurs in the internal forces of the beams on the 1st and 2nd floors with a maximum increase of 170% for the shear force, and 184% for the bending moment, while the increase is not significant for the columns.
4. The STBA Prayoga building is strong in withstanding earthquake loads. However, when tsunami loads were applied, the shear capacity of the column on the 1st floor and the bending moment and shear capacity of the beams on the 1st and 2nd floors are not strong enough in capacity to withstand the working loads.

REFERENCE

[1] National Center for Earthquake Studies, Source and Hazard Map of the 2017 Indonesian Earthquake, Ministry of PUPR, 2019.

[2] Boediono B., Dewi N. T. H., Kristalya M., Manik S. L. C. and Ong. E. H. K., Examples of Earthquake Resistant Building Designs, ITB, 2017.

[3] Dian O. and Manurung S., Geospatial Model of Potential Tsunami Vulnerability in Padang City, BMKG, 2010.

[4] Intan S. U., The Effect of the Tsunami Burden on the New Building of the West Sumatra Provincial Parliament, Universitas Andalas, 2017.

[5] Siregar N., The Effect of Tsunami Load on the Pasar Raya Inpres Block III Building in Padang City Based on FEMA P-646 / April 2012. Universitas Andalas, 2017.

[6] Alfianto R. and Rahmat D., Analysis of Calculation of Buildings with Methods ETABS Version 9.7.2, Journal of Civil Eng., Building and Transportation, Vol.2, No.1, 2018, pp28-33.

[7] Indonesian National Standardization Agency, SNI 1727:2020 Minimum Load for Planning of Buildings and Other Structures, 2020.

[8] Indonesian National Standardization Agency, SNI 1726:2019 Seismic Resistance Design Codes for Building and Other Structures, 2019.

[9] Applied Technology Council, FEMA P646-2019 Guidelines for Design of Structures for Vertical Evacuation from Tsunami, 2019.

[10] Zaidir, Reinforced Concrete Construction. Padang: Civil Engineering, Andalas University Press, 2015.

[11] Indonesian National Standardization Agency, SNI 2847:2019 Structural Concrete Requirements for Buildings, 2019.

[12] Huda Z., The Effect of Tsunami Burden on the Building of SD Negeri 23/24 Padang, Universitas Andalas, 2021.

[13] Setiawan A., Design of Reinforced Concrete Structures (Based on SNI 2847:2013). Erlangga. 2016.

[14] Edyasmar W. P., Planning Structure for Case Studies: Building, TPTC (Teacher Professional Training Center) Padang State University, Universitas Andalas, 2019.

8th Int. Conf. on Structure, Engineering & Environment (SEE), Mie, Japan, Nov.10-12, 2022, ISBN: 978-4-909106094 C3051

STRUCTURAL EVALUATION OF THE MELATI HOSPITAL BUILDING AT SUNGAI PENUH CITY

Fauzan[1], Lukman Nulhakim[1], Dyan Adhitya Nugraha M[1] and Zev Al Jauhari[2]
[1]Enginseering Faculty, Andalas University, Indonesia
[2]Department of Civil Engineering, Bengkalis Polythecnic, Indonesia

ABSTRACT

Melati Hospital is one of the health buildings in Sungai Penuh City, Jambi Province, Indonesia. The building, which was previously the main maternity clinic, plans to upgrade its status to a maternity hospital. Based on field investigations, the concrete compressive strength (fc') was 15.77 MPa, which did not meet the requirement in the Indonesian building codes. Therefore, a structural evaluation should be done to the building structure. Structural analysis was performed with ETABS v18 software using two methods, the open frame and the masonry wall infill frame methods. The performance of the building structure was evaluated in terms of the moment and shear capacities in columns and beams, as well as the inter story drift in the existing building. The results obtained by modeling the structure as the open frame found that the capacity of the existing structure was not strong enough to resist the working loads, especially on the second-floor columns, beams, and inter story drift that did not meet the permit limit in the building codes. Meanwhile, the modelling of the structure using frame with masonry infilled frame, this hospital building structure is strong enough to withstand the working loads. From these results, it was found that the ability of this building to resist earthquake loads largely depends on the walls contribution to withstand lateral loads. The masonry is a brittle material that is prone to crack or fail so that the retrofitting of the masonry wall using ferrocement layers is highly recommended for this hospital building.

Keywords: Hospital building, Structural evaluation, Earthquake loads, Structural elements capacity

INTRODUCTION

Health is very important for humans in order to survive and do activities properly. To manifest good health in the community, not only medical personnel and good medical support equipment are needed but also a good structural building. So that the health building can function safely and its strength can ensure the safety of the humans in it [1]. It is necessary to plan the structure in accordance with Indonesian standards building.

In Indonesia, the building standards are always changing along with the development of science and the latest circumstances. An example is that in 2012 the regulation on earthquake-resistant buildings was contained in SNI 1726:2012 [2], but after 7 years, this regulation had changed along with research on the response to major earthquakes in Indonesia which damaged many buildings in Indonesia, so a new regulation was issued, namely SNI 1726:2019 [3].

The Melati Hospital Building is one of the health buildings in the city of Sungai Penuh City, Jambi Province, Indonesia, as shown in Fig. 1. The building, which was previously the main clinic, wants to upgrade its status to a maternity hospital. This hospital was the first maternity hospital in the city of Sungai Penuh. This hospital building is a three-story building, and the construction uses reinforced concrete construction. The reason of choosing reinforced concrete construction is because considering the function of the building is designed to have high strength against the influence of external loads that may occur [4]. This building was located in an earthquake-prone area, which was designed using previous Indonesian building standard SNI 1726:2012 [2]. In the hammer test result, it was found that the compressive strength of concrete was quite low, which is 15.77 MPa. Therefore, a structural evaluation should be carried out on the existing structure of the Melati Hospital Building using the current Indonesian building standards [5].

Fig. 1 3D modelling of Melati Hospital Building.

STRUCTURE ANALYSIS

Building Data

The three-story Melati Hospital Building is made

of reinforced concrete structures with the size of 28.16m length and 13m width. The yield strength of steel (fy) was 240 MPa and 400 MPa for plain and deformed reinforcements, respectively, while the compressive strength of the concrete (fc') was 15.77 MPa. Figures 1, 2 and 3 show the lay-out building and the beam column position on first, second, and third floors. The dimensions of the structural elements are:
1. Beam: B1, B3 (30 x 40cm), B2 and RB (15 x 20cm)
2. Sloof: S1 (40 x 60 cm) and S2 (15 x 20 cm)
3. Column: K1 (35 x 35 cm), K2 and K3(30 x 400 cm)
4. Slab thickness: 13 cm.

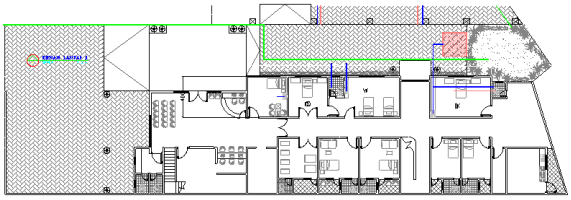

Fig. 2 The plan view of the building at 1st floor.

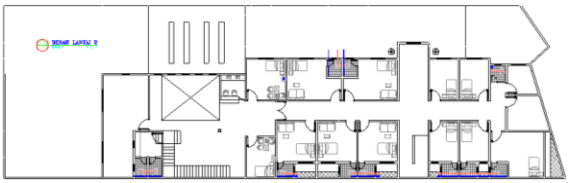

Fig. 3 The plan view of the building at 2nd floor.

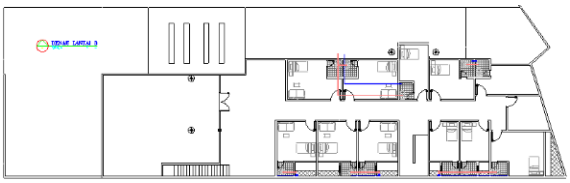

Fig. 4 The plan view of the building at 3rd floor.

Structural Modeling

Structural modeling for open frame method

In the modeling of the open frame method, columns and beams are modeled as frame elements, while floor slabs as slab elements [6]. The modeling is carried out in accordance with the existing conditions of the Melati Hospital building, as shown in Fig. 5. The spectrum response method was used in analysis of the earthquake load.

Structure modeling for masonry infilled-frame method

In relation to the results obtained in the modeling of the open frame method, another analysis was carried out using the frame method with a filler wall [4]. In the modeling of the frame with filler walls columns and beams are modeled as frame elements, floor plates as slab elements, and walls as wall elements with masonry material [6]. The properties of the masonry walls are modeled according to Fig. 6. Modeling of the masonry infilled-frame is carried out with definition:
1. The compressive strength (fc') of plaster for the walls is 5.23 MPa.
2. Specific gravity of plaster 2130 kg/m^3.
3. The compressive strength (fc') of masonry is assumed 1 MPa.
4. Specific gravity of masonry 1700 kg/m^3.

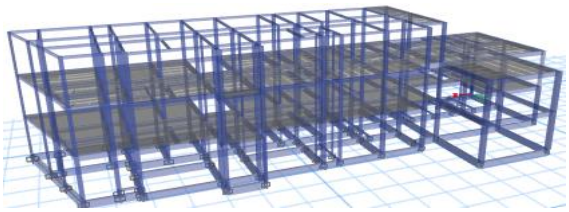

Fig. 5 Modeling of building structures with an open frame method.

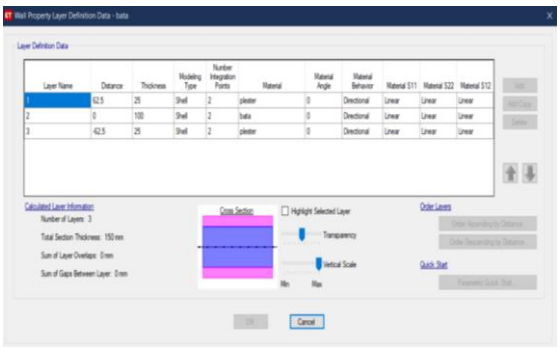

Fig. 6 Properties of masonry walls.

The results of modeling the masonry infilled-frame is shown in Fig. 7.

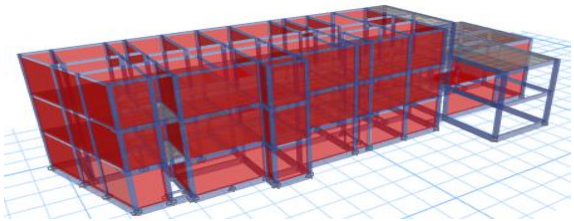

Fig. 7 Structural modeling of masonry infilled-frame method.

Loading Analysis

Dead load

The dead load on the building was calculated based on the Indonesian Standards Building (SNI

1727:2020) [3]. The dead load acting on the floor plate of the Melati Hospital Building at Sungai Penuh City shown in Table 1.

Table 1 Dead load on the building structure

Load	Load value
Floor coverings	48 kg/m^2
Floor plaster	42 kg/m^2
Plafond	20 kg/m^2
Rainwater	50 kg/m^2

Live load

The live load calculated based on SNI 1727:2020 must be the maximum load expected to occur due to the occupancy and the use of the building [7], but it must not be less than the minimum load set. The live load on the building is based on the floor plan:

a. Patient Room = 1.92 kN/m^2
b. Lobby/corridor = 4.79 kN/m^2
c. Lobby above the 1st floor = 3.83 kN/m^2
d. Operating room/laboratory = 2.87 kN/m^2

Earthquake load

The spectrum response is used as an analysis of dynamic earthquake loads. The spectrum response earthquake load is calculated based on SNI 1726:2019 [3]. Based on the design spectral acceleration parameter values for soft soil in the hospital building location, the value of spectral design SD1 and SDS are 0.663g and 1.459g, respectively. Figure 8 shows the spectrum response for Sungai Penuh City with soft soil conditions.

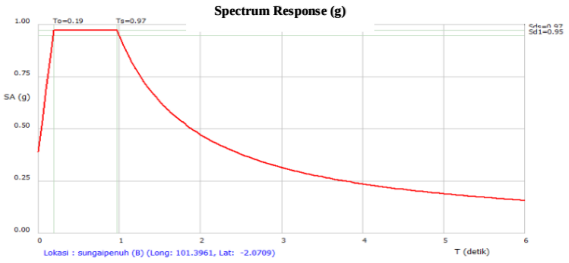

Fig. 8 Earthquake response spectrum design of Sungai Penuh City.

Load combination

Based on SNI 1726:2019, to simulate the direction effect of the random earthquake plan to the structure of the building, the effect of earthquake loading in the main direction determined must be considered to be 100% effective and must be considered to occur together with the effect of deep earthquake loads with a perpendicular direction to the main direction of the load, with an effectiveness of only 30% [3]. The load combination for this analysis is as follows:

1. 1.4 DL
2. 1.2 DL + 1.6 LL+ 0.5 R
3. 1.2 DL + 1.0 LL ± 1.0 EQx ± 0.3 EQy
4. 1.2 DL + 1.0 LL ± 0.3 EQx ± 1.0 EQy
5. 0.9 DL ± 1.0 EQx ± 0.3 EQy
6. 0.9 DL ± 0.3 EQx ± 1.0 EQy

Building priority factors (Ie) and response modification coefficient (R)

Based on SNI 1726:2019, the earthquake reduction factor (R) is 8 for the frame structure of the special moment-bearing frame system, and the building importance factor (Ie) is 1.5 for risk category IV [3]. The spectrum response data are inputted into the structural modeling and scale factor calculations was performed on ETABS using Eq. (1).

$$SF = G.I/R \quad (1)$$

RESULTS AND DISCUSSION

Cross-Sectional Capacity for Open Frame Method

Column capacity

To determine the cross-sectional capacity of the building structure, it is necessary to review the cross-sectional capacity of the columns and beams in the Melati Hospital Building. The review of the structural elements is grouped by dimensions, type, and position of those columns and beams. From the results of the structural analysis, it will be known the cross-sectional capacity of the structural elements such as beam momen capacity, beam shear capacity, column interaction diagrams and column shear capacity [8]. From the results of this cross-sectional capacity, it will be known whether the cross section is able to withstand the working load. The cross-sectional capacity of the column can be seen with the following interaction diagram of P-M and shear capacity results.

The calculation results of the interaction diagram of the first floor, second floor, and third floor columns of the building are shown in Fig. 9.

From the P-M interaction diagram in Fig. 9 above, it can be seen that the columns on the 1st and 3rd floors are still strongly carrying the working loads on the structure because the moment and axial do not cross the permit limit in the P-M interaction diagram. Meanwhile, the column on the 2nd floor is not strong enough to carry the working load because there is a moment and axial that passes the line permit limit in the P-M interaction diagram.

The shear capacity of the building columns is shown in Table 2. From the table, it is clearly seen that the column is able to withstand the shear forces acting on the structure.

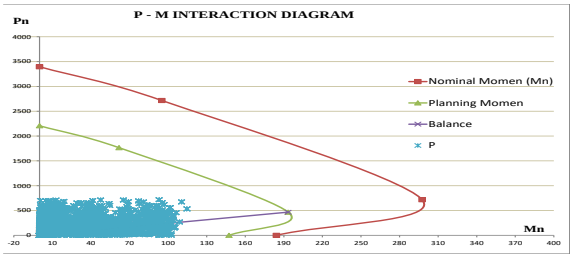

(a)

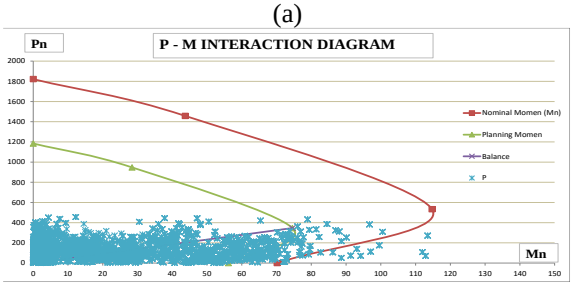

(b)

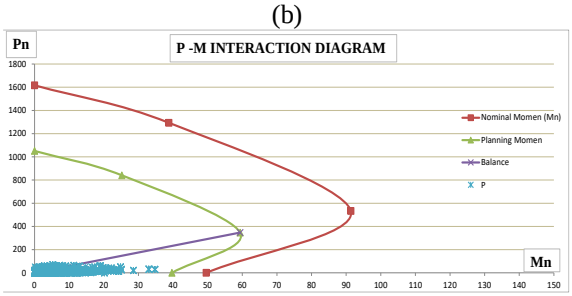

(c)

Fig. 9 P-M interaction diagram at 1st floor (a), 2nd floor (b) and 3rd floor (c) for open frame method.

Table 2 Shear capacity column

Story	Dimension (mm)	ϕ (mm)	Space (mm)	ϕVn (kN)	Vu (kN)	Description
1	350 x 350	10	100	141.5	60.9	OK
2	300 x 300	10	1100	112.2	59.4	OK
3	300 x 300	10	100	112.2	11.3	OK

Beam capacity

Table 3 Flexural capacity of beam

Type	Dimension (mm)	Comp. rebar	Tensile Rebar	ϕMn (kNm)	Mu (kNm)	Desc.
S1	400 x 600	6D19	8D19	378.86	77.23	OK
S2	150 x 200	2D10	2D10	7.28	3.86	OK
B21	300 x 400	6D13	6D13	84.05	107.61	NOT OK
B22	150 x 200	2D10	2D10	7.278	6.1	OK
B31	300 x 400	6D13	6D13	84.05	109.08	NOT OK
B32	150 x 200	2D10	2D10	7.28	3.9	OK
RB	150 x 200	2D13	2D13	11.48	11.15	OK

The cross-sectional capacity of the beam can be seen by comparing the moment capacity and shear plan with the working moment and shear ultimate [8].

From Table 3, it can be seen that the beams on the building structure are unable to withstand the loads acting on the structure. Meanwhile, the beam has enough capacity to resist the shear forces acting on the structure, as shown in Table 4.

Table 4 Shear capacity of beam

Type	Dimension (mm)	Comp. rebar	Tensile rebar	Vr (kN)	Vu (kN)	Desc.
S1	400 x 600	6D19	8D19	269.53	77.23	OK
S2	150 x 200	2D10	2D10	53.58	7.72	OK
B21	300 x 400	6D13	4D13	151.08	112.03	OK
B22	150 x 200	2D10	2D10	38.31	11.35	OK
B31	300 x 400	6D13	4D13	151.08	103.47	OK
B32	150 x 200	2D10	2D10	38.31	10.81	OK
RB	150 x 200	2D13	2D13	82.84	16.48	OK

Inter story drift

According to SNI 1726:2019, the determination of inter story drift (Δ) must be calculated as the difference in the drift at the center of mass above and below the level under review [3], [9]. Tables 5 and 6 show the results of the inter story drift building for X and Y directions.

Table 5 Inter story drift in X-direction

Story	H_{sx} (mm)	H (mm)	∂_e (mm)	Δ mm	Δ_i (mm)	Δ_{permit} (mm)	Desc.
3	12	4000	33.9	124.3	19.58	40	OK
2	8	4000	28.56	104.72	59.39	40	NOT OK
1	4	4000	12.26	45.32	45.32	40	NOT OK
Base	0	4000	0	0	0	40	OK

Table 6 Inter story drift in Y-direction

Story	Hsx (mm)	H (mm)	∂e (mm)	Δ (mm)	Δ_i (mm)	Δ_{permit} (mm)	Desc.
3	12	4000	40.38	148.05	-4.65	40	OK
2	8	4000	41.65	152.7	87.74	40	NOT OK
1	4	4000	17.72	64.96	64.96	40	NOT OK
Base	0	4000	0	0	0	40	OK

Based on Tables 5 and 6, it can be seen that the inter story drift in X and Y directions does not meet the permit limit as required on the SNI 1726:2019 [3].

Cross-Sectional Capacity for Masonry Infilled-Frame

Column capacity

Cross-sectional capacity for masonry infilled-frame [10] can be seen on the diagram of the P-M interaction, shown in Fig. 10.

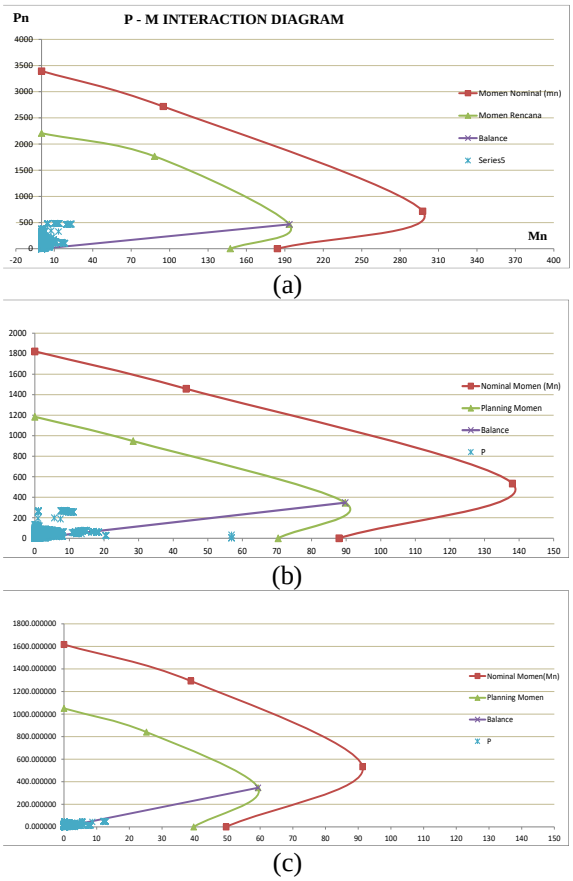

Fig. 10 P-M interaction diagram at 1st floor, 2nd floor and 3rd floor for masonry infilled-frame.

As seen in Fig. 10, the first, second, and third floor columns are strong enough to carry the working load because there are axial moment and compression force that not passes through the design axial compression moment line.

Table 7 shows the shear capacity on the columns. As seen in the table, the column is able to withstand the shear forces acting on the structure.

Table 7 Shear capacity column

Story	Dimensions (mm)	Diameter (mm)	Space (mm)	ϕVn (kN)	Vu (kN)	Desc.
1	350 x 350	10	100	141.5	10.16	OK
2	300 x 300	10	100	112.2	9.28	OK
3	300 x 300	10	100	112.2	2.77	OK

Beam capacity

Tables 8 and 9 shows the flexural and shear capacity of the beams. As can be seen in these tables, the beams are able to withstand the working loads.

Table 8 Beam flexural capacity

Story	Dimension (mm)	Comp. Rebar	Tensile Rebar	ϕMn (kN)	Mu (kN)	Desc.
S130x40	400 x 600	6D19	8D19	378.8	46.7	OK
S215x20	150 x 200	2D10	2D10	7.3	3.9	OK
B230X40	300 x 400	6D13	6D13	84.1	49.2	OK
B215X30	150 x 200	2D10	2D10	7.3	1.9	OK
B330X40	300 x 400	6D13	6D13	84.1	67.3	OK
B315X30	150 x 200	2D10	2D10	7.3	3.2	OK
RB	150 x 200	2D13	2D13	11.5	4.9	OK

Table 9 Beam shear capacity

Beam Type	Dimension (mm)	Comp. Rebar	Tensile Rebar	Vr (kN)	Vu (kN)	Desc.
S130x40	400 x 600	6D19	6D19	269.5	39.5	OK
S215x20	150 x 200	2D10	2D10	53.6	7.7	OK
B230X40	300 x 400	6D13	4D13	151.1	44.8	OK
B215X30	150 x 200	2D10	2D10	38.3	5.2	OK
B330X40	300 x 400	6D13	4D13	151.1	53.8	OK
B315X30	150 x 200	2D10	2D10	38.3	5.1	OK
RB	150 x 200	2D13	2D13	82.8	5.9	OK

Inter story drift

The calculation results of the inter story drift in the X and Y directions on the retrofitted building is shown in Tables 10 and 11.

Table 10 Inter story drift X direction

Story	H_{sx} mm	H mm	∂_e mm	Δ mm	Δ_i mm	Δ_{permit} mm	Desc.
3	12	4000	0.61	2.24	0.3	40	OK
2	8	4000	0.53	1.94	3.98	40	OK
1	4	4000	1.61	5.92	5.92	40	OK
Base	0	4000	0	0	0	40	OK

From Tables 10 and 11, it is clearly seen that the inter story drift that occur in X and Y directions have met the permit limit according to Indonesian building standard.

From the structural analysis results of the two methods, it can be seen that calculations with open frame modeling method shows that the Melati Hospital Building does not have strong enough capacity on resist the working loads, especially in the second-floor columns, beams, and the inter story drift. While the calculations with masonry infilled frame method [11], the structure of the hospital building is

strong enough to withstand the working load based on the current Indonesian building standards. However, masonry is a material that is vulnerable and easy to experience failure (brittle) so strengthening the building wall is highly recommended by using the mortar containing small wire mesh that was installed on a masonry wall (ferrocement layer retrofitting method) [12] – [16].

Table 11 Inter story drift Y direction

Story	H_{sx} mm	H mm	∂_e mm	Δ mm	Δ_i mm	Δ_{permit} mm	Desc.
3	12	4000	1.14	4.16	0.98	40	OK
2	8	4000	0.87	3.19	1.51	40	OK
1	4	4000	0.46	1.68	1.68	40	OK
Base	0	4000	0	0	0	40	OK

CONCLUSION

Based on the structural evaluation of the Melati Hospital Building, the following conclusions can be drawn:

1. The compressive strength of concrete in the beam and column elements of the Melati Hospital Building is quite low, fc' = 15.77 MPa (K-190), lower than that required in Indonesian Building Standards (fc' = 17 MPa).
2. The results of the analysis showed that the structural capacity of the Melati Hospital Building was not strong enough to resist the working loads, especially in the second floor column, the beams and inter story drift that was calculated with an open frame method. Whereas using modeling with masonry wall infilled frame method, this hospital structure is strong enough to withstand the working loads according to current Indonesian building standards.
3. The ability of Melati Hospital Building to withstand earthquake loads is highly dependent on the contribution of the wall to resist the lateral loads, so that the connection of the walls to the columns and beams should be properly designed and constructed.
4. Strengthening the walls of buildings with *ferrocement layer* improve the capacity of the building by reducing the internal force on columns and beams due to the working load on the building. In the observed column, it had a moment reduction of 16-17%, an axial force of 15-16%, and a shear force of up to 15%. While the beam had a moment reduction of 6-18%, and a shear force of 2-5%.

REFERENCES

[1] Haryanto Y., Sudibyo G. H. and Effendi F. C. A., Preliminary seismic hazard assessment of the oral and dental hospital of Jenderal Seodirman University, Proc. Eng. 171, 2017, pp1025-1034.

[2] Indonesian National Standardization Agency, SNI 1726:2012 Seismic Resistance Design Codes for Building and Other Structures, 2012.

[3] Indonesian National Standardization Agency, SNI 1726:2019 Seismic Resistance Design Codes for Building and Other Structures, 2019.

[4] Zengin B. and Kocak A., The Effect of the Bricks Used in Masonry Walls on Characteristic Properties, Sigma Journal of Engineering and Natural Science, Vol.35, No.4, 2017, pp.667-677.

[5] Putra N.S. A. and Lesmana C., Feasibility analysis of the structure of a 5-story public building in the Jakarta City, Jurnal Teknik Sipil, Vol.14, No.2, 2018, pp180-199.

[6] Alfianto R. and Rahmat D., Analysis of Calculation of Buildings with Methods ETABS Version 9.7.2, Journal of Civil Eng., Building and Transportation, Vol.2, No.1, 2018, pp28-33.

[7] Indonesian National Standardization Agency, SNI 1727:2020 Minimum Load for Planning of Buildings and Other Structures, 2020.

[8] Indonesian National Standardization Agency, SNI 2847:2019 Structural Concrete Requirements for Buildings, 2019.

[9] Akbar S. J., Chandra Y. and Yusriansyah, Analysis of Horizontal Deviation Value (Drift) in Earthquake Resistant Structures Using the Eccentric Bresing Frame System Type Braced V, Teras Jurnal, Vol.7, No.2, 2017, pp301-312.

[10] Pardeshi S. and Deshpande U. L., Repair, Restoration and Strengthening of Building, International Journal of Innovations in Engineering Research and Technology (IJIERT) Vol. 4, Issue 3, pp.121-124, 2017.

[11] Boen T., Earthquake Resistant Building Manual. World Seismic Safety Initiative. 2009.

[12] Barnaure M. and Stoica D. N., Analysis of Masonry Infilled RC Frame Structures Under Lateral Loading, Mathematical Modelling in Civil Engineering, Vol.11, No. 1, 2015, pp.29-39.

[13] Balamuralikrishnan R., AL Madhani M, and Al Madhani R., Study on Retrofitting of RC Column Using Ferrocement Full and Strip Warapping, C. Eng. Journal, Vol.5, No.11, 2019, pp.2472-2485.

[14] Fauzan, Ismail F. A., Zaidir and Amalia S. H., Experimental Study on Masonry Building Strengthened with Ferrocement Layers, Int. J. GEOMATE, Vol. 14, Issue 45, 2018, pp.84-90.

[15] Alam M. Z., Asif M. M. and Ahsan R., A study on The Performance of Ferrocement Retrofitted Masonry Wall Units under Cyclic Loading, Int. Con. on Adv. in Civ. Eng., 2018, pp. 451-455.

[16] Wang C., Sarhosis V. and Nikitas N., Strngthening/Retrofitting Techniques on Unreinforced Masonry Structure/Element Subjected to Seismic Loads: A Literature Review, Vol.12, 2018, pp.251-268.

8th Int. Conf. on Structure, Engineering & Environment (SEE), Mie, Japan, Nov.10-12, 2022, ISBN: 978-4-909106094 C3051

ANALYSIS OF REINFORCED CONCRETE STRUCTURES EMPLOYING KOHONEN SELF ORGANISING MAP

Omar Al Juboori[1] and Rabee Rustum[2]
[1]PEROrient Building Contracting LLC, UAE
[2]School of Energy, Geoscience, Infrastructure and Environment, Heriot Watt University, Dubai Campus,

ABSTRACT

Reinforced Cement Concrete (RCC) structure is most widely used in the construction industry alongside other types of structures such as steel structures, wooden structures and many other systems used globally. This paper employed Artificial Intelligent (AI) techniques for modelling the (RCC) elements in the buildings using the Kohonen Self Organizing Map (KSOM), A comparison between this technique and other techniques used in the field, such as the Artificial Neural Network (ANN) has been made. The results showed that the Kohonen Self Organizing Map (KSOM) is an attractive tool for modelling reinforced concrete structures. Moreover, this technique offers a magnificent tool for high-dimensional data visualization.

Keywords: Reinforced Cement Concrete, Artificial Intelligent, Kohonen Self Organizing Map, Artificial Neural Network

INTRODUCTION

The global trends nowadays for designing (RC) Structures as sustainable buildings direct the designer towards reducing the resources of concrete used in the structures by conserving the use of the environmental resources; hence an optimized design is required to establish any building. Thus, for the time-being, the researchers are trying to outline new ways, techniques, methods or procedures for the design to override the old ones [1].

The major limitations of the conventional methods are the safety factors presumed in the calculations that may lead to exaggerated material quantities, which will affect the cost of the building in the first place, time for construction and additional building mass where it will be critical in the seismic analysis. Futhermore, it requires a huge time for designing and analysis especially in complex buildings.

Subject to the above, the researchers/designers aim to employ artificial intelligence techniques to solve these critical issues, such as the artificial neural network (ANN) and Kohonen Self-Organizing Map (KSOM) [2].

LITERATURE REVIEW

The construction of any building requires a structural system to carry out the load applied to it; hence a proper design has to be considered. There are multiple ways to achieve this target, starting from the conventional methods that are highlighted in the international codes; however, nowadays, the main target is to use the artificial intelligence techniques such as but not limited to ANN and KSOM [3], [4].

The main technique that will be covered in this paper is one of the unsupervised techniques, which is the KSOM network, which was developed to solve problems such as clustering, visual analytics, and abstract thought, among others. The results reveal that when KSOM and the contiguity-constrained clustering approach are combined, the clustering results are comparable to those of other clustering methods. Then, using two well-referenced machine-learning scenarios, assess the method's applicability and compare the findings to those of several famous statistical clustering methods, referring to figure 1 for a simple illustration of KSOM technique [5], [6]. More information on training and visualization of the KSOM are available in the literature, and the reader can refer to Rustum and adeloye (2011) [7].

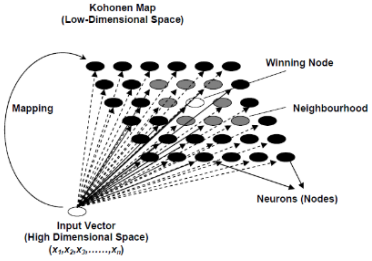

Fig. 1 – Illustration of winning node and its neighborhood in KSOM [8].

METHOD AND MATERIALS

Case Study

The methodology followed in this paper was applied to several data collected from several pieces of research for both selected cases, which are beams with stirrups and beams without stirrups. In both cases, the results of artificial neural network (ANN)

and the experimental results for shear force are also included, and this was used for validation and comparison between it and the KSOM method. Furthermore, several software was used to validate the data to get the most affected parts to the method in visualized maps.

The model for each case was developed and implemented using MATLAB Programming language and Neural Networks toolbox and the SOM toolbox developed at the CIS laboratory at Helsinki University of Technology [8].

MATLAB was chosen because neural networks require complicated matrix computations, and the tools within the software helped to provide a comprehensive design, implementation, and simulation of the model quickly. It is also flexible enough to do the necessary customization. The work was done using the software's package documentation and literature [8].

Microsoft Excel was chosen to visualize the data in figures and perform mathematical calculations to obtain the minimum, maximum, standard deviation, average, outlier, and other results needed for this study. The functions and definitions of the terms were obtained from the software package's documentation and the literature [9].

The parameters used in this are presented in Table 1 and 2 hereinafter.

Table 1 Notations Used for Beams with Stirrups Case

ID	Identification
b	Beam cross-section width (mm)
h	Beam cross-section height (mm)
d	The effective depth of section (mm)
a_v	The Shear span of a beam (mm)
f_c	Concrete compressive strength (MPa)
A_{sl}	Longitudinal reinforcement area (mm^2)
A'_{sl}	Compressive longitudinal reinforcement area (mm^2)
ρ (%)	Percentage of longitudinal reinforcement (%)
ρ ' (%)	Percentage of compressive longitudinal reinforcement ratio (%)
ρv (%)	Percentage of Transverse reinforcement ratio (%)
f_{yl}	Longitudinal reinforcement nominal yield stress (MPa)
f'_{yl}	Compressive longitudinal reinforcement nominal yield stress (MPa)
f_{yv}	Transverse reinforcement nominal yield stress (MPa)
A_{sv}	Stirrups reinforcement area (mm^2)
V_{EXP}	Experimental maximum shear (kN)
P_{EXP}	Experimental maximum load (kN)

Table 2 Notations Used for Beams with Stirrups Case

ID	Identification
b	Beam cross-section width (mm)
h	Beam cross-section height (mm)
d	The effective depth of section (mm)
a_v	The Shear span of a beam (mm)
f_c	Concrete compressive strength (MPa)
A_{sl}	Longitudinal reinforcement area (mm^2)
ρ (%)	Percentage of longitudinal reinforcement (%)
f_{yl}	Longitudinal reinforcement nominal yield stress (MPa)
V_{EXP}	Experimental maximum shear (kN)
P_{EXP}	Experimental maximum load (kN)

Models Performance Evaluation Criteria

The network should be evaluated and compared to other findings after it has been trained. In this study, the KSOM was employed and compared to the experimental and ANN techniques, and the following evaluation criteria were employed [8].

1. The Average Absolute Error (AAE) [8].
2. The relative average absolute error (RAAE) [8].
3. The normalized root mean squared error (NRMSE) [8].
4. The mean square error (MSE) [8].
5. The correlation coefficient (R) [8].
6. The classification error (CE) [8].

Analysis of Variance (ANOVA) Criteria

1. Sum of Squares (SS) [8].
2. Mean Square (MS) [8].
3. The Overall (F) [8].

4. Significance F [8].

Regression Summary Criteria

1. Coefficient: It gives the least squares estimate [8].
2. Standard Error [8].
3. t Stat [8].
4. P Value [8].
5. Lower & Upper 95% [8].

Regression Statistic Criteria

1. Multiple R [8].
2. R Squared (r^2) [8].
3. Adjusted R Square [8].
4. Standard Error [8].
5. Observations [8].

RESULTS AND DISCUSSION

To start the implementation of KSOM technique, two selected cases were used as described earlier, then the results were compared to those generated from ANN technique and the experimental results to judge the usefulness of this technique. It is worthy mentioning that the results obtained for this research went through a series of regressions (in sets), noting that the data analyzed was around 568 for the first case (Beams without stirrups) and 296 for the second case (Beams with stirrups).

Beams without stirrups case 1

In this case, the data obtained from the sources [10] were analyzed through 3 sets of regression, each set obtaining a serial number of results hereinafter, the results will be shown and discussed.

The below figures explain how each characteristic can affect the results using MATLAB Software; the higher the color appears in figure represents more contribution of this characteristic of the specimen.

The performance of the model is shown in figures 3 and 4, where the correlation between the modelled data using the KSOM and the experimental results was over 90%.

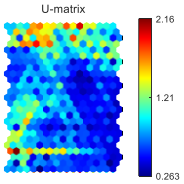

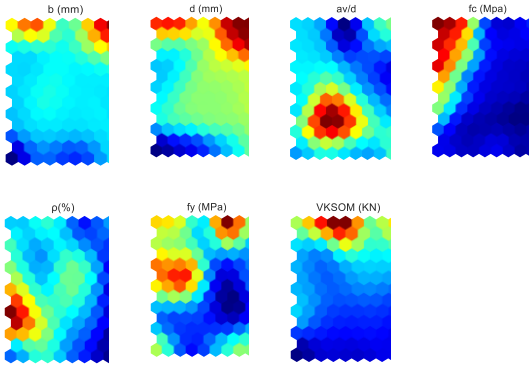

Fig. 2 – Affection of the specimen characteristic on the results – Case –1 – Set 1

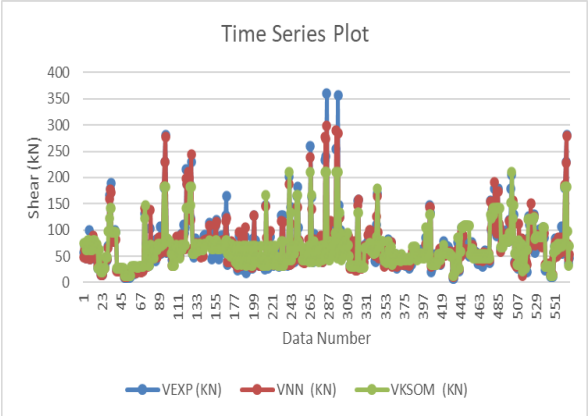

Fig. 3 – Time Series Plot for the regression analysis – Case –1 – Set 1

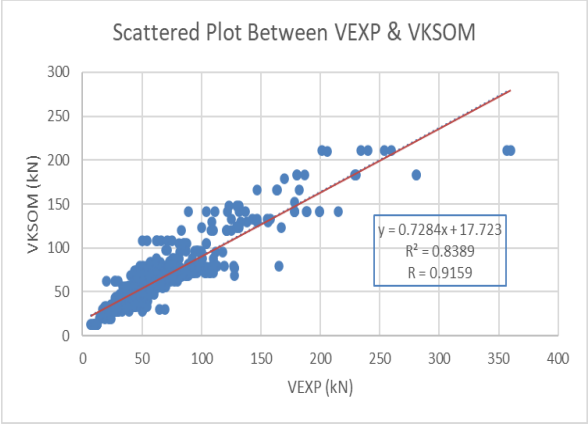

Fig. 4 – Scattered Plot between VEXP and VKSOM techniques – Case –1 – Set 1

Beams with stirrups case 2

In this case the data obtained from the sources [10] were analyzed through 4 sets of regression, each set obtaining a serial number of results hereinafter, the results will be shown and discussed.

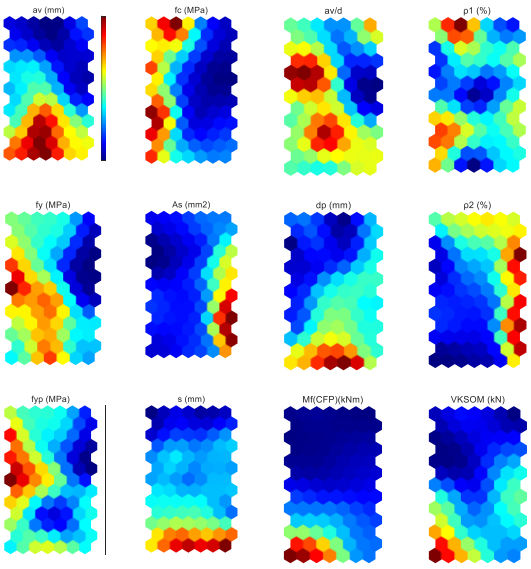

Fig. 5 – Affection of the specimen characteristic on the results – Case –2 – Set 1

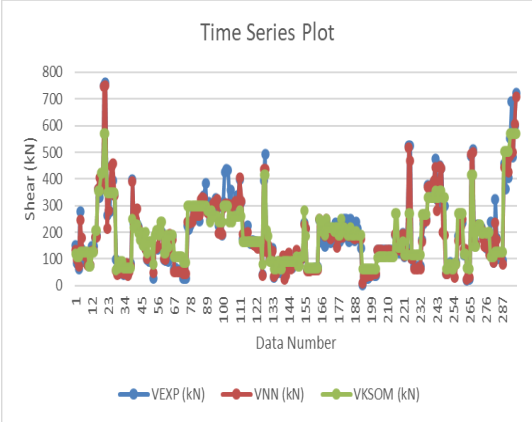

Fig. 6 – Time Series Plot for the regression analysis – Case –2 – Set 1

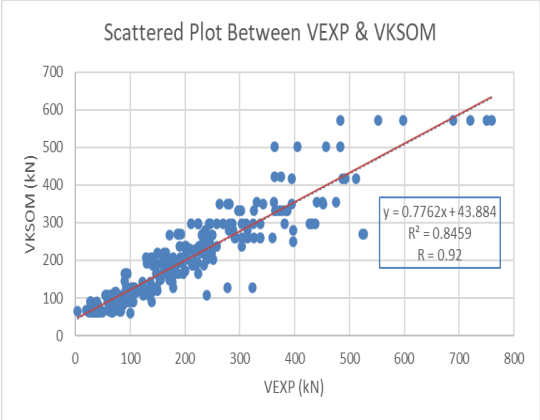

Fig. 7 – Scattered Plot between VEXP and VKSOM techniques – Case –2 – Set 1

And similarly, the calculations were obtained for the other sets in both cases, comparing all the results using the criteria described earlier to judge the technique for using it in the structural field.

CONCLUSION AND RECOMMENDATIONS

Based on the above calculations, the results found that using the Kohonen Self Organizing Map "KSOM" technique which is part of the artificial intelligence techniques in the structural field, is feasible and within the acceptable limits by comparing the obtained results along with the experimental results and those results obtained by using ANN, hence it is useful to use this kind of technology even when some data were missing, and the model didn't get affected by these missing data or the outliers and this one of the most important advantages of this technique.

The model training, as shown in both cases tested for this technique, got affected by the sectional dimension, location of the main reinforcement, and applied moment on the section, while the effect of the reinforcement percentage or the compressive strength of the section represents less important for the same.

Moreover, the model could be enhanced by adding other data from other sources to train it better and enhance it; this will tend to reduce the time requested to predict an acceptable design and reduce the time consumed using the conventional method procedure and the mathematical calculations.

Nevertheless, other types of structural elements could be entered into the model, train the model to get various type of designed elements and test it; the same will make this technique part of the next revolution in structural design and other engineering and non-engineering fields.

REFERENCES

[1] Saleem, M.U. and Qureshi, H.J., 2018. Design solutions for sustainable construction of pre-engineered steel buildings. Sustainability, 10(6), p.1761.

[2] Lee, S.C., 2003. Prediction of concrete strength using artificial neural networks. Engineering structures, 25(7), pp.849-857.

[3] Rustum, R., Adeloye, A. and Simala, A., 2007. Kohonen self-organising map (KSOM) extracted features for enhancing MLP-ANN prediction models of BOD5. In International Symposium: Quantification and Reduction of Predictive Uncertainty for Sustainable Water Resources Management-24th General Assembly of the International Union of Geodesy and Geophysics (IUGG) (pp. 181-187).

[4] Kumar, N., Rustum, R., Shankar, V. and Adeloye, A.J., 2021. Self-organizing map estimator for the

crop water stress index. Computers and Electronics in Agriculture, 187, p.106232.

[5] Kumar, N., Adeloye, A.J., Shankar, V. and Rustum, R., 2020. Neural computing modelling of the crop water stress index. Agricultural Water Management, 239, p.106259.

[6] Rustum, R.A.B.E.E. and Adeloye, A.J., 2006, September. Features extraction from primary clarifier data using unsupervised neural networks (Kohonen Self Organising Map). In the 7th International Conference on Hydroinformatics, HIC 2006, Nice, France.

[7] Rustum, R. and Adeloye, A., 2011. Artificial Intelligence modelling of wastewater treatment plants: Theory, applications and limitations.

[8] Rustum, R., 2009. Modelling activated sludge wastewater treatment plants using artificial intelligence techniques (fuzzy logic and neural networks) (Doctoral dissertation, Heriot-Watt University).

[9] Rustum, R. and Adeloye, A.J., 2007. Replacing outliers and missing values from activated sludge data using Kohonen self-organizing map. Journal of Environmental Engineering, 133(9), pp.909-916.

[10] Kotsovou, G.M., Cotsovos, D.M., 2017. Analysis Of Reinfored Concrete Structures Employing Neural Networks.

8th Int. Conf. on Structure, Engineering & Environment (SEE), Mie, Japan, Nov.10-12, 2022, ISBN: 978-4-909106094 C3051

EXISTING BRIDGE CAPACITY EVALUATION FOR TRANSPORTATION HAVEY TRAILER

Douangmixay DOUNSUVANH 1, Chanpheng PHOMMAVONE 2
1,2Department of Civil Engineering, Faculty of Engineering, National University of Laos, Lao PDR

ABSTRACT

At the present time, there are many mega projects have been popular constructed in Laos such as Hydropower Dam Projects. Which these projects require to transportation heavy machines and equipment such as transformers, generators, etc., crossing many existing old bridges along national roads, and most of bridges are no design information. It may difficult to bridge engineers to make decision for transportation heavy truck crossing the bridges which ensuring bridge are safe. This study is presenting for existing bridges capacity evaluation for transportation of heavy machine trailer crossing bridges along transportation routes of 60 km. The transportation route started from Thai-Lao border to dam project site at Khammuan Province, Lao PDR. All bridges along transportation road are no design information, which the allowable normal traffic trucks load is only 40 tones. However, the machine weight is up to 250 tones (not including trailer weigh). Two critical typical bridges namely PC-I girder and Steel I-Girder, span length 25m, and 25.5m respectably have been selected for presenting study bridges capacity and evaluation. The procedure of the bridges evaluation are including detail inspection, full loading testing by actual twelve wheel trucks, and 3D FEM model for comparing model and selecting proper tailor configuration (the total weigh of Machine and trailer weigh is 350 tones). After that the bridge response (Girders strain, deflection and vibration) were monitoring during heavy trailer crossing the bridges. It seen that this method is safe to bridge structure for carrying heavy trailer. The analysis results of bridge structure by 3D FEM are match to the actual testing and monitoring.

Keywords: Heavy Trailer, Bridge testing and monitoring, Bridge Capacity Evaluation.

INTRODUCTION

The bridge structure is very vital for highway engineering system, if it is lack of the capacity to carry traffic truck loads, consequently many problems would be occurred such as: structural cracking, successive deflection, shortening bridge service life, instability of the structural member leading to the whole structure collapse. Evaluation of the existing bridge is one difficult work for the Bridge Engineer, especially for the bridge that design and construction information are not known [2]. This study is for existing bridges capacity evaluation for transportation of heavy machine transformer to Dam site, Hydroelectric Power Project in Lao PDR. The project route for transportation is stating from Thai-Lao border to dam project site, 60 km at Khammuan Province, Lao PDR. Along the project route, there are 15 bridges and 10 culverts, all bridges are no design and construction information.

This study is presenting for existing bridges capacity evaluation for transportation of heavy trailer crossing bridges along transportation routes. The maximum transportation weight is 250 tones (not including trailer weigh), and 350 tones including trailer weigh). Two critical bridges along the project route are selected for study capacity by analysis model, actual load testing, after that, the bridges have been monitored their respond due to maximum heavy trailers.

BRIDGE ON PROJECT RUTE TRUCKS

The transportation route started from Thai-Lao border to dam project site which transportation routes is about 60 km at Khammuan Province, Lao PDR. Along the project route, there are 15 bridges and 10 culverts. All bridges along transportation road are no design information, which the allowable normal traffic trucks load is only 40 tones. Two critical bridges are selected for study their capacity such as PC-I girder (Bridge No.5) and Steel I-Girder (Bridge No.11), span length 25m, and 25.5m respectably for presenting study bridges capacity and evaluation. Due to that according to bridge inspection results, these two bridge are more critical than other bridges and cultivars along the transportation route.

Selected testing and monitoring bridges

The PC-I girder bridge is simple sport, spans length is 25m, lane width is 7m, and each span consisted of 3 Prestressed Concrete girders as show in the “Figure 1, PC-I girder bridge.”.

Fig. 1 PC-I girder Bridge (Brg No.5)

The Steel I-Girder (Brg No.11) is also simple supported bridge with spans is 25.5m, and consisted of 4 Steel composited I-girders as show in the "Figure 2, Steel I girder bridge.".

Fig. 2 Steel I-girder (Brg No.11)

The bridges information and material strength are selecting from actual inspection and assumption from general standard, for PC the concrete compression strength is 350.0 kg/cm2, PC ultimate strength of steel is fpu = 18, 730.0 kg/cm2; the steel structure the yield strength of steel is 3,250.0 kg/cm2.

Truck Loading and Heavy Trailer

The truck loading to evaluation bridge capacity are consisted such as AASHTO bridge design truck HS25-44 [1] (total weight 40,080.00 kg), tow traffics 12 wheel trucks namely TT12(weights of 65,050 kg and 67,000 kg, total of 132,050 kg) , and heavy trailer trucks namely T350(the total weigh of Machine and trailer weigh is 350 tones)

AASHTO HS25-44 is using for analysis to comparing analysis model of testing truck TT12 and heavy trailer trucks T345

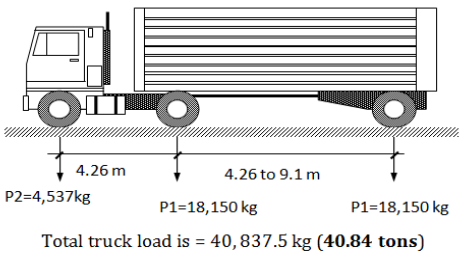

Fig. 3 AASHTO HS25-44

TT12 is using for calibration analysis model to testing results. Due to that this type of truck is popular unsung along project route.

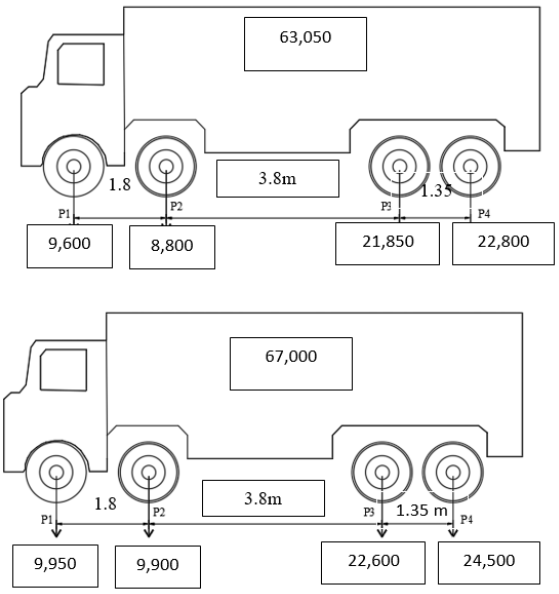

Fig. 4 Tow traffics 12 wheel trucks, TT12

Heavy trailer trucks, T350 is main purpose of transportation for the project, it will transport heavy transformer equipment of 250 tones (250,000 kg). The carefully special trailer is selected, the special trailer 32 axles and self weight of 100 tones (100,000 kg) is selected, the total weight of heavy trailer trucks, T350 is become 350 tones (350,000 kg). This heavy trailer truck therefor is using for both analysis and monitoring actual bridge respond during transporting crossing bridges.

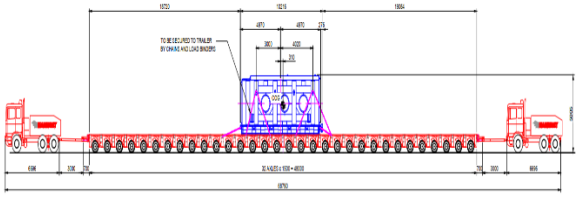

Fig. 5 Heavy trailer trucks, TT12.

32 Axle trailer with 1.5m spacing, cargo weigh = 250 tons + 100 (Trailer weigh) = total weigh 350 tons

BRIDGE ANALYAIA MODEL

The evaluation bridges No.5 and No.11 are modeled for analysis and evaluation capacity by 3D model FEM model using CSIBridge commercial software[5]. The loading models for analysis checking bridge capacity are included AASHTO truck load HS25-44, actual traffic trucks TT12, and heavy trailer trucks, T350 as indicated in the above.

The PC-I girder bridge (Brg. No.5) is modeled as 3 spans, simple supported bridge which each span length is 25m, bridge lane width is 7m, consisting of 3 PC girder as show in the "Figure 6, PC-I girder bridge.".

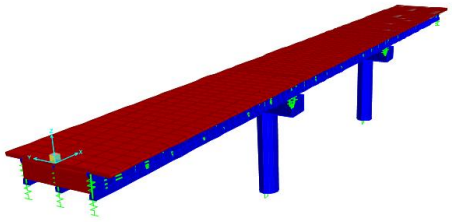

Fig. 6 Model of PC-I girder bridge (Brg. No.5)

The Steel I-Girder (Brg No.11) is modeled as one simple support, spans length 25.5m consisting of 4 Steel composited section as show in the "Figure 7, Steel I girder bridge.".

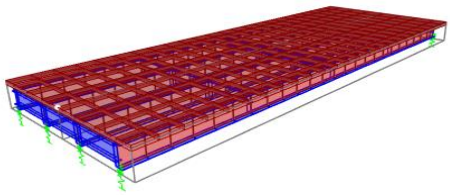

Fig. 7 Model of Steel I-Girder (Brg No.11)

Analysis Results

Three type of trucks loading namely HS25-44, TT12, T350, respectively are using to analysis for bridges No.5 and No.11. And all results are compared to consider bridge respond due to different truck loading.

The deformation shape of two bridges are shown in the below figure.

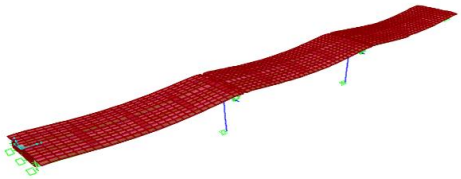

Fig. 8a Deformation shape of Brg. No.5

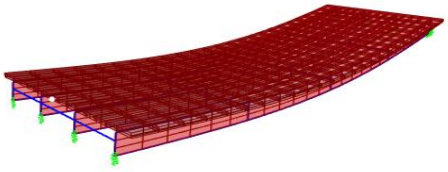

Fig. 8b Deformation shape of Brg. No.11

Table 1 shows the analysis results of total member forces of bridge No.5 due to three different types of truck loading. As the results in the table, the results of TT12 are higher than results of HS25-44 and results of T350. And results of HS25-44 are higher than results of T350. This is indicated that the special trailer truck configuration is proper selecting, it's respond is less than design accrual and design trucks model. The bridge may safe to using this trailer truck configuration.

Table 1 Summarized Member forced for Br. No.5

Items	M(Kgm)	V(Kg)	Def(mm)
Hs25-44	573,737.30	104,417.18	12.2
TT12	617,953.90	110,535.59	15.7
T350	515,078.00	90,150.00	11.2

Table 2 shows the analysis results of total member forces of bridge No.11. The analysis results of bridge No.11 are similar to that bridge No.5. The results of TT12 are higher than results of HS25-44 and results of T350. And results of HS25-44 are higher than results of T350.

Table 2 Summarized Member forced for Br. No.11

Items	M(Kgm)	V(Kg)	Def(mm)
Hs25-44	622,715.00	103,671.71	16.5
TT12	652,715.00	120,535.95	18.1
T350	563,401.00	92,275.00	14.1

BRIDGE TESTING AND MONITORING

To calibration analysis model before transportation heavy trailer trucks, T350, both bridges have been tested by full loading of TT12 which is consisted by tow 12 wheel trucks (weights of 65,050 kg and 67,000 kg, total of 132,050 kg) as show in the "Figure 4". The testing instruments are installed at midspan bridges. The results of testing than will compare to analysis models.

After model of bridge analysis due to TT12 have been proved with tested results, the bridges are also monitoring their respond due to heavy trailer trucks, T350

Testing and monitoring Bridge No.5

The testing instrument such as LVDT for measurement bridge deflection, concrete strain gage for measurement bridge strain, and accelerometer for measurement truck dynamic load are install at bottom middle span each PC-I girder.

Fig. 9 Installation testing instruments for Brg. No.5

Testing and monitoring Bridge No.11

Similar to the brg. No.5, steel I-girder bridge No.11 is also installed testing instruments such as LVDT for measurement bridge deflection, concrete strain gage for measurement bridge strain, and accelerometer for measurement truck dynamic load are install at bottom middle span.

Fig. 10 Installation testing instruments for Brg. No.11.

The testing procedure is done by using actual loading of two 12 wheels trucks, TT12 and two cases are tested for each bridge such as Test-Case-01: Static Loading testing by two truck, side by side stop on 5 locations; Test-Case-02: Dynamic Loading testing by running truck on one lane. Bridge response obtains from testing results are included as bridge deflection, strain at bottom midspan girders, and accelerometer.

The monitoring procedure is done after actual trucks tests results have been proved. The monitoring bridge is record during heavy trailer T350 is crossing overs bridges. Similar Bridge response of testing are record such as bridge deflection, strain at bottom midspan girders, and accelerometer.

Results of Testing and Monitoring

The testing results of actual truck loading, TT12 for bridge No.5 and No.11 are show in the Table 3. It is seen that deflection results from analysis are must higher that testing results, the strain from testing results are little comparing to normal allow strain of PC and steel structure. This is evident that bridge analysis model is much conservative.

Table 3 Summarized Testing Results, TT12

Items	Strain(Mcro)	Def-Test (mm)	Def-Anal (mm)
Brg. No.5	130	5.4	15.7
Brg. No.11	240	12.1	18.1

The monitoring results of the heavy trailer T350 for bridge No.5 and No.11 are show in the Table 4. The results also similar manner for testing results that the monitoring results are less those monitoring results.

Table 4 Summarized Monitoring Results, T350

Items	Strain(Mcr)	Def-Test (mm)	Def-Anal (mm)
Brg. No.5	122	3.4	11.2
Brg. No.11	230	11.5	14.1

It note that the results from acceleration are suing for checking bridge dynamic effect, for low speed track, the effect of dynamic load compare to static is less than 10%.

CONCLUSIONS

In this study, there are including analysis results by 3D FEM model of three types of truck loading HS25-44, actual traffic truck loading TT12, and heavy trailer truck loading T350. It is seen that the actual traffic truck produced member forces for bending and shear forces higher than HS25-44 and higher than heavy trailer T235. And analysis results HS25-44 are higher than heavy trailer T235. It is evident that selection of special trailer confabulation is suitable. However, to verify analysis model the bridges have been further conducting actual testing due to actual traffic truck loading TT12, and monitoring bridge during crossing heavy trailer T235. The testing and monitoring results are conservative, the results are less than analysis. It is evident that bridge are sate by proper selecting special trailer confabulation, and carefully evaluation by analysis and full loading testing.

ACKNOWLEDGMENTS

This study is supported by Transportation company namely **Hansa Meyer Global Tran. Co., LTD**, and corporation with Technical Division, Department of Road and Bridge, Ministry of Public works and Transportation (MPWT), Lao PDR.

REFERENCES

[1] AASHTO., Standard Specification for Highway Bridge, American Association of State Highway and Transportation Officials, Washington, DC., 17 Edition, 2002.

[2] J. M. Stallings, INSPECTION AND RATING OF TEN BRIDGES, Auburn University Highway Research Center, 2019.

[3] Umarani Gunasekaran, et al., Load rating of bridges – current practices and issues, ATI - Applied Technologies & Innovations, Vol. 2, Issue 2, August 2010, pp. 9-18.

[4] Rafael R. Armendariz, Mark D. Bowman, Bridge load rating, Joint Transportation Research Program Publication, 2018.

[5] Peng Keke. and Fikret Necati Catbas, Comparative Analysis of Bridges with AASHTO and Florida I-Beam Girders, Journal of Civil Engineering and Architecture, Feb. 2014, Volume 8, No. 2, pp. 151-159.

8th Int. Conf. on Structure, Engineering & Environment (SEE), Mie, Japan, Nov.10-12, 2022, ISBN: 978-4-909106094 C3051

AN INTRODUCTION TO LINI APPLICATION FOR EARTHQUAKE RESISTANT DESIGN OF BRIDGES IN INDONESIA

Desyanti[1] and Fahmi Aldiamar[1]
[1] Implementation Unit for Geotechnics, Tunnels, and Structures, Ministry of Public Works and Housing, Republic of Indonesia

ABSTRACT

As a country that is earthquake prone, the earthquake resistant design is inevitable for infrastructure in Indonesia. Indonesian standard for designing earthquake resistant bridges, SNI 2833:2016, has provided provisions and procedure, also maps of earthquake hazard at bedrock, for the purposes of earthquake resistant bridge design, mainly for conventional bridges. The Standard states that the earthquake load is taken as the horizontal force which is determined based on the multiplication of the elastic response coefficient (Csm) with the equivalent structure weight modified by the response modification factor (R). The Standard also determines that the earthquake hazard on bridges must be characterized using the earthquake acceleration response spectrum and site factors for the appropriate site class, so that the design response spectrum at ground level is obtained. To facilitate the designers with this response spectrum, a web-based application called LINI was developed based on the Standard, using the latest Indonesian seismic hazard map with probability of exceedance 7% in 75 years (equal to earthquake return period of 1,000 years). LINI strives to always be updated so that it is in line with the latest data and conditions. The latest update was the seismic hazard level zone maps, which was built based on the Standard, using the latest Indonesian seismic hazard map with probability of exceedance 7% in 75 years and site classification factors. These maps are expected to facilitate the designers in early stage of design and the stakeholders in prioritizing the existing bridges to maintain and/or to retrofit.

Keywords: Response spectrum, Earthquake resistant design of conventional bridge, Seismic hazard level zone maps, Web-based application

INTRODUCTION

Indonesia, tectonically speaking, is located among some main tectonic plates, i.e., Indo-Australian Plate, Eurasian Plate, and Pacific Plate; not to mention a minor one, the Philippine Plate. This condition makes Indonesia one of the countries with high-level seismicity. Earthquakes have occurred for many years in Indonesia, but the great Sumatra earthquake in 2004 had taken the attention of the public, nationwide and worldwide, as it caused a massive disaster in affected locations. Death tolls and the collapse of buildings and infrastructures were just some impacts of this event.

As a country prone to earthquakes, earthquake-resistant design is inevitable for buildings and infrastructure in Indonesia. In anticipating earthquake hazards on bridges, the Indonesian government already has a standard related to earthquake resistance design for bridges, namely SNI 2833:2016, entitled Bridge Design against Earthquake Loads [1]. It is stated in the Standard that bridges must be designed to have a small probability of collapse but can (or be allowed) significant damage and disruption to services due to an earthquake with a 7% probability of exceedance in 75 years (equivalent to an earthquake return period of 1,000 years). The Standard also states that the earthquake load is taken as the horizontal force which is determined based on the multiplication of the elastic response coefficient (Csm) with the equivalent structure weight modified by the response modification factor (R). Furthermore, the Standard determines that the earthquake hazard on bridges must be characterized using the earthquake acceleration response spectra and site factors for the appropriate site class so that the design response spectra at the ground surface are obtained.

To facilitate the designers with the design response spectra, an application has been developed based on the Standard.

BRIDGE DESIGN STANDARDS IN INDONESIA

Indonesia has had a standard for planning earthquake resistance for highway bridges since 1992. The standard was revised in 2008. Then another review study was carried out to improve the performance of bridge construction against earthquakes and to revise the Standard. In 2016, the latest Standard was published as a replacement for 2008 one.

The significant improvement was the return period and updated earthquake hazard maps used in

the Standard. The 2008 Standard only used one map of the 500-year return period Peak Ground Acceleration (PGA). Meanwhile, the 2016 one used three maps of the 1,000-year return period PGA, 0.2-sec spectral acceleration (S_S), and 1.0-sec spectral acceleration (S_1). The maps used in the 2016 Standard referred to the Indonesia Earthquake Map which was previously prepared by the Indonesian Earthquake Map Revision Team and published in 2010, which is expected to represent the state of seismicity in Indonesia.

Another significant change was the development of design response spectra. The 2008 Standard used only PGA to develop the design response spectra, while the 2016 one used three points, i.e., PGA, S_S, and S_1 to develop the design response spectra.

LINI APPLICATION

LINI is a web-based application to determine the design response spectra at the ground surface for earthquake return period of 1,000 years. It is a tool and an integral part of the Standard and was developed based on general procedure stated in the Standard. The general procedure is the determination of the design response spectra at ground surface for the site classes of hard soil (SC), medium soil (SD), and soft soil (SE) with the help of standard maps and amplification factors provided in the Standard.

LINI Application was developed in 2014 to facilitate the designers in determining the design response spectra. It is a web-based application with GIS platform; hence users can use LINI wherever there is an internet connection.

LINI can be accessed on https://lini.binamarga.pu.go.id.

Figure 1 shows the home of LINI Application.

The application home displays some maps that users can choose to see. As default, it displays the map of horizontal Peak Ground Acceleration (PGA) coefficient with 1,000-year return period. The other maps are horizontal response spectral acceleration coefficient at period of 0.2 s (S_S) with 1,000-year return period, horizontal response spectral acceleration coefficient at period of 1.0 s (S_1) with 1,000-year return period, horizontal Peak Ground Acceleration (PGA) coefficient with 100-year return period, horizontal Peak Ground Acceleration (PGA) coefficient with 500-year return period, seismic zones for all site classes, also cities and active faults lines.

Features

Location

Since it is developed with the GIS platform, LINI can locate any place on land in the Indonesia region. Meaning that LINI can determine design response spectra as long as the place is located more than 10 km from active faults.

LINI provides both cities and coordinates to locate the place. Users can choose to pick any city or input the coordinates (longitude and latitude in decimal format) to get their desired locations.

Values of acceleration coefficients

LINI provides users with values of acceleration coefficients without distance restriction.

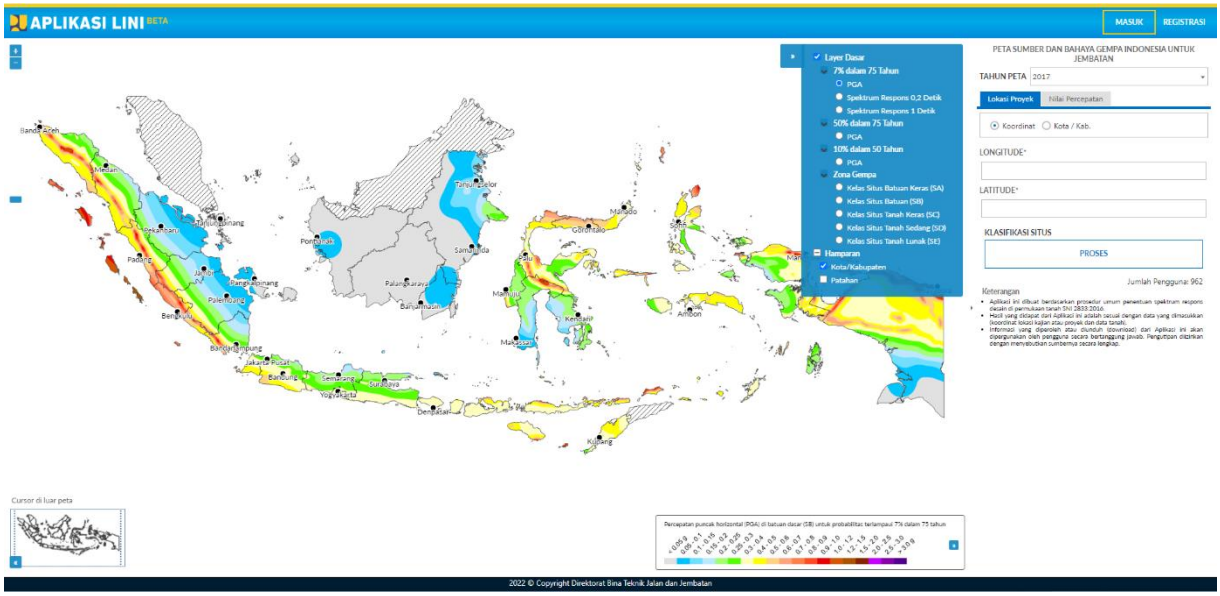

Fig. 1 Home of LINI application

Site class determination

LINI facilitates the users in determining the site class of their desired locations as long as they have the soil data to input (see Fig. 2).

Design response spectra

After the site class is obtained, the application then can give the users with the design response spectra. Nevertheless, if users have no soil data to input to obtain the site class, LINI still provides them with the design response spectra for all site classes (see Fig. 3).

UPDATE OF LINI APPLICATION

The 2014 LINI used the 2010 Indonesia seismic hazard maps. In 2017, the National Center for Earthquake Studies (PuSGeN) published an Indonesian Seismic Sources and Hazard Maps [2] using additional identified active earthquake sources. Accordingly, LINI has the urge to be updated to keep the LINI application in line with the latest data.

Hazard maps

LINI application adopted the 2017 Indonesia seismic hazard maps using spline interpolation

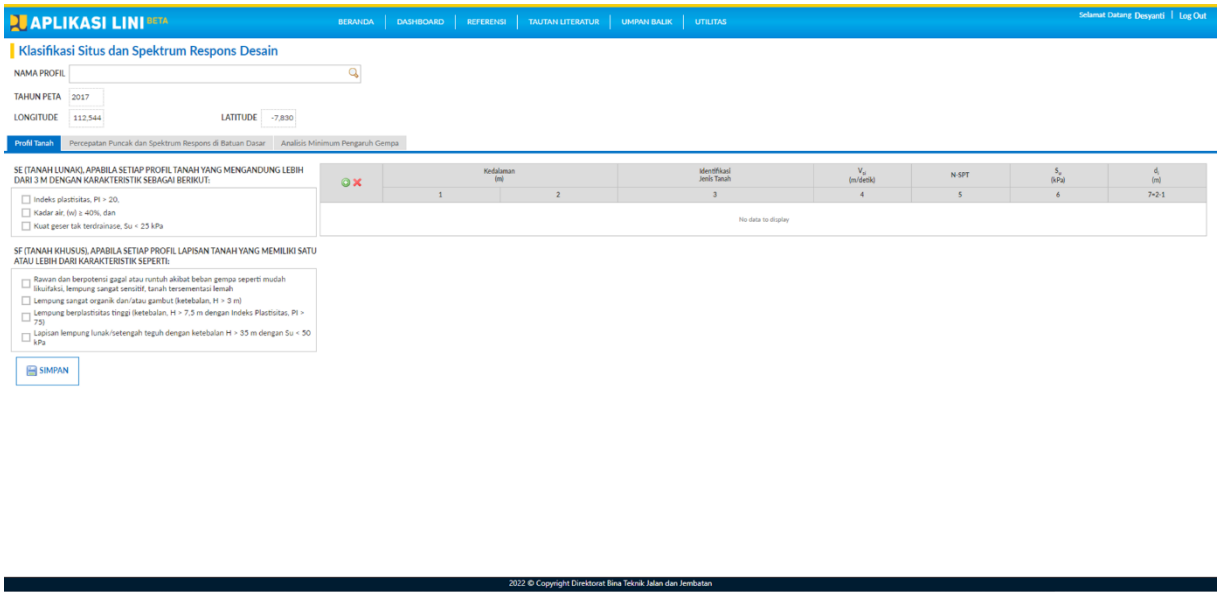

Fig. 2 Page of site class determination on LINI

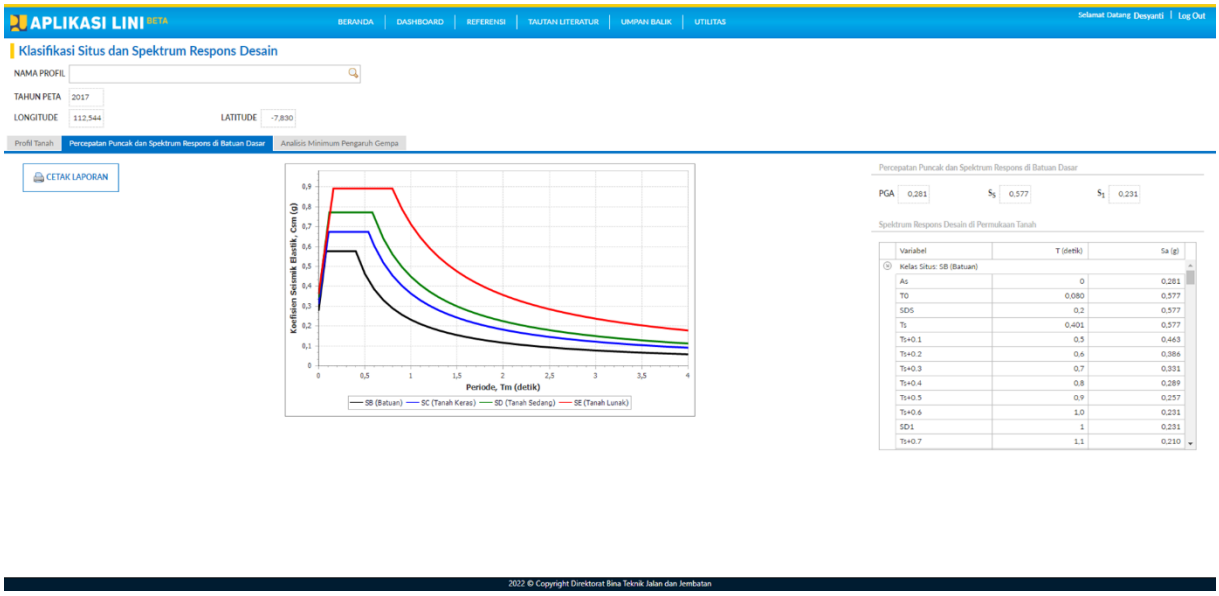

Fig. 3 Page of design response spectra on LINI

method so it was close to the one in PuSGeN's. This method estimated the value using a mathematical function that minimizes the overall curvature of the surface, resulting in a smooth surface that passes right through the input point.

Seismic zone maps

The seismic zone describes the variation of seismic risk and and is used to determine the method of analysis. Its maps were developed based on horizontal response spectral acceleration coefficient at 1.0-sec period modified by a long-period site factor (S_{D1}) (see Table 1).

Table 1 Seismic zone

Acceleration coefficient, S_{D1}	Seismic zone
$S_{D1} \leq 0.15$	1
$0.15 < S_{D1} \leq 0.30$	2
$0.30 < S_{D1} \leq 0.50$	3
$S_{D1} > 0.50$	4

LINI application provides seismic zone maps for all site classes, i.e., SA (hard rock), SB (rock), SC (very dense soil and soil rock), SD (stiff soil), and SE (soft soil). An example of a seismic zone map of site class SD is shown in Fig. 4.

Minimum analysis requirements for seismic effects

The 2016 Standard stipulates the minimum analysis requirements for seismic effects according to seismic zones. Since LINI already has the seismic zone maps, LINI also provides it to facilitate the users with which minimum analysis to use when calculating the seismic effects.

An example of minimum analysis to use is shown in Fig. 5.

CONCLUSIONS

LINI application is a systematic, practical, and integrated solution for knowing the value of seismic acceleration coefficients for locations located > 10 km from the active fault, the location of the seismic source of the active faults, the seismic zones based on SNI 2833:2016, the site class of a location, and getting the design response spectra at ground surface and determining the minimum analysis requirements for seismic effects.

ACKNOWLEDGMENTS

We thank the National Center for Earthquake Studies (PuSGeN) for the Indonesia Seismic Hazard Maps.

REFERENCES

[1] SNI 2833:2016, Perencanaan jembatan terhadap beban gempa (Bridge design against earthquake loads).
[2] National Center for Earthquake Studies (PuSGeN), Indonesian Seismic Sources and Hazard Maps 2017.

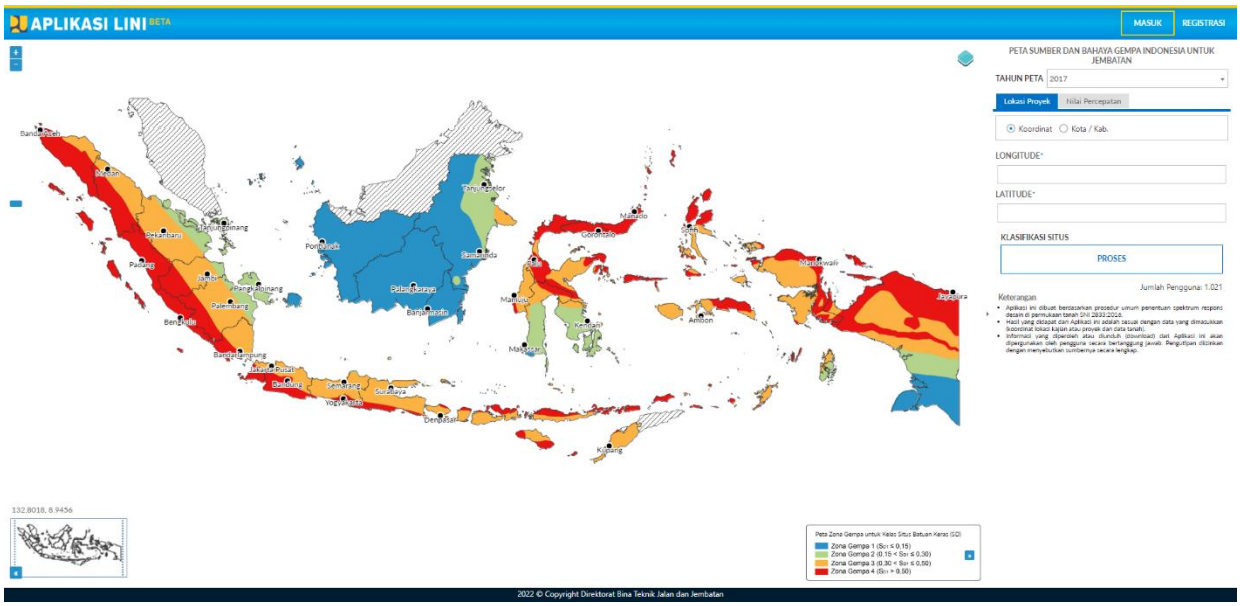

Fig. 4 Seismic zone map of site class SD on LINI

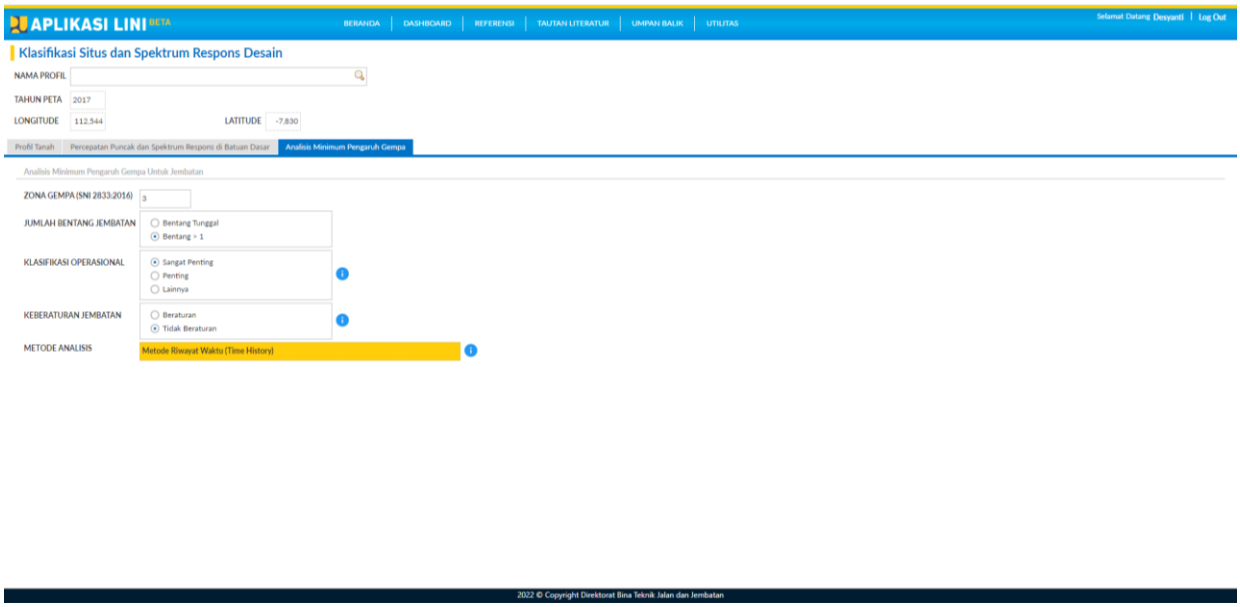

Fig. 5 An example of the minimum analysis required for seismic effects on LINI

12th Int. Conf. on Geotechnique, Construction Materials & Environment, Bangkok, Thailand, 22-24 November 2022, ISBN: 978-4-909106087 C3051

EXPERIMENTAL MEASUREMENT OF THE LOAD-BEARING CAPACITY OF WIRE HOOKS AND BENDS USED IN GABION RETAINING WALLS

Radim Cajka[1], Kamil Burkovic[2], Zdenka Neuwirthova[3], Petr Mynarcik[4] and David Bujdos[5]

[1,2,3,4,5] Faculty of Civil Engineering, VSB Technical University of Ostrava, Czech Republic

ABSTRACT

Gabion walls are today a very popular and ecological solution for retaining walls in civil engineering. Gabions are made of stones placed in wire baskets made of galvanized wire, which are interconnected by hooks and bends. Their advantage is the natural appearance, good conditions for landscaping and catching climbing plants. Unlike concrete or masonry retaining walls, they cannot have cracks and therefore resist uneven subsidence of the subsoil. However, the decisive factor for their load-bearing capacity is the quality of the quarry stone, its placement and the load-bearing capacity of the individual wires and, above all, their joints. In the laboratories of the Faculty of Civil Engineering of the Technical University of Ostrava, a number of tests of wire basket hook joints were performed, which were taken from damaged gabions on construction sites. The results of these tests will enable better prediction of the static effect of gabion walls in their design and implementation in construction practice. The paper presents the results of these tests and recommendations for their design and planning.

Keywords: Gabion retaining walls, experimental measurement, load-bearing capacity of wire hooks and bends

INTRODUCTION

A gabion is a wire stone element in the shape of a cube or cuboid, made of hexagonal steel mesh or welded steel nets and filled with natural or quarry stone, or suitable recycled material. Gabions are used for the construction of supporting and anti-erosion structures, noise barriers, facing walls, etc. The usual width and height of bonded gabions is 1 m, the length is a multiple of 1 m. For welded gabions, the dimensions can be arbitrary (according to the documentation) “Fig. 1”, [1], [2].

For the filling of gabions that have a structural function (retaining walls, securing landslides, etc.), only solid rock fragments or boulders that are not subject to weathering, do not contain water-soluble salts, do not swell and are not brittle must be used. Rocks with higher specific gravity and low porosity are preferred. The dimensions of the rock fragments must be larger than the diameter of the mesh (net) so that the stone does not fall out. Fragments of min. size equal to 1.5 to 2 times the diameter of the eye. For the purposes of the support structure, it is necessary to use clean stone, without admixture of fine-grained soil.

However, all this affects their load-bearing capacity and it may be hard to predict the bearing capacity precisely. Therefore, numerous of scientists trying to predict and improve designing methods [3], [4]. Precise calculations ensure safe and long-lasting design and prevents failure [5], [6]. Therefore, several test were made in the laboratories of the Faculty of Civil Engineering of the Technical University of Ostrava to help better prediction in the future and to predict in which part the bearing capacity will be reached.

GABION WALLS DESIGN

There are no standards on how to design a gabion wall in the Czech Republic. There are only recommendations, general procedures and technical regulations.

It is recommended that gabions that fulfill a static function (retaining or frame wall) are designed according to the principles stated in Eurocode 7-1 (ČSN EN 1997-1) [7].

Gabions that have only an aesthetic function (covering) are assessed together with the supporting structure. Under normal conditions, the height of the gravity gabion structure should not exceed 6 m. The gabion lining can also be part of a reinforced soil structure. In this case, the stabilizing elements are horizontal reinforcements (extended steel gabion nets or polymer grids fixed to the gabion basket, or between the layers of individual baskets) and the gabions fulfill the function of face fortification in the sense of ČSN EN 14475 [8] and TP 97 [9].

Gabions with a static function

For the filling of gabions that have a structural function (retaining walls, securing landslides, etc.), only solid rock fragments or boulders that are not subject to weathering, do not contain water-soluble salts, do not swell and are not brittle must be used. Rocks with higher specific gravity and low porosity are preferred. The dimensions of the rock fragments

must be larger than the diameter of the mesh (net) so that the stone does not fall out. Fragments of min. size equal to 1.5 to 2 times the diameter of the eye. The maximum stone size is 2.5 times the mesh width in mm. Stones larger than 2.5 times the size of the mesh mesh can occur only occasionally and their total volume must not exceed 5% of the gabion volume. Fragments smaller than the diameter of the mesh mesh can be used in an amount not exceeding 10% of the total volume for filling gaps and wedging larger stones inside the gabions (outside the faces). For the purposes of the support structure, it is necessary to use clean stone, without admixture of fine-grained soil.

Gabions without static function

The stone used in the face of gabions that do not have a static function (anti-noise and cladding walls) must meet the same requirements as gabions with a load-bearing function. Other material can be used behind the facing layer of stone according to the documentation (unsorted stone, concrete fragments, recycled gravel, etc.). The growth of vegetation can also be allowed for these gabions.

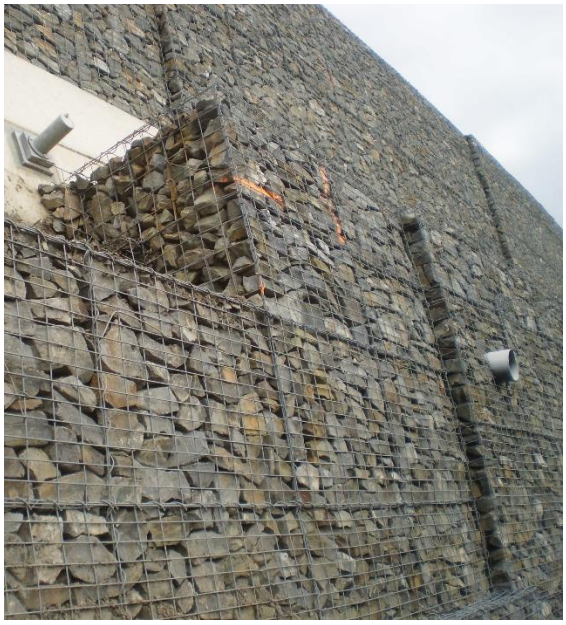

Fig. 1 Example of gabion wall

Fig. 2 Detail of steel wire attachment partially unfolded during usage

Design problems

With this very broad information it is very hard to design a proper designing method. The main concern is how to properly design bearing capacity of anchoring wires which provide the main bearing function and secure the gabions against overturning “Fig. 2”. Due to lack of designing information and incorrect suggestion it may result even in pull out of the wire and therefor a construction damage “Fig. 3”.

Fig. 3 Detail of steel wire attachment after reaching its bearing capacity

LABORATOR TESTS

In the laboratories of the Faculty of Civil Engineering of the Technical University of Ostrava were performed tensile tests of the supplied anchor wires, which were used for anchoring the gabion wall.

Tested wires

Steel wires with corrosion protection, probably ZnAl, were supplied for the tests. The exact material characteristics of the wire were not the subject of the

assignment of the assessment. The specimens were supplied with bends which were used in anchoring the gabion wall. The length of the wires ranged from 680 to 800 mm, with a bend length of 100-110 mm "Table 1". The cross-section of the wire is round and smooth, i.e. without ribs, with a diameter of 6 mm.

Table 1 The shape of the bends of the tested wires

No.	Wire bend opening [mm]	Length of the bent part of the rod from the bending axis [mm]	Length of the straight part of the rod from the bend axis to the jaw [mm]
1	130	110	190
2	130	110	230
3	70	110	210
4	90	100	250
5	90	100	240
6	150	100	240

Course of the test

The tests were carried out on an EU 40 hydraulic press with mechanical jaws. A wire with a longer bend was placed in the upper jaws so that the jaws of the press would grip both ends of it. The upper wire basically represented part of the metal structure of the gabion. A wire with a bend was placed in the lower jaws, which was used on the assessed object, i.e. with a bend length of 100 110 mm. The cross-section of the wire is round and smooth, i.e. without ribs, with a diameter of 6 mm.

The wire samples showed quite significant shape deviations from the plane. The largest irregularities were partially eliminated before the tensile tests began. Before the test, the shapes of the bends were roughly measured for individual wires with an accuracy of 10 mm "Table 1".

As part of the experimental tensile tests of wire bends, the loading speed according to ČSN EN ISO 6892-1: Metallic materials – Tensile testing – Part 1: Test method at room temperature (1/2017) was used. Table 2 and Figure 4 shows the results of the tensile tests.

Figure 5 and Figure 6 shows the test itself. There is a wire with a hook in the bottom and from the upper there is a hydraulic press measuring the lead. Figures are in respective order how it looks during the test.

Table 1 The shape of the bends of the tested wires

No.	*Length of the displacement of the crossbar (stretching of the wire in the bend) [mm]*	*Maximum pull force [kN]*
1	86,7	0,84
2	87,9	0,63
3	87,8	1,51
4	104,2	1,32
5	106,3	1,86
6	108,8	0,75
Minimum tensile force:		0,63 kN
Average tensile strength:		1,15 kN

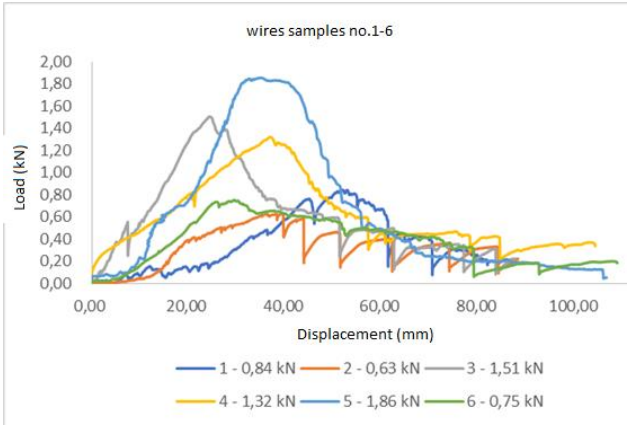

Fig. 4 Working diagram of tensile tests of wire bends

Fig. 5 Progress of the tensile test of wire – unfolding the bend. (Sample no. 4 at the start of the test – left, sample no.5 during the test)

Fig. 6 Progress of the tensile test of wire – unfolding the bend. (Sample no.3 in two different stages)

CONCLUSIONS

Based on the conducted experiments, it can be stated that during the tensile tests, the bends of the wires were straightened at a maximum force in the range of 0.63 - 1.86 kN. The average value of the maximum tensile force required to straighten the bend is 1.15 kN. Tensile strength of steel was not exceeding and therefore, the tensile force of unfolding bend is the bearing capacity of this anchor element.

At the same time, it is necessary to draw attention to the fact that the wire connection test was carried out in free space, in real conditions (when the wire is covered with aggregate) the bending failure would probably occur at a higher tensile force.

Considering the bearing capacity of the wire itself the force opening the bend is the limiting capacity of the gabion. In addition, this force will be affected by manner, if and how the eye will be closed and fixed. In this case, the least load-bearing variant without ties was verified.

ACKNOWLEDGMENTS

This result was obtained with the financial support of the contribution of the conceptual development of science, research and innovation for 2022 VSB - Technical University of Ostrava.

REFERENCES

[1] Chikute GC, Sonar IP. Gabion wall: Eco-friendly and cost-efficient retaining wall. Lect Notes Civ Eng 2021;124 LNCE:229-49.

[2] Lamerdonov, Z. G., T. Yu Khashirova, S. A. Zhaboev, M. A. Enaldieva, A. M. Chochieva, and K. Z. Lamerdonov. 2020. "Operational Experience of Gabion Shore Protection Structures on Mountain Rivers and some Suggestions for their Improvement." Ecology and Industry of Russia 24 (10): 8-12. doi:10.18412/1816-0395-2020-10-8-12

[3] Saravanapriya S. Experimental investigation on improvement in strength characteristics of gabion wall. Int J Civ Eng Technol 2018;9(9):628-41.

[4] Zhang H, Liu G, Liu W, Chen Z, Liu Q, Xu G. Experimental study on failure mode and mechanical characteristics of gabion material. Constr Build Mater 2022;344.

[5] Carneiro D, Barros PLA, Labaki J. Ground vibration attenuation performance of surface walls. Comput Geotech 2022;149.

[6] Chikute GC, Sonar IP. Failures of gabion walls. Int J Innov Technol Explor Eng 2019;8(11):1384-90.

[7] EN 1997-1 EUROPEAN STANDARD. Eurocode 7: Geotechnical design. 2004.

[8] European Standard EN 14475:2006. Execution of special geotechnical works - Reinforced fill. 2006.

[9] Technical quality conditions of road constructions, chapter 30, Special earth construction, Ministry of Transport, Department of Road Infrastructure, Approved: MD-OSI No. 1001/09-910-IPK/1, dated 17/12/2009 with effect from January 1, 2010, with the simultaneous cancellation of the second version of this chapter of the TKP, approved by MDS-OPK No. 24610/97-120, Prague, ARCADIS Geotechnika, a.s., December 2009

Engineering

8th Int. Conf. on Structure, Engineering & Environment (SEE), Mie, Japan, Nov.10-12, 2022, ISBN: 978-4-909106094 C3051

A NEW TYPE OF ELECTROMAGNETIC-VIBRATION PUMP WITH HIGH EFFICIENCY AND FLOW RATE

* Hiroyuki Yaguchi[1], Takuya Watanabe[1] and Toshiki Mishina[1]
[1] Faculty of Engineering, Tohoku Gakuin University, Japan

ABSTRACT

Small pumps with excellent performance are in demand in various industrial fields. In the present study, a new type of small underwater insertion pump that combines electromagnetic force and mechanical resonance was developed. A prototype electromagnetic-vibration pump with a one-valve structure in which the vibration component and water are separated by a thin film was constructed. The shape of this pump was optimally designed for the casing and valves. Rod and piston-type casings have been proposed to effectively use the displacement of the vibration component. By the inertial effect of water due to the operating principle, thin film separation, and shape optimization, the maximum efficiency of this pump was 19.1%, which exceeds that of previously proposed small pumps. In addition, as a normal use of the prototype pump, the pump with an acrylic pipe attached to the inlet port was improved, and its flow rate characteristics were examined. These two pumps can be directly driven by the power of a power outlet by tuning the resonance frequency of the vibration component. The proposed pump can be used in two ways depending on the application.

Keywords: pump, vibration, one-valve pump, optimized shape, pumping head, efficiency, mass flow.

INTRODUCTION

Small pumps with excellent performance are in high demand in various industrial fields, such as the fields of machinery, civil engineering, agriculture, chemical analysis, and medical care. For this reason, various types of small pumps have been developed. In particular, the axial flow pump [1], centrifugal pump [2], and diaphragm pump [3] have been actively studied. An electromagnetic motor is used as a drive source for these pumps because the efficiency of the pump depends on the efficiency of the electromagnetic motor. Accordingly, due to the low efficiency of the small motors installed, the efficiency of the small pumps is quite low.

A piezoelectric pump [4 - 6] is a typical pump that does not use an electromagnetic motor. Although this pump is characterized by high efficiency, it has a problem with respect to durability and is expensive. Even so, the efficiency of the small piezoelectric pump is less than 5%.

Therefore, considering environmental problems of note in recent years, pumps and motors are incorporated in many devices, and improving the efficiency of these basic devices is an important engineering problem.

For this reason, the authors prototyped a vibration-type pump [7], in which a drive unit having a vibration component was inserted into water, and showed the flow rate characteristics of the prototype pump. However, the efficiency of this pump is low, and the operation principle has not been clarified.

In the present study, a new type of small underwater insertion pump that combines electromagnetic force and mechanical resonance was developed. This small vibration-type pump converts the generated resonance energy into kinetic energy and effectively discharges water. A prototype pump with a one-valve structure in which the vibration component and water are separated by a thin film was prototyped. The shape of this pump was optimally designed with respect to the casing and valves. Rod and piston-type casings have been proposed to effectively use the displacement of the vibration component. By the inertial effect of water due to the operating principle, thin film separation, and shape optimization, the maximum efficiency of this pump was 19.1%, which exceeds that of previously proposed small pumps. In addition, as a normal use of the prototype pump, the pump with an acrylic pipe attached to the inlet port was improved, and its flow rate characteristics were examined. It was clarified that this small vibration-type pump has a very simple structure and can discharge water with a pumping head exceeding 1,000 mm. Two types of pump with high performances capable of use in two ways are described in the present paper.

OUTLINE OF THE VIBRATION-TYPE PUMP

Fig. 1 shows a small electromagnetic-vibration pump for an underwater insertion-type pump. This vibration-type pump consists of an acrylic casing, a thin silicone rubber film, a vibration component, an acrylic bar, and a discharge valve. In this pump, a thin silicone rubber film with a thickness of h (mm) was installed on top of the vibration component to

prevent contact between water and the vibration component. The part above the silicone rubber film is defined as the head portion, and the portion below the silicone rubber film is defined as the vibration portion. As a result, water flows into the head portion, and only air is injected into the vibration portion. Since the vibration component vibrates in the atmosphere, no viscous resistance of water is generated. The valve is a one-valve system with only discharge and has a very simple structure.

The acrylic rod and piston-type casings have been developed to effectively use the displacement of the vibration component. An inlet port and an outlet port having a diameter of 6 mm are attached to the head part, as shown in Fig. 1.

The vibration component consists of a ring-shaped permanent magnet and a compression coil spring. The permanent magnet is a neodymium ring magnet with an outer diameter of 12 mm, an inner diameter of 9 mm, and a height of 5 mm. As the spring, a compression coil spring with a free length of 25 mm, an outer diameter of 12 mm, and a spring constant of k = 2,691 N/m was used.

As shown in Fig. 2, an iron core with a bobbin shape was used as an electromagnet for exciting the vibration component. A copper wire with a diameter of 0.2 mm was wound 1,200 times to make an electromagnet. By combining a ring-type permanent magnet and the bobbin-type permanent magnet, the electromagnetic force can be efficiently converted into excitation force [8]. As shown in Fig. 2, for the iron disk, the diameter is R = 8 mm, and the thickness is b = 1 mm. In addition, the shaft diameter is r = 3 mm, and the length is B = 26 mm. The acrylic bar was mounted on the vibration component to increase the effect of pushing up the water.

Fig. 3 shows the structure and dimensions of the valve. A triangular acrylic support was attached to an acrylic disc with a thickness of 2 mm, an outer diameter of 19 mm, and an inner diameter of d (mm). The dimensions of the thin silicone rubber material for the valve are 8 mm wide, 10.5 mm long, and 0.05 mm thick. By attaching a thin silicone material to the triangular acrylic support, stable bending rigidity in the valve was obtained.

This pump is inserted into water, and AC power is input to the bobbin-type electromagnet to resonate the vibration component. An acrylic bar with a diameter of 12 mm and a length of L (mm) attached to the top of the vibration component via the silicone rubber film vibrates in the vertical direction. As shown in Fig. 1, when the acrylic bar is displaced upward, the pressure near the valve increases. The thin silicone material in the valve is pushed up, and water is drained. On the other hand, when the acrylic bar is displaced downward, the pressure near the valve decreases. For this reason, the valve closes and prevents backflow of water. Thus, since the pressure at the head portion is reduced, water can be sucked up from the inlet port. Based on the results of a previous study [7], a clearance of 1.5 mm was provided between the rod and the casing so that water could flow between them. Water is discharged intermittently by repeatedly increasing and decreasing the pressure over one cycle of vibration.

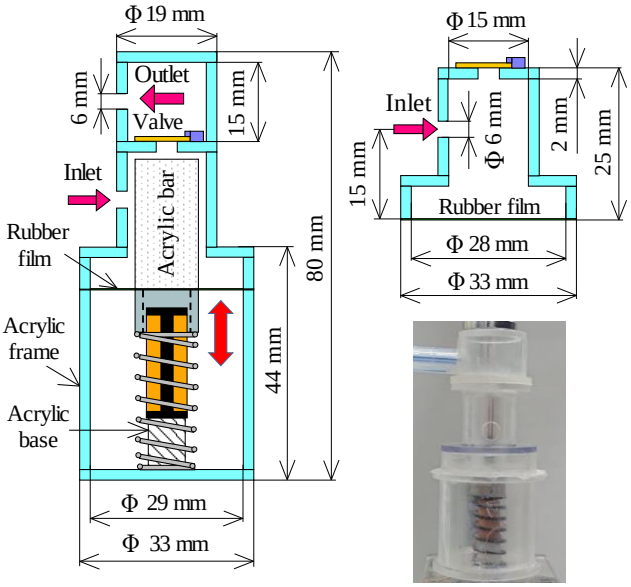

(a) Outline (b) Head portion and photograph

Fig. 1. Structure of the vibration-type pump.

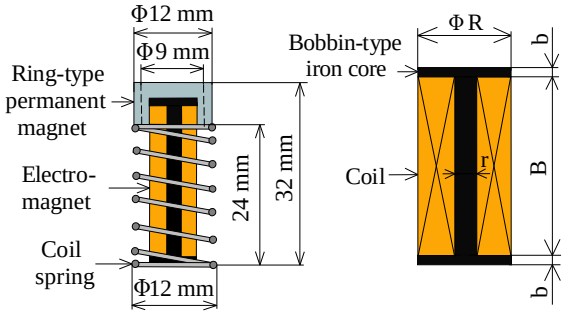

Fig. 2. Vibration component and electromagnet.

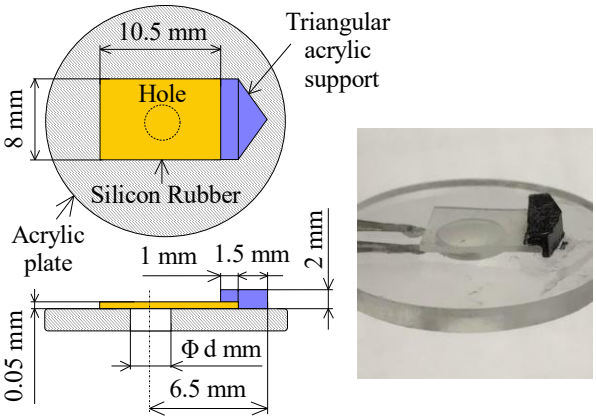

Fig. 3. Structure of the one-valve pump and photograph.

As shown in Fig. 1, the dimensions of the head portion are when the length of the acrylic bar is 25 mm. The prototype pump has a height of 80 mm, an outer diameter of 33 mm, and a total mass of 41 g.

OPTIMUM DESIGN FOR THE SHAPE OF THE VIBRATION-TYPE PUMP

As shown in Fig. 1, the shape of the vibration-type pump for an underwater insertion-type was optimized for the following three items:

(1) Length of the acrylic rod: L (mm)
(2) Thickness of the silicone rubber film for water separation: h (mm)
(3) Diameter of the outlet port in the valve: d (mm)

The prototype pump was inserted into an acrylic tank having a width of 350 mm, a length of 250 mm, and a height of 200 mm.

As shown in Fig. 4, the pumping head was 200 mm, and the flow rate was measured. An acrylic pipe with an inner diameter of 6 mm was used as the pipe from the outlet port. The vibration component was driven at the resonance frequency by a signal generator and amplifier. The resonance frequency is 70 Hz. The input voltage, current, and power to the electromagnet were measured using a power analyzer. The mass of discharged water was measured for 30 seconds using an electronic balance. The water temperature was measured as 20 degrees.

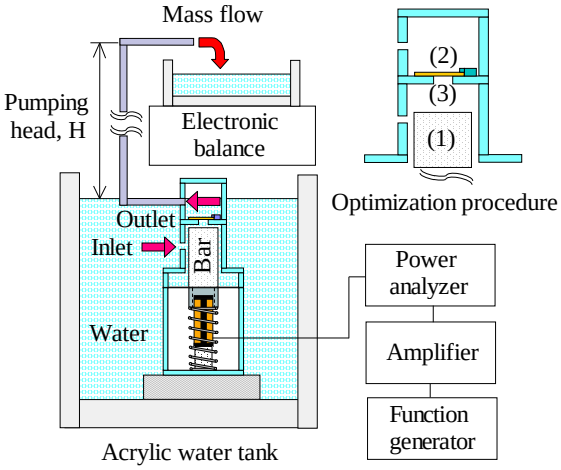

Fig. 4. Experimental apparatus and optimization procedure.

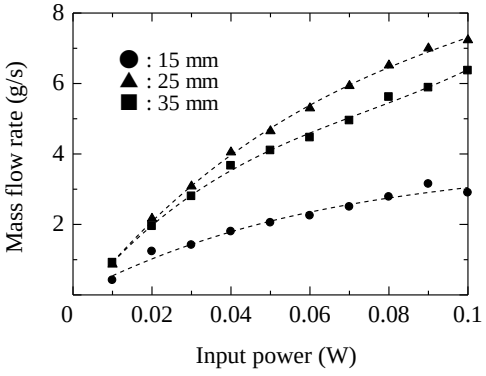

Fig. 5. Relationship between input power and mass flow rate (length of the acrylic rod).

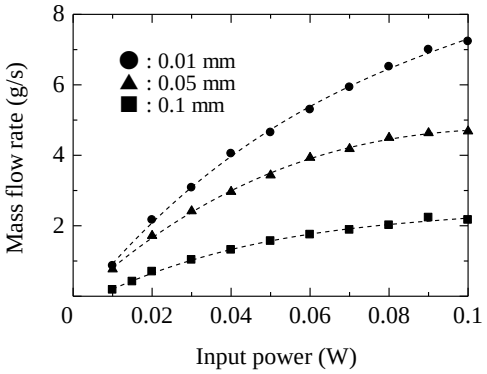

Fig. 6. Relationship between input power and mass flow rate (thickness of the silicone rubber film).

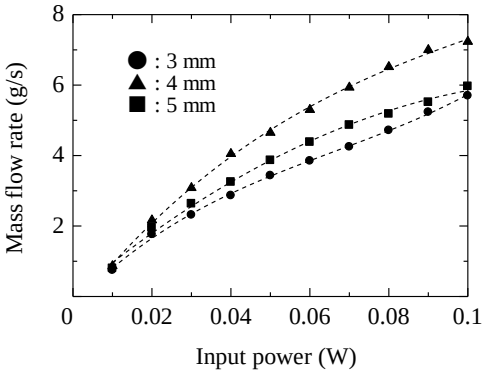

Fig. 7. Relationship between input power and mass flow rate (diameter of outlet port in the valve).

The pumping head (H = 200 mm), the diameter (d = 4 mm) of the outlet port in the valve, the thickness (h = 0.01 mm) of the silicon thin film, and the effect of the length, L (mm), of the acrylic rod were examined. Fig. 5 shows the relationship between the input power to the electromagnet and the flow rate per second by changing the length, L (mm), of the acrylic rod to 15 mm, 25 mm, and 30 mm. The highest efficiency was shown when the rod length was 25 mm. This indicates the existence of an optimum rod length. As the rod length increases, the effect of pushing out water increases. However, as the rod length increases, the contact area between the water and the rod increases and the viscous resistance to the vibration component increases. Therefore, it is considered that the optimum length of the rod exists.

The effects of the thickness, h (mm), of the silicone rubber film for water separation were examined with the pumping head (H = 200 mm), length (L = 25 mm) of the acrylic rod, and the outlet port diameter of the valve (d = 4 mm). Fig. 6 shows the relationship between the input power to the electromagnet and the flow rate per second by varying the thickness, h (mm), of the thin silicone

rubber film to 0.01 mm, 0.05 mm, and 0.1 mm. From the figure, the flow rate increases as the input power increases. When the silicone rubber film thickness is thin, this pump shows good flow rate characteristics. As the silicone rubber film thickness increases, the viscous resistance of the membrane material to the vibration component increases. Therefore, when the silicone rubber with a thickness of h = 0.01 mm is used, the flow rate characteristics are the best.

The pumping head (H = 200 mm), the length (L = 25 mm) of the acrylic rod, the silicon thin film thickness (h = 0.01 mm), and the effect of hole diameter, d (mm), at the outlet port in the valve were examined. Fig. 7 shows the relationship between the input power to the electromagnet and the flow rate per second by varying the hole diameter, d (mm), of the outlet port in the valve as 3 mm, 4 mm, and 5 mm. From the figure, the highest efficiency occurs when the hole diameter is 4 mm. However, the diameter of the hole in the valve portion is considered to be affected by the pumping head.

By examining three items, the value of (1) the length (L = 25 mm) for the acrylic rod, (2) the thickness (h = 0.01 mm) for the silicone rubber film for water separation, and (3) the diameter (d = 4 mm) for the outlet port in the valve are selected to maximize the flow characteristics of this pump.

INERTIA EFFECT DUE TO VIBRATION DISPLACEMENT OF THE ROD

This pump creates a pressure difference by the combination of the acrylic rod and the casing. Water cannot be sucked in and drained if the acrylic rod is not mounted on the vibration component at this pump. In addition, if the clearance between the acrylic rod and the casing is 0 mm, then water cannot be sucked from the inlet port. As mentioned above, the clearance between the rod and the casing was set to 1.5 mm, and the water discharge characteristics due to the vibration displacement of the rod were examined.

It is difficult to directly measure the displacement of a vibration component inserted in water with various sensors. The displacement was measured using the experimental apparatus shown in Fig. 8. In the experiment, the sine wave generated by the signal generator was amplified by an amplifier, and the exciter was vibrated harmonically. The vibration part of the exciter, two beams, and three rods were connected and inserted into the casing of the pump.

As shown in Fig. 9, when forced displacement is generated by the exciter, rod 3 is displaced. The acrylic rod attached to the vibration component, and rod 3 has the same dimensions. In addition, the casing and valve have the same dimensions as the optimized vibration-type pump. The vibration

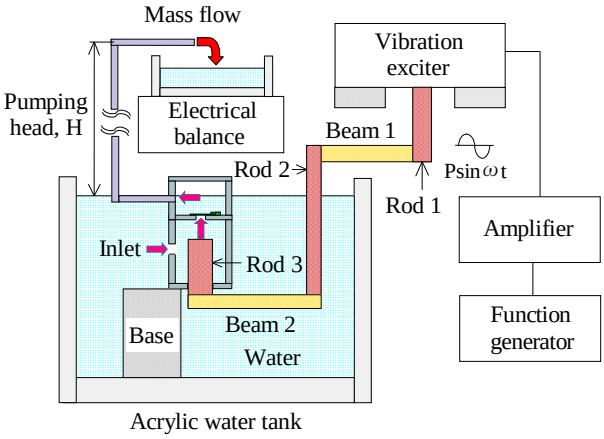

Fig. 8. Experimental setup for the operating principle.

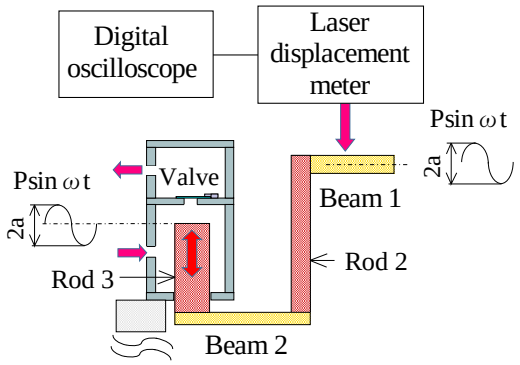

Fig. 9. Details of the experimental setup.

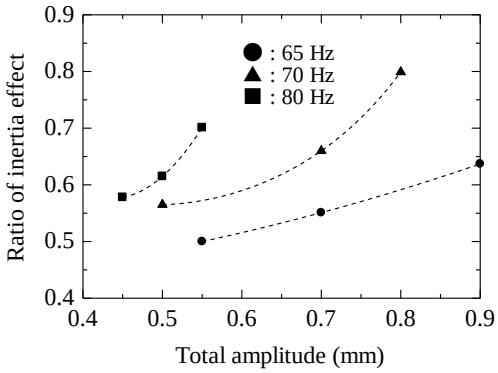

Fig. 10. Relationship between total displacement and ratio of inertia effect.

displacement of rod 3 was substituted by measuring the displacement of beam 1 using a laser displacement meter and a digital oscilloscope.

When the vibration component vibrates at a frequency, f (Hz), the change in the flow rate characteristics due to the displacement amplitude was investigated. For the purpose of clarifying the operation of this pump, the ratio of the inertial effect was defined as follows:

$$I_r = (Q / f) / V, \quad V = 2a\pi d^2 \qquad (1)$$

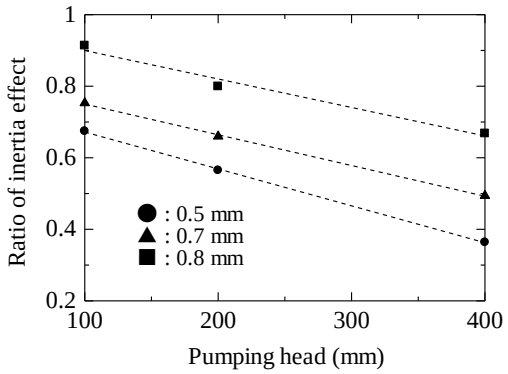

Fig. 11 Relationship between pumping head and ratio of inertia effect.

where I_r is the ratio to the volume, V (mm^3), when the acrylic rod with radius d (mm) vibrates with a total amplitude of 2a (mm) and a flow rate per second of Q (mm^3/s).

Fig. 10 shows the ratio, I_r, of the inertia effect by changing the drive frequency of the exciter when the pumping head, H, is set to 200 mm. As the total amplitude increases, the inertial effect increases. In addition, when the frequency is 70 Hz and the total amplitude is 0.8 mm, approximately 80% of the volume, V, of water due to vibration is discharged.

Fig. 11 shows the pumping head, H, and the ratio, I_r, of the inertial effect by changing the total amplitude of rod 3 when the drive frequency is 70 Hz. The inertial effect decreases as the pumping head, H, increases. On the other hand, when the pumping head is H = 100 mm, the ratio I_r of the inertial effect exceeds 90%, and approximately the same volume of water as the volume due to vibration displacement can be discharged. The obtained results are summarized as follows:

1) The inertial effect is proportional to the increase in drive frequency.

2) As the amplitude of the vibration component increases, the inertial effect increases.

3) When the pump head, H, is low, even if there is a clearance between the rod and the casing, the same amount of water as the volume due to the total amplitude of vibration can be discharged.

FLOW CHARACTERISTICS OF THE OPTIMIZED VIBRATION-TYPE PUMP

As shown in Fig. 1, an underwater insertion-type pump with three shape optimizations was prototyped and tested. The drive frequency of the vibration component is 70 Hz. The efficiency, η, of the pump is expressed as follows:

$$\eta = 100 \times M_f \, g \, H / P \, t \qquad (2)$$

where M_f (kg) is the mass flow, g (m/s^2) is the acceleration due to gravity, H (m) is the pumping head, P (W) is the input power to the electromagnet,

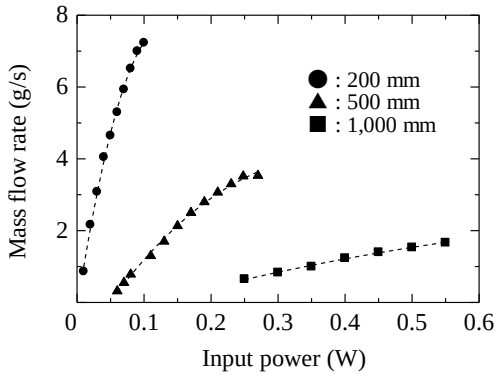

Fig. 12. Relationship between input power and mass flow rate (underwater insertion-type pump).

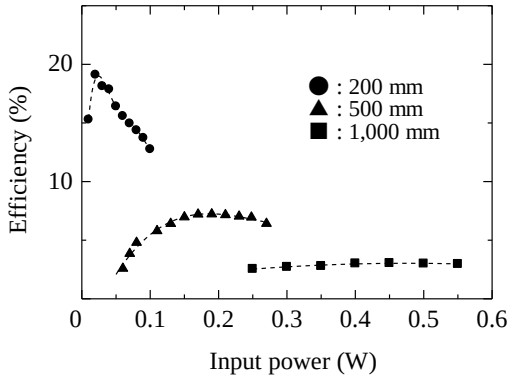

Fig. 13. Relationship between input power and efficiency (underwater insertion-type pump).

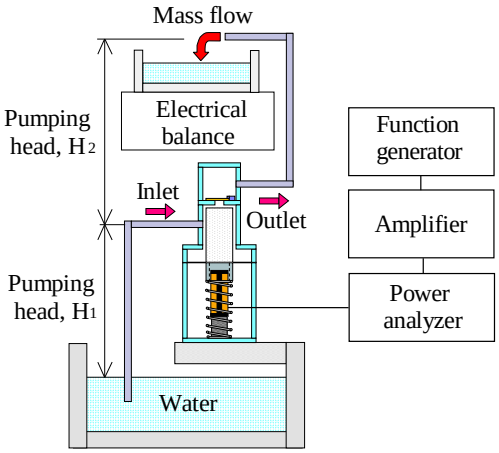

Fig. 14. Outline of the one-valve normal-type pump.

and t (s) is the measurement time. The mass flow was measured with an electronic balance.

Figs. 12 and 13 show the relationships between the input power to the electromagnet and, respectively, the flow rate per second and efficiency by changing the pumping head, H. The flow rate increases approximately linearly as the input power increases. Furthermore, when the pumping head is H = 1,000 mm, approximately 1.8 g of water can be discharged per second. On the other hand, when the input power is 0.02 W and the pumping head is

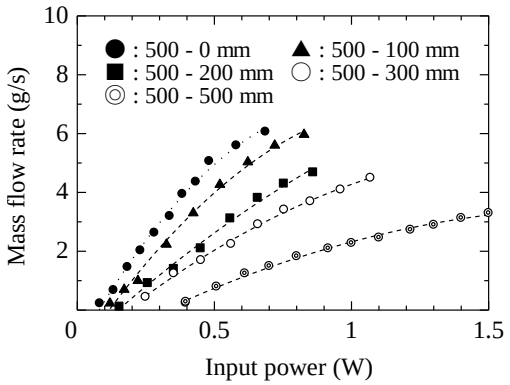

Fig. 15. Relationship between input power and mass flow rate (normal-type pump).

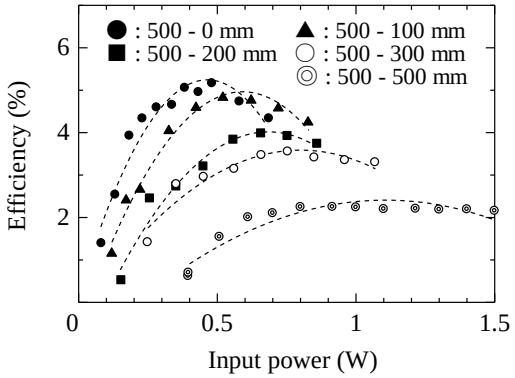

Fig. 16. Relationship between input power and efficiency (normal-type pump).

H = 200 mm, the maximum efficiency of this pump is 19.1%. This is because the inertia effect of the acrylic rod is acting. Due to the inertial effect, when the pumping head, H, is low, the efficiency of the prototype pump is significantly higher than that of commercial products.

As a normal application of the pump, an acrylic pipe with an inner diameter of 6 mm was attached to the inlet, as shown in Fig. 14, and the flow rate characteristics of the pump were investigated.

Figs. 15 and 16 show the relationships between the input power to the electromagnet and, respectively, the flow rate per second and efficiency by varying the pumping head (H_1 = 500 mm) and H_2 from 0 mm to 500 mm. The prototype one-valve pump can discharge 2.16 g of water per second at a pumping head of 1,000 mm. The maximum efficiency was approximately 5.1% at an input power of 0.38 W when the total pumping head, H (= H_1 + H_2), was 500 mm.

CONCLUSIONS

A small one-valve electromagnetic-vibration underwater insertion-type pump was proposed, and the optimum shape of the pump was designed. When this vibration-type pump was inserted into water, the pump had a maximum efficiency of 19.1%. Furthermore, the operating principle of this pump was clarified experimentally, and the effect of the inertial effect of water was clarified.

As a normal application of the prototype pump, an acrylic pipe was attached to the inlet port, and the suction characteristics of the pump were examined. The maximum efficiency of this pump was 5.1%, which was shown to exceed that of commercially available pumps. This vibration-type pump has a very simple structure and can send water exceeding 1,000 mm to the pumping head.

The proposed pump can be used in two ways depending on the application. The underwater insertion-type pump can be applied to circulation in water tanks and cooling devices, and the normal-type pump can be applied to specific industrial applications. In addition, these vibration-type pumps can be directly driven by the power of a power outlet by tuning the resonance frequency of the vibration component.

REFERENCES

[1] S. Momosaki, S. Usami, S. Watanabe and K. Okuma: 'Experimental Study on Rotational Speed Control of Contra-Rotating Axial Flow Pump', Journal of TSJ, Vol. 39, No. 2, pp.119-125 (2011).

[2] T. Shigemitsu, J. Fukutomi, M. Takumi and S. Masahiro, 'Unsteady Flow Condition of Centrifugal Pump for Low Viscous Fluid Food', International Journal of Fluid Machinery and Systems, Vol. 10, No. 4, pp. 432-438 (2017).

[3] C. Cabuz, W. Herb, E. Cabuz and S. Lu, 'The dual diaphragm pump 14th IEEE Int. Conf. on Micro Electro Mechanical Systems', DOI: 10.1109/MEMSYS.2001.906593 (2001).

[4] J. Kim, ,C. Kang and Y. Kim : 'A disposable polydimethylsiloxane – baseddiffuser pump actuated by piezoelectric-disc', Microelectron. Eng.,Vol. 71, No. 2, pp. 119-124 (2004).

[5] J. Sateesh1, K. Rao, K. Sravani1, K. Guha and R. Kumar : 'Design and Optimization of MEMS Based Piezo-ElectroMicro Pump',4th International Conference on Microelectronics, pp. 1200-1206 (2017).

[6] Q. Yan, Y. Yin, W. Sun and J. Fu : 'Advances in Valveless Piezoelectric Pumps', Applied science, Vol. 11, No. 15, pp. 1-12 (2021).

[7] H.Yaguchi, T. Mishina and K.Ishikawa : A New Type of Magnetic Pump with Coupled Mechanical Vibration and Electromagnetic Force, Journal of Mechanical Engineering and Sciences, Vol. 13, No. 3, pp 5212 - 5227 (2019).

[8] H. Yaguchi and S. Sakuma : Improvement of a Magnetic Actuator Capable of Movement on a Magnetic Substance, IEEE Transactions on Magnetics, Vol. 52, No. 7, pp.1-4 (2016).

8th Int. Conf. on Structure, Engineering & Environment (SEE), Mie, Japan, Nov.10-12, 2022, ISBN: 978-4-909106094 C3051

GEOPHYSICAL INVESTIGATION OF GROUNDWATER RESOURCES USING ELECTRICAL RESISTIVITY AND INDUCED POLARIZATION METHOD

Jannatul Hasni Omar[1], Nordila Ahmad[1], and Jestin Jelani[1], Zuliziana Suif[1] and Maidiana Othman[1]
Faculty of Engineering, National Defence University of Malaysia, 57000 Kuala Lumpur[1]

ABSTRACT

Identifying potential groundwater is crucial, especially in the area that faced water stress issue. However, when utilizing 2-D resistivity and Induced Polarization (IP) survey, it can be challenging to distinguish groundwater from soil particles. When drilling in the subsurface layers, many researchers struggled to determine the exact position of the aquifer or missed the aquifer's full capacity. In order to assess the potential groundwater in Sungai Besi, Kuala Lumpur, and to distinguish the saturated zones between an aquifer and unconsolidated sediments, this study combines resistivity and IP analyses. The pole-dipole array was used to build up two resistivity survey lines; 200 metres (m) and 800 metres long. According to the results of the 2-D resistivity and IP survey, low resistivity values between 10 and 100 m (Ohm-m) and low chargeability values between 0 and 1 millisecond can be used to identify potential groundwater areas in the subsurface (msec). Silty sand and sandy clay make up alluvium, which has a resistivity range of 125 to 255 m and a chargeability range of 7 to 10 msec. The presence of groundwater may also be indicated by type of soil profile from borehole data in the subsurface. By separating the soil particles from unconsolidated sediments, the study's finding provides useful information on the presence of groundwater. This study is limited to two lines of 2D resistivity and Induced Polarization with 400m and 800m long.

Keywords: Groundwater, Geophysical, Resistivity, Imaging and Potential.

INTRODUCTION

Water of poor quality is a significant issue today. Particularly in rural regions, identifying potential groundwater is crucial. Compared to water sources above the ground, including lakes and rivers, groundwater is beneath the ground and higher quality. When surface water is scarce or poor quality, finding a groundwater supply is one of the primary goals.

Geophysical surveys are one of the most reliable ways to find a groundwater supply. The common approach for geophysical survey is resistivity method where it is able to identify sources of groundwater potential [1]. This method is based on the composition and layering of the subsurface, interpretation of the soil's physical characteristics, and underground structures, cavities, and bodies from various geological environments [2]. It is also helpful for figuring out an aquifer's boundary, thickness, and depth [3].

According to[5], combines 2-D resistivity techniques with Induced Polarization (IP) imaging for groundwater exploration in a sedimentary environment is the most popular geophysical methodology for hydrological research. Since both clay and saturated sand formations have low resistivity, it might be challenging to distinguish them apart. Through the integration of all available data from previous research, boreholes and geology, the lithology of the indicated layers was established [4].

[6] stated that groundwater is described as water that is found in soil pores and rock formation fractures that is below the surface of the Earth. Finding the exact position of the groundwater accumulation zone in the subsurface layer is a challenge for engineers. The 2D resistivity method is utilized as initial step in any groundwater exploration. With the help of 2D resistivity inversion and supporting borehole data, reliable groundwater information can be generated.

However, when performing a resistivity survey, there is uncertainty in distinguishing between soil particles and groundwater. Therefore, the objective of this research is to apply the combination of induced polarization (IP) investigation and resistivity to identify the groundwater potential in National Defence University of Malaysia, Sungai Besi, Kuala Lumpur. The study area has experienced of water stress issue and it is important to have clean water supply to the campus. The best option for this issue is groundwater, and one benefit is that it can continue to exist even when all surface water has dried up or becoming more scarce.

Geological and Study Area

The study area for this research was selected at the National Defence University of Malaysia in the Sungai Besi Military Camp in Federal Territory of Kuala Lumpur, at approximate 3° 3'2.16"N, 101°43'45.16"E, as shown in Fig. 1. The ground level

elevation of the study area is from 90m to 161m relative to Mean Sea Level (MSL). There is a tropical climate in this region. The rainfall in Kuala Lumpur is a great deal, even in the driest month. In Kuala Lumpur, the average temperature is 27.1°C around 80.8°F. The annual rainfall is huge, with 220 rainy days during the year and an average humidity of over 80%, to the tune of 2540 mm (100") [7]. Geology formation in National Defence University of Malaysia, Sungai Besi, Kuala Lumpur is classified as an intrusive rock of granite as shown in Fig. 2.

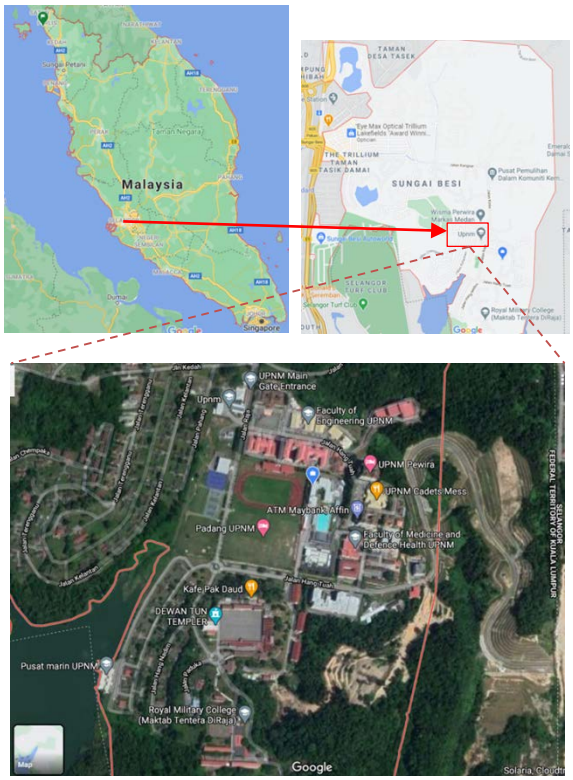

Fig. 1 Location of study area

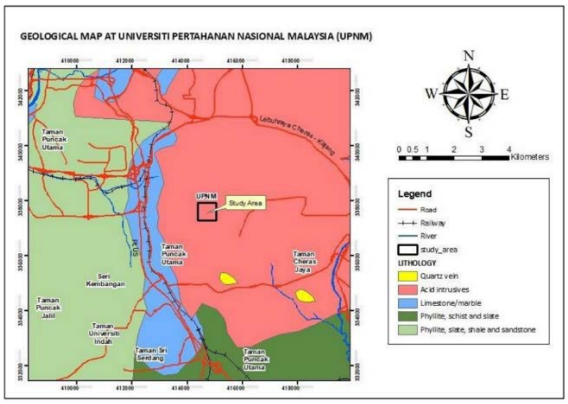

Fig. 2 Geological map of study area

MATERIAL AND METHODLOGY

Electrical resistivity imaging (ERI) and induced polarization (IP) surveys are two hydrogeophysical techniques that have been conducted for groundwater exploration in UPNM. Two survey lines conducted at the proposed area with length of 400m and 800m. The length of 400m cable was laid with the minimum spacing between electrode is 5 m and maximum spacing is 10m. Whereas, for 800m cable was laid with the minimum spacing between electrode is 10 m and maximum spacing is 20m. The newest Terrameter LS2 from ABEM was used for measurement, which including several equipment as shows in Fig. 3 for the electrical resistivity and induced polarization survey. Instruments used such as 4 units of multi-purpose cable, 64 units of jumper cable, 61 units of stainless-steel electrode, 2 units of cable connector, 1 unit of 12-volt battery, and 1 unit of remote cable. A 2D multielectrode ERI survey using the instrument in Fig. 3 are conducted using 61 units of stainless-steel electrode connected to a multicore cable. The electrode cable will be split into parts of controllable length, which are then attached end-to-end. Electrodes attach to the cable take-outs are then placed along a survey line into the ground at a specified daily interval [8]. The ABEM Terrameter LS2 is set up to measure resistivity and induced polarization at the same time during data gathering. Data processing will be conducted using the RES2DINV software when the data acquisition is finished [8]. The field data were processed using the RES2DINV version 4.5.16 software package to create a 2D electrical resistivity and induced polarization image. By using an inversion method, the resistance measurements of earth materials are converted to apparent resistivity readings. The ground resistivity is affected by a number of geological factors, including mineral and fluid composition, porosity, and water saturation. Sedimentary rocks are often more porous and have a larger water content than igneous and metamorphic rocks, resulting in lower resistivity values. The resistivity contour value is modified based on geological data that corresponds to the resistivity range with various colours. Finally, correlations between the borehole record and the contouring inversion model from this survey will be made.

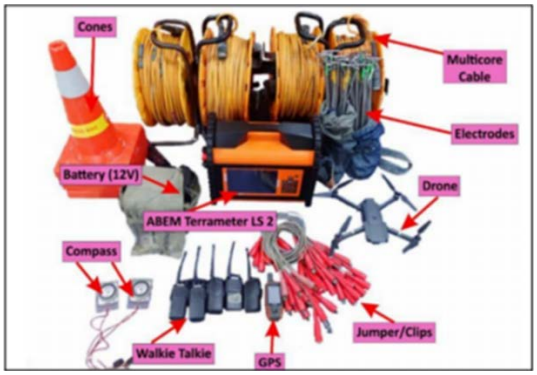

Fig. 3 Multi electrode resistivity system tools

RESULTS AND DISCUSSION

Figure 4 depicts how Line 1 was routed from North-Northeast to South-South west). The borehole was located 270 m from the first electrode. The resistivity values were between 125 and 7400 m. (Ohm-m). According to [9], the resistivity values of the top layer with soil along the line range from 0.1 to 10 m. High resistivity values are represented by the dark purple colour, whereas low resistivity values are represented by the blue colour. The resistivity values are influenced by a number of geological factors, including mineral content and fluid, water saturation, and rock porosity [3]. In accordance with the resistivity distribution, the groundwater potential zone is located within the distance from 255m to 275m with the depth from 25m to 50m. However, this water potential area is not within the fractured zone in order to exhibit a higher chance of groundwater in granite formation. In fact, the water potential zone in this area probably associated with weathered granite environment. Low resistivity anomalies below 100 Ωm have been observed and are thought to be an aquifer zone or a water-saturated layer [10]; [11].

Next, integrated with induced polarization profile, low chargeability values (<7.5ms) give a supportive interpretation of water containing zone for this area. As mentioned before, in water zone, the low values of chargeability are reflecting to water saturated zone as water is a poor medium to retain electrical charges. The chargeability values for induced polarisation indicate gravel, sandstone or alluvium. In contrast to coarse soil, such as gravel and sand, fine grain soils like silt and clay have a substantial composition of minerals, such as vermiculite, kaolinite, and montmorillonite, that makes the current flow easily and produces low resistivity values [12]. Two zones have low values for chargeability. The initial zone exhibits low chargeability between 20 and 270 metres from the first electrode and up to a penetration depth of 70 metres. Groundwater is represented by blue at a chargeability value of 0 to 1 milliseconds (msec), alluvium is represented by light green at a chargeability value of 1 to 4 msec, and gravel is represented by dark green at a chargeability value of 3 to 9 msec [15]. Low chargeability is present in the second zone, which extends from a depth of 40 m to a distance of 280 m to 310 m.

Figure 5 illustrates the correlation between the borehole record and the results of resistivity and chargeability surveys. From the borehole record, topsoil was discovered between 0 and 4 m. From 4 to 6 m and 6 - 25 m, sandy clay and silty sandy was discovered. Next, from 25 - 45 m alluvium was found. According to [15], alluvium, which is made up of sandy clay and sand, has resistivity values ranging from 125 to 255 Ωm and chargeability ranges from 7.5 to 10 msec. The chargeability value was out of range when compared to the Telford theory range of 1 to 4 msec for alluvium. Sandstone with resistivity ranges of 170 to 340 Ωm and chargeability ranges of 7.5 to 9.75 msec is found at depths of 45 to 55 m, but the theory of Telford provides a range from 3 to 12 msec. Schist is found with resistivity values of 1200 to 1700 Ωm at depths of 55 to 60 m, still overlapped on the resistivity value scale. However, Telford's theory, which specifies a range of 5 to 20 msec, a little bit slipped from the measured chargeability for schist from 7.5 to 10 msec. The granite layer that makes up the last layer of the borehole, has resistivity values ranging from 1700- 5700 Ωm at 60–100 m depth, which is slightly different from Frischknecht and Keller's range of 2000–1,000,000 Ωm, and chargeability values between 7.5 and 12 msec. which is a little bit outside of the acceptable range for granite according to the Telford theory, which is 10 to 50 msec

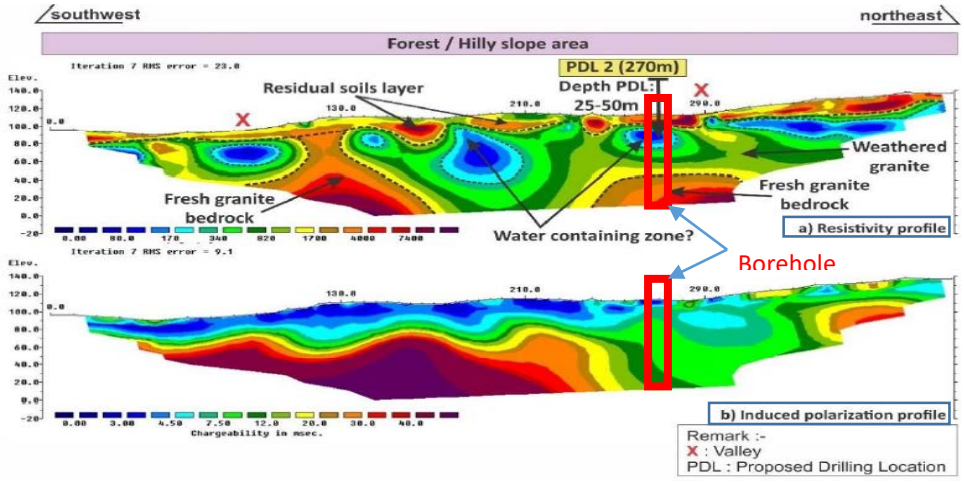

Fig. 4 Inversion model of (a) 2D resistivity and (b) chargeability for line 1

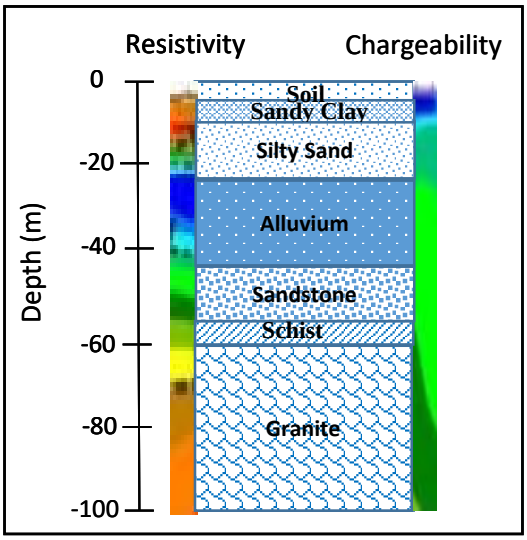

Fig. 5 Result of resistivity aligned with the borehole record at line 1

As a result, the resistivity value was more accurate than the chargeability value, which had a larger range. However, the groundwater potential zone that situated between 255 and 275 meters distance at a depth 25 – 50 m is not located within the fractured zone in order to demonstrate a greater likelihood of groundwater in granite formation. Tables 1 and 2 provide a summary of resistivity and chargeability values based on [15] and [16] 's theories, respectively.

Table 1: Resistivity value for soil and rocks [15]

Material	Resistivity (Ωm)
Fresh groundwater	10 - 100
Clay	1-100
Sand	60-1000
Alluvium	80-100
Sandstone	10-1000
Shale	20-2000
Limestone	50 - 4000
Schist	20 - 10,000
Granite	2000 – 1,000,000
Gneiss	10, 000 – 3,000,000

Table 2: Chargeability value [16]

Material	Chargeability (msec)
Groundwater	0 - 1
Alluvium	1 - 4
Gravels	3 - 9
Sandstones	3 - 12
Schist	5 - 20
Gneiss	6 - 30
Granite	10 - 50
Limestone	10 - 20
Shale	50 - 100

Lines 2 were set up in NWW (North West-west) to SEE (South wast-East), intersecting line 1 at 300 m from the first electrode. The line is straightened up to 800 m long; roughly 250 m is on the region of very thick shrubs area and from 500 m onwards, is area with a moderate to steep slope face. Other than that, the area is classify as flat landform. For survey line 2, water containing zone is less potential than the area of survey line 1. This is because the water containing zone is mainly located in rock formation which is indication of low volume than survey line 1. It is located at the distance from 580 m to 590 m with the depth from 20m to 30m only as shown Figure 6. This survey line was carried out on undulating topography. Hence, the water containing zone probably infiltrated from high topography (south) and accumulated towards low topography region (north). Resistivity value in line 2, at the bottom layer start of from high resistivity at depth 140 m to top layer with low resistivity value at a depth of 20 m. The resistivity values vary from 1 Ωm to 9000 Ωm. The layer with the highest concentration of resistivity is coloured dark purple based on the results of the resistivity distribution, indicating the presence of a massive rock at a depth of 140 m, which is interpreted as granite with resistivity value > 5000 Ωm. At a depth 120 m, the green and yellow coloured area depicted in the data as sandstone. Saturated layer presumed as blue colour in the data at a depth of 20 m until 30 m due to its low resistivity values of below 100 Ωm. This survey line was carried out on undulating topography. Hence, the water containing zone probably infiltrated from high topography (south) and accumulated towards low topography region (north).

The induced polarization in the survey lines, meantime, indicates some potential groundwater and alluvium. Resistivity values will lowered by the present of groundwater, and silt will also bring down the resistivity value below groundwater. The subsurface area that has been coloured in dark and light blue at a depth of 0 to 30 m could be classified as saturated zone with chargeability from 1 to 5 msec [14]. Therefore, the maximum depth of potential groundwater is at depth of 20 to 30 m with distance 580 to 590 m from the induced polarization (IP) at the first electrode. The high probability of finding groundwater was when the chargeability value for the groundwater was between 0 and 4.5 msec. The light green colour at a depth of 60 -100 m could be consider as sandstones. High chargeability can be found in orange colour with chargeability value of 20 to 30 msec and it can be represented as gneiss, while yellow colour at 16 to 20 msec of chargeability value showed schist. The bigger resistivity values between these rocks is the best approach to distinguish a schist to a gneiss with the value of resistivity greater than 5000

Ωm. This is consistent with the results of previous studies conducted within the same geologic environment [13].

Unconsolidated sediments and groundwater in the study area can be distinguished using induced polarization method to support the exploration due to its different chargeability values and not relying solely on resistivity method only. Table 3 shows the summary of the lithology in Sungai Besi, Kuala Lumpur.

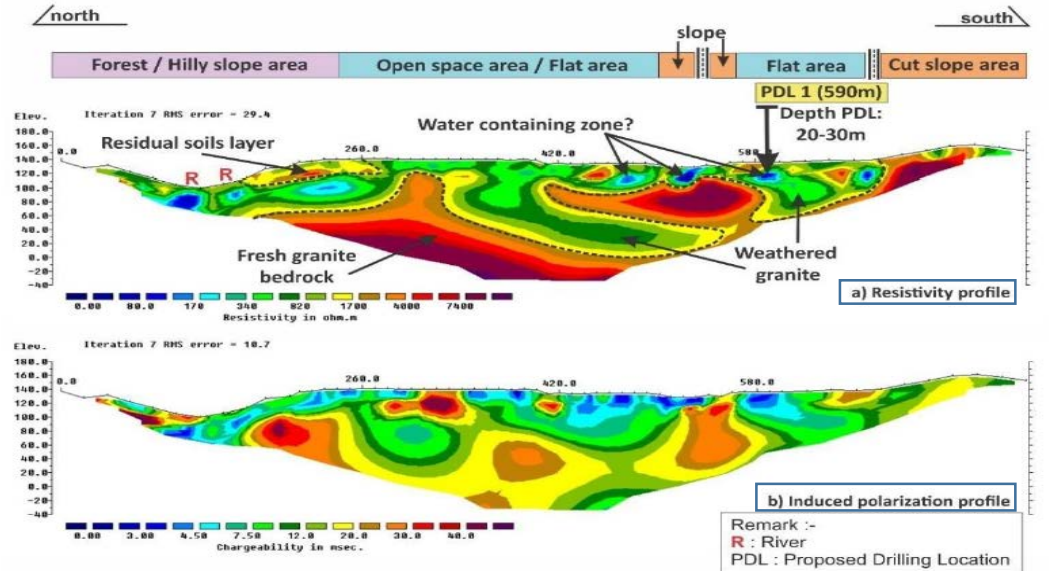

Fig. 6 Inversion model of (a) 2D resistivity and (b) chargeability for line 2

Table 3 Summary of geophysical and geological of area Sungai Besi, Kuala Lumpur

Study Area	Geology	Method	Values	Lithology
Sungai Besi, Kuala Lumpur	This area is consisting of as schist, sandstone and granite due to the area is in acid intrusive.	2-D resistivity	125 - 255 Ωm	Alluvium
			0 - 125 Ωm	Saturated zone
			170 - 340 Ωm	Sandstone
			1200 - 1700 Ωm	Schist
			1700 - 5700 Ωm	Granite
		Induced polarization	0 - 1 msec	Groundwater
			1 – 4.5 msec	Alluvium
			3 - 12 msec	Sandstones
			16 – 20 msec	Schist
			20 - 30 msec	Gneiss
			30 - 40 msec	Granite

CONCLUSIONS

This study's primary significance is the comprehensive investigation of the groundwater potential zone of granitic formation at National Defence University of Malaysia, Sungai Besi, Kuala Lumpur. This study used resistivity and induced polarisation techniques in granitic rock formation to assess the groundwater potential zone using a geophysical approach called electrical resistivity survey. At the site, two (2) profile lines of measurements were conducted at the proposed area within National Defence University of Malaysia. From the results, water containing zone interpreted approximately about resistivity values below 100 Ωm and chargeability values below 7.5 ms. Integrated with induced polarization profile, low chargeability values make survey line 1 have more potential in term of water containing zone. Thus, survey line 1 give a higher chance of groundwater containing zone than survey line 2. Also, the porosity and permeability of sediments; clay, silt and sand indicate presence of water due to its water-flow when the area is being recharged. From the analysis of induced polarization results, the uncertainty between unconsolidated sediments and groundwater was able to be deduced.

Some recommendations for further studies are more borehole wells purposes should be drilled due for better understanding on the groundwater at Sungai Besi, Kuala Lumpur. This study is limited to two lines of 2D resistivity and Induced Polarization with 400m and 800m long.

ACKNOWLEDGMENTS

The authors are grateful to the National Defence University of Malaysia management, research and innovation office for providing fund (Project code: UPNM/2021/GPJP/PK/1) for this research.

REFERENCES

[1] Oseji J., Atakpo E and Okolie (2005). Geoelectric investigation of the aquifer characteristics and groundwater potential in Kwale, Delta State, Nigeria. Journal Applied Science and Environmental Management., 9, 157 – 160.

[2] Dor (2011). Verification of surface groundwater connectivity in an irrigation canal using geophysical, water balance and stable isotope approaches. Water Resources Management, 25 (11), 2837 - 2853

[3] Omoyusi G. Adeyemo, A., and Adegoke (2007). Investigation of groundwater prospect using electromagnetic and geoelectric scounding at afunbiowo near Akure, Southwestern Nigeria. Pacific Journal of Science and Technology, 8, 172 - 182

[4] Aizebeokhai and Oyeyemi (2014). The use of the multiple-gradient array for geoelectrical resistivity and induced polarization imaging. Journal of Applied Geophysics, 111, 364 – 376.

[5] Ahzegbobor, Aizebeokhai, Kehinde, Oyeyemi and Emmanuel, S (2016). Electrical resistivity and induced polarization imaging for groundwater exploration convenant. SEG International Exposition and 87th Annual meeting, 2487 – 2491.

[6] Muchingami I., Hlatywayo D., Nel J., and Chuma C. (2012). Electrical resistivity sirvey for groundwater investigations of the basaltic greenstone formation of the urban Bulawayo aquifer. Physics and Chemistry of the Earth, Parts A/B/C, 50, 44-51.

[7] Arsene B., Elvis G., Daniel N. (2018). Investigation for Groundwater Resources from Electrical Resistivity Tomography and Self-Potential Data in the Meiganga Area, Adamawa Cameroon. International Joirnal of Geophysics. Vol, 2018 doi: 10.1155/2018/2697585.

[8] Arjwech and M. E. Everett (2015). Application of 2D electrical resistivity tomography to engineering projects: Three case studies. Songklanakarin Journal of Science and Technology, Vol. 37, no. 6, pp. 675–681.

[9] Riwayat, A. I., Nazri, M. A., & Abidin, M. H. (2018). Detection of Potential Shallow Aquifer Using Electrical Resistivity Imaging (ERI) at UTHM Campus, Johor, Malaysia. *Journal of Physics.*

[10] Amsir and Marwan (2015). The investigation of groundwater using geophysical techniques in Baitussalam Sub district, Aceh Besar District, Aceh province, Indonesia. Electronic Journal of Geotechnical Engineering, 20(205).

[11] Marsan, D., Azimmah, A., Adli, D, Muthi, Yuantoro & Fatkhan (2017). Aquifer characterization using 2D Electrical Resistivity Imaging in Kidangpananjung, Cililin District, West Java, Southeast Asian Conference on Geophysics. Earth and Environmental Science, 62.

[12] Zainal A., Raqib A., Aziman M., Azhar A., Khaidir A., Fairus Y., Rosli S., Fakhrurrazi and Izzaty (2017). Preliminary Groundwater Assessment Method at Quaternary Deposits Area using Electrical Method at Quarternary Deposits Area. IOP Conference Series: Materials Science and Engineering, 12042

[13] Nordiana and Haziq (2002). Evaluation of Aquifer Potential Using 2D Resistivity and Induced Polarization in Machang, Kelantan. Journal of sustainability Science and Management. Vol 17 No 1, 259-270

[14] Sowers G. (1979). Introductory soil mechanics and foundations. Geotechnical Engineering. 4th Edition. New York: Macmillan Publishing Co., Inc.

[15] Frischkecht F. and Keller G. (1996). Electrical methods in geophysical prospecting. Oxford: Pergamon Press Inc.

[16] Telford W., Geldart and Sheriff R (1976). Applied Geophysics. Cambridge University.

8th Int. Conf. on Structure, Engineering & Environment (SEE), Mie, Japan, Nov.10-12, 2022, ISBN: 978-4-909106094 C3051

MACHINE LEARNING MODELS TO DETERMINE THE COEFFICIENT ANGLE OF FRICTION OF MAKATI CITY, PHILIPPINES SOIL LAYERS

Joenel Galupino[1] and Jonathan Dungca[1]

[1]Faculty, De La Salle University, Manila, Philippines

ABSTRACT

Seismic activity in the Philippines is caused by the country's unique geographic location, which results in frequent volcanic and tectonic activity. This has resulted in the varied soil types and irregular soil thicknesses found throughout the country. As a result, local Geotechnical Engineers face a difficult task, as they require accurate soil and rock information in order to plan and design geotechnical construction projects in the country. Only a few borehole logs are conducted due to the project's limited budget and timeline, thus, geological and geotechnical data can be collected only at the project's location, leaving unknown subsurface data in other locations. The purpose of this study is to use Machine Learning Regression Models to determine the angle of internal friction between soil layers in Makati City, Philippines. Linear Regression Model, Tree Regression Model, Boosted Trees Model, and Artificial Neural Network are the competing Machine Learning Regression Models. Coefficient of Determination (R^2) and Root Mean Square Error (RMSE) values were calculated to compare and validate the regression models. Among the models, the Linear Regression Machine Learning Model had the highest Coefficient of Determination (R^2) and the lowest Root Mean Square Error (RMSE), and was used to deploy in the research locale. Another output was a map of Makati City represented by its internal friction angle.

Keywords: Geotechnology, Geospatial intelligence, Machine learning, Friction Angle, Philippines

INTRODUCTION

Foundations are frequently buried beneath the surface layers of soil and their loads affect the underlying soil strata, this comprehension can be attained through soil investigation tests. Engineers must fully understand the soil-foundation interaction in order to design and select the most suitable foundations [1]. The added seismic activity in the Philippines is caused by the country's unique geographic location, which results in frequent volcanic and tectonic activity. This has resulted in the varied soil types and irregular soil thicknesses found throughout the country. As a result, local Geotechnical Engineers face a difficult task, as they require accurate soil and rock information in order to plan and design geotechnical construction projects in the country [2-19]. In general, these examinations are costly and time-consuming. However, engineers are not always able to perform these experiments, so they depend on the findings of earlier studies conducted by their peers in nearby locations to estimate approximate values for certain soil qualities [20]. With the advancement of science and technology, it is now simpler to interpolate a collection of data to get values for non-spatial data regions, a technique that has been utilized by several researchers across the globe [21-26].

However, there are few researches on the angle of internal friction, which is a crucial shear strength metric for evaluating the stability of soil and slopes since it represents soil shear resistance [27]. Soil angle of internal friction is a measure of the soil's resistance to shear forces and corresponds to the angle between the normal stresses [28] and the resultant force within the soil that is produced shortly before collapse owing to shear stresses [29-30].

This study aims to determine the angle of internal friction between soil layers in Makati City, Philippines using Machine Learning Regression Models. The competing Machine Learning Regression Models are the following: Linear Regression Model, Quadratic Regression Model, Tree Regression Model, Boosted Trees Model, and Artificial Neural Network. In addition to describing the types of soil and evaluating its strength based on the angle of internal friction, a 3-D soil profile of Makati City, Philippines will be previewed representing the degree of angle of internal friction that may assist designers, engineers, and decision-makers in determining the site's appropriateness and the most suitable form of foundations.

METHODOLOGY

The process of the study is shown in Fig. 1. and explained in the later sections.

Research Locale

Makati City is a premier, highly urbanized city in the National Capital Region of the Philippines,

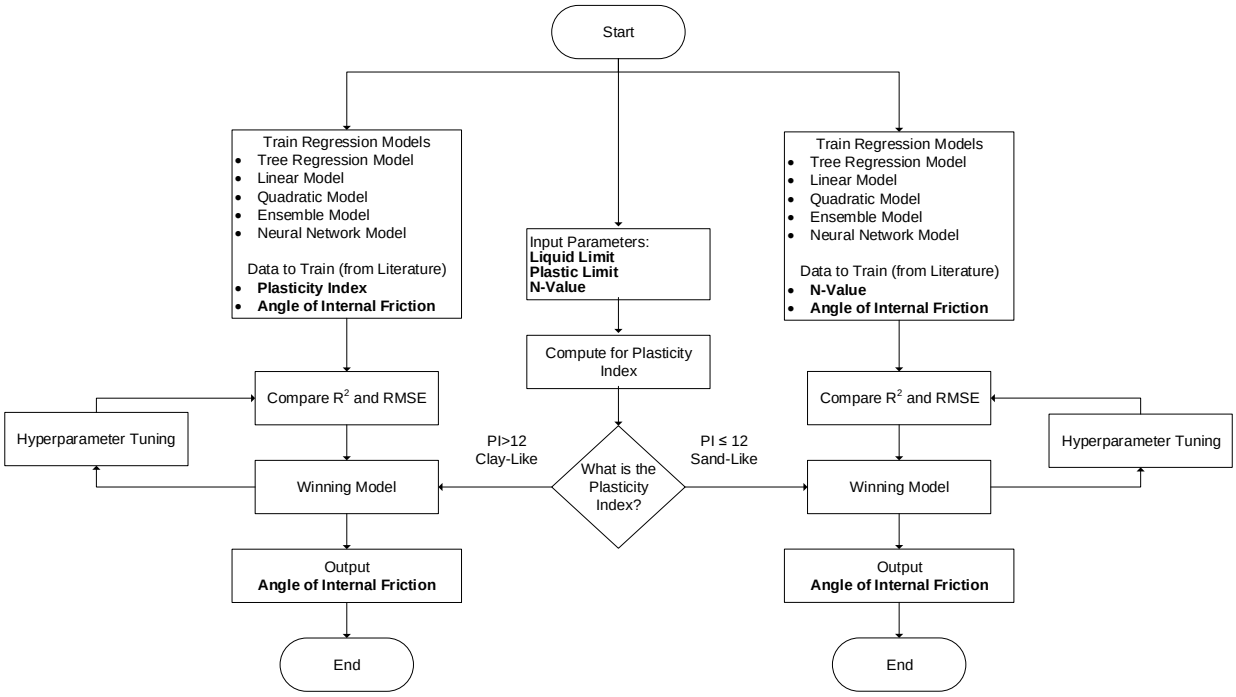

Fig. 1 Methodology of the Study

shown in Fig. 2. In terms of revenue from domestic sources and per capita income, Makati City remains the richest local government unit (LGU) in the Philippines. Makati is the financial hub of the Philippines, with the biggest concentration of global and domestic firms. Numerous banks, enterprises, department shops, and foreign embassies are located in Makati. Consequently, structures are being constructed to house these advancements, and as noted earlier, soil explorations are required for these projects.

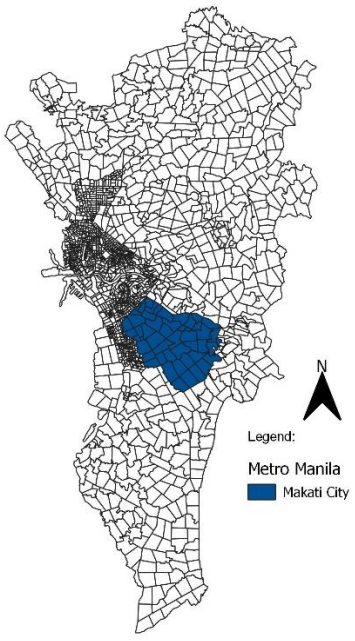

Fig. 2 Location of Makati City in Metro Manila

Data

The collection of soil borehole logs are from within and around Makati City. The soil profile was described using a density of one drill log per square kilometer. The distribution was visually evaluated, and data-deficient regions were identified. Erroneous logs from boreholes were also removed and discarded [22]. The locations of thirteen (13) boreholes were mapped based on their official investigation reports, as shown in Fig. 3. The 13 boreholes have 247 data layers.

The independent and dependent variables are displayed in Table 1. The soil data output is a numeric parameter, which is ideally suited for a Machine Learning Model.

Table 1 Dependent and Independent Variables of the Study

Independent Variable(s)	Dependent Variable(s)
1. Longitude	1. N-Value
2. Latitude	2. Liquid Limit
3. Elevation	3. Plastic Limit

Angle of Internal Friction and its Relationships

Angle of Internal Friction, Ø

The Angle of Internal Friction (Ø) is calculated using Mohr's Circle and a graph of the shear stress and normal effective stresses at which shear failure occurred. The combination of friction angles and slope is based on the connection established by the Mohr-Coulomb failure criteria, which implies that

soil friction angle is a component of shear strength, shown in Eq. 1:

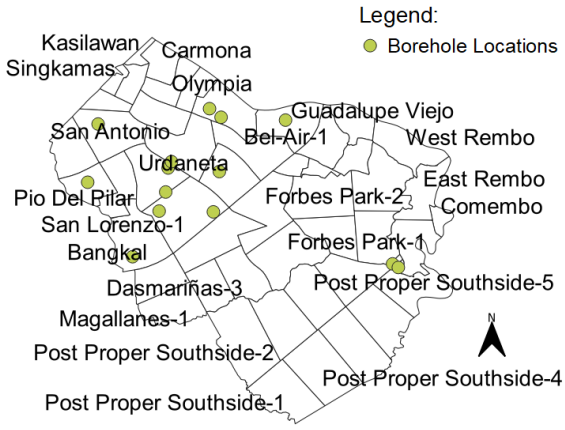

Fig. 3 Collected Boreholes for Makati City

$$\tau = c + \sigma' tan\emptyset \quad (1)$$

Where: τ is shear strength, c is cohesion, σ' is effective overburden pressure, and $\emptyset$ is angle of internal friction.

The Angle of Internal Friction (Ø) can be determined in the laboratory by the Direct Shear Test or the Triaxial Stress Test. However, due to lack of resources, the Angle of Internal Friction (Ø) is sometimes correlated with (1) N-Values for cohesionless soils or sand-like and (2) Plasticity Index, derived from Liquid Limit and Plastic Limit, for soils classified as sands but with clay-like properties.

The most trustworthy approach for determining shear strength parameters of subterranean soils is soil sampling coupled with laboratory testing. Due to limited funds, short deadlines, or a lack of concern, initiatives may not always obtain adequate laboratory recommendations. In many instances, however, soil type, water table depth, and standard penetration test (SPT) blow counts can be used to assess subsurface soil conditions. In the absence of laboratory data, it is usual practice to estimate the shear parameters based on the SPT findings.

Clay also has his own frictional properties. Among the pure clay minerals, sodium montmorillonite (composed of filmy particles) has the lowest Ø' value, while attapulgite (composed of interlocking fibers) has the greatest value. The range of typical Ø' values for soft clay, stiff clay, and shale components is 25˚ to 35˚, 20˚ to 35˚, and 15˚ to 35˚, respectively [31].

Correlations

Various researches on the correlation of Angle of Internal Friction (Ø) and N-values were gathered [32-37].

Various researches on the correlation of Angle of Internal Friction (Ø) and Plasticity Index values were gathered [31, 38-49]. At each plasticity index, different values of Ø ' result from the difference in clay size fraction of soils and from the difference in effective normal stress at which Ø' was measured.

These relationships also underwent machine learning modeling, with Linear Regression Model, Tree Regression Model, Boosted Trees Model, and Artificial Neural Network as competing models, Table 2 and Table 3 show the independent and dependent variables for the modeling.

Sand-like or Clay Like

Recent research, such as those by Boulanger and Idriss [50] and Bray and Sancio [51], have provided valuable information and recommendations for the management of soils:

- PI < 12: This group of soils should be deemed "sand-like" and examined using either the simplified technique for sands and non-plastic silts or site-specific studies that include laboratory testing on high-quality soil samples.

- PI > 12: The behavior of soils categorized under this category is thought to be "clay-like." Importantly, certain clay soils can experience considerable strength loss due to seismic shaking; hence, designating these soils as non-liquefiable does not mean that they are intrinsically stable.

Thus, for PI < 12, Table 2 was used for the correlation, while PI > 12, Table 3 was used.

Machine Learning Modelling

Machine Learning Competition

Machine learning automates models for analyzing soil data by learning from the data, detecting its patterns, and making judgments with minimum human input. This study focused on generating the soil profile of Makati City, Philippines using Machine Learning Models such as the Linear Regression Model [52], Quadratic Regression Model [53], Tree Regression Model [54], Boosted Trees Model [55] and Artificial Neural Network [56-57]

Table 2 Dependent and Independent Variables for Sand-Like Soils Relationship

Independent Variable(s)	Dependent Variable(s)
1. N-Value	1. Angle of Internal Friction

Table 3 Dependent and Independent Variables for Clay-Like Soils Relationship

Independent Variable(s)	Dependent Variable(s)
1. Plasticity Index	1. Angle of Internal Friction

Data Split Ratio

There are studies that give extensive analysis of the machine learning training and testing process [58]. Obtaining meaningful data has gotten increasingly difficult due to the explosion of data. To make sense of data, the discipline of data mining has emerged. Data mining is a collection of techniques used to derive meaning from data [59]. To identify the activities of a machine learning model, observations not used during training must be employed. Otherwise, the model's evaluation will be distorted. (1) Training Dataset, (2) Validation Dataset, and (3) Test Dataset are the datasets. The split ratio for the dataset is 70% Training Data, 15% Validation Data, and 15% Testing Data.

Coefficient of Determination (R^2) and Root Mean Square Error (RMSE)

Each model's Coefficient of Determination (R^2) were collected. The model with the highest Coefficient of Determination (R^2) among the five (5) competing Machine Learning Models was deployed; this is also known as a Competition. In this investigation, the approach of Cheng et al. [60] was utilized. Coefficient of Determination is a tool which determines and assesses the ability of a statistical model to explain and predict future outcomes., as illustrated in Eq. 2:

$$R^2 = \left\{ \frac{\sum[(X - X_m) * (Y - Y_m)]}{\sqrt{\sum(X - X_m)^2 * \sum(Y - Y_m)^2}} \right\}^2 \qquad (2)$$

Where: X – Data points in Data set X, Y – Data points in Data set Y, X_m – Mean of Data set X and Y_m – Mean of Data set Y

While the Root Mean Square Error (RMSE) is the square root of the mean of all errors squared [61], equation is shown in Eq. 3:

$$\boldsymbol{RMSE} = \sqrt{\frac{\sum_{i=1}^{N} ||\boldsymbol{y}(i) - \hat{\boldsymbol{y}}(i)||^2}{\boldsymbol{N}}} \qquad (3)$$

Where: N is the number of data points, y(i) is the i-th measurement, and ŷ(i) is its corresponding prediction.

The Matlab Regression Learner program employed the parameters listed in Tables 1, 2 and 3. As a foundation for training and verifying regression models, the program was employed. After training the competing models, compare their validation errors side-by-side to choose the optimal model. The following is a typical method for training regression models within the program Regression Learner:

a) Selection and Validation of Data
b) ML Regression Model Tuning (Hyperparameter Tuning)
c) ML Regression Model Training
d) Assess the ML Regression Model based on the Accuracy Rates (Competition)
f) Implement the chosen ML Regression Model

To calculate the soil stratification of an unknown location, the software employed the model with the best rate of accuracy. In addition, it is fine-tuned to evaluate whether the accuracy rates may be enhanced further, as described in the next section.

Hyperparameter Tuning

The hyperparameters of the chosen model were adjusted to determine whether the accuracy rates might be enhanced. The challenge of hyperparameter tuning is the selection of the optimal set of hyperparameters for a machine learning system [62]. The number of neighbors (k) for the k-NN model is an example of a hyperparameter.

Deployment

At the Barangay/Zone Level, the Machine Learning model with the best Accuracy Rate was deployed. To be consistent with the density of 1 borehole per square kilometer, these barangays were subdivided into zones, as seen in Fig. 4.

Geographic Information System was used to determine the latitude and longitude coordinates of each Barangay/Zones's centroid.

Predicted Soil Profile and Geographic Information System (GIS) Maps

Once the required data has been imported into a GIS platform, it may be integrated with other data layers to generate many unique maps. The soil profile is also delineated isometrically.

RESULTS AND DISCUSSIONS

Accuracy Rates and RMSE of ML Models

Accuracy is the ratio of correct predictions to the

total number of input samples [61], and it is determined using Eq. 2. In contrast, the Root Mean Square Error (RMSE) is the square root of the squared mean of all errors [62], shown in Eq. 3. Multiple Machine Learning Models were employed to train the data, and these models provided various accuracy rates, as shown in Tables 4 to 8. The model with the greatest accuracy rate was selected for deployment. Initial testing utilized the simplest types of hyperparameters. If the machine learning model had the greatest rate of accuracy, it was adjusted further.

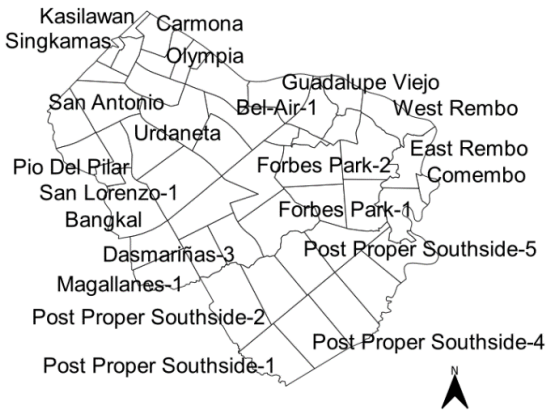

Fig. 4 Generated Map of Makati City Zones

Shown in Tables 4, 5 and 6 are the performances of the ML Models in Predicting N-Values, Liquid Limit and Plastic Limit, the Tree Regression Model was used for the deployment. The Longitude, Latitude and Elevation were the independent variables.

Table 4 Performance of ML Models in Predicting N-Value

Models	R^2	RMSE
Tree Regression Model	0.88	7.3277
Linear Model	0.09	20.238
Quadratic Model	0.25	18.405
Boosted Tree	0.5	15.088
Neural Network	0.46	15.729

Table 5 Performance of ML Models in Predicting Liquid Limit

Models	R^2	RMSE
Tree Regression Model	0.74	0.10728
Linear Model	0.72	0.10743
Quadratic Model	0.71	0.10771
Boosted Tree	0.44	0.11706
Neural Network	0.23	0.78019

These variables do not require normalization and/or scaling. Tree regression model is very suitable since the splitting has placed N-values, Liquid Limit and Plastic Limit in their proper subsets.

Table 6 Performance of ML Models in Predicting Plastic Limit

Models	R^2	RMSE
Tree Regression Model	0.69	0.11242
Linear Model	0.66	0.11668
Quadratic Model	0.65	0.11635
Boosted Tree	0.41	0.12042
Neural Network	0.44	0.11694

Table 7 Performance of ML Models in Predicting Angle of Internal Friction for Sand-Like Soils

Models	R^2	RMSE
Tree Regression Model	0.62	3.3497
Linear Model	0.77	3.1337
Quadratic Model	0.76	3.139
Boosted Tree	0.58	3.5096
Neural Network	0.65	3.1828

Table 8 Performance of ML Models in Predicting Angle of Internal Friction for Clay-Like Soils

Models	R^2	RMSE
Tree Regression Model	0.12	6.8151
Linear Model	0.18	5.8424
Quadratic Model	0.15	5.9295
Boosted Tree	0.01	6.4608
Neural Network	0.06	6.2284

For Tables 7 and 8, Linear Regression Model was used, among all the ML models, it had provided a more stable model compared to the other ML Models. A linear relationship was also provided by various studies [27-49] to determine the Angle of Internal Friction whether it is sand-like or clay-like. The Machine Learning Models Predicting the Angle of Internal Friction of Sand-Like Soils and Clay-Like Soils is shown in Fig. 5 and 6, respectively.

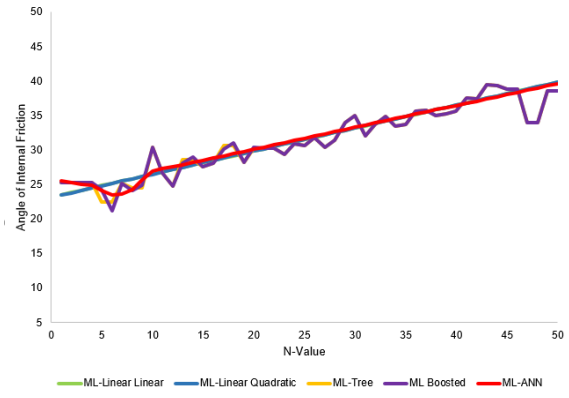

Fig. 5 Machine Learning Models Predicting the Angle of Internal Friction of Sand-Like Soils

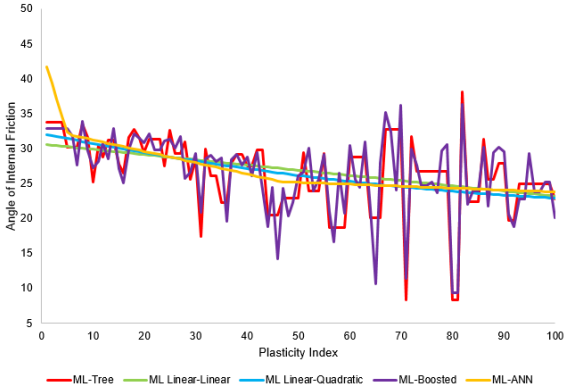

Fig. 6 Machine Learning Models Predicting the Angle of Internal Friction of Clay-Like Soils

Generated Angle of Internal Friction Soil Profile and Geographic Information System (GIS) Map

The western part of Makati City is dominated by hard strata, as shown in Fig. 7, N-values 40-50 is prevalent in these areas. The layers around these areas are reworked deposits of primary tuff and pyroclastic-flow deposits, thus providing a higher value of N. The Eastern area of Makati are dominated by marine epiclastic sediments, which can be loose, thus providing a lower value of N. Almost 59% of the soil layers have high N-values.

For the Atterberg Limit properties of Makati City, shown in Figs. 8 and 9, the surficial layers are dominated by low values of Liquid Limit and Plastic Limit, this may be attributed by the dominating soil types in the area. Non-plastic soils are prevalent. Almost 77% of the layers are non-plastic, while the remaining 23% are plastic soils.

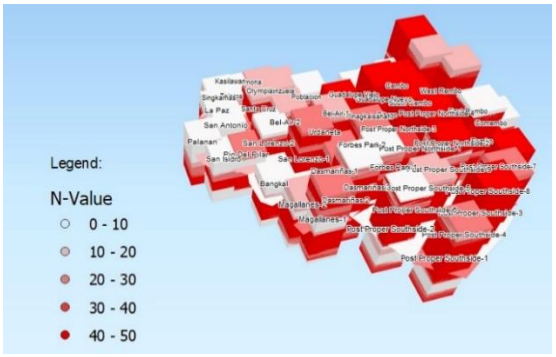

Fig. 7 N-Value Profile Generated for Makati City

As validation, shown in Fig. 10, the southeast side of Makati City experiences a greater shear wave velocity than the northwest side. This has the same configuration as the soil profile generated by the model and depicted in Fig. 11. In these regions, resistance is significantly more formidable. The PHIVOLCS Shear Wave Velocity Map was utilized to validate the subsurface soil profile generated by the Model.

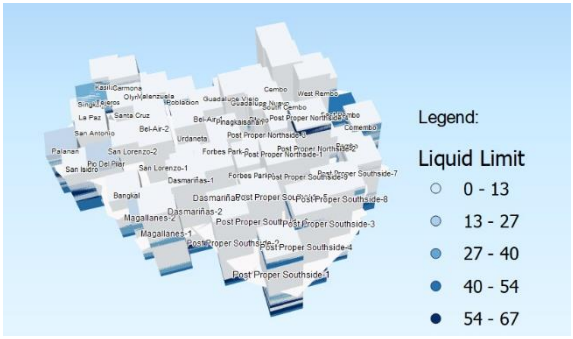

Fig. 8 Liquid Limit Profile Generated for Makati City

Fig. 9 Plastic Limit Profile Generated for Makati City

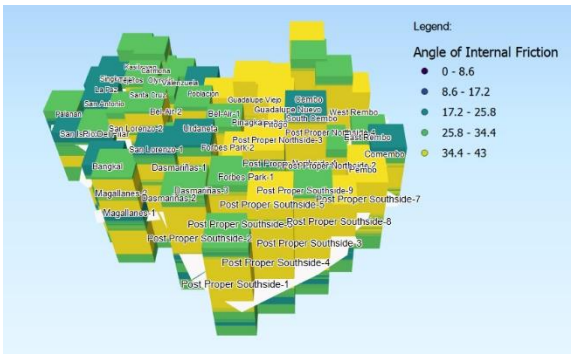

Fig. 10 Angle of Internal Friction Profile Generated for Makati City

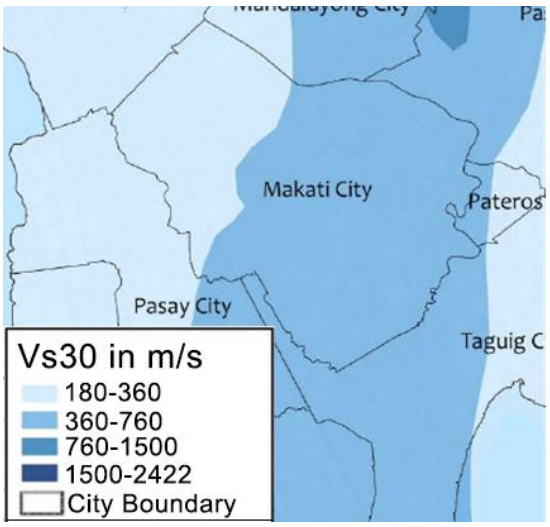

Fig. 11 Shear Wave Velocity Map showing Makati City [63]

CONCLUSION

For the Angle of Internal Friction of Makati City, shown in Fig. 10, almost 50% of the soil layers have a high Angle of Internal Friction. The higher value of the internal friction angle shows the higher of the material can withstand the lateral force. The 3-D profile of Makati City, Philippines for the Angle of Internal Friction has previewed representing the degree of angle of internal friction that may assist designers, engineers, and decision-makers in determining the site's appropriateness and the most suitable form of foundations.

The study aims to determine the angle of internal friction between soil layers in Makati City, Philippines using Machine Learning Regression Models. The competing Machine Learning Regression Models are the following: Linear Regression Model, Quadratic Regression Model, Tree Regression Model, Boosted Trees Model, and Artificial Neural Network.

For the ML Models in Predicting N-Values, Liquid Limit and Plastic Limit, the Tree Regression Model was used for the deployment. Tree regression model is very suitable since the splitting has placed N-values, Liquid Limit and Plastic Limit in their proper subsets.

For the ML Models in Predicting Angle of Internal Friction for Sand-Like and Clay-like Soils, Linear Regression Model had provided a more stable model compared to the other ML Models. A linear relationship was also provided by previous studies.

Once the all the data has been imported into a GIS platform, 3-D profile maps were created which has previewed representing the degree of angle of internal friction that may assist designers, engineers, and decision-makers in determining the site's appropriateness and the most suitable form of foundations

ACKNOWLEDGEMENT

The authors would like to express their sincerest thankfulness to Department of Science and Technology (DOST) for funding their project Geotechnical Mapping of Metro Manila Subsoil (GEMMMS).

REFERENCES

[1] Kareem Al-Mamoori, S., L. Kareem, S., A. Al-Maliki, L., & El-Tawil, K. (2021). Geotechnical Maps for Angle of Internal Friction of An-Najaf Soil-Iraq Using GIS. Wasit Journal of Engineering Sciences, 8(2).

[2] Hu, Y., Zhao, T., & Wang, Y. (2020). Bayesian Learning of Site-Specific Spatial Variability Using Sparse Geotechnical Data. 553–558.

[3] Galupino, J. G., & Dungca, J. R. (2015). Permeability characteristics of soil-fly ash mix. ARPN Journal of Engineering and Applied Sciences, 10(15), 6440-6447.

[4] Dungca, J. R., & Galupino, J. G. (2016). Modelling of permeability characteristics of soil-fly ash-bentonite cut-off wall using response surface method. International Journal of GEOMATE, 10(4), 2018-2024.

[5] Dungca, J., Galupino, J., Sy, C., & Chiu, A. S. F. (2018). Linear optimization of soil mixes in the design of vertical cut-off walls. International Journal of GEOMATE, 14(44), 159-165.

[6] Dungca, J. R., Galupino, J. G., Alday, J. C., Barretto, M. A. F., Bauzon, M. K. G., & Tolentino, A. N. (2018). Hydraulic conductivity characteristics of road base materials blended with fly ash and bottom ash. International Journal of GEOMATE, 14(44), 121-127.

[7] Adajar, M., Galupino, J., Frianeza, C., Faye Aguilon, J., Sy, J. B., & Tan, P. A. (2020). Compressive strength and durability of concrete with coconut shell ash as cement replacement. International Journal of GEOMATE, 17, 183-190.

[8] Dungca, J. R., & Dychangco, L. F. T. (2016). Strength properties of road base materials blended with waste limestones. International Journal of GEOMATE, 11(3), 2493-2498.

[9] Adajar, M. A. Q., Aquino, C. J. P., dela Cruz, J. D.,II, Martin, C. P. H., & Urieta, D. K. G. (2019). Investigating the effectiveness of rice husk ash as stabilizing agent of expansive soil. International Journal of GEOMATE, 16(58), 33-40.

[10] Adajar, M. A. Q., & Cutora, M. D. L. (2018). The effect of void ratio, moisture content and vertical pressure on the hydrocompression settlement of copper mine tailing. International Journal of GEOMATE, 14(44), 82-89.

[11] Adajar, M. A. Q., de Guzman, E., Ho, R., Palma, C.,Jr.III, & Sindico, D. (2017). Utilization of aggregate quarry waste in construction industry. International Journal of GEOMATE, 12(31), 16-22.

[12] Uy, E. E. S., & Adajar, M. A. Q. (2017). Assessment of critical-state shear strength properties of copper tailings. International Journal of GEOMATE, 12(32), 12-18.

[13] Uy, E. E. S., & Dungca, J. R. (2018). A comparative settlement prediction of limestone blended materials using asaoka and hyperbolic method. International Journal of GEOMATE, 14(43), 63-69.

[14] Ubay, I. O., Alfaro, M., Alfaro, M., & Blatz, J. (2020). Stability assessment of an aging earth fill dam considering anisotropic behaviour of clay. International Journal of GEOMATE, 18(66), 84-91.

[15] Adajar, J. B., Ubay, I. O., Alfaro, M., & Chen, Y. (2020). Discrete element model parameters to simulate slope movements. International Journal of GEOMATE, 18(65), 192-199.

[16] Adajar, J. B., Ubay, I. O., Alfaro, M., & Chen, Y. (2020). Discrete element modelling of undrained consolidated triaxial test on cohesive soils. Paper presented at the Geotechnical Special Publication, 2020-February (GSP 317) 172-182.
[17] Elevado, K. J. T., Galupino, J. G., & Gallardo, R. S. (2019). Compressive strength optimization of concrete mixed with waste ceramics and fly ash. International Journal of GEOMATE, 16(53), 135-140.
[18] Elevado, K. J. T., Galupino, J. G., & Gallardo, R. S. (2018). Artificial neural network (ANN) modelling of concrete mixed with waste ceramic tiles and fly ash. International Journal of GEOMATE, 15(51), 154-159.
[19] Dungca, J. R., & Galupino, J. G. (2017). Artificial neural network permeability modeling of soil blended with fly ash. International Journal of GEOMATE, 12(31), 76-83.
[20] Valverde-Palacios, I., et al., (2014). Geotechnical map of Holocene alluvial soil deposits in the metropolitan area of Granada (Spain): a GIS approach. Bulletin of Engineering Geology and the Environment, 73(1):(177-192).
[21] Dungca, J., & Chua, R. (2016). Development of a Probabilistic Liquefaction Potential Map of Metro Manila. International Journal of GEOMATE, 2016(April), 1804–1809.
[22] Dungca, J. R. (2020). A reference for the allowable soil bearing capacities in Quezon city, Philippines. International Journal of GEOMATE, 19(71), 42–47.
[23] Galupino, J. G., Garciano, L. E. O., Paringit, M. C. R., & Dungca, J. R. (2017). Location based prioritization of surigao municipalities using probabilistic seismic hazard analysis (PSHA) and geographic information systems (GIS). Paper presented at the HNICEM 2017 - 9th International Conference on Humanoid, Nanotechnology, Information Technology, Communication and Control, Environment and Management, 2018-January 1-7.
[24] Galupino, J. G., & Dungca, J. R. (2019). Quezon City soil profile reference. International Journal of GEOMATE, 16(58).
[25] Dungca, J. R., Concepcion, I., Limyuen, M., See, T., & Vicencio, M. (2017). Soil bearing capacity reference for Metro Manila, Philippines. International Journal of GEOMATE, 12(32), 5-11.
[26] Uy, E. E. S., Paringit, M. C. R., Cutora, M. D. L., Galupino, J. G., Garciano, L. E. O., & Dungca, J. R. (2020). Characterization of cebu province municipalities using probabilistic seismic hazard assessment (PSHA) and geographic information system (GIS). Paper presented at the IOP Conference Series: Earth and Environmental Science, 479(1)
[27] Bareither, C.A., et al., (2008). Geological and physical factors affecting the friction angle of compacted sands. Journal of geotechnical and geoenvironmental engineering, 134(10): 1476-1489.
[28] Roopnarine, R., G. Eudoixe, and D. Gay, (2012). Soil physical properties as predictors of soil strength indices: Trinidad case study. Geomaterials, 2(01): 1.
[29] Coulomb, C.A., (1973). Essai sur une application des regles de maximis et minimis a quelques problemes de statique relatifs a l'architecture.
[30] Skempton, A., (1964). Long-term stability of clay slopes. Geotechnique, (14):77-102.
[31] Terzaghi, K., Peck, R. B., and Mesri, G. (1996). Soil Mechanics in Engineering Practice, 3rd ed., Wiley, New York.
[32] Hatanaka, M., & Uchida, A. (1996). Empirical Correlation Between Penetration Resistance and Internal Friction Angle of Sandy Soils. Soils and Foundations, 36(4), 1–9.
[33] Mujtaba, H., Farooq, K., Sivakugan, N., & Das, B. M. (2018). Evaluation of relative density and friction angle based on SPT-N values. KSCE Journal of Civil Engineering, 22(2), 572–581.
[34] Hettiarachchi, H., & Brown, T. (2009). Use of SPT Blow Counts to Estimate Shear Strength Properties of Soils: Energy Balance Approach. Journal of Geotechnical and Geoenvironmental Engineering, 135(6), 830–834.
[35] Kulhawy, F. H., and Mayne, P. W. (1990). "Manual on estimating soil properties for foundation design." Electric Power Research Institute, Palo Alto, Calif.
[36] Terzaghi, K., and Peck, R. B. (1967). Soil mechanics in engineering practice, 2nd Ed., Wiley, New York.
[37] Salari, P., Lashkaripour, G. R., & Ghafoori, M. (2015). Presentation of Empirical Equations for Estimating Internal Friction Angle of GW and GC Soils in Mashhad, Iran Using Standard Penetration and Direct Shear Tests and Comparison with Previous Equations. Open Journal of Geology, 05(05), 231–238.
[38] T. C. Kenney, 1967, The influence of mineral composition on the residual strength of natural soils: Proc. Oslo Conf. on Shear Strength Properties of Natural Soils and Rocks, v. 1, pp. 123-29
[39] T. C. Kenney, 1959, Discussion: Journal of the Soil Mechanics and Foundation Engineering Division, ASCE, v.85:SM3, p. 67-79
[40] Bjerrum, L., and Simons, N. E. 1960. Comparison of shear strength characteristics of normally consolidated clays. In Proc. Res. Conf. Shear Strength Cohesive Soils. ASCE, New York, pp. 711–726.
[41] Ladd, C. C., Foote, R., Ishihara, K., Schlosser, F., and Poulos, H. G. 1977. Stress-deformation and strength characteristics. In Proc. 9th Int. Conf.

Soil Mech. Found. Eng., Tokyo, 2:421–494.
[42] Nonveiller E, (1967) Shear strength of bedded and jointed rock as determined from Zalesina and Vajont slides. Proceedings of Geotechnical Conference. Oslo(1). pp. 289-294.
[43] SKEMPTON, A. W. & PETLEY, D. J. 1967. The strength along structural discontinuities in stiff clays. In: Proceedings of Geotechnical Conference, Oslo, Vol. 2, 55– 69
[44] Hutchinson, J.N., 1967, The free degradation of London Clay Cliffe. Proc. Geotechnical Conf. (Oslo) 1, 113-118.
[45] Hutchinson, 1969. A reeconsideration of the coastal landslides of Folkestone Warren, Kent. Geotechnique 19, 6-38.
[46] Chandler, 1969. No AccessThe Effect of Weathering on the Shear Strength Properties of Keuper Marl. Géotechnique 19, 321-334.
[47] Pichumani, R. & D 'Appolonia, E. 1967. Theoretical distribution of loads among piles in a group. Proc. 3rd Panam. Conf. Soil M ech. & Found. Eng., Caracas
[48] Hamel, J.v. (1970). Stability of slopes in soft, altered rocks. Ph.D. Thesis, University of Pittsburg.
[49] Voight, B. 1973. Correlation between Atterberg plasticity limits and residual shear strength of natural soils. Géotechnique 23, 265-267.
[50] Idriss, I.M. and Boulanger R.W. (2008). Soil Liquefaction during Earthquakes, MNO–12, Earthquake Engineering Research Institute, 242p.
[51] Bray, J.D. and Sancio, R.B. (2006). 'Assessment of the Liquefaction Susceptibility of Fine-Grained Soils,' Journal of Geotechnical and Geoenvironmental Engineering, 132 (9), 1165–1177.
[52] Rath, S., Tripathy, A., & Tripathy, A. R. (2020). Prediction of new active cases of coronavirus disease (COVID-19) pandemic using multiple linear regression model. Diabetes and Metabolic Syndrome: Clinical Research and Reviews, 14(5), 1467–1474.
[53] Sun, Y., & Wang, Q. (2020). Function-on-function quadratic regression models. Computational Statistics and Data Analysis, 142.
[54] Pekel, E. (2020). Estimation of soil moisture using decision tree regression. Theoretical and Applied Climatology, 139(3–4), 1111–1119.
[55] Elith, J., Leathwick, J. R., & Hastie, T. (2008, July). A working guide to boosted regression trees. Journal of Animal Ecology.
[56] Hopfield, J.J., Artificial neural networks. IEEE Circuits and Devices Magazine, 1988. 4(5): p. 3-10.
[57] Bhardwaj, A. and A. Tiwari, Breast cancer diagnosis using genetically optimized neural network model. Expert Systems with Applications, 2015. 42(10): p. 4611-4620.
[58] Uçar, M. K., Nour, M., Sindi, H., & Polat, K. (2020). The Effect of Training and Testing Process on Machine Learning in Biomedical Datasets. Mathematical Problems in Engineering, 2020.
[59] I. H. Witten, E. Frank, and M. A. Hall, Data Mining-Practical Machine Learning Tools and Techniques, Morgan Kaufmann, Burlington, MA, USA, 2013.
[60] Cheng, C. L., Shalabh, & Garg, G. (2014). Coefficient of determination for multiple measurement error models. Journal of Multivariate Analysis, 126, 137–152.
[61] Willmott, C. J., & Matsuura, K. (2005). Advantages of the mean absolute error (MAE) over the root mean square error (RMSE) in assessing average model performance. Climate Research, 30(1), 79–82.
[62] Ghawi, R., & Pfeffer, J. (2019). Efficient Hyperparameter Tuning with Grid Search for Text Categorization using kNN Approach with BM25 Similarity. Open Computer Science, 9(1), 160–180
[63] PHIVOLCS. (2017). The Philippine earthquake model.

8th Int. Conf. on Science, Engineering & Environment (SEE), Mie, Japan, Nov.10-12, 2022, ISBN: 978-4-909106032 C3051

A STUDY ON VIBRATION AND SOUND SIGNALS OF AN ELECTRIC VEHICLE

Suphattharachai Chomphan
Faculty of Engineering at Sriracha, Kasetsart University, Thailand

ABSTRACT

Nowadays, electric vehicles have been continuously developed and become increasingly popular compared to conventional combustion engine vehicles. Their polluting emissions are less than those of petroleum-powered vehicles. Moreover, they are expected to produce noticeably less noise and vibration, however, the issue has not been concretely conducted. Therefore, an analysis of vibration and sound signals of an electric vehicle driving at six different engine speeds at three distinct positions within the passenger room to evaluate the quality of service comparatively has been performed in this paper. The FOMM ONE Y2018 model with a gross battery capacity of 11.84 kWh and a system power of 14 Hp has been selected in this study due to its popularity. The vibration and sound measuring positions are at the right front or driver's seat, the left front seat, and the rear seat. The measurement is performed at different speeds, i.e., 0, 10, 20, 30, 40, and 50 km/h, using a set of accelerometers and a microphone, respectively. The experimental data are statistically measured, and subsequently, the dominant frequency extraction is performed. The experimental results have been finally concluded. From the experiment, when the electric car starts to work by increasing the speed, its vibration and sound magnitudes measured at three distinct positions increase accordingly. When comparing the magnitude of vibration and sound occurring at the measuring locations, it was found that the left seat was the highest and the rear seat was the lowest, obviously at the standstill.

Keywords: Electric vehicle, Vibration signal analysis, Sound signal analysis, Fast Fourier transform, Dominant frequency extraction

INTRODUCTION

On the path of industrial reform in developing countries to drive macroeconomics causing enormous consumption of petroleum products. The incremental use of petroleum poses a serious threat to the environment with the problem of global warming, The disruptive innovation of electric vehicles (EV) has received a huge pinnacle of attention in the present global situation for several decades, A trend of its popularity has occurred intermittently, however it still can not be used as a replacement for internal combustion engine vehicles due to price factors, battery quality and performance (mileage per charge), the limited number of available electric vehicle models, as well as the value for resale. The popularity of engine vehicles can be divided into 3 periods as follows.

First of all, the beginning popularity occurred in 1993, the state of California of the United States announced the zero-emission vehicle standards. Owing to the vehicle performance limitations, however, the developed vehicle remains unpopular.

The second wave of popularity resurfaced in 2010 with the introduction of Tesla's Roadster, Mitsubishi's i-MiEV, and Nissan's Leaf models. Limitations of 200 km on a single charge and the number of public charging stations caused difficult decisions for the consumers.

The 3rd trend of popularity from the year 2017 until the present is caused by the problem of cumulative air pollution. The combustion of internal combustion engine vehicles has various polluting effects. Greenhouse gases, dust, and exhaust gases cause global warming and more severe disasters. The agreement in the Paris treaty (COP-21) to reduce greenhouse gas emissions by 20-25% by 2030, the advances in materials science technology development, and the better battery efficiency provoked the prevalence of the new electric vehicle popularity. Electric vehicles are expected to be sold at prices comparable to those of conventional cars in the same performance [1].

As a result, electric vehicle technology has been tremendously developed both in terms of related technology and usage patterns to meet user needs. In 2021, Rolls-Royce YASA and Electro-flight jointly developed the world's fastest electric aircraft at 480 km/h [2]. Besides, Spark Racing Technology company of China launched a Formula-E electric motor racing project with an increasing number of participants [3].

Recently, United Airlines has invested in United Airlines Ventures with Breakthrough Energy Ventures and Mesa Airlines in Heart Aerospace

company to develop a small electric-powered aircraft capable of carrying 19 passengers with several preorders in 2026 [4].

During the transition period, many automotive manufacturers focused on producing hybrid electric vehicles (HEVs) while gaining the advantages of both pure electric vehicles and traditional internal combustion engines. However, the noise and vibration produced during the HEV operation reduce the comfort of the passengers. They also cause stress, and fatigue, and adversely affect the drivers. The analysis of the noise and vibration of an HEV has been studied in 2022 [5].

In particular, competition in the automotive market is required to have a vehicle's acoustic and vibration dampening properties for optimal performance [6]. The analysis of vibration and sound signals has been previously performed for decades. The external and internal factors which affect the working conditions of the vehicles have been continuously studied.

Focusing on the external factors, several research have been conducted. In 2018, the environmental effects of the road surface types and conditions on the traffic flow management mode in the case of directive management have been investigated by Novikov et al., [7]. It has been found that there is a correlation between the friction coefficient and the capacity of the managed area resulting in the change of the traffic lights cycle, which is also corroborated by the conducted field experiment on a signalized intersection. Besides, an external factor affecting vehicle durability was studied by Hu and Zhong in 2019. A conventional finite element model for linear and nonlinear analysis for multibody full-vehicle-durability simulation was applied. Six different kinds of test road surfaces were conducted in the simulation, and the study concluded that the explicit–implicit co-simulation techniques are efficient and accurate enough for engineering purposes [8].

In addition, the interaction between the type and technical condition of road surfaces, dynamic vehicle loads, and the level of vibration propagated to the environment was studied by Czech in 2016 [9]. The study summarized that the type of road surface, the technical condition, and the varied dynamic vehicle loads explicitly affected the level of vibration propagated to the environment.

In 2019, the discomfort caused by vibration for three models of micro commercial vehicles running in four types of road conditions was studied by Huang and Li, since the main environmental stress of vibration affected the vehicles implicitly [10]. Furthermore, external factor analysis was conducted by Litak and his colleagues in 2008. They investigated the chaotic vibration which was the effect of critical Melnikov amplitude of the road surface profile to a quarter car model [11]. Moreover, Blekhman and Kremer also conducted a study of the effect of road unevenness on the dynamics of the averaged longitudinal motion of a vehicle in 2017 [12].

On the other hand, the internal factor analysis has been also studied. The studies of detection and diagnosis of the faults in rotating machinery have been tremendously pursued [13]-[15]. Investigating the associated signal processing for machine diagnosis in 2013, an amount of research on signal processing adaptation has been performed for fault diagnosis [14]. In 2012-2013, the discrete wavelet transform (DWT) was used with the vibration signal for the engine fault diagnosis of the diesel engine and the gearbox [14], [15]. The power spectrum analysis with high order, cepstrum analysis, and neural network approach was applied with fault diagnosis and an indication of some of the specific induction motors in 2013 [16]. Furthermore, the Fourier transform has been substantially utilized, for instance, the Fourier transform coefficients were adopted in the features of mel-cepstral HMM-based speech modeling for speech synthesis in 2009 [17]. Consequently, it was adapted to the correlation analysis of vibration and sound signals for a gasoline-engine car in 2020 [18]. Besides, in 2016 the power of signal analysis with less time consumption and a low computational cost was conducted in a comparative study of LPG-modified engines and regular oil-usage engines [19], and also in a fault diagnosis of rolling element bearings [20]. Moreover, the issue of gasoline substitution with LPG boiling system installation caused some significant variation in vibration and sound signals of the modified engines [21]-[24]. In addition, some analysis techniques of the vibration and sound signals were proposed to differentiate between the LPG-modified engine and the conventional gasoline engine, accordingly, some significant attributes were used to indicate the irregularities of the corresponding engines [25], [26]. In 2019, an internal factor study of vibration and sound signal analysis for a motorcycle and a gasoline engine with LPG installation and some specified fault simulations was investigated by Chomphan et al., LPG installation and the specified faults concretely affected the engine efficiency degradations [27], [28].

This paper applies engineering knowledge to study and analyze the vibration and sound of an EV car from one worldwide manufacturer of the FOMM ONE Y2018 model as depicted in Fig. 1. The analysis applies driving at six different engine speeds at three different positions within the passenger room to evaluate the quality of service comparatively. The measuring positions of vibration and sound are at the right front or driver's seat, the left front seat, and the rear seat, respectively.

Fig. 1 EV car of FOMM ONE Y2018 model.

A couple of principle purposes are to compare the vibration and sound signal attributes with three different measuring positions and different engine speeds. The Fast Fourier Transform (FFT) is adopted to extract the signal spectrum and the corresponding features in the analysis procedure [5], [18], [19], [28].

MATERIAL AND METHODS

In this section, electric vehicles have been generally explained in principle. The experimental procedure modified from the study in [5] has been illustrated step by step. Finally, the experimental setups have been therefore presented.

Electric Vehicles

This type of car uses only electric power to drive the whole body. The way a pure electric vehicle works is not as elaborate and complex as a petrol car. There are only three main driving components contributing to the efficiency of driving. These three components include a battery, an inverter, and an electric motor.

Experimental Procedure

The experimental procedure consists of a couple of consequential stages of data preparation and signal processing sub-procedures as depicted in Fig. 2. A brief explanation of the procedure is presented as follows.

Experimental Design

First of all, the experimental design process has been initiated. All experimental equipment includes an EV car of the FOMM ONE Y2018 model with a gross battery capacity of 11.84 kWh and the system power of 14 Hp, a number of vibration sensors and their peripheral devices, a condenser pre-polarized CCP free-field QC microphone with G.R.A.S. 40PP and its complementary parts, an NI 9234 module of National Instruments corporation with 4-channel, ±5V, 24-bit software-selectable IEPE, AC/DC analog input specifications, NI cDAQ-9171 USB chassis for interfacing with a computer, and a computational program for signal processing.

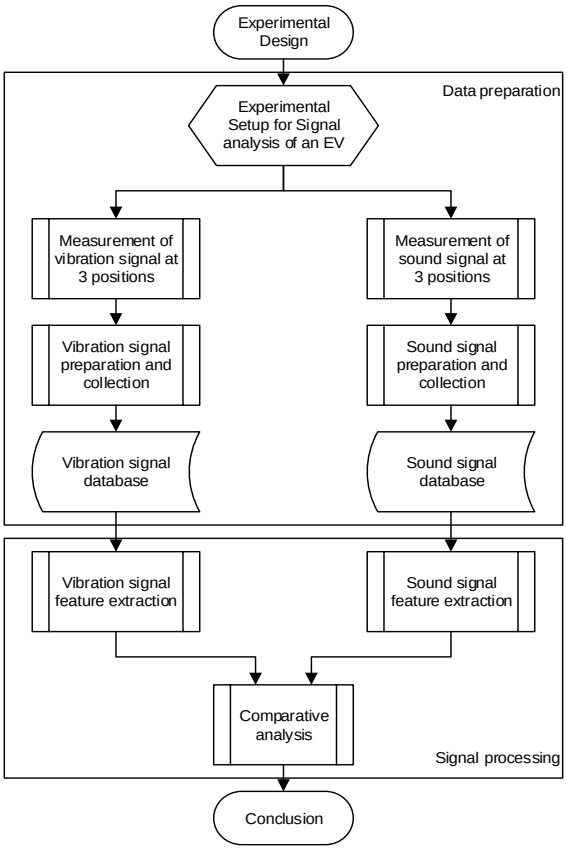

Fig. 2 Experimental Procedure.

Data Preparation

During the data preparation, the experimental setup is conducted to retrieve the vibration and sound signals simultaneously from the experimental car with six different numbers of engine speeds, i.e., 0, 10, 20, 30, 40, and 50 km/h. Thereafter, the measurement, preparation and collection, and database implementation are performed respectively.

Experimental Setup

The vibration and sound signal retrieving setups have been arranged during the experimental setup process. Three sets of high-frequency vibration sensors and a condenser microphone are allocated at different positions within the passenger room. The corresponding signals are then transferred into the processing computer through a group of NI interfacing cards.

The vibration sensors and the microphone are allocated at three positions including at the right front or driver's seat, the left front seat, and the rear seat. Three vibration sensor wires and the microphone wire are connected to the NI cards which are attached to the NI rack. The rack is also connected to the computer where the signals are retrieved into the Labview program.

Measurement of vibration (sound) signal at 3 positions

In the measuring process of signals of the EV car, three different positions are defined. All of the sensors apply the sampling frequency of 50,000 Hz. The signals are measured with 10 samples and 5-second periods of time at six different engine speeds of 0, 10, 20, 30, 40, and 50 km/h, respectively.

Vibration (sound) signal preparation and collection

The preliminary process of signal segmentation is performed after the signals arrive at the input ports through the Labview program. The collection of signals from all different sensor positions with all different engine speeds is categorized.

Vibration (sound) signal database

After signal categorization, a group of databases of the categorized signal is constructed. Three sets of categorization include the signals from the right front seat, the signals from the left front seat, and the signals from the rear seat. In each set, the signal portions are divided into six groups corresponding to each engine speed as mentioned in the previous section.

Signal Processing

At the signal processing, the feature extraction and comparative analysis are performed respectively.

Vibration (sound) signal feature extraction

The signal analysis technique of Fast Fourier transform has been applied to all of the portions of the signals for all groups within the database to obtain their corresponding frequency spectrum. From the output frequency spectrum, the most dominant peak appearing in the frequency domain is extracted. The frequency and magnitude at the peak are analyzed. Monitoring the frequency spectrum brings about some frequencies at the dominant peak points and their corresponding amplitudes. These highest peaks are assumed to represent the important components of the signal inherited from the movement of the EV. These extracted features are consequently utilized in the final process of the comparative analysis.

Comparative analysis

The extracted features are averaged among all corresponding samples. Several comparative analyses are conducted with different aspects. As for the first objective of position comparison, the corresponding features of vibration and sound signals at different positions of sensors are compared. Last but not least, the observation of the corresponding features of vibration and sound signals at different speeds has been conducted to achieve the second objective of speed comparison.

Conclusion

The interpretation of the output comparative analysis is performed. Finally, the discussion for all aspects has been completed.

EXPERIMENTAL RESULTS

In the signal feature extraction process, the FFT technique has been adopted to extract the significant features as described in the previous studies [5]. The extracted features are consequently utilized in the final process of the comparative analysis using the statistical averaging technique. The following bar charts are constructed and presented in this section.

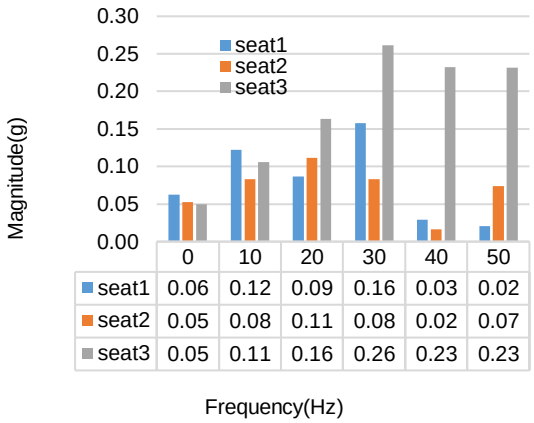

	0	10	20	30	40	50
seat1	0.06	0.12	0.09	0.16	0.03	0.02
seat2	0.05	0.08	0.11	0.08	0.02	0.07
seat3	0.05	0.11	0.16	0.26	0.23	0.23

Fig. 3 The averaged magnitude of the emerging peak of the frequency spectrum of the vibration signal measured at three distinct positions.

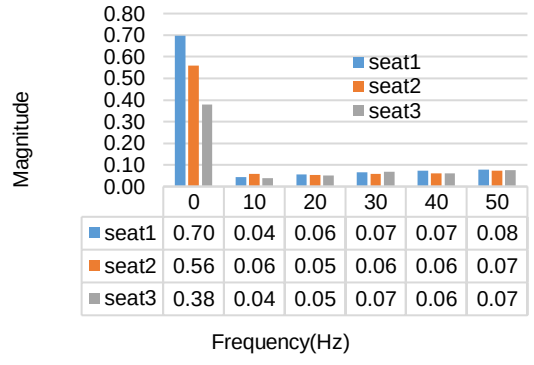

	0	10	20	30	40	50
seat1	0.70	0.04	0.06	0.07	0.07	0.08
seat2	0.56	0.06	0.05	0.06	0.06	0.07
seat3	0.38	0.04	0.05	0.07	0.06	0.07

Fig. 4 The averaged magnitude of the emerging peak of the frequency spectrum of the sound signal measured at three distinct positions.

As for vibration comparative analysis, the comparisons of the averaged magnitude of emerging peak of the frequency spectrum of the vibration signal measured at three different positions in gravitational acceleration unit (g) with different engine speeds are presented in Fig. 3.

As for sound comparative analysis, the averaged magnitude of the emerging peak of the frequency spectrum of the sound signal measured at three different positions with different engine speeds has been presented in Fig. 4.

From the experiment results, it can be observed from Fig. 3 that when the engine speed of the EV car is raised until reaching 30 km/h, the averaged magnitude of the emerging peak of the frequency spectrum of the vibration signal trends to increase accordingly for all three different positions. After that, the average magnitude gradually decreases. Moreover, comparing among three different positions, the averaged magnitudes of emerging peaks at the left-front seat (seat 1) are higher than those of the other positions for the first two speeds (0 and 10 km/h), meanwhile, the averaged magnitudes of emerging peaks at the rear seat (seat 3) are mostly highest than those of the other positions for the other four speeds (20 to 50 km/h).

On the other hand, it can be seen from Fig. 4 that when the engine speed of the EV car is raised from 10 km/h to 50 km/h, the averaged magnitude of the emerging peak of the frequency spectrum of the sound signal trends to increase accordingly for three different positions. The averaged magnitudes of emerging peaks at the standstill (speed of 0 km/h) are at the highest levels compared with those of other speeds for three different positions. Moreover, comparing among three different positions, the averaged magnitudes of emerging peaks at the left-front are mostly higher than those of the other positions, meanwhile, the averaged magnitudes of emerging peaks at the rear seat are mostly lowest than those of the other positions.

CONCLUSIONS

An analysis of vibration and sound signals of an electric vehicle at three different positions within the passenger room has been proposed. The locations of vibration sensors and microphones are at the left-front seat, the right-front seat, and the rear seat. The important frequency spectral features have been extracted for six different engine speeds, i.e., 0, 10, 20, 30, 40, and 50 km/h. As for the vibration analysis with positioning focus, the averaged magnitudes of emerging peaks at the left-front seat are higher than those of the other positions for the first two speeds (0 and 10 km/h), meanwhile, the averaged magnitudes of emerging peaks at the rear seat are mostly highest than those of the other positions for the other four speeds (20 to 50 km/h). As for the sound analysis, the averaged magnitude of the emerging peak of the frequency spectrum of the sound signal trends to increase accordingly for three different positions. The averaged magnitudes of emerging peaks at the standstill are at the highest levels compared with those of other speeds for three different positions. For further interest, the other popular types of electric vehicles and improved signal processing techniques will be studied.

ACKNOWLEDGMENTS

The related facilities were arranged by the members of the Mechanical System and Signal Processing research group. Besides, this research was supported by Kasetsart University, Faculty of Engineering at Sriracha.

REFERENCES

[1] Ribeiro F. N. D., Umezaki A. S., Chiquetto J. B., Santos I., Machado P. G., Miranda R. M., Almeida P. S., Simões A. F., Mouette D., Leichsenring A. R., Ueno H. M., Impact of Different Transportation Planning Scenarios on Air Pollutants, Greenhouse Gases and Heat Emission Abatement, Science of The Total Environment Journal, Vol. 781, 2021, 146708.

[2] Bolam R. C., Vagapov Y., Anuchin A., Review of Electrically Powered Propulsion for Aircraft, Int. Conf. International Universities Power Engineering Conference, 2018, pp. 1-6.

[3] Schoeggl, P., Haimann, A. Ress, L. Electrification in Motorsports, MTZ worldwide eMagazine, Vol. 73, 2012, pp. 4–11.

[4] Baumeister S., Leung A., Ryley T., The Emission Reduction Potentials of First Generation Electric Aircraft (FGEA) in Finland, Journal of Transport Geography, Vol. 85, 2020, 102730.

[5] Chomphan S., Contemplation of Vibration and Sound Signals of A Hybrid-engine Car. in Proc. Int. Conf. on Structure, Engineering & Environment, 2021, pp. 85-90.

[6] Liao L. Y., Zuo Y. Y., Liao X. H., Study on Hybrid Electric Vehicle Noise and Vibration Reduction Technology. Advanced Materials Research, Vol. 764, 2013, pp. 141-148.

[7] Novikov A., Novikov I., Shevtsova A., Study of the Impact of Type and Condition of the Road Surface on Parameters of Signalized Intersection, Transportation Research Procedia, Vol. 36, 2018, pp. 548-555.

[8] Hu H., Zhong Z., Explicit–Implicit Co-Simulation Techniques for Dynamic Responses

of a Passenger Car on Arbitrary Road Surfaces, Engineering, Vol. 5, Issue 6, 2019, pp. 1171-1178.

[9] Czech K. R., The Impact of the Type and Technical Condition of Road Surface on the Level of Traffic-Generated Vibrations Propagated to the Environment, Procedia Engineering, Vol. 143, 2016, pp. 1358-1367.

[10] Huang Y., Li D., Subjective Discomfort Model of the Micro Commercial Vehicle Vibration over Different Road Conditions, Applied Acoustics, Vol. 145, 2019, pp. 385-392.

[11] Litak G., Borowiec M., Friswell M. I., Szabelski K., Chaotic Vibration of a Quarter-Car Model Excited by the Road Surface Profile, Communications in Nonlinear Science and Numerical Simulation, Vol. 13, Issue 7, 2008, pp. 1373-1383.

[12] Blekhman I., Kremer E., Vibrational Resistance to Vehicle Motion Due to Road Unevenness, Journal of Sound and Vibration, Vol. 405, 2017, pp. 306-313.

[13] Yujun L., Peter W. T., Xin Y., Jianguo Y., EMD-Based Fault Diagnosis for Abnormal Clearance between Contacting Components in a Diesel Engine, Mechanical Systems and Signal Processing, Vol. 24, Issue 1, 2010, pp.193–210.

[14] Xia W., Changwen L., Fengrong B., Xiaoyang B., Kang S., Fault Diagnosis of Diesel Engine based on Adaptive Wavelet Packets and EEMD-Fractal Dimension. Mechanical Systems and Signal Processing, Vol. 41, Issue 1-2, 2013, pp. 581–597.

[15] Binqiang C., Zhousuo Z., Chuang S., Bing L., Yanyang Z., Zhengjia H., Fault Feature Extraction of Gearbox by using Over Complete Rational Dilation Discrete Wavelet Transform on Signals Measured from Vibration Sensors. Mechanical Systems and Signal Processing, Vol. 33, Issue 11, 2012, pp. 275–298.

[16] Liang B., Iwnicki S. D., Zhao Y., Application of Power Spectrum, Cepstrum, Higher Order Spectrum and Neural Network Analyses for Induction Motor Fault Diagnosis. Mechanical Systems and Signal Processing, Vol. 39, Issue 1-2, 2013, pp. 342–360.

[17] Chomphan S., Towards the Development of Speaker-Dependent and Speaker-Independent Hidden Markov Model-Based Thai Speech Synthesis. Journal of Computer Science, Vol. 5, Issue 12, 2009, pp. 905-914.

[18] Chomphan S., Wongchai B., Correlation Analysis of Vibration and Sound Signals of a Gasoline-Engine Car, International Journal of GEOMATE, Vol.18, Issue 67, 2020, pp. 195-201.

[19] Chomphan S., Chaimanatsakun A., Sakornsin R., Khumneungratavongsa S., Rattanarat K., A Comparative Study of LPG-modified Engine and Normal Oil-usage Engine. in Proc. Int. Conf. on Engineering and Applied Sciences, 2016, pp. 219-225.

[20] Akhand R., Upadhyay S. H., A Review on Signal Processing Techniques Utilized in the Fault Diagnosis of Rolling Element Bearings, Tribology International, Vol. 96, Issue 4, 2016, pp. 289-306.

[21] Ahmad T. A., Barat G., Teymour T. H., Seyed S.M., Vibration Analysis of a Diesel Engine Using Biodiesel and Petro Diesel Fuel Blends, Fuel, Vol. 102, Issue 12, 2012, pp. 414–422.

[22] Zunmin G, Jin C., Barry H., Analysis of Engine Vibration and Design of an Applicable Diagnosing Approach. International Journal of Mechanical Sciences, Vol. 45, Issue 8, 2003, pp. 1391–1410.

[23] Xianhua L., Randall R. B., Jerome A., Blind Separation of Internal Combustion Engine Vibration Signals by a Deflation Method. Mechanical Systems and Signal Processing, Vol. 22, Issue 5, 2008, pp.1082–1091.

[24] Xianhua L., Randall R. B., Blind Source Separation of Internal Combustion Engine Piston Slap from other Measured Vibration Signals. Mechanical Systems and Signal Processing, Vol. 19, Issue 6, 2005, pp. 1196–1208.

[25] Zbigniew S., Jan W., Application of Vibration Signals in the Diagnosis of Combustion Engines – Exploitation Practices. Journal of KONES Powertrain and Transport, Vol. 18, Issue 3, 2011, pp. 405-412.

[26] Carlucci A. P., Chiara F. F., Laforgia D., Analysis of the Relation Between Injection Parameter Variation and Block Vibration of an Internal Combustion Diesel Engine. Journal of Sound and Vibration, Vol. 295, Issues 1–2, 2006, pp. 141–164

[27] Chomphan S., Vibration Signal Analysis of a Motorcycle, International Journal of GEOMATE, Vol.16, Issue 56, 2019, pp. 27-32.

[28] Chomphan S., Kingrattanaset T., Boonsit S., Signal Analysis for LPG-modified Gasoline Engine with Engine Faults, International Journal of GEOMATE, Vol.16, Issue 56, 2019, pp. 65-72.

8th Int. Conf. on Structure, Engineering & Environment (SEE), Mie, Japan, Nov.10-12, 2022, ISBN: 978-4-909106094 C3051

CONSTANT VOLUME SHEAR TESTS ON COMPACTED SILTY SOIL UNDER CONSTANT WATER CONTENT CONDITION

Tufail Ahmad[1], Riko Kato[1] and Jiro Kuwano[1]

[1]Department of Civil & Environmental Engineering, Saitama University, Japan

ABSTRACT

Majority of the earth structures such as embankments, roadways, foundations, slopes and retaining walls are commonly built above the ground water table whenever possible, which implies that the soil used in construction of such structures is commonly unsaturated in nature. The behavior of unsaturated soil is less predictable as compared to saturated soil. Usually, triaxial tests are carried out on unsaturated soils at various net axial stress and matric suction under constant confining pressure. There is limited research regarding the constant volume, i.e., constant void ratio triaxial test on unsaturated soil. In this study a series of triaxial compression tests were performed under constant water content conditions using a double cell triaxial test apparatus. The samples were prepared with 80% degree of compaction and at optimum water content of 20%. All the soil specimens were consolidated isotropically under three different confining pressures of 100kPa, 300kPa and 500kPa before being sheared with constant volume. The soil specimen's volume was controlled by manually altering the cell pressure during the shearing phase (depending on the volume change measurement). A pre-shear infiltration test was also carried out to understand the influence of matric suction in unsaturated soil when sheared with constant volume. The results show that the normally consolidated specimen exhibit anomalous behavior of temporary sudden drop in axial stress within axial strain range of 0-2% which can be attributed to the collapse of soil particles held together by suction.

Keywords: Unsaturated soil, Constant water content tests, Constant Volume, Isotropic Consolidation, Axial strain

INTRODUCTION

For most of their lifespan, earthen structures and slopes that have been engineered remain in unsaturated state. In recent years, it has become clear that unsaturated soil mechanics can shed light on how compacted soils behave in a variety of situations, e.g., foundation engineering, retaining walls, earthen embankments and slopes, roads and pavements, mining engineering and underground pipelines [1-2]. In unsaturated compacted soils, the presence of matric suction can enhance the soil's shear strength and decrease its compressibility while also increasing the soil's effective stress. Additionally, suction helps to maintain larger void ratios and principal stress ratios at a given confining pressure [3]. Numerous experimental works have already been conducted to investigate the behavior of unsaturated soil [4-7].

Since rainfall and water infiltration are closely related to unsaturated slope failures, a thorough and in-depth seepage analysis is necessary to understand their behavior [8]. Both geotechnical and hydrological properties, such as the development of pore water pressure, rate of water infiltration and the rate of change in shear strength, which are influenced by a change in matric suction, are significant when studying the behavior of unsaturated slopes [9].

Usually, triaxial compression tests on unsaturated soils are carried out under unconfined, constant confining pressure (low or high) or constant matric suction conditions. There is limited research regarding the constant volume, i.e., constant void ratio triaxial test on unsaturated soil. This study investigates the mechanical behavior of unsaturated soil using triaxial tests executed with constant volume during shearing. Constant water content tests are carried out in this study to simulate sudden failure conditions in the field, and a pre-shear infiltration test is performed to simulate the condition and failure mechanism of a soil slope following a rainy period in which the soil above the water table has been wetted.

TESTING PROGRAMME

The physical properties of soil, specimen preparation, test apparatus and procedure will be discussed in this part.

Physical Properties of Soil

The fine soil used in this study is known commercially as DL Clay; it has low plasticity. The color of fresh, loosely deposited DL clay is yellowish-brown. DL clay is homogenous and easy to procure. It is classed as non-plastic silt (ML) by the USCS (Unified Soil Classification System) (ASTM D2487-11 2011) with 90% silt and 10% clay, and it has a larger grainsize than ordinary clay. This soil has a

uniform grain size distribution, with a mean grain size D50 of about 0.03 mm [10].

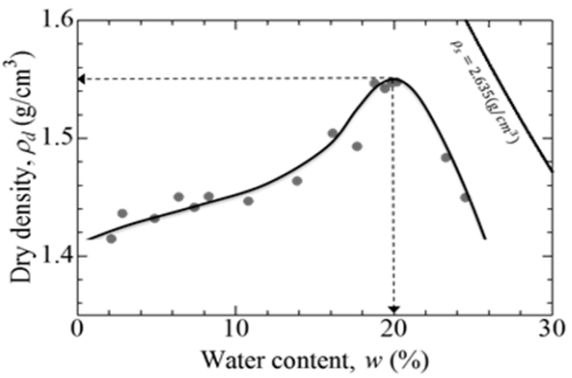

Fig. 1 Compaction Curve for the studied soil [11]

This soil is used because, at the same degree of saturation, it has a lower initial matric suction than kaolin clay. Table 1 and Fig.1 shows the physical properties and compaction curve of DL Clay.

Table 1 Physical Properties of DL Clay

Properties	Unit	Value
Specific gravity	g/cm^3	2.635
Percentage of fine content	%	99
Consistency	-	Non-Plastic
Maximum dry density, ρ_{dmax}	g/cm^3	1.55
Optimum water content	%	20

Specimen Preparation

To achieve a uniform density along the specimens' length, the soil was compacted in five layers, each being 2 cm thick, in a cylindrical mold with a diameter of 5 cm using a static compaction machine having a hydraulic jack [12]. The low energy of static compaction can provide a homogeneous density in the specimen, preventing the formation of a weaker zone [13]. Water was mixed with dry DL clay prior to compaction to make specimens at optimum water content of 20%. The samples were compacted to 80% degree of compaction and had a dry density of 1.24g/cm^3. During preparation, the specimen underwent a pre-consolidation pressure of about 210kPa and were initially 46.5% saturated with void ratio of about 1.125. All specimens had initial matric suctions of ≈19-20 kPa, indicating that the preparation steps were always meticulously followed to maintain a suction condition of about 20 kPa. All prepared specimens were 10 cm in height and 5 cm in diameter as shown in Fig. 2.

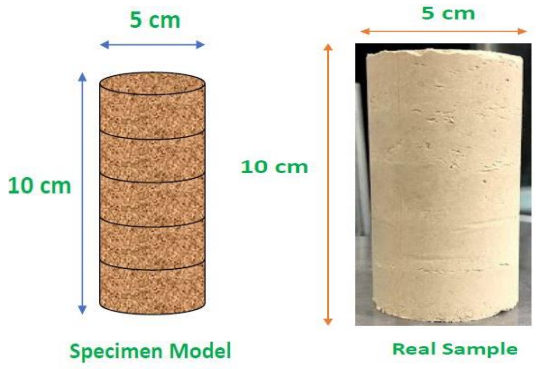

Fig. 2 Prepared Sample

Test Apparatus

Modern strain-controlled triaxial equipment suited for evaluating unsaturated soils was utilized for this research. It is comprised of a double cell, pore water pressure (PWP), cell pressure and pore air pressure (PAP) transducers. Loading system for exerting axial load, Low-Capacity Differential Pressure Transducer (LCDPT) to measure volume change, external Linear Variable Displacement Transducer (LVDT) to measure the vertical deformation of the specimens and a suitable computer application to track test sequence and record experimental results. The triaxial device is additionally coupled to a balance with an external load cell to quantify the amount of water drained or infiltrated into the specimen.

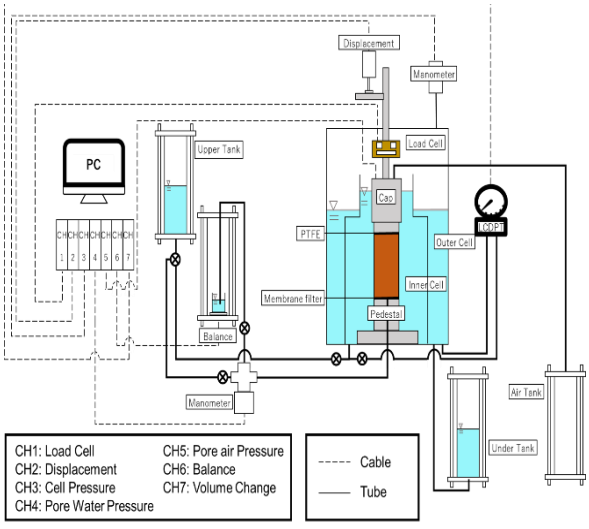

Fig. 3 Schematic Diagram of Triaxial Test Apparatus

Figure 3 depicts a schematic representation of the triaxial system employed in this study. The load cell along with all the transducers were properly

calibrated according to standards before commencing the experiments.

A thin membrane "Supor 450" and a Polytetrafluoroethylene (PTFE) sheet were used to effectively control and measure the pore water and pore air. The thin membrane was put on the bottom pedestal to allow water to flow while blocking the air passage [14]. It had a pore size of 0.45 µm, a thickness of 140 µm, and an air entry value of 250 kPa. The PTFE sheet was glued to the underside of the top cap to prevent water flow into the top cap (Fig. 4). To reduce the amount of air in the pore air drainage line, a solenoid-controlled exhaust air valve is also installed within the top cap.

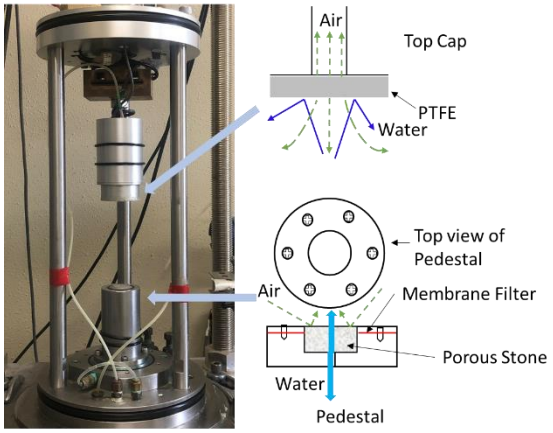

Fig. 4 Schematic of Top Cap and Bottom Pedestal

Test Procedure

The bottom pedestal was fully saturated before each test, so that no air bubble is trapped inside the porous stone of the pedestal. The suction pump was used to apply vacuum pressure to de-air the water in the exterior upper and lower tanks for at least 24 hours.

After the specimen was prepared, it was wrapped in a rubber membrane using a membrane holder and set over a pedestal with a thin membrane to measure the initial suction value. After measuring initial suction, the Axis translation technique (ATT) was carried to prevent formation of cavities inside the pedestal, which would ultimately affect the reading of pore-water pressure. To make pore water pressure zero, the pore air pressure and confining pressure were both increased at the same time, leaving the specimen volume unchanged [15].

During consolidation, the specimens were consolidated isotropically by applying the required net confining pressures of 100kPa, 300kPa and 500kPa, to get the sample to the desired state before shearing. The drain valve was kept open throughout the consolidation phase, to dissipate the excess pore water pressure. The axial stress was automatically controlled by the load control system to keep deviatoric stress (q) equal to zero.

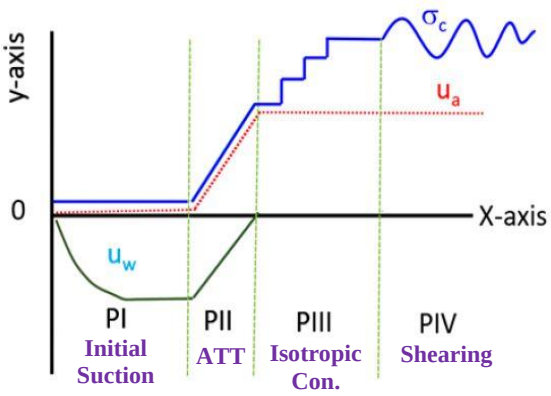

Fig. 5 Test phases involved

Figure 5 depicts the test stages involved in the current research. During shearing, the drainage valve for the pore water pressure was kept closed while the pore air pressure was continuously drained and controlled, and the soil specimens were sheared with constant void ratio (constant volume) at a strain rate of 0.05 mm/min under constant water content conditions. When fill materials are compacted in the field, the excess pore-air pressure that is developed during compaction will vanish instantly, while the excess pore-water pressure will dissipate over time. Constant water content test (CWC) can simulate this condition [16]. By adjusting the confining pressure in response to the specimen's volume change (i.e., reading of the LCDPT value), the sample volume was kept constant. The shearing phase was automatically terminated when the axial strain reached 15%, in accordance with standards of Japan Geotechnical Society "JGS 0527-2020".

For the pre-shear infiltration test, water in the soil sample was infiltrated through the waterline from the bottom pedestal, which was connected to a beaker and the pore water pressure transducer. The beaker was mounted on an external load cell and enclosed in a pressure chamber (balance). The rate of infiltration was regulated by varying the pressure of air applied on top of the water surface in the beaker [13], [17]. For this test, when isotropic consolidation was achieved after initial suction measurement and ATT, the matric suction value of the soil sample was reduced to 5kPa. This was accomplished by carefully applying infiltration pressure of 15kPa on the balance to increase the pore water pressure. When no further change in the flow of water entering the specimen was detected, the water infiltration step was completed. Following the infiltration stage, the pore water drainage valve was closed, and the specimen was subjected to shear under constant water content conditions.

TEST RESULTS

Up to a 15% axial strain, the sample was sheared at a rate of 0.05% per minute. The water drain valve was closed while the air drain valve was open so that the shearing could be done in constant water content conditions. The cell pressure was adjusted manually in accordance with the LCDPT value to keep the void ratio of sample constant, since the samples had to be sheared with zero volumetric strain. Fig. 6 shows the constant void ratio of samples maintained during shearing phase.

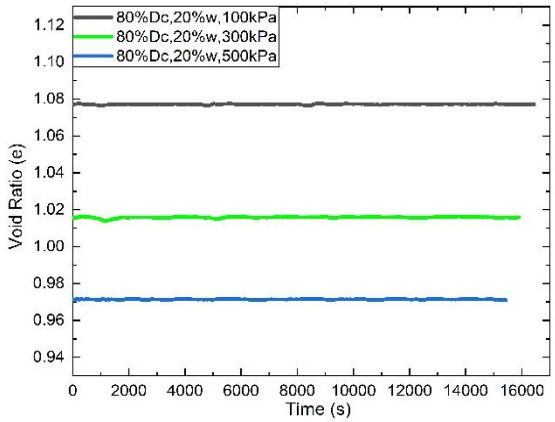

Fig. 6 Constant Void Ratio during shearing

Figure 7 shows the relationship between deviatoric stress and axial strain when sheared with constant volume. It can be observed that the deviatoric stress reaches a peak value within axial strain range of 0-2%, and then decreases afterwards exhibiting post peak behavior. The shear strength is greater for specimen consolidated under high confining pressure.

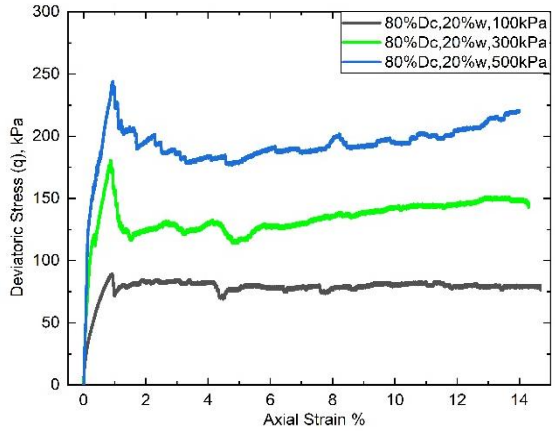

Fig. 7 Stress-Strain behavior

Figure 8 show that there is some peculiar behavior over an axial strain range of 0-2%. The effective stress gradually grows, then abruptly lowers, then gradually increases, and decreases again until the specimen reaches the critical condition. This phenomenon may be caused by the abrupt loading impact during shearing, which may cause the suction-held soil particles to quickly collapse and subsequently reorient. However, as the confining pressure is decreased the peculiar behavior is minimized as can be seen from the stress paths depicted in Fig. 9. It should be noted that the samples consolidated with 300 and 500kPa are normally consolidated as the confining pressure is greater than the pressure experienced during sample preparation while the sample consolidated with 100kPa is lightly over consolidated as the confining pressure is less than the pressure for sample preparation. The critical state line (C.S.L) has a slope of 1.3.

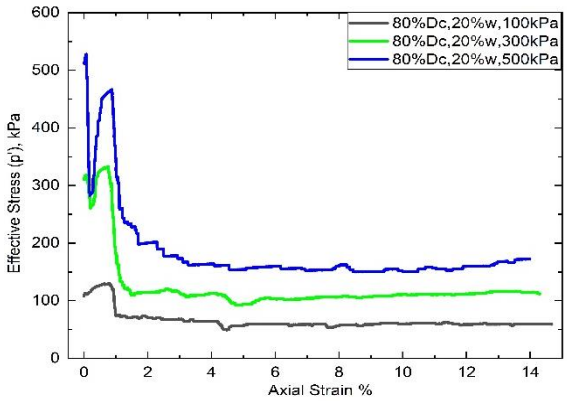

Fig. 8 Effective Stress Vs Axial Strain

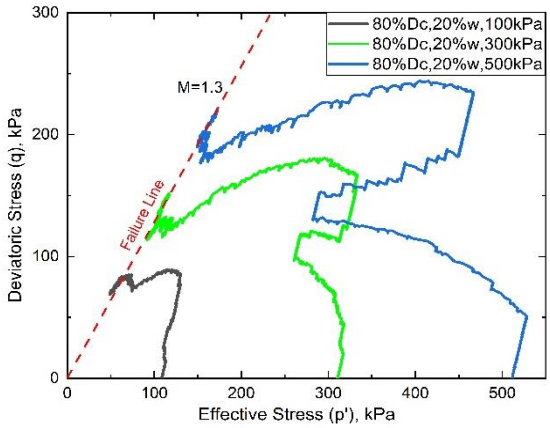

Fig. 9 Stress paths of specimen in CWC tests

Throughout the shearing phase, pore water and pore air pressure both reduced, as shown in Fig. 10. The drop in pore water pressure, however, was greater than the drop in pore air pressure. As a result, there was a modest rise in matric suction as well. Since the water drainage valve was closed and a fixed void ratio was kept during the testing, the degree of saturation of the samples remained almost constant throughout shearing.

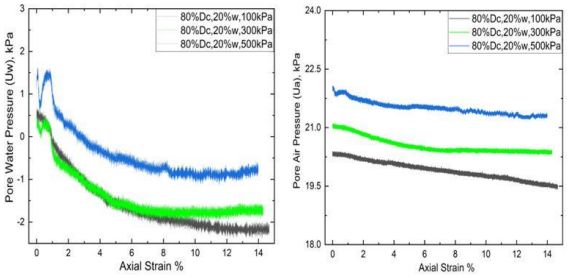

Fig. 10 Pore Air Pressure and Pore Water Pressure during shearing

To authenticate the suction-based assumption devised for the unusual behavior of effective stress during 0-2% axial strain range, a pre-shear infiltration test was carried out. This type of test replicates the state and mechanism of failure of a soil slope following a period of rain during which the soil above the water table undergoes a wetting process [12]. To reduce matric suction, the pore water pressure was increased prior to beginning the shear process. Attempts were made in a few early trial tests to infiltrate water into specimens without increasing the pore water pressure; however, only a little volume of water could be infiltrated into the specimens, which was not sufficient. As a result, water infiltration was conducted by lowering the matric suction (from 20kPa to 5kPa). This was attained by exerting 15kPa infiltration pressure on the balance. The volume of infiltrated water into the specimen was 23cm3 in a time of 3.5 hours when matric suction was reduced to 20kPa from 5kPa. The degree of saturation was increased from 46.5 to 77%.

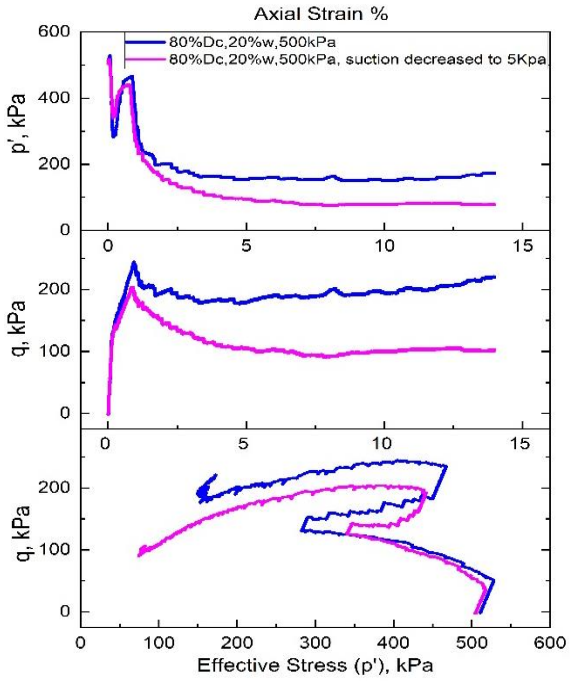

Fig. 11 Effect of water infiltration on stress-strain

It is evident from Fig. 11 that as matric suction reduces, so does the overall stiffness and strength. This is due to the effect of matric suction on inter particle contact forces, which tends to maintain the soil structure. However, with a decrease in matric suction it can be observed that the peculiar behavior within axial strain range of 0-2% has reduced. This phenomenon can be one of the reasons for the very sudden failure of slopes following an earthquake during a non-rainy period.

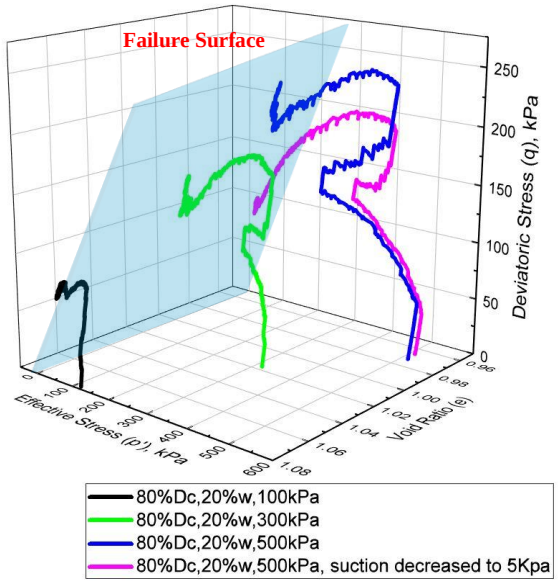

Fig. 12 Stress paths followed in p'eq space.

Figure 12 depicts a 3D illustration of the relationship between deviatoric stress, mean effective stress, and void ratio at failure. The state boundary surface (SBS) is formed by all of the stress paths lying on the same failure plane. SBS distinguishes between achievable and impossible stress states. It can also be noted that the constant volume test generates contour-like lines, which aid in determining the geometry of the state boundary surface.

CONCLUSIONS

In this study, constant volume shearing tests were carried out to explore the mechanical behavior of compacted silty soil under constant water content conditions. Following conclusions can be drawn from this study:

- To maintain constant volume of specimen during shearing, the cell pressure was adjusted manually corresponding to the change in volume indicated by LCDPT.
- The deviatoric stress reaches a peak value within axial strain range of 0-2%, and then decreases afterwards exhibiting post peak behavior. The effective stress also exhibits peculiar behavior

(increased and decreased twice) within axial strain range of 0-2%.

- The matric suction slightly increased during shearing due to decrease in pore water pressure.
- The overall shear strength decreased with decrease in matric suction. However, as matric suction reduces there is a drop in the peculiar behavior observed within axial strain range of 0-2%.
- Constant volume test present contour lines which help in defining the state boundary surface.

ACKNOWLEDGEMENTS

The Japanese Ministry of Education, Culture, Sports, Science and Technology (MEXT) is gratefully acknowledged for research facilities and financial assistance.

REFERENCES

[1] Kodikara, J., T. Islam, and A. Sounthararajah, Review of Soil Compaction: History and Recent Developments. Transportation Geotechnics, Vol. 17, Part B, 2018, pp. 24–34.

[2] Fredlund DG, Rahardjo H, Soil Mechanics for Unsaturated Soils. New York: John Wiley and Sons Inc., Soil Dynamics and Earthquake Engineering, Vol. 12, No. 7, 1993, pp. 449–450.

[3] Alonso, Eduardo E., Enrique F. Ortega Iturralde, and Enrique E. Romero, Dilatancy of coarse granular aggregates. Experimental unsaturated soil mechanics, Springer, Berlin, Heidelberg, 2007, pp.119-135.

[4] Rahardjo, H., Lim, T. T., Chang, M. F., & Fredlund, D. G., Shear-strength characteristics of a residual soil. Canadian Geotechnical Journal, Vol. 32, No. 1, 1995, pp. 60-77.

[5] Peters, S. B., Siemens, G., & Take, W. A., Characterization of transparent soil for unsaturated applications. Geotechnical Testing Journal, Vol. 34, No. 5, 2011, pp. 445-456.

[6] Li, L., and Zhang, X., A new triaxial testing system for unsaturated soil characterization. Geotechnical Testing Journal, Vol. 38, No. 6, 2015, pp. 823-839.

[7] Bagherieh, A. R., Baharvand, M., Meidani, M., & Mahboobi, A., Prediction of wetting-induced swelling using effective stress in an unsaturated kaolin. Iranian Journal of Science and Technology, Transactions of Civil Engineering, Vol. 43, No. 1, 2019, pp. 59-67.

[8] Yeh, H. F., Lee, C. C., & Lee, C. H., A rainfall-infiltration model for unsaturated soil slope stability. Sustainable Environment Research, Vol. 18, No. 2, 2008, pp. 271-278.

[9] Mahmood K, Ryu JH, Kim JM, Effect of anisotropic conductivity on suction and reliability index of unsaturated slope exposed to uniform antecedent rainfall. Landslides Vol. 10, No. 1, 2013, pp. 15–22.

[10] Chae, Jonggil, Byeongsu Kim, Seong-wan Park, and Shoji Kato., Effect of suction on unconfined compressive strength in partly saturated soils. KSCE Journal of Civil Engineering, Vol. 14, No. 3, 2010, pp. 281-290.

[11] Rasool, Ali Murtaza, and Mubashir Aziz, Advanced triaxial tests on partially saturated soils under unconfined conditions. International Journal of Civil Engineering Vol. 18, No. 10, 2020, pp. 1139-1156.

[12] Rasool AM, Kuwano J, Influence of matric suction on instability of unsaturated silty soil in unconfined conditions. International Journal of GEOMATE, Vol. 14, No. 42, 2018, pp. 1–7.

[13] Melinda F, Rahardjo H, Han KK, Leong EC, Shear strength of compacted soil under infiltration conditions, Journal of Geotechnical Eng. Div. ASCE, Vol. 130, No. 8, 2004, pp. 807–817.

[14] Habasimbi P, Nishimura T, Soil water characteristic curve of an unsaturated soil under low matric suction ranges and different stress conditions. International Journal of Geosciences, Vol. 10, No. 1, 2019, pp. 39-56.

[15] Hilf JW, "An investigation of pore water pressure in compacted cohesive soils" U.S. Department of Interior Bureau Reclamation Technical Memo. no. 654, 1956.

[16] Thu, Trinh Minh, Harianto Rahardjo, and Eng-Choon Leong, Critical state behavior of a compacted silt specimen. Soils and Foundations, Vol. 47, No. 4, 2007, pp. 749-755.

[17] Farooq, Khalid, Rolando Orense, and Ikuo Towhata, Response of unsaturated sandy soils under constant shear stress drained condition. Soils and foundations, Vol. 44, No. 2, 2004, pp. 1-13.

8th Int. Conf. on Structure, Engineering & Environment (SEE), Mie, Japan, Nov.10-12, 2022, ISBN: 978-4-909106094 C3051

NUMERICAL SIMULATION OF ENERGY EXTRACTION FROM A RESONATING RESERVOIR

Bang-fuh Chen, Hsing-nan Wu and Po-hung Yeh
Department of Marine Environment and Engineering, National Sun Yat-sen University, Taiwan

ABSTRACT

Wave energy harvest can be implemented through wave energy converters (WECs), including oscillating water columns (OWCs). Since the working mechanism of present paper bears resemlance to OWC, the possibility to garner energy from a resonant harbor is presented. Firstly, present study is carried out by a small-scaled 2D numerical wave tank, with a simulated downsized chamber which resembles a harbor reservoir attached to the end side. Second, the model in is validated by comparison with previous studies. The 3D model simulation where parametric settings and mesh layout are based on the results in 2D numerical calculation is performed. From experimental dimensional analysis and numerical prediction, it is indicated that the possible velocity inside the connecting channel can reach up to 1.44 m/s and can be used for future energy excavation.

Keywords: Energy harvest, Resonant harbor, numerical wave tank, OWC

INTRODUCTION

Of all types of sustainable energies that can be harnessed from the ocean, wave energy is estimated to have the most deposit [1]. That is the reason why the world has been turning more and more attention toward wave energy excavation. According to European Marine Energy Center Ltd., wave energy extraction can be classified into several types, which are attenuator, point absorber, oscillating wave surge converter, oscillating water column (OWC) and five others [2]. Each type, particularly OWC, has received more and more attention and researched these years due to the soaring demand for renewable energy worldwide. In present study, the possibility to extract energy from a resonant harbor is to be investigated. Although our current study doesn't analyze the aforementioned nine types directly, yet since the model in this paper bears a striking resemblance to an OWC, this present work will be availed of the similar research method used in other wave energy converters (WECs) to explore the energy acquisition from both resonant harbors and OWCs.

In contrast to other WECs, OWC has its advantages over others. Since most OWCs are built near the coast, the installation is less difficult, which also makes the upkeep easier. Besides, some OWCs serve to break waves. It is further estimated that 10%~60% of the wave energy can be collected. Morris-Thomas, Irvin and Thiagarajan disclosed that an increase in front wall submergence can reduce the hydrodynamic efficiency in short waves, and so can an increase in front wall thickness. The findings also reveals that the efficiency vaies with kh (k and h are wave number and wave elevation, respectively), with the average of 30%, and maximal efficiency being 70% [3]. In the work performed by Teixeira et al. (2013), 40%~50% of average energy capture ratio is reported [4].

However, regarding the front wall geometry, the study conducted by Tsai, Ko and Chen (2018) indicates that through a modified device, the incoming flow can form a U-type flow pattern inside the OWC, thus enhancing OWC's efficiency [5]. Also from [6], the turbine efficiency obtained by the new-generation turbine can reach up to 70%-80%.

From what is stated above, it is learned that the efficiency of wave energy transfer from progression to OWC, also considering the turbine energy capturing rate, may range from 20% to 30%. Moreover, Kuo et al. (2017) reported the hydrodynamic efficiency is less than 10%. On account that their chamber-orifice ratio was smaller, the efficiency in their research work was lower than others. As a result, to capture energy from the NDD connecting between the tank and the chamber is assumed to be the direct approach [7].

In the following sections, the simulated model is constructed to begin with, and the problem description is then made. Research methods is delineated afterwards, followed by some preliminary results and discussion. Lastly, concluding remarks are made in the last section.

RESEARCH METHODS

Model description

In view of the geometry being more complicated in present study, simplification of the harbor needs to be done in the first place to be fitted in the tank so as to further help conduct simulation. The constructed

model is exhibited in Fig. 1. The left region where the wave travels from left to right is analogous to the outer sea. The left-most boundary is likened to the wave maker. The upper in the left is atmosphere; the middle is the wave zone where the waves progress; the lower is the water body area. The chamber, representative of a simplified reservoir harbor, is in the right region.

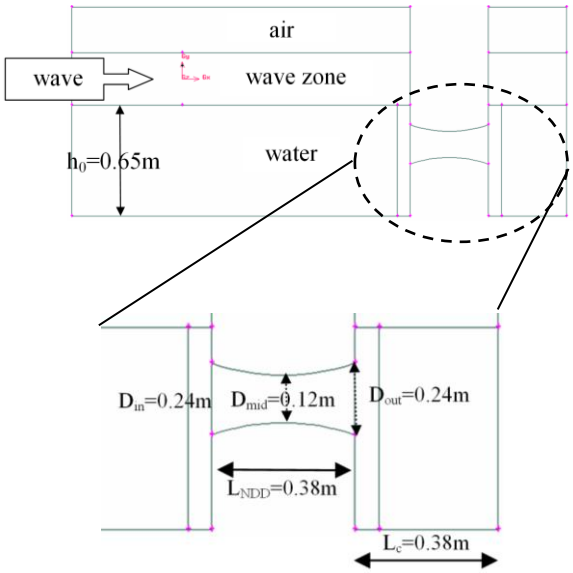

Fig. 1 (a) Schematic representation of simulation model; (b) magnified view at the end of the tank.

In principle, the atmospheric area is mainly occupied by air, and water body area is mainly water. Seeing that the waves propagate chiefly in the wave zone, the grids in this area are created more densely in particular. Meanwhile, the waves when traveling in this area are not made to be so large as to flood into or even out of the atmosphere area. The connecting channel is known as the nozzle-diffuser duct (NDD).

Fig. 2 Culverts serving as caisson breakwaters in connection with the ocean and the harbor

The device of NDD acts to simulate the culvert, shown in Fig. 2, where the current velocity flowing through this area can be augmented, so that the energy harvest can be achievable. Size of model components are also revealed in Fig. 1. The inlet diameter, central diameter, outlet diameter, total length, chamber length and water depth are denoted as D_{in}, D_{mid}, D_{out}, L_{NDD}, L_C and h_0, respectively.

The computational domain and mesh distribution in present study is displayed in Fig. 3. The far-view of the domain is shown in Fig. 3(a), while Fig. 3(a) is the magnified view of the front part near the piston-type wave maker, which is designated with a green arrow. The enlarged view of NWT's rear part is displayed in Fig. 3(b). Point A is where the virtual wave gauge is stationed; their respect positions are 10m and 20m away from the wave maker at the left side. Additionally, as illustrated in Fig. 3(c), a NDD, namely a nozzle-diffuser duct, is installed between the tank and the chamber to increase the pressure difference, thus accelerating the current speed. In doing so, the energy harvest can be possible.

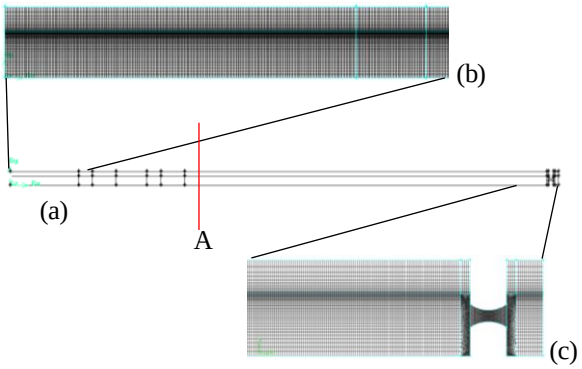

Fig. 3 (a) the computational domain. Point A (red line) is the location where virtual wave height meter is set up. The length of the numerical wave tank (NWT) is 40m. (b) Enlarged view near the front of the NWT. (c) Enlarged view near the rear part of the tank comprised of a chamber.

Governing equations

In present study, ANSYS Fluent, a commercial software in which computational fluid dynamics method is adopted, is utilized for numerical analysis. The two fundamental equations, listed in Eq.(1) and (2), are continuity equation and Navier-Stokes equations, respectively. The equations using SIMPLE algorithm are solved to obtain the velocity and pressure field. Second-order upwind method is employed in pursuit of better accuracy.

$$\frac{\partial \rho}{\partial t} + \rho \nabla \cdot \vec{U} = C \quad (3)$$

$$\rho \frac{D\vec{U}}{Dt} = \rho \vec{g} + \nabla \cdot \left[-p\vec{I} + \vec{\tau} \right] \quad (4)$$

The calculation is also coupled with volume of fluid (VOF) method in multiphase model, so the free surface is evaluated, and the wave height can be measured. During the computational procedures, turbulent model is applied as suggested in [8]. Thus in present research work, k-ε realizible model is adopted.

Wave-making theory

In present NWT simulation, the wave-making should be considered first and foremost. Wave-making methods are generally categorized into flat-type and piston-type. In 1960s, the relation between wave height H and flap-type wave maker stroke is expressed as Eq. (10).

$$\frac{H}{S}=\frac{\omega^2\cosh kh_0}{gk}=\frac{\int_0^h\left[1-y/h_0\right]\cosh k(h_0-y)dy}{\int_0^h\cosh^2 k(h_0-y)dy}=\frac{4\sinh kh_0}{kh_0}\frac{kh_0\sinh kh_0-\cosh kh_0+1}{\sinh kh_0+2kh_0} \quad (5)$$

, where k is the wave number, h_0 is the still water depth, with the velocity as a function of stroke S can be written in Eq. (6). [9]

$$U(y)=\frac{1}{2}S\omega\left[1-y/h_0\right] \quad (6)$$

For a small-amplitude wave, Dean and Dalrymple (1991) proposed that given the elevation $\eta=-a\sin(kx-\omega t)$, the wave maker's displacement with respect to time can be described as Eq. (7). [10]

$$\xi=-\xi_0\cos\omega t \quad (7)$$

, where $\xi_0=\frac{an_1}{\tanh kh_0}$, $n_1=\frac{1}{2}\left(1+\frac{2kh_0}{\sinh 2kh_0}\right)$, and h_0 is the still water depth. a is the wave amplitude, and ω is the angular frequency.

The foregoing expression pertaining to the displacement and time are revised to be Eq.(8) by Madsen (1970). [11]

$$\xi=\xi^{(1)}+\xi^{(2)}=-\xi_0\cos\omega t-\xi_0\left[\frac{a}{2h_0n_1}\left(\frac{3}{4\sinh^2 kh_0}\right)-\frac{n_1}{2}\right]\sin 2\omega t \quad (8)$$

Differentiating Eq.(8) yields Eq.(9).

In general, researchers often apply this velocity profile, namely Eq.(9), into the velocity inlet boundary condition incorporated with the continuity equation and the momentum equation to calculate the flow field [12]. Our current paper also follows suit to apply this velocity profile into the boundary condition, so that further physical quantities in the flow field can be obtained.

$$u=\frac{d\xi}{dt}=+\xi_0\omega\sin\omega t-2\omega\xi_0\left[\frac{a}{2h_0n_1}\left(\frac{3}{4\sinh^2 kh_0}\right)-\frac{n_1}{2}\right]\cos 2\omega t \quad (9)$$

Boundary conditions

The following boundary conditions provided by ANSYS Fluent are applied to execute the numerical calculation.

1. Moving wall: the moving wall acts as the piston-type wave maker positioned at the left side of the numerical wave tank (NWT). As mentioned in the previous section, the piston-type wave-making movement can be implemented by means of user-defined function (UDF) to be imported to the wall boundary condition. Noteworthy is that the moving mesh technique is required if piston-type or flap-type wave-making method is used. Nonetheless, if only stationary boundary is chosen, then velocity profile needs to be appended and instead of the moving boundary, which means moving mesh technique is not needed. In present study, piston-type movement is used, meaning that moving mesh technique is included.

2. Pressure outlet: This boundary condition is applied on top of the tank for the air be the outlet connected with the atmosphere, like it is set in the open-channel flow condition.

3. Wall: the left, right and bottom of the tank and the chamber (known as the reservoir/harbor) are set as walls. No physical quantities will penetrate through this boundary condition.

RESULTS AND DISCUSSION

Prior to more in-depth investigation, validation of current model is to be executed. Firstly, grid independence test has to be done. Afterwards, comparison between present research and previous studies are made to lay a foundation for forthcoming parametric analysis.

Grid independence test

Suggestions brought up in [13] by Lloyd, O'Doherty and Mason-Jones (2019) is referred to in the present grid independence test. Their criterion

outlines that the wave height spans at least 10 grid points. Besides, Dong and Huang (2004) also stated that time step size might as well be equaled to or less than $\Delta t/T \sim 0.001$. Their description is also taken into consideration in our present work.

The grid test outcome is presented in Fig. 4. Five different densities of grid number are used, which are named from Case A to Case F, with the mesh number being from 36458, 60391, 61657, 82941, 83656 and 115070 separately. From the figure, as the grid number increase, the data converge between Case D and Case E, with the difference being less than 2%. Therefore, the mesh number of 2D model in present work is set to range between 80000 and 100000 or so.

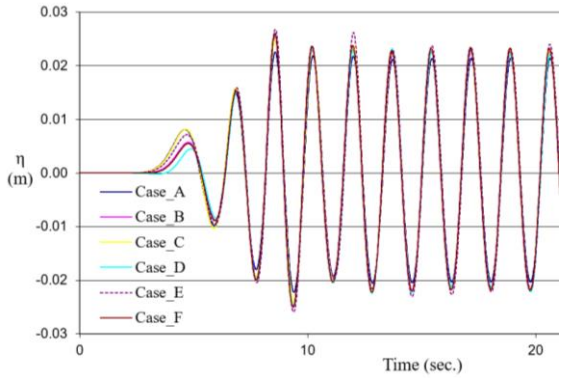

Fig. 4 Grid independence test (wave condition: water depth h_0=0.65m, T=1.73s, wave height H=4.76cm)

Validation

Posterior to the convergence test, validation with other studies is accomplished. First, comparison with analytical solution is made. The result is presented in Fig. 5. From the figure, an overall agreement is revealed, with the wave shape being basically overlapping. In terms of wave elevation, the result obtained in present research work approximates the analytical solution. The difference is less than 2%.

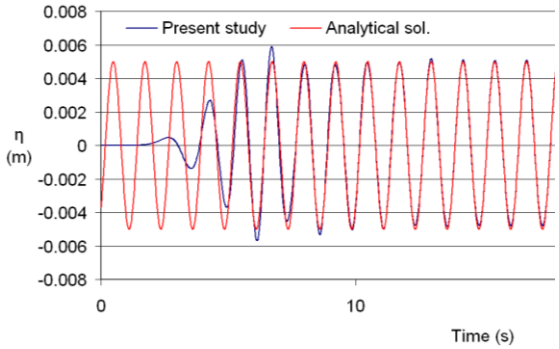

Fig. 5 Wave elevation η comparison with analytical solution (wave condition: water depth h_0=0.4m; T=1.25; wave height H=1cm)

Fig. 6 is the comparison between a previous study conducted by Dong and Huang (2004) and the current work. It is understood that a general tendency is observed despite some insignificant discrepancies, and that both datasets, using Stokes second-order terms, demonstrate the flattened trough due to nonlinear phenomenon.

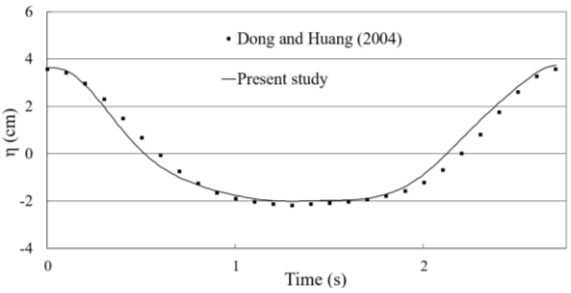

Fig. 6 Wave elevation comparison with Dong and Huang (2004) (wave condition: water depth h_0=0.38m, T=2.75, wave height H=5.7cm)

2D and 3D simulation comparison

After the validation, forthcoming exploration can be conducted. For starters, the actual size of Hualien Harbor is scaled down, and so is the wave condition dimensions. The original wave conditions are T=8.65s, h_0=16m, H=1.19m. After the scaling, the modified wave conditions become T=1.73s, h_0=0.65m, H=4.76cm. Downsizing the domain serves the purpose of comparing the present simulation result with the experimental data when future tank experiment is conducted. Once the comparison of both datasets is made, the in-situ measuring data can be predicted.

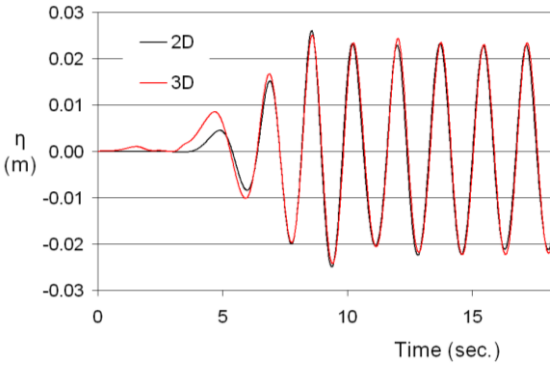

Fig. 7 Time history of wave elevation (0s-28s) at point A, sketched in Fig. 3. (Wave condition: T=1.73s; water depth h_0=0.65m; wave height H=4.76cm; flume length=40m.)

According to the aforestated wave conditions, 2D and 3D NWT simulations are carried out. For the reason that 3D simulation requires huge amounts of computational time, 2D result that is complete and

established serves to lay the benchmark for 3D calculation. As soon as 2D simulation converges, a 3D model can adopt similar grid layout in 2D as a reference to go on further analysis.

Fig. 7 presents the wave elevation comparison. Broadly speaking, the wave height of 2D and 3D are 4.51cm and 4.55cm individually, both of which show insignificant disparity of 5% and 4.4% in contrast with the actual observation value 4.76cm. From the figure, both 2D and 3D simulation data demonstrate a trend in agreement despite some discrepancy caused by the reflection from the wall on the right side.

Simulated velocity in central NDD

Once the data acquired from 2D and 3D simulation is validated, the simulation case of a 3D model is then performed based on the criteria set in 2D case. The velocity at the entrance and in the middle of NDD (namely the inlet and mid position in Fig. 8) is numerically calculated and obtained using high performance computing cluster since the mesh number exceeds more than 2 million, thus taking more time to run a case.

As shown in Fig. 9, where velocities in inlet and mid facets of NDD are exhibited, the simulation case is only executed 40 seconds (physical time) before the wave reflects from the reservoir (harbor). From the figure, one can observe the wave reaches the entrance of the NDD at around 15s, and the velocity inside the NDD attains the steady state after 25s. It is revealed that after 25 seconds the maximal velocity at the inlet of NDD is around 0.07 to 0.08 m/s, while the maximal velocity in the middle reaches up to 0.23 to 0.29 m/s. That is to say, the middle velocity is more than 3 times the inlet velocity. It is evident that the NDD has the function to accelerate the water current.

The average velocity magnitude during 3 periods from 30s to 35.25s is taken, the average is measured to be 0.16 m/s. When the use of Froude scaling, namely Eq.(10) is applied, the velocity in the center of NDD in actual ocean condition (V_{proto}) can be predicted.

$$\frac{V_{sim}}{V_{proto}} = \frac{\sqrt{L_{sim}}}{\sqrt{L_{proto}}} \qquad (10)$$

, where sim and proto stand for simulation and ocean prototype. Given V_{sim}, L_{sim} and L_{proto}, then V_{proto} can be obtained. The estimated values of V_{proto} are listed in Table 1.

Table 1 Estimated value of V_{proto}

	V_{sim}	L_{sim}	L_{proto}	V_{proto}
AVG	0.16m/s	0.65m	16m	0.79m/s
MAX	0.29m/s	0.65m	16m	1.44m/s

From Table 1, when the velocity is converted to the real situation in the coast caisson breakwater, the velocity ranges from 0.79m/s to 1.44m/s. In comparison with other current velocities in most locations worldwide running at the speed of 1 to 1.5 m/s, the site of NDD situated in the culvert acting as caisson breakwaters between the ocean and the harbor which is discussed previously can be a potential energy excavation place having stronger current velocities. That means future energy capture at this location can be seen possible.

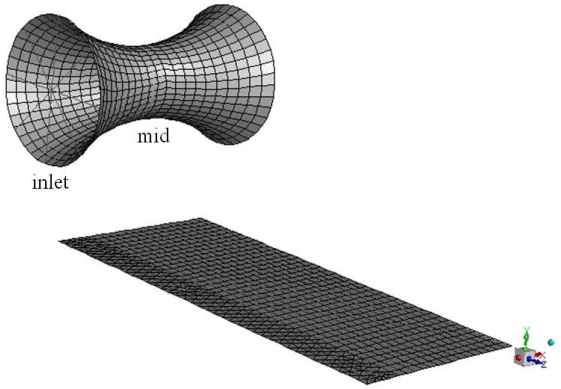

Fig. 8 Part of the facet mesh distribution near NDD in 3D model.

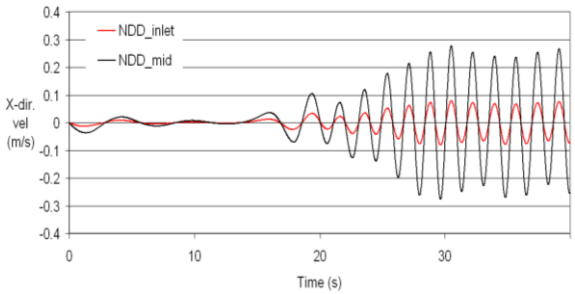

Fig. 9 Time history of current velocity at the entrance and in the middle of NDD (Wave condition: T=1.73s; water depth h_0=0.65m; wave height H=4.76cm; flume length=40m.)

CONCLUSIONS

After the the investigation is carried out numerically by a commercial software package, and also after the model case in present paper is validated by two different studies, it is known that the present model is reliable for future numerical prediction.

Also from what has been discussed, 2D simulation serves to set the mesh distribution benchmark for the 3D simulation case after 2D cases converge and are in line with 3D counterparts. It is then concluded that this carefully chosen 3D case is reliable enough gain good results and then executed by virtue of high-performance computing cluster as it

is computaionally costly. Further, it can be concluded that the channeling device, i.e. NDD, which acts as a connecting bridge between the tank (ocean) and the reseroir (harbor), functions to accelerate the current flow. The accelerated velocity can attain up to more than three times the original velocity. The estimated velocity in the center of NDD ranges from 0.79m/s to 1.44m/s. When compared with the general current velocity in the ocean at the speed of 1m/s, this makes the energy harvest from the culvert (casisson breakwater) feasible.

The result in present investigation has drawn the blueprint for future roadmap. The energy transmission efficiency through each component during wave propagation may be analyzed by virtue of wave incident and reflection, together with wave energy balance. Once the energy balance mechanism is established, the method can be broadly used to assess the efficiency of WECs as well as the installation possibility.

ACKNOWLEDGEMENTS

The authors would like to express their gratitude to the Ministry of Science and Technology for the kind financial support of Thousand Mile Horse Grant (Graduate Students Study Abroad Program) under the contract number 110-2917-I-110-003.

REFERENCES

[1] Ocean Energy Technology Overview, 2009 (can be accessed at http://large.stanford.edu/courses/2013/ph240/lim2/docs/44200.pdf)

[2] EMEC (European Marine Energy Center Ltd.), 2018. (can be accessed at http://www.emec.org.uk/marine-energy/wave-devices/

[3] Morris-Thomas M.T., Irvin R.J. and Thiagarajan K.P., An investigation into the hydrodynamic efficiency of an oscillating water column, Journal of Offshore Mechanics and Arctic Engineering, Vol. 129, Issue 4, 2007, pp. 273-278.

[4] Teixeira P.R.F., Davyt D.P., Didier E., Ramalhais R., Numerical simulation of an oscillating water column device using a code based on Navier-Stokes equations, Energy, Vol. 62, 2013, pp. 513-530.

[5] Tsai C.P., Ko C.H. and Chen Y.C., Investigation on performance of a modified breakwater-integrated OWC wave energy converter, Sustainability, Vol. 10, Issue 3, 2018. pp. 643-662

[6] Falcao A.F.O. and Henriques J.C.C., Oscillating-water-column wave energy converters and air turbines: A review, Renewable Energy, Vol. 85, 2016. pp. 1391-1424.

[7] Kuo Y.S., Chung C.Y., Hsiao S.C., and Wang Y.K., Hydrodynamic characteristics of Oscillating Water Column caisson breakwaters. Renewable Energy, Vol. 103, 2017, pp. 439-447.

[8] Thompson D.A., Karunarathna H. and Reeve D., Comparison between wave generation methods for numerical simulation of bimodal seas, Water Science and Engineering, Vol. 9, Issue 4, 2016, pp. 3-13.

[9] Ursell F., Dean R.G. and Yu Y.S., Forced small-amplitude water waves: a comparison of theory and experiment, Journal of Fluid Mechanics, Vol. 7, Issue 1, 1960. pp. 33-52.

[10] Dean R.G. and Dalrymple R.A., Water wave mechanics for engineers and scientists, Advanced Series on Ocean Engineering, Vol. 2, World Scientific, 1991. pp. 172-177.

[11] Madsen O.S., On the generation of long waves, Journal of Geophysical Research, Vol. 76, Issue 36, 1971. pp. 8672-8683.

[12] Dong C.M. and Huang C.J., Generation and Propagation of Water Waves in a Two-Dimensional Numerical Viscous Wave Flume, Journal of waterway, port, coastal and ocean engineering, Vol. 130, Issue 3, 2004. pp. 143-153.

[13] Lloyd C., O'Doherty T. and Mason-Jones A., Development of a wave-current numerical model using Stokes 2nd Order Theory, International Marine Energy Journal, Vol. 2, No. 1, 2019, pp. 1-14.

8th Int. Conf. on Structure, Engineering & Environment (SEE), Mie, Japan, Nov.10-12, 2022, ISBN: 978-4-909106094 C3051

DURABILITY PERFORMANCE OF CONCRETE INCORPORATING DIMENSION LIMESTONE WASTE AS FINE AGGREGATES REPLACEMENT

Jasmin M. Panganiban[1] and Mary Ann Q. Adajar[2]
[1]Faculty, University of Rizal System, Philippines;
[2]Faculty, De La Salle University, Philippines

ABSTRACT

Quarrying and production of dimension limestone produced a considerable amount of solid and slurry waste. Because of its great potential to be used as alternative material in concrete, these dimension limestone waste (DLW) have been the interest of many researchers. Several studies focus its investigation on the effect of DLW addition on concrete particularly on its mechanical properties. Although review of related literatures suggested the used of DLW in concrete because of its positive effect on concrete's mechanical properties, there still remains doubt on the its acceptability due to the lack of studies regarding its durability performance. Thus, this study aimed to assess the durability performance of concrete made with DLW as fine aggregate replacement. The investigation included test for sorptivity and resistance to sulfate attack using specimens with DLW replacements of level of 0%, 20%, 40% and 60%. Sorptivity test reveals that incorporation of up to 60% of DLW as sand replacement reduces the permeability of concrete. In terms of sulfate resistance, it was found that addition of DLW reduces length expansion and mass change due to sulfate attack. Furthermore, change in compressive strength test showed that after 15 weeks of sodium sulfate immersion, DLW concrete exhibited a less than 25% reduction in compressive strength. Based on the findings of this study, it has been concluded that replacement of sand by DLW can result to concrete having comparable durability performance.

Keywords: Durability performance, Sorptivity, Sulfate resistance, Limestone waste

INTRODUCTION

In a global scale, the construction industry is in great demand for raw materials particularly sand which is one of the component in making concrete. According to the United Nations Environmental Programme, the demand for sand has tripled over the last two decades as a result of the ballooning population, expanding urbanization, infrastructure development and ever-changing consumption patterns [1]. The estimated global sand consumptions have reached a volume of more than 20 billion tons annually, 75% of which is used in concrete production. Because of this huge consumption, many regions around the world is bound to face an increased rate of resource depletion.

In the Philippines, because of the current trend in infrastructure development, both public and private, the demand for fine aggregates or sand remains high and is expected to continuously grow. The country is rich in natural resource for raw materials such as river sand, stone and boulders, however over-exploitation of this non-renewable resources will eventually lead to its depletion causing sand scarcity in the country. The construction industry is therefore compelled to search for alternative for natural fine aggregate.

Similar to sand, dimension stone also has an increasing domestic and international demand. Limestone is one of the most used dimension stone by the construction industry. It is often cut into blocks and slab panel that are used for flooring, cladding, stair thread and many other applications. The quarrying and processing of these materials produced considerable amount of solid and slurry waste which are quite often left dumped in the quarry site. In one of the local manufacturing plant in the Philippines, it was reported that an average of 280 cu.m filtered sludge and 112 cu.m solid waste were collected every month. These wastes are considered a big problem from the aspects of disposal, environmental pollution, and health hazards. Given that we cannot totally reduce the amount of waste, neither at the quarrying stage nor at the dimension limestone production, the industry is therefore obligated to find a way to utilize these industrial wastes.

Useful application of solid waste particularly as substitute for fine aggregates in concrete is a promising solution to avoid severe problem associated with solid waste disposal and help construction industry in finding solution to the onset shortage of sand [2]. Earlier studies showed that limestone waste exhibits properties that is nearly comparable to that of the natural river sand [3]–[4]. Because of this, utilization of dimension limestone waste (DLW) as fine aggregate replacement becomes a viable solution to address the problem of both the

sand and dimension limestone industry.

Review of literatures on the properties of concrete with limestone concludes that, in general, incorporation of an appropriate amount of limestone as fine aggregate replacement enhances the compressive strength [4], flexural strength [3] and splitting tensile strength [5]. Several researchers have also reported that limestone aggregate could reduce the total shrinkage, water permeability and sorptivity coefficient of concrete [6]. Evaluation of sulfate resistivity, however, has contradicting results. Therefore, this study further investigated the durability performance DLW concrete exposed to sulfate-rich environment which is common in the Philippines being an archipelagic country where seawater is abundant. Specifically, this study aims to assess the effect of using DLW as fine aggregate replacement in the sorptivity and sulfate resistance of concrete. It is hoped that the result of this study will be a valuable input in the development of local standards to gain widespread acceptance and deployment of DLW concrete.

EXPERIMENTAL PROGRAM

Materials

DLW concrete test specimens were prepared using locally available materials. For cementitious materials, Ordinary Portland Cement Type 1, complying with PNS 7:2005, was used. Well graded crushed gravel with a maximum size of 20mm (3/4in) were used as coarse aggregates, while fine aggregates consist of a combination of sand and DLW. The mixing water were free from organic material and any deleterious minerals.

The DLW used as partial replacement for sand were dry limestone waste in slurry form collected from dump yard of a local dimension stone manufacturing plant and was sieved for particle size ranging from 75µm to 4.75mm. A comparative analysis of sand and DLW fine aggregate was conducted in terms of specific gravity, absorption and fineness modulus.

Properties of dimension limestone waste

The physical properties of DLW and sand were determined in accordance with ASTM test standards and the results are presented in Table 1. The specific gravity and absorption of DLW fall within the range for normal weight aggregates specified in ACI standard. The specific gravity of DLW is slightly lower whereas their water absorption is roughly 75% higher as compared with sand.

The particle size distribution of sand and DLW was measured through sieve analysis in accordance with ASTM C136. Figure 1 summarizes the gradation of DLW and sand. As shown in the figure, both sand and DLW exhibited a continuous grading. Sand shows a grading that fits within the limit whereas the fineness of DLW exceeded the upper limit set forth in ASTM C33. DLW has fineness modulus of 1.54 which is 37% lower compared to the 2.44 fineness modulus of sand, indicating that DLW is a finer material compared to sand. Based on ASTM C33, the fineness modulus of fine aggregates generally ranges from 2.0 to 3.3. In some cases, however, aggregates with fineness modulus less than 2.0 are used, an example of which is manufactured fine aggregates which contains finer natural sand [7].

Table 1 Physical properties of fine aggregates

Property	DLW	Sand
Specific Gravity (SSD)	2.58	2.72
Absorption (%)	1.42	0.81
Fineness Modulus	1.54	2.44

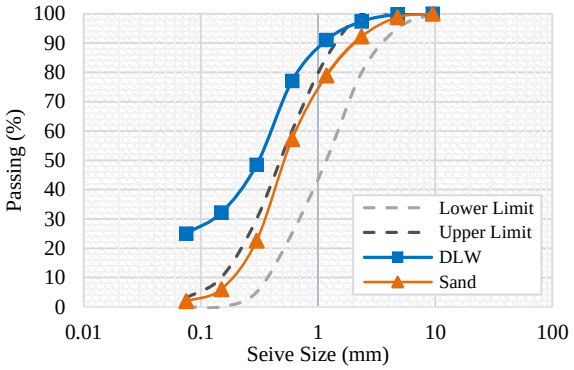

Fig. 1 Particle size distribution curves

Mix Proportion

A total of four (4) concrete mixtures were used in order to evaluate the effect of dimension limestone waste as sand replacement on the durability performance of concrete. Design mix proportion of concrete without DLW, designated as C-L0, as per ACI specification for a target strength of 20 MPa normal weight concrete and slump in the range of 50-90mm were used as reference or control mixture. DLW concrete mixtures were then determine by partially replacing sand with DLW. The replacement level investigated were 20%, 40% and 60% by weight thus each DLW concrete mixture were correspondingly designated as C-L20, C-L40 and C-L60, respectively. In all four mixes, no chemical admixture has been added and the water-to-cement ratio used was 0.65. Except for the ratio of dimension limestone waste and sand, the amount of other materials such as cement, coarse aggregate and mixing water were kept constant.

Preliminary tests were conducted to pre-assessed

if the design mix are suitable for the experimental program. Initial compressive strength test has been carried out on C-L0 mixture to determine if the design strength of 20MPa were achieved after 28 days of curing. Simultaneously, slump test for C-L60 were also conducted to check if the workability is within acceptable limit. After the initial test, resulting to C-L0 having achieved the design strength and C-L60 yielding slump above tolerance level of 25mm, the design mix proportions were adopted for the purpose of this study. Table 2 summarizes the details of the concrete mix proportion used.

Table 2 Details of concrete mix proportion

Mix Proportion in kg/m3				
Material	C-L0	C-L20	C-L40	C-L60
Cement	316	316	316	316
Gravel	1007	1007	1007	1007
Sand	853	682.4	511.8	341.2
DLW	0	170.6	341.2	511.8
Water	205	205	205	205

Methodology and Test for the Study

Durability of DLW concrete in terms of sorptivity and sulfate resistance was evaluated through series of laboratory experiments in accordance to ASTM standard. For each durability test, five replicate samples per mixture were tested.

To determine the sorptivity e, the standard test method in accordance with ASTM C1585 was followed. The test was carried out on concrete specimens having diameter of 100 mm and height of 50 mm after 28 days and 90 days curing period.

Sulfate resistance of DLW concrete was evaluated in terms of change in length, mass and compressive strength. For change in mass and compressive strength, 100mm concrete cube specimens were fabricated while for length change evaluation, 25mm by 25mm by 285mm mortar prism specimens were used as established by ASTM C157M. After the initial 28-day curing, each concrete specimens were subjected to sulfate attack by immersing it in a sodium sulfate solution with a concentration of 5% by mass. The volume proportion of sulfate solution to concrete specimens was maintained at 4±0.5 to ensure full immersion. The sulfate solution was stirred every week and replenished each month to maintain same concentration throughout the study.

Compressive strength test in accordance with ASTM C39 was performed on concrete cube specimens at the end of 28 days curing period and after 2, 4, 8, 13 and 15 weeks of sulfate immersion. Concurrently, for a set of concrete cube specimens, weight in saturated surface dry condition were measured and recorded as basis for mass change evaluation. Parallel to this, length change measurement of mortar prisms specimens was carried out in accordance with ASTM C1012. The initial length measurement was taken before sulfate immersion and then length change measurement was taken after 1, 2, 3, 4, 8, 13, 15, 19, 24 weeks of sulfate immersion.

TEST RESULTS AND DISCUSSION

Sorptivity

Durability of concrete is largely dependent on its ability to absorb water. Soptivity is widely used to characterize the concrete's ability to absorb water and transmit it via capillary action. It provides indications of pore structure and connectivity which is an important factor that influences the concrete's resistance to attack of aggressive substance when exposed to severe environment [8]. Increased sorptivity potential can lead to rapid concrete deterioration. Figure 2 presents a typical absorption curve of DLW concrete.

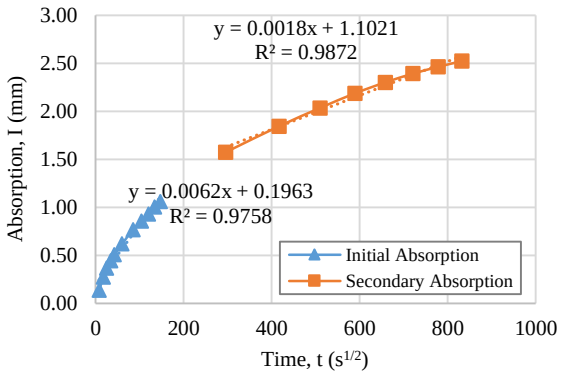

Fig. 2 Typical absorption curve of DLW concrete (C-L20 at 90 days)

Notice that absorption was more intense during the first 6 hours of the test, and then tends to gradually decreases afterwards. The rate of absorption during the first 6 hours is known as the initial sorptivity which is equal to the slope of the line that is the best fit to absorption plotted against the square root of time and was determined through linear regression analysis using all the points from 1 minute to 6 hours. On the other hand, the secondary sorptivity was taken as the slope of the line that best fitted the plot of absorption versus square-root of time using all points from day 1 to day 8.

The results of sorptivity tests are summarized and illustrated in Figure 3. Comparison of the results recorded at test age of 28 and 90 days shows that the addition of DLW generally reduces the sorptivity values. At 28 days, concrete with 20%, 40% and 60% DLW exhibits 27%, 20% and 17% reduction, respectively, in initial sorptivity as compared to control concrete. For secondary sorptivity, 14% and

10% reduction were observed for replacement level of 20% and 40%, respectively, which is contrary to the 32% increase noticed when replacement level is 60%. At 90 days testing age, the effect of DLW on sorptivity is more defined. A consistent reduction in both initial and secondary sorptivity with increasing DLW content was observed. The initial sorptivity of all mixes are comparable, with C-L60 having a slightly noticeable reduction of 9%. In terms of secondary sorptivity, 19%, 20% and 28% reduction relative to control concrete was recorded when replacement level is 20%, 40% and 60%, respectively. The reduction in sorptivity was more pronounced in the 20% replacement level at 28 days and 60% replacement level at 90 days. It is important to note that, all concrete mixes are considered acceptable in terms of sorptivity property since any value less than 0.10 mm/s$^{1/2}$ indicates an excellent quality concrete.

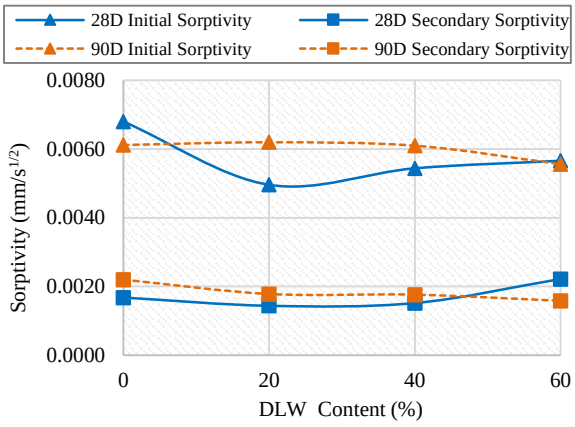

Fig. 3 Sorptivity of DLW concrete

Through Analysis of Variance, an overall look at the sorptivity results reveals that there is no significant variation in both initial and secondary sorptivity values due to percent replacement and curing period. The variation, however small, indicates that incorporation of up to 60% DLW as sand replacement improves the sorptivity. The improvement signifies a denser concrete microstructure making them more impermeable compared to control concrete. This could be attributed to the filler effect of the much smaller and finer particles of DLW blocking the interstitial and capillary pores of the binder phases of the mixture [9].

Resistance to Sulfate Attack

Sulfate resistance is one of the main concerns in terms of durability performance of concrete containing limestone. It has been previously reported that addition of limestone in concrete resulted to its poor performance under sulfate exposure. Some studies confirmed that expansion of concrete increased significantly when limestone is incorporated while other scholars found that the presence of limestone improves sulfate resistance [6]. Results of sulfate resistance evaluation of DLW concrete are hereby presented.

Change in length

The resistance to sulfate attack is commonly evaluated through expansion measurements. Figure 4 presents the average expansion of 5 mortar bars immersed in sodium sulfate solution measured after 1, 2, 3, 4, 8, 13, 15, 19 and 24 weeks of immersion as per ASTM C1012. During the test, increased expansion was observed in all mortar samples. Considering the expansion after 6 months, all tested mixes expanded less than the ACI stipulated expansion limit of 0.10%. Among the studied mixes, control samples exhibited the highest expansions.

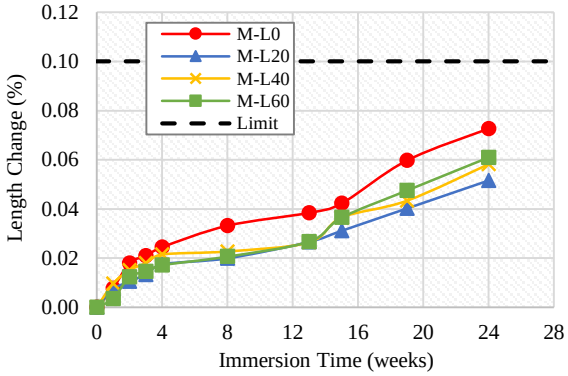

Fig. 4 Length change of DLW mortar prism

Statistical analysis revealed a significant decrease in length change between each DLW mortar samples and control samples. The percent decrease in length change were 29%, 19.9% and 16% for M-L20, M-40 and M-60, respectively. This indicates that incorporating DLW does in fact reduces the length expansion caused by sulfate attack. Nevertheless, it is important to note that although samples prepared with DLW have expanded less than the control concrete, expansion increases as the amount of DLW increases. This is because adding limestone in higher quantity increases the calcite content which also increases the possibility of ettringite and gypsum formation that leads to length expansion [10].

Change in mass

Mass loss is another indicators of concrete deterioration. The curve shown in Fig. 5 presents the percent change in mass measured after immersing concrete cube sample in sodium sulfate solution for a period of 1, 2, 3, 4, 8, 13, and 15 weeks. All samples demonstrate a similar trend. In the first week of immersion, a slight drop in mass was observed, then followed by a gradual increase in the subsequent

immersion time. The initial drop in mass can be attributed to the leaching of hydration products into the solution while the succeeding increase in mass was caused by the formation of expansive compound during the sulfate attack [11].

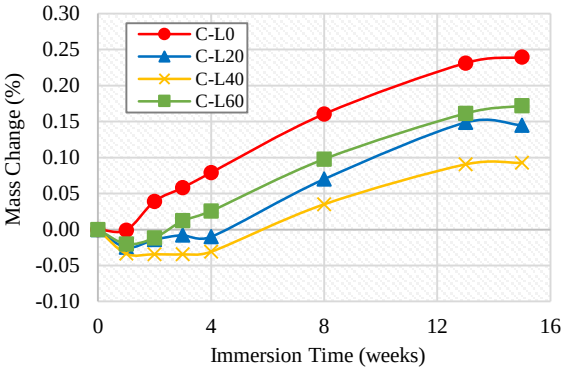

Fig. 5 Mass change of DLW concrete

ANOVA showed a significant difference in mass change of DLW concrete and control concrete. The concrete incorporated with DLW showed a lower mass change at the increasing stage compared with control concrete. After 15 weeks of exposure, mass increase was 39.5% lower for C-L20, 61.3% for C-L40 and 28.1% for C-L60. By inspection, concrete with 40% DLW has more pronounced effect in reducing mass change. Though the change in mass is relatively small, the resulting increase in mass indicates a formation of expansive compounds due to continuous exposure to sulfate. Evidently, from the mass and length change test, concrete incorporated with DLW has improve resistance to sulfate attack. This can be attributed to the effective reduction in sorptivity due to the filler effect of DLW. The reduced sorptivity decreases the change of sulfate ions ingress inside the hydrated cement matrix which consequently improves the resistance to sulfate attack.

Change in compressive strength

Prior to sodium sulfate immersion the average 28th day compressive strength was determined and the results are shown in Table 3. The compressive strength of all mixes satisfactorily exceeded the designed value of only 20MPa. Furthermore, it is obvious that as the DLW content increases, compressive strength gradually increases until the maximum compressive strength was developed at a replacement level of 40%. On the other hand, even though concrete specimen containing 60% DLW presents a compressive strength lower than the maximum recorded value, its compressive strength is still higher than the control specimen.

The compressive strength of concrete after immersion in sodium sulfate solution for a period of 2, 4, 8, 13, and 15 weeks were also determined and the corresponding change in compressive strength were recorded. As depicted in Fig.6, all concrete mix experienced a continuous compressive strength development in the first 8 weeks of exposure to sodium sulfate solution. After that, decrease in compressive strength related to increase in immersion time was observed. It can therefore be concluded that sulfate attack affects the compressive strength of concrete whether or not DLW were incorporated, particularly when exposed for a longer duration. The initial development of compressive strength even after sulfate exposure may be attributed to the continuous formation of hydration products and the formation of expansive product from the reaction of sulfate ions with hydrated cement components [11]. As this reaction product was formed, it filled the pores and strengthened the concrete. But, later on, when the formation of expansive product becomes more dominant, it induced cracking, spalling and loss of strength.

Table 3 Compressive strength of DLW concrete

Sample ID	% DLW	28th-day Compressive Strength (MPa)
C-L0	0	24.84
C-L20	20	25.00
C-L40	40	27.59
C-L60	60	27.03

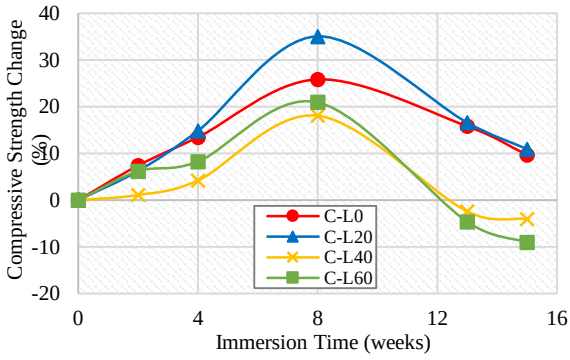

Fig. 6 Compressive strength change of DLW concrete due to sulfate attack

At the end of testing, 15 weeks after immersion, C-L0 and C-L20 maintained a compressive strength 9.7% and 10.9% higher, respectively, compared to their respective compressive strength prior to immersion. On the other hand, mixture with 40% and 60% DLW substitution rate showed an initial compressive strength reduction of 2.4% and 4.6%, respectively, after 13 weeks of exposure. After 15 weeks of exposure, C-L40 and C-L60 retained only 96% and 91% of their compressive strength prior to immersion, respectively. Considering the 25% limit in strength loss recommended by Mehta [12] for sulfate resistance concrete, it can still be concluded

that all concrete mixes exhibited good performance on sulfate resistance despite the observe decrease in compressive strength change.

CONCLUSIONS

Durability performance measures the concrete ability to resist the damaging effect of weathering, chemical attack and other deterioration process. In this study, the effect of utilizing DLW as fine aggregates in durability performance of concrete was investigated through examination of sorptivity and resistance to sulfate attack. Based on the finding of this study the following conclusions were established.

Replacement of sand by DLW shows good durability potential. In terms of sorptivity, it was concluded that incorporating up to 60% DLW fine aggregates slightly improved the permeability of concrete. All DLW concretes has sorptivity values less than 0.10 mm/s$^{1/2}$, hence DLW concretes can be classified an excellent quality concrete in terms of sorptivity.

The reduced sorptivity of DLW concrete gives way to the improvement of its resistance to sulfate attack. In terms of expansion, significant decrease in length change was observed in all DLW concrete as compared to the control concrete. Similarly, all DLW concretes showed lower mass change compared with control concrete. With regards to compressive strength loss, 20% DLW concrete retained a compressive strength higher than control concrete while a slight reduction in compressive strength was observed in 40% and 60% DLW concrete. Generally, it was inferred that DLW concrete has better sulfate resistance than conventional concrete. This was particularly evident from the evaluation results of length and mass change after immersion in sulfate solution.

Hence, based on the test results it can be concluded that dimension limestone waste (DLW) can be used as sand replacement to produced concrete with improved durability performance, reduce depletion of our non-replenishable aggregate deposits and alleviate environmental problems associated with DLW disposal. However, appropriate ratio of DLW replacement must be considered in order to achieve an optimum durability performance without any detrimental effect on strength and workability. SEM-EDX analysis of DLW concrete before and after sulfate exposure is recommended to get an idea about the reactive products formed due to exposure. Furthermore, other durability parameters such as chloride permeability, carbonation resistance and corrosion resistance should also be investigated.

REFERENCES

[1] Gallagher, L and Peduzzi, P., Sand and Sustainability: Finding New Solutions for Environmental Governance of Global Sand Resources, United Nations Environment Programme, 2019.

[2] Adajar, M. A. Q., de Guzman, E., Ho, R., Palma Jr, C., and Sindico, D., Utilization of Aggregate Quarry Waste in Construction Industry, GEOMATE Journal, Vol. 12, Issue 31, 2017, pp. 16-22.

[3] Chouhan, H. S., Kalla, P., Nagar, R., and Gautam, P. K., Gainful Utilization of Dimensional Limestone Waste as Fine Aggregate in Cement Mortar Mixes, Construction and Building Materials, Vol. 221, 2019, pp. 363-374.

[4] Bederina, M., Makhloufi, Z., Bounoua, A., Bouziani, T., and Quéneudec, M., Effect of Partial and Total Replacement of Siliceous River Sand with Limestone Crushed Sand on the Durability of Mortars Exposed to Chemical Solutions, Construction and Building Materials, Vol. 47, 2013, pp. 146-158.

[5] Omar, O. M., Abd Elhameed, G. D., Sherif, M. A., and Mohamadien, H. A., Influence of Limestone Waste as Partial Replacement Material for Sand and Marble Powder in Concrete Properties, HBRC Journal, Vol. 8, Issue 3, 2012, pp. 193-203

[6] Wang, D., Shi, C., Farzadnia, N., Shi, Z., and Jia, H., A Review on Effects of Limestone Powder on the Properties of Concrete, Construction and Building Materials, Vol. 192, 2018, pp. 153-166.

[7] ACI Committee E701, "Aggregates for Concrete", ACI Education Bulletin E1-16, 2016.

[8] San Nicolas, R. V. R., Walkley, B., & van Deventer, J. S. J., Fly Ash-Based Geopolymer Chemistry and Behavior, Coal Combustion Products, 2017, pp. 185-214.

[9] Githachuri, K., and Alexander, M. G., Durability Performance Potential and Strength of Blended Portland Limestone Cement Concrete, Cement and Concrete Composites, Vol. 39, 2013, pp. 115-121.

[10] Tosun, K., Felekoğlu, B., Baradan, B., and Altun, İ. A., Effects of Limestone Replacement Ratio on the Sulfate Resistance of Portland Limestone Cement Mortars Exposed to Extraordinary High Sulfate Concentrations, Construction and Building Materials, Vol. 23, Issue 7, 2009, pp. 2534-2544.

[11] Tang, Z., Li, W., Ke, G., Zhou, J. L., and Tam, V. W., Sulfate Attack Resistance of Sustainable Concrete Incorporating Various Industrial Solid Wastes, Journal of Cleaner Production, Vol. 218, 2019, pp. 810-822.

[12] Ghafoori, N., Diawara, H., and Beasley, S., Resistance to External Sodium Sulfate Attack for Early-Opening-To-Traffic Portland Cement Concrete, Cement and Concrete Composites, Vol. 30, Issue 5, 2008, pp. 444-454

8th Int. Conf. on Structure, Engineering & Environment (SEE), Mie, Japan, Nov.10-12, 2022, ISBN: 978-4-909106094 C3051

RECYCLING OF FISHERY WASTE AS PLANTING BASE POROUS CONCRETE AIMED AT ACHIEVING CARBON NEUTRALITY

Ayane Yanaka[1], Hidenori Yoshida[2], Shinichiro Okazaki[2], Yui Oyake[2], Yoshihiro Suenaga[2]
[1] Graduate School of Engineering, Kagawa University, Japan; [2] Faculty of Engineering and Design, Kagawa University, Japan

ABSTRACT

The Paris Agreement was adopted as the international framework against global warming, and the global movement to reduce greenhouse gas emissions is progressing. On the other hand, the final disposal amount will be reduced to 13 million tons in 2025 with considering the situation of waste disposal in Japan. Concrete, which is a typical recycled civil engineering material, is a very useful material for drastically reducing waste, while its constituent material, cement, emits a large amount of CO_2 in its manufacturing process. Additionally, due to the Japanese eating habits, a large amount of fishery waste including fish residues and shellfish are discharged. Although these are recycled, only about 30% of them are recycled. In this study, because the hydroxyapatite can contribute to reduction of the amount of cement and the plant growth promoted by phosphorus content, the hydroxyapatite produced from fish bones (Fishbone Powder, FbP), which is a fishery waste, is adopted as an alternative material to cement of planting base porous concrete. In addition, from the viewpoints of various physical properties (porosity, permeability and compressive strength), plant growth conditions and CO_2 emission reduction, the potential of recycling FbP as a binder for planting base porous concrete is also examined. As the result, CO_2 emission of about 2.6 kg per 1 m^3 of porous concrete can be reduced by using FbP as a binder for planting base porous concrete. Additionally, the plant growth ability is also improved while the compressive strength is maintained above 10 N/mm^2.

Keywords: Carbon neutrality, FbP, recycling, planting base porous concrete, CO_2 emission reduction

INTRODUCTION

The current global average temperature is approximately 1°C higher than that before the industrial revolution. In Japan, the average temperature in 2020 is the highest since records began in 1898, and the global warming is still becoming unstoppable. In response to serious global warming, "The Paris Agreement" was adopted as a new initiative to replace the Kyoto Protocol in order to reduce greenhouse gas emissions after 2020 at the 21st Conference of Parties (COP21) to the United Nations Framework Convention on Climate Change which was held in Paris, 2015. The global movement to achieve carbon neutrality is progressing with the adoption of the agreement. In 2020, Japanese government declared that "Greenhouse gas emissions would be reduced to zero as a whole by 2050". On the other hand, in Japan, the final disposal amount of Japan will be reduced to 13 million tons in 2025 with considering the situation of waste disposal in recent years [1]. As an effective means to reduce the amount of final disposal, construction wastes, industrial by-products, general wastes (incinerated ash, molten slag, etc.) and sewage sludge are used as recycled civil engineering materials. Concrete, which is a typical recycled civil engineering material, is a very useful material for drastically reducing waste, while its constituent material, cement, emits a large amount of CO_2 in its manufacturing process. In order to reduce the environmental load and CO_2 emission, "Low-carbon concrete", in which industrial waste and by-products such as fly ash, blast furnace slag and silica fume instead of cement are used, is noticed [2]. In addition to the wastes mentioned above, due to the Japanese eating habits, approximately 3.86 million tons of fishery waste, including fish residues such as bony parts of fish and shellfish such as scallops and oysters excluding those discharged by households, are discharged annually. Although these are recycled into feed and fertilizer, only approximately 30% of them are recycled [3]. Against this background, in order to reuse fish bones, which are discarded drastically at fish farms and fisheries processing plants, the hydroxyapatite produced from fish bones was developed by some of the authors, and its use as an adsorbent was proposed. In previous studies, the authors have clarified that the hydroxyapatite produced from fish bones has ability to adsorb for heavy metals such as zinc (Zn^{2+}), cadmium (Cd^{2+}), mercury (Hg^{2+}) and manganese (Mn^{2+}), and radioactive substances such as strontium (Sr^{2+}) in solution [4][5]. However, the use of adsorbents alone will not lead to a significant reduction in fishery waste. Additionally, the main component of hydroxyapatite produced from fish bones is calcium phosphate containing phosphorus which is one of the three major nutrients of plants.

Thus, in this study, because the hydroxyapatite can contribute to the reduction of the amount of cement and the plant growth promoted by phosphorus, the hydroxyapatite produced from fish bones (Fishbone Powder, FbP), which is a fishery waste, is adopted as an alternative material to cement of planting base porous concrete. In addition, from the viewpoints of various physical properties (porosity, permeability and compressive strength), plant growth conditions and CO_2 emission reduction, the potential of recycling FbP as a binder for planting base porous concrete is also examined.

FISHBONE POWDER (FbP)

Hydroxyapatite is one of the typical apatites, that are a group of crystalline compounds with $M_{10}(ZO_4)_6X_2$ as a basic composition, and is a basic calcium phosphate represented by $Ca_{10}(PO_4)_6(OH)_2$ as chemical formula. The manufacturing method of the hydroxyapatite produced from fish bones (Fishbone Powder: FbP, see Fig. 1) is as follows. First, fish residues with organic matter adhering to fish bones are immersed and boiled in high-temperature water. Next, the organic matter residues are removed from the fish residues by spraying high-pressure water, and the fish bones from which organic matter residues are removed are forced to dry at 200°C. After that, the fish bones are burned at 700-900°C in a heating furnace, and the burned fish bones are pulverized with a ball mill [6]. Here, in order to calculate the reduction of CO_2 emission in porous concrete for planting base using FbP as a binder, it is necessary to take into account CO_2 emission in the manufacturing process of FbP. However, Wada *et al*. [7] report that the temperature for the combustion reaction of the solid component (carbide) is 400-540°C in the oxidative pyrolysis reaction of food waste such as carbohydrate, protein and fat. In other words, the temperature at which organic matter residues are burned and CO_2 is emitted is 400-540°C. The organic matter residues, such as fish meat, are removed from the fish bones in FbP production. Additionally, even if a small amount of organic matter residues adheres to the fish bones, the drying temperature before burning is lower than the combustion temperature at which the CO_2 is emitted. Furthermore, even though the fish bones are burned at 700-900°C, CO_2 is hardly emitted due to the small amount of organic matter residues. Therefore, in this study, CO_2 emission in the manufacturing process of FbP is almost zero, and the reduction of CO_2 emission in using FbP as a binder is calculated.

Fig. 1 Fishbone Powder (FbP)

TEST METHOD

Mix design and test specimen preparation

Table 1 shows the mix proportions of porous concrete in the test. The mix proportions are determined with reference to the study by Nakamura *et al*. [8]. The water-cement ratio is 25% and the target porosity is 26%. "BLANK" represents an ordinary porous concrete (porous concrete without FbP), and "FBP" represents porous concrete in which FbP is mixed as a binder (1% replacement of cement mass). Ordinary Portland cement is used for cement, No. 5 crushed stones of 13 mm to 20 mm in diameter is used for coarse aggregate, and polycarboxylic acid-based air entraining (AE) and water-reducing admixture is used for chemical admixture. In addition, 1% is added to the cement mass as AE water reducing admixture. Cement, FbP and crushed stones are mixed in a concrete mixer, and then water in which chemical admixture is dissolved is put into the mixer. Then, the mixer is rotated to mix the materials. After that, the materials are put into a cylindrical mold of 100 × 200 mm (diameter × height), and struck with rods and wooden hammers at each time. The size of the sample for the grass growth test is 100 × 180 mm. Five specimens are prepared for each physical property test and cured in water for 7 or 28 days. On the other hand, four specimens are prepared for the grass growth test and cured in water for 28 days.

Physical property test

The porosity, permeability and compressive strength tests are conducted to confirm the physical property of porous concrete in which FbP is mixed as a binder. Porous concrete used as a planting base in the embankment is classified as "Strength emphasis type" or "Plant growth emphasis type". The porosity and strength for these two classifications are different. In the test, referring to "Plant growth emphasis type" of porous concrete, 21-30% of porosity, 2.5-5.0 cm/s of permeability, and 10 N/mm^2 of compressive strength are set as target values. As a reference to the report of the committee on the

Table 1 Mix proportions (kg/m^3)

	W	Binder		G	A
		C	FbP		
BLANK	84	337		1547	3.37
FBP	84	337.63	3.37	1547	3.37

*W: Water, C: Cement, G: Coarse Aggregate, A: Chemical admixture

establishment of design and construction methods of porous concrete of the Japan Concrete Institute [9], the porosity test is conducted according to the volumetric method, and the constant head permeability test is conducted. In addition, the upper end surface of the specimen is covered with gypsum in order to smooth the loading surface, and the uniaxial compression test is conducted in compliance with the compressive strength test method of concrete (JIS A 1108).

Grass growth test

In order to examine the plant growth ability of porous concrete in which FbP is mixed, a growth test of western grass is conducted on porous concrete without FbP (BLANK) and porous concrete in which FbP is mixed as a binder (FBP). The test period is 42 days from November 17 to December 29, 2021, and the test is conducted in the vinyl greenhouse installed outdoors. The cylindrical porous concrete of 100 × 180mm (diameter × height) is filled with peat moss in slurry type by a water-powder ratio of 1: 1 as the planting base (see Fig. 2). Fig. 3 shows the cross section of the planting base specimen. Since the test period is winter season, the blend of cold-district type turfgrass of Kentucky bluegrass, tall fescue, bent grass and others are selected as the test plant. The peat moss of 2 cm thickness is covered on the porous concrete. In order to make the western grass uniform, the seeds are added to the soil covering part at the ratio of 1 g per one porous concrete. Water is supplied once a day, around 11:00 a.m. after seeding. Leaf length is measured once a week from 14 days after seeding. Referring to the study by Tsukioka *et al*. [10], leaf length is measured at five places one per porous concrete specimen, and the average of five measured length is defined as the leaf length in the porous concrete specimen. The average of each leaf length in four porous concrete specimens is adopted as the test result for the whole case. In addition, the pH value of the soil cover and inside the porous concrete is measured after the grass growth test because it is considered that the soil pH value of the planting base influences the growth of the plant [11]. The mixture of soil 1 to distilled water 2.5 is shaken for 30 minutes. In the test, 6g of soil and 15mL of distilled water are used. After then, the measured pH of the supernatant is defined as the pH of the test soil.

Fig. 2 Planting base used in grass growth test

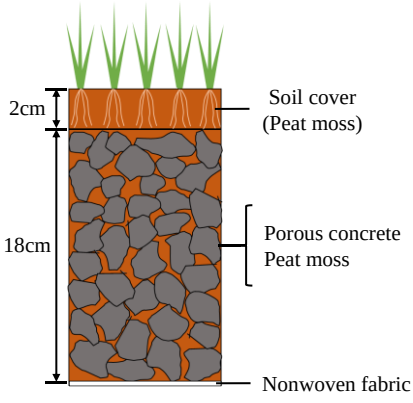

Fig. 3 Cross section of planting base specimen

RESULT AND DISCUSSION

Results of physical property test

As the results of the porosity test, Fig. 4 and Fig. 5 show the total and continuous porosity, respectively. The horizontal and vertical axes in Fig. 4 and Fig. 5 are the curing period and porosity of the porous concrete, respectively. Fig. 4 and Fig. 5 show that the porosity of both BLANK and FBP are higher than 26% of the target porosity in the design, and the porosity at 28 days of curing is above 21-30% of the application range for the plant growth emphasis type, except for the BLANK of the continuous porosity. According to Saito *et al*. [12], it is indicated that in the porous concrete filled in the mold, the continuous porosity in the vicinity of the mold increases, because the filling property of coarse aggregate is deteriorated near the form surface. It is considered that the measured values exceed the target value due to the wall effect of the mold. On the other hand, Koshi *et al*. [13] state that the porosity is affected by the specimen size, and the larger the aggregate size, that the larger the void size near the surface in contact with the mold, and that the continuous existence of voids also increases the porosity. In this study, the No. 5 crushed stones are selected to ensure suitable voids for the growth of plant roots in porous concrete. However, the No. 5 crushed stones are slightly larger than the specimen size of porous concrete. This is also considered to be the cause of the actual porosity exceeding the target one. In general, the porosity of porous concrete tends to decrease as the curing days pass because cement hydration products become dense, while, the results obtained in the test differ from the general tendency. Further investigation is needed to obtain more detailed information on the porosity of porous concrete. Furthermore, the ratio of the continuous voids to total voids is calculated and the ratio of both BLANK and FBP exceeds 99%. It is confirmed that most of the voids in those porous concrete are continuous voids. It can be said that both

BLANK and FBP are the porous concrete suitable for plant growth.

Fig. 6 shows the results of the permeability test. The horizontal and vertical axes in Fig. 6 are the curing period and permeability coefficient of the porous concrete, respectively. Fig. 6 shows that the permeability coefficient in the test deviates from 2.5-5.0 cm/s of the target range, except for the BLANK which is cured for 7 days. As with the porosity, it is considered that the results are due to the wall effect. Additionally, the permeability coefficients of both BLANK and FBP increase with the curing period. The permeability coefficient is strongly affected by the porosity. As the porosity in the test increases with the curing period, the permeability coefficient is also presumed to increase.

Fig. 7 shows the results of the uniaxial compression test. The horizontal and vertical axes in Fig. 7 are the curing period and compressive strength of the porous concrete, respectively. Fig. 7 shows that both BLANK and FBP are satisfied with 10 N/mm^2 of the target compressive strength, while the compressive strength of FBP is slightly lower than that of BLANK. This may be attributed to the fact that the amount of cement in the FBP is less than in the BLANK. In addition, the compressive strength of BLANK decreases with the curing period. Since the compressive strength is affected by the porosity as with the permeability coefficient, it is presumed that the results are due to an increase in the porosity. On the other hand, the compressive strength of FBP is maintained above 10 N/mm^2 despite an increase in porosity as the curing period progresses. It is necessary to examine the extent to which FbP contributes to strength from the relationship between the replacement ratio of FbP and the strength of porous concrete by changing the replacement ratio of FbP to cement mass.

Results of grass growth test

The measurement result of the leaf length of grass growth and the condition of each specimen at the end of grass growth test are shown in Fig. 8 and in Fig. 9, respectively. The horizontal and vertical axes in Fig. 8 are the elapsed period and leaf length, respectively. Fig. 8 shows that the leaf length of FBP is longer than that of BLANK consistently from the beginning to the end of the measurement of leaf length. In addition, the growth rate of leaf length in FBP is higher than that in BLANK. FbP contains phosphorus that is one of the three major nutrients of the plant. It is suggested that the phosphorus in FbP mixed in the porous concrete is supplied to it, which brings about a positive effect on the grass growth. It is necessary to analyze the amount of phosphorus contained in the grass growth test in which porous concretes mixed with and without FbP as planting base so as to confirm that the phosphorus in FbP is supplied to porous concrete. Additionally, Fig. 9 seems that FBP is slightly superior to BLANK regarding the root thickness, root length and root quantity of the grass

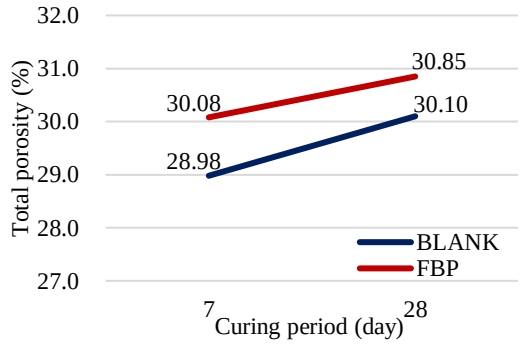

Fig. 4 Porosity test results (Total porosity)

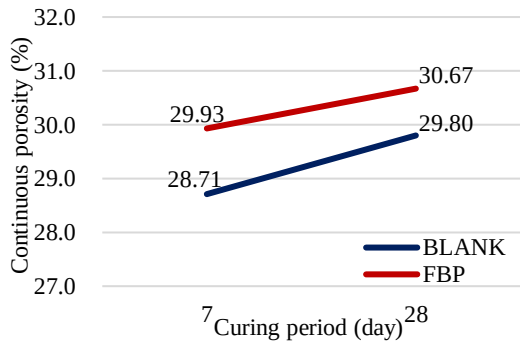

Fig. 5 Porosity test results (Continuous porosity)

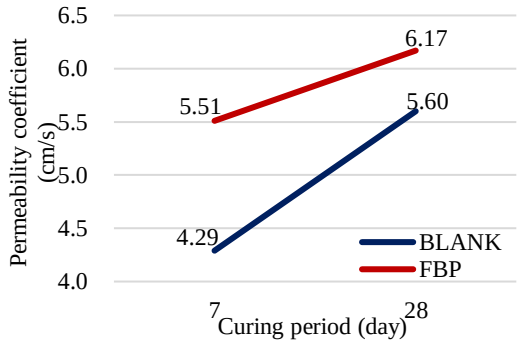

Fig. 6 Permeability test results

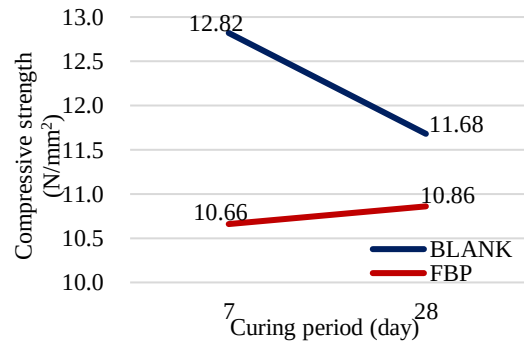

Fig. 7 Uniaxial compression test results

comparing BLANK and FBP. Yoneyama *et al*. [14] report that there is a proportional relationship between the root mass of plant and the absorbed amount of phosphorus. The growth of roots is presumed to be promoted by the supply of phosphorus contained in FbP. In the future, it is needed to conduct the quantitative investigations such as measurement of root dry mass.

The results of the pH value in the soil is listed in Table 2. Table 2 shows that the pH value in the cover soil of FBP is almost the same as that of BLANK. In addition, there is only about 0.1% difference between soil pH inside the void of BLANK and that of FBP. The difference is a category of error. Calcium phosphate, the main component of FbP, is from neutral to weakly alkaline, and it is presumed that the soil pH of BLANK and FBP is almost the same due to the use of FbP. Yokozeki *et al*. [15] indicates that there is a relatively high correlation between the soil pH and the volume of plant growth, and that the lower the pH, the better for plant growth. In order to further improve the growth amount of plant, it is necessary to examine a method of decreasing pH.

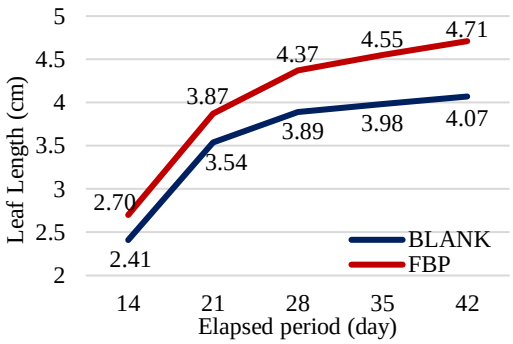

Fig. 8 Grass growth test results

Fig. 9 Planting base specimens at the end of grass growth test (left: BLANK, right: FBP)

Table 2 Measuring soil pH value test results

	BLANK	FBP
Cover soil	8.00	7.99
Inside of concrete	8.00	8.08
Peat moss (Original)	7.39	

Calculation of CO_2 emission reduction

By applying FbP mixed in porous concrete to an actual revetment, CO_2 emission reduction is calculated. Here, the Aizawa river embankment repair work in Yamagata Prefecture [16] is referred. CO_2 emission in manufacturing FbP is not considered, as described in Chapter 2. By substituting 1% of FbP for cement mass, it is possible to reduce cement content by 3.37 kg per 1 m^3 of porous concrete. According to the Japan Federation of Construction Contractors [17], roughly 770 kg of CO_2 is emitted in the production per 1 ton of cement. Compared with conventional porous concrete, CO_2 emission by approximately 2.6 kg per 1 m^3 of porous concrete can be reduced when FbP is used as a binder. The volume of the porous concrete used in the repair work is estimated to be 900 m^3 considering the construction scale and thickness of the embankment. Thus, CO_2 emission by approximately 2,335 kg can be reduced. Saiki *et al*. [18] states that a gasoline automobile emits 2.38 kg of CO_2 per 1 L of gasoline. Applying this to the repair work mentioned above, the amount of CO_2 emission reduced by substituting cement for FbP in porous concrete is equivalent to the amount of CO_2 produced when about 981 L of gasoline is consumed in a gasoline automobile. In the case of the automobile which runs 20 km per 1 L of gasoline, it can run approximately 19,620 km with 981 L of gasoline. This is equivalent to half a world' s circumference. Therefore, it is expected that the use of FbP as a binder for the planting base porous concrete brings useful results toward achieving carbon neutrality.

CONCLUSIONS

In this study, the hydroxyapatite produced from fish bones (Fishbone Powder, FbP), which is a fishery waste, was focused on an alternative material to the cement of planting base porous concrete, and the potential of recycling FbP as a binder for planting base porous concrete was examined. The findings obtained are as follows.

- Porous concrete in which FbP was mixed has the physical properties required for "Plant growth emphasis porous concrete" used as a planting base in a revetment.
- The compressive strength of porous concrete in which FbP was mixed as a binder was lower than that of porous concrete without FbP. Although the compressive strength of porous concrete without FbP decreased with the curing period, that of the porous concrete in which FbP was mixed did not decrease and was maintained above 10N/mm^2.
- The leaf length of grass in the porous concrete in

which FbP was mixed was longer than that in porous concrete without FbP. It is suggested that phosphorus in the FbP mixed in the porous concrete has a positive effect on the grass growth.

- CO_2 emission by approximately 2.6 kg per 1 m^3 of porous concrete can be reduced by using FbP as a binder. When porous concrete in which FbP is mixed is applied to the Aizawa river embankment repair work in Yamagata Prefecture, it is expected to reduce CO_2 emission by approximately 2,335 kg.

In the future, in order to investigate the effect of FbP on the strength of porous concrete, it is necessary to examine the relationship between the replacement rate of FbP to cement and its strength. Additionally, it is needed to analyze the amount supplied of phosphorus in the grass and measure the dry mass of the leaves and roots of the grass so as to quantitatively evaluate that FbP influences plant growth.

ACKNOWLEDGMENTS

This work has been supported by JSPS KAKENHI Grant Number JP20K04684. Also, in carrying out this study, Nihon Kogyo Co., Ltd. provided FbP. We express our gratitude here.

REFERENCES

[1] Ministry of the Environment, Annual Report on the Environment, the Sound Material - Cycle Society and Biodiversity in Japan 2021, 2021, pp. 183-202.

[2] Kobayashi T., Ichise K. and Namiki K., Technical Report, Low Carbon Emission Concrete “Crean-crete”, Report of Obayashi Corporation Technology Research Institute, No. 80, 2016, pp. 1-4.

[3] Demura M., Current Status and Issues of Fishery Waste Disposal –Focusing on the Recycling of Fish Residue-, Monthly review of agriculture, forestry and fishery finance, Vol. 57, No. 11, SN. 705, 2004, pp. 666-680.

[4] Shibata K., Yoshida H., Matsumoto N. and Suenaga Y., Study on adsorption ability of hydroxyapatite for strontium in solutions, Japanese Geotechnical Society Special Publication, Vol. 14, No. 7, 2016, pp. 163-167, DOI: 10.3208/jgssp.v04.j26.

[5] Shibata K., Yoshida H., Inoue T., Matsumoto N. and Suenaga Y., STUDY ON ADSORPTION PERFORMANCE OF FOOD WASTES FOR VARIOUS HEAVY METALS, Vo. 16, Issue 55, 2019, pp. 46-52, DOI: 10.21660/2017.34.2661.

[6] Kagawa University, NIHON KOGYO CO., LTD. Suenaga Y., Yoshida H., Honjo T., Tada K., Ichimi K., Matsuyama T., Kameyama T., Yamaji K., Hydroxyapatite produced from fish bone, JP6351008B2, 2018-07-04.

[7] Wada Y., Norose Y., Iwabuchi K. and Taniguro K., Pyrolysis Characteristics of Food Wastes, Journal of the Japan Society of Material Cycles and Waste Management, Vol. 22, No. 3, 2011, pp. 225-230.

[8] Nakamura K., Ishikawa Y., Yanagibashi K and Ando S., An Application of Porous Concrete to the Bank of Reservoir, Concrete Journal, Vol. 43, No. 4, 2005, pp. 41-45.

[9] Japan Concrete Institute, Report of the research committee on the establishment of design and construction methods for porous concrete, 2003.

[10] Tsukioka S., Yonemoto T., Growth Experiment of the turf Grass Using the Vegetation Type Concrete, Journal of the Japanese Society of Irrigation, Drainage and Reclamation Engineering, Vol. 74, No. 2, 2006, pp. 127-130.

[11] Research Committee of Japanese Institute of Landscape Architecture, Ground Maintenance Manual in Landscape Planting, Journal of the Japanese Institute of Landscape Architecture, Vol. 63, No. 3, 2000, pp. 224-241.

[12] Saito T. and Demura K., INFLUENCE OF WALL EFFECT OF MOLD FOR SPECIMEN ON VOIDS DISTRIBUTION AND COMPRESSIVE STRENGTH OF POROUS CONCRETES, Cement Science and Concrete Technology, Vol. 70, No. 1, 2016, pp. 290-296.

[13] Koshi T., Shimazaki I., Kunieda M. and Rokugo K., Evaluation of Void Ratio and Void Distribution of Porous Concrete, Proceedings of the Japan Concrete Institute, Vol. 21, No. 1, 1990, pp. 259-264.

[14] Yoneyama T., Horie H., Takebe M., Tanno F., Absorption of Phosphorus from Soil by Crops: II. The Relationship between Root Mass and Phosphorus Absorption, Journal of the science of soil and manure, Japan, Vol. 61. No. 4, 1990, pp. 382-385.

[15] Yokozeki K., Torichigai T., Takayama H., Higuchi T., Study on Improving Plant Growth Capacity of Porous Concrete, Proceedings of the Japan Concrete Institute, Vol. 35, No. 1, 2013, pp. 1405-1410.

[16] Japan Federation of Construction Contractors, Towards Promoting of Low Carbon Concrete – Contributing to the Construction of a Low Carbon and Recycling Oriented Society-, No. 0237, 2016

[17] Asano K. and Sato K., Construction of Cast-in-place Porous Concrete, Proceedings of JCI Symposium on Design, Construction and Recent Applications of Porous Concrete, 2003, pp. 127-130.

[18] Saiki Y. and Nakazawa M., CO2 Emission from Gasoline Vehicle of Running Mode, Journal of Japan Society for Atmospheric Environment, Vol. 25, No. 4, 1990, pp. 287-293.

8th Int. Conf. on Structure, Engineering & Environment (SEE), Mie, Japan, Nov.10-12, 2022, ISBN: 978-4-909106094 C3051

EXAMINATION OF SEDIMENT GRAIN-SIZE MEASUREMENT AND CALUCULATION AT MULTIPLE POINTS ON THE SANDBAR IN CLASS B RIVER

Yoshitaka Jiken[1], Kazuya Watanabe[2] and Noritoshi Saito[3]
[1,2,3] Graduate School of Engineering Science, Akita University, Japan

ABSTRACT

In recent years, flood damage was occurring frequently by the flow rate of rivers has increased due to heavy rains such as typhoons in Japan. Therefore, understanding the particle size distribution of riverbed materials was an important factor in river planning and sediment outflow forecasting. However, in many cases, the grain size considered in numerical calculations was only for the surface layer because collecting sediment heavy labor, and it has not been studied much in the depth direction. In this study, sediment was collected from multiple locations on the sandbar in the middle reaches of the Babamegawa River, which was a Class B River in Akita Prefecture. Then, the particle size analysis was performed in the cross-sectional and longitudinal directions. Sediment was collected twice to see the change in grain size before and after the flood. At the results, the D50 of the sediment collected after the flood tended to be larger than that of the sediment collected before the flood in both the cross-sectional and longitudinal directions. In the depth direction, it was confirmed a layer in which the particle size changes and a layer in which the particle size does not change.

Keywords: Babamegawa River, sandbar, particle size, diameter50, numerical calculation

INTRODUCTION

Flood damage caused by typhoons and heavy rains has occurred frequently in Japan [1]. The particle size distribution of riverbed materials in river roads was also an important index from the viewpoint of sediment management [2]. In addition, the average particle size obtained from the particle size distribution was also used for grasping the characteristics of rivers and river planning using numerical calculations in recent years. The particle size distribution of riverbed materials has been widely carried out in past studies [3][4]. However, the collection of sediment was a heavy labor, and it was costly to use heavy machines [5]. Therefore, there were many things related to the surface layer of the riverbed in consideration of the particle size. The examination of the riverbed material in the deeper point has not been done much. In this study, sediment was collected from multiple locations on the sandbar in the middle reaches of the Babamegawa River [6], which was a Class B River in Akita Prefecture. Then, the particle size analysis was performed in the cross-sectional and longitudinal directions. Sediment was collected twice to see the change in grain size before and after the flood. In addition, the numerical calculation of the studies using the middle basin of the Babamegawa River as the calculation area was reproduction calculation of the flow in which the roughness coefficient of Manning was changed depending on the location [7], Study on the Behavior of sandbar using UAV (Unmanned Aerial Vehicle) [8][9], but numerical calculations set for the mixed particle size have not been performed. Therefore, numerical calculations were performed using particle size distribution and exchange layer thickness obtained from actual riverbed materials, and the calculation results of uniform particle size and mixed particle size were compared.

RESERCH AREA

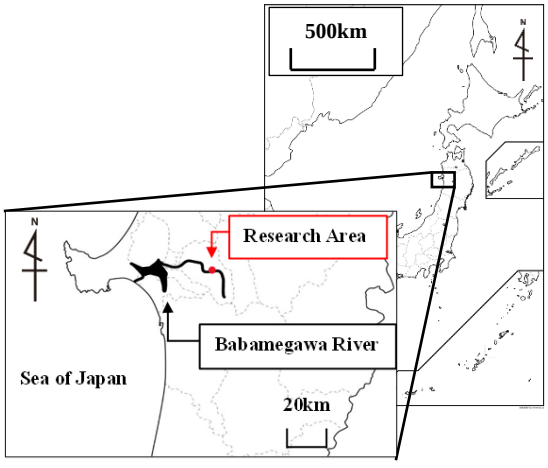

Fig. 1 Study Area.

Fig. 1 was shown the Babamegawa River flowed into the Sea of Japan and was the largest Class B The calculation area was shown in Fig.2. It was Babamegawa River at Hiranoshita area. The calculated area was an extension of about 850 m section of the Babamegawa River middle basin flat,

and the survey data of the river improvement work in 2014 was used for the topographical condition. The river width is about 40 m in all sections, and from the embankment to the riverbed was about 4 m. In this study, in order to compare with the calculated result, three measuring lines (No.1~3) were determined as shown in Fig.2.

RESEARCH METHODS

Riverbed Material Survey

Riverbed materials were collected from the sandbar indicated by the red frame in Fig.2(top). The details of the collected point were shown below. All seven stations(0~6) in Fig.2(bottom) were surveyed, and the points collected in November, 2020 were St.0, and the points collected in 2021 were St.1 to 6. St.1 to 3 were cross-sectional directions and St.4 to 6 were the longitudinal directions.

Fig. 3 was shown the river discharge variation of the Babamegawa River at the Kubo Observatory, which is several kilometers downstream from the survey site, from August to November, 2021. A flood of river discharge over 40 m^3/s has occurred twice during that period. Sediment samples were collected twice before and after the flood of river discharge 40 m^3/s shown in Fig. 3

At seven sites, about 6,000 g of riverbed material was collected from each layer, about 50 cm square from four layers of surface layer, depth of 30 cm, 50 cm, and 70 cm. In addition, the collected earth and sediment was dried, and the sifting test was carried out according to JIS A1204 [10] using about 4,000 g as a sample.

Particle Size Analysis Results and Discussions

Vertical Direction

Figs.4 and 5 were shown grain size accumulation curve and the occupancy of the sample stopped in each sieve of St.0 sediment. When the median diameter(D50) of each hierarchy was compared, it was about 13 to 14 mm in the range of 19 mm in the surface layer and 30 to 70 cm deep. The peak occupancy values were 9.5 to 26.5 mm. The grain size accumulation curve of St.0 did not difference in the grain size accumulation curve in the range of 30 to 70 cm deep. However, when the particle size addition curve of the riverbed material collected in August to November, 2021 is seen, the tendency by the depth like St.0 were almost non-existent.

In addition, the thickness of the exchange layer has not been formulated mechanically at present from the particle size distribution. Therefore, the grain size accumulation curve in the middle basin changes greatly depending on the time and position.

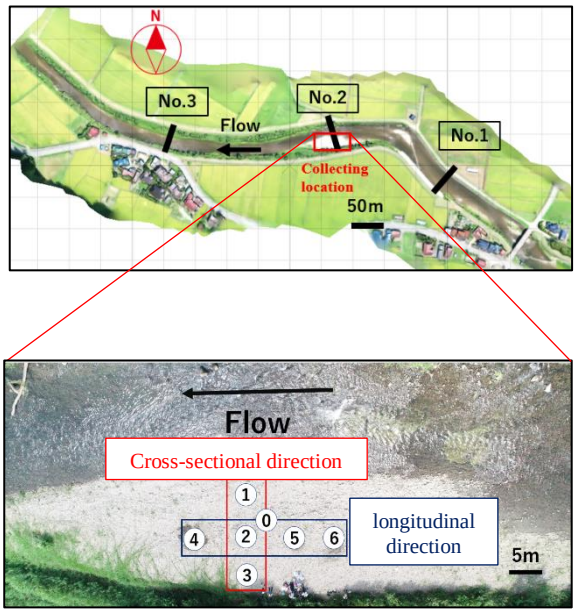

Fig. 2 Aerial photograph by UAV(August, 2021).

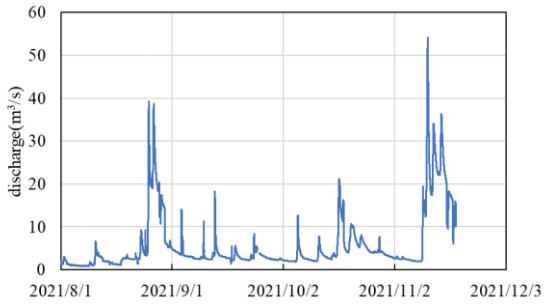

Fig. 3 River discharge variation from August to November, 2021.

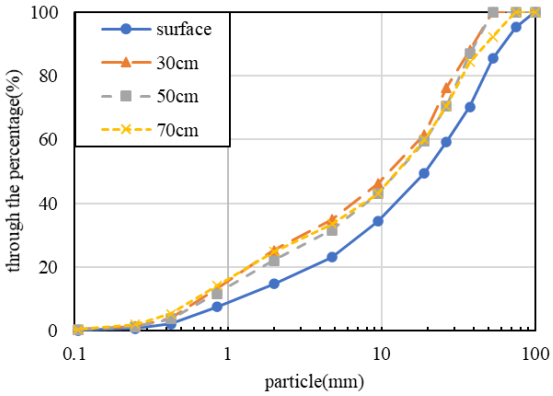

Fig. 4 Grain size accumulation curve at St.0. (November, 2020).

Particle size Comparison before and after the Flood

Fig. 6 was shown D50 in the cross-sectional direction of August and December, 2021. St.3 located on the shore showed a tendency to have a coarser particle size in December than in August at a depth of 30 cm and 70 cm. The D50 of the sediment collected in August ranged from 6.1 to 13.6 mm, regardless of the sampling point or depth. On the other hand, when the sediment collected in December was compared, st.1 was 6.9 to 9.5 mm, and St.2 and 3 were more than 10 mm. D50 after the flood tended to be larger than before the flood. it was thought to be due to the flood of a river discharge of over 40 m^3/s that occurred in the second half of August and the first half of November, and a small particle sediment flowed out of the sandbar. St.3 significantly increased particle size change and became coarser. As a reason, since the shore side was not flooded at normal times, it was considered that more fine sediment was washed away than other points.

Fig. 7 was shown D50 in the longitudinal direction of August and December,2021. D50 in August was 5.0 to 13.0 mm regardless of the location and depth of collection. On the other hand, D50 in December showed st.4 was 8.1 to 10.0 mm, while St.2, 5 and 6 were 9.5 to 19.0 mm except for depth 50 cm. D50 was bigger after the flood tendency to become the same as the cross-sectional direction, but there was no change as much as the cross-sectional direction.

In the longitudinal direction, the grain size tended to be coarse in the upper part of the sandbar and fine in the middle and downstream areas in the Tamagawa River of the Class A River[11].

Numerical Calculation

Calculation Model

In this study, the two-dimensional calculation model was used based on the past studies[7]-[9]. The continuous equations and equations of motion used this time were shown in equations (1) to (3).

$$\frac{\partial h}{\partial t}+\frac{\partial (hu)}{\partial x}+\frac{\partial (hv)}{\partial y}=q+r \tag{1}$$

$$\frac{\partial (uh)}{\partial t}+\frac{\partial (hu^2)}{\partial x}+\frac{\partial (huv)}{\partial y}=-hg\frac{\partial H}{\partial x}-\frac{\tau_x}{\rho}+D^x \tag{2}$$

$$\frac{\partial (vh)}{\partial t}+\frac{\partial (huv)}{\partial x}+\frac{\partial (hv^2)}{\partial y}=-hg\frac{\partial H}{\partial y}-\frac{\tau_y}{\rho}+D^y \tag{3}$$

Where h was the water depth, t was the flow velocity in the x direction, v was the flow velocity in the y direction, q was the amount of inflow by the

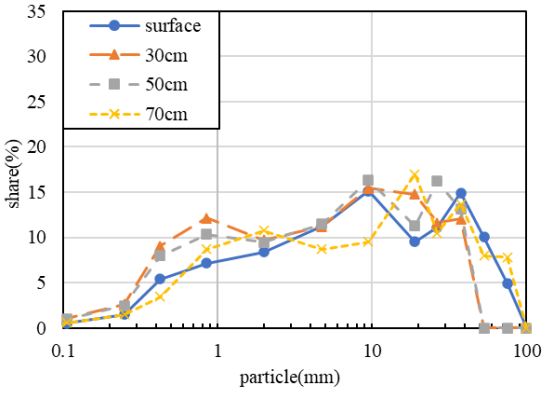

Fig. 5 Occupancy of sediment at St.0. (November, 2020).

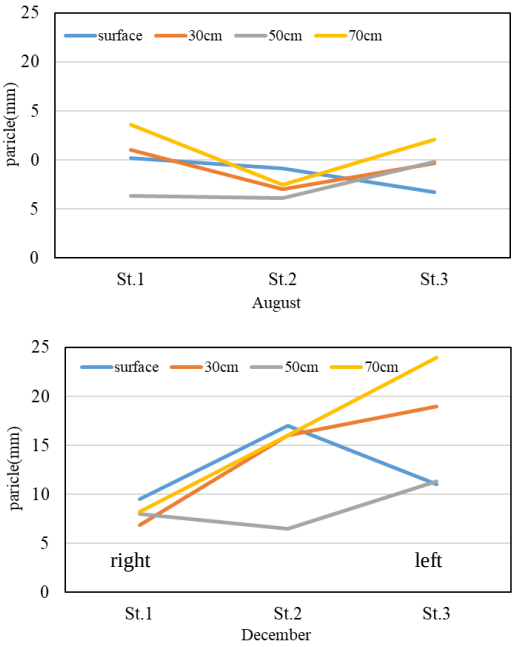

Fig. 6 Cross-sectional direction in 2021(D50).

culvert, gutter, and pump per unit area, r was the amount of rain, g was the gravitational acceleration, H was the water level, τx was the riverbed shear force in the x direction, τy was the riverbed shear force in the y direction, and v was the density of water.

Calculation Case

The typical particle size used for numerical calculation of uniform particle size was generally using the central particle size D50 of the surface layer. However, the difference was large between the peak value of the occupancy and the D50, and the particle size distribution of the surface layer was different depending on the collection time. In this study, we used the particle size distribution obtained numerical

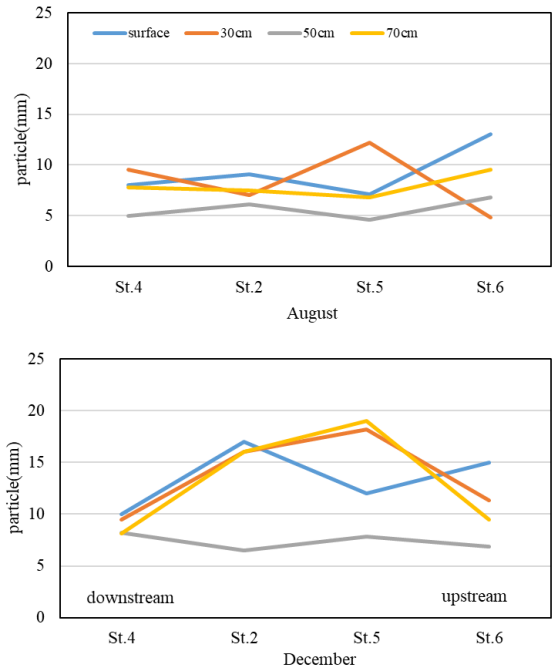

Fig. 7 Longitudinal direction in 2021(D50).

Table 1 Particle size input pattern

pattern		Particle size setting	particle size
a	1	Uniform particle size	7.8 mm (2020/10 D50)
	2		14.3 mm (2020/10 occupancy)
	3		19.0 mm (2020/11 D50)
	4		23.5 mm (2020/11 occupancy)
b	1	Mixed particle size	Deep 50 cm（2020/11）

Table 2 Calculation conditions

	Uniform particle size	Mixed particle size
Manning number	riverbed 0.03 other 0.04	riverbed 0.03 other 0.04
Time step	0.1s	0.1s
Exchange layer		30 cm
Sedimentary layer		40 cm
Number of layer thicknesses		25

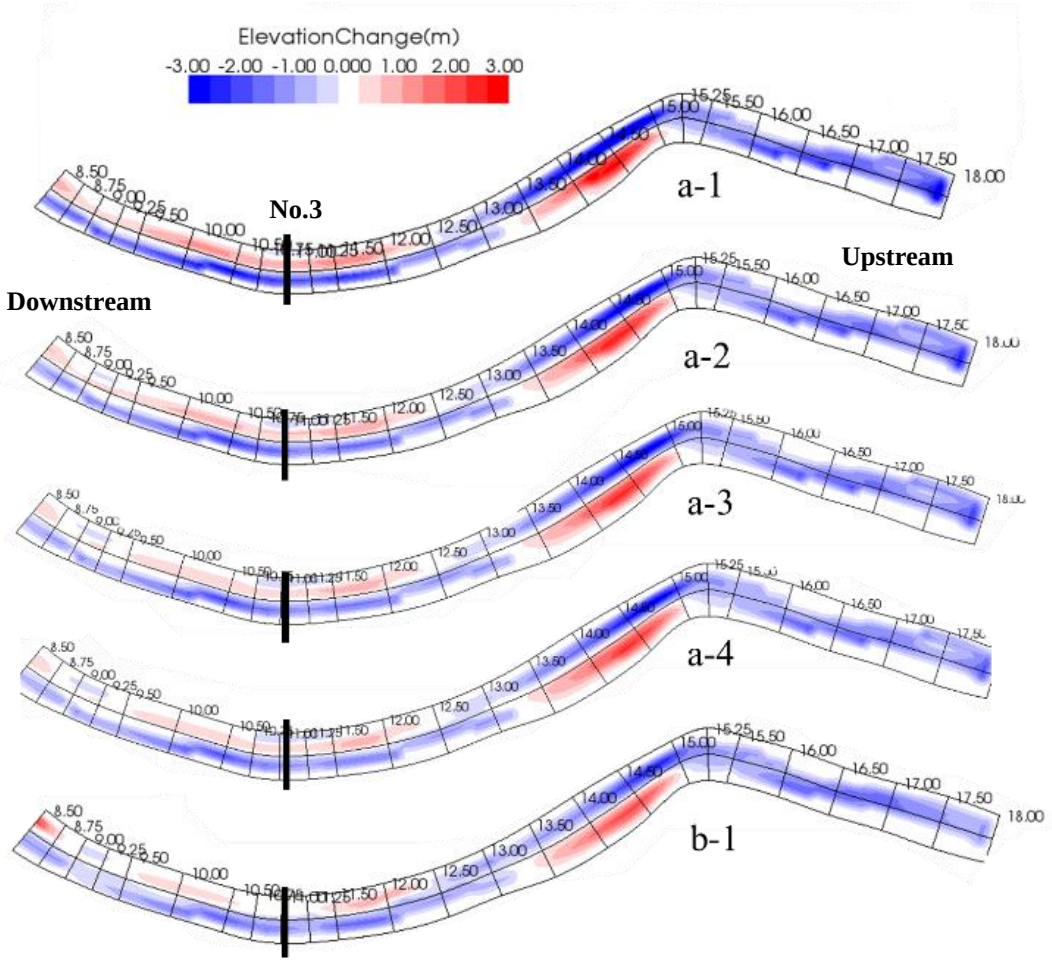

Fig. 8 Elevation change during peak river discharge.

calculations of 5 patterns shown in Table 1 based on the past study. The input particle size values used the D50 and occupancy peak values of the surface layer of sediment collected in October and November 2020. Table 2 showed the calculation conditions. The boundary conditions at the upstream end were 24 hour river discharge from 6:00 p.m. 24th to 6:00 p.m. 25th August, 2018 at the Observatory.

In this study, the longitudinal direction interval was set to 5 m and the cross-sectional direction was set to 10 divisions, and a computational lattice was created using a non-positive lattice.

Calculation Results and Discussions

Fig. 8 showed the change in the riverbed height at the peak river discharge. The numeral was displayed for each cell relative to the downstream end of the calculation area. The red color of the figure shows sedimentation and blue shows scour. When pattern a was compared as a whole, the larger the particle size, the smaller the fluctuations in the riverbed. However, the tendency of the scoring and deposition was similar regardless of the particle size. On the other hand, the amount of riverbed variation in pattern b was smaller than that of pattern a. And sedimentation was observed on the right bank of pattern a near the line, but no deposition was observed in pattern b.

The following meandering part where the flow velocity difference occurred was examined by paying attention. There was no difference visible from the flow velocity in numerical calculations of uniform particle size and mixed particle size around the peak river discharge (11 hours later). In addition, the river discharge was almost the same without approaching the size of the particle size even if it was compared by numerical calculation of uniform particle size. Only the calculation result of the mixed particle size (b-1) after 15 hours shown in Fig. 9 showed that the flow velocity did not come out on the right bank of the downstream end, and the tendency of the deposition was able to be read.

Fig. 10 showed the calculation results of a-1, a-2, and b-1 in No. 3 and the cross-sectional map of the research area. In the calculation result of pattern a, the scouring in the left bank was seen, while in pattern b, The shape of the riverbed remains the same as the initial state and the riverbed decreased overall.

When the survey results were seen, there was no tendency of scouring and sedimentation, and it was the same tendency as pattern b. Furthermore, when a-1 and a-2 were compared, a-1 had a smaller particle size, so the scoring and sedimentation were large.

In the case of numerical calculations in mixed particle size, the entire riverbed sediment not only did the Volume Conservation law hold, but also satisfies the Volume Conservation rule in the soil and sand of each particle size hierarchy constituting the particle size distribution. Therefore, in places where the particle size distribution varies, such as in the middle reaches of rivers, mixed particle size seems to have been able to reproduce the fluctuation tendency.

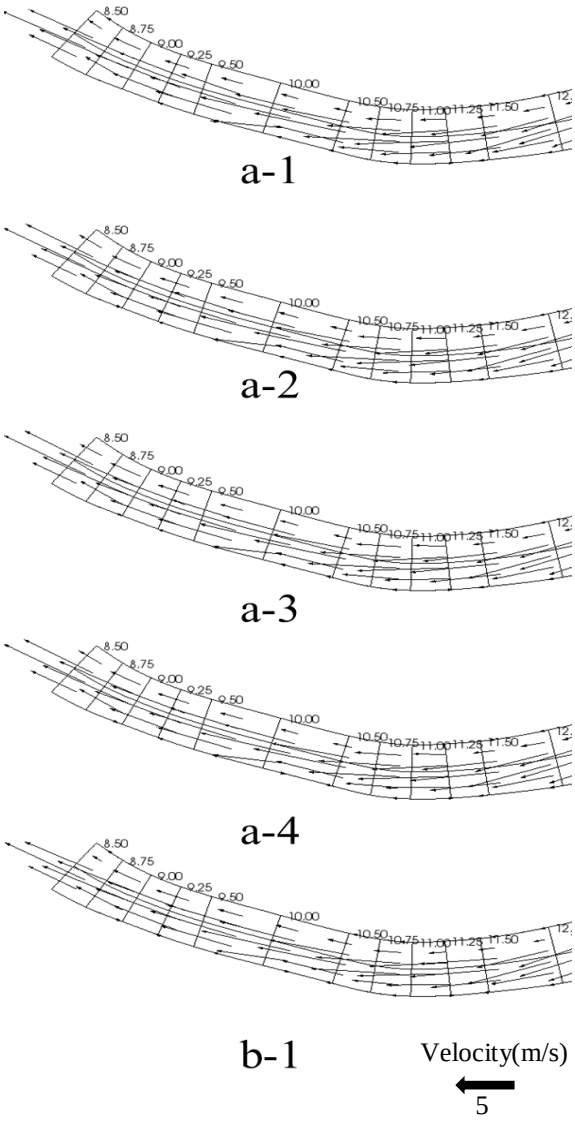

Fig. 9 Flow velocity (after 15 hours).

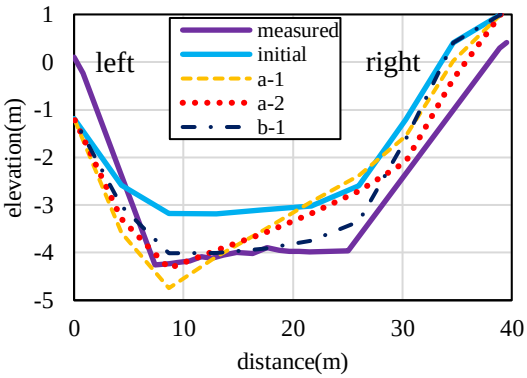

Fig. 10 Cross section map in No. 3

CONCLUSIONS

In this study, riverbed material was collected from the middle basin of the Babamegawa River in the plane direction and the vertical direction, and the particle size distribution was examined.

And numerical calculations were carried out at the mixed particle size and uniform particle size using the obtained particle size distribution and exchange layer thickness.

As a results of particle size analysis of riverbed materials,

- There was no tendency due to depth at most points, and the exchange layer could not be considered. It was thought to be because the particle size accumulation curve varies greatly depending on the collection time and position.
- Both the cross-sectional and longitudinal directions tended to increase the D50 of the earth and sand collected after the flood than the earth and sand collected before the flood. It seems to be due to the outflow of sediment with a small particle size from the sandbar with the flood flow rate of 40 m^3/s.

As a results of the numerical calculations on sediment transfer at uniform particle size and mixed particle size using local particle size,

- In the middle river basin, where the particle size distribution varies, it seems that the mixed particle size was able to reproduce the fluctuation tendency of the riverbed rather than the uniform particle size.
- In the case of a uniform particle size assuming all riverbed sediment as the same particle size, the peak value of the occupancy is closer to the setting condition than the D50 value, and it was considered that it approaches the real phenomenon as a result of calculation.

In this study, the reproducibility of sediment movement was qualitatively improved by calculating at the mixed particle size, but it was considered that it is necessary to consider factors other than particle size to quantitatively evaluate it in the future.

ACKNOWLEDGMENTS

This research was partially supported by the Ministry of Education, Science, Sports and Culture, Grant-in-Aid for Scientific Research (A), (20H00256, So Kazama)

REFERENCES

[1] Japan Meteorological Agency, Ministry of Land, <http://www.jma.go.jp/jma/index.html> (accessed on May 23, 2021).

[2] Harada D, Chibana T, and Agus SANTOSO., Characteristics of grain size distribution of riverbed and their determining factors, Proceedings of the Japan Society of Civil Engineers Paper B2, Vol.73, No.4, I_931-I_936, 2017(in Japanese).

[3] Pan B, Pang H, Zhang D, Guan Q, Wang L, Li F, Guan W, Cai A, and Sun X., Sediment grain-size characteristics and its source implication in the Ningxia–Inner Mongolia sections on the upper reaches of the Yellow River, Geomorphology, Volume 246, 2015, pp.255-262.

[4] Abeshu G W, Li H Y, Zhu Z, Tan Z, and Leung L R., Median bed-material sediment particle size across rivers in the contiguous US,Earth Syst. Sci. Data, 14, 2022 pp.929-942,.

[5] Murakami M., Riverbed Material Survey, Journal of the Japan Society of Erosion Control Engineering, Vol.71, No.6, 2019, pp.59-63, (in Japanese).

[6] Akita Prefecture. Class B River Babamegawa River water system River maintenance basic policy,<http://www.pref.akita.lg.jp/pages/arghive/10601> (accessed on April 23, 2021).

[7] Hagiwara T, Aita S, and Kazama S., A study on the variation calculation considering the particle size in the Babamegawa River, Conference of Tohoku Branch of Japan Society of Civil Engineering, 2015(in Japanese) (CD-ROM).

[8] Taniguchi J, Watanabe K, Saito N, and Fujisawa N., Study on the Behavior of Sandbar in a River Channel at the Babamegawa River, 6th Int. Conf. on Structure, Engineering & Environment (SEE), 2020, pp.149-154.

[9] Taniguchi J, Watanabe K, and Saito N., Study on the Behavior of Sandbar in a River Channel at the Babamegawa River, International Journal of GEOMATE, 2020 Vol.20, Issue 78, pp.115-120.

[10] JISA1204:2020<https://www.kikakurui.com/a1/A1204-2020-01.html> (accessed on April 25, 2021).

[11] Tadatsu T, Shimojo Y, Uchida T, Fukuoka S, Particle size composition of sandbars in gravel rivers and movement and deformation of sandbars due to flood flows, Kanto Branch is one of the Branches of JSCE, 2011, Ⅱ-26.

8th Int. Conf. on Structure, Engineering & Environment (SEE), Mie, Japan, Nov.10-12, 2022, ISBN: 978-4-909106094 C3051

RESIDUAL STRUCTURAL CAPACITY EVALUATION OF BRIDGE PIERS AFFECTED BY THE LOCAL SCOURING WITH A WATER LEVEL FORCASTING MODEL USING MACHINE LEARNING

Ryosuke Takahashi[1], Takuma Kadono[2] and Shinichiro Okazaki[3]
[1] Graduate School of Engineering, Kagawa University, Japan; [2]Department of Creative Technology Engineering, Course of Civil Engineering Lecturer, National Institute of Technology, Anan College, Japan; [3]Faculty of Creative Engineering Associate Professor, Kagawa University, Japan

ABSTRACT

In recent years, damage and subsequent destruction of bridge piers due to localized scouring has frequently occurred in many parts of Japan as one of the most serious heavy rain disasters. To properly maintain and manage infrastructures against such disasters, the residual capacity of piers affected by local scour should be evaluated to determine the health of the piers, and preventive measures against local scour should be implemented after assessing the risk caused by local scour. In this study, an evaluation method for the residual structural capacity of piers affected by localized scouring was proposed. The model is based on a machine-learning model for predicting river water levels using effective rainfall as an explanatory variable, and a model for evaluating the residual structural capacity of piers in response to fluctuations in river water levels and the development of local scour, using existing formulas for calculating pier bearing capacity.

Keywords: Machine learning, Effective rainfall, Prediction of river water level, Bridge pier, Evaluation of residual structural capacity

INTRODUCTION

In recent years, damage to bridge piers due to the local scouring and the resulting failures have become frequent in several parts of Japan, as one of the most severe heavy rainfall disasters. Once this type of disaster occurs, it is necessary to limit the use of bridges according to the situation and secure evacuation routes for neighboring residents. In addition, the "Paris Agreement" adopted by the Conference of the Parties to the United Nations Framework Convention on Climate Change (COP21) states that the global average temperature rise should be kept below 2 ° C as a long-term goal common to the world. According to the Ministry of Land, Infrastructure, Transport and Tourism's estimation, when the temperature rises by 2 ° C, the rainfall increases 1.1 times. Furthermore, focusing on the rainfall and flow rates targeted in the current river planning, it is estimated that the frequency of floods will double. In this way, although global efforts to combat global warming have been clearly shown, further extreme heavy rainfall and associated disasters are expected in Japan in the future. Therefore, even in the case of a local pier scouring disaster caused by heavy rain, it is necessary to establish appropriate maintenance and methods and implement rational disaster prevention measures.

Therefore, in this study, machine learning is used from the observed meteorological information for the purpose of constructing a method for quantitatively evaluating the soundness of local piers around piers that fluctuate depending on rainfall conditions, etc. in the future. In addition to proposing a model that predicts fluctuations in river water level, we also propose a model that evaluates the residual strength of piers according to the predicted river water level.

MAIN ARTICLE

Predicting River Water Level using Machine Learning

Study methods

Support vector regression (SVR) [1], which is one of the machine learning algorithms suitable for multivariate nonlinear regression problems, is used to construct a river water level prediction model. The objective variable was the future river water level of river X (basin area 155.5 km²) observed during the month of July 2018 and was calculated from the rainfall observed several hours ago in the catchment area of the target river. The effective rainfall [2] [3] [4] was used as the explanatory variable. The explanatory variables [5] [6] used in the river water level prediction model in previous studies generally include the river water level. On the other hand, if the river water level is used as an explanatory variable, a permanent water level gauge is required, which requires a large cost. Therefore, we considered whether it would be possible to predict the river water

level using only rainfall information and focused on the effective rainfall that can be calculated from the hourly rainfall.

Where, the effective rainfall is calculated by reducing the influence of past rainfall on the occurrence of sediment-related disasters with the passage of time, and the calculation formulas are as shown in Eq. (1) and (2).

$$\boldsymbol{R_t = r_t + \sum_{n=1}^{x} a_n r_{t-n} = r_t + a_1 r_{t-1} + \cdots + a_x r_{t-x}} \quad (1)$$

$$\boldsymbol{a_n = 0.5^{n/T}} \quad (2)$$

Where, R_t is the effective rainfall at time t, r_t is the hourly rainfall at time t, a_n is the reduction coefficient n hours ago, r_n is the hourly rainfall n hours ago, and T is the half-life. R_t approximately expresses the amount of water in the soil and indicates that the decrease coefficient decreases with the passage of time, resulting in the loss of water from the soil due to runoff and evapotranspiration. By setting the limit effective rainfall for the occurrence of slope failures such as landslides, the risk of landslide disasters can be evaluated from the evaluation of dangerous slopes during heavy rains, and from the precipitation including cumulative and regional characteristic data of topography, geology, and land use. Evaluation is being carried out. In the railway field in Japan, effective rainfall with half-life of 1.5, 6, 24 and 72 hours is the standard for train operation regulation.

Fig. 1 shows the positional relationship map of river X and each observation site store. This is a plot of each observation point, etc. on the Geographical Survey Institute map released by the Geospatial Information Authority of Japan. Fig.2 shows the time history of the effective rainfall calculated from the river water level for one month in July 2018 observed nearby Bridge A crossing River X and the actual rainfall observed at the rainfall observatory located in the catchment area of the river. The half-life of effective rainfall shown in the figure is calculated as 1.5 hours, 6 hours, 24 hours, and 72 hours, which is the half-life mainly used in the risk assessment of sediment-related disasters. This is for reference. Of the half-lives shown in Fig. 2 , the outline of the half-life of 24 hours is considered to be the closest to the outline of the time history of the river water level.

Next, Fig. 3 shows the relationship between the effective rainfall and the river water level with a half-life of 24 hours. This uses the data observed at the points in Fig. 1. The correlation coefficient r is also shown in the figure. Focusing on the relationship between effective rainfall and river water level shown in Fig. 3, the correlation coefficient r is 0.921, and there is a strong positive correlation, and although some non-linear relationships remain, the relationship between the two is linear as a whole. It turns out that there is. The part where the non-linear relationship remains is between 100 hours and 200 hours in Fig. 1 where the river water level is rising due to the heavy rain in July 2018. It was confirmed that the relationship was non-linear.

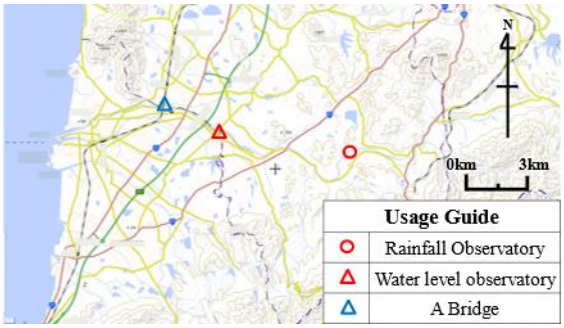

Fig. 1 Positional relationship map of river X and each observation site store

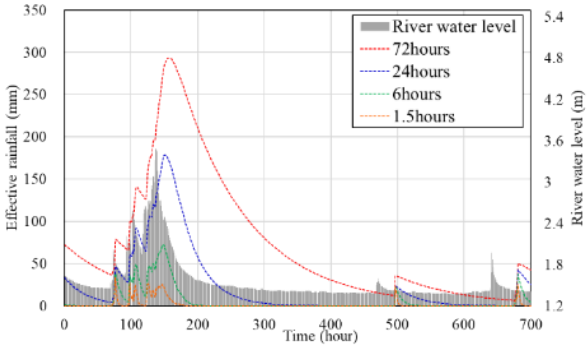

Fig. 2 Time history of the effective rainfall and the river water level

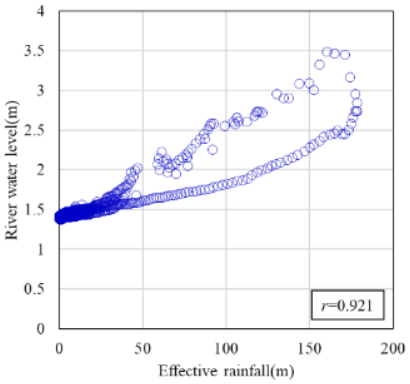

Fig. 3 Relationship between the effective rainfall and the river water level

When predicting the river water level, it is important to set the explanatory variables appropriately. As shown in Table 1, we decided to set up a case in which the effective rainfall range, which is an explanatory variable, was changed, and examined it.

Table 1 Consideration case of predicting the river water level

Case	Explanatory variable	
	Effective rainfall	Half-life
1	-12	24
2	-11,-12	
3	-10,-11,-12	
4	-9,-10,-11,-12	
5	-8,-9,-10,-11,-12	
6	-7,-8,-9,-10,-11,-12	
7	-6,-7-,8-,-9,-10,-11,-12	
8	-5,-6,-7-,8-,-9,-10,-11,-12	

Note: The "-" notation in the table means to use the effective rainfall n hours before the time you want to predict.

Study results

Table 2 shows the prediction results of the river water level. It was found that the coefficient of determination became higher as the explanatory variables were increased. The highest prediction accuracy was obtained when the effective rainfall calculated with the half-life of Case 8 as 24 hours was used as the explanatory variable from 5 hours to 12 hours before the time to be predicted. Fig.4 shows the time history of the water level prediction results. The continuity of the river water level was almost reproduced, and the coefficient of determination was 0.927. Furthermore, the prediction error of the maximum value of the river water level was 0.05 m, and it was confirmed that the prediction accuracy was sufficient even assuming that it would be used in practice.

Table 2 The results of predicting the river water level

Case	Predicted value (Maximum)	R^2
1	2.30	0.554
2	2.46	0.701
3	2.91	0.777
4	3.09	0.830
5	3.19	0.867
6	3.36	0.889
7	3.41	0.908
8	3.43	0.927

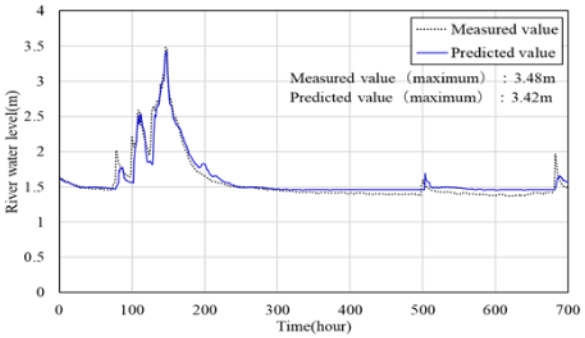

Fig. 4 Time history of water level prediction result (river X)

Additional study methods

In order to examine whether the constructed river water level prediction model can be applied to other rivers, the same water level prediction was performed for river Y (basin area 113.2 km²) and river Z (basin area 60.2 km²). The positional relationship diagrams are shown in Fig. 5 and Fig. 6. In addition, these figures are also plotted each observation point etc. on the Geospatial Information Authority of Japan map published by the Geospatial Information Authority of Japan.

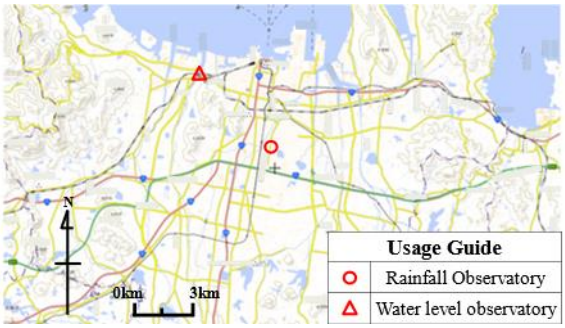

Fig. 5 Positional relationship map of river Y and each observation site store

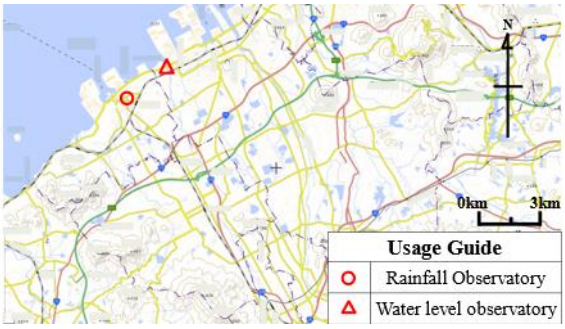

Fig. 6 Positional relationship map of river Z and each observation site store

Additional study results

The prediction results are shown in Fig. 7 and Fig. 8. For river Y, the fluctuation of the river water level could be reproduced, and the coefficient of determination was 0.973. In addition, the prediction error of the maximum value is 0.05 m, which shows that the prediction can be made with sufficient accuracy for practical use. On the other hand, river Z is considered to have been affected by the ebb and flow of the tide because the water level observation point is located near the estuary (about 0.6 km upstream from the estuary).

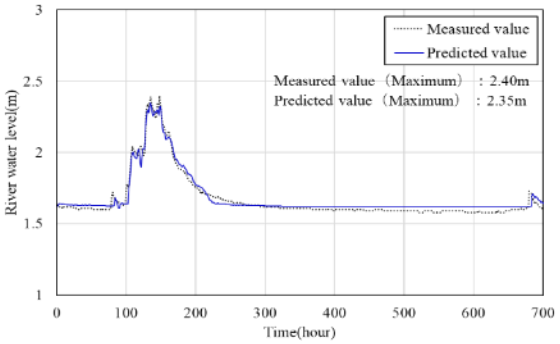

Fig. 7 Time history of water level prediction result (river Y)

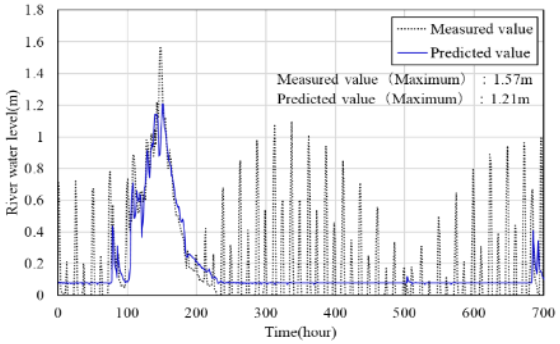

Fig. 8 Time history of water level prediction result (river Z)

Therefore, the relationship between the tide level and the river water level observed near the mouth of river Z is shown in Fig. 9, and when focusing on the fluctuation of the tide level and the river water level, it is found that the cycle of the rise of the river water level and the high tide are almost the same.

From these results, it was found that the proposed river water level prediction model can predict the river water level with sufficient accuracy in places where the river water level fluctuates gently, such as river X and river Y. On the other hand, it was found that it is necessary to add the tide level to the explanatory variables in the place where the river water level is affected by the tide level, such as river Z.

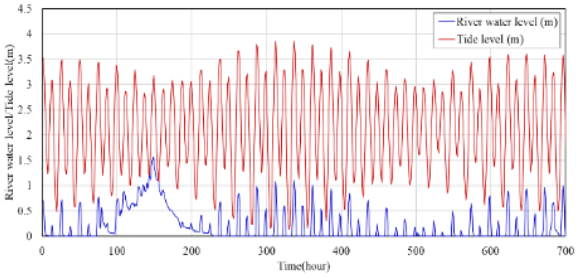

Fig. 9 Relationship between tide level and river water level

Evaluating Residual Structural Capacity of Bridge Piers

Study method

For the purpose of evaluating the safety of the pier with the progress of local scouring of the pier, the safety is evaluated according to the predicted future river water level. Fig. 10 shows a conceptual diagram of the action of the pier and the limit value. Where, h in the figure is the water level, D_f is the effective penetration depth, R_{vd} is the design vertical structural capacity of the direct foundation (kN), R_{hd} is the design horizontal structural capacity of the direct foundation (kN), and M_{md} is the maximum design. It is the resistance moment (kN ・ m). R_{vd}, R_{hd}, and M_{md} were calculated from Eq. (3) to (11) [7] [8].

$$R_{vd} = q_{vd} + \overline{\gamma_{e2}} D_f A' \tag{3}$$

Where, q_{vd} is the design vertical structural capacity of the direct foundation against increased load (kN / m^2), and A' is the effective area of the footing bottom surface (m^2). The effective area A' and the effective width B' of the direct foundation were calculated by the following Eq. (4) and (5).

$$A' = B'L \tag{4}$$

$$B' = B - 2e_x \tag{5}$$

Where, e_x is the eccentricity (m) of the point of action of the resultant force on the bottom of the footing and was calculated by the following Eq. (6).

$$e_x = \frac{M_d}{V_d} \tag{6}$$

Where, M_d is the design moment (kN ・ m) acting on the center of the footing bottom, and V_d is the design effective vertical load acting on the footing bottom.

$$R_{hd} = f_{rb} R_{hb} + f_{rp} R_{hp} \tag{7}$$

Where, R_{hb} is the horizontal structural capacity (kN) of the bottom surface of the footing, R_{hp} is the horizontal structural capacity (kN) of the front surface

of the footing, and f_{rb} and f_{rp} are the ground resistance coefficients for the horizontal structural capacity. The horizontal structural capacity R_{hb} on the bottom of the footing and the horizontal structural capacity R_{hp} on the front surface of the footing were calculated by the following Eq. (8) and (9).

$$R_{hb} = V_d \tan \delta_b \tag{8}$$

Where, V_d is the design effective vertical load (kN) acting on the bottom of the footing, and δ_b is the friction angle (degrees) between the bottom of the footing and the support layer.

$$R_{hp} = \alpha_h L\left(\sum p_{pi} H_i \cos \delta_{pi}\right) \tag{9}$$

Where, α_h is the shape coefficient of the front surface of the footing, p_{pi} is the passive soil pressure level (kN / m^2) of the front surface of the footing at the center of the layer of interest, and δ_{pi} is the front surface of the footing and the soil in the layer of interest. Friction angle (degrees). The passive soil pressure p_{pi} in front of the footing at the center of the layer of interest was calculated by the following Eq. (10).

$$p_{pi} = \left(\overline{\gamma_{ei}} h_i + \frac{\overline{\gamma_{ei}} H_i}{2}\right) K_{pi} + 2c_i K_{pi}{}^{1/2} \tag{10}$$

Where, $\overline{\gamma_{ei}}$ is the average effective unit volume weight (kN / m^3) above the section, h_i is the effective penetration depth to the upper surface of the layer of interest (m), and H_i is the layer of interest. Thickness (m), K_{pi} is the passive earth pressure coefficient in the layer of interest, and c_i is the degree of soil adhesion (kN / m^2) of the layer of interest.

$$M_{md} = \frac{BV_d}{2} - \frac{V_d^2}{2q_d L} \tag{11}$$

Where, q_d is the design vertical structural capacity (kN / m^2) considering the effects of eccentricity and inclination.

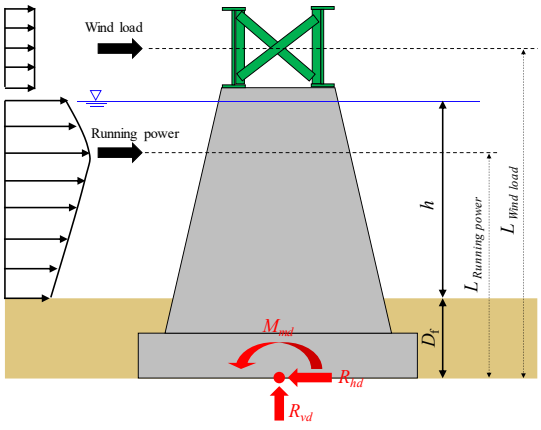

Fig. 10 Conceptual diagram of piers

We decided to calculate the risk of subsidence, sliding, and tipping by varying the penetration depth D_f to the bottom of the footing, assuming the river water level. The degree of risk is defined as the ratio of the response value acting on the pier to the limit value, and if this value is less than 1, the response value is below the limit value, so it is safe, and if it exceeds 1, the response value exceeds the limit value. Therefore, it is judged to be dangerous.

Study results

Fig. 11, Fig. 12, and Fig. 13 show the transition of the degree of risk according to the fluctuation of the effective embedding depth when the flow velocity is assumed to be 5 m / s for each subsidence, sliding, and tipping. The figure shows the cases where the river water level is 1m, 3m and 5m, and if the danger level exceeds 1, it is judged to be dangerous. From these results, in each case, the degree of risk decreases as the effective rooting depth increases. It was found that the change in the degree of risk was relatively small for sliding, and the effect on safety was small. On the other hand, it was found that the risk of subsidence and falls increases as the effective rooting depth decreases, which has a large effect on safety.

After obtaining the flow velocity of the river from the results of this calculation, the effective rooting depth is reduced as the local scour progresses, and the calculation is performed according to the water level predicted by the examined river water level prediction model. The degree of risk is calculated. In other words, it is possible to connect the judgment result of whether the risk level exceeds 1 to the safety evaluation of the pier.

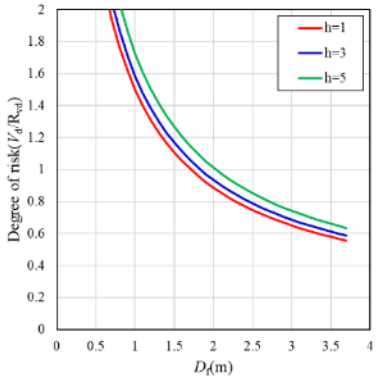

Fig. 11 Transition of risk level according to fluctuation of effective rooting depth (subsidence)

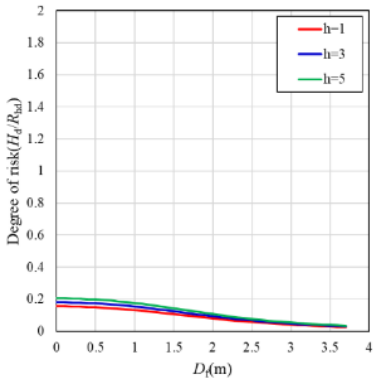

Fig. 12 Transition of risk level according to fluctuation of effective rooting depth (inclined)

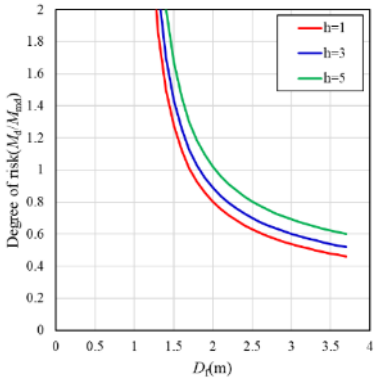

Fig. 13 Transition of risk level according to fluctuation of effective rooting depth (fall down)

From these results, it was shown that the residual strength of the pier can be calculated from the predicted future river water level and the safety can be evaluated. It was confirmed that the greater the local scour depth of the pier, the greater the risk level, leading to the judgment of danger. For this reason, if any one of the three items shown in the figure exceeds 1, it is necessary to restrict the use of railway bridges and road bridges and to reinforce the riverbed.

CONCLUSION

In this study, we used SVR, which is one of the machine learning algorithms, and created a river water level prediction model using effective rainfall as an explanatory variable. Therefore, it was shown that the structural capacity of the pier can be calculated from the predicted future river water level and the safety evaluation can be carried out.

The water level prediction model was possible, and the coefficient of determination was the coefficient of determination for the overwater level at the moment of land rainfall. The coefficient of determination was the total water level, which was determined by moving the most.

In the evaluation of the residual strength of the pier, the degree of risk associated with the fluctuation of the effective embedding depth was calculated by expressing the progress of local scouring by the decrease of the effective embedding depth. As a result, it was found that it is possible to quantitatively evaluate the decrease in the safety of piers due to the progress of local scouring and the increase in river water level.

ACKNOWLEDGEMENTS

This research was carried out by the Cabinet Office's Strategic Innovation Creation Program "Disaster Prevention / Disaster Mitigation Function Enhancement" (Representative: Yoshiyuki Kaneda). We would like to express our gratitude here.

REFERENCES

[1] Koji Tsuda, What is a support vector machine, Journal of the Institute of Electronics, Information and Communication Engineers, Vol.83, 2020, pp.460-466.
[2] Naomasa Honda, A Study on Setting the Half-Life in Effective Rainfall as a Debris Flow Generation Criteria, JSCE Proceedings B1 (Hydraulic Engineering), Vol.73, No.4, 2017 pp.I_247-I_252.
[3] Shiro Hayashi and Takashi Yamada, Regarding the characteristics of the effective rainfall coefficient in recent sediment-related disasters, Journal of Japan Society of Erosion Control, Vol.66, No.2, 2013, pp.31-39.
[4] Takuya Takeda, Haruka Tokuda, Toshiyuki Oyama, and Shigeru Koyama, Risk assessment of sediment-related disasters using effective rainfall and regional information, JSCE Proceedings F6 (Safety Issues), Vol.69, No.2, 2013, pp.1_81-1_86.
[5] Masayuki Hitokoto, Masaaki Sakuraba, and Yuichi Kiyoichi, Development of River Water Level Prediction Method Using Deep Learning, JSCE Proceedings B1 (Water Engineering), Vol.72, No_4, 2016, pp. 1_187-1_192.
[6] Masayuki Hitokoto and Masaaki Sakuraba, Hybrid river water level prediction method combining deep neural network and distributed model, JSCE Proceedings B1 (Water Engineering), Vol.73, No.1, 2017, pp.22-33.
[7] Railway Technical Research Institute, Design Standards for Railway Structures and Explanations: Basic Structures, 2012, pp148-155.
[8] Railway Technical Research Institute, Design Standards for Railway Structures and Explanations: Concrete Structures, 2004, pp55-58.

8th Int. Conf. on Structure, Engineering & Environment (SEE), Mie, Japan, Nov.10-12, 2022, ISBN: 978-4-909106094 C3051

TIME, STRESS AND STRAIN DEPENDENCY OF PILE STIFFNESS: IMPACT ON PILE BEHAVIOR AND STATIC PILE LOADING TESTS RESULTS

Fabien Szymkiewicz[1], Wassim Mohamad[1], Nader Elayni[1] and Carlos Minatchy[1]
[1]Université Gustave Eiffel, France

ABSTRACT

Static pile loading tests are carried out for different purposes: feed extended databases from which design bearing capacity of piles are derived, control the design, develop new piling methods, but also in some cases better understand the behaviour of a deep foundation submitted to additional solicitations such as temperature variations, in the case of geothermal foundations systems. These tests are conducted on any type of piles, themselves made from very different materials. For cast-in-place piles made of a combination of cementitious materials (either cement paste, mortar or concrete for example) and steel, the stiffness of the pile is a combination of the stiffnesses of the different materials. Furthermore, cementitious materials are well known to be evolutive materials, especially regarding their strength. By contrast, the strain-, stress- and time- dependency of the stiffness of the cementitious materials and therefore of the cast-in-place piles is not so well known, and therefore generally not taken into account when analysing static pile loading tests. The aim of this publication is to impart the importance of the evolution of pile stiffness with time and under stress, through different practical examples, and comparisons are made with results obtained with more classical analysis methods.

Keywords: deep foundations, time-dependency, stress-dependency, stiffness, pile load tests

INTRODUCTION

Determination of the bearing capacity is the main purpose of a static load test carried out up to the failure, in which case the test is called a conformity test. However, another purpose can be the study of the behavior of the pile under a certain load, usually under SLS load, or slightly higher. Some tests, called control tests, are carried out on the express purpose of assessing the settlement under this load.

Furthermore, piles are often instrumented, whether it be to determine the load distribution along the shaft or to study their behavior under particular conditions such as the boring of a tunnel nearby [1] or a thermal loading [2].

Therefore, to be able to evaluate the evolution of the loads at different depth, as well as to be able to predict the settlement of a pile in any given situation, it is necessary to know its stiffness under any level of stress [3].

This stiffness can be in a first approach assumed to be equal to 20 GPa for a short term solicitations or 10 GPa for long term behavior [4].

However, concrete is a non-linear elastoplastic material, its execution conditions affect its homogneneity. Results achieved on cored samples shows the great variability of the modulus of pile concrete [5]

It is also important to keep in mind that moduli determined in laboratory are often determined using a test method non representative of the pile solicitation, with very small deformations achieved through one or multiple loading cycles [6].

Furthermore, the formulation of the concrete has to be taken into account. Following Eq. (1), it is possible to estimate the concrete modulus from its uncompressive strength (Eurocode 2):

$$\mathbf{E_{cm} = 22(f_{cm}/10)^{0,3}} \quad (1)$$

However, it is also necessary to take into account the reinforcing steel bars of the cage inside the pile. The French standard NF P 94-150-1 [7] proposes the equivalent modulus method, taking into account the modulus of each material in the pile as well as their respective cross sectional area. This method is however often non-representative of the stiffness of the pile. Indeed, and as stated before in the case of cored samples, the values of the concrete modulus are given for a unique strain level, generally very small, leading to modulus values higher than in reality and, if used as it is, to incorrect interpretations.

This paper focuses on the stress, strain and time dependency of pile stiffness: it presents several examples highlighting the importance of the adequate consideration of the stiffness variability for a correct exploitation of the results of a static load test, as well as the assessment of a pile behavior.

STRESS AND STRAIN DEPENDENCY OF PILE STIFFNESS

Design Calculations

Taking into account the evolution of the pile stiffness in relation to the level of stress (or strain) has a big impact on the theoretical load-displacement curve.

Indeed, Fig. 1 shows the results of multiple calculations carried out with a pile stiffness kept constant along a pile, realized in a multi-layered soil, but ranging for 20 to 50 GPa. It is clear that while the impact on the bearing capacity of the pile is null, as the overall shape of the curve is minimally impacted, it is on the contrary of the upmost importance around the SLS load.

On this example, the SLS load of the pile, which would be in part defined as a fraction of the bearing capacity and by the tolerated displacement of the structure, would vary from 3800 kN to 5300 kN.

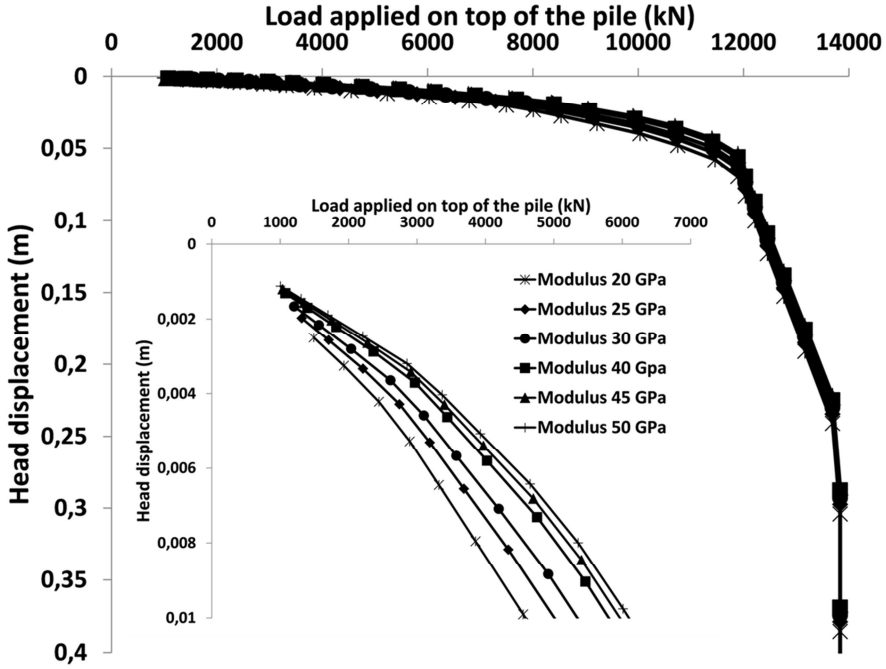

Fig. 1 Load-settlement curves for a same pile with different modulus (with a focus on the first part of the curve)

Furthermore, it is interesting to look at the theoretical mechanism of load distribution. Mobilization of the unit shaft friction q_s and base pressure q_b depends on displacement, which is due to the settlement of the pile as well as the deformation of the shaft.

The order of mobilization of the layers resistances also depends on the pile stiffness. Going on with the same example as before, it is clear that a higher modulus will imply a faster solicitation of the deep layers and of the base resistance, while the surface layers will not be solicited at first. This is due to the fact that with a shaft being stiffer, the shaft does not strain enough to allow for the mobilization of the q_s. Figure 2 clearly shows this trend. It is important to note that the shape of the curves is due to the shape of the t-z curves.

Of course, each geotechnical model is different, so that it is difficult to generalize the impact of this behavior. However, it can be seen on Fig. 2 that the difference at the base is negligible, while for the layers above, and more importantly for the first layer, it may be important in some cases to have this information in mind.

On Fig. 2c and Fig.2e, which represent mobilization of the shaft friction under its SLS load, it is possible to note that the difference, in terms of mobilization of q_s, can go as high as 20 kPa, in this particular case, which is approximately 10% of the $q_{s;max}$.

Regarding the base resistance, under the SLS load, the effect of the modulus is negligible, as the base is barely solicited. Furthermore, from Fig. 2b, it can be concluded that the mobilization of q_b is barely impacted by a change in modulus. This can be explained by the fact that the friction of the first layers is fully mobilized approximately when the base begins to be really solicited.

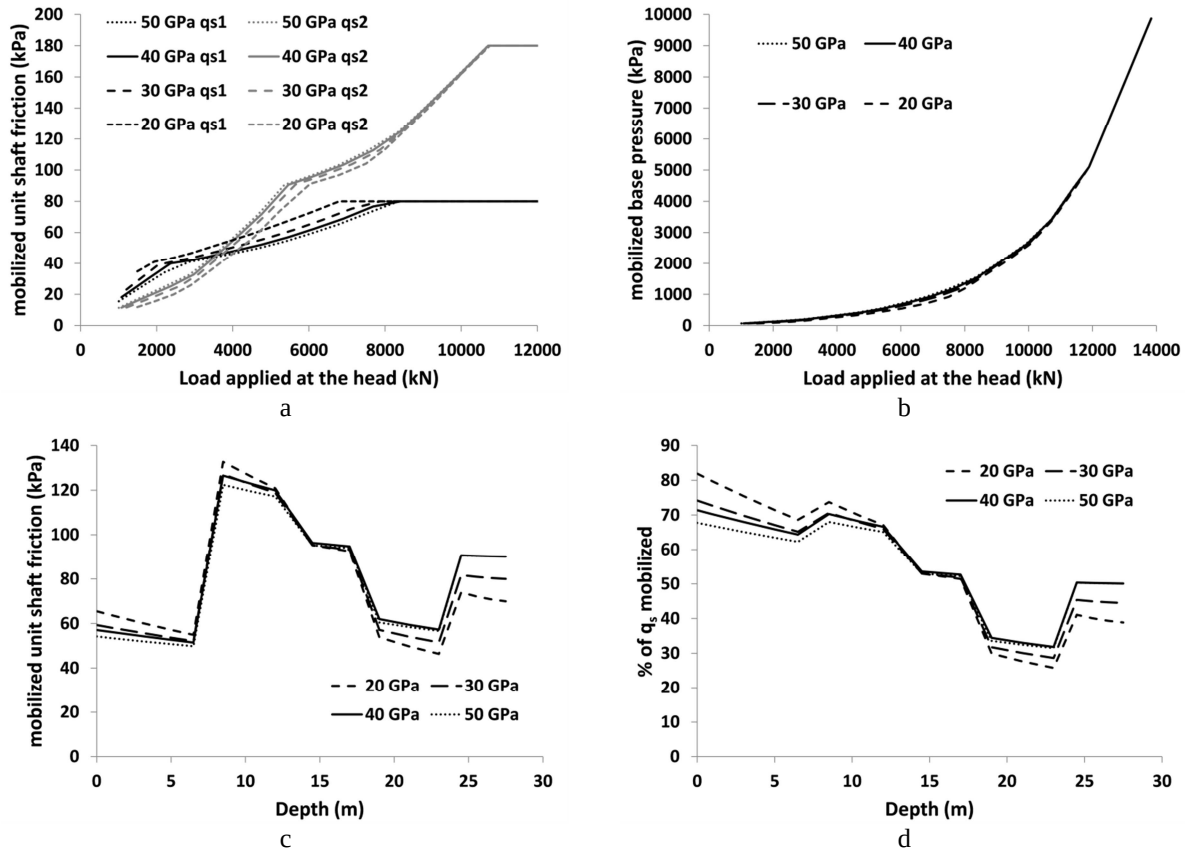

Fig. 2 Mobilization of q_s (a) and q_b (b) in function of the load applied at the head, and mobilization of q_s in function of the depth ((c) and (d)), depending on the pile stiffness

Finally, Fig. 3 shows the distribution of the axial load along the pile, under SLS load. The difference of pile stiffness between a very stiff pile (50 GPa) and a soft pile (20 GPa) results in a change of load distribution, as expected from the Fig. 3. However, this difference is not so pronounced, with a maximum difference load at any given depth less than 400 kN, or 8% of the load applied at the pile head.

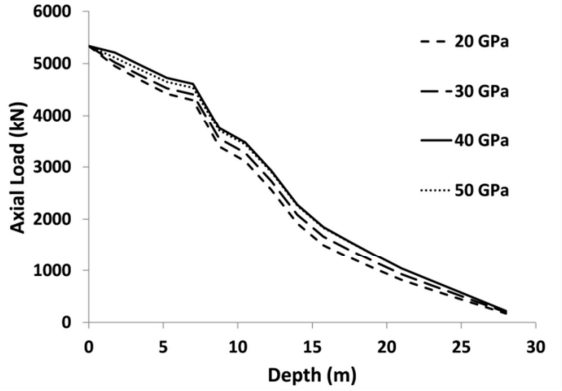

Fig. 3 Axial load distribution in a pile under SLS load, in function of its stiffness.

From what has been said above, it is clear that it is of the upmost importance to take into account the strain-dependency of pile stiffness. This is a crucial point when calculating the pile load-displacement curve. However, it is not so true when trying to assess the actual mobilization of unit shaft friction for each layer, as seen above, and even more as the dispersion of this value is quite large. This variability alone has a bigger impact on the incertitude of the mobilization of the friction along the shaft than the incertitude caused by the choice of the modulus.

Pile Load Tests Analysis

As stated in the introduction, determination of the pile stiffness through laboratory tests achieved on cored samples is not representative of the actual stiffness of the pile: neither the level of stress nor the representativity of the material is pertinent in this case.

Therefore, it is mandatory to take into account the strain-dependency of the modulus to analyze the data of the strain gauges (or assimilated) used during a pile load test. To do so, multiple authors proposed different methods, summarized by Lam and Jefferis (2011). Of these methods, the one proposed by

Fellenius (2001) seems one of the most commonly used.

However, a simpler method would be to use, the first level of strain gauges to assess the stiffness of the pile, in function of the applied load. Then, knowing the cross sectional area of the pile, the modulus can be easily estimated.

Figure 4 shows the evolution of the modulus derived from the strains measurements at the pile head, for four similar piles, realized on the same site, with the same machine and the same concrete formulation. The discrepancy in the results implies that it is necessary to carry out this study every time a pile is tested, even on if multiple piles are tested on the same site.

The purpose of an instrumented pile load test is mainly to differentiate the shaft resistance from the base resistance: therefore, an accurate estimation of the load distribution along the shaft is needed. The loads at different depths are derived from the strains measurements at each level, and from the strain measured at the pile head, as stated above.

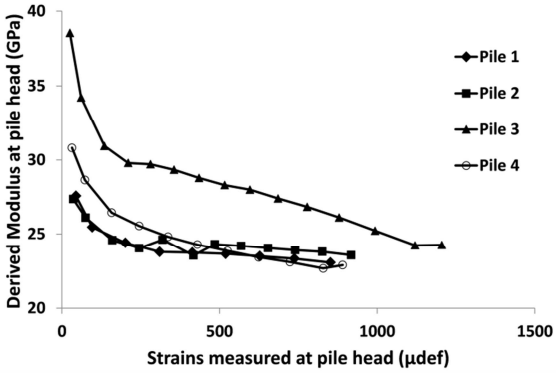

Fig. 4 Evolution of strains and modulus during load test for four similar piles realized on the same site

Continuing to use the pile example first used on Fig. 1, Fig. 5a shows the differences in terms of axial load distribution caused by the choice of pile stiffness. The most accurate hypothesis is to use a strain-dependent modulus to derive the axial load at each strain level: the evolution of the modulus can be established by segments or using a polynomial fit curve that relates the modulus to the strain level.

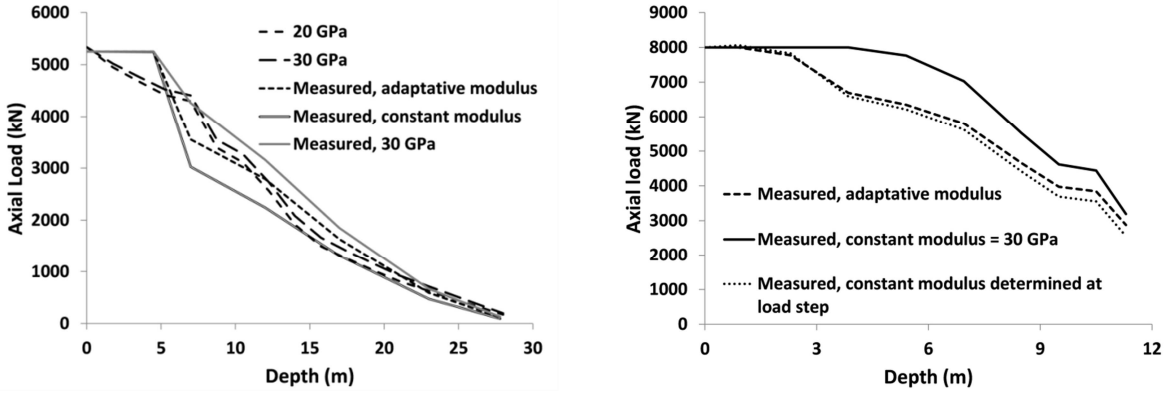

Fig. 5 Axial load distribution in two piles: comparison between calculated values and measured values, with different choices of pile stiffness under SLS load (a) and at failure (b)

Figure 5 shows a clear difference between the use of a modulus equal to 30 GPa (a common practice) and the adaptation of the modulus value in function of the depth (and therefore the stain level). While, under SLS load, the main difference is observed along the shaft, with almost no difference for the base pressure (as it should be, as SLS load is only a fraction of the bearing capacity), at failure, the differences are much more notable, with the base pressure being impacted too, by the modulus choice. Differences can amount for more than 1 MN at certain depths, with the solution of using a constant modulus of 30 GPa clearly over-estimating the base resistance as well as the shaft friction at the deeper levels, and therefore overestimating and underestimating q_s values by as much as 35%.

It is therefore of the upmost importance to analyse the data of a pile load test, having in mind the strain dependency of the pile stiffness.

Other factors related to this issue should also be taken into account, such as the age of the pile at the date of the test or the formulation of the concrete of the test pile, as the cementitious materials are getting stiffer as days goes by, and performing a test on such a pile at a young age or with a formulation different from the formulation which will be used during the actual project could lead to the overestimation of the pile head displacement, and could therefore lead to overdesign of the piles for a project.

The example showed on Fig. 1 can also be

scrutinized on from the 'time' point of view, as it relates in some way to the hardening process of the concrete.

TIME DEPENDENCY OF PILE STIFFNESS

Creep Strains

As stated above, concrete, as well as other cementitious materials, is an evolutive material that hardens with time, up to a point.

Another important point to take into account is also creep, or time dependent deformation.

As piles are subjected to creep, the calculation of their deformation, and therefore of their settlement, shall take into account this phenomenon. This is partly done, for example in France, where the long-term modulus of a pile should be considered equal to 10 GPa, as stated above.

A pile was subjected to a constant loading (equivalent to the SLS load) for more than 4 months, and strains at different levels were monitored (Fig. 6). The pile was loaded gradually, with load steps of equal magnitude. An automated hydraulic pump kept the load constant on top of the pile. Slight variations were caused by the differences in temperatures, which impacted the pump as well as the load cell.

It can be seen on Fig. 6 that the strains never stopped increasing, whether at the levels close to the surface or more in depth. However, the rate of strain was different, depending on the depth: the lower the level, the slower the rate of creep

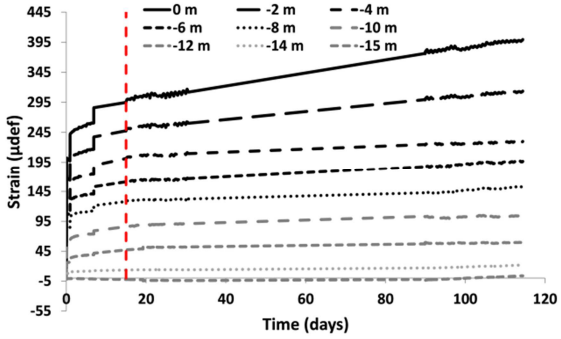

Fig. 6 Strains in function of time, for a pile loaded under SLS load

Therefore, at the end of the four months loading period, it was seen that the pile had been subjected to creep, with a maximum accumulation of strains of 100 µm/m at the pile head (Fig. 7a).

For the lowest levels, the creep strains were much lower, as they were subjected to smaller loads. Therefore, it seems that the creep strains were very much dependent on the load level.

However, when looking at Fig. 7b, which represent the ratio between creep strains and instantaneous strains, it is clear that the creep is independent from the load level, as all the strain gauges (here vibrating wires) recorded the same ratio creep strains over instantaneous strains. This ratio is on average equal to twenty percent.

The two lowest levels present somewhat abnormal values because of the low level of strain they recorded to begin with: a slight variation of the strain measurement creates a larger than really measured ratio.

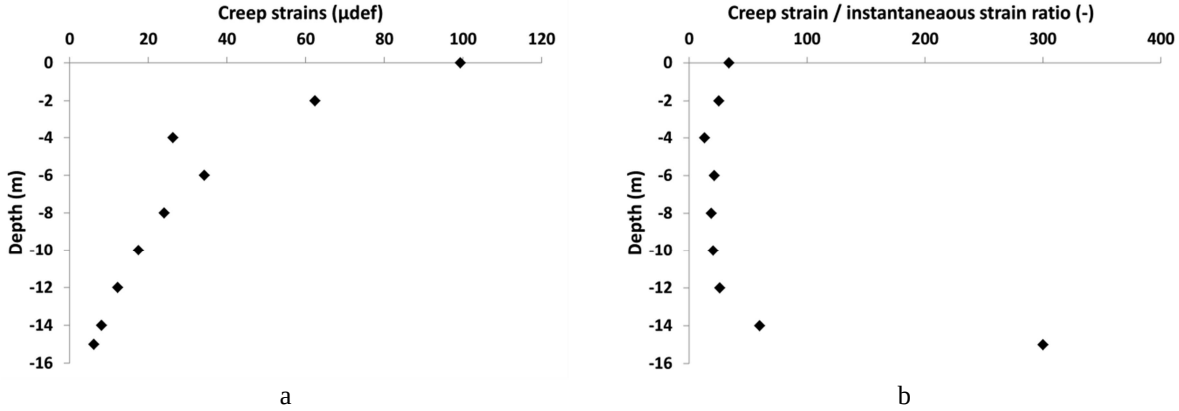

a b

Fig. 7 creep strains (a) and creep strain / instantaneous strain ratio at different levels, for a pile under SLS load for 4 months

From these measures, it is clear that the impact on the way to analyze the data for long-term pile monitoring has to be adjusted.

Pile Stiffness Adaptation

Figure 8 shows the initial axial load distribution along the pile, as well as the calculated distribution after four months of loading, using the initial

modulus of the pile.

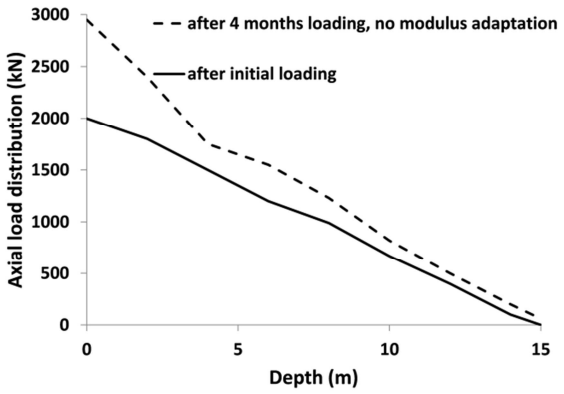

Fig. 8 Axial load distribution just after loading and after four months of loading

Looking at the new distribution, it seems obvious that the pile stiffness needed an adjustment, so as to fit with the initial distribution. Indeed, as creep occurs, strains are increasing while the applied load stays the same. Therefore, it means that the pile stiffness has to be decreased to keep the axial load distribution along the shaft constant, as the pile was not subjected to any other solicitations.

Creep strains over instantaneous strains ratio being fairly constant along the length of the pile, it is clear that the degradation of the pile stiffness must also be of the same magnitude, at every levels.

This is in accordance with the Eurocodes [8], which states that creep should be taken into account, and that creep is depending on the ambient humidity, the dimensions of the concrete element considered, the age at the moment of the loading and the type of cement.

For long term considerations, creep strains equal two times instantaneous strains, meaning that the pile stiffness must be degraded by a factor of three.

Incidentally, in this study, it can be seen that a loading of a pile for four months does not represent at all a long term behavior of the pile, creep strains only equaling for 20% of the instantaneous strains.

CONCLUSIONS

Static pile load tests are expensive, long tests, the results of which can considerably impact the design of the foundations of a structure or building.

Because of these high stakes, it is a priority to plan thoroughly these tests, and to carry them out in the best conditions, but also to analyze the data in the best possible way.

Taking into account the strain dependency of the material constitutive of the pile is therefore mandatory, as values given in the codes are default values, not taking into account the exact formulation of the cementitious material as well as the overall context (soil humidity, execution conditions, etc.).

Therefore, it was shown it this publication that this is of particular importance when deriving loads from strains.

However, it is not so important for design studies such as the distribution of loads along the shaft under SLS load, for example, as other variables are much more impacting. Also, while estimating the modulus of the pile precisely is very important for the prediction of the load-settlement curve, it is not mandatory to take into account its strain-dependency.

Finally, for long-term studies of a pile behavior, the time dependency of the pile stiffness shall be taken account and studied in details.

REFERENCES

[1] Mohamad, W.; Bourgeois, E.; Le Kouby, A.; Szymkiewicz, F.; Michalski, A.; Branque, D.; Berthoz, N.; Soyez, L.; Kreziak, C. Full scale study of pile response to EPBS tunnelling on a Grand Paris Express site. Tunnelling and Underground Space Technology. Vol. 124, 2022

[2] Bourne-Webb, P. J.; Amatya, B.; Soga, K.; Amis, T.; Davidson, C. and Payne, P. Energy pile test at Lambeth College, London: geotechnical and thermodynamic aspects of pile response to heat cycles. Géotechnique 59:3, 2009, pp.237-248

[3] Lam, C. and Jefferis, S.A.. Critical assessment of pile modulus determination methods, Canadian Geotechnical Journal, 48, 2011, pp.1433-1448.

[4] AFNOR. NF P94-262: Justification of geotechnical work - National application standards for the implementation of Eurocode 7 - Deep foundations, 2012, design standard.

[5] Szymkiewicz, F.; Sanagawa, T.; Nishioka, H. and Le Kouby, A. Feedback on static axial pile load tests for better planning and analysis, 2021, Proceedings of the Second International Conference on Press-in Engineering, Japan.

[6] AFNOR, NF EN 12390-13: Testing hardened concrete - Part 13 : determination of secant modulus of elasticity in compression, 2021, test standard.

[7] AFNOR. NF P94-150-1: Essai statique de pieu isolé sous effort axial en compression, 1999, test standard.

[8] AFNOR. NF EN 1992-1-1. Design of concrete structures Part 1-1: General rules and rules for buildings, 2005, design standard.

8th Int. Conf. on Structure, Engineering & Environment (SEE), Mie, Japan, Nov.10-12, 2022, ISBN: 978-4-909106094 C3051

A STUDY ON THE PROPERTIES OF CONCRETE WITH FLY ASH AND GARBAGE MOLTEN SLAG FINE AGGREGATE

Zihao Liu[1], Koji Takasu[1], Hidehiro Koyamada[1], and Hiroki Suyama[1]
Dept. of Architecture, Faculty of Environmental Engineering, The University of Kitakyushu, 1-1 Hibikino Wakamatsu, Kitakyushu, Fukuoka 8080135, Japan

ABSTRACT

This experiment investigated the properties of fly ash concrete replacing sand with garbage molten slag fine aggregate. The time development of compressive strength, elastic modulus, drying shrinkage, creep and pore structure were tested. The relationship between pore structure and compressive strength, relationship between pore structure and drying shrinkage were analyzed. A total of 4 mixes of concrete were prepared: the control concrete, one mix including cement replaced with fly ash (30% by strength contribution rate), two mixes including sand replaced with garbage molten slag fine aggregate (25%, and 50% by volume). The experimental results showed that by replacing cement with fly ash according to the strength contribution rate, the early strength (7d, 28d) of concrete not decreased, and the 91-day strength increased. Incorporation of recycled fines reduced drying shrinkage and creep. The pore volume in the range of 0.003 ㎛ to 0.1 ㎛ is considered to have a large effect on the drying shrinkage of concrete.

Keywords: Fly ash, Garbage Molten Slag, creep, Drying shrinkage, Pore structure

INTRODUCTION

With the rapid development of industrialization and urbanization, concrete was widely used in the construction industry, around 10 billion cubic meter of concrete was used every year [1], aggregate accounts for about 60% to 80% of the concrete volume [2]. As a result, a large amount of natural aggregate is consumed [3]. In 2012, the amount of direct incineration of general waste in Japan was 33.99 million tons per year, of which 12.35 million tons, or 36%, was melted to produce 790,000 tons of molten slag. The manufactured molten slag is used as road aggregate, concrete aggregate, ground improvement material, and the like. The garbage molten slag (GMS) generated from the melting facility for general waste is being effectively used from the viewpoint of recycling and quality stability, but the utilization rate as an aggregate for concrete is currently low. Therefore, with the aim of increasing the amount of molten slag used, it is necessary to consider a formulation that exhibits the same performance as when using natural aggregate. In another hand, the world produces about 900 million tons of fly ash every year, of which only about 53.5% is effectively utilized [4]. Many scholars have studied the properties of fly ash concrete, pointing out that the application of fly ash can improve the working performance of concrete, improve durability, reduce shrinkage, and improve the microscopic pore structure [5-9]. However, the research on the effect of fly ash on concrete containing recycled aggregate is not enough. Therefore, in this study, we evaluated the durability of concrete with different mixing ratios of garbage molten slag and fly ash.

MATERIALS AND EXPERIMENT METHOD

Materials and mix proportion

Table 1 shows the physical properties of the materials used in this experiment. As the cement, ordinary Portland cement was used, sea sand and garbage molten slag were used as fine aggregate, and crushed stone was used as coarse aggregate. Fly ash corresponding to Class II in JIS A 6201. Table 2 shows the mix proportions, and the unit water volume was 170 kg / m^3, the water-binder ratio was 45.5% for the control concrete, and 52.3% for the concrete with fly ash. Keep the compressive strength of concrete at 28d remain the same as the control group, cement replaced with fly ash (30% by strength contribution rate). In addition, the unit coarse aggregate bulk volume was set to 0.5 m^3 / m^3 to make it a high-fluidity concrete, target air volume is 5.0 ± 1%.

Experiment method

Measurement items are compressive strength, drying shrinkage and creep properties. The compressive strength test was conducted according to JIS A 1108, the drying shrinkage test was conducted according to "Method of measurement for length change of mortar and concrete" of JIS A1129-2, and 100 × 100 ×400mm prismatic specimens were produced. After casting, they were demolded at 1 day of age, then cured in water at 20 ° C for 7 days or in a constant temperature room with a temperature of 20 ° C and a

humidity of 60%. Specimens were taken out of the water at 7 days of age, and a stainless-steel chip was attached to both end faces of the specimens, and then both end faces were sealed to measure the base length. The specimens for measuring the drying shrinkage were cured in a constant temperature and humidity room with a temperature of 20 ± 1.0 ° C and a relative humidity of 60 ± 5%. In the creep test, the strain was measured according to JIS A 1157 “Method of test for compressive creep of concrete”. This constant temperature room could not strictly control the initial one-month humidity. The creep test uses a loading device of a separate type of hydraulic jack. Three test specimens were stacked vertically. The loading load was set to 1/3 of the maximum load of compressive strength at 28 days, and loading started from 28 days. Three strain gauges were attached to three places in the center of the test specimen, and the average value of the three strain gauges was taken as the total measured strain of the test specimen. And the average value of three test specimens was taken as the total strain of the mix proportion. In order to calculate the creep strain, measuring the no-load strain by preparing two pieces no-load specimen of Φ100 x 200 mm in each mix proportion similar to the creep test, attaching the strain gauges, and storing in a constant temperature room where the creep test is performed, and the measurement was performed with a data logger simultaneously with creep strain.

Table 1 Properties of materials used in experiment

Materials	Type	Properties	Symbol
Cement	Portland cement	Density 3.16 [g/cm^3]	C
Water	Tap water	-	W
Fine aggregate	Sean sand	Oven-dried density 2.59[g/cm^3] Water absorption 1.14% Soild content 62.1% Fineness modulus 2.35	S
	Garbage molten slag	Oven-dried density 2.79[g/cm^3] Water absorption 0.81% Soild content 59.7% Fineness modulus 2.75	RS
Coarse aggregate	Crushed stone	Oven-dried density 2.55[g/cm^3] Water absorption 0.50% Soild content 61.34% Fineness modulus 7.16	G
Admixture	Fly ash (adapted to JIS Ⅱ)	Density 2.20 [g/cm3] LOI 2.1% Specific surface area[3.41cm^2/g]	FA
Agent	AE water reducer	alkyl ether anionic surfactant	

Table 2 Mix proportions

Symbol		unit mass[kg/m^3]					
	W/B	W	C	FA	S	RS	G
FA0-0	0.455	170	374	0	952	0	814
FA30-0	0.523		325	139	828	0	
FA30-25			325	139	621	220	
FA30-50			325	139	414	439	

For porosity measurement, a specimen (φ100×200mm) that had been cured in water to the target material age was crushed, and a sieve was used to make a particle group of 2.5 to 5.0mm, and then the hydration reaction was stopped by immersion in acetone, and vacuum drying for 72 hours, then the sample was used. The measurement was performed with a mercury intrusion porosimeter (MIP).

RESULTS AND DISCUSSION

Compressive strength

Figure 1 shows the results of compressive strength. At 7 days of age (in water), the higher the substitution rate of both FA and garbage molten slag, the lower the compressive strength tends to be, but at 28 days of age (in water), FA0-0, FA30-0, FA30-25 compressive strength showed similar values. Therefore, it can be said that the strength contribution rate of 30% by compounding was appropriate. FA30-0 has the largest increase in strength after 28 days of age. This considered the increase in strength due to the pozzolan reaction. In addition, FA30-25 and FA30-50 were also expected to have a pozzolan reaction due to the inclusion of FA, but the increase in strength did not increase as much as FA30-0. From this, the effect of suppressing the increase in strength after 28 days of age was observed by mixing the garbage molten slag. For concrete with fly ash, up to 28 days of age, the compressive strength increase was larger in the air curing, at 28-91 days of age, water curing tends to increase strength more. From this, it is considered that water curing has the effect of enhancing the pozzolan reaction by fly ash as compared with air curing.

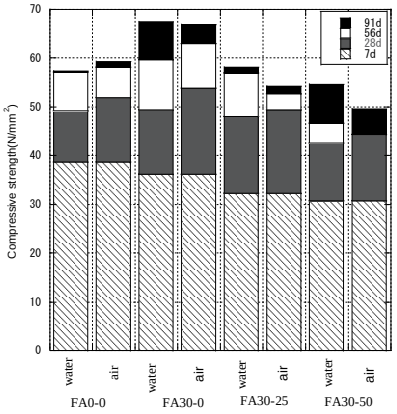

Fig. 1 The compressive strength of concrete

Drying shrinkage

Figure 2 shows the development over time in the drying shrinkage. Comparing FA0-0 and FA30-0, it was found that the drying shrinkage when fly ash was mixed tended to be reduced. In addition, FA30-25 showed a larger strain and FA30-50 showed a smaller strain than FA30-0. From this, it is considered that the replacement rate of garbage molten slag does not have the effect of suppressing shrinkage at 25%, but

the replacement rate of 50% has a certain effect of suppressing shrinkage. Figure 3 shows the mass reduction rate. Compared with Fig. 2, it can be seen that mass decreases with strain. The results show that drying shrinkage is not only related to water evaporation, but also related to the replacement rate of fly ash and aggregate.

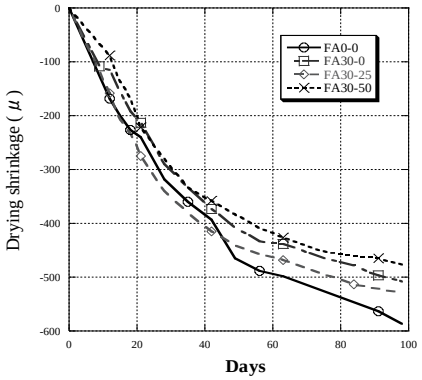

Fig. 2 The development over time in drying shrinkage.

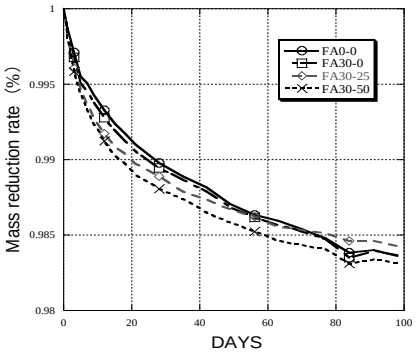

Fig. 3 The mass reduction rate over time

Creep

Figure 4 shows the change over time in the unit creep strain. FA30-0 and FA30-25 have lower creep strain than FA0-0. From this, it was confirmed that mixing FA has the effect of suppressing creep strain. However, the strain of FA30-50 showed a larger value than the strain of FA0-0. Therefore, when the replacement rate of molten slag is 25%, the effect on strain is small, but when it is increased to 50%, the strain tends to increase.

In this study, we investigated the correspondence between the experimental results of creep obtained by the experiment and the predicted value obtained by the creep strain prediction formula shown in the previous studies. The predicted results of the AIJ formula (Architectural Institute of Japan proposed) has been reported to have the highest adaptability for ordinary concrete [10], so we only analyzed the AIJ formula. The predicted values of FA0-0, FA30-0, and FA30-25 tended to be overestimated with respect to the experimental values. The predicted value of FA30-50 was a result close to the experimental value. While the AIJ formula is applied to ordinary concrete, the test specimen of this study is positioned in high-strength concrete with a water-bonding material ratio of around 40%, so it is considered that the result is significantly lower than the prediction formula. In addition, the prediction accuracy in the numerical prediction problem is evaluated using the RMSE value, which indicates how much the predicted values obtained from these prediction formulas deviate from the experimental values. When using high-strength concrete, by regression analysis we examined the correction factor to match the predicted value with the experimental value. Table 3 shows the correction coefficients analyzed, FA0-0 was 0.52, FA30-0 was 0.56, FA30-25 was 0.60, and FA30-50 was 0.95. As a result, in the AIJ formula, when calculating the predicted value when fly ash is mixed, and garbage molten slag is replaced with high-strength concrete, the predicted value can be calculated more accurately by using the above correction coefficient.

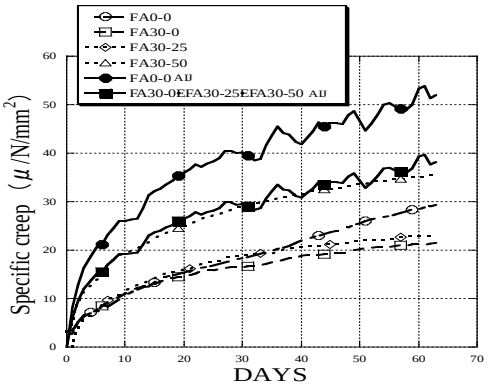

Fig. 4 The change over time in specific creep strain.

Table 3 The correction coefficients

	FA0-0	FA30-0	FA030-25	FA30-50
coefficients	0.52	0.56	0.6	0.95

The relationship between pore structure and compressive strength or drying shrinkage

Fig. 5 shows the pores volume of concrete. Comparing the amount of decrease in pore volume between 7 and 91 days of age, the amount of decrease in concrete with fly ash showed a larger decrease. In addition, when combined with the results of compressive strength, it is supported that the increase in the strength of the FA mixture after 28 days of age is due to the pozzolan reaction. Moreover, since no significant difference can be confirmed even when comparing FA30-25 and FA30-50, it is considered that the effect of the substitution rate of garbage molten slag on the pore structure is small. Figure 6 shows the relationship between the pores volume and the compressive strength. It was found that there is no

relationship between the compressive strength and the pore volume regardless of whether the pore volume is 50 nm or more or the total pore volume. Therefore, we think that the compressive strength of concrete is affected by the aggregate material in addition to the pore structure. Figure 7 shows the relationship between the pore volume and the dry shrinkage. The pore volume showed a particularly high correlation in the range of 0.003 ㎛ to 0.1 ㎛. Therefore, it is considered that the pore volume in this range has a large effect on the drying shrinkage of concrete.

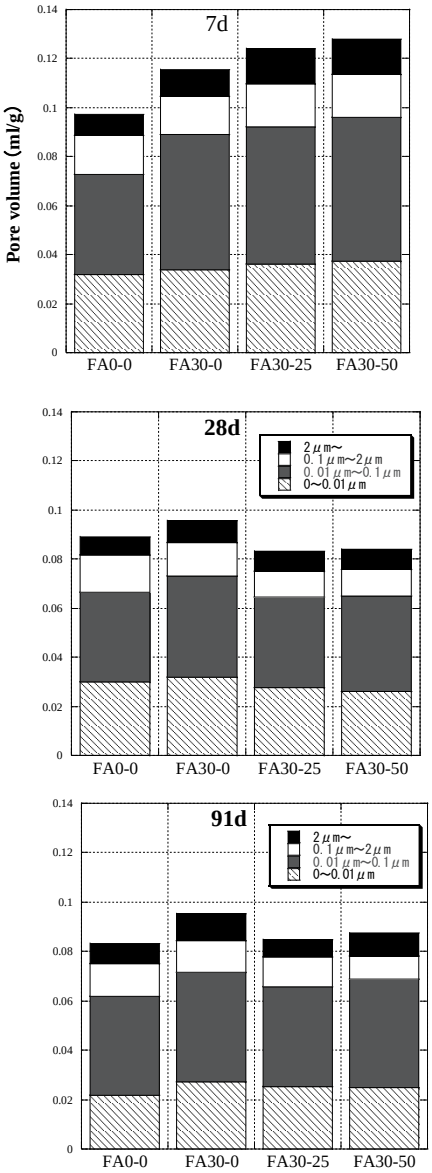

Fig. 5 The pores volume of concrete.

CONCLUSION

1. Regarding compressive strength, FA30-0 has the largest increase in strength after 28 days of age. This is considered the increase in strength due to the pozzolan reaction. Furthermore, by mixing garbage molten slag, the effect of suppressing the increase in strength after 28 days of age was observed.
2. Regarding the drying shrinkage strain, it was found that the drying shrinkage when fly ash was mixed tended to be reduced. And the shrinkage reduction effect by replacing the molten slag was better than fly ash.
3. Regarding the unit creep strain, it was confirmed that the strain tends to be suppressed by mixing fly ash in concrete. It is considered that the creep strain tends to increase when the replacement rate of the molten slag is increased to 50%, although the effect on the creep strain is small at 25%.
4. Regarding the pore volume, the mixtures with fly ash showed a larger decrease in the age of 7 to 91 days.

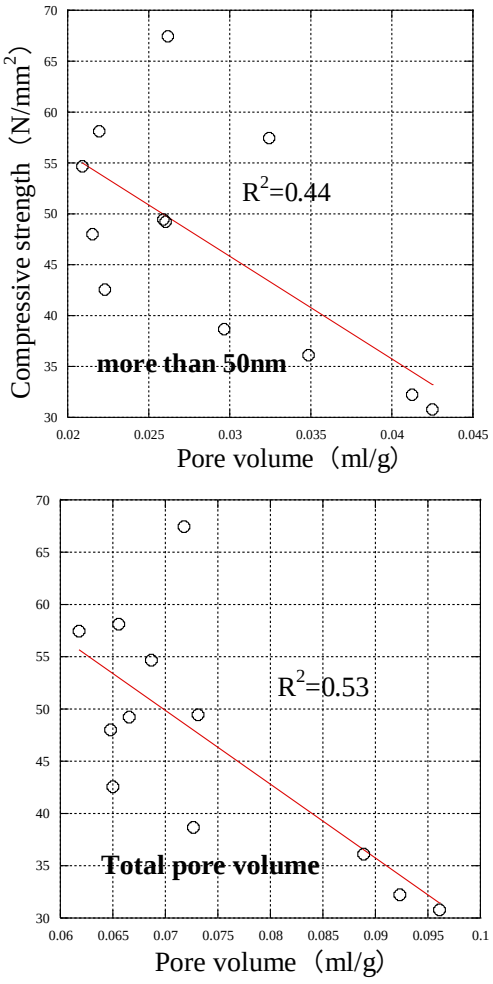

Figure 6 The relationship between the pores volume and the compressive strength.

ACKNOWLEDGMENTS

The authors acknowledge the assistance in this work provided by Eiji Mikura. This work was supported by KAKENHI (20H02300).

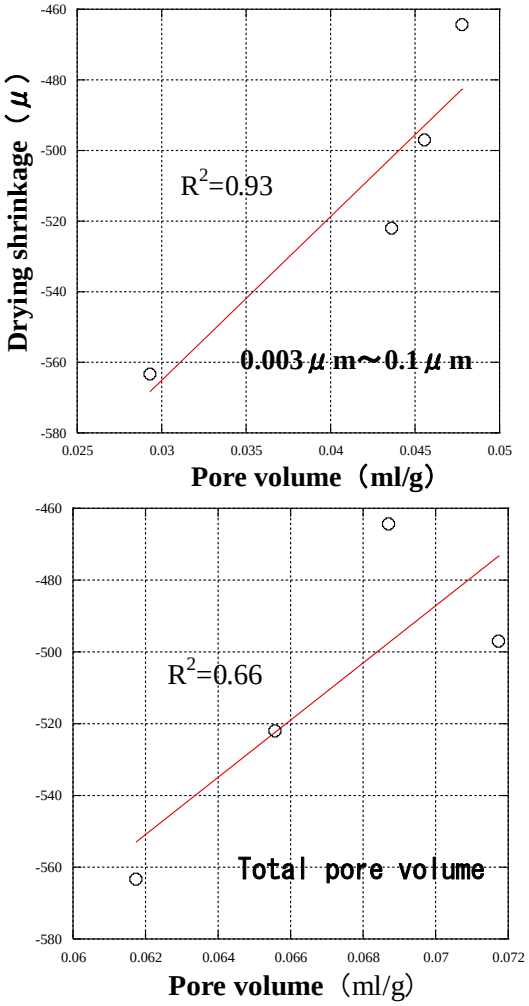

Fig. 7 The relationship between the pore volume and the dry shrinkage.

REFERENCE

[1] Meyer, Christian. "The greening of the concrete industry." Cement and concrete composites 31.8 (2009): 601-605.

[2] L. Evangelista, M. Guedes, J. de Brito, A.C. Ferro, M.F. Pereira, Physical, chemical and mineralogical properties of fine recycled aggregates made from concrete waste, Construct. Build. Mater. 86 (2015) 178–188.

[3] Kumar, G. S. (2019). Influence of fluidity on mechanical and permeation performances of recycled aggregate mortar. Construction and Building Materials, 213, 404-412.

[4] Heidrich, Craig, Hans-Joachim Feuerborn, and Anne Weir. "Coal combustion products: a global perspective." World of coal ash conference. 2013.

[5] De Maeijer, P.K.; Craeye, B.; Snellings, R.; Kazemi-Kamyab, H.; Loots, M.; Janssens, K.; Nuyts, G. Effect of ultra-fine fly ash on concrete performance and durability. Constr. Build. Mater. 2020, 263, 120493.

[6] Moghaddam, F.; Sirivivatnanon, V.; Vessalas, K. The effect of fly ash fineness on heat of hydration, microstructure, flow and compressive strength of blended cement pastes. Case Stud. Constr. Mater. 2019, 10, e00218

[7] Saha, A.K. Effect of class F fly ash on the durability properties of concrete. Sustain. Environ. Res. 2018, 28, 25–31.

[8] Moffatt, E.G.; Thomas, M.D.; Fahim, A. Performance of high-volume fly ash concrete in marine environment. Cem. Concr. Res. 2017, 102, 127–135.

[9] Kristiawan, S.A.; Aditya, M.T.M. Effect of High Volume Fly Ash on Shrinkage of Self-compacting Concrete. Procedia Eng. 2015,125, 705–712

[10]Liu, Zihao, et al. "A study on engineering properties and environmental impact of sustainable concrete with fly ash or GGBS." Construction and Building Materials 316 (2022): 125776.

8th Int. Conf. on Structure, Engineering & Environment (SEE), Mie, Japan, Nov.10-12, 2022, ISBN: 978-4-909106094 C3051

LABORATORY STUDY OF PHYSICAL AND THERMAL PROPERTIES OF CONCRETE MIXED WITH BAKELITE

Sitthiphat Eua-apiwatch[1] and Worasit Kanjanakijkasem[2]
[1]Department of Civil Engineering, Faculty of Engineering, Burapha University, Thailand;
[2]Department of Mechanical Engineering, Faculty of Engineering, Burapha University, Thailand

ABSTRACT

This research aims to study the physical and thermal properties of concrete blocks mixed with Bakelite. The main goal of this research is to use Bakelite plastic to replace the total mass of concrete blocks. The laboratory tests include compressive strength test, density test, water absorption test, and thermal conductivity test. The concrete blocks are mixture of Portland cement type one, dust stone, sand, and Bakelite plastic. The mixing ratio of concrete blocks with a binder to total mass is 1:5 by weight. The percentage of plastic varies from 0% to 20% and the curing method of concrete blocks is air curing for 7, 14, and 28 days. The compressive strength and density tests were conducted after the completion of each curing period, while the water absorption test was conducted only for the curing period of 28 days. Two groups of concrete block samples, 50x50x50 mm^3 and 65x125x145 mm^3, were used in the physical properties tests, while 10x10x10 cm^3 concrete block samples with the curing period of 28 days were used in the thermal conductivity test. The result shows that an increasing in the percentage of Bakelite decreases the compressive strength and density of concrete block samples. The water absorption is in proportion to the increasing of percentage of Bakelite. Finally, an increasing of Bakelite ranging from 0% to 20% roughly reduces the thermal conductivity of concrete block samples from 0.5 W/m-K to 0.3 W/m-K.

Keywords: Bakelite plastic, Compressive strength, Density, Water absorption, Thermal conductivity

INTRODUCTION

The total amount of plastic waste generated in Thailand is approximately 2 million tons per year, and only about 0.5 million tons per year can be recycled. The remaining 1.5 million tons is a single-used plastic and cannot be recycled. Most of them will be disposed of as solid waste and continuously increasing. In 2020, a study on the amount of plastic waste [1] stated that there was approximately 6,300 tons of plastic waste per day during the coronavirus disease 2019 epidemic, or a 15% increase in plastic waste compared to the same period under normal circumstances in 2019. Due to the epidemic situation, people have changed their behaviors in using online shopping services coupled with less waste sorting for recycling due to fear of infectious waste that was mixed with community solid waste.

In 1907, a Belgian chemist, Leo Baekeland developed polyoxybenzylmethylenglycolanhydride or Bakelite [2]. It has gotten more important role in the industry because it can be manufactured with less effort and its cost is low. While its properties such as low thermal conductivity and low electrical conductance can satisfy various requirements of several products. To eliminates the Bakelite waste, It is prohibited from direct disposed to the landfilling and open burning [3] therefore the cost of Bakelite waste treatment is very high.

In this study, Bakelite will be used as an element of aggregate for concrete block forming to be an approach to reduce Bakelite waste. Then, the basic physical properties and thermal conductivity of concrete block samples mixed with Bakelite are investigated to obtain basic information for using such concrete blocks as a construction material.

MATERIAL AND ITS PROPERTIES

Bakelite

Bakelite is the commercial name of a thermosetting phenol formaldehyde resin formed from the condensation reaction of phenol with formaldehyde. Its main chemical components consist of carbon, hydrogen, and oxygen. Compounds found in Bakelite by X-Ray diffraction (XRD) technique are reported in Table 1 which calcium oxide is the main compound with a small amount of silica and sulfur trioxide. The specific gravity of Bakelite used in this study is ranging from 1.3 to 1.4.

Table 1 Chemical compounds in Bakelite.

Compound	Percentage by weight (%)
CaO	94.23
SiO_2	5.14
SO_3	0.33

Aggregate

Quarry dust, sand, and ordinary Portland cement type 1 used in forming concrete blocks have specific gravity of 2.70, 2.65, and 3.13, respectively. The particle size distribution of quarry dust is shown in Fig. 1.

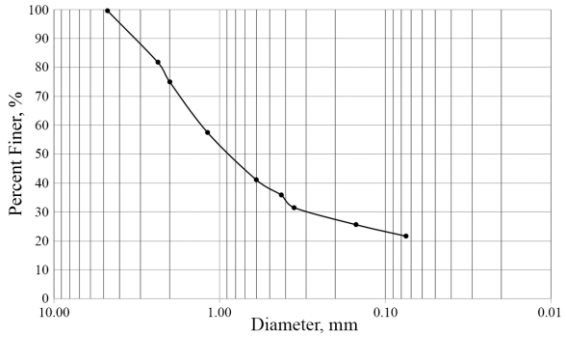

Fig. 1 Particle size distribution of quarry dust.

METHODOLOGY

Physical Properties Testing

Physical properties testing includes compressive strength testing, density testing, and water absorption testing. Sample concrete blocks for all tests were prepared using one kilogram of Portland cement type 1 mixed with quarry dust, sand, and Bakelite. The mixtures of concrete block samples are shown in Table 2.

Table 2 Mixtures of concrete block samples.

No.	Mass (kg)		Fine Bakelite plastic (kg)	Water (cc.)
	Quarry Dust (kg)	Sand (kg)		
1	4.00	1.00	0	800
2	3.80	0.95	0.25	900
3	3.60	0.90	0.50	1000
4	3.40	0.85	0.75	1100
5	3.20	0.80	1.00	1200

Sample concrete blocks were formed with a dimension of 100x1250x250 mm^3 as shown in Fig. 2 and were cured for 7, 14, and 28 days. After the curing period, they were cut into concrete block samples with dimensions of 50x50x50 mm^3 as shown in Fig. 3. For each mixture, five concrete block samples were tested. Firstly, their densities were found. Then, they were dried at a temperature ranging from 105ºC to 110ºC and immersed in water for 24 hours to find water absorption. Finally, the compressive strengths of concrete block samples were tested by a concrete compression machine.

Fig. 2 Sample of concrete blocks

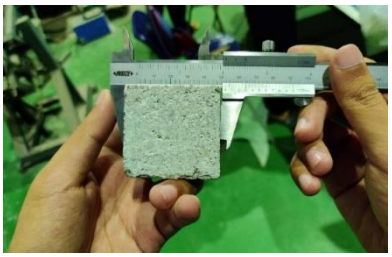

Fig. 3 Sample concrete blocks for physical properties testing.

Thermal Conductivity Testing

The mixtures of concrete blocks in the physical properties testing are also used in the thermal conductivity testing. The dimension of concrete block samples for this purpose is 100x100x100 mm^3 with a curing period of 28 days and three concrete block samples are employed for each mixture. Five thermocouples of type K, calibrated at the melting point and boiling point of distilled water, were placed on the middle plane of the concrete block sample and equally spaced along the vertical line passing through its centroid as shown in Fig. 4.

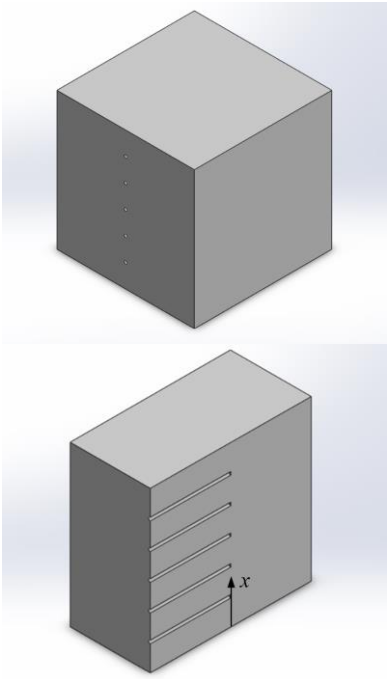

Fig. 4 Locations of thermocouple installation.

The concrete block sample was three-layer insulated on all vertical surfaces as shown in Fig. 5 and on the top surface (not shown in Fig. 5) to prevent heat losses to ambient air. On the top surface, a heat flux sensor was placed at its centroid. After assembling all stuff, it was heated from the bottom surface by a compact heater.

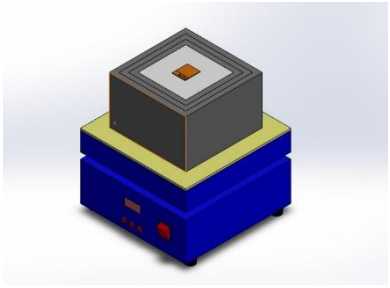

Fig. 5 Heating of concrete block samples.

Placing of all thermocouples as explained results in obtaining temperature distribution along the vertical line passing through the centroid of the concrete block sample which can be considered as one-dimensional conduction heat transfer. The temperature gradient at steady state, dT/dx, can be computed from temperatures at five locations, while the corresponding heat transfer rate on the top surface, q_x, can be obtained by the heat flux sensor.

Consequently, the thermal conductivity of the concrete block sample, *k*, can be computed from Fourier's law of conduction [4] in Eq.(1).

$$q_x = -k \cdot \frac{dT}{dx} \tag{1}$$

The temperature gradient along the vertical line passing through the centroid of the concrete block sample can be computed via the method of undetermined coefficients [5]. It starts by writing the first derivative of a function at any point, *x*, as a summation of the weighted of that function at five points in Eq.(2). Then, all terms on the right-hand side are replaced by Taylor series expansion about a point, x, as in Eq.(3). Finally, a system of equations in Eq.(4) is set up from the coefficients of the first five terms of all series, i.e., the coefficients of $f(x)$, $f'(x)$, $f''(x)$, $f^{(3)}(x)$, $f^{(4)}(x)$. This can yield the formula for numerical differentiation after obtaining all weighting factors from the system of equations. After putting the location, *x*, of the top surface into the formula, the temperature gradient can be immediately computed. It should be noted that the locations of thermocouples will be a part of the input for this approach, so it is not necessary to be seriously concerned about precision in equally spacing them.

$$f'(x) = a \cdot f(x_1) + b \cdot f(x_2) + c \cdot f(x_3) + d \cdot f(x_4) + e \cdot f(x_5) \tag{2}$$

$$\begin{aligned} f'(x) = {} & a \cdot \left[f(x) + f'(x) \cdot (x_1 - x) + \frac{1}{2!} \cdot f''(x) \cdot (x_1 - x)^2 + \frac{1}{3!} \cdot f^{(3)}(x) \cdot (x_1 - x)^3 + \ldots \right] \\ & + b \cdot \left[f(x) + f'(x) \cdot (x_2 - x) + \frac{1}{2!} \cdot f''(x) \cdot (x_2 - x)^2 + \frac{1}{3!} \cdot f^{(3)}(x) \cdot (x_2 - x)^3 + \ldots \right] \\ & + c \cdot \left[f(x) + f'(x) \cdot (x_3 - x) + \frac{1}{2!} \cdot f''(x) \cdot (x_3 - x)^2 + \frac{1}{3!} \cdot f^{(3)}(x) \cdot (x_3 - x)^3 + \ldots \right] \\ & + d \cdot \left[f(x) + f'(x) \cdot (x_4 - x) + \frac{1}{2!} \cdot f''(x) \cdot (x_4 - x)^2 + \frac{1}{3!} \cdot f^{(3)}(x) \cdot (x_4 - x)^3 + \ldots \right] \\ & + e \cdot \left[f(x) + f'(x) \cdot (x_5 - x) + \frac{1}{2!} \cdot f''(x) \cdot (x_5 - x)^2 + \frac{1}{3!} \cdot f^{(3)}(x) \cdot (x_5 - x)^3 + \ldots \right] \end{aligned} \tag{3}$$

$$\begin{bmatrix} 1 & 1 & 1 & 1 & 1 \\ x_1 - x & x_2 - x & x_3 - x & x_4 - x & x_5 - x \\ \frac{1}{2!} \cdot (x_1 - x)^2 & \frac{1}{2!} \cdot (x_2 - x)^2 & \frac{1}{2!} \cdot (x_3 - x)^2 & \frac{1}{2!} \cdot (x_4 - x)^2 & \frac{1}{2!} \cdot (x_5 - x)^2 \\ \frac{1}{3!} \cdot (x_1 - x)^3 & \frac{1}{3!} \cdot (x_2 - x)^3 & \frac{1}{3!} \cdot (x_3 - x)^3 & \frac{1}{3!} \cdot (x_4 - x)^3 & \frac{1}{3!} \cdot (x_5 - x)^3 \\ \frac{1}{4!} \cdot (x_1 - x)^4 & \frac{1}{4!} \cdot (x_2 - x)^4 & \frac{1}{4!} \cdot (x_3 - x)^4 & \frac{1}{4!} \cdot (x_4 - x)^4 & \frac{1}{4!} \cdot (x_5 - x)^4 \end{bmatrix} \begin{Bmatrix} a \\ b \\ c \\ d \\ e \end{Bmatrix} = \begin{Bmatrix} 0 \\ 1 \\ 0 \\ 0 \\ 0 \end{Bmatrix} \tag{4}$$

RESULTS

Compressive Strength

From Fig. 6, it was found that the compressive strength of concrete block samples increased with respect to the curing period but decreased with respect to the percentage of Bakelite by weight. The compressive strength of the concrete block sample without mixing of Bakelite with a curing period of 28 days is 261 ksc which is the highest compressive strength of the concrete block sample in this study.

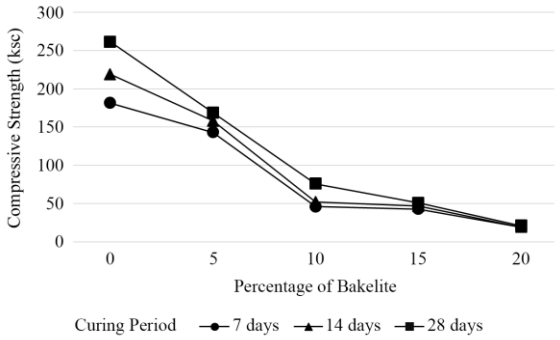

Fig. 6 Relationship between compressive strength and percentage of Bakelite.

Density

From Fig. 7, it was found that the density of concrete block samples decreased with respect to the percentage of Bakelite. This resulted from several tiny voids that occurred after the setting of concrete block samples. The curing period of 28 days which is the longest curing period in this study seems to yield the lowest density of concrete block samples for all mixtures. While the curing period of 7 and 14 days tends to yield a comparable density of concrete block samples and is higher than that of concrete block samples with a curing period of 28 days.

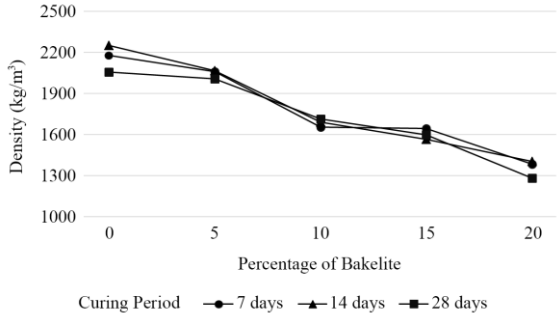

Fig. 7 Relationship between density and percentage of Bakelite.

Water Absorption

From Fig. 8, it was found that water absorption of concrete block samples increased with respect to percentage of Bakelite. This is because higher percentage of Bakelite had caused the concrete block samples to have higher porosity from the expansion of Bakelite due to the hydration reaction of cement and water. The lowest absorption is at 9% for the concrete block sample with no mixing of Bakelite

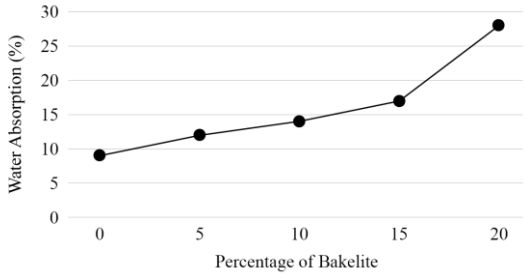

Fig. 8 Relationship between water absorption and percentage of Bakelite.

Thermal Conductivity

Three concrete block samples with curing period of 28 days were tested for each mixture. Each case was lasting about 3 to 8 hours to reach steady state of heat conduction, i.e., the temperature of the location closest to the heater was constant about 10 minutes. This location was selected because it could have the largest temperature change from room temperature. Or it can be said that the temperature at this location is the most sensitive one among all five locations. Although the precision in placing all thermocouples was not the issue to be concerned with, they were equally spaced in this study and all the results are shown in Table 3. The format of sample name is the combination of the percentage of Bakelite and number of samples, e.g., sample 0-1 means sample number 1 of concrete block with 0% of Bakelite, sample 5-1 means sample number 1 of concrete block with 5% of Bakelite, etc.

Thermal conductivities of all concrete block samples computed from temperature gradients and heat fluxes in Table 3 are presented in Table 4 and as bar chart in **Error! Reference source not found.**. It was roughly found that thermal conductivities of concrete block samples linearly decreased from 0.5 W/m-K to 0.3 W/m-K with respect to the percentage of Bakelite ranging from 0% to 20%.

Table 3 Temperature distributions along the line passing through the centroid of concrete block samples and temperature gradients at the top surface of concrete block samples.

Sample	Temperature (°C) at Locations along *x*-axis					dT/dx	$q_x \pm 2$S.D.
	1.67 cm	3.33 cm	5.00 cm	6.67 cm	8.33 cm	$(\frac{K}{m})$	$(\frac{W}{m^2})$
0-1	79.212	72.730	70.050	67.895	64.486	-258.369	136.820 ± 0.639
0-2	76.725	71.430	69.415	67.568	64.610	-211.506	113.216 ± 0.370
0-3	78.530	73.400	70.697	68.440	65.640	-191.981	97.740 ± 0.385
5-1	78.553	74.790	42.546	70.309	64.456	-191.427	88.700±0.402
5-2	78.520	72.955	70.790	68.653	65.715	-181.545	83.020±0.379
5-3	77.208	72.780	69.200	66.747	63.980	-232.899	107.320±0.485
10-1	77.670	73.594	69.140	66.587	63.550	-317.369	129.382±0.494
10-2	76.963	74.355	70.481	67.790	65.065	-246.627	97.797±0.445
10-3	76.937	72.408	69.012	66.899	64.427	-221.367	90.460±0.315
15-1	76.383	72.584	67.290	63.882	60.947	-265.49	90.992±0.313
15-2	76.961	72.338	67.170	64.960	62.520	-320.081	112.963±0.410
15-3	77.789	72.932	68.190	65.950	63.700	-261.65	90.991±0.233
20-1	74.772	68.445	66.676	64.943	60.427	-388.442	112.963±0.420
20-2	76.382	69.870	66.013	63.400	60.154	-261.591	83.291±0.303
20-3	73.690	68.619	64.910	61.921	58.051	-308.610	95.997±0.363

Table 4 Thermal conductivity of concrete block samples.

Percentage of Bakelite (%)	Thermal Conductivity $(\frac{W}{m \cdot K})$		
	Sample 1	Sample 2	Sample 3
0	0.529553 ± 0.002473	0.535286 ± 0.001751	0.509113 ± 0.002023
5	0.463362 ± 0.002100	0.457297 ± 0.002087	0.460801 ± 0.002083
10	0.407671 ± 0.001556	0.396538 ± 0.001804	0.408643 ± 0.001424
15	0.342732 ± 0.001179	0.352920 ± 0.001280	0.347758 ± 0.000891
20	0.290810 ± 0.001082	0.318402 ± 0.001580	0.311063 ± 0.001770

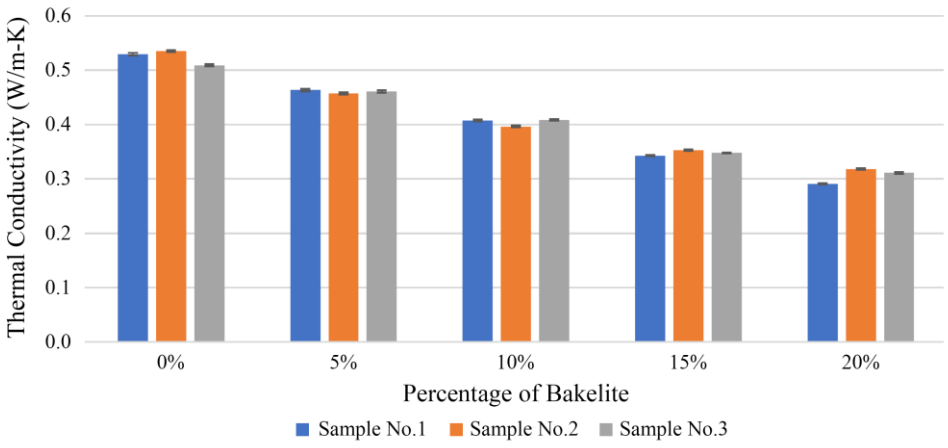

Fig. 9 Bar chart of thermal conductivity of concrete block samples.

CONCLUSIONS

Physical properties testing and thermal conductivity testing of concrete mixed with Bakelite are carried out in this study. The experimental results reveal that the increasing in the percentage of Bakelite bring about the decreasing in compressive strength and density of the concrete block samples, while the water absorption of the concrete block samples is heightened. Additionally, the increasing of Bakelite ranging from 0% to 20% roughly reduces the thermal conductivity of the concrete block samples from 0.5 W/m-K to 0.3 W/m-K.

ACKNOWLEDGEMENTS

This research is partly supported by the Research Fund No. PJ 6/2563 from Faculty of Engineering, Burapha University

REFERENCES

[1] Pollution Control Department, Situation of Municipal solid waste in Thailand (in Thai). 2021.
[2] Dharanidharan S., Srivithya N., and Meena N., Experimental Study on the Flexural Behavior of E-Waste Plastics in Concrete. International Journal of Engineering Science & Research Technology, Vol. 4, No.11, 2015, pp. 660-669.
[3] Seree T., Nopagon U., and Sirawan R.T., A Study Bakelite Plastics Waste from Industrial Process in Concrete Products as Aggregate. International Journal of Structural and Civil Engineering Research, Vol. 6, No.4, 2017, pp. 263-267.
[4] Incropera F.P., DeWitt D.P., Bergmann T.L., and Lavine A.S., Fundamentals of Heat and Mass Transfer. 6th ed., Wiley, 2006.
[5] Kanjanakijkasem W., Numerical Methods (in Thai). 2nd ed., 2020.

8th Int. Conf. on Structure, Engineering & Environment (SEE), Mie, Japan, Nov.10-12, 2022, ISBN: 978-4-909106094 C3051

ELECTROCHEMICAL EVALUATION OF CORROSION PROTECTION OF REINFORCING STEEL BARS USING SUGARS

Yoko Sakakihara[1], Kiyofumi Yamagiwa[2], Kyosuke Isoda[3], and Shinichiro Okazaki[3]
[1] Graduate School of Engineering, Kagawa University, Japan;
[2] Faculty of Life & Environmental Sciences, Teikyo University of Science, Japan;
[3] Faculty of Engineering and Design, Kagawa University, Japan

ABSTRACT

This study reports the effect of adding sugars to prevent corrosion of reinforcing bars. The reducing sugars aldose (sugar with an aldehyde group) and, ketose (sugar with a ketone group), and a non-reducing sugar and syrup with an expiration date were used in the experiments. Fehling's reaction, Benedict's reaction, and cyclic voltammetry (CV) tests were performed to investigate the effect of the various sugars on the reductive ability. Because the electrochemical oxidation of sugars requires electro-catalysts, electrodes containing particulate CuO catalysts were used in the experiments. The measurements were performed under alkaline conditions to, simulate a reinforcing bar in the concrete. The experimental results revealed the influence of different types of sugars on the reductive ability. In Fehling's reaction, fructose was observed to be highly reductive, and its reaction rate was high. In Benedict's reaction, waste syrup (WS) obtained results similar to those of fructose, thereby confirming that WS can be used as a reducing sugar. The oxidation initiation potentials in the electrochemical experiments were lower for fructose, WS, and glucose, in that order, which was the same as the order of the reaction rates in Benedict's reaction.

Keywords: Corrosion protection, Cyclic voltammetry, Fehling's reaction, Benedict's reaction, sugar

INTRODUCTION

Several structures were built during the rapid economic growth period in the 1960s in Japan for infrastructure development. The life span of reinforced concrete (RC) structures is generally around 50 years, and many structures currently require inspection and repair [1]. The decrease in the durability of RC structures is primarily owing to corrosion of the reinforcing steel bars [2], [3].

Because reinforcing bars are generally located inside concrete, and the pore solution in concrete is alkaline, a nonconductive film is applied on the surface of the reinforcing bars to prevent corrosion. However, this non-conductive film can be destroyed by the carbonation of concrete and intrusion of chloride ions, and when both water and oxygen reach the film, the steel starts to corrode. As the rebar corrodes, its volume expands by a factor of two or more, and the expansion force destroys the concrete. Additionally, water and oxygen penetrate through cracks and accelerate the corrosion. Controlling corrosion is the key to maintaining the durability of concrete.

Methods such as using a thicker concrete cover or a lower water–cement ratio have long been employed to control the corrosion of steel bars [4]. A surface impregnating material is also commonly applied to prevent water from penetrating into the steel [5], [6], but it is preferable to omit such laborious methods and use a corrosion-preventive admixture to maintain the durability of a structure.

In recent years, amidst calls for a shift to a recycling-oriented society, reusing waste syrup (WS) has been in focus from the perspective of sustainable development goals and recycling [7]–[9]. By mixing sugar waste from the food industry into concrete, we aim to not only reuse the waste, but also have the secondary effect of preventing rebar corrosion caused by the reducing performance of sugar [10]. Currently, there is no admixture that increases corrosion resistance; therefore, reducing sugar was selected with the expectation that adding a reducing agent would have a sacrificial anode effect. Electrochemical experiments were conducted to investigate the reducing ability of sugar and its potential use in corrosion protection of rebar.

In this study, we first investigated the reduction performance of WS and other sugars in the Fehling's reaction and Benedict's reaction, and then through cyclic voltammetry (CV) measurements. By comparing the results of these three experiments, the influence of the reduction power of sugars on the electrochemical properties of rebar was confirmed.

MATERIALS AND METHODS

Materials

Referring to the study by Inoue et al [11], glucose was selected as the reference substance. The WS used in the experiment consisted of 75% solids and 25%

water. The main component of the WS was glucose, constituting approximately 40% of sugars. Fructose was the next most abundant component, constituting approximately 30%. The remaining 30% contained a few percent each of other sugars. Fructose was selected as one of the materials because the main contents of the WS were glucose and fructose. Sucrose was added as a material for comparison because it was known as a non-reducing sugar.

Fehling's Reaction

As shown in Fig. 1, fructose, and glucose have the same alcohol configuration from the third to sixth carbon positions. These four sugars including sucrose and WS were used in the experiment.

Distilled water was used as the solvent to prepare the reagents and in the experiments. Fehling's solution A was prepared by dissolving 6.92 g of copper (II) sulfate pentahydrate in water to make 100 ml of solution. For Fehling's solution B, 34.6 g of potassium sodium tartrate tetrahydrate and 10.0 g of sodium hydroxide were dissolved in water to make 100 ml of solution [12]. One milliliter each of Fehling's solutions A and B were added into a test tube containing 9 mg of sugar (12mg in case of WS) to completely dissolve the sugar. The test tubes were covered with Parafilm and heated in a water bath at 80 °C for 1, 2, 3, and 5 min, and then filtered through a filter paper (No. 5C). The filter paper was then dried and quantified.

The WS was set to 12 mg because it contains 75% sugars and 25% water.

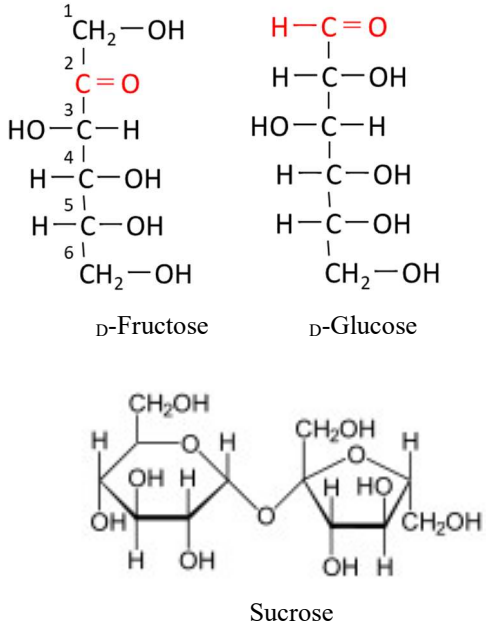

Fig. 1 Molecular structures of sugars.

Benedict's Reaction

Benedict's solution is a commercially available reagent (Hayashi pure chemical Inc., LTD.) and is sold for clinical testing. Two milliliters of Benedict's solution were added into a test tube containing 9 mg of sugar (12 mg in case of WS). The test tubes were covered with Parafilm and the tube was immersed in water heated to 80 °C for 1, 2, 3, and 5 min. Thereafter, the solution was filtered through the filter paper, which was then dried and weighed.

Electrochemical Measurements

CV measurements were performed to characterize the reducing properties of sugars. CV measurements require an electro-catalyst that facilitates the oxidation of sugars [13]–[16]. Recently, it has been discovered that metal oxides such as copper oxide (CuO) catalyze the electrochemical oxidation of sugars, especially under alkaline conditions; therefore, a CuO-based catalyst was used in this experiment.

The CuO-based catalyst was synthesized by heat-treating a carbonate mineral containing Cu [17]. The catalyst and carbon paste (conductive material) were mixed with a dispersant to form a slurry, which was poured onto a carbon paper and dried to form electrodes.

D-glucose (aldose), D-fructose (ketose), sucrose (non-reducing sugar), and WS were used to study the electrochemical behaviors of the sugars. The concentration of D-glucose, D-fructose, and sucrose in 0.1 M NaOH solutions was 10 mM. The concentration of WS was also set the same. The composition of the WS was 75% sugars and 25% water. All sugars of WS were assumed to be monosaccharides, and the WS solution was set to have a concentration of 10 mM in 0.1 M NaOH solution.

The CuO electrode was used as the working electrode. A saturated silver-silver chloride electrode (Ag/AgCl) was used as the reference electrode, and a platinum electrode was used as the counter electrode. The measurements were performed in a three-electrode cell with a potentiostat (Hokuto Denko model HZ-7000). A cyclic voltammogram was obtained in the potential range of -0.1 to 0.6 V. The electrode was then changed, and measurements were performed in the range of -0.1 to 0.2 V. In all cases, three cycles with a scan rate of 10 mV s^{-1} were recorded. The third cycle was used for evaluation. The electrochemical measurements were performed at 25 °C and without stirring.

RESULTS AND DISCUSSION

Fehling's Reaction

The experimental cases are shown in Table 1. The amounts of Cu_2O formed by the reactions of glucose, fructose, sucrose, and WS with Fehling's solution were compared (the blanks indicate the case where only distilled water was used as the sample).

Figure 2 shows a photograph of the precipitation obtained through Fehling's reaction after 5 min. As shown in Figs. 2 and 3, Cu_2O was not formed from sucrose. For validation through a blank case, an experiment with only water was also performed, which showed similar results.

Figure 3 shows photographs of the experiment. From left to right: fructose, WS, glucose, sucrose, and blank. After 1 min, a color change began in fructose and WS, followed by a color change in glucose, and after 5 min, fructose, glucose, and WS turned red [18].

The results of the reaction of Fehling's solution with sugars that exhibited reducing properties are shown in Fig. 4. In the reduction reaction of Fehling's solution, Cu_2O was produced from fructose, glucose, and WS, in that order. It was obtained the fastest from fructose, indicating a high reaction rate.

Table 1 Weight of sugars used in the experiment.

Cases	Sugars	Weight of sugar
1	Fructose	9 mg
2	Glucose	9 mg
3	Sucrose	9 mg
4	WS	12 mg
5	Blank	-

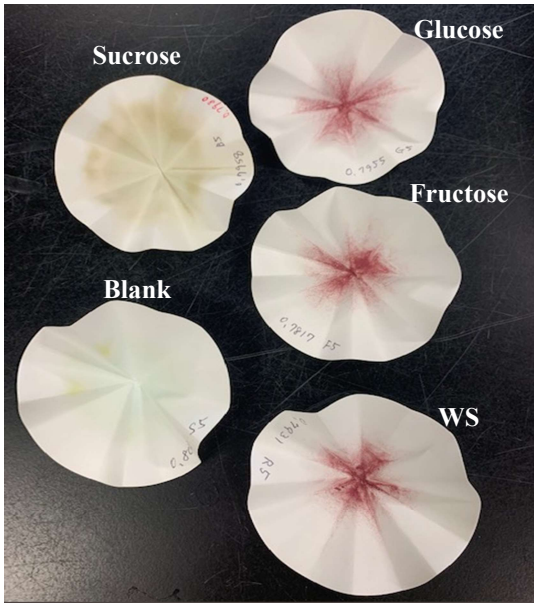

Fig. 2 Photograph of precipitation obtained through Fehling's reactions after 5 min.

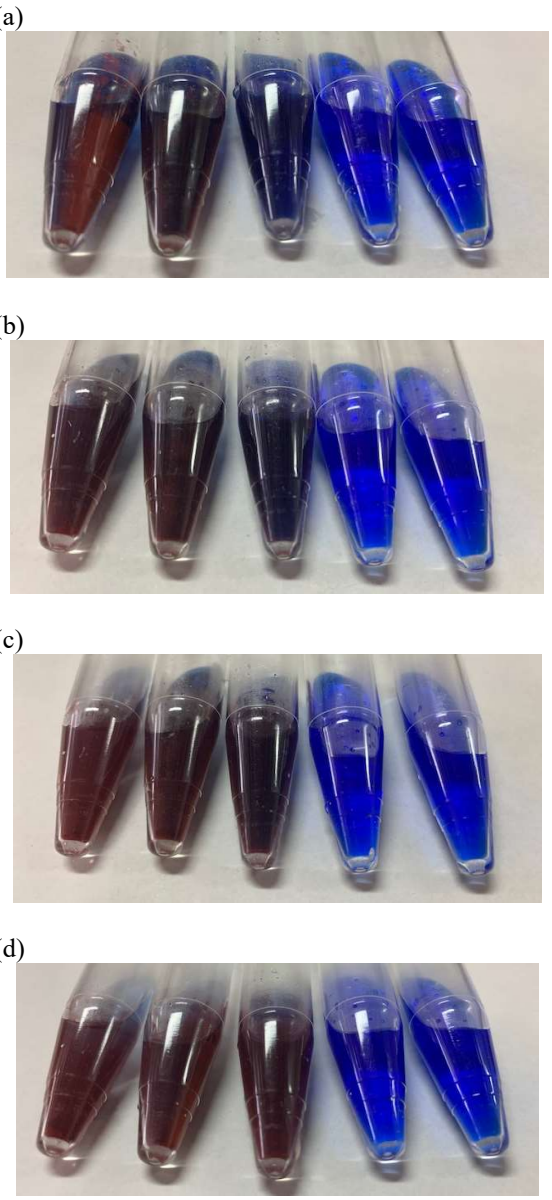

Fig. 3 Color changes in Fehling's reactions. (a: after 1 min, b: after 2 min, c: after 3 min, d: after 5 min)

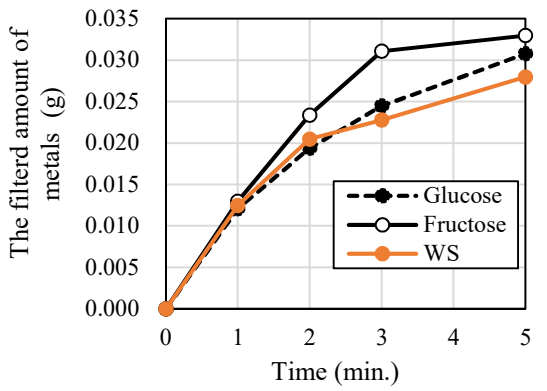

Fig. 4 Increase in the weight of filter papers after Fehling's reactions.

Benedict's Reaction

Figure 5 shows photographs of color changes in Benedict's solution. From left to right: fructose, WS, glucose, sucrose, and blank. The weights of the precipitates obtained via Benedict's reaction are shown in Fig. 6. Although the results for the reductions using fructose, glucose, and WS were marginally different in Fehling's reaction, there was a marked difference between them in Benedict's reaction. Fehling's solution is a strong alkali with a pH of 14, whereas Benedict's solution has a pH of approximately 10, which indicates that Benedict's reaction is gradual. Although glucose was easily oxidized in Fehling's solution, Benedict's reaction was slightly slower [19]. This result is similar to that reported by Inoue et al. [11].

(a)

(b)

(c)

(d)

Fig. 5 Color changes in Benedict's reactions. (a: after 1 min, b: after 2 min, c: after 3 min, d: after 5 min)

Fructose reacted the fastest in Benedict's reaction, similar to Fehling's reaction. In Benedict's reaction, WS and glucose, in that order, yielded Cu_2O. As shown in Fig. 5, sucrose did not oxidize [18]. For validation through a blank case, an experiment with only water was also performed, which showed similar results.

Results of CV Measurement

We performed cyclic voltammetry to confirm the functionality of the CuO electrode. The cyclic voltammogram of glucose is shown in Fig. 7. The system with glucose shows that an oxidation current originating from the electrochemical oxidation of glucose is at high potentials, and a significant oxidation current density of ~3 mA cm^{-2} is observed at 0.6 V. The measurement of the oxidation current of glucose using a CuO electrode has been reported in other studies [20], [21], and similar results were obtained in this experiment, wherein its function as a catalyst for glucose oxidation was confirmed.

The cyclic voltammograms of the CuO-containing electrode in each sugar solution (potential range: -0.1 to 0.6 V (vs. Ag/AgCl)) are shown in Fig. 8. Significant oxidation currents were observed at 0.6 V for all carbohydrates. Sucrose, similar to the other sugars, also showed oxidation currents. The details of the reaction mechanism of the electrochemical oxidation are still unclear. Although there was no significant difference in the current density, the experiment showed that the oxidation initiation potentials differed among the different sugars. Fructose showed a rise in oxidation current from a lower potential than WS.

The cyclic voltammograms of the CuO-containing electrode in each sugar solution (potential range: -0.1 to 0.2 V (vs. Ag/AgCl) are shown in Fig. 9. The order of the fastest rising oxidation initiation potentials was fructose, WS, and glucose, which is similar to that in the Fehling's reaction.

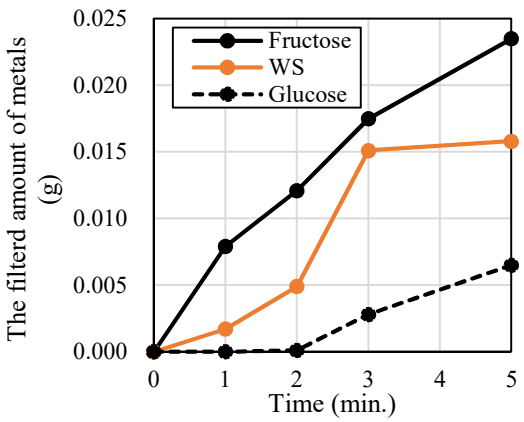

Fig. 6 Increase in the weight of filter papers after Benedict's reactions.

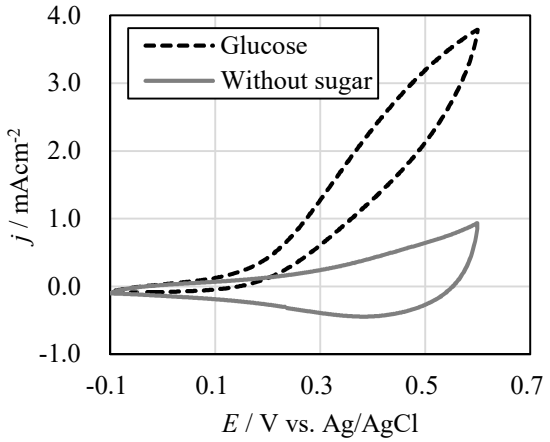

Fig. 7 Cyclic voltammograms of the CuO-containing electrode in the glucose solution (electrolite: 0.1 M NaOH, 10 mM glucose).

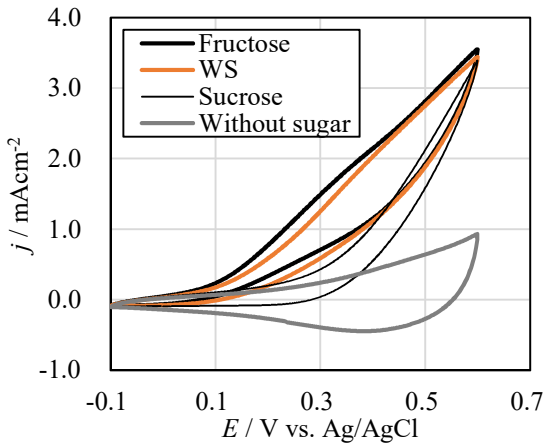

Fig. 8 Cyclic voltammograms of the CuO-containing electrode in each sugar solution (potential range: -0.1 to 0.6 V (vs. Ag/AgCl)).

CONCLUSIONS

The Fehling's reaction, Benedict's reaction and electrochemical experiments were used glucose, fructose, sucrose, and WS. In Fehling's reaction, it was observed that fructose was highly reductive and its reaction rate was high. The result of WS was similar to that of fructose and glucose. In Benedict's reaction, the differences were observed in the amount of precipitation and the reaction rate. Fructose was fastest, next was WS, and glucose. The reaction rate of Fehling's solution is a strong alkali with a pH of 14, whereas Benedict's solution has a pH of approximately 10, which indicates that Benedict's reaction is gradual. Although glucose was easily oxidized in Fehling's solution, Benedict's reaction was slightly slower. The oxidation initiation potentials in the electrochemical experiments were lower for fructose, WS, and glucose, in that order, which was the same as the order of the reaction rates in Benedict's reaction. To our knowledge, no study has yet obtained the same order of reaction intensity in electrochemical redox as in the Fehling and Benedict reactions. The results of the Fehling's reaction, Benedict's reaction, and electrochemical experiments indicate that WS has a reducing ability similar to that of fructose and glucose.

The Fehling's reaction, Benedict's reaction, and electrochemical experiments were all conducted under alkaline conditions. In the electrochemical experiments, inorganic catalysts that function under alkaline conditions were selected instead of enzymes; therefore, the conditions were more similar to those of concrete. In the comparison at -0.1 to 0.2 V, both the low oxidation initiation potential and the current density at 0.2 V confirmed an ordering that corresponds to that of the Fehling's and Benedict's reactions. It can be expected that the electrochemical viewpoint can also help in the selection of the best sugar to add reinforced concrete.

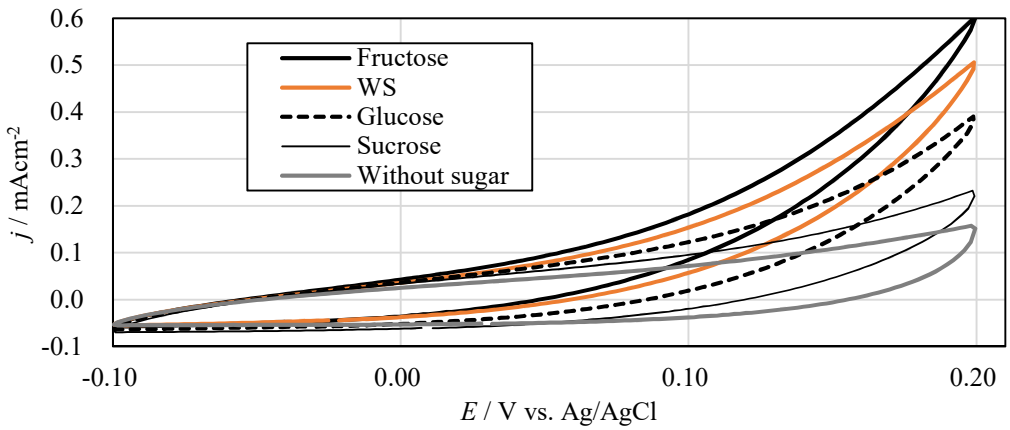

Fig. 9 Cyclic voltammograms of the CuO-containing electrode in each sugar solution (potential range: -0.1 to 0.2 V (vs. Ag/AgC

ACKNOWLEDGMENTS

This research was supported by the Regional Innovation Ecosystem Program of the Ministry of Education, Culture, Sports, Science, and Technology, Japan.

REFERENCES

[1] Oyamoto T., Efforts to Extend the Life of Existing Reinforced Concrete Buildings, Concrete Journal, Vol. 57, No. 5, 2015, PP. 346-351.
[2] Morinaga S., Irino K., Ohta T. and Tsuchimoto Y., Life Prediction of Reinforced Concrete Structures determined by Corrosion, Concrete Research and Technology, Vol. 1, No. 1, 1990, pp. 177-189.
[3] Ueda T. and Miyagawa T., Deterioration of Concrete Structures and Some Relevant Issues, Zairyo-to-Kankyo, Vol. 59, No. 4, 2010, pp. 111-116.
[4] Otsuki N., Miyazato S., Shibata T., Hisada M., Md. Tarek U. and Nagataki S., The influence of W/C on corrosion mechanism near bending crack, Journal of Jaoan Society of Civil Engineers, No. 66, 1998, pp. 63-73.
[5] Someya N. and Kato Y., Fundamental study on modification effect and penetration mechanism of silicate-based surface penetrants, Concrete Research and Technology, Vol. 25, 2014, pp. 181-189.
[6] Date S., Goryozono Y., Hahimoto S. and Miyazato S., The evaluation of performance of hydrophobic impregnation –comparison with European Norm (EN 1504-2)-, Journal of Advanced Concrete Technology, Vol. 50, No. 4, 2012, pp. 331-337.
[7] Niida R., Nitta H. and Nishizaki I., Method for reducing hexavalent chromium eluted from recycled base courses material using reducing sugar, Journal of Japan Society of Civil Engineers, Vol. 71, No. 3, 2015, pp. I._211-I_216.
[8] Shibata K., Study on recycling of the food wastes considering environmental load, Thesis of Kagawa University, Vol. 139, 2020.
[9] Shibata K., Yamaya K., Yoshida H., Suenaga Y., Okazaki S. and Matsumoto N., Japanese Geotechnical Society Special Publication, Vol. 8, Iss. 4, 2020, pp. 130-135.
[10] Rbaa M., Dohare P., Berisha A., Dagdag O., Lakhrissi L., Galai M., Lakhrissi B., Ebn Touhami M., Warad I. and Zarrouk A., New Epoxy sugar based glucose derivatives as eco friendly corrosion inhibitors for the carbon steel in 1.0 M HCl: Experimental and theoretical investigations, Journal of Alloys and Compounds, Vol. 833, 2020, 154949.
[11] Masuda Y., Konno T. and Inoue M., Determining the structure that causes reducing properties of sugars, Chemistry & Education, Vol. 68, No. 10, pp. 434-437.
[12] Ohki M., Ohsawa T., Tanaka M., Chihara H., Encyclopedic dictionary of chemistry, Tokyo Kagaku Dozin Co., Ltd., 1989, pp.1971.
[13] Jin J., and Miwa T., Electrochemical behavior of Ni-Ti alloy electrode and its application to the amperometric detection of sugars, BUNSEKI KAGAKU Vol. 47, No. 10, 1998, pp.665-672
[14] Sugawara K., Construction of Electrodes modified with biopolymers for biomolecular sensing, BUNSEKI KAGAKU, Vol. 67, No. 2, 2018, pp. 73-79
[15] Takahashi M., Iwabata K., Torigoe K., Endo T., Sakaguchi K., Sakai H. and Abe M., Effects of stabilizer concentration on the electrochemical performance of Au-Pt anode catalysts for direct glucose fuel cell, J. Jpn. Soc. Colour Mater., Vol. 90, No. 2, 2017, pp. 61-66
[16] HandaY., Watanabe K., Chihara K. Katsuno E., Horiba T., Inoue M. and Komaba S., The Mechanism of Electro-Catalytic Oxidation of Glucose on Manganese Dioxide Electrode Used for Amperometric Glucose Detection, Journal of The Electrochemical Society, Vol. 165, 2018, H742.A
[17] Yamaguchi N., Wakatabe T. and Yamagiwa K., Synthesis of particulate catalysts from natural mineral pigments, Bulletin of Teikyo University of Science, Vol. 17, 2021, pp. 69-74.
[18] Schlesner S. K., Voss M., Helfer G. A., Costa A. B., Cichoski A. J., Wagner R. and Barin J. S., Smartphone-based miniaturized, green and rapid methods for the colorimetric determination of sugar in soft drinks, Green Analytical Chemistry, Vol. 1, 2022, 100003.
[19] Singh S. V., Saxena O. C. and Singh M. P., Mechanism of copper(II) oxidation of reducing sugars. I. Kinetics and mechanism of oxidation of D-xylose, L-arabinose, D-glucose, D-fructose, D-mannose, D-galactose, L-sorbose, lactose, maltose, cellobiose, and melibiose by copper(II) in alkaline medium, Journal of the American Chemical Society, Vol. 92, 1970, pp. 537-541.
[20] IAshok A., Kumar A. and Tarlochan F., Highly efficient nonenzymatic glucose sensors based on CuO nanoparticles, Applied Surface Science, Vol. 481, 2019, pp. 712-722.
[21] Jin J., Zheng G., Ge Y., Deng S., Liu W. and Hui G., A non-enzyme electrochemical qualitative and quantitative analyzing method for glucose, D-fructose, and sucrose utilizing Cu foam material, Electrochimica Acta, Vol. 153, 2015, pp. 594-601.

8th Int. Conf. on Structure, Engineering & Environment (SEE), Mie, Japan, Nov.10-12, 2022, ISBN: 978-4-909106094 C3051

PHYSICAL AND MORPHOLOGICAL PROPERTIES OF POLYURETHANE MODIFIED BITUMEN UNDER AGEING CONDITIONS

Faridah Hanim Khairuddin[1], Siti Zubaidah Mohd Asri[2], Noor Aina Misnon[3], Nur Izzi Md Yusoff[4], and Ahmad Nazrul Hakimi Ibrahim[5]
[1,2,3] Faculty of Engineering, Universiti Pertahanan Nasional Malaysia, 57000, Malaysia
[4,5] Faculty of Built and Engineering, Universiti Kebangsaan Malaysia, 43600, Malaysia

ABSTRACT

The aim of this research is to evaluate the effects of ageing on 60/70 penetration grade bitumen modified with polyurethane (PU). Effects of ageing were evaluated by performing consistency test through ageing index and morphology evaluation. The results of these tests show that adding 3 wt% of PU stiffens the bitumen in comparison to base bitumen. A very high increase in viscosity was observed due to the hardening effect of PU. The computed ageing index shows that this alternative material reduces ageing effects on the physical properties of the bitumen, as indicated by the lower ageing index value of physical testing subsequent to ageing. Therefore, the addition of PU results in improved bitumen resistance to oxidative ageing. Optical microscopy shows the sample was homogeneously blended. Atomic Force Microscopy (AFM) was conducted to evaluate the catana phase, peri phase, and para phase topography images of PU modified bitumen. Topography image from AFM test indicates that the inclusion of PU and ageing conditions has decreased the bee-like structures of the bitumen, showing larger dispersion in the sample.

Keywords: Polyurethane Modified Bitumen, Ageing, Atomic Force Microscopy, Morphology, Topography

INTRODUCTION

The past several decades has witnessed hot mix asphalt (HMA) being used as the primary material in the paving industry, where bitumen is used as a coating for aggregates. Bitumen is a sticky, dark brown or black, semisolid material and is highly viscous at ambient temperature [1]. A strong bond between bitumen and aggregate is required to accommodate traffic loading. This is to ensure that pavements are strong and durable, and provide a smooth surface for road users. However, the increase in traffic volume, pressure and load in recent years had an adverse impact on pavement performance. In order to deal with these problems, the quality of existing pavements have to be improved. Additions of modifier or replacement to bitumens are done to improve its resistance to rutting, fatigue, and temperature susceptibility [2]. Recent research has shown that bio-binders can be used as modifiers (<10% bitumen replacement), extenders (25% to 75% bitumen replacement), or 100% replacement for bitumen [3].

One study investigated the effects of using waste cooking oil and spent coffee ground as a modifier on the physical and chemical properties of bio-binders. Results showed that longer oxidation time improved the viscoelasticity of the waste oil [4]. A study conducted by Al-Omari et al. [5] used waste vegetable oil as a modifier; the researchers observed improvement in temperature susceptibility, penetration, ductility, flash and fire points, fluidity, and m-value, along with a decrease in the bitumen's softening point, rotational viscosity, and creep stiffness A research using bio-oil generated from waste wood source found that the bio-binders lower the mixing temperature of bituminous mixtures and improved the performance of the bitumen. Khairuddin et al. [6] conducted a study on bitumen modification using polyurethane (PU). The outcomes of this study show that the addition of PU at intermediate and higher temperatures has stiffened the bitumen properties and increased resistance to fatigue and rutting.

Besides investigating the physical and chemical properties of the modified bitumen, the interrelationship of structure-property is important to obtained the bitumen optimum performance by interpretation the morphology using microscopic method. Surface morphology using Atomic Force Microscopy (AFM) is widely used by researchers to study the topography, roughness, adhesion and local mechanical properties of the bitumen [3] - [7]. As bitumen consist of 'bumble bees' structures, it is important to investigate the effect of modifier in term of dispersion and matrix domains [8].

One of the causes of road pavement deterioration is bitumen oxidation [9]. Short-term ageing (STA) occurs during the mixing and compacting of mixtures, where higher temperatures results in higher

oxidation rate. Long-term ageing (LTA) occurs during the service life of a pavement. Oxidation occurs when bitumen reacts with oxygen diffused in the air voids on aggregate surface [10]. The higher viscosity caused by oxidation process increase the stiffness of pavements, which then causes cracking [11]. As ageing occurs, the physical and chemical properties of bitumen alter the behavior of bitumen significantly. Ageing affects the physical properties of bitumen, such as penetration, viscosity, ductility and stiffness [9]. Therefore, investigation of ageing process and its effect on modified bitumen is very important in real application.

This study seeks to evaluate the physical, morphological and ageing effect of a new material, palm kernel oil polyol (PKO-p) and 2,4-diphenylmethane diisocyanate (MDI) under STA and LTA conditions. The addition of these two materials will form PU. The morphology of the modified bitumen was observed to evaluate the homogeneity, separation and dispersion of bee-like structure in the bitumen with the inclusion of the new material. The following section will present a comprehensive discussion of the tests and their results.

METHODOLOGY

Materials

In this study, a 60/70 penetration grade bitumen was used as the control sample. The physical characteristics of the control sample is given in Table 1. The sample was modified by adding PU to the bitumen. In order to produce PU, pre-polymerization method of PKO-p from palm kernel oil were done at first stage. Next, polymerization will occur during mixing process of PKO-p with MDI that will produced PU.

Table 1 Physical properties of control sample

Physical test	Bitumen Grade 60/70	
	Value	Specification
Penetration (0.1 mm) at 25 °C	66	60-70 (ASTM D5)
Softening point (°C)	49	47-52 (ASTM D36)
Ductility (cm) at 25 °C	100	100 (ASTM D113)
Viscosity (mPa.s) at 135 °C	550	- (ASTM D4402)
Specific gravity (g/cm^3) at 25 °C	1.03	1.0-1.06 (ASTM D70

Sample preparation

Modification of the bitumen was carried out by heating the base bitumen (B-B) at 145℃ for about 30 minutes until it turned liquid. PU in the amount of 3% by weight of bitumen was used to produce the polyurethane modified bitumen (B-PU) [6],[12]. This optimum percentage of 3 wt% PU was predetermined by Design Expert Software using Response Surface Method. PKO-p and MDI were then added at a ratio of 1:0.6 by weight of PU. The PKO-p and bitumen were blended for 15 minutes at 110℃ and 2000 revolutions per minute using shear mechanical mixer; MDI was then added and blended using the same parameter. Prior to obtain a homogeneous blend, penetration and softening point results were monitored until consistent results were obtained and taken as indicators of a well-blended mix.

Laboratory Testing

Penetration test

The penetration test was conducted in compliance with ASTM D5. The value of penetration is dependent upon the hardness or softness of a bitumen. Higher value of penetration measured in tenths of millimetre indicates a bitumen with softer characteristic.

Softening point and storage stability

The softening point test was carried out to measure the temperature at which the bitumen starts to flow. It was carried out in compliance with ASTM 36. For bitumen with a given penetration (determined at 25 ºC), higher softening point indicates lower temperature sensitivity. Storage stability test was conducted to evaluate the homogeneity of a blend as well the stability during storage. This test was conducted in compliance with ASTM-D5976 (2000).

Viscosity test at 135 ℃

Evaluation of bitumen's viscosity at high temperature is important to determine the optimal temperature for the mixing and compacting of bituminous mixture at site. It indicates the extent to which the bitumen can be pumped through bitumen plant. This test was conducted in compliance with ASTM D4402.

Ageing of bitumen

To simulate STA, the samples were prepared using the Rolling Thin Film Oven procedure in accordance with ASTM D2782. STA of a bitumen occurs during the production of bituminous mix at the plant. Simulation of LTA were carried out using the Pressure Aging Vessel method in accordance with ASTM D6521. LTA is an indication of the service life of a pavement.

Ageing Index

The effects of ageing on B-PU were measured using the penetration, softening point, and rotational viscosity tests, and the results were compared with the B-B. The ageing index (AI) for each test was computed using Eq. (1) below to evaluate the ageing susceptibility.

$$\boldsymbol{AI} = \frac{\boldsymbol{T\ aged}}{\boldsymbol{T\ unaged}} \quad (1)$$

where T_{aged} is the penetration/softening point/viscosity test value of the aged sample and T_{unaged} is the penetration/softening point/viscosity test value of the unaged sample.

Microscopic DINO-LITE

The morphological property of B-B and B-PU were observed using the optical microscope DINO-LITE Pro Digital, 500X. The sample was heated at 145°C until it turned viscous. Then, the sample was dropped on a glass slide to form an even surface and leave for 30 minutes before being viewed under a microscope. The DINO-LITE is capable to capture high image resolution and good image quality of a sample.

Atomic Force Microscopy

To further investigate the morphology characteristics of B-B and B-PU sample, AFM test was conducted using the XE-10 AFM from Park Systems Corporation. To evaluate the surface and bee characteristics of the bitumen, heat cast method was applied where sample were heat until it turned liquid and dropped on a glass slide. For this study, 20 x 20 µm area at 1 Hz scan rate was selected. The sample was tested using a silicon cantilever tip sized < 10 nm tip radius by non-contact mode method, at 0.2 N/m constant force for the quantifications of sample surface.

RESULT AND DISCUSSION

Physical Testing

Penetration test

Penetration test was used to evaluate the fluidity of bitumen before and after modification with PU under unaged (UA), STA, and LTA conditions. Figure 1 shows the results of the penetration tests for B-B and B-PU. The addition of 3% of PU to bitumen decreased the penetration value by 7.3% for UA, 10.7% for STA, and 10.3% for LTA. This shows that the samples become stiffer subsequent to modification and ageing. This is consistent with the previous findings made by another researcher that the addition of PU had a hardening effect on the bitumen.

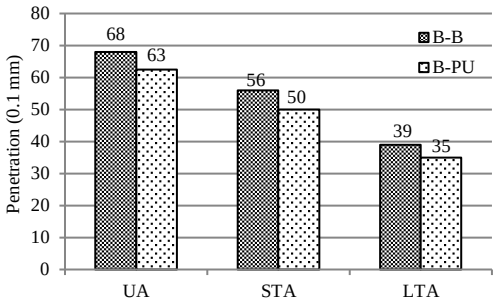

Fig. 1 Penetration values for UA, STA and LTA.

Softening point and storage stability test

Figure 2 shows the softening point values for B-B and B-PU under UA, STA, and LTA conditions. The general trend shows that adding PU to bitumen improves softening point by 10% for UA, 8.5% for STA, and 7.6% for LTA. This indicates the extent to which the bitumen hardened after modification and ageing. The increase in softening point is due to the change in the structural molecules in the bitumen's content of fraction during the ageing process [13].

In addition, storage stability test conducted shows the differences between the top and bottom section for softening point value of B-PU is 0.50 °C which is less than 2.2 °C. This result indicates that there is no separation occurred between the top and bottom section and the B-PU sample are homogeneously, storage stable blended [14].

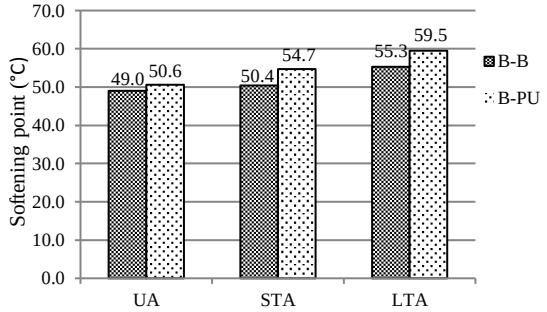

Fig. 2 Softening point values for UA, STA and LTA.

Viscosity test

Figure 3 shows the experimental value for viscosity at 135 °C, which is the average mixing and compaction temperatures for bituminous mixture. The addition of PU markedly increased viscosity by 64% for UA, 22% for STA, and 12% for LTA. This increase is still within specification permitted by the Strategic Highway Research Program which states that the increase in viscosity should not exceed 3000

mPa.s [10]. The increase in viscosity occurred due to the increase in bitumen stiffness which limited molecule movement during the test. The addition of PU is the contribution of higher viscosity value [14].

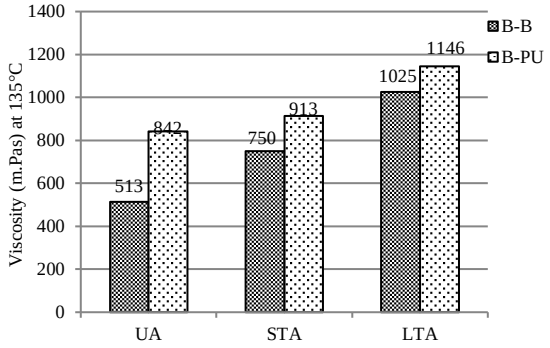

Fig. 3 Viscosity value for UA, STA and LTA.

Ageing Index

Table 2 shows the penetration aging index (PAI) computed using AI equation. The table shows that the value of PAI decreased after STA and LTA, which indicate that B-PU has a higher ageing resistance in comparison to B-B. The softening point ageing index (SPAI) is listed in Table 3 showing an increased value due to the change in the structural molecules in the bitumen's content of fraction during the ageing process. Thus, the addition of PU improved the bitumen's resistance to oxidative ageing [15]. Table 4 presents the viscosity aging index (VAI). It shows that VAI decreased with the addition of PU, thus reduce the ageing sensitivity.

Table 2 PAI for B-B and B-PU

Bitumen	STA	LTA
B-B	0.825	0.568
B-PU	0.807	0.566

Table 3 SPAI for B-B and B-PU

Bitumen	STA	LTA
B-B	1.029	1.129
B-PU	1.080	1.175

Table 4 VAI for B-B and B-PU

Bitumen	STA	LTA
B-B	1.462	1.998
B-PU	1.084	1.361

Morphological properties of Bitumen

Optical microscopic test

Figures 4(a) and (b) show the image of B-B and B-PU used in this research. No separation was observed in the microscopy images. Fig. 4(b) shows clearly the image of a homogeneous blend of the B-PU, which indicate that the PU has been uniformly dispersed and evenly spread during the mixing process. There are no lumps observed after mixing 3 wt% PU with bitumen at selected parameters showing analogous mix was formed. This is in agreement with the result of storage stability test.

(a)

(b)

Fig. 4 Optical Microscopic for (a) B-B, (b) B-PU.

Atomic Force Microscopy test

The typical bee structure was clearly found in both unmodified and modified sample with reduction off bee lines with ageing condition. As stated by Lyne et al. [7] there are three phases observed in bitumen namely the catana phase, the peri phase and the para phase respectively as shown in Figure 5(a). The catana phase represents the black line like a bee structure that indicate the high and low of the topography image, the peri phase that is outerpart to the catana phase while the para phase is alongside the peri phase. In bitumen, the bee structure occurred because of the crystallization of the wax composition as well dispersion of the molecule [16]. The existence of various nonpolar alkane chains together with the wax are the contribution factors to the 'bee-like structures' appearance in bitumen [8].

Figures 6(a)-(f) and Figures 7(a)-(f) represent the 2D and 3D topography images of B-B and B-PU before and after ageing, respectively, obtained from AFM test. The presence of bee-like structures or catana phase for UA sample can be clearly seen in accordance with Fig. 6(a) and Fig. 7(a). This indicates that the addition of PU did not affect the bitumen bee-like structures. The dispersion in the aged samples,

however, decreases remarkably, particularly for both B-B and B-PU samples after ageing. This showed that during STA and LTA there was a great interaction of the distributed domains in bitumen. It can be clarified that oxidation leads to the reduction of the difference in chemical properties between the distributed domains and the matrix during STA and LTA. The domains can spread in the matrix gradually before ageing, but not after ageing [17].

The topographic image in Fig. 7(c) and 7(e) shows that after STA and LTA for the B-PU sample, the dimension and quantity of bee-like structures are significantly reduced. The bee-like structures seem to float much and obviously spread throughout as seen in Fig. 7(e). In addition, with the inclusion of PU, at certain points in STA and LTA, it is noted that the dimension of bee-like structures is reduced compared to the B-B sample in Fig. 6(c). This shows that the addition of PU and the hardening of bitumen from ageing have led to the substantial decrease in the bee-like structure as well as the absence of the boundary. This outcome is comparable to the research performed by Zhang et al. [18] using AFM to perform morphology analysis on unmodified and modified organo-montmorillonite bitumen. The findings showed that bitumen showed a 'bee-like' structure and, with the introduction of the organo-montmorillonite, the dimension of the 'bee-like' structures was reduced to some degree. Due to the increased solubility of microcrystalline waxes (>C40) and waxy molecules in bitumen during ageing, which can impede their crystallization, the dimension and quantity of 'bee-like' structures have been reduced after ageing.

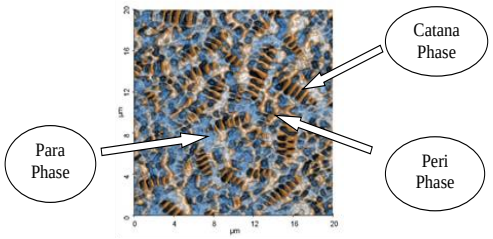

Fig. 5 Sample showing the catana phase, peri phase and para phase in bitumen structure.

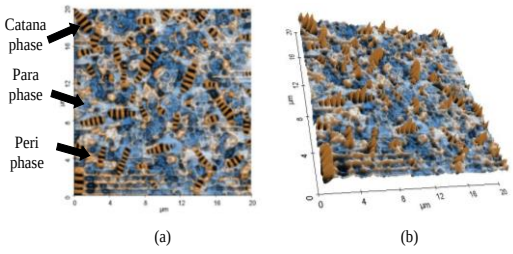

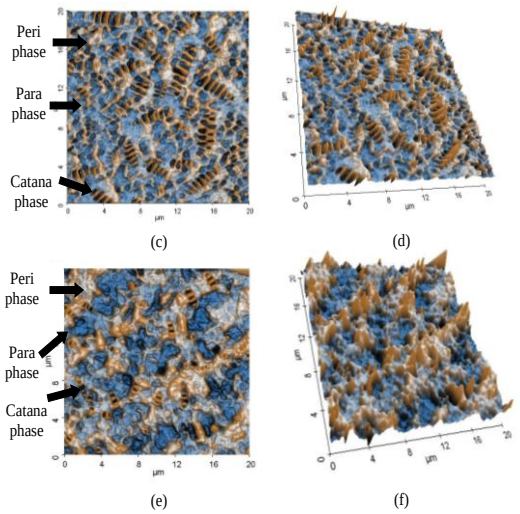

Fig. 6 2D & 3D topography image of B-B for (a)-(b) UA, (c)-(d) STA and (e)-(f) LTA

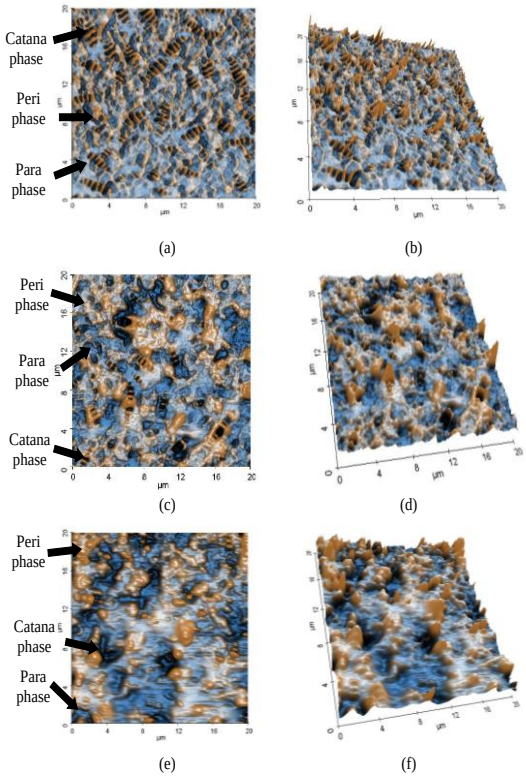

Fig. 7 2D & 3D topography image of B-PU for (a)-(b) UA, (c)-(d) STA and (e)-(f) LTA

CONCLUSION

The present study evaluates the effect of ageing on the physical and morphological properties of B-PU and compares the results with those of conventional bitumen. Result reveals that the addition of PU to B-B decreased the penetration value, which shows that harder bitumen has been formed while softening point value increased with the addition of PU. This is consistent with the results of the

penetration test, where stiffer bitumen increases the melting point of the bitumen. The AI for both penetration and softening point indicate that the B-PUs have higher ageing resistance in comparison to B-B. Besides, viscosity test shows that the addition of PU significantly increased viscosity value at 135 °C; the lower VAI shows that addition of PU reduced the ageing sensitivity of the bitumen. Image analysis from optical microscopic test shows that no separation occurred in the B-PU sample. This shows that the sample has been homogeneously blended and uniformly dispersed during the mixing process. The topography images from AFM test indicate that the inclusion of PU and ageing conditions has decreased the bee-like structures of the bitumen, showing larger dispersion in the sample.

ACKNOWLEDGMENT

The authors would like to express their gratitude to Ministry of Education Malaysia and Universiti Pertahanan Nasional Malaysia for the financial support for this work (FRGS/1/2020/TK0/UPNM/03/4).

REFERENCES

[1] Ibrahim A. N. H., Khairuddin F. H., Md Yusoff N. I., Borhan M. N., and Mohd Akhir N., Sifat Mekanik dan Tingkah Laku Resapan Air Bitumen Terubahsuai Geopolymer. Jurnal. Teknologi, 2017, 79(4): 107-111.

[2] Rahmad S., Yusoff N. I. M., Rosyidi S. A. P., Badri K. H., and Widyatmoko I., Effects of Rediset on The Adhesion, Stripping, Thermal and Surface Morphologies of PG76 Binder. Const. and Build. Mat, 2020, 241(117923).

[3] Airey G. D., and Mohammed M. H., Rheological Properties of Polyacrylates Used as Synthetic Road Binders. Rheol Acta, 2008, 47: 751–763.

[4] Jalkh R., El-Rassy H., Chehab G. R., and Abiad M. G., Assessment of The Physico-Chemical Properties of Waste Cooking Oil and Spent Coffee Grounds Oil for Potential Use as Asphalt Binder Rejuvenators. Waste and Biomass Valorization, 2017, 1–8.

[5] Al-Omari A. A., Khedaywi T. S., and Khasawneh M. A., Laboratory Characterization of Asphalt Binders Modified with Waste Vegetable Oil Using SuperPave Specifications. Int. Jour. of Pave. Research and Tech, 2018, 11(1): 68–76.

[6] Khairuddin F. H., Alamawi M. Y., Yusoff N. I. M., Badri K. H., Ceylan H., and Tawil S. N. M., Physicochemical and Thermal Analyses of Polyurethane Modified Bitumen Incorporated with Cecabase and Rediset: Optimization Using Response Surface Methodology. Fuel, 2019, 254.

[7] Lyne Å. L., Wallqvist V., and Birgisson B., Adhesive Surface Characteristics of Bitumen Binders Investigated by Atomic Force Microscopy. Fuel, 2013, 113: 248–256.

[8] Magonov S., Alexander J., Surtchev M., Hung A. M., and Fini E. H., Compositional Mapping of Bitumen Using Local. 2017.

[9] Lu X., and Isacsson U., Effect of Ageing on Bitumen Chemistry and Rheology. Const. and Build. Mat, 2002, 16(1): 15–22.

[10] Omar H. A., Yusoff N. I. M., Sajuri Z., Ceylan H., Jakarni F. M., and Ismail A., Evaluating the Effect of Mixing Process on Nano-Clay Modified Binders Using the Pull-Off Test Method. Applied Mechanics and Materials, 2015, 802: 357–362.

[11] Al-Rub R. K. A., Darabi M. K., Kim S. M., Little D. N., and Glover C. J., Mechanistic-Based Constitutive Modeling of Oxidative Aging in Aging-Susceptible Materials and its Effect on The Damage Potential of Asphalt Concrete. Const. Build and Mat, 2013, 41: 439–454.

[12] Khairuddin F. H., Yusoff N. I. M., Badri K. H., Koting S., Tawil S. N. M., Ng C. P., and Misnon N. A., Effect of Aging on The Chemical, Morphological and Wettability Characteristics of Polyurethane Modified Binder, Adv. in Civil Eng. Mat, 2021, 261–270.

[13] Cong P., Chen S., Yu J., and Wu S., Effects of Aging on The Properties of Modified Asphalt Binder with Flame Retardants. Const. and Build. Mat, 2010, 24(12): 2554–2558.

[14] Awazhar N. A., Khairuddin F. H., Rahmad S., Fadzil S. M., Omar H. Ali., Yusoff N. I, M., and Badri K., Engineering and Leaching Properties of Asphalt Binders Modified with Polyurethane and Cecabase Additives for Warm-Mix Asphalt Application. Const. and Build. Mat, 2020, 238.

[15] Ali A. H., Mashaan N. S., and Karim M. R., Investigations of Physical and Rheological Properties of Aged, Rubberised Bitumen. Adv. Mat. Sci. and Eng, 2013, 1–8.

[16] Pauli, T., Grimes W., Beiswenger J., and Schmets A. J. M., Surface Structuring of Wax in Complex Media. Jour. of Mat. Civil Eng, 2015, 27(8): 1–9.

[17] Zhang, H. L., Yu J. Y., Feng Z. G., Xue L. H., and Wu S. P., Effect of Aging on the Morphology of Bitumen by Atomic Force Microscopy. Jour. of Microscopy, 2012, 246(1): 11–19.

[18] Zhang, H. L., Wang H. C., and Yu J. Y., Effect of Aging on Morphology of Organo-montmorillonite Modified Bitumen by Atomic Force Microscopy. Journal of Microscopy, 2011, 242(1): 37–45.

8th Int. Conf. on Structure, Engineering & Environment (SEE), Mie, Japan, Nov.10-12, 2022, ISBN: 978-4-909106094 C3051

PUSHOVER ANALYSIS OF RC FRAMES WITH SUBSTANDARD BEAM-COLUMN JOINTS

Zaidir[1], and Syafri Wardi[2]
[1]Faculty of Engineering, Andalas University, Indonesia; [2]Faculty of Engineering, Padang Institute of Technology, Indonesia

ABSTRACT

Recent earthquakes in developing countries showed that the failure of substandard beam-column joints often contributes to heavy damage or collapse of reinforced concrete (RC) buildings. Static nonlinear pushover analysis is one of the methods to evaluate the seismic capacity of RC frames/buildings. However, the pushover analysis commonly neglects the failure at beam-column joints because of the complex behavior. In this study, a nonlinear pushover analysis procedure considering the failure of exterior beam-column joints without shear reinforcement is presented. Specifically, the performance limit is assumed as a point at the failure of beam-column joints from the literature of experimental study and a simplified backbone of joint shear stress-strain response. The proposed analysis procedure is applied to one RC frame with substandard beam-column joints representing a collapsed building due to a recent earthquake in Indonesia. The proposed analysis procedure is applicable to estimate the seismic capacity of RC frames considering the failure of exterior beam-column joints.

Keywords: Beam-column joint failure, Plastic hinge, Reinforced concrete, Seismic capacity evaluation

INTRODUCTION

The beam-column joints that do not satisfy the requirements of the standard for seismic detailing often caused severe damage or collapse of RC buildings, as observed in recent earthquakes in developing countries [1]–[3]. Figure 1 shows a collapsed RC building with failure on the beam-column joint, in which the joint area had no shear reinforcement. The previous study by one of the authors [4], [5] also showed that beam-column joints without shear reinforcement still exist in newly built construction in an area that had experienced significant damage due to a past earthquake (Fig. 2). These indicated that many stocks of RC buildings with substandard beam-column joints exist in developing countries in earthquake-prone areas.

Fig. 1 A collapsed building and its damaged exterior beam-column joint [2].

Fig. 2 Substandard detail of exterior beam-column joint in construction [4].

The behavior and seismic capacity of existing buildings need to be evaluated using non-linear analysis, i.e. static nonlinear pushover analysis. Pushover analysis of RC frames/buildings commonly considers the nonlinear behavior of beam and column members, assuming rigid beam-column joints. However, this assumption may mislead the analysis results in the case of substandard beam-column joints, because the failure of the joint may occur.

Many literatures (e.g. [6]–[8]) have developed detailed numerical models for the analysis of RC beam-column joints. However, the models are not easy to be used by a practical engineer. Therefore, this study presented a simplified nonlinear pushover analysis procedure to evaluate the seismic capacity of RC frames with sub-standard beam-column joints, assuming the performance limit of the frames is at the failure of beam-column joints observed in previous experimental studies from the literature of experimental study and a simplified backbone of joint shear stress-strain response.

REVIEW ON PERFORMANCE LIMIT OF SUB-ASSEMBLAGE BEAM-COLUMN JOINTS WITH SUBSTANDARD DETAILS

Many experimental studies have been conducted on the seismic performance of substandard beam-column joints. This section focuses on the experimental studies of exterior beam-column, without shear reinforcement in which the joint shear failure occurred before yielding of adjacent beam [1], [9]–[11]. This kind of failure exhibited brittle failure, where the strength and the deformation capacity of the specimens significantly drop after the peak strength was observed. Therefore, in the current study, the drift ratio at the peak strength is assumed as the performance limit for the exterior beam-column joint without shear reinforcement.

Table 1 summarized the drift ratio at the peak strength of the sub-assemblage exterior beam-column joint specimens without shear reinforcement from the literature on experimental study. The data used in table 1 was restricted only to the case of sub-assembled exterior beam-column joint specimens which were given static cyclic load at the beam end. The data was also restricted for the specimens with deformed bars with standard hooks; thus, anchorage failure of beam reinforcement in the joint did not occur.

Table 1 The drift ratio at peak strength of sub-assemblage exterior beam-column joints

Specimen ID	Drift ratio at peak strength	Case study
as-is joint [9]	2,0%	1960s building in the US.
C1 [10]	2,3%	Poorly - detailed joint.
C2 [10]	1,8%	
Test#1 [11]	1,5%	The 1960s-1990s building in Italy.
J2 [2]	1,5%	Indonesian building.

The experimental results in table 1 showed that the conservative value of drift ratio at peak load of the specimens is 1,5%. This value is also confirmed as the median value of drift ratio at peak joint shear strength of unconfined exterior beam-column joint in the database used in a study by Hassan [12], in which most of the specimens with joint shear failure had a drift a peak strength around 1% - 2% as shown in Figure 3. In the figure, data for specimens with joint shear failure is indicated by a red open circle and a red solid circle.

In the next section, one sub-assemblage beam-column joint specimen representing an Indonesian building with the drift ratio at peak strength of 1,5% was used as the reference for verification of the numerical modeling.

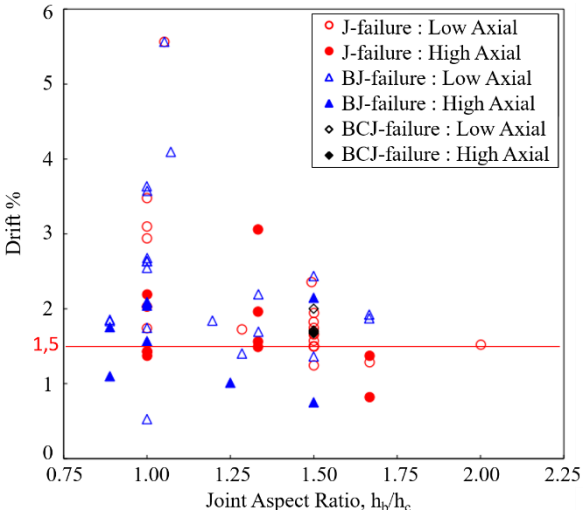

Fig. 3 Drift ratio at the peak strength in the experimental database [12] (some notes in the figure were added by authors)

MODELLING OF SUB-ASSEMBLAGE BEAM-COLUMN JOINTS WITH SUBSTANDARD DETAILS

A commercial finite element-based software Seismostruct is used for modeling the structure. The column and beam members are modeled using an inelastic force-based flexure type element (Fig. 4), that used the force-based finite element formulation [13], [14] in modeling geometric nonlinearity and material inelasticity of the member.

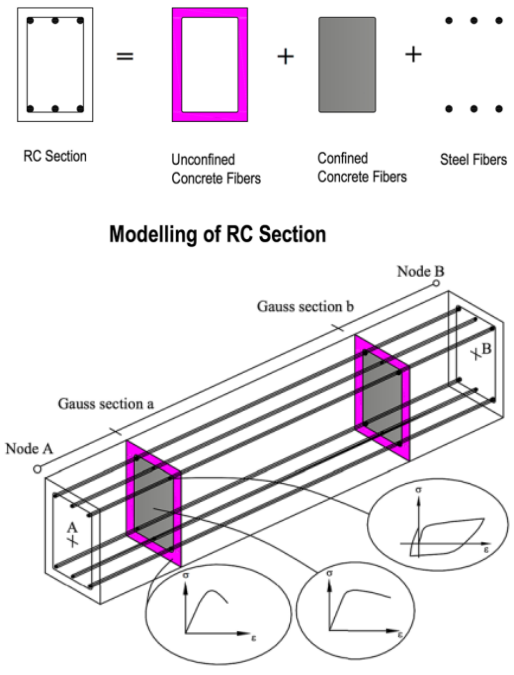

Fig. 4 Modeling of columns and beams.

This study used a simplified modeling technique to model the failure of the beam-column joint in one sub-assemblage beam-column joint specimen in the literature, specimen J2 [2]. The joint panel was idealized as rigid links with a rotational spring at the center of the joint, as shown in Fig. 5. This model was used widely in the literature (e.g. [15], [16]).

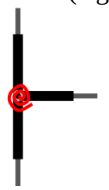

Fig. 5 Beam-column joint modeling.

The rotational spring at the center of the joint is defined by the backbone of joint shear stress – shear strain response. The backbone is generally controlled by four damage states: cracking of concrete, pre-peak strength, peak strength, and residual strength, as shown in Figure 6. These damage states were adopted in many constitutive models in the literature (e.g. [11], [17], [18]).

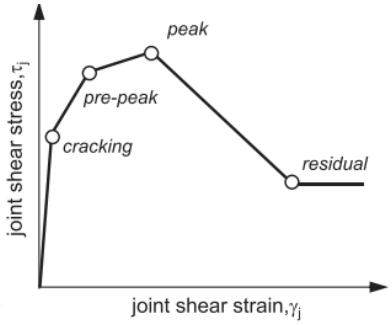

Fig. 5 Backbone of the joint shear stress-strain and damage states.

This study considered a backbone of the joint shear stress-strain developed by DeRisi [11], as shown in Figure 6. The model was developed for unreinforced exterior beam-column and verified with the experimental database. The summary of the key parameters defining the shear stress (τ_j) of the backbone curve for the exterior beam-column with joint shear failure before yielding of the beam is shown in Table 2. However, in this study, the backbone curve is simplified as follows:

1. $\tau_{j,max}$ is determined as a conservative value of $0{,}42\sqrt{f_c'}$. This value is used widely in the literature (e.g.[19]–[21]) as a conservative value of shear stress of unreinforced exterior beam-column joint with beam rebars bent into joint.
2. The performance limit of the joint is assumed as the first point when the maximum shear stress is achieved because the literature of the experimental studies (e.g. [2], [9]–[11]) showed that the unreinforced exterior beam-column specimens exhibit a brittle failure after this point. Therefore, the backbone curve for the post-peak behavior is not considered.

The simplified backbone curve used in this study is shown in Figure 7. The backbone of the tensile stress–shear response was converted into a moment-rotation response by applying the equations by Celik and Ellingwood [15].

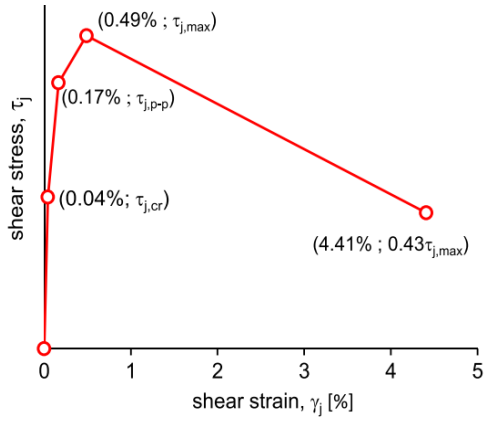

Fig. 6 Backbone of shear stress-strain [11]

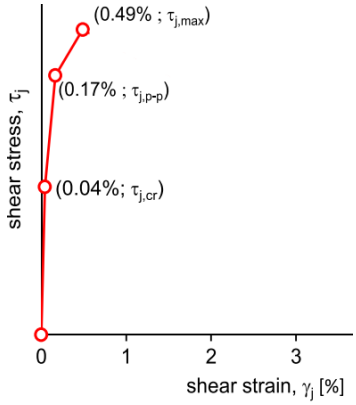

Fig. 7 Simplified principal tensile stress–shear deformation (adapted form [11], modified by authors).

Table 2 Summary of the key parameters defining the shear stress (τ_j) of the backbone curve for the exterior beam-column [11]

Backbone point	τ_j
Cracking ($\tau_{j,cr}$) [22]	$\tau_{j,cr} = 0{,}29\sqrt{fc}\sqrt{1+0{,}29\frac{P}{A_j}}$
Pre-peak ($\tau_{j,p-p}$)	$\tau_{j,p-p} = 0{,}85\ \tau_{j,max}$ if J-failure
Peak ($\tau_{j,max}$) [23]	$\ln(\tau_{j,max}) = -0{,}81 + 0{,}46\ln(fc) + 0{,}50\ln(\tau_d) + 0{,}68\ln(JP) + 0{,}62\ln(TB) - 0{,}25\ln(h_b/h_c) + 0{,}08\ln(M_R) + 0{,}14\ln(\theta)$
Residual	$0{,}43\ \tau_{j,max}$

The modeling technique explained above was applied to a sub-assemblage beam-column joint specimen from the literature [2] using static pushover analysis. Figure 8 shows the comparison between the numerical modeling with pushover analysis (red line) and the experimental hysteretic curve (black line) from the literature.

The numerical pushover curve was close to the experimental results, especially in estimating the stiffness. The numerical pushover curve also conservatively estimates the peak strength and the drift at the peak strength. This shows the soundness of the proposed modeling procedure in simulating the behavior of the sub-assemblage exterior beam-column joints without shear reinforcement in the joint; thus, it can be applied for pushover analysis of RC frames/RC buildings with such kind of details in the joints.

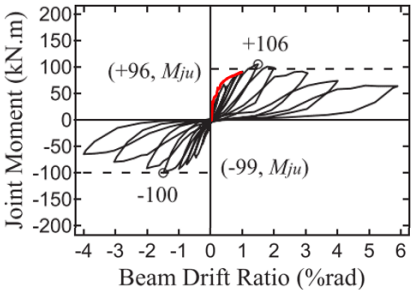

Fig. 8 Numerical pushover results vs experimental hysteretic curve for specimen J2 [2]

PUSHOVER ANALYSIS OF RC FRAMES WITH SUBSTANDARD BEAM-COLUMN JOINT

Case Study

A plane frame of a three-stories office building in Indonesia is examined in this study. The building collapsed due to the 2018 Earthquake in Palu [24]. The photos from the field investigation in Figure 9 show that no shear reinforcement was installed in the exterior joint and buckling of column longitudinal reinforcement was observed in the joint. This indicated that the collapse of the building might occur because of the failure of the joint.

The plane frame of the building and the details of the structural member is shown in Figure 10. In this study, the analysis is conducted only for one plane frame of the focused building, because the building has a similar plane frame in both directions of the building. The design strength of concrete used in the building is 22.8 MPa for concrete. The specified yield strength of reinforcement is 390 MPa and 240 MPa for longitudinal and transverse reinforcement, respectively.

Fig. 9 A collapsed building due to the 2018 Palu Earthquake and damage to the exterior beam-column joints. (Photo courtesy of Syafri Wardi)

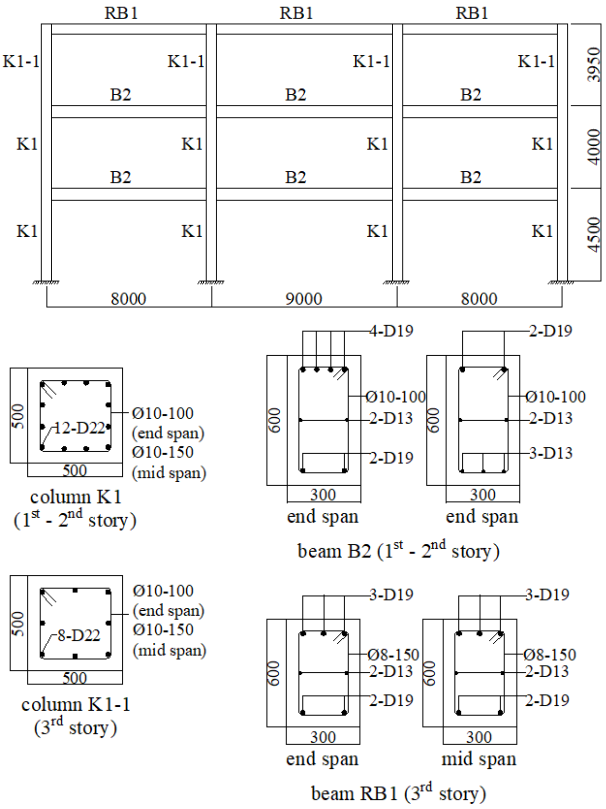

Fig. 10 Plane frame of the building and the details of the structural member.

Analytical Assumptions

Seismostruct 2022 is used for modeling the plane frame. The assumptions for modeling are similar to those in the modeling of sub-assemblage beam-column joint specimens in the previous section of this article. Two models were analyzed in this study. The first model is the frame without nonlinear modeling of the beam-column joint, in which the beam-column

joints were assumed as a rigid zone. The second model is the frame with non-linear modeling of the exterior beam-column joints with the same assumption as those in the analysis of the sub-assemblage beam-column joint in the previous section. For the second model, interior joints are also idealized as rigid links with a rotational spring, but the rotational spring is as assumed as linear elastic.

The gravity load of the building was calculated based on the Indonesian code [25]. The distribution of lateral load for pushover analysis was assumed as an inverted triangular distribution and the analysis was performed using a displacement control approach.

The performance limit of the frame was set to the point at the failure of the exterior beam-column joints. The failure of exterior beam-column joints is more critical than interior beam-column joints, as confirmed in literature by Priestley [19].

Analysis Results

The capacity curve (base shear vs roof displacement) relationship of the first model without modeling the beam-column joints is shown in Figure 11 The figure also includes the target displacements at the performance level of life safety (LS) and Collapse Prevention (CP) under the earthquake hazard level of BSE-1E and BSE-2E, according to ASCE 41-17 [26]. The capacity curve shows that the frame maintained its strength and ductility exceeding the target displacement. This result misleads the behavior and seismic performance of the building.

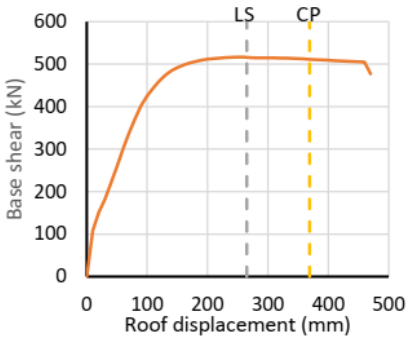

Fig. 11 Base shear vs. roof displacement for the frame without joint modeling.

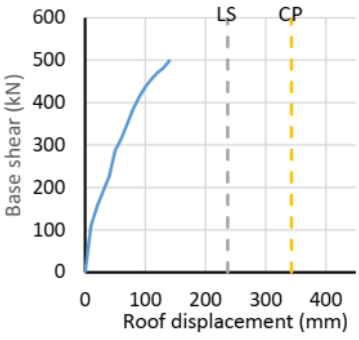

Fig. 12 Base shear vs. roof displacement for the frame without joint modeling.

CONCLUSIONS

This study presented a nonlinear pushover analysis procedure considering the failure of exterior beam-column joints without shear reinforcement, in which the performance limit of the frames is assumed as a point at the peak strength of the joints. A simplified numerical modeling assumption for the joints was presented and verified to a sub-assemblage exterior beam-column joint. The numerical pushover curve had a good agreement in estimating the stiffness and conservatively estimates the peak strength and the drift at the peak strength of the sub-assemblage exterior beam-column joint.

The pushover analysis procedure was applied to one RC frame with substandard beam-column joints representing collapsed buildings due to the 2018 Earthquake in Palu, Indonesia. Application of the analysis procedure is applicable to estimate the seismic capacity of RC frames/buildings considering the failure of beam-column joints, especially in the case of the unreinforced beam-column joints using deformed bars and beam rebars bent into joints with sufficient anchorage length.

REFERENCES

[1] Y. Li, Y. Sanada, S. Takahashi, K. Maekawa, H. Choi, and K. Matsukawa, “Seismic Performance Evaluation and Strengthening of RC Frames with Substandard Beam-Column Joint: Lessons Learned from the 2013 Bohol Earthquake,” *J. Earthq. Tsunami*, vol. 10, no. 03, p. 1640007, Sep. 2016, doi: 10.1142/S1793431116400078.

[2] Y. Li and Y. Sanada, “Seismic strengthening of existing RC beam-column joints by wing walls,” *Earthq. Eng. Struct. Dyn.*, 2017, doi: 10.1002/eqe.2890.

[3] S. Wardi, Y. Sanada, N. Saha, and S. Takahashi, “Improving integrity of RC beam-column joints with deficient beam rebar anchorage,” *Earthq. Eng. Struct. Dyn.*, vol. 49, no. 3, pp. 234–260, Mar. 2020, doi: 10.1002/eqe.3229.

[4] S. Wardi, Y. Sanada, M. Kita, J. Tanjung, and M. Maidiawati, “Common Structural Details and Deficiencies in Indonesian RC Buildings: Preliminary Report on Field Investigation in Padang City, West Sumatra,” *Int. J. Adv. Sci. Eng. Inf. Technol.*, vol. 8, no. 2, p. 418, Mar. 2018, doi: 10.18517/ijaseit.8.2.4207.

[5] S. Wardi, Y. Sanada, M. Kita, J. Tanjung, and Maidiawati, “Investigation on implementation of seismic detailing of reinforced concrete buildings in West Sumatra Indonesia,” in *Proceedings of the 7th Asia Conference on Earthquake Engineering (7ACEE)*, 2018, p. Paper ID ACEE0069.

[6] L. N. Lowes and A. Altoontash, “Modeling Reinforced-Concrete Beam-Column Joints

Subjected to Cyclic Loading," *J. Struct. Eng.*, vol. 129, no. 12, pp. 1686–1697, Dec. 2003, doi: 10.1061/(ASCE)0733-9445(2003)129:12(1686).

[7] M. Shin and J. M. LaFave, "Testing and modelling for cyclic joint shear deformations in RC beam-column connections," in *Proceedings of the Thirteenth World Conference on Earthquake Engineering*, 2004, p. Paper No. 0301.

[8] Y. C. Sung, T. K. Lin, C. C. Hsiao, and M. C. Lai, "Pushover analysis of reinforced concrete frames considering shear failure at beam-column joints," *Earthq. Eng. Eng. Vib.*, vol. 12, no. 3, pp. 373–383, Sep. 2013, doi: 10.1007/s11803-013-0179-8.

[9] C. Pantelides, C. Clyde, and L. Reaveley, "Rehabilitation of R/C Building Joints With FRP Composites," in *12th World Conference on Earthquake Engineering*, 2000, p. Paper No. 2306.

[10] C. P. Antonopoulos and T. C. Triantafillou, "Experimental Investigation of FRP-Strengthened RC Beam-Column Joints," *J. Compos. Constr.*, vol. 7, no. 1, pp. 39–49, Feb. 2003, doi: 10.1061/(ASCE)1090-0268(2003)7:1(39).

[11] M. T. De Risi, P. Ricci, and G. M. Verderame, "Modelling exterior unreinforced beam-column joints in seismic analysis of non-ductile RC frames," *Earthq. Eng. Struct. Dyn.*, vol. 46, no. 6, pp. 899–923, May 2017, doi: 10.1002/eqe.2835.

[12] W. M. Hassan, "Analytical and Experimental Assessment of Seismic Vulnerability of Beam-Column Joints without Transverse Reinforcement in Concrete Buildings," University of California, Berkeley, 2011.

[13] A. Neuenhofer and F. C. Filippou, "Evaluation of Nonlinear Frame Finite-Element Models," *J. Struct. Eng.*, vol. 123, no. 7, pp. 958–966, Jul. 1997, doi: 10.1061/(ASCE)0733-9445(1997)123:7(958).

[14] E. Spacone, V. Ciampi, and F. C. Filippou, "Mixed formulation of nonlinear beam finite element," *Comput. Struct.*, vol. 58, no. 1, pp. 71–83, Jan. 1996, doi: 10.1016/0045-7949(95)00103-N.

[15] O. C. Celik and B. R. Ellingwood, "Modeling Beam-Column Joints in Fragility Assessment of Gravity Load Designed Reinforced Concrete Frames," *J. Earthq. Eng.*, vol. 12, no. 3, pp. 357–381, Mar. 2008, doi: 10.1080/13632460701457215.

[16] J. S. Jeon, L. N. Lowes, and R. DesRoches, "Numerical models for beam-column joints in reinforced concrete building frames," *ACI Spec. Publ.*, vol. 297, pp. 1–26, 2014, [Online]. Available: https://www.concrete.org/publications/internationalconcreteabstractsportal/m/details/id/51686900

[17] M. Anderson, D. Lehman, and J. Stanton, "A cyclic shear stress–strain model for joints without transverse reinforcement," *Eng. Struct.*, vol. 30, no. 4, pp. 941–954, Apr. 2008, doi: 10.1016/j.engstruct.2007.02.005.

[18] A. C. Birely, L. N. Lowes, and D. E. Lehman, "A model for the practical nonlinear analysis of reinforced-concrete frames including joint flexibility," *Eng. Struct.*, vol. 34, pp. 455–465, Jan. 2012, doi: 10.1016/j.engstruct.2011.09.003.

[19] M. J. N. Priestly, "Displacement-Based Seismic Assesment of Reinfirced Concrete Buildings," *J. Earthq. Eng.*, vol. 1, no. 1, pp. 157–192, 1997.

[20] S. Pampanin, G. M. Calvi, and M. Moratti, "Seismic behavior of R.C. beam-column joints designed for gravity only," in *Proceedings of the 12th European conference on earthquake engineering*, 2002, p. Paper No. 726.

[21] A. Sharma, R. Eligehausen, and G. R. Reddy, "A new model to simulate joint shear behavior of poorly detailed beam–column connections in RC structures under seismic loads, Part I: Exterior joints," *Eng. Struct.*, vol. 33, no. 3, pp. 1034–1051, Mar. 2011, doi: 10.1016/j.engstruct.2010.12.026.

[22] S. M. Uzumeri, "Strength and Ductility of Cast-In-Place Beam-Column Joints," *Symp. Pap.*, vol. 53, pp. 293–350, 1977.

[23] J.-S. Jeon, A. Shafieezadeh, and R. DesRoches, "Statistical models for shear strength of RC beam-column joints using machine-learning techniques," *Earthq. Eng. Struct. Dyn.*, vol. 43, no. 14, pp. 2075–2095, Nov. 2014, doi: 10.1002/eqe.2437.

[24] USGS, "M 7.5 - 72 km N of Palu, Indonesia." https://earthquake.usgs.gov/earthquakes/eventpage/us1000h3p4/executive (accessed Jun. 01, 2022).

[25] National Standardization Agency of Indonesia (BSN), "Design Load Procedure for Homes and Buildings," Jakarta, 1989.

[26] *Seismic Evaluation and Retrofit of Existing Buildings*. Reston, VA: American Society of Civil Engineers, 2017. doi: 10.1061/9780784414859.

8th Int. Conf. on Structure, Engineering & Environment (SEE), Mie, Japan, Nov.10-12, 2022, ISBN: 978-4-909106094 C3051

LIFE CYCLE ASSESSMENT IN THE PRODUCTION PROCESS OF CRUDE PALM OIL (CPO) ON PALM OIL PLANTATION AND MILLS

Deffi Ayu Puspito Sari[1,] *, Malikhatun Nikmah[1] and Nugroho Adi Sasongko [2]

[1] Universitas Bakrie; malikhatunnikmah97@gmail.com; deffiayu@gmail.com
[2] National Research and Innovation Agency; nugroho.adi.sasongko@brin.go.id
***** Correspondence: deffiayu@gmail.com

Abstract

Life Cycle Assessment (LCA) could be used to assess the environmental impact. The purposes of this research are: 1)to collect data of energy and material inventory used in oil palm plantations and mills of PT Y in 2019; 2)to analyze the results of LCA and Crude Palm Oil (CPO) production with several impact categories such as Global Warming Potential, Acidification, and Eutrophication, and 3)to provides the recommendation on reducing emissions from CPO production based on the LCA results. To processed data, this research use SimaPro and excell base with CML-IA Baseline method. The system boundary used is cradle to gate. The result showed that the biggest emission comes from the Mills with Global Warming Potential impact value is 21,655,029 kg CO_2-eq/kg CPO/year, Acidification value is 177,462 kg SO_2-eq/kg CPO/year, and Eutrophication value is 6,958 kg PO_4-eq/kg CPO/year.

Keywords: oil palm plantations and mills; life cycle assessment; global warming potential; acidification; eutrophication

INTRODUCTION

Oil palm plantations are starting to develop very quickly in Indonesia. Of the 34 provinces in Indonesia, oil palm plantations are growing in 22 provinces. This oil palm plantation can generate the largest foreign exchange for Indonesia. The potential of oil palm plantations in the economic field is very large and Indonesia is the largest exporter of oil palm (Masykur, 2013).

Currently, the demand to land for oil palm plantations is increasing, this has led to the construction of many palm oil mills with large production capacities. To reduce the amount of agricultural land and production forests can use biomass. Types of biomass, namely those from soil, forest and cultivated plants (Falatehan & Sari, 2020). The most economical and reliable source of energy is hydroelectric power. Efforts to reduce dependence on the use of fossil fuels can be done by increasing renewable energy production capabilities (Bahtiar, Falatehan, Sari, & Thamrin, 2019). Electrical energy can also be said to be energy that is very easy to use because it is easy and efficient in converting electrical energy into other forms (Thamrin, Sari, & Setyoningrum, 2019).

Palm oil mills produce emissions from each process, one example of which is the emission of greenhouse gases such as carbon (CO2), methane (CH4), nitrous oxide (N2O) and other gases (Sari, Mutaqin, Pawenary, & Majlan, 2019). In palm oil mills, the production process, energy consumption, and the waste degradation process can produce greenhouse gases (Sari, Fadiilah, Azizi, & Pawenary, 2019). Other environmental impact are Acidification and Eutrophication which can be harmful to the environment. Waste from palm oil mills is in the form of solid and liquid waste. Liquid waste comes from the sterilization and clarification process or commonly called Palm Oil Mill effluent (POME), this POME can trigger climate change because it produces methane gas (Sari, Fadiilah, & Azizi, 2019).

PT Y's palm oil mill has a production capacity of 60 tons of fresh fruit bunches/hour. Therefore, this research will be conducted on PT Y's plantations and palm oil mills using the Life Cycle Assessment (LCA) method. The method can assess the environmental impact associated with each product, process and activity (Ciambrone, 1997). Life Cycle Assessment can be used to determine the amount of energy, costs, and environmental impact caused by the stages of the product life cycle. Starting from the time of taking raw materials until the product is finished being used by consumers (Susanto, Santoso, & Suwedi, 2017). The reliability and adequacy of the object data inventory to be assessed is very influential for the LCA results. The Life Cycle Assessment (LCA) has four stages, namely the purpose and scope definition stage, the inventory analysis stage, the impact assessment stage and the interpretation stage.

MATERIALS AND METHODS

This research was conducted with the Life Cycle Assessment (LCA) approach which has 4 stages, namely data collection, life cycle inventory, life cycle impact assessment, life cycle assessment and interpretation. The data used in this study are secondary data obtained from routine company reports in 2019. The method used is the CML-IA Baseline. This method is an LCA methodology

developed by the Leiden University Center for Environmental Sciences (CML) in the Netherlands and released by CML in April 2013 and has been standardized by the IPCC.

In this study, using 3 impact categories, namely Acidification, Climate Change, and Eutrophication. The system limit used is Cradle to gate which covers all processes from raw material extraction through the production stage, used to determine the environmental impact of a product's production. Analysis through the LCA approach by entering inventory data derived from the cultivation process and the processing of oil palm in the SimaPro and Microsoft Excel software. Based on the analysis carried out, environmental impacts will be generated and alternative improvements in each production activity will be obtained.

RESULTS

Palm oil plantation and mill PT Y

PT Y's garden is divided into 4 Afdeling. Afdeling I area of 1,057 hectares, Afdeling II area of 709 hectares, Afdeling III covering 626 hectares and Afdeling IV covering 782 hectares. The land of PT Y's oil palm plantations before being turned into oil palm plantations was a rubber plantation. Meanwhile, geologically, the oil palm plantation area of PT Y is included in the tertiary formation (S3) with clay rock and sandstone (Randa, 2011). The process of cultivating oil palm at PT Y is as follows:

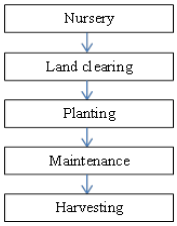

Figure 1. Flow chart of the process of oil palm cultivation at PT Y (SOP of PT Y Oil Palm Plantation).

Fresh fruit bunches that have been harvested are then transported by truck to the factory to be used as crude palm oil (CPO). The following is a diagram of the process of processing fresh fruit bunches into CPO at the PT Y palm oil mill:

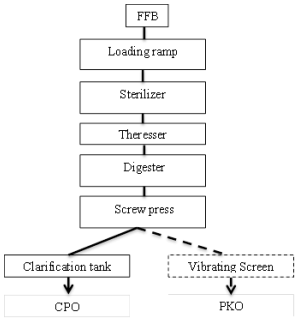

Figure 2. The process of processing fresh fruit bunches into crude palm oil at PT Y's palm oil mill (SOP of PT Y Palm oil processing).

Life Cycle Inventory

The data obtained in this research are secondary data obtained from routine reports of PT Y's plantation and palm oil mill companies. The data are in the form of material and energy usage data in each process of oil palm cultivation to produce crude palm oil for one year, namely in 2019.

Table 1. PT Y's oil palm plantation and mill inventory data for 2019.

Activity	Type of activity	Type	amount	unit
TM Maintenance	Fertilization	NPK 15-7-24-1	618	Kg
		Dolomite	293	Kg
	Herbicide	Glyphosate	1414	liter
BBM Energy (Solar)	Transportation	D 1048 AAF	3687	liter
		D 8178 DT	1513	liter
		D 8643 EJ	7087	liter
		D 8808 EZ	5927	liter
		D 8809 EZ	7223	liter
		D 8807 EZ	8393	liter
		Loader	27600	liter
		Excavator	14433	liter
Electrical Energy	Cummins 2	PLN (20%)	8648	kWh
		Biomass (80%)	34591	kWh
	Turbine	PLN (20%)	808719	kWh
		Biomass (80%)	3234876	kWh
	Fuel	Shell	12415304	kg
		Fiber	20560264	kg
Biomass	Water energy	Factory washing water	9747	m3
		Boiler feed	78177	m3
		Process	108626	m3
		Domestic	113939	m3
		Boiler	78177	m3

Life Cycle Impact Assessment

Impact Assessment is carried out on PT Y oil palm plantations and mills by multiplying inventory data with characterization factors. The multiplication is done using SimaPro software and Excel base. The following is a table of Life Cycle Assessment (LCA) results on Global Warming Potential, Acidification, and Eutrophication at PT Y's oil palm plantations and mill:

Table 2. Life Cycle Assessment (LCA) Results on Global Warming Potential, Acidification, and Eutrophication at PT Y.

Activity	Type of activity	Type	Impact factor GWP (kg CO2 eq/kg cpo/tahun)	Acidification (kg SO2 eq/kg cpo/tahun)	Eutrophication (kg PO4 eq/kg cpo/tahun)
TM Maintenance	Fertilization	NPK 15-7-24-1	2384	12	4
		Dolomite	13	0	0
	Herbicide	Glyphosate	7941	53	38
BBM Energy (Solar)	Transportation	D 1048 AAF	50733	202	48
		D 8178 DT	20819	83	20
		D 8643 EJ	97517	388	92
		D 8808 EZ	81556	325	77
		D 8809 EZ	99388	396	94
		D 8807 EZ	115488	460	109
		Loader	379776	1512	358
		Excavator	198598	791	187
Electrical Energy	Cummins 2	PLN (20%)	8907	51	40
		Biomass (80%)	1584	26	4
	Turbine	PLN (20%)	832981	4763	3712
		Biomass (80%)	148157	2439	343
Biomass	Fuel	Shell	899563	7616	2759
		Fiber			
	Water energy	Factory washing water	82795	248	59
		Boiler feed	664070	1988	475
		Process	922717	2762	660
		Domestic	967848	2897	692
		Boiler	21655029	177462	6958

Source: calculation results.

Table 2. shows the results of the multiplication of inventory data for 2019 with the characterization factor of the Global Warming Potential, Acidification, and Eutrophication in PT Y's oil palm plantations and mills which produce impact factor values. In oil palm plantations which have the biggest impact on the 3 impact categories are the use of glyphosate herbicides, which is 7,941 kg CO2-eq / kg cpo / year on Global Warming Potential, amounting to 53 kg SO2-eq / kg cpo / year against Acidification and 38 kg PO4-eq / kg cpo / year to Eutrophication. Glyphosate type herbicides in oil palm plantations are used to eradicate weeds. Weed is one of the pests that has the potential to reduce the productivity of oil palm plants.

Whereas at the palm oil mill which has the biggest impact is the use of boilers that is equal to 21,655,029 kg CO2-eq / kg cpo / year on Global Warming Potential, amounting to 177,462 kg SO2-eq / kg cpo / year on Acidification and 6,958 kg PO4 -eq / kg cpo / year against Eutrophication. Boilers are closed vessels for turning water into high pressure steam with the help of heating obtained from combustion. The fuel used by PT Y's palm oil mills is shells and fibers. Boilers are the main provider of energy needs in palm oil mills. The following are the results of networking using SimaPro software in PT Y's oil palm plantations and mills:

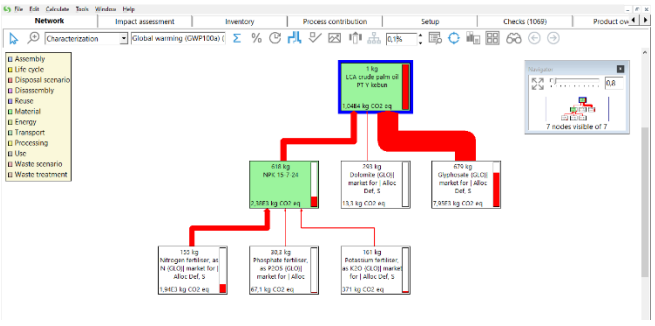

Figure 3. Results of SimaPro networking software on oil palm plantations on Global Warming Potential (calculation results).

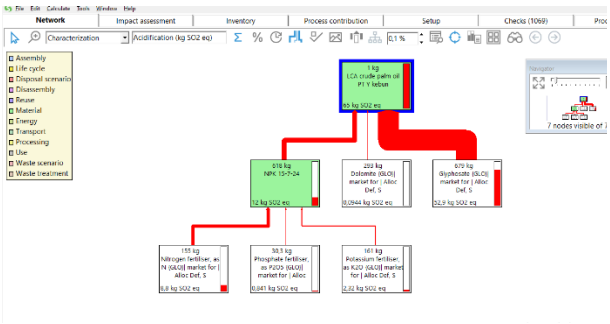

Figure 4. Results of SimaPro networking software on oil palm plantations on Acidification (calculation results).

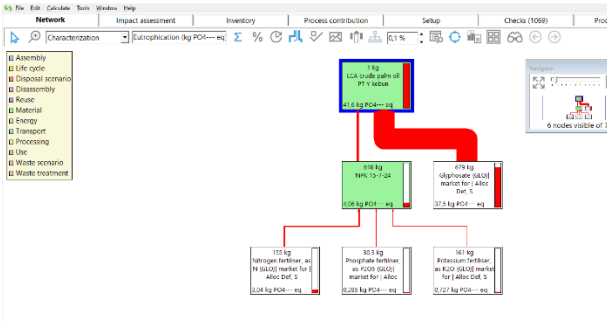

Figure 5. Results of SimaPro networking software on oil palm plantations for Eutrophication (calculation results).

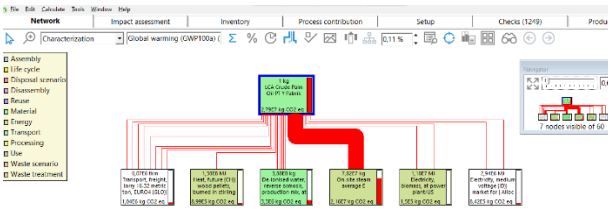

Figure 6. Results of SimaPro networking software on palm oil mills on Global Warming Potential (calculation results).

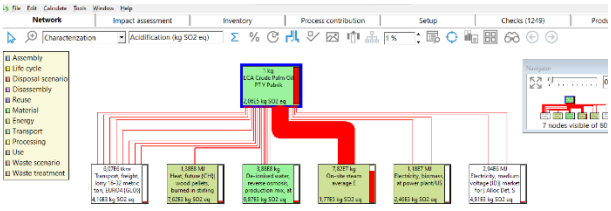

Figure 7. The results of SimaPro networking software on palm oil mills against Acidification (calculation results).

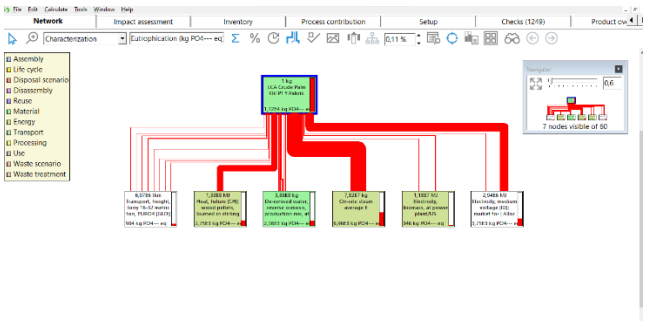

Figure 8. Results of SimaPro networking software on a palm oil mill for Eutrophication (calculation results).

The results of networking for oil palm plantations show differences in the thickness of the red line. The thickness of the line shows the percentage of volume or material flow ratio, which means that the process or stage has more use than the other processes and has the greatest impact on the environment.

DISCUSSION

After an LCA analysis, it is known that the biggest impact produced from such an activity. The following are the linkages between the activities of the activities and their impacts, as well as providing alternative improvements in the future.

Palm Oil Plantation

In oil palm plantations, herbicide use activities are activities with the greatest environmental burden. This herbicide use activity is an activity to eradicate weeds. Where this weed will potentially cause a decrease in productivity of oil palm plants. Herbicide with active glyphosate is widely used by farmers and planters in Indonesia because it is effective, inexpensive and safe.

However, excessive use of herbicides will cause soil fertility is reduced and can give symptoms to farmers such as eye irritation, blurred vision, burning or itchy skin, nausea, sore throat, asthma, difficulty breathing, headaches, nosebleeds and dizziness. An alternative that can be used to reduce the use of herbicides is to pay attention to the dose used. Farmers need to be educated to provide farmers with knowledge about the selection, preparation, handling and application of herbicides on oil palm lands.

Palm Oil Mill

At the palm oil mill, the use of boilers is the activity with the greatest environmental burden. The use of steam boilers has the greatest impact on global warming potential, one example of which can cause greenhouse gases. Climate change can cause losses for farmers because it can cause land drought, reduced water sources, crop failure and unpredictable rainfall (Sari, Falatehan, Irawan, Sedana, & Rahim, 2018). Alternatives to reduce the use of this boiler need further research.

CONCLUSIONS

The conclusions that can be drawn from this study are: 1) Inventory data on oil palm plantations in the form of fertilizer and herbicide use. Fertilizers used during 2019 are NPK 15-7-24 with 618 kg and 293 kg of dolomite. The herbicide used was 1,414 liters of glyphosate type herbisisda; 2) Inventory data on palm oil mills in the form of solar energy, electricity, fuel and water energy; 3) The results of the life cycle assessment of oil palm plantations and mills which have the greatest impact on Global Warming Potential, Acidification, and Eutrophication are the use of boilers in the amount of 21,655,029 kg CO2-eq/kg cpo/ year for the Global Warming Potential impact factor, 177,462 kg SO2-eq /kg cpo / year for impact factor Acidification and 6,958 kg PO4-eq/kg cpo/year for impact factor Eutrophication; 4) Hotspots that have the greatest impact on the environment on PT Y plantations are on the use of glyphosate herbicides; 5) Hotspots that have the greatest impact on the environment at the PT Y plant are on the use of boilers.

RECOMMENDATION

From this research, it can be given recommendation that are expected to be useful for companies, among others, as follows:

The use of glyphosate type herbicide during 2019 has the greatest impact on the environment, namely 7,941 kg CO2-eq/kg cpo/year for Global Warming Potential impact factors, 53 kg SO2-eq/kg cpo/year for Acidification impact factors and of 38 kg PO4-eq/kg cpo/year for the Eutrophication impact factor, so it is necessary to educate farmers about the use of herbicides for oil palm land.

The use of boilers during 2019 had the greatest impact on the environment, amounting to 21,655,029 kg CO2-eq/kg cpo/year for Global Warming Potential impact factors, 177,462 kg SO2-eq/kg cpo/year for impact factors Acidification and of 6,958 kg PO4-eq/kg cpo/year for the impact factor Eutrophication, it is necessary to use an air filter in the boiler chimney so that emissions released are more environmentally friendly.

Recommendations for further research

The need for interrelation of all parties to ensure the availability of complete data. Complete data in the form of material and energy use data and emission loads released.

Further research needs to be done on alternatives that can be used to reduce the impact on the environment.

ACKNOWLEDGEMENT

This research has been funded by Ministry Education, Culture, Research and Technology, Indonesia (PTUPT Scheme), with contract number 234/E4.1/AK.04.PT/2021; 3585/LL3/KR/2021; 115/SPK/LPP-UB/VII/2021 and Universitas Bakrie with contract number 130/SPK/LPP-UB/VII/2021.

REFERENCES

1. Bahtiar, R., Falatehan, A., Sari, D., & Thamrin, S. (2019). *Economic Impact of Microhydro Power Project in Jambi Province, Indonesia*. 1–6. https://doi.org/10.4108/eai.18-7-2019.2288677

2. Falatehan, A. F., & Sari, D. A. P. (2020). Characteristics of Peat Biomass as an Alternative Energy and Its Impact on the Environment. *Solid State Technology*, *63*(5), 4700–4712. Retrieved from www.solidstatetechnology.us

3. Masykur. (2013). Pengembangan Industri Kelapa Sawit Sebagai Penghasil Energi Bahan Alternatif dan Mengurangi Pemanasan Global. *Jurnal Reformasi*, *3*, 96–107.

4. Randa, D. G. (2011). *Penjadwalan Transportasi Tandan Buah Segar dan Tandan Kosong Kelapa Sawit*.

5. Sari, D. A. P., Fadiilah, D., & Azizi, A. (2019). Utilization of palm oil mill effluent (Pome) for biogas power plant; its economic value and emission reduction. *Journal of Advanced Research in Dynamical and Control Systems*, *11*(7), 465–470. https://doi.org/10.31227/osf.io/bhfd9

6. Sari, D. A. P., Fadiilah, D., Azizi, A., & Pawenary. (2019). Energy Sector CO2 Emission In Palm Oil Mill. *Journal of Physics: Conference Series*, *1364*, 012003. https://doi.org/10.1088/1742-6596/1364/1/012003

7. Sari, D. A. P., Falatehan, F., Irawan, D. S., Sedana, G., & Rahim, R. (2018). Mitigation and Adaptation Analysis of the Climate Change Impact Using Sustainable Livelihood Model. *International Journal of Engineering & Technology*, *7*(2.5), 108–114. https://doi.org/10.14419/ijet.v7i2.5.13963

8. Sari, D. A. P., Mutaqin, P. A. Z., Pawenary, & Majlan, E. H. (2019). Methane capture installation for greenhouse gasses emission reduction in palm oil mill. *Journal of Advanced Research in Dynamical and Control Systems*, *11*(7), 459–464. https://doi.org/10.31227/osf.io/n5x3j

9. Susanto, J. P., Santoso, A. D., & Suwedi, N. (2017). Perhitungan Potensi Limbah Padat Kelapa Sawit untuk Sumber Energi Terbaharukan dengan Metode LCA. *Jurnal Teknologi Lingkungan*, *18*(2), 165. https://doi.org/10.29122/jtl.v18i2.2046

10. Thamrin, S., Sari, D. A. P., & Setyoningrum, A. (2019). *Energi Baru dan Terbarukan.pdf* (A. H. Tambunan, Ed.). Bogor: Universitas Pertahanan.

8th Int. Conf. on Structure, Engineering & Environment (SEE), Mie, Japan, Nov.10-12, 2022, ISBN: 978-4-909106094 C3051

SEDIMENT EXPERIMENTAL STUDY ON BARK STRIPPING PROCESS USING DRIFTWOOD MODEL

Kazuya WATANABE [1], Noritoshi SAITO [2] and Yoshitaka JIKEN [3]
[1]Graduate School of Engineering Science, Akita University, Japan

ABSTRACT

Due to heavy rain such as typhoons, landslides and slope failures are caused, and driftwood occurs along with debris flows. Since the bark of driftwood peels off during flow, elucidating the bark peeling process will lead to the estimation of the source of driftwood. It is also considered to be useful for river management. In this study, a driftwood model was created using the bark of grown cedar (Cryptomeria japonica) and fixed in a waterway for peeling experiments. As a result, when fresh water and earth and sand were circulated, the bark peeling rate increased in the order of upstream side, side surface, downstream side due to the collision of earth and sand. Furthermore, the separation rate on the riverbed side was higher than that on the water surface side. We confirmed two cases, one in which the peeling progressed mainly in the place where the peeling occurred due to friction with the earth and sand, and the other in which the bark mass peeled off.

Keywords: driftwood, bark, separation, cedar (Cryptomeria japonica), circular waterway, image analysis

INTRODUCTION

As the influence of the heavy rains such as typhoons, the landslide and slope failure were caused. As a result, driftwood occurs with a debris flow. And damage such as bank rip, flooded, the collapse of the house was caused in the downstream by driftwood flowing down. The damage that it looks like it occurs frequently [1] [2]. The driftwood is flowing down, and the bark exfoliates. Elucidating a bark exfoliation process may lead to an outbreak source estimate of the driftwood. It is useful for river management.

Previous studies were as follows. It was gotten three main conditions about outbreak of the driftwood caused by hydraulic experiment and field survey with a debris flow [3]. In addition, the rotating cylinder elucidated segregation phenomenon of the driftwood during a debris flow [4]. As stated above, the study of debris flow and the driftwood were conducted from various viewpoints. Furthermore, it was considered using a plane circulating water channel about the bark exfoliation process of the driftwood [5]. However, to use branch of the cedar (Cryptomeria japonica) as a driftwood model, there was the problem that the bark was easy to exfoliate than real driftwood thinly.

In this study, made a driftwood model using the bark of the cedar which grew up enough. The driftwood model was locked to the channel and the bark exfoliation experiment was carried out.

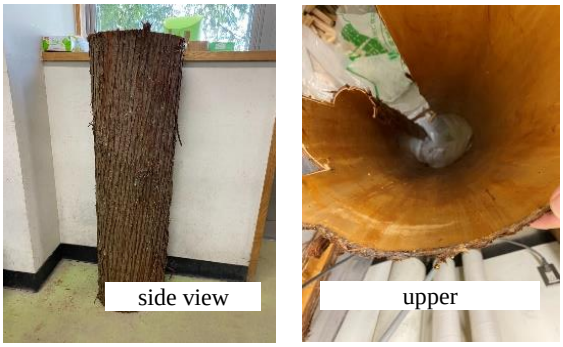

Fig. 1 The bark of the cedar (Cryptomeria japonica)

DRIFTWOOD MODEL

(1) The choice of the tree class

It was the flood that occurred in Omono River of Akita in July, 2017, and cedar deposited on a bridge and farmland as driftwood [6]. A cedar was more likely to flow out in Akita that had abundant cedar forest [7] and used the bark of the cedar for a driftwood model in this study.

The bark of the cedar was shown Figure 1. The cedar was a product in Akita-City Iwami, three of 40~50 years old. It was 1m in width, 1m in height, thickness 6.7mm and specific weight was 0.348 [8].

(2) Manufacture of the driftwood model

The driftwood model was made using except the node. Driftwood model was shown Figure 2.

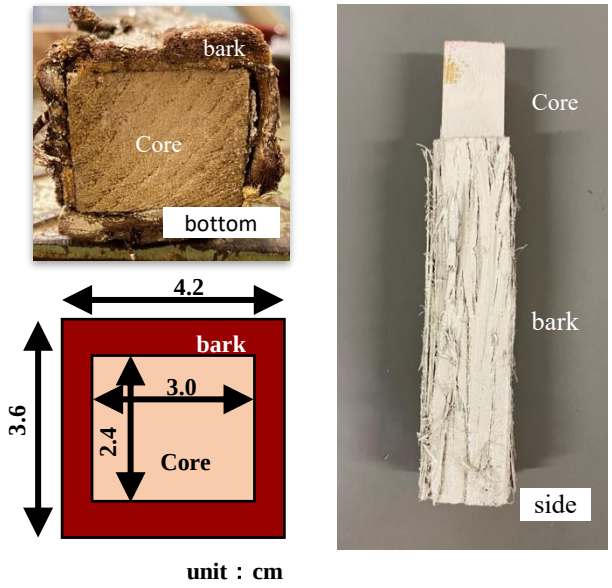

Fig. 2 Driftwood model

Fig. 3 Gravel and sediment at Babamegawa River

The bark of the driftwood model was cut into a strip of paper form and made a prism. (4.2*3.6cm in width, 17.0cm in height)

As a result of having carried out a preliminary experiment using the driftwood model, it was difficult to confirm the bark detachment by visual observation. Therefore spray of the white was applied to the model before an experiment to make an exfoliation point clear. In addition, the model was applied thinly as possible because there might be influence in exfoliation when spray was too thick.

OUTLINE OF EXPERIMENT

(1) Condition of sand

Sand were gathered by Babamegawa River. Image of sand was shown Figure 3 and grain size accumulation curve was shown Figure 4. Sand were constructed by sand and gravel. Gravel was about 60%. In addition, it was maximum particle size 31.5mm, uniformity coefficient was 7.60.

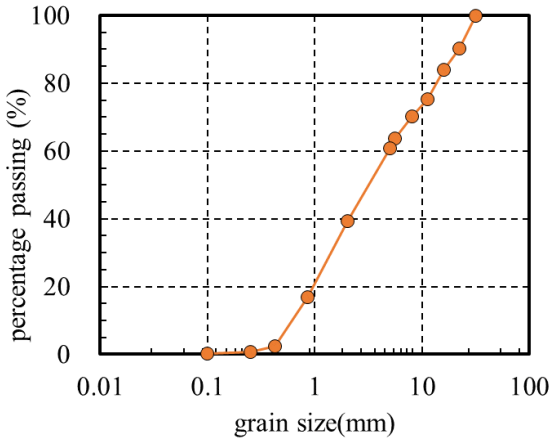

Fig. 4 Grain size accumulation curve

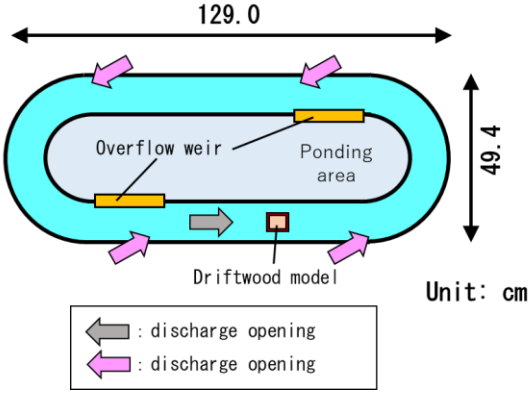

Fig. 5 plane circulating water channel

(2) Experiment channel

In this study, it was performed using a plane circulating water channel [5] about the bark exfoliation process of the driftwood. Plane circulating water channel was shown Figure 5. It is 129.0cm in width, 49.4cm in depth of the whole waterway, circumferential 280.0cm in length of the waterway, 81.5cm in length of the straight line, curve part 58.5cm, waterway 11.5cm in width. The current produces by drainage pump, but the water level of ponding water area decreases to continue drawing water. Therefore the overflow weir at the curve part exit of the channel was made to ponding water area. The system was such that the water was circulated through. The pump to circulate water used three.

(3) Method of experiment

The diminishing scale of the driftwood model assumed it 1/7 from the ratio of a circumference of the bark and the length of four sides of driftwood models. And the speed of the plane circulation waterway is 0.91m/s and is equivalent to 2.4m/s in the

conversion speed. However, as for the speed of this study, it was the value that was slightly lower than a debris flow. Because the speed of the debris flow in the actual phenomenon was 3~10 m/s [9]. The driftwood model fixed it to the plane circulating water channel (Figure 6). The setting side of the model assumed a side of upper reaches, the downstream side, the orthogonality direction side 1 and 2 for a current. The current mixed for water and sand was produced for 480 minutes. Then the image analysis of exfoliating stopped a pump every 30 minutes to be performed. The experiment performed 2 patterns. It was a case only for fresh water and a case of the waters and sand.

(4) Image analysis

The image of each plane of driftwood model were taken pictures. Then the area of the exfoliation was calculated by image analysis. Exfoliation rate calculated from Eq (1). The driftwood model was evaluated from exfoliation rate.

$$foliation\ ratio = \left(\frac{exfoliation\ area}{driftwood\ area}\right) \times 100 \qquad (1)$$

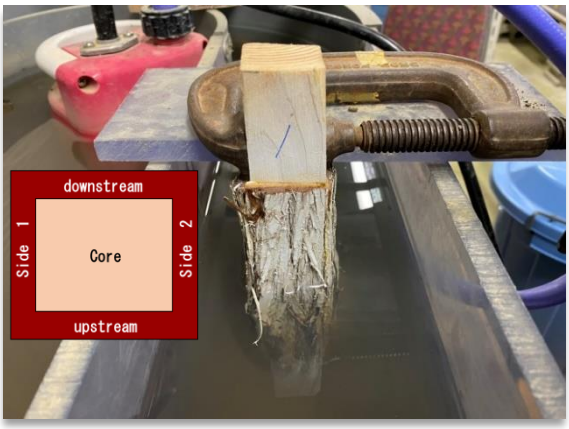

Fig. 6 The fixed situation of the driftwood model

RESULT OF EXPERIMENT AND DISCUSSION

In this study, the experiment performed 2 patterns. It was a case only for fresh water and a case of the waters with sand. The exfoliation rate of the bark was calculated, and the exfoliation situation was observed.

(1) Case only for fresh water

As the case that only for fresh water circulated, water level was experimented on as 18.0cm. Relations of experiment time and the exfoliation rate was shown Figure 7 and the exfoliation situation of the driftwood model (the upper side) was shown Figure 8. The exfoliation rate of upper reaches was 0.03% passed for 480 minutes and other sides were 0.00%. In addition, the change except the exfoliation including abrasion and the breaking was not seen when looked at the side of the driftwood model of upper reaches every 30 minutes. There was the same tendency to other three. Therefore, it was revealed that the fluid power did not influence the bark exfoliation.

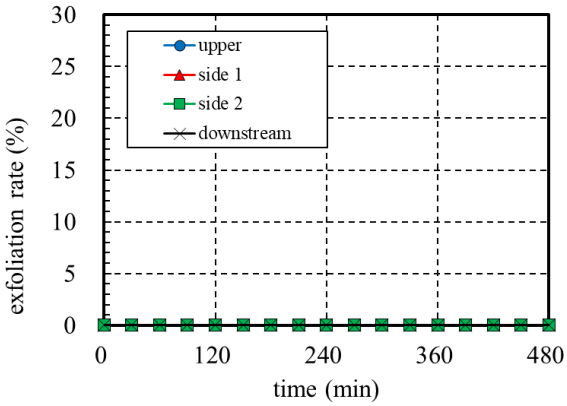

Fig. 7 Relations of experiment time and the exfoliation rate (fresh water)

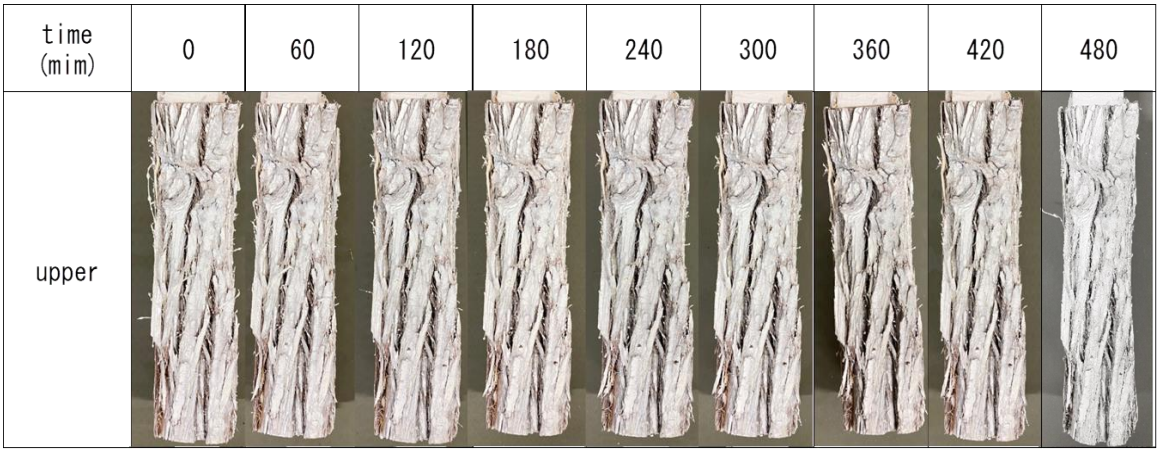

Fig. 8 The exfoliation situation of the driftwood model

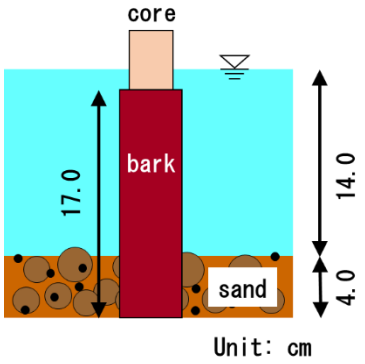

Fig. 9 Experimental condition

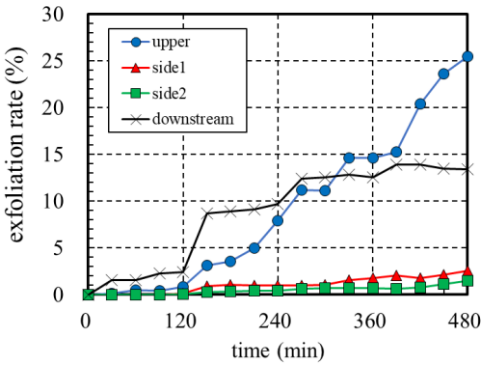

Fig. 10 Relations of experiment time and the exfoliation rate

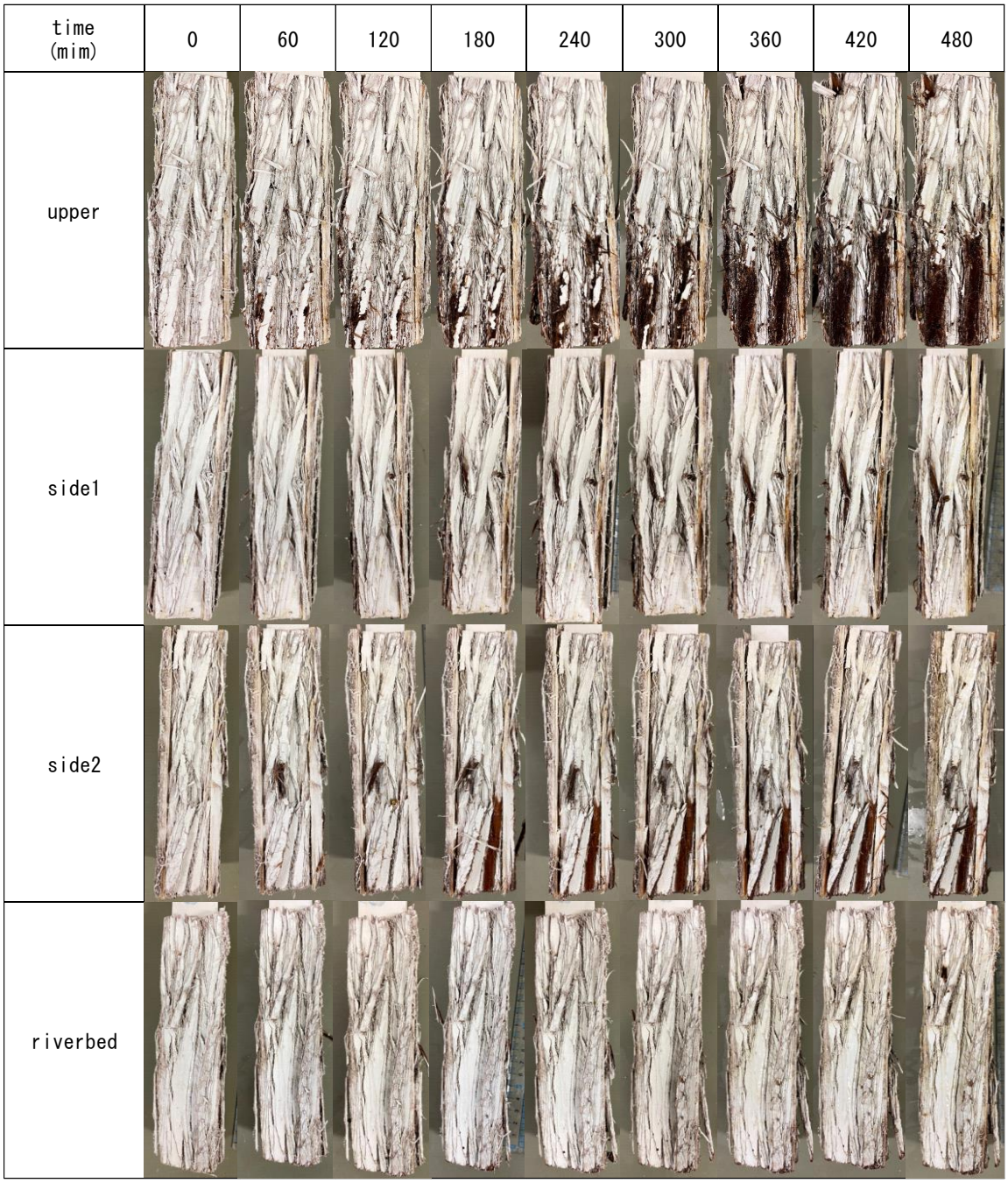

Fig. 11 The exfoliation situation of the driftwood model (fresh water and water with sand)

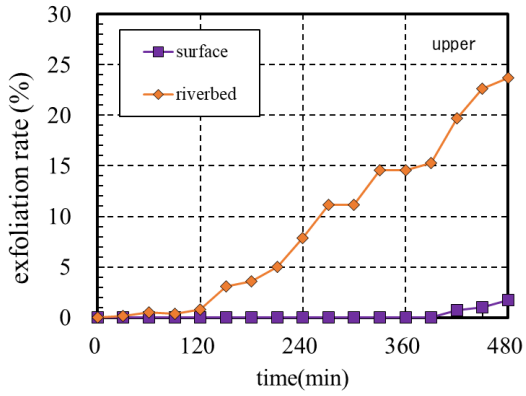

Fig. 12 The time history of exfoliation rate (upper)

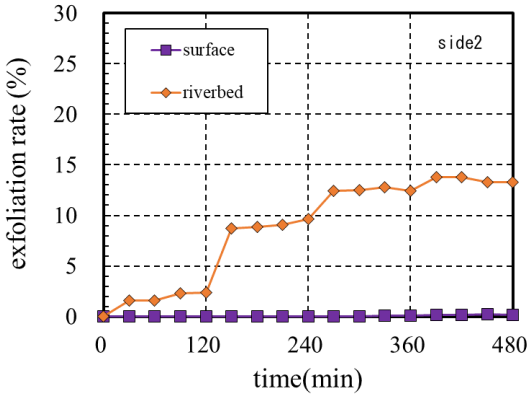

Fig. 14 The time history of exfoliation rate (side2)

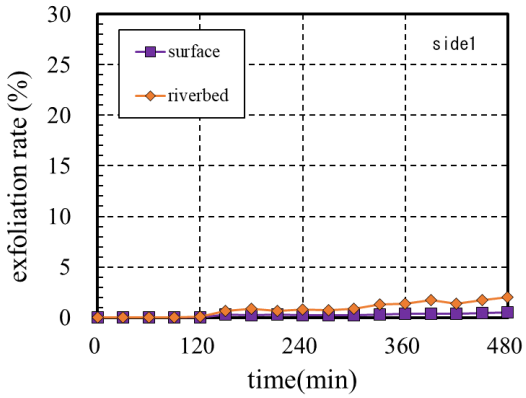

Fig. 13 The time history of exfoliation rate (side1)

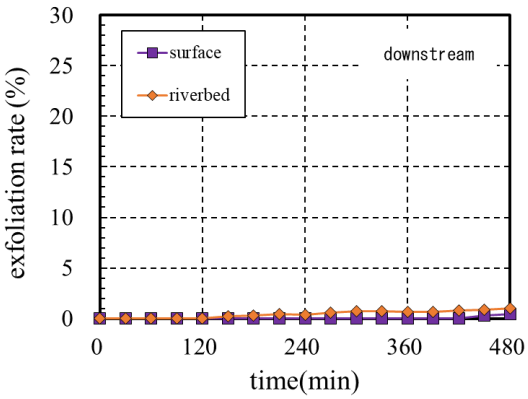

Fig. 15 Time history of exfoliation rate (riverbed)

(2) Case of the waters with sand.

Influence of the installation surface

Experiment condition at the waters with sand was shown Figure 9. The depth of the water was 18.0cm same as only fresh water. The sand spread layer thickness 4.0cm in the channel. Time history of exfoliation rate was shown Figure 10. Exfoliation was seen in the upper side and the side 2 soon after the experiment start. As for the upper side where the sand collided with most, it was 25.4% when exfoliation rate 480 minutes later, as for the side 1 that drifted so that the upper s side and sand after having collided rubbed against the bark for 2.5%, the side 2 was 13.4%. Furthermore, as for the downstream side which friction produced by the complicated basin including the countercurrent [10] having been formed, it was in 1.4%. It was revealed that the influence of the sand was dominant as for the bark exfoliation of the driftwood to greatly vary in a detachment rate than a result of Figure 7.

The exfoliation situation of the driftwood model was shown Figure 11. Bark exfoliation occurred on the upper side near a riverbed 60 minutes later, and exfoliation progressed to spread after it around the point where exfoliation occurred first. On the other hand, the increase of the exfoliation rate was seen by one piece of the bark exfoliating with the side 2 120 minutes later. Sand got into the gap of the bark when observed exfoliation point in detail. Therefore the possibility that the bark exfoliation progressed was suggested by not only the outside but also the inside by the small sand of the particle size.

Influence of the depth direction

The calculation of the exfoliation rate was carried out with driftwood model as a riverbed and surface side.

The time history of exfoliation rate on the upper was shown Figure 12. A exfoliation rate rose 390 minutes later, and the surface of the water side became 1.8% 480 minutes later, but a exfoliation rate

rose to the riverbed side from after for 120 minutes, and it was 23.7% 480 minutes later.

Time history of exfoliation rate on side1 was shown Figure 13. The surface side, the increase of the exfoliation rate was small together a riverbed side, as for surface of the water side 0.4% of 480 minutes later, the riverbed side was 2.0%. Although the exfoliation rate was different, in comparison with a side to shown in Figure 12 of upper, the tendency that the exfoliation rate on the riverbed side grew larger than the surface of side were agreed. Because exfoliation rate became around 2% on the surface side, the small sand to float with a strong flow were a few, but it became clear that it was a factor to cause exfoliation.

The time history of exfoliation rate on side2 was shown Figure 14. As for 0.1%, exfoliation rate of the riverbed side, it was 13.3%, and exfoliation rate of the surface side 480 minutes later was greatly different from a result of the side 1 to show to Figure 14.

Time history of exfoliation rate on downstream was shown Figure 15. As for 0.1%, exfoliation rate of the riverbed side, it was 13.3%, and exfoliation rate of the surface side 480 minutes later was greatly different from a result of the side 1 to show to Figure 14. Time history of exfoliation rate on downstream was shown Figure 15. As for 0.4%, exfoliation rate of the riverbed side, it was 0.1%, exfoliation rate of the surface side 480 minutes later became small in four driftwood models most both.

CONCLUSIONS

In this study, the driftwood model was made using the bark of the cedar which grew up and the exfoliation experiment circulated fresh water and water with sand was performed. The conclusion was shown as follows.

(1)As the case that only for fresh water circulated, it was revealed that the fluid power did not influence the bark exfoliation.
(2) Then only for fresh and water with sand circulated, exfoliation rate grew large in order of upper side > side view > downstream side. In addition, regardless of the setting side of the driftwood model, exfoliation rate of the riverbed side was the tendency that became larger than surface side.
(3) From observation of the progress of the exfoliation confirmed two cases, exfoliation produced by the friction with sand and lump of the bark exfoliates.

ACKNOWLEDGMENTS

This research was partially supported by the Ministry of Education, Science, Sports and Culture, Grant-in-Aid for Scientific Research (A), （20H00256, So Kazama）.

REFERENCES

[1] Yuichi SUZUKI, Yasuharu WATANABE, BEHAVIOUR OF DRIFTWOOD IN THE SARU RIVER DURING TYPHOON NO.10, PROCEEDINGS OF HYDRAULIC ENGINEERING, Vol. 48, pp.1633-1638, 2004.
[2] Ministry of Land, Infrastructure, Transport and Tourism. Preliminary Figures for Summary of t he earth and sand disaster caused by the July, 20 17 North Kyushu heavy rain <http://www.mlit.g o.jp/river/sabo/h29_kyushu_gouu/gaiyou.pdf > (in Japanese) (accessed on July 1, 2022).
[3] Yoshiharu ISHIKAWA, Takahisa MIZUYAMA and Makoto FUKUZAWA, Generation and Flow Mechanisms of Floating Logs associated with Debris Flow, Journal of the Japan Society of Erosion Control Engineering, Vol. 42 No. 3(164), pp.4-10, 1989. (in Japanese)
[4] Kentaro Matsumura, Kazuki Saito, Toshiyuki Horiguchi and Satoshi Katsuk, Segregation of water and gravel using large ball mill device with roughness bed, Japan Society of Civil Engineers, Journal of structural engineering. A., Vol.62 A, pp.1097-1110, 2016. (in Japanese)
[5] JUNYA TANIGUCHI, KAZUYA WATANABE, NORITOSHI SAITO: EXPERIMENTAL STUDY ON PROCESS OF EXFOLIATION FROM DRIFTYWOODS IN FLOOD AT OMOTOGAWA RIVER, Proceedings of APD-IAHR Congress, 1-5-5, 2020.
[6] Toshinori OGASAWAR and Yuriko MATSUBAYSHI, Report of the Research Mission on the Heavy Rain Disaster of 2018, Survey of the Omono River tributary Yodogawa River, Japan Soc. of Civil Engineers, pp29-36, 2018.
[7] Third natural environment preservation basic research, Vegetation working papers, Ministry of the Environment, 7p, 1988.
[8] Yutaka ISHIMARU, Yuzo FURUTA and Masaki SUGIYMA, Physics of wood, Kaiseisha Press, 210p, 2017.
[9] Hiroshi IKEYA, Debris flow disaster, Iwanami Shoten, 221p, 1999.
[10] Shoji FUKUOKA, Tomohiro MIYAGAWA and Masaru TOBIISHIMeasurements of Flow and Bed Geometry around a Cylindrical Pier, PROCEEDINGS OF HYDRAULIC ENGINEERING, Vol. 41, pp.729-1734, 1997.

8th Int. Conf. on Structure, Engineering & Environment (SEE), Mie, Japan, Nov.10-12, 2022, ISBN: 978-4-909106094 C3051

BUDGET PRIORITIZATION OF RURAL ROAD MAINTENANCE USING THE INTEGRATED AHP – TOPSIS METHOD TO DECISION SUPPORT SYSTEM.

*Pawarotorn Chaipetch[1], Chisanu Amprayn[1] Paijit Pawan[1] and Vatanavongs Ratanavaraha[2]
[1]School of Engineering, Sripatum University, Thailand; [2]Suranaree University of Technology, Thailand

ABSTRACT

The Department of Rural Roads (DRR) in Thailand is responsible for road maintenance of 48,974 kilometers. The budget prioritization is primarily based on two factors: traffic volume and the international roughness index (IRI). The benefits of low-volume roads will not be enough to justify the benefit, many sections of rural roads with low traffic volumes were ignored. As a result, road agencies are unable to effectively develop and maintain roads within their responsibilities. A decision support system is necessary for decision makers to decide on the evaluation and strategy for overcoming budget constraints by identifying appropriate projects. The Analytical Hierarchy Process (AHP) and the Technique for Order Preference by Similarity to Ideal Solution (TOPSIS) methodologies were used in this study's decision support system to analyze and allocate performance scores to DRR' decision-making process for road maintenance, as well as performance score ranking considering factors such as economic, engineering, environmental, and social factors. The AHP method is used to determine each factor's weight, and TOPSIS methodologies were used to analyze the performance score in order to select the most appropriate road project for maintenance and rehabilitation. Finally, the findings are expected to the decision-makers were able to identify the most important roads from a large network of roads due to this prioritization and the suggested the projects. Implementation of the project has become important for the state road network and reached at a reasonable approach to the project selection as well as the best usage limited resources.

Keywords: Prioritization, AHP, TOPSIS, Low Volume Road, Decision Support System, IRI

INTRODUCTION

Road accessibility allows people to be connected to public facilities such as hospitals, schools, police stations, temples, and transportation hubs. Furthermore, road infrastructure contributes to a better society, such as poverty reduction and economic development. [1] Communities can develop local economies as transportation infrastructure improves, allowing them access to resources, capital, goods, and the labor market. [2] In addition, road improvements influence land use and market expansion, as well as encourage investment and employment. [3]

The Department of Rural Road (DRR) in Thailand is responsible for road maintenance of 48,974 kilometers, which includes 2,563 kilometers of concrete, 45,868 kilometers of asphalt, and 542 kilometers of gravel. [4] The deterioration of pavement is in exponential function and is affected by pavement age, traffic volume, the volume of heavy trucks, rainfall, and topographical gradient. [5,6] DRR allocated funding for road network maintenance by road strategies and the nation's development policy, including strategies for logistic and integrated transport systems, tourism, reducing traffic congestion in urban areas, and developing transportation to strengthen competitiveness and rural economic development.

Any facility's performance degrades with time as a result of hard environmental conditions and several inherent characteristics, as shown in fig. 1. Maintenance planning used to be limited to contingency planning in the case of an emergency, resulting in excessively high maintenance costs. [7]

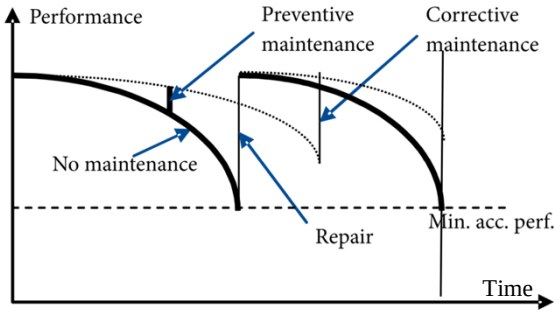

Fig. 1 Performance with time for different maintenance scenarios.

Maintenance is necessary throughout the facility's planned service life to prevent loss of performance at acceptable levels. The efficient and planned execution of maintenance actions also helps to a sustainable built environment by reducing the demand for new facilities and optimizing the use of resources available. In addition, the planning and implementation of these strategies must be cost-

effective without compromising the users' safety and comfort, and a maintenance program must be established on a short, medium, and long-term basis.

Because maintenance budget is constantly limited, it is necessary to prioritize and select the alternatives that are most aligned with the asset management governance's objectives, which in the case of infrastructure, should also reflect public demands. It can be shown in many countries that present maintenance spending was much less than what is required to keep public ownership infrastructure in good condition. The annual funding for maintenance in the European Union (EU), which would ensure that road infrastructure functions properly, is estimated to be between 1% and 2% of the total asset value. Particularly in the budget allocation of DRR, it was found that DRR was allocated a budget that was less than the requirement for maintenance in the past 10 years. The budget is typically allocated 60-65 percent of the total budget requirement as shown in fig. 2. [4] As a result, the allocated budget for maintenance needs in each area, especially the low-volume roads, may be insufficient or inadequate.

The budget prioritization is primarily based on two factors: traffic volume and the international roughness index (IRI). The benefits of low-volume roads will not be enough to justify the benefit, many sections of rural road with low traffic volumes were ignored. As a result, road agencies are unable to effectively develop and maintain roads within their responsibilities. A decision support system is necessary for decision makers to decide on the evaluation and strategy for overcoming budget constraints by identifying appropriate projects.

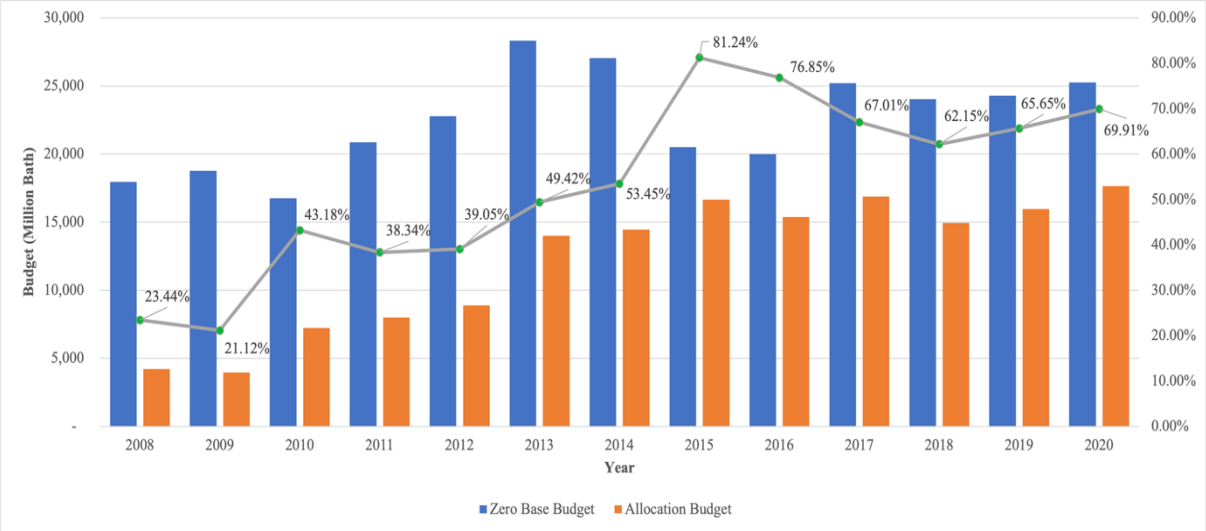

Fig. 2 The Annual Budget Report for Maintenance of Department of Rural Road. (Department of Rural Road, 2020)

Due to the widespread road network, a considerable investment in maintenance is required to maintain a acceptable level of service. However, because the funding is limited, DRR must plan carefully to define road priorities and allocate the budget proportionally for maintenance in road strategies and the nation's development policy.

A decision support system is required to provide support in the decision-making process for a more objective and on-target evaluation of road priority. This study had to use a performance score to evaluate and allocate budget to DRR's road maintenance decision-making process, as well as the addition of factors such as cost and financial aspect, road condition, and socio-economic aspect, among others. The Analytical Hierarchy Process (AHP) and the Technique for Order Preference by Similarity to Ideal Solution (TOPSIS) were used as analytical methods in this research. The AHP method is used to determine each factor's weight, and TOPSIS methodologies were used to analyze the performance score in order to select the most appropriate road project for maintenance and rehabilitation. Moreover, it is expected that findings will assist the policymakers and agencies in developing transportation appraisal methods that are both cost-effective and beneficial to the region.

OBJECTIVE

The study's objective was to use the AHP and TOPSIS to analyze and allocate performance scores by considering economic, engineering, and social factors to prioritize road sections for appropriate budget allocation on Thailand's Department of Rural Roads' Strategic Driving Plan.

A LITERATURE REVIEW

The decision-makers in Multi-Criteria Decision

Making (MCDM) problems are provided with a set of alternatives and various types of criteria, and each one has varying degrees of importance. As a result, multi-criteria enables decision makers to weigh various criteria for a large number of options at the same time. To put it differently, MCDM analysis assists decision makers in making better decisions and selecting the best possible options from current candidates based on a variety of criteria. [8]

Factor to Prioritization Road Maintenance

Criteria are qualitative and quantitative properties that performance of the road maintenance is evaluated according to factor. This study evaluated the factor that should be considered when prioritizing road maintenance, and it is divided into three groups based on the findings of a literature review. [9,10]

Economic factor

It is an evaluation of all of the costs and benefits of projects to determine their monetary value. The most important monetary benefits are reduced vehicle operating costs, travel time savings, and accident reduction cost compared with maintenance and rehabilitation cost. As a result, the benefit-cost ratio must be greater than one.

Engineering factor

It's a direct factor in the design, management, maintenance, and rehabilitation of a road, and it includes physical, functional, distress, condition, connectivity, and accident data. For example,

- International Roughness Index (IRI) is a standardized roughness measurement used to define as a serviceability.
- Traffic Volume and Volume of Heavy truck.
- Volume Capacity Ratio (V/C ratio).
- Lifeline Road is a way of transportation for which there is no substitute or for which the substitute requires a significant increase in time or money. It has a significant impact on a community's social or economic viability, especially in a disaster situation.
- Connectivity to the road network represents the significance of a road about the existing road network, which may include national highways, rural roads, and local roads.
- Accident data.

Social factor

It's a direct factor that is related to social, environmental, land use, community area, and attractive point of Interest within 2 kilometers on both sides of the road. As an example,

- Population density.
- Tourist spots.
- Government office.
- School, colleges, and university.
- Hospital.
- Business center and market.
- Industrial area and warehouse.

ANALYSIS

Weighting the evaluation criteria

Pavement Maintenance Prioritization Using Multi – criteria Decision Approach. The main multi – criteria decision making approach is the AHP which was a structured method for organizing and analyzing complex decisions that are based on math and psychology. It was created in the 1970s by Thomas L. Saaty [11] and it has been extensively studied and refined since then.

It is a precise method of quantifying the weights of decision criteria. Pair-wise comparisons are used to estimate the relative magnitudes of factors based on individual experts' experiences. Using a specially designed questionnaire, each respondent compares the relative importance of each pair of items. With these rating values as elements of matrix a_{ij} of the criteria i and j (where a_{ij} are the geometric mean value of responses), a pairwise comparison matrix A has been developed as follows Eq. (1)

$$\mathbf{A} = \begin{bmatrix} \mathbf{1} & \mathbf{a12} & \dots & \mathbf{a1n} \\ \frac{\mathbf{1}}{\mathbf{a12}} & \mathbf{1} & \dots & \mathbf{a2n} \\ \dots & \dots & \dots & \dots \\ \frac{\mathbf{1}}{\mathbf{a1n}} & \frac{\mathbf{1}}{\mathbf{a2n}} & \dots & \mathbf{1} \end{bmatrix} \quad (1)$$

The next stage is to evaluate the weight of each evaluation criterion after the criteria have been identified. The relative and overall importance of a set of criteria is indicated by their weight compared to all other criteria. As a result, it is an important part of the analysis. The value of such weights is difficult to ascertain because the requirements are given in several measurement units. In this regard, reasoning, and the use of tried-and-true elicitation procedures aid in determining the weights' values. When experts have in-depth knowledge of the criteria, including their relative values and the connections between them, the weights are set in accordance with their professional judgements.

In this study, the weight assigned to the employed criteria are determined by the AHP as described in detail by Chaipetch et al. (2021) [12], that was purposive in the authority of budget planning and prioritization on road maintenance of decision – making authority on planning policy, which is 20 respondents.

Their values are presented in Table 1. It can be

seen that facility rating is considered the most important factor to be taken into account in the decision process.

Table 1 Summary of the analysis of Priority Factor by AHP method.

Factor/Strategic	LIS Priority Value 27	TCA Priority Value 27	TSM Priority Value 22	CED Priority Value 24
Economic (B/C)	**46**	**40**	**43**	**45**
Engineering	**29**	**28**	**23**	**20**
IRI	-	-	13	-
V/C Ratio (VC)	17	24	21	17
Traffic Volume (TV)	19	21	16	15
The volume of Heavy Truck (HV)	21	-	-	-
Lifeline (LL)	-	-	-	14
Connectivity to the road network (CN)	23	24	25	27
Accident data (ACC)	20	31	25	27
Social	**25**	**32**	**33**	**35**
Population density (PPD)	19	29	17	25
Tourist spots (TS)	18	20	40	26
Business Center (BC)	23	26	23	27
Hospital (HOS)	-		20	-
Industrial Area (INA)	40	25		22

Ranking and Prioritization

TOPSIS, an MCDM model developed by Hwang and Yoon in 1981 [13], is an ideal point technique that ranks alternatives according to their proximity to the positive ideal solution and distance from the negative ideal solution. This method is rational, intuitive, and relatively easy to comprehend; it also lacks the strict assumptions of other MCDM models and provides a cardinal value. The general step of the TOPSIS method includes alternative selection; defining evaluation criteria; weighting the evaluation criteria; normalizing the criteria value; ranking; and prioritization of alternatives.

The selected item will be ranked based on a value so that the alternative with shortest distance with an ideal positive solution is the best alternative item. Alternative with bigger score is the best to choose.

The TOPSIS method is based on the Euclidean distance-based idea of proximity to the ideal solutions. In other words, alternatives are suggested as the best options that are close to both the positive and the negative ideal solutions at the same time or in the opposite direction. The collection of optimal performance values for each criterion represents the ideal solution. The following methods are used systematically in the TOPSIS methodology to evaluate and prioritize road maintenance.

1. The process begins with the formation of a decision matrix D in Eq. (2), which is a rectangular matrix m×n, where m is the number of alternatives, and n is the number of criteria. For all elements of the decision matrix to be expressed in dimensionless size, it is necessary to normalized the matrix using the Eq. (3).

$$D = \begin{bmatrix} x_{11} & \cdots & x_{1n} \\ \vdots & \ddots & \vdots \\ x_{m1} & \cdots & x_{mn} \end{bmatrix} \quad (2)$$

$$r_{ij} = \frac{x_{ij}}{\sqrt{\sum_{i=1}^{m} x_{ij}^2}} \quad (3)$$

2. Calculate weighted normalized decision matrix (v_{ij}). The weight of the criterion (w_j) from the AHP technique is multiplied by the normalized matrix (r_{ij}), which is shown in Eq (4). The weighted normalized decision matrix is showed in Table 2.

$$v = \begin{bmatrix} r_{11}w_1 & \cdots & r_{1n}w_n \\ \vdots & \ddots & \vdots \\ r_{m1}w_1 & \cdots & r_{mn}w_n \end{bmatrix} \quad (4)$$

3. Determine both positive and negative ideal solutions. The best performance value of each criterion, as shown in Eq. (5), provides the positive ideal solution (B+). Whereas the negative ideal solution (B-) is determined from the lowest performance value as indicated in Eq. (6). The calculation's result is shown in Table 8,

$$B^+ = max\{v_1^+, v_2^+, \ldots, v_i^+, \ldots, v_n^+\} \quad (5)$$

$$B^- = min\{v_1^-, v_2^-, \ldots, v_i^-, \ldots, v_n^-\} \quad (6)$$

4. Calculate the Euclidean distance between ideal solutions. The closeness of each alternative to the positive ideal solution can be measured by the n-dimensional Euclidean distance using Eq. (5). Similarly, Eq. (6) indicates the separation of each alternative from the negative ideal solution is

shown in table 3.

$$S_i^+ = \sqrt{\sum_{j=1}^{n}(v_{ij} - v_j^+)^2} \quad (5)$$

$$S_i^- = \sqrt{\sum_{j=1}^{n}(v_{ij} - v_j^-)^2} \quad (6)$$

Table 2 Example of the weighted decision matrix of each road maintenance section

Road ID	Km.	B/C	VC	TV	HV	CN	ACC	PPD	TS	BC	INA
AY. 2005	7 - 8	0.0019	0.0002	0.0001	0.0001	0.0004	0.0000	0.0002	0.0001	0.0000	0.0010
SP. 4002	4 - 5	0.0181	0.0020	0.0019	0.0011	0.0047	0.0000	0.0018	0.0002	0.0043	0.0094
CM. 3002	2 - 3	0.0029	0.0001	0.0001	0.0001	0.0003	0.0003	0.0001	0.0000	0.0000	0.0000
NS. 3022	4 - 5	0.0003	0.0003	0.0002	0.0000	0.0003	0.0000	0.0002	0.0000	0.0000	0.0003
SK. 2017	2 - 3	0.0160	0.0002	0.0004	0.0007	0.0004	0.0000	0.0001	0.0000	0.0004	0.0001
AD. 3072	5 - 6	0.0061	0.0002	0.0002	0.0002	0.0003	0.0000	0.0002	0.0000	0.0000	0.0002

Table 3 Positive – ideal (B^+) and negative – ideal solution (B^-) for each criterion

Criterion	B^-	B^+
B/C	0.0000	0.0181
VC	0.0000	0.0025
TV	0.0000	0.0023
HV	0.0000	0.0059
CN	0.0004	0.0000
ACC	0.0000	0.0048
PPD	0.0000	0.0018
TS	0.0000	0.0019
BC	0.0000	0.0052
INA	0.0000	0.0111

5. Calculate similarity indexes (C_i) implies the relative closeness to the ideal solution and it will be used for the prioritization of road maintenance. It is obtained by Eq. (7) and range in the interval from zero to one hundred. Prioritizing the road maintenance section list is made with respect to C_i values in descending order. The Euclidean deviation, the relative distance of alternatives from ideal solutions, and the final rank of maintenance priorities in the first iteration are shown in Table 4.

$$C_i = S_i^+ / (S_i^+ + S_i^-) \quad (7)$$

Table 4 Example of S^+, S^- and C_i of each road maintenance section

Road ID	Km.	S^-	S^+	C_i
AY. 2005	7 - 8	0.0022	0.0202	9.7609
SP. 4002	4 - 5	0.0689	0.0659	51.1058
CM. 3002	2 - 3	0.0003	0.0222	1.4617
NS. 3022	4 - 5	0.0006	0.0219	2.5062
SK. 2017	2 - 3	0.0255	0.0236	51.9323
AD. 3072	5 - 6	0.0061	0.0175	25.7195

When using the TOPSIS method to calculate, it is critical to select values that represent both a positive and a negative ideal solution. Based on these data, the n-dimensional Euclidean deviation from the positive and negative ideal points is calculated. The relative distance from the ideal solution gives a ranking list of sections of the road network according to maintenance priorities. The best alternative is the one whose value of the relative distance to the alternative is close to 100, while the other alternatives are ranked in descending order.

DISCUSSION AND CONCLUSION

Because maintenance budget is constantly limited, it is necessary to prioritize and select the alternatives that are most aligned with the asset management governance's objectives, which, in the case of infrastructure, should also reflect public demands. Particularly in the budget allocation of the DRR, the budget is typically allocated 60-65 percent of the total budget requirement. As a result, the allocated budget for maintenance needs in each area, especially the low-volume roads, may be insufficient or inadequate.

In this study presented a methodology overview on the use of multi-attribute decision making using AHP and TOPSIS for the prioritization of road maintenance section alternatives. By considering economic, engineering and social factor, the approach enable decision makers to capture the complex road maintenance prioritization procedure, in a more objective way for example based on DRR' Strategic Driving Plan.

As it was mentioned, TOPSIS method is based on aggregating function that representing the closeness to ideal solutions and the remoteness from the negative ideal solution simultaneously or reverse. In this study, the "similarity index" was defined by combining the proximity to the positive – ideal.

The results of this study are expected to assist policymakers and agencies in developing transportation appraisal methods that are both cost-effective and beneficial to the region. The similarity index, comprising of thirteen different indexes, helped in identifying the priority of road maintenance that will result in a better road network system as a whole and is vital to the socio-economic growth of the region. The economic factor reflects the value of an investment. Second, the engineering factors provide network connectivity and ensure traffic continuity. Transporting goods and services and making public services and attractive places more accessible increases the quality of traffic flow and congestion, particularly in urban areas. Finally, social factors have a variety of socioeconomic benefits associated with their development; for example, increased economic activity in terms of connectivity, accessibility, regional growth, and a key component of rural development, such as public service access, which is important for both goods movement and labor markets and is a contributing factor to higher income.

The decision-makers were able to identify the most important roads from a large network of roads due to this prioritization method and the suggested phasing of the projects. Implementation of the project has become important for the state road network because of the strategic value of the identified road sections, improvement treatments, and their satisfactory feasibility results. The decision-makers reached at a reasonable approach to the project selection as well as the best usage limited resources due to the screening process of the road sections.

ACKNOWLEDGMENTS

I would like to thank the Bureau of Road Maintenance, Department of Rural Road and Center of Excellence in Infrastructure Management, Chulalongkorn University for their valuable data, expert opinion, and constructive suggestions.

REFERENCES

[1] Walle D. V. D., Choosing Rural Road Investments to Help Reduce Poverty, World Development, Vol.30, No.4, 2002, pp. 575 – 589.

[2] W. Sangthammkijkul, “Determining Rural Roads Importance Degree”, M.S. Thesis, 2014, Department of Civil Engineering, Kasetsart University, Bangkok, Thailand.

[3] Amornchaisakda C., and Subsompon W., Analytical Framework of Road Serviceability Level Corresponding to Road Strategies, Proceeding of the 14th National Civil Engineering Convention, Engineering Institute of Thailand, 2009, pp. 635-642.

[4] Department of Rural Road, Annual Report of Bureau of Road Maintenance, 2020, Thailand.

[5] Subsompon W., et. al., Road Deterioration Model based on International Roughness Index (IRI), Proceeding of the 6th National Civil Engineering Convention, Engineering Institute of Thailand,2000, Bangkok Thailand.

[6] Subsompon W., and Chaipetch P., Work Estimation Model for Pavement Routine Maintenance, Research and Development Journal, Vol.21, No.4., 2010, pp. 57-64.

[7] Miyamoto A., Konno M., Nakmura H., and Bruhwiler E., Maintenance plan optimization system for existing concrete bridge groups, Structure and Infrastructure Engineering, Vol.2, No.2, 2006, pp. 91-115.

[8] Teng J., and Tzeng G., A multiobjective programming approach for selecting non-independent transportation investment alternatives, Transportation Research Part B: Methodological, Vol.30, No.4, 2015, pp. 291-307.

[9] Moya M., Gallego E., Garcia A. I., and Ayuga F., A Proposed Methodology for the Management of Low-Volume Roads in Spain, The Baltic Journal of Road and Bridge Engineering, Vol. 6, No. 3, 2011, pp. 153-162.

[10] Menendex J. R., Budget Allocation Planning for Small Road Systems in Peru, Proceedings of the 25th World Road Congress - Seoul 2015: Roads and Mobility - Creating New Value from Transport, 2015.

[11] Satty, L. T., Fundamentals of Decision Making and Priority Theory with The Analytic Hierarchy Process, 2014, RWS Publication, USA.

[12] Chaipetch P., Amprayn C., Pawan P., and Ratanavaraha V., Analytical of multi-criteria approach for identifying the weight and factor of rural road maintenance prioritization, International Journal of GEOMATE, Vol.22, Issue 91, 2021, pp. 70-79.

[13] Hwang C., and Yoon K., Multiple attribute decision making: methods and applications: a state-of-art survey, 1981, Springer, USA.

8th Int. Conf. on Structure, Engineering & Environment (SEE), Mie, Japan, Nov.10-12, 2022, ISBN: 978-4-909106094 C3051

FIXATION OF SOYBEAN EXTRACT METHOD FOR BIOCATALYST IN CALCITE PRECIPITATION METHOD AND ITS APPLICABILITY AS A SOIL IMPROVEMENT TECHNIQUE

Heriansyah Putra[1]*, Baiq Heny Sulistiawati [2,3], Hideaki Yasuhara[2], Minson Simatupang[4], and Dede Heri Yuli Yanto[5]

[1]Department Civil and Environmental Engineering, IPB University, Bogor, 16680, Indonesia
[2]Department of Civil and Environmental Engineering, Ehime University, Matsuyama, 790-8577, Japan
[3]Faculty of Civil Engineering, State Polytechnic of Semarang, Semarang, 50275, Indonesia
[4]Department Civil Engineering, Halu Oleo University, Kendari, 93232, Indonesia
[5]Research Center for Applied Microbiology, National Research and Innovation Agency (BRIN), Bogor, 16911, Indonesia

ABSTRACT

This study evaluated the extraction method of soybean as a plant-derived urease enzyme. The soybean powder was prepared in a suspension and extracted in two different ways, namely filtered and centrifuged, to separate the particle and solution and thus obtain the purified soybean solution. The efficacy of purified soybean as the biocatalyst was evaluated using a test-tube experiment to obtain the hydrolysis rate of urea and production of precipitated materials. The unconfined compression strength (UCS) tests evaluated its effect on soil strength at various curing times. The highest hydrolysis rate was obtained using 50 g/L of soybean extract in both extraction methods of the centrifuge and filtered with the rate of 1100 u/g and 500 u/g, respectively. The maximum precipitation ratio of 100% was achieved using a soybean concentration of 20 g/L, and thus constantly, even the soybean concentration was increased. This study shows that both extraction methods result in a similar UCS value ranging from 300 to 400 kPa. In conclusion, the soybean concentration of 20 g/L prepared by a simple extraction method of filtration has a great potential to apply in the calcite precipitation technique for soil improvement.

Keywords: Calcite precipitation, Centrifuged, Filtered, Soil improvement, Soybean extract

INTRODUCTION

In recent years, many soil improvement techniques have been developed for their application to various soil problems, such as geotextile [1], [2], aggregate piers [3], [4], deep soil mixing [5], [6], and grouting with chemical compounds [7], [8]. A variety of substances can be applied to chemical grouting, consisting of cement, lime, or other chemical solutions, depending on the stabilization and soil's characteristics. Recently, bio-grout-based ground improvement practices have been proposed as a potential and effective technique, especially for soil strengthening under the existing building [9]–[11]. Bio-grouts are produced by various mineral formations caused by chemical reactions, managed and controlled through biological activities [12]. However, these techniques are related to major environmental issues such as CO2 emissions and high energy costs for production and applications [13], [14]. Furthermore, the reagents for bio-grout are produced at relatively low temperatures compared to ordinary cement that involves heating ingredients to temperatures up to about 1500°C [15], [16]. Therefore, many alternative methods and materials of bio-grouting have been proposed to extend its applicability, reduce the environmental impact, and promote the advantages of less energy during the production process, such as the calcite precipitation methods [17].

Calcite precipitation methods are the bio-grout technique that utilizes the reagent and bio-agent to produce calcite crystal after the biochemical reaction [18], [19]. Many previous studies have investigated the applicability of this technique using the catalyst derived from bacteria and purified enzyme to hydrolyze the urea and thus, promote the carbonate ion [20]–[22]. The use of bacteria as bio-agent in the calcite precipitation method has several limitations, especially related to controlling the bacteria growth and its activities [22], [23]. Yasuhara et al. [23] utilize the purified enzyme extracted from jack bean instead the bacteria called enzyme-induced calcite precipitation (EICP). These methods promoted the significant improvement of soil strength parameters and were applied for various purposes such as liquefaction prevention, erosion control, and bearing capacity improvement [10], [24]. However, jack bean urease is reported as ineffective material due to its high production cost caused by the high purity level of the urease enzyme [25]–[27]. Using urease enzyme extracted by jack bean consumed about 90% total material cost to produce the calcite solution [13], [14], [26].

Several studies using the urease enzymes of plant origin to replace the jack bean urease enzyme have been developed in recent years, such as legume varieties from melons, flask, the pine family, watermelon, pumpkin, and soybean [12], [28]–[30]. A mixture of urea and crude extract of watermelon seeds that produces a reagent solution can effectively produce the deposition of the calcium phosphate compounds [30]. After a curing time of 28 days, a maximum UCS of 125.6 kPa was achieved by this method [30]. Recently, the examination of soybean extract for the source of urease enzyme was conducted [27], [31], [32]. The UCS strength of treated soil was increased by more than 100% with a single injection [26]. Pratame et al. [26] used the centrifuged method to extract the soybean and collected the purified soybean solution, thus mixing it with the reagent to produce the calcite precipitation. However, using the centrifuged method for large applications is challenging due to its quantity and time-consuming.

This work evaluates the applicability of soybean powder as the replacement of commercial urease enzyme with two extraction methods, namely filtration and centrifugation. The experimental work included the extraction of soybean and testing the hydrolysis rate of urea and $CaCO_3$ precipitation. In addition, XRD tests were used to verify the microstructures of the deposited materials to observe the effects of soybean crude extract on the substance of the precipitated materials. Finally, the selected concentration of reagent solution in both extraction methods is applied to the soil samples and cured for various curing times prior to the unconfined compressive strength (UCS) tests.

MATERIALS AND METHODS

Materials

The treatment solution in this study was prepared using pro analysis grade of urea reagent ($CO(NH_2)_2$) and dihydrate of calcium chloride ($CaCl_2 \cdot 2H_2O$), which are obtained from EMSURE® ACS, Reag. Ph. Eur. Soybean powder was obtained from PT. Gasol Pertanian Organik, Indonesia. The sandy soil of graduated sand SO-404, classified as poorly graded sand (SP) with e_{max}, e_{min}, coefficient of uniformity (Cu), and specific gravity (Gs) of 0.802, 0.543, 2.26, and 2.61, respectively, is using as soil sample is this study.

Plant-Derived Urease Enzyme

Various concentrations of soybean were prepared and thus extracted in two methods, namely filtered and centrifuged. Firstly, the soybean powder was mixed with distilled water and stirred for 5 minutes. Then, the suspension was eliminated using the centrifuged and filtered method. The centrifuges process was conducted following the method proposed by Gao et al. (2019) with a rotation rate of 3,000 rpm for 15 minutes. Meanwhile, in the filtration method, the soybean solution was filtered using sieve No. 200 (0.0075 mm). The purified soybean solution was obtained and thus, prepared for mixing with the reagent solution composed of urea and calcium chloride.

Hydrolysis Rate

The rate of hydrolysis was carried out to assess the ability of crude soybean extract as a urea biocatalyst. The procedure introduced by Whiffin [33] is followed in this study. Firstly, a standard curve was created by calculating the conductivity generating from the replete hydrolysis of several urea concentrations. The varying concentration of purified soybean crude extracts resulted in both methods being prepared and mixed with urea. The rate was measured immediately after mixing using a conductance meter of Hanna Edge Multiparameter 230. The rate of hydrolysis was determined by calculating the slope of the conductivity change gradient with time, which is expressed as Eq (1).

$$Hydrolysis\ rate\ \left(\frac{u}{g}\right) = \frac{\theta_{ms}}{\theta_{sc}}.v.N \qquad (1)$$

Where θms is the slope of the measured sample gradient; θsc is the standard curve gradient slope; v is the sample volume (L), and N is the final concentration of ammonia (mMol/L).

Test-Tube Experiments

The calcite precipitation was conducted in clear test tubes to assess the amount of the precipitation mass as a result of the chemical reaction of the reagent and biocatalyst of soybean extracts. The solution of reagent and the extract of soybean were prepared separately and mixed thoroughly with distilled water to a total volume of 30 mL for each sample. The soybean solutions were prepared in two extract methods, namely centrifugation and filtration. The tubes containing the improving solution were treated at room temperature for five days to allow for the precipitation process.

The amount of precipitation was examining the number of the particles remaining in the tubes. Firstly, the tube was filtered using a filter paper No 40 (size 0.02 mm) and dried at 60℃ for 24 h to eliminate the water and obtain the precipitated material. Next, the mass of the deposited substance was assessed by associating the mass of the deposited substance stored in the test tubes with that residing on the strainer paper. Two similar tests were performed for each substance to verify for a duplicate. In this

study, the varying soybean concentration of 10 g/L to 50 g/L with two extraction methods of filtration and centrifugation were combined with the reagent solution was used at one mol/L. The experimental condition of tube experiments is shown in Table 1.

Table 1. Various concentrations of the solution for precipitation tests.

Case	Concentrations		
	$CO(NH_2)_2$ (mol/L)	$CaCl_2.2H_2O$ (mol/L)	Soybean extract (g/L)
1	1.0	1.0	10.0
2	1.0	1.0	20.0
3	1.0	1.0	30.0
4	1.0	1.0	40.0
5	1.0	1.0	50.0

The precipitation mass is expressed as the ratio of precipitation. This is the percentage of the real amount of the deposited substance, and the maximum amount of the calcite deposited theoretically.

Unconfined Compressive Strength Test

Unconfined compressive strength tests were conducted using a sample of 5 cm and 10 cm in diameter and height, respectively. The PVC cylinders were prepared, and the sandy soil with emin, emax, Cu (uniformity coefficient), and Gs (specific gravity) of 0.818, 0.586, 1.533, and 2.643, consecutively, were poured into the mold with the density relative (Dr) of 50%. The persistent solution volume was grouted into the formed sand columns. Two extraction methods of soybean, i.e., filtered and centrifuged, were applied to prepare the purified soybean prior mixed with the reagent. The grouting amount was boundaries by the amount of pore volumes (PV), one PV being ~80 mL. The sand columns were treated by single injection with various curing times, e.g., 7, 14, and 28 days. After curing time, the handled samples were taken out from the PVC tubes. The surface of the specimens was leveled before the UCS tests were performed. Two tests were carried out for each condition to verify the duplicate. The UCS tests were performed under wet conditions to prevent any unexpected deposition that may happen when specimens are consciously dried out.

RESULT AND DISCUSSION

Hydrolysis Rate

The hydrolysis rate analysis was performed to examine the influence of the crude extract methods on the urea hydrolysis rate. A standard curve for hydrolysis was prepared by the maximum conductance values. The conductance measurements were performed for 10 min, and the results were plotted on a curve for the measured conductance. The one mol of urea was prepared and mixed with various concentrations of soybean powder of 10 - 50 g/L—the change in conductance with time for both extraction methods of filtration and centrifugation.

The hydrolysis rate in various concentrations of soybean extract was calculated using Eq (1), which is shown in Fig. 1. As is apparent, the activity was linearly related to the increase in the concentration of soybean. The rate result in centrifuged method shows a higher value than in the filtered method. The hydrolysis rate of 1100 u/g (note that one u of activity corresponds to 1 µmol/L of urea hydrolyzed per minute) was obtained using 50 g/L of soybean extract centrifuged. This result revealed that the use of 1 g/L of soybean extract was estimated to be around 25 u/g.

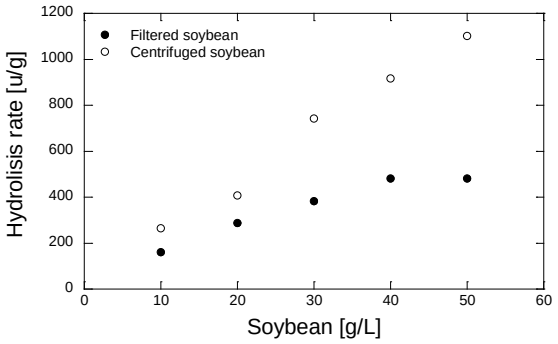

Fig. 1 Hydrolysis rate with various concentrations of soybean extract

The hydrolysis rate results in both soybean extraction methods lower than the rate resulting in the commercial urease of jack bean reported by Putra et al [34] and relatively higher than previous investigations especially seated on crude solutions extracted from crushed seeds of watermelon [14], [27], [30]. In addition, the higher hydrolysis rate was reported as the main factor in reducing of uniformity of calcite distribution within the soil. Hence, reducing the rate may improve the uniform distribution of precipitated material within the treated soi [35].

Precipitation Test

Precipitation tests were conducted to examine the efficacy of soybean crude extract as a replacement for commercial urease enzyme in producing calcite precipitation. The effect of the extraction method, i.e., filtration and centrifugation in various concentrations of soybean, was evaluated in this study. The reagents composed of urea and calcium chloride of 1 mol/L were combined with soybean varying from 10 – 50 g/L. The summary of test results is displayed as the ratio of precipitation, which is the percentage of obtained mass during the experiment, and the maximum theoretical mass of the $CaCO_3$, which is shown in Fig. 2.

The results indicated that both extraction methods, filtered and centrifuged, were effective in producing the purified enzyme result in soybean powder. Fig. 2 shows that soybean with a concentration of 20 g/L can produce a maximum precipitation ratio of 100%. The amount of precipitation increases significantly at low concentration soybean of 10 g/L to 20 g/L. Then, the amount is stable at the maximum value. Therefore, the addition of the crude extract concentration does not significantly affect the mass of precipitation materials. Considering to the amount, these results may indicate that the soybean of 20 g/L is the optimum concentration for precipitated calcite production. Pratama et al. [26] reported that the high concentration (more than 10 g/L) of soybean prepared by the centrifuged test is high enough to be used as a bio-catalyst in the EICP method.

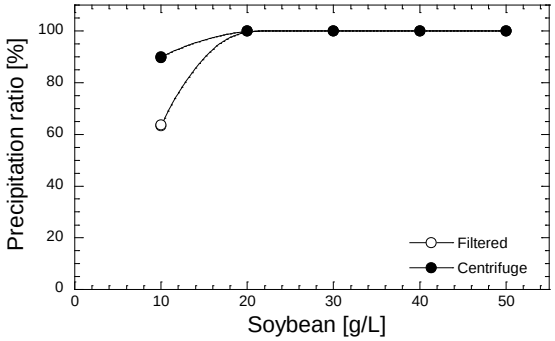

Fig. 2 Precipitation ratio of precipitated calcite

XRD tests were performed to assess the mineral types of calcites generated during the precipitation stage. The mineral types of the precipitated material are indicated by the intensities of the primary peaks in XRD patterns, as shown in Fig. 3.

The result shows that the precipitated minerals are mainly composed of calcite—the extraction methods of filtered and centrifuged result in a similar trend of XRD pattern for all samples. Calcite is the most stable carbonate mineral and polymorph of calcium carbonate [36]. The vaterite form was also detected in XRD result in both of treatment. The using of high concentration of soybean may be promoted more undissolved organic matter and thus, hamper the calcination process. Konopacka-łyskawa et al. (2020) reported that the presence of organic solvent promoted the vaterite form in addition to calcite. However, this study has not yet conducted a detailed analysis of the amount of each mineral in precipitated minerals. It should be considered essential in further study.

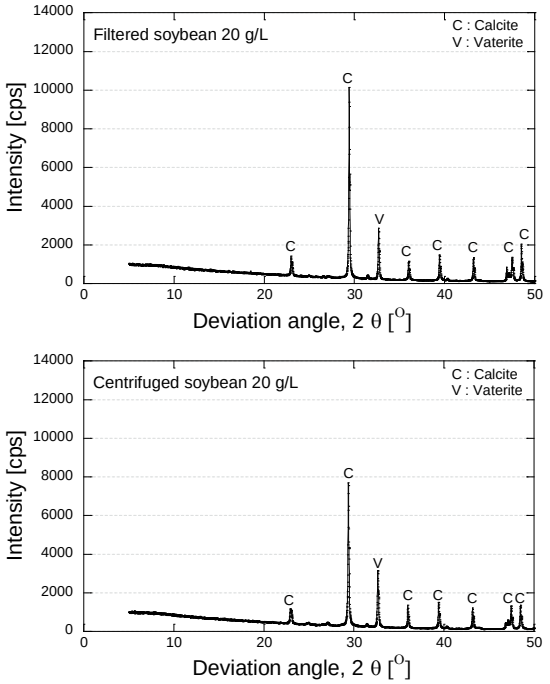

Fig. 3 X-Ray Diffraction (XRD) results

Shear Strength Improvement

The unconfined compressive strength (UCS) tests were performed to evaluate the impact of soybean extract methods on improving the soil strength. The optimum soybean concentration of 20 g/L was prepared using both extraction methods of filtration and centrifugation. Thus, mixed them with a reagent to produce the treatment solution. The soil samples were treated by a single injection of 1 pore volume and incubated for varying curing times of 7, 14, and 28 days to assess the impact of time elapsed on soil improvement. The UCS result in Fig. 4 shows the similar relative strength for the whole varying samples. The UCS ranging from 340 - 400 kPa were achieved with the maximum strength obtained by the filtered method in curing times of 14 and 28 days.

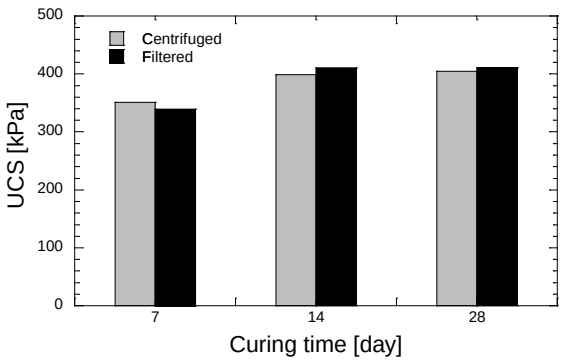

Fig. 4 Results of UCS tests with various curing time

CONCLUSION

The plant-derived urease enzyme was examined to assess the potential new urease enzyme source, especially soybean powder. The extraction of soybean was conducted by two different methods, e.g., filtered and centrifuged methods. The effect of the preparation for crude extract was examined in terms of rate of hydrolysis, precipitation ratio, type, and shape of mineral. The hydrolysis rate increases with the increase in soybean concentration. A hydrolysis rate of 1100 u/g was obtained using 50 g/L of soy powder. Thus, the soybean had a high-enough hydrolysis rate to be used instead of commercial urease enzymes as the biocatalyst in the calcite precipitation method. The precipitation test results show that the method of preparation of crude extract using filtered and centrifuged method has no significant impact on the precipitation mass. The precipitation ratio significantly increased when the soy powder concentration was increased from 10 g/L to 20 g/L in both extraction methods. Using soybean of more than 20g/L results in the maximum precipitation ratio of 100% and thus is selected as an optimum concentration of soybean. The UCS test result also shows that the extraction method has no significant effect on soil strength. A single injection in the treated sample achieved a relatively similar UCS ranging from 340 to 400 kPa. The varying curing time resulted in a similar trend, with a maximum strength of 0.4 MPa in 14 days. Hence, this study confirms that soybean's filtration extraction method may be a more effective and applicable technique to prepare the catalyst in the calcite precipitation method cause its impact and simplicity.

ACKNOWLEDGMENTS

The research described in this paper was financially supported by the Minister of Education, Culture, Research, and Technology of the Republic of Indonesia, grant number 082/E5/PG.02.00.PT/2022

REFERENCES

[1] Khoury CN, Miller GA, Hatami K. Unsaturated soil-geotextile interface behavior. Geotext Geomembranes. 2011;29(1):17–28.
[2] Cheng H, Yamamoto H, Thoeni K, Wu Y. An analytical solution for geotextile-wrapped soil based on insights from DEM analysis. Geotext Geomembranes. 2017;45(4):361–76.
[3] Saftner DA, Zheng J, Green RA, Hryciw R, Wissmann K. Rammed aggregate pier installation effect on soil properties. Proc Inst Civ Eng Gr Improv. 2018;171(2):63–73.
[4] Hamidi M, Lajevardi SH. Experimental Study on the Load-Carrying Capacity of Single Stone Columns. Int J Geosynth Gr Eng. 2018;4(3):0.
[5] Madhyannapu RS, Puppala AJ, Nazarian S, Yuan D. Quality Assessment and Quality Control of Deep Soil Mixing Construction for Stabilizing Expansive Subsoils. J Geotech Geoenvironmental Eng. 2010;136(1):119–28.
[6] Chen J-J, Zhang L, Zhang J-F, Zhu Y-F, Wang J-H. Field Tests, Modification, and Application of Deep Soil Mixing Method in Soft Clay. J Geotech Geoenvironmental Eng. 2013;139(1):24–34.
[7] Modoni G, Bzówka J. Analysis of Foundations Reinforced with Jet Grouting. J Geotech Geoenvironmental Eng. 2012;138(12):1442–54.
[8] Njock PGA, Chen J, Modoni G, Arulrajah A, Kim YH. A review of jet grouting practice and development. Arab J Geosci. 2018;11(16).
[9] Reeksting BJ, Hoffmann TD, Tan L, Paine K, Gebhard S. In-Depth Profiling of Calcite Precipitation by Environmental Bacteria Reveals Fundamental Mechanistic Differences with Relevance to Application. Kelly RM, editor. Appl Environ Microbiol [Internet]. 2020 Mar 18;86(7):1–16.
[10] Cheng L, Cord-Ruwisch R. Upscaling Effects of Soil Improvement by Microbially Induced Calcite Precipitation by Surface Percolation. Geomicrobiol J [Internet]. 2014 May 28;31(5):396–406.
[11] Spairani Y, Cisternino A, Foti D, Lerna M, Ivorra S. Study of the Behavior of Structural Materials Treated with Bioconsolidant. Materials (Basel). 2021. 14(18):5369.
[12] R.A.N. Dilrukshi SK. Plant-derived urease induced sand cementation used in geotechnical engineering applications. Int Conf Geomech Geo-energy Geo-resources. 2016;
[13] Gao Y, He J, Tang X, Chu J. Calcium carbonate precipitation catalyzed by soybean urease as an improvement method for fine-grained soil. Soils Found. 2019;59(5):1631–7.
[14] Hamed Khodadadi T, Javadi N, Krishman V, Hamdan N, Kavazanjian EJ. Crude urease extract for biocementation. J Mater Civ Eng. 2020; 32(12)
[15] Gerilla GP, Teknomo K, Hokao K. An environmental assessment of wood and steel reinforced concrete housing construction. Building and Environment, 2007; 42(7), 2778-2784
[16] Olagunju BD, Olanrewaju OA. Life cycle assessment of ordinary Portland cement (OPC) using damage oriented (endpoint) approach. Proc Int Conf Ind Eng Oper Manag. 2021;2050:113–9.
[17] Akiyama M, Kawasaki S. Microbially mediated sand solidification using calcium phosphate compounds. Eng Geol [Internet]. 2012 Jun;137–

138:29–39.
[18] Yasuhara H, Neupane D, Kinosita N, Hayashi K, Unno T. Solidification of sand soils induced by calcium carbonate precipitation utilizing biocatalyst. JJpn Soc Civ Eng Ser C (Geosph Eng). 2014;70(2):290–300.
[19] Akiyama M, Kawasaki S. Improvement in the unconfined compressive strength of sand test pieces cemented with calcium phosphate compound by addition of calcium carbonate. Ecol Eng. 2012;47:264–7.
[20] Whiffin VS, van Paassen LA, Harkes MP. Microbial carbonate precipitation as a soil improvement technique. Geomicrobiol J. 2007; 24(5):417–23.
[21] DeJong JT, Fritzges MB, Nüsslein K. Microbially Induced Cementation to Control Sand Response to Undrained Shear. J Geotech Geoenvironmental Eng. 2006;132(11):1381–92.
[22] Neupane D, Yasuhara H, Kinoshita N, Putra H. Distribution of grout material within 1-m sand column in insitu calcite precipitation technique. Soils Found. 2015; 55(6):1512–8.
[23] Yasuhara H, Neupane D, Hayashi K, Okamura M. Experiments and predictions of physical properties of sand cemented by enzymatically-induced carbonate precipitation. Soils Found. 2012 52(3):539–49.
[24] Simatupang M, Okamura M. Liquefaction resistance of sand remediated with carbonate precipitation at different degrees of saturation during curing. Soils Found. 2017;57(4):619–31.
[25] Pratama GSB, Yasuhara H, Kinoshita N, Putra H. Application of soybean powder as urease enzyme replacement on EICP method for soil improvement technique. IOP Conf Ser Earth Environ Sci. 2021 1;622(1):012035.
[26] Baiq HS, Yasuhara H, Kinoshita N, Putra H, Johan E. Examination of Calcite Precipitation Using Plant-Derived Urease Enzyme for Soil Improvement. Int J GEOMATE. 2020; 19(72):231–7.
[27] Almajed A, Lateef MA, Moghal AAB, Lemboye K. State-of-the-Art Review of the Applicability and Challenges of Microbial-Induced Calcite Precipitation (MICP) and Enzyme-Induced Calcite Precipitation (EICP) Techniques for Geotechnical and Geoenvironmental Applications. Crystals. 2021 Apr 1;11(4):370.
[28] Sumner JB. Enzyme Urease. J Biol Chem. 1926;69(2):435–41.
[29] Dilrukshi RAN, Nakashima K, Kawasaki S. Soil improvement using plant-derived urease-induced calcium carbonate precipitation. Soils Found. 2018;58(4):894–910.
[30] Imran M Al, Nakashima K, Kawasaki S. Bio-Mediated Soil Improvement Using Plant Derived Enzyme in Addition to Magnesium Ion. Crystals. 2021 6;11(5):516.
[31] Cuccurullo A, Gallipoli D, Bruno AW, Augarde C, Hughes P, La Borderie C. Soil Stabilization Against Water Erosion via Calcite Precipitation by Plant-Derived Urease. Lect Notes Civ Eng. 2020;40:753–62.
[32] Lofianda L, Putra H, Erizal E, Sutoyo S, Yasuhara H. Potentially of Soybean as Bio-Catalyst in Calcite Precipitation Methods for Improving the Strength of Sandy Soil. Civ Eng Archit. 2021;9(7):2317–25.\
[33] Whiffin VS. Microbial CaCO3 Precipitation for the Production of Biocement. Murdoch University; 2004.
[34] Putra H, Erizal, Sutoyo, Simatupang M, Yanto DHY. Improvement of organic soil shear strength through calcite precipitation method using soybeans as bio-catalyst. Crystals. 2021;11(9):1044.
[35] Putra H, Yasuhara H, Kinoshita N, Hirata A. Application of magnesium to improve uniform distribution of precipitated minerals in 1-m column specimens. Geomech Eng [Internet]. 2017;12(5):803–13.
[36] Wang Y, Mao X, Xiao W, Wang W. The Influence Mechanism of Magnesium Ions on the Morphology and Crystal Structure of Magnetized Anti-Scaling Products. Minerals. 2020;10(11):997.
[37] Konopacka-łyskawa D, Czaplicka N, Łapiński M, Kościelska B, Bray R. Precipitation and transformation of vaterite calcium carbonate in the presence of some organic solvents. Materials (Basel). 2020;13(12):1–14.

8th Int. Conf. on Structure, Engineering & Environment (SEE), Mie, Japan, Nov.10-12, 2022, ISBN: 978-4-909106094 C3051

PERFORMANCE COMPARISON OF GEOMETRIC SHAPE OF DESILTING BASIN RECTANGULAR AND VORTEX DESILTING BASIN

*Muhammad Isnaeni[1], Muhammad Syahril Badri Kusuma[2], Joko Nugroho[2], Mohammad Farid[2], and Muhammad Cahyono[2]

[1]Doctoral Program of Water Resources Engineering, Faculty of Civil and Environmental Engineering, Institut Teknologi Bandung, Indonesia; [2]Water Resources Engineering Research Group, Faculty of Civil and Environmental Engineering, Institut Teknologi Bandung, Indonesia

*Corresponding Author, Received: 00 June. 2022, Revised: 00 June. 2022, Accepted: 00 June. 2022

ABSTRACT: Vortex desilting basins have inherent advantages over other types of sediment-removal desilting basins. The advantage is that they require smaller dimensions and a lower removal discharge to achieve specific sediment removal efficiency. An increase in the incoming velocity generates a powerful centrifugal forced vortex, resulting in higher hydraulic efficiencies of the basin. The streamlines and velocity vectors in the horizontal superimposed sections were drawn and analysed then for incipient motion of sediment. This study presents the results of experimental research that was accomplished in a vortex desilting chamber to observe the slope orifice chamber with 1:10, 1:5 and 1:2. The method uses numerical methods with CFD simulations by Ansys R.21 Student to similarity geometric, kinematics and dynamic, then laboratory experiments with a model scale 1:40 prototype to an undistorted 3-D physical model. Comparing the magnitude of the velocity and streamlined path in horizontal sections with the occurrence of secondary in radial sections revealed that the flow in the vortex direction plays a higher role in the removal efficiency of the desilting basin. In comparing the performance, as a result, the slope orifice chamber of 1:5 is further effective in case of deposition and removal faster than other slope chamber types; in the same time model scale, 4 days in a prototype similar to 11 hours on the model scale settled 82.12% sediment and within 4 hours which is similar to 35 minutes on the model scale or more effectively 87.91% of the chamber slope of 1:2 and 1:5.

Keywords: Vortex desilting basin, sediment removal, removal efficiency, deposition, undistorted 3-D physical model.

1. INTRODUCTION

Rapid land-use change during the last decades has resulted in a decrease in irrigation areas and an increase in urban/developed areas. Although water demand for irrigation areas tends to decrease as affected by land-use change, even East Tarum canal and irrigation infrastructures are still in the same dimension [1], [2]. Land-use change on the main island of Indonesia is inevitably increased due to the demographic growth and regional development activity in the last two decades [3], [4].

One of the primary constraints to sustainable agricultural production is a lack of irrigation water supplies. In recent years, the development of alternative water sources and the application of irrigation water-saving technologies are two key strategies to alleviate the scarcity of agricultural water resources [5], [6]. Nowadays, surface irrigation is the most extensively used irrigation method due to its long tradition and low energy consumption. However, this method may pose more erosion and pollution risks than drip or even semi-technique irrigation methods. The concentrated water flow in the canals may erode the soil and disperse the agrochemicals adsorbed to the sediments in the environment [7]. Therefore, evaluation of the transport process requires improved techniques to determine sediment concentration in the narrow, concentrated flow of irrigation canals, especially if the bed and suspended loads are to be evaluated separately. Similar improvements are required in flow velocity determinations [8].

While fresh sediment deposits are often close to fluid mud, older and deeper riverbed sediments tend to be consolidated, with the state of consolidation higher for deeper sediment. These vertical gradients complicate the modelling of sediment erosion, transport, and deposition [9], [10].

A considerable effort is required to improve irrigation operations and modernise them. A desilting basin is a temporary sediment control structure to intercept sediment-laden runoff and retain the sediment. It aims to detain sediment-laden runoff from the disturbed area for sufficient time and allow most deposits to settle within the sediment trap [11]. Decrease the flow velocity in the basin to assure the sediment particle's remaining

time is longer than the settling time is the primary design idea of settling basins. This phenomenon results in the flow of water for irrigation required that is diverted through the weir, resulting in a decreased supply of irrigation water [7]. Water flowing in the canal taking off from head works on such rivers also carries sediment load, the canal gets silted if it receives sediment load over its transporting capacity, and effective measures are not taken for its control. This results in a decrease in the discharge carrying capacity of the canal. Further, the canal slope is generally smaller than the main river; hence, sediment always tends to be deposited in the irrigation canal [12]. To address it, the weir as a head structure requires a sediment trap that can deposit non-cohesive type sediments and quickly remove out because the water required for irrigation is complicated to stop during the cropping pattern because farmers need it.

Previous authors investigated the vortex settling chamber; Cecen and Bayazit (1975), Curi et al. (1975), Ogihara and Sakaguchi (1984), Sanmuganathan (1985), Mashauri (1986), Paul et al. (1991), Athar (2000), Athar et al. (2002), Athar et al. (2005), Keshavarzi et al. (2006), Ansari (2008) and Ansari and Athar (2013) The vortex settling chambers can also separate solids from their transporting fluids, such as in treating sewage and industrial wastes. However, the development by the previous study is to deposit sediment in a power plant and electrical energy to avoid a larger diameter of non-cohesive sediment entering the turbine drive system. In irrigation, sediment gradation allowed and neglected to enter the irrigation canal is cohesive type sediment whose diameter is < 0.06mm [9]. It is challenging to deposit this type of sediment because it is suspension sediment that moves with the water flow [13], [14].

As a case study for head structure in the weir for sediment traps, the Macan weir was designed in a narrow space located in Subang Regency, West Java Province, Indonesia. This weir services a technical irrigation area of 9,670 ha, where the current condition of the wet perimeter section area is reduced by ±35%, caused by sedimentation. The existing conventional plan will construct rectangular sediment traps located right side of the head structure [15].

The present research examines and develops the modern shape of sediment traps as a proposed to replace sediment traps with conventional geometric shapes for the future. This research aims to improve the vortex desilting basin sediment trap performances, depositing non–cohesive sediment > 0.06mm and removing out sediment fraction as trapped settling basins.

Fig. 1 Macan Weir, Located in West Java, Indonesia

The slope orifice chamber of 1:5 is further effective in case of deposition and removal faster than 1:10 and 1:2 slope chamber types.

The shape of the sediment trap must meet the hydraulics rules, design criteria and standardised. So that, non – cohesive sediment is deposited, and increasing removal efficiency to the maximum requires different characteristics and velocity. If hydraulically it can be fulfilled, then the aspect of operational costs is undoubtedly a consideration as well as research significance. This proposed geometric shape is recommended for a weir that does not yet have sediment traps and can only be built in a narrow space.

2. METHODS

2.1 Sediment Properties

2.1.1 Primary data extracted

This research started and was carried out by taking sediment properties obtained by primary data in 2019 and tested at the Laboratory of Engineering Geology, Padjajaran University in Bandung, to obtain sediment properties and physical properties.

Fig. 2 Samples extraction on site (2019).

The sediment particle was tested by comparing the data around the study site, such as on the Cibeet

and Ciasem rivers, and sediment properties in the Macan weir sediment trap were taken at upstream (3 samples) and downstream (3 samples) sampling points, with laboratory test results at 20°C water temperatures [16].

2.1.2 Sediment's laboratory test for the physical model test (2022)

There are four key classifications of sedimentation processes, each characterised by different settling behaviour; describes these as [13], [17]:

a) Type I: Discrete particle settling – particles settle individually without interaction with neighbouring particles.
b) Type II: Flocculant settling – flocculation causes the particles to increase in mass and settle at a faster rate.
c) Type III: Hindered or Zone settling – a mass of particles tends to settle as a unit with individual particles remaining in fixed positions with respect to each other.
d) Type IV: Compression settling – the concentration of particles is so high that sedimentation can only occur through compaction of the structure.

Discrete particle settling occurs in dilute mixtures where there is no particle interaction, with discrete particles being defined as particles whose size, shape and specific gravity do not change with time [18]. The settling velocity of a single spherical particle undergoing discrete settling under laminar conditions [19]. Using a settling tube (Settling Tube), an effective settling velocity is measured, which can be converted into an equivalent particle diameter. Parameters C_1 and C_2 are taken at values of 18 and 0.3 for fine-grained particles but somewhat higher values for natural particles, as discussed later. For particles that can be considered redundant, so the following equation is obtained:

$$V_s = \frac{\rho_s \, gD^2}{18\,\mu + \sqrt{0.3\,\rho_s \rho g D^3}} \qquad (1)$$

Where, V_s deposition velocity, g acceleration gravity, D spheres particles diameter, ρ_s sediment density, ρ water density, μ viscosity. Before the results of the sediment deposition rates are obtained, this settling tube is carried out as shown in Fig.3, Fig.4 and Fig.5 as below:

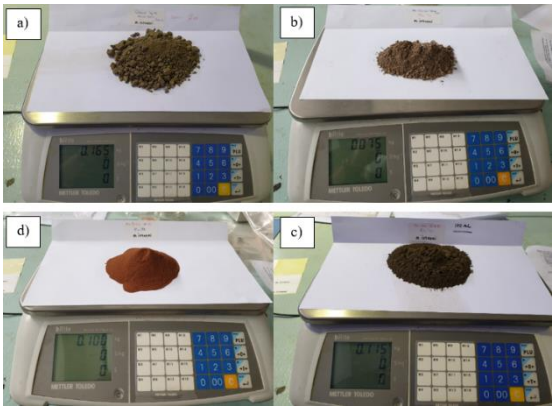

Fig. 3 Equivalent weighing of test sediment samples a) Ex. Field Sediments, b) Passed sieve #400 Ex. Stone Crusher, c) Passed sieve #400 Ex. Coal, and d) passed sieve #400 Ex. Brick in the Fluid Laboratory ITB (2022)

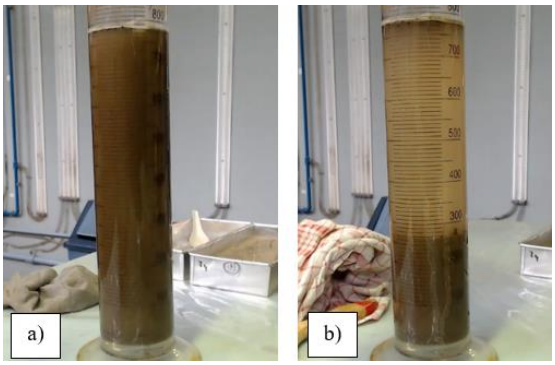

Fig. 4 Field sample testing (Prototype), a) initial deposition, b) sediments deposition

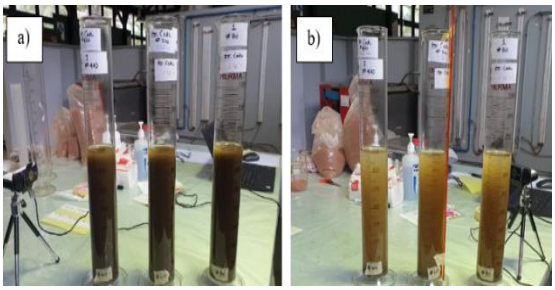

Fig. 5 Deposition rate test Ex. Brick's sample passed sieve #80, #200, and #400. a) initial deposition, b) sediments deposition

Referring to Eq.1, the analysis results are calculated using four (4) formulas and calibrated by laboratory tests with four (4) samples. As a result, the deposition rates result of 0.735cm/s with a comparative curve as follows:

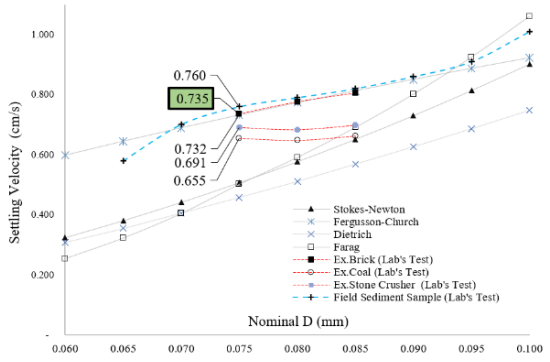

Fig. 6 Comparison curve as calculated four (4) formulae versus settling tube test in laboratories

The analysis has calibrated the results of differences in values from the predictions of a model as an estimate of the observed values, as shown in Fig.6. Root Mean Square Error (RMSE) results from the square root of the Mean Square Error. The accuracy of the measurement error estimation method is characterised by the presence of a small RMSE value. Estimation methods with a smaller Root Mean Square Error (RMSE) are more accurate than estimation methods with a more significant Root Mean Square Error (RMSE).

2.2 Numerical Analysis by Computational Fluid Dynamic (CFD)

In recent years, the growing availability of computational sources and progress in the accuracy of numerical methods has helped researchers to solve fluid mechanics. The method used in CFD to analyse the flow behaviours is a numerical approach. CFD complements testing and experimentation, reducing the efforts and costs required for experimental procedures and data acquisition [20], [21]. This simulation will be carried out by modelling three fluid phases, namely air, water, and sediment or mud so that the sediment's flow characteristics can be obtained against time (transient). Because in this simulation, several fluids have different phases (air, water, and mud), multiphase modelling must be used. For flows with a clear separation between one phase and another, the Volume of Fluid (VoF) model is used. This model is also relatively simple and efficient compared to eulerian or mixture [22].

2.3 Dimensional Analysis

Dimensional analysis is formulating fluid mechanics problems in the case of non-dimensional variables and parameters. Physical problems are described by relations, which are determined by quantities having a certain dimension—length, time, mass, force, temperature, etc. These relations must be so structured that dependent and independent quantities are combined so as to yield dimensionally correct formulas [23]. Dimensional analysis can sometimes provide a complete set of dimensionless products constructed from the pertinent process variables [2], [24]. Similitude by dimensional analysis requires that the dimensionless products have the same value in the prototype as in the model, the similarities that have been tested in this study are geometric, kinematic and dynamic [25].

2.4 Experiment Set-up in Laboratory

Physical model tests are performed to investigate the hydraulic behaviour of the entire sediment trap or each component. Physical model tests often solve fluid mechanics and hydraulics problems to discover the hydraulic behaviour not obtained in numerical models with CFD **[26]**. This physical model test is intended to test or check the performance of sediment traps in the efficiency of deposition and desilting that have been previously tested in numerical analysis with CFD.

2.4.1 Accessories of the Experimental Set-up

Simple ADV performance interface, enabling fast data collection by a data logger by a computer. Laboratory test used 2 unit Micro ADV 16MHz down and side-looking, 1 unit Probe Propeller Current Meter H33 with data logger and 8 unit Camera Highspeed DSLR.

2.4.2 Schematic of Laboratory Test

A 3-D test of this physical model was carried out in the hydraulics laboratory of the Faculty of Civil and Environmental Engineering Institut Teknologi Bandung (ITB), and an undistorted scale 1:40 3-dimension physical model was conducted from February to May 2022 (see Fig.7). The determination of the scale model in the analysis of the relationship between scales prototype to model, considering: space in a laboratory, accuracy, facilities/accessories, and visual view of the undistorted physical model with a scale of 1:40.

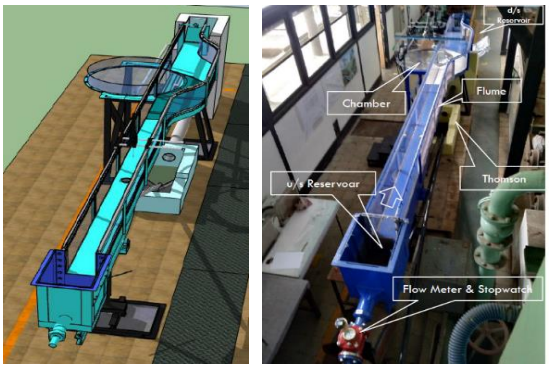

Fig. 7 View of undistorted 3-D lab physical model.

2.4.3 Experimental Procedures

The sediment removal efficiency of the vortex settling/desilting basin used was measured by systematically varying the inlet discharge, underflow removal discharge, sediment size, underflow outlet orifice diameter and the width of the channel. The sediment trap efficiency is defined as the ratio of deposited sediment to the total sediment inflow for a given period within the sediment trap economic operation [27], [28].

2.6 Limitations

In this study, the authors limited several variables so that the focus of the study became clear and not pseudo; here are the limitations of the research: a). Laboratory 3D Physical Model, Undistorted Scale 1: 40; b). Inlet Irrigation Main Canal length at Model: 5.5 m equal Prototype 220 m and static with 0.2m in model equal to 8.00 m at prototype; c). A circular cylindrical type of vortex settling basin having a diameter at model 1.00m equal to 40m at prototype was used for experimentation in the present study; d). Sediment to be deposited cohesionless type > 0.07mm, and <0.07mm neglected and allowable enter to the main system; e). Water depth has variations based on Q 50%, 100% and 120% by NFR; f). The underflow outlet orifice static diameter is 0.025 m, equal to a diameter of 1.00m; g). Cohesion-less uniform sediments having sizes 0.008 mm to 0.825 mm were used, and: h). Suspended sediment concentration in the vortex settling basin varied from 11,200 ppm to 190,000 ppm by weight.

3. RESULTS AND DISCUSSIONS

Decrease of the flow velocity in the basin to assure the sediment particle remaining time longer than the settling time is the main design idea of the settling basin. To achieve this goal, the common procedures are widening the basin width and lowering the basin bottom. However, different combinations of length, width, and depth may attain the same deposition efficiency. The economic design of the settling basin with the specific efficiency is the focus of this study.

3.1 Rectangular Shape Sediment Trap

The performance of a sediment trap is expressed in how effectively it is depositing and quickly removing the sediment fraction. As a comparison, in 2018, there was an undistorted 3-D of physical model of the rectangular shape of sediment traps in the Hydraulics Laboratory of PUSSAIR Bandung, (see Fig. 8).

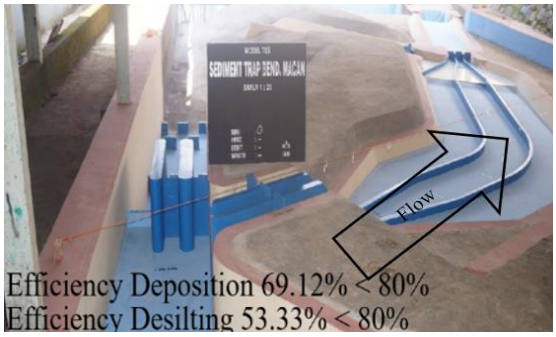

Fig. 8 Undistorted physical model test scaling 1:20 for conventional rectangular sediment trap

In such irrigation systems, sediment in canal structures has both technical and economic implications in developing and utilising water resources; hence, its control is essential. With a similar location and parameters, due to the Macan main canal's alignment in the irrigation system's direction, if it is built on a space with curved alignment is not optimal in terms of performance. The alignment of sediment traps on the curved line leaves significant sedimentary fractions in the inner curve and under sluice, see Fig. 9 and 10. The results of physical modelling on conventional sediment trap forms with a model scale of 1:20 are not very optimal, the deposition efficiency is measured at 69.12%, and this deposited sedimentary fraction can only be removed by 53.33%, see Table 2.

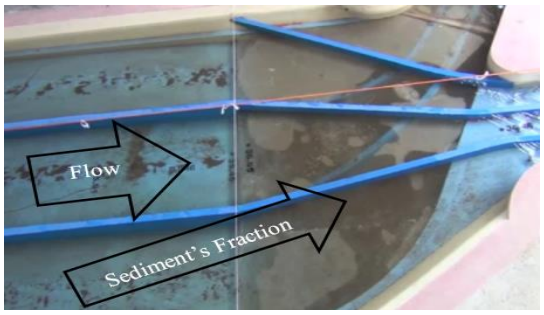

Fig. 9 Unremoved sediment at under sluice space

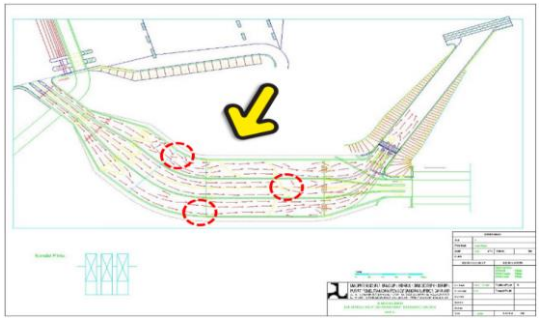

Fig. 10 Fraction of sediment on dashed line – break the red circle in rectangular sediment trap.

In the Design Criteria (KP-02, 2015) issued by the Ministry of Public Works and Housing, sediments deposited in diameter >0.07mm, for diameters <0.07mm are allowed to be neglected and then move the irrigation system with operational routine and periodic maintenance conditions extracting [29].

Table 2 Performance of Rectangular Conventional Sediment Trap, 2018

No	Parameters	Rectangular Conventional Sediment Trap	
		Prototype, Scale 1:1	3-D Physical Model, 1:20
a	Q 100%	10.64 m^3/s	1.057 lt/s
b	Daily Sediment Transport	52.66 m^3/day	5,367.80 cm^3/day
c	Continue Settling Time	7 Days	24.63 Hours
d	Volume/Fraction Settled	37.50 m^3	3,710.22 cm^3
e	Desilting Time	1 Days	5.4 Hours
f	Volume/Fraction Desilted	21.08 m^3	1,978.66 cm^3
g	Velocity	1.261 m/s	20.430 cm/s
h	Froude Number	0.560 -	2.0151 -
i	Reynold Number	1.58.E+03 -	4.63E-01 -
j	Sediment Consentration	190,751 ppm	96,774 ppm
k	Trap Efficiency (TE)	**71.21%**	**69.12%**
l	Desilting Efficiency (η_0)	**56.21%**	**53.33%**

3.2 Simulation for Approach Geometric Shape by CFD

In all 22 runs were conducted for sediment removal efficiency of vortex settling/desilting basin by varying slope chamber of underflow outlet, whereas 44 runs were conducted for this study.

Here are the inputs used in boundary conditions: Mass-flow-Inlet: a). In the inlet section, it is defined as a mass flow inlet either for water or mud. b). Wall: On walls, it is defined as a wall with a no-slip condition to represent the friction between the fluid and the wall. c). Surface: At the top of the domain, the effects of wall friction are removed to represent atmospheric air, and d). Outlet: The outlet section is defined as a pressure outlet representing the flow's "exit".

Computational Fluid Dynamics (CFD) is the art of transforming fluid dynamics set equations in the form of integrals and derivatives into discrete algebraic forms, which a computer can solve to obtain the values of the flow field at a particular discrete point or time. As for the regulatory equations in fluid dynamics: the continuity equation, the momentum equation and the energy equation [20], [21]. Here are the equations used in CFDs;

Continuity equation of integral forms:

$$\frac{\partial}{\partial t}\iiint_V \rho dV + \iint_A \rho\vec{V}\cdot d\vec{A}=0 \quad (1)$$

The continuity equation of the differential form:

$$\frac{\partial \rho}{\partial t}+\rho\vec{\nabla}\cdot\vec{V}=0 \quad (2)$$

The equation of momentum in the direction of the x-axis:

$$\frac{\partial(\rho u)}{\partial t}+\vec{\nabla}\cdot(\rho u\vec{V})=-\frac{\partial p}{\partial x}+\frac{\partial \tau_{xx}}{\partial x}+\frac{\partial \tau_{yx}}{\partial y}+\frac{\partial \tau_{zx}}{\partial z}+\rho f_x \quad (3)$$

The equation of momentum in the direction of the y-axis:

$$\frac{\partial(\rho v)}{\partial t}+\vec{\nabla}\cdot(\rho v\vec{V})=-\frac{\partial p}{\partial y}+\frac{\partial \tau_{xy}}{\partial x}+\frac{\partial \tau_{yy}}{\partial y}+\frac{\partial \tau_{zy}}{\partial z}+\rho f_y \quad (4)$$

The equation of momentum in the direction of the z-axis:

$$\frac{\partial(\rho w)}{\partial t}+\vec{\nabla}\cdot(\rho w\vec{V})=-\frac{\partial p}{\partial z}+\frac{\partial \tau_{xz}}{\partial x}+\frac{\partial \tau_{yz}}{\partial y}+\frac{\partial \tau_{zz}}{\partial z}+\rho f_z \quad (5)$$

The energy equation is written in the form of internal energy:

$$\frac{\partial}{\partial t}\left[\rho\left(e+\frac{V^2}{2}\right)\right]+\vec{\nabla}\cdot\left[\rho\left(e+\frac{V^2}{2}\right)\vec{V}\right]=\rho\dot{q}-\frac{\partial(\rho p)}{\partial x}-\frac{\partial(vp)}{\partial y}-\frac{\partial(wp)}{\partial z}+\rho\vec{f}\cdot\vec{V} \quad (6)$$

Where, ρ is Liquid density (kg m^{-3}), A is mass area, $\vec{V}$ is Velocity vector (m s^{-1}) or velocity fluid parcel, e for internal energy, three velocity components are u, v, w, $\vec{\nabla}$ vector, f any vector function. The solution of a partial differential analytical equation results in a continuously closed-form dependent variable expression across domains. In contrast, the solution of numerical equations can only give

values to discrete points in the domain, also called grid points. As a shaping approach to the vortex geometric shape settling/desilting basins proposed, as shown in Fig. 11, then input all the hydraulic variables and applying Eq.1 – Eq. 6 above in CFD resulted shape as follows:

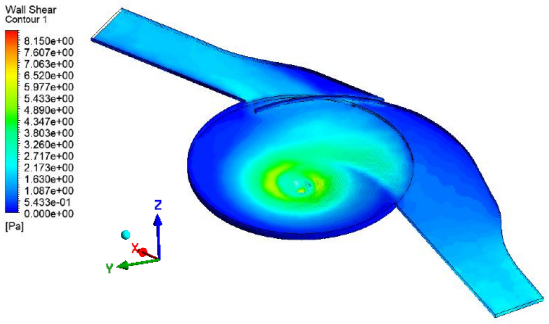

Fig. 11 Wall shear contour, in valve-way closed condition

As shown in Fig.11, it showed that the wall shear contour on the free vortex flow along the forced vortex flow side of the chamber is relatively high and states that sediment is well deposited, the percentage of sedimentary volume deposited from sediment transport within continues flow in 7 days of flow amounting to 82.11%. On the longitudinal section of this sediment trap is shown a fraction of sediment deposited present by the predominance of red in the following Fig.12 below:

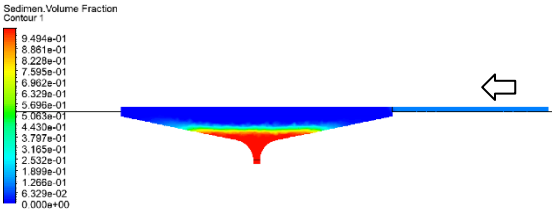

Fig. 12 Sediment volume fraction – longitudinal section view (deposition time)

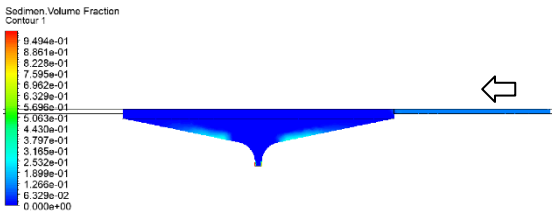

Fig. 13 Sediment volume fraction – longitudinal section view (desilting time)

In addition, the rheological process of sedimentary sediments also exerts an influence on the classification of this type of sediment. Of the 82.11% of sediment deposited, as shown in Fig. 12 and Fig. 13, a total of 69.31% of the sediment fraction can be drained. Leaving approximately 30.69% in cyan colour cannot be remove-out due to the position of the sediment in the transition of the free vortex flow to the forced vortex.

3.3 Result Laboratory Undistorted 3-D Physical Model Test

The geometric approach of the vortex settling/desilting basin with a numerical approach to its results was tested with a physical model in the laboratory.

After the dimensional analysis, stages are carried out, and geometric, kinematic, and dynamic similarity tests and the available space, a model scale of 1:40 is determined.

Table 3 Summary of geometry similitude

Parameter	Prototype		Model	
Daily Sediment Rate	52.66	m^3/day	822.78	cm^3/12.32 Hr
Flushing Period	3.25	day	12.32	Hour
Sediment Trap Area	170.91	m^3	2,670.55	cm^3

The following equation calculates the deposition efficiency value:

$$T_{ef}=\frac{V_{in}-V_{out}}{V_{in}}\times 100 \quad (7)$$

Where T_{ef} is trap efficiency (%), V_{in} is the volume of sediment entering the sediment trap, V_{out} is volume of sediment as remove at outlet.

To calculate the efficiency of removing/desilting, use the following equation:

$$\eta_0=\frac{\text{Ws removed+Ws Settled}}{\text{Total Ws Feeding}}\times 100 \quad (8)$$

Where η_0 is removal efficiency (%), Ws removed is the volume of a sediment chamber, and Ws Settled as sediment deposited. Ws feeding the total amount feeding of sediment transport rates [23], [30].

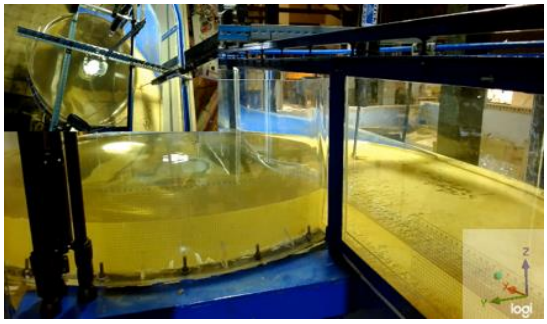

Fig. 14 Deposition time condition in 3.25 of 12 hours running.

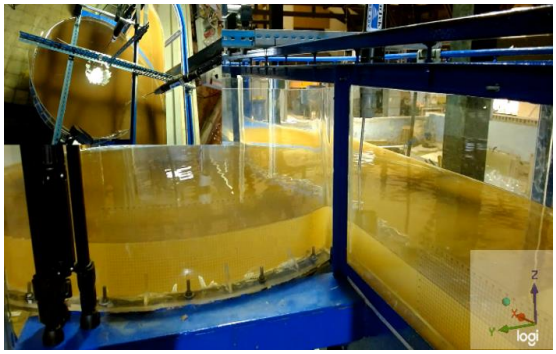

Fig. 15 Measurement of sediment fraction in 8.25 of 12 hours running

As shown in Fig. 14 and Fig. 15, 11 runs were conducted for this study and feeding the sediment through a sediment feeder to determine the volume of deposition and the removal efficiency refer to Eq.7 and Eq.8. The maximum result for chamber 1:5, with the effectiveness, deposited 84.90%>80%. Of these sediment fractions, 87.90% were removed within 0.3 hours and left a sediment fraction of 12.1%. The deposition conditions yielded the maximum, with flow conditions Q=0.53lps, V=8.18cms, water level height 8.23cm in flume and Fr 0.98. A regulator is required on the operation gate to maintain and implement this parameter.

4. CONCLUSION

Present research for steady, vortex, and open channel flows over smooth, rough, and movable beds, independent and based on Reynolds and Froude numbers. As a comparison of 2 different geometric shapes of sediment traps with hydraulic parameters such as discharge, the exact characteristics of sediments to deposition and removed-out, the running results showed an increase in the number of volumes that could be settling from 69.12% to 84.90%. Meanwhile, for removal, the sediment fraction of 53.33% increases to 87.90% from the deposited can be removed. For future research, it is optimising the geometric shape of the chamber to be optimum based on the diameter ratio chamber effect.

5. ACKNOWLEDGMENTS

This study aims to develop a 3-D rectangular sediment trap to a vortex desilting/settling basin shape. The authors would like to thank the Ministry of Public Works and Housing for their assistance regarding the data collection required for this paper. Furthermore, the authors would also like to express gratitude to this research, the Water Resources Engineering Research Group of the Faculty of Civil and Environmental Engineering Institut Teknologi Bandung, for supporting this publication.

6. REFERENCES

[1] M. S. B. Kusuma, A. A. Kuntoro, and R. Silasari, "Preparedness Effort toward Climate Change Adaptation in Upper Citarum River Basin, West Java, Indonesia," p. 8.

[2] M. S. B. Kusuma, R. A. Rahayu, and M. Cahyono, "Development Study of Turbulent κ-ε Model for Recirculation Flow III: Two Dimension Recirculation Flow in a Reservoir," p. 16.

[3] Bappenas RI, *ATLAS Pengelolaan Sumber Daya Air Terpadu Wilayah Sungai Citarum*. BAPPENAS, Asian Development Bank, 2012.

[4] M. S. B. Kusuma, L. M. Hutasoit, B. Kombaitan, M. Syafila, and T. Setiadi, "Strategi pengelolaan terpadu penyelesaian permasalahan DAS Citarum," *Forum Guru Besar ITB*, 2018.

[5] L. Mateos and J. V. Giráldez, "Suspended load and bed load in irrigation furrows," *CATENA*, vol. 64, no. 2–3, pp. 232–246, Dec. 2005, doi: 10.1016/j.catena.2005.08.007.

[6] M. S. Badri Kusuma, "EXPERIMENTAL MODEL OF DAM BREAK FLOW AROUND SEVERAL BLOCKAGES CONFIGURATIONS," *Int. J. GEOMATE*, vol. 16, no. 58, Jun. 2019, doi: 10.21660/2019.58.97684.

[7] M. R. Morris, A. Hussain, M. H. Gillies, and N. J. O'Halloran, "Inflow rate and border irrigation performance," *Agric. Water Manag.*, vol. 155, pp. 76–86, Jun. 2015, doi: 10.1016/j.agwat.2015.03.017.

[8] Y. Shen, J. Puig-Bargués, M. Li, Y. Xiao, Q. Li, and Y. Li, "Physical, chemical and biological emitter clogging behaviors in drip irrigation systems using high-sediment loaded water," *Agric. Water Manag.*, vol. 270, p. 107738, Aug. 2022, doi: 10.1016/j.agwat.2022.107738.

[9] J. Lepesqueur, R. Hostache, N. Martínez-Carreras, E. Montargès-Pelletier, and C. Hissler, "Sediment transport modelling in riverine environments: on the importance of grain-size distribution, sediment density, and suspended sediment concentrations at the upstream boundary," *Hydrol. Earth Syst. Sci.*, vol. 23, no. 9, pp. 3901–3915, Sep. 2019, doi: 10.5194/hess-23-3901-2019.

[10] P. I. Kinnell, "Discussion on 'GIS Based Distributed Model for Soil Erosion and Rate of Sediment Outflow from Catchments' by Manoj K. Jain, Umesh C. Kothyari, and Kittur G. Ranga Raju," *J. Hydraul. Eng.*, vol. 133, no. 7, pp. 843–844, Jul. 2007, doi:

10.1061/(ASCE)0733-9429(2007)133:7(843).

[11] A. Ali, A. E. Mynett, and M. H. Azam, "Sediment Dynamics in the Meghna Estuary, Bangladesh: A Model Study," *J. Waterw. Port Coast. Ocean Eng.*, vol. 133, no. 4, pp. 255–263, Jul. 2007, doi: 10.1061/(ASCE)0733-950X(2007)133:4(255).

[12] M. A. Ansari and M. A. Khan, "Performance assessment of vortex settling chambers," *ISH J. Hydraul. Eng.*, vol. 20, no. 3, pp. 324–338, Sep. 2014, doi: 10.1080/09715010.2014.925330.

[13] J. Chapokpour, "Turbulent Flow Measurement in Vortex Settling Basin," *Iran. J. Energy Environ.*, 2011, doi: 10.5829/idosi.ijee.2011.02.04.3098.

[14] M. A. Ansari and M. Athar, "Design parameters of vortex settling basin," *Proc. Inst. Civ. Eng. - Water Manag.*, vol. 166, no. 5, pp. 262–271, May 2013, doi: 10.1680/wama.11.00098.

[15] Isnaeni, M., Kusuma, MSB., Nugroho, J., "Rheological Relationship to Sediment Deposition Rate in Macan Weir Sediment Traps," *Int. J. GEOMATE*, vol. 21, no. 87, Nov. 2021, doi: 10.21660/2021.87.j2370.

[16] Isnaeni, M., Kusuma, MSB., Nugroho, J., "Comparison of Four Particle Deposition Rate Formulae in Laminar Flow," *Int. J. GEOMATE*, vol. 21, no. 84, Aug. 2021, doi: 10.21660/2021.84.j2160.

[17] W. E. Dietrich, "Settling velocity of natural particles," *Water Resour. Res.*, vol. 18, no. 6, pp. 1615–1626, Dec. 1982, doi: 10.1029/WR018i006p01615.

[18] K. Hutter, Y. Wang, and I. P. Chubarenko, "Dimensional Analysis, Similitude and Model Experiments," in *Physics of Lakes*, Cham: Springer International Publishing, 2014, pp. 307–396. doi: 10.1007/978-3-319-00473-0_30.

[19] O. E. Agwu, J. U. Akpabio, S. B. Alabi, and A. Dosunmu, "Settling velocity of drill cuttings in drilling fluids: A review of experimental, numerical simulations and artificial intelligence studies," *Powder Technol.*, vol. 339, pp. 728–746, Nov. 2018, doi: 10.1016/j.powtec.2018.08.064.

[20] R. Ramirez, E. Avila, L. Lopez, A. Bula, and J. Duarte Forero, "CFD characterisation and optimisation of the cavitation phenomenon in dredging centrifugal pumps," *Alex. Eng. J.*, vol. 59, no. 1, pp. 291–309, Feb. 2020, doi: 10.1016/j.aej.2019.12.041.

[21] T. M. Ravens and R. A. Jepsen, "Computational Fluid Dynamics Analysis of Flow in a Straight Flume for Sediment Erodibility Testing," *J. Waterw. Port Coast. Ocean Eng.*, vol. 132, no. 6, pp. 457–461, Nov. 2006, doi: 10.1061/(ASCE)0733-950X(2006)132:6(457).

[22] M. E. Mohammad, N. Al-Ansari, S. Knutsson, and J. Laue, "A Computational Fluid Dynamics Simulation Model of Sediment Deposition in a Storage Reservoir Subject to Water Withdrawal," *Water*, vol. 12, no. 4, p. 959, Mar. 2020, doi: 10.3390/w12040959.

[23] K.-C. Yeb and E.-T. Lin, "Efficiency Simulation and Design of Settling Basin," p. 12.

[24] G. Piton and A. Recking, "Design of Sediment Traps with Open Check Dams. I: Hydraulic and Deposition Processes," *J. Hydraul. Eng.*, vol. 142, no. 2, p. 04015045, Feb. 2016, doi: 10.1061/(ASCE)HY.1943-7900.0001048.

[25] M. J. Briggs, "Basics of Physical Modeling in Coastal and Hydraulic Engineering," p. 12, 2013.

[26] Z. Xu, X. Song, G. Li, Z. Pang, and Z. Zhu, "Settling behavior of non-spherical particles in power-law fluids: Experimental study and model development," *Particuology*, vol. 46, pp. 30–39, Oct. 2019, doi: 10.1016/j.partic.2018.07.006.

[27] S. Shahi and E. Kuru, "Experimental investigation of the settling velocity of spherical particles in Power-law fluids using particle image shadowgraph technique," *Int. J. Miner. Process.*, vol. 153, pp. 60–65, Aug. 2016, doi: 10.1016/j.minpro.2016.06.002.

[28] S. Uhlenbrook and A. Sieber, "On the value of experimental data to reduce the prediction uncertainty of a process-oriented catchment model," *Environ. Model. Softw.*, vol. 20, no. 1, pp. 19–32, Jan. 2005, doi: 10.1016/j.envsoft.2003.12.006.

[29] M. of P. W. DGWR, "Design Criteria," *Minist. Public Works Indones.*, vol. KP-06, 2015, [Online]. Available: https://sda.pu.go.id

[30] M. A. Eizel-Din *et al.*, "Trap efficiency of reservoirs on the Nile River," p. 7.

8th Int. Conf. on Structure, Engineering & Environment (SEE), Mie, Japan, Nov.10-12, 2022, ISBN: 978-4-909106094 C3051

CASE STUDY AND EVALUATION OF ROAD LANDSLIDE OVER TUFF-MATERIAL

Fahmi Aldiamar[1], and Dea Pertiwi[3]
[1,2]Implementing Unit for Geotechnical, Tunnel and Structures, Directorate General of Highway, Ministry of Public Works and Housing, Indonesia

ABSTRACT

Muara Tebo-Sei Bengkal National Road in Jambi province are constructed over Kasai Formation consisted of tuff sandstone, clay, gravel and thin layer of coal according to regional geological map. This formation usually consists of young loose fine-grained material that is porous and easily eroded when infiltration and surface runoff due to raining is occurred. In 2018, longitudinal cracks, which were propagated creating crown of landslide on road shoulder, were occurred in this road section. Geogrid-reinforced earthwork was constructed to overcome this problem. Unfortunately, this construction did not work well due to inundation of embankment toe during high intensity rainfall, and sliding plane developed below geogrid-reinforced earthworks (MSE Wall) construction. Evaluation on the depth of sliding plane was conducted using inclinometer measurement and re-evaluation on soil stratification according to soil testing across the road section. Sliding plane was predicted to develop down to 7 meters depth which is the interface between impervious material (clay) that underlie below surface material (silty sand) which is more porous. It is indicated that softening of the embankment toe triggered progressive instability to the road embankment and geogrid-reinforced earthworks, acted as additional load causing the sliding occurred faster. Evaluation on this case showed that meticulous examination on geotechnical aspects will provide a more thorough determination on problems, and bored-pile using retaining wall as a slope stabilization solution is more effective when dealing with deep sliding plane.

Keywords: Road landslide, Tuff material, Geogrid reinforcement, Bored pile

INTRODUCTION

Volcanic tuffs are very porous rock and are prone to weathering [1]. Tuff is pyroclastic rocks produced by volcanic eruptions due to endogenous forces. The material forms the volcanic eruption were deposited before being transported by water [2]. Residual tuff soil was formed by weathering process and become relatively soft especially in saturated condition.

Road construction over volcanic tuff material should be design carefully especially when surface water run-off was uncontrollable and ground water level are high. When landslide occurred on National Road, disruption to road user and traffic jam were major problems especially when the National Road are strategic and the only connection road between district.

Tebo district economic income were depend on palm and rubber farm also mining such as coal, crude oil and small-scale gold mining. Jambi is a province of Indonesia that is located on the east coast of central Sumatra. National road connecting Tebo district and Jambi province were vital due to its strategic trading route.

In this paper, forensic geotechnical investigation using numerical method were conducted to utilize, simulate and analyze landslide behavior [3]. The geotechnical analysis involves soil characterization, water level, displacement and main cause of road landslide were evaluated to draw conclusions and present the solution for the failure in the construction [4].

CHRONOLOGY OF ROAD LANDSLIDE AND PREVIOUS COUNTERMEASURE

In 2018 erosion at embankment slope surface due to surface water runoff induced instability of road embankment at Muara Tebo-Sei Bengkal National Road in Jambi province (Fig. 1).

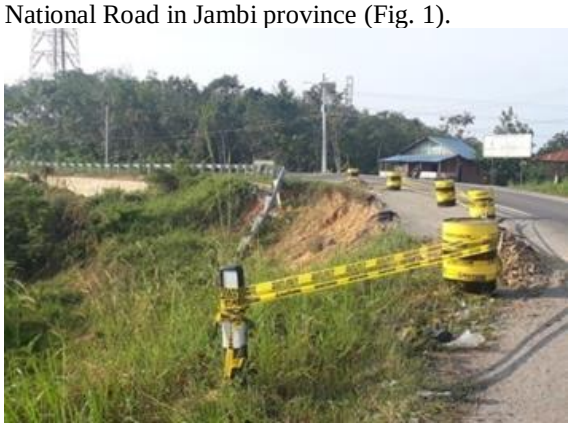

Fig. 1 Slope surface instability due to water runoff

Since the instability were indicated shallow and only influenced roadside, Mechanically Stabilized Earth (MSE) Wall consist of compacted backfill and soil reinforcement using uniaxial geogrid were design and constructed as seen in Fig. 2 until Fig. 5.

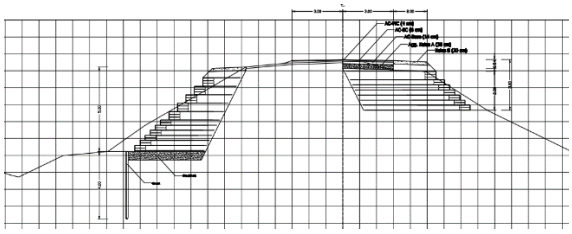

Fig. 2 Design drawing of MSE Wall

Fig. 3 Soil reinforcement using uniaxial geogrid

Fig. 4 Compaction of embankment above soil reinforcement

Fig. 5 Finished construction of MSE Wall

Unfortunately, in 2019, cracks at roadside follow by large displacement occurred at the MSE Wall construction is shown in Fig. 6.

Fig. 6 Large displacement at MSE Wall

Evaluation on rainfall intensity for the past 3 years from 2017 until 2019 showed that when the landslide occurred in November 2019, heavy rainfall with intensity until 60 mm/day happened. These intensities were the largest in the range of observation data (Fig. 7).

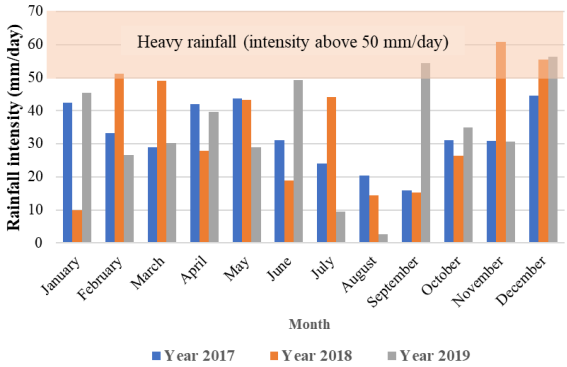

Fig. 7 Rainfall intensity data from 2017 until 2019

REGIONAL AND LOCAL GEOLOGY OF THE REGION

Muara Tebo-Sei Bengkal National Road in Jambi province are constructed over Kasai Formation (QTk) consisted of tuff sandstone, clay, gravel and thin layer of coal according to regional geological map (Fig. 8). This formation usually consists of young loose fine-grained material that is porous and easily eroded when infiltration and surface runoff due to raining is occurred.

Evaluation on the outcrop of tuff material at toe of the embankment (Fig. 9) show that the material was saturated, loose and some places show waterway that indicated material erosion due to surface runoff.

Fig. 8 Geological map of Muarobungo, Sumatera [5]

Fig. 9 Visualization of tuff material at toe of embankment

SOIL STRATIFICATION

To evaluate the cause of landslide, three (3) soil investigation (BH-1, BH-2 and BH-3) conducted in 2020 at different position crossing the landslide (Fig. 10). After completion of drilling work, instrumentation to define position of sliding plane namely inclinometers were installed at BH-2 according to National Standard method [6], while instrumentation to measure elevation of ground water level i.e., open standpipe piezometers were installed according to National Standard method [7], at BH-1 and BH-3.

Five (5) layers of soils were identified according to National Standard method [8], as seen in Fig. 10. Thickness of surface layer that is soft-medium stiff tuff were ± 5.0 m, while interlude of silty sand, sandy silt and clay are identified below the tuff material. Surface elevation measured at that time indicated that lateral displacement of MSE Wall were around 11m, while vertical displacements were approximately 5m.

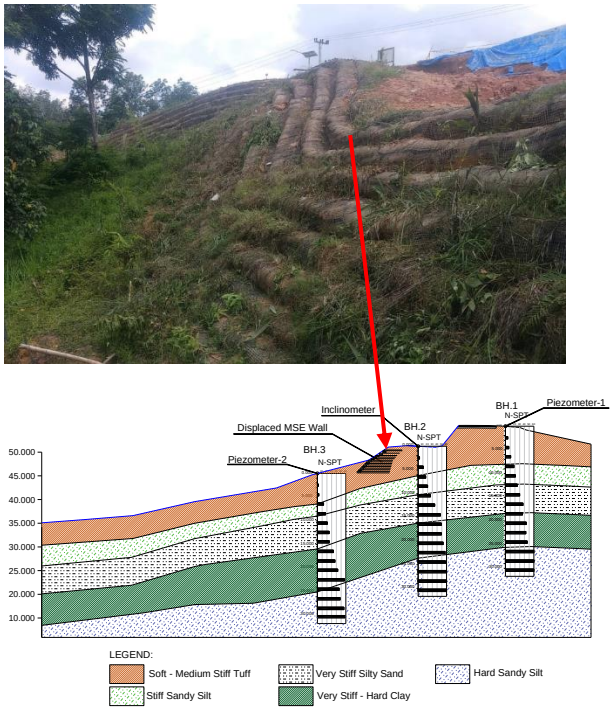

Fig. 10 Soil stratification and condition of displaced MSE Wall

IDENTIFICATION OF SLIDING PLANE ACCORDING TO INSTRUMENTATION MEASUREMENT

According to piezometer measurement, ground water level were expected at -12.0 m below pavement elevation, while sliding plane were indicated at 2 (two) position i.e. shallow sliding plane at -1.50 m and deep sliding plane at -7.0 m below surface elevation of BH-2 as seen in Fig. 11 and Fig. 12.

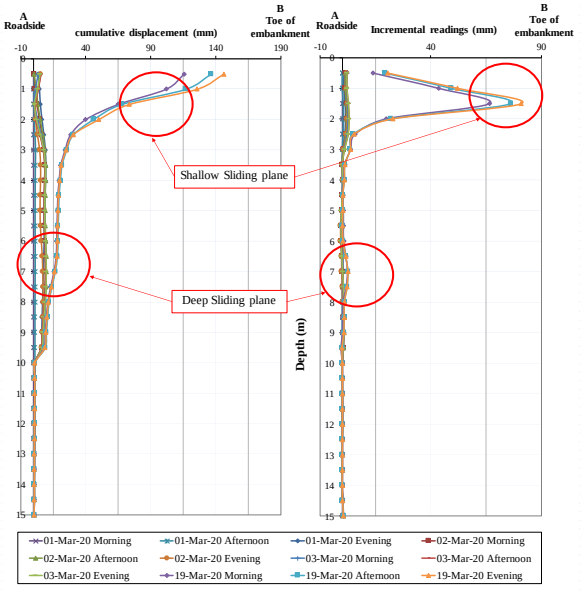

Fig. 11 Cumulative and Incremental displacement from inclinometer readings

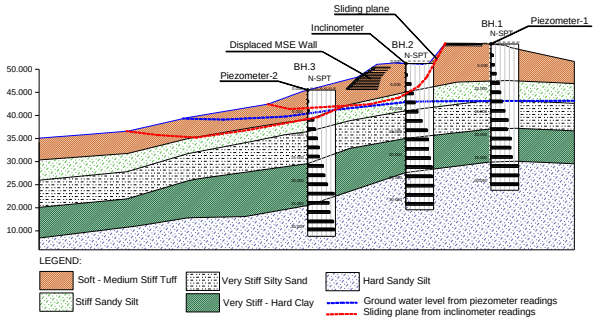

Fig. 12 Position of ground water level and sliding plane according to monitoring readings

This information confirms that sliding plane were below MSE-Wall base construction. The prediction of the sliding place is at the boundary of a slightly impermeable layer (tuff material) that is above the porous layer, namely sandy silt.

It is estimated that the groundwater table saturating the toe of the slope that resulted in weathering of the tuff material and reduce the shear strength. The landslide were progressive, starting at the toe of the embankment slope that softened due to weathering and saturation.

SOIL PARAMETER AND STABILITY ANALYSIS RESULT

To identify the appropriate landslide countermeasure for road embankment over tuff material, mechanism of embankment failure was analyze using back analysis methodology and finite element numerical modelling.

Soil parameters used in the stability analysis were based on N-SPT correlation for sandy soils [9] and tuff [2]. Back calculation analysis conducted only on Soft-Medium Stiff Tuff parameter by reducing cohesion (c') until Factor of Safety (FoS) nearly 1 (one) (Fig. 13) and the sliding plane represent the actual condition as seen in Fig. 12.

Soil parameter resulted from back calculation analysis and geogrid used in the MSEW finite element method modelling using Plaxis 2-Dimension software were resumed in Table 1 and Table 2.

Table 1 Soil parameters

Description	γ (kN/m^3)	E (kN/m^2)	c' (kPa)	ϕ' (deg)
Soft-Medium Stiff Tuff	18	5000	0.1	27
Stiff Sandy Silt	18	10000	1	30
Very Stiff Silty Sand	19	28000	5	35
Very Stiff – Hard Clay	17	35000	15	30
Hard Sandy Silt	18	27000	5	32
Embankment	17	25000	15	25

Table 2 Geogrid parameters

Description	Tensile strength (kN/m)	Elongation at break (%)	EA (kN/m)
Uni-axial geogrid	100	13	12.7

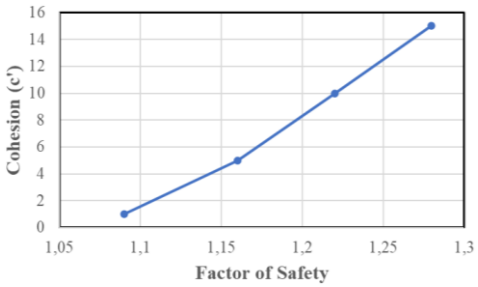

Fig. 13 Correlation between cohesion reduction to decreasing of FoS

Analysis by reducing tuff cohesion parameter conducted to closely represent soil softening and as seen in Fig. 14, sliding plane are relatively close to the actual displacement measured at field. In this illustration we can confirmed that the actual sliding plane were deep below the position of MSE Wall.

Furthermore, for this kind of situation it is also concluded that retaining structure are not effective to overcome deep sliding plane. The weight of the retaining structure could give an extra weight or dead load in the slope that trigger large displacement, especially when the shear strength at toe of embankment were reduced due to softening by surface water runoff.

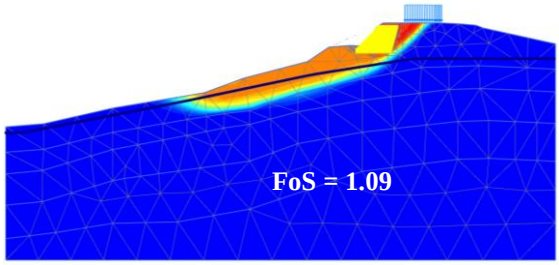

Fig. 14 Sliding plane according to back calculation analysis

Since the depth of sliding plane are 7.0 m below position of BH-2, the expected depth of piles for slope reinforcement are minimum 14.0m or two times the depth of sliding plane. Since the location of the research are in rural area, and there are difficulties to get large diameter of boring machine. The diameter of bored piles that used in this evaluation are 0.8 m based on the availability of local machinery close d to the project area. To avoid visco-plastic flow [10] between piles, spacing of piles evaluated were 2 times diameter of piles (1.6 m spacing center to center) and reinforced concrete retaining structure are constructed above pile cap.

First evaluation (Fig. 15) show that after application of 14 m length of bored pile below concrete retaining structure and 15 kPa traffic load, the FoS increased into 1.2 and sliding plane moved at toe of embankment. This condition indicated that the embankment condition relatively stable after application of bored pile and retaining structure. To evaluate the global stability of road embankment, regrading at toe of embankment slope were conducted in the second evaluation (Fig. 16) to reduce the acting force and check the overall stability, especially at roadside. According to the result on the second evaluation, FoS increased into 1.28 which is above the minimum required by National Standard [11] 1.25.

Evaluation using combination of bored pile and retaining structure also regrading at toe of embankment shown good result and recommended to use as deep landslide problem of embankment over tuff material.

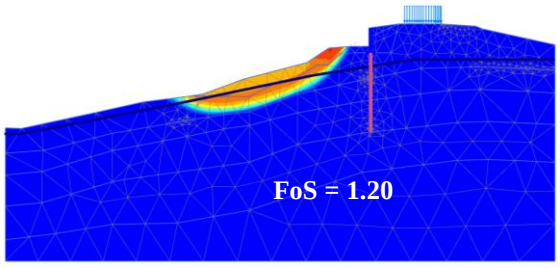

Fig. 15 Sliding plane according to back calculation analysis

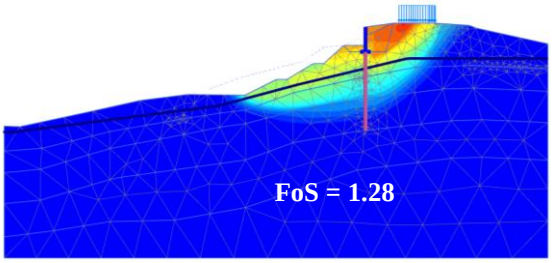

Fig. 16 Sliding plane according to back calculation analysis

CONCLUSIONS

Softening of tuff material at the embankment toe could triggered progressive instability to the road embankment and shallow reinforcement such as geogrid-reinforced earthworks (MSE Wall). MSW wall or retaining structure could acted as additional load to the embankment slope and when the embankment slope saturated could cause instability.

Evaluation on this case showed that meticulous examination on geotechnical aspects, especially with good soil investigation and proper instrumentation placement such as inclinometer and piezometer could help engineer to evaluate the cause of instability of road embankment construction.

Thorough forensic geotechnical investigation using numerical method will provide a more clear determination on landslide problems and how to increase the stability of the embankment using the appropriate reinforcement.

According to the numerical simulation, reinforcement of slope using bored-pile combine with retaining structure and slope regrading at toe of embankment could solve the deep sliding plane and increase the slope factor of safety.

ACKNOWLEDGMENTS

Author would like to thanks Implementation Unit of National Road, Jambi and Institute of Road Engineering for sharing of knowledge and data sharing throughout the landslide evaluation process.

REFERENCES

[1] Torok A., Basri A., Bogoly G., Lovas T., Somogyi A., and Gorog P., Slope Stability and Rockfall Asessment of Volcanic Tuffs Using RPAS with 2-D FEM Slope Modelling. Nat. Hazards Earth Syst. Sci., 18, 583-597, 2018.

[2] Asniar N., Purwana Y. M., Surjandari N. S., Tuff as Rock and Soil: Review of The Literature on Tuff Geotechnical, Chemical and Mineralogical Properties Around. AIP Conference Proceedings, 2114, 050022, 2019.

[3] Naveed A. M., Ali Z., Qadir A., Latif U. N., Hamid S., Sarwar U., Geotechnical Forensic Investigation of a Slope Failure on Silty Clay Soil. Front. Struc. Civ. Eng., 14, 501-517, 2020.

[4] Clough G. W., O'Rouke T. D., Construction Induced Movement of in-situ Walls. ASCE Conference Proceeding on Performance of Earth Retaining Structures, Geotechnical Special Publication No. 25, ASCE 439-470, 1990.

[5] Simandjuntak T. O., Budhistrisna T., Surono., Gafoer S., Amin T. C., Geological Map of The Muarabungo Quadrangle, Sumatera, Geological Research and Development Centre, 1994.

[6] National Standardization Agency, Guidance of Inclinometer Installation and Monitoring the Horizontal Movement of the Ground, Indonesian Standard, SNI 3404:2008, 2008.

[7] National Standardization Agency, Guidance of Soil Pore Water Pressure Measurement using Open Standpipe Casagrade, Indonesian Standard, SNI 8134:2015, 2015.

[8] National Standardization Agency, Guidance of Recording and Identification on Core Drilling Result, Indonesian Standard, SNI 2436:2008,

2008.
[9] Hatanaka M., Uchida A., Empirical Correlation Between Penetration Resistance and Internal Friction Angle of Sandy Soils, Japanese Geotechnical Society, Soils and Foundations Vol. 36, No 4, 1-9, 1996.
[10] Firat S., Stability Analysis of Pile-Slope System, Scientific Research and Essay vol. 4 (9), pp. 842-852, 2009.
[11] National Standardization Agency, Geotechnical Design Requirement, Indonesian Standard, SNI 8460:2017, 2017.

8th Int. Conf. on Structure, Engineering & Environment (SEE), Mie, Japan, Nov.10-12, 2022, ISBN: 978-4-909106094 C3051

FIELD PERFORMANCE EVALUATION OF ENVIROMENTALLY FRIENDLY PREFABRICATED VERTICAL DRAIN (PVD)

Dea Pertiwi
Geotechnical, Tunnel, and Structure Division, Ministry of Public Works and Housing, Indonesia

ABSTRACT

The application of natural materials for soil improvement has recently been highly considered. Prefabricated Vertical Drain (PVD) is widely used in Indonesia to accelerate the process of settlement of soft soil. PVD made from jute fibers tend to decompose easily in the soil after the service period is over, thus not storing plastic waste underground. After providing good hydraulic and mechanical performance when tested in the laboratory, jute PVD was tested in the field, which is in a small pond area in Kendal Regency, Central Java. The depth of the soft soil is 20-24 m and is still influenced by tides. Through the installation and monitoring of geotechnical instrumentation, it turns out that up to 120 days (4 months) after construction, the consolidation rate in natural and synthetic PVD areas has reached > 90%. Under preloading, the settlement is estimated 10% greater than the synthetic PVD area. Monitoring results also predict the effective depth of jute PVD installation is 14 m, in the transition from soft silty clay to clayey sandy silt with the largest permeability coefficient (k) of 9 x 10^{-8} cm/s and consolidation coefficient (Cc) of 0.86. At this depth, the largest value of vertical compression and excess pore pressure were detected. It can be concluded that in a limited (very small) experimental scale area, the installation of pre-construction instrumentation must consider the effect of heavy equipment loads working on the instrumentation points because it will greatly affect the accuracy of the monitoring results.

Keywords: PVD, Natural materials, Field performance, Geotechnical instrumentation

INTRODUCTION

Prefabricated Vertical Drain (PVD) technology made from polymer has been widely recognized as one of the soil improvement technologies with its main function of dealing with the problem of settlement on soft soil by accelerating the consolidation process. The demand for the use of PVD technology in Indonesia is very large because the soft soil area in Indonesia covers 10 million hectares or about 10% of Indonesia's land area [1]. Preloading with PVD is one of the technologies used, beside other soil improvement technologies.

In addition to synthetic PVD, natural PVD is also widely used, especially outside Indonesia (Japan, Korea, Bangladesh, India) mainly because of environmental preservation considerations. The advantages of PVD made from natural materials are non-toxic, recyclable, high liquid absorption, relatively fast disintegration time in the soil due to the nature of the material that is easily biodegradable. Thus, in less than a year the PVD material has decomposed in the soil. This is very suitable for dense urban areas because the location of the former PVD installation can be used for other underground constructions.

In 2015 to 2017 a study was conducted on natural fibers that have the potential as raw materials for making PVD on a laboratory scale with a variety of natural materials and PVD geometries to obtain a PVD model with the best technical performance [2] and [3]. In 2018, verification of the model studied in 2017 was carried out through the creation of a trial scale physical model to monitor actual performance in the field and compare it with synthetic PVD [4].

LOCATION OF OBSERVATIONS

Figure 1 shows the geological map of Kendal regency. From the map, it is known that there are recent alluvial deposits consisting of sand and gravel along the main rivers. The Holocene Formation is a very soft grey clay containing layered shells and is in the form of a sand lens towards the highlands in the south.

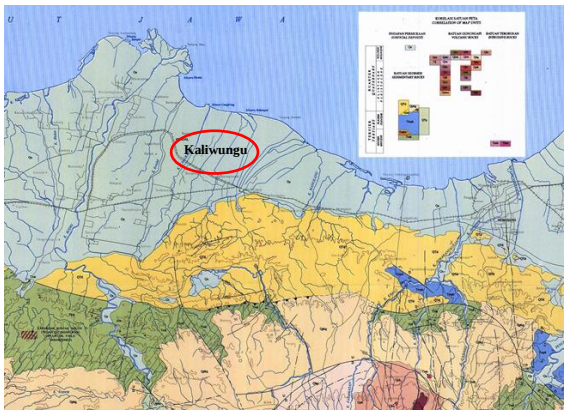

Fig. 1 Geological condition

The location of observations is in Kaliwungu district, located at Kendal Regency port highway and is ± 2.5 km before the Kendal port location so that the ponds around the site are still affected by the tides. Considering its hydrogeological conditions, Kaliwungu is an area that often experiences flooding with a flood water level that is regulated so that it can irrigate rice fields of residents (Fig. 2).

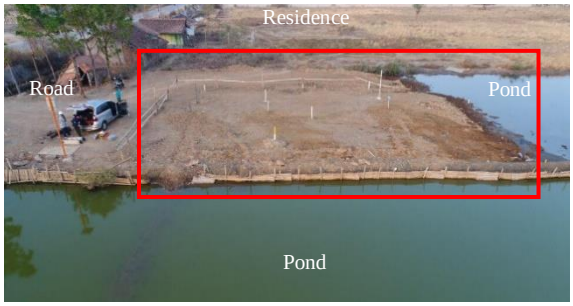

Fig. 2 Area of observation

The soil layer investigated from two boreholes, BH-1 and BH-5 data are grey soft clayey sandy silt with very soft consistency to a depth of 6.00 meters. Underneath there is a grey clayey sandy silt with a soft consistency to a depth of 20.50 – 21.00 meters. Borehole 1 (BH 1) indicates grey clayey sandy silt was found with a firm to stiff consistency, up to a depth of 30.00 meters.

Three locations of Cone Penetation Test (CPT) are plotted into a correlation graph for mechanical sondir [5] and showed in Fig. 3 and Fig. 4. From CPT-1 up to a depth of 16.40 meters found very soft to soft clayey sandy silt with a predicted value of undrained shear strength (c_u) 12.5 to 25 kPa. At a depth of 16.60 – 21.20 meters found clayey sandy silt with soft consistency and a predicted c_u of 25 to 30 kPa, and below it is followed by silty clay and sandy silt with firm consistency and a predicted c_u of 50 kPa. Estimation of undrained shear strength refers to [1].

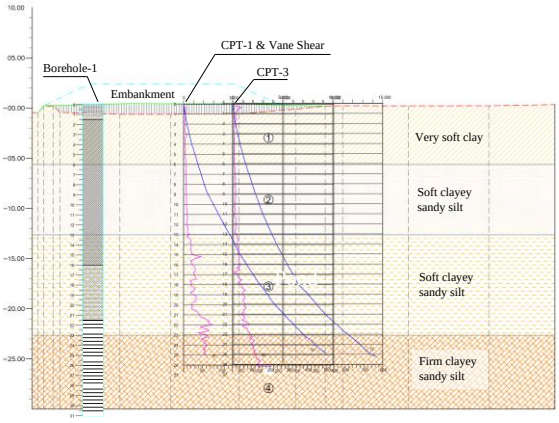

Fig. 3 Longitudinal section of observation area

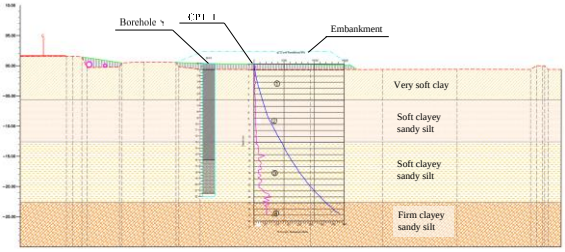

Fig. 4 Cros section of observation area

PREFABRICATED VERTICAL DRAIN (PVD)

The type of PVD installed is natural PVD. The filter blanket material is woven jute fiber, while the core material is coconut fiber. PVD is 9.5 cm wide and 11 mm thick. Synthetic PVD as a comparison in this study is made of non-woven geotextile material and polypropylene core with a width of 5.25 m and a thickness of 1.2 mm. PVD is installed up to a depth of 23.5 m with an installation space of 1.2 m using a triangular pattern. The working platform is 1.0 m high; sand (horizontal drainage) is 0.5 m thick, and the embankment (preloading) is 1.5 m high, which has considered the critical embankment height. Layout of PVD installation and instrumentation modified from [6] and given in Fig. 5.

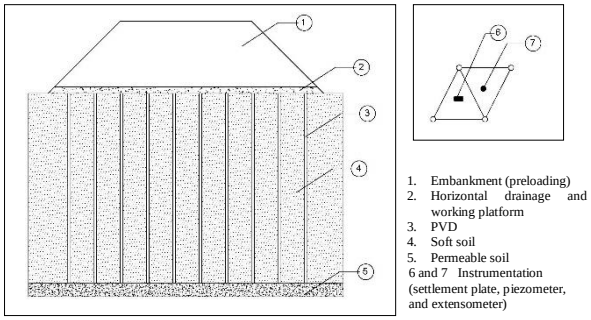

Fig. 5 PVD and instrumentation layout

FIELD OBSERVATIONS

Instrumentation installation aims to observe the field performance of embankment after being improved with PVD and preloading. The procedure follows the Indonesian Standard for Geotechnical Design Criterias [7], PVD specification [8], and instrumentation specification [9]. Figure 5 illustrates the layout of the instrumentation installation.

Piezometers are installed to determine the pore water pressures that occur at different layer depths and are positioned between the installed PVDs (see Fig. 5). The number of installations is a minimum of one observation point in each layer [10].

The inclinometer is installed at the toe of the embankment to determine the lateral direction of soil movement with the installation procedure that refers to [11] and [12]. The inclinometer must be installed on the part of the embankment slope that is most prone to stability or with the inclinometer depth entering to a hard soil layer where lateral soil movement will not occur**.**

Settlement plates are installed at distance of 50 meters above the original soil surface and 3 (three) points are installed in a cross section at the centre of the embankment and both left and right sides to describe the settlement contour. The installation of fixed reference points on soil conditions that are not affected by subgrade subsidence aims to determine the subgrade settlement of soft soil. The monitoring of the settlement plate aims to observe the magnitude of the settlement when PVD and preloading are constructed [9].

Extensometers or deep settlement probes are installed to determine the movement in each soil layer in the vertical direction. The extensometer is placed in each soil layer which has different soil properties and soil consistency [9].

RESULTS AND DISCUSSION

Prediction of post-construction settlement using the ASAOKA method as well as the actual reduction of geotechnical instrumentation monitoring results indicate that up to 120 days (4 months) post-construction, consolidation in natural PVD and synthetic PVD areas has reached > 90%. However, monitoring was continued for up to 210 days (7 months). Predicted settlement 7 months after construction is 104 cm.

Settlement plates and surface markers

Under preloading, the settlement of natural PVD is estimated 10% greater than the synthetic PVD. Monitoring of settlement plates and surface makers in the natural PVD installation area, showed that the surface settlement at the embankment ranges from 90 – 100 cm, while at the toe of the embankment 20 cm. In the synthetic PVD installation area, the surface settlement at the embankment is between 70 – 90 cm, while at the toe of the embankment it is 40 – 50 cm.

Magnetic extensometers

In natural PVD area the largest vertical compression due to PVD installation and embankment filling occurred in Extensometer-1 at a depth of 14 m, in the transition between very soft to soft clayey sandy silt with c_u = 19 kPa, ϕ' = 24°, the largest permeability coefficient (k) of 9 x 10^{-8} cm/s and consolidation coefficient (Cc) of 0.86. The vertical compression in this layer is 55 cm and is the largest post-construction compression.

Post-construction spider magnet readings in synthetic PVD area occurred in Extensometer-3 at a depth of 3.5 m, in very soft clay layer. Similar with Extensometer-1, the last reading on the spider magnet at a depth of 11 m, 16 m and 21 m was only able to take before PVD installation and preloading. It is suspected that heavy equipment traffic above the extensometer point caused the hole to be clogged with sand, because the hole was not properly protected.

However, the Extensometer-3 in the area between natural PVD and synthetic PVD can still be monitored until the end of construction. The reading results indicate that the data fluctuates during the PVD installation process, and the compression of soft soil gradually becomes consistent after both types of PVD installation and preloading (Fig. 6).

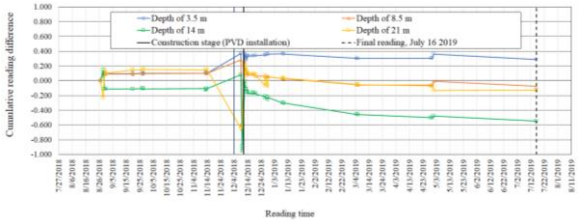

Fig. 6 Compression of soft soil by extensometer reading in PVD area

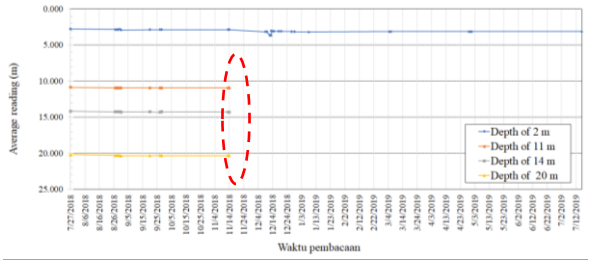

Fig. 7 Monitoring average depth of Extensometer-1 (area of natural PVD)

Inclinometer

At this observation site, the inclinometer is placed at toe of the embankment. The lateral movement in the transverse direction of the embankment or A-B direction (Southeast) is 56.11 mm (in very soft clay at a depth of 2 m) with an incremental displacement of 13 mm per month (Fig. 8). Meanwhile in the transverse direction of the embankment or C-D direction (Southwest) is 76.05 mm (on very soft soil at a depth of 4 m) with an incremental displacement of 20 mm per month. Readings are taken pre-construction, during construction and post-construction.

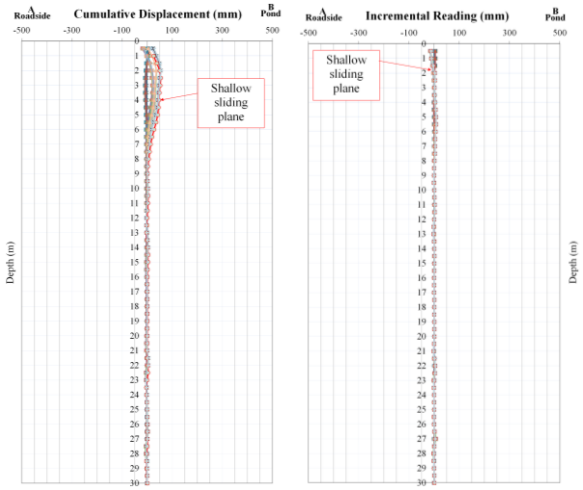

Fig. 8 Inclinometer readings

Piezometers

Four months after construction, equilibrium conditions have been reached in the natural PVD area. However, data collection still continues to seven months. Constant pore water pressure near zero in Piezometer-1 at reaches values of -159 kPa (10 m depth), -4 kPa (20 m depth), and -3 kPa (30 m depth). In the synthetic PVD installation area which was monitored using a Piezometer-2, equilibrium condition has also been reached with constant pore water pressure approaches zero at values of -19 kPa (5 m depth), 1.2 kPa (15 m depth), and -14 kPa (25 m depth).

The largest excess pore water pressure occur at a depth of 10-15 m. Below that, the effect of PVD installation and embankment filling did not appear too significant. As with the extensometer, the piezometer tip cannot be read after PVD installation. It is suspected that heavy equipment traffic above the piezometer point caused the borehole to be clogged with sand, because it was not properly protected.

Figure 9 illustrates pore pressure reading before, during, and 3 to 7 months after the PVD installation and preloading. Final fully instrumented embakment shown in Figure 10. The procedure for embankment filling and preloading refers to Division 3 of the General Specifications of Highways [13].

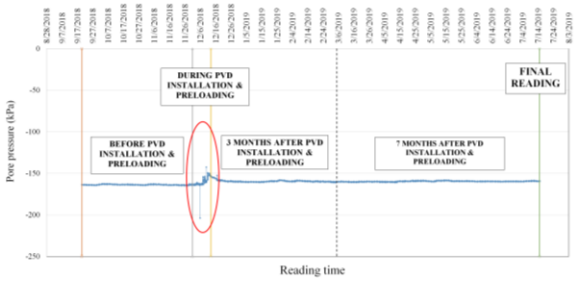

Fig. 9 Piezometer reading

The findings from field observations are summarized as follows:

1) Seven months after construction, both types of PVD showed great field performance and provided a significant settlement acceleration.
2) Installation of PVD is effective up to a depth of 14 m, in the transition from soft silty clay to clayey sandy silt with values of c_u of 19 kPa and ϕ' of 24°, the largest coefficient of permeability, k is 9 x 10-8 cm/s and Cc of 0.86.
3) The vertical compression in this layer is 55 cm and is the largest post-construction compression.
4) The results of monitoring excess pore water pressure show that the largest excess pore water pressure during construction and post construction occurs at a depth of 10-15 m. In addition, the calculation of the stress distribution using the Boussinesq analysis gives the greatest increase in effective stress occurring up to a depth of 15 m.

Fig. 10 Final area of embankment

CONCLUSIONS

In field application natural PVD can match the performance of synthetic PVD. On a laboratory scale, PVD made from natural materials has also been proven to have good properties.

Observations of external factors such as fluctuations in rainfall and the influence of tides should be considered in determining the design parameters, and they are easier to simulate through numerical modeling. Direct field observation is possible by making an observation pipe to get groundwater level fluctuations during the construction period until the service period is exceeded.

The installation of instrumentation must pay attention to the effects of construction work to avoid damage to the instrument due to heavy equipment traffic during construction. The security of the installed instrumentation must be done properly.

It can be concluded that in a limited (very small) experimental scale area, the installation of pre-

construction instrumentation must consider the effect of heavy equipment loads working on the instrumentation points because it will greatly affect the accuracy of the monitoring results.

ACKNOWLEDGMENTS

The author would like to thank the Geotechnical, Tunnel, and Structure Division for providing the opportunity to write down the results of research, development, and evaluation of the field performance of natural PVD, so it can be used as a lesson learned.

REFERENCES

[1] Ministry of Settlement and Regional Infrastructure. Pt T-08-2002-B. Geoguide 1 – Occurrence and General Nature of Soft Soils, Guideline of Road Embankment on Soft Soils. 2002.

[2] Moelyani, D. The Development of Local Materials for Prefabricated Vertical Drain (PVD) Technology. ISBN: 978-602-264-141-4. Road and Bridge Research and Development Center (Pusjatan). December 2015.

[3] Pertiwi, D., Iqbal, M., Aldiamar, F. Performance Evaluation of Natural-Based Indonesian Made Prefabricated Vertical Drain (PVD). ISBN: 978-602-264-136-6. Road and Bridge Research and Development Center (Pusjatan). December 2017.

[4] Pertiwi, Dea. Trial Scale of Natural-Based Indonesian Made Prefabricated Vertical Drain (PVD). Road and Bridge Research and Development Center (Pusjatan). December 2018.

[5] CUR. Building on Soft Soils. A.A Balkema/Rotterdam/Brookfield/1996. The Netherlands. 1996.

[6] BSI. 2007. BS-EN: 2007 Execution of Special Geotechnical Works – Vertical Drainage. BS EN 15237:2007. British Standard. United Kingdom.

[7] National Standardization Agency. Geotechnical Design Requirement, Indonesian Standard, SNI 8460:2017. 2017.

[8] Directorate General of Highways. SKh-2.3.6. Special Specification (Interim-2) of Prefabricated Vertical Drain (PVD). February 2017.

[9] Directorate General of Highways. SKh-1.3.7 Special Specification (Interim) of Geotechnical Instrumentation. December 2015.

[10] National Standardization Agency (BSN). SNI 6461:2012. Procedure for Installation and Reading of Vibrating Wire Piezometer. 2012.

[11] National Standardization Agency (BSN). SNI 3404:2008. Guidance of Inclinometer Installation and Monitoring the Horizontal Movement of the Ground. 2008.

[12] TRB. Use of Inclinometers for Geotechnical Instrumentation on Transportation Project. Transportation Research Board. http://onlinepubs.trb.org/onlinepubs/circulars/ec129.pdf. 2018.

[13] Directorate General of Highways. General Specifications for Road and Bridge Construction Works. September 2018.

8th Int. Conf. on Structure, Engineering & Environment (SEE), Mie, Japan, Nov.10-12, 2022, ISBN: 978-4-909106094 C3051

AN APPROACH STUDY OF REDUCING THE SUB-BALLAST THICKNESS OF RAILWAY USING GEOTEXTILES

Prof.Dr. Saad F.I. AL-Abdullah[1], Mr. Zaman T. Teama [2], Maysaloon A. Zaidan[3] and Dr.Suha Aldahwi [4]

[1] B.Sc., M.Sc., PhD (CE).MISSMGE.M.I.ASCE, Faculty of Engineering. Isra University, Jordan

[2] B.Sc., M.Sc., Baghdad University, Baghdad, Iraq[2]

[3] B.Sc. Faculty of Engineering, Mustansiriyah University, Baghdad, Iraq

[4] B.Sc., M.Sc., PhD Faculty of Engineering. Isra University, Jordan

ABSTRACT

The Iraq transportation system suffers from poor and deformation in railways due to less maintenance and updating of the railroad. The country needs thousands of kilometers of new railways to develop the transportation system to transport goods and people. This paper will investigate the behavior of railways when changing the thickness of the sub-ballast and use geotextile above ballast, ballast/ sub-ballast interface, and sub-ballast/ subgrade interface through using the finite element approach by simulating the railway by the ABAQUS program. The sub-ballast thicknesses used are; 150, 200, 250, 300, 350, and 400 mm with 200mm ballast thickness and 4 m subgrade thickness. The results showed when the thickness of the sub-ballast increased by 50 mm it led to a reduction in deformation of about 7.2 %. Also illustrated that the best position to reduce deformation in the railway was when putting a geotextile above the ballast. The results illustrate that using geotextile above the ballast layer Equivalent to increasing the thickness of the sub-ballast layer by about 3.57 cm in decreasing deformation in the rail track.

Keywords: ABAQUS; Railway, Sub-ballast, Geotextile, Sub-ballast, and Equivalent Thickness

INTRODUCTION

Iraq considers a growing country, and its infrastructures suffer from destruction due to the wars and the absence of maintenance and updating of its railways. Iraq needs to construct a new railroad to improve the transportation system and carry people and heavy goods. So we need a stable railway able to resist track degradation and lateral instability, which may become a complex problem if we construct a weak railway structure under conditions of railroad loading [1].

The railway ballast layer consists of particles of course, aggregate due to the repeated heavy load of train become deteriorated let to increasing compressibility [2][3][4][5]. The effectiveness of geosynthetics in railroad tracks has signified investigated in the past, and it's established that geosynthetics generally increase road performance by decreasing the deformation and degradation of ballast [6][7][8][9][10][11][12][13][14]. Limited research has studied the interaction between geosynthetics ballast aggregates when large strain happens due to heavy repeated loading [15][16]. Suiker and de Borst [16] were studied by A numerical model to demonstrate the maximum plastic deformations produced during repeated loading. The effect of geotextile on improving railway was investigated by [11][12][17] [18] [19].

The investigation aims to estimate the effect of using geotextile instead of increasing the thickness of sub-ballast layers and studying the structural effect of using geotextile at different positions in railway structure on deformation, vertical settlement, and lateral displacement of the railway. The laboratory tests do not provide a comprehensive understanding of what happens and the mechanisms of stresses, strains, and deformations distribution in the layers of the railway when the train passes over the rail, so the numerical analysis (FEM) approach was used [15] to illustrate the effect of using geotextile of railway stability.

ESTABLISHMENT OF FINITE ELEMENT MODEL

The FE approach has been established to be a useful and valid method for predicting the responses of railway structures under loading conditions [1][20][21]. The researchers have used the FE approach to investigate the behavior of rail track response below heavy loads by numerical simulations, which focused on

the behavior ballasts layer with and without geotextile [12] [15] [21].

MODELING

ABAQUS has proved its validation in the analysis of geotechnical problems[22][23].Inthis investigation, a three-dimensional finite element model was built by simulating the railway with all its parts, multi-layer geotechnical material, including subgrade, sub-ballast, ballast, sleeper, and rail, as illustrated in Fig 1.

The rail track was simulated in the model with dimensions. The width and height of the subgrade are 12 and 4 m, respectively. For studying the effect of change thicknesses of the sub-ballast layer, five models were built with five sub-ballast thicknesses, 200, 250, 300, 350, and 400 mm, and the thickness of ballast and sleeper was 200 and 150 mm, respectively, for all models. For investigating the effect of geotextile and its position in the behavior of railroad, four models were built with layer thicknesses of sub-ballast. Ballast and sleeper were 200, 200, and 150 mm, respectively, with different positions of placing geotextile.

The gauge between the two rails of the track is 1.68 m, and the length of the sleeper is 2.5m. The rail is simplified as a rectangle with a width of 16 cm and a height of 5cm to ensure that the total area is equivalent to a 60 kg/m rail [21][24].

MATERIAL PROPERTIES FOR MAIN COMPONENTS

The input material properties of the ABAQUS models play important role in the results of the program. Table 1 illustrate the material properties used in the railway simulation, which are used in finite element analysis for railways [21] The linear response is used for simulating the subgrade, granular layers, and geotextile [13][22].

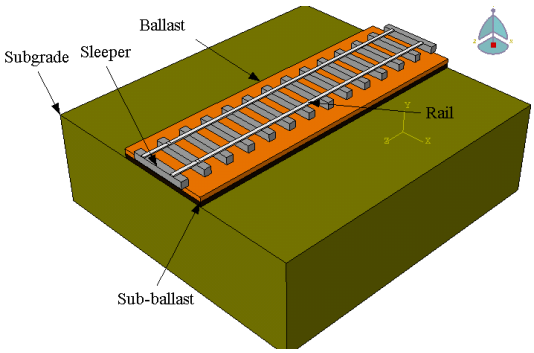

Fig.1 ABAQUS Model Geometry

Table 1 Input Materials Properties

Property	Subgrade	Sub Ballast	Ballast
Modulus of elasticity (N/m)	125×10^5	800×10^5	1200×10^5
Density (Kg/m3)	1632	1700	1590
Poisson's Ratio	0.4	0.35	0.25

EFFECT OF CHANGE THICKNESS OF SUB-BALLAST

To investigate the effect of change thickness of the sub-ballast layer in decrease deformation, vertical settlement, and lateral displacement the railway five thicknesses of the layer were used which are 200, 250, 300, 350, and 400 mm.

Use at most three levels of headings that correspond to chapters, sections and subsections. The first level headings for chapter titles should be in 10pt, bold, justified, and upper case font. Leave one blank line before and after the first level headings, respectively.

EFFECT OF USING GEOTEXTILE

The effect of using geotextile in decrease deformation, vertical settlement, and lateral displacement of railway investigate by putting the geotextile layer in different positions; at subgrade/ sub-ballast interface (above subgrade), at sub-ballast/ ballast interface (above sub-ballast), and at ballast/ sleeper interface (above ballast) and evaluate which position gives minimum deformation, vertical settlement, and lateral displacement in the rail track.

ELEMENT TYPE AND MESH SIZE

All parts of the models were used finite element type 8-node continuum three-dimensional brick element (C3D8R) [22]. The mesh size of elements changes from medium for subgrade to fine for rail as shown in Fig.2.

LOAD CALCULATION

The load which used in the simulation of train load was dynamic wheel load is empirically expressed as the static load wheel, with the value of 178.71 KN was considered to simulate a train speed of 80 km/h and a wheel diameter of 970 mm,[21] [25][26].

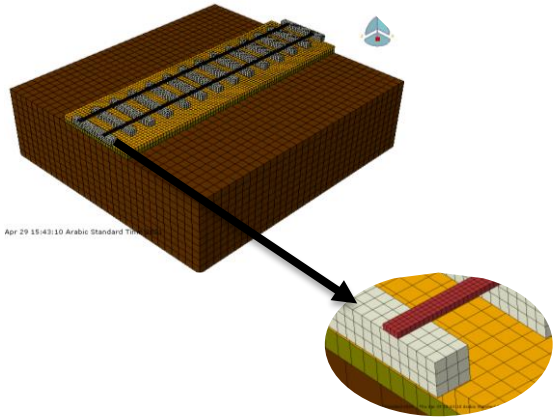

Fig. 2 mesh size of FE model

RESULTS AND DISCUSSIONS

Effect of Change Thickness of Sub-Ballast

The deformation, vertical settlement, and lateral displacement were measured at the surface of the ballast layer under the sleeper which plays a very important role in the stability of the railway and safe pass of the train, for each thickness of sub-ballast layers which are 200,250,300, 350 and 400 m. The results of the analysis illustrated that the increasesing the thickness of sub-ballast lare led to decreases in deformation, vertical settlement, and lateral displacement of rail track as shown in Figs 3-5 respectively.

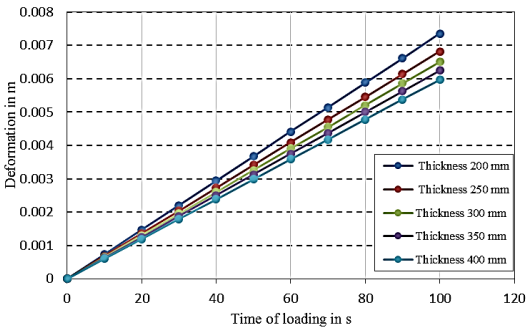

Fig.3 Shows the relationship between deformation and thickness of sub-ballast for thicknesses 200,250,300,350 and 400 mm

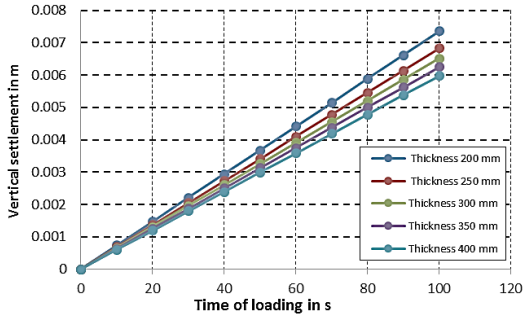

Fig. 4 Shows the relationship between vertical settlement and thickness of sub-ballast for thicknesses 200,250,300,350 and 400 mm

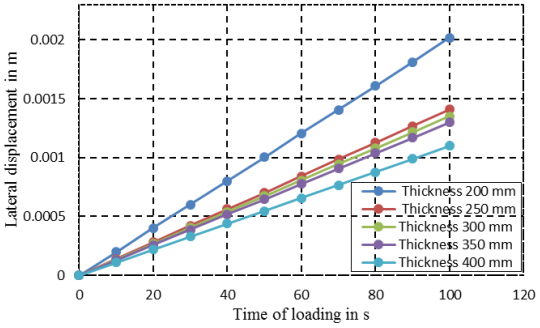

Fig. 5 Shows the relationship between lateral displacement and thickness of sub-ballast for thicknesses 200,250,300,350 and 400mm

Figs. 6-9. Shown the relationship between the deformation, vertical settlement, and lateral displacement in railtrack and thickness of the sub-ballast layer which illustrated that the deformations decrease as the thickness of sub-ballast increased.

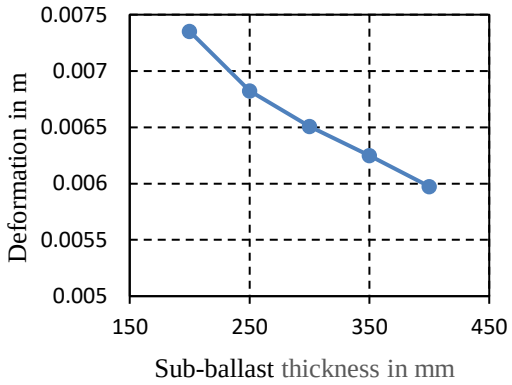

Fig. 6 Shows the relationship between deformation and sub-ballast thickness

Effect of Using Geotextile

to investigate the effect of geotextile in reduce deformation, settlement, and lateral displacement in rail track the geotextile was putted in three positions, above subgrade, above sub-ballast, and above ballast layer, the result shows that the maximum

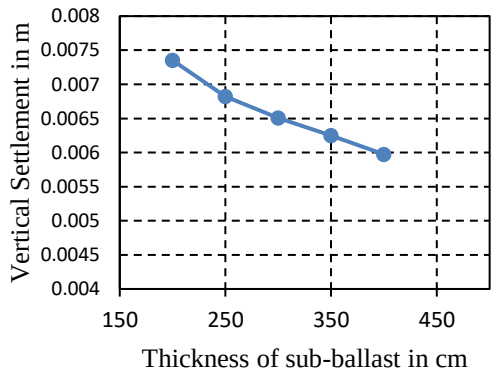

Fig. 8 Show the relationship between the lateral displacement and sub-ballast thickness

Effect of geotextile in reducing deformations and vertical settlement was when putting it above the ballast layer as shown in figs. 9-10, respectively. The results also show that the putting of geotextile above sub-ballast layer was less effective than putting it above ballast in decrease deformations and vertical settlement and the putting geotextile above subgrade was given minimum effect in

reducing deformation as illustrated in Figs. 9-10.

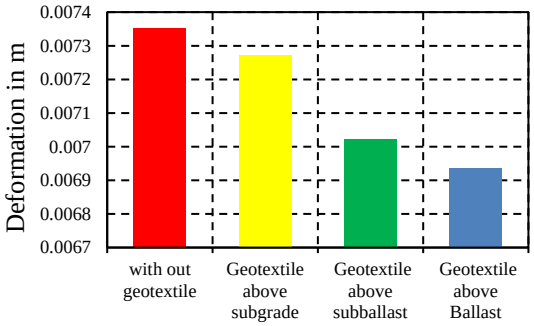

Fig. 9 shows the relationship between the position of geotextile and deformation in the rail track

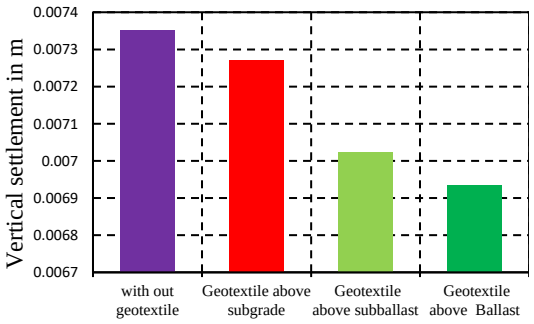

Fig. 10 shows the relationship between the position of geotextile and vertical settlement on the rail track

Comparison between models

thickness of sub-ballast and the effect of position of reinforcement of geotextile in reduce deformation, vertical settlement, and lateral displacement of rail track. The Colum with the red color shown in the figures represents a railway without reinforcement and with a sub-ballast thickness of 20 cm, which is considered a reference (origin) model for comparison between all models,

Fig. 11. Demonstrated the deformation for all models, from the figure, we can see the increase in thickness of the sub-ballast layer effected in decreasing the deformation of the rail track, the fig. 11. illustrated that are two models with deformation

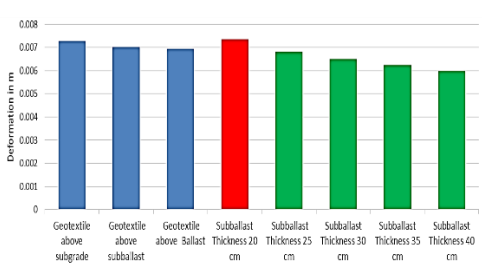

Fig. 11 Shows the deformation for all models

so close each one to other, one of the models with a thickness of sub-ballast 25 cm which has deformation 0.00682 m and another one with geotextile reinforcement was putted above a ballast layer which has deformation 0.00693 m.

Fig. 12 shows the vertical settlement for all models, illustrating that the change in thickness of sub-ballast was more effective in reducing vertical settlement than geotextile. Also, the figure shows that the least deformation, vertical settlement, and lateral displacement in rail track were for rail track with a sub-ballast thickness of 40 cm. The rail track with large deformation (excluding the reference model), was in rail track with reinforcing geotextile above subgrade.

Fig.13. Shown the lateral displacement for all tracks, the figure is illustrated that the use of geotextile led to an increase in lateral displacement at the surface of the ballast, while the increased thickness of the sub-ballast led to a decrease in lateral displacement.

Percentage of Reduction in Deformations

Fig. 14. Shown the percentage of reduction in rail track deformation for each model illustrated that the model with a sub-ballast thickness 40 cm has the largest percentage of reduction in deformation and the model with reinforcement at subgrade has the smallest percentage of reduction in deformation

The Sub-Ballast Thickness that Geotextile Equivalent it

This part will determine how much geotextile is equivalent to the thickness of sub-ballast in reduce the same value of deformation, the value of deformation obtained from using geotextile was 0.00693 when putting the reinforcement above ballast layer, from the relationship between deformation and The thickness of sub-ballast thickness, we can find that geotextile is equivalent to 3.57 cm of sub-ballast thickness as shown in Fig. 15. Table 2 shown the equivalent thickness of the sub-ballast and the position of the geotextile

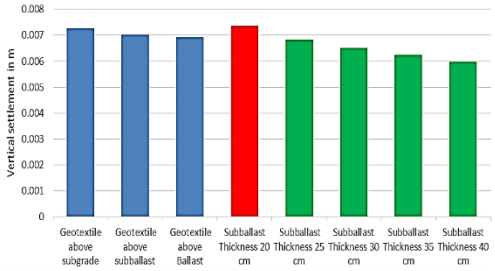

Fig. 12. Shown the vertical settlement

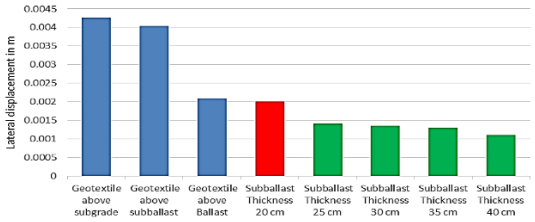

Fig. 13. Shown the vertical settlement

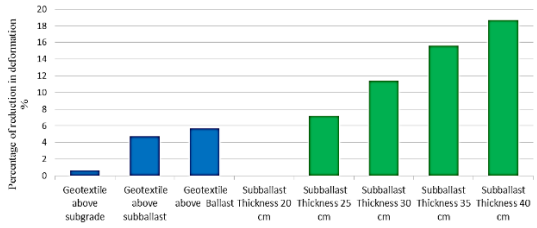

Fig. 14. percentage of reducing deformation in rail track

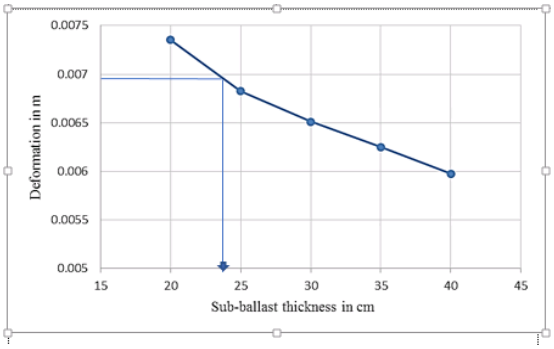

Fig. 15. Shown the calculation of equivalent thickness of sub-ballast

Table 2. Illustrate the Geotextile position equivalent to the thickness of sub-ballast

Geotextile position	Equivalent to sub-ballast thickness (cm)
Above ballast	3.57
Above sub-ballast	2.85
Above subgrade	N/P

CONCLUSIONS

The simulation of railway track has investigated the behavior of rail track under train loading when the sub-ballast layer change thickness and the behavior of track when reinforced by a geotextile. The following conclusions are obtained from this research;

1. The increase in the thickness of the sub-ballast layer by 5 cm decreases the deformation by about 7.2% by reducing the stress reaching the subgrade and increasing the track's strength and stability.
2. The increase of the sub-ballast layer led to a decrease in the vertical settlement in the rail track through an increase in the distribution of loads come from the train.
3. As the thickness of the sub-ballast increase the lateral displacement decrease through decrease the stress at sub-ballast/ subgrade interface.
4. The use of geotextile reinforcement at ballast (sleeper/ ballast interface) led to a decrease in the deformation in the rail track by about 5.71 % through the distribution of the stresses at the sleeper/ ballast interface.
5. The use of geotextile at ballast/ sub-ballast interface led to a decrease in the deformation about 4.65%
6. The using of geotextile at sub-ballast/ subgrade interface (above subgrade) led to decrease deformation about 0.68 %.
7. The maximum useful position of geotextile as reinforcement layer to reduce deformation in rail track was above ballast layer and the minimum influence of position reinforcement was in above a subgrade layer
8. The maximum percentage of reduction in deformation was for rail track with sub-ballast thickness 40 cm and the minimum percentage of reduction deformation was when reinforcing the rail track with geotextile above subgrade layer.
9. The use of geotextile as a reinforcement layer at the sleeper/ballast interface equivalent to increasing the thickness of the sub-ballast layer by about 3.57cm.

LIMITATIONS OF THIS STUDY

The properties of geotextile play a very important role increase the benefit of using it, in this paper the modules of elasticity of geotextile was 120 MPa, the geotextile which has a modulus of elasticity less than 120 MPa not evaluated The result and conclusion represented in this paper shows that we need more investigation before used geotextile above subgrade, sub-ballast, and ballast.

REFERENCES

[1] Selig, E. T. and Waters, J. M., (1994). Track geotechnology and substructure management, Thomas Telford, London (reprint 2007).

[2] Anderson, W. F., and Fair, P. (2008). "Behavior of railroad ballast under monotonic and cyclic loading." J. Geotech. Geoenviron. Eng., 134(3), 316–327.

[3] Lackenby, J., Indraratna, B., McDowell, G., and Christie, D. (2007). "Effect of confining pressure on ballast degradation and deformation under cyclic triaxial loading." Geotechnique, 57(6), 527–536.

[4] Lu, M., and McDowell, G. R. (2006). "Discrete element modelling of ballast abrasion." Geotechnique, 56(9), 651–655.

[5] Indraratna, B., Nimbalkar, S., Christie,D., Rujikiatkamjorn, C., andVinod, J. S. (2010a). "Field assessment of the performance of a ballasted rail track with and without geosynthetics." J. Geotech. Geoenviron. Eng., 136(7), 907–917.

[6] Göbel, C. H., Weisemann, U. C., and Kirschner, R. A. (1994). "Effectiveness of a reinforcing geogrid in a railway subbase under dynamic loads." Geotextile Geomembr., 13(2), 91–99.

[7] Raymond, G. P. (2002). "Reinforced ballast behavior subjected to repeated load." Geotextile Geomembr., 20(1), 39–61.

[8] Shin, E. C., Kim, D. H., and Das, B. M. (2002). "Geogrid-reinforced railroad bed settlement due to cyclic load." Geotech. Geol. Eng., 20(3), 261–271. [9] Brown, S. F., Kwan, J., and Thom, N. H. (2007). "Identifying the key parameters that influence geogrid reinforcement of railway ballast."Geotextile Geomembr., 25(6), 326–335.

[10] Indraratna, B., and Salim, W. (2003). "Deformation and degradation mechanics of recycled ballast stabilized with geosynthetics." Soils Found.,43(4), 35–46.

[11] Indraratna, B., Khabbaz, H., Salim, W., and Christie, D. (2006). "Geotechnical properties of ballast and the role of geosynthetics in rail track stabilization." Ground Improv., 10(3), 91–101.

[12] Indraratna, B., Shahin, M. A., and Salim, W. (2007). "Stabilising granular media and formation soil using geosynthetics with special reference to railway engineering." Ground Improv., 11(1), 27–44.

[13] Ibraheem. Farhan., G. Sofia, and Z. Teama.(2016) Evaluation of Using Geosynthetic Material and the Process of Grouting to Improve Pavement Performance over Sand Dunes Subgrade, International Conference on Transportation and DevelopmentASCE.https://doi.org/10.1061/9780784479926.078

[14] Rowe, P.K., and Jones, C. J. F. P. (2000). "Geosynthetics: Innovative materials and rational design." Proc., GEOENG 2000, Technomic, Lancaster, PA

[15] Indraratna, B., Nimbalkar, S. (2013) Stress-Strain Degradation Response of Railway Ballast Stabilized with Geosynthetics DOI:10.1061/(ASCE)GT.1943-5606.0000758

[16] Suiker, A. S. J., and de Borst, R. (2003). "A numerical model for the cyclic deterioration of railway tracks." Int. J. Numer. Methods Engrg., 57(4), 441–470.

[17] Raymond, G. P., and Ismail, I. (2003). "The effect of geogrid reinforcementon unbound aggregates." Geotextile Geomembr., 21(6), 355–380.

[18] Jirousek, O., et al. (2010). "Numerical modeling of the reinforcing effect of geosynthetic material used in ballasted railway tracks., Proc., Inst. Mech Eng. F: J. Rail Rapid Transit, 224(4), 259–267.

[19] Montanelli, F., and Recalcati, P. (2003). "Geogrid reinforced railways embankments: Design concepts and experimental test results." Proc., IABSE Symp., Antwerp, Netherlands, 212–213.

[20] Esveld, C. (2001). Modern railway track, MRT Productions, Zaltbommel, Netherlands.

[21] Jiang and Nimbalkar, (2019) Finite Element Modeling of Ballasted

[22] Ibraheem Farhan, G. sofia, Zaman teama. (2017) An approach in study behavior of sand dunes to use as subgrade in paved road under moving loads. congress on technical advancement ASCE

[23]Ahmed H. Hussein and Al-Zaidee S. Rohaima. (2020) Three-Dimensional Explicit Finite Element Simulation of Piled-Raft Foundation. Journal of Engineering Number 3 Volume 26 March.

[24] Doyle, N. F. (1980). "Railway track design: a review of current practice," in Occasional Paper no. 35, Bureau of Transport Economics, Canberra, ACT: Commonwealth of Australia.

[25] Jeffs, T., and Tew, G. P. (1991). A Review of Track Design Procedures, Vol. 2- Sleepers and Ballast. Melbourne, VIC: BHP Research Melbourne Laboratories

[26] Sun, Q. D., Indraratna, B., and Nimbalkar, S. (2015). Deformation and degradation mechanisms of railway ballast under high frequency cyclic loading. J. Geotech. Geoenviron.Eng.142:04015056.doi:10.1061/(ASCE)GT.1943-5606.0001375

8th Int. Conf. on Structure, Engineering & Environment (SEE), Mie, Japan, Nov.10-12, 2022, ISBN: 978-4-909106094 C3051

EVACUATION RISK ASSESSMENT OF FLOODED SLOPING ROAD IN THE CITY OF KAMAISHI

Yuriko Matsubayashi[1] and Mako Ebina[2]
[1]Faculty of Science and Engineering, Iwate University, Japan; [2] Aomori, Japan

ABSTRACT

As heavy precipitation due to climate change increase, need of quantitative assessment of flood risk gain in importance. Studies have been made on evacuation risk evaluation of flooded road. However, there is little agreement on risk assessment of flooded sloping road. The purpose of this work is to establish method of estimating risk of evacuation on flooded, water flowing slopes.

In the hazard map of the city of Kamaishi, hazardous areas in the events of heavy rain, such as flooded area, debris flow and steep slopes are shown. It also describes the danger of water flow running over the sloping roads, which prevented evacuation in the past disaster. However quantitative risk assessment of the sloping roads is not performed. This paper presented risk evaluation of evacuation on foot on the slopes, using fluid force calculated using estimated velocity and water depth with the maximum rainfall in the past. Velocity and water depth are estimated using rational runoff formulae and velocity formulae,

As a result, more than 30% of the 86 sloping roads described in the hazard map are unsuitable for evacuation route and a positive correlation is observed between the risk and upstream area.

In conclusion, a simple evacuation risk assessment on sloping road with water flow could be performed with calculating fluid force using estimated velocity and water depth.
Keywords: Flood, Inundation, Sloping road, and Evacuation

INTRODUCTION

On 12th, October, 2019, Hagibis made landfall on Izu Peninsula in Shizuoka prefecture, Japan. After that, Hagibis made its way to northward, weakened to an extratropical cyclone by 12 a.m 13th. Heavy rain induced by Hagibis caused great damages especially in Tohoku region in Japan. 105 people are killed by flood and sediment disasters and 3 people are missing. In Iwate prefecture, At Fudai forecast point in north area of Iwate, rainfall of 95.0mm per hour is recorded. 3 people are killed and 7 people are injured by disaster induced by Hagibis.

We carried out an interview survey for residents in Iwate prefecture. The result of the survey shows that people are exposed to danger during evacuation.

At Touni town in city of Kamaishi (Fig. 1 and 2), several evacuees obstructed by water flow on the sloping road. As shown in Fig.2, the sloping road is evacuation route to Touni elementary and junior high school, which is the designated evacuation shelter and refuge place. Around 0 a.m. on 13th, the sloping road was inundated. As water was flowing over like a waterfall, some residents couldn't arrive at the evacuation shelter.

In the city of Kamaishi, they GIS hazard map published on the internet. The hazard map shows predicted flood, sedimentary disasters, tsunami hazard and the designated evacuation shelters and refuge places [4]. The map also shows past disaster information caused by heavy rains. The past disaster

Fig. 1 Location of the city of Kamaishi in Iwate prefecture, Japan.
An arrow and text are added on map [5]

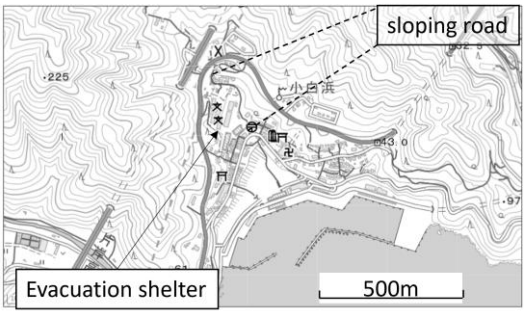

Fig.2 Sloping road at Touni town.
Arrows and text are added on map [5]

information is collected from local resident. It shows many sloping roads which water or debris had flown over while past heavy rain disaster. The sloping road danger in Touni town has been indicated in the hazard map as past disaster information; nevertheless, evacuees were exposed to danger.

It is well known that evacuation under flooding condition is affected by water depth and velocity, Suga et al [1] investigated safety threshold of water depth and velocity. They proposed evaluation index using fluid force, buoyant power and friction force [1]. Asai et al [2] use specific power to calculate safety index for evacuation. Dias et al [3] carried out an experimental study to investigate human walking behavior under inundation.

Although there are studies of evacuation under flooding conditions, there are few knowledge about the danger of walking on sloping road under flooding. In this study, we assessed evacuation risk using estimated water depth and velocity calculated with runoff volumes, slope and width of roads. We extracted roads which are pointed out past inundation in the hazard map in the city of Kamaishi. Precipitation data at Kamaishi station of AMeDAS from 12th to 13th in October in 2019 are used for estimation. There are various reasons for inundation or water flow over sloping roads. We categorized the roads by reasons and determined catchment areas to calculate runoff volumes in the catchment basin.

The results indicate that 30% of the roads shown as flooded in the past are at risk for impassable during heavy rain.

METHOD

We extract 86 roads from the hazard map which flooded in the past. Fig. 3 shows location of targeted roads in 7 areas which are Unosumai, Kurihashi, Nakatsma, Kasshi, Kosano, Kamaishi and Hirata/Touni. The gradation shows elevation. 7 areas are administrative districts in the city of the Kamaishi. Each area has geographical characteristic. Unosumai area includes lower reaches of Unosumai river and cape, while Kurihashi area is in upper reach of Unosumai river. Kasshi, Nakatsuma, Kosano and Kamaishi areas are located along Kasshi river. Most houses are built in floodplain of Kasshi river or on steep slopes along tributary rivers. Hirata/Touni area is in the south of the city. Houses are built along small rivers or on a hill.

All targeted roads are paved with asphalt. The roads have gutters for drainage, stream flowing along roads or culvert installed under the road.

The roads are categorized by area, number of houses along the road and cause of flooding. The specifications of roads, length, width, elevation slope, number of houses along the roads and detour route for evacuation, are calculated from GIS map [5]. Table 1 shows the categorized road number. A road without

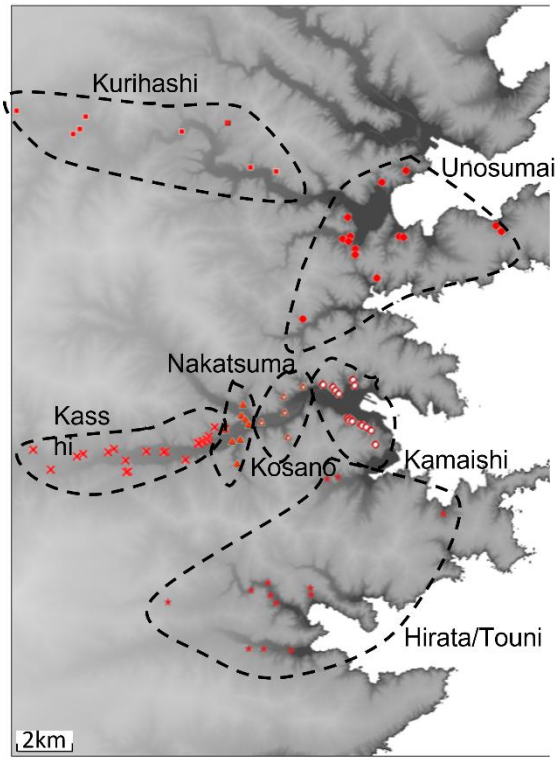

Fig. 3 Location of extracted roads.
Markers and dot lines are drawn on map [5]

Table 1 road numbers in areas

Area name	Total	No catchment area	No house
Unosumai	14	0	2
Kamaishi	15	0	1
Hirata	13	1	4
Kurihashi	8	1	3
Kasshi	23	7	1
Nakatsuma	6	1	0
Kosano	7	3	0
Total	86	13	11

catchment area is inundated by Kasshi river flooding or due to poor drainage. A road without house along it has low possibility being used for evacuation route. For the 86 roads, most causes of flooding are according to overflowing of stream along the road or culvert under the road. With heavy rainfall, increasing of flow rate or clogging by debris make water elevation higher, therefore overflown water run over the road. Hence, in this paper, we consider predicted runoff volume of stream along or under a road as flow rate flowing over the road.

In the example of Touni town, a river flowing under the road clogged therefore water flow over the road. As the slope of the road is steep, water ran down over the road at high speed, thus evacuees are

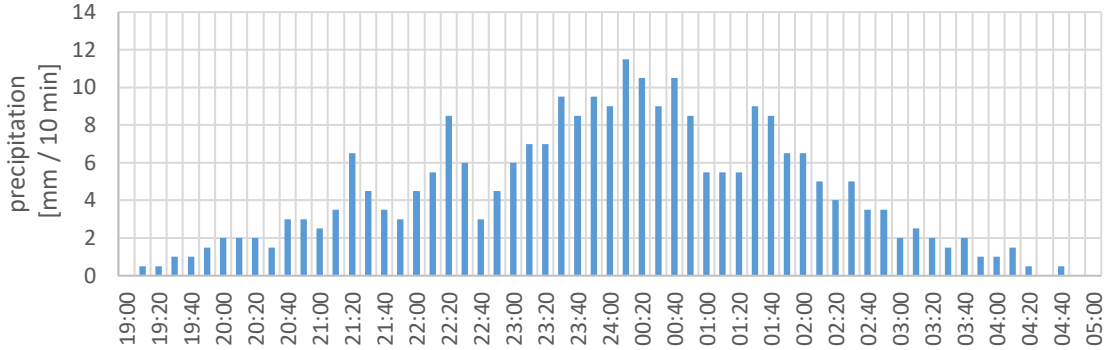

Fig. 4 AMeDAS rainfall at Kamaishi station. p.m.9, 12th, October ~ a.m.5, 13th October

obstructed evacuation.

Velocity and water depth on the roads

Evacuation risk of each road is indicated in two ways using estimated velocity and water depth on the roads.

Velocity and water depth of water flow on the roads are estimated with runoff volume calculated with rational formulae (Eq. (1), (2) and (3)) using catchment area and precipitation data shown in Fig. 4 [6].

$$Q = \frac{1}{3.6} \times f \times r \times A \tag{1}$$

$$t = \frac{30\sqrt{A}}{\sqrt{2}} \tag{2}$$

$$T = \frac{1}{3600} \times \frac{L}{W} \tag{3}$$

Where q is unit width flow rate, f is discharge coefficient, r is the design rainfall intensity, A is catchment area, t is inlet time, T is flow time, time of concentration is summation of $t + T$, L is Length of river channel from its outlet point to its farthest point, W is flow velocity by Kraven's formulae.

We obtained velocity and water depth with Manning's formula for rectangular channel (Eq. (4) and Eq. (5)) on the assumption of that the roads are very wide rectangular channel with constant width and slope.

$$v = \frac{Q}{bh} = \frac{1}{n} \times R^{\frac{2}{3}} \times i^{\frac{1}{2}} \tag{4}$$

$$h = \left(\frac{nQ}{bi^{\frac{1}{2}}}\right)^{\frac{2}{5}} \tag{5}$$

Where v is flow velocity, b is width of road, n is Manning's roughness coefficient, R is hydraulic radius and i is slope. As the roads are considered as very wide channel, we regarded R as h.

Assessment of evacuation risk

We compared results of risk assessment calculated with comparison between fluid force and resistance force [1] and specific force per unit width [2].

Fluid force and resistance force

Suga et.al. [1] compared fluid force and resistance force (hereinafter this is called $2D - F$) to evaluate risk for walking under water flow. We calculated fluid force with Eq. (6) Resistance force is friction force between shoe sole and the ground, calculated with Eq. (7). Eq. (8) is criterion. We added terms considering slope effect to the equations shown in Suga et.al.[1].

$$D = C_d \times \frac{\rho(u+v)^2 \times a}{2} + G_0 \sin i \tag{6}$$

$$F = f \times (G_0 \sin i - W) \tag{7}$$

$$F \geq \alpha D \tag{8}$$

Where D is fluid force, C_d is drag coefficient for human body, ρ is density of water, u is walking speed (0.4 m/s in this study), a is projected area of human body, G_0 is body weight (60kg ×9.8 m/s^2 in this study), F is resistance force, W is buoyant force and α is safety factor. α is set to 2 following Suga et. al. [1]

Specific force per unit width

We calculate specific force per unit M (hereinafter this is called M) with Eq. (9) to evaluate risk of walking under flooding following Asai et. al. [2]. Where g is gravity acceleration. Table 2 shows the criterion of M classified for man in twenties,

woman in twenties, elderly man and elderly woman, proposed by Asai et. al. [2]

$$M = \frac{v^2 h}{g} + \frac{h^2}{2} \tag{9}$$

Table 2 Criterion of specific force per unit [2]

	Safe for evacuation	Obstruction from flooding
Male 20s	$\boldsymbol{M < 0.125}$	$\boldsymbol{M > 0.250}$
Female 20s Male senior	$\boldsymbol{M < 0.100}$	$\boldsymbol{M > 0.200}$
Female senior	$\boldsymbol{M < 0.080}$	$\boldsymbol{M > 0.160}$

RESULTS

Catchment area and road slope are important element for flow condition. Fig. 5 shows relationship of catchment area and slope of roads. The developing standard of steep slope is fixed by law in Japan. From the viewpoint of concern for the wheelchair, installation criterion of slopes at public spaces has been decided. Sloping path steeper than 1/12 needs arm rail on both side of the path. Sloping path instead of stairs in buildings must be milder than 1/8.[7]

We see from Fig.5 that most roads are milder than 1/15 and have small catchment area. 1/15 slope is enough gentle for walking in dry condition, however it's steep as river slope. Fig. 4 shows that target roads include many roads laid along or over the steep river or mountain stream.

To compare the characteristics of each area, Fig. 6 shows road slope in each area. In Kasshi area, 15 of 23 roads are milder than 1/15. Although the roads are gentle, water flow from catchment area lying on steep slopes on both side of Kasshi river, induce flooding on roads.

Table 3 shows the results of risk assessment with water depth, $2D - F$ and M value, for each area. The assessment results are different for each method. Estimated water depth are sufficiently low for on-foot evacuation under flooding condition on most of targeted roads. With the assessment using $2D - F$, 28 roads are considered not safe for on-foot evacuation.

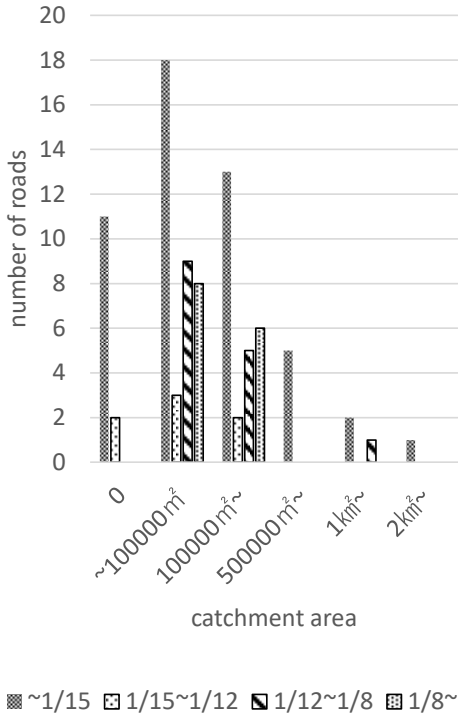

Fig. 5 Catchment area and road slope

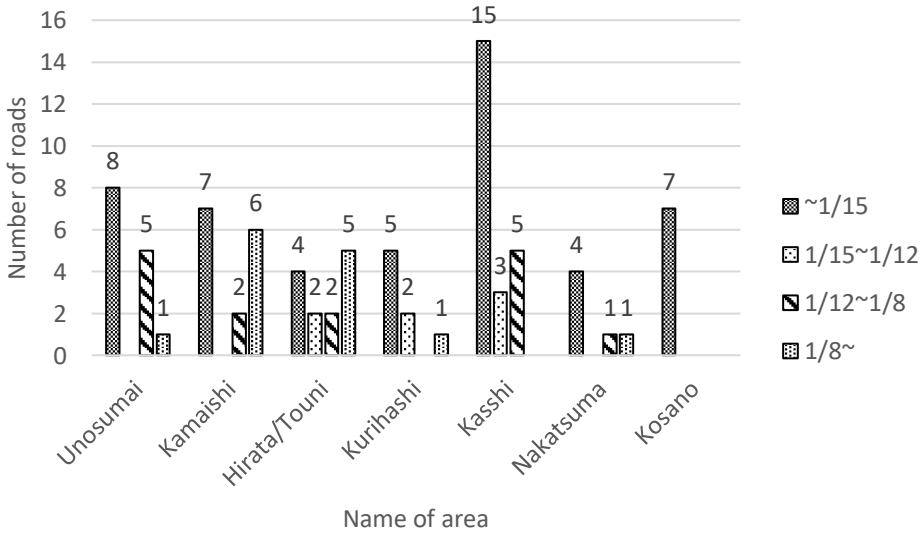

Fig. 6 Road slope in each area

Table 3 Result of evacuation risk assessment

	water depth > 0.3m	Comparison between fluid force and resistance force	specific force per unit width		
			M > 0.123	M > 0.100	M > 0.08
Unosumai	1	8	8	9	10
Kamaishi	1	4	4	4	5
Hirata/Touni	1	7	7	7	8
Kurihashi	0	3	5	5	5
Kasshi	1	2	3	4	4
Nakatsuma	0	3	3	3	4
Kosano	1	1	1	1	2
total	5	28	31	33	38

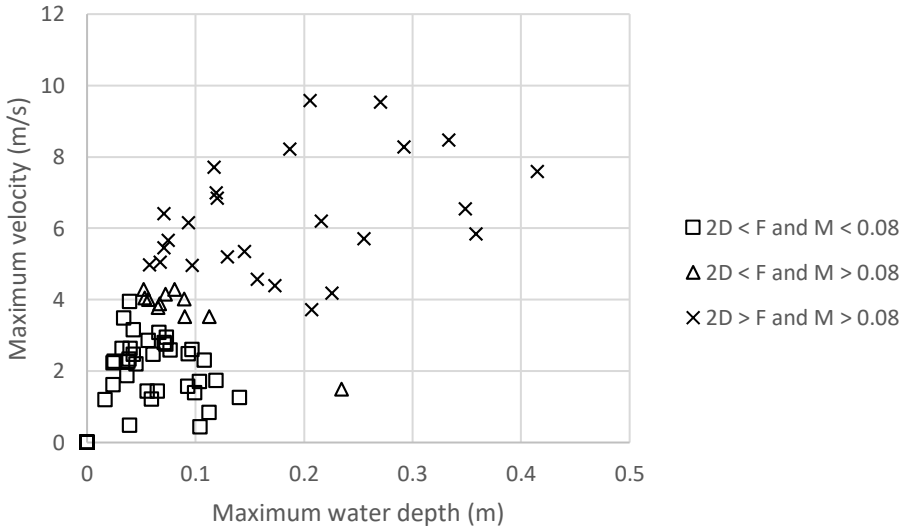

Fig. 7 Maximum velocity, maximum water depth and results of assessment

With the assessment using M, 38 roads are considered not safe for on-foot evacuation of elderly women. The results of roads in Touni (Fig. 2) are safe assessed by water depth while not safe using $2D - F$ and M.

We compared the assessment results with $2D - F$ and M. Fig 7 shows the relationship between maximum velocity and maximum water depth of each road. The roads are categorized by results of two risk assessment method, $2D - F$ and M. Fig. 7 shows that criterion of M is stricter than $2D - F$. In Fig.7, an outlier data is excluded. Maximum velocity and maximum water depth of the excluded road are 15.1m/s and 0.72m since the catchment area is much larger than others. Besides, the road with outlier data is in Kasshi area and not safe for risk assessment with $2D - F$ and M.

DISCUSSION

This paper describes the result of risk assessment of on-foot evacuation under flooding condition in the city of Kamaishi. The assessment is carried out for roads extracted from hazard map. The studies introduced a simple method to assess evacuation risk of sloping road with catchment area. The results show the different between the assessment method and evaluated disaster scales of evacuation route. Therefore, from the point of view of risk assessment of inland flooding and publishing hazard map, it is recommended to establish cause of flooding and effect of sloping roads so that the risk would be adequately estimated. On the other hand, because of

work cost and smallness of disaster-scale, only few hazard maps present accurate disaster prediction for inland flooding. In addition, as the assessment in this paper includes assumptions concerning estimation of flow rate over the roads, it needs further study to enhance accuracy.

CONCLUSIONS

In the city of Kamaishi, roads flooded in the past disaster are shown in hazard map. Many of the flooded roads are sloping and have streams along or under them. On-foot evacuation risk of the roads under heavy rain condition is estimated, under the assumption that these inland flooding are occurred by overflowing of river, stream, or culvert along or under each road. The results show difference of the assessment results between assessment methods.

ACKNOWLEDGMENTS

The author would like to thank to all members of construction division of Kamaishi city hall for helpful suggestions and approval for survey.

REFERENCES

[1] Suga K, Uesaka T, Yoshida T, Hamaguchi K, Chen Z, Preliminary Study on Feasible Safe Evacuation in Flood Disaster, Annual journal of hydraulic engineering, JSCE. 1995 Volume 39 Pages 879-882. in Japanese

[2] Asai Y, Ishigaki T, Baba Y and Toda K,Safety Analysis of Evacuation Routes Considering aged Persons During Underground Flooding, Annual journal of hydraulic engineering, JSCE. Volume 53 Pages, 859-864. in Japanese

[3] Dias. C., Rahman, N. A., Zaiter, A., Evacuation under flooded conditions: Experimental investigation of the influence of water depth on walking behaviors, International Journal of Disaster Risk Reduction, 58(2021) 202192

[4] The city of Kamaishi, Kamaishi city floods and landslide hazard map ,https://kamaishi.nigedoki-map.com/ , in Japanese

[5] Ministry of infrastructures, Transport and Tourism Geospatial information Authority of Japan, GIS MAPs, https://maps.gsi.go.jp, in Japanese

[6] Kagoshima prefecture, Design Criteria of River Works https://www.pref.kagoshima.jp/ah07/infra/kasen-sabo/kasenseibi/sekkeikijyun.html, in Japanese.

[7] Ministry of infrastructures, Transport and Tourism Japan Meteorological Agency, https://www.jma.go.jp/jma/index.html , in Japanese.

8th Int. Conf. on Structure, Engineering & Environment (SEE), Mie, Japan, Nov.10-12, 2022, ISBN: 978-4-909106094 C3051

EXPERIMENTAL STUDY ON ECO-BINARY MORTAR AT HIGH -TEMPERATURE EXPOSURE

R.A Malek[1,2] and S. Gooven[2]
[1]Centre of Excellence for Frontier Materials Research, Universiti Malaysia Perlis, Jalan Kangar-Alor Setar, Kampung Seriab, 01000 Kangar, Perlis, Malaysia
[2]Faculty of Chemical Engineering Technology, Universiti Malaysia Perlis, Taman Muhibbah, 02600 Jejawi, Perlis, Malaysia

ABSTRACT

Concrete or mortars exposed to high temperatures has impact in their strength and durability. One of the strategies to overcome this issue is by replacing cement with other alternative pozzolanic materials. In this study, the non-beneficial agricultural waste, namely rice husk ash (RHA), which has high silica content under controlled burning conditions makes it appropriate to be used as partially replacement in mortar. The addition of RHA ranging 5 to 20 wt. % has significantly influenced the appearance of mortars as they perform darker grayish color as the increasing amount of RHA. Unexpectedly, this study revealed that greater compressive strength was obtained almost doubled the value for 5 wt.% addition of RHA followed by 10 and 15 wt.% addition of RHA, respectively. However, addition of 20 wt.% RHA was not a preferable mixture as it achieved only 12.49 MPa of compressive strength which is below than the conventional mortar. Due to high temperature exposure up to 1,093 °C, the process influenced the moisture content in the cement paste and change the appearance of the sample into whitish-gray color as well as their physical and residual mechanical properties. All samples recorded relative strength values between 0.35 and 0.16. All these findings have correlation with thermal analysis conducted for all samples. Overall, the samples has started to evaporate the free water contained in the cement past at temperature of 82 to 140 °C followed by decomposition of Ca(OH)2 at 445 to 454 °C. It can be concluded that, 5 wt.% of RHA addition provided reasonably good properties in comparison to other mixture. This study exhibited the consumption of these economical and feasible agricultural waste materials is acceptable to be implemented in concrete industry and thus bearable to solve dumping and environmental issues.

Keywords: rice husk ash, high temperature, mortar, supplementary cementitious materials

INTRODUCTION

Supplementary cementitious materials (SCM) with pozzolanic properties, such as blast furnace slag, silica fume, fly ash, and rice husk ash, have played an important role and are widely adopted in the construction industry nowadays. Among SCM candidates, it was found that more researchers have been involved in the possibility of using rice husk ash (RHA) than other agricultural waste and other byproducts due to high siliceous content ranging from 85 to 95% [1] with pozzolanic or hydraulic properties in proper controlled burning conditions [1]–[3].

It was reported by [4] that the amount of rice production globally had hit 501 million tons (MT), involving more than 160 thousand hectares of harvested area in 2016. By comparing the South Asian countries as presented in Table 1, Malaysia has a relatively small production of rice as it only covers 0.21% of Malaysia's land area. However, data provided by [1] shows a significant increment of 56% growth rate in paddy production as well as RHA between 2002 and 2022. To some extent, the utilization of no-beneficial use of RH to produce secondary byproducts has been spotlighted as it is bearable to overcome a few issues related to environment and disposal of RH in landfills.

Table 1 Comparison data on rice production and area harvested in the South Asian Region [4].

Country	Population (10^3)	Production (MT)	Area harvested (10^3 ha)
World	7,466,964	501.5	162,521
Asia	4,462,677	453.2	143,072
Indonesia	261,115	45.6	13,870
Philippines	103,320	12.1	4,722
Vietnam	94,569	28.1	7,743
Thailand	68,864	21.6	10,780
Malaysia	31,187	1.8	700

Among these justifications, a major concern on their effect to sustain good strength during fire exposure could be considered since utilization of RHA in mortar or concrete would impact their properties. When exposed to high temperatures, the chemical composition and physical structure of the concrete changes considerably due to dehydration released by bound water of calcium-silicate-hydrate (C-S-H) starting at 200 °C, disintegrates calcium hydroxide

($Ca(OH)_2$) and C-S-H breakdown at 400-600 °C, followed by loss of strength, durability and microstructural changes as it reaches temperatures greater than 1,000 °C [1], [2].

RESEARCH SIGNIFICANCE. RHA has been identified as an acceptable pozzolans replacement for cement in mortar. However, utilization of RHA as supplementary cementitious materials that are capable of resisting high temperatures has been given far too little attention by previous researchers. Therefore, it is important to understand if the alteration in mortar composition would affect the properties of the mortar at high temperatures.

EXPERIMENTAL PROCEDURES

RAW MATERIALS. Materials used in this study were ordinary Portland cement (OPC), fine aggregate, and rice husk ash. Rice husks (RHs) are locally available in the Northern state of Malaysia, Perlis, sourced from a rice milling factory known as Kilang Beras BERNAS Sdn. Bhd., Simpang Ampat, Perlis, Malaysia.

RICE HUSK ASH (RHA) PREPARATION AND CHARACTERIZATION. RH was prepared under controlled burning conditions at 650 °C for 1 hour with a heating rate of 10 °C/min, followed by grinding and sieving processes to obtain 63 µm particle size. The RHA was analyzed using X-ray Fluorescence (XRF) technique for chemical composition, which are listed in Table 1. Meanwhile, the outer and inner epidermis of RHA and their respective XRD patterns that proved the ashes contained mostly amorphous silica phase are shown in Figures 1 and 2.

Table 1 The necessary details of Perlis RHA used in the study.

Parameters	RHA
SiO_2 (wt.%)	88.991
Al_2O_3 (wt.%)	0.050
Fe_2O_3 (wt.%)	0.117
CaO (wt.%)	1.177
MgO (wt.%)	0.596
K_2O (wt.%)	6.499
Na_2O (wt.%)	0.048
SO_3 (wt.%)	0.713
Other (wt.%)	1.809
Mean Particle size (µm)	386.4
Specific gravity	0.360

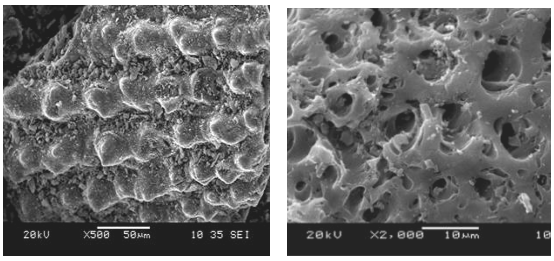

(a) (b)

Fig. 1 The (a) outer and (b) inner parts of RHA after completed burning process at 650 °C for 1 hour duration observed using scanning electron microscopy (SEM).

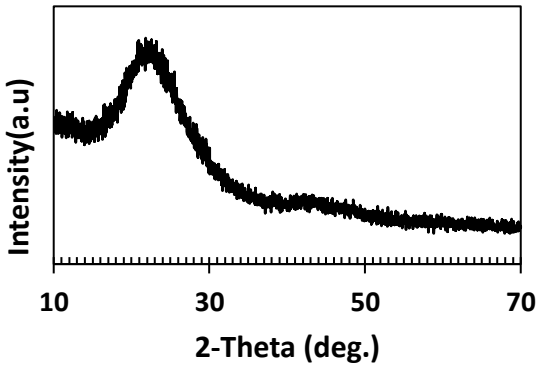

Fig. 2 XRD pattern of RHA

MIXING PROCEDURES. The amount of RHA, OPC, fine aggregates, and water required for the cube mold with a dimension of 50 x 50 x 50 mm was calculated as shown in Table 2. The first mixture was the control sample, while the subsequent mixtures, identified as M1 to M4, were mortar that was mixed with RHA at different compositions between 5 and 20% to be used for comparison. Water to binder (w/b) ratio demand was set at 0.4 for all mixtures. All the mortar mixtures were de-molded after 24 hours and then water cured for 28 days.

Table 2 Designations and mix proportions of mortar mixtures.

Mixture ID	OPC (wt.%)	RHA (wt,%)	Fine Aggregate (kg/m^3)	Water (kg/m^3)
Control	100	…	544	170
M1	95	5	544	170
M2	90	10	544	170
M3	85	15	544	170
M4	80	20	544	170

TESTING ON FIRE RESISTANCE. The mortars were heated up to 1,093 °C in an electric muffle furnace by following the ASTM E119 (ASTM International, 2020). This test method provides a standard time-temperature curve to which materials

and components are exposed to evaluate their resistance to fire as presented in Fig. 3.

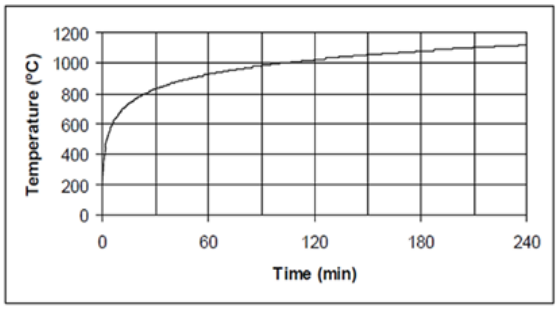

Fig. 3 Standard time-temperature curve according to ASTM E119 fire exposure.

RESULTS AND DISCUSSION

The forensic analysis by comparing the surface of mortar usually starts with visual observation of color change, cracking, and spalling of mortar surface that have been conducted to all samples after exposure to high temperature. Fig. 4 shows the mortar surfaces before and after exposure to high temperature. Color changes affected by high temperature can be easily identified by means of visual inspection. Before firing the samples, it can be seen obviously that samples with addition of RHA appear darker greyish color compared to the control sample. As the amount of RHA increases, a darker gray color will be obtained. However, discoloration occurred in all samples after the firing process was completed, which gave a final color of whitish-gray.

As per the abovementioned findings, it resulted in physical and chemical modification in the heated samples. As a consequence, cement paste experienced moisture evaporation or dehydration as well as shrinkage or mass loss; and thermal expansion characteristics between aggregate and cement paste caused samples to crack when exposed to high temperature. Detailed investigation by [5] found that water removal from the calcium-silicate-hydrate (C-S-H) structure has a relationship between water-binding energy and solids. Therefore, water contained in C-S-H structure will be eliminated starting from evaporation of free water followed by capillary water and physically bound water. There were voids spotted on all mortar surfaces, but long external cracking lines were visible for the control and M1 samples. As the amount of RHA increased greater than 5 wt. %, only shorter external cracking lines appeared. Surprisingly, no thermal spalling occurred that broke samples into pieces when heated up to 1,093 °C for all mixtures.

The effect of high temperature gave variations in mass loss at different mixtures in this study. By referring to Table 2, two different types of mass rates were calculated. Firstly, the mass difference after completing the curing procedure (denoted as Mass rate I), and secondly, the mass difference after completing the heating procedure (denoted as mass rate II). For mass rate I,

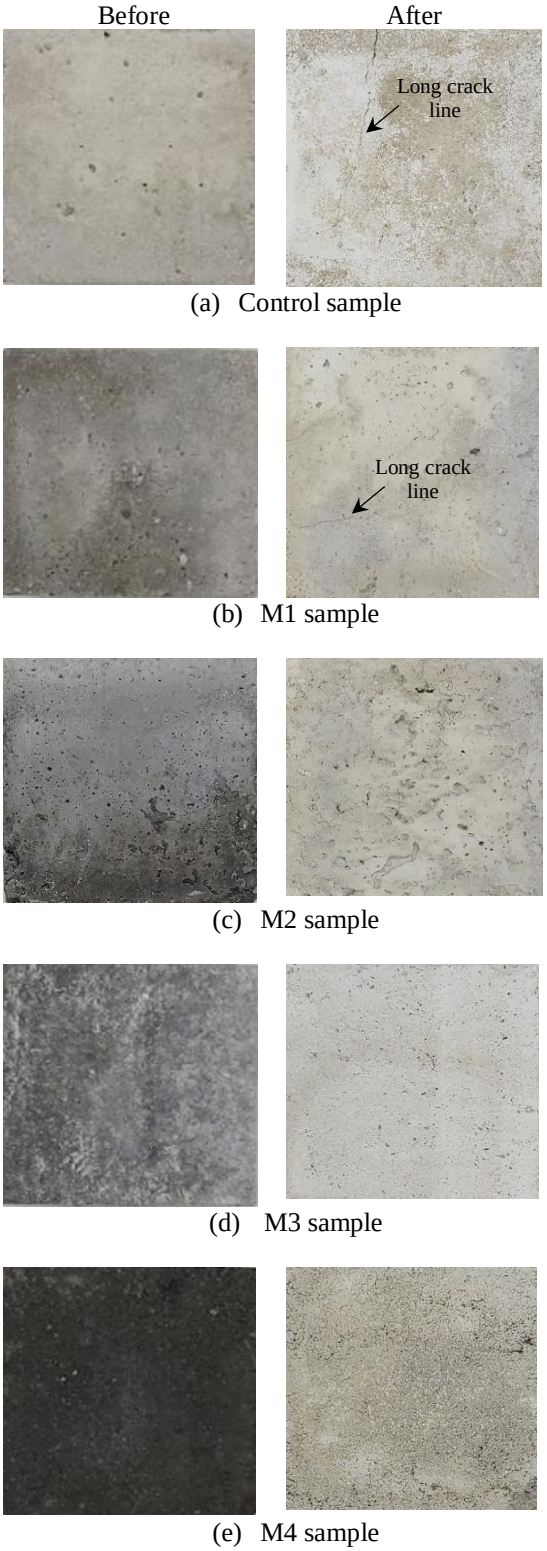

(a) Control sample

(b) M1 sample

(c) M2 sample

(d) M3 sample

(e) M4 sample

Fig. 4 Comparison on surface texture before and after exposed to 1,093 °C.

it shows that there was no mass loss during the curing process, but all the samples gained mass throughout the process as expected since the porous structure of RHA tends to absorb more water during the curing procedure. The sample ranging from 0 to 15 wt. % of RHA replacement showed comparable mass gain but increasing the amount of RHA up to 20 wt.% has resulted in more than double adsorption of water in C-S-H structure. Meanwhile, a similar trend in mass rate II was recorded ranging 4.9 to 6.3% as all the water binds in C-S-H structure were gradually removed during the heating process. To some extent, this finding fits well with the outcome of the visual observation.

The density variation in the RHA-based and conventional mortars could create the variation in compressive strength. Based on the experimental results of density, it was found that the control sample was denser than RHA containing mortars. As the amount of RHA increases in mortar, a greater amount of water will be absorbed in RHA porous particles. As water gets evaporated during the heating process, it forms voids that contribute to less dense mortars. The density of the control sample was 2.14 gcm^{-3} and diminished to 2.10, 1.97, 198, and 1.82 gcm^{-3} for M1 to M4 samples, respectively. Consequently, these voids that are filled with air will lead to detrimental effects on their strengths.

Table 2: Calculated data of mass loss in different conditions.

Mixture ID	Mass loss rate I (%)	Mass loss rate II (%)
Control Sample	0.6	5.1
M1	0.6	5.2
M2	0.6	4.9
M3	0.6	5.4
M4	1.7	6.3

The influence of RHA replacement on the compressive strength development of hardened mortar paste in two different conditions, namely unheated and post-heated, are presented in Fig. 5. It is evident from the results that the compressive strength of unheated samples in the control sample gave an average value of 25.73 MPa. This value is consistent with the conventional mortar made of a full mixture of ordinary Portland cement (OPC). Remarkably, the addition of RHA showed greater compressive strength values reaching 43.10 MPa for 5 wt. % RHA addition, followed by 37.22 MPa and 28.37 MPa for 10 and 15 wt. % RHA replacement, respectively, compared to the control sample. However, replacement of 20 wt. % showed that the mortar had drastically lost its compressive strength by more than half of the control sample. The relative compressive strength values of the concrete was recorded ranging 0.35 to 0.16 in parallel to the amount of RHA.

This trend is somehow related to the formation of portlandite at the early stages of the hydration reaction between cement and water. The amount of RHA replacement up to 20% in this study seemed to affect the efficiency of silica from the RHA reacting with free portlandite [2]. Nonetheless, the overall unheated compressive strength result in this study signifies that the mortar mixtures, regardless of the amount of RHA replacement, are superior for use as mortar for construction purposes.

Overall, it can be seen that the heated samples lose massive compressive strength with losses ranging from 64% up to 88%. The ranking is M1 > Control sample > M2 > M3 > M4, respectively. The relative strength was obtained as the percentage retained strength with respect to the unheated strength. The relative strength of concrete significantly decreased after high temperature exposure as expected since the moisture evaporation during high temperature exposure would have altered their mechanical properties [6], [7].

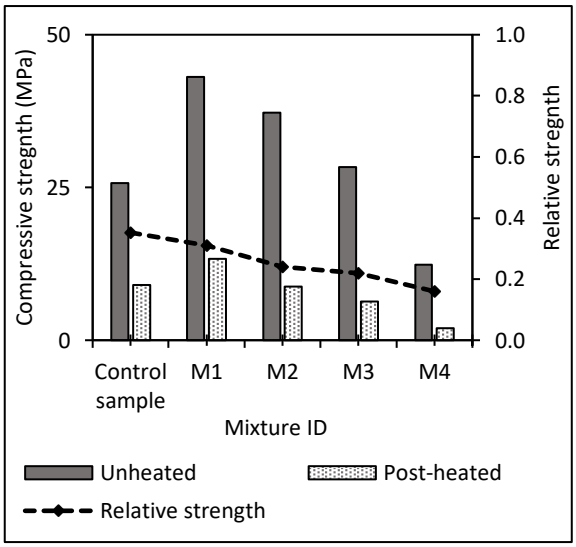

Fig. 5 Compressive strength of unheated and post-heated mortar samples at various RHA replacement amount.

All explanations on the effect of high temperature can be linked to the thermal analysis. Cement paste plays a vital role in the strength of mortar exposed to high temperatures. All the mortar samples were tested using thermogravimetric analysis (TGA) to determine the reaction of the samples at elevated temperatures and the results were compared and analyzed as presented in Fig. 6. After all the TGA patterns were compared with the control mix, it was found that mortars containing 5% to 15% RHA had a similar pattern with the control sample. However, the

sample containing 20% RHA showed an inconsistent pattern.

For the control mix, the first endothermic peak was observed at 48 °C, while for the M1 sample, the first endothermic peak was at 55 °C. For samples M2 and M3, their first endothermic peak was observed at 49 °C and 47 °C, respectively. This shows that the evaporation of free water takes place earlier in the control, M2, and M3 samples compared to the M1 samples. Another endothermic peak appeared denoted as (B) for all samples, except the M4 samples, which occurred at a temperature of 82 °C, 85 °C, 83 °C, and 140 °C, respectively. This shows that the dehydration of water still continues after the first endothermic peak due to further release of water from the samples.

In addition, all the samples experienced exothermic peaks within a certain temperature. The control and M1 samples had a single exothermic peak, with the exothermic reaction having a maximum peak at 224 °C and 321 °C, respectively. However samples of M3 and M4 had multiple exothermic peaks which ranged from 118 °C to 436 °C. This reaction indicates that gas was released from the samples.

The third endothermic peak (C) is considered the calcium hydroxide peak [8]. For this peak, all samples experienced the third endothermic peak at similar temperatures, which were at 445, 455, 454, and 454 °C, respectively. This peak is important as it indicates the decomposition of $Ca(OH)_2$ [9]. From the results, it was determined the decomposition of $Ca(OH)_2$ initiates faster in the control mix compared to other mortars containing RHA. The last peak is indicated as (D), and is the fourth endothermic peak (D) that represents the dehydration of C-S-H gel in the samples, which occurs at temperatures ranging from 692 to 710 °C and shows the possible generation of new phases due to high temperature.

Enormous mass changes were also found for all the samples. At the early stage (i), control samples had a mass loss of about 5%, followed by M1 (7.5%), M2 (6%), and M3 (10%) because of free water evaporation. The next mass loss (ii) takes place at a temperature range of 500 °C to 850 °C. During this temperature, the control sample had a mass loss of 6.7%, M1 sample had a mass loss of 5.8%, M2 sample had a mass loss of 5.5%, and M3 sample had a mass loss of 6%. This mass loss is due to the decomposition of $CaCO_3$. The sample containing 20% RHA (M4) could not be analyzed as it does not have any proper peaks. The TGA graph that was obtained showed a fluctuating pattern with endothermic and exothermic reactions that had taken place repeatedly. The mass loss was also continuous and the sample seemed to have a mass reduction of 20% throughout the process.

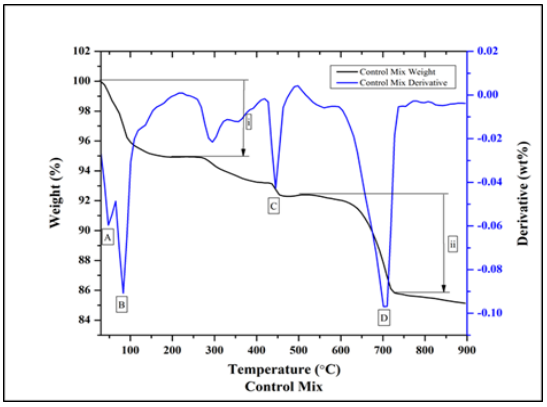

(a)

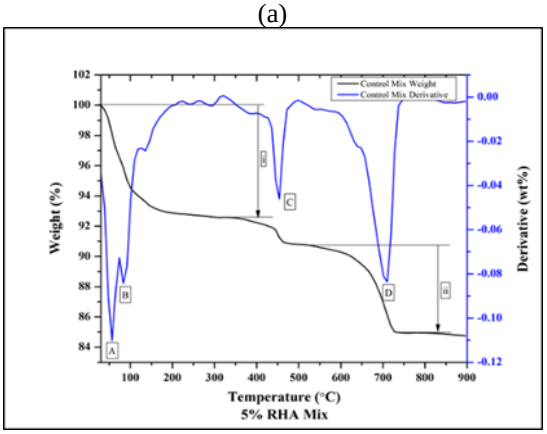

(b)

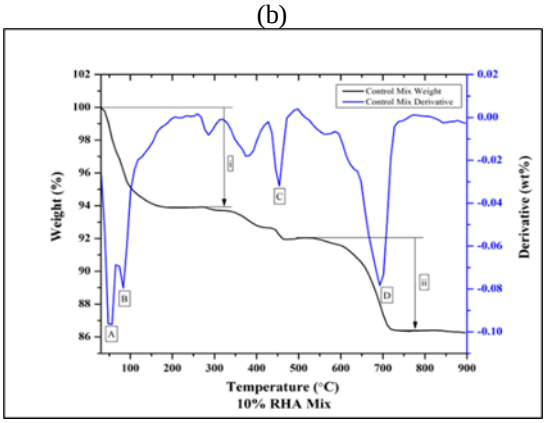

(c)

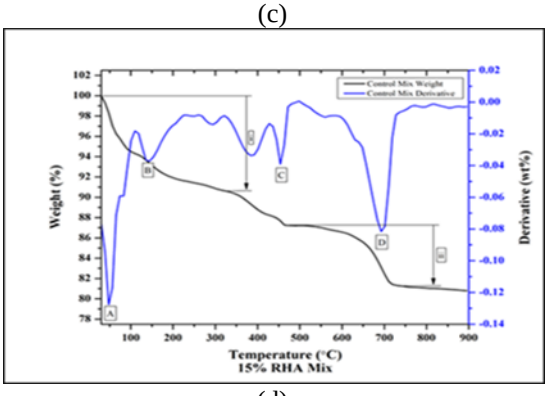

(d)

Fig. 6: TGA graphs for (a) control sample (b) M1 (c) M2 (d) M3 and (e) M4 of RHA replacement.

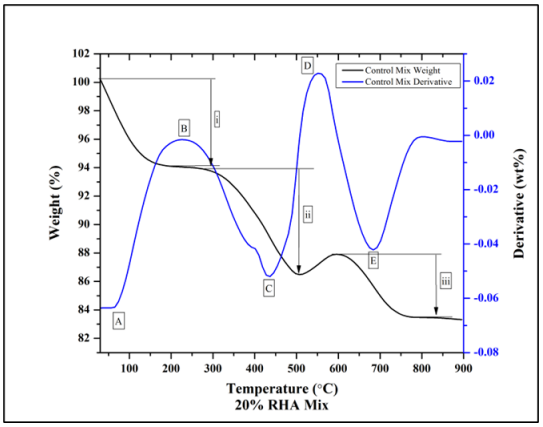

(e)

Fig. 6 (cont.): TGA graphs for (a) control sample (b) M1 (c) M2 (d) M3 and (e) M4 of RHA replacement.

CONCLUSIONS

This paper presented an experimental investigation on the effects of mortar to high temperature exposure with different amounts of RHA replacement. In general, this study generated an acceptable mortar property produced by using RHA as SCM that gives higher compressive strength and denser mortar since the porous structure of RHA increased the water demand in cement paste. However, exposure to high temperature revealed the color changes of the appearance of mortar from darker grayish to whitish-gray influenced by dehydration of cement paste. The residual compressive strength reduced more than half of the initial value as consequence of dehydration that altered their mechanical properties. Overall, the addition of 5 wt.% of RHA poses good characteristics and has potential to be used in construction fields.

ACKNOWLEDGMENTS

The authors would like to acknowledge the support from the Fundamental Research Grant Scheme (FRGS) under grant number of FRGS/1/2019/TK06/UNIMAP/02/6 from the Ministry of Higher Education (MoHE), Malaysia.

REFERENCES

[1] M. Amran *et al.*, "Rice husk ash-based concrete composites: A critical review of their properties and applications," *Crystals*. 2021.

[2] M. Thiedeitz, W. Schmidt, M. Härder, and T. Kränkel, "Performance of rice husk ash as supplementary cementitious material after production in the field and in the lab," *Materials (Basel).*, 2020.

[3] L. Hu, Z. He, and S. Zhang, "Sustainable use of rice husk ash in cement-based materials: Environmental evaluation and performance improvement," *J. Clean. Prod.*, 2020.

[4] "(PDF) The Status of the Paddy and Rice Industry in Malaysia." https://www.researchgate.net/publication/351223058_The_Status_of_the_Paddy_and_Rice_Industry_in_Malaysia (accessed Jul. 05, 2022).

[5] I. Hager, "Colour Change in Heated Concrete," *Fire Technol.*, 2014.

[6] F. M. Nazri, S. Shahidan, N. K. Baharuddin, S. Beddu, and B. H. Abu Bakar, "Effects of heating durations on normal concrete residual properties: Compressive strength and mass loss," 2017.

[7] K. Selvaranjan *et al.*, "Thermal and environmental impact analysis of rice husk ash-based mortar as insulating wall plaster," *Constr. Build. Mater.*, 2021.

[8] O. Arioz, "Effects of elevated temperatures on properties of concrete," *Fire Saf. J.*, 2007.

[9] W. H. Wang, Y. F. Meng, and D. Z. Wang, "Effect of rice husk ash on high-Temperature mechanical properties and microstructure of concrete," *Kem. u Ind. Chem. Chem. Eng.*, 2017.

8th Int. Conf. on Structure, Engineering & Environment (SEE), Mie, Japan, Nov.10-12, 2022, ISBN: 978-4-909106094 C3051

FAULT DETECTION USING PALSAR-1/2 IMAGE DATA FOR GROUNDWATER ANALYSIS (STUDY AREA: CENTRAL AND SOUTHWEST OF DJIBOUTI)

Yessy Arvelyna[1], Sawahiko Shimada[2], Sergio Azael May Cuevas[2], Fadoumo Ali Malow[3]

[1]Remote Sensing Technology Center of Japan, Tokyo, 105-0001, Japan
[2]Faculty of Regional Environment Science, Tokyo University of Agriculture, Tokyo, 156-8502, Japan
[3] The World Bank in Djibouti

ABSTRACT

Fault detection analysis on PALSAR-1/2 data has been observed using the implementation of a series of adaptive and gradient filters to derive a Relief Image. This method is applied to delineate good resolution faults distribution, and to add and revise faults mapping derived from existing geology maps over the Djibouti region. Fault mapping is done in order to observe the possibility of fault-driven groundwater flow into the fault systems. Study areas are located in central and southwest of Djibouti, where faults exist because of continental plate movements, contact of geological formation and tectonics activities. The result shows that the processed Relief Image can delineate the fault lines and remove artefacts from PALSAR-1/2 data. The Geology Setting Index is introduced in this study to analyze the correlation of groundwater data with the geology setting of borehole sites such as geological formation, fault system, distance to rivershed, type of aquifer, etc. It is shown that the occurrence of fault systems possibly increases the groundwater volume of boreholes at study areas. The proposed study is useful to locate the potential area for groundwater resources in Djibouti.

Keywords: ALOS-2, PALSAR-2, Fault Detection, Groundwater Analysis, Djibouti.

1. INTRODUCTION

Fractures in volcanic aquifers have been analyzed as the main water resources in Djibouti, as shown by the pumping test data, which consist of major basaltic series, e.g. the Stratiform series (3.4 Ma to 1 Ma) and the Dalha series (9 Ma to 3.4 1 25 Ma) with a thickness more than 200 m [1]. The geochemical and isotopic surveys in the southwest of Djibouti show a common evolutionary pattern of groundwater i.e., a recharge from wadi-rivers flown into the alluvium layer, then, circulated downward into the basalt layer through major faults, and mixed with a more geochemically evolved groundwater [2]. Affected by semi-arid and arid weather, Djibouti has low rainfall, about 130 mm/year, which mostly evaporates to the air (83.5 %) and the rest flows on the ground surface (6 %), penetrates into sub-surface (5.5 %) and sub-ground (5 %), form the renewable groundwater resources estimated about 300 Mm3/year [3].

Therefore, it is necessary to delineate the faults distribution in order to locate areas with high possibility of groundwater resources. On Synthetic Aperture Radar (SAR) image data, fault distribution can be detected by using the interpretation of bright and dark signatures of backscattering data [4]. This study aims to detect the distribution of fault systems using open and free data products of PALSAR-1/2 (Phased Array type L-band Synthetic Aperture Radar) image data over Djibouti by analyzing fault distribution on the Relief Image processed using the gradient filter method. The location of boreholes and boreholes data are analyzed to retrieve the correlation of the faults and groundwater resource characteristics. This study is done under the project on "Advanced and Sustainable Methods on Water Utilization Associated with Greening Potential Evaluation" aimed to create sustainable agropastoral practices in the Djibouti desert through developmental management of water resources, designated by Tokyo University of Agriculture, Japan, from FY2018 for a 5 years period [5].

2. DATA

2.1. SAR Image Data

SAR (Synthetic Aperture Radar) data has been widely used in volcanic and tectonic terrains. Because imaging radar is sensitive to changes of slope, rough-ground surface scatters higher radar signals on the front, while lower radar signals are backscattered on the back slope [4]. Thus, fault lines and their associated topographic scarps are emphasized by highlight (whitish feature) and shadow (blackish feature) on a SAR image [6]. In the SAR image, a thrust fault can be detected by different trends of underlying rocks, and strike-slip faults are often shown by aligned notches, shutter ridges, linear terraces and offset stream channels [4]. The

advantage of using a SAR image is that a radar signal can penetrate clouds and observe the ground surface night and day; thus, it can produce image data without cloud problems. Radar backscatters, derived from satellite observation with high look angle, can produce an extreme topographic distortion, hence, it needs geometric terrain correction to produce a good image data. The processed PALSAR-1/2 data in this study are described below.

2.1.1. PALSAR-1 ASF RT1 data

PALSAR-1 sensor was aboard on Japanese ALOS (Advanced Land Observing Satellite) for land observation using L-band frequency with the main objective to contribute on cartography, regional observation, disaster monitoring and resources surveying [7]. The Alaska Satellite Facility (ASF) has processed Radiometrically Terrain Corrected (RTC) ALOS PALSAR products which are accessible to users on GeoTIFF format since 2014 [8].

The PALSAR RTC product has been corrected for geometry terrain by correcting geometric distortions that lead to geolocation error, and radiometric correction by removing topography influence on backscatter values [9]. This study selected 8 scenes of RT1 high-resolution product which has gamma naught power on pixel data with 12.5 m resolution over Djibouti region. For the Djibouti region, the geometric correction uses SRTM GL1 DEM (Digital Elevation Model) data up-sampled 30-m mapping function to 12.5 m mapping function. The RT1 image data can be downloaded from ASF Data Portal under Product License Agreement and Citation [10].

2.1.2. PALSAR-2 global mosaic data

Started in 2014, the ALOS-2 PALSAR-2 data is the continuation of the PALSAR-1 program ended in 2011. The PALSAR-2 Global Mosaic Data is a seamless mosaic of the backscattering coefficients of PALSAR-2 image with 25 m resolution within 10x10 degrees in latitude and longitude released by JAXA in 2018. Geometric distortion correction (ortho-rectification) and topographic effect on image intensity (slope correction) are applied [11]. Temporal interval of the mosaic is generally 1 year. This data is aimed for understanding and responding to global environmental changes such as global warming and loss of biodiversity, timely assessment of deforestation and forest degradation. Users can access for free and open dataset with a registration on JAXA site under specific JAXA's Terms of Use of Research Data [12]. This study has acquired 4 scenes of PALSAR-2 Global Mosaic data over the Djibouti region.

2.2 Geology Map

The geology map over Djibouti (Fig.1) [13][14] is used to observe the geological formation of borehole, e.g., basaltic or sedimentary formation, the distance to rivershed (wadi), type of nearby fault system and type of aquifer that correlate with the production level of groundwater.

2.3 Borehole Data

The source of borehole data analyzed in this study is a collection of past boreholes data in Djibouti obtained by a FAO project [15]. Spatial distribution of borehole site and groundwater discharge data for each borehole are used to analyze the impact of fault distribution into groundwater resources. The description of borehole data for the target area is noted below.

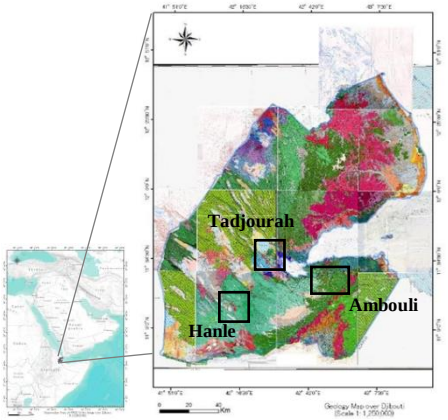

Fig. 1 Geology map of Djibouti and study area

3. STUDY AREA

3.1. Ambouli Watershed

The Ambouli watershed is located in the southwest of Djibouti city, whose main water resource came from the wadi Ambouli. The aquifers at the Ambouli watershed are mainly composed of volcanic aquifers and part of sedimentary aquifers. Normal faults with throw less than 20 m and faults without throw are mostly observed in NW-SE, W-E and NESW direction [14]. About 58 boreholes are distributed in the Ambouli watershed and from these, 36 boreholes with groundwater discharge data were used for groundwater data analysis.

3.2. Hanle Watershed

The Hanle watershed is stretched from the west into the southwest of Djibouti. The aquifers in the Hanle watershed are mainly composed of the sedimentary aquifers and regional volcanic aquifers. In this region, the formation of older basalt of Stratoid series (βD), middle Stratoid basalts of the Afar (βSI I), and the Dalha basaltic series (βD) are widely

covered and in some parts are overlaid by younger sedimentary layers of alluvial deposits (Qa, A3 -A5) observed from the north into south part region of the watershed [14] with depth about 100 m [16]. From 30 boreholes located in the Hanle watershed, only 9 boreholes, which have groundwater discharge data, were analyzed in this study.

3.3. Tadjourah Region

In the Tadjourah region, complex fault systems are observed, such as in the Asal rift zone, central part of Djibouti. The aquifers at this region are mainly composed of volcanic aquifers and minor sedimentary aquifers. The geology setting shows complex layers from basaltic series of Dalha (βD) in the north side, basalts of external margins of the Asal (βG1, recent Quartenary) in the central part, initial basalt series of the opening of the gulf of Tadjourah (βi) along the coastal area and in between overlaid with recent sedimentary formations (Qa) from upper Pliocene to middle Pleistocene era [14]. Normal faults and faults without throw are observed mostly in NW-SE and NE-SW direction, respectively (Fig.1). Twenty boreholes are distributed in this region.

4. IMAGE PROCESSING METHOD

4.1. Preprocessing

On pre-processing, the PALSAR-1/2 data are re-projected to have the same datum and projection, e.g., WGS 1984 Lat/Long. The PALSAR-1 ASF RT1 data uses WGS 1984 datum and UTM 37N projection and the PALSAR-2 global mosaic data uses WGS1984 latitude/longitude. Therefore, the RT1 data is re-projected into WGS 1984 Lat/Long. The DN pixel value of backscattering of RT1 image (HH or HV band) can be converted into gamma naught values in dB (decibel) using the equation [8] as follows,

$$dB = 10*Log10(sqrt(DN)) \quad (1)$$

The PALSAR-2 global mosaic data products are stored as the DN number in unsigned 16 bit and the conversion into gamma naught in dB can be done using following equation [12]:

$$dB = 10*Log10\langle DN2\rangle + CF \quad (2)$$

Where, CF is a calibration factor (value is -83 dB for PALSAR-1 mosaic data), and < > is the ensemble averaging.

Since SAR data is filled with speckle noise due to the interferences during signal transmission [17], adaptive filters, such as Enhanced Lee Filter, etc., are applied on PALSAR-1/2 data to reduce speckle noise on the image. Adaptive filters use standard deviation of pixels within a moving window/box to calculate new pixel values. Enhanced Lee filter can be used to reduce speckles in SAR images while preserving texture information [18]. The filtering process utilizes the Damping Factor, an exponential damping in the weighted average for heterogeneous class, where larger damping produces less averaging. Homogenous is the pixel value replaced by the average of the filter window and Heterogeneous is the pixel value replaced by a weighted average.

4.2. Fault Detection Analysis using the Relief Image

Since the fault lines on SAR image are associated with the dark-light transition, this feature contains edges that possess gradients with a large magnitude on the X-Y plane [19]. Therefore, it can be emphasized using gradient filters. In this study, fault distribution is delineated from the processed Relief image composed by applying gradient filter on ortho-rectified PALSAR-1/2 image data to emphasize the relief features of fault lines. On ENVI ver. 5.5.3, this process can be done by applying Convolution High Pass Filter with 3x3 Kernel Size on X and Y direction by applying Kernel in X direction: [-1, 0, 1]; [-2, 0, 2]; [-1, 0, 1] and Y direction: [1, 2, 1]; [0, 0, 0]; [-1, -2, -1].

Then, the Relief image is derived by composing the X and Y direction gradient filtered image (b1+b2), such as the Band Math of ENVI or the raster tool of ArcMap. Fault detection analysis is done by overlaying the Relief image derived from gradient filtering of PALSAR-1/2 data on geology map over Djibouti using ArcMap ver.10.6 with transparency setting about 45%. The correlation of the fault line from geology map over study area and the Relief image are observed under image scale from 1:30,000 or higher scale.

4.3. Scoring Index for Geology Setting Analysis of Borehole Site

The correlation between the groundwater volume from borehole and the geology setting of borehole site are analyzed using the Geology Scoring Index which is designed according to the information derived from the geology map over Djibouti, e.g., basaltic or sedimentary formation, the distance to rivershed (wadi), type of nearby fault system and type of aquifer that correlate with the production level of groundwater (Table 1). The borehole data at study area, i.e., groundwater volume and deep profile, borehole elevation, etc., are analyzed and visually compared using graphs.

5. DISCUSSION AND ANALYSIS

5.1. Fault Detection Analysis

The proposed method of the Relief image by applying gradient filter on PALSAR-1/2 image data was capable of delineating the fault system at study area. This method can enhance the difference of backscattering data from ground surface occurred by fault system retrieved as higher backscattering coefficients. The Relief Image shows that fault lines and dry rivers are associated with rugged features on image (Fig.2, top), where the fault line appears as straight lines and the river system as curved lines.

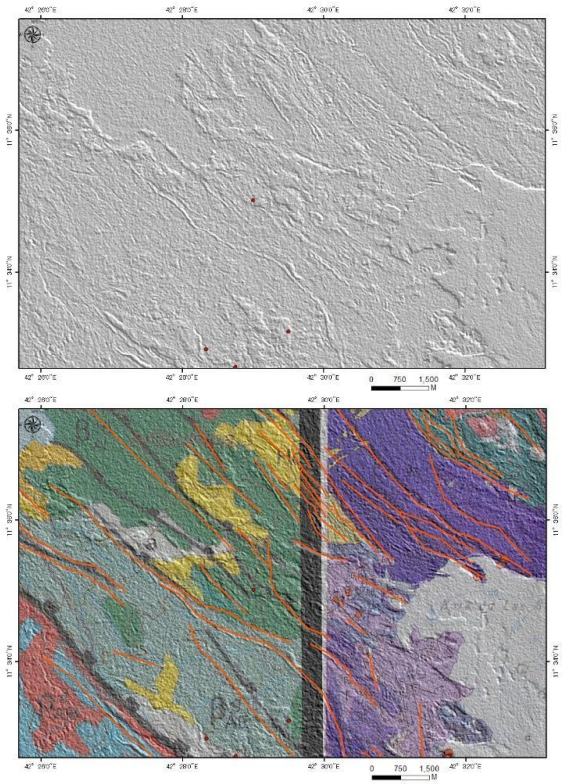

Fig. 2 Processed the Relief image derived from PALSAR-1 ASF RT1 data at the Asal rift zone (top), is overlaid with geology map (bottom) to extract fault lines (orange).

The overlay with the geology map (Fig. 2, bottom) shows that the extracted fault lines from the Relief image are consistent with fault lines from the geological map. Normal faults such as in the Asal rift zone, appear as a straight and deep relief. Additional several fault lines were delineated from the Relief image which can add the fault system distribution from the geology map. The source data for the Relief image, e.g., orthorectified image data of PALSAR-1 RT1 and PALSAR-2 Global Mosaic data, can produce accurate position of fault lines from the Relief image, which can improve the fault lines distribution from the geology map over Djibouti.

Table 1. Geology Setting Index (GSI) for borehole site

Group	No	Class	Index Name	Index	Category
I. Geology formation	1	Sedimentary formation	SedF_i	2	The capacity to absorb water
	2	Basaltic formation	BasF_i	1	
II. Rivershed	3	Dry rivershed	Rv_i	2	Distance to a rivershed
	4	Near dry rivershed	Rv_i	1	
III. Fault	5	Along normal fault	F_i	3	Correlation to fault
	6	Along fault	F_i	2	
	7	Possibly along fault	F_i	1	
IV. Aquifer type	8	Local sedimentary aquifer	SedAq_i	2	The capacity to absorb water

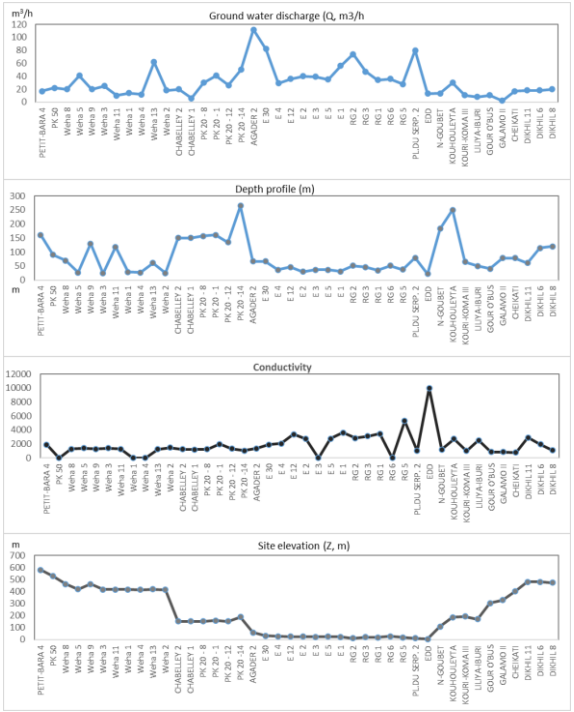

Fig. 3 Borehole data for study area: a) groundwater discharge per hour (Q); b) depth profile (m); c) groundwater static level (NS in m); d) conductivity (µs/cm); and e) elevation (Z in m).

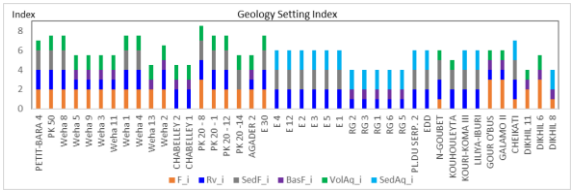

Fig. 4 Geology Setting Index for borehole sites introduced by this study

5.2. Boreholes Data Analysis

The result of the Geology Setting Index (GSI) of boreholes introduced by this study (Table 1) shows that it is capable of evaluating the correlation of geology setting of borehole sites and groundwater resources at the study area (Fig. 4). It is revealed that the boreholes at study areas are mostly located at or near dry river bed of wadi (blue) and more than half of borehole sites are located at the fault systems (orange).

At the Ambouli watershed, higher conductivity level with range between 2850 and 5300 μs/cm, is shown for borehole data located at basaltic formation (RG1-RG3, RG5), in comparison with boreholes data at sedimentary formation (E1-E5) with range 2240 - 3625 μs/cm (Fig.3.d). At the Hanle watershed, the borehole data (Dikhil6, Dikhil11) from volcanic aquifers at basaltic formation in fault regions also show high conductivity level 1950 – 2900 μs/cm. High conductivity shows mineralization of groundwater from water-rocks interaction in basalt formations. In Djibouti, the recharge of basaltic aquifers is involved with downward circulation of surface water into deeper basalt layers through major faults [2].

For borehole sites closer to the Djibouti city, higher conductivity levels are retrieved. The highest conductivity is shown at the EDD borehole located in Djibouti city. This result possibly shows the salinization of groundwater. The observed conductivity level of groundwater of some boreholes exceed the WHO standard for drinking water (< 1,500 μS/cm) and FAO standard for water quality agriculture, i.e. >700 μS/cm is slightly restricted to use and >3000 μS/cm is strictly restricted to use and assumed inadequate for irrigation from past field survey in Dikhil region [20].

The occurrence of large fault system possibly increases the groundwater resource as shown at PK20-8 (Q=30 m^3/h) and PK-201 (Q=41 m^3/h) boreholes, which are located in a fault region, in comparison with borehole sites without the impact of fault system, such as Chabelley-1 and Chabelley-2 (Q=6 - 20 m^3/h) in the Ambouli watershed (Fig. 3). Those boreholes are located about in the same elevation and depth profile (150 - 157 m). The borehole data of N-Goubet at elevation of 183 m in the Tadjourah region, e.g., deep depth profile (183 m), low groundwater discharge (13.33 m^3/h) and the highest NS data (122.76 m) show the possibility of high fluctuation of the groundwater in faults region. High fluctuation of the NS data is also shown for boreholes data on at the Hanle watershed (Kouri Koma III, Liliya Iburi Cheikati, Dikhil 6 and Dikhil 8) with deep depth profile (41 – 120 m), high elevation (184 – 474 m) and low discharge (2.2 – 30 m^3/h).

These results correlate with past studies that show the groundwater discharges in faults region increase linearly with the width and the number of fractures (faults) and decrease linearly with the increase in depth [21] and the magnitude of fluctuation increase to depth [22].

6. CONCLUSION

This study demonstrates that the proposed application of the Relief Image for fault detection using PALSAR-1/2 image data and the Geology Setting Index analysis are useful to locate an area with high possibility of groundwater resources. By evaluating the correlation between the geology setting of borehole sites, e.g., geological formation, occurrence of fault system, aquifer type, etc. with borehole data, i.e. groundwater discharge, conductivity, depth profile, etc., potential sites for groundwater resources can be mapped. In study areas, potential groundwater resources are located in or near dry rivershed (wadi), sedimentary aquifers and regions where fault systems exist. From the observation of study area in the southwest and central of Djibouti, the fault regions in the west part (i.e., site of Weha 3, Weha 5, Weha 13) and the north part (PK 20-8, PK 20-1, PK 20-12) of the Ambouli watershed and the southwest of Djibouti city (site of Agader 2) show good potential of groundwater for irrigation and drinking water. At these regions, the groundwater discharge ranges between 25 - 62 m^3/h, depth profile of boreholes 24 – 67 m and conductivity of borehole data below 1500 μS/cm.

ACKNOWLEDGMENTS

This study acknowledged the copyright notice for ALOS PALSAR RTC © NASA [2006-2007], includes material © JAXA, METI [2006-2007]. The PALSAR-2 Global Mosaic data have been provided by the Japan Aerospace Exploration Agency. The copyright of the Relief image and fault analysis products (includes the Geology Setting Index analysis) derived from PALSAR-1/2 data over Djibouti is belong to RESTEC and the usages is granted to Tokyo University of Agriculture/ SATREPS JST/JICA project through “Fault detection analysis using PALSAR-1/2 image data throughout Djibouti” project in FY2020.

REFERENCES

[1] Jalludin, M. and Razack, M., Analysis of Pumping Tests, with Regard to Tectonics, Hydrothermal Effects and Weathering, for Fractured Dalha and Stratiform Basalts, Republic of Djibouti, Journal of Hydrology, Vol. 155, 1994, pp.237–250.

[2] Awaleh, M. O., Baudron, P., Soubaneh, Y. D., Boschetti, T., Hoch, F. B., Egueh, N. M., Mohamed, J., Dabar, O. A., Masse Dufresne, J.,

and Gassani, J., Recharge, Groundwater Flow Pattern and Contamination Processes in an Arid Volcanic Area: Insights from Isotopic and Geochemical Tracers (Bara Aquifer System, Republic of Djibouti), Journal of Geochemical Exploration, Vol. 175, 2017, pp.82–98.

[3] Malow, F. A., Development of a 3D Water Flow Modelling based on Scarce Data for Arid Land Water Resources Management: Case Study of Ambouli and Kourtimalei Watersheds in Djibouti, Ph.D. Thesis, Tokyo University of Agriculture, Tokyo, Japan, 2018, pp.22.

[4] Ford, J., Blom, R., Coloman, J., J.R., Farr, T., J.J, P., Pohn, H., and Jr., F. S., Radar Geology, in Henderson, F M, and Lewis, A J., Principles and Applications of Imaging Radar. Manual of Remote Sensing: 3rd ed., Vol. 2, 2013, pp.525-526.

[5] JST, Advanced and Sustainable Methods on Water Utilization Associated with Greening Potential Evaluation, JST, 2018. https://www.jst.go.jp/global/english/kadai/h300 2_djibouti.html.

[6] Sabins, F. F. J., Remote sensing: Principles and Interpretation, Freeman and Co, New York, 2nd ed., 1987, pp.423.

[7] JAXA, ALOS Data Users Handbook - Revision C, Earth Observation Research and Application Center, Japan Aerospace Exploration Agency, 2018, pp.2. https://www.eorc.jaxa.jp/ALOS/en/doc/fdata/ALOS_HB_RevC_EN.pdf.

[8] ASF, ASF Radiometrically Terrain Corrected ALOS PALSAR Products - Product Guide, The Alaska Satellite Facility, Revision 1.2, 2015, pp.9.

[9] ASF, View Radiometrically Terrain Corrected (RTC) Images in QGIS, The Alaska Satellite Facility, 2018. https://asf.alaska.edu/wp-content/uploads/2019/02/view_rtc_in_qgis_v5.2 .pdf.

[10] ASF, ALOS PALSAR – Terms and Conditions, 2021. https://asf.alaska.edu/data-sets/sar-data-sets/alos-palsar/alos-palsar-terms-and-conditions, Accessed: 2021-10-04.

[11] JAXA, ALOS Data Users Handbook - Revision C, Earth Observation Research and Application Center, Japan Aerospace Exploration Agency, 2008. https://www.eorc.jaxa.jp/ALOS/en/doc/fdata/ ALOS_HB_RevC_EN.pdf.

[12] JAXA, Global PALSAR-2/PALSAR/JERS-1 Mosaic and Forest/Non-forest Map (FNF) - Dataset Description, Japan Aerospace Exploration Agency, 2019. https://www.eorc.jaxa.jp/ALOS/en/palsar_fnf/DatasetDescription_PALSAR2_Mosaic_FNF_revI.pdf.

[13] ISERST, Carte Geologique de la Republique de Djibouti a 1:100,000, ORSTOM, Office de la Recherche Scientifique et Technique Outre Mer, Paris, France, 1983, 1985, 1986, 1987, 1995.

[14] CERD, Geological map of the Republic of Djibouti, 1:200,000, Centre d'Etude et de Recherche de Djibouti, Djibouti, 2015.

[15] Maudho, A., Water Resource Management in the Republic of Djibouti, FAO, Rural Hydraulic Directorate's Database Study Report, 2018.

[16] JICA, Information Gathering and Confirmation Survey (Geophysical Exploration) for Djibouti Geothermal Development, 2015. https://www.jst.go.jp/global/english/kadai/h3002_djibouti.html, (in Japanese).

[17] Skolnik, M. I., Introduction to Radar Systems, McGraw-Hill, Inc., 2nd ed., 1981, pp.537.

[18] Lopes, A., Touzi, R., and Nezry, E., Adaptive Speckle Filters and Scene Heterogeneity, IEEE Transactions on Geoscience and Remote Sensing, Vol. 28, 1990, pp.992–1000.

[19] Duda, R. O. and Hart, P. E., Pattern Classification and Scene Analysis, A Wiley-Interscience Publication, 1973, pp.268.

[20] JICA, The Republic of Djibouti, the Master Plan Study for Sustainable Irrigation and Farming in Southern Djibouti, Final Report, 2014.

[21] Basak, P., Lekha, K. R., and Prasad, P., Flow through Fractured Rocks: A Field Correlation between Fracture Parameters and Yield, in Workshop on Water Management: India's Groundwater Challenge, Ahmedabad, India, 1993.

[22] Moench, M., Burke, J., and Moench, Y., Rethinking the Approach to Groundwater and Food Security, Water Reports, Food and Agriculture Organization of the United Nations, Rome, Vol.24, 2003, pp.40.

8th Int. Conf. on Structure, Engineering & Environment (SEE), Mie, Japan, Nov.10-12, 2022, ISBN: 978-4-909106094 C3051

THE EFFECTS OF RICE HUSK ASH DOSAGE ON COMPRESSIBILITY AND MICROSTRUCTURAL DEVELOPMENT OF STABILIZED CALCITE-RICH RIVER SLUDGE

Alex Otieno Owino[1], and Zakaria Hossain[1]
[1]Graduate School of Bioresources, Mie University, Japan

ABSTRACT

The maintenance and construction operations along riverways often lead to large amounts of river sludge that can cause severe environmental pollution problems if not disposed of properly. To reduce the risk of such environmental concerns, alternative handling methods such as stabilizing the river sludge are effective in improving the geotechnical properties of such wastes, making them useful in the construction industry. This study aims to chemically stabilize river sludge using control-burnt rice husk ash with high amorphous silica content. The study experimentally investigated the effects of different rice husk ash dosages on the compressive strength (q_u), modulus of deformation (E_{50}), microstructural developments, and the ultimate chemical compositions in the stabilized river sludge specimens during the curing period. The methods applied in this study to reveal the intrinsic mechanisms included an unconfined compressive strength test, scanning electron microscopy test (SEM), and X-ray powder diffraction (XRD). The results showed maximum peaks of calcium aluminosilicate hydrates gels (CAH-gels) at 5%RHA, a pozzolanic reaction product, which formed strong cementation bonds in the river sludge-RHA composite. Identifying CSH gels and the firmly cemented microstructure provided an insightful interpretation for the strength evolution of RHA stabilized river sludge. This proposed stabilization methodology proved to be an essential parameter in solving the uncontrolled disposal of river sludge and as a conservation measure in saving RHA and river sludge disposal costs. Additionally, the innovative incorporation of RHA was an efficient and sustainable approach to justifying river sludge's potential use as subgrade material for designing light-duty farm roads and footpaths.

Keywords: River sludge, Unconfined compressive strength, Modulus of deformation, RHA, SEM, XRD

INTRODUCTION

The maintenance and construction operations along riverways often lead to large amounts of river sludge generation, and their disposal poses vast challenges worldwide. Due to the serious environmental concerns associated with river sludge pollution (from toxic substances to dust when dry), illegal dumping should be significantly discouraged [1][2][3]. Also, the accumulation of river sludge in rivers and waterways can cause a significant decrease in the downstream river water flow capacities [4]. The poor geotechnical properties, high water content, and organic matter have disfavored its application in engineering construction works [5]. However, with the current developments in material science technologies, the practicality of pioneering river sludge as a construction material is rising. Some of the recent research has utilized sludge treatment procedures, including the introduction of additives such as phosphor-gypsum, slag, cement, lime, fly ash, blast furnace slag, and magnesium oxychloride cement, among others [1][4][6][7].

However, it is essential to establish a suitable approach for river sludge stabilization to counter further environmental degradation concerns on matters of carbon footprints associated with the manufacture of some of these treatment additives. Currently, the use of amorphous silica-based alternatives such as rice hush ash is gaining tremendous attention in the construction industry owing to its pozzolanic reactivity, the abundance of rice husks worldwide, and the low carbon footprints in its production [8][9][10][11]. As discussed in this study, the above advantages permit rice husk ash to be applied as a stabilizing additive. The excellent characteristics of RHA, specifically abundant micropores and large specific areas, can rapidly influence the moisture content of river sludge or soil and improve the compaction characteristics hence showing a great potential of its application in geotechnical engineering. Furthermore, previous studies have shown that the main chemical components of RHA are SO_2 and carbon dioxide. It also includes metallic and non-metallic oxides such as CaO, AL_2O_3, Fe_2O_3, K_2O, MgO, P_2O_5, and MnO, depending on the rice husk combustion temperatures [12]. When rice husks are subjected to combustion temperatures between 600-700 °C, the morphology of the SO_2 mainly consists of amorphous silica particles that exhibit very high pozzolanic reactivity [14]. The high pozzolanic reactivity proves that RHA has the potential to generate cementitious gels such as calcium silicate hydrates that can be used as stabilizing agents for river sludge instead of the additives with high carbon footprints.

Several researchers have used RHA combined with conventional stabilizers such as cement and lime

to stabilize soils. These combinations indicated a decrease in soil's maximum dry density and increased optimal moisture content [14][15]. Concerning the compressibility of RHA stabilized soils, studies showed that the unconfined compressive strength (UCS) increased then decreased with increasing RHA content. For instance, Owino (2022) suggested that the optimal contents of RHA with nominal dosages of cement (3% cement) was 5%, above which the UCS reduced significantly [16]. Similar developments in UCS with RHA stabilization have also been recorded in other studies [17][18][19][20][21]. Additionally, through micro-structure analysis (SEM, EDS, and XRD), several studies recorded that the structure of the ultimate RHA stabilized soils was mainly composed of hydrated calcium silicate (C-S-H) and sodium-based aluminosilicate (N-A-S-H) at low RHA contents, justifying the structural developments reflected in the improved UCS [9][22][23]. However, in literature, there is little to almost no research demonstrating the effects of RHA dosages on the compressive strength and microstructural developments in stabilized river sludge.

To address the shortcoming of the available pieces of research, the main objective of this study was to comprehensively evaluate RHA's feasibility in stabilizing river sludge. A thorough experimental analysis through a series of unconfined compression tests was performed to investigate the compressive strength of the stabilized river sludge considering the curing period. Also, further examinations by scanning electron microscopy (SEM) and X-ray diffraction (XRD) tests were conducted to identify pore structure and hydration products, respectively, to reveal the associated micro-mechanisms of RHA stabilized sludge with the curing period. The obtained findings provided a basic framework for developing an appropriate and eco-friendly stabilization technology for the usage of river sludge.

MATERIAL AND METHODS

Materials

River sludge

The sludge was dredged from a river in Saga prefecture, Japan. The collection point and processing steps are shown in Fig. 1a-c. The sludge was black due to organic matter and became light gray during the open-air dewatering process. The river sludge was air-dried before evaluating the specific gravity, particle size distribution, and the Atterberg limits following the Japan Industrial standards JIS 1204, JIS 1205, and JIS 1202, respectively [24][25][26]. The characterization of the dewatered river sludge is illustrated in Table 1 and Fig. 2. As specified by the American Association of State Highway and Transportation Officials (ASSHTO) soil classification systems, the river sludge was classified as silty and clayey gravel sand, A-2-5 (0). The modified Proctor compaction tests showed that the optimum water content and maximum dry density were 33% and 1.25 g/cm^{3,} respectively. It was also noted that the chemical composition of river sludge was mainly quartz (SO_2) and calcite (CaO) with some traces of iron sulfates ($FeOHSO_4$), as shown in Figure 3a.

Rice husk ash (RHA)

Make Integrated Technologies Ltd, Osaka; Japan provided the RHA used in this study. RHA was produced through a combustion process with temperatures between 600 and 700 °C and a burning time of 27 hours. The particle distribution chart showed an average particle size between 0.001 and 0.3 mm, as shown in Fig. 2. The main chemical components of RHA were SO_2 and carbon dioxide. It also included some metallic and non-metallic oxides such as CaO, AL_2O_3, Fe_2O_3, K_2O, MgO, $P_2O_{5,}$ and MnO in varied proportions, as illustrated in Table 2. The wide SO_2 peak from XRD tests, shown in Figure 3b, justified the high concentration of amorphous silica content, a fundamental parameter in pozzolanic reaction processes during river sludge stabilization.

Table 1 Properties of river sludge

Property	Value
Specific Gravity	2.15
Maximum dry Density	1.25 g/cm^3
Optimum water content	33%
Liquid limit, LL	62.31%
Plastic limit, PL	52.27%
Plasticity Index, PI	10.04%
AASHTO classification	Silty and Clayey Gravel sand A-2-5 (0)

Table 2 Properties of RHA

Physical properties	Values
Specific gravity	1.47
Average Particle Size,	0.001 to 0.30 mm
Loss of Ignition	4.00-6.00
Silica (SiO_2),	91.10%
Carbon dioxide (CO_2)	4.35%
Potassium Oxide (K_2O)	2.40%
Calcium Oxide (CaO)	0.57%
Iron Oxide (Fe_2O_3)	0.05%
Alumina (Al_2O_3)	0.03%
Others	1.50%

Testing methodology

The experimental procedures to analyze the

stabilization of river sludge included determining optimum water content (OMC) and maximum dry

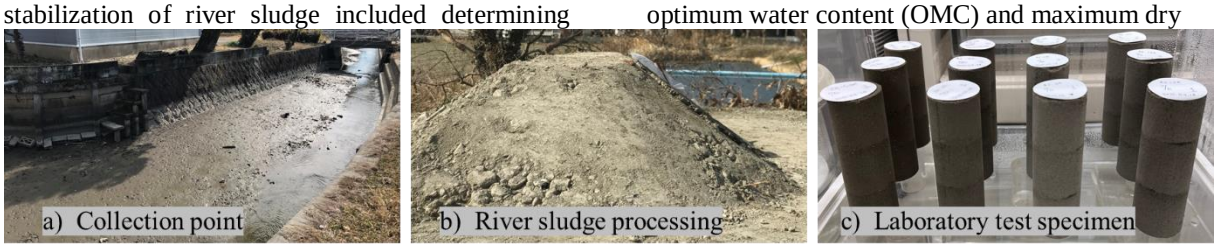

Fig. 1 (a) Location of river sludge collection, (b) River sludge processing on-site, (c) River sludge test specimen.

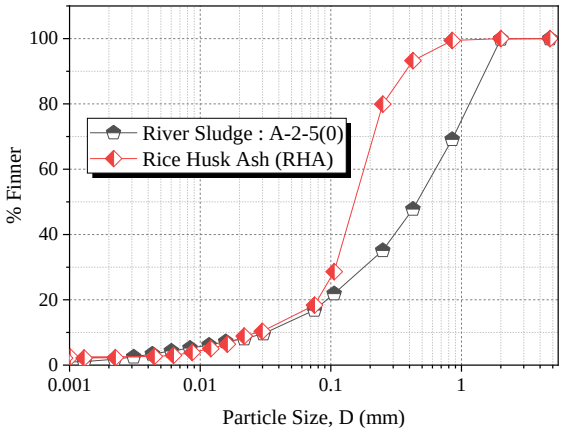

Fig. 2 Particle size distribution for river sludge and RHA

density (MDD) of each mixing scheme, specimen preparation, compressive strength evaluation, and microstructure analyses. The air-dried river sludge was sieved through a 2mm sieve and mixed with RHA following the schemes illustrated in Table 3. The dry aggregates were then mixed by hand for 10 minutes to achieve a homogeneous mixture, after which water was added according to the OMC, as shown in Table 3. Next, the mixture was compacted in three layers inside a mold, measuring 5cm in diameter and 12.5 cm in height using a 1 kg rammer at a falling height of 30 cm. A record of 20 blows was registered for each layer to maintain constant compaction energy. Subsequently, the molded specimens were placed in a desiccator and wet cured at a standard temperature of 25°C for 1 day, 7 days, and 28 days.

The unconfined compressive strength test (UCS) was done using the uniaxial compression tester with a maximum loading of 500N at a axial displacements rate of 1mm per minute. All the UCS testing procedures followed the Japan Industrial standards JIS 1216 [27]. Upon completion of the tests, 50 grams of river sludge-RHA composite was taken from each specimen to evaluate the specimen morphology and mineralogical compositions through SEM and XRD analyses.

Table 3 Specimen mixing schemes

Mixing scheme	River sludge (%)	RHA (%)	OMC (%)	MDD (g/cm^3)
RS	100	0	33	1.237
RS+5RHA	100	5	40	1.135
RS+10RHA	100	10	31	1.329
RS+15RHA	100	15	36	1.209

Note: RHA amount = *i*% weight of the dry weight of river sludge

RESULTS AND DISCUSSION

Compaction characteristics

According to Japan Industrial standards JIS 1210, the standard Proctor compaction tests were conducted, and the compaction curves were plotted as shown in Fig. 4 [28]. The optimum moisture content (OMC) increased sharply by 7% for the RS+5%RHA specimen due to the high-water absorption capability of RHA compared to the control specimen. Additionally, the maximum dry density (γ_{dmax}) decreased to 1.135 g/cm^3 for the RS+5%RHA specimen due to the replacement of the dense river sludge particles with lightweight RHA particles upon stabilization and chemical reactions taking place in the compacted specimen. The replacement phenomenon decreased the weight of the proctor molds containing the compacted river sludge-RHA mixtures, lowering the γ_{dmax}. These observations agreed with the findings of previous studies [29[[30] [31].

However, for the RS+10RHA and RS+15RHA specimens, the OMC and γ_{dmax} results were found to be irregular. The irregularity was attributed to the more significant differences in the particle sizes in the stabilized river sludge specimen due to the excess accumulation of fine materials and the differences in the specific gravities between river sludge and RHA. Basha (2005) and Harichane (2011) also observed a similar deviating trend in OMC and γ_{dmax} while examining the compaction responses of RHA stabilized residual soils [32] [33]. Moreover, the compaction curves did not pass the saturation line (S_r), demonstrating the accuracy of the relationships between OMC and γ_{dmax}.

Unconfined compressive strength test results

To understand the bearing capacity of the stabilized river sludge, the variation of compressive strength of RHA stabilized river sludge with curing time is presented in Fig. 5. The full stress-strain curves can

evaluate parameters such as the maximum strain and the unconfined compressive strength. The stress-strain relationship of the control specimen (river sludge only) is also provided in the plots for a better comparison.

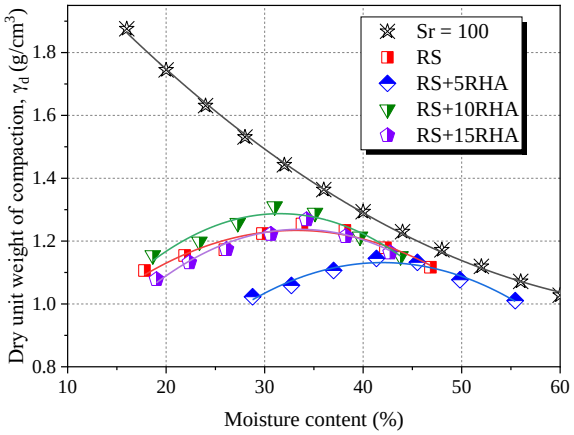

Fig. 4 Compaction characteristics

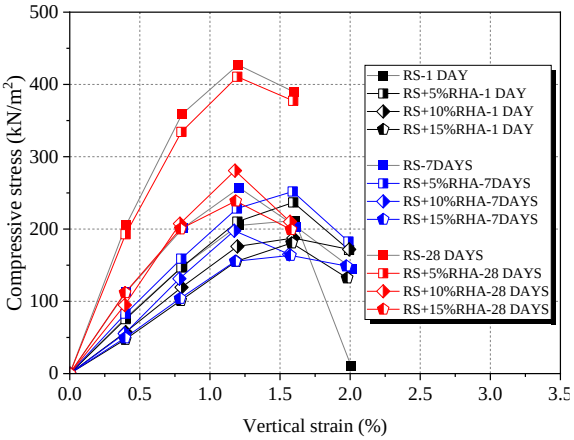

Fig. 5 Stress-strain relationship with curing period

It was observed that the compressive stresses increased with the axial strains, but the increment rate varied depending on the RHA content and curing period. A similar relationship between compressive stress, axial strain, and curing period has also been recorded in other studies [1] [34] [35] [36]. It was also noted that the maximum compressive stresses were achieved after 28 days of curing across all specimens.

Additionally, increasing the RHA content reduced the compressive stresses due to the structural modifications of the stabilized river sludge and the limited pozzolanic activity associated with the accumulation of excess RHA in the specimen matrix. Furthermore, the maximum axial strains were reduced by 0.4% after 28 days of moist curing due to the increased stiffness in the specimens during stabilization.

In Fig. 6a, the variation of the compressive strength (q_u) with the curing period was presented. Evidently, the rate of q_u development in RHA stabilized river sludge was influenced by the RHA dosage and the curing period. For instance, significant improvements in q_u were noticeable for specimen RS and RS-5%RHA with values 427.14 and 420.61 kN/m^{2,} respectively, after 28 days curing period. The increase in q_u was attributed to the flocculation and cementation processes in the calcite-rich river sludge and the enhanced pozzolanic reactions at low RHA contents in the stabilized matrix.

However, for higher RHA contents, the pozzolanic reactivity of the stabilized matrix was insubstantial due to the accumulation of excess porous RHA within the specimen, producing a highly compressible matrix hence the reduction in compressive stresses. On the other hand, the strain at the maximum compressive stress (q_u) decreased noticeably with the curing period, as shown in Fig. 6b. Generally, the variation of the RHA dosage had minimal effects on the axial strain development across all the tested specimens, with an almost constant strain value ranging between 1.20% to 1.58%.

For the sake of calculating the modulus of deformation (E_{50}), the values corresponding to the 50% compressive strength ($q_u/2$) and the corresponding axial strain (ε_{50}) values were calculated for all the tested specimens. The equivalent E_{50} values considering RHA dosage and curing period were determined Using Eq. (1) and plotted as illustrated in Fig. 6c.

$$\boldsymbol{E_{50} = \frac{\frac{q_u}{2}}{\varepsilon_{50}} / 10} \qquad (1)$$

Where; E_{50} is the modulus of deformation of the stabilized river sludge in MPa and ε_{50} is the compressive strain at 50% compressive strength ($q_u/2$). It was evident that the moduli of deformations (E_{50}) increased remarkably with the curing period for all the RHA dosages. Similar results were obtained by Muntohar (2013) [37] and Jongpradist (2018) [10] while studying the effects of RHA on E_{50} during the curing period. It was also noted that the RHA dosages greatly influenced the E_{50} in the stabilized river sludge. For example, the modulus of deformation for specimen RS, RS-5%RHA, RS-10%RHA, and RS-15%RHA was 49.67 MPa, 4.052 MPa, 26.82 MPa, and 27.98 MPa, respectively.

This study proposed using 5%RHA content for river sludge stabilization as it proved to be an essential parameter in solving the uncontrolled disposal of river sludge. Additionally, using river sludge-5%RHA composites can reduce disposal costs and act as an environmental conservation measure to reduce the carbon footprint obtained from manufacturing conventional stabilizer agents.

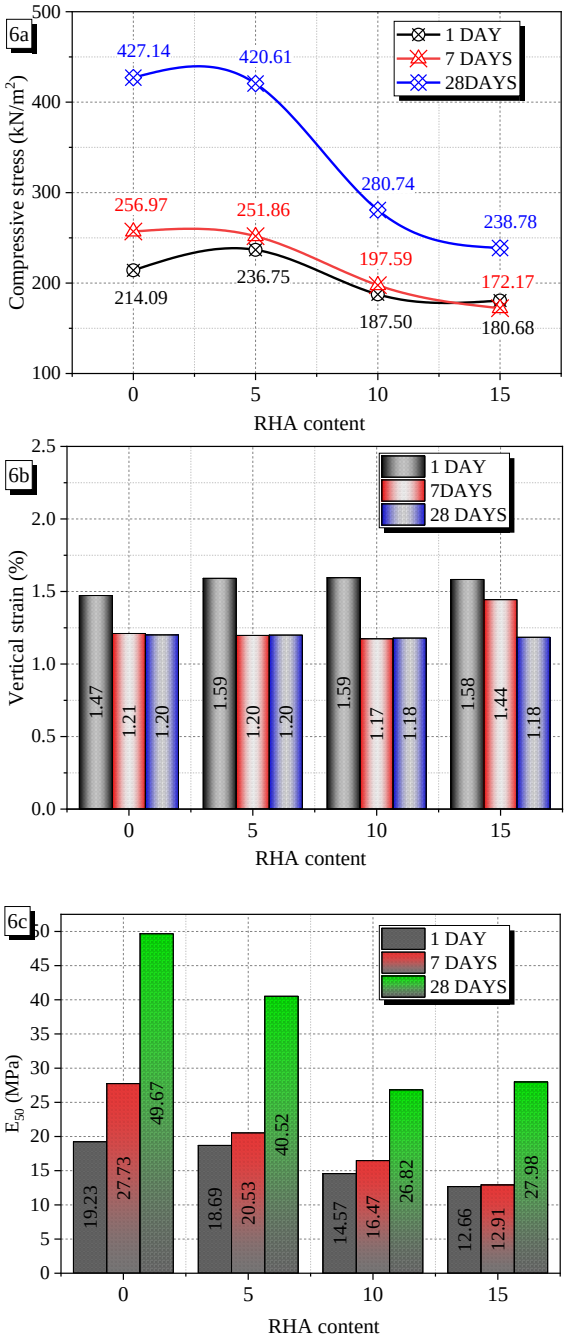

Fig. 6 (a)Relationship between q_u and RHA content(b) Relationship between ε and RHA content (c) Relationship between E_{50} and RHA content

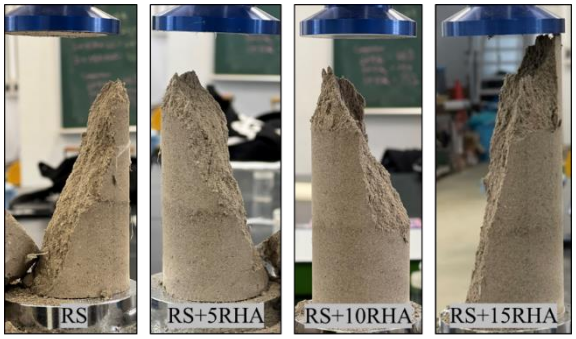

Fig. 7 Specimen failure patterns after 28 days curing period

Specimen failure patterns

In this study, it was observed that the failure modes of the tested specimens under the unconfined compressive strength tests varied depending on the amount of RHA in the stabilized river sludge matrix. The failure modes after 28 days of curing are shown in Fig. 7. A simple shear failure pattern was evident for specimen RS, RS-5%RHA, and RS-10%RHA at axial strains of 1.20%, 1.19%, and 1.18%, respectively. Further increase in RHA dosage to 15% led to a tensional failure pattern at a corresponding axial strain of 1.18%, as indicated by the almost axial failure plane. Moreover, it was observed that for all specimens tested, no diagonal cracks were evident during the early stages of testing until the maximum axial strains were attained, indicating the considerable development in shear strength with RHA stabilization.

Microstructure analyses

This section emphasized understanding the structural and mineralogical characterization of the RHA stabilized river sludge through SEM and XRD tests. The SEM images for the specimen stabilized with 0%RHA, 5%RHA, 10%RHA, and 15%RHA, and the corresponding XRD graphs were presented and analyzed.

It was observed that the control specimen's microstructure after 28 days of curing consisted of coarser and angular particles and a porous morphology, as shown in Fig. 8a. Additionally, secondary particles dominated the microstructure due to flocculation and agglomeration during the hydration processes within the calcite-rich river sludge. On the other hand, the microstructure of the RS-5%RHA specimen displayed the development of a more compact and highly cemented stabilized river sludge matrix, as shown in Fig. 8b. Through XRD analyses, the observed microstructural evolutions were justified by the presence of high peaks of calcium aluminosilicate hydrate gels (CAH-gels) alongside calcium silicates for specimen RS and RS+5%RHA as shown in Fig. 8c and Fig. 8d, respectively. The dominant peaks of CAH-gels enhanced interparticle attractions that ultimately increased the compressive strength, as shown in Fig. 5a. These results were consistent with the RHA stabilization results reported by previous researchers [38][39][40].

To further evaluate the effects of RHA dosages, the representative SEM images and XRD plots for RHA content of 10% and 15% are shown in Fig. 9. The SEM micrographs revealed that the higher RHA dosages led to the development of smaller packets of

aggregates, and larger pore spaces gradually developed in the specimen structure, as presented in Fig. 9a and 9b. The larger pores existed because of the limited production of hydrated products that was validated by the detection of the reduced high peak of CAH-gels for specimen RS+10%RHA and increased peaks of calcium silicates in the XRD graphs as shown in Fig. 9c. Similarly, a higher concentration of un-hydrated calcium silicates was also detected for the RS+15%RHA specimen, as shown in Fig. 9d. This significant finding coincided well with the UCS results, thus providing a reasonable explanation for the strength reduction in the RHA stabilized river sludge as indicated earlier in Figure 5a.

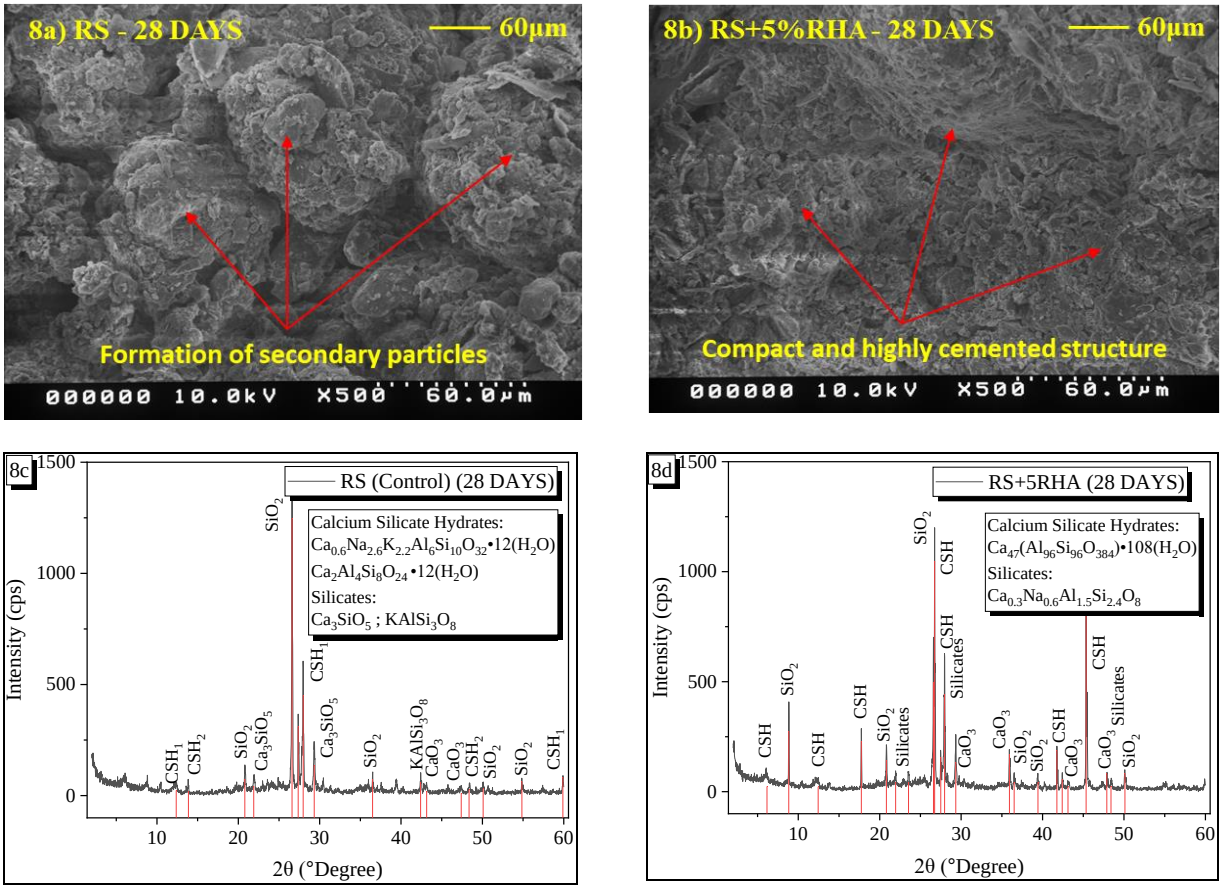

Fig. 8 (a) SEM image for the RS (control) specimen (b) SEM image for the RS+5%RHA specimen (c) XRD graph for the RS (control) specimen (d) XRD graph for the RS+5%RHA specimen

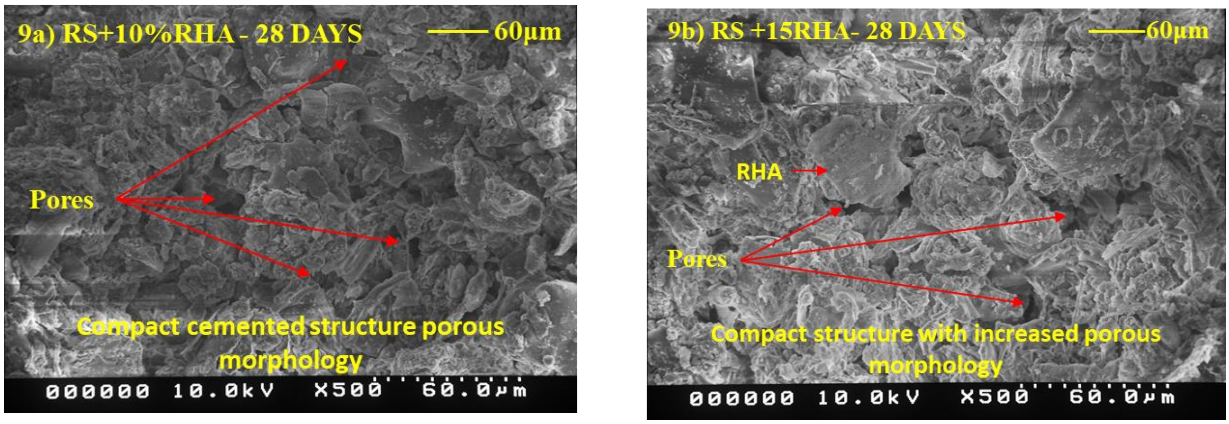

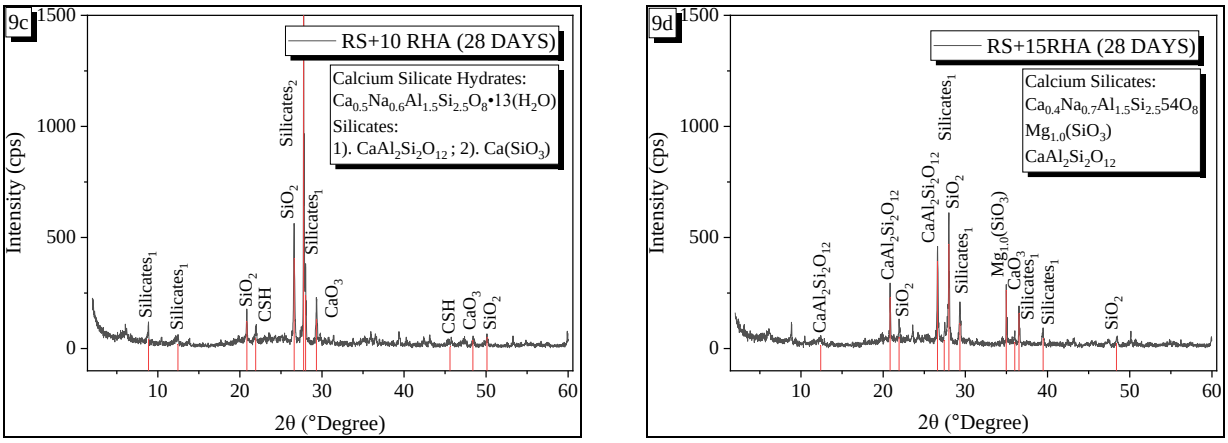

Fig 9 (a) SEM image for the RS+10%RHA specimen (b) SEM image for the RS+15%RHA specimen (c) XRD for the RS+10%RHA specimen (d) XRD graph for the RS+15%RHA specimen

CONCLUSION

An eco-friendly material, rice husk ash, was utilized to stabilize river sludge and proved effective in improving the geotechnical and microstructural characteristics. The influence of RHA dosage and curing time was systematically investigated by a series of unconfined compression, SEM, and XRD tests. The findings drawn from the investigation were summarized as follows:

1. The UCS of the RHA stabilized river sludge was greatly affected by the RHA content and curing period. Specimen mixing schemes RS and RS+5%RHA improved the compressive strength, with values 427kN/m^2 and 411kN/m^{2,} respectively, after 28 days curing period. These conditions proved to be the appropriate parameter values to improve the mechanical response of RHA stabilized river sludge.
2. SEM analyses showed a dense structural framework in the new composite material containing 5%RHA, indicating strength development. Identifying the less porous morphology by SEM provided a reasonable explanation for the improved compressive strength in the RHA stabilized river sludge.
3. The XRD results demonstrated that the strength development at 5%RHA was due to the development of Calcium Aluminosilicate Hydrates minerals in the hydration products of the studied RHA stabilized river sludge. Additionally, river sludge had a dominant crystalline phase containing Calcite (CaO_3) and $SiO_{2,}$ which had the capacity to precipitate within the spaces between particles, forming a hard mass within the specimen.

ACKNOWLEDGMENTS

The authors would like to acknowledge the Japan Ministry of Education, Culture, Sports, Science and Technology for providing the MEXT scholarship through Mie University, where this study was conducted. This research was also supported by Make Integrated Technology Limited, which provided experimental materials.

REFERENCES

[1] Wang, D., Di, S., Gao, X., Wang, R. and Chen, Z., Strength properties and associated mechanisms of magnesium oxychloride cement-solidified urban river sludge. Construction and Building Materials, 250, 2020, pp.118933. https://doi.org/10.1016/j.conbuildmat.2020.118933

[2] Lang, L., Song, C., Xue, L. and Chen, B., Effectiveness of waste steel slag powder on the strength development and associated micro-mechanisms of cement-stabilized dredged sludge. Construction and Building Materials, 240, 2020, pp.117975. https://doi.org/10.1016/j.conbuildmat.2019.117975

[3] Lang, L., Liu, N. and Chen, B., Investigation on the strength, durability and swelling of cement-solidified dredged sludge admixed fly ash and nano-SiO2. European Journal of Environmental and Civil Engineering, 26(7), 2022, pp.2913-2933. https://doi.org/10.1080/19648189.2020.1776160

[4] Maierdan, Y., Haque, M.A., Chen, B., Maimaitiyiming, M. and Ahmad, M.R., Recycling of waste river sludge into unfired green bricks stabilized by a combination of phosphogypsum, slag, and cement. Construction and Building Materials, 260, 2020, pp.120666. https://doi.org/10.1016/j.conbuildmat.2020.120666

[5] Lang, L., Liu, N. and Chen, B., Strength development of solidified dredged sludge containing humic acid with cement, lime and nano-SiO2. Construction and Building Materials, 230, 2020, pp.116971. https://doi.org/10.1016/j.conbuildmat.2019.116971

[6] Mymrin, V., Stella, J.C., Scremim, C.B., Pan, R.C., Sanches, F.G., Alekseev, K., Pedroso, D.E., Molinetti, A. and Fortini, O.M., Utilization of sediments dredged from marine ports as a principal component of composite material. Journal of Cleaner Production, 142, 2017, pp.4041-4049. https://doi.org/10.1016/j.jclepro.2016.10.035

[7] Said, I., Missaoui, A. and Lafhaj, Z., Reuse of Tunisian marine sediments in paving blocks: factory scale experiment. Journal of Cleaner Production, 102, 2015, pp.66-77. https://doi.org/10.1016/j.jclepro.2015.04.138

[8] Sandhu, R.K. and Siddique, R., Influence of rice husk ash (RHA) on the properties of self-compacting concrete: A review. Construction and Building Materials, 153, 2017, pp.751-764. https://doi.org/10.1016/j.conbuildmat.2017.07.165

[9] Owino, A.O., Nahar, N., Hossain, Z. and Tamaki, N., Dimensional influence of basalt fiber reinforcements on the consolidation behaviour of rice husk ash stabilized soils. Construction and Building Materials, 339, 2022, pp.127686. https://doi.org/10.1016/j.conbuildmat.2022.127686

[10] Jongpradist, P., Homtragoon, W., Sukkarak, R., Kongkitkul, W. and Jamsawang, P., Efficiency of rice husk ash as cementitious material in high-strength cement-admixed clay. Advances in Civil Engineering, 2018. 11pages https://doi.org/10.1155/2018/8346319

[11] Taiwo, L.A., Obianyo, I.I., Omoniyi, A.O., Onwualu, A.P., Soboyejo, A.B. and Amu, O.O., Mechanical behaviour of composite produced with quarry dust and rice husk ash for sustainable building applications. Case Studies in Construction Materials, 17, 2022, pp. e01157. https://doi.org/10.1016/j.cscm.2022.e01157

[12] Chen, R., Congress, S.S.C., Cai, G., Duan, W. and Liu, S., Sustainable utilization of biomass waste-rice husk ash as a new solidified material of soil in geotechnical engineering: A review. Construction and Building Materials, 292, 2021, pp.123219. https://doi.org/10.1016/j.conbuildmat.2021.123219

[13] Bie, R.S., Song, X.F., Liu, Q.Q., Ji, X.Y. and Chen, P., Studies on effects of burning conditions and rice husk ash (RHA) blending amount on the mechanical behavior of cement. Cement and Concrete Composites, 55, 2015, pp.162-168. https://doi.org/10.1016/j.cemconcomp.2014.09.008

[14] Choobbasti, A.J., Ghodrat, H., Vahdatirad, M.J., Firouzian, S., Barari, A., Torabi, M. and Bagherian, A., Influence of using rice husk ash in soil stabilization method with lime. Frontiers of Earth Science in China, 4(4), 2010, pp.471-480. https://doi.org/10.1007/s11707-010-0138-x

[15] Nahar, N., Hossain, Z. and Tamaki, N., Optimum utilization of rice husk ash waste for ground improvement. International Agricultural Engineering Journal, Vol 30, No. 1, 2021, pp1-10

[16] Owino, A.O., Nahar, N., Hossain, Z. and Tamaki, N., Effects of basalt fibres on strength and permeability of rice husk ash-treated expansive soils. Journal of Agricultural Engineering, 53(1) 2022. https://doi.org/10.4081/jae.2022.1315

[17] Ghorbani, A. and Salimzadehshooiili, M., Evaluation of strength behaviour of cement-RHA stabilized and polypropylene fiber reinforced clay-sand mixtures. Civil Eng J, 4, 2018, pp.2628-41. http://dx.doi.org/10.28991/cej-03091187

[18] Ghorbani, A. and Salimzadehshooiili, M., Dynamic characterization of sand stabilized with cement and RHA and reinforced with polypropylene fiber. Journal of Materials in Civil Engineering, 31(7), 2019, pp.04019095. https://doi.org/10.1061/(ASCE)MT.1943-5533.0002727

[19] Jiang, X., Huang, Z., Ma, F. and Luo, X., Analysis of strength development and soil–water characteristics of rice husk ash–lime stabilized soft soil. Materials, 12(23), 2019, pp.3873. https://doi.org/10.3390/ma12233873

[20] Salehi, M., Bayat, M., Saadat, M. and Nasri, M., Prediction of unconfined compressive strength and California bearing capacity of cement-or lime-pozzolan-stabilised soil admixed with crushed stone waste. Geomechanics and Geoengineering, 2022, pp.1-12. https://doi.org/10.1080/17486025.2022.2040606

[21] Ayodele, F.O., Fajimi, M.S. and Alo, B.A., Stabilization of tropical soil using calcium carbide residue and rice husk ash. Materials Today: Proceedings, 60, 2022, pp.216-222. https://doi.org/10.1016/j.matpr.2021.12.465

[22] Phummiphan, I., Horpibulsuk, S., Sukmak, P., Chinkulkijniwat, A., Arulrajah, A. and Shen, S.L., Stabilisation of marginal lateritic soil using high calcium fly ash-based geopolymer. Road Materials and Pavement Design, 17(4), 2016, pp.877-891. https://doi.org/10.1080/14680629.2015.1132632

[23] Arulrajah, A., Yaghoubi, M., Disfani, M.M., Horpibulsuk, S., Bo, M.W. and Leong, M., Evaluation of fly ash-and slag-based geopolymers for the improvement of a soft marine clay by deep soil mixing. Soils and foundations, 58(6), 2018, pp.1358-1370. https://doi.org/10.1016/j.sandf.2018.07.005

[24] JIS A 1204, Soil particle density test. Japanese Industrial Standard, Guidance and Basic - Soil Test, The Japan. Geotech. Soc. (in Japanese) (2010) pp.19-26.

[25] JIS A 1204, Soil particle size test. Japanese Industrial Standard, Guidance and Basic - Soil Test, The Japan. Geotech. Soc. (in Japanese) (2010) pp.27-38.

[26] JIS A 1217, Soil liquid limit and plastic limit test. Japanese Industrial Standard, Guidance and Basic - Soil Test, The Japan. Geotech. Soc. (in Japanese) (2010) pp.39-48.

[27] JIS A 1217, Soil unconfined compressive strength test. Japanese Industrial Standard, Guidance and Basic - Soil Test, The Japan. Geotech. Soc. (in Japanese) (2010) pp.151-158.

[28] JIS A 1217, Soil compaction test. Japanese Industrial Standard, Guidance and Basic - Soil Test, The Japan. Geotech. Soc. (in Japanese) (2010) pp.71-78.

[29] Kumar, A. and Gupta, D., Behavior of cement-stabilized fiber-reinforced pond ash, rice husk ash–soil mixtures. Geotextiles and Geomembranes, 44(3), 2016, pp.466-474. https://doi.org/10.1016/j.geotexmem.2015.07.010

[30] Phanikumar, B.R. and Nagaraju, T.V., Effect of fly ash and rice husk ash on index and engineering properties of expansive clays. Geotechnical and Geological engineering, 36(6), 2018, pp.3425-3436. https://doi.org/10.1007/s10706-018-0544-5

[31] Lu, S.G., Sun, F.F. and Zong, Y.T., Effect of rice husk biochar and coal fly ash on some physical properties of expansive clayey soil (Vertisol). Catena, 114, 2014, pp.37-44. https://doi.org/10.1016/j.catena.2013.10.014

[32] Basha, E.A., Hashim, R., Mahmud, H.B. and Muntohar, A.S., Stabilization of residual soil with rice husk ash and cement. Construction and building materials, 19(6), 2005, pp.448-453. https://doi.org/10.1016/j.conbuildmat.2004.08.001

[33] Harichane, K., Ghrici, M. and Missoum, H., Influence of natural pozzolana and lime additives on the temporal variation of soil compaction and shear strength. Frontiers of Earth Science, 5(2), 2011, pp.162-169. https://doi.org/10.1007/s11707-011-0166-1

[34] Owino, A.O., Nahar, N., Hossain, Z. and Tamaki, N., Effects of basalt fibres on strength and permeability of rice husk ash-treated expansive soils. Journal of Agricultural Engineering, 53(1). 2022. https://doi.org/10.4081/jae.2022.1315

[35] Shibi, T. and Ohtsuka, Y., Influence of applying overburden stress during curing on the unconfined compressive strength of cement-stabilized clay. Soils and Foundations, 61(4), 2021, pp.1123-1131. https://doi.org/10.1016/j.sandf.2021.03.007

[36] Eskisar, T., Influence of cement treatment on unconfined compressive strength and compressibility of lean clay with medium plasticity. Arabian Journal for Science and Engineering, 40(3), 2015, pp.763-772. https://doi.org/10.1007/s13369-015-1579-z

[37] Muntohar, A.S., Widianti, A., Hartono, E. and Diana, W., Engineering properties of silty soil stabilized with lime and rice husk ash and reinforced with waste plastic fiber. Journal of materials in civil engineering, 25(9), 2013, pp.1260-1270. https://doi.org/10.1061/(ASCE)MT.1943-5533.0000659

[38] Safi, W. and Singh, S., Efficient & effective improvement and stabilization of clay soil with waste materials. Materials Today: Proceedings, 51, 2022, pp.947-955. https://doi.org/10.1016/j.matpr.2021.06.333

[39] Zhang, C., Wang, W., Zhu, Z.D., Li, N., Pu, S.Y., Wan, Y. and Huo, W.W., Triaxial mechanical characteristics and microscopic mechanism of graphene-modified cement stabilized expansive soil. KSCE Journal of Civil Engineering, 26(1), 2022, pp.96-106. https://doi.org/10.1007/s12205-021-0778-2

[40] Jafer, H.M., Majeed, Z.H. and Dulaimi, A., Incorporating of two waste materials for the use in fine-grained soil stabilization. Civil Engineering Journal, 6(6), 2020, pp.1114-1123. http://dx.doi.org/10.28991/cej-2020-03091533

8th Int. Conf. on Structure, Engineering & Environment (SEE),
Mie, Japan, Nov.10-12, 2022, ISBN: 978-4-909106094 C3051

ANAYSIS OF UNREINFORCED CONCRETE BEAMSON SOIL BY FINITE ELEMENTS

*Radhi Alzubaidi ,Husain M Husain[1] and Samir Shukur[3]
*University of Sharjah,Civil Engineering Department, Sharjah
[1]University of Baghdad, Civil Engineering Department, Baghdad, Iraq,
[2]University of Kufa, Civil Engineering Department, Najif, Iraq.

ABSTRACT

Using unreinforced concrete foundations in construction building leading to a distinctive reduction in cost. A nonlinear three-dimension finite element analysis has been used to predict the load -deflection behavior of unreinforced concrete beams on soil by using a computing program (ANSYS5.4). The 8- nodded brick elements with 24 degrees of freedom is used to represent the concrete and soil. Nonlinearities of material due to cracking, crushing of concrete and soil are taken into consideration during the analysis. The model by Willam , K and Warnke (1975) been used to represent the concrete behavior while the modal by Drucker- Prager been used to represent the soil[1]. The nonlinear equations of equilibrium have been solved using an incremental- iterative technique operating under load procedure. The modified Newton-Raphson method is used for nonlinear solution algorithm and force or displacement criteria been used as a convergence criterion. Four applications are analyzed and a comparison is made with experimental and theoretical load deflection curves, where a good agreement been observed. The effects of some parameters ,like depths, width and length of foundations, modulus of elasticity of soil and Poisson's of soil on load -deflection behavior been studied , where these parameters showed distinctive effects on the results. The finite element used in present showed a good agreement with experimental results. The results showed some differences of 6% in the ultimate load prediction and 15.6% in deflection when using interface element and critical state model.

Keywords: Finite element, One-way slab, Foundation, Deflection, Load

1. INTRODUCTION

The development in analysis and design of various type of foundations has led to the concept of transmitting the load to soil through a special members system, which resists the load through direct stress. The types of foundations are varied according to different requirements. The problem of the beam or plate rest on soil has attracted the attention of both structural and geotechnical engineers and it merges the effect on both superstructure and substructure elements. Winkler (1967) [2] presented his theory of the modulus of subgrade reaction, the basic assumption of this model is the relation between the applied surface pressure and the vertical surface deflection at every point[2]. Rao et al (1995) studied interaction analysis for the design of open plane frame resting on soil, the soil has been modeled as 4-node isoparametric element, a plane strain approach is adopted for representing the soil. A comparison is made between the more realistic half-space continuum and the plane-strain approach to examine the approximation involved in the letter type of representation of the soil. They concluded sagging moments in superstructure beams as obtained using plane-strain model were always greater than those obtained from the elastic half[3]. Boudaa et al (2019) presented a finite element modeling of beam resting on a two-parameter layered soil, in their model analysis, they consider the strain energy solutions, the shear strain of the beam element and soil foundation. They concluded that the shear deformations showed crucial influence on the beam, on the structure and on the interface behaviors[4]. Deb and Dhar (2013) studied the development of a methodology for the identification of optimal design parameters for a system of beams resting on a stone column–improved soft soil. They conducted a finite difference–based simulation model and an evolutionary multiobjective optimization model. In their study tried to minimize the settlement at the center of the beam and the maximum shear force. They concluded that the evaluation of the system showed that stiffness of the stone columns or modular ratio and flexural rigidity of the beam are the most important parameters for optimal design[5]. Haldar and Basu (2016) presented a developed method for nonlinear analysis of Euler-Bernoulli beams resting on heterogeneous

multilayered soil. They obtained the governing differential equations for beam and soils displacements using the virtual work, the equations been solved using one-dimensional finite-element and finite-difference methods, the analysis showed that beam responses with accuracy comparable with those obtained from equivalent two-dimensional finite-element analysis are obtained within seconds[6]. AI et al (2014) studied a boundary element method to analyze the elastic foundation finite beams on 2D plane-strain and 3D multilayered isotropic soils. They tried to explore the solution of multilayered elastic soils that obtained to be a kernel function of BEM analysis. They found that with the displacement and stress condition of coordination between beam and soil, the solution is acquired for beams resting on multilayered soils [7]. Zhang et al (2011) studied the beam-soil interface resistance and developed a deformation governing differential equation for a finite beam resting on the Winkler elastic foundation. In their solution the coupling effect between vertical and horizontal displacement is considered [8]. Kousik (2012) presented soil –structure interaction analysis for beam resting on multilayered granular fill reinforced with geosynthetic. The governing differential equations been solved by finite difference techniques. He concluded that using the reinforced geosynthetic is not very effective for maximum settlement reduction and also not effective for shear force reduction for very rigid beam. The multilayered reinforced system found very effective for bending moment and differential settlement reduction[9]. Naeij et al (2021) used the iterative finite element method in the field differences to design a safe steep slopes in a cut. They also showed that, for steep slopes and vertical cuts, the method showed a distinctive underestimate the factor of safety compared to the Limit equilibrium methods [10]. Bayatet al (2018) developed a semi-analytical solution for nonlinear vibration of Euler- Bernouli beams resting on linear elastic foundation. The study include the effects of many parameters on the ratio of nonlinear to linear frequency of the system. They concluded that the results were compared with numerical solution and showed that the maximum and minimum approach can extended in nonlinear partial differential equations [11]. Mohebkhah (2017) studied a two-dimensional numerical model utilizing the discrete element method to predict the ultimate load-bearing capacity of a strip footing on weak clay reinforced with stone masonry trench. The study showed that using a stone masonry trench of optimum dimension I a weak clay can increase the bearing capacity of a strip foundation up a factor of 3.5[12] . Khatri et al (2017) investigate into the behavior of the Pressure-settlement of square and rectangular skirted footings resting on sandy soil where the footing is subjected to a vertical load. They carried out load tests on samples using a model tank and the results showed when using skirt structures a distinctive increase in bearing capacity and a decrease in settlement[13]. Friswell et al (2007) proposed a non-local viscoelastic foundation model to analyze the dynamics of beams with different boundary conditions using the finite element method. They conclude that the case study, predicted that the finite element technique is efficient for the dynamic analysis of beams with non-local viscoelastic foundations [14]. Verma and Mohanty (2018) investigate into behavior of shallow foundation resting on multi layered and homogeneous soil under dynamic loading[15].

2. FINITE ELEMENT REPRESENTATION OF INTERFACE

The present study describes a technique for solving two and three dimensional interface problems. The elements (contact 52) shown in Fig. 1 are adopted in present research.

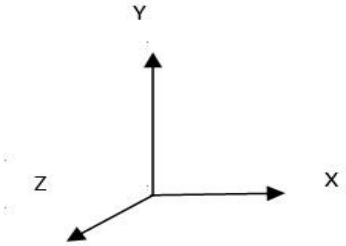

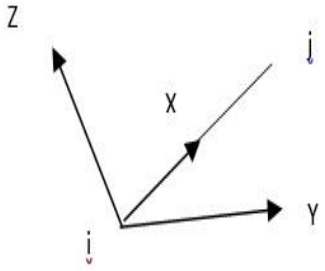

Figure. 1 CONTAC52 3-D point–to–point (ANSYS Manual 1997)

The interface element includes normal and sliding forces ([16] and [17]). This element has one of two condition if the elastic COULOMB friction is used :

1- Stuck element (no sliding)

$\mu|f_n| > |f_s|$

Where:
μ= coefficient of friction
f_n= normal force
$f_n = K_n (u_{n,j} - u_{n,i} + d)$

K_n = normal stiffness
$u_{n,j}$=displacement of node j in normal direction
$u_{n,i}$= displacement of node i in normal direction
d= distance between nodes.

Also
$f_s = K_s (u_{s,j} - u_{s,i} - u_o)$
f_s= sliding force
K_s=sticking stiffness
$u_{s,j}$= displacement of node j in sliding direction
$u_{s,i}$= displacement of node i in sliding direction

u_o= distance that nodes i and j have slide with respect to each other

Writing:

$$\{F\} = [K]\{\Delta\} \qquad (1)$$

$$F\} = \begin{bmatrix} fn \\ fsy \\ fsz \\ -fn \\ -fsy \\ -fsz \end{bmatrix} \qquad (2)$$

Where :
fn = normal force
fs = stick force (in y and z direction)

$$\{\Delta\} = \begin{bmatrix} u_i \\ v_i \\ w_i \\ u_j \\ v_j \\ w_j \end{bmatrix} \qquad (3)$$

$$[K] = \begin{bmatrix} kn & 0 & 0 & -kn & 0 & 0 \\ 0 & ks & 0 & 0 & -ks & 0 \\ -kn & 0 & 0 & kn & 0 & 0 \\ 0 & -ks & 0 & 0 & ks & 0 \\ 0 & 0 & -ks & 0 & 0 & ks \end{bmatrix} \qquad (4)$$

1. Sliding element

If $\mu|f_n| = |f_s|$

Then sliding occurs in both directions, the stiffness matrix (in element coordinate) is:

$$[K] = \begin{bmatrix} kn & 0 & 0 & -kn & 0 & 0 \\ 0 & 0 & 0 & 0 & 0 & 0 \\ 0 & 0 & 0 & 0 & 0 & 0 \\ -kn & 0 & 0 & kn & 0 & 0 \\ 0 & 0 & 0 & 0 & 0 & 0 \\ 0 & 0 & 0 & 0 & 0 & 0 \end{bmatrix} \qquad (5)$$

3.ANSYS COMPUTER PROGRAM

[18] in the present study used a computer program ANSYS 5.4 to analyze plain concrete beams rested on soil. The program has the capacity to solving linear and nonlinear problems including the effect of cracking, crushing, yielding of reinforcement (if existing) ,creep ,bond slip, temperature change ,with 165 different elements conducted in the program.

4.NUMERICAL APPLICATIONS

Numerical actual cases are conducted to compare the results obtained by the present method of finite elements with those obtained from experimental or analytical solutions.

A number of numerical examples have been also analyzed by the computer program ANSYS 5.4. The examples also used to check the validity of the material models used and the applicability and capability of the analysis method adopted in present research where different types of elements are employed. The theoretical study is approximate in nature due to different factors mainly:

1- Approximation in the material modeling of concrete and soil.
2- Approximation inherent in discretization in finite element technique.
3- Approximation in the integrations used in the numerical analysis.
4- Approximation introduced due to the type of procedure used in solving the nonlinear system of equations.

The main results obtained by the solution introduced through present study are the load – deflection response, crack propagation and stress distribution.

4.1. Two- Way Concrete Slab

A two way unreinforced concrete slab with dimension 2.67 m x 2.67 m x 0.762 m was tested under uniform distributed pressure by [19] , details of the concrete slab are shown in Table. 1. The geometry of the slab is modeled by (144) 8 brick elements (solid 65). Figure.1 shows the details of the finite element mesh for the two way- slab.

Table.1 Material properties of Two-Way Slab

Material properties and material parameters	Symbol	Value
Young `s modulus	Ec (N/mm^2)	29000
Compressive Strength	f `c (N/mm^2)	20.67
Tensile strength	f t (N/mm^2)	2.067
Poisson `s ratio	υ	0.2

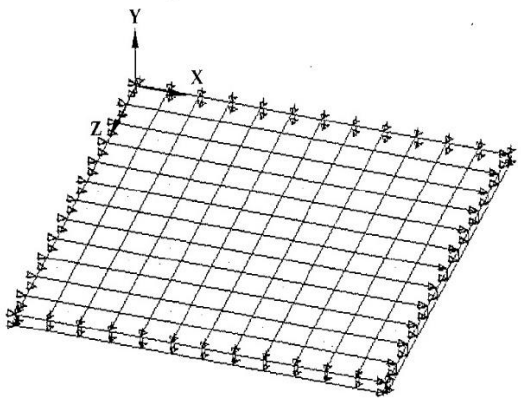

Figure 1 Finite Element Mesh of Two-Way Slab

The distributed of load was lumped to nodes, the load deflection curve for center point is shown in Fig. 2.The deflection increases as the load increases. The maximum deflection was found equal to 67.7 mm at maximum load of 10 kpa, after which no convergence was possible.

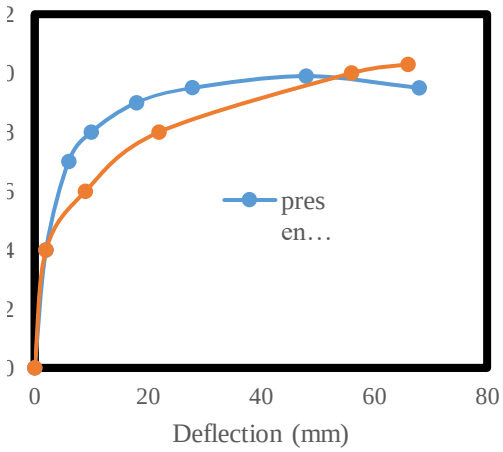

Figure 2 Load –Deflection Curve at Center of Two- Way Slab

Results of finite element give a good agreement with the experimental results of Mosallam et al (2000).

4.2 Rigid Footing on Soil

A cast rigid circular footing was tested experimentally by [20] by resting the footing in a rectangular metal filled with sand. Due to symmetry, only a quarter of the footing system is modeled by the 8 node brick elements (solid 45) and by interface elements (contact 52). The soil considered as homogenous sand, underlain by the rigid bottom of the tank. The boundary condition of the structure- soil problem is considered as the bottom of the tank is fixed with no movement in x, y and z- directions. The main purpose of studying this test, is to verify the behavior of the soil under footing by the present soil model. Material properties are given in Table 2.

The load- deflection curve for the circular footing is shown in Fig.3. The present study results showed a good agreement with experimental works of Rasheed (1998).

Table 2 Material Properties of Rigid Footing

Soil	Young`s modulus	E (N/mm^2)	10
	Poisson`s ratio	υ	0.25
	Cohesion	C (N/mm^2)	0
	Angle of Internal friction	Ø	39.5
Steel	Young`s modulus	Es (N/mm^2)	20000
	Yield stress	*Fy* (N/mm^2)	295
Interface	Factor of friction	μ	0.25

4.3 Slab-Beam Foundation

The case of slab-beam foundation of [21]is considered and solved by (ANSYS 5.4) program. The dimensions of the foundation is shown in Fig.4, and the properties of the properties of soil can be shown in Table 3. Due to symmetry of loading and geometry, only one half of the slab –beam foundation is analyzed by using (2316) elements as shown in Fig. 5 . The load - deflection response at the position of column on slab is shown in

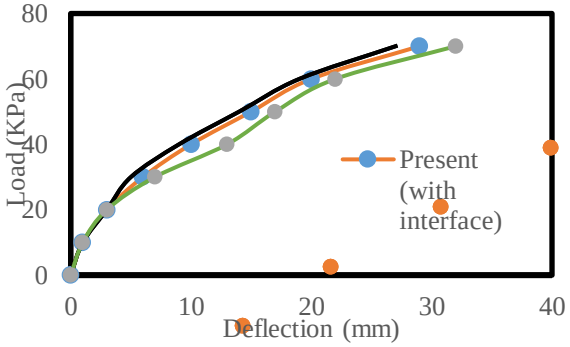

Figure 3 Load –Deflection Curve of Rigid Footing

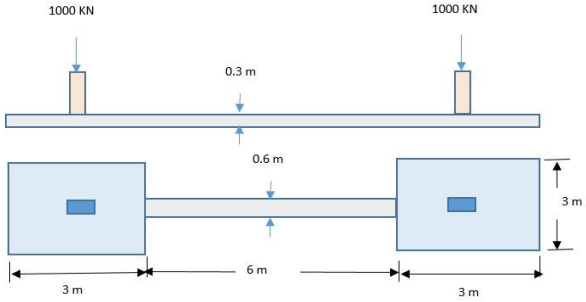

Figure 4 Geometrical and loading details of Slab – Beam Foundation

Table 3. Material Properties of Slab –beam foundation

Concrete	Young` s Modulus	E_c (N/mm^2)	21560
	Compressive strength	f `$_c$ (N/mm^2)	28
	Tensile Strength	f t (N/mm^2)	1.75
	Poisson`s Ratio	υ	0.15
Soil	Young` s Modulus	E_{so}	15
	Poisson`s Ratio	υ_{so}	0.3
	Cohesion	C (N/mm^2)	0

	Angle of Internal Friction	Ø	36
Interface	Factor of friction	μ	0.3

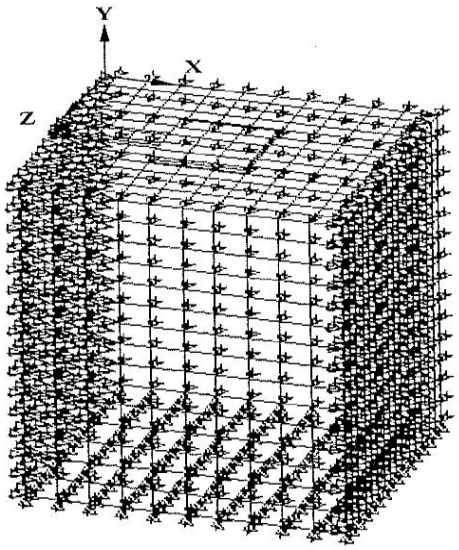

Figure 5 Finite Element Mesh of Slab-Beam foundation

in Fig.6 ,the computed deflection shows a good agreement with the theoretical results , the crack patterns of the slab – beam at different load levels are

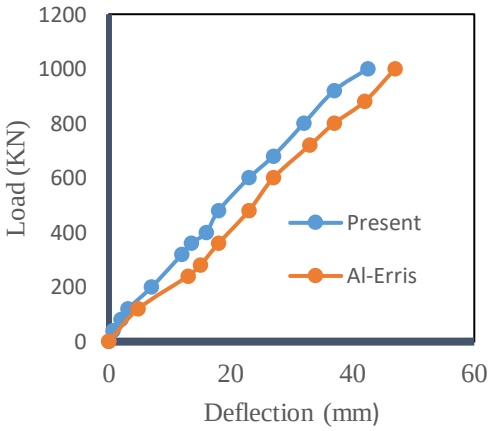

Figure 6 Load – Deflection Curve of Slab – Beam Foundation

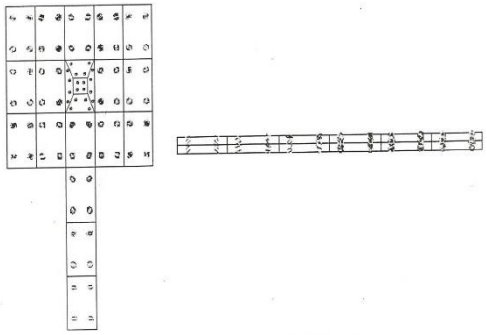

(a)TopView (b) Side View

Figure 7 Crack Patterns of Slab – Beam Foundation at Final Load (1000 KN)

Shown in Fig. 7 . The first crack initiates at a load of about 375 KN. The cracks separate in all three directions of the beam, through the increase of load levels.

5. PARAMETRIC STUDY

The influence of some parameters on the behavior of the same slab- beam foundation under static load is studied. These parameters include the effect of thickness of foundation, modulus of elasticity and Poisson's ratio of soil.

5.1 Effect of Foundation Thickness

The effect of foundation thickness is investigated (slab and beam), three values of thickness 0.3, 0.5, and 0.8 m were considered at constant value of Poisson's ratio (0.2) for soil with different values of modulus of elasticity of soil of 10,17,24 MPa . Figure 8 shows the relation between the maximum displacement beneath the foundation and the modulus of elasticity of soil for different values of thickness foundation. It can be seen that the increase of thickness would considerably decrease maximum displacement.

5.2 Effect of Modulus of Elasticity

The effect of modulus of elasticity of soil also investigated, three values for the modulus of 10, 17 and 24 MPa used for three values of thickness of 0.3,0.

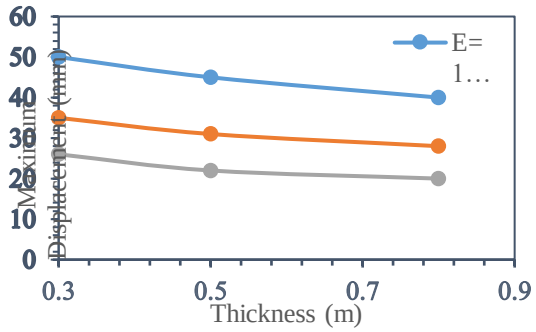

Figure 8 Effect of Foundation Thickness on Maximum Displacement

and 0.8 m with constant passion's ratio of 0.2 and analyzed numerically. The results showed that the increase in the values of modulus lead to a distinctive decrease in the displacement for all values of thickness. This is due to the increase in the rigidity or stiffness of the soil as can be seen in Fig.9

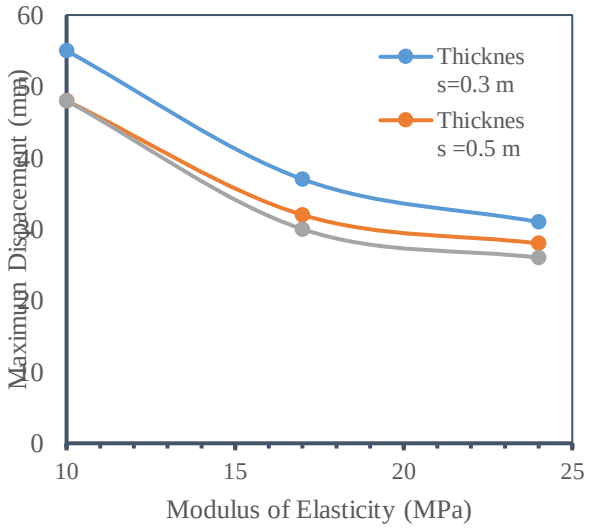

Figure 9 Effect of Soil modulus on Maximum Deflection

5.3 Effect of POISSON'S Ratio

To investigate the effect of Poisson's ratio for the soil, three values are adopted 0.2 ,0.275 and 0.35 at three values of thickness 0.3 ,0.5 and 0.8 m , while the modulus of elasticity for the soil is constant at value of 10 MPa . Fig.10 shows when increasing the values of Poisson's ratio lead to distinctive decrease in displacement of the foundation for all values. This may attributed to the increasing of the rigidity of the soil.

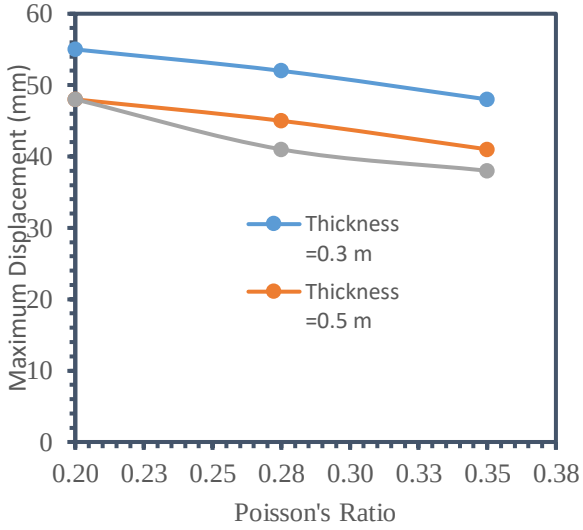

Fig.10 Effect of Poisson's Ratio of Soil on Maximum Displacement

6. CONCLUSSIONS

The present research developed a numerical method of analysis, include the analysis of unreinforced concrete foundations under static load. 8-nodes brick element has been used to model the concrete foundation. Also ,8-node brick element has been used to model the soil ,while the interaction between the soil and the concrete foundation is simulated by contact interface element. Based on the present finite element developed program ,which been conducted through the present work , the following conclusions can be drawn as follows:

1- The ability of using unreinforced concrete beams in the foundation with a good performance even after occurrence some cracks.

2-The results obtained from the present finite element method showed that the computational model adopted in present research is suitable for prediction of load-deflection behavior of unreinforced concrete foundation under static load. The comparison between the numerical and the available experimental results showed a good agreement.

3- The comparison of the numerical results obtained by using the present solution with experimental testing of two way slab. The deflections increase as the loads

increase. The results of the finite element showed a good agreement with experimental results.

4- The results of the load –deflection finite element solution showed a considerable agreement with the experimental results of a cast –iron rigid circular footing.

5- The slab – beam foundation tested load –deflection results showed a good agreement with finite element solution developed in presented study.

6- The numerical results obtained when taking into account the effect of using contact interface element showed a better simulation to the interaction between the soil and the concrete foundation. It is found that the behavior of foundation will be softer when the interface behavior is neglected.

7- The parametric studies showed that there is a distinctive effect when increasing the length, depth, and width of the concrete beam and Poisson's ratio and modulus for the soil. These parameters showed different effects on load – deflection behavior of the foundation.

8- The effects of foundation thickness, Poisson's ratio and modulus of elasticity of soil are found to have the most distinctive factors that affect the load – deflection behavior of slab-beam foundation, when these parameters increase the rigidity of the soil increase.

7. **REFERENCES**

[1] Willam , K and Warnke (1975) , Constitutive Model For The Triaxial Behavior of Concrete , Proceeding International Association for Bridge and Structural Engineering ,Vol.19, Issue 15,Bergam, Italy

[2] Winkler (1967), E. "Die Lehre Von Der Elastizitatune Festigkeit " Dominicus, Prague, 1976.

[3] Rao, P, Rambabu, K.V, and Allam, M.M, (1995) "Representation of Soil Support in Analysis of Open Plan Frames", Computers and Structures, Vol.56, No.6, pp.917-925

[4] Boudaa, S, Khalfallh, S, and Bilotta, E. (2019) "Static interaction analysis between beam and layered soil using a two-parameter elastic foundation. International Journal of Advanced Structural Engineering volume 11, pp21–30.

[5] Deb, K and Dhar, A. (2013) " Parameter estimation for a system of beam resting on stone column-reinforced soft soil. International Journal of Geomechanics ,vol.13 ,issue 3.

[6] Haldar ,S and Basu , D (2016) " Analysis of Beams on Heterogeneous and Nonlinear Soil " .International Journal of Geomechanics , Vol.16 , Issue 4.

[7] AI,Z , Li, Z, and Cheng ,Y(2014) " BEM analysis of elastic foundation beams on multilayered isotropic soils " Soils and Foundations ,Vol.54, Issue 4,pp667-674

[8] Zhang ,L, Zhao, M and Xiao , Y. (2011) . "Nonlinear analysis of finite beam resting on Winkler foundation with consideration of beam-soil interface resistance effect". Structural Engineering and Mechanics ,Vol.38, Issue 5,pp 573-592.

[9] Kousik, D (2012) " Soil-structure interaction analysis of beams resting on multilayered geosynthetic-reinforced soil, Interaction and Multiscale Mechanics ,Vol.5, Issue 4

[10] Naeij , M, Ghasemi, D,Ghafarian ,D and Javanmardi,Y, (2021) Explicit finite element analysis of slope stability by strength reduction, Geomechanics and Engineering,Vol.26,Number2 pp133-146

[11] Bayat, M, Bayat, M, Kia ,M , Ahmadi , H and Pakar, I (2018) Nonlinear frequency analysis of beams resting on elastic foundation using max-min approach , Geomechanics and Engineering ,Vol.16,Number 4 ,pp355-361.

[12] Mohebkhah, A (2017) Bearing capacity of strip footing on a stone masonry trench in clay, Geomechanics and Engineering,Vol.13,Number 2 ,pp255-267

[13] Khatri, V, Debbarma, S , Dutta ,R and Mohanty , B (2017) Pressure-settlement behavior of square and rectangular Skirted footing resting on sand Geomechanics and Engineering ,Vol.12, No.4 ,pp 689-705

[14] Friswell. , M, Adhikari. , S and Lei,Y (2007) , Vibration analysis of beams with non-local foundations using the finite element method.International journal for numerical methods in engineering,Vol.71,pp 1365-1386.

[15] Verma ,A and Mohanty ,S. (2018) Finite element analysis of foundation on layered and homogeneous soil deposit under dynamic loading. Indian geotechnical conference, Bengaluru, India

[16] Mazurkiewics, M, and Ostachowicz, W (1983) "Theory at Failure Element Method for Elastic Contract Problems of Solid Bodies" Computers and Structures, 17(1)

[17] ANSYS Manual (1997) ,Version 5.4 , Swanson Analysis System ,Inc., Houston , Pennsylvania.

[18]Shukur ,S (2002) Analysis of Unreinforced Concrete Beams on Soil By Finite Elements, MSc thesis ,College of Engineering ,University of Kufa, Iraq.

[19] Mosallam, A., Kreiner, J., Lancey , T,. Haroun, M. and Elsandedy ,H.,(2000) Experimental and Numerical Analysis of Two Concrete Slabs Repaired with Polymer Composites ,Division of Engineering California State University – Fullerton. Ca 92834, USA .

20] Rasheed, K, (1998) . A Study of the Behavior of Conical and Inverted Spherical Shell Foundations. PhD thesis, University of Baghdad, Baghdad, Iraq.

[21] AlEriss, H ,(1982), Interaction of Soil –Footings Connected by Grade beams . MSc thesis, university of Technology, Baghdad, Iraq.

8th Int. Conf. on Structure, Engineering & Environment (SEE), Mie, Japan, Nov.10-12, 2022, ISBN: 978-4-909106094 C3051

EXPERIMENTAL STUDY ON RETROFITTING OF HOLLOW BRICK MASONRY HOUSES USING A FERROCEMENT LAYER

Fauzan[1], Jonathan Vincensius Osman[1], Geby Aryo Agista[1], Naurah Daffa Carol[1] and Yundha Syah Putra[1]

[1]Engineering Faculty, Andalas University, Indonesia

ABSTRACT

An experimental study on a hollow brick masonry house with and without a ferrocement layer was carried out to investigate the effect of retrofitted houses using ferrocement layer. Two specimens of the hollow brick masonry house with the scale 1/4 of the actual size (104 cm x 110 cm) were prepared. The first specimen (B1) is a hollow brick house without retrofitting and mortar plastering, which is tested to suffer heavy damage, while the second specimen (B2) is a brick wall house retrofitted using a ferrocement layer with bandage system on both sides of the specimen wall. Both specimens were tested on a shaking table of 304cm x 190cm with a load variation of 0.3g - 1g. The first test aims to make B1 specimen severely damaged, where the heavy damage occurs when the input load is 0.6 g with an additional evenly distributed load is 200 kg. After testing, the cracked B1 specimen was repaired and retrofitted using ferrocement layer with bandage system. The second test is then carried out on the retrofitted B1 and B2 specimens. The test result shows that no visible damage was observed on both specimens up to a variation of the input load of 1 g with an additional uniform load of 500 kg. This proves that the ferrocement layer with bandage system can be applied for retrofitting the damaged hollow brick houses after an earthquake, which significantly improves the seismic behavior of hollow brick houses.

Keywords: URM house, Hollow brick, Earthquake, Shaking table, Ferrocement layer

INTRODUCTION

Indonesia is a country that often experiences natural disasters, especially earthquakes. Major earthquakes that have occurred in Indonesia such as Aceh earthquake in 2004, the West Sumatra earthquake in 2009, Lombok and Palu earthquakes in 2018, Mamuju Earthquake in 2021 and West Pasaman Earthquake 2022. These earthquakes caused enormous losses, not only claimed many lives but also damage to infrastructure and buildings, especially simple houses/community houses, ranging from minor-to-major damage.

Community houses are generally built using unreinforced masonry (URM) buildings. This house is not strong against earthquake loads, because the building does not have structural elements such as beams and columns, while the walls thickness are not in accordance with earthquake resistant house standards [1]. The house was usually built without involving construction experts such as Architects and Civil Engineers [2]–[4].

The behavior of the brick/hollow brick material makes this house brittle and has almost no ductility that makes the brick wall does not have the resistance to horizontal loads or earthquake loads. When an earthquake occurs, this simple unreinforced hollow brick building can suffer light damage to heavy damage, as shown in Fig. 1.

Fig. 1 Damage to brick wall houses due to the 2022 West Pasaman earthquake [5].

In order to retrofit the damage houses, many methods had been published, one of them is Ferrocement layer method. Ferrocement is a type of plaster (mortar) that is reinforced with woven wire. Many studies have been conducted on the use Ferrocement layer as retrofitting method for the damaged non-engineering buildings such as houses [6]–[8]. Testing results of the brick house retrofitted with ferrocement layer showed that the retrofitting method improve the capacity of the house, which was effective in preventing wall collapse during an earthquake [9]–[12].

In this research, an experimental study on hollow brick masonry houses with and without a ferrocement layer was carried out to investigate the effect of the retrofitted damage house using ferrocement layer with a bandage system. The house

specimens were tested on a shaking table test, which apply the earthquake load to these specimens.

TEST SPECIMENS

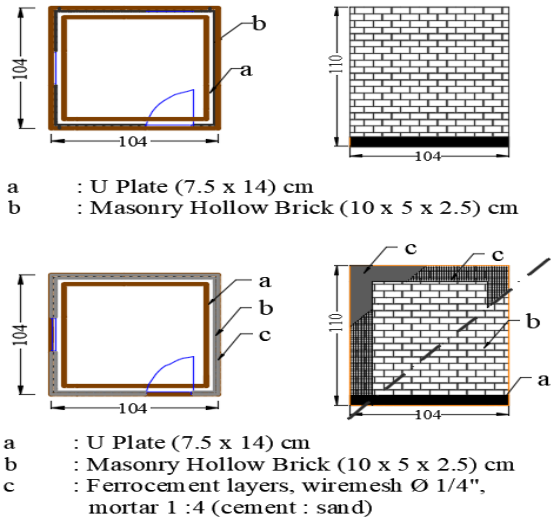

Fig. 2 Plans and sections of B1 and B2 specimens.

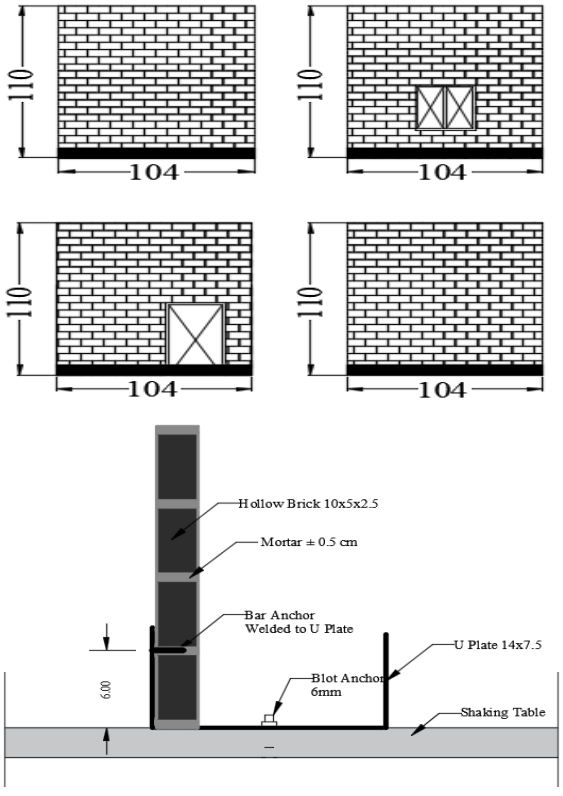

Fig. 3 View and detail of B1specimens.

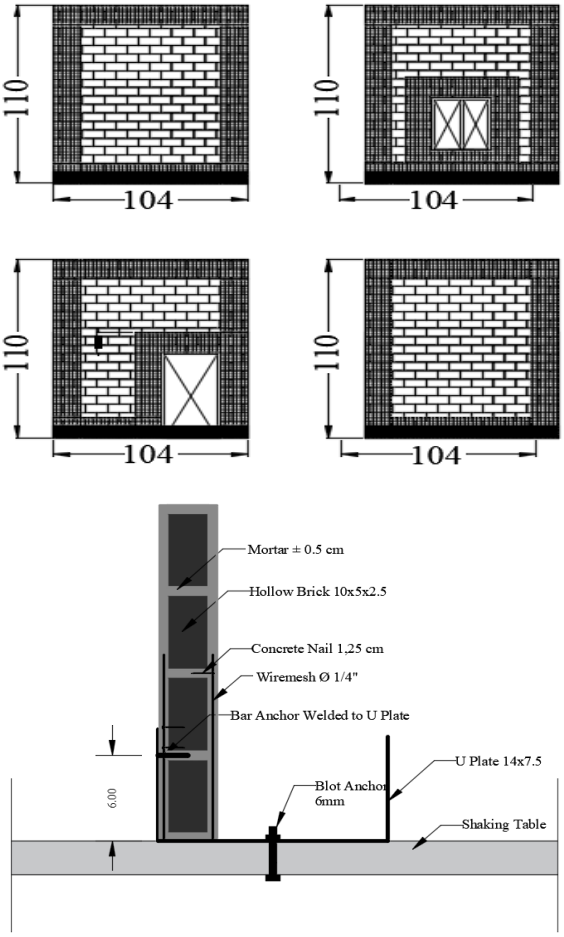

Fig. 4 View and details of B2 specimens.

In this study, two hollow brick masonry house specimens were prepared. The first specimen (B1) is a simple hollow brick house, which is tested until it suffered heavy damage and then, it retrofitted with a ferrocement layer with a bandage system. The second specimen (B2) is a simple hollow brick house made using a ferrocement layer with bandage system as shown in Fig. 2. Both specimens are scaled 1/4 from the original house size. These two specimens were scaled due to the limitations of the shaking table used to test the two specimens.

Both specimens with the size of 1.04m x 1.1m were constructed, as shown in Figs. 2 to 4. The hollow brick material used was 100 x 50 x 25mm, which is the scale of the actual material size. The composition of the cement and sand mixture to make the material is 1 : 5 by volume. The mortar used for spacing and plaster has a 1 : 4 mixture of cement and sand by volume. The thickness of the spacing is 5mm. The width of the ferrocement layer is 125mm. The thickness of plaster for coating the woven wire is 5mm. Material properties such as compressive strength of hollow brick and plaster ranged from 2.5 MPa and 9.9 MPa which were tested at the Materials and Structural Laboratory, Department of Civil

Engineering, Andalas University. The process of making B1 and B2 specimens can be seen in the following figure (Fig. 5 and Fig. 6).

Fig. 5 Process of B1 specimen.

Fig. 6 Construction process of B2 specimens.

According to the Indonesian Seismic Standard (SNI 1729–2019), clause 7.5.3 stated that the load is applied separately in all two orthogonal directions. The effect of the most critical load due to the direction of application of earthquake forces on the structure is considered fulfilled if the components and foundations are designed to carry the load combination specified as follows: 100 percent of the force for one direction plus 30 percent of the force for the perpendicular direction [13]. Therefore, the slope of the specimen is set at 16˚ towards the positive x-axis, as shown in Fig. 7.

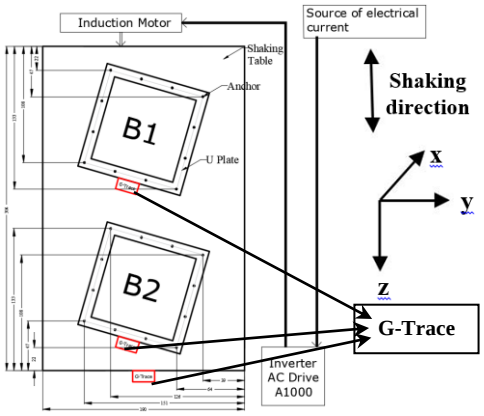

Fig. 7 Set-up of specimens on shaking table.

TEST PROCEDURES

In this study, both specimens were tested using a horizontal uniaxial motion shaking table at the Soil Mechanics Laboratory, Andalas University [14]. Table 1 shows the input motions of this test with variations in earthquake frequency, such as Moderate Earthquake (ME), Strong Earthquake (SE), and Very Strong Earthquake [10]. The input motion of 0.6g is the Peak Ground Acceleration (PGA) of Padang City based on the 2019 Indonesia Earthquake Map. The excitation given to the test object: a = 2.94 m/s^2, 5.88 m/s^2, and 9.81 m/s^2.

Table 1 Variation of input earthquake load

Type of input motions	a (m/s^2)
ME (0.3g)	2.94
SE (0.6g)	5.88
VSE (1g)	9.81

B1 dan B2 specimens were tested on a shaking table, in which the test was stopped when the B1 specimen is severely damaged. This test (P1) consists of 3 times of loading, namely: 0.3g – no load, 0.3g – 200 kg additional uniform load, and 0.6g – 200 kg additional uniform load. After B1 specimen was severely damaged, the specimen was repaired and strengthened using a ferrocement layer with a bandage system.

Both specimens were tested again on the shaking table. This retest (P2) consists of four times of loadings, namely: 0.3g – 400 kg additional dead load, 0.6g – 400 kg additional dead load, 0.6g – 500 kg additional dead load, and 1g – 500 kg additional dead load. The additional dead load referred to is the load using a sand-filled sack placed on top of the specimen, as shown in Fig. 8. In this research phase, the earthquake load given also refers to the September 30, 2009 Padang Earthquake.

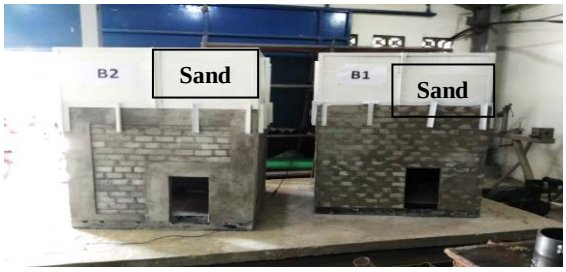

Fig. 8 Specimen with additional uniform load using sacks filled with sand (sandbags).

RESULT AND DISCUSSION

The test results from this experimental study include failures such as crack patterns that occur in the specimen and the maximum acceleration obtained from the readings of the G-Trace vibration reader. This experimental study was divided into 2 tests, namely testing B1 specimen until it was severely damaged (P1) and testing after B1 specimen was strengthened using a ferrocement layer with bandage system.

The Test of B1 Specimen Until It Was Heavily Damaged

This test aims to make B1 specimen severely damaged to see whether the retrofitting using ferrocement layer can be applied to strengthen houses that have suffered heavy damage due to the earthquake.

Test with input motion of 0.3g and no additional uniform load (P1-A)

In this test, both specimens were subjected to an earthquake load of 0.3g and no additional load. From the test result, it appears that the two specimens did not suffer any damage because the earthquake strength was not enough to damage the building, as shown in Fig. 9.

Fig. 9 Specimens that have been tested with 0.3g input motion and no applied additional load.

Tests with an input motion of 0.3g and an additional uniform load of 200 kg (P1-C)

Both specimens in this test were given an earthquake load of 0.3 g with an additional uniform load of 200 kg. The test result shows that the two specimens also did not suffer damage.

Tests with an input motion of 0.6 g and an additional uniform load of 200 kg (P1-C)

In this test, both specimens were given an earthquake load of 0.6 g with an additional uniform load of 200 kg, where the results of this test show that B1 specimen suffered heavy damage on all sides of the specimen wall, as shown in Fig. 10, while B2 specimen did not suffer any damage. The condition of damage as in B1 specimen is stated as the condition of the specimen experiencing severe damage.

Fig. 10. Specimens that have been tested with Input motion of 0.6 g and an additional uniform load of 200 kg.

Testing B1 Specimen After Retrofitting

Due to B1 specimen having been severely damaged, B1 specimen is then repaired and retrofitted using ferrocement layer with bandage system, which was tested again on the shaking table.

Both specimens were subjected to an earthquake load of 0.3 g with an additional uniform load of 400 kg (P2-A), 0.6g with additional uniform load of 400 kg (P2-B) and 500 kg (P2-C), 1g with additional uniform load of 500 kg (P2-D). The test results shows that there is no damage was observed on both specimens after each test until P2-D test, as shown in Fig. 11. This is because the contribution of ferrocement layers in improving the specimen capacity to withstand earthquake loads. This result also proves that the retrofitting using ferrocement layer can be applied to houses that has been damaged

by the earthquake. The retrofitted house can be safe without damage and cause no casualties when another earthquake occurs. This test is only carried out until this stage due to the limitations of the shaking table equipment.

Fig. 11 Specimens that have been tested with an input motion of 1g and an additional uniform load of 500 kg.

Comparison of Cracks Pattern That Occurred During Testing

Figure 12 shows the crack pattern on B1 specimen tested until it is severely damaged. From the figure, it can be seen that the cracks occurred at an earthquake load of 0.6g with an additional evenly distributed load of 200 kg. From the acceleration reading obtained using G-Trace shown in Fig. 13, the maximum acceleration (a_{max}) of B1 specimen when the cracks occur is 2.5g at t = 2.5 seconds.

After retrofitting the B1 specimen, the test is continued until the input motion of 1 g and additional uniform load of 500 kg. For this test, neither the reinforced B1 specimen nor the B2 specimen experienced cracks, as shown in Fig. 14. The a_{max} of the B1 and B2 specimens at this test were 2.52g and 1.27g, respectively, as shown in Fig. 15. The test was carried out for 30 seconds, but there was no damage to both specimens, although the acceleration that occurred in both specimens was quite large.

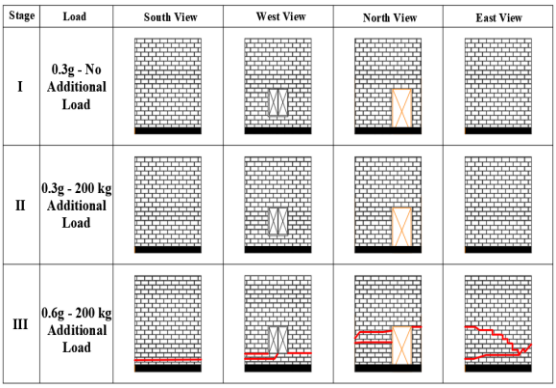

Fig. 12 Schematic of cracking pattern on B1 specimen until it is severely damaged.

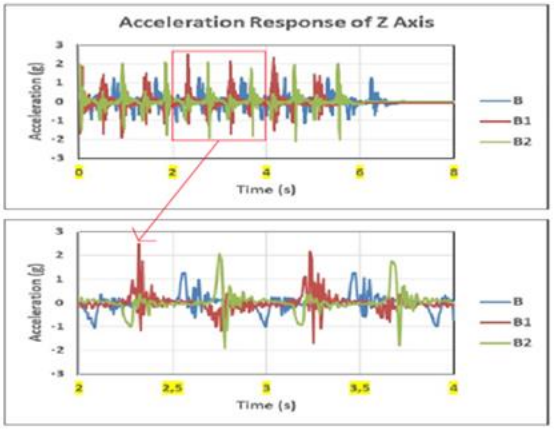

Fig. 13 Graph of acceleration response for shaking table (b), B1 and B2 specimens with an earthquake load of 0.6 g and an additional uniform load of 200 kg.

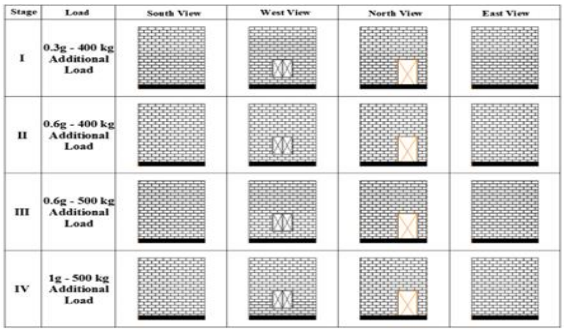

Fig. 14 Schematic of cracks pattern of the retrofitted B1 specimen until the end of the test.

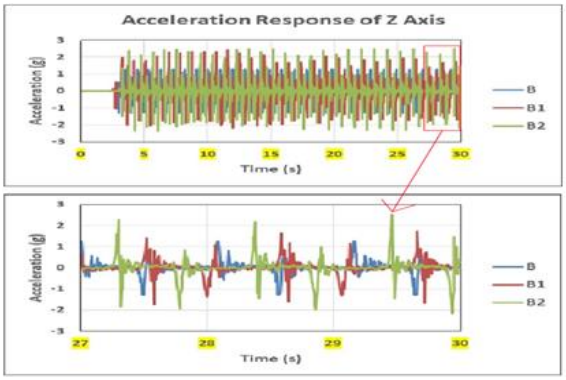

Fig. 15 Graph of acceleration response for vibrating table (b), B1 and B2 specimens with an earthquake load of 1 g and an additional even load of 500 kg.

CONCLUSION

Based on the experimental results carried out on the retrofitting the hollow brick houses using ferrocement layer, the following conclusions can be drawn:

1. B1 Specimen suffered heavy damage at the input motion of 0.6g and an additional evenly distributed load of 200 kg because the damage occured on all sides of the hollow brick wall of the specimen.
2. No damage or cracking was observed in both specimens until the input motion of 1g and an additional uniform load of 500 kg when the testing was conducted after retrofitting the B1 specimen.
3. The maximum acceleration (a_{max}) of B1 specimen when the cracks occur was 2.5g at t = 2.5 seconds, while the a_{max} of the retrofitted B1 specimen at the end of the test was 2.52g without any crack appeared on the specimen.
4. The results of this study prove that ferrocement layer with a bandage system can be used for retrofitting the damaged hollow brick houses after an earthquake, which can significantly increase the seismic behavior of hollow brick houses.

REFERENCES

[1] Gumilang AA, and Rusli M., Seismic Performance of earthquake resistant simple residential confined masonry house structure based on PUPR regulation No. 5 of 2016 specification, 2nd International Conference on Disaster and Management, 2021, 708 012085.

[2] Boen T., Learning from Earthquake Damage: Non-Engineered Wall Buildings in Indonesia, Yogyakarta: Gadjah Mada University Press, Indonesia: 2016 (In Bahasa).

[3] Ismail FA, Asmirza MA, Hakam A., Fauzan, Ferrocement – Brick Sandwich Wall Applied to Non – Engineered Houses, International Journal of GEOMATE, April., 2018, Vol. 14, Issue 44, pp.47-51.

[4] Hakam A., Fauzan, Ismail FA and Istijono B., Capacity Building of Local Home Builders on Application of Earthquake Safe House for Disaster Risk Reduction, 4th Annual meeting of Indonesian Disaster Expert Association, May 2017, Jakarta.

[5] CNN Indonesia., 8 Meninggal Akibat Gempa Pasaman Barat, 103 Rumah Rusak Berat, https://www.cnnindonesia.com/nasional/20220226122239-20-764392/8-meninggal-akibat-gempa-pasaman-barat-103-rumah-rusak-berat. Retrivied 21 September 2022.

[6] Ferrocement Technology., Definition of Ferrocement.http://tebeceria09.blogspot.com/2012/12/technology-ferrocement.html. Retrieved 10 May 2018.

[7] Sandeep K., Ferrocement Materials for Construction, International Journal of Engineering Research and Applications, 2018, Vol. 8, No. 3, pp.53-55. ISSN: 2248-9622.

[8] Al-Rifaie WN, and Mohammad K, Load Carrying Capacity of Clay Brick Masonry Wall Encased by Ferrocement, International Journal of Emerging Engineering Research and Technology, 2017, Vol. 5, No. 4, pp.26-35. ISSN 2349-4395 (Print) & ISSN 2349-4409 (Online).

[9] Boen T, Brief Report of Shaking Table on Masonry Building Strengthened with Ferrocement Layer, 16th World Conference on Earthquake, 2017, Paper no. 1393.

[10] Fauzan, Ismail FA, Hakam A., Zaidir, and Amalia SH, Experimental Study on Masonry Building Strengthened with Ferrocement Layers, International Journal of GEOMATE, May., 2018, Vol. 14, Issue 45, pp.84-90.

[11] Fauzan, Hakam A., Ismail FA, and Osman JV, Experimental Investigation of Hollow Brick Unreinforced Masonry Building Retrofitted by Ferrocement Layers, 4th International Conference on Science, Engineering & Environment (SEE), Nagoya, Japan, Nov. 12 – 14, 2018, ISBN: 978-4-909106018 C3051 (Proceeding).

[12] Asif MM, Alam MZ, and Ahsan R., An Experimental Investigation of Ferrocement Retrofitted Masonry Wall Units Subjected to Cyclic Loading, Proceedings of the 5th International Conference on Advances in Civil Engineering (ICACE 2020), 4-6 March 2021, CUET, Chattogram -4349, Bangladesh.

[13] National Standardization Agency, Earthquake Resistance Planning Procedures for Building Structure and Non-Building Structure (SNI 1726-2019), 2019, Jakarta.

[14] Hakam A., Ismail FA, and Fauzan, Liquefaction Potential Assessment Based on Laboratory Test, International Journal of GEOMATE, Oct., 2016, Vol. 11, Issue 26, pp.2553-2557.

Environment

8th Int. Conf. on Structure, Engineering & Environment (SEE), Mie, Japan, Nov.10-12, 2022, ISBN: 978-4-909106094 C3051

LABORATORY INVESTIGATION ON WATER QUALITY OF SPRING WATER FOR SMALL COMMUNITY FOR WATER SECURITY

Mohamad Nazrul Hafiz[1], Maidiana Othman[1], Noor Afiza Mat Razali[1], Zuliziana Suif[1], Jestin Jelani[1] and Nordila Ahmad[1]

[1]Faculty of Engineering, Department of Civil Engineering, National Defence University of Malaysia, Malaysia

ABSTRACT

Water has become a necessity in our daily life. The lack of clean water will be forced people to drinks unsafe water and lead to more diarrhea cases which is the second leading cause of death for children. The impact of unsafe water on the consumer is critically alarmed and has contributed human health problem. An alternative clean water sources as a water supply should be sustainable solution to overcome this problem. Malaysia is located at the equator to have rain and hot weather along the year. Therefore, the possible use of spring water as an alternative clean water source will improve the quality of water consumption especially for small community in rural area and provides a benefit to surrounding flora and fauna. The aim of this study is to investigate the performance of spring water sources located in National Defence University of Malaysia (NDUM) campus to support the Green Campus champaign. The spring water analysis was performed for various physicochemical during February 2020 to May 2020. Temperature, pH, electrical conductivity, total dissolved solid, total suspended solid and dissolved oxygen were measured to generate water quality index. The results demonstrated the water samples were found to be suitable for use were within permissible limits except pH were close to or exceeded the permissible limit of standards, which indicates that requirement of treatment prior to use. The outcome of this study may contribute to propose the new way of monitoring water quality in campus by using real-time system. In addition, the outcome also to provides the baseline information about water quality for the welfare of society, support the Green campus campaign and that may also help in future water security and sustainability planning for the NDUM campus area.

Keywords: Spring Water, Water Quality Monitoring, Sustainability, Water Security.

INTRODUCTION

Water has become a necessity in our daily lives. In 2013, the average usage of water per day for Malaysians is 210 liters, while in 2014 the value increase by 2 which means 212 liters or about 141 bottle of 1.5 liters water bottle (Abdullah, 2015). However, the amount of water usage in 2018 has increase to 300 liters per person. The value set by United Nations (UN) is 165 liters per person. The amount set by UN is enough for a person's basic daily needs and yet Malaysians use almost double that value. The trend of excessive usage of water in Malaysia might rise water shortage problems. The lack of clean water will be forced people to drinks unsafe water, this will lead to more diarrhea cases which is the second leading cause of death in children.

World water day celebrate water and raises awareness of the 2 billion people living without access to safe water. It is about taking action to tackle the global water crisis. The main focus is to support the achievement of Sustainable Development Goal (SDG) 6: Water and sanitation for all by 2030. This year, 2022 theme is "Groundwater is invisible, but its impact is visible everywhere". This event is to support three theme which is to minimize the contaminant in groundwater, implement integrated water management at all planning levels and to maximize water efficiency and adapt withdrawals to water availability (Stefan Siepman, 2022).

Besides natural water resources like stream, lake, and river basin, alternative water sources are also started eagerly by human to overcome the scarcity of water in the future. By exploring the new water resources and invent new technologies, the current agencies generate extra or replace current water supply to reach the water demand for current situation and future generation (Li and Boyle, 2010).

In Malaysia, surface water and groundwater are the main source of water supply for drinking, domestic, industrial and agricultural purposes. Spring water is one of the most important for human as a source of fresh water, especially in arid regions which have relatively lac of annual rainfall. Spring is an opening at or near the surface of the Earth for the discharge of water from underground sources or directly into the lake, sea or steam.

The quality of spring water sources varies widely, depend on the location and environmental factors. The quality of water discharged by a spring depends

on the type of aquifer and rock strata through which the water has passed, the temperature along the route and the volume of circulating water, past and present (Britannica, 2020). Water quality expresses the suitability of water for various application including drinking, industrial water supply, irrigation and generation of hydro power. Water quality is indicated by various physical parameters such as pH, total solids, total dissolved solids (TDS), total suspended solid (TSS), hardness, chlorine content many other parameters related. Recently, several studies have focused on monitoring spring water quality in Malaysia (Simon et al. (2019), Razali et al. (2017), Awang (2015), Ngadiman et al. (2015), Zaini et al. (2013)). In Malaysia, spring water quality evaluation and monitoring have received little attention, therefore, these types of analyses are needed to understand the physiochemical and quality changes of spring water.

Green campus campaign has been introduced in NDUM campus as one of efforts to support sustainable development goal set by United Nation. Several studies have been performed to identify the potential of natural and environment resources in NDUM campus for further action including wetland (Othman et al. 2021a), recycle waste (Othman et al. 2021b), solar energy (Hashim et al. 2021) and other study related (Jelani et al. 2021) This study supports the green campus campaign in UPNM by providing the initial data collection for water security and sustainability planning in future.

In this study, the water quality of spring water located in NDUM campus were measured and classified based on National Water Quality Standard. Five parameters (Dissolved Oxygen, Temperature, Total Suspended Solids, Total Dissolved Solids and pH) is chosen as the initial factors in determining the spring water quality.

MATERIAL AND METHODS

Study area and sampling sites

The study area is located in the NDUM campus area situated near Sg. Besi at a distance of 10 km from city of Kuala Lumpur, Malaysia. The community in the campus has about 3000 persons. The map and the location of the investigated springs are presented in Fig. 1. Sg. Besi is a town and suburb area, and the climate is considered humid weather throughout the year. The average daily temperature is between 21^{o}C and 32^{o}C. The area receives an annual rainfall of 750-900 mm. The major water sources are streams, rivers and groundwater. Spring water sampling points were spotted in the NDUM campus.

Sampling and sample analysis

A total of 16 water samples were collected from the spring water points. Sampling was undertaken from February to April 2020 in between wet (Northeast Monsoon from October to March) and dry (Southwest Monsoon from April to September). The water samples were placed in 500 ml bottles rinsed with distilled and later washed with the sample's water. These bottles containing water samples were later transferred into a cooling box and stored in a refrigerator at 20^{o}C for water quality analysis.

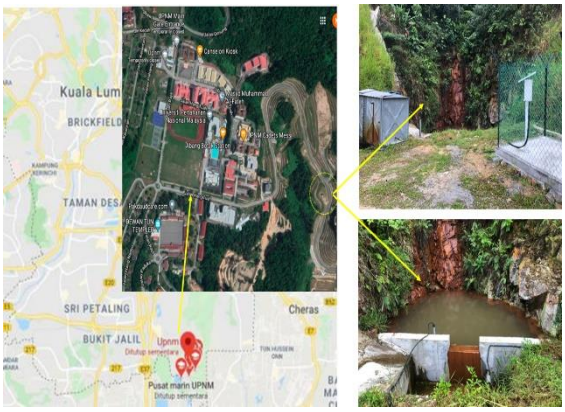

Fig. 1 The location of NDUM and the spring water

The water quality analysis involved several parameters including temperature (°C), pH, electrical conductivity (EC), total dissolved solid (TDS), total suspended solid (TSS) and dissolved oxygen (DO) in accordance with the procedures delineated in the standard guideline described by WHO (2011) and NSDWQ (2004). Electrical conductivity (EC) and pH of each water sample were measured in-situ. The water quality assessment from other water resources around UPNM (i.e. groundwater (Omar (2021), tap water (Jamid (2018) and rainfall (Munikanan et al. (2019)) was used as a control. Table 1 shows the technical and methods used for the analysis of different parameters, along with the instruments and units used in this study.

(a) Temperature
Temperature is one of the factors that affect the water density and dissolved oxygen levels in water. Moreover, temperature control rate reactions and growth of living organism in water. The variation in temperatures may influence by various condition along its path to the surface. WHO (2011) stated that there is no requirement for temperature as it changes depending on the location of the water source.

(b) pH
pH refers to the degree of acidity or alkalinity of a water.

(c) Electrical conductivity
The conductivity in water is the ability of water to conduct an electric current. This is proportional to the ion concentration in the water.

(d) Total suspended solids
TDS is a measure of the dissolved combined

content of all inorganic and organic substances present in a liquid in molecular, ionized, or micro-granular (colloidal sol) suspended form. TDS also used as a parameter to evaluate the quality of drinking water.

(e) Dissolved oxygen

The amount of oxygen dissolved in water is referred to as dissolved oxygen (DO). The atmosphere and aquatic vegetation both provide oxygen to water bodies. Running water, such as a fast-moving stream, dissolves more oxygen than stagnant water, such as that found in a pond or lake.

Table 1 The Method used for the analysis the different parameters

Parameters	Unit	Reference Method Of Analysis
Total Dissolved Solids (TDS)	mg/L	TDS Meter
pH	unit	pH meter
Temperature	°C	Temperature
Conductivity	S/m	Conductivity Meter
Dissolved Oxygen (DO)	mg/L	DO Meter

RESULTS AND DISCUSSION

The water quality analysis of spring water was determined. The summary of parameters measured are presented in Table 2.

Table 2 Water quality of spring water in UPNM

Parameters	Unit	Range	Mean	Std Dev	Recommended WHO (2017)	Recommended NDWQS (2000)
Total Dissolved Solids (TDS)	mg/L	30-300	206	10.8	1000	500
pH		6-6.4	6.3	0.6	6.5-8.5	6.5-9.0
Temperature	°C	22-27	25	1.5	-	-
Conductivity	µS/cm	10-100	52	5.8	400	1000
Dissolved Oxygen (DO)	mg/L	5-8.5	6.5	0.8	7	-

The results of TDS for the spring water samples shows in Fig. 2. The results reflected that the TDS for spring water and groundwater was around 30 to 300 mg/L and nearly the same reading. The mean TDS was 206 mg/L with standard deviation of 10.8. These values are acceptable based on recommended values by WHO (2011) which is within 1000 mg/L and 500 mg/L for NDWQS (2000).

Similar trends of result were obtained by Hamzah et al. (2013) but Razali et al (2017) recorded lower concentration of TDS in ground water samples in Selangor, Malaysia. Usually, EC and TDS are directly related to each other. The more the number of ions, the more will be the value of TDS and furthermore will be the EC (Rusydi, 2018).

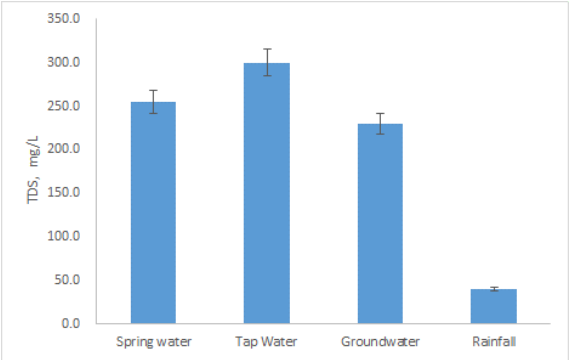

Fig. 2 NDUM campus spring water TDS

The results of pH values for spring water sampling was in range of 6 to 6.4 as shown in Fig. 3. The recommendation of drinking water pH range stated by WHO (2011) is in between 6.5 and 8.5. The mean pH was 6.3 with standard deviation of 0.6. Most of the data are around the mean value. Overall, the samples sites and controls were found to be acceptable. These values aligned with the finding by Simon et al. (2019) and Razali et al. (2017) for spring water flow from fractures in granite rocks in Semenyih, Malaysia with pH range of 6.7. Hamzah et al. (2013) and Simon et al. (2019) reported that the pH of water sources in hot spring around Selangor, Malaysia are characterized as alkaline and this might be due to geological composition of the region. Ngadiman et al. (2015) tested a spring water from the hill of Ulu Yam also shows the pH value for hill water is 6.8 and almost neutral.

The temperature of spring water as shown in Fig. 4 were consistent with other types of water resources in UPNM campus with 25°C with standard deviation of 1.5. the error bar also show the result is significant. The present study shows similar results on range of temperature of spring water flow from fractures in granite rocks near SILK Highway in Malaysia reported in Razali et al. (2017). Hamzah et al. (2013) and Simon et al. (2019) reported the high temperature in hot spring water with temperature range between 36°C to 68°C. The difference in temperature may due to the geothermal heating. The temperature values in this study is within the normal temperature.

Fig. 5 show the results of conductivity for the spring water in NDUM campus. The graph shows the value for the location fluctuate slightly throughout the testing period. The conductivity values in all sampling were in the range of 10 µS/m to 100 µS/m. The highest conductivity recorded is 100 µS/m. On the other hand, the lowest data recorded is 10 µS/m. The low value of conductivity indicates a smaller number of ions present in the water sample, making it suitable to consume. The similar trend was found in the work conducted by Razali et al. (2017). The research conducted by Hamzah et al. (2013) shows an average results of 505.9 µS/m. According to Simon et al. (2019) the spring water has an average conductivity value of 443 µS/m. The average value for the conductivity for this spring water is within the limit of NDWQS (2000) and WHO (2011). Therefore, it is safe to be use for consumption.

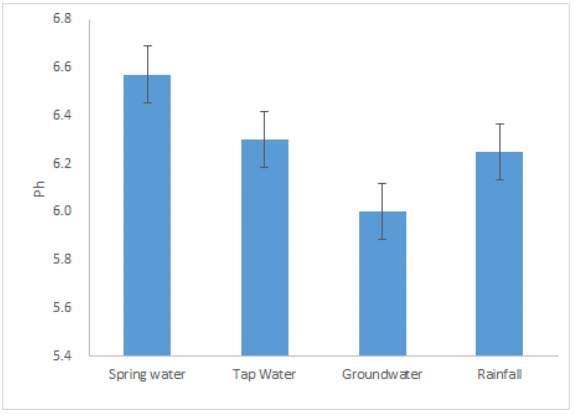

Fig. 3 NDUM campus spring water pH.

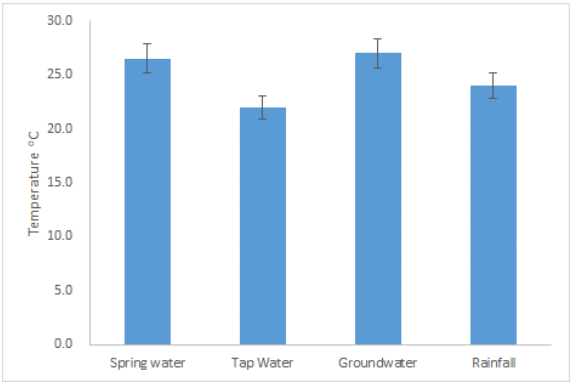

Fig. 4 NDUM campus spring water temperature

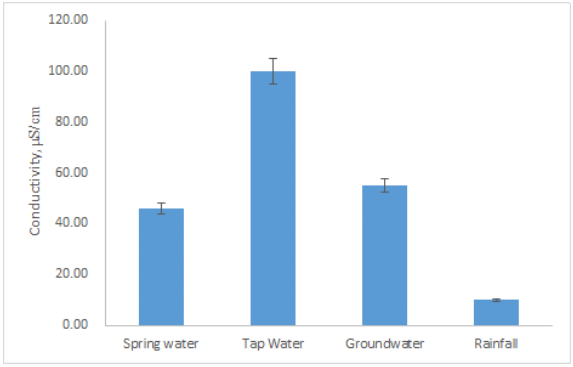

Fig. 5 NDUM campus spring water Electrical conductivity (EC)

The graph (Fig. 6) shows the value for the spring water locations fluctuate slightly throughout the testing period. The DO values in all sampling were in the range of 5.00 mg/L to 8.50 mg/L. The highest turbidity recorded is 8.50 mg/L. On the other hand, the lowest data recorded is 5 mg/L. Therefore, the spring water for this source is safe for consumption as the results the within limit set by WHO and NDWQS. The DO value in the present study shows that it is higher compared to values reported in Simon et al. (2019). The turbidity of spring water flow from the spring water in Jordan by Al-Khashman shows that the DO value of 4.63 mg/L. A study on hot spring in Selangor by Hamzah et al. (2013) shows a lower DO value with an average of 3.38 mg/L.

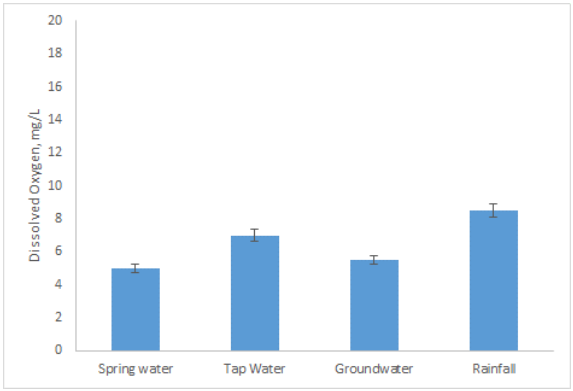

Fig. 6 UPNM campus spring water DO

CONCLUSION AND RECOMMENDATION

The present study has been conducted to determine the quality of spring water in NDUM campus based on several parameters. The water samples were found to be suitable for use were within permissible limits except for pH were close to or exceeded the permissible limit of Malaysia standards, which indicates that requirement of treatment before can be safely consumed. The outcome of this study may contribute to propose the new way of monitoring water quality in campus by using real-time system.

In the future, the biological and chemical testing

should be conducted in order to fully assess the quality of the spring water to be used for drinking. However, it is also important to investigate other potential water contamination such as microbial and radiological for longer period to assess the overall water quality of NDUM.

ACKNOWLEDGEMENT

The authors wish to thank the Department of Civil Engineering, Faculty of Engineering and Research and Innovation Centre (PPPI) at National Defence University of Malaysia especially for their support. This work is also supported by National Defence University of Malaysia under Short Term Grant Project entitles “Sustainable Spring Water Treatment System for Small Community” with grant number UPNM/202/GPJP/PK/1. The appreciation is also extended to my beloved parents, family, lecturers and fellow colleagues for their continuous help and support.

REFERENCES

[1] Rusydi A.F. Correlation Between Conductivity and Total Dissolved Solid In Various Type Of Water: A Review. IOP Conference Series: Earth and Environmental Science, 2018, 118(1).
[2] Asmoe M.A. Feasibility Study on Groundwater Extraction in Sungai Besi Camp. First Degree Thesis. Universiti Pertahanan Nasional Malaysia, 2010.
[3] Florence L.J.E Alternative Water Resources In UPNM Campus. First Degree Thesis. Universiti Pertahanan Nasional Malaysia,2018.
[4] WHO. Guidelines for drinking-water quality, Fourth edition incorporating the first addendum. WHO Library Cataloguing-in-Publication Data, 2011.
[5] Engineering Services Division, Ministry of Health Malaysia. National standard for drinking water quality. Kementerian Kesihatan Malaysia, 2004.
[6] Suriyani Awang. A Water Quality Study of Selangor River. Degree for Doctor of Philosophy School of Environmental Sciences University of East Anglia Norwich England, 2015.
[7] WHO, Guidelines for Drinking-Water Quality. 2nd ed., Volume 2, Health Criteria and Other Supporting Information. International Program on Chemical Safety, Geneva, 2011.
[8] Appalaraju Yarral and Siva Krishna Kotha, A Water Quality Monitoring system based on Wireless Sensor Network., 2017.
[9] Bartram J. and Ballance R. Water Quality Monitoring - A Practical Guide to the Design and Implementation of Freshwater Quality Studies and Monitoring Programmes. United Nations Environment Programme and the World Health Organization, 1996
[10] Othman, M., Suif, Z., Jelani, J. Ahmad, N., Che Osmi, S.K., M. Nadzri, M, N. (2021a). Performance of Pilot-scale Constructed Wetland for Treating Stormwater. Jurnal Kejuruteraan SI 4(2) 2021: 141-145. UKM.
[11] Razali M. F., Roslan F., Ismal F. I. and Noor W.S.A.W.M. Analisis kualiti air bawah Tanah di Lebuhraya SILK Kajang Sungai Long, Hulu Langat, Selangor. Undergraduate Research Journal for Earth Sciences ISSN, 2017, 2600 – 8009.
[12] Engineering Services Division, Ministry of Health Malaysia, National Standard for Drinking Water Quality. Kementerian Kesihatan Malaysia, 2004.
[13] American Public Health Association (APHA), Standard Methods for the Examination of Water and Wastewater, 22nd edition, 2012.
[14] Ngadiman N., Kaamin M. and Hamid N.B. Water Quality of Hills Water, Supply Water and RO Water Machine at Ulu Yam Selangor. IOP Conf. Series: Materials Science and Engineering, 2015, 136: 012081.
[15] Zaini, H., Abd Rani, N.L., Saat, A. and Wood, A. K. Determination of Hot Springs Physico-Chemical Water Quality Potentially Use For Balneotherapy. Malaysian Journal of Analytical Sciences, 2013, Vol 17 No 3 : 436 – 444.
[16] Al-Khashman O.A., Ainawafleh H.M, Jrai A.A. and Al-Muhtaseb A.A. Monitoring and Assessing of Spring Water Quality in Southwestern Basin of Jordan. Open Journal of Modern Hydrology, 2017, Vol 7, 331-349.
[17] Hashim, F.R., Nagappan, P., Ishak, M.T., Joini, N.F., Makmor, N.F., Saleh, M.S., and Zolkiply, N. Solar Location Estimation Using Logsig Based Activation Function using Artificial Neural Network Approach. Zulfaqar Journal of Defence Science, Engineering and technology. Vol. 4 (1).
[18] Simon N., Unjah T., Yusry M. and Dzulkafli M. A. Physico-chemical Characterisation and Potential Health Benefit of the Hulu Langat Hot Spring in Selangor, Malaysia. Sains Malaysiana, 2019, 48(11)(2019): 2451–2462.
[19] Aaruththiran M., Yujia Z. and Bagherian M. A. Smartphone-based Real-Time Water Quality Monitoring System, Master of Engineering The University of Nottingham, Faculty of Engineering Department of Electrical and Electronic Engineering, 2019.
[20] Munikanan, V, Mon, A.A., M. Sahkrin, N.N.S, Md Nor, M.A., Yahya, M.A. Yusof, M.A. and E.Jing, F.L. (2019). Alternative Water Resources in UPNM. International Journal of Recent Technology and Engineering (IJRTE). ISSN: 2277-3878, Vol. 7, Issue-5S4.

[21] Othman, M., Ahmad, N., Suif, Z., Jelani, J. Munikanan, V. and Md Farid, F. (2021b). Recycling Waste Practice in Campus Towards a Green Campus and Promotion of Environmental Sustainability. Jurnal Kejuruteraan SI 4(1) 2021: 13-17. UKM.

[22] Jelani, J., Adli Hah, M.S., M Daud, M.N., Ahmad, N., Othman, M. and W. M. Sabri,m W.M. S. (2021). Stability Analysis of a Man Made Slope: A Case Study on the UPNM Campus, Sg Besi, Kuala Lumpur. Sustainable Development of Water and Environment. Springer Nature Switzerland, AG 2021, H-Y. Jeon (ed.).

[23] Britannica, T. Editors of Encyclopaedia (2020, January 16). spring. Encyclopedia Britannica. https://www.britannica.com/science/spring-water

[24] Ebraheem, A. A., Sherif, M., Al Mulla, M., Alghafli, K. and Sefenasr, A. (2022). Assessment of Groundwater Resources in Water Springs Areas using Geophysical Methods, Northern UAE. Natural Disaster Science and Mitigation Engineering: DPRI Reports. Wadi Flash Floods. Springer Open Access.

8th Int. Conf. on Structure, Engineering & Environment (SEE), Mie, Japan, Nov.10-12, 2022, ISBN: 978-4-909106094 C3051

POTENTIAL FOR DESCENDING METEORIC WATER RECHARGE IN HYDROTHERMAL SYSTEMS AS A PATHWAY FOR CARBON DIOXIDE SEQUESTRATION

John Victor Smith[1]
[1]Faculty of Engineering, RMIT University, Australia

ABSTRACT

The disposal of carbon dioxide (CO_2) by sequestration in geological zones below the ground surface has been identified as an important potential contributor to maintaining climate stability. Most attention has been on reservoirs which are depleted in oil or gas or in saline aquifers more generally. Pumping carbon dioxide into basalt host rocks to promote carbonate mineralization is also being undertaken. In this paper another environment in which CO_2 is naturally introduced into geological materials and stored below ground is reviewed. The environment is the natural hydrothermal systems which are commonly found in magmatically active locations. In these areas it is common for the cool near-surface (meteoric) water to descend as a replacement (recharge) of the warm or hot magmatic water in the hydrothermal-magmatic system. The role of CO_2 in such modern and ancient hydrothermal systems is reviewed. Examples of hydrothermal systems, particularly in the western Pacific, show the common occurrence of naturally descending meteoric water recharge in hydrothermal systems. It is also noted that the descending waters are commonly enriched in CO_2. The descending CO_2 can react with existing rocks and minerals to form carbonates of calcium and other cations. Studies of modern and ancient hydrothermal systems show the ways in which formation of carbonate can occur. It is proposed that introduction of CO_2 into naturally descending meteoric water recharge in hydrothermal systems may be a mechanism for CO_2 sequestration by mineral trapping. Further investigation of this process and its potential is proposed.

Keywords: CO_2 Sequestration, Hydrothermal Systems, Meteoric Water, Recharge

INTRODUCTION

One of the responses to an increase in carbon dioxide (CO_2) in the atmosphere is to sore it underground in a process referred to as geological sequestration [1]. The various ways this can be achieved are being studied and implemented in many countries [2]. Understanding the natural cycle of CO_2 in the Earth may provide additional opportunities for geological sequestration.

Water plays an important role in the transfer of heat and matter in geothermal systems [3]. CO_2 can become fixed within carbonate minerals, for example calcite, dolomite and magnesite through hydrothermal alteration, which is a common occurrence in many parts of the Earth's crust [4]. Water also plays a significant role in the transfer of pressure and the initiation of movement on brittle structures [5]. In this way water can contribute to a fault-valve cycle and once fluid pressure exceeds the lithostatic load, accumulating shear stresses trigger failure on faults. This is supported by observed relationships of faults and other evidence of fluid-pressure cycling within gold veins and other metallic deposits [5].

The process of hydrothermal alteration which transforms large volumes of rock into different mineral assemblages has occurred through geological history including the formation of greenstone belts. Such belts, surrounded by extensive granite, may be 300 m to 12 km wide and 100 to 700 km long and the presence of carbonate minerals in greenstone belts is well known [6].

In this paper it is proposed that introduction of CO_2 into naturally descending meteoric water, which commonly recharges hydrothermal systems, may be a mechanism for CO_2 sequestration by mineral trapping. Further investigation of this process and its potential is proposed.

FORMATION OF CARBONATE MINERALS

Geothermal systems such as Wairakei in New Zealand have been observed to form deposits of calcite mineral scale in wells [7]. Some other wells in geothermal systems produce no calcite scale and are inferred to be a result of waters entering the wells being undersaturated in CO_2 or suitable cations. It is inferred that, during recharge of shallow water deeper into the geothermal reservoir, an insufficient quantity of CO_2 was transported into the system to saturate the water with calcite. [3].

Carbonate minerals are commonly found within the rocks affected by hydrothermal systems. These minerals are found over a wide range of pH and temperature conditions. Carbonates are also found in

association with a wide range of other minerals (Table 1). The types of carbonate minerals, as determined by their cations, can also vary with increasing fluid pH. This effect has been observed as zoning of carbonate minerals as has been observed in some hydrothermal systems [8]. Based on these observations, it has been inferred that Fe, Mn and Mg become less mobile as pH increases toward neutral.

The solubility of carbonate minerals in an aqueous solution at pH 4-8 can be represented by Eq. (1):

Table 1 Associations of carbonate and clay minerals [8]

Carbonate cations	Mineral names	Associated minerals	pH conditions
Fe, Mn	Siderite, rhodocrosite	Kaolin, illite	Low
Ca, Mn, Mg, Fe	Rhodocrosite, ankerite, kutnahorite, dolomite	Illitic and chloritic clays	Mod.
Ca, Mg	Dolomite, calcite	Chlorite, calc-silicates	Neutral

$$MCO_3+CO_2+H_2O=M^{2+}+2HCO_3^- \quad (1)$$

Where M represents the cations: Ca, Mn, Mg, Fe.

At pH less than 4 carbonates are dissolved. At temperatures less than 100°C and neutral conditions (pH 6-7) bicarbonate dominates over CO_2. The controls on carbonate solubility under high temperature saline conditions is the subject of current research.

Carbonate minerals are present in all levels in hydrothermal systems from low temperature surficial conditions to deep magmatic conditions. The dominant control on carbonate deposition is increasing temperature. In comparison, dilution and pressure drop are secondary factors in affecting carbonate deposition. Therefore, the heating of descending CO_2-rich waters leads to carbonate mineral deposition [8].

If a fluid with significant concentrations of dissolved CO_2 undergoes boiling, carbonate deposition can also occur. The most common cause of boiling in nature is the reduction in pressure rather than an increase in temperature. Such a reduction in pressure can occur gradually by ascending fluids having decreased overburden or rapidly by faulting or large-scale landslides [8].

A comprehensive review of hydrothermal systems in the southwest Pacific rim [8] showed that many of these systems incorporate meteoric water recharge.

METEORIC WATER RECHARGE IN HYDROTHERMAL SYSTEMS

Geothermal systems can be characterized according to the chemistry of the water emanating from a magma intrusion. Geothermal systems can also be characterized by the depth of the magma intrusion and therefore the distance from the heat source to the geothermal activity observed near the surface. The class of geothermal systems known as ‘epithermal’ refer to the significant distance that can exist between the heat source (magma intrusion) and the ground surface. The epithermal system refers to the areas in which near surface waters circulate through the ground such that the chemistry of the waters is a mixture of juvenile magmatic water and groundwater known as ‘meteoric’ water. In these epithermal systems it is common for CO_2-rich water to descend from above an intrusion and mix with magmatic fluids in the conduits [8]. The conduits of fluid flow may be permeable rocks or structures such as faults. The magmatic fluids typically contain dissolved reactive gases. The chemistry of the fluids can be affected by interaction with rock and dilution by the circulating meteoric waters. The meteoric waters typically capture a significant amount of the magmatic gases, including CO_2, as the mixing occurs [8].

Mineral Deposition

The cool, descending, low pH, CO_2-rich meteoric water mixes with hot, silica-saturated, deep magmatic fluids resulting in deposition of carbonates in response to increasing temperatures [8]. Hydrothermal systems are commonly located in tectonically active areas such that major fracture zones and faults can be periodically reopened by fluid pressure permitting both the ascent of magmatic fluids and the descent of meteoric water to progressively deeper levels [5].

Where mineral precipitation occurs in permeable rocks, the rock is described as ‘altered’. Where mineral precipitation occurs in fractures the rocks are described as ‘veined’. The overall effect of these processes is to seal the most permeable zones by precipitation of minerals including carbonates.

A review of geothermal systems in the Philippines showed that cool, low pH, CO_2-rich water has been detected as deep as 2000 m [8]. Evidence that these CO2-rich waters have mixed with warmer magmatic waters include the precipitation of carbonates with a range of cations including dolomite (Ca, Mg-carbonate), siderite (Fe-carbonate) and ankerite (Mg, Ca, Fe-carbonate).

Observations of the occurrence of various carbonate minerals at depths of 600-1200m in the Broadlands hydrothermal system in New Zealand are also considered to be indicative of the drawing down

of CO_2-rich waters into a saline aquifer dominated by magmatic water [8]. At Rotakawa in New Zealand, the occurrence of Mn-carbonates has been inferred to be the result of deep circulation of CO_2-rich surficial waters [8].

In summary, calcium carbonate (calcite) can be deposited from either magmatic or meteoric waters. However, magmatic fluids are typically depleted in magnesium and therefore the presence of Mg-carbonates (dolomite, ankerite) at deep levels in active geothermal systems is inferred to be related to the incursion of CO_2-rich meteoric waters into deeper parts of magmatic hydrothermal systems [8].

Evolution of Hydrothermal Systems

Hydrothermal systems pass through a series of stages, principally driven by the cooling of the intrusive pluton. According to [8] the stages are evidenced by the following features: 1) contact metamorphism, 2) release of a magmatic volatile plume, 3) convective hydrothermal alteration and 4) draw down of surficial waters.

Meteoric waters can be involved in each stage but become more dominant as the system evolves. In the earlier stages the descent of surface water occurs farther away from the thermal center and in the final stage the descent of water can occur directly on top of the waning thermal system [8].

This evolutionary model of hydrothermal systems provides a framework for studying and understanding individual examples of hydrothermal systems. The evolutionary model applies to active hydrothermal and geothermal systems and ancient systems preserved in rock. Both active and ancient systems are of great interest as they are a common host to the formation of metallic mineral deposits. Many of the ancient systems can be hosted within active hydrothermal areas. For example, a magmatic intrusion which has become fully cooled will be surrounded by its fossil hydrothermal system. If further magmatic intrusions occur, complex overprinting of the rock alteration and mineralogy will occur.

A summary of active and ancient hydrothermal systems in which evidence of descending meteoric waters has been observed is provided in Table 2.

Composite Volcanic Terrains

An example of descent of water toward a magmatic volatile plume is the Alto Peak system in northern Leyte, Philippines. In that system the magma is over 2 km below surface (Fig. 1). There is deep meteoric water recharge from multiple kilometers around the magma intrusion to around 2 km depth in the system. Concurrently, in shallower parts of the system meteoric water descends hundreds of meters to form a wide-spread zone of CO_2-rich water.

An example of descent of water toward a zone of convective hydrothermal alteration is the Tongonan system also located in northern Leyte, Philippines. In that system the magma is within 1 km below surface (Fig. 2). There is deep meteoric water recharge from multiple kilometers around the magma intrusion to around 2 km depth in the system. Concurrently, in shallower parts of the system, meteoric water descends hundreds of meters along major faults.

An example of near-surface water being drawn down to deeper levels is the Palinpinon geothermal field in southern Negros, Philippines. This final stage of geothermal waning occurs as the pluton cools. In this stage cool dilute meteoric waters and shallow, low pH and CO_2-rich waters descend to considerable depth within the reservoir of saline groundwater. The Palinpinon geothermal field and surrounding geothermal activity is driven by the intrusion and cooling of a large monzonite intrusion [8].

Table 2 Examples active and fossil hydrothermal systems with descending CO_2-rich/meteoric water [8]

Country	System	A/F
Philippines, northern Leyte	Alto Peak, Tongonan	A
Philippines, southern Negros	Palinpinon	A
Philippines, southern Luzon	Bacon-Manito	A
Philippines, eastern Mindanao	Amacan	A
Sumatra, Indonesia	Miwah	A
PNG, Lihir Island	Ladolam	A
Australia, Queensland	Kidston	F
Indonesia, Kalimantan	Kelian	F
PNG	Porgera	F
PNG	Morobe	F
PNG, Woodlark Island	Busai	F
PNG	Maniape	F
PNG	Mt Kare	F
Solomon Islands	Gold Ridge	F
New Zealand, Coromandel	Golden Cross	F
Japan, Kyushu	Hishikari	F

A=active geothermal system, F= fossil hydrothermal system

One of the characteristics of a waning geothermal field is that CO_2-rich water can be descending directly at the center of the field as is occurring in the fault zones that mark the focus of the Palinpinon

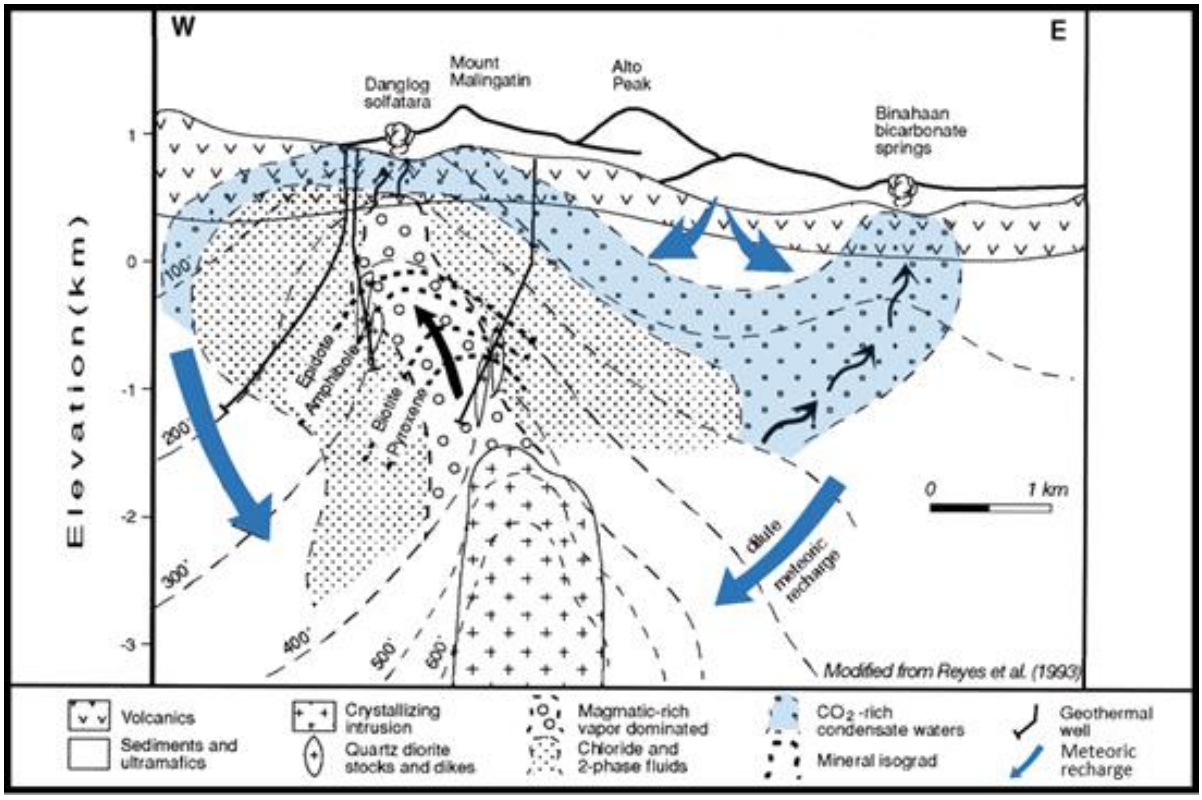

Fig. 1 Alto Peak (Philippines) hydrological model [8]. Descending meteoric waters shown in blue arrows. CO_2-rich waters shown in blue.

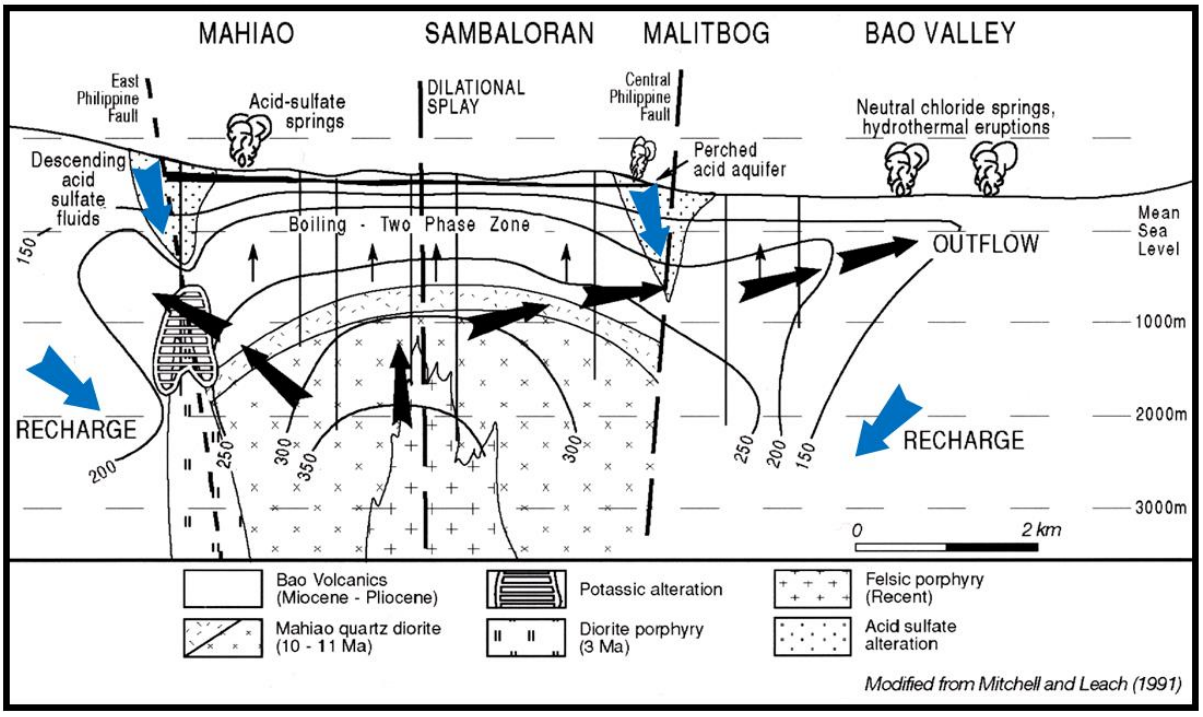

Fig. 2 Tongonan (Philippines) hydrological model [8]. Descending meteoric waters shown in blue arrows.

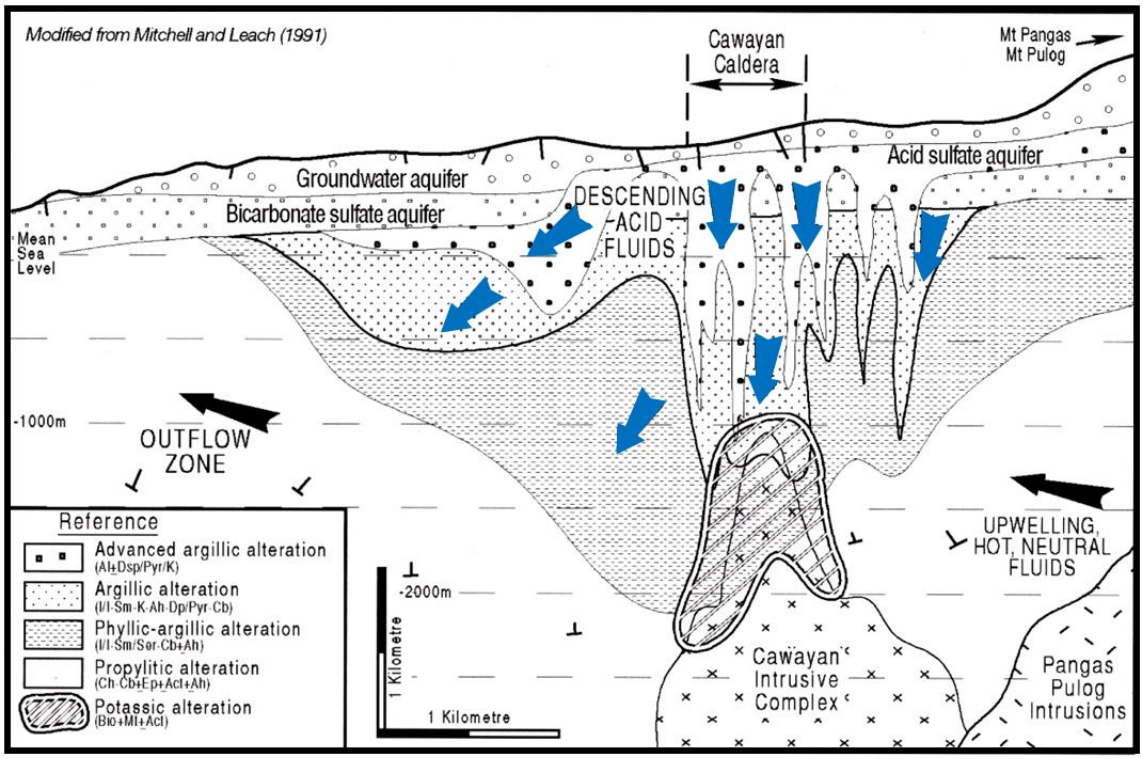

Fig. 3 Bacon-Minato (Philippines) hydrological model [8]. Descending meteoric waters shown in blue arrows.

geothermal field. A pluton emplaced during the Miocene initiated the system and progressively cooled. Smaller and younger intrusions have occurred on tectonic structures. These younger intrusions and deeper extensions of them, provide the current heat source for the geothermal field.

In the Palinpinon geothermal field, meteoric waters also move laterally through permeable strata toward the center of the geothermal field. According to [8] the Palinpinon geothermal field is in an early stage of waning or thermal collapse such that cool CO_2-rich meteoric waters are descending in response to pressure draw down. The dilute nature of the fluids in the central part of the system show that the meteoric waters are dominant over the residual presence of magmatic water.

The Bacon-Manito geothermal field in southern Luzon, Philippines, has a complex volcanic and intrusive geological history which has been interpreted as a waning system (Fig. 3). It has been observed that CO_2-rich waters move down structures and caldera margins to depths exceeding 1,500 m. This descent of cool waters into hotter environments has resulted in widespread deposition of carbonates and other minerals. As a consequence of mineral precipitation, the upper 1000 m is relatively low in permeability [8].

Cordillera-style Hydrothermal Systems

Volcanic mountain chains, commonly called cordillera are also associated with hydrothermal activity. In the Philippines, the northern Luzon and eastern Mindanao regions can be considered to be cordillera-style hydrothermal systems. In these areas upflow of magmatic water can be restricted to vertical channels. Mixing of magmatic fluid and CO_2-rich surficial water occurs near the surface.

An example of a Cordillera-style geothermal system is the Amacan geothermal system eastern Mindanao, Philippines. Abundant bicarbonate springs with as much as 4 wt% CO_2 occur in the area. This is inferred to be the result of meteoric waters intercepting CO_2 from the magmatic source and redistributing it within the geothermal system [8].

FOSSIL HYDROTHERMAL SYSTEMS

One of the most significant sources of information on hydrothermal systems is from those systems where metals have been deposited. Many of these systems are extinct or nearly extinct so they can be considered to be fossil hydrothermal systems.

Meteoric water played a significant role in many such hydrothermal systems. Of the mineral deposit-forming processes the epithermal or more specifically, the low sulfidation porphyry system is one environment in which meteoric water interaction is most crucial.

An example of such a system is the Ladolam gold mine on Lihir Island, Papua New Guinea. The gold mineralization is understood to have formed in an

earlier phase of the evolving geothermal field. The current geothermal system is inferred to be in a waning stage. Currently, low pH, CO_2-rich waters are being drawn down into the geothermal system. These waters are understood to be groundwaters that have absorbed gases from the earlier magmatic systems. The temperature and pH of the water near the surface allowed dissolution of carbonate and later re-deposition of the carbonate deeper in the system as the descending water was heated [8].

The Kidston gold mine in Queensland Australia is hosted by a Permo-Carboniferous age volcanic breccia pipe. The sequence and distribution of minerals shows that descending cool, low pH, CO_2-rich waters descended into the hydrothermal system and deposited carbonate minerals [8].

There is an entire class of mineral deposit known as carbonate-base metal-gold systems. These systems have characteristics similar to other hydrothermal systems including the importance of the mixing of rising magmatic water with meteoric CO_2-rich water.

The fluid flow model for these deposits involves hot mineralized fluids which evolve from cooling intrusions. The fluids rise along permeable zones which may be fracture systems. At depth, these fluids mix with circulating meteoric waters. Gases evolve from these upwelling fluids by boiling and vapor loss and are absorbed by groundwater near the surface to form CO_2-rich waters. Cooling of the intrusions leads to draw down of these fluids deep into the hydrothermal system. Carbonate minerals are precipitated as a result.

An example of these processes is the Kelian mine, Kalimantan, Indonesia. In this system carbonate minerals are zoned with depth. Fe and Mn carbonates are encountered at shallow depth whereas Mg and Ca carbonates are found deeper in the deposit [8].

The Porgera deposit in Papua New Guinea is also classified as a carbonate-base metal-gold deposit. Carbonate minerals are zoned in a similar manner to the Kelian deposit. Carbon and oxygen isotope data from carbonates at Porgera support the model of progressive mixing of magmatic and meteoric waters to produce the observed zonation of carbonate minerals [9].

DISPOSAL OF CO2

It is known that geothermal systems can undergo steam eruptions due to changes in pressure [10-11]. Therefore, any ground engineering activities in a geothermal system must be conducted with careful risk assessment being applied.

Disposal of CO_2 usually involves pumping water through wells. In disposal into oil fields and saline reservoirs the depths of CO_2 introduction are very deep and the gas is in a supercritical state and dry of water. Shallower injection of CO_2 gas can be used where mineral carbonation is the aim. These gases are typically not in a critical state and water can be present with the gas.

It is proposed in this paper that the existing downward flow of meteoric water in natural geothermal systems introduces the possibility of using a syphon system to introduce CO_2 to the ground. This means that highly pressurized pumping may not be needed for the gas and/or gasified water to be introduced to the ground. It is anticipated that a well would be required to ensure that the gas becomes entrained in a downward flow. The depth of the well would depend on the nature of the natural flows.

It is anticipated that meteoric waters that are not currently saturated in CO_2 would be the most favorable for disposal of CO_2. Identification of suitable sites for CO_2 disposal would require a detailed understanding of the geothermal system. This assessment would include assessment of the presence of rock with sufficient cation potential for the formation of carbonate minerals in combination with the introduced CO_2.

Exploration of geothermal systems is a well developed field of research including the use of geochemistry [12] and geophysics [13]. The concept of using existing downward flowing water to sequester CO_2 through mineralization has not been previously considered and may have significant barriers and limitations. It is hoped that this review may prompt further investigation into this possibility.

CONCLUSIONS

Descending water with CO_2 occurs naturally and is common in areas of geothermal activity. It is known that carbonate minerals form abundantly in many of these systems.

It is proposed that active geothermal systems in which descending waters are not saturated in CO_2 could accommodate the introduction of CO_2 for the purpose of reducing atmospheric carbon. Because these are naturally down-flowing waters there is potential to use the syphon effect to draw water enriched in CO_2 into the descending flow without the requirement for highly pressurized pumping.

ACKNOWLEDGMENTS

Discussions on carbon sequestration with colleagues at RMIT University and CMW Geosciences are acknowledged.

REFERENCES

[1] IPCC, 2022: Climate Change 2022: Impacts, Adaptation, and Vulnerability. Contribution of Working Group II to the Sixth Assessment Report of the Intergovernmental Panel on Climate Change. Cambridge University Press.

[2] Kelemen P., Benson S.M., Pilorgé H., Psarras P., and Wilcox J., An Overview of the Status and Challenges of CO2 Storage in Minerals and Geological Formations. Frontiers in Climate, Vol. 15, 2019, pp. 1:9.
[3] Arnórsson S. Deposition of calcium carbonate minerals from geothermal waters—theoretical considerations. Geothermics. 1989 Vol. 18, Issue 1-2, pp. 33-9.
[4] Gorczyk W, Gonzalez CM, Hobbs B. Carbon dioxide as a proxy for orogenic gold source. Ore Geology Reviews. 2020, Vol. 1, Issue 127, pp. 103-29.
[5] Sibson RH, Robert F, Poulsen KH. High-angle reverse faults, fluid-pressure cycling, and mesothermal gold-quartz deposits. Geology. 1988, Vol. 16, Issue 6, pp. 551-5.
[6] Elmer FL, White RW, Powell R. Devolatilization of metabasic rocks during greenschist–amphibolite facies metamorphism. Journal of Metamorphic Geology. 2006, Vol. 24, Issue 6, pp. 497-513.
[7] Mahon WA. Chemistry in the exploration and exploitation of hydrothermal systems. Geothermics. 1970, Vol. 2, Issue 13, pp. 10-22.
[8] Corbett, G.J., and Leach, T.M. Southwest Pacific Rim gold-copper systems: structure, alteration, and mineralization. Vol. 6. Colorado: Society of Economic Geologists, 1998.
[9] Richards JP, Kerrich R. The Porgera gold mine, Papua New Guinea; magmatic hydrothermal to epithermal evolution of an alkalic-type precious metal deposit. Economic Geology. 1993, Vol. 88, Issue 5, pp. 1017-52.
[10] Hedenquist JW, Henley RW. Hydrothermal eruptions in the Waiotapu geothermal system, New Zealand; their origin, associated breccias, and relation to precious metal mineralization. Economic geology. 1985, Vol. 80, Issue 6, pp. 1640-68.
[11] Global Volcanism Program, Report on Yakedake (Japan) (Wunderman, R., ed.). Bulletin of the Global Volcanism Network, 20:2. Smithsonian Institution. 1995. https://doi.org/10.5479/si. GVP. BGVN199502-283070.
[12] Ii, H., Kanbara, H., Kawabata, Y., Geothermal and Hot Spring Water Origin Determination Using Oxygen and Hydrogen Stable Isotope in The Toyohirakawa Catchment, Hokkaido, Japan. International Journal of GEOMATE, 2017, Vol. 13, Issue 37, pp. 127-132.
[13] Rokhmatuloh, S., Sobirin, R., Suhanto, E., The Effect of Gravity Measurement Distribution Points on Interpretation of Gravity Data in the Gunung Endut Geothermal Prospect Area, Indonesia International Journal of GEOMATE, 2018 Vol.14, Issue 41, pp.60-67.

8th Int. Conf. on Structure, Engineering & Environment (SEE), Mie, Japan, Nov.10-12, 2022, ISBN: 978-4-909106094 C3051

CU,ZN,FE AND MN CONCENTRATIONS OF SOME GASTROPODS IN THE WAKAGAWA ESTUARY TIDAL FLAT

Kazuko Kubo[1] and Hiroyuki Ii[2]

[1]641-0033, Imabuku, Wakayama City
[2]Faculty of Systems Engineering, Wakayama University, Japan

ABSTRACT

Mudflat is an important place for changing organic material into inorganic compound. Benthos in mudflat play a big role of decomposing organic material. In the past, factory wastewater such as dyes and the chemical industries flowed into the Wakagawa River, which is located in the northern part of Wakayama Prefecture, and the estuary was severely polluted. After that, the inflow of contaminated water was restricted by various measures, and the organic pollution of the tidal flats gradually decreased. However, it is thought that various metallic elements remain in the tidal flats and affect benthos. Some of them, especially detritus-feeder, might accumulate metals and could be index organism of environmental contamination. In this study, Cu, Zn, Fe, Mn concentrations of some snails sampled on January-September 2016 were measured using ICP-AES. No clear difference was found between the collection points in this tidal flat, and the accumulated elements differed depending on the species. The Zn concentration was higher in the detritus feeder than in the algae feeder.

Keywords: Snails, Batillaria, Pirenella, Clithon, Heavy metals

INTRODUCTION

Wakagawa estuary is located in the northern part of Wakayama prefecture. The tidal flat area is about 35 hectares. It is thought that more than 300 species of benthos and fish inhabit there, and it has been selected as one of the "500 Important Wetlands in Japan" by the Ministry of the Environment (Ministry of the Environment Nature Conservation Bureau 2001)[1]. However, during the period of high economic growth, there was terrible contamination due to wastewater from factories (leather, dyes, chemical industries, etc.) and domestic wastewater. Since then, the environment in the estuary has improved considerably due to drainage regulations and various measures[2]-[4]. However, it is presumed that the factory effluent at that time contained various metals, and most of these may remain on the tidal flats in some way, affecting benthic organisms.

Many papers have attempted to evaluate metal pollution in environmental water and soil using seaweeds, river insects, and river plants[6-10]. However, there are not many surveys of metal pollution using various benthic animals on tidal flats. In this study, the metal concentrations of some gastropods (snails) of the Wakagawa estuary tidal flat were measured. The gastropods investigated were mainly three species of genus *Batillaria* and *Pirenella nipponica*, which are detritus feeders, and *Nerita japonica* and *Clithon oualaniensis*, which are algae feeders.

STUDY AREA

Wakagawa Estuary Tidal Flat is located in the northern part of Wakayama Prefecture. Fig. 1 shows the location of the Wakagawa estuary on a map, and Fig. 2 shows the sampling points. Fig. 2 is a part of the photo that seems to have been taken at low tide. At high tide, all sampling points sink into the sea, leaving small islets with a plus mark and bridges. The area around the islet is sandy, and the mud increases as it gets closer to the water's edge. The front and south sides of the small islet are relatively sandy, and the wide area on the north side is relatively muddy. Site E is a little low across the channel from Site Front, it's difficult to walk there unless it is at the lowest tide. Sampling was mainly performed at Site Front, and was also performed at Site S, N, E as a reference.

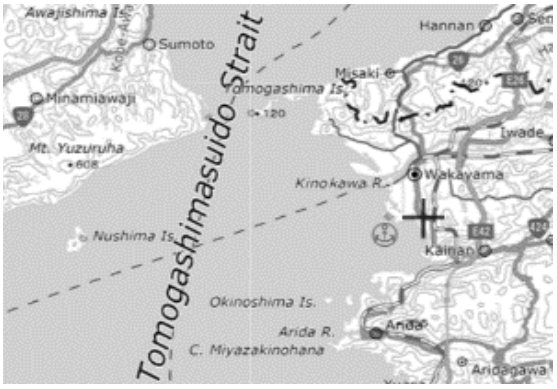

(Map form Geospatial Information Authority of Japan)

Fig. 1 Study area

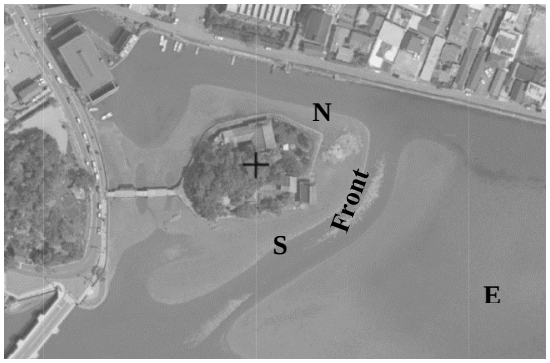

Fig. 2 Sampling site

METHOD

The snails were collected at Site Front on January 12, 2016, May 24, and September 18, 2016 at low tide. On March 22nd, in addition to Site Front, Site N and S were also used as references. On April 11th, only Site E was used for collection. After washing off the mud, the snails brought back were fasted in 50% artificial seawater for about a week to expel the contents of the digestive tract. Then, the whole snail was ultrasonically cleaned, and then the soft bodies was carefully taken out and washed with Millipore water. After sufficiently drying them in a dryer at 60 ° C, they were weighed and dissolved with concentrated nitric acid. After filtering with the 0.45μm membrane filter, the concentrations of Cu, Zn, Fe, and Mn were measured using ICP-OES (AMETEK Inc. SPECTRO ARCOS). For some samples, the previous model Seiko Instruments Inc. SPS1700HVR was used.

RESULTS AND DISCUSSION

Figure3-(a) to (e) show the distribution of Cu concentrations of *Batillaria cumingii*, *B.mulutiformis*, *B.zonalis*, *Pirenella nipponica*, and *Clithon oualaniensis* resupectively. For the four species except *Batillaria cumingii*, no significant difference in Cu concentration was observed depending on the collection site and collection month. For *B. cumingii*, the concentration at Site E seems to be slightly low (Fig. 1-a), but the difference between the mean values is 57.8, which is smaller than the variation in the measured values(Max.-Min.=66.0).

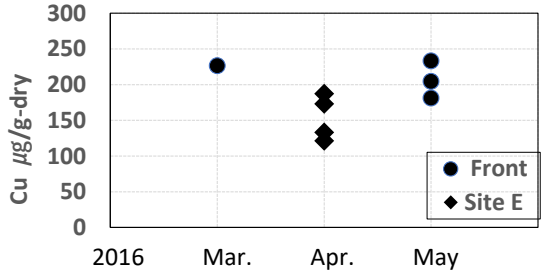

Fig.3-a Cu concentrations of *Batillaria cumingii*

Since the number of samples is small, statistical tests have not been performed.

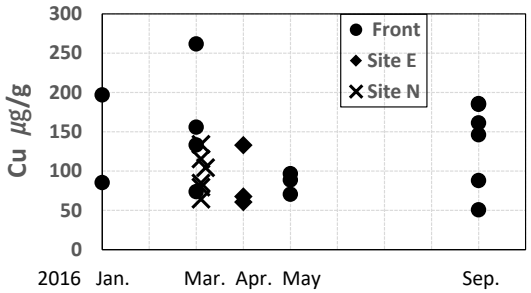

Fig.3-b Cu concentrations of *Batillaria mulutiformis*

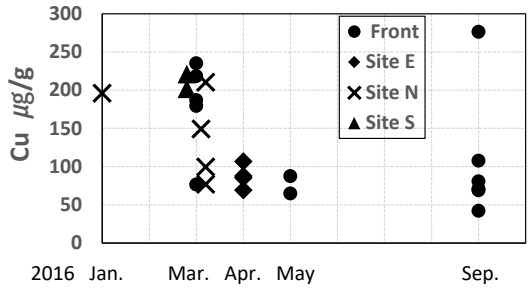

Fig.3-c Cu concentrations of *Batillaria zonalis*

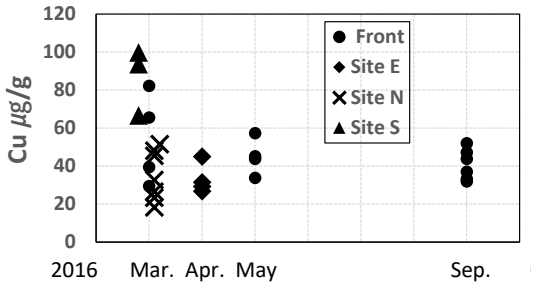

Fig.3-d Cu concentrations of *Pirenella nipponica*

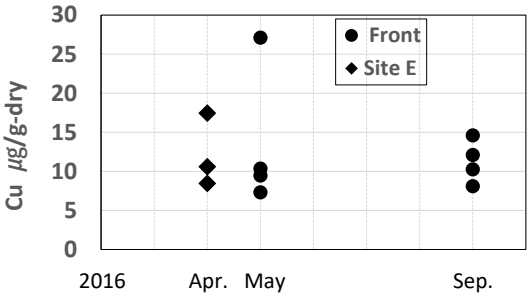

Fig.3-e Cu concentrations of *Clithon oualaniensis*

Figure 4 shows the Cu concentrations of all snails investigated. Six species from *Batillaria* to *Clithon oualaniensis* showed lower values than *Littorinidae* and *Rapana venosa* measured for comparative reference. Among these 6 species, the genus *Batillaria* tended to show higher values than *Pirenella nipponica* and 2 species of family Neritidae, *Nerita japonica* and *Clithon oualaniensis*. No

significant difference was found among the three species of the genus *Batillaria*. The Cu value of *Batillaria cumingi* was about the same as that of Nakatsu tidal flat of [5] and slightly lower than that of Banzu tidal flat (about 300 μg / g). However, care must be taken in the comparison, as they remove the stiff muscles of the foot and use only the internal organs (they call it soft tissue) for measurement.

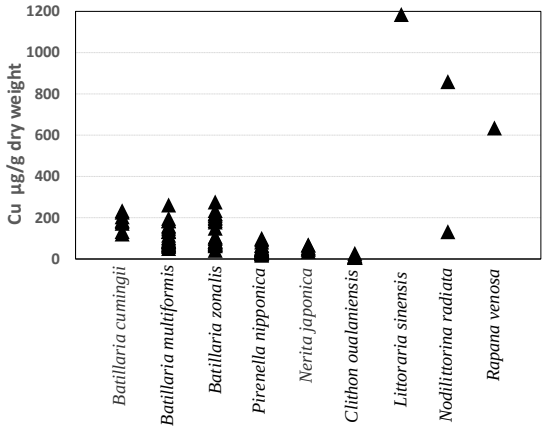

Fig. 4 Cu concentrations of all snails investigated

Figure5-(a) to (e) show the distribution of Zn concentrations of *Batillaria cumingii*, *B.mulutiformis*, *B.zonalis*, *Pirenella nipponica*, and *Clithon oualaniensis*, resupectively. At the Site N, Some individuals showed high values in *B.mulutiformis*, and *B.zonalis*, In *Pirenella nipponica*, the variation of the value was very large at the Site N, and many of them showed higher values than the other sites, and the highest value was 952 μg / g. No difference was found between the E point and the Site Front in all four species.

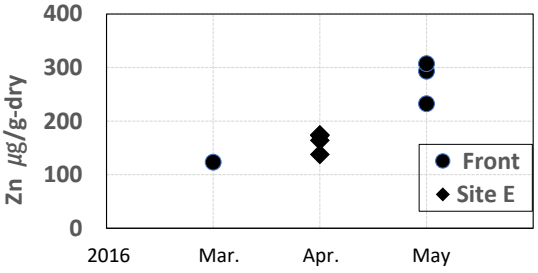

Fig.5-a Zn concentrations of *Batillaria cumingii*

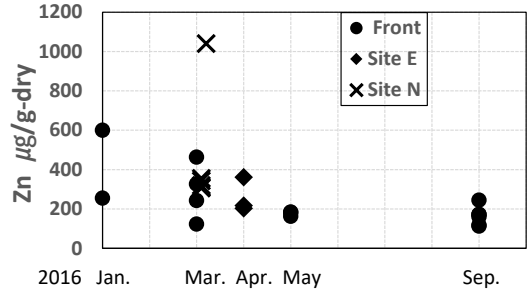

Fig.5-b Zn concentrations of *Batillaria mulutiformis*

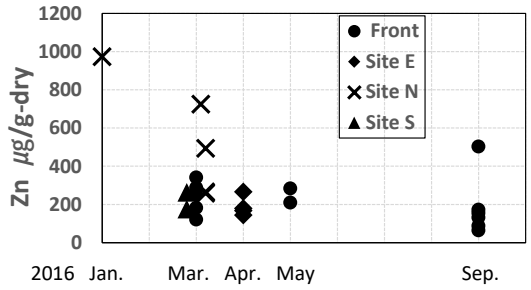

Fig.5-c Zn concentrations of *Batillaria zonalis*

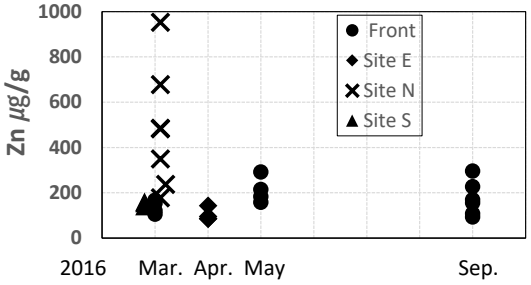

Fig.5-d Zn concentrations of *Pirenella nipponica*

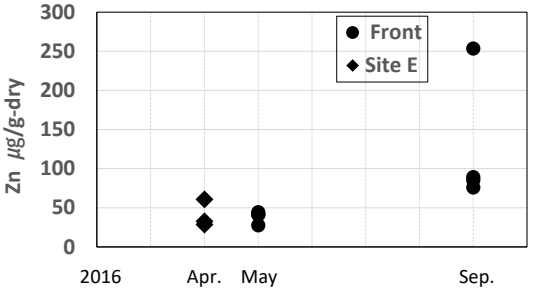

Fig.5-e Zn concentrations of *Clithon oualaniensis*

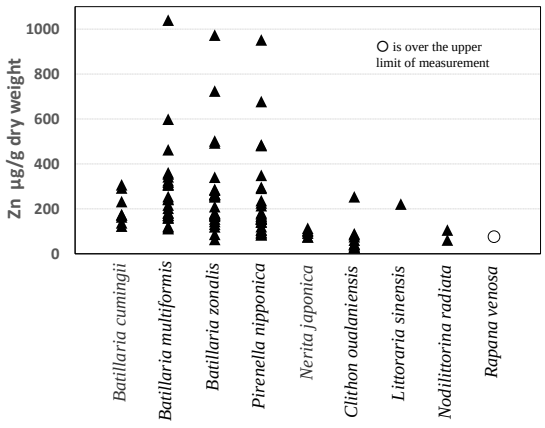

Fig. 6 Zn concentrations of all snails investigated

Figure 6 shows the Zn concentrations of all snails investigated. The Zn value of *Batillaria cumingii* was about the same as or slightly higher than that of Nakatsu and Banzu tidal flat of [5]. Several individuals of *Batillaria mulutiformis*, *B.zonalis* and

Pirenella nipponica showed very high Zn concentrations.

Figure7-(a) to (e) show the distribution of Fe concentrations of *Batillaria cumingii*, *B.mulutiformis*, *B.zonalis*, *Pirenella nipponica*, and *Clithon oualaniensis* resupectively. No significant difference in Fe concentration was observed depending on the site. Some individual of *B.zonalis* showed rather high values. At Site N, one individual of *Pirenella nipponica* showed extremely high value.

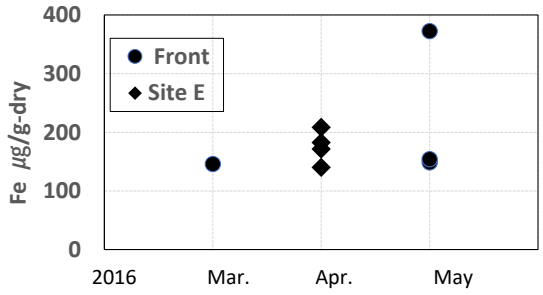

Fig.7-a Fe concentrations of *Batillaria cumingi*

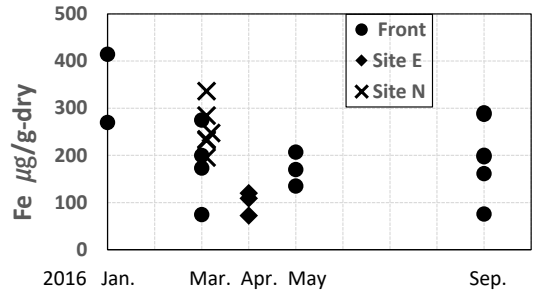

Fig.7-b Fe concentrations of *Batillaria mulutiformis*

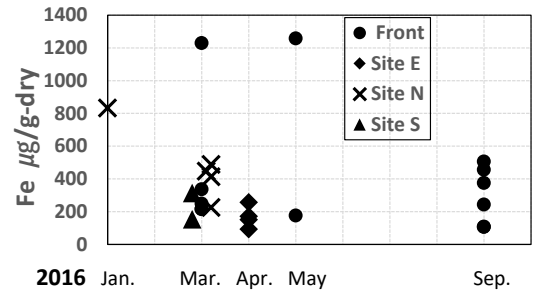

Fig.7-c Fe concentrations of *Batillaria zonalis*

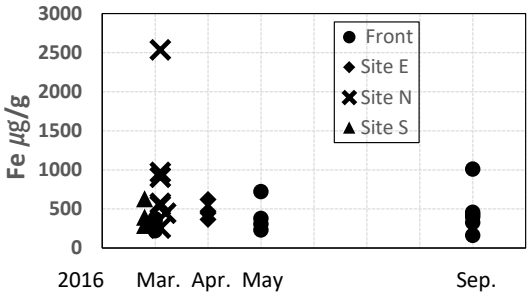

Fig.7-d Fe concentrations of *Pirenella nipponica*

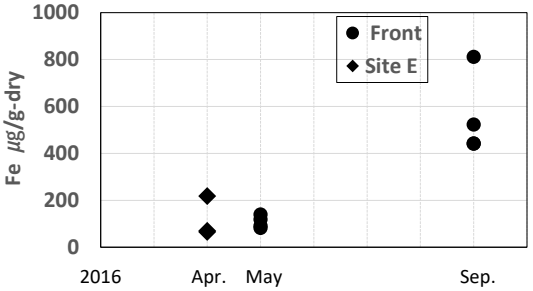

Fig.7-e Fe concentrations of *Clithon oualaniensis*

Figure 8 shows the Fe concentrations of all snails investigated. Some individuals of *Batillaria zonails*, *Pirenella nipponica* and *Clithon oualaniensis* showed very high Fe concentrations. Especially,one individual of *Pirenella nipponica* showed extremely high value. These three species are Near Threatened Species or Endangered Species II. *Batillaria multiformis* is also Near Threatened Species, but it showed similar concentrations to the common species *Batillaria cumingii*. None of the reference species Littorinidae and *Rapana venosa*, showed high concentrations. For Fe, no clear relationship between concentrations and eating habits was found.

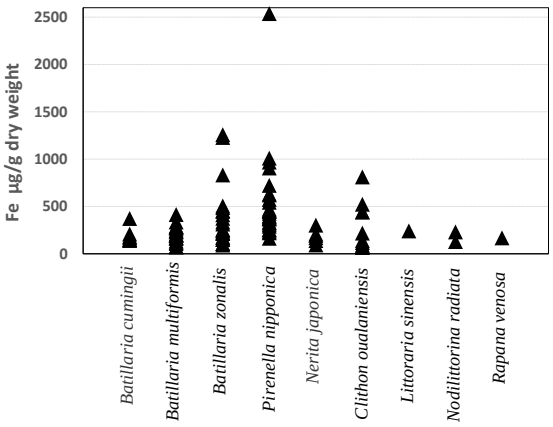

Fig. 8 Fe concentrations of all snails investigated

Figure 9-(a) to (e) show the distribution of Mn

concentrations of *Batillaria cumingii*, *B.mulutiformis*, *B.zonalis*, *Pirenella nipponica*, and *Clithon oualaniensis* resupectively. There was no clear difference between the Sites in any species except *Batillaria cumingi.* In this species, Site E showed a slightly higher concentration than Site Front, but the difference was less than 250 μg, which is not large compared to the variation in values in other species.

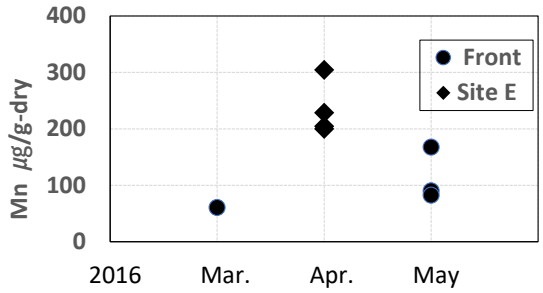

Fig.9-a Mn concentrations of *Batillaria cumingi*

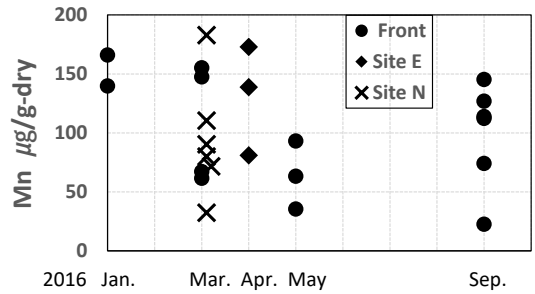

Fig.9-b Mn concentrations of *Batillaria mulutiformis*

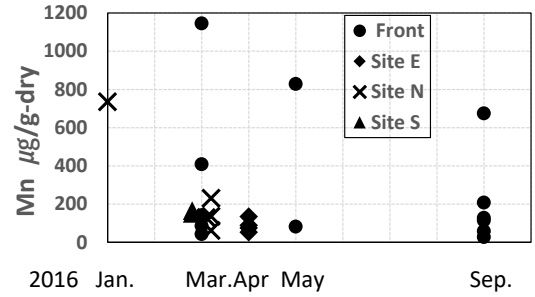

Fig.9-c Mn concentrations of *Batillaria zonalis*

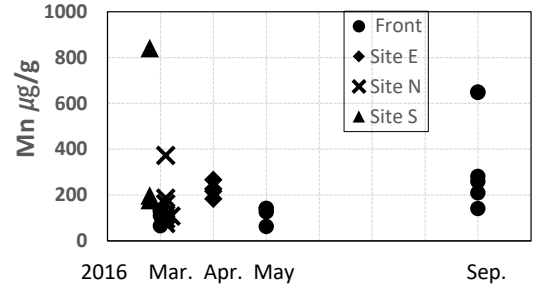

Fig.9-d Mn concentrations of *Pirenella nipponica*

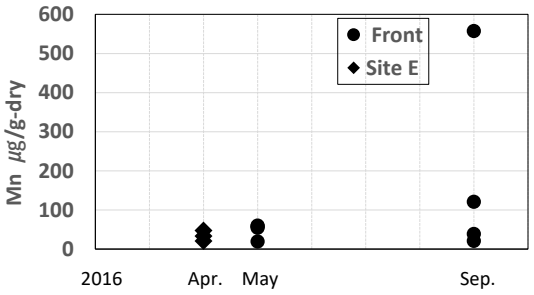

Fig.9-e Mn concentrations of *Clithon oualaniensis*

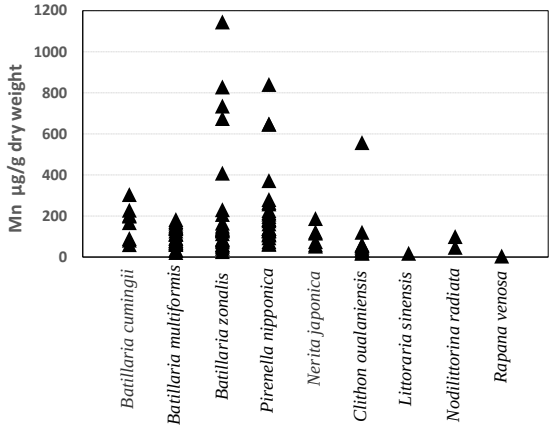

Fig. 10 Mn concentrations of all snails investigated

Figure 10 shows the Mn concentrations of all snails investigated. The genus *Batillaria*, *Pirenella nipponica*, and family Neritidae tended to show higher Mn concentrations than the reference species Littorinidae and Rapana venosa. In particular, several individuals of Batillaria zonails and *Pirenella nipponica*, and one individual of *Clithon oualaniensis* showed very high Mn concentrations. As with Fe, no clear relationship between concentrations of Mn and eating habits was found.

CONCLUSIONS

Regarding the Cu, Fe, Mn concentrations of snails, no clear difference was found between the sites in the tidal flats at the mouth of the Wakagawa River.

The Cu concentration of the three species of the genus *Batillalia* did not differ greatly from the values reported by [5] (about 300 μg/g). *Pirenella nipponica*, which also detritus feeder, showed lower values (less than 100 μg/g) and was similar to algae feeder *Nerita japonica*.The genus *Batillaria* may have some characteristics regarding the accumulation of Cu.

Contrary to the concentration distribution of Cu, the reference species Littorinidae and *Rapana venosa* showed lower concentrations in Fe and Mn. Among the genus *Batillalia*, some individuals of *B.zonalis* showed high concentrations of Fe and Mn. *Pirenella nipponica* also showed the same tendency as

B.zonalis. However, the relationship between the concentrations and the species rarity, relatives or feeding habits could not be seen.

The Zn concentrations of *Batillaria cumingii* (mean 201 μg/g) were similar to or slightly higher than those of the same species in Nakatsu and Banshu tidal flats [5]. Compared to these values, very high Zn concentrations were shown by several individuals of *Pirenella nipponica*, *Batillaria mulutiformis* and *B.zonalis*. Especially high values were found in Site N, where is partially surrounded by land, and the water flow is poor compared to other sites. Therefore, when the pollution was severe, the area just below the surface of the mud flat at this site was in an anaerobic state, and even a little digging of the mud smelled like hydrogen sulfide. Currently, there is almost no such bad odor, but there are many muddy places.

Regarding the Zn concentration, the variability was much larger in the detritus feeders than in the algae feeders, and many individuals showed extremely high values. From these results, it is possible that there is partial Zn contamination of the mud in places where water and mud tend to stay in the Wakaura tidal flat.

On the other hand, among the detritus feeders, only *Batillaria cumingii* didn't show an extremely high concentration. *Batillaria cumingii* thrives on tidal flats across the country, even where other species of the genus *Batillaria* are declining due to environmental deterioration. It is said that this species is resistant to environmental pollution because it has direct development and does not have a floating larval stage. Zn is an essential element for living organisms, but overdose shows toxicity to living organisms. They may have some mechanism to prevent excess Zn from accumulating in the body.

REFERENCES

[1] Ministry of the Environment Nature Maintenance Bureau 2001 "500 Important Wetlands in Japan" https://www.env.go.jp/nature/important_wetland/index.html

[2] Kinki Regional Development Bureau, Ministry of Land, Infrastructure, Transport and Tourism. History of environmental maintenance.

[3] Wakayama River National Highway Office About efforts to improve the water quality of the Daimon River by introducing environmental water

[4] Wakayama Prefectural Land Development Department. Removal of Wakagawa "temporary weir" and construction of rubble revetment.

[5] Akari F.,Motoo U.,Kunihiro O.,Takaaki S.,An Assesment of the *Batillaria* Snails,*Batillaria cumingii*, as an Indicator of Heavy Metals Contamination in Banzu and Nakatsu Tidalflats,Japan. Japanese Society of Water Treatment Biology,Vol.43,No1,2007, pp.1-8

[6] Hiroyuki Ii, As,Sr,Zn,Fe,Mn,Pb and Cu Concentrations of Seaweed at the Kii Peninsula,Japan. International Journal of GEOMATE, Vol. 10, Issue 22, 2016, pp. 2036-2042.

[7] Kubohara T and Ii H., Cu,Co,Cr and Ni of River Insect and Water Plant in the Kinokawa River Catchment, International Journal of GEOMATE, Vol. 10, No.1(Sl.No.19),2016, pp. 1600-1606.

[8] Kubohara T and Ii H., Cu,Co and Ni Contamination Index for River Using River Insects and Water Plants, International Journal of GEOMATE, Vol. 11, Issue 26, 2016,pp. 2651-2658.

[9] Kubohara T and Ii H., Evaluation of Metal Contamination for River Using Bryophyte in the Kinokawa River Catchment, International Journal of GEOMATE, Vol. 13, Issue 37, 2017, pp. 108-115.

[10] Zn and Fe Contamination Index for River Using River Insects and Water Plants in the Kinokawa River Catchment, International Journal of GEOMATE, Vol.19, Issue 75, 2020,pp.76-83.

8th Int. Conf. on Structure, Engineering & Environment (SEE), Mie, Japan, Nov.10-12, 2022, ISBN: 978-4-909106094 C3051

EFFECTIVENESS OF COMPACTED POLYURETHANE-CLAY AS A SANITARY LANDFILL LINER

Cielo Frianeza[1] and Mary Ann Adajar[2]
[1]Civil Engineer, De La Salle University, Philippines; [2]Faculty, De La Salle University, Philippines

ABSTRACT

Sanitary landfill is a waste disposal facility that has control over the potential impact of solid waste by using impermeable liners to prevent contamination of the environment. Several studies improved the impermeability of compacted clay liners by adding bentonite. However, bentonite is an expansive soil susceptible to volume change that would cause the deterioration of the sanitary landfill liner. Hence, the study aimed to investigate the effectiveness of compacted clay mixed with polyurethane as a sanitary landfill liner since polyurethane is a polymer known for its stability and impermeability. Through experimentation using a rigid wall permeameter, it was inferred that the hydraulic conductivity of the compacted polyurethane-clay is acceptable as a sanitary landfill liner. On the other hand, the compacted clay with the same void ratio as the compacted polyurethane-clay is not an acceptable landfill liner. Thus, the changes in the soil structure induced by adding polyurethane to the compacted clay has a significant effect on the permeability characteristics.

Keywords: Polyurethane, Clay, Sanitary Landfill Liner, Permeability

INTRODUCTION

It was believed that the leachate produced from the degradation of waste was filtered by the soil; however, several studies showed that leachate contaminates the surrounding soil and eventually will contaminate the groundwater system [1]. Thus, sanitary landfill (SLF), a waste disposal facility, was developed to have an impermeable layer that prevents the infiltration of leachate and the contamination of the surrounding environment [1].

There are different kinds of impermeable materials that may be used as an SLF liner, such as clay, geomembrane, geotextiles, geosynthetic clay liner, geonet, or a combination of these materials [1]. Among these materials, compacted clay liner is preferred due to the abundance and availability of native clay. A layer of clay used as an SLF liner is compacted to lower the hydraulic conductivity, a measure of permeability, and to remold the soil aggregates into a homogenous soil mass. Different factors such as moisture content of the clay, method of compaction, and compactive effort influence the hydraulic conductivity of the compacted clay liner [2]. In actual practice, the hydraulic conductivity of clay is further reduced by incorporating bentonite. It was inferred that the addition of bentonite in the native clay mixture is effective in reducing the permeability of bentonite-modified clay [3]. However, bentonite, which consists of montmorillonite minerals, increases the shrinkage capability of the soil mixture when subjected to a decrease in moisture content [3]. Thus, the study aims to incorporate an impermeable and stable material into the soil matrix of a local clay, which would yield a hydraulic conductivity that is acceptable as an SLF liner based on the standard design criteria. Such material that may be incorporated into the soil matrix are polymers.

Polymers stabilize soil through the reduction of the rate of water invasion into the soil structure [4]. The effectiveness of polymers in increasing the water-stable aggregation is related to the strength of interparticle bonding induced by the material [4]. Polyurethane (PU) is a polymer formed from the chemical reaction between polyol and isocyanate that produce the repeating unit in the polymer, urethane [5]. Polyurethane is widely used in the construction industry for ground improvement of expansive soils. Inclusion of polyurethane foam in the soil mass through mixing successfully increased the shear strength of marine clay, a soil characterized by excessive volume change [5]. Application of polyurethane also includes decreasing soil settlement when used as a grout; moreover, polyurethane grout micro piles improve the response of the ground to dynamic forces [5]. A study has also shown that polyurethane foam, when injected into the ground, is found to improve strength, stiffness, and bearing resistance [5]. Aside from the ground improvement in terms of strength, polyurethane injection was also inferred to lower permeability of cracked expansive soils. A study about the effects of polyurethane resin injection in desiccated expansive soil mass showed that the veins of the injected polyurethane resin acted as a moisture barrier better that intact clay; in addition, the injected polyurethane resin did not increase the swelling of the soil mass [6].

EXPERIMENTAL PROGRAM

Materials

The two components of the compacted polyurethane-clay include the local clay and the rigid polyurethane foam. The expansive soil used in the study was from a proposed SLF site in Kauswagan, Lanao del Norte and was excavated at least 2 meters below the ground to ensure that no organic matter is present in the soil mass. ASTM standards were used to determine the different soil properties necessary for computational purposes and to analyze the control specimen, the compacted local clay. The soil properties of the excavated soil from Kauswagan, Lanao del Norte is tabulated in Table 1.

Table 1 Soil properties of local clay

Standard	Soil property	
D698	Optimum moisture content	31.15%
D854	Specific gravity	2.41
D4318	Liquid limit (%)	73
D4318	Plastic limit (%)	47
D4318	Plasticity index (%)	26
D4943	Shrinkage limit (%)	28
D4253	Maximum void ratio	1.55 [7]
D4254	Minimum void ratio	1.07 [7]
D2487	Soil classification	MH
D7928	D_{60} (mm)	0.00480

The rigid polyurethane foam used in the study was purchased from Polymer Product (Phil.), Inc. The rigid polyurethane foam is produced from the two components, polyol and isocyanate. The properties and reaction data of the rigid polyurethane foam is shown in Table 2.

Table 2 Polyurethane properties

Property	Value
Specific gravity	1.1 to 1.2
Viscosity at 25°C	100 cps to 400 cps
Cream time	19 seconds to 27 seconds
Gel time	117 seconds to 130 seconds
Tack free time	230 seconds to 262 seconds

Mix Proportion

The obtained optimum moisture content of the local clay was 31.15%, which served as a basis to determine the moisture content upon compaction that would yield the desirable hydraulic conductivity of the compacted local clay. According to previous studies, compacting the specimen at a higher moisture content would yield a lower hydraulic conductivity [8]. Thus, five trials were conducted to approximate the compaction moisture content that would yield an acceptable hydraulic conductivity of the compacted local clay. In which, the trial specimen for this study was targeted to have a similar hydraulic conductivity with the specimen from the study of Tiongson and Adajar [7] that used the same type of expansive soil from the same site in Kauswagan, Lanao del Norte. The compaction moisture content established from the trial tests was 46.5%, which was used in the mix proportion of the specimens used in the experimentation to obtain the hydraulic conductivity of the compacted polyurethane-clay. The mix proportion of the two kinds of specimen, local clay and polyurethane-clay is tabulated in Table 3, wherein the mass of the rigid polyurethane foam is 0% and 3% of the dry mass of the specimen. In addition, the mixing ratio for the rigid polyurethane foam is 1 part polyol and 1 part isocyanate by weight.

Table 3 Sample mix proportion

PU content	Dried clay (kg)	PU (kg)	Dried clay and PU (kg)	Water (kg)
0%	68.26	0.00	68.26	31.74
3%	66.22	2.04	68.26	31.74

Mixing and Curing

The local clay used to produce the specimen was oven-dried to ensure that the water in the mixture is controlled. The rigid polyurethane foam was synthesized in a single step by directly mixing the polyol and isocyanate. Mixing of the polyurethane components was conducted within the cream time before the dried local clay was added. The dry mixing of the rigid polyurethane foam and the dried local clay was done as fast as possible to prevent the solidification of the polyurethane before it is evenly integrated into the local clay matrix. The polyurethane-clay mixture was placed in an airtight container for 20 minutes before adding the amount of water required to meet the compaction moisture content, so that further reaction between components may occur. The mixture of polyurethane, clay, and water was cured for at least 24 hours in a plastic bag before it was compacted to ensure that the water is evenly distributed in the mixture. The same methodology was applied to the local clay used to produce the compacted local clay specimen with 0% polyurethane content with the exclusion of incorporating the rigid polyurethane foam**.**

Manual Compaction

The soil properties of the polyurethane-clay mixture are tabulated in Table 4. Based on the tabulated soil properties of local clay and polyurethane-clay, it can be observed that the liquid limit of the local clay is higher than the liquid limit of the polyurethane-clay. In addition, the liquid limit and plasticity index of both local clay and polyurethane-

clay intersect below the "A" line of the plasticity chart in ASTM D2487. Thus, both soils are classified as MH or elastic silt; however, the polyurethane-clay consists of 16.5% sand, which denotes that its classification is elastic silt with sand. Furthermore, it can be observed that the specific gravity of the local clay and polyurethane-clay differs, which are 2.41 and 2.86, respectively. The difference denotes that there will also be a difference in the void ratio of the local clay and polyurethane-clay specimen when compacted with the same effort. Hence, two compaction efforts were applied that yielded three kinds of compacted specimen labeled as compacted clay liner (CCL), clay liner (CL), and compacted polyurethane-clay liner (CPCL). The summary of the void ratio and the description of the manual compactive effort applied for the three kinds of compacted specimen are tabulated in Table 5. The compactive effort that produced the CCL, with an initial void ratio of 1.06, compaction moisture content of 46.5%, and an acceptable hydraulic conductivity based on the study of Tiongson and Adajar [7] that used the same type of soil, was applied to polyurethane-clay that produced the CPCL. CPCL had the same compactive effort as CCL, but a higher void ratio of 1.44. Less compactive effort was applied to the third type of compacted specimen, CL, to obtain the same void ratio as CPCL, which is 1.44. All test specimens were cured for 24 hours after compaction in the airtight permeameter mold. After curing, all specimens were saturated for 14 days to initiate the permeability test.

Table 4 Soil properties of polyurethane-clay

ASTM	Soil property	
D854	Specific gravity	2.86
D4318	Liquid limit (%)	68
D4318	Plastic limit (%)	48
D4318	Plasticity index (%)	20
D4943	Shrinkage limit (%)	29
D2487	Soil classification	MH with Sand
D7928	D_{60} (mm)	0.02025

Table 5 Compaction effort and initial void ratio

Specimen	PU	Initial void ratio	Compaction
CCL	0%	1.06	Standard
CPCL	3%	1.44	Standard
CL	0%	1.44	Less

Permeability Test

The ASTM standard test method used in the study to determine the hydraulic conductivity is ASTM D5856 [9], or the standard test method for measurement of hydraulic conductivity of porous material using a rigid wall, compaction-mold permeameter. The components used to conduct the test included the flow measurement system and a rigid wall permeameter as shown in Fig. 1. In addition, the falling head method was used with a hydraulic gradient of 1.07. Since the expected hydraulic conductivity is low, it was anticipated that a single run of the experiment would take approximately 60 days; thus, each run was conducted simultaneously. The diameter of each specimen is 63.5 mm, and the height is 110 mm. The hydraulic conductivity of each specimen tested in a rigid wall permeameter under the falling head system was calculated using Eq. (1).

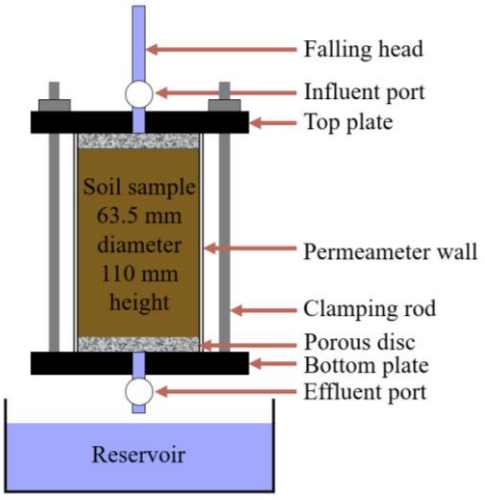

Fig. 1 Rigid wall permeameter setup

$$k = \frac{aL}{At} ln\left(\frac{h_1}{h_2}\right) \quad (1)$$

Where k is the hydraulic conductivity in m/s, a is the cross-sectional area of the standpipe in m^2, L is the length of the specimen in m, A is the cross-sectional area of the specimen in m^2, t is the time between determination of h_1 and h_2 in seconds, h_1 is the head loss across the specimen at time t_1 in m, and h_2 is the head loss across the specimen at time t_2 in m.

TEST RESULTS

XRD Analysis

The x-ray diffraction (XRD) analysis of the local clay and polyurethane-clay are shown in Fig. 2 and Fig. 3, respectively. The XRD analysis determined that aluminum silicate hydroxide and silicon oxide, which are also known as Kaolinite and Quartz, are present in both local clay and polyurethane-clay. Furthermore, the multiplot of both soil types have the same trend and spikes, denoting that the soil types are similar in composition; however, it should be noted that the amount of polyurethane in the polyurethane-clay mixture is only 3% of the dry weight of the specimen, which may not be a significant amount to produce a change in the spikes plotted.

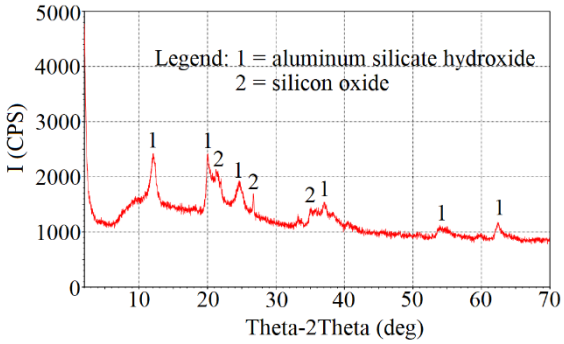

Fig. 2 XRD analysis of local clay

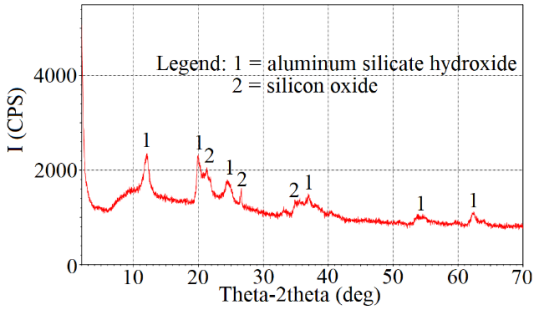

Fig. 3 XRD analysis of polyurethane-clay

One of the minerals found on both soil types is Kaolinite, which is a non-swelling, soft clay mineral that is plastic in nature; moreover, Kaolinite is assumed to be the least reactive among the clay minerals [10]. It can also be noted that the obtained plasticity index of local clay and polyurethane-clay when tested using the ASTM standard reflected a highly plastic property, which agrees with the highly plastic characteristic of Kaolinite [10]. The other mineral detected through XRD analysis is Quartz, which is a mineral present in almost all parent materials and inherited by silt and sand [11]. Considering the classification of the local clay and polyurethane-clay, which is elastic silt and elastic silt with sand, it can be inferred that the presence of Quartz agrees with the soil classification.

EDX Analysis

The energy dispersive x-ray (EDX) analysis of the local clay and polyurethane-clay detected traces of oxygen, silicon, bromine, carbon, and iron, tabulated in Table 6. The dominant elements in the analysis are oxygen and silicon, which are commonly found in soils. Moreover, it can be observed that polyurethane-clay has more carbon than local clay; thus, it can be inferred that incorporating polyurethane into the soil matrix of the local clay increases the carbon content of the mixture. An increase in carbon content denotes that the soil mass has a more stable structure and a better water holding capacity [12]. Thus, a higher carbon content in the soil mass also results in reduced soil erosion because of the improved capability of the soil mass to hold particles together [13]. Therefore, based on the elemental distribution established through the EDX analysis that exhibited an increase in carbon content, it can be inferred that polyurethane-clay is more stable than local clay.

Table 6 EDX analysis of uncompacted specimen

Element	Weight Percentage	
	Local Clay	Polyurethane-clay
Oxygen	44.69	41.26
Silicon	14.69	14.29
Bromine	28.73	27.29
Carbon	2.99	9.96
Iron	8.90	7.20

SEM Analysis

The scanning electron microscope (SEM) image of the local clay and polyurethane-clay are shown in Fig. 4. It can be observed that both soil types are clustered and have intergranular and intragranular voids. However, it can be observed that the SEM image of polyurethane-clay exhibits spherical particles on the surface of the clay particle, which is inferred to be polyurethane foam based on the existing SEM image of polyurethane foam. The SEM image of pure polyurethane foam is shown in Fig. 5, in which spherical particles are predominant.

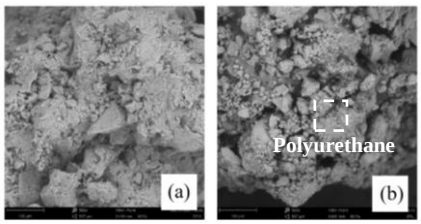

Fig. 4 Image of (a) clay and (b) polyurethane-clay

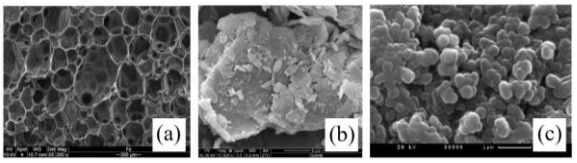

Fig. 5 SEM images of (a) polyurethane [14], (b) Kaolinite [15], and (c) Quartz [16]

SEM images shown in Fig. 4 also exhibit characteristics of Kaolinite and Quartz, which were the elements detected on the local clay and polyurethane-clay through XRD analysis. Kaolinite, which is described as thick, rigid, and plate-like with a hexagonal shape [17], appears flaky and plate-like on Fig. 4. On the other hand, the spheroidal particles observed in Fig. 4 are inferred as Quartz based on the similarity of the particle shape shown in Fig. 5. It can

be observed in Fig. 4 that more spheroidal-shaped particles are found in polyurethane-clay, which agree with the grain size distribution established for the polyurethane-clay that shows more sand particles as compared to the composition of the local clay.

Hydraulic Conductivity

The hydraulic conductivity obtained from the experimentation for the three kinds of compacted specimen are tabulated in Table 7. Hydraulic conductivity is one of the major parameters considered to determine if a material is a suitable SLF liner; thus, CL and CPCL, were compared considering that the two specimen types have relatively the same void ratio. It was opted that the void ratio would be held constant instead of the compactive effort because a constant void ratio denotes that the volume of voids that water could occupy between soil particles are also constant for both specimen types, CL and CPCL.

Table 7 Hydraulic conductivity

Specimen	PU	Void ratio	Hydraulic conductivity, *k*
CCL	0%	1.09	2.27×10^{-8} cm/s
CL	0%	1.38	6.47×10^{-5} cm/s
CL	0%	1.42	8.08×10^{-5} cm/s
CPCL	3%	1.50	2.36×10^{-8} cm/s
CPCL	3%	1.53	3.44×10^{-8} cm/s

The decrease in hydraulic conductivity as polyurethane was incorporated into the soil matrix of the local clay may be due to the impermeable nature of polyurethane. A previous study inferred that polyurethane, in its pure form, is relatively water resistant due to the closed porosity of its microstructure; in addition, polyurethane injected into cracked clays are observed to have a low permeability of 10^{-8} cm/s [14]. Therefore, the polyurethane improved the impermeability of the polyurethane-clay mixture based on the comparison between the hydraulic conductivity of CPCL and CL, which are specimens with the same void ratio. However, the difference in hydraulic conductivity of CL and CPCL may also be attributed to the difference in compactive effort applied. The compactive effort applied on CPCL and CCL is greater compared to the compactive effort applied to CL, since the compactive effort used on CL had an objective to attain the high initial void ratio of CPCL.

Estimated Compactive Effort

By utilizing the model proposed by Tiongson and Adajar [7] to predict the hydraulic conductivity for the same local clay, the compactive effort of the manually compacted specimen in the study may be determined. The actual hydraulic conductivity of CCL is similar to the predicted value for specimen in which the Standard Proctor effort of 600 kN-m/m^3 was applied as the compactive effort. On the other hand, the predicted hydraulic conductivity of CL is two orders of magnitude lower than the actual hydraulic conductivity of CL as shown in Table 8.

Table 8 Predicted hydraulic conductivity

	Void ratio	Actual *k* (cm/s)	Predicted *k* (cm/s)	
			Reduced Proctor	Standard Proctor
CCL	1.09	2.27×10^{-8}	2.07×10^{-8}	2.29×10^{-8}
CL	1.42	6.47×10^{-5}	1.50×10^{-7}	2.39×10^{-7}
CL	1.38	8.08×10^{-5}	1.17×10^{-7}	1.78×10^{-7}

Thus, this indicates that the compactive effort of CL is considerably smaller than the compactive effort of CCL. Moreover, it should be noted that the manual compactive effort applied on CCL is relatively the same as the manual compactive effort applied on CPCL. Therefore, it can be inferred that the manual compactive effort applied on CPCL may also be the Standard Proctor effort.

Effectiveness of CPCL as SLF Liner

Most of the related literature that discussed the suitability of landfill liner material utilized a maximum hydraulic conductivity of 10^{-7} cm/s. Furthermore, the said hydraulic conductivity was utilized by most studies to ensure that the landfill liner material is less permeable to avoid the contamination of the surrounding environment. The lowest permeability required for a compacted SLF liner in the Philippines is 10^{-7} cm/s or 10^{-9} m/s [18]. Thus, for a material to be considered as a suitable SLF liner for all SLF categories, the obtained hydraulic conductivity should be equal to or lower than 10^{-9} m/s.

Based on the design standards, it can be inferred that the compacted polyurethane-clay liner is a suitable SLF liner for all SLF categories with regards to its permeability. Moreover, the clay specimen compacted to have the same initial void ratio as CPCL is not a suitable SLF liner for any SLF category.

One-way analysis of variance was used to statistically compare the hydraulic conductivity of CPCL and CL. The result of the analysis of variance, tabulated in Table 9, indicates that the model and the polyurethane content are significant since the P-values are less than 0.05. Thus, incorporating polyurethane into the soil mixture, statistically, has an effect on the hydraulic conductivity. It can be inferred that the polyurethane in the soil mixture decreased the hydraulic conductivity of the specimen, which can be considered as a suitable SLF liner as opposed to the compacted clay without polyurethane that have the same initial void ratio as CPCL.

Table 9 Statistical analysis of hydraulic conductivity

Source	P-value	
Model	0.0120	Significant
Polyurethane content	0.0120	Significant

CONCLUSION

Bentonite-modified clay is often used in the industry as sanitary landfill liners; however, the characteristic of bentonite makes the clay susceptible to deterioration due to volumetric changes. Thus, the local clay was mixed with polyurethane, a polymer often used to stabilize soil. Changes in the soil structure induced by incorporation of the polyurethane into the soil matrix, such as increase in carbon content, improved the water holding capacity of the compacted specimen when compared to the compacted local clay with the same void ratio. Furthermore, the impermeable nature of polyurethane was inferred to have contributed to the decrease in hydraulic conductivity. Thus, the compacted polyurethane-clay was classified as a suitable landfill liner in accordance with the Philippine design standard for all sanitary landfill categories.

RECOMMENDATION

Since excessive volume change could deteriorate the impermeability of SLF liners made from expansive soil, it is recommended that future studies explore the shrinkage resistance of polyurethane-clay. Furthermore, it is recommended that future studies explore the unsaturated hydraulic conductivity of polyurethane-clay since SLF liners are not always saturated in actual conditions.

REFERENCES

[1] National Solid Waste Management Commission, & Japan International Cooperation Agency, Technical Guidebook on Solid Wastes Disposal Design, Operation and Management (Second ed.) (Philippines, National Solid Waste Management Commission), National Solid Waste Management Commission Office of the Secretariat, 2010.

[2] Daniel, D. E., Case Histories of Compacted Clay Liners and Covers for Waste Disposal Facilities, International Conference on Case Histories in Geotechnical Engineering, 1993.

[3] He, J., Wang, Y., Li, Y., & Ruan, X., Effects of leachate infiltration and desiccation cracks on hydraulic conductivity of compacted clay, Water Science and Engineering, 2015, pp. 151-157.

[4] Fink, J., Chapter 8 - Clay stabilization, Hydraulic Fracturing Chemicals and Fluids Technology, 2020, pp. 119-139.

[5] Saleh, S., Yunus, N. M., Ahmad, K., & Ali, N., Stabilization of marine clay soil using polyurethane, MATEC Web of Conferences, 2018.

[6] Buzzi, O., Fityus, S., & Sloan, S. W., Use of expanding polyurethane resin to remediate expansive soil foundations, Canadian Geotechnical Journal, 2010, pp. 623-634.

[7] Tiongson, J. M., & Adajar, M. A., Compaction characteristics of a fine-grained soil potential for landfill liner application, International Journal of GEOMATE, 2020, pp. 211–218.

[8] Wagner, J. F., Chapter 9 Mechanical Properties of Clays and Clay Minerals, In Developments in Clay Science, Vol. 5, 2013, pp. 347-381.

[9] ASTM International, ASTM D 5856-95: standard test methods for measurement of hydraulic conductivity of porous material using a rigid-wall, compaction-mold permeameter, In Annual book of ASTM standards 1995, 1995, pp.1-8.

[10] Pourhakkak, P., Taghizadeh, M., Taghizadeh, A., & Ghaedi, M., Adsorbent, Interface Science and Technology, 2021, pp. 71–210.

[11] Gutiérrez-Castorena, M. del., Pedogenic siliceous features, Interpretation of Micromorphological Features of Soils and Regoliths, 2018, pp. 127–155.

[12] Rice, C. W., Carbon cycle in Soils | Dynamics and management, Encyclopedia of Soils in the Environment, 2005, pp. 164–170.

[13] Pimentel, D., & Burgess, M., Maintaining sustainable and environmentally friendly fresh produce production in the context of climate change, Global Safety of Fresh Produce, 2014, pp. 133–139.

[14] Buzzi, O., Fityus, S., Sasaki, Y., & Sloan, S., Structure and properties of expanding polyurethane foam in the context of foundation remediation in expansive soil, Mechanics of Materials, 2008, pp. 1012-1021.

[15] Namdar, A., Kaolinite Chemical Composite and Morphology in Geotechnical Engineering, Advances in Natural and Applied Sciences, 2011, pp. 93–99.

[16] Baawuah, E., Fosu, B., Ofori-Sarpong, G., & Addai-Mensah, J., Influence of Alkaline Type on Quartz Pulp Particle Interactions and Interfacial Chemistry in Aqueous Media, In 3rd Biennial UMaT International Mining and Mineral Conference, 2021, pp. 220–227.

[17] Rouquerol, F., Rouquerol, J., & Sing, K., Adsorption by clays, pillared layer structures and zeolites, Adsorption by Powders and Porous Solids, 1999, pp. 355–399.

[18] Department of Environment and Natural Resources Administrative Order No. 10, 2006.

8th Int. Conf. on Structure, Engineering & Environment (SEE), Mie, Japan, Nov.10-12, 2022, ISBN: 978-4-909106094 C3051

FEASIBILITY OF OYSTER SHELL PERVIOUS CONCRETE WITH DIFFERENT PARTICLE SIZE AS A SEAWEED BED

Shuta Hiura[1], Itaru Horiguchi[2] and Yoichi Mimura[3]
[1]Advanced course, National Institute of Technology (KOSEN), Kure College, Japan;
[2,3] National Institute of Technology (KOSEN), Kure College, Japan

ABSTRACT

Global warming, due to a large amount of greenhouse gas emission, is one of the most important issues for the entire world. Japan has already pledged to achieve net zero greenhouse gas emissions, carbon-neutrality, by 2050. The use of plants is one of the measures being used to solve the problem because plants utilize carbon dioxide by photosynthesis. In this study, the feasibility of pervious concrete (OyPC) used oyster shell aggregates with different particle size as a seaweed bed was investigated because the oyster shells of about 90,000 tons are annually produced as a by-product in Hiroshima Prefecture. The porosity, compressive strength, and water permeability of OyPC were also studied. From the test results, OyPC using aggregates ranged from 5.0 to 0.3 mm (Oy5003) had the lowest porosity, resulting in the highest compressive strength and relatively low water permeability. Oy5003 would be effective as a seaweed bed because thick seaweeds grew densely on Oy5003 with graded aggregates compared with the other OyPC with single-sized aggregates from the results of immersion tests with cylindrical specimens.

Keywords: Oyster shell pervious concrete, seaweed bed, porosity, compressive strength, water permeability

INTRODUCTION

Global warming due to a large amount of greenhouse gas emission is one of the most important issues for the entire world. Japan has already pledged to achieve net zero greenhouse gas emissions, carbon-neutrality, by 2050. The use of plants is one of the measures being used to solve the problem because plants utilize carbon dioxide by photosynthesis. Recently, carbon captured by the world's ocean and coastal ecosystem is receiving a lot of attention for carbon sequestration, which is called "blue carbon". Coastal blue carbon ecosystems include seaweed beds, mangroves, tidal marshes, and so on [1], [2].

Hiroshima Prefecture is famous for its high oyster productivity, contributing 17,928 metric tons or 64.6% of Japan's total production levels (27,742 metric tons) for 2019 [3]. The production of oysters generates oyster shells as a by-product. Oyster shells are used commercially as livestock feed for chickens, pigs, and cows and as a soil conditioner. However, the reuse of oyster shells remains limited. Pervious concrete is a special concrete in which single-sized aggregates are bound together with a cement paste or mortar. Pervious concrete has a large volume of interconnected pores ranging from 15 to 30%. In previous researches, the plat-growing performance of pervious concrete (OyPC) containing crushed oyster shell aggregates was investigated, and OyPC was found to have higher plat-growing performance than crushed stone pervious concrete [4], [5].

In this study, the feasibility of OyPC used oyster shell aggregates with different particle size as a seaweed bed which was one of coastal blue carbon ecosystems was investigated. The porosity, compressive strength, and water permeability of OyPC were also studied.

Fig. 1 Storage facility of oyster shells.

MATERIALS AND METHODS

Materials

In this study, oyster shells were collected from a storage facility in Kure City, Hiroshima Prefecture (Fig.1). The oyster shells were washed by a tilting mixer to eliminate impurities such as salt and seaweeds attached to shells, which could adversely affect the cement hydration. The washed oyster shells were dried in the sun and crushed by a shell crusher (Fig.2). The crushed oyster shells were sieved to

Table 1 Physical properties of the oyster shell aggregates.

Specimen	Particle size (mm)	Saturated surface-dry denisty (g/cm^3)	Oven-dry density (g/cm^3)	Absorption (%)	Bulk density (kg/L)	Solid content (%)
Oyster shell aggregate	0.3-5.0	1.98	1.57	25.9	0.838	53.3
	5.0-10.0	1.92	1.59	21.2	0.581	36.7
	2.5-5.0	2.08	1.72	20.7	0.796	46.2
	1.2-2.5	1.99	1.58	25.8	0.736	46.5
	0.6-1.2	1.93	1.48	30.3	0.656	44.3

Table 2 Proportions of materials in each mixture.

Specimen	Particle size (mm)	W/C (%)	p/a (%)	Unit weight (kg/m^3)			
				Water	Cement	Oyster shell aggregate	Admixture
Oy5003	0.3-5.0	25	30	62	248	950	1.24
Oy10050	5.0-10.0			43	171	634	0.86
Oy5025	2.5-5.0			54	215	865	1.08
Oy2512	1.2-2.5			54	217	833	1.08
Oy1206	0.6-1.2			52	207	773	1.04

Fig. 2 Shell crusher.

prepare for 4 types of single-sized aggregates, of which particle sizes were 0.6 to 1.2 mm, 1.2 to 2.5 mm, 2.5 to 5.0 mm, 5.0 to 10.0 mm, and graded aggregates of 0.3 to 5.0 mm. Saturated surface dry oyster shell aggregates were used for production of specimens. The oyster shell aggregates were immersed in water for 24 hours and the excessive water was removed from the wet aggregates by left into sandbags for more than 24 hours. To dry the surface of the aggregates in the sun, the aggregates were spread on plastic sheets. The saturated dry surface condition of aggregates was decided by the flow cone method based on JIS A 1109.

Table 1 shows the physical properties of oyster shell aggregates. In this study, Portland blast-furnace slag cement-type B was used as cement to reduce the amount of alkaline components which may inhibit seaweed growth. Tap water and air-entraining and high-range water-reducing admixture were also used. Table 2 shows mixture proportions of OyPC. For all

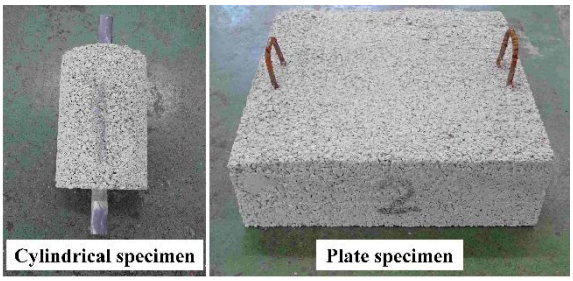

Fig. 3 Specimens for the immersion test in the Sea.

mixtures, the water to cement ratio by mass (W/C) was 25%, and the cement paste to aggregate ratio by volume (p/a) was 30%. An omni mixer of which capacity was 10 liters was used for the mixing. First, aggregates and cement were mixed for 30 seconds in the mixer. Next, water with the admixture was put into the mixer and mixed for 90 seconds. The cylindrical specimens of Φ100×200 mm were used for the porosity, compressive strength, and water permeability test. On the other hand, cylinder of Φ100 ×150 mm and plate of 300×300×100 mm were used for the immersion test in the sea (Fig. 3). A polyvinyl chloride (PVC) pipe of which inner, outer diameter, and length were 13, 18, and 300 mm, respectively, was inserted in the center of the cylindrical specimen. Two hooks bent round steel bars of 6mm diameter were mounted on the plate specimen.

Each mixture was filled into a mold in a single layer for both cylindrical and plate specimens. The specimens were compacted with a table vibrator for 10 seconds, and the surfaces of specimens were leveled using an external vibrator. Once placed in the

molds, the specimens were covered with wet gunny bags and plastic sheets for 24 hours to prevent drying before consolidation. The specimens were demolded and placed in 20±2℃ water for 6 and 27 days.

Test method

The porosity and the water permeability coefficient were measured according to JCI-SPO2-1 and JCI-SPO3-1, respectively. The specimen was weighed in casting and the porosity (A_t, %) was calculated using the following Eq. (1)

$$A_t = \left(1 - \frac{W_1/V_1}{W_2/V_2}\right) \times 100 \quad (1)$$

where W_1 (kg) and V_1 (m^3) are the weight and volume, respectively, of the specimen, and W_2 (kg) and V_2 (m^3) are the total weight and volume, respectively, of water, cement, aggregate, and admixture used in $1m^3$ of pervious concrete.

The water permeability test was performed by using the apparatus provided in Fig. 4. A specimen was set into a PVC pipe with an inner diameter of 100 mm and a pipe collar was connected to the pipe. A sponge rubber sheet was wrapped around the side of the specimen to prevent water from permeating the interface between the specimen and the pipe. The pipe collar had a drain outlet for keeping the water level of 40 mm. The amount of water permeated the specimen for 30 seconds was measured three times. The water permeability coefficient could be calculated by Eq. (2)

$$K = \frac{Q}{TA} \times \frac{h}{H} \quad (2)$$

where K (cm/sec) is the water permeability coefficient. Q (cm^3) is the amount of water flow within T, and T (sec) is the test time. A (cm^2) is the cross section of a specimen, h (mm) is the height of a specimen, and H (mm) is the water head.

The compressive strength test was carried out based on JIS A 1108. The specimens cured for 7 and 28 days were tested by using an Amsler type universal testing machine at a loading speed of 0.01 N/mm^2/sec until the specimens were damaged. Sulfur mortar was prepared for capping the ends of specimens to prevent stress concentration.

The immersion test in the sea was started at an oyster farm in Kure City, Hiroshima Prefecture from November 5, 2021 and is still ongoing (Fig. 5). Four types of cylindrical specimens, which were Oy5003, Oy10050, Oy5025, and Oy2512, were prepared in the test. Seven specimens for each of the mixtures were connected at intervals of about 350 mm with a polyethylene rope. The connected specimens were suspended carefully from a bridge across shore to a floating pier (Fig. 6). The distance between a top

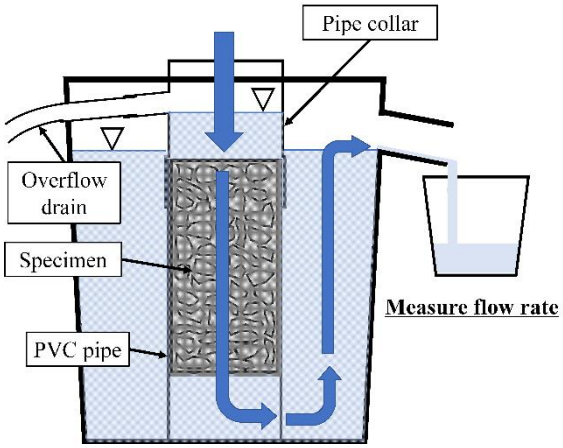

Fig. 4 A schematic diagram of water permeability test.

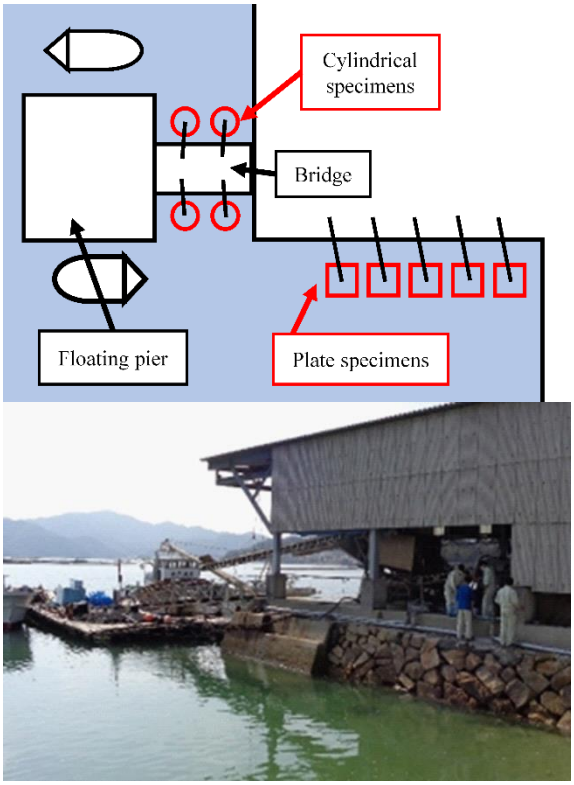

Fig. 5 Immersion test in the sea at an oyster farm.

surface of a topmost specimen (No. 7) and the seabed was about 3 m; however it was fluctuated because the pier sank and floated due to tidal action.

Five types of plate specimens, which were Oy5003, Oy10050, Oy5025, Oy2512, and Oy1206, were also immersed in the sea. The hooks mounted on the plate were tied to a heavy steel wire basket with a polyethylene rope in order not to wash away by waves. Both of the cylindrical and the plate specimens were temporarily pulled up from the sea for the visual observations at 31 and 84 days after the start of the test.

RESULTS AND DISCUSSION

Porosity, compressive strength, and water permeability

The porosity of specimens for the compressive strength and water permeability test are shown in Fig. 7. According to Fig. 7, Oy5003 with graded aggregates had the lowest porosity of about 35%. While the porosities of Oy10050, Oy5025, Oy2512, and Oy1206 with different size of single-sized aggregates were almost the same value of 45%, which was higher than that of Oy5003.

Figure 8 shows the compressive strengths of OyPC curing for 7 and 28 days. Regardless of the curing age, Oy5003 with graded aggregates showed the highest strength of about 2.5 N/mm^2 among all of the specimens. While the strengths of Oy10050 with the largest single-sized aggregates were 1.1 and 1.0 N/mm^2 at 7 and 28 days, respectively, which were as small as 40% of that of Oy5003. The 28-day strengths of OyPC were higher than the 7-day strengths, with the exception of Oy10050; although these differences were small due to the significantly low strength of oyster shell aggregate.

Figure 9 presents the water permeability coefficients of OyPC. As shown in Fig. 9, the water permeability of OyPC with single-sized aggregates decreased while decreasing the particle size, and Oy1206 had the lowest water permeability coefficient of 0.21 cm/sec. The water permeability coefficient of Oy5003 with graded aggregates was 0.81 cm/sec which was similar to that of Oy2512.

The compressive strength and the water permeability of pervious concrete depend on its pore structure, such as porosity, pore diameter and tortuosity, which is determined by the particle size and the shape of aggregates and the amount of cement paste. Pervious concrete with smaller single-sized aggregates generally has smaller pores and a more tortuous pore structure than pervious concrete with larger aggregates. Compared with pervious concrete with single-sized aggregates, pervious concrete with graded aggregates has fine pore structure because of the high packing density of aggregates. Therefore, Oy5003 with graded aggregates had the lowest porosity, resulting in the highest compressive strength and relatively low water permeability.

The immersion test results

The appearance of cylindrical specimens No. 1, 2 3, and 4 immersed in the sea for 31 and 84 days is shown in Fig. 10. From the visual observations no changes were observed in specimens No. 5, 6, and 7 where distance from the seabed was over 1.4 m.

According to Fig. 10, surfaces of the specimens immersed for 31 days turned light brown regardless of particle size, although the color changes occurred

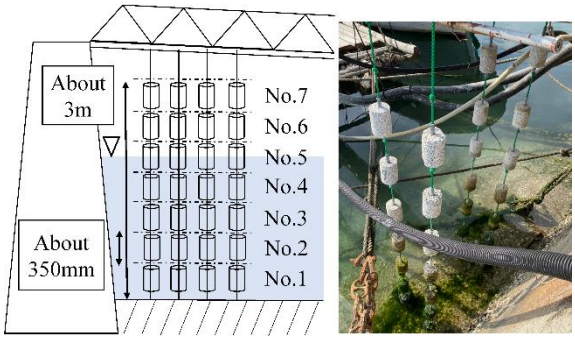

Fig. 6 Cylindrical specimens suspended from a bridge

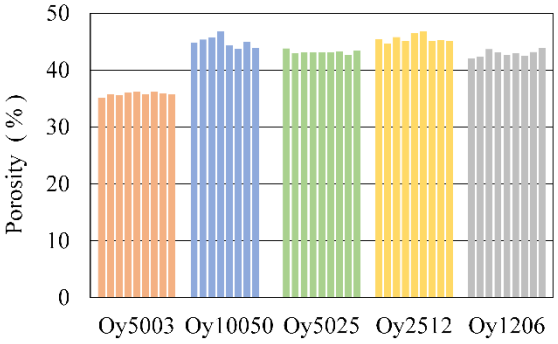

Fig. 7 Porosity of specimens for the compressive strength and water permeability test.

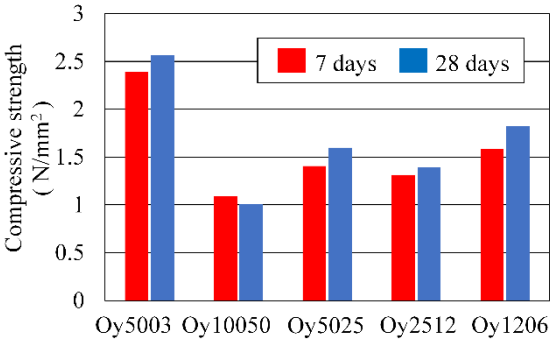

Fig. 8 Compressive strength of OyPC curing for 7 and 28.

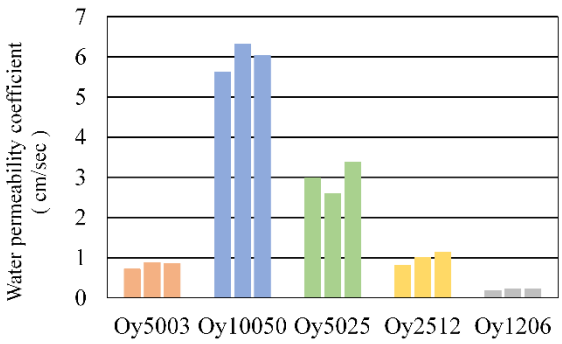

Fig. 9 Water permeability coefficient of OyPC.

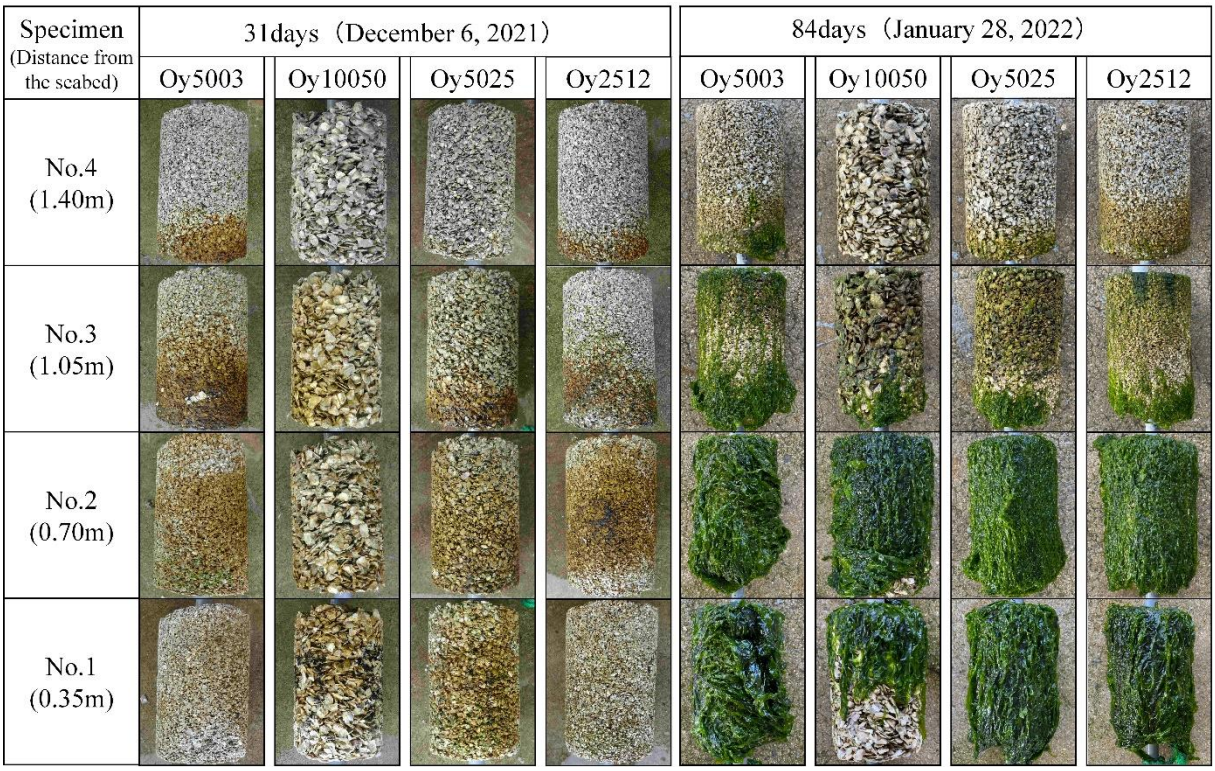

Fig. 10 Appearance of cylindrical specimens immersed in the sea for 31 and 84 days.

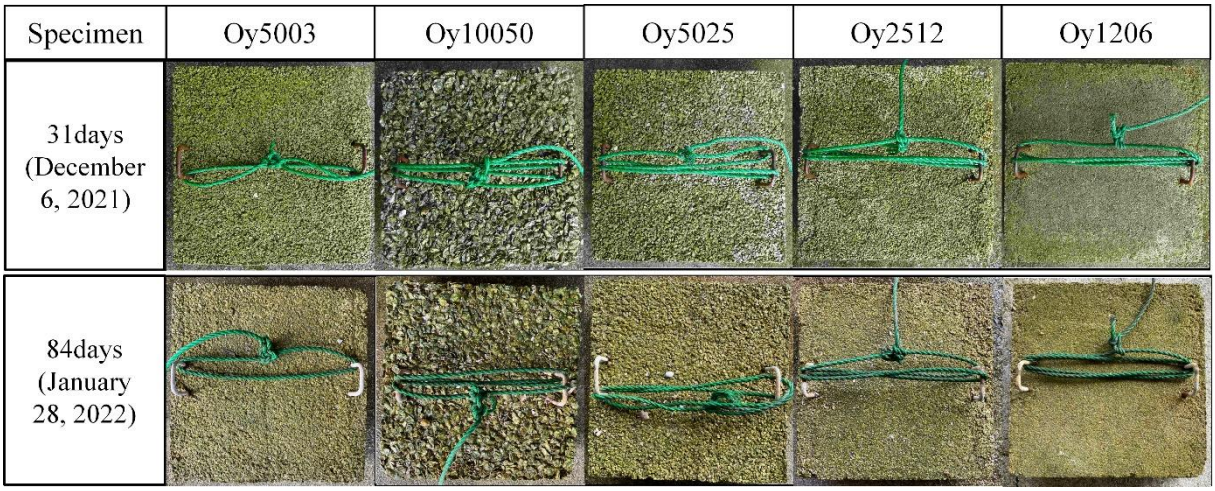

Fig. 11 Appearance of plate specimens immersed in the sea for 31 and 84 days.

partially. Very tiny seaweeds were found on the top and the side of Oy5003 No. 2, 3, and Oy5025 No. 1.

Seaweeds grown on the specimens were observed for all of specimens immersed for 81 days. In particular, specimens No. 1 and 2 for all of the mixtures which were close to the seabed had a lot of seaweeds. Thick seaweeds grew densely on Oy5003 No. 1 and 2 with graded aggregates compared with the other OyPC with single-sized aggregates. The specimens No. 1 and 2 of Oy5025 and Oy2512 had seaweeds grown densely, however those were slightly thin. Seaweeds grew sufficiently on the top of Oy10050 No. 1 and 2 while there was a small number of seaweeds on the side of specimens.

The results of the immersion test with cylindrical specimens suggested that Oy5003 with graded aggregates would be effective as a seaweed bed. The reason why seaweeds could grow on the OyPC has not been clear, however the water retention of the OyPC would strongly affect on the growth of seaweeds on the specimens. In this immersion test, sea level was lower than the bottom surface of the lowermost specimen (No. 1) at low tide. Therefore, seaweeds became easy to dry on the specimens with

high water permeability, namely low water retention, resulting in the inhibition of seaweeds growth. Additionally, seasonal changes in sunlight and seawater temperature also have an effect on the growth of seaweeds, and further observations over one year will be needed.

Figure 11 shows the appearance of plate specimens at 31 and 84 days. The top surface of all specimens at 31 days after the start of the test became partially green, and green colored area spread widely at 84 days regardless of mixtures. In contract to the cylindrical specimens, no seaweed grown on the plate specimens could be found. This is because the plate specimens were immersed in the shallow sea and the immersion time of the plate specimens was shorter than the cylindrical ones.

CONCLUSIONS

The present study investigated the feasibility of OyPC used oyster shell aggregates with different particle size as a seaweed bed which was one of coastal blue carbon ecosystems. The porosity, compressive strength, and water permeability of OyPC were also studied. The main conclusions of this study are highlighted below:

(1) Oy5003 would be effective as a seaweed bed because thick seaweeds grew densely on Oy5003 with graded aggregates compared with the other OyPC with single-sized aggregates from the results of immersion tests with cylindrical specimens.
(2) The results of the immersion test with plate specimens showed that the top surface of all specimens became green; however no seaweed grown on the plate specimens could be found.
(3) Compared with OyPC with single-sized aggregates, Oy5003 with graded aggregates had the lowest porosity, resulting in the highest compressive strength and relatively low water permeability.

REFERENCES

[1] Ministry of Land, Infrastructure, Transport and Tourism, The white paper on land, infrastructure, transport and tourism in Japan, 2021
[2] Nellemann C., Corcoran E., Duarte C. M., Valdes L., De Young C., Fonseca L., Grimsditch G., Blue carbon. A Rapid Response Assessment. United Nations Environment Programme, GRID, Arendal, 2009
[3] Hiroshima Prefectural Agriculture, Forestry and Fisheries Department, Guidelines for production and shipping of oysters in Hiroshima, 2021
[4] Hiura S., Horiguchi I., Mimura Y., Matsubara S., The evaluation method of the void structure and the water pumpability of oyster shell porous concrete with different particle size. Journal of Japan Society of Civil Engineers Chugoku region branch, Vol. 62, 2021, pp. 365-366
[5] Horiguchi I., Mimura Y., Monteiro P. J. M., Plant-growing performance of pervious concrete containing crushed oyster shell aggregate. Cleaner Materials, Vol. 2, 2021, 100027

8th Int. Conf. on Structure, Engineering & Environment (SEE), Mie, Japan, Nov.10-12, 2022, ISBN: 978-4-909106094 C3051

PHYSICAL PROPERTY AND HEAVY METAL LEACHING BEHAVIOR OF CONCRETE MIXED WITH WOODY ASH

Takuto Ueno[1], Ayane Yanaka[1], Shinichiro Okazaki[2], Naomichi Matsumoto[2] and Hidenori Yoshida[2]
[1] Graduate School of Engineering, Kagawa University, Japan; [2] Faculty of Engineering and Design, Kagawa University, Japan

ABSTRACT

In recent years, the woody biomass power generation attracts a lot of attention since woody biomass is an alternative energy source to fossil fuels. In the future, further implementation of woody biomass power generation is expected, and a large amount of woody ash will be discharged. Several studies have been conducted on the effective use of woody ash for construction materials. However, woody ash has not been practically used because of concerns about the leaching of heavy metals from concrete mixed with woody ash. If the above problem can be solved, a large amount of woody ash is expected to be used. In this study, the fresh property and hardened properties, such as compressive strength and length change were measured to evaluate the feasibility of using concrete mixed with woody ash. Furthermore, a heavy metal leaching test was conducted to assess the environmental impact caused by concrete mixed with woody ash. As the result, the concrete mixed with woody ash has the slump and air content similar to that of normal concrete, the compressive strength meeting the standard durability design strength in Japan, and the shrinkage is similar to that of normal concrete. Additionally, the concentration of heavy metals exceeding the soil environmental quality standards in Japan was partially detected, but the leaching amount of heavy metals from the concrete mixed with woody ash was similar to that from normal concrete.

Keywords: Woody ash, Recycling, Concrete admixture, Heavy metals

INTRODUCTION

In recent years, global energy consumption has been increasing due to population growth and economic growth in developing countries. On the other hand, most of the energy resources consumed in the world are fossil fuels, and the reduction of carbon dioxide emissions generated by power generation has become an issue. As the initiative to reduce carbon dioxide emissions, the parties to the United Nations Framework Convention on Climate Change (UNFCCC) have set a long-term goal in the Paris Agreement to hold the increase in the global average temperature to well below 2 ° C above pre-industrial levels and pursuing efforts to limit the temperature increase to 1.5 °C. Woody biomass is a renewable resource and absorbs carbon dioxide through photosynthesis during growth. In addition, woody biomass is an alternative energy resource to fossil fuels. For these reasons, the spread of woody biomass power generation attracts a lot of attention in recent years. In the future, further implementation of woody biomass power generation is expected, and a large amount of woody ash will be discharged. As reported in [1], about 70% of the woody ash generated is currently landfilled. As shown in [2], [3], [4], and [5], several studies have been conducted on the effective use of a large amount of woody ash for fertilizer and construction materials. However, as reported in [2] and [6], the leaching of heavy metals which are contained in the woody ash is worried due after the service. On the other hand, as shown in [7], hardened cement has the performance of preventing the leaching of heavy metals contained in the waste and it is most commonly used in solidification and stabilization processes. Therefore, if wood ash can be used as a concrete material, a large amount of wood ash can be reused. Although the physical and chemical properties of woody ash are influenced by species of tree and tree growing regions, a decrease in the strength of concrete mixed with woody ash has been reported, as shown in [5]. Therefore, if woody ash is mixed into the concrete, the strength of the concrete may be lower than the strength required for the structure. In this study, the fresh property and physical properties after hardening, such as strength and length change were measured to evaluate the feasibility of using concrete mixed with woody ash. Furthermore, a heavy metal leaching test was conducted to assess the environmental load caused by concrete mixed with woody ash.

MATERIALS

Cement, Aggregate and Chemical Admixture

Ordinary Portland cement (3.16 g/cm3 of density) specified in JIS R 5210 Japanese Industrial Standards

was used for cement. Mountain sand with 2.5 mm of maximum grain size and 2.57 g/cm3 of surface dry density for fine aggregate and crushed stone with 12 mm of average particle size and 2.62 g/cm3 of surface dry density for coarse aggregate were used, respectively. The air entraining and water reducing agent (AE-WRA) whose main components are a complex of a lignin sulfonic acid compound and a polycarboxylic acid ether was used for chemical admixture.

Woody Ash

Incinerated ash discharged from woody biomass power plants is classified into bottom ash and fly ash. As described in [8], most of the ash generated in the incinerator is bottom ash, which comprises about 80% in total. Therefore, in order to reuse a large amount of woody ash, it is important to examine the feasibility of using concrete mixed with woody bottom ash. In this study, woody bottom ash generated from a woody biomass power plant in Kochi Prefecture, Japan, was used as a concrete admixture. The woody bottom ash contained many coarse particles with 9.5 mm of a maximum grain size. Therefore, in order to obtain a suitable shape for concrete material, woody bottom ash was dried at 100°C for 24 hours and ground in a ball mill until there were no coarse particles. Fig. 1 shows the woody bottom ash after crushing. The density of the ground bottom ash is 2.47 g/cm^3. Next, the composition of the woody bottom ash was analyzed by XRD (X-ray Diffraction) analyzer. Fig. 2 shows the spectrum of the woody bottom ash analyzed by XRD analysis. As a result of XRD analysis, the composition of the woody bottom ash was 56.5% of SiO_2, 23.7% of $CaCO_3$, 11.6% of Fe_2O_3, 7.9% of MgO and 0.4% of CaO by weight. Although the woody ash contained SiO_2, it was not amorphous which promotes the pozzolanic reaction. In addition, in order to confirm the leaching of heavy metals from woody ash, the leaching test was conducted based on the Environmental Agency Notification No.46. The heavy metals analyzed in the leaching test were arsenic (As), hexavalent chromium (Cr (VI)) and fluorine (F), which are confirmed to be contained in trees in Japan. Cr (VI) and F were analyzed by a monomeric water analyzer based on diphenylcarbazide spectrophotometry, and As was analyzed by ICP-AES. Table 1 shows the concentration of heavy metals leached from woody bottom ash, and all concentrations exceeded the soil environmental quality standard values in Japan.

Table 1 Concentrations of heavy metals leached from woody ash (ppm)

	Woody bottom ash	Soil environmental quality standards
As	0.166	0.01
Cr (VI)	0.413	0.05
F	1.465	0.80

Fig. 1 Woody ash

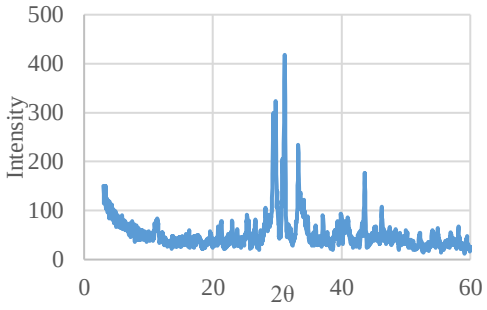

Fig. 2 Spectrum of woody bottom ash by XRD

TEST METHOD

Concrete Mix Design

As reported in [9] and [10], woody ash mixed into the concrete may absorb water and the workability of concrete may decrease. Therefore, when woody ash is mixed into the concrete, it is necessary to increase the unit water volume in concrete in order to achieve the same level of workability as normal concrete. In this test, all concrete mixes were designed with water cement ratio and fine aggregate ratio at 55% and 43%, respectively. In addition, the workability of the concreate mixed with woody ash equivalent to that of a normal concrete was ensured by changing the addition quantity of the air entraining and water reducing agent. Table 2 shows the concrete mix proportions in the test. “Blank” and “WBA” represent normal concrete (concrete without woody bottom ash) and concrete mixed with woody bottom ash, respectively. The woody bottom ash mixed into the concrete was woody bottom ash in which heavy metals were leached at concentrations exceeding the

soil environmental quality standard values in Japan in the leaching test. In this test, 10% of the mass of cement used in Blank concrete was replaced with the woody bottom ash. In order to make the workability of the two types of concrete equivalent, the amount of the air entraining and water reducing agent added to the cement mass was 1.0% for Blank concrete and 1.8% for WBA concrete. Concrete preparation was carried out based on Japanese Industrial Standard JIS A 1138. The order in which the materials were charged into the mixer was a half amount of aggregate (coarse aggregate and fine aggregate), cement, and the remaining aggregate, to prevent the floatation of powder. The woody bottom ash was mixed into cement in advance and charged into the mixer. After charging the materials into the mixer, the mixer was rotated for 30 seconds to mix the materials. Then, the water added with AE-WRA was poured into the mixer and mixed for 90 seconds.

Slump Test and Air Content Test

The slump test and air content test were conducted immediately after the fresh concrete was made.
The slump test and air content test were conducted based on Japanese Industrial Standards JIS A 1101 and JIS A 1128, respectively. In the slump test, first, the fresh concrete was filled into the slump cone in three times. The fresh concrete in each layer was struck 25 times with a rod, and after the fresh concrete in the third layer was struck, the fresh concrete was made flat to match the top edge of the slump cone. When the top surface of the fresh concrete was lower than the that of the slump cone, the same concrete sample was added into the slump cone. Next, the slump cone was quickly lifted vertically at a constant speed, and the slump value was measured 0.5 cm unit in the center of the concrete. In the air content test, the air content in fresh concrete was measured based on the air chamber pressure method using a Washington-type air meter. As a method of air content test, fresh concrete was filled into the air content measuring container in the same way as the above-mentioned slump test, and the side of container was tapped with a wooden mallet. The fresh concrete protruding from the container was removed and the top of the concrete was leveled. Next, after the lid was attached to the container, high pressure was applied to air bubbles in the fresh concrete by operating an air meter, which causes volume change. Then, the air content in the concrete sample was measured to the order of 0.1% based on Boyle's law. In this test, the target slump value and air content value were set at 12 ± 2.5 cm and 4.5 ± 1.5%, respectively.

Preparing of Test Specimens for Concrete

A ϕ100 × 200 mm cylindrical specimen was prepared for compressive strength test based on Japanese Industrial Standard JIS A 1132. A cylindrical specimen was removed from the mold, and after that, the specimen was cured in water from the time of specimen preparation until 28 days later. The loading surface (upper surface) of cylindrical specimen was ground with a polishing grinder so that the specimen loading surface (upper surface) became flat. In addition, a 100 × 100 × 400 mm prismatic specimen was prepared for length change measurement. The prismatic specimen was removed from the mold, and then cured in water for 7 days from the time of specimen preparation.

Compressive Strength Test

After 28 days in water curing of the specimens, the compressive strength test was conducted based on Japanese Industrial Standard JIS A 1108. The compressive strength was calculated by the following Eq. (1).

$$f_c(\mathrm{N/mm^2}) = \frac{P}{\pi d^2/4} \quad (1)$$

where "*fc*" is the compressive strength, "*P*" is the maximum load, and "*d*" is the diameter of the cylindrical specimen measured by a caliper. The compressive strength test was conducted three times for each mix, and the mean value was adopted for the test results.

Length Change Measurement

The length change of concrete due to drying shrinkage was measured based on the contact gauge method of Japanese Industrial Standard JIS A 1129. As the procedure of the length change measurement, contact tips were affixed to the specimen after curing so that the base length of the tips was 100 mm near the center of the specimen. The contact chips were

Table 2 Mix proportions of concrete (kg/m^3)

	Water	Cement	Woody Bottom Ash	Fine Aggregate	Coarse Aggregate	AE-WRA
Blank	175	318	0	734	992	3.18
WBA	175	286	32	731	988	5.73

affixed at two locations on both sides of each side adjacent to the concrete placing surface of the specimen. After that, the concrete specimens were stored in a room at 20°C and the length change of the concrete specimens was measured. The length change measurement was conducted at 1, 7, 14, 28, and 56 days after the specimens were cured in water. Fig. 3 shows the specimen after contact tips were attached.

Fig. 3 The specimen after contact tips were attached

Heavy Metal Leaching Test

As has mentioned above, the concrete has the performance to prevent the leaching of heavy metals. However, there are few studies on the leaching of heavy metals from concrete mixed with woody ash when it is demolished. Therefore, in this study, the heavy metal leaching test on the crushed concrete was conducted based on the Environmental Agency Notification No.46. First, a concrete specimen was crushed with an electric hammer. The crushed one was subjected to sieving with a 2 mm mesh opening, and the one which passed through it was utilized as a sample for the leaching test. Next, 50 mL of distilled water was poured into the centrifuge tube, and 5 g of the sample was also added into the centrifuge tube. It was defined as the specimen in this test and shaken for 6 hours at 200 rpm at 20°C. After shaking, the specimen was allowed to stand for 30 minutes and then centrifuged at 3000 rpm for 20 minutes. After centrifugation, the supernatant solution of the sample was filtered through a membrane filter with 45 μm of pore size, and the concentration of heavy metals in the filtered solution was analyzed. Cr (VI) and F were analyzed by a monomeric water analyzer based on diphenylcarbazide spectrophotometry, and As was analyzed by ICP-AES. The solution analyzed by ICP-AES was acidified by adding a small amount of nitric acid as a pretreatment. The leaching test was conducted three times, and the mean value of concentrations analyzed was adopted as the test result.

RESULTS AND DISCUSSION

Slump and Air Content of WBA Concrete

Table 3 shows the slump value and the air content value of Blank concrete and WBA concrete. The slump value and the air content value for both fresh concretes were within the target range. From the results, it was found that when 10% of the mass of cement used in Blank concrete was replaced with the woody ash, the slump value of WBA concrete equivalent to that of Blank concrete could be ensured by adding 0.8% more the air entraining and water reducing agent than the Blank concrete. Fig. 4 and Fig. 5 show the shapes of Blank concrete and WBA concrete after the slump test, respectively. When the shapes of Blank concrete and WBA concrete were compared after the slump test, there was not any significant difference. Therefore, from the results of the slump test and the air content test, it can be said that WBA concrete has a slump and air content without any problems in construction. These facts are consistent with those described in [9] and [10].

Table 3 Slump value and air content value for Blank and WBA concretes

	Slump value (cm)	Air content value (%)
Blank	12.5	5.5
WBA	14.0	5.5

Fig. 4 Shape of Blank concrete

Fig. 5 Shape of WBA concrete

Result of Compressive Strength Test

Fig. 6 shows the compressive strengths of Blank

concrete and WBA concrete. The compressive strength of WBA concrete decreased by about 19% compared to that of Blank concrete. The reason why the compressive strength of WBA concrete decreased is considered that the binding force between aggregates decreased by the reduction of cement content in concrete. From the result, it was confirmed that the woody bottom ash did not contribute to the development of compressive strength for the concrete at the age of 28 days. However, the compressive strength of WBA concrete is 25.6 N/mm^2, which exceeds 24 N/mm^2, one of the standard design strengths applied to concrete structures in Japan. Therefore, even when 10% of the mass of cement used in ordinary concrete is replaced with the woody ash, it is possible to use WBA concrete in the same way as ordinary concrete. According to the report [11], even though the amorphous components were not detected in the woody bottom ash, the long-term strength of the mortar mixed with woody bottom ash increased and exceeded the strength of the normal mortar. Therefore, it is considered that further examination such as the long-term water curing of concrete is needed to obtain more clear knowledge on the strength development of WBA concrete.

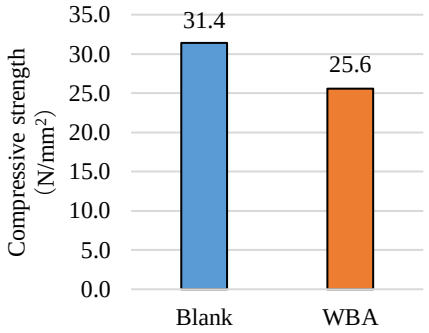

Fig. 6 Result of compressive strength test (28 days)

Results of Length Change Measurement

Fig. 7 shows the length changes of Blank concrete and WBA concrete. From Fig. 7, the shrinkage of WBA concrete was about 20% and 7% smaller than that of Blank concrete on 14 and 28 days after the start

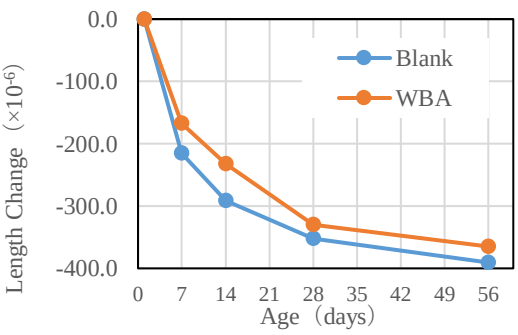

Fig. 7 Result of length change measurement

of measurement, respectively. This suggests that the drying shrinkage of concrete can be suppressed by replacing cement used in concrete with woody ash. However, it is necessary to clarify the relationship between the amount of woody ash substitution for cement and drying shrinkage in the future because it is not clear how much cement to be replaced with woody ash is rational and economical.

Result of Heavy Metal Leaching Test

Table 3 shows the concentrations of As, Cr (VI) and F leached from each concrete. From Table 3, it can be seen that the leaching amount of heavy metals from WBA concrete is equivalent to that from Blank concrete. This fact suggests that there is no significant difference in the amount of leached heavy metals between concrete with and without woody ash containing heavy metals. The soil environmental quality standard values in Japan for As, Cr (VI) and F are 0.01 ppm, 0.05 ppm and 0.80 ppm, respectively. In this test, the concentrations of As and Cr (VI) leached from all concretes sample exceeded the soil environmental quality standard values in Japan. In this study, it is considered that the concentrations of heavy metals exceeding the soil environmental quality standard values in Japan were leached because the leaching test was conducted for the finely crushed concrete. These facts are consistent with those described in [12]. Therefore, when WBA concrete is demolished, it is considered that the treatment to reduce the leaching amount of heavy metals from WBA concrete is needed.

Table 3 Result of heavy metal leaching test (ppm)

	Blank	WBA
As	0.24	0.23
Cr(VI)	0.07	0.05
F	<0.40	<0.40

CONCLUSION

In this study, the fresh property and physical properties after hardening, such as strength and length change were measured for ordinary concrete (Blank) and concrete mixed with woody bottom ash (WBA) to examine the feasibility of using WBA concrete. Furthermore, the heavy metal leaching test was conducted to assess the environmental load caused by WBA concrete.

- From the results of the slump test and the air content test, it was proven that WBA concrete has slump and air content without any problem in construction.

- Although the compressive strength of WBA concrete was slightly lower than that of Blank concrete, it exceeded the standard design strength in Japan.

- The drying shrinkage of concrete was suppressed by replacing cement used in concrete with woody bottom ash.

- The leaching amount of heavy metals from WBA concrete was equivalent to that from Blank concrete. In the meantime, the concentrations of heavy metals exceeding the soil environmental quality standard values in Japan were leached because the leaching test for the finely crushed concrete was conducted.

These findings indicated that the physical properties of WBA concrete after hardening are not significantly different from those of Blank concrete. On the other hand, there is a possibility that the concentrations of heavy metals exceeding the soil environmental quality standard values in Japan are leached from the demolished WBA concrete. Therefore, it can be said that the woody ash can be used as a concrete material by treating the demolished WBA concrete to reduce the leaching amount of heavy metals. However, it is not clear how much cement to be replaced with woody ash is rational and economical. For this reason, it is necessary to clarify the relationship between the amount of woody ash substitution for cement and the properties of WBA concrete, such as the strength development and drying shrinkage, in the future. Additionally, further examination such as a long-term water curing of concrete is needed to obtain more clear knowledge on the strength development of WBA concrete.

ACKNOWLEDGMENTS

This work has been supported by JSPS KAKENHI Grant Number JP20K04684. Also, in carrying out this study, Amron Corporation provided woody ash. We express our gratitude here.

REFERENCES

[1] Siddique R., Utilization of wood ash in concrete manufacturing, Resources, Conservation and Recycling, Volume 67, October 2012, pp. 27-33

[2] Yang Z., Huddleston J., and Brown H., Effects of Wood Ash on Properties of Concrete and Flowable Fill, Journal of Materials Science and Chemical Engineering, Vol.4, No.7, July 2016, pp. 101-114

[3] Chowdhury S., Mishra M., and Suganya O., The incorporation of wood waste ash as a partial cement replacement material for making structural grade concrete: An overview, Ain Shams Engineering Journal, Volume 6, Issue 2, June 2015, pp. 429-437

[4] Raheem A. A., Adenuga O. A., Wood Ash from Blead Bakery as Partial Replacement for Cement in Concrete, International Journal of Sustainable Construction Engineering & Technology, Volume 4, No 1, 2013, pp.75-81

[5] Batt A. S. and Garg A., Partial Replacement of Wood Ash with Ordinary Portland Cement and Foundry Sand as Fine Aggregate, Journal of Civil & Environmental Engineering, Volume 7, Issue 2, January 2017

[6] Obernberger I., Biedermann F., Widmann W., and Riedl R., Concentrations of inorganic elements in biomass fuels and recovery in the different ash fractions, Biomass and Bioenergy, Volume 12, Issue 3, 1997, pp. 211-224

[7] Gougar M. L. D., Scheetz B. E., and Roy D. M., Ettringite and C-S-H Portland cement phases for waste ion immobilization: A review, Waste Management, Volume 16, Issue 4, 1996, pp. 295-303

[8] Sklivaniti V., Tsakiridis P. E., Katsiotis N. S., Velissariou D., Pistofidis N., Papageorgiou D., and Beazi M.,Valorisation of woody biomass bottom ash in Portland cement: A characterization and hydration study, Journal of Environmental Chemical Engineering, Volume 5, Issue 1, February 2017, pp. 205-213

[9] Elinwa A. U., Mahmood Y. A., Ash from timber waste as cement replacement material, Cement and Concrete Composites, Volume 24, Issue 2, April 2002, pp. 219-222

[10] Abdullahi M., Characteristics of Wood ASH/OPC Concrete, Leonardo Electronic Journal of Practices and Technologies, Issue 8, January-June 2006, pp. 9-16

[11] da Luz Garcia M., Sousa-Coutinho J., Strength and durability of cement with forest waste bottom ash, Construction and Building Materials, Volume 41, April 2013, pp. 897-910

[12] Eckbo C., Okkenhaug G., Hale S. E., The effects of soil organic matter on leaching of hexavalent chromium from concrete waste: Batch and column experiments, Journal of Environmental Management, Volume 309, May 2022, 11470

8th Int. Conf. on Structure, Engineering & Environment (SEE), Mie, Japan, Nov.10-12, 2022, ISBN: 978-4-909106094 C3051

TECHNOLOGY FOR IMPROVING OCTOPUS RESOURCE PRODUCTIVITY USING ARTIFICIAL REEFS AND AI

Takafumi Yamamoto[1], Yoshihiro Suenaga[2], Tetsuya Tamaki[2], Shinichiro Okazaki[2], Hidenori Yoshida[2]
[1] Graduate School of Engineering, Kagawa University, Japan; [2] Faculty of Engineering and Design, Kagawa University, Japan

ABSTRACT

In recent years, the decrease in the catch of useful fish and shellfish has become serious in Japan. In particular, in the Seto Inland Sea area including Kagawa Prefecture, we have focused on octopus as a useful fishery resource since 1999, and have been trying to increase and cultivate it in the actual sea area. In addition, there is a growing demand for fishery cooperatives and fishermen in the Setouchi region to increase octopus's production and catch. Therefore, in this study, we focused on the porous substrate attached to the artificial reef that was developed by the authors and is effective in improving the productivity of fishery resources, and examined the conditions necessary for octopus to inhabit the artificial reef. First, we conducted octopus breeding experiments and examined the ecology of octopus, such as preferring concrete substrates to unglazed jars commonly used in octopus fishing. Next, we aimed to develop a technology for improving the resource productivity of octopus by proposing a structure suitable for octopus and examining a method for discriminating octopus using AI. In this study, we investigated the aggregation of octopus by diving in the sea area where artificial reefs were installed, and quantitatively evaluated the amount of prey organisms and seaweeds attached to the structures. In addition, by using AI, we will develop a method for discriminating octopus in the sea, quantitatively evaluate the distribution area of octopus and the utilization rate of artificial reefs, and proposed efficiently promotion method for recruit octopus's resources.

Keywords: Fishery resource, Productivity of octopus, Artificial Reef, Porous substrate, AI

INTRODUCTION

It is becoming even more serious that the fisheries catch is decreasing every year in Japan. Special attention is placed on to valuable fisheries resources such as octopuses (Octopus: *Octopus sinensis*) and rockfish (Black Rockfish: *Sebastes inermis,* Red spotted grouper: *Epinephelus akaara* etc.) in Seto Inland sea area (i.e. Kagawa prefecture). It is understood that the demand for octopus' catch is increasing based on surveys and interviews for fisherman and their union.

In this study, an artificial reef was developed and environmental conditions necessary for octopuses was explored. This artificial reef is made of porous material which provides adherence of preferable prey organisms for fish juveniles and has a current control function. It would form the better habitat for them with these two remarkable functions.

Also, based on the research by the substrate selection breeding experiment of octopus, it was found that they prefer concrete substrates to other materials (e.g. glass, ceramics, iron etc.) as one of the environmental conditions.

The study also examined the method to increase productivity. AI was used for quantitative assessment of the usage rates of artificial reef and distribution of octopuses in the case study area (Shinoo Bay and Kamano Bay, Aji town, Kagawa Prefecture, Japan).

OCTOPUS' HABITAT

The ecology of octopuses and habitat conditions were extracted and organized, and as a result, the conditions necessary for octopus' habitat were (1) preferred substrate, (2) shape, and (3) securing of seaweeds and feed organisms. We have conducted the substrate selection breeding experiment of octopus (octopus: *Octopus sinensis*). It was found that octopus has a strong tendency to prefer concrete substrate to octopus trap made of unglazed pottery (see Fig. 1). In addition, octopuses have a habit of digging octopus traps and holes and inhabiting in hiding, and it is generally accepted that female parents do not feed and protect eggs in the habitat even during spawning. From this, it was confirmed that octopuses prefer to inhabit concrete substrates and hole shapes. From the research by *Kadowaki et al. 2018* [1], there was a significant difference in the growth of octopus depending on the presence or absence of seaweed (sea lettuce), and it was concluded that the growth of seaweed is preferable for the growth of octopus. From this, it was decided that seaweeds are necessary for the octopus' habitat. Adult octopuses are carnivorous with a strong appetite and prey on prey organisms such as shrimp, crabs and fish [2], [3]. In addition, it is said to eat shellfish, and it is said that small bivalves can be pried open by the force of their arms, but if they do not open, they make a small hole in the shell

and inject anesthetic poison from there to prey on it. When these prey biomasses are inadequate, octopuses may cannibalize each other or eat their own arms, which is one of the factors that reduce octopus' fecundity.

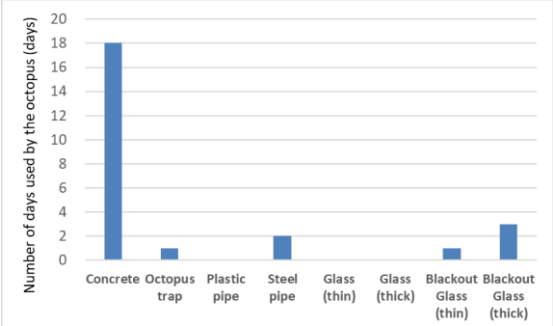

Fig. 1 Substrate selection breeding experiment

ARTIFICIAL REEF

We investigated the collection of octopus species in structures aimed at protecting and nurturing fry and improving the environment associated with the creation of stable seagrass beds (see Fig. 2). The structure integrates a porous body and a concrete block foundation, and is also equipped with a growth substrate that has a detachable function for creating seaweed beds. The existing structures in Shinoo and Kamano, Aji-cho, Takamatsu City, Kagawa Prefecture and the surrounding sea area were used as the survey sea area in this study.

We developed one structure that increases the seaweed rootage by its current control function. This structure is made of one special porous material which provides excellent adherence of preferable prey organisms for fish juveniles. This structure would form the better habitat for them with these two remarkable functions.

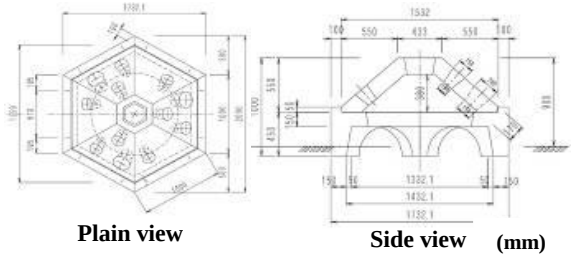

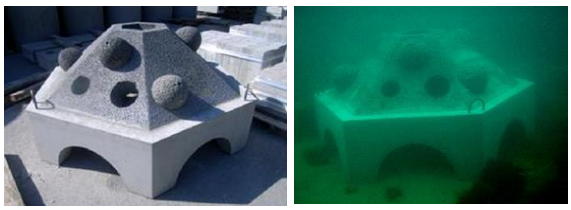

Fig. 2 Artificial reef for octopus

TEST METHODS

Hydraulic experiment

We verified these functions by two methods. One is hydraulic experiment and the second is field research. In hydraulic experiment we arranged 1/25 scale model and visualized the flow situation around the model. In field research we settled experimental structure and some components of the structure for the purpose of measuring the change of amount of rooted seaweed and adhered prey organisms. In hydraulic experiment we confirmed that many small retention areas formed on the surface of the upper part of the structure (see Fig. 3). This area would contribute to accumulation of spores of seaweed.

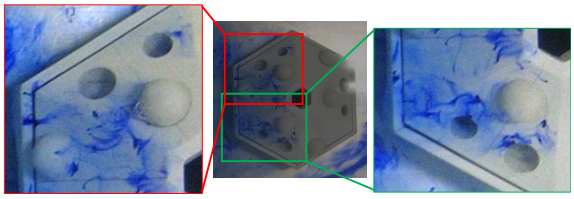

Fig. 3 Hydraulic experiment of artificial reef

Installation of the artificial reef

We selected the installation area for the experimental structures using the multi-level numerical model. Before installation, we conducted the carbonation of porous materials because carbonation is very effective for promoting prey abundances and seaweeds seeds to adhere the porous materials [4], [5]. We developed full scale experimental structures in the area indicated in Fig. 4 in December 19th, 2020. Installation depth was 4-5 m and the bottom sediment were sand and gravel. The predominant direction of the tidal current in the installation site was north and south.

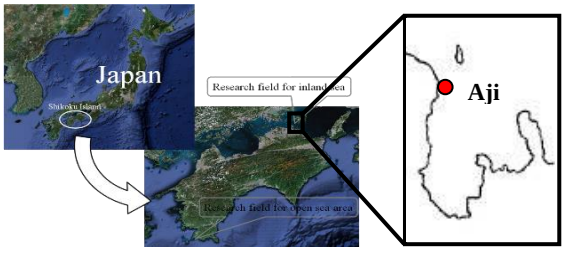

Fig. 4 Study area (Aji-Kamano, Takamatsu City, Kagawa Pref., Japan)

We settled 20 porous material specimen plates and 2 concrete plates, 2 steel plates and 5 clusters of stones and porous material for the purpose of comparison around the experimental structures and measured the quantity of adhered preferable prey organisms in the specimens collected 4 times after the

settlement. We confirmed the quantity of attached seaweeds by mowing the surface of the experimental substrates 7 times during April 2020 to May 2022. Furthermore, we examined the number of fishes aggregated around this experimental structure by visual observation 2 times during the same period.

Identification of octopuses in the sea using AI

Currently, the method of confirming the collection of octopus is visual confirmation. However, due to their habits, octopuses may be difficult to visually confirm because they assimilate with surrounding substrates or hide themselves. Therefore, in this research, we tried to detect an object using AI [6]. We propose a method for confirming the habitat of octopus using an underwater robot or an underwater camera through object detection. In this study, as a method of confirming octopus, image/video recognition using object detection by AI was performed. YOLOv5 is the latest object detection method released in 2020, featuring fast data processing speed and high accuracy. YOLO can identify what kind of object is reflected in the image by integrating the results of the data obtained by the analysis of annotations. Annotation is a term that expresses the act of adding additional information that explains the data to data such as sentences, images, sounds, and videos, or the information itself. There are many annotation specifications, and they vary depending on the work content of the target data. Image/video recognition also includes object detection, area detection, and image classification. A typical annotation in object detection is a bounding box. A bounding box is a box-shaped figure used to determine the approximate range of each object in an image. Each bounding box has an axis that represents its position in the image, and the possibility that what is contained in that box is an object is also calculated numerically. With this numerical value, it is possible to judge whether the image in each box is an object or a background, and to estimate the size of the entire object. By integrating the class probability and the bounding box, it is possible to roughly infer what kind of object is in what range in the image (see Fig. 5: Octopus in blue box).

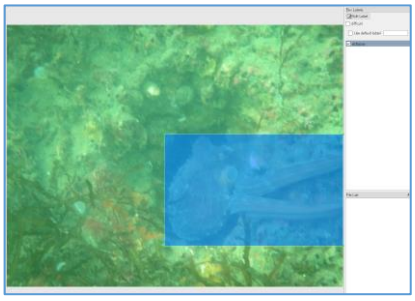

Fig. 5 Detection of octopus by bounding box

Learning method

1) Image preparation

Apart from the images to be verified, we used an online search to prepare images of approximately 110 adult octopuses and 20 octopuses guarding their eggs for this analysis. Assuming that an underwater camera will be used in the future, we prepared a total of 2,069 images by performing processing such as blurring, rotation, inversion, hue conversion, light/dark conversion, and lowering the resolution [6].

2) Annotation:

This time, we used an annotation tool called labelImg for a total of 2,069 images prepared in 1). After starting labelImg, the image file was opened and the image was selected. The bounding box of the octopus was specified in the selected image, and the YOLO format text file was saved. The class probability here is octopus.

3) Preparation of Python:

YOLOv5 runs on Python, so we prepared a virtual environment. A dedicated file was created in the personal computer, and the annotated image and the label text describing the axis were put in the specified location in the file.

4) Operation with Anaconda Prompt:

YOLOv5 was started at the command prompt called Anaconda Prompt. We entered the learning code and spent 5 to 8 hours learning. After the learning was completed, the image to be verified (the image not used for learning) was put in the specified place different from the file in 3). With Anaconda Prompt again, I entered the verification code and verified it over 10 to 15 minutes.

RESULTS AND DISCUSSION

The abundance of prey organism settled on each substrate

Quantity of the adhered preferable prey abundances in the experimental porous material was shown in Fig. 6. The adherence of prey abundance in and around the carbonation porous material (PMPS) was 2-20 times larger against other substrates. Also, the porous material with porosity 30% had the highest quantity of adherent prey abundance [4], [5].

We conducted the fish catch around the artificial reefs using fish net to confirm the fish bait those prey abundances or not. The result of juvenile fish catches, it was verified the rockfish juvenile could feed the adherent prey abundance by dissecting their stomach. We confirmed that the volume of them increased as time progressed. An example of a prey organisms is shown in Fig. 7.

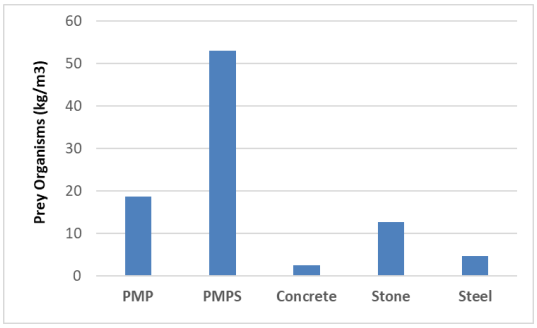

Fig. 6 Temporal changes of adhered preferable prey organisms wet weight biomass per unit volume after 36 months. (PMP: Porous material plate, PMPS: PMP in the structure)

Fig. 7 The adhered preferable prey organisms

Attached seaweeds

We observed that seaweed attached to the porous material through the research on April 24th 2020 to May 8th 2022. We confirmed the abundance of attached seaweed (dry weight) on the porous material. It was shidamoku (*Sargassum filicinum Harvey*), a kind of brown algae. It decreased sharply from October to November 2020. We call this algae shidamoku hereinafter. Furthermore, we show the volume of attached seaweed shidamoku on the surface of porous material specimen and other specimens for comparison. The maximum value 39.0kg/m^2-dw was indicated in the sample of the porous material in the experiment structure in April 24th and exceeded the remarkable value 14.1kg/m^2-dw in the porous material specimen plate (see Fig. 8). Also, we confirmed the recovery of seaweed and it was expected smooth growth of shidamoku in spring season. From those results, the porous structure is the effective base foundation for seaweed to root.

We observed extremely larger amount of seaweed rooted on the upper part of the structure than some other materials. Furthermore, we measured large amount of adhered preferable prey organisms on the seaweeds. An example of the adhered seaweeds on the artificial reefs are shown in Fig. 9 and prey organisms that have settled on seaweed leaves shown in Fig. 10.

It is considered that the porous structure of the artificial reef contributes to fixing the roots of seaweed. Also, it was possible to verify that the seaweed itself serves as a feeding ground for fish juveniles.

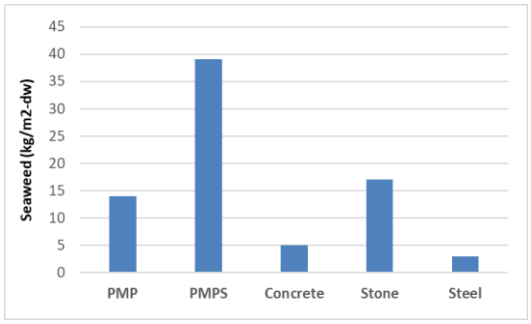

Fig. 8 Difference of attached Seaweed (shidamoku) on the specimens on April 24th 2020. (PMP: Porous material plate, PMPS: Porous material in the structure)

Fig. 9 The adhered Seaweed on the Artificial Reefs

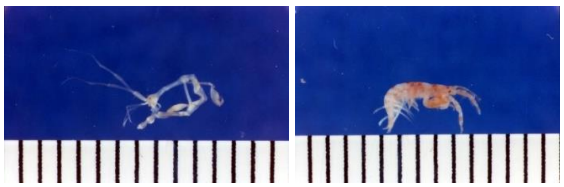

Fig. 10 Prey organisms that have settled on seaweed leaves

Fish aggregation

We investigated the temporal change of the observed number of fishes, such as Black Rockfish (*Sebastes inermis)*, Red Seabream (*Pagrus major)* and Thread-sail filrfish (*Stephanolepis cirrhifer) and* octopus, aggregated around the artificial reefs. The increase in black rockfish was especially remarkable. Also, Redspotted grouper (*Epinephelus akaara)* began to be observed during August 2020.

At the beginning of the survey, only about 5 juvenile rockfish were found per fish, but in 2020, 35 fish were also seen. In addition, the average body length is also on the rise, and although it was 8 cm on average at the start of the survey, it grew to an average of 20 cm in 2020 (see Fig.11-12). It was found that the average body length gradually increased as the amount of collection increased, and there was a positive correlation. In the survey after October every year, it became possible to confirm the inhabitation of octopus in the hole of the artificial reef. Also, octopus would prey on shellfish that have settled on artificial reefs. (see Fig.13). In particular, octopus was

assimilated with the surrounding color and was difficult to confirm, but it was suggested that this artificial reef is suitable for octopus' habitat due to its holes and porous structure.

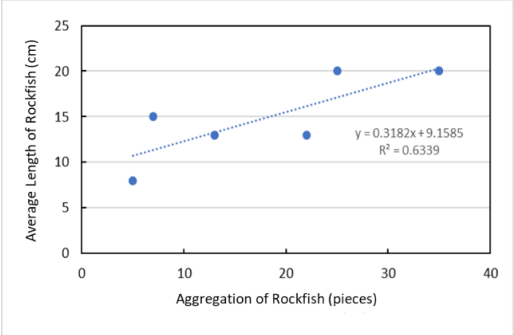

Fig. 11 Relationship between average body length (cm) of rockfish and aggregation amount (pieces)

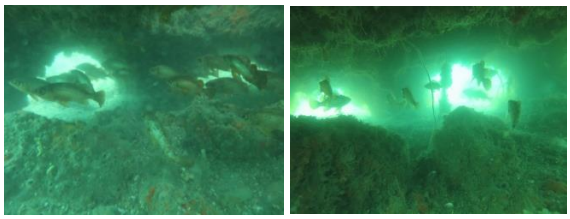

Fig. 12 Aggregation of rock fish in the artificial reefs

Fig. 13 Aggregation of octopus in and around the artificial reefs

Results of collection in survey area

In the existing structures in the survey area, seaweed epiphytes, prey organisms, and octopus' collections were confirmed under the above-mentioned conditions. In the biological collection survey conducted in 2020-2022, it was confirmed that rockfish and wrasse were as stable as before, and that the artificial reef function was maintained. As for seaweed, epiphytes of hondawara (*Sargassum fulvelus)*, etc. were confirmed. Especially in octopuses, it was confirmed that they lived in two holes of the 10 structures investigated, spawned, and predated by shellfish. On the other hand, no collection of octopus was found in the octopus trap used for octopus fishing near the structure.

From the collection results, it was verified that the structure functions as a "habitat" sufficiently, and that the characteristics of the target structure make it a convenient hiding place for foreign enemies even when protecting octopuses' eggs. Furthermore, the structure in which artificial upwelling occurs makes it easy to give fresh currents to eggs, so it can be said that it is an environment in which both larvae and adults of octopus can easily inhabit. If the target structure becomes established as a habitat for octopus, it is possible to improve the fisheries resources productivity. However, since these structures are specialized for seaweed bed construction, we thought that it was necessary to improve the structures more suitable for octopus. This structure would provide better habitat for fish juveniles both with many hiding spaces realized by good rootage of seaweed and abundant prey organisms adhered to the porous materials consisting the structure.

Learning results by AI

First, some of the results of the first verification are shown in Fig.14. The closer the number in the photo is to 1, the better the accuracy. It can be said that the accuracy is not good because both of figures are 0.5 or less. In addition, it can be said that the accuracy of left photo of Fig. 14 is low because there are many areas that are identified as octopuses and some of the reefs are misrecognized.

Fig. 14 Results of image verification (Accuracy Left:0.49, Right:0.40)

From the first learning result, we focused on the spawning situation of octopus. Since the appearance of octopus eggs does not change until hatching, the second learning added an image of the octopus holding an egg mass as imparted information. The appearance of protecting eggs was also classified into the same classification as adults of octopus, and AI was trained. Some of the results of the second verification are shown in Fig.15 -17. Comparing Fig. 15 with the results of the first time as Fig. 14, it can be seen that the accuracy is improved. Although it is a little, the range of object detection has narrowed, and no misrecognition has occurred. The images of the octopus holding the egg mass were successfully detected, and the accuracy was high at 0.73 (see Fig. 16), [7]. Since the octopus egg mass was used for the second time, the image verification in which the octopus is assimilated with the surrounding environment, failed to detect the object both times. The accuracy was generally improved except for the

images in which the octopus used for other verifications did not cause anabolic action and the images in which only a part of the body was hidden and visible (see Fig. 17). It can be said that the accuracy was improved by learning not only the adult octopus but also the state of holding the egg.

Fig. 15 Results of image verification (Accuracy Left:0.62, Right:0.46)

Fig. 16 Learning results of octopus holding an egg [7]

Fig. 17 Image verification that octopus is assimilated with the surrounding environment

CONCLUSIONS

In this study, the octopus' habitat and spawning were confirmed on the developed artificial reef, indicating that it is an effective structure for octopus. Since the octopus and the egg mass could be recognized by the image verification, it is considered that it becomes easier to find the octopus spawned in the actual sea area at the time of spawning of the octopus. After the discovery of octopus, their production is carried out by artificially protecting and hatching octopus' larvae, and artificially raising and releasing octopus for about one month, which is said to shift from floating life to submarine life. It is effective for improving the production of octopus' resources. Although the image recognition accuracy of octopus has improved by performing image verification twice, it can be said that the number of learning sheets is not sufficient because some images cannot be detected with octopus. Since mollusks behave unpredictably, it is also necessary to learn various forms of octopus. In addition, we thought that the reason why the detection range of octopus was large in the verification image was due to the annotation method. The bounding box was used as the annotation method this time, but the long arm of the octopus learns other information such as the background as the octopus when the bounding box is selected. In order to detect octopus accurately, it is necessary to try segmentation used for region extraction and polygonal polygons.

ACKNOWLEDGMENTS

This work has been supported by JSPS KAKENHI Grant Number JP20K06209. Also, in carrying out this study, Nihon Kogyo Co., Ltd. constructed artificial reefs and supported field reserach. We express our gratitude here.

REFERENCES

[1] Kadowaki H., Fujiwara H., Kasedo T., Onoe T., Common octopus hanging basket farming and suitable environment using horticultural pots, Bulletin of Faculty of Fisheries, Kagoshima University, Vol. 67, 2018, p.7-12.

[2] Yoshioka F., and Suenaga Y., Research on aquatic resource breeding structures with environmental control function, Technical Report, Department of Agricultural Eng., Faculty of Agriculture, Kagawa University, pp.1-12, 2000, pp.9-12.

[3] Okutani T., ed., Japanese Octopus, Tokai University Press, 2013, pp9-10.

[4] Kagawa University Setouchi Area Research Center: Takamatsu City Aji-cho Shinoo area Report of Artificial Reef, 2020-2021, pp.1-24.

[5] Kameyama T., Matsuyama T., Yasuoka K., Honjo T., Tada K. and Suenaga Y., Study on the Creation of Seaweed Beds by Artificial Reef Includes the Porous Material, Recent Advances in Marine Science and Technology - PACON International, 2012, pp.29-36.

[6] Shahinfar, S., Meek, P., and Falzon, G. "How many images do I need?" Understanding how sample size per class affects deep learning model performance metrics for balanced designs in autonomous wildlife monitoring. *Ecological Informatics,* 57: 101085, 2020.

[7] Uozu Aquarium: A word from the keeper, 2015. http://uozu-aquarium.jp/hitorigoto/wp-content/uploads/2015/06/kimura601.jpg

8th Int. Conf. on Structure, Engineering & Environment (SEE), Mie, Japan, Nov.10-12, 2022, ISBN: 978-4-909106094 C3051

NUMERICAL AND ANALYTICAL STUDY FOR SOLVING HEAT EQUATION OF THE REFRIGERATION OF APPLE

Dalal Adnan Maturi [1]

[1]Departement of Mathematics, Faculty of Science, King Abdulaziz University, Jeddah, Saudi Arabia

ABSTRACT

In this paper, we study the mathematical Heat and Mass transfer model, Apple shipments from Australia to England began to decline several decades ago. Due to a disorder known as "brown heart," which developed due to insufficient cooling. When placed on deck, the apples are normally warm and must be refrigerated to keep them fresh. Storing in the cold Breathing generates heat as well. This heat was thought to be the cause. The generation successfully counteracted the apple's cooling, resulting in dark fruit. "Brown Heart ".This was the issue that resulted in the Awberry. To investigate how heat is distributed within a room. The location where heat is produced. At first, Awberry assumed the apple was in the beginning.at a constant temperature In the suitable value, we can assume that this temperature is zero. Select a temperature scale from the drop-down menu. t = 0 is the current time. It must be concluded that the generation of heat inside the apple is not "Brown Heart "cause.
We now know that the brown core is caused by an excessive concentration of carbon dioxide and an insufficient amount of oxygen in the stockpile. It affects the metabolic activities that occur in apples and leads to a decrease in temperature separation. We have solved the heat equation for cooling apples using the method of separating variables in addition to numerical methods and clarification of the results obtained, including comparing the exact solution with the numerical solution. In terms of discovering analytical and numerical solutions, the approach is quite effective and useful.

Keywords: Heat Equation, Refrigeration of Apple, Numerical Method ,Matlab.

INTRODUCTION

To reduce post-harvest deterioration, agricultural goods should be chilled from ambient temperatures to their optimal storage temperatures [1]. After harvest, there is a significant loss of fresh fruits due to rot and shriveling as a result of inappropriate storage and handling conditions [2]. In practice, storage facility managers frequently define and apply storage conditions based on past experience, allowing for certain product losses due to non-optimal storage conditions. Local heat and mass transfer intensities are usually overlooked while assuming global heat and mass transfer rates through product layers.

As a result, the complex interactions between products in the same layer as well as between layers are ignored. Computer modeling and computational fluid dynamics have been used to investigate challenges in the agriculture and food industries [1-5] . For decades, numerical and experimental methods have been used to study conjugate heat transfer and fluid flow in a channel containing heated components [6-9]. Despite the fact that such issues were primarily focused on the cooling of electronic components, several post-harvest processing processes make use of the same problem configuration. The conjugate heat transfer problem for laminar flow over a three-heated obstacle array.

[10] used a control volume model to tackle the problem. A similar correlation was utilized to explore the same topic in reference [11], but this time with experimental data rather than numerical simulations. Young and Vafai [12] looked into the cooling of heated blocks, focusing on the heat transfer process's conjugate behavior. Fruit cooling is a conjugate heat transfer phenomenon, and a thorough understanding of the problem requires modeling and simulation, in which the local air velocity fields, as well as the mutual heat transfer between each fruit and the surrounding cooling agent, are analyzed. Fuji apples are often stored and chilled in rectangular crates with lateral holes to allow cool air to enter. The temperature is normally controlled at or below freezing.

Two consecutive apples will be separated by around one diameter. As a result, the heat emitted by the leading apple will almost surely delay the cooling of the following lining apples during the chilling process. The influence of the leading apple on the following apple as a function of the coolant air flow can be used to investigate the overall cooling performance of two apples.

HEAT EQUATION OF REFRIGERATION OF APPLE

The nonhomogeneous heat equation becomes

spherical because of the spherical geometry.

$$\frac{1}{\alpha^2}\frac{\partial u}{\partial t} = \frac{1}{r^2}\frac{\partial}{\partial r}\left(r^2\frac{\partial u}{\partial t}\right) + \frac{F}{\kappa}, 0 \le r < b, \ \ 0 < t, \qquad (1)$$

where α^2 represents the thermal diffusivity, b represents the apple's radius, κ is the thermal conductivity, and F is the heating rate (per unit time per unit volume).When we try to employ variable separation on Equation (1), we find that the $\frac{F}{\kappa}$ It prevents us from doing so. To get around this problem, we ask the more straightforward issue of what occurs after a very long time.

We expect a balance to be reached eventually, in which conduction takes the heat generated within the apple to the surface, where the environment absorbs it. We hope for a steady-state solution $w(r)$ where heat conduction removes the heat generated within the apples. The differential equation in its most basic form

$$\frac{1}{r^2}\frac{d}{dr}\left(r^2\frac{\partial w}{\partial t}\right) = -\frac{F}{\kappa'}, \qquad (2)$$

Provides the steady-state value. In addition, just as we added a transient solution to allow our solution to satisfy the starting condition, we must have one here as well, and the governing Equation

$$\frac{\partial w}{\partial t} = \frac{a^2}{r^2}\frac{\partial}{\partial r}\left(r^2\frac{\partial v}{\partial r}\right). \qquad (3)$$

First, solve Equation (3).

$$w(r) = C + \frac{D}{r} - \frac{Fr^2}{6\kappa} \qquad (4)$$

Because the answer must be finite at r = 0, the constant D equals zero. Therefore, the steady-state solution must satisfy the boundary condition w(b) =.

$$C = \theta + \frac{Fb^2}{6\kappa} \qquad (5)$$

We introduce a new dependent variable y(r, t) = RV in the transient issue (r, t). Equation 3 can be replaced with Equation 3 thanks to the new dependent variable.

$$\frac{\partial y}{\partial t} = a^2\frac{\partial^2 y}{\partial r^2}, \qquad (6)$$

We can resolve The R(r) equation to become R(r)T(t) if we assume y(r, t) = R(r)T(t) and only have a negative separation constant.

$$\frac{d^2R}{dr^2} + k^2R = 0, \qquad (7)$$

which has the answer

$$R(r) = Acos(kr) + Bsin(kr) \qquad (8)$$

Because the solution, Equation 8, must disappear at r = 0 in order for v(0, t) to stay finite, the constant A equals zero. However, because for every time = w(b) + v(b, t) and v(b, t) = R(b)T(t)/b = 0, R(b) = 0. As a result, $k_n = n/b$, and

$$u_n(r,t) = \frac{B_n}{r}\sin\left(\frac{n\pi r}{b}\right)\exp\left(-\frac{n^2\pi^2a^2t}{b^2}\right) \qquad (9)$$

The entire solution is obtained via superposition, which equals

$$u(r,t) = \theta + \frac{F}{6\kappa}(b^2 - r^2) + \sum_{n=1}^{\infty}\frac{B_n}{r}\sin\left(\frac{n\pi r}{b}\right)\exp\left(-\frac{n^2\pi^2a^2t}{b^2}\right) \qquad (10)$$

Finally, we use the initial condition u(r, 0) = 0 to calculate the coefficients B_n.Therefore,

$$B_n = \frac{-2}{b}\int_0^b r\left[\theta + \frac{F}{6\kappa}(b^2 - r^2)\right]\sin\left(\frac{n\pi r}{b}\right)dr = \frac{2\theta b}{n\pi}(-1)^n + \frac{F}{\kappa}\left(\frac{b}{n\pi}\right)^3(-1)^n \qquad (11)$$

The entire package is

$$u(r,t) = \theta + \frac{2\theta b}{r\pi}\sum_{n=1}^{\infty}\frac{(-1)^n}{n}\sin\left(\frac{n\pi r}{b}\right)\exp\left(-\frac{n^2\pi^2a^2t}{b^2}\right) + \frac{F}{6\kappa}(b^2 - r^2) + \frac{2Fb^3}{rk\pi^3}\sum_{n=1}^{\infty}\frac{(-1)^n}{n^3}\sin\left(\frac{n\pi r}{b}\right)\exp\left(-\frac{n^2\pi^2a^2t}{b^2}\right) \qquad (12)$$

The temperature distribution due to the imposition of the temperature on the apple's surface is given by the first line of Equation 12. In contrast, the second line raises the temperature due to interior heating.

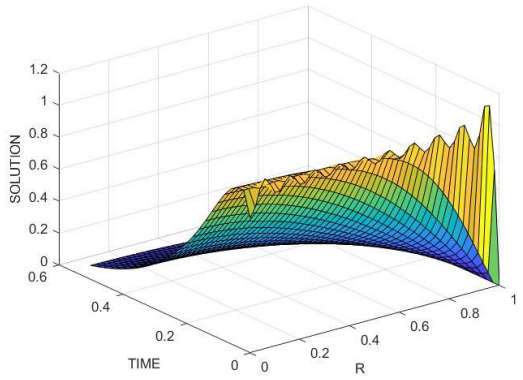

Fig. 1 The temperature $u(r,t)/T_0$ within an infinitely long cylinder at various points r/b and times a_2t/b_2 that we heated to the beginning temperature T_0 temperature uniformity After that, the surface was forced to cool.

Returning to our original question of whether the inside heating is powerful enough to offset the cooling caused by refrigeration, we apply the second line of Equation 12 to determine how much the temperature deviates from what we predict. Because of this, the maximum temperature is found in the center of each apple, and it is the only one of its kind. This problem has piqued your curiosity. Assuming that the radius of the apple is b = 4 cm, a1 G/ = 1.33105C/s, as well as a

2.55 103 = 2.55 103 = 2.55 103 = 2.55 103 = 2.55 103 =The temperature effect of heat generation is particularly high at cm2/s.

When the temperatures within the apples reach 0.0232 C after around 2 hours, the temperature inside the apples is small, only 0.0232 C.

Equilibrium. As a result, we must conclude that heat generation within the apples is not the cause of the

problem. brown heart's cause .Brown heart is now known to be caused by an excess of carbon dioxide in the storage hold and an insufficient amount of oxygen. This environment, it's assumed, impacts the apple's metabolic activities, leading to low-temperature disintegration.

TRANSIENT CONDUCTION WITH A HEAT SOURCE

The following equation governs one-dimensional transient conduction (1).

By introducing the following nondimensional quantities, we may reduce this equation to a dimensionless form

$$\xi = \frac{x}{L} \qquad \tau = \frac{\alpha t}{L^2} \qquad Bi = \frac{hL}{k}$$
$$\theta = \frac{T - T_\infty}{T_i - T_\infty} \qquad \sum = \frac{L^2 F}{k(T_i - T_\infty)}$$
$$\chi = \frac{-F'' L}{k(T_i - T_\infty)}$$

Where $\theta = \theta(\xi, \tau)$, L, is the domain length, T_i is an arbitrary temperature that usually represents the beginning temperature, F'' is the heat flux, and for T_∞ a convective boundary is the fluid temperature. When a convective boundary condition is not employed, is an arbitrary temperature that must deviate from. The governing equation changes when these variables are included

$$\frac{\partial \theta}{\partial \tau} = \frac{\partial^2 \theta}{\partial \xi^2} + \sum \qquad (13)$$

Fixed Temperature

$$\theta = \theta_w$$

Specified Flux

$$\frac{\partial \theta}{\partial \xi} = \chi_w$$

Convective

$$\frac{\partial \theta}{\partial \xi} = -Bio\theta_w$$

The boundary at is represented by the negative sign in the convective boundary condition, while the values at the wall are represented by the subscript. Equation (13) is a parabolic partial differential equation with one spatial dimension. Separation of variables is one approach of solution that is applicable to a limited number of boundary conditions. This is an example of a solution of this typ

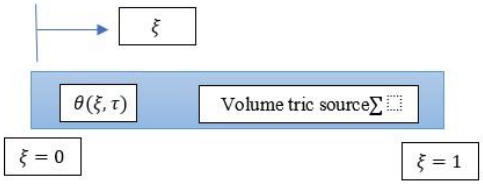

Fig. 2 Source geometry for a one-dimensional transient heat transfer.

due to the equal spacing of the curves at The temperature at which convection occurs is represented by the upper curve in Figure 3. The temperature drops quickly at tiny levels of due to convection and conduction. As the steady-state temperature profile determined by the energy source approaches, the temperature of the surface begins to climb. The profile at the moment of lowest temperature is displayed as a dotted line in Figure 4. Running pdepe for a long time yielded the steady-state solution. The steady-state curve depicted in Figure 4 was generated using bvp4c to corroborate that finding.

Table 1 Input Values

Parameter	Value
BC	$\sum = \mathbf{1}$
$\boldsymbol{\xi = 0}$	$\boldsymbol{Bi = 0.1}$
$\boldsymbol{\xi = 1}$	$\boldsymbol{\theta(1,\tau) = \theta_w = 0.55}$
IC	$\boldsymbol{\theta(1,\tau) = 1 - 0.55\xi}$
$\boldsymbol{0 < \xi < 1}$	**41**
$\boldsymbol{0 < \tau < 1}$	**101**

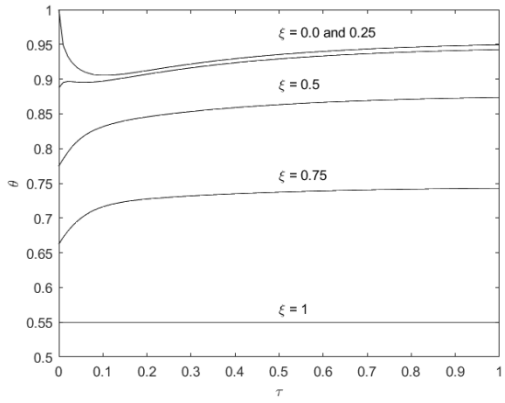

Fig. 3 For the same data plotted against the spatial coordinate with time as a parameter, one-dimensional heat conduction using the data

in Table 1.

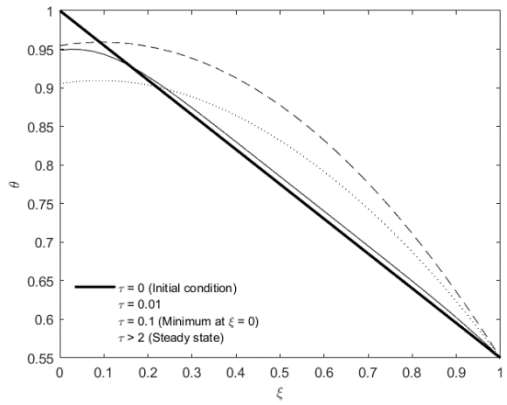

Fig. 4 Heat conduction in one dimension using data from Table 1. Figure 3 shows the same data displayed versus time with location as a parameter.

CONCLUSIONS

The development and performance of a computer algorithm that calculates latent and sensible heat loads, as well as moisture loss and temperature distribution in the environment, are presented in this work.

Apples should be refrigerated in quantity. This algorithm was created as a helper for both the is a refrigeration facility designer and operator who can simulate a wide range of commodities. In addition, the thermophysical properties of commodities and flow field parameters were discussed in this paper.which regulates heat and mass transmission in fresh apple.

ACKNOWLEDGMENTS

This paper was supported by the Deanship of Scientific Research (DSR), King Abdulaziz University, Jeddah.

REFERENCES

[1] Lopes D.C., Martins J.H., Lacerda Filho A.F., Melo E.C., Monteiro P.M.B., & Queiroz D.M., Aeration strategy for controlling grain storage based on simulation and on real data acquisition. Computers and Electronics in Agriculture, 63, 2008,pp.140-146..

[2] Mohsenin N.N. Thermal Properties Of Foods And Agricultural Materials. CRC Press, New York, US. 1980.

[3] Sun D.S., Computational Fluid Dynamics (CFD) - A design And Analysis Tool For the Agri-Food Industry. Computers and Electronics in Agriculture, Vol.34, 2002,pp.1-3.

[4] Jun S., Sastry S., Modeling And Optimization Of Ohmic Heating Of Foods Inside A flexible Package, Journal Of Food Process Engineering, Vol.28, 2005,pp. 417-436.

[5] Roy J.C., Vidal C., Fargues J., & Boulard T., CFD Based Determination Of Temperature And Humidity At Leaf Surface. Computers and Electronics in Agriculture, Vol.61, 2008,pp. 201-212.

[6] Ortega A., Writh U.S. & Kim S.J, Conjugate Forced Convection From Discrete Heat Source On Aplane Conducting Surface: A benchmark Experiment. Heat Transfer in Electronic Systems, Vol.292, 1994 ,pp.25-36.

[7] Sablani S.S., Ramaswamy H.S. & Mujumdar A.S., Dimensionless Correlations For Convective Heat Transfer To Liquid And Particles In Cans Subjected To End-Over-End Rotation, Journal of Food Engineering, Vol.34, 1997,pp. 453-472.

[8] Jensen B.B.B., Friis A., Prediction Of Flow In Mixproof Valve By Use Of CFD - Validation By LDA, Journal of Food Process Engineering,Vol. 27, 2004,pp. 65-85.

[9] De-bonis M.V., & Ruocco G. A., Generalized Conjugate Model For Forced Convection Drying Based On An Evaporative Kinetics, Journal of Food Engineering, Vol.89, 2008,pp. 232–240.

[10] Davalath J., & Bayazitoglu Y. Forced Convection Cooling Across Rectangular Blocks. 1987.

[11] Garron K., & Garimella S.V., Composite Correlations For Fonvective Heat Transfer From Arrays Of Three-Dimensional Obstacles, International Journal of Heat and Mass Transfer, Vol.40, 1997,pp. 493-498.

[12] Young T.J., & Vafai K., Convective Flow And Heat Transfer In Channel Containing Multiple Heated Obstacles, International Journal of Heat and Mass Transfer, Vol.41, 1998,pp.3279- 3298.

[13] Wazwaz A.M., The variational iteration method; a reliable tool for solving linear and nonlinear wave equations, Comput. Math. Appl., 54 (2007) 926–932.

[14] Wazwaz A.M., A First Course in Integral Equations, World Scientific, Singapore, (1997).

[15] Wazwaz A.M., Suheil A. Khuri, The variational iteration method for solving the Volterra integrodifferential forms of the lane-Emden and the Emden-Fowler problems with initial and boundary value conditions, DE GRUYTER Open Eng. (2015);5:31-41.

[16] Maturi A.D., Numerical Solution of System of Two Nonlinear Volterra Integral Equations, International Journal of Computers & Technology, Vol12, No.10, 2014, pp.3967-3975.

[17] Maturi A.D., Bajamal. Z.A, AlGethami M.B., Numerical Solution of Volterra Integral Equation of Second Kind Using Implicit Trapezoidal,

Journal of Advances In Mathematics, Vol8, No.2,2014, pp.1540-1553.

[18] Maturi A.D., Adomian Decomposition Method of Fredholm Integral Equation of the Second Kind Using Maple, Journal of Advances In Mathematics, Vol9, No.1,2014, pp.1868-1875.

[19] Maturi A.D., Application of Adomian Decomposition Method for Solving of Fredholm Integral Equation of the Second Kind, European Journal of Science and Engineering, Vol9, No.2,2014, pp.1-9.

[20] Sorkun H.H., Yalcinbas S., Approximate solutions of linear Volterra integral equation systems with variable coefficients, Applied Mathematical Modeling, 34(2010) 3451-3464.

[21] Maturi A.D., Malaikah M.H., Numerical Solution of System of Three Nonlinear Volterra Integral Equation Using Implicit Trapezoidal, Journal of Mathematics Research; Vol. 10, No. 1; February 2018, ISSN 1916-9795doi:10.5539/jmr.v10n1p44URL: https://doi.org/10.5539/jmr.v10n1p44.

[22] Maturi A.D., The Modified Decomposition Method for Solving Volterra Integral Equation Of The Second Kind Using Maple, International Journal of GEOMATE, Oct., Vol.17, Issue 62,2019 pp. 23-28.

[23] Maturi A.D., Aljedani I.A., Alaidarous S.E., Finite Difference Method For Solving Heat Conduction Equation Of The Granite, International Journal of GEOMATE, Sept., Vol.17, Issue 61, 2019 pp. 135 -140. ISSN: 2186-2982 (P), 2186-2990 (O), Japan.

[24] Maturi A.D., Finite Difference Method For Solving Heat Conduction Equation Of The Brick, International Journal of GEOMATE, April, Vol.18, Issue 68, 2020, pp. 114-119.

[25] Maturi A.D., Simbawa A.E., The Modified Decomposition Method For Solving Volterra Fredholm Integro-Differential Equation Using Maple, International Journal of GEOMATE, March Vol.18, Issue 67,2020, pp. 84-89.

8th Int. Conf. on Structure, Engineering & Environment (SEE), Mie, Japan, Nov.10-12, 2022, ISBN: 978-4-909106094 C3051

THE INVESTIGATION OF BIOGAS PERFORMANCE AFTER PURIFICATION USING NATURAL ZEOLITE AND RICE-HUSK BIOCHAR

Ambar Pertiwiningrum[1], Margaretha Arnita Wuri[2], Alva Edy Tontowi[3], Andang Widi Harto[4] and Misri Gozan[5]

[1]Faculty of Animal Science, Universitas Gadjah Mada, Indonesia; [2]Center for Energy Studies, Universitas Gadjah Mada, Indonesia; [3,4]Faculty of Engineering, Universitas Gadjah Mada, Indonesia; [5]Faculty of Engineering, Universitas Indonesia, Indonesia

ABSTRACT

Renewable energy is expected to gain a larger share of Indonesia's Mix Energy in 2030. To increase renewable energy sharing in the energy mix, biogas technology is encouraged to improve its performance. The challenge is to purify biogas on the community biogas scale to overcome well-established technologies and the current heavily fossil fuel-based energy. The study aims to investigate the effect of the substitution of natural zeolite with biochar to decrease investment costs. For our analysis, the researchers used four different times in biogas purification: 10, 15, 20 and 25 minutes of adsorption time to find the best performance. The performance was measured from biogas's CO2 and CH4 methane composition after biogas purification. In this study, biogas purification using natural zeolite and rice-husk biochar decreased either CO_2 or CH_4 methane composition in biogas. It's related to the characteristics of adsorbents. The researchers concluded that the mesopore characteristic of the pore structure of biochar didn't selectively adsorb CO_2 molecules only by analysis using a surface area analyzer. The results showed that natural zeolite and biochar have pore sizes of 4.74 and 3.26 nm respectively. Both of them were dominated by meso-sized pore volume with a volume of 0.057-0.093 cc/g. The characteristic of adsorbent needs to be improved to encourage the acceleration of biogas adoption in Indonesia.

Keywords: CO_2 Adsorption, Rice-husk biochar, Biogas, Purification

INTRODUCTION

Indonesia has many plans to achieve greenhouse gas (GHG) mitigation. Some policies and regulations have been proclaimed to support the achievement of this goal, including the National Action Plan on Greenhouse Gas Emissions Reductions (RAN-GRK) through Presidential Regulation No. 61/2011 [1] and Inventory of Greenhouse Gases through Presidential Regulation No. 71/2011 [2]. In the energy sector, the government has determined the energy mix policy which is also contained in Government Regulation no. 79/2014. The main energy mix is organized as follows: (1) new renewable energy is at least 23% in 2025 and at least 31% in 2050, (2) the oil must be less than 25% in 2025 and less than 20% in 2050, (3) the coal is at least 30% in 2025 and at least 25% in 2050, and the last (4) the gas is at least 22% in 2025 and at least 24% in 2050 [3].

Throughout 2019, Indonesia added 385 MW of renewable energy. The increase in the role of renewable energy substitutes for the declining share of oil and natural gas. Renewable energy supply keeps being pushed along with increasing concern about the increase of fossil fuel prices and the environmental impact of fossil fuel. Unfortunately, in terms of generation, renewable energy only contributed to 12.2% of the installed capacity mix in 2019 [4]. To accelerate the implementation of these policies, many plan actions to adopt renewable energies have been conducted in Indonesia such as biogas technology. Until today, the renewable energy supply is still dominated by biofuels, biomass, hydropower, and geothermal. Meanwhile, the other renewable energies, wind energy, solar cell, and biogas, have a very small share [5].

There are some challenges to biogas program adoption in the energy mix policy in Indonesia [6]. Rachmawan [7] reported that there are still many obstacles that can be classified as problems of (1) market, (2) economics and finance, (3) institutional, (4) technical, and (5) social and culture. From a technical point of view, according to this study, the biogas system was not capable to deliver gas, even at a distance of 10 m from the digester. Moreover, in general, biogas did not meet the expected cooking and lighting needs of households [8]. It means the use of biogas didn't fully replace the use of fossil fuels. Dintani [9] also reported that the implementation of the communal biogas wasn't able distributed to all households due to biogas having low pressure.

The low pressure of biogas is caused by biogas components that are not pure methane. Biogas consists mainly of methane and carbon dioxide, but also contains several impurities. To transfer biogas that has high methane components, a major step

offered is a cleansing process to remove the trace components or biogas purification. The presence of the other components in biogas causes a detrimental effect on the structure of the downstream implementation of biogas such as corrosion of engines and lower calorific value and gas pressure. If these components are removed, the purified biogas would have high-quality methane and can be used for a wider variety of uses, either for cooking or electricity or vehicle fuels. In this study, the researchers focused on CO_2 removal, as the biggest impurities in biogas. As the CO_2 component gas is removed, the relative density decreases and the calorific value increases [10]. The lower calorific value of biogas compared to natural gas is also the reason that biogas purification is important.

But, Sahota [11] also reviewed that biogas purification in small-scale plants is too expensive due to high investment costs for the pieces of equipment. Thus, for now, a simple biogas purification needs to be developed and can be developed by reduction of the complexity of the control system and the use of cheap material as adsorbent. Ryckebosch [10] reviewed the advantages and disadvantages of techniques for the removal of CO_2 and the adsorption method is suitable for the small capacity of a biogas plant.

The study aims to develop a simple biogas purification system that uses an adsorbent-based biowaste. As the researchers know, according to Statistics Indonesia [12], rice husk, a major by-product of rice milling industries, is abundant. To capture CO_2, rice husk is required to convert to biochar. Biochar is a solid material obtained from the carbonization of biomass. Biochar is non-expensive, environmental-friendly, and can capture CO_2 [13]. In the previous study, the researchers investigated five formulations with different ratios of zeolite and rice husk based-biochar: A1 (100% of natural zeolite), A2 (75%:25%), A3 (50%:50%), A4 (25%:75%), and A5 (100% of biochar) to decrease carbon dioxide composition. The substitution of 25% volume of zeolite with rice husk-based biochar adsorbed CO_2 optimally with a CO_2 reduction of 43.13%. In this study, the researchers investigated the effect of time of adsorption on CO_2 reduction in biogas purification using the combination of 25% volume of biochar and 75% volume of zeolite.

METHODOLOGY

Rice husk-based biochar production

The rice husk was collected from the paddy farmers near Yogyakarta. The rice husk was sun-dried overnight and then pyrolyzed at the temperature of 255ºC for 3 hours in the furnace. After that, biochar was characterized by a surface area analyzer.

Biochar preparation for biogas purification

The biochar and natural zeolite samples prepare for biogas purification. In this study, the substitution of a 25% volume of zeolite with rice husk-based-biochar adsorbed CO_2 was carried out. Biogas purification was conducted in a packed second-level bed column with a column length of 20 cm and a diameter of 3 cm. The placement of the adsorbent in the column is sorted where the natural zeolite (75% volume) is at the bottom of the column then rice husk biochar (25% volume) is on top for each column (Fig. 1).

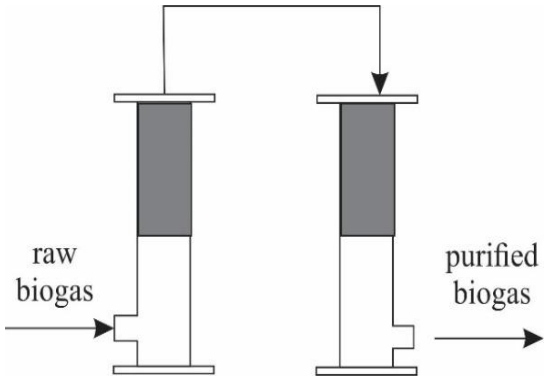

Fig. 1 The CO_2 adsorption column in biogas purification.

Four variations of adsorption time were carried out (10, 15, 20, and 25 minutes). Biogas before and after biogas purification were analyzed of CH_4 and CO_2 contents by gas chromatography. Sampling was carried out in three repetitions for each variation adsorption time. Sample names are following Table 1.

Table 1 Samples in the variation's adsorption time

Adsorption time (minutes)	Samples
10	ZR1
15	ZR2
20	ZR3
25	ZR4

Surface Properties

The specific surface area of adsorbents was measured with a surface area analyzer using the N_2 adsorption method to determine the macro and micropore surface area.

RESULTS AND DISCUSSION

Carbon dioxide content in biogas

Carbon dioxide (CO_2) is the biggest impurities in biogas contents. In this study, the change in CO_2 content in biogas between before and after biogas purification represented that biogas purification run well. It means the adsorbents, the combination of natural zeolite and rice husk biochar, were capable to capture CO_2. Our previous study reported that the optimal adsorbents formula with a composition of 75% volume of natural zeolite and 25% volume of biochar for each column gave the highest CO_2 reduction so in this study, for investigating the variations of adsorption time, used the adsorption composition.

Many references [13]-[14] reported that the variation in adsorption time continually gave different impacts on CO_2 adsorption capacity. Figure 2 showed the correlation between adsorption time and CO_2 reduction.

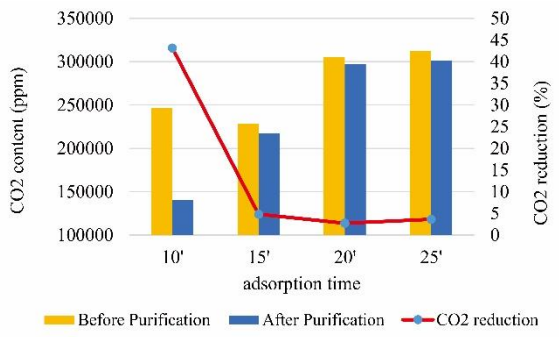

Fig. 2 The different CO_2 compositions of biogas before and after biogas purification.

For all samples, biogas purification by CO_2 adsorption in the variations of adsorption time (10, 15, 20, and 25 minutes) succeeded reduce CO_2 content compared to CO_2 content in biogas before biogas purification. The highest CO_2 reduction is shown by biogas purification with an adsorption time of 10 minutes. There is a decrease in CO_2 content from 246,370.98 to 140,107.09 ppm or with a CO_2 reduction of 43.14% (Fig. 2). Above 10 minutes of adsorption time, the adsorbents' capability to capture CO_2 molecules is reduced. Figure 2 shows that the CO_2 adsorption process occurred very fast in the first 10 minutes and became slow after 10 minutes. For 15 minutes of adsorption time, there is a decrease in CO_2 content from 228,503.73 to 217,554.23 ppm or with a CO_2 reduction of 3.49%. For 20 and 25 minutes of adsorption time, there are a CO_2 reduction of 2.72 and 3.16% respectively. There is a tendency for the CO_2 adsorption ability to stagnate after biogas purification is carried out for more than 10 minutes. It means the combination of adsorbents undergoes CO_2 adsorption equilibrium at 15 to 25 minutes of adsorption. The trend was consistent with the previous studies [13]-[14] of CO_2 adsorption on biochar and natural zeolite. The result predicts that there was an increase in surface area by the substitution of 25% by volume of natural zeolite with biochar, which played an important role in the capability of CO_2 adsorption. Therefore, surface area analysis was also conducted in this study.

Methane content in biogas

The consequence of the implementation of biogas purification by CO_2 adsorption is an increase in CH_4 content in biogas [10]-[11],[15]. As the CO_2 content in biogas is removed, the CH_4 content increases [10] and impacts the calorific value. Figure 3 showed the correlation between adsorption time and the CH_4 composition in biogas.

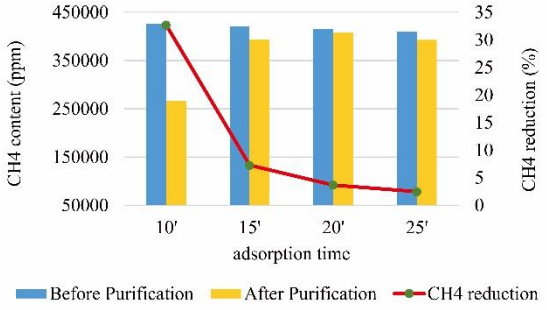

Fig. 3 The different CH_4 compositions of biogas before and after biogas purification.

Unlike the previous studies, biogas purification by CO_2 adsorption has the effect of reducing CH_4 content at the same time. For all samples, biogas purification by CH_4 adsorption in the variations of adsorption time (10, 15, 20, and 25 minutes) s reduced CH_4 content compared to CH_4 content in biogas before biogas purification. The highest CH_4 reduction is shown by biogas purification with an adsorption time of 10 minutes, the trend is as same as CO_2 reduction. There is a decrease in CH_4 content from 426,727.56 to 266,451.89 ppm or with a CH_4 reduction of 32.67% (Fig. 3). Above 10 minutes of adsorption time, the adsorbents also captured CH_4 molecules. Figure 2 shows that the CH_4 also happened after biogas purification for 15 minutes, with a decrease in CH_4 content from 420,435.56 to 393,761.63 ppm or with a CH_4 reduction of 7.26%. For 20 and 25 minutes of adsorption time, there are a CH_4 reduction of 2.72 and 3.16% respectively. The trend of the decrease in CH_4 content is in line with the decrease in CO_2 content in biogas.

The facts showed that either natural zeolite or rice husk-based biochar not only captures CO_2 molecules but also CH_4 in biogas. This phenomenon can be explained further by investigating the characteristics of the adsorbents. This probably can

be attributed to micro or mesopore surface area on adsorbents, which could promote the physisorption of CO_2 and CH_4. To provide evidence of the mechanism the physisorption of CO_2 and CH_4 has related to adsorbents characteristics so adsorbents' surfaces are measured in this study.

Surface area properties

Based on the experimental data showed that rice husk-based biochar combined with natural zeolite could be a promising framework for CO_2 capture. But, the use of rice husk-based biochar combined with natural zeolite as adsorbents in the biogas purification system still has to be developed further.

The BET surface area, total pore volume, and micro and mesopores size were measured by a surface area analyzer. The results are shown in Table 2. The combination of adsorbents, natural zeolite and rice husk-based biochar, adds the specific surface areas that have a role in capturing CO_2 when the biogas is passed through the adsorption column at a gas pressure of 5-7 bar. The CO_2 reduction value by ZR1 is higher than the 100% volume of natural zeolite with a CO_2 reduction of 25% [16].

Table 2 The adsorbents' characteristics

Characteristics	Natural zeolite	Rice husk-based biochar
Specific surface area (m^2/g)	47.66	50.40
Pore radius (nm)	4.74	3.26
Total pore volume (cc/g)	0.110	0.082
Micro-sized pore volume (cc/g)	0.017	0.025
Meso-sized pore volume (cc/g)	0.093	0.057

However, the adsorbents have the potential capability as the CO_2 adsorption in biogas purification, the adsorbents also can adsorb the CH_4 molecules. One possible reason is that due to both natural zeolite and biochar are still dominated by a meso-sized pore with a size pore diameter range of 2-50 nm (Table 2). For selective adsorbents that capture CO_2 molecules only, the adsorbents must have a micro-sized pore dominantly. The dominant meso-sized pores cause CH_4 molecules to be captured by adsorbents. Lee [17] observed the presence of abundant narrow micro-sized pores has an important role in doing the best CO_2 adsorption capacity. Therefore, based on this study, biochar synthesis or biochar pyrolysis becomes key factor to develop micropore-sized adsorbent. Temperature of pyrolysis must be investigated deeply for the further study. In addition, surface modification and pore size control are essential for CO2 capture selectively.

CONCLUSIONS

Results from this study indicated that the combination of natural zeolite and rice husk-based biochar (with a volume ratio of 3:1) could be a promising adsorbent for CO_2 capture. The best CO_2 adsorption was performed by adsorbents after 10 minutes of biogas purification and reached adsorption equilibrium after 25 minutes of adsorption.

It's also concluded that surface modification to make micro-sized pores of the adsorbent is suggested to be a concern for the next study. In this study, the adsorbents not only captured CO_2 but also CH_4 molecules at the same time and trend. The dominant meso-sized pores on adsorbents caused adsorbents were not selectively in adsorbing CO_2 because CH_4 molecules belong to the meso-sized molecule with a molecule size of 0.38 nm.

ACKNOWLEDGEMENTS

In this study, it is impossible to thank everyone individually, so the researchers give our thanks to many people and individuals who have assisted us over the years, and to the colleagues, students and volunteers who have similarly offered their support. The researchers also wish to express our sincere thanks to the Directorate General of Higher Education, Ministry of Education and Culture for its funding and support through the PTUPT research grant.

REFERENCES

[1] Government Regulation Number 79/2014. National Energy Policy, 2014.
[2] Presidential Regulation Number 61/2011. National Action Plan on Greenhouse Gas Emissions Reduction (RAN-GRK), 2011.
[3] Presidential Regulation Number 71/2011. National Inventory of Greenhouse Gases, 2011.
[4] Author H., A Book New York Publisher, Year, pp.1-200.
[5] Institute for Essential Services Reform (IESR), IESR Publisher, 2019, pp.1-69.
[6] The Agency of the Assessment and Application Technology, Center for the Study of Process Industry and Energy (PPIPE), 2020, pp.1-70.
[7] Rachmawan B., Ridwan, Mohammad K.R., Andianto H., Yogana S.A., Suhono and Kutut S., Sustainability Challenge for Small Scale

Renewable Energy Use in Yogyakarta, Procedia. Vol.17, 2013, pp.513-518.

[8] Florence L., Johnny M., Peter N.W., Jo S., and Bedru B., Dis-adoption of Household Biogas Technologies in Central Uganda., Energy for Sus. Dev., Vol. 37, 2017, pp. 124-132.

[9] Dintani Y.N.N., Margaretha A.W., Ambar P., Rachmawan B., and Tiwi P.H., Technical and Social Assessment of Biogas in Yogyakarta and Gorontalo, Indonesia, in Proc. 2019 ICESE, Vol. 471, 2020, pp. 1-8.

[10] E. Ryckebosch, M. Drouillon, and H. Vervaeren, Techniques for Transformation of Biogas to Biomethane, Biomass and Bioenergy, Vol. 35, 2011, pp. 1633-1645.

[11] Sahota S., Shah G., Ghosh P., Kapoor R., Sengupta S.m Singh P., Vijay V., Sahay A., Vijay V.K., and Shekhar T., Reviews of Trends in Biogas Upgradation Technologies and Future Perspectives, Biores. Tech. Reports, Vol. 1, 2018, pp. 79-88.

[12] Statistics Indonesia, Statistics Indonesia, 2018, pp. 12

[13] Cha, J.S., Park S.H., Jung S., Ryu C., Jeon J., Shin M., and Park Y., Production and Utilization of Biochar: A Review, J. of Industrial and Eng. Chem., Vol. 40, 2016, pp. 1-15.

[14] Xu X., Kan Y., Zhao L., and Xinde C., Chemical Transformation of CO2 during Its Capture by Waste Biomass Derived Biochars, Env. Pollution, Vol. 213, 2016, pp. 522-540.

[15] Anne E.C., Bin G., and Ming Z., Carbon Dioxide Capture Using Biochar Produced from Sugarcane Bagasse and Hickory Wood, Chem. Eng. Journal, Vol. 249, 2014, pp. 174-179.

[16] Margaretha A.W., Ambar P., Rachmawan B., Misri G., and Andang W.H., The Waste Recycling of Sugarcane Bagasse-Based Biochar for Biogas Purification. in Proc. JESSD, Vol. 940, 2021, pp. 1-6.

[17] Lee S. and Park S., A Review on Solid Adsorbents for Carbon Dioxide Capture, Journal of Industrial and Eng. Chem., Vol. 23, 2015, pp. 1-11.

8th Int. Conf. on Structure, Engineering & Environment (SEE), Mie, Japan, Nov.10-12, 2022, ISBN: 978-4-909106094 C3051

WATER AND SANITATION SERVICE: A PRIORITY TO IMPROVE QUALITY OF SLUM AREAS IN PONTIANAK CITY BASED ON STAKEHOLDERS' PREFERENCES

Zulfa Amala[1], Ahmad Soleh Setiyawan[1], Prasanti Widyasih Sarli[1], Prayatni Soewondo[1], and Dion Awfa[2]
[1]Faculty of Civil and Environmental Engineering, Bandung Institute of Technology, Indonesia; [2]Faculty of Environmental Engineering, Sumatera Institute of Technology, Indonesia

ABSTRACT

Water and sanitation facilities of an area are important aspects that affect the quality of life, health and environment. Pontianak City, Indonesia is known as the "Equator City." There are 150.16 hectares of slum areas in this city. The existence of these slum areas is mostly due to the lack of basic facilities and infrastructure, and lack of public understanding about the importance of a healthy and quality environment. The government has made efforts over the past 5 years to improve the quality of water and sanitation infrastructure in slum areas in order to achieve the 2030 SDGs and to ensure the universal accessibility of water and sanitation and their sustainable management. This research was conducted to determine the priority of stakeholders in Pontianak City in improving the provision of water and sanitation infrastructure in slum areas. The methods of Analytic Hierarchy Process (AHP) were used, with the approach referring to the Indonesian Minister of PUPR No. 14 of 2018 concerning Prevention and Quality Improvement of Slum Housing and Settlements. The results (CR value < 0.1) showed that the Pontianak City stakeholders prioritized 0.30 the provision of drinking water in slum areas, 0.25 solid waste management, 0.23 wastewater management, and 0.22 environmental drainage. An in-depth priority study by various relevant stakeholders is needed to improve the quality of slum areas.

Keywords: Pontianak City, Slum area, Stakeholders, Water and sanitation

INTRODUCTION

Along with the development of Pontianak City, the population of slum settlements has increased over the last 5 years. It's influenced by population growth and urbanization [1]. The resident built these areas spontaneously and privately alongside the rivers and ditches. It is well-known as "river culture" due to the adaptive characteristics of its residents in their physical, social, and economic life [2]. There were slum settlements of 70.51 hectares with various levels of slum in 2015 (light, medium and heavy) and due to the results of the latest regulation issued by the Pontianak Mayor Decree Number 1063.1/D-PRKP/2020, it becomes 150.16 hectares of slum settlements with a light level. The existence of these slum settlements in Pontianak is mostly due to the lack of basic facilities and infrastructure quality and also lack of public understanding about the importance of a healthy and quality environment [3]. Because of this failure, there will be serious repercussions for both the health of humans and the environment. At a crucial stage in the process of sanitation planning, the lack of involvement from both governmental and nongovernmental stakeholders is one of the primary factors that contributes to the problems [4].

The Analytic Hierarchy Process (AHP) technique is one way to facilitate users' access to the relative weights of a number of criteria or options in relation to a specific criterion in an approach that is both straightforward and easy to understand. Raters are still able to determine whether one criterion is more important than another, even if quantitative ratings are not available. This method is simple, rational, and most often used for weighting. In this paper, AHP is used in the consideration of priorities for improving clean water and sanitation in the slum areas of the study site in Pontianak City. This makes it possible to identify stakeholder priorities, and to compare them with the current condition of clean water and sanitation management. As a result, valuable information can be obtained regarding stakeholder preferences and their impact on current existing conditions and the appropriateness of water and sanitation management which may be conflicting.

STUDY AREA

The study was conducted in three slum areas in Pontianak City, namely the Panglima A. Rani Area (RT 01, 02, and 03) in Tambelan Sampit Subdistrict, RA Kartini (RT 01) in Tengah Subdistrict and Kayu Manis in Sungai Jawi Luar Subdistrict (RT 04, 05, and 08). The selection of this area refers to the Decree of the Mayor of Pontianak Number 1063.1/D-PRKP/Year 2020, which is the determination of slum areas in Pontianak City. The selection of the area is

based on Deltares data where the area is in a water sensitive area, besides that it also has the characteristics of a densely populated area, high poverty rate, flood risk, and passes through drainage channels or rivers.

RESEARCH METHODS

Data Collection Method

Descriptive research is used to describe the existing conditions related to water and sanitation at the study site. The survey method was used to collect primary data, where closed-ended questions were used as a tool. This is done to compare field conditions with stakeholder priorities related to increasing access to clean water and sanitation.

The existing condition data collection uses cluster random sampling to ensure the probability of respondents in the selected group. The Yamane method was used to determine the number of samples using the formula in Eq. 1. The total sample in this study amounted to 127 households with a margin of error of 10%. In Yamane's formula, refers to the sample size (n), population size (N), and margin of error (e).

$$n = \frac{N}{1 + Ne^2} \quad (1)$$

Prioritization is needed to determine the level of importance and contribution of each exposure indicator to its impact. Criteria and indicators for increasing access and demand for drinking water, environmental drainage conditions, facilities and infrastructure for domestic wastewater management, and solid waste management systems, refer to the Indonesia Minister of PUPR Regulation No. 14 of 2018 concerning Prevention and Quality Improvement of Slum Housing and Settlements. Stakeholders who responded include: Department of Environment and Forestry (DLHK) of West Kalimantan Province, Department of Environment (DLH) of Pontianak City, Department of Health (Dinkes) of Pontianak City, Department of Public Housing and Settlement Areas (DPRKP) of Pontianak City, Department of Public Works and Public Housing (DPUPR) Pontianak City, Head of each study location, Head of RW and non-governmental groups.

A weighting method is required to determine the priority of these indicators. Therefore, the method used in this study is AHP because this method is simple, rational and most often used for weighting indicators. The type of questionnaire used for determining priorities is a pairwise comparison questionnaire. The principle that must be applied to the pairwise comparison method is Logical Consistency, the ratio of consistency by looking at the consistency index. Logical consistency states a measure of whether or not an assessment/weighting is consistent in the pairwise comparison matrix. This happens because of the inconsistency of respondents in giving preferences [5]. One way to measure consistency is through a consistency index (CI). n represents the alternative being compared and λ max represents the largest eigen value of the pairwise comparison matrix.

$$CI = \frac{(\lambda\, max - n)}{(n - 1)} \quad (2)$$

If the CI is 0 then the assessment decision is the same as the number of criteria being compared. The higher the CI value, the higher the level of inconsistency of the comparison decisions that have been made. The consistency index of the random matrix with a scale of 9 (1-9) and its inverse is called the Random Index/RI. Based on Saaty and Vargas (2006) obtained the average value of the Random Index as in Table 1 [6].

Table 1 Average value of random index

1	2	3	5	6	7	8	9
0	0	0,58	0,90	1,12	1,24	1,41	1,45

If the values of CI and RI have been obtained, then the next step is to find the value of Consistency Ratio (CR) formulated by:

$$CR = \frac{CI}{RI} \quad (3)$$

Next is to make a combined assessment, namely by using the geometric mean [5]. X represents the sample value and n represents the number of samples. The geometric mean is formulated as follows:

$$G = \sqrt[n]{x_1 \times x_2 \times \ldots \times x_n} \quad (4)$$

Data Analysis

The results of the closed questions and the AHP were analyzed using descriptive statistics, and Microsoft Excel was used for the processing and illustration of the results. The information that was gathered, which was supported by documentation and direct observation, will be used to describe the current state of the slum area that is located in the area under study [7].

RESULT AND DISCUSSION

Water and Sanitation in slum household

In this study, the classification of drinking water refers to the three-step ladder used by the WHO/UNICEF Joint Monitoring Program (JMP), piped water inside buildings, as well as other improved sources and unimproved sources [8]. Fig. 1 exhibit the source of drinking water in the study area based on JMP classification. The use of community drinking water is generally classified into the other improved sources category, where the source of drinking water is rainwater. The remainder is from unimproved sources, where the source of drinking water is refilled water and bottled water. However, in the RA Kartini and Kayu Manis areas, some people do not treat rainwater first. Rainwater is not always a good clean water source that is ready to be consumed; physically, it does not have color, taste, and clarity, however, rainwater is affected by the area where the rain falls [9].

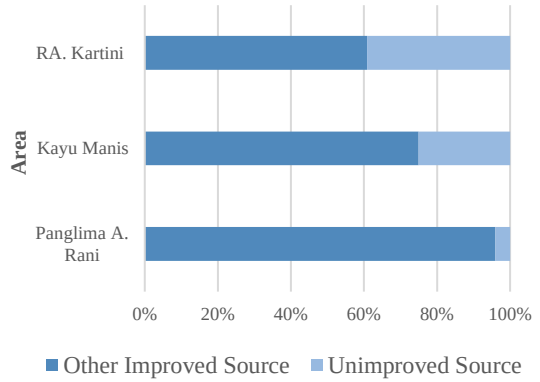

Fig. 1 Drinking water sources of households in slum areas based on the JMP three-ladder classification (n=127).

Table 2 Clean water sources of households in slum areas

Household Water Source	Area		
	Panglima A. Rani	Kayu Manis	RA. Kartini
River water	88	62	-
Portable water	12	34	78
Well water	2	34	22
Rainwater	2	7	22

Table 2 shows that the majority of riverside households used river water directly without any treatment. Households in the city used portable water, whereas wells and rainwater were also used for bathing and washing needs. According to the PUPR standard Number 14/PRT/M/2018, a community's minimum drinking water needs are < 60 liters/person/day. As much as 83% of households in slum settlements in this study's location did not meet minimum water needs.

The management of domestic wastewater at the study sites showed that the management was 100% unsafe. As shown in Table 3, generally, households that were located on the riverside were at the basic level of sanitation, and households in the city were at the level of shared sanitation. Moreover, the septic tanks that the community owns did not meet technical standards. Meanwhile, in households that did not have a septic tank, some directly discharged their waste into water bodies and drainage channels. Therefore, the function of the drainage channel was still mixed with domestic wastewater discharge. This was made worse by the fact that there was still a practice of defecation in the river, the highest occurrence being in the Kayu Manis Area. The practice of defecating in public is one of the problems that plague the developing world and is the root cause of the spread of diseases that cause diarrhea [10]. The unsafe management of domestic wastewater can produce high levels of nutrients in the waters and cause environmental degradation, such as eutrophication [11].

The condition of solid waste in slum areas, especially in the Kayu Manis and Panglima A. Rani areas, which is located on the riverside, can be seen by the large mass of garbage scattered or piled in the area. This is partly due to the habit of riverside residents throwing garbage into the Kapuas River. For household solid waste management, as shown in Fig. 2, generally, the community collected their waste individually into containers that have been provided at several locations. The waste transportation system used was the HCS (Hauled Container System) system. However, the management of solid waste transported to landfills only reached around 53-87%. The community managed the remaining household waste by burning and throwing their waste into the river.

Table 3 Sanitation ladder of households in slum areas

No	Sanitation Ladder	Area		
		Panglima A. Rani	Kayu Manis	RA. Kartini
1	Safety Managed	-	-	-
2	Basic	84%	66,2%	30,4%
3	Shared	2%	-	65,2%
4	Unimproved	2%	-	-
5	Open Defecation	12%	33,8%	4,3%

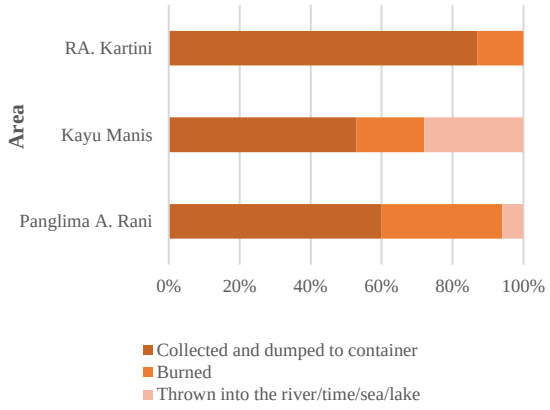

Fig. 2 Solid waste management of households in slum areas

Burning trash and throwing it in rivers due to a lack of public awareness is a bad habit that can have long-term implications. In most cases, children will model their behavior after their parents. If children see their parents throwing trash into the river, there is a significant likelihood that the children will follow in their parents' footsteps and do the same [12]. The negative effects of littering can range from lessening a city's appeal from an aesthetic standpoint to polluting waterways and ecosystems [13].

The drainage concept that is still widely applied is the principle that rainwater needs to be dumped into the river as soon as possible. This causes the river to receive a load that exceeds its capacity, while not much water seeps into the ground [14]. Likewise, in this study, not all households had drainage channels. Especially in the Kayu Manis and Panglima A. Rani areas, several community houses were located above the river on stilts. In addition, the function of the drainage channel was still combined with the disposal of domestic wastewater such as bathing and washing. As much as 84.4% of households dispose of gray water in drainage channels.

Table 4 indicates the incidence of flooding in the studied slum area. This research found that Panglima A. Rani and RA. Kartini areas were more vulnerable to flooding. Flood heights could reach the knee height of adults, with the receding time being less than 1 hour to half a day. At the study site, the factors that influenced the amount of flooding/ puddle were the lack of drainage channels, drains for surface runoff, and high tides, especially in low-lying areas. Flooding/puddle was also caused by the small drainage potential of Pontianak City due to the area's flat topography. Therefore, the small drainage potential and influence of rising tides causes the water to flow slowly, so the process of determining flood areas takes a long time.

Table 4 Flood incidences of households in slum areas

Criteria	Area		
	Panglima A. Rani	Kayu Manis	RA. Kartini
Flood incidences	24% Several times a year	47% Once a year	48% Several times a year
Flood height	Adult knee	Adult knee	Adult knee
The flood dries up	Half-day	Less than 1 hour	Less than 1 hour

Stakeholder's Priority

Standard and interest groups are the two categories that can be used to classify the stakeholders in the water and sanitation planning process [4]. In this study, the opinions of interest groups were obtained as stakeholders because they are the most familiar with slum areas. Interest groups include political parties, civic organizations, and residents of the impact area. Each interest group has its point of view for evaluating potential alternatives and often has different relational systems of preference, thus creating competition and conflicts based on different group values [15]. According to the priority results by stakeholders shown in Table 5, the consistency value obtained was 0.043. The CR value was less than 0.1, so the results can be declared consistent. Therefore, the stakeholders' priorities according to priority weights are the provision of drinking water, followed by waste management, domestic wastewater management, and environmental drainage.

This information was used to create the decision hierarchy structure shown in Fig. 3. From the existing criteria, each indicator that supported stakeholders in preventing and improving the quality of slum areas was also identified.

Table 5 Priorities for increasing access to water and sanitation

No.	Criteria	Priority vector	Rank
1	Drinking water supply	0.30	1
2	Domestic wastewater	0.23	3
3	Solid waste	0.25	2
4	Environmental drainage	0.22	4

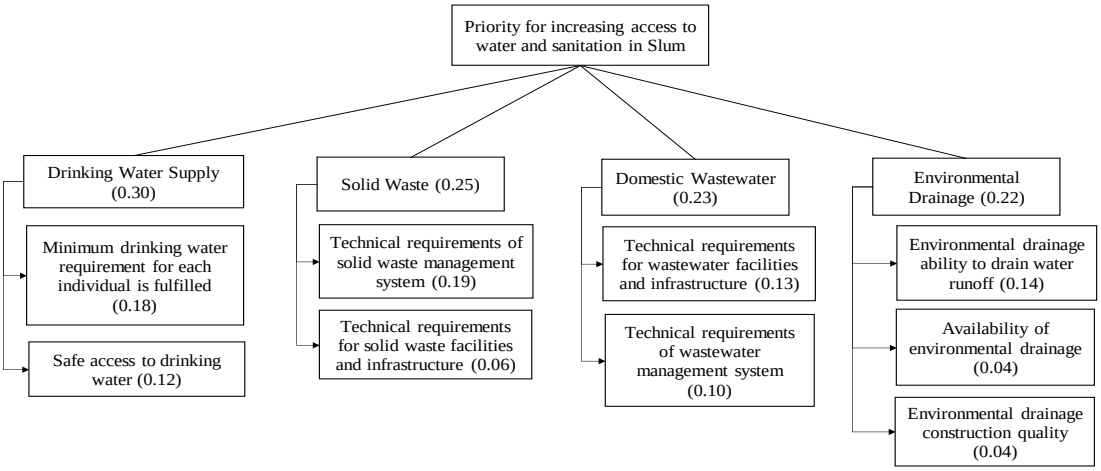

Fig. 3 Hierarchy priority for increasing access to water and sanitation for households in slum areas

Fig. 3 shows the priority of stakeholders was as much as 0.30 in increased drinking water supply in slum areas. In supporting the increase in water supply, stakeholders prioritize the minimum drinking water requirements for each individual being met, which then provides safe access to drinking water. The existing condition of slum households, it shows that there were still 83% of households whose minimum water needs had not been met. Meanwhile, the provision of secure access is still not fully fulfilled. Households are still very dependent on rain water and refill water to meet their drinking water needs. In fact, the management of rainwater is still not well managed by households.

In the second priority, 0.25 of stakeholders prioritized solid waste management. Indicators supporting the improvement of solid waste management are the technical requirements of the solid waste management system (domestic collection and sorting, environmental collection, environmental transportation, and environmental treatment) and technical requirements for solid waste facilities and infrastructure (household-scale waste segregation, TPS 3R, transportation facilities, transportation of environmental scale waste, and TPST). From the existing condition of slum households, 53-87% of solid waste was transported to landfills. Some households still managed their solid waste by throwing it into the river or burning it. Meanwhile, only 10.6% of waste sorting activities were conducted, with the selected waste being organic, plastic, or glass waste.

In the third priority, 0.23 of stakeholders prioritized domestic wastewater. The supporting indicators include the technical requirements for wastewater facilities and infrastructure (latrine/closet connected to a septic tank and the availability of a local or centralized sewage treatment system) and technical requirements for a wastewater management system (basic, proper and safe services). Based on the existing condition of slum households, households on the riverside were still at the basic level of sanitation, and households in the city center were at the level of shared sanitation. Meanwhile, households that did not have a septic tank would directly discharge their waste into water bodies or drainage channels.

For the last priority, as much as 0.22 of stakeholders prioritized environmental drainage. The supporting indicators include the ability of environmental drainage to drain water runoff, the availability of environmental drainage, and the quality of environmental drainage construction. Based on the existing conditions of slum households, the availability of environmental drainage already existed, but it was still unable to accept high water runoff in cases of changes in the climate. In addition, drainage channels were still mixed with domestic wastewater which caused environmental pollution. The majority of waterway managers and researchers also concentrated their attention on the contaminants that were already widely known to be present in urban waterways. These contaminants include nutrients, heavy metals, sediment, and various other types of physical and chemical contaminants. Freshwater ecosystems are also affected by a variety of other chemical properties of the water, such as the pH level, electrical conductivity, and ionic composition [16]. Therefore, it is difficult from a management point of view to identify urban pollutants and appropriately control them [17]. Within urban areas, it has come to everyone's attention that the imperviousness of catchment areas and the lack of drainage infrastructure are significant factors that influence the water quality, hydrology, and form of urban rivers [16].

However, despite the stakeholders' expression on the prioritization of clean water, there has not been an increase in access to clean water and sanitation in slum households, as the domestic wastewater management has a fairly severe condition, and the sanitation ladder is at the basic sanitation and shared sanitation levels. Finally, domestic wastewater has been indicated to contaminate the soil and/or the Kapuas River.

CONCLUSION

The priorities for increasing access to clean water and sanitation were determined based on stakeholder perceptions. These priorities include drinking water management (0.30), solid waste management (0.25), domestic wastewater management (0.23), and environmental drainage management (0.22). The existing conditions of water and sanitation in slum areas were still unsafe and unsustainable. Domestic wastewater management and drainage had the highest risk of affecting environmental quality. This indicates that the priority of stakeholders in slum areas has not been able to improve the quality of slum areas. Therefore, stakeholders need to conduct deeper studies on the priorities of clean water and sanitation supply and management in slum areas. One of them is by considering improvements in the management of the most at-risk priority to improve the quality of clean water and sanitation in these areas.

ACKNOWLEDGMENTS

The authors would like to extend their gratitude toward the Netherlands Organization for Scientific (NWO) and Indonesian Ministry of Education, Culture, Research, and Technology (KEMENDIKBUDRISTEK) for funding this research. This research was part of the Resilient Indonesia Slum Envisioned project (RISE). This research was also supported by the Global Sanitation Graduate School (GSGS) program.

REFERENCES

[1] E. B. Santoso and L. V. Therik, Faktor Penentu Bertempat Tinggal Pada Kawasan Kumuh Di Kota Malang Berdasarkan Teori Doxiadis, tataloka, vol. 18, no. 4, p. 261, Nov. 2016, doi: 10.14710/tataloka.18.4.261-273.

[2] M. V. Michiani and J. Asano, Physical upgrading plan for slum riverside settlement in traditional area: A case study in Kuin Utara, Banjarmasin, Indonesia, Frontiers of Architectural Research, vol. 8, no. 3, pp. 378–395, Sep. 2019, doi: 10.1016/j.foar.2019.03.005.

[3] A. Yamri, Studi Penanganan Terpadu Kawasan Permukiman Di Tepian Sungai Kapuas Kota Pontianak, p. 16, 2016.

[4] P. N. Bao, T. Aramaki, and K. Hanaki, Assessment of stakeholders' preferences towards sustainable sanitation scenarios: Assessment on sanitation scenarios, Water Environ J, vol. 27, no. 1, pp. 58–70, Mar. 2013, doi: 10.1111/j.1747-6593.2012.00327.x.

[5] R. Putra, Analisis Faktor Penentu Pengembangan Sistem Pengolahan Air Limbah Terpusat Kota Tangerang (Studi Kasus: Kecamatan Tangerang. Bandung: Institut Teknologi Bandung, 2016.

[6] Saaty, Pengambilan Keputusan. Jakarta: Pustaka Binaman Pressindo, 1968.

[7] W. M. Fatimah, P. W. Sarli, P. Soewondo, and N. M. Zakiyya, Strategic thinking to improve sanitation in Kampung Pelangi 200, Bandung City: in comparison with Kampung Jodipan-Ksatrian, Malang City, IOP Conf. Ser.: Earth Environ. Sci., vol. 592, no. 1, p. 012018, Nov. 2020, doi: 10.1088/1755-1315/592/1/012018.

[8] A. Nastiti et al., Water And Sanitation In Urban Slum: A Case From Bandung Municipality, West Java, Indonesia, p. 15, 2013.

[9] K. Khayan, A. Heru Husodo, I. Astuti, S. Sudarmadji, and T. Sugandawaty Djohan, Rainwater as a Source of Drinking Water: Health Impacts and Rainwater Treatment, Journal of Environmental and Public Health, vol. 2019, pp. 1–10, Jul. 2019, doi: 10.1155/2019/1760950.

[10] P.-M. Stathatou, P. Dedousis, G. Arampatzis, H. Grigoropoulou, and D. Assimacopoulos, Energy savings and reduced emissions in combined natural and engineered systems for wastewater treatment and reuse: the WWTP of Antiparos Island, Greece, DWT, vol. 159, pp. 13–23, 2019, doi: 10.5004/dwt.2019.23995.

[11] I. Suryawan and E. Sofiyah, Cultivation of Chlorella sp. and Algae Mix for NH3-N and PO4-P Domestic Wastewater Removal, Civense, vol. 003, no. 01, pp. 031–036, Apr. 2020, doi: 10.21776/ub.civense.2020.00301.4.

[12] R. Adawiah, Instilling the Environmental Care Characters to the Elementary Schools Located on the River Banks, jwem, vol. 6, no. 2, p. 84, Feb. 2019, doi: 10.20527/jwem.v6i2.177.

[13] H. P. Johannes, R. Maulana, and H. Herdiansyah, Prevention of Littering through Improved Visual Design, EREM, vol. 77, no. 4, pp. 86–98, Dec. 2021, doi: 10.5755/j01.erem.77.4.25043.

[14] A. Wahyuningtyas, S. Hariyani, and F. R. Sutikno, Strategi Penerapan Sumur Resapan Sebagai Teknologi Ekodrrainase Di Kota Malang (Studi Kasus: Sub Das Metro), vol. 3, p. 8, 2011.

[15] R. Lahdelma, P. Salminen, and J. Hokkanen, Using Multicriteria Methods in Environmental Planning and Management, Environmental Management, vol. 26, no. 6, pp. 595–605, Dec. 2000, doi: 10.1007/s002670010118.

[16] I. A. Wright, P. J. Davies, S. J. Findlay, and O. J. Jonasson, A new type of water pollution: concrete drainage infrastructure and geochemical contamination of urban waters, Mar. Freshwater Res., vol. 62, no. 12, p. 1355, 2011, doi: 10.1071/MF10296.

[17] V. Novotny and H. Olem, Water Quality. Prevention, Identification and Management of Diffuse Pollution. New York: Van Nostrand Reinhold, 1994.

8th Int. Conf. on Structure, Engineering & Environment (SEE), Mie, Japan, Nov.10-12, 2022, ISBN: 978-4-909106094 C3051

IDENTIFICATION OF POTENTIAL URBAN SLUM SETTLEMENTS TO IMPLEMENT WATER-SENSITIVE URBAN DESIGN

Nico Halomoan[1], Ahmad Soleh Setiyawan[1], Prayatni Soewondo[1],
Prasanti Widyasih Sarli[1], Dion Awfa[2]
[1,] Faculty of Civil and Environmental Engineering, Institut Teknologi Bandung, Indonesia;
[2]Department of Environmental Engineering, Institut Teknologi Sumatera, Indonesia

ABSTRACT

Slums are settlements that do not meet the quality standards of buildings, facilities, and infrastructures, and this is affected by the increasing population and the strategic value of the city. Water sensitivity can be interpreted as an effort to utilize the water cycle in sustainable water management. Manado city, Indonesia, has a strategic location but still has slums and flood-prone areas. This study aims to identify urban slum areas in Manado City, Indonesia, in the context of implementing water sensitive urban design (WSUD). The WSUD is an integration of structural planning through an engineering approach. It combines several objectives of water cycle management through engineering design approaches that are beneficial for water conservation, rainwater management, and improvement of rainwater runoff quality, including flood control and environmental sanitation. Interviews and questionnaires addressed to stakeholders and the community were carried out to identify urban slum area. Three urban villages were reviewed as case studies by comparing settlements based on their topological characteristics, namely hills, river banks, and coastal areas. The feasibility of implementing WSUD is carried out by looking at the features of the availability of sanitation infrastructure, water management, potential disasters, and socio-economic aspects. Based on the identification results, the environmental and water conditions of each site topology indicate the need to provide adequate facilities with the application of WSUD.

Keywords: Identification, Manado City, Slum Settlement, WSUD

INTRODUCTION

Slum settlements arise due to minimal and inadequate facilities and infrastructure that not meet standards in a developing municipality. The inadequate public services including water, sanitation, and hygiene conditions that cause environmental degradation and lack adequate water [1]. Physical and non-physical characteristics, which do not meet the requirements, become the basis for formulating criteria and indicators of slum symptoms. Physical aspects include housing and settlement units and building conditions. Non-physical aspects include community behavior, legal, and business certainty. This is the process of identifying the location of slum settlements. Poor planning with poor infrastructure and inadequate sanitation facilities for most households has been one of the reasons[2].

Water sensitivity is an effort to prevent and mitigate runoff that is not handled/utilized in water management, including water supply, sanitation, and flood protection, in realizing environmental protection services that ensure long-term sustainability, viability, and resilience. The water-sensitive concept developed on a city scale is a water-sensitive city applied in urban planning under Water Sensitive Urban Design (WSUD) [3]. WSUD is one of the urban settlement planning concepts with the use of a sustainable water cycle, one of which is rainwater being used as a water source with the development of appropriate technology and design. In the WSUD application, all aspects of the urban water cycle are considered a valuable resource. WSUD also takes an engineering approach through integration the urban water cycle, including rainwater, groundwater, and wastewater management, as a resource that can be stored on land, public spaces, or open spaces, for reuse or through filtration process [4].

This WSUD can be implemented as a stand-alone system or combined with centralized rainwater and waste distribution system[5]. The advantages of WSUD are that floods can be utilized and mitigated, protected forms of the environment, liveability can be improved and it requires community commitment and understanding [6].

The research location identified was the city of Manado, the capital of the province of North Sulawesi, Indonesia. The city is located downstream of the river and the coast which has 20 rivers, with five of them large rivers flowing into Manado Bay, where in 2014 there was a flash flood overflowing Lake Tondano. This city has a slum location due to urbanization and population growth. The basis for determining the location to be studied is the Decree

of the Mayor of Manado Number 163/KEP/LT.02/Bappeda/2015 concerning the Determination of the Location of Slum Settlement Areas in Manado City based on the determination of the location of slum areas in Manado City which includes 25 sites in 9 sub-districts.

The implementation of WSUD in slum areas is expected to result in the availability of alternative water sources, this includes aquifer filling schemes, captured surface and roof rainwater runoff, and recycling. Through a fundamental approach to proactive, sustainable rainwater management planning with environmental facilities management design, it is possible to maintain environmental health and improve community quality [3]. WSUD that has been implemented currently is limited to common residential areas. In contrast with the advantages of WSUD and its applications, such as the use of green roofs, and porous pavements, can actively operate in mitigating flood risk and increasing city resilience[6], it is necessary to use it to slum settlements to improve the quality of life, this has been done with visual improvement in slum settlements to improve the quality of life [7]. WSUD which is applied to slum areas is expected to support improving the quality of life and improving infrastructure. This study is expected to see the initial potential of slum settlements to implement WSUD applications.

METHODOLOGY

Slums Identification

Identification of slum settlement in location study considers several factors, including physical conditions, the potential for disasters, settlements, population density, clean water and sanitation facilities. The study desk data is deemed, this is based on the Decree of the Mayor of Manado Number 163/KEP/LT.02/Bappeda/2015 concerning the Determination of the Location of Slum Settlement Areas in Manado City, then several locations are selected, which will be verified by visiting the selected area. , then search for information through structured interviews with regional management stakeholders.

The method used to obtain information is a structured interview method through field visits, this is done in slum locations and coordination is carried out through meetings with community representatives, this is done because one solution to improving the quality of slum areas must be location-specific [8]. Interviews attempt to ask a representative group of respondents open-ended questions to obtain qualitative responses [9]. In this study, structured interviews were conducted with the head of the area, accompanied by a direct visit to the location. Structured interviews to determine the location of the study were conducted with information from secondary data which was also taken into account by regional regulations and desk studies. The main questions asked were about the physical condition of settlements, residents, disasters, and water and sanitation facilities in general in the area. The results will be displayed descriptively and followed up with interviews using a questionnaire at a later stage.

Identification of WSUD Implementation

Identification by questionnaire interview was conducted on 93 household samples from a population of 1345 households; the sample calculation used the Yamane formula with a margin of error of 10%. The interview material focused on questions related to the potential for implementing WSUD in slum areas by reviewing the design characteristics of the housing environment, the condition of water management in the environment and the socio-economic factors of the population. The structure of the questionnaire questions will ask about the design characteristics of the housing environment, socio-economic aspects, conditions for managing sanitation facilities, as well as management conditions and water availability.

RESULT AND DISCUSSION

Three locations of slums settlements are determined from several of locations contained in the regional regulations of Manado City, these locations are located with different physical characteristics or topologies, these locations are North Titiwungen Village, Sario District on the sea side; Singkil Satu Village, Singkil District which is a location with a hilly; Wawonasa Village, Singkil District with a riverbank. The basis for identifying the study sites can be seen in Table 1. The characteristics of the three locations have the potential water sensitivity in congested and slum areas with problems with sanitation infrastructure.

Table 1. General characteristics and conditions Study site

Criteria	Location of Study		
	North Titiwungen	**Singkil Satu**	**Wawonasa**
Location of Study	Lingkungan 02 dan half of lingkungan 03 Titiwungen Utara Village	Lingkungan 2 Singkil Satu Village	Lingkungan 02 and 03, Wawonasa Village
Settlement Conditions	Residential density with a density of 10,347 people/km^2	Densely populated settlements with a density of around 14,439 people/km^2	Densely populated settlements with an average number of 15,872 people/km^2
Topology	Location flat land close to the Sulawesi Sea and located in the coastal area of the sea.	Located on hilly land with a sharp downward contour.	Situated on flat land very close to the Tondano watershed
Potential Disaster	Frequent rob floods and no flood protection.	Potential landslide disaster	Potential for flood disaster
Drainage Infrastructure Condition	The drainage channels are mixed with greywater from households with some drains containing garbage.	With inadequate drainage channels, rainwater runoff is difficult to drain and mixes with greywater.	The flow in the drainage channel is disrupted by the presence o garbage and greywater mixed in the stream.
Wastewater Infrastructure Condition	Most of the houses already have family latrines with septic tanks and a few use a centralized system from the nearest mall.	Most of the houses have family latrines, there are no public toilets.	Most of the houses have family latrines with septic tanks and there are public toilets.
Water Infrastructure Condition	Most residents have been served by the water drinking water services company, but it has not been continuous, mainly using shallow and deep well water.	Most residents use water from pipe network services provided by residents, some use shallow and deep wells.	Most residents use water from wells and rivers, and drinking water company services are inadequate, but houses still do not have safe access.

Social and Economy Aspects

Social and economic aspects that support this identification analysis are income, employment, and house ownership. Economically, in the three areas reviewed, households have a low average economic capacity, with less than 33% of the population having an income above 3 million per month (Fig. 1) . At the same time, the most common occupations are traders/entrepreneurs in each area. This will also affect the availability and willingness to improve the quality of residential facilities owned.

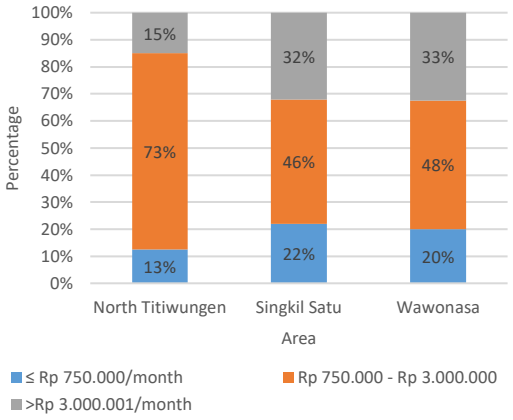

Fig. 1 Percentage of household economic income capacity

The condition of the house will also affect the readiness to implement the WSUD, some applications from the WSUD will modify the function of part of the house such as changing the function of the roof, yard or drainage channel, including harvesting rainwater. Most of the houses in the study area were permanent homes, but not all of them became homeowners. The majority of Singkil Satu (68%) and Wawonasa (50%) residents live in their own homes, while in the North Titiwungen area, more than 48% live with their families.

With the majority having permanent and private homes, there is potential to be able to implement WSUD in residents' homes (Fig. 2), because it is recognized that there is a need for ownership and involvement in implementing WSUD thereby increasing risk awareness and greatly influence the community's decision to provide access to clean water and proper sanitation.

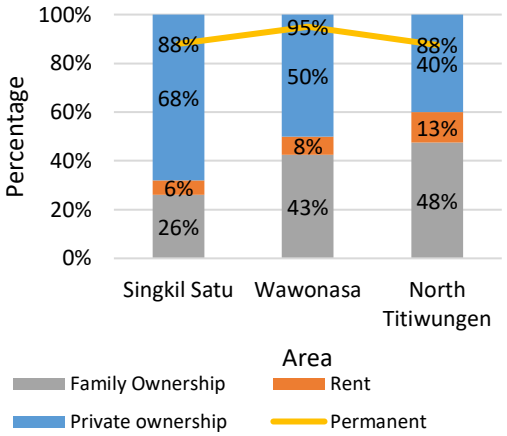

Fig. 2 Percentage of household ownership in the study area

Sanitation Infrastuctures

Some residents in the study area use inadequate domestic wastewater management, although 97% of residents stated that they have private latrines (Fig. 3), using septic tanks that are not waterproof which are grouped as cubluk (Fig. 4), this has the potential to cause ground water pollution. The potential for contamination can be reduced by carrying out further treatment of effluent from sanitation facilities. Several WSUD systems have been used to improve the quality of rainwater by removing contaminants by either infiltration or sedimentation methods[4]. The combination of waste treatment in sanitation facilities with WSUD facilities has the potential to improve the quality of the water produced.

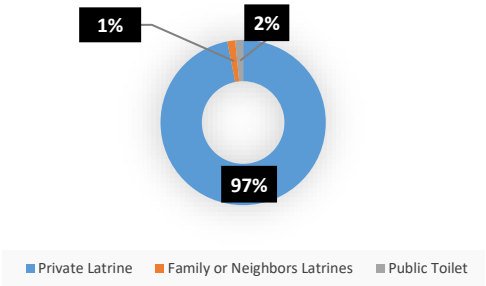

Fig. 3 Ownership of private latrines at the study area

Drainage channel is one of the infrastructure for WSUD implementation. However, the condition in the study area shows that most of the drainage channels are not functioning properly, because more greywater is channeled into the canal. Another problem is the inadequate width of the drainage channel; blockage or clogging by garbage, oil and grease from kitchen activities; Drainage channels that are higher than the road cause inundation and flooding during the rainy season.

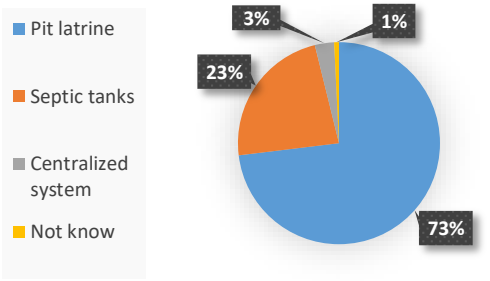

Fig. 4 Percentage of use of domestic wastewater system

Water Management

The water supply aspect is considered in this identification. the majority of residents in North Titiwugen use groundwater as a source of clean water, as well as most residents in Singkil Satu and Wawonasa, only a few residents use tap water, because it is not optimal in providing water (Fig. 2).On the other hand, as a source of drinking water, the community prefers refilled water compared to ground water or tap water. Based on these two conditions, it is indicated the need for continuous availability of water as a source of clean water; With the implementation of WSUD, the potential use of rainwater as a water source will support the availability of water from pipelines and groundwater.

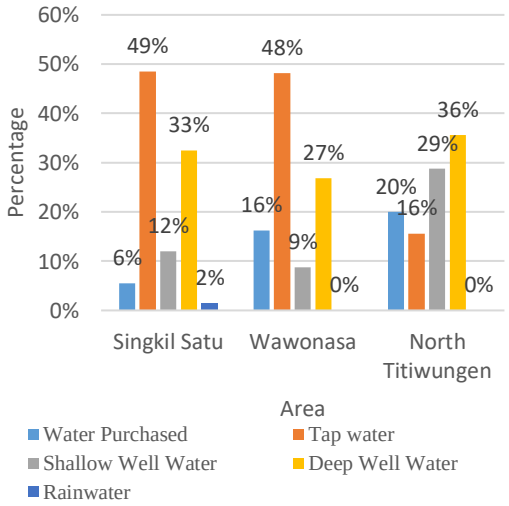

Fig. 5 Percentage of water sources used by residents

The aspect related to water management is the potential for disasters caused by water. Wawonasa area, which is very close to the Tondano watershed, the potential for flood events often occurs during the

rainy season; 60% of the community stated that flooding occurred several times a year (Fig. 6), this area is prone to flooding. North Titiwungen is an area that is very close to the Sulawesi Sea. Most of the flooding occurs when high tides occur, or the potential for being affected by tidal flooding. On the other hand, in Singkil Satu, water only passes when it rains, but no flooding occurs due to the area's contours. Regional topology also affects flood events, the impact of flood events can be reduced if they can seep into the ground, and the application of WSUD in several flood-affected and inundated areas has the potential to support the reduction of inundation due to flood events.

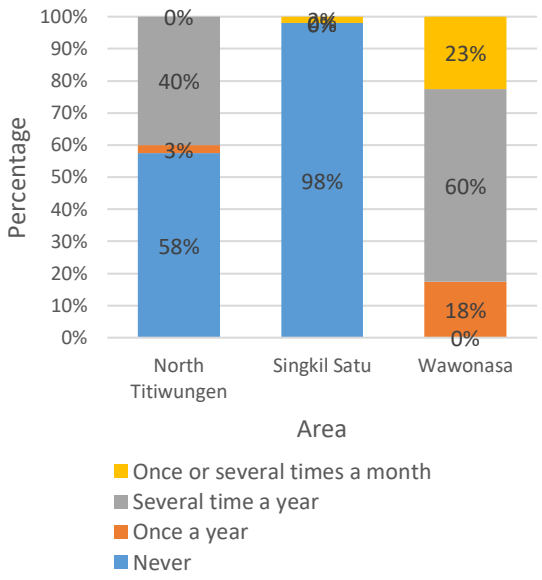

Fig. 6 Percentage of flood events at the study area

WSUD potential implementation

Based on the results presented, the potential for implementing WSUD in slum areas in Manado City, it is indicated that there are significant challenges but there are still opportunities to be able to implement WSUD. The first challenge is the high population density with adjacent houses; this makes it difficult to provide land for implementing WSUD; some design options require land for infiltrated water and growing vegetation. Another WSUD method is water infiltration, where the limited drainage canal can be used as eco drainage for rainwater absorption, but first prepared management for greywater and sediment barriers[10]. WSUD potential to be implemented is rainwater harvesting used as potable water, where the roof is used as a rainwater receiver and supports the supply of water as a backup for each household. Still, it is necessary to add a supporting unit so that the water produced can be used directly as a source of clean water.

Another challenge is that the characteristics of each regional topology result in a more specific application, so further research is needed at the location to find the most suitable WSUD design to be applied in each location.

CONCLUSIONS

The identification of the potential for implementing WSUD in slum areas has been studied in three slum areas in Manado City by conducting surveys and interviews related to socio-economic conditions, water management, sanitation infrastructure and flood potential. Socio-economic conditions are a challenge with the majority of residents earning below 3 million/month, but private home ownership will support the potential willingness to apply WSUD technology. The condition of drainage and sanitation infrastructure has not functioned properly, this needs to be supported by community understanding and water availability. People still rely on groundwater and do not use rainwater, drinking water relies on refilled gallon water, this technical condition has great potential in the WSUD application, especially increasing the availability of water for residents, but there needs to be research on the potential of rainwater and soil absorption. Seeing the challenges and opportunities that exist, further research is needed by involving technical studies and focusing on each location to find the appropriate WSUD technology to be applied.

ACKNOWLEDGMENTS

This research was part of the Resilient Indonesia Slum Envisioned (RISE) project 2021-2023. It was funded by the Netherlands Organization for Scientific (NWO) and the Ministry of Education, Culture, Research and Technology (KEMENDIKBUDRISTEK).

REFERENCES

[1] H. Taubenböck and N. J. Kraff, "The physical face of slums: a structural comparison of slums in Mumbai, India, based on remotely sensed data," *J Hous and the Built Environ*, vol. 29, no. 1, pp. 15–38, Mar. 2014, doi: 10.1007/s10901-013-9333-x.

[2] I. K. Tumwebaze, C. G. Orach, C. Niwagaba, C. Luthi, and H.-J. Mosler, "Sanitation facilities in Kampala slums, Uganda: users' satisfaction and determinant factors," vol. 23, no. 3, pp. 191–204, Aug. 2012, doi: 10.1080/09603123.2012.713095.

[3] T. H. F. Wong, B. C. Rogers, and R. R. Brown, "Transforming Cities through Water-Sensitive Principles and Practices," *One Earth*, vol. 3, no. 4, pp. 436–447, Oct. 2020, doi: 10.1016/j.oneear.2020.09.012.

[4] A. K. Sharma, S. Rashetnia, T. Gardner, and D. Begbie, "WSUD Design Guidelines and Data Needs," in *Approaches to Water Sensitive Urban Design*, Elsevier, 2019, pp. 75–86. doi: 10.1016/B978-0-12-812843-5.00004-6.

[5] A. Sharma *et al.*, "Water Sensitive Urban Design: An Investigation of Current Systems, Implementation Drivers, Community Perceptions and Potential to Supplement Urban Water Services," *Water*, vol. 8, no. 7, p. 272, Jun. 2016, doi: 10.3390/w8070272.

[6] A. Dada, C. Urich, F. Berteni, M. Pezzagno, P. Piro, and G. Grossi, "Water Sensitive Cities: An Integrated Approach to Enhance Urban Flood Resilience in Parma (Northern Italy)," *Climate*, vol. 9, no. 10, p. 152, Oct. 2021, doi: 10.3390/cli9100152.

[7] W. M. Fatimah, P. W. Sarli, P. Soewondo, and N. M. Zakiyya, "Strategic thinking to improve sanitation in Kampung Pelangi 200, Bandung City: in comparison with Kampung Jodipan-Ksatrian, Malang City," *IOP Conf. Ser.: Earth Environ. Sci.*, vol. 592, no. 1, p. 012018, Nov. 2020, doi: 10.1088/1755-1315/592/1/012018.

[8] P. Jones, "Formalizing the Informal: Understanding the Position of Informal Settlements and Slums in Sustainable Urbanization Policies and Strategies in Bandung, Indonesia," *Sustainability*, vol. 9, no. 8, p. 1436, Aug. 2017, doi: 10.3390/su9081436.

[9] A. Davis, A. Javernick-Will, and S. M. Cook, "A comparison of interviews, focus groups, and photovoice to identify sanitation priorities and increase success of community-based sanitation systems," *Environ. Sci.: Water Res. Technol.*, vol. 4, no. 10, pp. 1451–1463, 2018, doi: 10.1039/C8EW00391B.

[10] T. H. F. Wong and Engineers Australia, Eds., *Australian runoff quality: a guide to water sensitive urban design*. Crows Nest, N.S.W: Engineers Media, 2006.

8th Int. Conf. on Structure, Engineering & Environment (SEE), Mie, Japan, Nov.10-12, 2022, ISBN: 978-4-909106094 C3051

THE CHARACTERISTICS AND DISTRIBUTION OF DEEP GROUNDWATER IN DJIBOUTI

Yasuhiro Asakura[1], Sawahiko Shimada[1], Ko Hinokidani[1] and Yasuhiro Nakanishi[1]
[1]Tokyo University of Agriculture, Japan

ABSTRACT

Djibouti is one of the most arid areas in the world and rivers are not formed regularly in this region. So, groundwater has been used as the main water resource for humans and livestock. Therefore, necessary to understand the state of groundwater in terms of utilizing of sustainable water resources in this country. In this study, we measured ion contents (Li^+, Na^+, NH_4^+, K^+, Mg^{2+}, Ca^{2+}, F^-, Cl^-, NO_2^-, Br^-, SO_4^{2-}, NO_3^-, PO_4^{3-}, HCO_3^-) in groundwater using ion chromatography, and analyzed characteristics groundwater quality using by multivariate analysis based upon groundwater quality with stable isotope ratio of hydrogen and oxygen and tritium concentrations, with reference to their locations and examined the distribution analysis using GIS data of watershed maps. As a result of groundwater quality measurements, the most of groundwater samples in this study mixed with seawater or hot spring water and fossil seawater. And the concentration of NO3- in groundwater was over 50 mgL-1 at 4 sites. In addition, as a result of the hierarchical cluster analysis, groundwater in this study showed different chemical characteristics even in the same watershed. As results of this study, although some important data of groundwater quality in Djibouti has been obtained, it is considered necessary to study in groundwater dating and water stable isotope ratios more wide area in order to understand its complex groundwater distribution and water quality characteristics.

Keywords: Ion chromatography, Arid area, water resources, GIS, Stable isotope ratio

INTRODUCTION

Djibouti is located at the northeastern end of the African continent, called the "Horn of Africa", where the climate is extremely arid belonging to the Hot Desert or Semi-arid Climate of BWh in the Köppen classification. The climate of this region shows two seasons, a cold (winter) season from October to April and a warm season (summer) from May to September. Winters are relatively cool (20~30 °C) due to the northeast trade winds blowing from the Gulf of Aden, while in summer, the equatorial westerly winds blow over the mountains from Ethiopia and Somalia, which further enhances the hot and dry climate (35~45℃) due to the foehn phenomenon [1]. As a result, precipitation is extremely low (c.a. 150 mm^{yr-1}), in this region and occurs irregularly as a short time event. Hence, rivers are not formed regularly in this region, and groundwater has been used as the main water resource for humans and livestock.

In recent years, however, as the lifestyle of nomads has shifted from pastoralism to a combined agro-pastoralism [2][3], the demand for groundwater resources, mainly for irrigation, has increased, and groundwater pollution due to human impacts and starvation of groundwater resources due to over-pumping have become problems. Therefore, it is necessary to understand groundwater conditions from the perspective of sustainable use of limited water resources in this country with extremely low precipitation. Although some studies have been conducted to find out groundwater quality, age and flow system, the data is still scarce for understanding the spatial characteristics of groundwater in Djibouti [4] In press [5] [6]. Accumulating of the basic database on the quality and the location of the groundwater in Djibouti, which flows through complex geological structures is necessary.

In this study, we analyzed characteristics of groundwater quality using multivariate analysis and hierarchical cluster analysis based upon ion structure (Li^+, Na^+, NH_4^+, K^+, Mg^{2+}, Ca^{2+}, F^-, Cl^-, NO_2^-, Br^-, SO_4^{2-}, NO_3^-, PO_4^{3-}, HCO_3^-) with stable isotope ratio of hydrogen and oxygen (δ D and $\delta^{18}O$), and tritium contents with reference to their locations and examined the distribution analysis using GIS data of watershed maps.

MATERIALS & METHODS

Sites description

We selected 16 deep wells from 4 areas in Djibouti: Djibouti city area, Arta, Ali-Sabieh, and Dikihil. Djibouti city facing Tajoura Bay is the most urbanized area in Djibouti. More than 60% of the nation is concentrated in this area. Arta area has one of the largest wadis in the country called Ambli Wadi, and most of the 250 wells are drilled along the wadi. Ali-Sabieh area is close to Somalia and has over 300 wells drilled. Dikihil area is close to Ethiopia and has

Table 1 Details of study points for the groundwater samples.

No.	District	Latitude	Longitude
1	Dikhil	N11°12'23.8"	E42°25'54.6"
2		N11°05'10.6"	E42°24'25.9"
3		N11°16'09.1"	E42°13'45.5"
4		N11°06'04.68"	E42°10'49.43"
5		N11°00'13.32"	E42°12'27.35"
6	Alih-Sabieh	N11°12'42.6"	E42°45'19.0"
7		N11°09'40.2"	E42°57'49.6"
8	Arta	N11°26'23.6"	E42°48'12.6"
9		N11°29'16.4"	E42°50'19.0"
10		N11°31'22.1"	E42°54'45.0"
11		N11°31'22.1"	E42°54'45.0"
12		N11°26'15.79"	E42°47'1.11"
13		N11°26'14.86"	E42°46'57.16"
14		N11°25'24.24"	E42°45'37.59"
15	Djibouti	N11°33'9.95"	E42°57'47.24"
16		N11°32'42.35"	E42°43'00.72"

the second largest population in Djibouti. Most of the about 270 wells are concentrated in densely populated areas, and some wells are in suburban areas.

Collection of groundwater samples

We collected groundwater samples from 16 deep wells (100-200m depth) in Feb. 2020 (Table 1). All groundwater samples were filtered using a 0.22 μm syringe filter and put into a 100 mL plastic bottle. All the bottle samples were refrigerated until analysis in Japan.

Ion structures of groundwater quality

Ion concentrations of groundwater were measured by ion chromatography (Shimadzu; HIC-SP) for 6 cations (Li^+, Na^+, NH_4^+, K^+, Mg^{2+}, Ca^{2+}) and 7 anions (F^-, Cl^-, NO_2^-, Br^-, SO_4^{2-}, NO_3^-, PO_4^{3-}, HCO_3^-). HCO_3^- concentrations were measured at pH 4.8 and by the alkalinity titration method. Water temperature (WT), pH, electric conductivity (EC), oxidation-reduction potential (ORP), and dissolved oxygen (DO) in groundwater samples were measured at study sites using portable instruments.

The characteristics of ion structure in the groundwater samples were classified by piper [7] and hexa-diagrams using equivalent concentrations of ion components measured by ion chromatography.

Chemical characteristics of groundwater

The chemical characteristics of groundwater were classified by hierarchical cluster analysis (Ward's method). These analyses were based upon equivalent concentrations of 14 major ion components (Li^+, Na^+, NH_4^+, K^+, Mg^{2+}, Ca^{2+}, F^-, Cl^-, NO_2^-, Br^-, SO_4^{2-}, NO_3^-, PO_4^{3-}, HCO_3^-), EC, hydrogen and oxygen stable isotope ratio (δ D and δ ^{18}O) and tritium concentrations [8]. Principal component analysis (PCA) using the values of EC, DO, ORP, pH, water temperature (WT), Na, Ca_2, Cl, Mg_2, SO_4^2

Watershed map with study points

Watershed map of Djibouti was sourced from database of Ministry of Agriculture, Water, Fishery and Livestock in Charge of Marine Resources of Djibouti. All study points were plotted on this map using Arc GIS and indicated by classification using hierarchical cluster analysis.

RESULTS

Ion structures of groundwater

The characteristics of the groundwater quality composition were classified by piper and hexa-diagrams based upon the value of ionic constituents

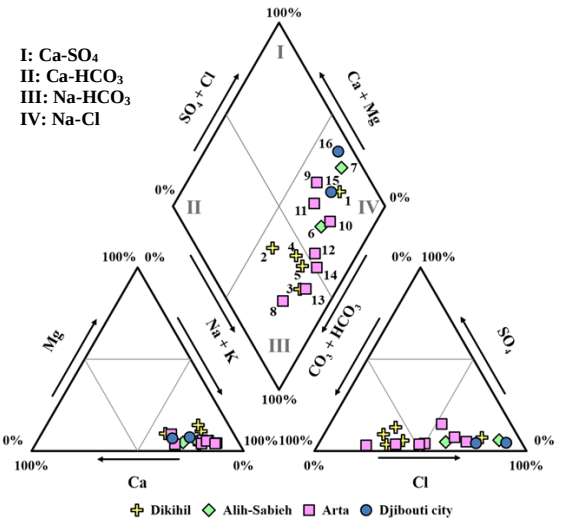

Fig. 1 A piper diagram of groundwater samples in Djibouti.

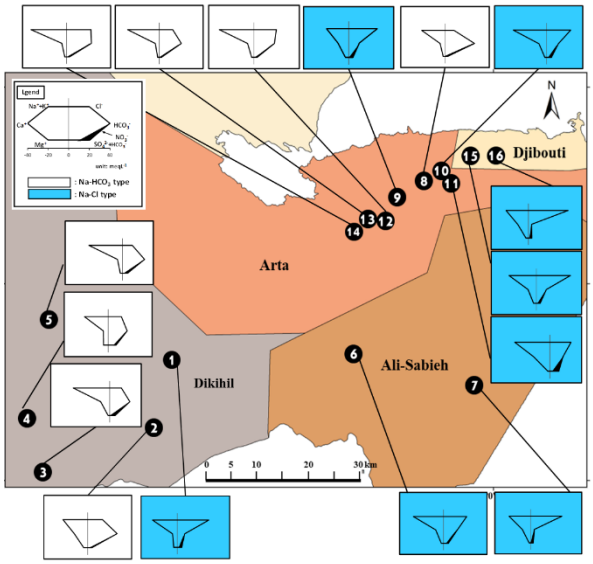

Fig. 2 Hexa-diagram of groundwater samples on study sites map in Djibouti.

in the groundwater. According to the piper diagram (Fig.1), the groundwater in this study was classified into two main types. All groundwater of Djibouti City and Ali-Sabieh area were classified as Na-Cl type, while most of groundwater of Dikihil and 3 points of Arta were classified as Na-HCO_3 type. However, Point 1 in Dikihil and Point 9, 10, 12 and 11 in Arta were classified as Na-Cl type. According to the hexa-diagram (Fig. 2), the groundwater in this study was classified into two main types of water quality composition. In Djibouti area, located on the coast, and in Ali-Sabieh area, Na-Cl type was predominant. On the other hand, in Dikihil area, located furthest from the sea, and in Arta area, Na-HCO_3 type was predominant.

The equivalent concentration ratio of Cl^- to Na^+ in groundwater was richer than in seawater (Cl^- : Na^+ = 1 : 0.85) at most of the study sites (Fig. 3).

The equivalent concentration ratio of Cl^- to Br^+ in all groundwater samples was plotted on seawater between halite (Fig. 4).

Table 2 shows the values of EC, DO, ORP, pH, and water temperature of groundwater collected at study sites. The values of EC showed high at all sites (0.84 to 6.90 $mScm^{-1}$), there was no significant correlation with elevation or distance from the ocean. Water temperature was over 30°C at all sites, with a maximum of 52°C. There was a significant negative correlation between water temperature and elevation.

pH was around 7.5, maximum was 8.5 with no significant correlation with water temperature. DO ranged from 2.61 to 6.90 mgL^{-1}.

The concentration of NO_3^- in groundwater was over 50 mgL^{-1} at 4 sites (Table 2). The concentrations of HCO_3^- in groundwater were high at all study sites.

Chemical characteristics of groundwater

Hierarchical cluster analysis using values of 14 major dissolved ions and EC and DO, all groundwater collected at study sites were classified into three clusters at a height of 20. At Cluster 3, only Point 7 was classified (Fig. 5). As a result of PCA, the factorial axis 2 represented 53.6 % of the variance

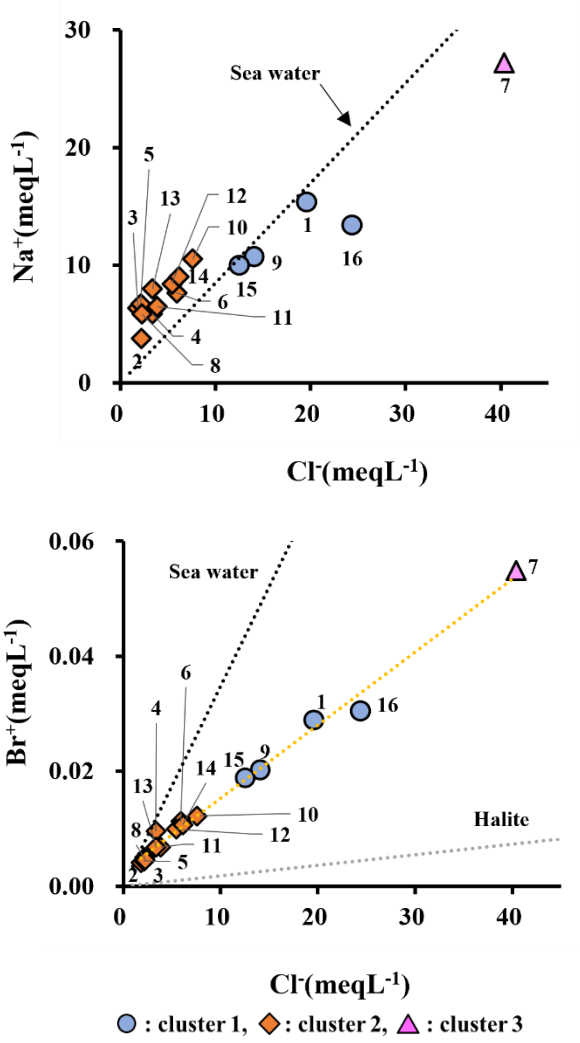

Fig. 3 and 4 Relationship between concentrations of Cl^- and Na^+ in groundwater samples. Relationship between concentrations of Cl^- and Br^+ in groundwater samples.

and groundwater classified in Cluster 2 was characterized by positive factor in pH, DO and HCO_3. The factorial axis 1 represented 20.5 % of the variance and groundwater classified in Cluster 1 and 3 were characterized by positive factor in EC, Na, Ca_2,

of groundwater samples.

Table2 NO_3^-, DO, EC, ORP, water temperature, pH

No.	DO	EC	WT	pH	NO_3^-
	mgL^{-1}	$mScm^{-1}$	℃		mgL^{-1}
1	6.08	2.78	31	7.87	50.9
2	5.68	0.84	37	7.98	24.4
3	6.40	0.91	32	8.28	20.1
4	5.47	1.20	36	8.12	94.2
5	6.43	1.00	32	8.52	10.0
6	6.90	1.26	32	8.35	47.2
7	5.90	4.42	32	7.34	39.1
8	6.50	0.91	38	7.84	14.5
9	6.85	2.15	34	7.39	63.3
10	6.16	1.48	30	7.99	37.3
11	2.61	1.16	31	7.86	34.5
12	5.32	1.28	39	7.64	22.4
13	6.07	1.08	37	8.14	16.1
14	6.08	1.29	36	8.30	16.3
15	3.71	1.93	52	7.45	38.3
16	5.87	2.83	48	7.77	61.1

Cl, Mg_2, SO_4^2 and negative factor in ORP, water temperature (Fig. 6).

Watershed map with study points

Fig. 7 showed study points on watershed map of Djibouti. In the Dikihil area, study points were distributed in 3 watersheds. Points 3 and 4 were in the same watershed and were also classified in the same cluster, Points 2 and 5 were also in the same watershed and in the same cluster. Point 1 was classified in a different cluster from other four points, and its watershed was also different from the other four sites. Although all study points in Arta and Djibouti area were distributed in same watershed, these points classified two clusters. In Ali-Sabieh area, study points were distributed two watersheds.

DISCUSSION

Ion structures of groundwater quality

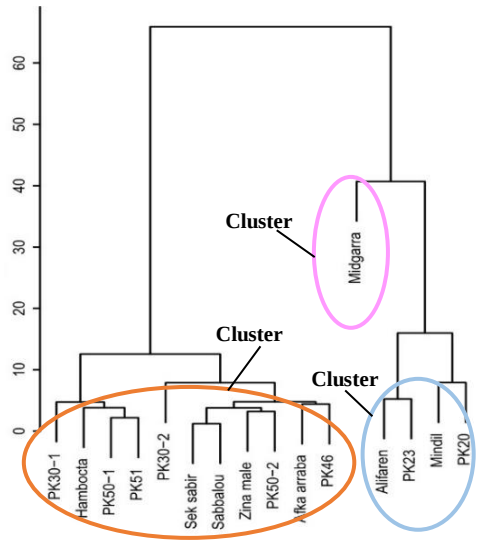

Fig. 5 Hierarchical cluster analysis of groundwater samples in Djibouti.

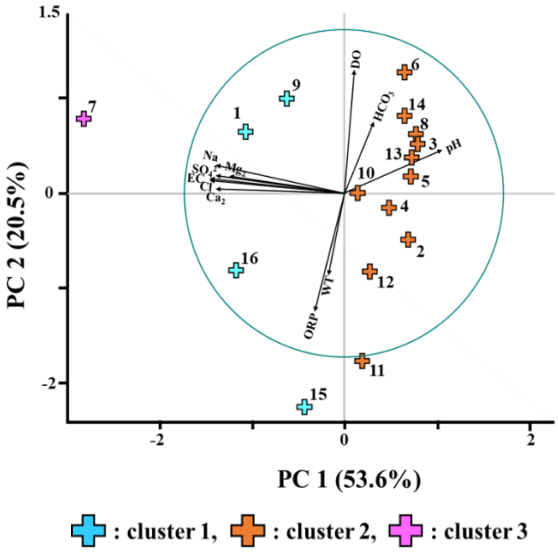

Fig. 6 Principal component analysis (PCA) using the values of EC, DO, ORP Water temperature (WT), pH, Na, Ca_2, Cl, Mg_2, SO_4^2.

Various factors such as mixing with seawater, weathering of bedrocks, and leaching of inorganic constituents from minerals may be influenced the differences in values of EC in groundwater (0.84 to 6.90 $mScm^{-1}$).

In general, it has been reported that groundwater quality classified as Na-Cl type is likely affected by mixing with fossil seawater confined in the underground [9]. Therefore, the mixing of fossil seawater and groundwater was considered at the

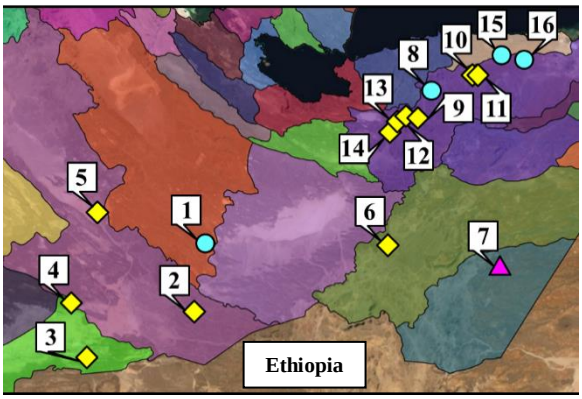

○ : cluster 1, ◇ : cluster 2, △ : cluster 3

Fig. 7 Study site with watershed map of Djibouti. The area divided by color gradients shows watershed (source: Ministry of Agriculture, Water, Fishery and Livestock in Charge of Marine Resources).

study sites classified as Na-Cl type groundwater. In this study, piper diagram classified groundwater quality into four types to estimate the origin of ions in groundwater. Ca-SO_4 type (I): This type is the commonly found in shallow groundwater in Japan. Ca-HCO_3 (II): This type is commonly found in deep groundwater with very old age. Na-HCO_3 (III): This type contains hydrothermal water and fossil seawater. Na-Cl type (IV): This type is commonly found in seawater and hot spring water. Therefore, in this study, groundwater classified as Na-HCO_3 type may be mixed with fossil seawater or geothermal water, and groundwater classified as Na-Cl type may be mixed with seawater or hot spring water [10]. The relationship between the equivalent concentration ratios of Na^+ and Cl^- suggests possibility that groundwater at most of study sites may be affected by sodium leaching from volcanic rocks and by mixing seawater and fossil seawater [11].

Origin of NO_3^- in groundwater

As a result of ion chromatography, the concentration of NO_3^- in groundwater was over 50 mgL^{-1} at 4 sites. Generally, NO_3^- in groundwater may be derived from fertilizers, livestock manure, domestic wastewater, and soil organic matter. In particular, it has been reported that high concentrations of NO_3^- in groundwater in arid areas are likely to originate from natural soil sources [12]. But most of the wells in study sites are also used by local nomads as drinking water for their livestock too, it is possible that NO_3^- in the groundwater was also originated from livestock manure.

Chemical characteristics of groundwater

The results of the hierarchical cluster analysis indicated that Point 7 in the Ali-Sabieh area has different characteristics compared to the other study points. The results of the principal component analysis also indicated the characteristics were positive factors in EC, Na, Ca_2, Cl, Mg_2, and SO_4^2. This suggest that inorganic constituents into the groundwater primarily cause to weathering of the basalts and seawater intrusion [13]. Groundwater at Points 1, 9, 15, and 16 were classified in the same Cluster 1 in the hierarchical cluster analysis, and the principal component analysis results also characterized groundwater at these Points by similar factors. But there was difference between groundwater at Points 1, 9 and Points 15, 16 based on water temperature and ORP. The water temperature of groundwater at Points 15 and 16 was approximately 50°C, and they were plotted as Type IV in piper diagram, suggesting that these groundwaters was influenced by the mixing of hot spring water and seawater [14]. Groundwater classified as Cluster 2 was characterized primarily by positive factors in pH and HCO_3. The high concentrations of HCO_3^- detected in groundwater are reported to be supplied from soil [15]. Therefore, high concentrations of HCO_3^- means groundwater age is old. So, groundwater at these study points were likely to have been in residence for a long time. However, point 11 was plotted in a different direction than the groundwater in the same cluster 2. This was mainly due to positive water temperature and ORP factors, with a negative direction for the HCO_3^- factor. This result suggests that the groundwater at this site is relatively young in age and may have been mixed with hot spring water [14].

Relationships between cluster of groundwater and watersheds

Distribution of watersheds of Djibouti are characterized by the Great Rift Valley that crosses the country. At Arta and Djibouti City area included more than half of the study points, they were plotted within the same watershed. Cluster analysis also showed that 6 of the 9 sites were classified in the same cluster, suggesting that groundwater quality in eastern Djibouti is characterized by inorganic component runoff due to weathering of basaltic rocks. However, the characteristics of groundwater quality was not unitary even in the same watershed, since there are groundwaters influenced by hot springs or geothermal waters, such as at Points 11 and 12. On the other hand, groundwater plotted in different watershed in Dikihil area was in the same cluster, suggesting that groundwater characterized by the

same sediments or basalt were widely distributed.

CONCLUSIONS

As results of this study, although some important data of groundwater quality in Djibouti has been obtained, it is considered necessary to study in groundwater dating and water stable isotope ratios more wide area to understand its complex groundwater distribution and water quality characteristics. In addition, it is considered important to conduct long-term monitoring studies at a large number of study sites in order to consider anthropogenic influences on groundwater. In Djibouti, groundwater is the only freshwater resources of domestic water for local nomads. Although there have been no reports of groundwater being affected by nitrogen contamination due to human activities, it was considered important to estimate the origin of NO_3^- in groundwater using nitrogen stable isotope ratio in this study and to understand groundwater contamination in detail to propose appropriate management for sustainable and stable groundwater resources in Djibouti.

ACKNOWLEDGMENTS

This study was supported by Japan Science and Technology Agency (JST) and Japan International Cooperation Agency (JICA) under the project of Science and Technology Research Partnership for Sustainable Development (SATREPS GRANT NUMBER: JPMJSA1802).

REFERENCES

[1] Assowe, O.D., Awaleh, M.O., Kirk-Davidoff, D., Olauson, J., Söder, L., Awaleh, S.I., Wind resource assessment and economic analysis for electricity generation in three locations of the Republic of Djibouti. Energy Vol 185, 2019, pp.884–894.

[2] JICA, The Master Plan Study Project for Sustainable Irrigation and Farming in South- ern Djibouti. The Republic of Djibouti. Final Report, 2014, pp.52–172.

[3] Awaleh M.O., Boscheti T, Adaneh A.E., Chrdon M.A., Ahmed M.M., Dabar O., Soubaneh Y.D., Egueh E.M., Kawalieh A.D., Kadieh I.H., Chaheire M., Origin of nitrate and sulfate sources in volcano-sedimentary aquifers of the East Africa Rift System: An example of the Ali-Sabieh groundwater (Republic of Djibouti). Science of the Total Environment, Vol. 804, Issue 15, 2022, pp.1-13.

[4] Aboubaker M., Jalludin M., Razack M., Hydrochemistry of a complex volcano-sedimentary aquifer using major ions and environmental isotopes data: Dalha basalts aquifer, southwest of Republic of Djibouti. Environmental Earth Science, 2013, Vol. 70, pp.3335-3349

[5] Awaleh M., Paul B., Youssouf D. S., Tiziano B., Farhan B. H., Nima M. E., jalludin M., Omar A. D., Janie M. D., Jean C., Recharge, groundwater flow pattern and contamination processes in an arid volcanic area: Insights from isotopic and geochemical tracers (Bara aquifer system, Republic of Djibouti). Journal of Geochemical Exploration, 2017, Vol. 175, pp.82-98.

[6] Ahmed A.H., Rayaleh W.E., Zghib A., Ouddane B., Assessment of chemical quality of groundwater in coastal volcano- sedimentary aquifer of Djibouti, Horn of Africa. Journal of African Earth Science, 2017, Vol. 131, pp.284-300.

[7] Piper A.M., A graphic procedure in the geochemical interpretation of water-analyses. EOS, American Geophysical Union Transaction, 1944, Vol. 25, Issue 6, pp.914–923.

[8] Asakura Y., Nakanishi Y., Ofleh B.H., Values of δ D and δ ^{18}O and concentrations of ^{3}H and ^{14}C of deep groundwater in Djibouti. Journal of Arid Land Studies, Unpublished Work but Accepted.

[9] Frape S.K., Fritz P., McNutt R.H., Water-rock interaction and chemistry of groundwaters from the Canadian Shield. Geochemica et Comochimica Acta, Vol. 48, Issue 8, pp.1617-1627.

[10] Editorial Board of Handbook of Groundwater, For Chapter 9 in Handbook of Groundwater, 1980, Research Institute of Construction and Industry, Tokyo, pp. 358-367.

[11] Join J.L., Coudray J., Longworth K., Using principal components analysis and Na/Cl ratios to trace groundwater circulation in a volcanic island: the example of Reunion. Journal of Hydrology, 1997, Vol. 190, Issue1-2, pp.1–18.

[12] Kendall, C., Elliott. E.M., Wankel. S.D., For Chapter 12 in Stable Isotopes in Ecology and Environmental Science, second ed., 2007, Blackwell Publishing, New York, pp. 375-449.

[13] Freeze R.A., Cherry J.A., For Chapter 3 in Groundwater, 1979, Prentice-Hall Inc., Englewood Cliffs, Vol. 7632, pp.80-139.

[14] Awaleh M.O., Hoch F.B., Boschetti T., Soubaneh Y.D., Egueh N.M., Elmi S.A., jalludin M., Khaireh M.A., The geothermal resources of the Republic of Djibouti - II: geo- chemical study of the Lake Abhe geothermal field. Journal of Geochemical Explorer. Vol. 159, pp.129-147.

[15] Nordstrom D.K., Ball J.B., Donahoe R.J., Whittemore D., Groundwater chemistry and water-rock interactions at Stripa. Geochemica et Cosmochimica Acta, 1989, Vol.53, pp. 1727-1740.

8th Int. Conf. on Structure, Engineering & Environment (SEE), Mie, Japan, Nov.10-12, 2022, ISBN: 978-4-909106094 C3051

HYDROCHEMICAL CHARACTERISTIC OF THE EASTERN SLOPES OF MOUNT KARANG, WEST JAVA, INDONESIA

Hadi Hidayat[1], Deden Zaenudin[1], Boy Yoseph CSS Syah Alam[1]
[1]Faculty of Geology, Padjadjaran University, Bandung, West Java, Indonesia

ABSTRACT

Population and industrial growth in Java are the most significant compared to other regions in Indonesia, which triggers high groundwater use. The Eastern slopes of Mount Karang (a volcano in West Java, Indonesia) has the potential to be a significant groundwater source. Analyzing the characteristics of groundwater is significant for the rational management of groundwater resources. Samples were collected from springs, dug wells and drill wells. We use information about aquifer systems, hydrogeological conditions and hydro-chemical data to investigate groundwater sources and groundwater quality resulting from water-rock interactions. Chemical data showed that samples belonged to the Ca-Mg-HCO_3 type, Mg-HCO_3 type, Na+K-HCO^3 type and Na+K-Cl type. Ca^{2+} indicates that this water may have flowed through a rock formation composed of andesitic rocks with Ca-plagioclase minerals. The presence of Mg^{2+} shows that the water has flowed from shallow to the deeper aquifer. HCO_3^- originates from either infiltration of rain water that has been equilibrated with CO_2 in the atmosphere, or from CO_2 that has been generated by respiration of organic material. The different types of groundwater detected (Na+K-Cl type) indicate that groundwater on this slope has flowed in rocks of different geological products. Groundwater chemical characteristic is mainly controlled by changes in volcanic deposits.

Keywords: Groundwater, hydro-chemical, water-rock interactions, Mount Karang

INTRODUCTION

Population and industrial growth in Java are the most significant compared to other regions in Indonesia, Thus, urbanization is one of the major triggers' high groundwater use, Jakarta was the example of a decrease in groundwater reserves [1], as well as several buffer areas of the capital city that were affected, such as the Banten area. So that research on groundwater must be done a lot to meet the needs of many people. The Eastern slopes of Mount Karang (a volcano in West Java, Indonesia) has the potential to be a significant groundwater source [2].

The aims of this study were to identify groundwater sources, groundwater quality as a result of the interaction between water and rocks, as well as the influence of geological conditions (changes in volcanic lithofacies), hydrogeological conditions on hydrochemistry and groundwater flow. Analyzing the characteristics of groundwater is significant for the rational management of groundwater resources.

This research was carried out on the eastern slope of Mount Karang, Pandeglang, Banten, Indonesia (Fig. 1), which is geographically located at 106°3`28" E 6°13`18" S and 106°8`39" E 6°17`51" S.

GEOLOGICAL SETTING

The research area is located on the morphology of the slopes of the mountain at the foot of the mountain and solitary hills at the foot of the mountain, with a slope from sloping to steep. The difference in slope is caused by the diversity of landforms which are influenced by different types of lithology.

Based on the results of geological mapping of the eastern slope of the Karang Mountain, it is divided into 11 (eleven) volcanic lithofacies which are interpreted as the result of 5 (five) eruptions of Karang Mountain (Fig.1), the results of the 1st eruption depositing the old rough lapilli rock facies (Fbl) autoclastic facies with lava (ALKa). Well sorted lapilli tuff facies (PDct) and the grain supported pyroclastic-breccia breccia facies (ALHb), then the 2nd eruption produces pyroclastic breccia-tuff grain supported facies (ALHbr), the result of the 3rd eruption is andesite lava facies (ALK), coarse tuff facies – matrix supported graded bedding facies (JPbt) tuff breccia, poorly sorted matrix supported tuff breccia facies (APbt), 4th eruption of Karang Mountain produced andesite sheeting joint (ALsj) lava facies, medium tuff facies – breccia tuff matrix supported graded bedding (Jpt). As well as the 5th eruption of Mount Karang which produces auto-clastic with lava facies (ALKal).

The geological structures that developed in the study area are the Cilenggor sinistral horizontal fault, the Cikirup normal fault, the Cikarang normal - dextral fault and the Cilalaki normal - sinistral fault (Fig.1).

AQUIFER SYSTEM

Three different aquifer systems in the study area based on the survey, including the aquifer system in autoclastic lithology, lava and andesite lava (fractured system), aquifer system in pyroclastic breccia lithology and tuff grain supported (combined between contact and porus) aquifer system in tuff and lapilli lithology (porus).

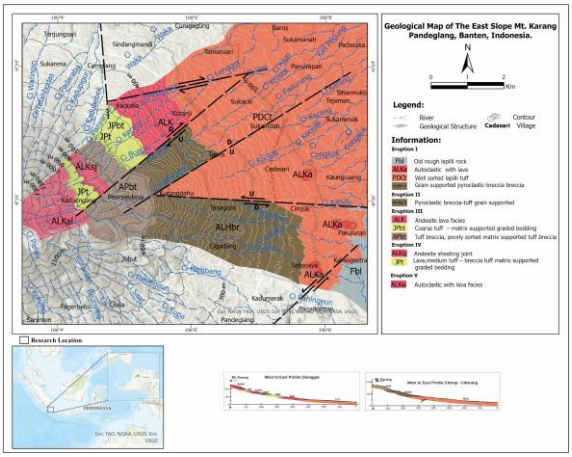

Figure 1. Geological Map of Study Area

METHODOLOGY

Sampling Location

This study reports analytical data for 20 groundwater sources located at elevations ranging from 167 to 928 m a.s.l. and springs, and wells (Figure 2). Springs are generally found on the contact between volcanic lithofacies and at varying morphology of the valley. Two dug wells are located at elevations of 297 m and 239 m asl with their depth of water level as 3.9 m and 0 m respectively.

Sampling methods

Field survey was carried out from January-March 2020.

Water sampling was performed using 500-mL polyethylene bottles. Prior to sampling, the bottles, ladle, filtration units and messzy inder were rinsed three times with the filtered water. The water samples were filtered in situ using 0.45 µm Syringe filter. As much as 500 mL of sample was collected for cation and anion analyses. The bottles containing the water samples for thesealed.

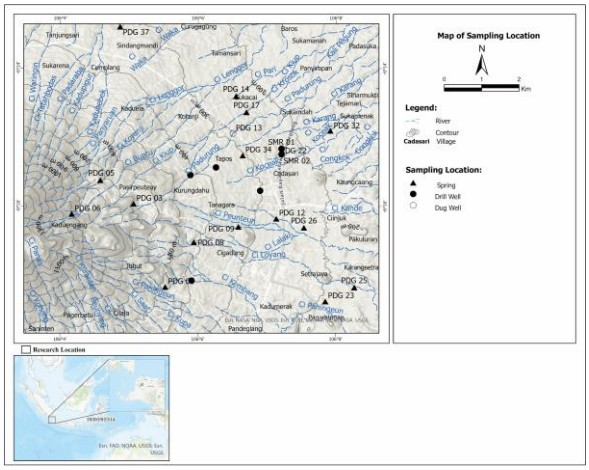

Figure 2. Map of Sampling Location

Analysis methods

pH, electrical conductivity (EC), total dissolved solid (Tds) and temperature using HANNA Instruments HI9811-5 were measured on site. The cations (Li^+, Na^+, K^+, $NH_4^+Ca^{2+}$and Mg^{2+}) and anions (Cl^-, NO_3^-, SO_4^{2-}) were determined by ion chromatography (IC- metrohm type 930 Compact), in laboratory. HCO_3^- was analyzed using the titration method with a 0.1N HCl, methyl red and bromocresol green were used as tritants.

A 5% difference in the electrical balance between cations and anions is required and was obtained for all samples.

RESULT AND DISCUSSION

Physical Properties

Groundwater parameter such as Electric Conductivity (EC), Total dissolved solid (Tds), pH, Temperature, together with analytical data for the major ions are presented in Table 1. The measured Electrical Conductivity (EC) values for springs, river and wells were 50 -460 µS/cm which shows that the groundwater in the study area is freshwater. Total dissolved solid (Tds) were 20 – 220 mg/L, pH range of springs and wells from slightly acidic to neutral (5.5 -7.8) and then the temperature from 23-31 ^{o}C.

Major Ions

Chemical contents especially major ions showed Ca^+ 3.16- 41.17 ppm, Na^+ from 3.47 to 30.37, K^+ from 2.76 to 13.52, Mg^{2+} from 0.84 to 19.37 ppm, Cl^- from 1.23 to 38,32 ppm, HCO_3^- from 13.85 to 249.74 ppm and SO_4^{2-} from 1.12 to 18.71 ppm.

Table 1. Physical properties and chemical analysis of water saples

Sample ID	Type	EC	TDS	T	pH	Li^+	Na^+	NH_4^+	K^+	Ca^{2+}	Mg^{2+}	F^-	Cl^-	NO_2^-	Br^-	NO_3^-	SO_4^{2-}	HCO_3^-
		µS/cm	mg/L	◦ C		ppm												
PDG 01	Spring	80	20	23	7,6	0,02	6,17	0,03	2,85	3,16	0,88	0,23	1,67	0,00	0,00	3,10	3,14	30,10
PDG 03	Spring	60	20	23	6,5	0,03	6,11	0,09	2,76	3,98	0,84	0,14	1,59	0,00	0,00	3,95	2,97	15,00
PDG 05	Spring	290	140	24,9	6,9	0,00	12,61	0,06	4,04	26,21	9,29	0,13	17,88	0,00	0,00	54,63	3,81	57,19
PDG 06	Spring	50	20	23,6	7,2	0,00	3,47	0,03	2,87	4,91	1,26	0,12	1,23	0,60	0,00	2,49	1,79	13,85
PDG 08	Spring	150	70	25	6,8	0,00	9,90	0,18	3,31	9,86	6,53	0,15	1,73	0,00	0,00	1,50	1,34	77,69
PDG 09	Spring	130	60	24,8	7	0,02	8,73	0,06	4,62	9,97	5,24	0,17	2,46	0,63	0,00	2,58	2,79	67,71
PDG 12	Spring	140	60	25,9	6,4	0,00	9,07	0,04	4,89	11,30	5,01	0,16	2,61	0,00	0,00	4,26	2,72	93,05
PDG 13	Dug Well	460	220	25,9	6,3	0,00	13,29	0,10	13,52	41,17	19,37	0,14	5,68	0,65	0,00	17,54	18,71	249,74
PDG 14	Spring	230	110	23,3	6,5	0,02	11,21	0,06	5,03	20,51	12,55	0,20	2,16	0,00	0,00	3,09	1,45	170,05
PDG 17	Spring	180	80	27,4	7,4	0,00	8,44	0,07	8,15	18,08	4,20	0,16	5,76	0,00	0,00	2,04	6,56	57,15
PDG 22	Dug Well	160	70	26,6	6,5	0,00	9,73	0,06	4,88	14,26	6,67	0,16	2,04	0,00	0,00	3,09	1,92	89,01
PDG 23	spring	190	80	25,2	6,5	0,00	11,45	0,06	4,94	16,83	10,72	0,18	4,23	0,00	0,00	6,27	2,63	81,76
PDG 25	spring	320	150	26,5	5,5	0,00	30,37	0,14	7,86	15,39	5,52	0,13	38,32	0,60	0,53	12,87	15,38	57,38
PDG 26	spring	150	70	26,3	6,6	0,00	9,75	0,04	4,73	11,58	6,17	0,17	1,75	0,00	0,00	2,20	2,16	65,65
PDG 31	spring	140	80	30,4	6,7	0,00	13,66	0,00	4,49	24,52	9,02	159,22	0,00	0,00	0,00	0,00	6,29	154,15
PDG 32	spring	210	90	31	6,4	0,00	15,46	0,14	5,52	27,69	12,15	0,17	4,62	1,34	3,71	1,34	3,71	187,12
PDG 34	spring	130	50	25,4	6,1	0,00	10,16	0,11	4,30	15,95	5,20	0,13	1,42	0,85	1,25	0,85	1,25	96,61
PDG 37	spring	140	60	25,5	6,2	0,00	10,08	0,07	4,57	12,72	5,07	0,14	1,34	1,84	1,12	1,84	1,12	92,03
SMR 01	Drill Well	120	50	27,8	7,8	0,00	11,09	0,00	5,42	10,42	4,81		3,51	0,00	0,00	0,00	4,90	101,99
SMR 02	Drill Well	130	60	29,3	7,10	0,00	9,76	0,05	4,90	13,89	6,97	0,16	1,43	2,06	1,60	2,06	1,60	96,20

The results of chemical analysis for the waters were plotted on a piper diagram and stiff diagram as shown in Figure 3 and Figure 4. From Fig. 3 waters are divided into 5 (five) groups based on their chemical characteristics: Ca-Mg-HCO_3, Mg-Ca-HCO_3, Mg-HCO_3, Na+K-HCO_3, and Na-+K-Cl.

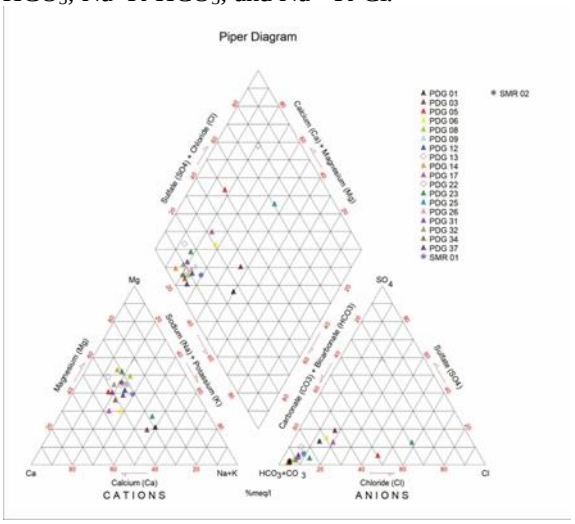

Figure 3. Piper Diagram

Twelve waters Samples of Ca-Mg-HCO_3 type, are located on elevations from 167 to 928 ma.s.l.. That groundwater facies is the type of groundwater that dominates in the study area. One sample belong to Mg-Ca-HCO_3 type is located on 437 m.a.s.l. two samples belong to Mg-HCO_3 type are located on elevation 199 and 251 m.a.s.l. Then two waters of Na+K-HCO_3 type are located in the elevation 459 m.a.s.l. and one water sample belong to Na+K-Cl is located in the elevation 180 m.a.s.l.

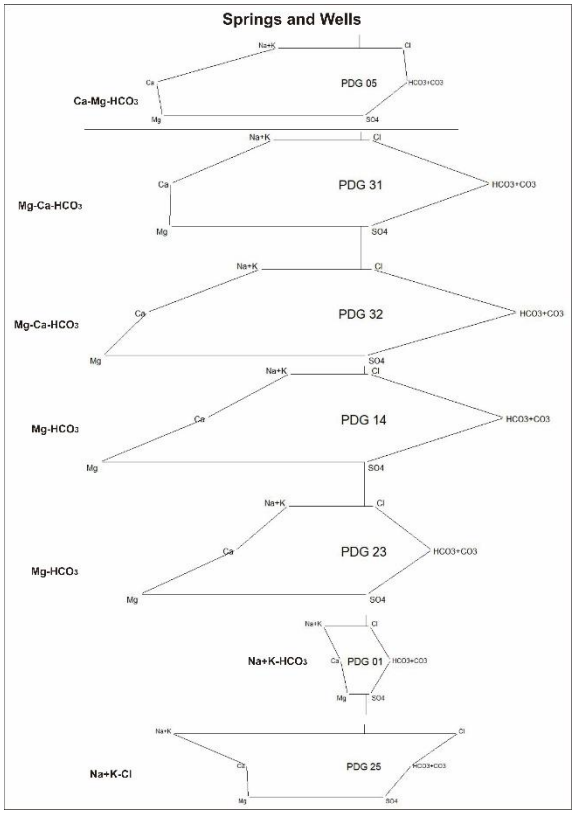

Figure 4. Stiff diagram for major ion of water samples

From the stiff diagram in Fig.4, Ca2+ is a dominant cation in Ca-Mg HCO_3 type water in PDG 5 which is located at an elevation of 750 m.a.s.l. This water has flowed in the volcanic facies of andesitic rock that contains Ca-plagioclase.

The presence of Mg^{2+} shows that the water has flowed from shallow to the deeper aquifer. As in PDG 14 and PDG 23 where these cations are elements that are quite widely dissolved in groundwater samples with concentrations of 12.55 ppm and 10.72 ppm, respectively.

Variations in the presence of cations in groundwater samples in the study area are indicated by the dominance of Na+K cations in groundwater samples from PDG 1 and PDG 25 points with

concentrations of 6.17 ppm and 30.37 ppm, respectively. shows that the interaction of groundwater with rocks lasts quite a long time. PDG1 is associated with the ALHbr volcanic facies which is composed of breccia lithology, so that the dominance of Na+K elements is the result of dissolution of plagioclase minerals.

Meanwhile, HCO_3 is derived from infiltration of rainwater equilibrated with CO_2 in atmosphere or is CO_2 generated by root respiration organic material. These ype indicated for local flow system. In general, surface water is controlled by the type of groundwaters.

The concentration of Cl^- anions in PDG 25 showed a value of 38.32 pp, so it was an anomaly compared to the anions contained in other water samples. The PDG 5 sample point is associated with the oldest volcanic facies in the study area, namely Fbl which is composed of lapilli lithology. In addition, the emergence of these springs is associated with a sinistral horizontal fault, so it is interpreted that groundwater that appears at the PDG 5 point has flowed into the deep groundwater aquifer

Groundwater flow system

Based on the water table and water types in the study area, groundwater flow in the volcanic aquifer system can be determined. In the upstream part, the Ca-Mg-HCO_3 type indicated that it is close to the source. The presence of the Mg-Ca-HCO_3 type at elevation 437 and the Mg-HCO_3 type indicates the groundwater flow is quite far from the recharge area and the groundwater has flowed into the aquifer which is deep enough. The appearance of the Na+K-Cl type indicates that in the study area there is groundwater flowing very deep and far from its infiltration source and its appearance is influenced by the geological structure (fault). The direction of groundwater flow is generally from West to East and shown in Figure 5.

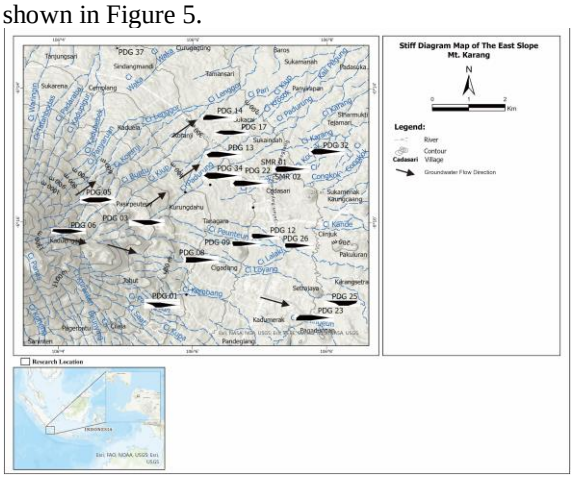

Figure 5. The stiff diagram map and shallow groundwater flow.

CONCLUSION

Physical properties of groundwater identified as a result of the interaction of groundwater with rocks, it shows that the water in the study area is included in fresh water. Lithological variations and changes that compose various volcanic facies in the study area control the chemical composition of groundwater as indicated by variations in groundwater types identified from various groundwater samples including Ca-Mg-HCO^3, Mg-Ca-HCO_3, Mg-HCO_3, Na+K-HCO_3 and Na+K-Cl. In addition, the various types of groundwater show differences in groundwater flow which are controlled by geological events. The direction of shallow groundwater flow from west to east is also controlled by the morphology of the study area.

ACKNOWLEDGMENTS

The authors would like to thank deeply to Faculty of Geology, Universitas Padjadjaran and the Unpad team for their invaluable participation in this study. We would also like to express our gratitude for the valuable comments provided by reviewers and the editor of GEOMATE.

REFERENCES

[1] Anna Rusyidi, Mitsuyo Saito,Seiichiro Ioka, and Rizka Maria., Estimation of Ammonium Sources in Alluvial Groundwater Using Cl^- and GIS A Case Study Of Indramayu, Indonesia. Int. Conf. on Science, Engineering & Environment (SEE), 12-14, 2018,pp.203-207

[2] Boy Yoseph CSS Syah Alam, Yuichi Itoi, Sachihiro taguc=hi and Rie Yamashiro, Spatial variation in groundwater type of the volcanic aquifer system based on hydro-chemical and stable isotopes (δD and δ18O) at Mt. Karang, West Java, Indonesia. Modern Applied Science; Vol 8 No.6 2014.

[3] Muhammed Haji,Dajun Qin,Yi Guo,Lu LiDongdong Wang Shankar Karuppannan,Hassen Shube, Origin and geochemical evolution of groundwater in the Abaya Chamo basin of the Main Ethiopian Rift: application of multi-tracer approaches. Hydrogeology Journal (2021) 29:1219–1238.

[4] Appelo, C.A.J.andPostma, D.,Geochemistry, Groundwater and Pollution. A.A. Balkema(2005).

[5] Domenico,P.A. and Schwartz, W.F., Physical and chemical hydrogeology.John Wiley and Sons, Inc., Canada, 824p (1990).

[6] Fetter, Jr.C.W., Applied hydrogeology.Bell and Howell Company, 488p (1980).

[7] Freeze R.A. and Cherry, J.A., Groundwater. Prentice-Hall, 604p (1979).

[8] Fury W,.Hydrochemical characterization of complex volcanic aquifers in a conteinental rifted zone: the Middle Awash basin, Ethiopia. Hydrogeology Journal 20: 385-400(2011)

8th Int. Conf. on Structure, Engineering & Environment (SEE), Mie, Japan, Nov.10-12, 2022, ISBN: 978-4-909106094 C3051

RELATIONSHIP BETWEEN THE LIVING ENVIRONMENT AND THE SENSE OF TIME-SPACE

Kazuki Miyake[1], Kazunari Tanaka[2]
[1] Osaka institute of technology Graduate Course in Architecture, Civil Engineering and Urban Design,
[2]Osaka Institute of Technology

ABSTRACT

People's behavior in public spaces has been studied from different viewpoints and previous studies have shown that actions are influenced by the layout of the device and the shape of the space. The cognitive distance and means of transportation to and from school and workplace depends on where people live. Compared with urban areas, suburban areas have fewer stores. In other words, people living in urban areas and suburbs have different means of transportation and surroundings. They have different space-time senses. Depending on the living environment, such as the waiting time of public transportation and the distance of facilities used daily. The distance and the speed of transportation are changed depending on the location. The purpose of this study is to quantify the differences in distance perception, depending on the living environment. Focusing on the residence position of people with respect to the distance from the station, the residence data was displayed and visualized by GIS. The structure of distance intervals in people's lives was extracted.

Keywords: (Living environment, Kernel density estimation, distance intervals, GIS),

INTRODUCTION

Background

There is a large body of literature that addresses the influence of the surrounding environment, such as season and the placement of retention devices, on people's behavioral choices in retention spaces. However, we believe that behavior also varies depending on the experience that is the source of affordance. Currently, the population of Japan is aging rapidly, and the problem of depopulation in suburban areas has arisen due to population decline. Depending on where people live, the distance they travel to school and work and the means of transportation differ. In addition, there are fewer stores and residences in suburban areas than in urban areas. In other words, people living in urban and suburban areas have different means of transportation and different surrounding environments, and each has a different sense of time.

Purpose and Method

We believe that differences in perception such as near/distant and early/slow form due to living environment, such as waiting time for public transportation and distance to facilities used and change daily. Therefore, the purpose of this study is to quantify the differences in the perception of distance due to living environment, and to extract the structure of perceived distance in people's daily lives. The experiment will be conducted in Asahi-ku, Osaka City, Osaka Prefecture, and Sakurai City, Nara Prefecture. As a preliminary study, we conducted a survey on the location of people staying in Sakurai City, Nara Prefecture. Here, we focused on people's location in relation to the distance from the station and visualized the data by displaying it in a GIS. Next, a questionnaire survey was conducted to extract people's sense of distance and time axis. Since previous studies have shown that the perceived distance differs depending on the history of residence, a questionnaire survey was conducted targeting both visitors and residents of the city. In order to have subjects perceive distance, we asked them to describe their means of travel and travel time to a certain point and compared them with the actual distance and travel time.

EXPERIMENT

Experiment 1

The first study was conducted during the social experiment in front of Sakurai Station in Sakurai City, Nara Prefecture. The first study was a comparison of the different periods of time during which the social experiment was held in front of Sakurai Station in Sakurai City, Nara Prefecture, Japan. Figure 1 shows the results of the residential location of the passers-by for each period.

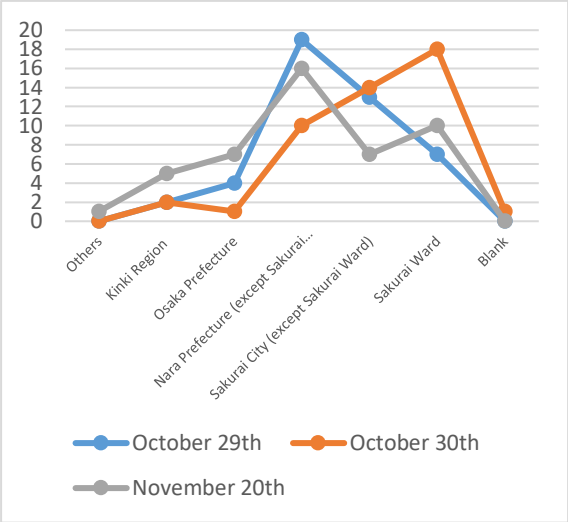

Fig. 1 Percentage of visitor residence

The survey was conducted by videotaping 90 minutes of data and counting the number of incoming and outgoing flows. The results are shown in Table 1.

Table 1 Day Number of in/out flows

	High school student	Others
	October 29 th	
①	14	318
②	5	330
③	4	190
	October 30th	
①	68	2229
②	30	1027
③	24	1149
	September 20 th	
①	282	330
②	22	311
③	44	190

Figures 2, 3, and 4 show the results of Table 1 as the size of the arrows on the map for each schedule. High school student counts are indicated by blue arrows and the general public by red arrows.

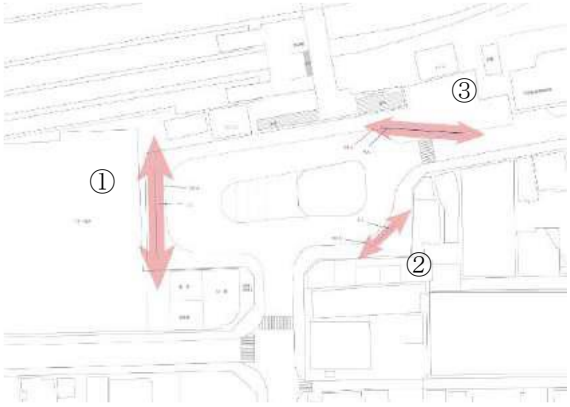

Fig. 2 October 29th Inflow/Outflow

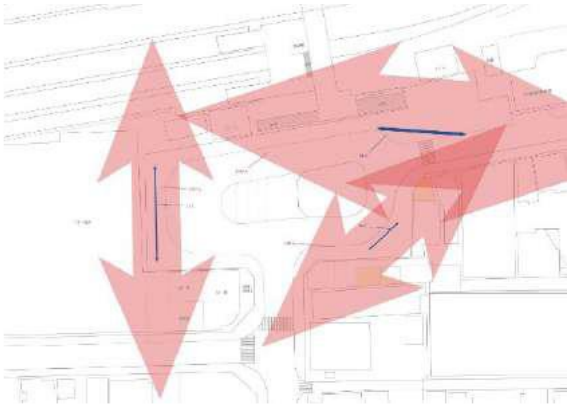

Fig. 3 October 30th Inflow/Outflow

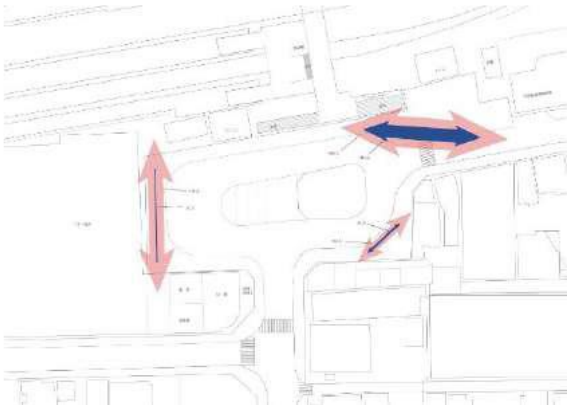

Fig. 4 November 20th Inflow/Outflow

October 29 was an experimental day with a relatively large number of residents, October 30 was an event held at a nearby location, and November 20 was an experimental day with a large number of non-local visitors during the fall foliage season. The traffic volume in the vicinity of the station was higher on the experimental days when there were more visitors, while on the experimental days when there were more residents, the traffic volume in front of the commercial facilities was higher. In the next section, we will visualize and verify the difference in dwell position by residential area.

Experiment 2

The second survey was conducted to determine the location of the visitors in the vicinity of the station plaza. The results of the questionnaire survey, shown in figure 5, revealed that there was a difference in the number of times the respondents visited the area and the location of their stay. We believe that the range of behavior may change depending on the residential area or the level of recognition of the area, and we compared the dwell time positions of residents and visitors to extract differences in behavior in the residential area.

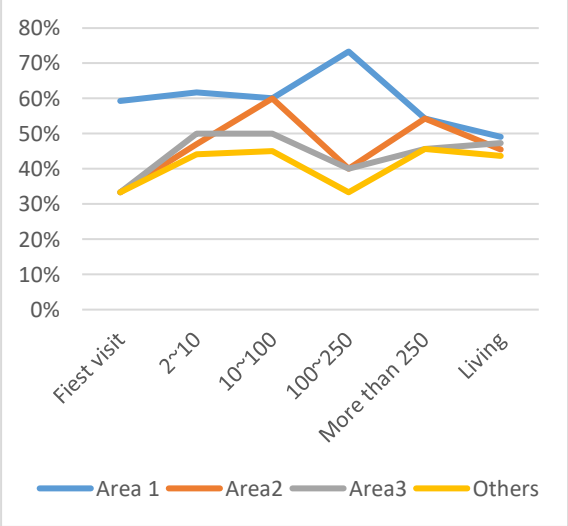

Fig. 5 Dwell position by number of visits

The purpose of the survey was to extract data on the place of stay by place of residence through a questionnaire survey and to compare the range of activities of the two groups. Plotting the stay locations of visitors and residents obtained from the questionnaire survey on a map was performed. The subject site is shown in Figure 5. Area 1 is in front of the commercial center as the target area. Area 2 is located in front of the east exit of Sakurai Station. Area 3 is the tourist information center. Area 4 is the bus stop Area 5 is Hommachi Street.

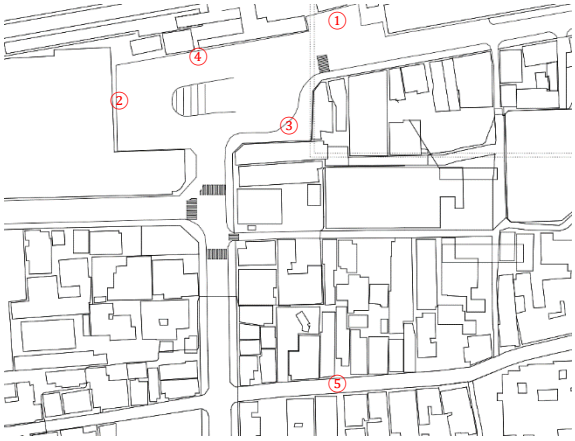

Fig. 6 Area Location

Table 2 shows the results of the location of stay by place of residence for a total of 5 days.

Table 1 Day Number of in/out flows

	Resident	Visitor
Area 1	24	15
Area2	23	24
Area3	22	15
Area4	7	11
Araa5	12	0

Figures 4 and 5 show heat maps created by kernel density estimation using GIS with the results shown in Table 2.

Fig. 7 Resident action range

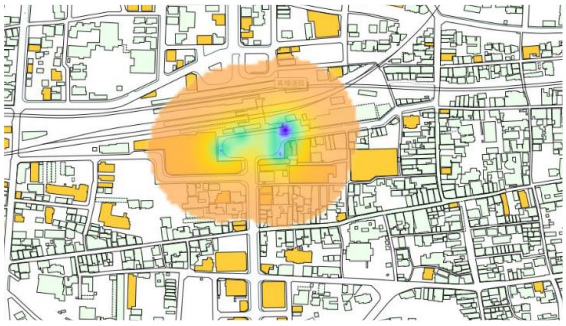

Fig. 8 Visitor Action Area

It was found that most of the visitors stayed at the bottom of the east staircase, while the residents stayed in relatively calm areas with little traffic, moving to various locations during events. These results indicate that the location of residence and the range of activities vary depending on the level of recognition of the town, and that each individual has a different sense of distance from the others.

3 CONCLUSION

Survey 1 revealed that the flow in and out of each area differs depending on the residential area, and Survey 2 revealed that the location of residence and the range of activities differ depending on the level of recognition of the town. The results indicate that people have a different sense of distance from each other depending on their residential environment. In an aging society with a declining birthrate, the sense of distance is an important perspective in promoting the mobility of residents in suburban areas through compact urban development and is considered to be fundamental information regarding the layout of facilities and target areas. We were able to obtain results that can be used as an indicator for the development of future residential environments.

REFERENCES

[1] Murata S., Morihara K., and Koda T., Analyses of Effect of Personality on Personal Space in Real World and Metaverse. The Japanese journal of Psychology, Vol. 52(2), 1981, pp. 124-127.

[2] Konishi H., Nozawa K., Study on Seating Behavior in the Train; the Influence of Prediction about Crowd on Seating Behavior. The annual bulletin of Musashino University Institute of Human sciences, Vol. 7, 2018, pp. 37-39.

[3] soshihiro O., Ayaka M., Distance Measure Based on Spatiotemporal Coexistence of Residents. J. Archit Plan., AIJ, Vol.80 No.715 2001-2010 Sep.,2015

8th Int. Conf. on Structure, Engineering & Environment (SEE), Mie, Japan, Nov.10-12, 2022, ISBN: 978-4-909106094 C3051

A REVIEW OF THE CURRENT LEGISLATION ON WASTE MANAGEMENT IN DEVELOPING AND DEVELOPED COUNTRIES

Kylie Douglas[1], Daniela Ionescu[2], Joe Petrolito[3] and Bandita Mainali[4]
[1]Council of Greater Bendigo, Bendigo, Australia
[2,3] School of Engineering and Mathematical Sciences, La Trobe University, Australia
[4] School of Engineering, Macquarie University, Australia

ABSTRACT

The management of municipal solid waste is a major problem worldwide. However, the approaches on SMW widely vary between countries due to in-place legislation. Developed countries are moving towards a Circular Economy and are developing policies and legislation to support this move. However, the policies and legislation makers are not always up to date with studies on the best practices on MSW, which results in few tangible outcomes. In developing countries, landfills are still an accepted means of disposal. The legislation mandates source segregation of recyclates. However, in some countries there is little desire to enforce this, resulting in tones of recyclates being discarded to landfill.

The aim of this paper is to review the strengths and weaknesses of the legislation governing solid waste management (SWM) in both developed and developing countries. It looks specifically at comparing the legislation and policies directly pertaining to SWM and how they are enacted at ground level using Regional Victoria, Australia, and Kathmandu Metropolitan City (KMC), Nepal as case studies. In addition, it examines the potential for the transfer of knowledge and learnings between Regional Victoria and KMC.

The results from the study strongly support the transfer of learnings between Regional Victoria and KMC, to actively enforce sustainable SWM practices. Moreover, the learnings from Regional Victoria's move towards becoming a truly Circular Economy can be directly applied to KMC. Conversely, learnings from KMC and their methods of production of high-quality recyclates can also be directly applied to Regional Victoria, aiding in the transition towards a Circular Economy.

Keywords: Solid waste management, Circular economy, Technology transfer, Waste reduction

INTRODUCTION

The spread of urbanization and intensified industrialization are phenomena that are observed in developed as well as developing economies, and they are associated with rapid population growth. Developments, growth and consumption of goods and services are on the increase. This causes an increased rate of municipal solid waste generation, which in 2016 was reported to be 0.75 kg/person/day and is expected to increase by 70% in 2050 [1]. The sustainable collection and management of this waste is critical to economic development, the environment, and society [2].

The challenges of solid waste management (SWM) are recognized at a global level, and they are not limited by boundaries or by the development status of countries. Common challenges include limited 'waste' disposal infrastructure, resource recovery and the availability of markets for the recovered materials, and the quality and 'cleanliness' of the recovered products. However, with the challenges come opportunities, and it is in realizing these opportunities that the differences between developed countries and developing countries become apparent.

It is reported that the amount of waste generated strongly reflects the economic status of the people [3] and also depends on socio-cultural patterns and climatic factors [4]. There is no agreement on the correlation between Gross Domestic Product (GDP) and waste generation. Othman et al. [5] reported that the average solid waste generation in developing countries is 0.7-0.8 kg/person/day, while it is 0.4-0.6 kg/person/day in developed countries. In contrast, [4] showed that the median generation rates in high-income countries is about six-fold greater than in low-income countries, as presented in Fig. 1.

The aim of this paper is to review the strengths and weaknesses of the legislation governing SWM in both developed and developing countries. It looks specifically at comparing the legislation and policies directly pertaining to SWM, and how they are enacted at ground level using Regional Victoria, Australia, and Kathmandu Metropolitan City (KMC), Nepal as case studies. In addition, it examines the potential for the transfer of knowledge and learnings between Regional Victoria and KMC.

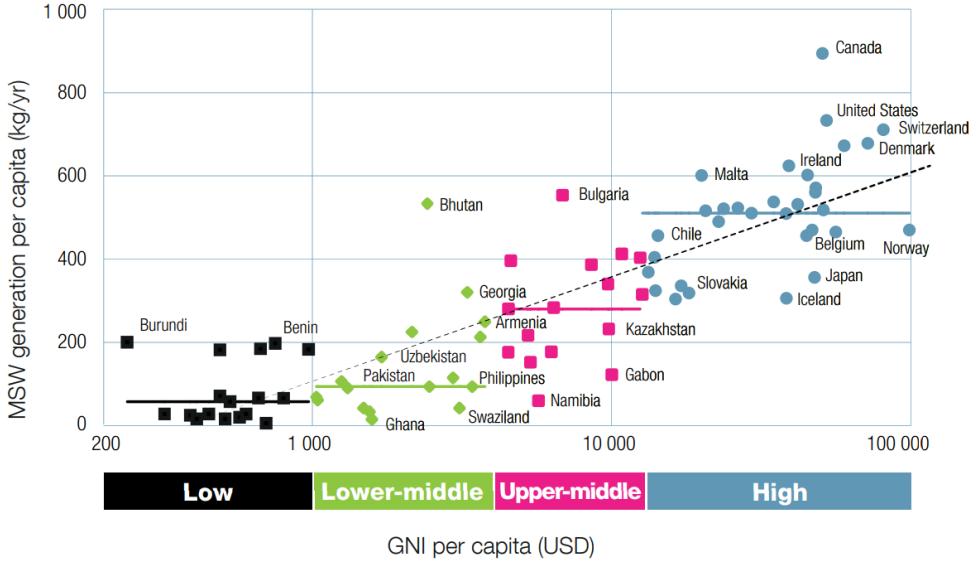

Figure 1. Waste generation versus income level by country [4]

EXISTING SOLID WASTE MANAGEMENT FACILITES

Geographic and Demographic Background

Kathmandu occupies an area of 49.45 km^2 in Central Nepal, at an average altitude of 1400 m. 74% of its surface is built-up area [6]-[8]. It has a temperate climate for most of the year, with four distinct seasons [9]. It currently has 1.521 million inhabitants, resulting in a population density of over 30,750 people/km^2 [10]. The terrain surrounding Kathmandu is primarily used for agriculture to support the growing population [11].

Kathmandu is a multicultural metropolitan area comprising of four major ethnic groups, namely Newar 30%, Matwali 25%, Khas Brahmins 20% and Chettris 18.5% [8]. The two major religions are Hinduism and Buddhism, and there are three main languages that are spoken, namely Nepali, Nepal Bhasa and English [8]. The city's infrastructure dates to the 10th Century.

Regional Victoria is located in South-Eastern Australia and has a topography that ranges from plains to mountainous, with elevations varying from 10 m to 2000 m [12]. The total land space of 226,267 km^2 supports a population of 6,681 million people, with a density varying from 1 people/km^2 to 37 people/km^2 [13]. Regional Victoria also has a temperate climate for most of the year, with four distinct seasons [11].

Australia was built on migration after the initial settlement by the British. Settlements in Regional Victoria date back to the mid-1800s [11]. Regional Victoria has a rich multicultural history. Although the Aboriginals are recognized as the first inhabitants of the land, a quarter of the Regional Victoria population originates overseas (UK, India, etc.), with 68% of the population being Australian-born citizens [13]. The varied range of migrants practice diverse religions, although Christianity is the largest. Similarly, multiple languages are spoken, with English being predominant.

Kathmandu Metropolitan City

SWM was formalized in KMC in the 1980s with the construction of the Teku composting facility, the Teku transfer station and the Gokarna landfill. During the 1990s, waste was disposed of without any segregation taking place [14]. The closure of the Teku composting facility in 1992 and then of the Gokarna landfill in 2005 resulted in a return to poor SWM and uncontrolled dumping in KMC [14].

The opening of the Sisdol landfill and the 2011 SWM Act in Nepal facilitate improved collection and disposal practices in KMC, as segregation of waste at the source and separation of organics from waste was implemented and promoted [15]. In 2012, KMC allocated 24% of its budget to SWM, of which between 60-70% was used in street sweeping to clean up the street-side dumping of waste, and 20-30% was used for waste transportation [6]. The adoption of the new constitution in 2015, and the merger of the central governmental offices with the local government, resulted in a lower proportion of the budget (6.3%) being allocated to SWM, although the overall funding was higher [16].

The waste collection occurs through a combination of KMC vehicles and staff, and private sector organizations (PSOs) [17]. Inconsistent fees for service are being charged throughout KMC, resulting in inconsistent collection services [16].

Currently, KMC and the surrounding region are

serviced by a single landfill located at Sisdol. A new landfill is being constructed at Banchare Danda [18].

Regional Victoria

During the gold rush era, until the late 1800s and into the 1900s, there was uncontrolled disposal of waste [19]. With the formation of Local Government Authorities (LGAs), waste management became more formalized, with the establishment of local 'tip sites' for the disposal of waste [19].

The Local Government reform of the 1990s resulted in the amalgamation of 210 shires into just 78 [20]. Many smaller disposal sites were closed, waste collection was mandated, and the remaining disposal sites were formalized and controlled. Collection services took place under a mandatory 'fee for service' model [20].

Hence, in contrast to the KMC practice, each of the municipalities of Regional Victoria has access to controlled waste disposal facilities. Resource and recovery facilities are common at the transfer stations and landfills. A kerbside waste collection occurs weekly, and most municipalities support a fortnightly collection of recyclable materials. A green waste collection service is offered by some municipalities, and private operators also provide, for a fee, a green waste collection service in other areas. The kerbside collection of waste is the responsibility of the municipality, although residents can access disposal and recycling facilities to deposit excess waste from properties.

LEGISLATION TO SUPPORT CURRENT PRACTICES

An overview of the legislation and policies currently in place for both KMC and Regional Victoria is provided in this section. How they are implemented and enforced, and the weaknesses and strengths of the legislation is also presented.

Kathmandu Municipal City - Legislation

The focus of regulations in KMC is on the timely collection and disposal of the waste material. The regulations include provisions for the recovery of recyclable materials, such as organics from the waste stream. The enforcement of the regulations is left to KMC Council, although, there is little evidence of active enforcement by KMC. This is evident in the lack of segregation of recyclable materials, as well allowing many PSOs to operate without the required license [15].

Local Self Governance Act - 1999

This Act allows municipalities to impose service charges for SWM, as well as for the authority to impose fines in the event of dumping of waste in undesignated areas. The fines can be up to Rs. 15,000 (approximately AUD $192), and if required can include additional clean-up costs. Although the Act covers dumping of waste in undesignated areas, street-side dumping is still an accepted practice in KMC.

Interim Constitution of Nepal - 2008

According to [21], this policy includes some provisions that broadly relate to SWM, and it states the right of each person to live in a clean environment, and that it is the state responsibility to maintain and provide the environment. However, the policy does not indicate how this is to be achieved, nor does it detail what it covers.

Solid Waste Management Act - 2011

This Act focused solely on SWM and allocates the responsibility of the construction and operation of any disposal facilities, including transfer stations, treatment plants and landfills, solely with the Local Government [7]. Although the Act makes provisions for the management of hazardous, medical, chemical, or industrial waste to be managed by the generator, these provisions lack detail and do not dictate how these hazardous waste streams must be disposed of or treated. Furthermore, the Act does not provide directions on the disposal of SW, except that it must be to a sanitary landfill, with no differentiation between waste types and classifications. However, the Act specifies that organics must be segregated at the source from SW and encourages the Local Body to promote, whenever possible, waste reduction, waster reuse and recycling [7].

The Act empowers the Local Body to charge a fee for the SWM services provided, to monitor the SWM, contract PSOs to carry out this work, assess, evaluate, and report on the effectiveness of SWM, and implement report recommendations. While the Act maintains that regular monitoring must be undertaken, it does not dictate how often it should be carried out and how it will be regulated.

The Act leaves the responsibility of SWM squarely with KMC to implement, manage and regulate. The Act also delegates power to the Local Body (KMC) to suspend services, such as power and telephone, and to prevent the sale of house and land by offenders for breaches of the Act [7].

Local Government Operation Act, 2074 FY - 2018

SWM activities are largely governed by this Act, with the roles, responsibilities and functions being spelt out in it [10]. The Act focuses on:

- Raising awareness on sanitation and waste management,

- Collection, re-use, re-cycle and disposal of waste, and tariffs and their regulation, and
- Coordination, collaboration and partnership with private sector and non-government agencies for waste management.

Environmental Protection Act 2076 FY - 2019

This is a recent Act that is the result of amending and consolidating older laws pertaining to environment protection into a single Act [10]. The Central Bureau of Statistics [10] lists the focus of this Act as follows:

- To protect the fundamental right of each citizen to live in a clean and healthy environment,
- To provide the victim with compensation by the polluter for any damage resulting from environmental pollution or degradation,
- To maintain a proper balance between the environment and development,
- To mitigate adverse environmental impacts on the environment and biodiversity, and
- To face the challenges posed by climate change.

Regional Victoria – Legislation

The regulations regarding SWM are actively enforced, and they include collection and the appropriate disposal and segregation of recyclates. Audits of LGAs are carried out regularly in accordance with several different pieces of legislation by different State Government bodies to ensure compliance. In addition, industries that specialize in waste treatment and disposal are also audited regularly to ensure compliance. Non-compliance penalties apply and are very high.

Environment Protection Act - 1970

In Victoria, the Environment Protection Act 1970 (EP Act) was established to protect the environment from harm through the generation, transportation, and disposal of waste from both industry and LGAs alike [22]. It sets the standards and requirements for acceptable operating requirements for industries, how waste is to be handled once generated, how it is to be transported, and the final disposal requirements. Hazardous wastes have very specific transportation, storage, and disposal requirements, to ensure not only the safety of those handling it, but also to protect the environment from harm. This is a distinct difference to KMC, whose regulations do not include such provisions. Hence, PSOs in KMC that undertake resource recovery are at a higher risk of exposure to hazardous wastes, due to a lack of separation of the waste at the disposal site.

To ensure the provisions of the Act are met, an independent regulating body oversees the management of waste within the State. The Environment Protection Authority (EPA) has the power to enforce, prosecute and impose penalties for any breaches of the Act [23].

It is noted that this Act has been superseded by the EP Act 2017, which places a greater focus on the prevention and risk management than the previous Act. The EPA is also the regulating authority for this Act and the subsequent regulations, and it has greater powers to investigate and prosecute where breaches of the Act have been identified.

Local Government Act - 2020

In Victoria, the Act pertaining to the provision of SWM services, such as household collections, leaves the responsibilities predominantly with LGAs, like the Solid Waste Management Act 2011 in Nepal. However, the regulation of the Act is different. Instead of self-regulation by LGAs, independent regulating bodies were set up by the State Government under the provisions of the Act, to ensure that the requirements under the Act were being met by each LGA. These governing bodies include Sustainability Victoria (SV) and Department of Environment, Land, Water and Planning (DELWP), with each body being responsible for different aspects and being able to feed into legislation for additional requirements. It should be noted that the regulating body, EPA, also reports to DELWP. The Act covers the requirement for LGAs to provide for specific services to residents, such as access to recovery and waste drop off facilities, the provision for collections of MSW and recycling where practicable and cost-effective.

In addition to regulating bodies, Waste and Resource Recovery Groups (WRRGs) were also established, and these are responsible for fixed zones that cover multiple LGA areas. The role of the WRRGs is to work directly with LGAs and industry to establish long-term SWM plans for the regions, including the mapping, evaluation, and the establishment of facilities for SW disposal and resource recovery.

LGAs have the authority to recover the costs for the provision of the required services and can independently set these costs. However, the charge to residents must be for cost recovery only, as opposed to making a profit. This is where the KMC private operators differ from the LGAs in the provision of waste collection and disposal services, since they are free to charge what they deem is appropriate, and they operate to make a profit.

ENFORCEMENT AND ENACTMENT

Kathmandu Municipal City

The City is divided into 35 wards, and the collection of waste from these areas is via a

combination of private and government resources [17]. In 2015, twelve wards were serviced by KMC, one ward was serviced solely by a PSO, and the remaining twenty-two wards were serviced by a combination of KMC and PSOs [15], although it was reported that only 8 wards are serviced solely by KMC [16].

The older and more central wards (35% of the area) are serviced by the staff of KMC at no charge, due to the difficulty of collecting a service fee in these areas. The waste in these areas is thrown on the side of the road and collected from there. The rest of the area is serviced by private operators who charge a small monthly service fee for the collection of waste. This fee is about AUD $4.26 per household, with higher fees being charged for hospitals and businesses [16]. The vehicles used in the collection of the waste vary extensively from hand carts through to collection trucks [15].

It is reported that waste generation in KMC is 0.464 kg/person/day [6], [15], producing over 669 tonnes/day, of which only 250 tonnes is disposed daily. Hence, the efficiency of collection appears to be only 37%, as opposed to the 86.9% that [6] and KMC [15] have quoted. The major barriers to SWM efficiency are the poor implementation of SWM by KMC Council itself and the lack of enforcement of the governing legislation. This has resulted in the accepted practice of street side dumping. While segregation is included in the legislation, the lack of support and enforcement from the KMC council results in minimal source segregation. While minimum segregation occurs, where it is performed by PSOs and the informal sector, the products are of high quality and cleanliness, resulting in good markets for the products.

Regional Victoria

The implementation of the EP Act 1970 initiated the segregation of paper, cardboard, glass, cans, and hard plastics from the waste at the source. Recycled materials were then collected and transported to the Material Recovery Facilities (MRF) for further segregation and consolidation, followed by the sale of the material to processors, to be converted into new products. The collection and transportation costs were passed on to serviced residents.

The LG reform of the 1990s resulted in smaller disposal sites being closed, waste collections implemented, and waste disposal sites formalized and controlled. The collection services took place under a mandatory ‘fee for service’ model [20].

In the late 1990s and early 2000s, the comingled service was established. All recyclates were placed into a single bin, instead of being separated by the product stream. Victoria became reliant on overseas markets and the income they generated, resulting in the closure of local markets. After the closure of China to Australian recyclates and the subsequent closure of other international markets, due to the contamination in the recyclates being recovered, recyclates were stockpiled in the hope that new markets would open. The unforeseen impact of this was the breakout of fires at several major recycling facilities [24]. Multiple studies and plans have been developed at a State level in an attempt to address the lack of local markets and processing infrastructure. However, these studies and plans have been developed largely in isolation of each other.

The disposal of waste at landfill incurs a levy set and collected by the State Government, with the intent of these funds going back into investment in SWM infrastructure. Large amounts of State Government support go to divert organics from landfill. However, the capacity of receiving facilities has not been analyzed or considered. Street-side dumping of waste is prohibited by law, and high monetary penalties apply for noncompliant actions.

The current legislation is actively enforced in Regional Victoria, resulting in household segregation of recyclates and clean streets. However, the focus of the government is on policies, as opposed to actively initiating change, and the same practices have been used for more than 20 years with minimal change. Change occurs at a very slow rate, with any new direction taking years to initiate.

The State Government is also heavily reliant on consultants to conduct studies to inform policy making. However, there is a lack of expertise to map out clear aims and objectives for the studies, and to analyze and link the separate studies that have been completed. In addition, large commercial operators also influence policy making by portraying themselves to be ‘experts’ in SWM, leaving smaller operators without a voice.

DISCUSSION

The examination of the legislation and the practices implemented on the ground in Kathmandu Metropolitan City identified large gaps in both. While the backbone of the legislation is there, it does not go far enough and fails to address problems such as street side dumping, leaving the problem solely with the municipality. The practices on the ground are also a clear indication of the lack of enforcement of the existing legislation. However, the waste segregation performed by PSOs results in products of high quality and cleanliness, ensuring good markets for them.

This contrasts with Regional Victoria. The legislation is actively enforced, resulting in clean streets, effective waste, and recycling collections. However, the legislation is too slow to change with updates in technology and trends in waste management. As Victoria is moving towards becoming a Circular Economy, the legislation is becoming outdated quickly, with Government bodies

struggling to make the necessary changes to ensure that it is still valid.

CONCLUSION

The existing SWM practices and the current legislation regulating these activities in Kathmandu Municipal City and Regional Victoria were reviewed and compared.

Learnings regarding the enforcement of existing legislation can be transferred to KMC from Regional Victoria. Conversely, learnings from KMC regarding the input and value of smaller operators can be taken back to Regional Victoria and would aid in the transition to a truly Circular Economy.

REFERENCES

[1] The World Bank, Solid Waste Management, 2022 https://www.worldbank.org/en/topic/urbandevelopment/brief/solid-waste-management.

[2] Heidari, R., Yazdanparast, R., and Jabbarzadeh, A., Sustainable Design of a Municipal Solid Waste Management System Considering Waste Separators: A Real-World Application, Sustainable Cities and Society, Vol. 47, May 2019, 101457, p. 14.

[3] Shekdar, A.V., Sustainable Solid Waste Management: An Integrated Approach for Asian Countries, Waste Management, Vol. 29, April 2009, pp. 1438-1448.

[4] Modak, P., Wilson, D.C. and Velis, C., Waste Management: Global Status, Global Waste Management Outlook, United Nations Environment Programme, 2015, pp. 51-124.

[5] Othman, S.N., Noor, Z.Z., Abba, A.H., Yusuf, R.O. and Hassan, M.A.A., Review on Life Cycle Assessment of Integrated Solid Waste Management in Some Asian Countries, Journal of Cleaner Production, Vol. 41, February 2013, pp. 251-262.

[6] Asian Development Bank, Solid Waste Management in Nepal: Current Status and Policy Recommendations, 2013, Mandaluyong City, Philippines.

[7] Government of Nepal Central Bureau of Statistics, National Population and Housing Census 2011, November 2012, Kathmandu, Nepal.

[8] World Population Review (2015) Kathmandu Population, http://worldpopulationreview.com/world-cities/kathmandu-population.

[9] Shreshta, V.P., A Concise Geography of Nepal: Climate, 2007, Mandal Publications, Kathmandu.

[10] Central Bureau of Statistics, Current Kathmandu Macroeconomic and Financial Situation, April 2021, Kathmandu, Nepal.

[11] Douglas, K., Ionescu, D., Mainali, B. and Petrolito, J., Integrated Waste Management – Technology Transfer Between Australia and Nepal – Proc. International Conference on Environmental Science and Sustainable Development (ICESSD2015), October 2015, pp. 25-26.

[12] State of Victoria, Department of Environment, Land, Water and Planning, 2015, http://maps.land.vic.gov.au/lassi/SmesUI.jsp.

[13] Australian Bureau of Statistics, National, State and Territory Population - Statistics About the Population and Components of Change (Births, Deaths, Migration) for Australia and Its States and Territories, 17 March 2022, Australia.

[14] Rakesh, T.L., Internationalization of Waste Management Company in Kathmandu, thesis, Turku University of Applied Sciences, Kathmandu, Nepal, 2010.

[15] Urban Development Ministry, Solid Waste Management of Kathmandu Municipal City, 2015, Kathmandu, Nepal.

[16] Pathak, D.R., Director Engineering Study and Research Centre, Kathmandu, Nepal, personal communication, 10 July 2019.

[17] Maze Solution, Kathmandu Valley Temples, http://kathmandu-valley-temples.com/ktmvalley_php/main.php?site=rundgang&object=079, August 2017.

[18] Pathak, D.R., Integrated Resource Recovery Approach for Sustainable Solid Waste Management in Developing Countries, 7 August 2021, Kathmandu, Nepal.

[19] Visit Victoria, Gold Rush History, https://www.visitmelbourne.com/Regions/Goldfields/Things-to-do/History-and-heritage/Gold-rush-history

[20] Connoley, R., Victorian Local Government Reform 1992-1999, Journal of Economic and Social Policy, Vol. 11, Issue 2, 2007, p.3-21.

[21] Kumar, A., Smith, S.R., Fowler, G., Velis, C., Kumar, S.J., Rena, S.A., Kumar, R. and Cheeseman, C., Challenges and Opportunities Associated with Waste Management in India, Royal Society Open Science, Vol. 4, Published:22 March 2017.

[22] Victorian State Government, Environment Protection Act 1970, 1 July 2010, Melbourne, State Government of Victoria.

[23] EPA Victoria, Compliance and Enforcement. https://www.epa.vic.gov.au/about-epa/what-we-do/compliance-and-enforcement.

[24] Hope, Z., Major Fire at Factory Belonging to Notorious Melbourne Recycler, The Age, 9 July 2019, Melbourne, Victoria, Australia.

8th Int. Conf. on Structure, Engineering & Environment (SEE), Mie, Japan, Nov.10-12, 2022, ISBN: 978-4-909106094 C3051

THE IMPACT OF THE COVID-19 PANDEMIC ON RESORT AREAS AND ITS RELEVANT TO AGRICULTURAL MARKETS -A CASE STUDY OF KARUIZAWA, NAGANO PREFECTURE, JAPAN-

Reiko MACHIDA[1], Yuya MIKAMI[2], Waya KOBAYASHI[1], Nobuhiko TANAKA[3], Teruaki IRIE[1], Hijiri SJIMOJIMA[1], Tomohiro KIMATA[4] and Shigeyuki MIYABAYASHI[1]
[1]Department of Regional Regeneration Science TOKYO UNIVERSITY OF AGRICULTURE, Japan, [2]Tohoku Nippon Ham Co., Japan; [3]TOKAI University, School of Tourism, Japan, [4]SATOYUME Co.Japan

ABSTRACT

In Japan, the development of resort towns in rural areas began during the Meiji period (1868-1912). Karuizawa Town in Nagano prefecture with a history of over 100 years has been the most prominent of these resort towns. In the 1850s, Japanese farm villages began facing challenges such as the weakening of local communities, and difficulties of continuing agricultural work because of shrinking and aging populations. On the other hand, due to the COVID-19 pandemic, agricultural towns have experienced increased popularity as people started relocating to the countryside or living in multiple locations. In this study, we conducted a literature review and an interview survey in Karuizawa, Nagano Prefecture, to shed light on the development of tourism in the postwar period, and to examine the impact of COVID-19 on resort areas and their relationship to the local economy, particularly agriculture. As a result, we have been able to confirm an increase in the town's population due to new residents moving in or increased long term stays in conjunction with working holidays and educational organizations. It also became clear that the population increase has led to a positive impact on the local economy for agricultural produce and a higher name recognition for local products..

Keywords: Tourism, Vila,Agricultural markets, COVID-19,Karuizawa

INTRODUCTION

The tourism industry has suffered a major economic blow from COVID-19 due to the government restrictions imposed on the movement and gathering of people. According to the UNWTO (World Tourism Organization), in 2020 the COVID-19 pandemic will result in a more than 70% year-on-year decline in international tourist arrivals which translates to 800 million to 1 billion fewer tourists worldwide and is also expected to result in a loss of 100 million jobs. In addition, in 2021, international tourism is expected to grow by a meagre 4%, significantly below pre-pandemic levels, and the recovery of the tourism industry is still expected to be sluggish[1].

On the other hand, the COVID-19 pandemic has led to an increased interest in relocating to rural areas and people living in two separate locations in Japan (Tanaka, 2020) [2]. The UNWTO report also revealed the criteria that were important to tourists following the outbreak of COVID-19. They were the following: "safety and security", "price", and "location and brand"[3].

Considering the changes in tourists' preferences following COVID-19, discussions toward sustainable tourism have become more active, specifically towards "tourism that is responsive to the needs of visitors, the industry, the environment, and the communities that host them, while taking full account of current and future economic, social, and environmental impacts."

According to a review of studies on sustainable tourism from an environmental, social, and economic perspective, Miyagawa (2020) points out that in order to manage cultural landscapes, it may be necessary to balance the needs of communities and tourism[4]. Putu Hermawati (2019) analyzed the characteristics of individual and group tours to the island of Bali in order to model the chains and modes of tourism. His research helped the government create effective marketing strategies, draft regulations, innovate new technologies and provide infrastructure to better manage traffic[5]. Lily Soraya (2017) highlights the importance of the role and involvement of the government and private sector in marine ecotourism related to biodiversity conservation in the Celib Islands[6]. Gunawan Prayitno (2019) reports that the better the social capital in the community, the better the management of environmental tourism[7].

However, there are still only a few research reports discussing the state of sustainable tourism after COVID-19. Following the outbreak of the COVID-19 pandemic in Japan, rural villages have gained increased attention. Karuizawa Town in Nagano Prefecture is one of the leading vacation home areas in Japan with a history of more than a hundred years as a holiday resort. The number of new residents who moved here following the outbreak of the pandemic has been increasing. In addition, local industries based on agriculture have also become more active, and the town is now gaining attention as a model for a sustainable tourist destination.

Therefore, this study conducted a literature

review and interview surveys to clarify the development process of postwar tourism development in Karuizawa, Nagano Prefecture, and to examine the impact of COVID-19 on tourism in Karuizawa and its relationship to the local economy, particularly agriculture. Specifically, we identified the new demands of tourism in Karuizawa after COVID-19, the relationship with holiday home residents, and the impact of the agricultural market on the local economy.

METHOD

This study analyzes the characteristics of tourism development and holiday home development in Karuizawa during the period between 1950, when holiday homes and transportation networks were developed and 2020, the beginning of the COVID-19 pandemic. This study also examines the process and sustainability of these developments in the town of Karuizawa.

A literature survey was conducted concerning the changes in holiday home development and tourism development during the 1950 to 2020 period broken down into decades. In this literature survey, we researched the history of holiday home development and tourism development and the current state of the resort areas. We examined the changes in the number of households, infrastructure, and transportation[8] [9].

An interview survey was conducted on September 9, 2020, with the Karuizawa Tourist Association and the Tourism and Economy Division of the Karuizawa Town Hall regarding the current state of Karuizawa and the resort areas in the wake of the COVID-19 pandemic. Then, on November 1, 2021, another interview survey was conducted with the officials of the Karuizawa Town Agricultural Market regarding the state of post-COVID-19 use of the agricultural market.

RESEARCH AREA

Karuizawa Town, located on the eastern edge of Nagano Prefecture right next to Gunma Prefecture, is a highland town spread out on the southern slopes of Mount Asama (2,568 m above sea level) at an elevation of 900 to 1,000 m above sea level. Mount Asama, the symbol of Karuizawa Town, is a triple stratovolcano representative of Japanese volcanoes, that has repeatedly erupted every year until the 1960s.

The area's climate is cool, befitting a summer resort area, with an average annual temperature of around 8 degrees Celsius. Even in the summer, the average temperature remains around 20 degrees Celsius, and the maximum temperature rarely exceeds 30 degrees Celsius. Karuizawa is also known for its foggy summers. Fogs occur on an average of 120 days per year due to the influence of air currents approaching from the Kanto region. Annual precipitation is 1,000 to 1,500 mm, and the lowest temperature in the winter is nearly 15 degrees below zero, although snowfalls of 30 cm or more has rarely been recorded.

Karuizawa town lies on an important, historical land transportation route between the Sekisoku region and Nagano Prefecture, but over time it has transformed into a separate, summer resort area. The city is still in the process of being redeveloped.

The number of farm households, the size of the farmer population, and arable land in Karuizawa have decreased in all categories except for tree-planting. Comparing the total number of farm households (units) between 1990 and 2015, the number has decreased by about half. The number of full-time farming households first increased from 69 in 1990 to 72 in 2005, and then decreased to 57 in 2015. The number of farmers per farming operation has also decreased from 4 to 1, indicating a lack of successors. In terms of the farmer population, the number of farmers has decreased from 1,608 in 1995 to merely 331 in 2015. Clearly, the aging of farmers and lack of successors has been a central issue.

On the other hand, the Karuizawa Hotchi Farmers Market has become a tourist attraction drawing 262,315 visitors annually (as of March 2020). It was opened in 2016 as a retail sales center offering a variety of popular, fresh local vegetables, including brand-name vegetables marketed under the name "Karuizawa Kirishita Vegetables" (Fig.1)..

Karuizawa Town's development into a resort area began in 1888 when Canadian missionary A.C. Shaw built a villa on Mt. Otsuka in the older area of Karuizawa (Kyu Karuizawa). The first Japanese vacation home was built there by Yujiro Hatta in 1893. Later, in the early Taisho period (1912-1926), with the inflow of private-sector real estate capital, development and subdivision of the area began. In the beginning, Kyu Karuizawa was the center of the villa area, but development gradually moved southward and westward, expanding the area in size which has continued to this day.

Fig.1 The Karuizawa Hotchi Farmers Market

THE CHARACTERISTICS OF TOURISM DEVELOPMENT AND HOLIDAY HOME

DEVELOPMENT IN KARUIZAWA

Japan's period of rapid economic growth after WWII (1950-1973)

During this period, along with the development of large-scale golf courses and ski resorts, Karuizawa experienced a rapid boost in popularity as a location for vacation homes for high-income earners and as a summer resort, with an increase in the number of summer homes and entertainment facilities built in the surrounding areas. During this development of vacation homes, private companies also developed areas to the north and south of the main town. In those areas, the Karuizawa Cultural Association and the Karuizawa Oiwakekai residential communities were established. In terms of tourism policies, the Karuizawa Town Nature Preservation Measures Outline was issued, establishing strict standards for the land area, floor-area ratios, and building-to-land ratios.

Period of stable growth (1974-1986)

Reflecting the "100 million people leisure boom", cultural facilities such as art museums and libraries were opened one after another, and the establishment of facilities where people could experience nature has also greatly increased. The development of holiday homes however resulted in conflicts between vacation home owners, permanent residents, and the local government. Frustration among local residents also grew due to rising land prices caused by the purchases of land for investment purposes.

Bubble economy period (1986-1991)

During this period, there was a holiday home boom, but unlike with other tourist destinations, there was no largescale development in tourism. It was mostly limited to the establishment of sports facilities and outdoor experience facilities. In terms of vacation home development, there was no development financed by private capital, but rather small-scale weekend home development and a gradual increase in the number of permanent residents.

Low-growth period (1992-2000)

This period is characterized by a stable and growing number of tourists due to the development of a new high-speed transportation network and the establishment of an enormous outlet mall, which has suddenly brought the area closer to the metropolitan area. In addition, although there have been no significant large-scale holiday home developments, the area has transformed into a shopping-oriented tourist destination in addition to an experience-oriented and nature-oriented tourist destination. There were few vacation home developments during this period, and what we can see here is predominantly long-term use of the villas.

Negative growth period (2001-2019)

This period is defined as a negative economic growth period because real disposable income was negative. This era can be characterized by the lack of major development and the town's active promotion of community development policies. In addition, vacation home development increased slightly during this period. Although the total number of holiday homes has continued to increase, the number of permanent homes has declined once again due to the sluggish growth in national income.

Trends of villas in Karuizawa Town in the COVID-19 Pandemic

According to our interview survey, there were various challenges and prospects faced by the Karuizawa area during the COVID-19 pandemic. The first is the growing need for vacation home sites. There was a tendency for residents who owned properties at two or more locations to move permanently to their vacation homes in Karuizawa Town beginning March 2021. The push towards teleworking has led to more spaces in the region allowing for telework and to an increase in the number of hotels and cottages that offer telework opportunities as a business. As a result of these trends, we can see a marked increase in land prices for vacation homes.

INTERVIEW SURVEY OF THE KARUIZAWA TOWN REGARDING THE STATE OF POST-COVID-19

The business concept of the Hotchi Farmers Market

Even though the Karuizawa area has long been a tourist destination, the Karuizawa Minami area has remained a primarily agricultural one. In 2002, residents requested from the town of Karuizawa to set up a tourist-type farmers' market facility. In 2014, the Karuizawa Town Office began plans to build the Hotchi Farmers Market.

The main objective of Hotchi Farmers Market was to promote Karuizawa's food culture. The idea was to make Hotchi Farmers Market not only a direct sales outlet, but also a place to promote Karuizawa's food culture. The concept of Hotchi Farmers Market is to function not just as a direct sales venue for the purpose of purchasing groceries like in a supermarket, but to serve as a physical space where people can gather. It offers facilities such as a sub-conference room, and provides space to various tenants such as several restaurants of Karuizawa, aiming to run a direct sales venue where people can not only shop, but enjoy their stay.

Number of customers at the Hotchi Farmers Market

The number of customers in April 2016, when the park opened was about 7,000, but in May it reached 20,000, showing a significant increase during consecutive holidays and other events. The highest number of visitors in each year was in August, most likely due to the summer vacation season and other long-term vacations. For the six-month period from May to November, the number of visitors recorded was over 20,000 per month, while the number of visitors in winter trended down. The number of users was on an increasing trend from 2016, the year of opening to 2018, but the number of users decreased due to the COVID-19 pandemic. Nevertheless, the number of users is expected to recover in 2021.

The Hotchi Farmers Market conducts regular vehicle license plate number checks. Accordingly, 90% of the vehicles had license plates from outside the prefecture, 20% of which were villa residents. In addition, the results of a customer surveys, which were conducted about once every four months, revealed that many tourists from Yokohama and other areas use the Ken-O Expressway, the Higashi-Kanto Expressway, and the Kan-Etsu Expressway.

Number of customers at the Hotchi Farmers Market

The number of customers in April 2016, when the park opened was about 7,000, but in May it reached 20,000, showing a significant increase during consecutive holidays and other events. The highest number of visitors in each year was in August, most likely due to the summer vacation season and other long-term vacations. For the six-month period from May to November, the number of visitors recorded was over 20,000 per month, while the number of visitors in winter trended down. The number of users was on an increasing trend from 2016, the year of opening to 2018, but the number of users decreased due to the COVID-19 pandemic. Nevertheless, the number of users is expected to recover in 2021.

The Hotchi Farmers Market conducts regular vehicle license plate number checks. Accordingly, 90% of the vehicles had license plates from outside the prefecture, 20% of which were villa residents. In addition, the results of a customer surveys, which were conducted about once every four months, revealed that many tourists from other areas use the Higashi-KantoExpressway,the Kan-Etsu Expressway.

Table 1 Number of visitors in Hocchi Farmaers Markket [9]

	2019 fiscal year	2020 fiscal year	2021 fiscal year
January	5,594	2,751	5,747
February	7,555	7,081	5,919
March	10,501	10,740	8,975
April	16,470	7,522	14,967
May	27,166	—	21,491
June	22,710	19,900	19,988
July	30,748	25,491	30,241
August	49,819	41,643	39,668
September	36,434	31,753	30,578
October	23,540	29,103	31,284
November	21,791	22,666	23,962
December	9,987	9,155	11,163
Total aomount	262,315	207,805	243,983

Characteristics of farmers who have stalls in the Hotchi Farmers Market

The Hotchi Farmers Market has a Karuizawa direct sales management committee, and farmers are members of this organization. There are two membership organizations: farm product producing members and souvenir/processed goods producing members. The designated manager selects the businesses for the fairs and the processed goods to be sold, which are managed in cooperation with the direct sales center.

About 60% of the 226 members of the Karuizawa direct sales center were local farmers of Karuizawa. There are some cases where the family members lived separately, such as when the wife and children were JA (Japan Agricultural Cooperation Agency) members and the husband is a member of the Hotchi Farmers Market. The average Karuizawa direct sales shop management committee member is in their late 70s. These previously retired farmers grow their produce as a hobby or to earn additional income.

The designated manager focuses on side dishes and processed foods when selecting farmers. Some of the members are farmers who have acquired qualifications for producing processed food items, such as jams, side dishes, and other processed products. Some members deliver both farm produce and processed food items.

Agricultural products and local brands sold at the Hotchi Farmers Market

The vegetables produced in Karuizawa and sold directly by the Hotchi Farmers Market are marketed as "Karuizawa Kirishita Vegetables". During the summer, when the temperature rises, Karuizawa's highland plateau produces fog in the morning, and thanks to the humidity, the highland vegetables grow without their surface drying out, which leads to the vegetables' softness and sweetness. This is the reason behind the name "Karuizawa Fog Vegetables". "Karuizawa Kirishita Vegetables" is the brand name personally registered by one of the current representatives of Hatsuchi Farmers Market. Therefore, only products sold at Hotchi Farmers Market can use the brand name Karuizawa Kirishita Vegetable. This brand name has helped raise awareness for the Hotchi Farmers Market and made it popular, especially among holiday home residents.

Typical vegetables sold at the Hotchi Farmers Market are cabbage, lettuce, Chinese cabbage, corn, and spinach. The number of cabbages grown under the fog shipped each morning is two to three hundred with more cabbages added during the peak season. The unsold produce for sale was 1 percent of the total shipment, which means it was almost completely sold out. According to interviews with the Hotchi Farmers Market, one of the reasons for the sell-out is that there are many repeat customers who are holiday home residents.

In addition, Hotchi Farmers Market tries to sell vegetables of high quality and freshness. For example, the direct sales staff checks the freshness of vegetables that have short shelf lives like eggplants and cucumbers when placing them on the store shelves. Farmers use a so called "Post System," in which they ship before opening and sales data for the morning is sent to their cell phones so that they can reship around noon. Highly motivated farmers may even visit the store to monitor the situation on the sales floor to determine their course of action for the afternoon.

Holiday home residents and THE IMPACT OF THE COVID-19 PANDEMIC

The users of Hotchi Farmers Market include few permanent residents, many of them are the vacation home residents. Therefore, the employees of Hotchi Farmers Market have made efforts to become acquainted with the holiday home users, and often ask these users directly about their requests. For example, holiday home residents often find the road to the Tsuruya Karuizawa supermarket heavily congested during the summer. For this reason, they requested that the Hotchi Farmers Market store carry regular daily food items such as olive oil. Therefore, as a new idea at the store additional supplementary cooking ingredients, such as dressings and pasta have been placed near the vegetables, allowing customers to purchase all ingredients necessary for cooking one stop at the Hotchi Farmers Market. By responding to the requests of villa residents in such a way, the store was able to see an increased number of customers.

Since the Hotchi Farmers Market facility is a close contact environment, it was treated equally to general supermarkets by the government in May 2020 when the state of emergency was declared, so the decision was made to temporarily close the store. Afterwards however, the company decided not to close the store, even when the state of emergency was declared again, based on the view that the store should remain open while ensuring safety since it is a facility closely connected to people's lives and the environment of Karuizawa.

As of March 2022, the number of visitors was 12,000, up 111% from the previous year. In addition, the average price per item purchased has also increased and total sales were up 131% from the previous year.

In the snacks and refreshments section, the upper section displays snacks and refreshments that are packaged in small bags and easy to eat by hand in the car, rather than the large boxes of local souvenirs typically displayed at direct sales venues of agricultural products. The local delicacies of Karuizawa, such as okowa also became popular among villa residents, and by 2021, after the Corona pandemic, sales at the side dish corner have reached 6 million to 10 million yen per month.

THE IMPACT OF THE COVID-19 PANDEMICON RESORT AREAS AND ITS RELEVANT TO AGRICULTURAL MARKETS

According to our interview survey, there were various challenges and prospects faced by the Karuizawa area during the COVID-19 pandemic. The first is the growing need for vacation home sites. There was a tendency for residents who owned properties at two or more locations to move permanently to their vacation homes in Karuizawa Town beginning March 2021. The push towards teleworking has led to more spaces in the region allowing for telework and to an increase in the number of hotels and cottages that offer telework opportunities as a business. As a result of these trends, we can see a marked increase in land prices for vacation homes.

The second trend is the newly transformed relationship between the local community and the vacation home residents as a result of the increase in the number of new residents moving to and settling down in the area. Following the outbreak of the COVID-19 pandemic and the push towards teleworking, the number of people moving out of the Tokyo Metropolitan area has increased. However, unlike in the case of the popular vacation home areas in the Hakone, Nasu, and Tateshina regions, the

residents of Karuizawa had formed unique communities in the vacation home areas, including the Karuizawa Association (1916), Karuizawa Minamihara Cultural Association (1932), Karuizawa Cultural Association (1953), and Karuizawa Cultural Association (1954), Karuizawa Oiwake-kai (1963), and Karuizawa Shirakaba-kai (2013). Unlike urban communities, these unique communities are places where people can enjoy entertainment, talk about business, share their values, and stimulate each other, which is one of Karuizawa's strengths.

Third, there is a growing demand for education, agriculture, and forestry as basic means of livelihood. The demand for education in Karuizawa is increasing due to the COVID-19 pandemic and the rising number of families moving to and settling down in the area. In particular, more and more businesspeople from the IT industry, mostly in their 30s and 40s are moving into the area bringing their families and children, further increasing the demand for schools. As an example, many parents in Karuizawa are enrolling their children into the Kazakoshi Gakuen, a private, integrated kindergarten, elementary, and middle school, and into United World College ISAK Japan, an international school.Table numbers and labels should be placed on top of the table, hanging by 12.5 mm, and left- and right-justified. Number the tables consecutively and locate them after and close to where they are first referenced. Leave at least one line space between the table, label and the text. Tables should be auto-fit to a single column or the whole width over two columns and no vertical lines or borders are needed.

Regarding agriculture, an increasing number of farmers are producing a wider variety of leafy vegetables in smaller quantities, growing for example not only regular lettuce, but also green curl lettuce and sunny lettuce. Furthermore, farmers are also beginning to grow rhubarb and other rare vegetables. While local residents tend to go to local, inexpensive supermarkets, the holiday home residents prefer to purchase fresh vegetables and fruits sold at the Karuizawa Hotchi Farmers Market which serves as a new source of motivation for the farmers to continue to work in agriculture. Karuizawa's agriculture and vegetables are gaining increased attention, and a project is underway to promote agriculture on the 19-hectare idle farmland in Karuizawa's southern district. There is also demand for agricultural employment from outside the prefecture, and it is expected that interest in and desire to work in agriculture among Karuizawa's vacation home residents and outsiders will increase even further.

In the forestry industry, Karuizawa Town has a lumberyard that aims to make effective use of harvested trees and recycled resources. Pruned branches are processed into chips, which are offered to people free of charge. Since holiday home residents spend about 400,000-500,000 yen per year on firewood, we believe that the demand for firewood will continue to increase in the future as well.

ACKNOWLEDGMENTS

This study was supported by the Town of Karuizawa and the Karuizawa Tourism Association. We are grateful to Dr. Yuichido Hirano, Forestry and Forest Products Research Institute, for helpful discussions. In addition, this research was partially carried out at Kakenhi 20H04442.

REFERENCES

[1] UNWTO., WORLD TOURISM BAROMETER, https://www.e-unwto.org/,2021

[2] Nobuhiko TANAKA.,A STUDY ON THE INFLUENCE WHICH COVID-19 BROUGT TO TOURISM AND ON THE WAY OF THE NEW TOURSIM IN JAPAN., Journal of the Japanese Institute of Landscape Architecture,2021,pp.246-249.

[3] UNWTO., TOURISM UNITED, RESILIENT AND DETERMINED, https://www.unwto.org/2021-a-year-in-review,2021

[4] Tomoko M, Sakura Y, Sayuri Y,Shinpei Y and Masahiro T.,CHARACTERISTICS OF CULTURAL LANDSCAPE IN THE GATEWAYTOWN OF KUDOYAMA, International Journal of GEOMATE Vol. 19, Issue76,2020, pp.1467-147

[5] Putu H, Sakti A. A, Muhammad I. R and Sumarni H.,CHOICES MODELS OF TRIP CHAIN AND TRANSPORTATION MODE FOR INTERNATIONAL TOURISTS IN TOURISM DESTINATION ISLAND, International Journal of GEOMATE, Vol. 66, Issue 55, 2019, pp. 195-203.

[6] Lily S, Eka P and Kuristiyanto., ROLE OF GOVERNMENT AND PRIVATE SECTOR IN MARINE ECOTOURISM RELATED TO CONSERVATION OF BIODIVERSITY IN SERIBU ISLANDS, International Journal of GEOMATE, Vol. 14, Issue 43, 2018, pp.140-147.

[7] Gunawan P, Nindya S, Ike K, Putri K,. SOCIAL CAPITAL IN POVERTY ALLEVIATION THROUGH PRO-POOR TOURISM CONCEPT IN SLUM AREA (CASE STUDY: KELURAHAN JODIPAN, MALANG CITY) . International Journal of GEOMATE, Vol. 16, Issue 55, 2019, pp.131-137.

[8] KARUIZAWA TOWN,. Karuizawa Town Directory, commemorating the 95th anniversary of the town's establishment. 2018, p.65

[9] KARUIZAWA TOWN,. The number of visitors of Hocchi Farmers Market, https://www.town.karuizawa.lg.jp/www/contents/1528425604611/simple/7.nougyou.pdf, 2021.1.13.

8th Int. Conf. on Structure, Engineering & Environment (SEE), Mie, Japan, Nov.10-12, 2022, ISBN: 978-4-909106094 C3051

SOCIAL COSTS BY OCCURRING ROADKILL OF AMAMI RABBIT IN KAGOSHIMA, JAPAN

Hideyuki Ito[1], Yosuke Imahashi[2] and Takahiro Fujii[3]
[1,3]Nihon University, Japan; [2] East Japan Railway Company, Japan

ABSTRACT

The Amami Oshima and Tokunoshima Islands in Kagoshima Prefecture, Japan are the main habitats of the endemic Amami rabbit (*Pentalagus furnessi*). As a result, it was listed as an endangered species on the Red List of the Ministry of the Environment, Japan. However, the Ministry of the Environment, Japan has implemented a mongoose control project on Amami Oshima, and both the population and habitat of the Amami rabbit have been increasing since around 2015. However, the number of traffic accidents involving Amami rabbit and vehicles has been increasing every year, and also recorded the worst ever record of 56 accidents in 2021. In addition, the United Nations Educational, Scientific and Cultural Organization (UNESCO) has pointed out the need to strengthen roadkill measures for the Amami Oshima Island in 2021, when the island is registered as a World Natural Heritage site. In this study, we estimated the economic value of Amami rabbit using the Contingent Valuation Method, and also estimated the social cost of roadkill. As the results, it was indicated that significant social economic losses have occurred due to roadkill outbreaks of the Amami rabbit.

Keywords: Roadkill, Contingent valuation method, Amami rabbit (Pentalagus furnessi), Social cost

INTRODUCTION

Amami Oshima Island in Japan is located in the ocean between the Kagoshima mainland and the Okinawa mainland and is rich in nature and biodiversity, and is home to manJPYdemic and rare species such as the Amami rabbit (*Pentalagus furnessi*) and the Lidth's jay (*Garrulus lidthi*), etc. It is recognized as a unique ecosystem, and on July 26, 2021, Amami Oshima and Tokunoshima were registered as a World Natural Heritage site together with the northern Okinawa Main Island and Iriomote Island were registered as "World Natural Heritage" together with the northern Okinawa Island and Iriomote Island.

The Amami Oshima and Tokunoshima Islands in Kagoshima Prefecture are the main habitats of the endemic Amami rabbit, but the introduction of mongooses in 1979 for the purpose of extermination of habu and other animals resulted in predation and a decline in both population numbers and habitat area. As a result, Amami Oshima was listed as Endangered on the Red List of the Ministry of the Environment. However, the Ministry of the Environment has implemented a mongoose control project on Amami Oshima, and both the population and habitat of the Amami rabbit have been increasing since around 2015.

However, the number of roadkills of Amami rabbit by vehicles running over them has been increasing every year, with Amami Oshima Island recording 50 road kills in 2020 and a record 56 road kills/year in 2021 [1]. Against this background, the United Nations Educational, Scientific and Cultural Organization (UNESCO) has pointed out the need to strengthen measures against roadkill by Amami rabbit and other animals in conjunction with the registration of Amami and Okinawa as World Heritage sites.

The purpose of this study is to estimate the economic value of the Amami rabbit in Amami Oshima using the Contingent Valuation Method (CVM) and to estimate the social costs of roadkill, and to show the importance of conservation of this animal.

LITERATURE REVIEW

The Ministry of the Environment, Japan [2] estimated the economic value of the Tsushima leopard cat (*Prionailurus bengalensis euptilurus*) conservation and propagation project to be about 52.7 billion JPY per year by estimating the Willingness To Pay (WTP) for the Tsushima leopard cat using CVM, assuming an increase in population due to the project.

Based on the occurrence of roadkill of Amami rabbit within Amami Oshima Island, Heijo et al. [3] found that road width may affect both the length of time animals stay on the road and the speed of vehicles, which in turn may induce roadkill.

Ito et al. [4] estimated the social external costs of accidents between Ezo sika deer (*Cervus nippon yesoensis*) and vehicles in Hokkaido using CVM, and found that 62.9% of the external costs were caused by Ezo sika deer running over and killing animals, which accounted for a high proportion of the total costs.

The Research Institute for Global Environmental

Strategies et al. [5] estimated the value of wildlife conservation in the Yanbaru region of Okinawa Prefecture using CVM, and found that the WTP per household was 772 JPY. They also conducted a selection experiment and found that the marginal willingness-to-pay for increasing the protected area of forest by one square kilometer is 2.9 JPY per household per year, the marginal willingness-to-pay for increasing the number of Yanbaru rail birds (*Hypotaenidia okinawae*) by one bird is 1.0 JPY, and it was estimated to be 2,423 JPY for special protection to avoid extinction of the Yanbaru long-armed scarab beetle.

Mitsui and Kubo [6] found that the highest BWS (Best-Worst Scaling) rating of the respondents' preference for the use rules in Kanehakubara, a virgin forest in the Amami Islands National Park, was "Mandatory guided tours," followed by "Shuttle buses," "Limit the number of people," and "Raise money for cooperation. The second highest BWS was "shuttle buses," followed by "limiting the number of visitors," and "asking for cooperation money. The results revealed that "free use" was the least desirable option.

Sasaki et al. [7] used CVM to estimate social losses caused by raccoons in Hokkaido, including ecosystem destruction, damage to the living environment, and infectious disease damage. The results indicated that the WTP was 153.3 JPY per household per month, which represents an annual loss of approximately 5.04 billion JPY in whole Hokkaido.

Qiu and Hashimoto [8] conducted an economic evaluation analysis of the tourism value of Amami Oshima Island using the travel cost method, and found that the portion of tourism services generated annually that corresponds to public recreation services is equivalent to about 10 billion JPY when evaluated in terms of consumer surplus. The result shows that the portion of the public recreation services generated every year is equivalent to about 10 billion JPY.

Kurt and Peter [9] examined the method of calculating the value of deer in deer-vehicle collisions. From the viewpoint of economics, they stated that most of the values of deer estimated in previous researches were basically expenditure indicators, not economic values, and suggested using consumer surplus or net WTP as a measure of deer value.

Previous studies have been conducted on various endangered species using CVM to calculate economic values and to estimate the social costs of roadkill. However, there is a few studies, and no studies have been conducted on the Amami rabbit.

SUMMARY OF AMAMI RABBIT

The Amami rabbit (Fig.1) is endemic only to Amami Oshima and Tokunoshima Island in Kagoshima Prefecture, Japan. It is designated as a special natural monument of Japan, a domestic rare wild animal and plant species, and an endangered species on the Ministry of the Environment's Red List of Threatened Species IB. In the past, the Amami Oshima Amami rabbit could be seen in almost all areas of the island. However, in 1979, mongooses and habu were released into Naze, Amami City, for the purpose of exterminating bear rats, and the number of mongooses continued to increase and their habitat expanded. In 2005, mongooses were designated as "Specified Invasive Alien Species" under the Invasive Alien Species Act, and extermination began in earnest, and the number of Amami rabbit inhabitants and their habitat area have been increasing since around 2015.

On the other hand, the number of roadkill incidents by Amami rabbit has been increasing every year, with Amami Oshima Island recording the worst ever record of 56 incidents/year in 2021. Amami rabbit is nocturnal, acting from nightfall to morning, and has a habit of defecating in open areas to avoid predators2) . In addition, their black body color and small body size make them less visible to drivers. For these reasons, roadkill is likely to occur. Also. Roadkill occurs throughout the year, but tends to occur more frequently in fall and winter, which coincide with the breeding season of the Amami rabbit as shown in Fig.2.

Fig. 1 Amami rabbit

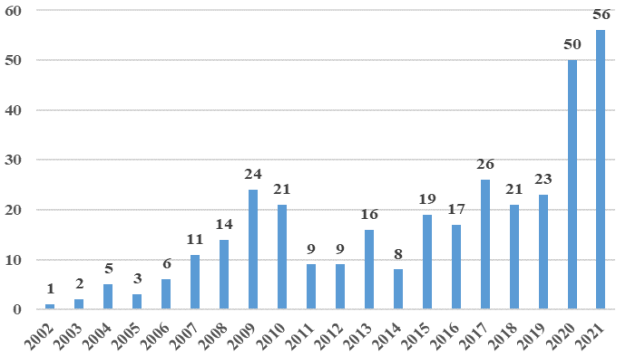

Fig. 2 Number of road kills on Amami Oshima

ESTIMATION OF SOCIAL COST BY ROADKILL OF AMAMI RABBIT USING CVM

Outline of Questionnaire Survey

To estimate the social costs of roadkill by the Amami rabbit, a web-based survey using Rakuten Insight company was conducted on December 22-24, 2021, targeting Rakuten Insight members aged 20-79 living in whole Japan (47 prefectures). The survey was conducted from December 22 to 24, 2021, and 1,500 samples (500 samples x 3 patterns) were obtained.

At the beginning of the questionnaire, we used charts and photographs to explain the survey and the current status of the Amami rabbit in order to give respondents an accurate understanding of the survey and the current status of the Amami rabbit. In the middle part of the questionnaire, we explained the utilization of the Amami rabbit and the status of roadkill occurrence. At the end of the questionnaire, questions were asked to confirm the level of understanding of the questionnaire content. The reason for this was to ensure that only those samples who correctly understood the content of the questionnaire were extracted for analysis. Questions asking about WTP for Amami rabbit conservation and questions asking about personal attributes were then asked. As a result, out of the 1,500 samples collected, 1,041 samples were used in the analysis.

In the question asking about the WTP for Amami Oshima roadkill conservation, it was assumed that in order to reduce the number of roadkills to zero on road segments where roadkills occur frequently on Amami Oshima, measures would be implemented to prevent roadkills by installing Amami Oshima roadkill prevention fences and warning signs and by installing speed humps in the road. We explained a scenario in which a nature conservation organization would solicit donations from the Japanese public only once to implement these measures, and asked the WTP in a two-step, dichotomous-choice approach as shown in Table 1.

We explained a scenario in which a conservation group would solicit donations from the Japanese public only once to implement these measures, and asked the WTP in double-bounded Dichotomous Choice. The initial amounts to be offered were set at 20 JPY, 40 JPY, and 60 JPY, and a scope response test was conducted by offering amounts for one, five, and ten Amami rabbits. Then, in order to eliminate resistant responses, "respondents who answered that they were unwilling to pay in all questions" were asked why they were against the payment.

Finally, to conduct an analysis of factors influencing WTP for Amami rabbit conservation, we asked about personal attributes. We asked respondents about their "awareness of protecting the natural environment and living creatures," "frequency of participation in activities to protect the natural environment and living creatures," "awareness of the term 'Amami rabbit," "awareness of the term 'roadkill,'" "awareness of the term 'over tourism,'" "car driving license possession status," "awareness of making trips to Have you ever visited Amami Oshima Island?", "Have you ever seen an Amami rabbit in the wild?," "occupation," "annual household income," "gender," and "age," respectively.

Table. 1 Amount offered for each pattern

	1 Amami rabbit		5 Amami rabbits		10 Amami rabbits	
	Initial offer	Second offer	Initial offer	Second offer	Initial offer	Second offer
Patter 1	40 JPY	YES 80 JPY No 20 JPY	300 JPY	YES 600 JPY No 150 JPY	200 JPY	YES 500 JPY No 100 JPY
Patter 2	20 JPY	YES 50 JPY No 10 JPY	300 JPY	YES 400 JPY No 100 JPY	600 JPY	YES 1,200 JPY No 300 JPY
Patter 3	60 JPY	YES 120 JPY No 30 JPY	100 JPY	YES 250 JPY No 50 JPY	400 JPY	YES 800 JPY No 200 JPY

Results of the Survey

The results of the questionnaire survey, in which 1,041 samples were collected, showed that 816 samples (78%) were in favor of respondents paying donations for roadkill control, with the most common reason given as "because I want to protect the endangered Amami rabbit," at 60.5%. This was followed by "because I think it is good to pay for something useful in the world" and "because I think it is important for society to protect the life of the Amami Owl Rabbit," at 21.6% and 11.9%, respectively. In all questions, 225 samples (22%) disagreed with the respondent's decision to pay the donation. Of the samples that were opposed, the most common response was "because I can't make a decision based on this information," at 44.4%. This was followed by 32.9% who were against the system of collecting money through donations.

Regarding the respondents' awareness of the importance of protecting the natural environment and living creatures, "agree" was the most common response, at 46.7% of the sample. This was followed

by "very much so" at 41.0% and "neither" at 10.3%.

Regarding the frequency of respondents' participation in activities to protect the natural environment and living creatures, the largest number of respondents (75.8%) answered that they "have never participated at all. This was followed by 14.3% who answered, "I do not participate now, but I have participated in the past," and 6.8% who answered, "I participate occasionally (a few times a year). The percentage of respondents who had visited Amami Oshima was 6.0%, and 43.9% of the respondents "knew" the name of the Amami rabbit, 22.6% had "heard only the word," and 33.5% "did not know.

Elimination of Resistance Responses

In some cases, respondents do not respond to the willingness-to-pay question because they compare the utility of implementing roadkill measures with the utility of not implementing roadkill measures. There are also resistant responses, in which the respondent does not respond "no payment" because of resistance to the scenario presented in the survey form or to the way the willingness-to-pay amount is collected. There are also cases in which respondents respond to the amount of willingness to pay because they value something other than the effects realized by the roadkill measure, or they agree to pay even though they do not value the implementation of the roadkill measure. In such cases, there is a risk that the willingness to pay may be overstated, and that an appropriate willingness to pay may not be obtained. Therefore, it is necessary to eliminate from the analysis the data of respondents who do not fully understand the questionnaire in an appropriate manner. In this survey, a total of 39 samples (29 samples that answered "Because I think it is inevitable if others also pay" as the reason for agreeing with the 809 samples that agreed with paying the donation and 10 samples from "other free statements" were excluded as resistant responses.

In the reasons for opposition to the 225 samples that opposed paying donations, a total of 193 samples (74 samples responded "I am opposed to the system of collecting money through donations," 100 samples responded "I cannot make a decision based on this information," and 19 samples from "other free statements") were excluded as resistant responses to estimate the WTP. The most common reasons given as opposition were "Taxpayers should pay for the conservation of the Amami Rabbit, not donations," and "The population of the Amami Rabbit is increasing.

WTP Results for Conservation of Amami Rabbit

The WTP to Amami rabbit conservation was estimated based on 809 samples after eliminating resistance responses from the 1,500 samples obtained. The estimation was performed using "CVM in Excel Version 4.0" provided by Kuriyama [10]. The Weibull survival distribution was applied to estimate a non-discrimination curve, and the median and mean values were calculated to estimate the WTP of the Amami rabbit. The WTP estimated for one, five, and ten Amami rabbit are shown in Fig. 3, Fig. 4, and Fig. 5, respectively.

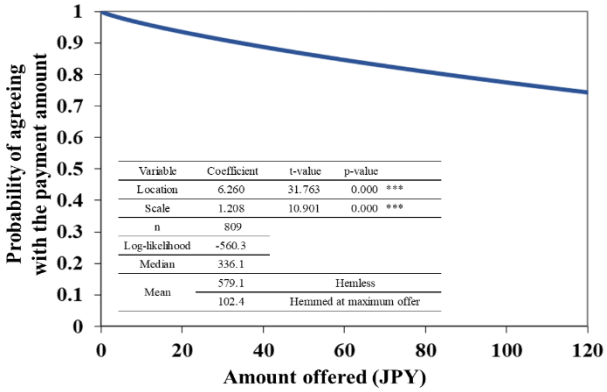

Fig. 3 Estimated WTP for 1 Amami rabbit

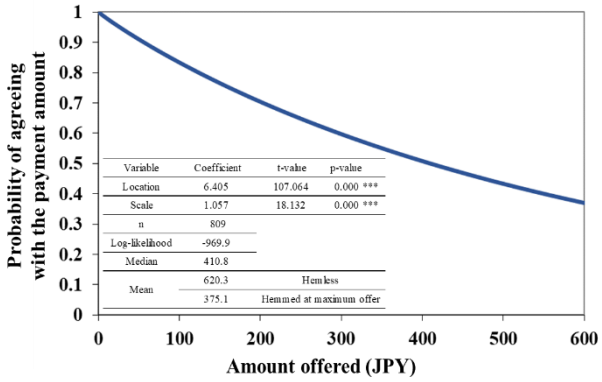

Fig. 4 Estimated WTP for 5 Amami rabbits

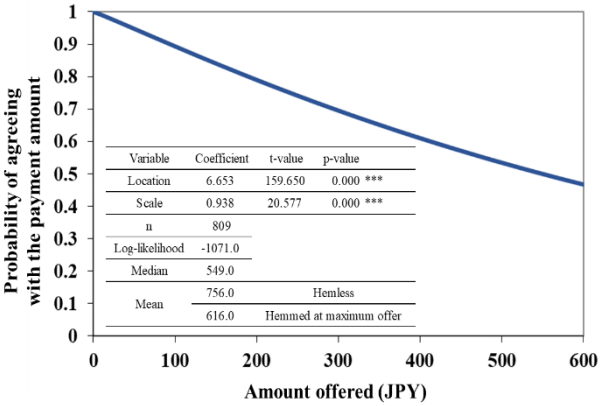

Fig. 5 Estimated WTP for 10 Amami rabbits

The estimated results of the WTP for the conservation of Amami rabbit for each number of animals are shown in Table.2. Therefore, in this study, the WTP for Amami rabbit conservation was estimated at 54.9 JPY/household, which was calculated by converting the median value per 10 animals, which showed the lowest value, into per animal (Table.2).

Table. 2 Amount offered for each pattern

WTP	1 Amami rabbit	5 Amami rabbit	10 Amami rabbit
Median	336 JPY/household	411 JPY/household (82.2 JPY per rabbit/household)	549 JPY/household (54.9 JPY per rabbit/household)
Average	102 JPY/household	375 JPY/household (75.0 JPY per rabbit/household)	616 JPY/household (61.6 JPY per rabbit/household)

Results of Social Cost by Roadkill of Amami Rabbit

The estimated WTP value was multiplied by the number of households in Japan (57,378,423 households) [11] and the number of roadkill cases of Amami Oshima by Amami rabbit in 2021 (56 cases), resulting in an estimated social cost of 176.04 billion JPY due to roadkill cases of Amami Oshima in 2021. The social cost of roadkill by Amami rabbit in 2021 was estimated at 176.04 billion JPY. The social cost due to roadkill by Amami Oshima hare (341 cases) during the 22 years from 2000 to 2021, when data were recorded, was estimated to be 1.07 trillion JPY.

In this study, Amami Oshima, the main habitat of the Amami rabbit, was targeted. But, using the WTP (54.9 JPY/household) for Amami rabbit conservation estimated in this study, the social loss for Tokunoshima and the Amami rabbit as a whole was also estimated using the same method. In Tokunoshima, 17 cases of roadkill of Amami rabbit were estimated to have occurred in 2021, resulting in a social loss of 53.6 billion JPY. The social cost of roadkill by Amami rabbit (95 cases) in Tokunoshima during the 22 years from 2000 to 2021, when records are available, was estimated to be 299.3 billion JPY.

The total number of roadkill by Amami Oshima and Tokunoshima in 2021 was 73, and the social cost was estimated to be 230.0 billion JPY. The social cost of roadkill by Amami rabbit (436 cases) during the 22-year period from 2000 to 2021, when records are available, was estimated to be 1.40 trillion JPY. Table.3 shows the social cost of roadkill by Amami rabbit.

Table. 3 Social costs by roadkill of Amami rabbit

	Evaluation period	Number of roadkills	Social cost
Amami Oshima	2021	56	176.04 billion JPY
	Total since 2000	341	1.07 trillion JPY
Tokunoshima	2021	17	53.6 billion JPY
	Total since 2000	95	299.3 billion JPY
Total	2021	73	230.0 billion JPY
	Total since 2000	436	1.40 trillion JPY

Analysis of Factors Affecting WTP

Factors influencing WTP for Amami rabbit conservation were analyzed based on the personal attributes obtained from the questionnaire. The following items were analyzed in the full log-linear logit model: "frequency of participation in activities to protect the natural environment and living creatures," "awareness of the term 'Amami rabbit'," "awareness of the term 'roadkill'," "awareness of overtourism," "car driving license ownership," "awareness of traveling," "have you visited Amami Oshima Island? ". Table 4 shows the results of the analysis of factors affecting WTP.

The results of the analysis showed that the three variables that met the 10% level of significance were "awareness of protecting the natural environment and living creatures," "awareness of the term 'Amami rabbit,'" and "awareness of the term 'roadkill'". Thus, the results indicated that WTP may be higher in the case of respondents who had these factors.

1) Those with high "awareness of the protection of the natural environment and living creatures" had a high awareness of the protection of living creatures and felt that the protection of the Amami rabbit was also important, which is thought to have resulted in a higher WTP.

2) Those with high "awareness of the term 'Amami rabbit'" had prior knowledge of the situation of the Amami rabbit and felt the need to conserve it, and thus their WTP was higher.

3) Those with high "awareness of the word roadkill" had some knowledge of traffic accidents between wild animals and vehicles, and the proportion of those who wanted to save wild animals from roadkill was also higher than that of the group with low awareness. Therefore, the proportion of people who wanted to save the Amami rabbit from roadkill would also be higher, which would have resulted in a higher WTP.

Table. 4 Results of analysis of factors affecting WTP

Variables	Coefficient	t-value	p-value	
Constant	4.352	7.147	0.000	***
ln(Bid)	-1.629	-20.508	0.000	***
Awareness of the natural environment and biological conservation (1: Not at all disagree - 5: Agree very much)	0.956	8.703	0.000	***
Frequency of participation in activities to protect the natural environment and living organisms (1: Not participating at all - 5: Participating frequently)	0.231	2.528	0.012	**
Awareness of the term "Amami rabbit" (1: Don't know - 3: Know)	0.246	3.002	0.003	***
Awareness of the term "Roadkill" (1: Don't know - 3: Know)	0.261	2.596	0.010	***
Age	0.106	2.388	0.017	**
n	809			
log-likelihood	-996.768			

CONCLUSION

In this study, we estimated the WTP for Amami rabbit conservation using CVM and estimated the social costs of Amami rabbit roadkill occurrence. The results indicated that the occurrence of roadkill by Amami rabbit has caused significant social losses. Therefore, it can be said that measures to prevent roadkill of the Amami rabbit should be implemented as soon as possible. However, the CVM used in this study requires further study to determine the appropriate number of exposed populations, since the social costs vary depending on the number of exposed population.

In addition, as a future issue, roadkill of endangered amphibian species, such as the Amami ishikawa frog (*Odorrana splendida*) and the Otton's frog (*Babina subaspera*), which are endemic to Amami Oshima and are listed as endangered in red data book of the Ministry of the Environment, Japan, is also occurring frequently. It is considered necessary to estimate the social costs of roadkill of these species.

REFERENCES

[1] Ministry of the Environment, Elucidation of the cause of death of rare mammals in Amami Oshima and Tokunoshima in 2021 https://kyushu.env.go.jp/okinawa/pre_2022/2021.html (last access: July 2, 2022)

[2] Ministry of the Environment, Results of the economic value evaluation of the Tsushima leopard cat conservation and propagation project by CVM, https://www.biodic.go.jp/biodiversity/activity/policy/valuation/pdf/t1_03-2_140311.pdf (last access: July 2, 2022)

[3] T. Hiragi, Y. Kimoto and C. Iwamoto, Road-kills of the Amami rabbit Pentalagus furnessi on Amami-Ohshima Island from April 2007 to March 2017, Mammalian science, Vol.57, No.2, 2017, pp.249-255.

[4] H. Ito, M. Wada and T. Fujii, EXTERNAL COSTS CAUSED BY HOKKAIDO SIKA DEER-VEHICLE COLLISIONS IN HOKKAIDO, JAPAN, Proceedings of 7th International Conference on Structure, Engineering & Environment, 2021, pp.328-334.

[5] Institute for Global Environmental Strategies, Kyoto Univ., Nagasaki Univ. and Nagoya Univ., 2011 Policy Research on Environmental Economy Research on policy options for sustainable use of ecosystem services through internalization of economic values Final Research Report, http://www.env.go.jp/policy/keizai_portal/F_research/f-09-03.pdf (last access: July 2, 2022)

[6] S. Mitsui and T. Kubo, Visitors' Evaluation of Management Rules in Amami Oshima "Kinsakubaru Native Forest": Application of Best-Worst Scaling, Journal of Forest Economics, Vol.64, No.3, 2018, pp.1-7.

[7] T. Sasaki, H. Nakamura and S. Suzuki, Estimation of Social Losses caused by Raccoon based on CVM, Annual Report of the Hokkaido Branch of the Civil Engineering Society, Paper No. 72. 2015. http://library.jsce.or.jp/jsce/open/00057/2016/72-D-0003.pdf (last access: July 2, 2022)

[8] C. Qiu and Y. Hashimoto, A Travel Cost Analysisof the Recreation Value of Amami Oshima, Journal of Japan Institute of Tourism Research, The Tourism Studies Quarterly , Vol.16, No. 1, 2003, pp.1-8.

[9] Kurt A. Schwabe and Peter W. Schuhmann, Deer-Vehicle Collisions and Deer Value: An Analysis of Competing Literatures, Wildlife Society Bulletin, Vo.30, No.2, 2002, pp.609-615.

[10] K. Kuriyama, CVM in Excel, Version 4.0, http://kkuri.eco.coocan.jp/research/introtxt/index.html (last access: July 2, 2022)

[11] Ministry of Internal Affairs and Communications HP: Population, Demographics and Number of Households based on the Basic Resident Ledger as of January 1, 2021 https://www.soumu.go.jp/main_sosiki/jichi_gyousei/daityo/jinkou_jinkoudoutai-setaisuu.html (last access: July 2, 2022)

8th Int. Conf. on Structure, Engineering & Environment (SEE), Mie, Japan, Nov.10-12, 2022, ISBN: 978-4-909106094 C3051

IMPUTATION OF OUTLIERS AND MISSING VALUES FOR ACTIVATED SLUDGE DISSOLVED OXYGEN DATABASE USING MULTIVARIATE IMPUTATION BY CHAINED EQUATIONS (MICE)

Hatem Nijim[1]and Rabee Rustum[2]
[1,2]Department of Civil Engineering, Heriot-Watt University, United Arab Emirates

ABSTRACT

Activated sludge process (ASP) is the most widely used process in wastewater treatment plants. The concentration of dissolved oxygen (DO) is a crucial controlling parameter in this process as the DO affects the efficiency of the treatment, operational cost, and system sustainability. While Field electrodes measure DO, maintaining regular and accurate records remains a challenge, even in the absence of aggressive climate conditions. Most of the DO probes are sensitive and require careful maintenance and calibration that may lead to non-accurate data recording. This paper discussed the validity of statistical models to impute missing DO values. Multivariate Imputation by Chained Equations (MICE) is used in R programming language to predict missing values and replace outliers in the DO measurements. The performance of this technique was very good as the correlation ranges between 0.999 and 0.821 when the missing values range from 1 to 15 % (424 to 6,360 of total data of 42,420). The method is highly effective and ready to be used for many other applications. Kohonen Self Organising Map (KSOM) is applied as an alternative model to verify the accuracy of the MICE.

Keywords: Activated sludge process; Dissolved Oxygen (DO); Multiple Imputations; Chained Equations

INTRODUCTION

The concentration of dissolved oxygen (DO) is a key variable in water resource recovery facilities [1]. DO is monitored to ensure oxygen is sufficient for aquatic species to survive [2]. In wastewater treatment, dissolved oxygen monitoring in aeration tanks in the activated sludge process is essential as it significantly impacts the efficiency of the treatment process.

There are two methods to measure the DO concentrations: Winkler titration method [3]. Or oxygen electrode sensors [1]. DO sensors are the most accurate method; however, instrumental errors are inevitable, and a certain procedure should be followed to obtain reliable data [4].

When the DO concentration levels are reduced, the number of filamentous microorganisms increases, which subsequently impacts the ability of the activated sludge to settle. If DO levels continue to decrease, effluent turbidity increases, and treatment will be reduced rapidly [5].

This study was based on Seafield wastewater treatment plant data in Edinburgh, UK. The Seafield wastewater treatment plant (WWTP) is the largest WWTP in Scotland and treats more than 300 million litres of wastewater per day. The main areas of Seafield WWTP Comprise of Eight sedimentation tanks with a volume of 9260 m^3, Eight final settlements tanks with a volume of 3974 m^3, and five rectangular aeration lanes. Data of DO values in these five lanes are used in this paper.

METHODOLGY

Outlier Detection

Data values with magnitudes that differ significantly from the majority of other data values are known as outliers. There are many possible reasons for outliers. Commonly, human errors such as errors in transferring the data or a fault in handling the measuring sensors can lead to unintentional outliers [6].

Identifying the outliers from the data sets and replacing them so the model will create more uniform sets of data, and accordingly, the results for the model performance will be more accurate. A Z-score test was used to identify the outliers. A Z-score test in Eq. 1 and 2 are used to obtain a Z-score [6].

$$z_i = \frac{(x_i - \bar{x})}{s} \quad (1)$$

$$s = \sqrt{\frac{\sum_{i=1}^{n}(x_i - \bar{x})^2}{n-1}} \quad (2)$$

Where

x_i Observed DO value,

$\bar{x}$ Mean for all observed DO,

S Standard deviation,

N sample size (total number of the data).

As per the Z-score equation, the z-score is 3.5 < Z < -3.5. The values beyond this range should be marked as an outlier and considered as missing values to be imputed by the models later.

Missing Data

Missing data are two types, ignorable and non-ignorable [7].

1- Ignorable Missing Data are two types:
   a. Missing Data Completely at Random (MCAR): they occur randomly, meaning the value of the missing and observed data is independent.
   b. Missing at Random (MAR): The value of the missing data and observed data might be dependent.

2- Non-Ignorable Missing Data: If the missing data are not at random (MNAR), then they are considered non-ignorable. The MNAR are when the value of the unobserved variable itself predicts missingness [8].

Multiple Imputations

The concept of Multiple Imputation (MI) uses the distribution of the observed data to estimate and predict a set of the possible values for the missing data. With MI, the missing values are replaced by many different values, and accordingly, many different full data sets are performed. Complete data sets will be created by multiple imputations, and these sets should slightly differ. The final step of the MI is to pool out from these imputed steps one complete data set as a final result [9].

Multivariate Imputation By Chained Equations (MICE)

Multivariate imputation by chained equations (MICE), also known as Sequential Regression Imputation [10]. It is a practical approach for imputing missing datasets based on a set of imputation models. MICE is a chain of equations used to impute missing values and is fully conditional. The missing values are imputed one by one. For example, in a data set $Y_1, Y_2, Y_3, \ldots\ldots, Y_{10}$, if Y_1 is a missing value, MICE will use the information from all other variables $Y_2, Y_3, \ldots\ldots, Y_{10}$, and the same procedure will be repeated for all missing values. The imputed values are modified by adding a residual error which can be added directly to the imputed values or to the parameters estimates of the MICE model. The residual error will improve the sampling variability to the imputations [11]. MICE assumes that missing data are missing at random[12]. MICE procedure is provided in many software, such as SPSS, STATS and S-Plus [13]. However, the most common software is R [11].

Kohonen Self-Organizing Map (KSOM)

KOSM is a nonlinear classification technique able to recognise a specific group from a complex data set [6]. The KSOM has been used in various research fields, as discussed in [6] [14]. KSOM converts the input signal pattern of complex data into a two-dimensional map. The tuned input pattern are shown as clusters where similar patterns are shown in the same output neurons or with its adjacent one; these clusters reduce the amount of huge data, and accordingly, the relationship between higher-dimensional data will be in lower dimension [6]. The KOSM consists of two layers, the input layer, and output layer, the layers are composed of neurons, and both layers are connected with a weight vector. The input layer consists of multi-dimensional layers, and the output layer consists of two-dimensional layers made of neurons. A specific dimensional weight vector represents each neuron in the two-dimensional map. Similar neurons are located together, and neurons which are not similar will be further apart. Map size varies depending on the number of neurons; the number of neurons affects the accuracy of KOSM. More details on the theory and application of the KSOM can be found in [6][15][16].

RESULTS AND DISCUSSION

Results for the predicted values of the dissolved oxygen by MICE and KOSM are compared with the observed one. The accuracy of the predicted values was evaluated by three statistical parameters namely the Correlation Coefficient R, the mean square error (MSE), and the Average Absolute Error AAE [6].

Figure 1 illustrates the component planes for the Kohonen self-organising map (KSOM) for all lanes when missing values are 15%; these planes visually show the relationship between DO values for each lane. As shown, lanes 1,2 and 3 are slightly correlated, and lanes 4 and 5 are less correlated. The more correlated vectors between each other lanes indicate better results.

Table 1 shows the results for MICE, and KOSM when 1 % up to 75 % of data are missing. The table summarises the results as an average for the five lanes. The values for R, MSE, and AAE almost have the same values for MICE and KOSM. The performance of the models is very good when 15%of DO data are missing, . The R values for MICE and KOSM are 0.884 and 0.919, the MSE is 0.308 and 0.211, the AAE is 0.158 and 0.124.

CONCLUSION

The performance of MICE is excellent when the missing data are 10% or less, very good performance when the missing data is between 10% and 15%, good performance when the missing data is between 15% and 20%, and poor performance when the missing data more than 20%. KSOM was used as an alternative model to validate the MICE results. KSOM is applied in previous case studies, and

therefore, KSOM results which are similar to MICE results, emphasise MICE application to predict the missing values.

LIMITATIONS AND RECOMMENDATIONS FOR MICE

Data quality is the major factor which will affect the accuracy of the predicted values. Replacing the outlier will improve the accuracy however if the outliers are more than 10% of the overall data, the accuracy of the predicted values after replacing the outliers will not be improved.

MICE can be applied regardless of the type of missing data. However, better performance for MICE when the missing data is MAR. The number of imputations affects the accuracy of the predicted values; 5 to 10 imputations are the default number of imputations; however, for the data with a big variance, more imputations should be applied. Increasing the number of imputations may have an impact on the software speed; delay is expected when the number of imputations is more than10.

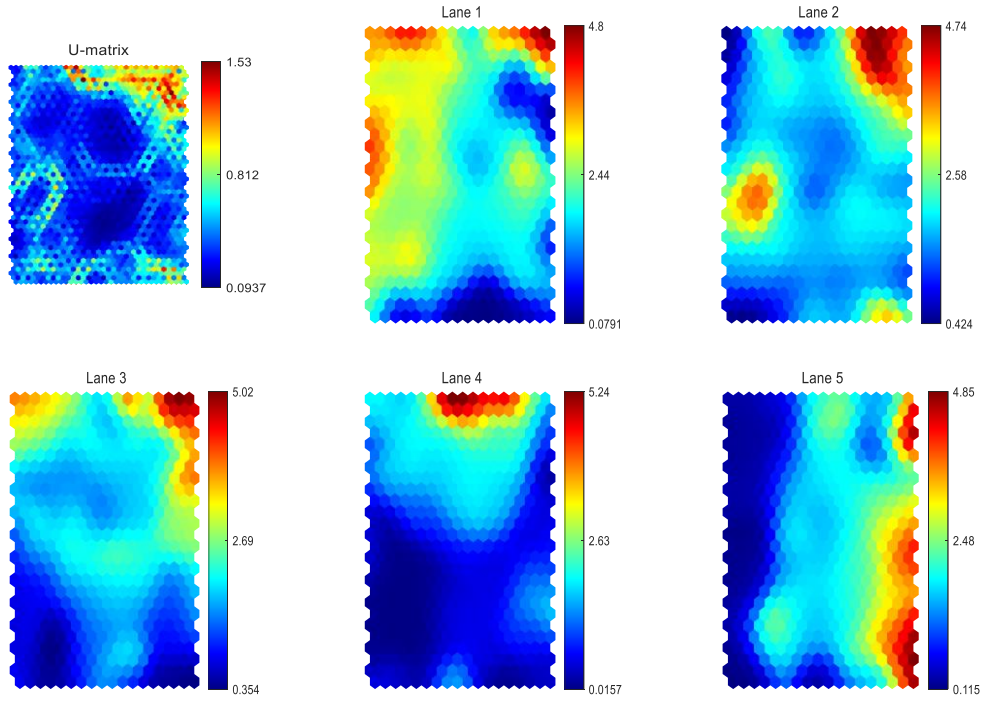

Figure 1 The component planes of the KSOM for all lanes when missing values are 15%

Table 1 Summary of Statistical values for MICE and KOSM performance

Percentage Of Missing Date	Results when Dates are Missing			
	Mice		KOSM	
	Statistical Parameters	Value	Statistical Parameters	Value
Results when 1% of Dates are Missing	R	0.994	R	0.997
	MSE	0.015	MSE	0.009
	AAE	0.009	AAE	0.007
Results when 5 % of Dates are Missing	R	0.96	R	0.975
	MSE	0.107	MSE	0.066
	AAE	0.054	AAE	0.039
Results when 10% of Dates are Missing	R	0.929	R	0.948
	MSE	0.21	MSE	0.136
	AAE	0.108	AAE	0.081
Results when 15% of Dates are Missing	R	0.884	R	0.919
	MSE	0.308	MSE	0.211
	AAE	0.158	AAE	0.124
Results when 20% of Dates are Missing	R	0.837	R	0.884
	MSE	0.435	MSE	0.302

	AAE	0.221	AAE	0.173
	R	0.837	R	0.794
Results when 30% of Dates are Missing	MSE	0.435	MSE	0.506
	AAE	0.221	AAE	0.305
	R	0.633	R	0.686
Results when 40% of Dates are Missing	MSE	0.945	MSE	0.729
	AAE	0.469	AAE	0.422
	R	0.63	R	0.791
Results when 50% of Dates are Missing	MSE	1.16	MSE	0.512
	AAE	0.599	AAE	0.389
	R	0.519	R	0.689
Results when 60% of Dates are Missing	MSE	1.538	MSE	0.739
	AAE	0.752	AAE	0.506
	R	0.235	R	0.291
Results when 75% of Dates are Missing	MSE	1.687	MSE	1.339
	AAE	0.864	AAE	0.782

REFERENCES

[1] Samuelsson, O., 2021. Sensor Fault Detection and Process Monitoring in Water Resource Recovery Facilities (Doctoral dissertation, Acta Universitatis Upsaliensis).

[2] Holenda, B., Domokos, E., Redey, A. and Fazakas, J., 2008. Dissolved oxygen control of the activated sludge wastewater treatment process using model predictive control. Computers & Chemical.

[3] Winkler, L.W., 1888. The determination of dissolved oxygen in water. Berlin DeutChem Gas, 21, pp.2843-2855.

[4] Wei, Y., Jiao, Y., An, D., Li, D., Li, W. and Wei, Q., 2019. Review of dissolved oxygen detection technology: From laboratory analysis to online intelligent detection. Sensors, 19(18), p.3995.

[5] Rustum, R., 2009. Modelling activated sludge wastewater treatment plants using artificial intelligence techniques (fuzzy logic and neural networks) (Doctoral dissertation, Heriot-Watt University).

[6] Rustum, R., Adeloye, A. and Simala, A., 2007. Kohonen self-organising map (KSOM) extracted features for enhancing MLP-ANN prediction models of BOD5. In International Symposium: Quantification and Reduction of Predictive Uncertainty for Sustainable Water Resources Management-24th General Assembly of the International Union of Geodesy and Geophysics (IUGG) (pp. 181-187).

[7] Rubin, D.B., 1987. Statistical analysis with missing data.

[8] Bouhlila, D.S. and Sellaouti, F., 2013. Multiple imputation using chained equations for missing data in TIMSS: a case study. Large-scale Assessments in Education, 1(1), pp.1-33.

[9] Harel, O. and Zhou, X.H., 2007. Multiple imputation: review of theory, implementation and software. Statistics in medicine, 26(16), pp.3057-3077.

[10] Van Buuren, S. and Groothuis-Oudshoorn, K., 2011. mice: Multivariate imputation by chained equations in R. Journal of statistical software, 45, pp.1-67.

[11] Zhang, Z., 2016. Multiple imputation with multivariate imputation by chained equation (MICE) package. Annals of translational medicine, 4(2).

[12] Ratolojanahary, R., Ngouna, R.H., Medjaher, K., Junca-Bourié, J., Dauriac, F. and Sebilo, M., 2019. Model selection to improve multiple imputation for handling high rate missingness in a water quality dataset. Expert Systems with Applications, 131, pp.299-307.

[13] Azur, M.J., Stuart, E.A., Frangakis, C. and Leaf, P.J., 2011. Multiple imputation by chained equations: what is it and how does it work?. International journal of methods in psychiatric research, 20(1), pp.40-49.

[14] Rustum, R. and Adeloye, A.J., 2007. Replacing outliers and missing values from activated sludge data using Kohonen self-organising map. Journal of Environmental Engineering, 133(9), pp.909-916.

[15] Kumar, N., Rustum, R., Shankar, V. and Adeloye, A.J., 2021. Self-organising map estimator for the crop water stress index. Computers and Electronics in Agriculture, 187, p.106232.

[16] Kumar, N., Shankar, V., Rustum, R. and Adeloye, A.J., 2021. Evaluating the performance of self-organizing maps to estimate well-watered canopy temperature for calculating crop water stress index in Indian mustard (Brassica Juncea). Journal of Irrigation and Drainage Eng, 147(2), p.0402004

THE EFFECT OF *FLEXIBLE WORKING ARRANGEMENT* AND *WORK LIFE BALANCE* ON EMPLOYEE PRODUCTIVITY IN GOVERNMENT OFFICES IN BEKASI CITY, WEST JAVA

Beti Nurbaiti[1], Waluyo[2] and Dwi Setyowati[3]

[1]Universitas Bhayangkara, Indonesia; [2]Aidhub Services; [3]Universitas Bhayangkara, Indonesia

ABSTRACT

The purpose of this study is to analyze the effect of Flexible Working Arrangement (FWA) and Work Life Balanced (WLB) on Employee Productivity in the City Government (Pemkot) of Bekasi, West Java. The approach used is a quantitative method using a survey questionnaire from primary data of 151 employees, at the Bekasi City Government, West Java during April 1 – May 30, 2022. The research equation is in the form of structural research (SEM) which is processed using Lisrel software. The results show that there is a significant positive relationship between FWA and WLB, as well as a negative relationship significant difference between WLB and PROD. This finding shows that the implementation of FWA during the COVID-19 pandemic in the Bekasi City Government of West Java has a positive impact on WLB, but does not necessarily increase employee productivity in the Bekasi City Government. The presence of employees is still required at the Bekasi City Government office as a place for community services and activities, even though they take turns because of the prokes during the pandemic. So it can be concluded that the application of flexible work from home is not effective if fully enforced in the office on employee productivity.

Keywords: Flexible Working Arrangement; Work Life Balance; Productivity; SEM

I. INTRODUCTION

The COVID-19 pandemic over the past 2 years has had a significant impact on people's lives in all parts of the world on economic conditions, as well as social, cultural, and daily activities. Social life has turned into face-to-face remotely by utilizing technology (*zoom, google meet, whatsapp*, and other social media *platforms).* On the one hand, the pandemic of giving is considered a disaster, but on the other hand, it creates a virtual communication technology that is more flexible without time and place limits. The ferocity of this flu mutation has forced many people to stay at home using digital technology with various policies/regulations. The Bekasi City Government has also implemented a policy of Enforcement of Community Activity Restrictions (PPKM) for both its employees and the local community, where the regulation continues the previous policy, namely Large-Scale Social Restrictions (PSBB) to break the chain of spread of the COVID-19 virus. However, it is necessary to study further whether the concept of flexible work or *Flexible Working Arrangement (FWA) is* in line with the concept of work *life balance* (WLB) and has an impact on employee productivity. To analyze these three variables, the authors conducted a study by taking saturated samples of all employees with the status of the government employee the Bina Marga dan Sumber Daya Air (BMSDA) Bekasi City.

II. LITERATURE REVIEW

2.1. Flexible Working Arrangement

COVID-19 pandemic has changed the behavior pattern of a person with a flexible work system that is not limited by time and place with the use of technology (Ko & Kim, 2018). Work flexibility offers employees a balance between their professional and personal lives, which leads to job satisfaction and high performance and overall improvement of the organization (Sethi & Saini, 2020). Work flexibility is very important, and with digital advancements and technological advancements, employees can continue their work anywhere they want, as long as they have an internet connection (Davidescu et al, 2020). Flexible working hours and home-based remote work are added values, (Dilmaghani, 2021).

There are three reasons why work-life measures that focus on flexibility can prevent employees from leaving the company: *First*, employees feel that the leader or company cares about the need for reconciliation and work-life balance. *Second,* flexibility measures imply greater autonomy with respect to employees' working time and workplace. *Third,* flexible work patterns are applied depending on the size of the company, generally the larger the size of the company, the more attractive flexible work systems are because of clear remuneration according to output (Marx et al, 2021).

There are several advantages obtained from FWA as expressed by FGD respondents, namely: a) Flexible time; b) work and family life balance; c) freedom to choose a comfortable workplace; d) safety and security; e) company budget savings for facilities and utilities; f) develop trust among employees; and g) and developing a digital work environment (Hasan & Butt, 2021). The application

of flexible options to employees has potential benefits and this type of arrangement ensuring work-life balance for employees (Anya et al, 2021). It is hoped that employees of organizations that provide flexible working hours have a much higher turnover intention low, influenced by collective culture and norms in the workplace (Gašić & Berber, 2021).

2.2 Working Life Balance (WLB)

WLB is defined as a balance of individual life activities between work/professional and non-work activities, in order to enable individuals to have sufficient autonomy to meet the demands of their professional and personal duties. (Johnson & College, 2021).

WLB practices can be categorized as follows:

(1) Time reduction practices, allowing employees to voluntarily reduce the number of hours they work by working part time or sharing jobs, temporarily reducing their workload and salaries;

(2) The practice of flexible work arrangements, including all employer policies that allow employees to control flexibly without reducing their salary (Martines-Leon et al, 2019).

WLB emphasizes eliminating difficulties related to gender and employee welfare, especially for women. Employees need a meaningful balance between work and life in order to be productive and focus on both areas (Uddin & Khan, 2022) and (Martinez-Leon et al, 2019). WLB is necessary for people to find a match between their personal and professional lives. An employee can be better at managing personal and work commitments if the company has a good functional information system to reduce employee problems (Paje et al, 2020).

2.3 Productivity (PROD)

Productivity is the relationship between outputs (goods or services) and inputs (labor, materials, money). Productivity is a measure of productive efficiency. A comparison between the output and input. For work, workers prefer FWA so that they can benefit from increased productivity and efficiency (Ko & Kim, 2018). Productivity and skill development of employees can be increased by improving the working life of employees in the workplace through flexible work (Kumar & Verma, 2022).

Flexible Work Arrangements (Flextime, Flexplace and Compressed Workweek) have a positive impact on employee engagement and thus lead to increased productivity, financial performance, customer satisfaction, quality improvement (Gašić & Berber, 2021). The idea of work-life balance is focused on developing a positive work atmosphere that encourages and enables workers to maintain a balance between their professional and personal lives, thereby increasing productivity and employee loyalty (Anya et al, 2021).

This type of flexible work will increase productivity if employees can reduce stress, rest more and are happier, and more prosperousOf course, this condition has an impact on higher organizational outcomes in production and income (Martínez-León et al, 2019). Monitoring and management of employee work stress is emphasized because it is a factor that affects productivity. (Rachmawati et al, 2021). Adequate funding for flexible work is important so that it is right on target and produces high work productivity (Hoggart et al, 2021).

III. METHODS, HYPOTHESES, AND RESEARCH RESULTS

The research method used quantitative by taking a of the entire population of Bina Marga and Sumber Daya Air Kota Bekasi yang berjumlah 158 people, with data returned and ready to be processed from 151 people. The research equation using a structured model (*Structural Equation Modeling*/ SEM) was processed with Lisrel software (Asra et al, 2015). Statistical tests used in this study include: (1) model fit test, measuring the suitability of the data with the model; (2) validity test, measuring what the researcher wants to measure; and (3) reliability test, test instrument reliability, and (4) structural model test/hypothesis test (Wijanto, 2008).

According to Wijanto (2008) the GOFI indicator is sufficiently represented by 9 (nine) indicators, which are: RMSEA $\leq$ 0.080, NFI $\geq$ 0.90, NNFI $\geq$ 0.90, CFI $\geq$ 0.90, RFI $\geq$ 0.90, IFI $\geq$ 0.90, Standardized RMR $\leq$ 0.050, GFI $\geq$ 0.90, dan AGFI $\geq$ 0.90. GOFI dengan Degrees of Freedom = 0; Chi-Square = 0.0 P = 1.00): *The Model is Saturated, the Fit is Perfect* in other words the fit is very good. Good validity to the construct or latent variable if the *Standardized Loading Factor* (SLF) value $\geq$ 0.50. Measurement of reliability seen from the value of *Construct Reliability* (CR) $\geq$ 0.70 and *Variance Extracted Mesure* (VE) $\geq$ 0.50.

There are 2 (two) research hypotheses, namely:

Hypothesis 1 (H1): There is a significant relationship between Flexible Working Arrangement (FWA) and WA, also Work Life Balance (WLB)

Hypothesis 2 (H2): There is a significant relationship between Work Life Balance (WLB) and Productivity (PROD).

Table 3.1 Goodness of Fit, Validity, Reliability of Flexible Working Arrangement (FWA) Result

Questionnaire Number	Questionnaire Statement	SLF Value	Error	Validity Test Results	Reliability Test Results
FWA2	I work more effectively with flexible working hours.	0.82	0.29	Good Validity	CR Value = 0.86 VE Value = 0.52 Good Reliability
FWA7	Flexible working hours are assessed according to work safety and security standards.	0.79	0.38	Good Validity	
FWA3	I feel more comfortable with flexible working hours.	0.73	0.47	Good Validity	
FWA5	Flexible working hours allow me to do two or more jobs more than normal working hours.	0.69	0.53	Good Validity	
FWA6	Flexible working hours are able to create a balance between working and family time.	0.61	0.62	Good Validity	
FWA4	The company's policy of implementing flexible working hours has a positive impact on my work motivation.	0.60	0.64	Good Validity	
FWA1	My income has increased with flexible working hours.	0.59	0.65	Good Validity	
FWA9	Flexible working hours contributes in reducing conflicts between me and my colleagues.	0.56	0.69	Good Validity	
RMSEA = 0.00; NFI = 0.99; NNFI = 1.00; CFI = 1.00; IFI = 1.00, RFI = 0.97; Standardized RMR = 0.039; GFI = 0.98 and AGFI = 0.90					
Conclusion: all variables observed in the latent variable FWA have good validity and reliability.					

Source: processed by researchers (2022)

The results of the survey data processing in the table 3.1 shows that FWA is considered by employees to be more effective, safer because it avoids the spread of the covid-19 virus according to the results of research Kumar & Verma (2022) and Reard et al (2021, Martínez-León (2018). Respondents' perceptions indicate that employees minimize conflicts between colleagues and FWA, as well as increased income due to savings from transportation costs due to working more from home in line with findings from Nwagbara (2020) and Rachmawati (2021).

Table 3.2 Goodness of Fit, Validity, Reliability of Work Life Balance (WLB) Result

Questionnaire Number	Questionnaire Statement	SLF Value	Error	Validity Test Results	Reliability Test Results
WLB1	I am able to find a balance between work activities and family activities with the implementation of FWA.	0.9 3	0.14	Good Validity	CR Value = 0.91 VE Value = 0.60 Good Reliability
WLB 9	I am able to harmonize work time with family or personally as a result of implementing FWA.	0.87	0.24	Good Validity	
WLB 6	I find it easier to meet work targets with the FWA concept.	0.77	0.40	Good Validity	
WLB 7	I am more motivated to work with the FWA concept.	0.77	0.41	Good Validity	
WLB 5	With the FWA concept, I feel more comfortable working because I have more time with my family.	0.76	0.42	Good Validity	
WLB 4	With the FWA concept, I feel more comfortable working because I have more time for my personal life.	0.69	0.52	Good Validity	
WLB 8	I can complete my work anywhere because of the application of the FWA concept.	0.59	0.65	Good Validity	
RMSEA = 0.00; NFI = 1.00; NNFI = 1.00; CFI = 1.00; IFI = 1.00, RFI = 0.99; Standardized RMR = 0.020; GFI = 0.99 and AGFI = 0.93					
Conclusion: all variables observed in the latent variable WLB have good validity and reliability.					

Source: processed by researchers (2022)

Referring to the results of the WLB variable data processing in the table 3.2 it can be seen that employees think that the FWA work concept can harmonize work and home or family affairs. This condition is in line with research from Bartsch et al (2021) where in order for this balance to occur, a leader/supervisor needs to take conducive actions by: (1) involving employees in virtual team work; (2) give their employees the necessary autonomy and support and (3) adequate internet supporting facilities related to digital technology to maintain a high level of performance among employees. The balance of work and personal according to research conducted by Marx et al (2021).

Table 3.3 Goodness of Fit, Validity, Reliability of Productivity (PROD) Result

Questionnaire Number	Questionnaire Statement	SLF Value	Error	Validity Test Results	Reliability Test Results
PROD 6	The punctuality of completion of work by employees is better with the application of the FWA concept.	0.80	0.35	Good Validity	CR Value = 0.89 VE Value = 0.50 Good Reliability
PROD 4	The quality of employee work results is better with the implementation of FWA.	0.73	0.47	Good Validity	
PROD 10	The application of the FWA concept demands the achievement of higher targets.	0.72	0.48	Good Validity	
PROD 2	I have more autonomy in my work with FWA concept.	0.71	0.50	Good Validity	
PROD 5	Achievement of work targets by employees is better with the application of the FWA concept.	0.68	0.54	Good Validity	
PROD8	The level of employee independence is higher with the application of the FWA concept.	0.68	0.54	Good Validity	
PROD 9	The responsibility of superiors in supervising subordinates/staff is lighter with the application of the FWA concept.	0.67	0.55	Good Validity	
PROD 3	Employees are more responsible for completing work with the FWA concept.	0.65	0.58	Good Validity	
PROD 7	Companies benefit from saving organizational resources as a result of applying the FWA concept to their employees.	0.65	0.58	Good Validity	
RMSEA = 0.00; NFI = 1.00; NNFI = 1.00; CFI = 1.00; IFI = 1.00, RFI = 0.99; Standardized RMR = 0.018; GFI = 0.99 and AGFI = 0.96					
Conclusion: all variables observed in the latent variable PROD have good validity and reliability.					

Source: processed by researchers (2022)

The majority of government employees in the Bekasi City Government think that the completion of work is the most important thing compared to the implementation of FWA work itself. This finding is in line with previous research from Dilmaghani (2021). Employee independence increases with the implementation of FWA in the office, supported by supervision and the necessary technological devices such as research results from Paje et al (2020). Employees have more responsibility with the application of FWA, and this phenomenon is in line with the findings of Nwagbara (2020).

Table 3.4 Research Hypothesis Test

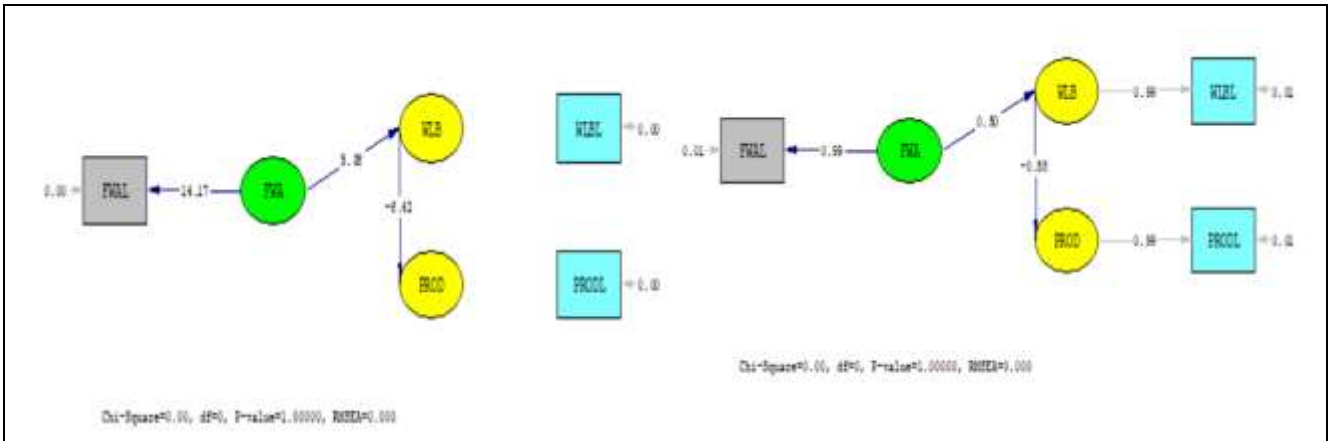

No	Questionnaire statement	T-Value	Coefficient Standard	Conclusion
1	H1: There is a significant relationship between the Flexible Working Arrangement (FWA) variable and the Work Life Balance (WLB).	5.38	0.50	Hypothesis 1 is accepted. There is a significant positive relationship between FWA and WLB.
2	H2: There is a significant relationship between the Work Life Balance (WLB) variable on Productivity (PROD).	- 6.42	- 0.58	Hypothesis 2 is accepted. There is a significant negative relationship between WLB and PROD.

Source: processed by the author (2022)

Based on the hypothesis test, it can be seen that both research hypotheses are accepted, where Hypothesis 1 answers that there is a positive relationship/correlation between the latent variable Flexible Working Arrangement (FWA) and Work Life Balance (WLB), or in other words, the higher the application of FWA, the better the WLB condition. Furthermore, hypothesis 2 answers that

there is a negative relationship/correlation between the latent variable Work Life Balance (WLB) and Productivity (PROD), or it can be concluded that a high WLB will reduce employees' PROD.

IV. DISCUSSION

The COVID-19 outbreak has an impact on work-life balance and employee job satisfaction. Employees who enjoy a favorable work-life balance tend to be more satisfied with their jobs. The positive impact that emerges from telecommuting reduces work-family conflict and improves well-being for employees, thus leading to positive outcomes such as increased performance and productivity. The supporting aspects of work-life balance signal to Bekasi City Government employees that they are valued by the organization, and employees feel included when the organization provides resources that meet employees' work-life balance needs. Work-life balance satisfaction is stronger among men and women without dependent children. The demands of work even if expressed in the realm of flexible work can interfere with domains of life, not just child-rearing responsibilities, such as health, friendships, and civic engagement. To overcome this in order to avoid work-family conflict requires more specific actions. Flexible work needs to be supported by bonuses and remuneration that are adjusted to the demands of the Bekasi City Government.

For the effective operation of the FWA, it is important not only to launch the flexible work program itself, but also to ensure that users are properly understood and evaluated fairly. Work-life programs such as flexible work arrangements, employee assistance programs, family and dependent care services, and health and wellness aim to provide a means for the workforce. This work system aims to meet performance expectations while managing their personal life needs and commitments, but the level of participation or response from the community can be negative.

However, not all types of flexible work arrangements are manageable or beneficial for all sizes and types of organizations. There are several things employers should consider what type of flexible scheduling will best suit their needs. On the other hand, previous research found a negative side that concerns all organizations, namely the lack of direct supervision of workers from their organizations during FWA can result in a decrease in intrinsic motivation and unethical behavior of these employees. In addition, flexible work can lead to work-family conflict as spouses need to multitask to take care of family responsibilities and work responsibilities at the same time. This is because flexible work arrangements can result in blurred boundaries between work and home roles leading to an increase in work and family conflicts. This is certainly a dilemma for organizations in implementing the FWA concept. Organizations offering FWAs should periodically assess whether employees find FWAs attractive and facilitate different circumstances of flexibility.

One's work-life balance must be measured and seen in the hope of providing a better future. The implementation of FWA must be balanced with the system so that employees are not trapped in a blurred time limit between work and personal or household. Most of the work done in developing countries related to the implementation of FWA creates family conflicts, especially for societies with a strong patriarchal culture. The main determinant of effective WLB implementation is HR policy that emphasizes a work-life balance culture. A flexible work system must be supported by good leadership. Leadership behaviors, particularly relationship-oriented leadership, can promote a supportive work environment and make it easier to cope with excessive work demands and establish appropriate boundaries between work and personal life. But on the other hand, if there is a state of excessive commitment to work (individual behavior) and high job demands, it will have a negative impact on the employee's life balance because of disturbed psychosocial factors.

The level of job flexibility does not necessarily have high flexibility. This is influenced by other factors such as functional flexibility, working time, and work space flexibility in increasing the level of satisfaction and work productivity of employees. WLB has an impact on organizational performance, productivity and sustainability. WLB is aligned with participatory human resource (HR) management, making it possible for mutual benefit (or win-win situation) for both employers and employees. This flexible working method will have a positive impact if the organization helps employees achieve more balance by offering various policies and initiatives that balance work and family pressures. One of the drawbacks of FWA is that the company may not be able to control every employee, and will not be able to see whether everyone is working or not, or whether they are productive. For this reason, work management is needed so that work stress does not occur, where this can trigger low productivity, illness and ineffectiveness of government employees in the Bekasi City Government.

V. CONCLUSION

The COVID-19 outbreak has affected the lives of individuals around the world, without any age limit and the type of work they are currently engaged in, including employees, so it can be concluded :

1) Flexible work began to be carried out as an adaptation to conditions during the pandemic due to restrictions on individual

movement out of the house to break the chain of the spread of the COVID-19 virus.
2) Employees will enjoy work-life balance if telecommuting reduces work-family conflict and increases welfare for employees, thereby increasing performance and productivity.
3) Flexible work needs to be supported by a flexible work environment, bonuses, and remuneration adapted to the demands of the Bekasi City Government work to avoid decreasing intrinsic motivation and employee unethical behavior.
4) The control function when implementing FWA needs to be arranged so that the performance of the Bekasi City Government can be maintained.

ACKNOWLEDGEMENTS

This research was supported by the Bekasi City Government, Bina Marga dan Sumber Daya Air (BMSDA) division's.

REFERENCES

[1] Anya, P. J., Adeniji, A. A., Salau, O. P., Balogun, O. M., Aribisala, S. O., & Ikeagbo, J. O. (2021). Examining employee engagement within the context of flexible work arrangement in Asian-owned Company in Lagos state. *Academy of Strategic Management Journal*, *20*(6), 1–12.

[2] Asra, A. d. (2015). *Sampling in Survey Research*. Jakarta: Rajawali. Pers.

[3] Davidescu, A. A. M., Apostu, S. A., Paul, A., & Casuneanu, I. (2020). Work flexibility, job satisfaction, and job performance among romanian employees-Implications for sustainable human resource management. *Sustainability (Switzerland)*, *12*(15). https://doi.org/10.3390/su12156086

[4] Dilmaghani, M. (2021). There is a time and a place for work: comparative evaluation of flexible work arrangements in Canada. *International Journal of Manpower*, *42*(1), 167–192. https://doi.org/10.1108/IJM-12-2019-0555

[5] Gašić, D., & Berber, N. (2021). The Influence of Flexible Work Arrangement on Employee Behavior During the COVID-19 Pandemic in the Republic of Serbia. *Management:Journal of Sustainable Business and Management Solutions in Emerging Economies*, *26*(3), 73–89. https://doi.org/10.7595/management.fon.2021.0026

[6] Hasan, T., Jawaad, M., & Butt, I. (2021). The influence of person–job fit, work–life balance, and work conditions on organizational commitment: Investigating the mediation of job satisfaction in the private sector of the emerging market. *Sustainability (Switzerland)*, *13*(12). https://doi.org/10.3390/su13126622

[7] Hoggarth, J. A., Batty, S., Bondura, V., Creamer, E., Ebert, C. E., Green-Mink, K., Kieffer, C. L., Miller, H., Ngonadi, C. V., Pilaar Birch, S. E., Pritchard, C., Vacca, K., Watkins, T. B., Zavodny, E., & Ventresca Miller, A. R. (2021). Impacts of the covid-19 pandemic on women and early career archaeologists. *Heritage*, *4*(3), 1681–1702. https://doi.org/10.3390/heritage4030093

[8] Ko, E. J., & Kim, S. S. (2018). Intention to use flexible work arrangements: The case of workers in Korea and gender differences in motivation. *Journal of Organizational Change Management*, *31*(7), 1438–1460. https://doi.org/10.1108/JOCM-01-2018-0001

[9] Kumar, I., Prakash, B., & Verma, J. K. (2022). *(QWL) OF BANK MANAGERS IN PUBLIC AND PRIVATE SECTOR BANKS IN BIHAR, INDIA : A*. *21*(1), 1–12.

[10] Martínez-León, I. M., Olmedo-Cifuentes, I., & Sanchez-Vidal, M. E. (2019). Relationship between availability of WLB practices and financial results. *Personnel Review*, *48*(4), 935–956. https://doi.org/10.1108/PR-12-2017-0402

[11] Marx, C. K., Reimann, M., & Diewald, M. (2021). Do work–life measures really matter? The impact of flexible working hours and home-based teleworking in preventing voluntary employee exits. *Social Sciences*, *10*(1), 1–22. https://doi.org/10.3390/socsci10010009

[12] Nwagbara, U. (2020).gh Exploring how institutions shape managerialist employment relations and work-life balance (WLB) challenges in Nigeria. *Employee Relations*, *42*(6), 1401–1421. https://doi.org/10.1108/ER-07-2019-0269

[13] Paje, R. C., Escobar, P. B. A., Ruaya, A. M. R., Sulit, P. A. F., & Paje, R. C. (2020). The Impact of Compressed Workweek Arrangements on Job Stress, Work-Life Balance, and Work Productivity of Rank-And-File Employees from Different Industries in Metro Manila. *Journal of Physics: Conference Series*, *1529*(3), 1–8. https://doi.org/10.1088/1742-6596/1529/3/032055

[14] Renard, K., Cornu, F., Emery, Y., & Giauque, D. (2021). The impact of new ways of working on organizations and employees: A systematic review of literature. *Administrative Sciences*, *11*(2). https://doi.org/10.3390/admsci11020038

[15] Sethi, G. K., & Saini, N. K. (2020). COVID-19: Opinions and challenges of school teachers on work from home. *Asian Journal of Nursing Education and Research*, *10*(4), 532–536. https://doi.org/10.5958/2349-2996.2020.00115.9

[16] Wijanto, S. H. (2008). Structural Equation Modeling dengan Lisrel 8.8. Graha Ilmu.

8th Int. Conf. on Structure, Engineering & Environment (SEE), Mie, Japan, Nov.10-12, 2022, ISBN: 978-4-909106094 C3051

ACOUSTIC EMISSION OF INTERNAL DRAINAGE IN MULTI-STOREY BUILDINGS

Anaebo Chike Emmanuel[1], Rabee Rustum[2,*], Lynne B Jack[3] and Adebayo J. Adeloye[4]

[1] Heriot-Watt University, Dubai Campus; UAE
[2] Heriot-Watt University, Dubai Campus; UAE
[3] Heriot-Watt University, Edinburgh Campus, UK
[4] Heriot-Watt University, Edinburgh Campus, UK

ABSTRACT

The number of multi-story buildings continues to increase around the world, and as a result, the quality of life for those people living in these buildings requires ongoing evaluation. Many residents of multi-story buildings complain about noise disturbances from internal drainage systems, mostly from toilets flushing in the upper levels. This paper seeks to establish whether or not the noise from internal drainage systems in multi-story buildings affects daily human activity and sleep patterns. A survey was undertaken on a 6-storey building and used a sound level meter to measure noise levels on different floors in the building. The results showed that the building height does not influence the noise, nor does the noise affect human activity and sleep patterns, principally because the noise does not last longer than a few seconds, with a typical duration of 15 seconds or less.

Keywords: Multi-storey building; Acoustics Emissions; Drainage; Flow.

INTRODUCTION

Multi-story buildings have seen a significant rise in number in recent years. Starting from around the middle of the 20th Century, the growth rate in their numbers has been considerable, particularly in cities in Asia and Europe. In developed cities across the globe, multi-story buildings are often the main feature of urbanisation[1]. Multi-story buildings also bring economic implications as they often increase the cost of buying land. In addition, they can also add aesthetic value and can influence the lifestyle of people living in and around these developments)[2].

However, modern structures must offer their residents comfort, of which curbing sound emissions is one significant aspect [3]. Unfortunately, sound emissions can be found in buildings where proper provisions have not been made to tackle such problems. Sound emissions in multi-storey buildings can come from, for example, floor impact noise, neighbours, and electronic and elevator equipment. In addition, it is not uncommon that emissions in new buildings arise from the plumbing systems. And while noise from sanitary facilities is not peculiar to multi-storey buildings, it is essential to tackle this problem as multi-story buildings are home to a large number of residents. Over time, occupants living with plumbing noise problems realise that such noises can be irritating during the day and can interfere with sleep at night[4].

In the construction industry, there is a range of materials that possess high sound insulation properties; in particular, studies show that multiple walled pipes can significantly reduce sound emissions[5]. Another method of reducing noise in pipes involves using sound insulation materials. Although these different materials can be tested and the material properties compared [6], there is no evidence that noise emissions have been completely eliminated in most buildings.

The research reported herein has reported the acoustic emissions generated from internal drainage systems in multi-floor occupancy buildings. In addition, a questionnaire has been circulated to understand the effects, if any, of noise from drainage on sleep behaviour and premature awakening and to gather subjective responses from residents. This study is an experimental one, looking at a 5-story building and focusing on the effect of sound transmission on occupants. Acoustic measurements were made to gain an understanding of the extent of transmission that might affect occupants' well-being. Thus, the work has been done so as to help propose a systematic approach to reducing sound emissions during the design and installation stages. Hence the goal is to ascertain the level of sound emissions from multi-storey building sanitary facilities and how best to properly mitigate any adverse effects by identifying suitable sound-insulation material. Information on methods and materials are presented along with detail on data collection techniques, followed by the main results and recommendations for future research.

REVIEW OF THE LITERATURE

From the beginning of civilisation, tall structures have fascinated humankind. This dates back to 2600 BC, when the Egyptian pyramids were constructed and are still regarded as one of the seven wonders of the ancient world [7]. Currently, the tallest building in the world is the Burj Khalifa, located in Dubai in the United Arab Emirates, standing at 828m tall [8].

However, multi-storey buildings require modern technology to aid their function, part of which is the provision of sanitary facilities for the removal of wastewater.

Sound emission from drainage

Sound is generated in pipes due to solid, gaseous, and liquid waste transport. Sound waves can travel through elastic mediums and liquid and various solid materials [9,10]. The majority of audible frequencies range between 20 and 20,000 Hz. Humans hear sound best between 1,000 and 5,000 Hz [11].

Audible ranges are divided into 10-octave bands, representing specific frequency spectrums. These range from 16,000 Hz to 31.5 Hz and sometimes are separated into third-octave bands for accuracy. If 500 Hz is taken as a medium frequency, its low and high frequencies will range between 300 Hz and 750 Hz, respectively. Hence, the knowledge of the third-octave bands aids the overall calculation of sound level[12].

Burk et al. (2011)[13] stated that an A-weighting is applied to sound measurements that consider the relative sound perceived by the human ear, recognising the ear's sensitivity to low audio frequencies, particularly below 1,000 Hz, with B-, C- and Z-weightings used to measure very low, medium and very high frequencies. Ray (2010) [14] also noted that a minor change in the decibel reading leads to a significant change in the sound produced, which has an impact on what the person hears. The NIH (2014) [15] pointed out that the duration of exposure to certain sounds is a significant factor in the amount of pleasure or discomfort experienced by the listener. Thus, humans should limit their exposure time to certain sounds beyond 85 dB, and for every 3 dB beyond 85 dB, the exposure time should be cut by half to avoid permanent hearing damage.

The average sound level in dwellings is typically around 25 dB, with 60 dB being the norm for offices, depending on the activity and overall quality. This results in noise rating (NR) curves for background noise evaluation as reported by Ref. [16].

Causes of noise in the drainage system

Causes of noise in drainage systems include water hammers, impact noises on bends and tees, flow noises, and falling solid matter noise. When the water closet, WC, is flushed, noise emissions are typically transmitted via connected structures. While a degree of noise within the room housing the sanitary facility is usually deemed acceptable, consequent sound in surrounding apartments is undesirable, and measures should be taken to prevent this[11]. In addition, water hammers can lead to the unwanted movement of improperly attached pipes, causing vibrations, noise and, in some cases, the loosening of joints and fittings [17]. Flow impact on bends and tees designed can also lead to noise, horizontal movement of sewage leads to flow noise as vertical movement leads to falling noise[18].

Transmission of noise in the building

Sound is transmitted through a building by air and solid-borne pathways. Structure-borne transmission involves sound emissions through solid materials and is regarded as the main noise path. Noise can also convert from one form to another, e.g. from structure-borne to airborne and vice versa. According to BS 8233: 2014[19], two stages of plumbing noise should be considered during the design and construction stages. Porous materials tend to absorb the sound of middle to high frequencies based on their thickness. Typical materials are:

- Hard finish: Plaster on a solid backing,
- Porous absorber: 50 mm mineral fibre 50 kg/m^3,
- Panel absorber: 9 mm ply, 50 mm cavity containing 25 mm mineral fibre,
- Perforated panel: 14% perforations, 25 mm cavity containing mineral fibre,
- Perforated gypsum tiles/board, 16% perforations, suspended with 200 mm plenum.

METHODOLOGY

The two major pieces of equipment required for this analysis are the Nor140 sound analyser and the calibrator. The Nor140 sound analyser is a precision handheld device used to record sound and monitor building acoustics in real-time. The calibrator is inserted within the microphone cartridge of the sound level meter.

Acoustic emission measurements

Measurements were collected from a 6-storey student residence with modern engineering design and technology. Each floor has the same layout from top to bottom, with each room having a toilet with a bathtub, WC and a washbasin. Care was taken to ensure that the faucets in the bathtub and washbasins were turned off, and there was no ongoing plumbing activity in the building before the test was carried out.

The Nor140 sound analysing device was placed on the ground floor, and the water closet was flushed on the 5th, 4th, 3rd, 2nd and 1st floors in turn and the results were recorded on the ground floor. This was repeated for each floor. The sound pressure level measurements were made using 1/3 octave bands because this produces more precise results. These were then converted to octave bands so as to make comparisons with required standards. Equation 1 aids in calculating the sound pressure level for different

octave [20].

$$L\boldsymbol{p} = 10 \log \left(\mathbf{10}^{\frac{L_1}{10}} + \mathbf{10}^{\frac{L_2}{10}} + \mathbf{10}^{\frac{L_3}{10}} + \ldots\ldots + \mathbf{10}^{\frac{L_n}{10}} \right) \quad (1)$$

Questionnaire

A series of questions were drafted for the purpose of understanding the effect of noise emissions from the drainage system on the sleep pattern and daily activities of the residents of the multi-storey building. The questionnaire was developed and delivered online and deployed a scaling system to assist respondents (aged 15-35 years). The questionnaire was designed in accordance with ISO (2003)[21] recommendations and uses a direct question method. The procedure used to choose the words for the questionnaire scale was done in a way that is consistent with its position on a numerical scale of 1 to 5 for most of the questions. The questionnaire was used to answer the following questions:

1. Have you lived or currently live in a multi-story building?
2. Are you satisfied or dissatisfied with the noise from your water closet as a result of flushing?
3. Are you satisfied or dissatisfied with the noise from your building drainage system?
4. Does the noise from your water closet as a result of flushing affect your daily activities?
5. How heavy or high do you sleep?
6. Does the noise from the flushing of the water closet from the upper floors affect your sleep?
7. Does the noise from the flushing of the water closet from your adjacent neighbour affect your sleep?

RESULTS AND DISCUSSION

Acoustic results

Using Equation 1, all the measurements were calculated in octave bands and plotted as shown in Figure 1. The frequencies analysed were for audible frequencies only, ranging from 16 Hz to 8 kHz, and compared with the NR curve. NR curves for dwellings are 25 and 30. The NR curve is used to ascertain where the SPL level exceeds standards by comparing the sound pressure level lines measured with the NR curve, representing typical sound pressure level values with respect to octave bands.

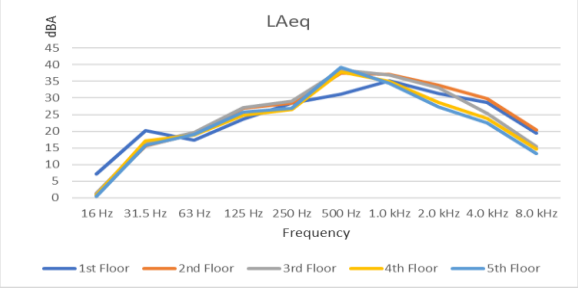

Fig. 1: Integrated average sound pressure level dBA.

Table 1 illustrates the results obtained from a series of noise tests run with the aid of a sound level meter on different levels of the multi-story building. The results show that the sound level from the five floors tested is similar, which means that when the toilet is flushed, irrespective of the level it is flushed from, the sound is transmitted through the pipes equally down the building. This means that the height of the building does not influence sound transmission through the internal drainage system of a multi-storey building. The results in Table 1 show the average value of the results presented graphically in Figure 3.

Table 1. The sound level from flushing at different levels in a building.

Location of measurement	LAeq, dBA
Background noise	26.0
Ground floor measurement from flush at 1st floor	42.0
Ground floor measurement from flush at 2nd floor	39.0
Ground floor measurement from flush at 3rd floor	41.6
Ground floor measurement from flush at 4th floor	40.9
Ground floor measurement from flush at 5th floor	42.2

Figure 2 shows the same measurements as in Table 2, but with octave bands, the result of the tests represented graphically for integrated average sound pressure levels. The results illustrated in Figure 2 show the corresponding values for the tests carried out. The green curve depicts the NR curve of 30. From the Figure, the sound measurements at frequencies just above 250 Hz to 4.0 KHz clearly fall above the acceptable values for dwellings. As a result, there is a need to further analyse the noise levels to ascertain the noise level that needs to be reduced in A-weighting frequency.

From the graph above, it can be seen that the noise from each floor is similar throughout; from the moment the toilet is flushed from any level, it follows the same pattern, with little difference, which may be caused by the speed of the sound takes from the source to arrive at the point of collection with the

sound level meter. The noise peaked at a frequency of 500 Hz and 39.2 dBA, which is well within the limit of 45 dBA for toilet flushing noise within a residential building.

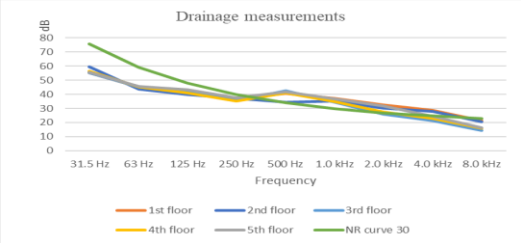

Fig. 2. Drainage measurement results.

Table 2 shows that only noise of frequencies ranging from 500 Hz to 4 kHz needs reduction with all sound pressure levels not exceeding 10 dB; this indicates that the acoustic emissions are not so high but can result in discomfort for residents. As such, it is pertinent that more insulation should be added to reduce the noise emissions in the drainage system.

Table 2: Loudest SPL octave band measurement analysis.

Frequency	31.5	63	125	250	500	1.0	2.0	4.0	8.0
Drainage measurement SPL, dB	57.7	45.8	43.7	37.7	42.4	37	32.6	28.8	21.5
NR 30 curve	75.8	59.2	48.1	39.9	34	30	26.9	24.7	22.9
Reduction needed	-18.1	-13.4	-4.4	-2.2	8.4	7	5.7	4.1	-1.4
A-weighting correction factor	-39.4	-26.2	-16.1	-8.6	-3.2	0	1.2	1	-1.1
Reduction needed in A-weighting	-	-	-	-	5.2	7	6.9	5.1	-

Questionnaire results

Results are presented in percentages illustrating the survey responses from 90 participants to understand their perception of noise from the flushing of WCs in the multi-storey building under consideration. Key findings are presented below, and graphical results are available in Appendix 1.

a) The tolerance level of respondents to noise from the flushing of the water closet: This aspect reflects how satisfied or dissatisfied respondents are about the noise emission from their water closet when flushed. The range spa was 'very dissatisfied' to 'very satisfied'. 33.3% of respondents were neither satisfied nor dissatisfied, followed by 31.1% who said they were satisfied, 26.6% who were dissatisfied, 5.5% very dissatisfied, and 3.3% very satisfied. This shows that most respondents are either indifferent about the noise from the flushing of the water closet or satisfied with it.
b) Respondents' satisfaction with noise insulation: This question aims to understand the overall satisfaction level of respondents with noise insulation in their building of residence. Out of the 90 respondents that participated in the survey, 35.5% were satisfied with the insulation level of their building, 27.7% were dissatisfied, 26.6% were neither satisfied nor dissatisfied, 6.6% were very satisfied, and just 3.3% were very dissatisfied. This shows that most of the respondents were either satisfied or indifferent.
c) Impact of water closet flushing noise on daily human activity: This question was drafted to understand if toilet flushing affects daily human activities such as reading, working, or watching a movie. 51.1% disagreed that noise from the flushing of the water closet affected their daily activity, 21.1% neither agreed nor disagreed, 14.4% agreed, 8.8% strongly disagreed, and 4.4% strongly agreed. This shows that most respondents are not affected by noise from toilet flushing, and others are indifferent, leaving just the small number who believe it bothers them. Those may be individuals who are more intolerant to the noise of any kind.
d) Impact of water closet flushing noise from upper floors on sleep: Ninety respondents gave their verdict on the impact of flushing water closets from upper floors on their sleep pattern. 46.6% of respondents noted that noise from the flushing of water closets from upper floors does not affect their sleep pattern, 21.1% agree, 17.7% neither agree nor disagree, 13.3% strongly disagree, and just 1.1% strongly agree. This shows that the majority of respondents are of the opinion that water closet flushing from upper floors has no impact on their sleep patterns. Those who felt their sleep was disturbed may be light sleepers whose sleep patterns can easily be interrupted by the mildest of sounds.
e) Impact of water closet flushing noise from a next-door neighbour on sleep: This survey showed that noise generated from the flushing of the water closets from the adjacent neighbours on the same floor has no impact on sleep patterns. Of the 90 respondents, 44.4% disagreed, 22.2% strongly disagreed, 16.6% agreed, 14.4% neither disagreed nor agreed, and only 2.2% strongly agreed. This is an indication that sleep is not affected by noise

from the flushing of the toilet from a neighbour's residence on the same floor.

From the analysis carried out, it is observed that while most respondents claim that the noise from flushing water closets does not disrupt their daily activity and sleep pattern, others believe it does. This finding is confirmed from the acoustic emissions levels presented herein. The analyses also show that there is a need for further insulation. Hence, the pipes should be insulated further to reduce noise emissions.

CONCLUSION

The tests carried out as reported herein lead to the conclusion that noise from the internal drainage system from flushing WCs at different levels in a multi-story building does not change with height. The test was run on a 6-storey residential building, and the average noise levels obtained were 42, 39, 41.6, 40.9 and 42.2 dBs, respectively. The variability in this range is negligible, showing that the noise difference is unchanged throughout the different levels. The questionnaire also provides results that show that noise from the water closet's flushing, although loud enough to be heard by its residents, whose ages range from 15 to 35 years, does not pose a major problem because it does not occur beyond 10 seconds. The noise does not disturb sleep patterns but can be problematic if it becomes continuous. Since the noise to be reduced is between the mid to high-level frequency, pipes should be covered thoroughly by insulation and placed behind a perforated gypsum board, 16% perforations, suspended with 200 mm plenum as recommended in BS 8233:2014. These results can be used to improve human health, comfort and general wellbeing. Furthermore, this article will aid better sound insulation in buildings, knowledge of the best materials for sound insulations and a proper understanding of what humans perceive as tolerable and intolerable noise levels.

RECOMMENDATION

To further reduce the noise level within a multi-story building, it is pertinent to run further tests to confirm the best materials to protect residents from unwanted noise. In addition, it is pertinent to analyse the acoustic emissions generated from the hydraulic jumps that occur at junctions between vertical and horizontal stacks and determine optimum places to create bends and velocity breaks, hence decreasing the acoustic emissions.

REFERENCES

[1] Farouk, A., 2011. High rise buildings and how they affect countries progression. E iataorC Leader. https://g-casa.com/conferences/zagreb/papers/Akram1-HighRise.pdf

[2] Hayati, H. and Sayadi, M.H., 2012. Impact of tall buildings in environmental pollution, , in Environmental skeptics and critics. IAEES, pp. 9, 10. http://taccire.suanet.ac.tz/handle/123456789/153

[3] Science for Environment Policy (2017) Noise abatement approaches. Future Brief 17. Produced for the European Commission DG Environment by the Science Communication Unit, UWE, Bristol. Available at: https://ec.europa.eu/environment/integration/research/newsalert/pdf/noise_abatement_approaches_FB17_en.pdf .

[4] Hye-kyung shin, Kyoung-woo kim, Jun-oh yeon, K. yang (2016) 'Suggest toilet noise standardfor multi-dwelling residential building', in Proceedings of the 22nd international congress on acoustics. Buenos Aires, p. 2. http://www.ica2016.org.ar/ica2016proceedings/ica2016/ICA2016-0301.pdf

[5] Marley-dBlue (2011) Acoustic soil and waste. https://www.marleyplumbinganddrainage.com/media/11322/marley-dblue.pdf.

[6] van der Schee W.G. (2012) 'Measurement of the noise production in drainage pipes', CIB W062 Symposium 2012. https://www.irbnet.de/daten/iconda/CIB_DC25341.pdf

[7] Institute for steel development growth, (2014) Multi-storey building. https://www.yumpu.com/en/document/read/36193244/multi-storey-buildings-ii-institute-for-steel-development-growth

[8] Khalifa, B. (2010) Fact sheet Burj Khalifa. Dubai. https://www.burjkhalifa.ae/img/FACT-SHEET.pdf

[9] Schmidt-Jones, (2005) 'Sound, physics and music', https://cnx.org/contents/GOQaowEz@1.52:ZSG7escu@10/Talking-about-Sound-and-Music

[10] Fahy, F. and Thompson, D. (2015) Fundamentals of sound and vibrations. Second Edi. Edited by F. Fahy and D. Thompson. Boca Raton: CRC Press. Taylor and Frances group. https://doi.org/10.1201/b18348

[11] Nataliya, D. (2016) Plumbing noises in water supply and sewage systems. Mikkeli University of Applied Sciences. https://www.theseus.fi/bitstream/handle/10024/109246/Danchenko_Nataliya.pdf?sequence=1&isAllowed=y

[12] Abel, E., Nilsson, P.E., Ekberg, L., Fahlén, P., Jagemar, L., Clark, R., Fanger, O., Fitzner, K., Gunnarsen, L., Nielsen, P.V. and Stoops, J., 2003. Achieving the desired indoor climate-energy efficiency aspects of system design. Studentlitteratur.

[13] Burk, P., Polansky, L., Repetto, D., Roberts, M. and Rockmore, D., 2011. Music and computers: a theoretical and historical approach. Preface to the Archival Version (Spring, 2011).

[14] Ray, E.F., 2010. Industrial Noise Series, Part IV, Modeling Sound Propagation. June, 16, p.2010.

[15] NIH Pub. No. 99-4233, 2014, Noise induced hearing loss. https://www.nidcd.nih.gov/sites/default/files/Documents/health/hearing/noise-induced-hearing-loss-english-8-2021.pdf

[16] Cirrus research Plc. (2013) Calculation of NR & NC Curves in the optimus sound level meters and NoiseTools software. North Yorkshire. pp. 4 – 14.

Available at: https://www.cirrusresearch.co.uk/library/documents/technical_papers/TN31_Calculcation_of_NR_and_NC_Curves_in_the_optimus_sound_level_meter_and_NoiseTools_software.pdf

[17] Choon, T. W. et al. (2012) 'Investigation of Water Hammer Effect Through Pipeline System', International Journal on Advanced Science, Engineering and Information Technology, pp. 48, 49. doi: 10.18517/ijaseit.2.3.196.

[18] Catron, F. and Fagerlund, A. (2009) 'Noise generation and propagation effects on piping system components', in Noise Control Engineering Journal. doi: 10.3397/1.3155382.

[19]

[20] BS 8233, (2014) Guidance on sound insulation and noise reduction for buildings. BSI standards limited 2014.

20- Nor 140 (2021), Nor Instruction Manual, https://www.akustik.lth.se/fileadmin/tekniskakustik/education/LjudBS_17/Nor-140_Instruction_Manual_v3R0.pdf

[22] ISO (2003) ISO-TS-15666: Acoustic-assessment of noise annoyance by means of social and socio-acoustic surveys. Geneva:ISO, International Organization for Standardization. https://www.iso.org/standard/28630.html

APPENDIX 1

Results of the survey

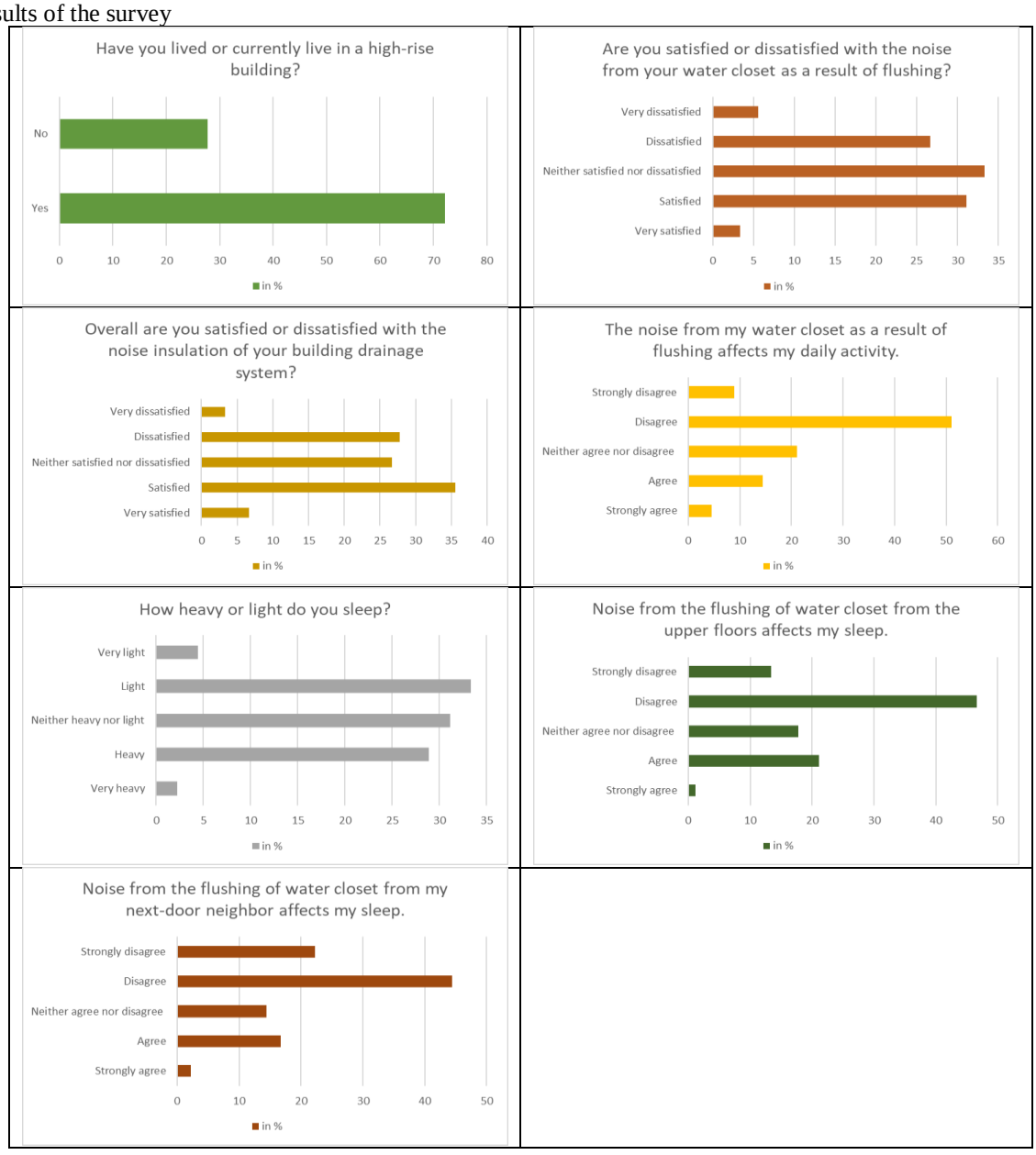

8th Int. Conf. on Structure, Engineering & Environment (SEE), Mie, Japan, Nov.10-12, 2022, ISBN: 978-4-909106094 C3051

INFRASTRUCTURE IMPACTS CALCULATOR: AN INFRASTRUCTURE ASSESSMENT TOOL USING CO-BENEFIT APPROACH

Nicanor R. Roxas, Jr.[1], Krister Ian Daniel Z. Roquel[2], Krista Danielle S. Yu[3], Alerik Ezekiel C. Ruiz[2], and Alexis M. Fillone[2]
[1]Department of Manufacturing Engineering and Management, De La Salle University, Philippines;
[2]Department of Civil Engineering, De La Salle University, Philippines;
[3]School of Economics, De La Salle University, Philippines

ABSTRACT

The 1992 United Nations Conference on Environment and Development recognized the concept of sustainable development which balances the economic, social, and environmental factors to meet our needs and the future. Succeeding climate actions such as the Clean Development Mechanism, Nationally Appropriate Mitigation Actions, Green Climate Fund, Intended Nationally Determined Contributions, and the Paris Agreement reinforce the support for co-benefits. The co-benefits approach considers both the development and climate benefits in a single policy. The Sustainable Technology Assisted Route Planning for Region VI, funded by the Department of Science and Technology – Philippine Council for Industry, Energy, and Emerging Technology Research and Development, considers this approach. It aims to support the development of a sustainable Local Public Transport Route Plan (LPTRP) that integrates the road and maritime transport network of Region VI through the use of developed technologies for the transport sector while considering its social, economic, and environmental impacts. The LPTRP is crucial in the implementation of the Public Utility Vehicle Modernization Program launched in 2017. In this regard, an Excel-based assessment tool compatible with a transport simulation tool is developed and presented. The tool facilitates a swift processing of information from the simulation results of different scenarios to the comparative assessment of transport infrastructure proposals and policies. It enhances the capabilities of local staff and researchers in assessing the effects of transport projects and programs using co-benefit analysis. This endeavor hopes to foster better local decision-making related to transportation planning and management affecting not only the economy but also the environment.

Keywords: Co-benefit analysis, Transportation planning, Impact assessment tool, Sustainability

INTRODUCTION

The 1992 United Nations Conference on Environment and Development recognized the concept of sustainable development which balances the economic, social, and environmental factors to meet our needs and the future. Succeeding climate actions such as the Clean Development Mechanism, Nationally Appropriate Mitigation Actions (NAMAs), Green Climate Fund (GCF), Intended Nationally Determined Contributions (INDCs), and the Paris Agreement reinforce the support for co-benefits. The co-benefits approach aims to consider both the development and climate benefits simultaneously in a single policy.

The transportation sector links the different sectors of our economies. Investments in the transportation sector affect the country's development. The movement of people, goods, and services almost always require the use of transportation. In this regard, being able to improve and optimize the transportation sector is critical to sustain economic growth. However, public health should never be overshadowed by the pursuit of economic growth. The strong relationship between transportation and health necessitates a more inclusive approach - one that would cover the interests of both the stakeholders and the society. In light of the broad evidence that climate change is occurring with potentially expensive and far-reaching health consequences, urgent and substantial actions are needed. Several researchers have employed the co-benefits (CB) framework to assess transport projects and policies beyond just transportation metrics [1]–[3]. Its use has become a predominant concept in scientific writing that focuses on reconciling environmental and developmental goals. This appears to be very promising for developed economies and emerging economies, as it offers a way of not compromising economic growth while still allowing environmental aspects to be taken into account. The literature is abundant with transportation and traffic studies offering various solutions for the many problems that face the transport sector. Experiences of other countries and best practices all over the world are now readily available. With these information, local

planners are given the opportunity to learn from previous mistakes and follow or even improve on the success of others for local projects implementations.

Back in 2018, local transportation planning specialists were commissioned to conduct a two-week hands-on training to municipal, city, and provincial representatives of Local Government Units (LGUs) to develop the Local Public Transport Route Plan (LPTRP). The expected output of the capacity building activity is the submission of LPTRPs. However, only a few LGUs were able to achieve. The LPTRP is an important document for the LGUs in order for the Public Utility Vehicle Modernization Program (PUVMP) to be implemented. The training has shown that the participants had limited exposure to both QGIS for spatial land-use planning and JICA STRADA v.3.5 for public transport planning. JICA STRADA software is highly complex and thus, participants were not able to utilize this tool in developing their respective route plans. A more user-friendly transportation planning tool is therefore proposed.

Transportation plans and policies crafted from sound and holistic approaches are needed in identifying a sustainable transportation development roadmap that would cater to the needs of all stakeholders. This research is part of an ongoing research program entitled Sustainable Technology-Assisted Route Planning for Region VI (STARPLANVI) which is funded by the Department of Science and Technology – Philippine Council for Industry, Energy, and Emerging Technology Research and Development (DOST-PCIEERD). The STARPLAN program aims to support the development of a sustainable Local Public Transport Route Plan (LPTRP) that integrates the road and maritime transport network of Region VI through the use of developed technologies for the transport sector. The LPTRP is crucial in the implementation of the Public Utility Vehicle Modernization Program of the Philippine government which was launched in 2017. STARPLAN will specifically train and provide both the software and hardware public transport planning tools to the local government staff and university faculty and staff for their use to sustain the public transport planning and management of Region VI. Through the STARPLAN VI, several computers installed with the necessary public transport planning tools and trainings are provided to the local government staff and partner educational institutions for their use to sustain the public transport research, planning, and management of Region VI. The program objective is very timely and appropriate as various projects are being constructed and many are still in the planning process. In this light, the trainings provided to the staff are quite apt. The level of understanding of the various concepts of the transportation planning process and the skills are further enhanced. In the various trainings, different participants have different level of understanding of the transportation planning concepts. In order to further streamline this process, the Traffic Infrastructure Impacts Calculator was conceived. This will facilitate LGU personnel and researchers to easily estimate the effects of certain policies and proposals from their simulations. The tool facilitates a swift processing of information from the simulation results of different scenarios to the comparative assessment of the proposals and policies for the region using Co-benefit Analysis. This endeavor hopes to foster better local decision-making related to transportation planning and management. To adopt a more systems-oriented approach and considering the archipelagic nature of the country, it is essential to plan towards an interconnected maritime and road transport network. Noting the case of Region VI wherein maritime transport services are available to provide linkages between Negros Occidental and Guimaras with Panay Island.

The targeted audience of the TIIC are LGUs, specifically those who are in charge of making local policies, transport projects and infrastructure. STARPLAN also provides training in various transportation tools and software to Region VI LGUs and providing the TIIC tool can provide huge benefit to them. This is because the TIIC can provide LGUs a way to quickly test and assess policies, infrastructures, and projects on their own.

REVIEW OF RELATED LITERATURE

Urban areas are generally centers of economic growth. Rapid development and expansion of these areas require a massive amount of investment in infrastructure and transportation for sustainability. The transportation sector is next to the industrial sector in terms of energy consumption accounting for about 30% of the world's total delivered energy. The transportation sector guzzles around 60% of the global oil demand and is responsible for approximately 22% of the CO2 emission in 2008 globally. Moreover, road vehicles account for around 81% of the total transportation energy demand [4]. In a research in Delhi, India, cobenefits was used in order to determine the effects of mode shifting to a non-polluting mass transit system. The study was motivated by the increasing population in the city resulting in an escalation of transportation demand and thus the problems of congestion and emissions from road vehicles [5]. In another study in Manila, Philippines, cobenefit analysis was also applied in determining the effect of mode choices of commuters along EDSA when hypothetical improvements are made with respect to the access and egress modes to MRT3. The difference of these scenarios in terms of environmental effects from baseline and hypothetical scenarios were examined [6]. The same research team also did a cobenefit analysis for the proposed Panay-Guimaras-Negros Bridge in Western Visayas

Region [7]. A study made in Beijing also looked into cobenefits. The study specifically looked into the effect of promoting NEVs (new energy vehicle) on energy consumption [8]. There are quite a lot of studies concerning the use of cobenefits to assess the effects of various proposed transportation projects and policies. Mayrhofer and Gupta [9] accredits the co-benefits approach as a positive and constructive "win-win" way to operationalize how economic, environmental, and social aspects can be integrated within the concept of sustainable development, instead of framing them in terms of trade-offs. In this study, by incorporating the benefits of travel time and vehicle operating cost (VOC) reduction with the primary CB of savings in accident losses and emission costs, an all-inclusive and long-term assessment will be performed, aiming to determine the optimum development roadmap that caters to the interests of both the industry and the community.

In this light, useful tools are required in order to further facilitate and improve transportation planning towards sustainability. A growing consensus among planners regarding the interaction between the integrated land-use and the transport policies results in better outcomes [10]. The researchers mentioned that accessibility planning is a key strategy in maximizing environmental sustainability and quality of life in urban areas brought about by more efficient transport systems. In this particular study, they developed a tool which assesses the location choices of new activities in Rome based on accessibility changes. This tool aids planners in assessing the effects of new location choices on mobility and the environment in monetary terms. Another study by Mateichyk et al [11] also developed a tool in the facilitation of the processes and analysis for EIAs in Ukraine. Their web-based tool was proven to work starting from encoding to reports generation to supervisory state agency. These tools aid in the planning and could therefore aid in achieving the various sustainability goals through the proper assessment of various projects and policies.

In the Philippines, one of the flagship projects of the current administration is the PUVMP. To shed more light on the importance of this program, based on an LTO report, there are more than 12 million motor vehicle units registered as of 2019 where around 18% are PUJs [12]. Buses and PUJs serve around 67% of the demand in Metro Manila. The PUVMP is not just about modernizing the PUJs as it also aims to consolidate the operators into cooperatives, reduce emission, encourage mode shift through improved services, and enhance the living standards of the PUJ industry/sector [12]. The new body make which costs at least 1.6 million pesos, minimum of EURO IV emission standards, global navigation satellite system (GNSS), automatic fare collection, free WIFI, CCTVs, speed limiters, dashboard cameras, and easy accessibility for PWDs are some of those which have been required by LTFRB. Under the modernization, the units will achieve being comfortable, accessible, reliable, environment-friendly, and sustainable (CARES) with due consideration to PWDS and the elderly. It is worth noting that 90% of the total PUJs nationwide are at least 15 years old [12]. The timeworn units contribute largely to air pollution and are getting obsolete. In order to aid the drivers and operators in this program, the Land Bank of the Philippines and the Development bank of the Philippines are providing special loan packages where the 5% equity or down payment of 80,000PHP can be shouldered by the government [12]. However, one of the requirements for the loan is to secure the Local Public Transportation Route Plan (LTPRP) from the LGUs which is also a problem due to non-submission of LGUs [13]. In the current fragmented set-up which is characterized by disorganized dispatching and on-street competition, drivers tend to be more aggressive in order to increase their profit. Jeepney units also stop anywhere causing congestion [14].

METHODOLOGY

The TIIC uses both Excel's and Visual Basic for Applications (VBA) Userform functions. The tool uses input based around EMME's output which are the Average speed of the network, Total VDT, and VHT in order to do the Co-benefits analysis. The output of the analysis would be in billions of Philippine Pesos per year for Time Savings, Vehicle Operating Cost, and Environmental Cost Savings. This enables a simple comparison among alternatives.

The Institute for Global Environmental Strategies (IGES) has promoted the use of the co-benefits approach to incorporate both the climate and development issues in project evaluations. The co-benefit analysis is a tool which provides invaluable information to policy makers. It incorporates savings in travel time, vehicle operating costs, traffic safety, and environmental emissions [15].

The travel time savings is quantified by taking the difference between the total travel cost of travellers with and without the project. The total travel time costs for the scenarios are computed as follows:

$$\boldsymbol{BT_i = \sum_j \sum_l \left(Q_{ijl} \times T_{ijl} \times \alpha_j\right) \times 365} \quad (1)$$

where

- $\boldsymbol{BT_i}$ – total travel time cost with/without the project
- $\boldsymbol{Q_{ijl}}$ – traffic volume for *j* vehicle type on link *l*, with/without the project (vehicle/day)
- $\boldsymbol{T_{ijl}}$ – average travel time for *j* vehicle type on link *l*, with/without the project (min)
- $\boldsymbol{\alpha_j}$ – value of time for *j* vehicle type
- $\boldsymbol{i}$: $\boldsymbol{i = w}$ **with project**; $\boldsymbol{i = 0}$ **without project**

The vehicle operating cost reduction is quantified by taking the difference between the vehicle operating costs between the two scenarios. The computation for the savings is shown as follows:

$$\boldsymbol{BR_i} = \sum_j \sum_l \left(\boldsymbol{Q_{ijl}} \times \boldsymbol{L_l} \times \boldsymbol{\beta_j}\right) \times \mathbf{365} \quad (2)$$

where

$\boldsymbol{BR_i}$ – total vehicle operating cost with/without the project

$\boldsymbol{Q_{ijl}}$ – traffic volume for j vehicle type on link l, with/without the project (vehicle/day)

$\boldsymbol{L_l}$ – link length of link, l (km)

$\boldsymbol{\beta_j}$ – value of vehicle operating cost for j vehicle type

$\boldsymbol{i : i = w}$ **with project**; $\boldsymbol{i = 0}$ **without project**

The environmental emissions are quantified using the top-down approach where the amount of fuel used for the scenarios are first quantified. This provides the basis for taking the difference in the emissions generated between the baseline and the with-project scenarios. The emissions included are the SOx, CO2, NOx, and the PM which are also monetized using the various marginal costs per air pollutant. Monetizing all the benefits enable the comparison of scenarios using a single unit. The overall savings provide policy makers an overview of the costs and benefits associated with the scenarios involving policy changes or project proposals being evaluated.

RESULTS AND DISCUSSION

In this particular research, Roxas City has been chosen as the pilot city to implement the TIIC. Roxas City, as seen in Fig.1, is in the island of Panay which is part of the Western Visayas Region where the STARPLAN VI project is deployed.

Fig. 1 Roxas City Location

The city has been chosen because they were among the first to gather data for their LPTRP. In this regard, the data, which includes traffic counts, origin and destination information, public transport routes, and other relevant information, gathered was used in order to develop the EMME model for the baseline scenario. The various traffic counts were used to calibrate the baseline model. Shown in Fig.2 is the volume of vehicles on links for the baseline scenario.

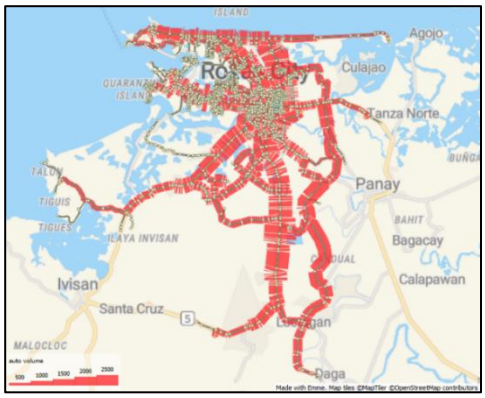

Fig. 2 Roxas City baseline Emme network

Two hypothetical scenarios were formulated as seen in Fig.3. The first one is related to the introduction of a circumferential road whereas the other scenario involves adding the same circumferential road with other new local roads.

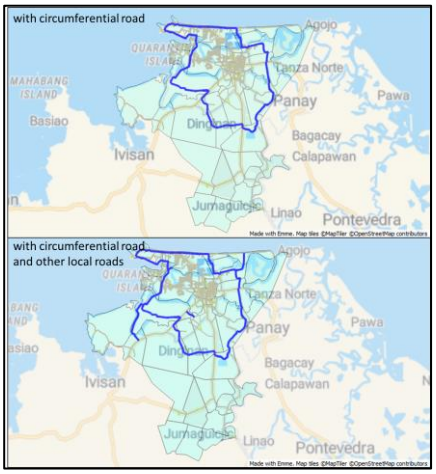

Fig. 3 Two formulated hypothetical scenarios

The traffic is forecasted for the 5, 10, and 20 year projections shown below. The comparison of the baseline scenario against the other two hypothetical scenarios are based on the projections shown in Fig.4.

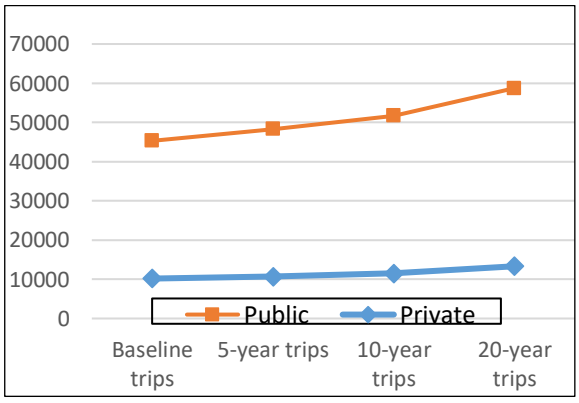

Fig. 4 Baseline and forecasted traffic

The different scenarios were simulated and were compared with the baseline scenario. Shown in Table 1 is the summary of the scenarios simulated in EMME. It can be seen that overall, the proposed scenarios will improve the current situation due to the enhancement in average zone to zone travel time and speed. The volume-capacity ratio (VCR) also shows a significant improvement brought about by the proposed roads.

Table 1 EMME Scenario modeling summary

Scenarios	Average zone to zone travel time (min)	VCR	Ave. speed (kph)	VDT (veh-km)	VHT (veh-hr)
baseline	23.55	0.16	26.75	63010.38	2306.13
with circumferential roads	20.86	0.11	28.10	60090.06	1779.55
with circumferential and additional road links	20.54	0.11	28.15	59512.49	1750.47

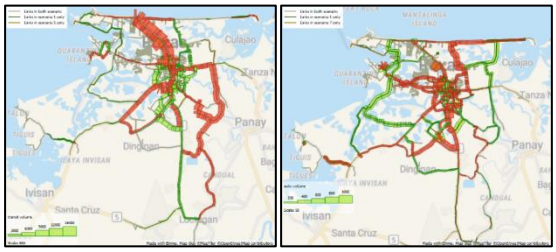

Fig. 5 Baseline and with-circumferential road scenarios comparison (left) and baseline and with-circumferential road plus other local roads scenarios comparison (right)

Figure 5 on the left shows the scenario comparison output of the baseline vs with-circumferential road and on the right, the comparison between baseline and with-circumferential plus other local roads. The green-colored links show reduction in traffic volume while those in red show increase in volume. The scenario comparison clearly shows the impact of the provision of the proposed roads. Though this tool, planners can visualize the extent of the effect of the projects, the TIIC can aid in accurately comparing the effects of these scenarios in terms of the cobenefits.

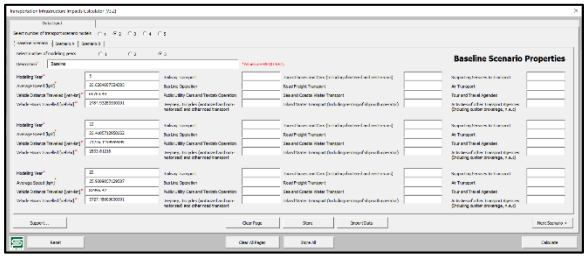

Fig. 6 TIIC GUI with EMME baseline results

After incorporating the two scenarios in EMME, separate simulations were prepared for each of them. After each run, results were exported and compiled. These information were directly fed into the TIIC as shown in Fig.6. The information can either be encoded manually or imported from the worksheet output of EMME. Once all the information is fed to the TIIC, the calculation may be started and several charts and a table can be seen in the output tab of the tool. Figure 7 contains four different charts for the different savings calculated. For travel time savings, the hypothetical scenarios are each compared with the baseline scenario and the savings are calculated based on the reduction in travel time for the entire network. The minimum wage rate is used to convert the travel time savings to monetary units. The next cobenefit included in the TIIC is the vehicle operating cost savings. This is computed based on the link speeds and estimated using equations developed by JICA [16]. Due to improved speed in the network, the vehicle operating cost for the scenarios indicate savings. More savings can be derived from the circumferential plus other local roads scenario due to better average speed in the network. The reduction in NOx, CO, CO2, SOx, and PM were considered for the environmental savings. The reduction also derived from the changes in speed and quantified through the values obtained from Clean Air Asia Initiatives. Figure 7 shows a similar result where scenario B involving the provision of the circumferential road along with other local roads yield the larger amount of savings.

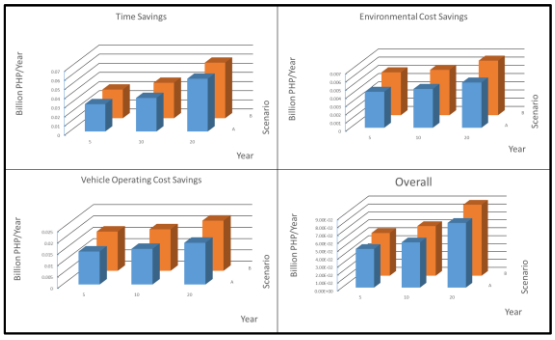

Fig. 7 TIIC comparison of various scenarios

CONCLUSIONS

This study is part of the government-funded research program STARPLAN VI which aims to support the development of the LPTRPs of various LGUs that integrates the road and maritime transport network of Region VI through the use of developed technologies for the transport sector. In order to aid government staff in assessing proposed transport infrastructure projects, the TIIC was conceived. The TIIC tool is able to perform co-benefit analysis in line with the outputs of EMME which is the transportation planning software used in the project. The tool streamlines the process of being able to compare various scenarios that are introduced in EMME through co-benefit analysis that is integrated in the

TIIC tool. This tool can either accept imported EMME CSV data or through manual encoding. Co-benefit analysis has been utilized as it not only looks into vehicle operating costs and value of travel time savings as well as environmental emission savings. This promotes the concept of sustainability which is essential especially during these times were climate change is a pressing issue.

In this paper, Roxas City, Philippines was chosen to be the pilot implementation of the TIIC. Two EMME scenarios were formulated and were separately compared with the baseline scenario. Not only can this tool accept various scenarios but it can also accept various projections from each scenario. It was determined that the second case will provide the more co-benefits to the city. Through this tool, this research aims to achieve its goal of assisting the LGUs in their task of crafting sustainable transport infrastructure projects and programs in Region VI.

ACKNOWLEDGMENTS

This project is funded by the Department of Science and Technology (DOST) through the Philippine Council for Industry, Energy and Emerging Technology Research and Development (PCIEERD). The authors would like to acknowledge DOST-PCIEERD, De La Salle University, and the University Research Coordinating Office for their support on this research. The authors would also like to extend their gratitude to the staff of the various LGUs from Region VI for their assistance.

REFERENCES

[1] Kwan, S., Tainio, M., Woodcock, J., Sutan, R., & Hashim, J. (2017). The carbon savings and health co-benefits from the introduction of mass rapid transit system in Greater Kuala Lumpur, Malaysia. Journal of Transport&Health, 6, 187-200.

[2] Shaw, C., Hales, S., Edwards, R., Howden-Chapman, P., & Stanley, J. (2017). What can fuel price increases tell us about the air pollution health co-benefits of a carbon price. Journal of Transport & Health. Advanced online publication.

[3] Alam, M., Hyde, B., Duffy, P., & McNabola, A. (2018). Analysing the co-benefits of transport fleet and fuel policies in PM2.5 and CO2 emissions. Journal of Cleaner Production, 172, 623-634.

[4] Atabani, A. E., Badruddin, I. A., Mekhilef, S., & Silitonga, A. S. (2011). A review on global fuel economy standards, labels and technologies in the transportation sector. Renewable and Sustainable Energy Reviews, 15(9), 4586–4610.

[5] Panwar, M., Singh, D. K., & Devadas, V. (2018). Analysis of environmental co-benefits of transportation sub-system of Delhi. Alexandria Engineering Journal, 57(4), 2649–2658.

[6] Roxas, N. R., Fillone, A. M., & Roquel, K. I. D. (2018). Estimating the environmental effects of car shifting behavior along EDSA. International Journal of GEOMATE, 14(44), 8–14.

[7] Roxas, N. R., & Fillone, A. M. (2017). Co-benefit analysis of the proposed Panay-Guimaras-Negros Bridge Project, Western Visayas, Philippines. Transportation Research Procedia, 25, 3568–3581.

[8] Yang, X., Lin, W., Gong, R., Zhu, M., & Springer, C. (2021). Transport decarbonization in big cities: An integrated environmental co-benefit analysis of vehicles purchases quota-limit and new energy vehicles promotion policy in Beijing. Sustainable Cities and Society, 71(August 2020), 102976.

[9] Mayrhofer, J. & Gupta, J. (2015). The science and politics of co-benefits in climate policy. Environmental Science and Policy, 57, 22-30.

[10] Coppola, P., & Papa, E. (2013). Accessibility Planning Tools for Sustainable and Integrated Land Use/Transport (LUT) Development: An Application to Rome. Procedia - Social and Behavioral Sciences, 87, 133–146.

[11] Mateichyk, V., Khrutba, V., Kharchenko, A., Khrutba, Y., Protsyk, O., & Silantieva, I. (2021). Developing a Tool for Environmental Impact Assessment of Planned Activities and Transport Infrastructure Facilities. Transportation Research Procedia, 55(2019), 1194–1201.

[12] Estipular, J. L. (2020). CPBRD Policy Brief Looking into the impLementation of pubLic utiLity VehicLe modernization program Congressional Policy and Budget Research Department House of Representatives.

[13] ARTA. (2021). ARTA to create TWG to address issues raised by transport coops in PUV Modernization Program - Anti-Red Tape Authority. https://arta.gov.ph/press-releases/arta-to-create-twg-to-address-issues-raised-by-transport-coops-in-puv-modernization-program/

[14] Pontawe, J., & Napalang, S. (2018). Examining the Potential Significance of Industry Consolidation and Fleet Management in Implementing the DOTr ' s PUV Modernization Program : A Case Study of 1TEAM. Philippine Transportation Journal, 1(2), 47–58.

[15] (IGES), I. for G. E. S. (2011). Mainstreaming Transport Co - benefits Approach. A Guide to Evaluating Transport Projects. In Institute for Global Environmental Strategies (IGES).

[16] JICA. (2014). Technical Report No. 2: Transport Demand Analysis. March. http://www.neda.gov.ph/wp-content/uploads/2015/03/FR-TR2-TECHNICAL-ANALYSIS.-12149639.pdf

8th Int. Conf. on Structure, Engineering & Environment (SEE), Mie, Japan, Nov.10-12, 2022, ISBN: 978-4-909106094 C3051

GROWTH CHARACTERISTICS OF PINUS DENSIFLORA IN SIMULATED HEAVY METAL CONTAMINATED SOIL

Takuma Kubohara[1], Hiroyuki Ii[2], Ryoichi Araki[3] and Masakazu Saito[4]
[1]Kinokawa City Office, Japan; [2]Faculty of Systems Engineering, Wakayama University, Japan; [3]Faculty of Education, Wakayama University, Japan; [4]Wakayama Prefectural Forestry Experiment Station, Japan

ABSTRACT

The effects of heavy metals on the growth and their accumulation patterns in *Pinus densiflora* in heavy metal contaminated soil were studied because the influences of heavy metals on the growth of *Pinus densiflora* have not been well revealed. The tree heights of *Pinus densiflora* grew 11 ~ 14 cm to 15 ~ 17 cm in 4 weeks with or without Zn, W, Cu, and Ni loading. Zn and W concentrations (37 to 140 for Zn and 10 to 52 mg/kg-dry for W) in *Pinus densiflora* in each metal load condition were higher than those in other load conditions (20 to 53 for Zn and 7 to 40 mg/kg-dry for W). Zn and W concentrations in roots of *Pinus densiflora* in each metal load condition (70 to 140 for Zn and 30 to 52 mg/kg-dry for W) were higher than those concentrations in leaves and stems of *Pinus densiflora* in each load condition (37 to 66 for Zn and 10 to 30 mg/kg-dry for W). Zn concentrations in leaves (37 to 50 mg/kg-dry), stems (49 to 66 mg/kg-dry), and roots (70 to 140 mg/kg-dry) of *Pinus densiflora* in Zn load condition were higher than those in other load conditions (20 to 40 for leaves, 30 to 45 for stems, and 30 to 53 mg/kg-dry for roots). Therefore, it was concluded that *Pinus densiflora* was not affected by growth abnormalities caused by heavy metal-contaminated soil and grew while accumulating Zn in the leaves, stems, and roots and W in the roots.

Keywords: Pinus densiflora, Heavy metal tolerance, Roots, Zn, W

INTRODUCTION

It is known that some plants accumulate large amounts of heavy metals. *Scopelophila cataractae*, a type of bryophyte, and *Athyrium yokoscense (Franch. et Savat.) Christ*, a type of fern are famous[1]-[2]. Those species are often found in heavy metal contaminated areas such as mining sites. On the other hand, *Pinus densiflora* is also often found in mining sites and is known to accumulate heavy metals [3]-[5]. However, the influences of heavy metals on the growth of *Pinus densiflora* have not been well studied. Therefore, in this study, we reveal the effects of heavy metals on growth and their accumulation patterns in *Pinus densiflora* under different heavy metal-contaminated soil conditions.

STUDY METHOD

Outdoor Experiment

Figure 1 shows the location of the outdoor experiment. The outdoor experiment was carried out in Kinokawa City, Wakayama Prefecture. In this experiment, *Pinus densiflora* seedlings provided by Wakayama Prefectural Forestry Experiment Station were used. Figure 2 shows the outline of pot experiment. *Pinus densiflora* seedlings that had been sown in the open field for about 10 months were used in the experiment. One seedling was transplanted into each pot, and the load of heavy metals was started approximately 2 months after transplanting. The experimental period was early May to early June 2022. *Pinus densiflora* seedlings were placed outside in a sunny place during the experiment. Table 1 shows the experimental conditions. The pot experiment was carried out under five conditions of copper, nickel, zinc, tungsten, and no load. Cu, Ni, Zn,

Fig.1 Location of the outdoor experiment.

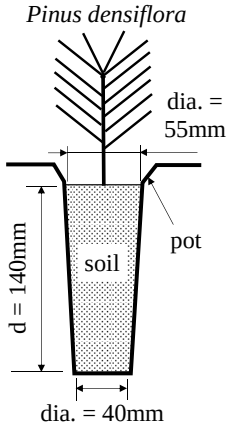

*At the experiment start.

Fig.2 The outline of pot experiment.

Table1 The experimental conditions.

Sample name	Loaded heavy metal	Heavy metal concentration (ppm)	Loadings
Zn	Zn ($ZnSO_4$ solution)	860	start and 1 week after the experiment start: 10mL/pot 2 and 3 weeks after the experiment start: 20mL/pot
W	W (K_2WO_4 solution)	33	
Cu	Cu ($CuSO_4$ solution)	2.5	
Ni	Ni ($NiSO_4$ solution)	2.6	
CTRL	Nothing	-	-

and W concentrations in solutions were 2.5, 2.6, 860 and 33ppm. Heavy metals were loaded at the experiment start, 1 week, 2 weeks, and 3 weeks after the experiment start. The amount of loaded heavy metal solutions was 10 mL/pot at the experiment start and 1 week after the experiment start, and was 20 mL/pot at 2 weeks and 3 weeks after the experiment start. The tree height of *Pinus densiflora* seedlings was measured in an outdoor experiment. 4 weeks after the experiment start, *Pinus densiflora* seedlings were pulled out from their pots to determine the heavy metals concentrations in the seedlings. After removing the soil from the roots of *Pinus densiflora* seedlings, the whole body was rinsed with pure water. Then, *Pinus densiflora* seedlings were divided into leaves, stems, and roots.

Laboratory analysis

Laboratory analysis was performed at Wakayama University. Three samples for analysis were prepared for leaves, stems, and roots. Leaves, stems, and roots of *Pinus densiflora* were desiccated by a dryer at 60 °C. After drying, they were dissolved with concentrated nitric acid and filtered with a membrane filter in 0.45 micrometer of pore size. After filtering, the Cu, Ni, Zn, and W concentrations in each part of

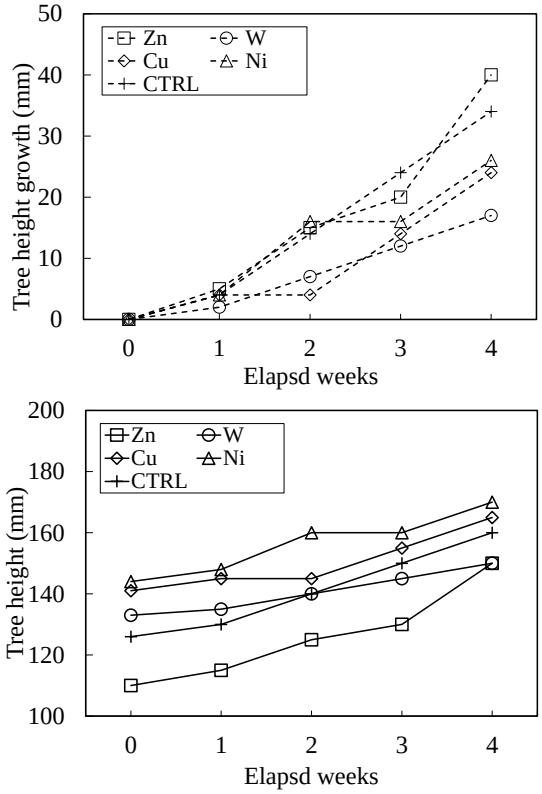

Fig.3 Changes of tree height growths and tree heights.

Pinus densiflora were measured by ICP-OES (AMETEK, Inc., SPECTRO ARCOS). The actual detection limit of ICP-OES is 0.01ppm for Cu, Ni, Zn, and W.

RESULTS AND DISCUSSION

Tree Height Growths of *Pinus densiflora* in Contaminated and Non-contaminated Soils

Figure 3 shows tree height growths and tree heights of Zn, W, Cu, Ni, and CTRL. At 4 weeks later from the experiment start, tree height growths of Zn, Cu, and Ni were almost the same as that of CTRL. However, tree height growth of W was lower than that of CTRL. At 4 weeks later from the experiment start, tree heights of Zn, W, Cu, and Ni were almost the same as that of CTRL. Moreover, at the experiment start, tree height of W was the third tallest of all and was already tall. Therefore, it was thought that tree height growth of W was small. And then, no appearance growth abnormalities such as wilting were observed in all seedlings during the experiment.

From the above results, it was found that *Pinus densiflora* can grow in Zn, W, Cu, and Ni contaminated soils.

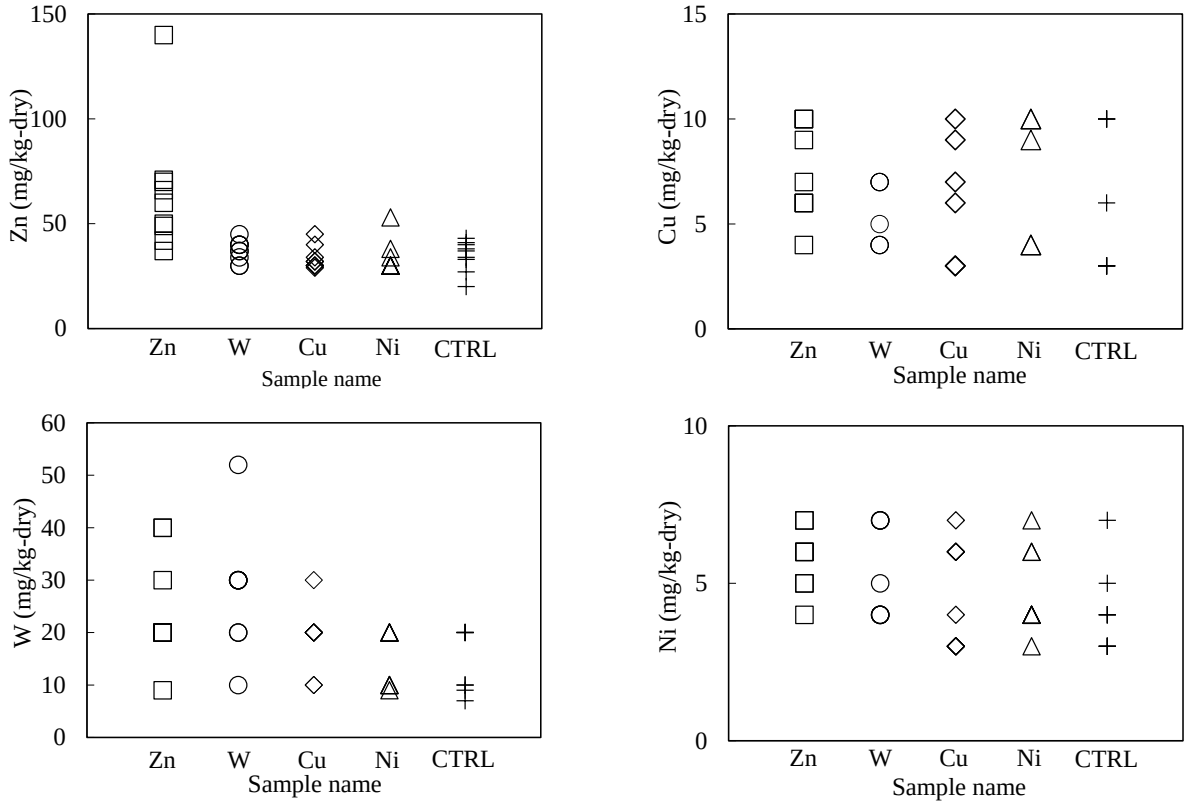

Fig.4 Zn, W, Cu, and Ni concentrations in *Pinus densiflora* in contaminated and non-contaminated soils.

Heavy Metal Concentrations in *Pinus densiflora* in Contaminated and Non- contaminated Soils

Figure 4 shows Zn, W, Cu, and Ni concentrations in *Pinus densiflora* in contaminated and non-contaminated soils.

Zn concentrations in Zn, W, Cu, Ni, and CTRL were 37 to 140, 30 to 45, 29 to 45, 30 to 53, and 20 to 43 mg/kg-dry, respectively. W concentrations in Zn, W, Cu, Ni, and CTRL were 9 to 40, 10 to 52, 10 to 30, 9 to 20, and 7 to 20 mg/kg-dry, respectively. Therefore, Zn concentrations in Zn and W concentrations in W were higher than those concentrations in other conditions. Cu concentrations in Zn, W, Cu, Ni, and CTRL were 4 to 10, 4 to 7, 3 to 10, 4 to 10, and 3 to 10 mg/kg-dry, respectively. Ni concentrations in Zn, W, Cu, Ni, and CTRL were 4 to 7, 4 to 7, 3 to 7, 3 to 7, and 3 to 7 mg/kg-dry, respectively. Therefore, Cu and Ni concentrations were almost the same as those concentrations in all conditions. Cu, Ni, Zn, and W concentrations in the loaded solutions were 2.5, 2.6, 860, and 33ppm. Zn and W concentrations in the solutions were higher than Cu and Ni concentrations in the solutions. Therefore, it was thought that the heavy metals concentrations in *Pinus densiflora* were influenced by the difference of heavy metals concentrations in the loaded solutions.

From the above results, it was deemed that *Pinus densiflora* absorbs a large amount of heavy metal in soils containing a large amount of heavy metal. Moreover, it was found that *Pinus densiflora* accumulate Zn and W.

Heavy Metals Concentrations in Leaves, Stems, and Roots of *Pinus densiflora*

Figure 5 shows Zn, W, Cu, and Ni concentrations in leaves, stems, and roots of *Pinus densiflora*.

Zn concentrations in leaves, stems, and roots of Zn were 37 to 50, 49 to 66, and 70 to 140 mg/kg-dry, respectively. Zn concentrations in leaves, stems, and roots of W were 30 to 40, 37 to 45, and 30 to 40 mg/kg-dry, respectively. Zn concentrations in leaves, stems, and roots of Cu were 29 to 34, 30 to 32, and 32 to 45 mg/kg-dry, respectively. Zn concentrations in leaves, stems, and roots of Ni were 30, 30, and 34 to 53 mg/kg-dry, respectively. Zn concentrations in leaves, stems, and roots of CTRL were 20 to 34, 33 to 38, and 40 to 43 mg/kg-dry, respectively. Therefore, roots Zn concentrations were higher than Zn concentrations in leaves and stems for Zn. Roots Zn concentrations were almost the same as Zn concentrations in leaves and stems for W, Cu, Ni, and CTRL. It is known that fern accumulates large amounts of Zn in its roots [2], [6-7]. Moreover, it is reported that Zn concentration in root of *Pinus*

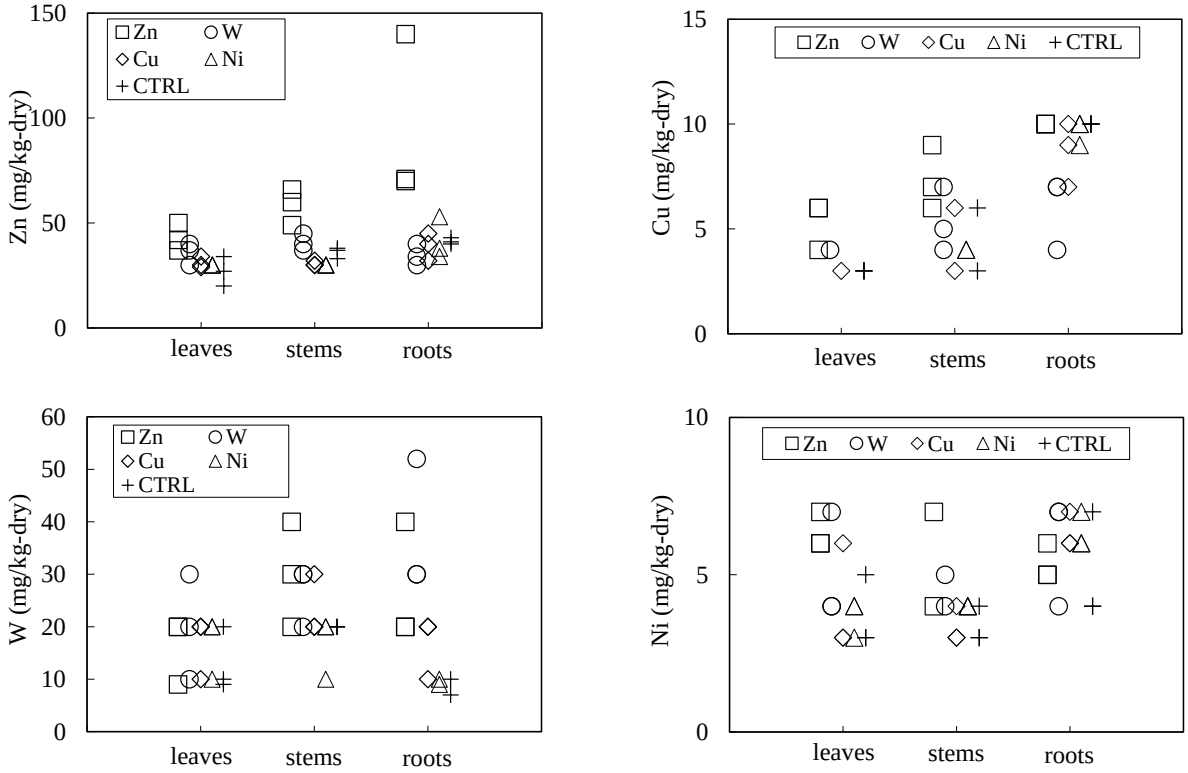

Fig.5 Zn, W, Cu, and Ni concentrations in leaves, stems, and roots of *Pinus densiflora.*

densiflora grown in heavy metal contaminated soil was higher than those in leave and stem [4]. Therefore, it was thought that *Pinus densiflora* can accumulate large amounts of Zn in its roots. And then, Zn concentrations in leaves, stems, and roots of Zn were higher than those concentrations of W, Cu, Ni, and CTRL. It is reported that *Athyrium yokoscense (Franch. et Savat.) Christ* and *Clethra barbinervis Sieb. et Zucc.* which live in the contaminated area, contain large amounts of Zn not only in their roots but also in their leaves and stems [2], [8-9]. Therefore, it was thought that *Pinus densiflora* also can accumulate large amounts of Zn in its leaves and stems.

W concentrations in leaves, stems, and roots of Zn were 9 to 20, 20 to 40, and 20 to 40 mg/kg-dry, respectively. W concentrations in leaves, stems, and roots of W were 10 to 30, 20 to 30, and 30 to 52 mg/kg-dry, respectively. W concentrations in leaves, stems, and roots of Cu were 10 to 20, 20 to 30, and 10 to 20 mg/kg-dry, respectively. W concentrations in leaves, stems, and roots of Ni were 10 to 20, 10 to 20, and 9 to 10 mg/kg-dry, respectively. W concentrations in leaves, stems, and roots of CTRL were 9 to 20, 20, and 7 to 10 mg/kg-dry, respectively. Therefore, roots W concentrations were higher than those in leaves and stems for W. Roots W concentrations were almost the same as W concentrations in leaves and stems for Zn, Cu, and Ni. Roots W concentrations of CTRL were lower than W concentrations in leaves and stems of CTRL. Moreover, roots W concentrations of W were higher than those of Zn, Cu, Ni, and CTRL, but W concentrations in leaves and stems of W were almost the same as those of Zn, Cu, Ni, and CTRL. It is reported that W concentrations in roots of Italian ryegrass grown in the nutrient solution containing tungsten were higher than those in leaves and stems [10]. Therefore, it was thought that *Pinus densiflora* also can accumulate large amounts of W in its roots.

In contrast, Cu concentrations in leaves, stems, and roots of Zn were 4 to 6, 6 to 9, and 10 mg/kg-dry, respectively. Cu concentrations in leaves, stems, and roots of W were 4, 4 to 7, and 4 to 7 mg/kg-dry, respectively. Cu concentrations in leaves, stems, and roots of Cu were 3, 3 to 6, and 7 to 10 mg/kg-dry, respectively. Cu concentrations in leaves, stems, and roots of Ni were under the detection limit, 4, and 9 to 10 mg/kg-dry, respectively. Cu concentrations in leaves, stems, and roots of CTRL were 3, 3 to 6, and 10 mg/kg-dry, respectively. Therefore, roots Cu concentrations were almost the same as Cu concentrations in stems and leaves for all conditions. Ni concentrations in leaves, stems, and roots of Zn were 6 to 7, 4 to 7, and 5 to 6 mg/kg-dry, respectively. Ni concentrations in leaves, stems, and roots of W were 4 to 7, 4 to 5, and 4 to 7 mg/kg-dry, respectively. Ni concentrations in leaves, stems, and roots of Cu were 3 to 6, 3 to 4, and 6 to 7 mg/kg-dry, respectively. Ni concentrations in leaves, stems, and roots of Ni

were 3 to 4, 4, and 6 to 7 mg/kg-dry, respectively. Ni concentrations in leaves, stems, and roots of CTRL were 3 to 5, 3 to 4, and 4 to 7 mg/kg-dry, respectively. Therefore, roots Ni concentrations were almost the same as Ni concentrations in stems and leaves for all conditions.

From the above results, it was found that *Pinus densiflora* accumulated Zn and W in the roots and Zn in the stems and leaves.

CONCLUSIONS

Zn, W, Cu, and Ni concentrations in *Pinus densiflora* and growth conditions (tree heights and appearances) were investigated to reveal the effects of heavy metals on the growth and their accumulation patterns in *Pinus densiflora* under different heavy metal-contaminated soil conditions. At 4 weeks later from the experiment start, the tree heights of *Pinus densiflora* in Zn, W, Cu, Ni, and CTRL were almost the same, and no appearance growth abnormalities were observed. it was found that *Pinus densiflora* can grow in Zn, W, Cu, and Ni contaminated soils. Zn concentrations in the Zn load condition and W concentrations in the W load condition were higher than those concentrations in other experimental conditions. Therefore, it was found that *Pinus densiflora* accumulate Zn and W. Roots Zn concentrations were higher than Zn concentrations in leaves and stems for the Zn load condition. W concentrations in roots were higher than those in leaves and stems for the W load condition. Therefore, it was found that *Pinus densiflora* can accumulate large amounts of Zn and W in its roots. Moreover, Zn concentrations in leaves, stems, and roots of Zn load condition were higher than those of other experimental conditions. Therefore, it was found that *Pinus densiflora* can also accumulate large amounts of Zn in its leaves and stems.

REFERENCES

[1] Satake K, "A "copper bryophyte" *Scopelophila cataractae* and copper (1) - Distribution of *Scopelophila cataractae* in the world", Proceedings of the Bryological Society of Japan, Vol.5, No.4, 1990, pp.49-53.

[2] Honjo T., Heavy Metals and Indicator Plants - Recovery of Natural Environment, Bulletin of the Japan Sea Research Institute Kanazawa University, No.30, 1999, pp.171-193.

[3] Hori K., Sakakibara M., and Sera K., Heavy Metal Accumulation in Trees on an Abandoned Mine Tailing in Southwestern Japan, NMCC Annual Report, 19, 2012, pp.198-205.

[4] Kyung W.S., Yowhan S., Charles C.R., Nam J.N., Jin W.K., and Jeong-Gyu K., Seedling Growth and Heavy Metal Accumulation of Candidate Woody Species for Revegetating Korean Mine Spoils, Restoration Ecology, Vol.16, No.4, 2008, pp.702-712.

[5] Honjo T., Studies on the Deposit of Heavy Metals in *Pinus densiflora* Leaves from the Kanazawa Castle Area, Kanazawa City, Ishikawa Prefecture, The Journal of Phytogeography and Taxonomy, Vol.XXVIII, No.2, 1980, pp.72–75.

[6] Nishioka H., Kodera H., Heavy metal content in fern plants, Journal of Environmental Conservation Engineering, Vol.34, No.4, 2005, pp.301-305.

[7] Kubohara T. and Ii H., Zn and Fe Contamination Index for River using River Insects and Water Plants in The Kinokawa River Catchment, International Journal of GEOMATE, Vol.19, Issue 75, 2020, pp.76-83.

[8] Morishita T. and Boratynski K. J., Accumulation of cadmium and other metals in organs of plants growing around metal smelters in Japan, Soil Science and Plant Nutrition, Vol.38, Issue 4, 1992, pp.781-785.

[9] Honjo T., http://kanazawa-sakurada.cocolog-nifty.com/blog/2009/06/2009626-9bd2.html

[10] Yamada. H., Nishimura K., Hattori T, and Takahashi E., Uptakes of Molybdenum and Tungsten by Italian Ryegrass, Japanese Journal of Soil Science and Plant Nutrition, Vol.60, Issue 5, 1989, pp.463-465.

8th Int. Conf. on Structure, Engineering & Environment (SEE), Mie, Japan, Nov.10-12, 2022, ISBN: 978-4-909106094 C3051

ANALYSIS OF FLOOD FLOW RATE CALCULATE FROM PRECIPITATION AT TYPHOON NO.19 IN 2019 IN THE ABUKUMA RIVER BASIN

Masanobu Taniguchi
Wakayama University

ABSTRACT

P Recent year, Japan has big typhoons, So the cities occurred flood, the Cities in Abukuma River Basin is damaged by the typhoon. The characteristic of flood runoff is not cleared. The Abukuma River is flooded by the typhoon, a part of the region of the Nasugawa City, the Hongu City, the Marumori Town, the Date City and the Hukushima City flooded. The Rain runoff calculation system is developed. The system can calculate the river runoff converted by precipitation, the system has river structure database and the small basin distribution. The rain runoff is calculated by Thiessen method at each rain observing station.

Keywords:Abukuma River, Typhoon, Flood, runoff, Flow rate

INTRODUCTION

The Abukuma River Basin was called "Abaregawa" its mean often flooded by the Typhoon in past. The Abukuma River has flood in 2019 at Typhoon No.19, some city were damaged by flood condition. The National major road No.349 which connects Miyagi and Fukushima prefectures, was broken by the flood, and the tunnel was filled with river and forest sediment. The Ministry of Land, Infrastructure, Transport and Tourism has rehabilitated the river to prevent flooding. The river was researched by some researcher, Sabo & Landslide Technical Center has surveyed the damaged from the typhoon. The Abukuma River Basin is 6th length in Japan. Therefore, it is difficult to clarify the flood phenomenon. The typhoon has moved slowly, thus the flood is occurred in 2019. It is necessary to analyze rain runoff quickly. The rain runoff calculation system is developed. The research objective is clear the relation between the precipitation and the river flowrate, and to calculate the river flows from the precipitation. The novelty of this study is to calculate the amount of runoff that arrives from the flow velocity and the distance of the river, and to predict the time when the rainfall water will arrive.

OVERVIEW OF RESEARCH AREA

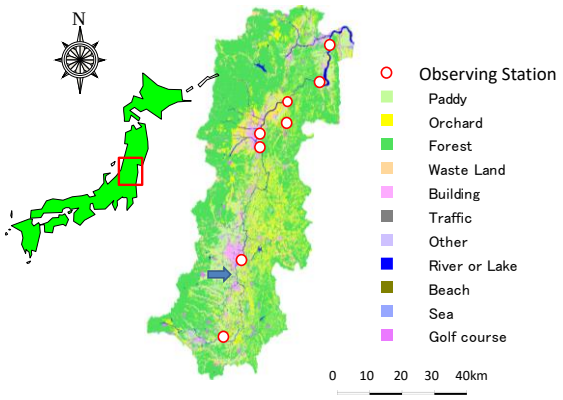

Fig.1 Overview of Abukuma River Basin

Fig.1 shows overview of Abukuma River Basin. The area in Abukuma River basin is 5,400 km². The flow path extension of the Abukuma River is 239km.[5] The length is 2nd long in Tohoku Area in Japan. The population is about 1.78 million people in the Basin. The Abukuma River has 17 cities in Fukushima Prefecture, has five cities in Miyagi Prefecture. The Abukuma River is originated at Asahidake in South - East of Fukushima. The land use of 56% in whole basin is forest, 16% is paddy, 14% is orchard, and 6% is building. The water of the Inawashiro lake inflows in the upper stream of Abukuma River Basin shown in arrow in figure. The sending water is mainly used for paddy.

THE METHOD OF CALCULETE RAIN RUNOFF

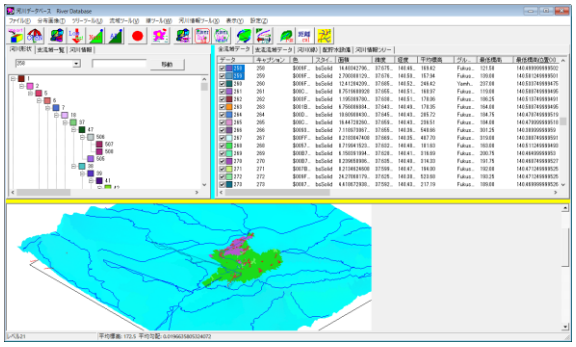

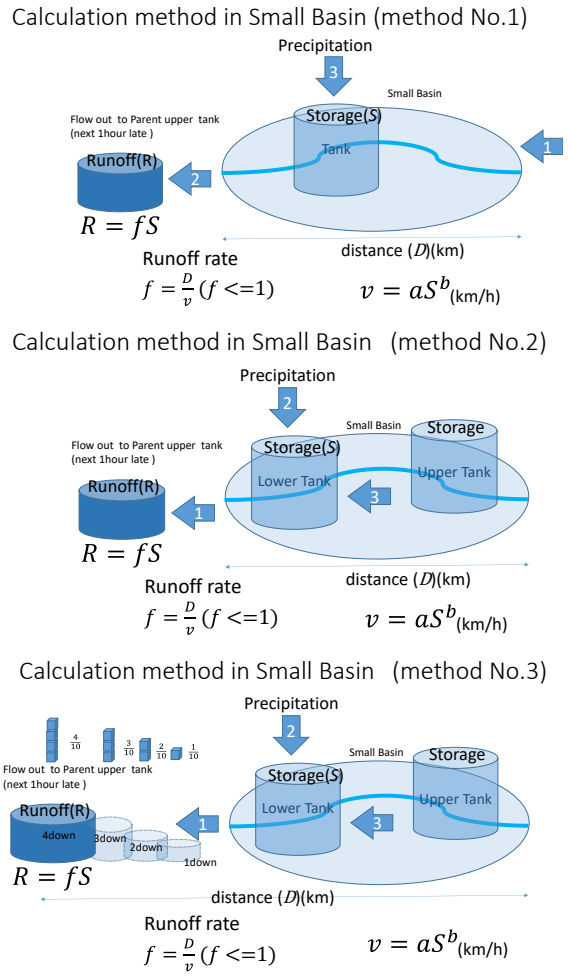

Fig.2 Method of calculation of rain runoff

Figure 2 shows the method of 3 types of calculation of rain runoff. The system has the river structure database, the river basin location data, river channel data, so the distance from upstream can be calculated. The distance is very important data to calculate the time of flood condition. The flow path is curved not straight, and location information is required to know the distance accurately. The rain runoff analyze system can calculate by location data of longitude and latitude. The runoff rate can be calculated by amount of rainfall per second calculated by precipitation and area, as the flow rate is per second. The calculation is performed from the upstream first, and the calculation is performed to the downstream. The amount of water reached is calculated by multiplying the amount of runoff by the coefficient obtained by the approximate formula. First type of method has one storage, next one has has two storages to reflect the value at the next time. And the third type of method is to calculate the runoff at higher speeds more accurately.

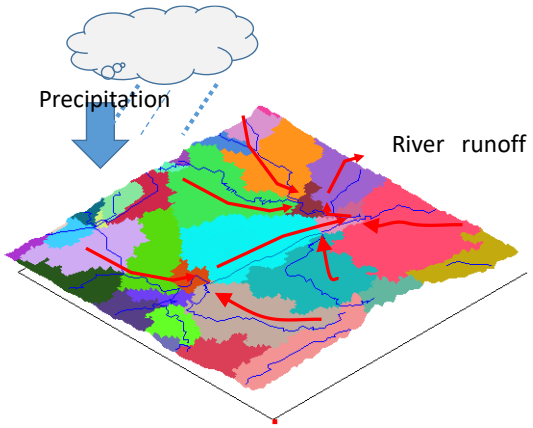

Fig 4. The overview of water flow.
Figure 4 shows overview of water flow.

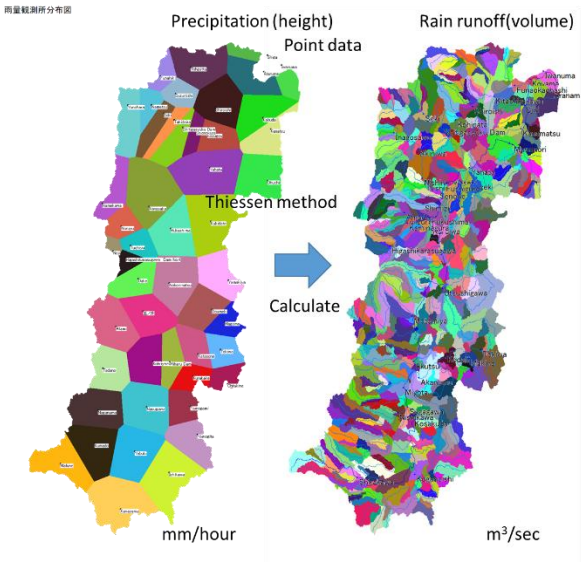

Fig. 5. The method of amount of rain runoff calculate by precipitation

Figure 5 shows the method of amount of rain runoff calculate by precipitation. There are 49 precipitation

stations in the Abukuma River basin. As, the data of precipitation is point data, the data need to calculated for each with small river basins. The point data is distributed by the Thiessen method. The amount of rain runoff is divided by the small basins, and collected by the rivers. The calculation of runoff needs to know relation between the basins.

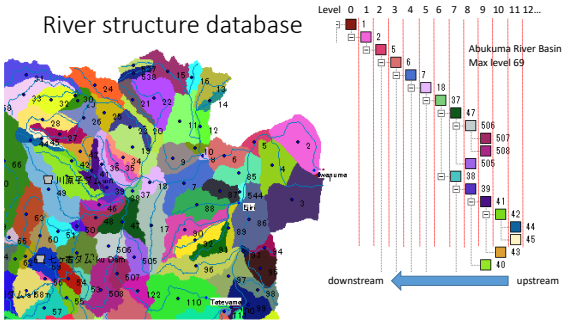

Fig.6. the small river basin structure database

Figure 6 shows the small river basin structure database. The rain runoff is collected by the river, the flow rate is calculated by each one hour time. The Abukuma River Basin has 543 places of the small basins. The max level of small basin is 69, the calculation of rain runoff is started from upper stream. The small basin has certainly one of river flow pass.

COMPARISON OF OBSERVED AND CALCULATED VALUES

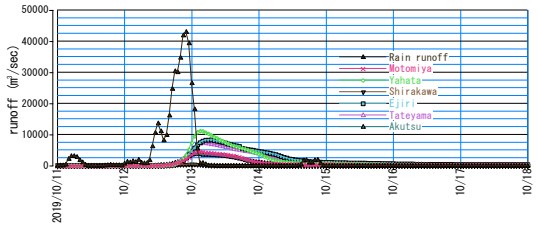

Fig 7. Time series of flow rate in the Abukuma river Basin at typhoon No.19 in 2019

Figure 7 shows the time series of flow rate in the Abukuma river Basin at typhoon No.19 in 2019. The max value of rain runoff is 43050m^3/sec, sum of amount of rain runoff from October 11 to 18 is 1,494,241,200m^3. The sum of water volume at Ejiri the lowest observing station is 1,044,104,400m^3.

RAIN RUNOFF CALCULATION

The distance of river pass is calculated by the Longitude latitude. The runoff velocity is showed by follow formula (1). The velocity is calculated by amount of rain runoff as "S" (m3/sec). The "a" and "b" are coefficients. The rain water runoff velocity is calculated by multiplying the power of "S" to "*b*" by "*a*". Next the runoff ratio is calculated by dividing the distance by the runoff velocity shown as formula (2). The runoff ratio is calculated by the distance and velocity of the river. Moreover the amount of runoff is calculated by multiplying the runoff ratio by the amount of runoff shown as formula (3).

$$v = aS^b \quad (1)$$

$$f = \frac{D}{v} \ (f <= 1) \quad (2)$$

$$R = fS \quad (3)$$

Using this formula, the flow rate can be predicted from the amount of precipitation.

RESULT OF RAIN RUNOFF DISTRIBUTION

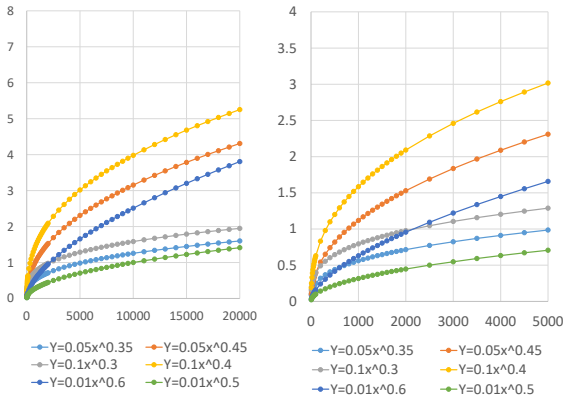

Fig 8. Approximate line between amount of rain runoff (m^3/sec) and velocity (km/hour)

Figure 8 shows the approximate line between amount of rain runoff and velocity. It is important to consider velocity in order to estimate the amount of water that will reach the downstream basin after one hour. Generally, when the amount of rain is heavy, the flow velocity tends to be high. However the velocity is unknown in flood condition, the velocity is estimated by some the approximate lines.

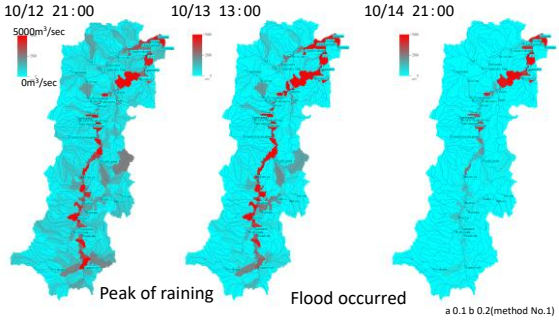

Fig 9. The result of rain runoff distribution (No.1)

Figure 9 shows the result of rain runoff distribution calculated by the method No.1. In the formula, Coefficient “a” was used 0.1, and “b” was 0.2.

The max of rain runoff is showed over 5000m^3/sec by red color. The peak of typhoon raining is October 12 21:00 in whole area. At October 13 13:00, the flooding in some area is occurred. As the flood is occurred, the result of lower stream of rain runoff was different value from observed flow rate. The No.1 method is the small basin has one tank, same time of water storage is include the upper stream of water runoff value, as the value is calculated from upper stream. The problem of the method is seemed to calculate higher value.

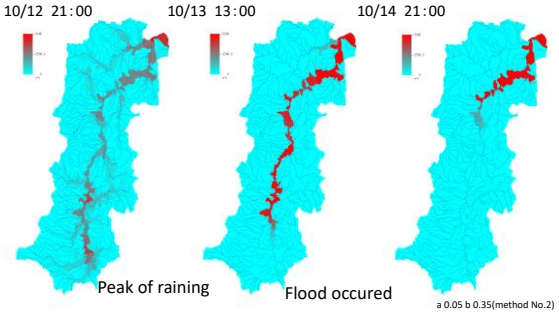

Fig 11. The result of rain runoff distribution (No.2)

Figure 11 shows the result of rain runoff distribution calculated by the method No.2. In the formula, Coefficient “a” was used 0.05, and “b” was 0.35. The No.2 method has two tanks, so upper stream of amount of water runoff is calculated one hour after. It is estimated to calculate water runoff was accurately, however the channel distance of the small basin is shorter than the calculated velocity. As a result, the calculated rain runoff was slower than the actual flow rate. Since the tanks are separated, the maximum value is also determined, and water is flowing in order.

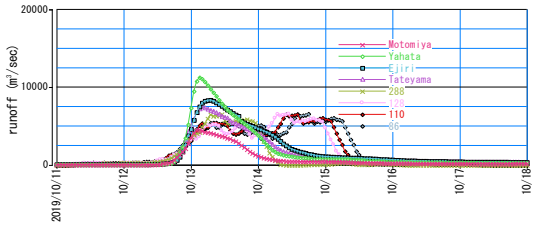

Fig 12. The time series of water runoff (No.2)

Figure 12 shows the time series of water runoff calculated by the method No.2. The peak of rainwater runoff is not sharp. The water flow is determined by the small basin, and it was estimated that Small basins need to be skipped.

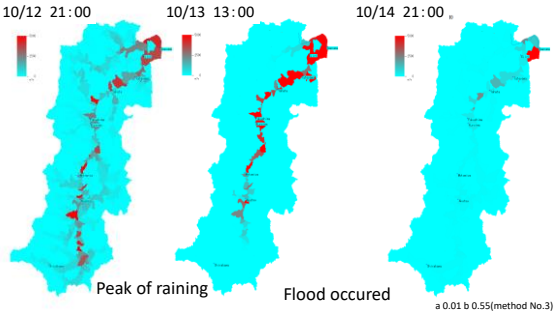

Fig 13. The result of rain runoff distribution (No.3)

Figure 13 shows the time series of water runoff calculated by the method No.3. The flow velocity fits well with the following coefficients. In the formula, Coefficient “a” was used 0.01, and “b” was 0.55. If the small basin is skipped, the water does not flow in the small basin. As the river flow is wave, it was assumed the rain runoff was triangle wave. However the calculation occurred noise.

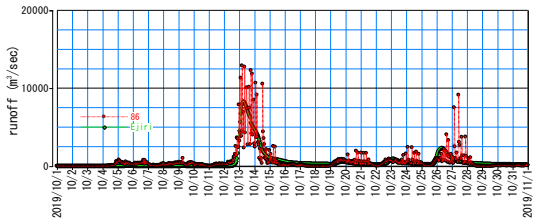

Fig 14. The time series of water runoff (No.3)

Figure 12 shows the time series of water runoff calculated by the method No.3. The peak time is seemed same time, and the shape of the peak is very similar.

CONCLUSIONS

The rain runoff analysis system is developed. The Abukuma Basin was flooding in 2019. The rain runoff was calculated, some method of calculation was tried. The peak time of the calculated amount of rain runoff is seemed same time to observed flow rate, and the shape of the peak is very similar in the method No.3. However the calculated rain runoff has noise, and the system is need to improve.

REFERENCES

[1] Tokuo KISHII, On the Flood Disaster in the Abukuma River Basin at the End of August 1998, Natural Disaster Research Report of the National Research Institute for Earth Science and Disaster Resilience 37 , pp. 91-105, 2001.

[2] Tsuyoshi KINOUCHI and Katumi MUSIAKE, Water quality and nutrient loads in the abukuma watershed under normal flow condition, Water Engineering paper, vol. 51, February 2007(in Japanese)

[3] Ralia,https://www.wakayama-u.ac.jp/~masa/profile/soft/index.html, 2018.

[4] Ministry of Land, Infrastructure and Transport, Japan, Water information system, http://www1.river.go.jp/

[5] Digital national land information, http://nlftp.mlit.go.jp/ksj/
Japan Meteorological Agency, http://www.jma.go.jp/jma/index.html

[6] Kazuyuki Mizumura, Hydrosphere hydrology, 1998.

[7] Isamu Kayane, Hydrology, Daimeido 1980.

8th Int. Conf. on Structure, Engineering & Environment (SEE), Mie, Japan, Nov.10-12, 2022, ISBN: 978-4-909106094 C3051

ANALYSIS OF SEASONAL AND SECULAR VARIATIONS IN DISSOLVED OXYGEN CONCENTRATION AT THE BOTTOM OF LAKE BIWA, JAPAN

Jinichi Koue[1,2]

[1]Graduate school of Maritime Sciences, Kobe University, Japan; [2]Graduate School of Engineering, Osaka University, Japan

ABSTRACT

Lake Biwa in Japan is a water resource utilized by approximately 14 million people in Kansai region, and its water pollution has a significant impact not only on people but also on the ecosystem, particularly in the bottom layer, where hypoxia can cause an environmental problem. Until the 1980s, eutrophication was the main cause of hypoxia of the lake bottom, and after the measures for eutrophication, it is not clear what the main cause quantitatively is such as the climate change and a regime shift in the ecosystem. In the present study, seasonal and secular variations of water quality in Lake Biwa over the past 30 years were analyzed by using vertical profile data of water temperature and dissolved oxygen concentration observed by Lake Biwa Environmental Research Institute in Shiga Prefecture at the deepest point of fixed-point observation and weather data at Hikone Local Meteorological Observatory. The results of the analysis showed that intensity of stratification increased in the surface layer of Lake Biwa, but conversely stratification weakened in the deeper layers. These changes in the physical environment of the lake have affected the decline of dissolved oxygen in the lake bottom of Lake Biwa. The seasonal changes in dissolved oxygen over 30 years could be classified into approximately three patterns, with the dominant factors being the strengthening of stratification due to the change in air temperature and wind speed, the shortening of the period of the overturning and the vertical mixing by wind during stratified season and cooling period.

Keywords: Dissolved Oxygen, Climate change, Overturning, Lake Biwa

INTRODUCTION

Water contains a variety of substances, including organic matter, minerals, and microorganisms, and physical, biological, and chemical reactions constantly occur. In rivers, there is a time span between the time the water originates at the source and the time it flows out to the sea, but that time span is only a few days. Therefore, as the water quality in the river changes, these physical, biological, and chemical reactions in rivers brought about less significant problem than in lakes and marshes. However, in lakes, once the water flows into the lake, water stays in the closed water body for a long period of time. During the residence process, physical, biological, and chemical reactions such as heat exchange with the atmosphere and elution of nutrients from the bottom sediment proceed, and hypoxia, eutrophication, and other visible changes in water quality eventually occur.

Lake Biwa is the largest freshwater lake in Japan. The lake has an area of approximately 674 km^2 (616 km^2 in the north and 58 km^2 in the south), a maximum depth of 103.6 m, a length of approximately 63.5 km from north to south, a maximum width of 22.8 km and a minimum width of 1.35 km (Figure 1). Lake Biwa is divided into northern part and southern part of the lake based on its shape, with an average depth of 43 m in northern part and 4 m in southern part. The total volume of Lake Biwa is approximately 27.5 billion m^3. The annual water inflow is about 5 billion m^3, and the average residence time is 5.5 years in North Lake and approximately 15 days in South Lake.

Hypoxia in the bottom layer of the northern part of Lake Biwa became pronounced around the 1960s, and it has been pointed out that the cause of the hypoxia in Lake Biwa is an increase in organic matter in the surface water layer due to eutrophication and sedimentation into the deep layer. There is concern that anoxia of the bottom layer may affect the habitat of the ecosystem living in the bottom layer, leading to water pollution in Lake Biwa. The concentration of dissolved oxygen of 2 mg/l or less in the bottom layer (90 m) in Imazu-Oki has been observed in some years since 1979. The concentration of 2 mg/l has significance as a value at which the basic metabolism of organisms declines. For example, in Lake Ikeda, the overturning (whole-layer circulation) did not occur every year, but partial circulation prevailed, and dissolved oxygen in the deep layer continued to decrease, becoming nearly anoxic in recent years [1]. In the case of Lake Biwa, it is necessary to pay

attention to future trends. However, even after the 1980s, when organic substances and nutrient loads from the land area were regulated, the dissolved oxygen concentration in the bottom layer of Lake Biwa remained below 2 mg/L. This is attributed to climate change around Lake Biwa in recent years ([2],[3]). Woolway stated that changes in stratification due to climate change have a significant impact on the hypoxia of the bottom layer in lakes worldwide. In particular, they reported that the increase in air temperature and decrease in wind speed may weaken vertical mixing of lake water and cause a decrease in dissolved oxygen concentration.

The effect of wind speed, precipitation, and inflows on stratification in relation to warm and cold weather was significant especially when observed climate patterns were expected to have effects on thermal characteristics [4]. For example, the global warming has reduced snowfall mainly in the northern basin of Lake Biwa, and that the amount of snowmelt water, which is colder and richer in oxygen than lake water during the snowmelt season, may be flowing into the bottom layer along the lake bottom. However, no such phenomenon of snowmelt water flowing along the lake bottom was observed, and studies of the relationship between the size of snowmelt runoff and the minimum annual dissolved oxygen level showed no effect. Vertical mixing by wind causes various phenomena such as blowdown flow and destruction of stratification by vertical mixing when wind blows. In addition, wind causes internal waves, and the breaking of these waves results in active mixing of the lake water. Wind-driven wind, vertical mixing, and internal waves have been observed by continuously monitoring the vertical distribution of water temperature using a mooring system [5]. Among these, wind influences on the deep-water layer are vertical mixing and internal waves caused by strong winds. They showed that vertical mixing is caused by the passage of such waves (internal surge) in Lake Biwa during summer. However, the seasonal and secular changes in dissolved oxygen at all depths due to strong winds and internal waves have not yet been fully investigated. In this study, environmental changes in Lake Biwa were investigated from the physical aspect using data from a fixed point in the northern part of Lake Biwa.

DATA ANALYSIS

The analysis used data on water temperature and dissolved oxygen concentration obtained from periodic surveys (once or twice a month) conducted by Lake Biwa Environmental Research Institute in Shiga Prefecture at the monitoring point of Imazu-oki (Fig. 1) (water depth: approximately 90 m). This periodic survey has been conducted since 1979. This monitoring point is the deepest point among the fixed points of the periodic surveys conducted on a multidecadal scale. The depths are 0.5 m, 5 m, 10 m, 15 m, 20 m, 30 m, 40 m, 60 m, 80 m, and 1 m just above the lake bottom (approximately 90 m). (Water temperature, dissolved oxygen concentration, and depth were measured in the field using a HYDOROLAB water quality sensor (Quanta). Air temperature, wind speed, wind direction, and precipitation were observed at Hikone District Meteorological Observatory (every 3 hours (only precipitation is a daily average)). The height from the ground of the thermometer, which observed air temperature, is 1.5 m. The height from the ground of the anemometer, which observed wind speed and direction, is 17 m. The minimum unit of water and air temperature, wind speed and precipitation are 0.1°C, 0.1 m/s and 0.1 mm respectively. The wind direction was observed in 16 directions. The stratification strength is estimated by the difference in water temperature between the surface layer (5 m) and the bottom layer (90 m). The surface layer is not at a depth of 0.5 m, where water temperature is likely to change due to wind mixing, but at a depth of 5 m below the surface layer, while the bottom layer is at a depth of 90 m. SSI (Schmidt stability index (kgm/m^2) was estimated in order to calculate the strength of stratification as follows.

$$SSI = \frac{1}{A_0}\int_{z_0}^{z_m} A_z(z - z_g)(\rho_z - \rho_g)dz \quad (1)$$

$$z_g = \frac{1}{\int_{z_0}^{z_m} A_z\rho_z dz}\int_{z_0}^{z_m} A_z\rho_z z dz \quad (2)$$

$$VMI = \frac{WSI}{SSI} \quad (3)$$

$$WSI = \kappa \times |\tau| \quad (4)$$

$$\tau = \rho_a C_D \lfloor U_a \rfloor U_a \quad (5)$$

where A_0 is surface area of lake (m^2), z is depth (m), z_m is maximum depth (m), z_0 is water surface depth (m), A_z is area at depth z (m^2), ρ_z is density at depth z (kg/m^3), ρ_g is density at depth z_g (kg/m^3), V is lake volume (m^3), and z_g is depth to the center of gravity of stratified lake (m). In this study, the density was calculated as a function of only water temperature. Vertical mixing index (VMI) indicates the parameter of expressing the proportion of the wind stress on the stratification. κ is the constant of 1.0. Wind stress index was calculated in order to evaluate the influence of the strong wind on the stratification. τ is the wind stress, ρ_a is the air density above the lake surface (1.2255 kg/m^3), U_a indicates the atmospheric wind speed at a height of 17 m above the lake surface, C_d represents the drag coefficient of lake surface, which performs the momentum transfer efficiency between atmosphere and lake, and is dependent on wind speed, currents, waves, lake surface roughness,

and stability amongst other factors.

Frequency analysis was used to determine whether a particular period of wind prevailed.

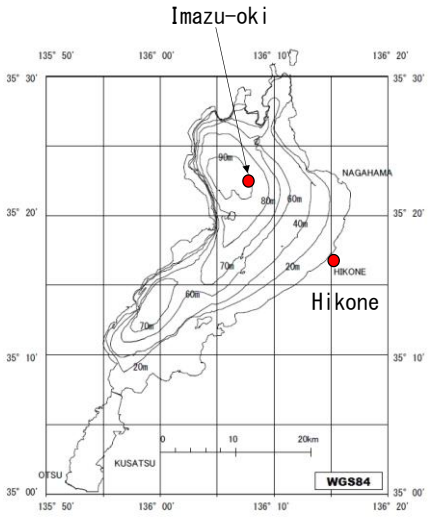

Fig.1 Monitoring point for each data in Lake Biwa

RESULTS AND DISCUSSIONS

Factors of the seasonal change of dissolved oxygen over 30 years

Seasonal changes in dissolved oxygen (DO) in the bottom layer (90 m depth) in the monitoring point of Imazu-oki over the past 30 years could be approximately classified into three patterns (Fig. 2). . Firstly, in A-pattern, DO began to decrease with the onset of stratification, reached a minimum around October, and then recovered somewhat before the overturning occurred. In this case, the minimum DO was often around 2 mg/l. On the other hand, in B-pattern, DO gradually decreased and maintained a value higher than the minimum DO in A-pattern before the overturning. In C-pattern, the decrease in DO continued until around December, but the minimum DO was 2-4 mg/l at most. The rate of decrease in DO was greatest in A-pattern, and decreased in the order of C-pattern and B-pattern.

in the 1990s, while C-pattern was observed after 1990 in all but one case.

Fig. 2 shows the averaged seasonal changes in DO for each pattern. Fig. 3, 4, 5 shows the secular change of SSI, VMI, period of overturning from 1980 to 2009. SSI of average of A-pattern was 197.93 and 7 higher than that of B and C-pattern. The strength of stratification in A-pattern was higher than that of B and C-pattern. The decreasing rate of DO was influenced by the strength of stratification. From Fig. 4, VMI of A-pattern was 6.98×10^{-5} and 4.42×10^{-6} lower than B-pattern, and 5.67×10^{-6} lower than C-pattern. Considering the effect of the wind stress, the correlation coefficient between VMI and decreasing rate of DO was 0.54, therefore the contribution of the wind stress to the vertical mixing plays an important role in the change of DO. As for A-pattern, the vertical mixing due to the wind stress less occurred compared with B, C-pattern. DO tended to decrease during the period of stratification due to the consumption of DO by bacteria under the thermocline. From the perspective of the amount of precipitation, the correlation between precipitation and decreasing rate of DO was rather low (Fig. 5). Fig.6 shows the secular change of period of overturning from 1980 to 2009. The correlation coefficient of the period of overturning and decreasing rate of DO was 0.54, hence as the period of overturning decreased, the decreasing rate of DO increased. The vertical mixing in winter occurred efficiently, DO in lake was enough in all layers, and hypoxia in the bottom of the layer less likely happened as in the case of B-pattern.

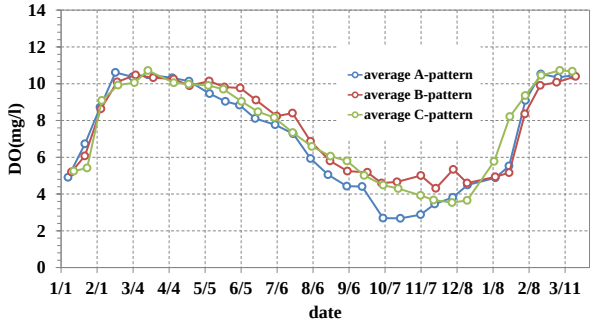

Fig.2 Average of seasonal change of DO over 30 years

Table 1 Three types of classification based on the shape of seasonal changes in DO concentration over 30 years (A-pattern 11 times, B-pattern 11 times)

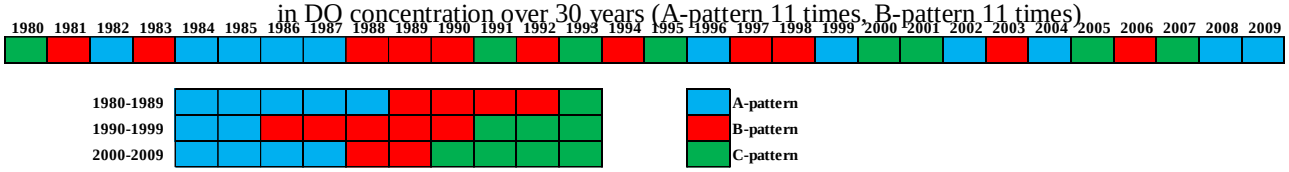

Seasonal changes in DO over the past 30 years can be divided into these three patterns: A-pattern 11 times, B-pattern 11 times, and C-pattern 8 times (Table 1). A-pattern was most frequently observed in the late 1980s and 2000s, with only two cases in the 1990s (1996 and 1999). B-pattern was more common

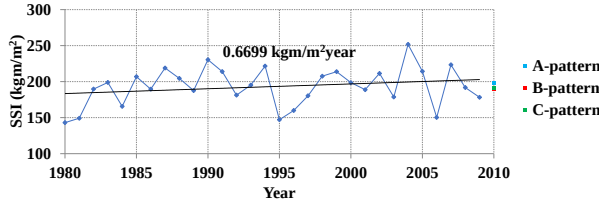

Fig. 3 Secular change of average SSI from the starting day of overturning to the day of minimum DO for 30 years

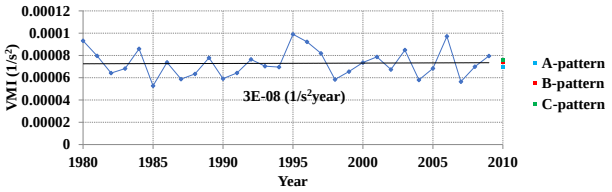

Fig. 4 Secular change of VMI from the starting day of overturning to the day of minimum DO for 30 years

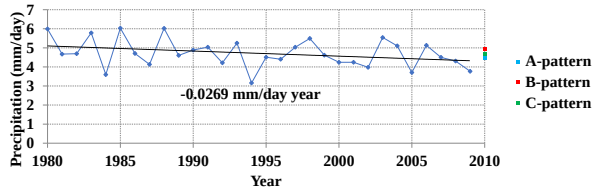

Fig. 5 Secular change of precipitation from the starting day of overturning to the day of minimum DO for 30 years

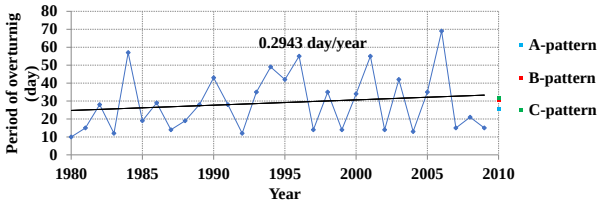

Fig. 6 Secular change of period of overturning from 1980 to 2009

Recovery of DO in the case of A-pattern

As for the case of A and C-pattern, DO decreased more than B-pattern. Only in the case of A-pattern, DO recovered slightly right before the overturning period. Fig. 7 shows the relationship between recovery of DO and VMI in A-pattern. The correlation coefficient of VMI and the amount of average recovery value of DO in A-pattern was 0.41. The amount of recovery value of DO was calculated by the averaging the values from the day of the minimum DO to the day right before the overturning. During the period of recovery in DO, as the stratification weakened and the strong wind blew, the vertical mixing between 80 m layer and 90 m layer more likely occurred. Minimum DO remained greater for B-pattern and C-pattern than for A-pattern. Therefore, the strong wind lead to the vertical mixing in the bottom layer, which supplied with the DO from the just above the bottom layer.

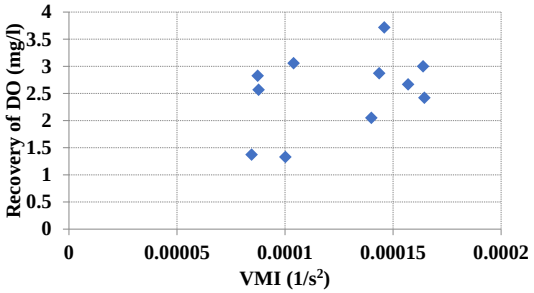

Fig. 7 The relationship between recovery of DO and VMI in A-pattern

The trend of secular change of DO

Fig. 8 shows the secular change of difference of DO between 90m and each depth from 1980 to 2009. Difference in DO between 90m and each depth was determined by annual moving average. Difference in DO between the bottom layer and each layer (from the surface layer (0.5 m) to the deep layer (20-60 m)) became larger as time passed.

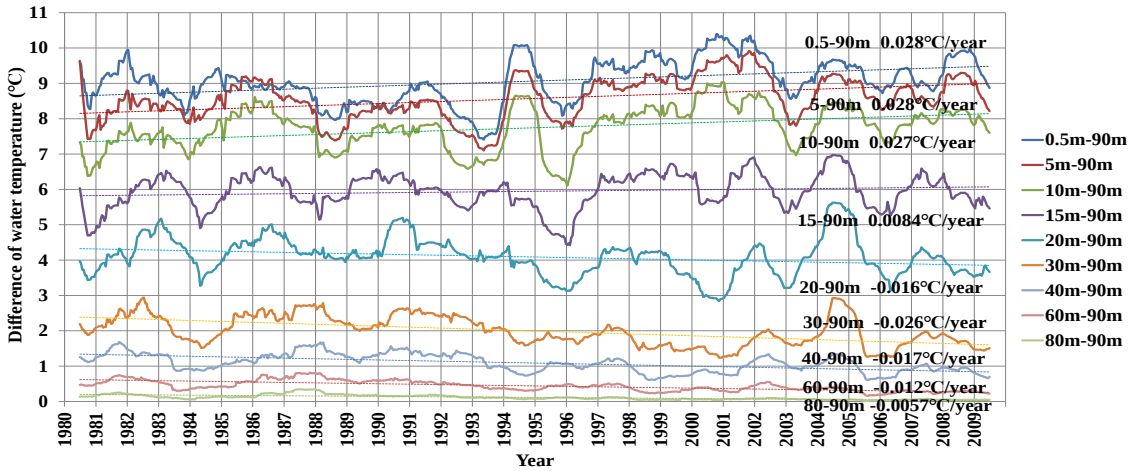

Fig. 8 Secular change of difference of DO between 90 m and each depth from 1980 to 2009

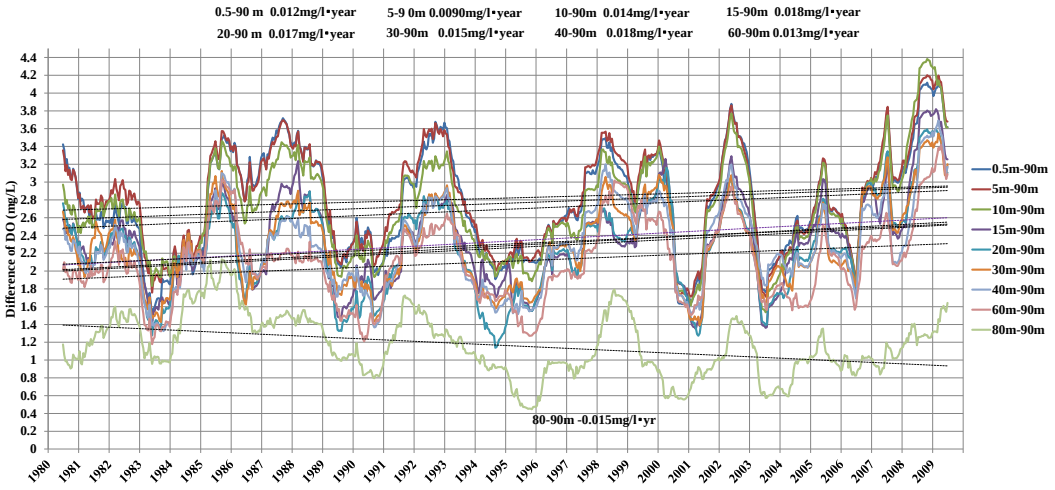

Fig. 9 Secular change of difference of water temperature between 90 m and each depth from 1980 to 2009

Difference in DO between 90 m and 80 m layer became less from 1980 to 2009, which means that the bottom layer from 80 m to 90 m became the homogeneous layer, taking into account that the difference of water temperature between 90 m and 80 m was not so large (From Fig.9). The increase of water temperature in the surface layer was closely related to the increase in air temperature during the stratification period. The air temperature at Hikone increased by about 1.3℃ as a linear trend over the past 30 years. On the other hand, it was reported that water temperature at the lake bottom was highly correlated with the air temperature in winter when the overturning (whole-layer circulation) occurred.

The difference in the trend of the increase in water temperature by depth showed an interesting feature in the temporal variation of the difference between the water temperature in each layer and that at the bottom of the lake. The difference between the water temperature at the surface and that at the bottom of the lake increased with depth from the surface to 15 m, while the difference decreased at depths deeper than 20 m. This means that the stratification was enhanced in the entire lake, while the stratification was weakened at depths deeper than the thermocline in summer (this is irrelevant in winter, when the water temperature was uniform).

The trend of water temperature uniformity in the stratified layer is considered to be related to the increase in wind intensity. The annual mean wind speed at Hikone showed an increasing trend with time, increasing by 0.29 m/s over 30 years (10%) as a linear trend. It is possible that the mixing of the deep water layer associated with enhanced winds caused the uniformity of water temperature. Another possibility is that the vertical mixing at the beginning of stratification has been enhanced in recent years. In other words, it is reasonable to assume that the conditions below the thermocline were not due to stratification period but were due to non-(weakly) stratified conditions (overturning period).

Fig.10 demonstrates the secular change of power spectrum of wind speed from April to December over 30 years. The power spectrum shows a relatively weak trend in the 1980s and 2000s and a strong trend in the 1990s. This trend was consistent with the fact that B and C-patterns were more frequent in the 1990s and A-pattern were more frequent in the 1980s and 2000s. Seasonal change of DO in 1990, 1992, 1994, and 1998 were classified as B-patterns, in those years, 24-hour period power spectra of wind speed were large. Seasonal change of DO in 1987 and 2008 were classified as A-pattern, and 1980, 1991, 1993, 2000, and 2005 as C-pattern, and their power spectra were relatively small. The periodic strong wind speed influenced seasonal change of DO over 30 years.

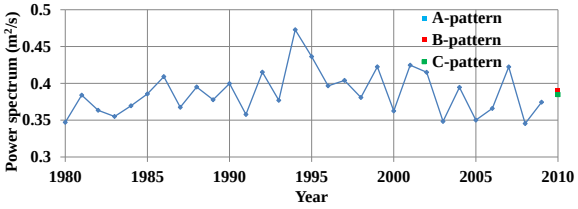

Fig.10 demonstrates the secular change of power spectrum of wind speed from April to December over 30 years

CONCLUSIONS

Seasonal and secular changes of water quality in Lake Biwa over the past 30 years were examined using data of water temperature and dissolved oxygen concentration observed by Lake Biwa Environmental Research Institute and data of air temperature, wind speed, and precipitation from Hikone Local Weather Station.

DO increased with time, except at depths of 80 and 90 m for 30 years. The increase in DO was inversely correlated with the increase in water temperature. The reason for the increase in DO in contrast to the increase in water temperature from 0.5

m to 15 m was unknown, but the increase in phytoplankton near the surface could have an effect. The decreasing rate in DO at 80 m depth was larger than that at 90 m depth. Therefore, in the bottom layer the DO concentration tended to decrease over 30 years.

Seasonal changes in DO at the lake bottom varied from year to year, but could be roughly classified into three patterns. A-pattern showed an earlier decrease in DO during the period of stratification than B and C-patterns, and a further decrease than the minimum of the B and C-patterns. In B-pattern, the decrease in DO during the stratification period was slower and the minimum value remained higher than in A-pattern, and then recovered during the overturning period. In C-pattern, DO decreased more slowly than in A-pattern and recovered earlier than in B-pattern. The minimum DO was higher than in A-pattern and DO rarely recovered before the overturning.

VMI (the average of the period from the start of the overturning to the lowest DO date) showed a corresponding relationship with the three patterns. The strength of stratification in A-pattern was stronger than the average of B-pattern except in 1982, 1996, and 2009, that of B-pattern was weaker than the average of A-pattern except in 1994 and 1998, and that of C-pattern was weaker than the average of A-pattern except in 1980, 1993, and 1995. The strength of stratification of the C-pattern was higher than that of the B-pattern except in 1980, 1993, and 1995. The strength of stratification mainly depends on the wind stress and air temperature.

The period of overturning was also related to the three patterns. In most cases, the short period of overturning corresponded to A-pattern, while the long period of overturning corresponded to B and C-pattern. For example, the A-pattern had a longer stratification period than the B-pattern. The overturning of A-pattern (except for 1984 and 1996) were shorter than those of B and C-pattern, while those of B-pattern (except for 1983, 1992, and 1997) tended to be longer.

Another factor controlling the pattern of seasonal changes in DO was the strong wind in the period of strong and weak stratification, and the secular variation of wind velocity over a 24-hour cycle. As for the recovery of DO in A-pattern in autumn, the strong wind such as typhoon played an important role in the vertical mixing in the bottom layer (80 m and 90 m) according to the calculation of VMI. On the other hand, the most prominent wind system in Lake Biwa during the period of stratification is the lake breeze, which is the most dominant wind system during this period. The secular variation of the power spectrum of wind speed showed a relatively weak trend in the 1980s and 2000s and a strong trend in the 1990s. This trend was consistent with the fact that B and C-pattern were more frequent in the 1990s, and A-pattern were more frequent in the 1980s and 2000s. In other words, the vertical mixing was relatively strong in the 1990s, when winds of this period were strong, and B-patterns were more likely to appear, while mixing was weaker in the 1980s and 2000s, when A and C-patterns were more likely to appear. the secular change of the 24-hour cycle of the lake breeze appeared to be consistent with DO pattern.

In this study, environmental changes in Lake Biwa were investigated from the physical aspect using data from a fixed point in the northern part of Lake Biwa. In order to examine changes of water quality in Lake Biwa as a whole in more detail, it will be necessary to study them in combination with model experiments as we developed [3]. In addition, changes in DO could be examined from a biochemical point of view, and a complex study that includes the physical environment is a major issue for the future.

REFERENCES

[1] Ito Y., Momii K., Impacts of regional warming on long-term hypolimnetic anoxia and dissolved oxygen concentration in a deep lake, HYDROLOGICAL PROCESSES 29(9) 2232-2242

[2] Kumagai, M., Vincent, W.F., Ishikawa, K., and Aota, Y, Lessons from Lake Biwa and other Asian lakes: Global and local perspectives, in Freshwater Management (eds. M. Kumagai, W.F. Vincent), Springer, Tokyo, 2003, pp.1-23.

[3] Koue J., Shimadera H., Matsuo T., Kondo A., Numerical Analysis of Sensitivity of Structure of the Stratification in Lake Biwa, Japan by changing Meteorological elements, Water, Vol. 10, 2018,1492.

[4] R. Iestyn Woolway., Sapna Sharma., Gesa A. Weyhenmeyer., Andrey Debolskiy., Malgorzata Golub, and Eleanor Jennings, Phenological shifts in lake stratification under climate change. Nature Communications volume 12, 2021, 2318.

[5] Stetler, J. T., S. Girdner, J. Mack, L. A. Winslow, T. H. Leach, and K. C. Rose. 2021. Atmospheric stilling and warming air temperatures drive long-term changes in lake stratification in a large oligotrophic lake. Limnol. Oceanogr. 66: 954–964.

[6] Saggio A. and Imberger J., ”Internal wave weather in a stratified lake.”, Limnology and Oceanography, Vol.43, 1998, pp.1780-1795.

8th Int. Conf. on Structure, Engineering & Environment (SEE), Mie, Japan, Nov.10-12, 2022, ISBN: 978-4-909106094 C3051

GREEN PROCESS FOR CRUDE PALM OIL BIODIESEL PRODUCTION USING COMMERCIAL LIPASE ENZYME

Mallika Tapanwong[1], Rayakorn Nokkaew[2], Pinsuda Viravathana[3] and Vittaya Punsuvon[4*]
[1,3,4]Faculty of Science, Kasetsart University, Thailand; [2,3,4]Center of Excellence-Oil Palm Kasetsart University, Thailand

ABSTRACT

Antioxidants such as carotene about 500-700 ppm and vitamin E (tocopherol and tocotrienol) about 600-1,000 ppm are abundant in crude palm oil (CPO). Those antioxidants have many beneficial effects to human health including enhancement of immune and reduction of the risk degenerative diseases such as cancer and cardiovascular diseases. Thus, the extraction of antioxidants from oil is interesting. Because oil, carotene and tocols are non-polar substances, they are good solubility with each other. One separation method is transforming CPO to biodiesel and then separating biodiesel out of the antioxidants, called as palm phytonutrients, by biodiesel distillation. The keys of this method are producing highly biodiesel yield while keeping the minimum destructiveness on palm phytonutrients. In this research, the enzymatic transesterification with commercial lipase was carried out. The 2-levels factorial design was performed to evaluate four parameters including enzyme amount, methanol molar ratio, water amount, and operation time, on fatty acid methyl ester (FAME), free fatty acid (FFA), carotene content, tocopherol and tocotrienol content. The ANOVA reported that enzyme amount was significant to all responses except FAME while the effect of methanol molar ratio was significant on FFA and tocotrienol content. The interactive effect between methanol to oil molar ratio and water amount had affected FAME and carotene content. In summary, the production of biodiesel synthesized by commercial lipase was a green process which non-waste water, gave highly biodiesel yield without using chemical catalysts, and especially preserved palm phytonutrients.

Keywords: Crude palm oil biodiesel, Enzymatic transesterification, Commercial lipase, Free fatty acid, Carotene content

INTRODUCTION

Palm is one of several economical plant in Thailand. It can produce a lot of oil comparing with other oil-based plants. In crude palm oil (CPO), the major component is saponified matter including free fatty acid and triglyceride. The minor part is a collection of phytonutrients such as carotenoids (500-700 ppm), tocopherol and tocotrienol (600-1,000 ppm), sterols (326-527 ppm) and squalene (200-500 ppm) [1]. The main carotenoids in CPO are β-carotene (70%) and α-carotene (30%) which are considered as a pro-vitamin A. The carotenoids have a function as a biological antioxidants and it has a lot of beneficial effect on human health that enhanced the immune response and reduced the risk of degenerative diseases such as cancer, cardiovascular diseases, cataract, and muscular degeneration [2]-[3]. Moreover, tocopherol and tocotrienol are also accepted as a potential antioxidant. They exhibit the biological activities on human health such as neuroprotective, anti-cancer, anti-inflammatory and cholesterol lowering properties [4]. In CPO, there is abundant of tocotrienol which shows a superior antioxidant activities and anti-inflammatory properties more than tocopherol [5].

Mainly, CPO can be used as a raw material for the production of two different groups. The first group is for human consumption such as palm olein oil, red palm oil and margarine. The second group is for energy consumption such as biodiesel. Biodiesel can be synthesized from CPO and alcohol especially methanol using several catalysts. In esterification reaction, the acid catalyst is used to reduce high content of free fatty acid in CPO to lower than 2%. After that, the transesterification reaction is performed to synthesize biodiesel from oil containing free fatty acid under 2% that obtained from esterification reaction. The catalyst in this step can be separated to two types. Firstly, the homogeneous catalysts are sodium hydroxide and potassium hydroxide which can synthesize highly biodiesel yield but it give waste water from purification process [6]. The second catalyst is heterogeneous catalyst such as calcium oxide and calcium hydroxide which are more benefit in terms of no waste water [7].

Normally, biodiesel synthesized from CPO presents the red color. It indicates that the carotene in CPO still contains within biodiesel. If this biodiesel is further distillated under reduced pressure, it will generate two products, pure biodiesel and a palm phytonutrients [8]-[10]. The palm phytonutrients are

a combination of carotene, tocopherol, tocotrienol and other antioxidants. From those process, CPO is not only originated a purified biodiesel but it also produces a value-added product as well. In this case, the process of biodiesel production is important. The reaction should perform under mild condition because the carotene, tocopherol and tocotrienol are sensitive by heat and chemical substance such as acid catalyst in esterification process and basic catalyst in transesterification process. Thus, the enzymatic transesterification using lipase enzyme is very interested because of low temperature operation, non-chemical catalyst and also easy for purification [11]-[17].

The objective of this research is to study the parameters that affected on biodiesel properties via enzymatic transesterification using commercial lipase enzyme. The four variables are enzyme amount, methanol to oil molar ratio, water amount and reaction time. The biodiesel properties such as fatty acid methyl ester content (FAME), free fatty acid (FFA), carotene content, tocopherol content and tocotrienol content are also evaluated.

MATERIAL AND METHODS

Materials

Oil palm bunches were obtained from Faculty of agriculture, Kasetsart University. All reagents were analytical grade from Merck (Germany). The commercial lipase enzyme was purchased from Sichuan Habio Bioengineering (China). All standard chemical are purchased from Sigma-Aldrich (USA).

Preparation of CPO

Oil palm bunches were chopped into oil palm spikelet. About 1.5 kg of palm spikelet was dried by household microwave (Samsung Co.,Ltd., Thailand) at 850 watt for 10 minutes. Then, the palm fruits was detached from its spikelet and separated a mesocarp out of its nut. After that, the CPO was extracted using hexane solvent after that the solvent was evaporated by rotary evaporator. The obtained CPO was analyzed the fatty acid composition using the AOAC Official Method 969.3. In addition, the CPO was also checked its free fatty acid (FFA), carotene content, tocopherol and tocotrienol content.

Enzymatic Transesterification

The enzymatic transesterification was carried out using 2^4 factorial design which was totally 16 experimental runs. The two level of each factor was shown in Table 1. CPO was weighed in an erlenmeyer flask. Then, methanol and water were added into CPO and covered the flask with aluminum foil. The flask was placed in the shaking incubator to operate the reaction at 45 ^oC and 250 rpm of the shaking speed. After that, the mixture was separated by centrifugation at 10,000 rpm for 15 minutes. The biodiesel locating in the upper layer was transferred into a beaker for removing the excess methanol by heating at 70 ^oC. Finally, the biodiesel in terms of a fatty acid methyl ester (FAME), free fatty acid (FFA), carotene content, tocopherol and tocotrienol content were analyzed. The statistical analysis was performed by SPSS software version 12.

Table 1 Actual value of studied parameters

Factor	unit	value	
		-1	1
Enzyme amount	%wt.	13	23
Methanol to oil molar ratio	mole	3	5
Water amount	%wt.	3	7
Time	h.	2	4

Analysis of Biodiesel Properties

Fatty acid methyl ester content (FAME)

A 30 mg of oil was dissolved with 1 ml of methyl heptadecanoate as an internal standard. The FAME content was measured by gas chromatograph with FID. Helium was used as a carrier gas. The solution was analyzed by DB-WAX column (30m x 0.25mm x 0.25µm). The injection mode was split as a split ratio of 30:1. The injector and detector temperature were set at 250 ^oC. The temperature program was initially set at 80 ^oC for 2 minutes. Then, it was increased to 250 ^oC with ramping of 10 ^oC/min and held at the final temperature for 5 minutes. The C_8-C_{24} of methyl ester was used as a standard. Equation (1) presented the calculation of FAME content.

$$\textbf{FAME}\ (\%\textbf{wt.}) = \frac{(\mathbf{A_{tot}-A_{IS}})}{\mathbf{A_{IS}}} \times \frac{(\mathbf{C_{IS}\times V_{IS}})}{\mathbf{W}} \times \mathbf{100} \qquad (1)$$

Where, A_{tot} and A_{IS} are the total area and the area of internal standard, respectively. C_{IS} is the concentration of internal standard (mg/ml). V_{IS} is the volume of internal standard (ml). W is the sample weight (mg)

Free fatty acid content (FFA)

The FFA content was performed according to AOCS official method ca5a-40. For a brief explanation, the sample was dissolved with ethanol and titrated with 0.1 N sodium hydroxide using phenolphthalein as an indicator. The FFA content was calculated following Eq. (2).

$$\textbf{FFA}\ (\%\textbf{wt.}) = \frac{(\mathbf{S-B})\times \mathbf{C}\times \mathbf{25.6}}{\mathbf{W}} \qquad (2)$$

Where, S and B are the volume of sodium hydroxide titrated with sample and blank, respectively. C is concentration of sodium hydroxide (normality; N). W is the sample weight (g)

Carotene content

Carotene content was analyzed by high performance liquid chromatograph equipped with UV detector at 450 nm (Yonglin Co., Ltd, Korea). The analytical column was YMC carotenoid (30cm x 8mm ID). A 100 mg of oil was dissolved with n-hexane in 10 ml of volumetric flask. The solution was injected to a column with the flow rate of 1 ml/min. The mobile phase was the mixture of solvent A and dichloromethane (70:30, respectively). Solvent A was a mixture of methanol, acetonitrile and ultrapure water (84:14:2, respectively). The carotene content was quantify comparing with the standard of α-carotene and β-carotene.

Tocopherol (TP) and tocotrienol (TT) content

100 mg of oil was dissolved with n-hexane in 10 ml of volumetric flask. A 20 µl of solution was analyzed tocopherol and tocotrienol content by high performance liquid chromatograph equipped with UV detector. The solution was directly injected to a UK-silica column (15cm x 4.6 mm ID) at a flow rate of 1 ml/min. The mobile phase was 99.5% n-hexane and 0.5% isopropanol and the measured wavelength was 292 nm. The tocopherols and tocotrienols content were quantify using external standard technique. The tocopherol and tocotrienol standard consisted of α-tocopherol, γ- tocopherol, δ-tocopherol, α-tocotrienol, γ- tocotrienol and δ- tocotrienol

RESULTS AND DISCUSSION

Characterization of CPO

Table 2 presented the properties of CPO that obtained from dried oil palm spikelet with microwave (MW).

Table 2 CPO Properties

Properties of CPO	Amount	
	Not using MW	Using MW
FFA (%wt.)	35.44	1.25
Carotene content (ppm)	382.23	490.68
Tocopherol content (ppm)	-	345.49
Tocotrienol content (ppm)	-	811.80

The FFA of CPO using microwave for drying decreased from 35.44% to 1.25%. This result indicated that CPO can directly produce biodiesel by transesterification reaction due to its low FFA content (less than 2%). While the carotene content increased from 382.23 ppm to 490.68 ppm. It indicates that the microwave drying is beneficial technique for CPO's quality improvement. In addition, the analysis of fatty acid composition in Table 3 revealed that the main component was palmitic acid (45.65%), oleic acid (39%) and linoleic acid (9.73%).

Table 3 Fatty acid composition of CPO

Fatty acid	Amount (%Area)
Myristic acid (C_{14})	1.22
Palmitic acid (C_{16})	45.65
Palmitoleic acid ($C_{16:1}$)	0.22
Stearic acid (C_{18})	3.23
Oleic acid ($C_{18:1}$)	39.00
Linoleic acid ($C_{18:2}$)	9.73
Linolenic acid ($C_{18:3}$)	0.41
Arachidic acid (C_{20})	0.39
Behenic acid (C_{22})	0.06
Lignoceric acid (C_{24})	0.10

Biodiesel Production

Statistical analysis

The four parameters such as enzyme amount, methanol to oil molar ratio, water amount and reaction time were used to evaluate the biodiesel properties in terms of FAME, FFA, carotene content, tocopherol and tocotrienols content that was shown in Table 4. All experimental data were tested the analysis of variance (ANOVA) at 95% confident interval. It revealed that enzyme amount, methanol to oil molar ratio and interactive effect between methanol molar ratio and water amount had affected biodiesel properties. The P-value of four responses including FFA content, carotene content, tocopherol and tocotroenol content on the effect of enzyme amount were 0.013, 0.008, 0.021 and 0.022, respectively. It indicated that the enzyme amount had affected those responses. The methanol to oil molar ratio had affected FFA content (P-value=0.011) and tocotrienols content (P-value=0.010). In addition, the interactive effect between methanol to oil molar ratio and water amount had also affected FAME content (P-value=0.033).

Optimum condition

The FAME content increased when enzyme loading increased (compared between run 1 to 7 and run 14 to 16). Therefore, selected enzyme loading in

Table 4 Full factorial design of biodiesel properties based on FAME, FFA, carotene content, tocopherols content and tocotrienols content

Run	Enzyme amount (%wt.)	Methanol to oil molar ratio (mole)	Water amount (%wt.)	Time (h)	FAME content (%wt.)	FFA content (%wt.)	Carotene content (ppm)	TP content[1] (ppm)	TT content[2] (ppm)
1	13	3	3	2	60.52	8.66	734.17	477.03	858.48
2	13	3	3	4	64.42	9.35	734.71	515.81	905.66
3	13	3	7	2	56.40	8.39	685.97	375.98	648.49
4	13	3	7	4	61.96	10.25	617.76	513.69	915.81
5	13	5	3	2	54.85	4.75	613.55	414.99	779.55
6	13	5	3	4	56.77	4.68	548.76	444.24	808.87
7	13	5	7	2	68.90	8.13	621.40	454.74	756.79
8	13	5	7	4	83.35	9.60	651.12	487.60	770.88
9	23	3	3	2	66.41	12.92	745.12	593.46	1,110.78
10	23	3	3	4	71.52	11.85	795.84	511.81	946.25
11	23	3	7	2	58.36	10.83	718.87	547.77	1,017.96
12	23	3	7	4	69.02	12.34	740.65	490.49	983.55
13	23	5	3	2	57.50	6.19	563.89	464.04	786.86
14	23	5	3	4	86.07	10.70	701.02	504.01	756.06
15	23	5	7	2	84.98	9.35	839.59	540.12	885.09
16	23	5	7	4	84.88	9.96	865.58	582.55	812.57

Note: [1]TP is tocopherol and [2]TT is tocotrienol.

this transesterification was 23%wt. When the reaction time was compared (run 15 with run 16), the result showed that the FAME content as well as FFA, carotene content, TP and TT were slightly changed. It can be said that the reaction time has not affected FFA, carotene content, TP and TT. For water amount (run 14 with run 16), it was found that 3% of water amount produced high FFA content, lower amount of carotene, TP and TT when compared with high amount of water (7%). For methanol to oil molar ratio (run 11 with run 15), it showed that high methanol to oil molar ratio gave high FAME, lower FFA content and higher carotene, TP and TT when compared with 5 mole. Therefore, run 15 is selected in this experiment to produce biodiesel by enzyme catalyst due to high FAME, carotene content, TP and TT of biodiesel production with lower FFA content.

Properties of Biodiesel

Free fatty acid content (FFA)

The FFA content of biodiesel presented in Table 4 was higher than FFA content of CPO. It was caused by the two competitive reactions. The main reaction was transesterification catalyzed by lipase enzyme for biodiesel production. However, the commercial lipase enzyme using in this work was a liquid lipase resulting to hydrolysis reaction was performed and it promoted the FFA molecule as shown in Fig. 1. Thus, a higher level of enzyme amount resulted in the increasing of FFA content as shown in run 1 and run 9 (Table 4). In run 1, the biodiesel produced by 13% of lipase presented the FFA content of 8.66% while the one produced by 23% of lipase (run 9) presented 12.92% of FFA content. In addition, the FFA content showed a direct proportion on the effect of water loading and reaction time while the methanol molar ratio had affected FFA content in terms of an inverse proportion. For example, the reaction using 3 mole of methanol (run 1) produced 8.66% FFA content of biodiesel comparing with 5 mole of methanol (run 5) generated 4.75% FFA content.

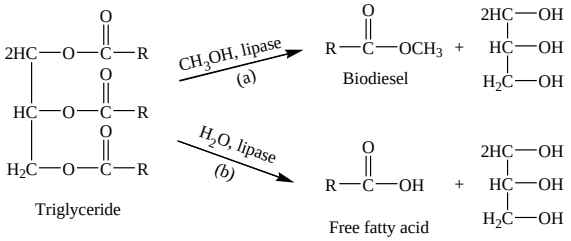

Fig. 1 Competitive reaction catalyzed by commercial lipase enzyme: (a) Transesterification reaction; (b) Hydrolysis reaction

Carotene content

All experiments showed that the carotene content in biodiesel was higher than CPO because of two reasons. Firstly, the enzymatic transesterification was

performed at low temperature (45 ºC), so it prevented carotene from destruction by heat. Secondly, carotene content was measured in terms of ppm (defined as carotene weight (mg) per oil weight (kg)) and the transesterification reaction of CPO eliminated the glycerol molecule out of the oil. Therefore, the proportion of carotene in oil was increased resulting to a high carotene content in biodiesel.

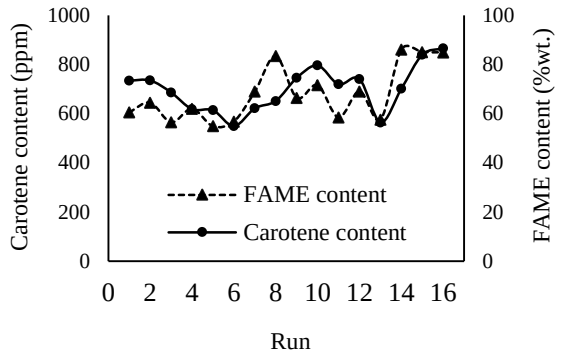

Fig. 2 Carotene content and FAME content containing in biodiesel of all experiment

The variation of carotene content containing in biodiesel presented mostly similar trend as the FAME content in Fig. 2. However, the proportional of α-carotene and β-carotene was the same in both CPO and biodiesel. It contained about 24% of α-carotene and 76% of β-carotene. At the same FAME content (about 85% in run 15), biodiesel catalyzed by enzyme gave carotene content about 840 ppm while biodiesel catalyzed by potassium hydroxide gave 465 ppm of carotene content. This high carotene content indicated that the enzymatic reaction can prevent the carotene destruction.

Tocopherol and tocotrienol content

In Table 4, the TP and TT content in biodiesel were in range of 375.98-593.44 ppm and 648.49-1,110.78 ppm, respectively, which is higher than in CPO (345.49 ppm of TP and 811.80 ppm of TT). The biodiesel given by suitable condition (run 15) consisted of 474.48 ppm α-TP, 65.64 ppm γ-TP, 299.83 ppm α-TT, 484.58 ppm γ-TT and 100.68 ppm of δ-TT while CPO had 301.17 ppm α-TP, 44.32 ppm γ-TP, 281.84 ppm α-TT, 431.15 ppm γ-TT and 98.81 ppm of δ-TT as presented in Table 5. It showed that TP and TT in biodiesel were higher than the ones in CPO. When compared between catalysts, the result showed that biodiesel synthesized by basic catalyst (potassium hydroxide) was γ-TT and δ-TT reduction while enzyme catalyst could save both γ-TT and δ-TT from destruction.

Table 5 Composition of tocopherol and tocotrienol containing in biodiesel and CPO

Run	Composition of TT and TP (ppm)				
	α-TP	γ-TP	α-TT	γ-TT	δ-TT
1	419.77	57.25	298.81	460.44	99.23
2	451.20	64.61	315.99	485.13	104.54
3	330.03	45.95	231.90	345.10	71.50
4	452.28	61.40	315.52	494.97	105.32
5	358.23	56.76	286.18	411.12	82.25
6	387.54	56.70	303.31	411.59	93.97
7	399.77	54.98	261.11	411.77	83.91
8	429.84	57.76	262.54	413.82	94.52
9	524.29	69.16	385.64	606.31	118.82
10	447.79	64.01	332.55	502.85	110.85
11	479.24	68.53	353.39	544.33	120.23
12	446.05	44.44	338.11	541.89	103.56
13	403.70	60.34	295.61	397.64	93.60
14	448.39	55.62	255.07	410.67	90.32
15	474.48	65.64	299.83	484.58	100.68
16	522.00	60.55	314.55	401.75	96.28
CPO	301.17	44.32	281.84	431.15	98.81
Biodiesel catalyzed by basic catalyst	810.70	111.20	510.27	360.11	89.87

Note: TP is tocopherol and TT is tocotrienol.

CONCLUSIONS

The commercial lipase enzyme was successfully catalyzed transesterification for biodiesel synthesis. The suitable condition was performed at 23% enzyme loading, 5 mole of methanol, 5% water loading, 2 hours of reaction time and 45 ^{o}C of reaction temperature that gave 84.98% of FAME content. In this condition, the biodiesel contained 839.59 ppm of carotene content, 540.12 ppm of tocopherols content and 885.09 ppm of tocotrienols content. The advantages of using commercial lipase as a catalyst for biodiesel production are high biodiesel yield, low energy consumption, easy purification, less chemical usage and saving palm phytonutrients (carotene and vitamin E). The synthesized biodiesel consisted of a high carotene and vitamin E content. When it was further distillated under reduced pressure, it improved the purification of biodiesel and amount of phytonutrients. However, using commercial lipase production had some drawback of a high FFA content.

ACKNOWLEDGMENTS

This research was supported by The Research and Researchers for Industries (RRI; PHDI0022), Center of Excellence-Oil Palm and Sang Arun Palm Oil Ltd., Co. and Thailand Institute of Nuclear Technology (TINT) under Thailand Science Research and Innovation (TSRI).

REFERENCES

[1] Choo Y.M., Palm Oil Carotenoids. Food and Nutrition Bulletin, Vol. 15, Issue 2, 1994, pp. 1-8.
[2] Namitha K.K. and Negi P.S., Chemistry and Biotechnology of Carotenoids. Critical Reviews in Food Science and Nutrition, Vol. 50, Issue 2, 2010, pp. 728-760.
[3] Sumita S.K. and Munish G., Pharmacological Effects of Carotenoids: a Review. International Journal of Pharmaceutical Sciences and Research, Vol. 3, Issue 1, 2012, pp. 42-48.
[4] Haseeb A., Amjid A., Jahangir I. and Waseem A S., Pharmacological Potential of Tocotrienols: A Review. Nutrition & Metabolism, Vol. 11, Issue 52, 2014, pp.1-22.
[5] Hong Y.P., Tan W.S.D., Wupeng L. and Wong W.S.F., Vitamin E Therapy beyond Cancer: Tocopherol versus Tocotrienol. Pharmacology & Therapeutics, Vol. 162, 2016, pp. 152-169.
[6] Man K.L., Keat T.L. and Abdul R.M., Homogeneous, Heterogeneous and Enzymatic Catalysis for Transesterification of High Free Fatty Acid Oil (Waste Cooking Oil) to Biodiesel: A Review. Biotechnology Advances, Vol. 28, 2010, pp. 500-518.
[7] Surbhi S., Ajay K.A., Rajendra P.B. and Deepak K. T., Biodiesel Production Using Heterogeneous Catalysts. Bioresource Technology, Vol. 102, 2011, pp. 2151-2161.
[8] Batistella C.B., Moraes E.B., Filho R.M. and Maciel M.R.W., Molecular Distillation Process for Recovering Biodiesel and Carotenoids from Palm Oil. Applied Biochemistry and Biotechnology, Vol. 98, 2002, pp. 1149-1159.
[9] C M., Ida I.M. and Eko S., Potential Source and Extraction of Vitamin E from Palm-Based Oils: a Review. Journal Teknologi, Vol. 69, Issue 4, pp. 43-50.
[10] Ramesh K.S. and Young S.K., Carotenoid Extraction Methods: a Review of Recent Developments. Food Chemistry, Vol. 240, 2018, pp. 90-103.
[11] Prakash S.B., Bhagwan S.S., Gulab S.T., Rakesh K.B. and Prasad G.B.K.S., Biodiesel Production with Special Emphasis on Lipase-Catalyzed Transesterification. Biotechnol Lett, Vol. 32, 2010, pp. 1019-1030.
[12] Adriana G., Marius R., Monica T., Csaba P. and Florin D.I., Biodiesel Production Using Enzymatic Transesterification – Current State and Perspectives. Renewable Energy, Vol. 39, 2012, pp. 10-16.
[13] Aarthy M., Saravananb P., Gowthamana M.K., Rose C. and Kamini N.R., Enzymatic Transesterification for Production of Biodiesel Using Yeast Lipases: an Overview. Chemical Engineering Research and Design, Vol. 92, 2014, pp. 1591-1601.
[14] Yang L., Wei D. and Dehua L., Free Lipase-Catalyzed Biodiesel Production from Phospholipids-Containing Oils. Biomass and Bioenergy, Vol. 71, 2014, pp. 162-169.
[15] Abhishek G., Bhaskar S., Taurai M., Kugen P. and Faizal B., Advances in Synthesis of Biodiesel via Enzyme Catalysis: Novel and Sustainable Approaches. Renewable and Sustainable Energy Reviews, Vol. 41, 2015, pp. 1447-1464.
[16] Xuebing Z., Feng Q., Chongli Y., Wei D. and Dehua L., Lipase-Catalyzed Process for Biodiesel Production: Enzyme Immobilization, Process Simulation and Optimization. Renewable and Sustainable Energy Reviews, Vol. 44, 2015, pp.182-197.
[17] Kareem S.O., Falokun E.I., Balogun S.A., Akinloye O.A. and Omeike S.O., Enzymatic Biodiesel Production from Palm Oil and Palm Kernel Oil Using Free Lipase. Egyptian Journal of Petroleum, Vol. 26, 2017, pp. 635-642.
[18] Cheng S.F., Mohd Nor L. and Chuah C.H., Microwave Pretreatment: a Clean and Dry Method for Palm Oil Production. Industrial Crops and Products, Vol. 34, 2011, pp. 967-971.

8th Int. Conf. on Structure, Engineering & Environment (SEE), Mie, Japan, Nov.10-12, 2022, ISBN: 978-4-909106094 C3051

QUANTIFICATION OF HYDRATION PRODUCTS IN RICE HUSK ASH (RHA)-BLENDED CEMENT CONCRETE WITH CRUMB WASTE RUBBER TIRES (CWRT) & ITS CORRELATION WITH MECHANICAL PERFORMANCE

John Mark L. David[1], Richard M. De Jesus[1] and Rodolfo P. Mendoza[1]
[1]Department of Civil Engineering, Gokongwei College of Engineering, De La Salle University, Philippines

ABSTRACT

Previous studies on the use of rice husk ash (RHA) as a replacement of cement focused on attributing the strength enhancements in mechanical strength in hardened concrete to its pozzolanic reactivity. Investigation of the pozzolanic reaction RHA in terms of cement hydration has yet to be examined. This study intended to assess the pozzolanic activity of RHA by quantification of calcium hydroxide (CH) and calcium silicate hydrate (C-S-H) gel in RHA-blended cement pastes using simultaneous thermogravimetric and differential-thermal analysis (TG-DTA). Moreover, the application of crumb waste rubber tire (CWRT) in concrete as fine aggregate replacement is known to reduce mechanical strength. Thus, the pozzolanic reaction of RHA compensating the strength loss by CWRT was also investigated. Two types of RHA, from open-air burning (RHA-O) and thermal power plant (RHA-T), were used in casting cement pastes and mortars with 0%, 7.5%, 12.5%, and 17.5% replacement of cement (by weight). Finally, concrete with fixed optimal RHA and 5%, 10%, and 15% CWRT (by volume) were tested for compression and splitting tensile strength. Results from TG-DTA revealed reductions in quantified CH contents and increase in C-S-H gel contents in cement pastes with RHA indicating pozzolanic reaction. Decreasing CH content corresponded to increasing compressive strength highlighting the strength enhancement by pozzolanic activity, optimal at 17.5% using RHA-O. For concrete, results showed that incorporating 17.5% RHA-O and 5% CWRT provided comparable compressive strength and higher splitting tensile strength than normal concrete, signifying the compensation of strength loss of CWRT by RHA.

Keywords: Rice husk ash, Pozzolanic effect, Thermogravimetric analysis, Hydration product, Crumb rubber

INTRODUCTION

Concrete remains the single most widely used material in the world. Production of cement contributes to about five percent of the global carbon dioxide (CO_2) production due to human activities [1]. One of the waste materials that have been investigated to be an effective supplementary cementitious material is rice husk ash (RHA). Combustion of rice husk to run milling processes will produce a huge amount of RHA, usually dumped on bodies of water that cause pollution and contamination [2]. RHA is described to have high silica (SiO_2) content ranging from 85% to 90% [3] making it very reactive and pozzolanic. Amorphous silica is highly reactive whereas crystalline silica has no pozzolanic activity [4].

Notable increase in mechanical strength has been observed in mortars and concrete with replacements of cement with RHA [3], [5]. The pozzolanic effect of RHA happens when the excess calcium hydroxide (CH) from the hydration of cement reacts with silica (SiO_2) of RHA to form additional calcium silicate hydrate (C-S-H) gel. The C-S-H gel is considered as the main carrier of strength in a hardened concrete hence increasing its overall mechanical strength [6].

Considering the abundant research on the effect of RHA on the mechanical strength, the mechanism of pozzolanic reaction by RHA in blended mortar and concrete has yet to be studied. Therefore, one of the main objectives of the study is to evaluate the pozzolanic activity of RHA through the quantification of hydration products. Simultaneous thermogravimetric and differential-thermal analysis (TG-DTA) has been considered as the easiest and most widely used methodology for the analysis of hydration reactions in cementitious pastes [7]. In this method, thermogravimetric analysis (TGA) monitors the weight of the sample upon heating to a constant rate while differential-thermal analysis (DTA) detects the temperature at which the reactions in the sample occur manifested by peaks in the curve.

The hydration products have unique decomposition temperatures. This allows the determination of their quantities based on the mass losses associated with the decomposition temperatures. For C-S-H gel, the temperature of decomposition ranges from 110°C to 400°C [7] whereas for CH, the decomposition ranges from 400°C to 600°C [8]. Using this method, reduction in the quantity of CH can be indicative of reaction with SiO_2 from RHA while increase in C-S--H can be

associated with the production of secondary C-S-H gel.

Another potential material replacement in the concrete mix is the crumb waste rubber tire (CWRT) as fine aggregates. Although the addition of CWRT reduces strength [9], the increase in strength provided by the pozzolanic reaction of RHA can compensate for this lack.

In this paper, two types of RHA will be examined: RHA from open-air burning (RHA-O) and RHA from a thermal plant (RHA-T). Using TG-DTA, C-S-H and CH contents from the hydration of RHA-blended cement pastes will be quantified and correlated to the compressive strength of mortar with and without RHA to evaluate strength improvement in relation to pozzolanic effect. The final output of this study is a blended concrete with optimal amount of RHA and CWRT.

THEORETICAL BACKGROUND

Hydration of Portland Cement with RHA

The hydration of C_3S and C_2S in Portland cement produces CH and C-S-H gel in the form $C_{1.7}SH_4$ where: C = CaO, S = SiO_2 and H = H_2O [10]. The reaction of amorphous silica (SiO_2) in RHA with the excess CH from the hydration of Portland cement forms another type of C-S-H given by the formula [11]: $2S + 3CH + H \rightarrow 2C_{1.5}SH_2$.

Quantification of Hydration Products by TG-DTA

Various authors have observed the following decomposition reactions that occur in cement pastes upon heating during TG-DTA: a) 30 °C to 105 °C: dehydration of evaporable water [12], b) 110 °C to 400 °C: dehydration or loss of chemically bound water from C-S-H molecules [7], c) 400 °C to 600 °C: dehydroxylation of CH [8] following the reaction: $Ca(OH)_2 \rightarrow CaO + H_2O$, and d) 600 °C to 1100 °C: decarbonation (loss of carbon dioxide) in $CaCO_3$ [10] based from the reaction: $CaCO_3 \rightarrow CaO + CO_2$.

The amount of CH can be estimated using [10]:

$$CH\ (\%) = CH_{loss} \cdot \frac{MW\ (CH)}{MW\ (H)} \quad (1)$$

where CH (%) is the percentage amount of CH, CH_{loss} is the mass loss in percentage due to dehydroxylation of CH, and MW (CH) and MW (H) are the molecular weights of CH and water, respectively. Calcium silicate hydrate (C-S-H) gel content can be computed using the equation [7]:

$$C\text{-}S\text{-}H\ (\%) = C\text{-}S\text{-}H_{loss} \cdot \frac{MW\ (C\text{-}S\text{-}H)}{Moles\ of\ water \cdot MW\ (H)} \quad (2)$$

where C-S-H (%) is the percentage amount of C-S-H, $C\text{-}S\text{-}H_{loss}$ is the mass loss in percentage due to dehydration of C-S-H gel between 110°C - 400°C and MW (C-S-H) and MW (H) are the molecular weights of C-S-H gel and water, respectively.

METHODOLOGY

Preparation of RHA

The burning of rice husks was performed in an open area using a cylindrical hollow steel plate. The fire was maintained for one hour without controlling the combustion temperature and cooled for 24 hours. Two types of RHA were utilized in this study: (a) RHA from open-air burning (RHA-O) and (b) RHA from a thermal plant (RHA-T). Both RHA were further ground using Los Angeles Abrasion machine to attain the required fineness of ASTM C618.

Characterization of OPC and RHA

Characterization of OPC and RHA were conducted as follows: a) Blaine Air-Permeability Test (ASTM C204) and No. 325 mesh fineness test (ASTM C430) for fineness, b) Scanning Electron Microscope (SEM) Imaging using JEOL JSM-5310 for microstructure, c) X-ray fluorescence spectrometry (XRF) for chemical compositions and d) X-ray Diffraction (XRD) analysis for crystallinity. The degree of crystallinity (DOC) of silica in each RHA was estimated using Eq. (3) based on areas of crystalline peaks and residual area in the diffraction curve attributed to the area of amorphous peaks [13]:

$$DOC(\%) = \frac{Crystalline\ area}{Crystalline\ area + Amorphous\ area} \times 100 \quad (3)$$

The weight fraction of amorphous silica is given by:

$$W_{amorphous}\ (\%) = 100 \times (1\text{-}DOC) \quad (4)$$

Thermogravimetric and Differential-Thermal Analysis (TG-DTA) of RHA Cement Pastes

Two sets of cement pastes were prepared with RHA-O and RHA-T, at levels of replacement of pure cement equal to 0%, 7.5%, 12.5% and 17.5% (Table 1). All pastes were mixed following ASTM C305, casted into plastic jars (Ø30mm) with 10 mm height and stored in a water bath 24 hours after casting.

All hardened cement pastes cured for 120 days were dried in an oven at 105 °C for at least 24 hours, pulverized using mortar and pestle, and then sieved using No. 200 sieve. Simultaneous thermogravimetric and differential-thermal analysis (TG-DTA) was performed using Perkin Elmer Simultaneous Thermal Analyzer (STA) 6000 available in Advanced Device and Materials Testing Laboratory (DOST-ADMATEL). Approximately 20 mg of each powdered sample was weighed and filled in a platinum crucible. The heating program was set in the following manner: (a) heat from 30 to 995 °C at 10 °C per min and (b) hold for 5 min at 995 °C. All samples were heated in Nitrogen gas atmosphere.

Quantification of CH and C-S-H contents in pure and blended cement paste samples were based on the proposed methods from previous works [7], [8] calculated using Eq. (1) and (2), respectively.

Mortar Mix Proportioning and Testing

Mortar cubes having 50 mm edge with 7.5%, 12.5% and 17.5% cement replacement (by weight) by each RHA type (RHA-O and RHA-T) were made using ASTM C109 and mixing per ASTM C305 as shown in Table 2. Mortar fragments were subjected to SEM imaging after testing.

Table 1 Mix proportion of pure Portland cement and RHA-cement pastes

Mix Design	Material			
	Cement, g	RHA, g		Water, mL
		RHA-O	RHA-T	
CP	100	0	0	48.5
7.5PO	92.5	7.5	-	48.5
12.5PO	87.5	12.5	-	48.5
17.5PO	82.5	17.5	-	48.5
7.5PT	92.5	-	7.5	48.5
12.5PT	87.5	-	12.5	48.5
17.5PT	82.5	-	17.5	48.5

Table 2 Mixture proportion of 6-cube batch RHA mortars

Mix Design	Material				
	Cement, g	RHA, g		Sand, g	Water, mL
		RHA-O	RHA-T		
CM	500	0	-	1375	242
7.5MO	462.5	37.5	-	1375	242
12.5MO	437.5	62.5	-	1375	242
17.5MO	412.5	87.5	-	1375	242
7.5MT	462.5	-	37.5	1375	242
12.5MT	437.5	-	62.5	1375	242
17.5MT	412.5	-	87.5	1375	242

Concrete Mix Proportioning and Testing

From the compression test on RHA mortars, the most optimal RHA type is RHA-O at 17.5% cement replacement. Concrete cylinders were prepared at fixed 17.5% RHA-O with CWRT at replacement levels 5%, 10% and 15% by volume. Mix proportioning per $1m^3$ of each batch in Table 3 was formulated according to ACI 211.1 at w/c equal to 0.5. Three replicates of Ø100mm×200mm cylinders were tested for compression and splitting tensile strength after 28 days as per ASTM C39 and ASTM C496, respectively.

RESULTS AND DISCUSSIONS

Properties of RHA and OPC

Chemical composition

Both RHA-O and RHA-T manifested high silica (SiO_2) contents equal to 93.38% and 82.73%, respectively, as shown in Table 4. Jamil et al. [11] demonstrated that amorphous silica from RHA reacts with CH from cement hydration process to form secondary C-S-H gel.

Crystallinity of silica in RHA

The silica phase of RHA-T is partly crystalline and partly amorphous due to narrow peaks at around 21.8° at the top of a broad peak between 10° and 28° and another at 29.4° as shown in Fig. 1. These sharp peaks are indicative of crystalline silica while the broad peak is attributed to amorphous silica. The broad smooth hump between 10° and 30° of RHA-O indicated amorphous silica content. From the DOC method, RHA-O and RHA-T contained 90.91% and 76.18% amorphous silica, respectively. Hence, it can be concluded that RHA-O will be more reactive than RHA-T since it has more amorphous silica content.

Table 4 Chemical composition of RHA-O, RHA-T and OPC

Chemical analysis (%)	RHA-O	RHA-T	OPC
Silicon Dioxide (SiO_2)	93.38	82.73	16
Aluminum Oxide (Al_2O_3)	-	-	3.69
Ferric oxide (Fe_2O_3)	1.35	1.1	2.93
Calcium oxide (CaO)	1.65	11.22	67.6
Moisture content (%)	0.36	0.29	-

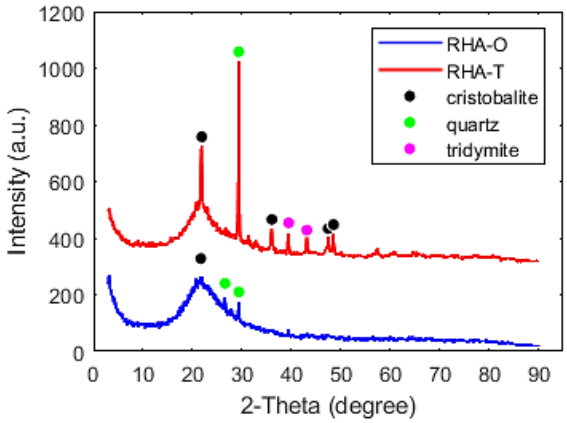

Fig. 1 XRD pattern of RHA-O and RHA-T

Thermogravimetric Analysis of Cement Pastes

Figures 2a show the profiles of thermogravimetric (TG) curves of 120-day cement pastes with RHA-O typical to cement pastes with RHA-T where gradual weight loss with increasing heating temperature can be observed. Differential Thermal (DTA) curves are also presented in the figure showing the temperatures at which reactions in the samples occur.

Thermogravimetric curves

From the DTG curves in Fig. 2b, four zones were defined where the sharp peaks occurred for all samples. Zone 1 is the first mass loss step corresponding to dehydration or loss of evaporable water [12]. Zone 2 characterizes the dehydration or loss of chemically bound water from C-S-H molecules [7]. Zone 3 indicates the dehydroxylation of calcium hydroxide (CH) [7]. Lastly, Zone 4 is associated with the decarbonation of calcium carbonate or calcite ($CaCO_3$) [8]. The temperature of peaks and decompositions for all cement pastes did

Table 3 Mixture proportion of concrete cylinders with RHA and CWRT in kg for 1 m^3 concrete production.

Mix	RHA (%)	CWRT (%)	Cement	RHA	FA[a]	CWRT	CA[b]	Water
R0C0	0	0	418	0	779	0	1151	241
R0C10	0	10	418	0	701	38	1151	241
R17.5C0	17.5	0	345	73	779	0	1151	241
R17.5C5	17.5	5	345	73	740	19	1151	241
R17.5C10	17.5	10	345	73	701	38	1151	241
R17.5C15	17.5	15	345	73	662	57	1151	241

Note: [a] fine aggregate, [b] coarse aggregate

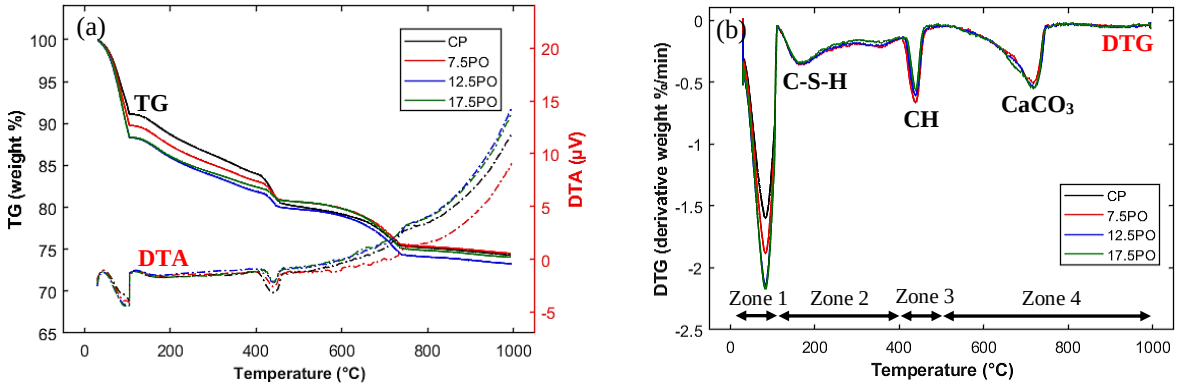

Fig. 2 TG-DTA results for RHA-O cement pastes: (a) TG-DTA curve and (b) DTG curve

not vary significantly thus no major change in phase chemistry of the products.

Calcium silicate hydrate (C-S-H) content

The formation of C-S-H gel with chemical composition $1.7CaO{\cdot}SiO_2{\cdot}4H_2O$ for cement pastes with pure Portland cement [10] and $2Ca_{1.5}SiO_{3.5}{\cdot}2H_2O$ for RHA-blended cement pastes [11] were considered for its quantification by TG-DTA. Figure 3 presents the computed C-S-H gel from 120 days of hydration with mass loss from 110 °C to 400 °C. The formation of C-S-H gel increased from 22.37% in CP (control) to 33.09%, 32.06% and 29.54% with 7.5PO, 12.5PO, and 17.5PO, respectively. Similarly, the C-S-H content in 7.5PT, 12.5PT, and 17.5PT increased by 31.82%, 29.89% and 30.14%, respectively. However, C-S-H gel does not vary significantly with the replacement level of RHA.

It can be inferred that the addition of both RHA types as cement replacement can cause a significant increase in the C-S-H content. The mechanism of C-S-H increase can be explained by the pozzolanic activity of RHA where secondary C-S-H is produced from the consumption of CH from Portland cement hydration [11]. For cement pastes with RHA-O, the amount of C-S-H is higher than pastes with RHA-T except at 17.5% replacement. This is due to higher amorphous silica content and higher fineness of RHA-O as compared to RHA-T.

Calcium hydroxide (CH) content

The quantity of CH in cement pastes was calculated from the mass loss from 400°C to 500°C as shown in Fig. 3. The amount of CH decreased from 16.22% in CP to 10.32%, 8.73%, and 7.35% for 7.5PO, 12.5PO and 17.5PO, respectively. The same trend was observed for cement pastes with RHA-T where CH content diminished to 10.43%, 8.30% and 7.89% for 7.5PT, 12.5PT and 17.5PT, respectively. Further, CH in blended cement decreases with increasing RHA content. Between RHA-O and RHA-T at same level of replacement, CH content does not vary significantly.

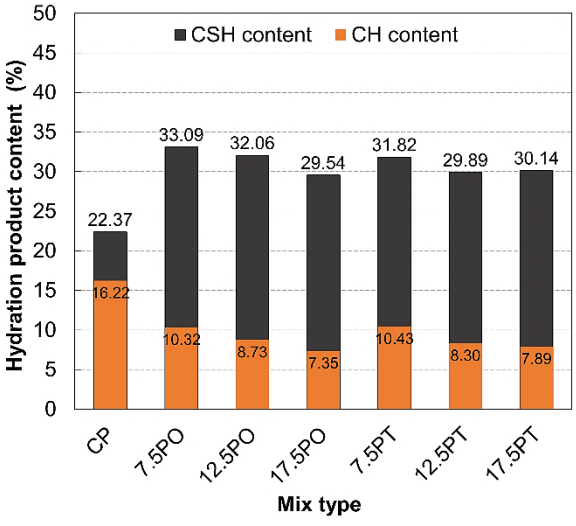

Fig. 3 Hydration product contents of cement pastes after 120 days

The reduction in the CH content confirmed the pozzolanic activity of RHA-O and RHA-T. This is consistent with the results of the quantification of C-S-H gel where cement pastes with RHA exhibited more C-S-H gel content than with plain Portland cement. Boualleg et al. [14] reported that as the

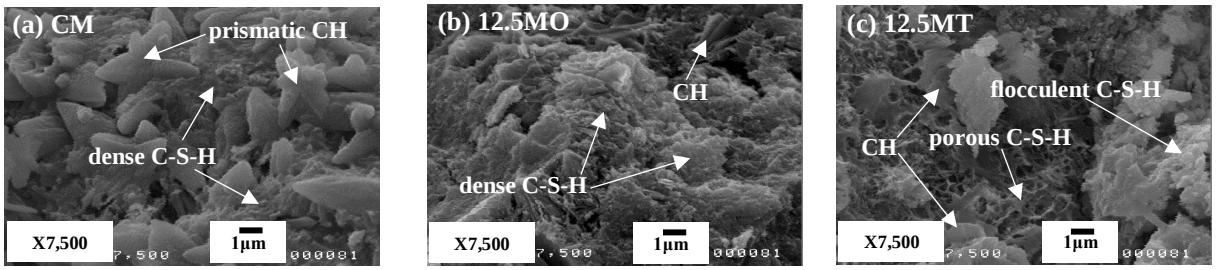

Fig. 4 Microstructure of (a) control mortar (CM), (b) mortar with 12.5% RHA-O (12.5MO) and (c) mortar with 12.5% RHA-T (12.5MT) after 120 days of curing

hydration of pure cement progresses, portlandite ions (Ca^{++} and OH^{-}) are released and captured by the pozzolan to form a new type of C-S-H gel. Based on the results, the reduction of CH is greatest in cement paste with 17.5% RHA-O (17.5PO) indicating the greatest pozzolanic reaction.

Effect of RHA in Mortar

Compressive strength

After 3 days, the compressive strengths of all mortars with RHA are lower than the control mortar (CM) except to the mortar with 7.5% RHA-O (7.5MO). For 28-day samples, 12.5MO and 17.5MO exhibited comparable strength increase equal to 29.1% and 27.3% of the control, respectively. Mortars with 12.5% RHA-T (12.5MT) and 17.5% RHA-T (17.5MT) also increased in strength by 15.5% and 3.6% of the control, respectively. After 120 curing days, similar trend to 28 days is observed where 12.5MO, 17.5MO, 12.5MT, and 17.5MT showed strength increase equal to 23.0%, 14.0%, 17.9%, and 1.6% of the control, respectively. It is also evident that mortars with 12.5% RHA-O and RHA-T performed slightly better than mortars with 17.5%. Habeeb and Mahmud [15] reported that CH from the hydration of Portland cement may be insufficient to react with the available silica in RHA, thus leading to the incomplete pozzolanic reaction.

Researchers have reported that the compressive strength increase of mortars with RHA may be partially due to its high fineness and pozzolanic reaction [11], particularly the presence of highly amorphous silica in RHA enhancing its reactivity [4].

Microstructure

Prismatic CH and dense C-S-H gel were visible on the surface of control mortar (CM) at 120 curing days as seen in Fig. 4a. The prismatic CH is abundant and embedded on the C-S-H matrix since it is one of the main products from the hydration of Portland cement. In Fig. 4b, mortar containing 12.5% RHA-O showed a denser C-S-H than CM. The presence of CH also diminished. Production of secondary C-S-H from the pozzolanic reaction of RHA-O contributed to a denser C-S-H matrix and less CH when compared to the control. Pore refinement of the microstructure of the mortar with 12.5% RHA-O resulted to the highest compressive strength. On the other hand, the microstructure of mortar with 12.5% RHA-T in Fig. 4c manifested porous and flocculent C-S-H gel with the presence of more voids and CH crystals.

Effect of RHA and CWRT on Concrete

Compressive strength

It can be observed in Fig. 5, R17.5C0 recorded the highest compressive strength improvement equal to 12.4% when compared to the control (R0C0). Comparing the results of sample concrete with CWRT only (R0C10) and samples with both RHA-O and CWRT (R17.5C5, R17.5C10, R17.5C15), it can be inferred that the incorporation of RHA-O can increase the compressive strength up to 10% CWRT. The compressive strength of R17.5C5 is comparable to the control with a slight decrease of 3.4%. The enhancement in strength by RHA-O is attributed to its pozzolanic effect. It is also observed that replacing fine aggregates with rubber decreases the compressive strength.

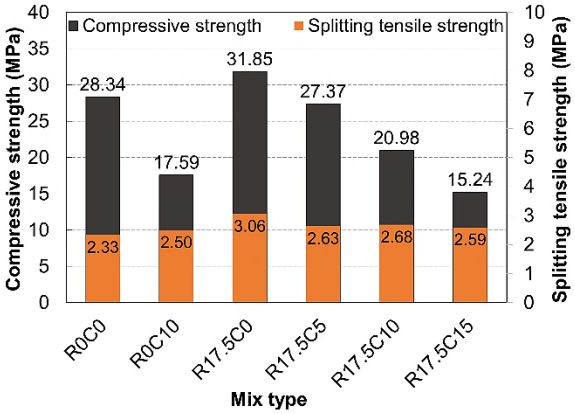

Fig. 5 Compressive and splitting tensile strength of concrete with RHA-O and CWRT after 28 days

Splitting tensile strength

In terms of splitting tensile strength, R17.5C0 gained the highest strength at 3.06 MPa with an increase of 31.2% of the control as shown in Fig. 5. It is also noted that additions of both RHA-O and CWRT showed remarkable tensile strength increases ranging from 7.2% up to 15.1% of the control unlike in compressive strength where strength enhancement is only due to RHA-O. When both RHA-O and CWRT are incorporated, the concrete is seen to

perform better than concrete with CWRT only (R0C10) but still lower strength than concrete with RHA-O only (R17.5C0).

CONCLUSIONS

Based on the analysis of results presented in the study, the following conclusions can be derived:

1. RHA- RHA-O and RHA-T exhibited high silica ($Si0_2$) contents equal to 93.38% and 82.73%, respectively. X-ray diffraction (XRD) analysis revealed that silica in RHA-O is mainly amorphous in form, whereas silica in RHA-T is partly amorphous and partly crystalline.
2. Simultaneous thermogravimetric and differential-thermal analysis (TG-DTA) can be used to quantify C-S-H and CH and examine the extent of pozzolanic reaction in blended cement pastes.
3. The amount of C-S-H gel is higher in RHA cement pastes than plain cement pastes after 120 days. C-S-H gel does not vary significantly with the RHA replacement level. Reductions in CH are observed on RHA-blended cement pastes at 120 days of curing. Increasing RHA content resulted in decreasing CH content confirming the pozzolanic activity of RHA.
4. Mortars prepared with 12.5% and 17.5% RHA-O showed excellent compressive strength gain after 28 and 120 days. To maximize RHA content, 17.5% RHA-O is used in concrete since their strengths are comparable.
5. Concrete with 17.5% RHA-O only yielded the highest compressive and splitting tensile strength after 28 days among all mix types. Increasing CWRT content decreases compressive strength. Additions of both RHA-O and CWRT resulted in higher splitting tensile strength than the control. Adding 17.5% RHA-O and 5% CWRT provided comparable compressive strength and higher splitting tensile strength than normal concrete which signifies the compensation of strength loss of CWRT by RHA.

ACKNOWLEDGEMENT

The authors acknowledge the Department of Science and Technology (DOST-ERDT) of the Philippines for providing the grant for this research.

REFERENCES

[1] Boden, T. A., Andres, R. J., & Marland, G., Global, regional, and national fossil-fuel CO2 emissions, carbon dioxide information analysis center, Oak Ridge National Laboratory, U.S. Department of Energy, Oak Ridge, Tenn., USA, 2017.

[2] Rodríguez De Sensale, G., Strength development of concrete with rice-husk ash. Cement and Concrete Composites, 28(2), 2006, pp. 158–160.

[3] Zareei, S. A., Ameri, F., Dorostkar, F., & Ahmadi, M., Rice husk ash as a partial replacement of cement in high strength concrete containing micro silica: Evaluating durability and mechanical properties. Case Studies in Construction Materials, 2017, pp. 73–81.

[4] Xu, W., Lo, T. Y., & Memon, S. A., Microstructure and reactivity of rich husk ash. Construction and Building Materials, 29, 2012, pp. 541–547.

[5] Isberto, C. D., Labra, K. L., Landicho, J. M. B., & De Jesus, R., Optimized preparation of rice husk ash (RHA) as a supplementary cementitious material. International Journal of GEOMATE, 16(57), 2019, pp. 56–61.

[6] Alex, J., Dhanalakshmi, J., & Ambedkar, B., Experimental investigation on rice husk ash as cement replacement on concrete production. Construction and Building Materials, 127, 2016, pp. 353–362.

[7] Singh, L. P., Goel, A., Bhattacharyya, S. K., & Mishra, G., Quantification of hydration products in cementitious materials incorporating silica nanoparticles. Frontiers of Structural and Civil Engineering, 10(2), 2016, pp. 162–167.

[8] Collier, N. C., Transition and decomposition temperatures of cement phases - a collection of thermal analysis data. Ceramics - Silikaty, 60(4), 2016, pp. 338–343.

[9] Bisht, K., & Ramana, P. V., Evaluation of mechanical and durability properties of crumb rubber concrete. Construction and Building Materials, 155, 2017, pp. 811–817.

[10] Mounanga, P., Khelidj, A., Loukili, A., Baroghel-Bouny, V., Predicting Ca (OH)2 content and chemical shrinkage of hydrating cement pastes using analytical approach. Cement and Concrete Research, Elsevier, 34 (2), 2017, pp. 255-265.

[11] Jamil, M., Kaish, A. B. M. A., Raman, S. N., & Zain, M. F. M., Pozzolanic contribution of rice husk ash in cementitious system. Construction and Building Materials, 47, 2013, pp. 588–593.

[12] Fagerlund, G., Chemically bound water as measure of degree of hydration: method and potential errors. In Division of Building Materials, 315, 2009.

[13] Madsen, I. C., Scarlett, N. V. Y., & Kern, A., Description and survey of methodologies for the determination of amorphous content via X-ray powder diffraction. Zeitschrift Fur Kristallographie, 226(12), 2011, pp. 944–955.

[14] Boualleg, S., Bencheikh, M., Belagraa, L., Daoudi, A., & Chikouche, M. A., The combined effect of the initial cure and the type of cement on the natural carbonation, the portlandite content, and nonevaporable water in blended cement. Advances in Materials Science and Engineering, 2017.

[15] Habeeb, G., & Mahmud, H., Study on properties of rice husk ash and its use as cement replacement material. Materials Research, 13(2), 2010, pp. 185–190.

8th Int. Conf. on Structure, Engineering & Environment (SEE), Mie, Japan, Nov.10-12, 2022, ISBN: 978-4-909106094 C3051

FEASIBILITY STUDY FOR ENVIRONMENTALLY FRIENDLY PROCESS IN PREMIUM CRUDE PALM OIL PRODUCTION

Sureerat Namwong[1], Vittaya Punsuwan[2], Pinsuda Viravathana[3] and Rayakorn Nokkaew[4]
[1,2,3] Faculty of Science, Kasetsart University, Bangkok, Thailand;
[2,3,4]Center of Excellence-Oil Palm Kasetsart University, Bangkok, Thailand

ABSTRACT

Thailand has more than 149 factories of small palm oil mills. Mostly, they produce with low quality of crude palm oil (CPO) with high free fatty acid (6-15% of FFA) and low Deterioration of Bleachability Index (≤2.0 of DOBI). This research investigated the application of microwave technology for the production of premium CPO. In this experiment, the CPO quality from two heating processes were compared. The first process is two times palm spikelet heating by microwave and the second one is heating by microwave and hot air drying. The results showed that two processes can produce the premium CPO with less than 1% of FFA, more than 4 of DOBI, about 500 ppm of carotenoids content, and less than 10 meq.kg^{-1} of peroxide value. The operating time of the first and the second process were 0.28 and 2.23 hr., respectively with the convention process was 10 -15 hr. Summarized, the microwave technology can reduce operating time and palm spikelet heating has the high potential process for premium CPO production.

Keywords: Premium crude palm oil, Microwave technology, Small palm oil mill, Low free fatty acid.

INTRODUCTION

Palm oil is currently the world's largest vegetable oil consumed for food, follow by soyabean and rapeseed oil [1], [2]. Thailand is the third palm oil producer inferior to Indonesia and Malaysia. There are 149 mills in Thailand estimates, they have the capacity to produce 2.8 million tonnes of CPO per year. About 0.24 million households across the country are involved in this sector, the majority (79%) of which are smallholders [3]. Half of mills are small palm oil mill. These were limited knowledge and technology making, it unable to produce premium CPO, can only produce low quality oil [4]. They are the main problem of small palm oil mills in Thailand. This research therefore focuses on study the feasibility of premium CPO production using microwave technology for small palm oil mill.

In the conventional palm oil milling process in Thailand provides 2 scales. There are a large scale and a small scale. The large scale mill; fresh fruit bunches are pretreated under sterilization process. It uses steaming as wet heat treatment. This process is to deactivate the oil splitting enzyme, soften the palm fruitlets and encourage detachment of fruitlets from bunches [5]. Fruits are stripped to separate the sterilized fruits from the sterilized bunch stalks. After that, loose fruits are preparative to screw pressing process for good CPO quality. However, the sterilization process was produced large amount of palm oil mill effluent (POME) [6]. Most small-scale mill use dry pretreatment of fresh palm fruits (Hot air pretreatment) that the mill is not occur POME problem. However, disadvantage of dry process is getting lower quality of CPO [4].

Microwave heat treatment for improving of CPO has been widely accepted and continually developed [7]. Many research was studied on sterilization of palm fruit bunch using microwave. The result found that the microwave consumed shot time when compared with the sterilized process of the large mill. However, microwave heating worked only the outer layer of the fresh fruit bunch due to limitation of microwave to penetrate inner layer of the bunch [8], [9], [10]. The spikelet without core of fresh fruit bunch microwave sterilization would be much more efficient and effective process.

Two times heat treatments were used sterilization process by microwave and hot air. These processes consumed less time and low temperature which reduced the destruction of antioxidants to effect on high quality of CPO [8]. Therefore, microwave heating and two times heat treatment processes were a good alternative for environmentally friendly process.

The aim of this research is feasibility study for premium CPO production using microwave heating and comparison between two times heating form palm spikelets by microwave and the second one is heating by microwave and hot air drying. The optimum conditions were collected on quality of premium CPO.

MATERIALS AND METHODS

Materials

Palm fresh bunch were obtained from the Faculty of Agriculture, Kasetsart University, Thailand. Solvents and chemicals were obtained as follow: *n*-hexane (99%), acetic acid, sodium thiosulfate, starch and hydrochloric acid were purchased from QReC, Newzaland. *n*-hexane (95%) for extraction was purchased from Burdick&Jeckson, South Korea. Sodium hydroxide and methanol (95%) were purchased from Merck Geramany. Ethanal (95%) was purchased from Liquor distillery organization. Potassium hydrogen phthalate, phenolphthalein, potassium iodine and sodium bicarbonate were purchased from Ajex Finechem, Newzeland. Chloroform was purchased from RCI Labscan limited, Thailand. Folin-Ciocalteu reagen was purchased from Sisco Research Laboratories, India. Gallic acid was purchased from Sigma-aldrich, USA.

Methods

Two times heating process were carried out: 1) collected of palm spikelet from bunch chopped for microwave treatment optimization study and 2) palm fruitlets from spikelet via microwave treatment at optimization for the second heating by microwave and hot air drying.

The pre-heating process for treatment premium CPO production

Palm spikelets were heated by a domestic microwave oven (Sumsung, Model MS28H5125BK, 28 liters, 2.4 GH) at medium power intensity (850 W). Duration of heating varied from 2-26 min. After that, palm fruitlets were analyzed heated by microwave (the fist process) and by hot air oven (the second process).

The first and second heating processes for treatment premium CPO production

The fruitlets from the pre-heating process were raw material for the first and the second processes The first process; the fruitlets were heated by microwave at 850 W for 1-5 min of heating time. The second process; the fruitlets were heated by hot air oven at 90°C for 1-3 hr. of heating time. Then mesocarp was oil extraction by solvent. After that, the CPO was analyzed the physical and chemical properties.

Each condition of two heating processes, measured the temperature on palm fruit after heating, then peeled mesocarp and extracted the oil by solution extraction. The oil was collected for chemical analysis. The overall of experiment shown in Fig.1.

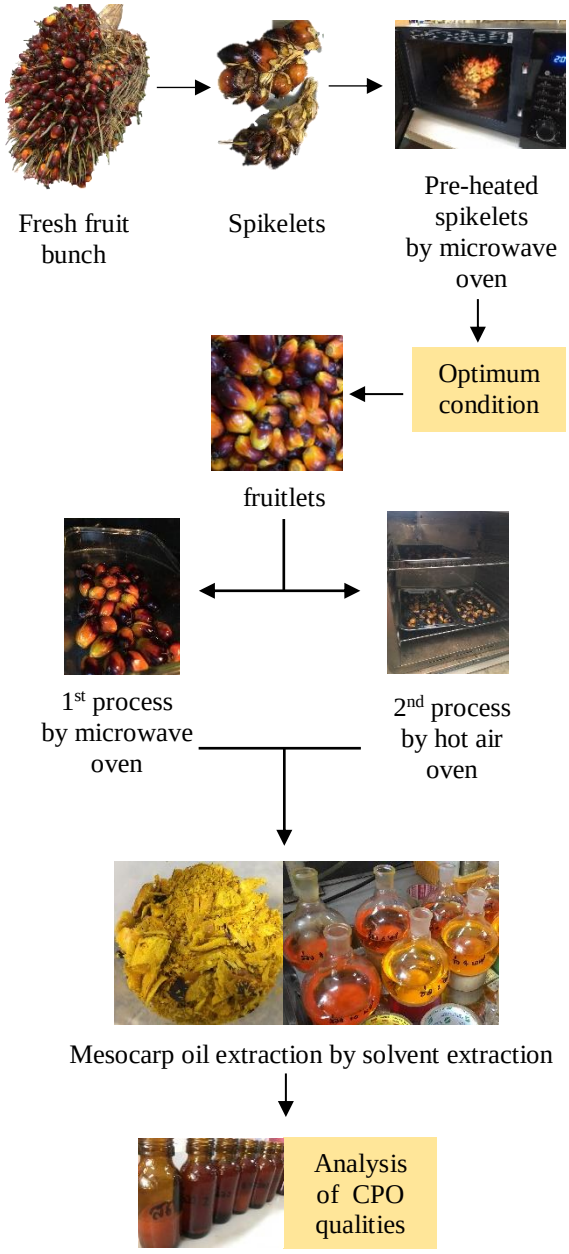

Fig. 1 The experimental diagram for premium CPO production.

Analysis of Palm Oil Properties

Determination of free fatty acid content (FFA)

FFA content of the oil sample was measured by dissolving oil in 95% ethanol and titrated with 0.1 N sodium hydroxide solution using a phenolphthalein indicator. The FFA content is calculated by following Eq. (1).

$$\text{FFA (\%)} = \frac{(S-B)\times N \times 25.6}{W} \quad (1)$$

Where, S is the volume of sodium hydroxide solution for oil titration, B is the volume of sodium hydroxide solution for blank titration, N is the concentration of sodium hydroxide, W is the weight of oil.

Determination of Deterioration of Bleachability Index (DOBI)

DOBI was determined followed MPOB test method (2004). DOBI is defined as the ratio of the spectrometric absorbance at 446 nm 269 nm 0.1 g of oil sample was weighed into 25 mL of volumetric flask and dissolved with hexane. The sample solution was measured absorbance at 269 and 446 nm using UV-VIS spectrophotometer. The value of DOBI is calculated followed Eq. (2).

$$\text{DOBI} = \frac{Absorbance\ at\ 446\ nm}{Absorbance\ at\ 269\ nm} \quad (2)$$

Determination of carotene content (CC)

Carotene content was carried using MPOB test method (2004). Briefly explained, 0.1 g of oil sample was dissolved with n-hexane in a 25 mL volumetric flask. The absorbance reading of the solution at 446 nm was taken using UV-VIS spectrophotometer. The carotene content is calculated as Eq. (3).

$$\text{Carotene content (mg.kg}^{-1}) = \frac{383\ (\text{A})(\text{V})}{100(\text{W})} \quad (3)$$

Where, A is the absorbance at 446 nm, V is the volume of oil solution and W is the weight of oil sample.

Determination of peroxide value (PV)

5 g of oil sample was dissolved in 30 mL mixture solution of (acetic acid and chloroform). Then added 0.5 mL of saturated potassium iodine solution and shaked the solution and shaked the solution. After that, added 30 mL of water and shaken vigorously to liberate iodine from the organic to aqueous layer. Iodine was titrated with a 0.1 N sodium thiosulphate solution using a starch indicator. A blank determination was made using the same procedure without the oil sample. PV was calculated using the Eq. (4).

$$\text{PV} = \frac{(\text{X}-\text{Y})\times\text{C}\times 1000}{\text{g}} \quad (4)$$

Where, X is the volume of sodium thiosulphate used to titrate with oil sample, Y is the volume of sodium thiosulphate used to titrate with blank, C is the concentration of sodium thiosulphate, g is the weight of oil.

Determination of total phenolic content (TPC)

Total phenolic content was determined the Folin-Ciocalteau colorimetric method by [11]. Gallic acid (GA) was standard for used to plot the standard curve that was constructed by a range of concentrations dissolved with the solvent. The equation was obtained, total phenolic content of the CPO as GA equivalent per gram of oil extract (mg GAE/ 100 g oil).

Determination of 1,1-diphenyl-2-picrylhydrazyl (DPPH) radical scavenging activity

DPPH analysis is the methods for evaluating antioxidant activity in oil. DPPH scavenging activity was determined using a modified method of yingngam and Chooklin [12], [13]. Different concentrations of sample dilution (0.3 mL) were mixed with 1.5 mL of 0.1 mM ethanolic DPPH solution. The resulting mixture was kept in the dark for 30 min and measured absorbance by UV-Vis spectrophotometer at 517 nm. The percentage of free radical inhibition of the palm oil was calculated according to the following Eq. (5).

$$\text{Inhibition (\%)} = \left[\frac{A_0-(A_1-A_2)}{A_0}\right] \times 100 \quad (5)$$

Where, A_0 is the absorbance of ethanol and DPPH mixed, A_1 is the absorbance of standard and DPPH mixed and A_2 is the absorbance of standard and ethanol mixed. Inhibition (%) was used to plot the standard curve. The equation was obtained DPPH antioxidant activity on μg Trolox/g CPO.

RESULTS AND DISCUSSIONS

Spikelets pre-heating by microwave heating

Table 1 show the physical properties of palm spikelet after microwave heating the criteria for optimum condition of pre-heating was completely loosing of palm fruit and premium CPO quality (FFA<3%, DOBI>3). The results found that at 14 min of duration heating consumed less time for 100% of fruitless. The characteristic of palm fruit was good physical. Mesocarp was slightly soft and kernel was white which whole palm fruit could produce crude palm oil and crude palm kernel oil. The temperature on palm fruit at 4 min was 89.14℃ to optimum temperature was more than 90°C to affect on

carotenoids degradation [14]. So, the optimum condition for spikelet preheating was 14 min of heating duration. The cause of loose fruitlets by the microwave heating was compensate steam heating and dielectric properties of the materials (water in material) that is major absorber of microwave energy. The microwave generated is distributed and absorbed by the component leading to rise in temperature. Consequently, palm spikelets received fast heating in kernel and mesocarp [8]. Although at 26 min of heating duration gave 6.68% of MC and completely fruitlet which the MC was optimum condition for oil production by screw press. The temperature was 108.34℃ to effect on antioxidants degradable which this condition gave lower TPC (table 2). The moisture content (MC) of mesocarp was decreased rapidly with higher heating duration because the water was rapidly evaporated from inside to outside of palm fruits. Moreover, over heat of microwave has effect on destruction of the physical structure, specially oil cell rupture, has effect on oil content (OC) [14]-[15].

Table 1 Physical properties of palm after microwave pre-heating

Heating duration (min)	T (℃)	MC (%)	OC (%)	fruitlets (%)	Condition	
					Mesocarp	Kernel
2	51.74	38.20	72.47	0.02	no changes	white
8	84.06	27.80	75.37	58.41	no changes	white
14	89.14	17.32	76.17	100.00	slightly soft	white
20	100.76	13.04	76.76	100.00	slightly soft	white
26	108.34	6.68	78.55	100.00	oily and soft	white

Note: T – Temperature (°C)

Heat penetration is key factor in palm sterilization via microwave heating. Notably, qualities of palm spikelet oil after microwave heating shown in Table 2. At the optimum pre-heating, DOBI, Peroxide value and FFA were 3.89, 3.28 mg.kg^{-1} and 0.60% respectively. The result showed that the CPO met premium palm oil standard. FFA reducing by microwave heating due to the lipase enzyme induced the hydrolysis reaction of triglyceride to generate the FFA with inactivated by microwave [4], [6]. The result of carotene content, peroxide value and total phenolic contents were slightly reduced due to deterioration of palm oil from high heating [8].

The advantage of spikelet pre-treat by microwave was reducing of FFA 1% of FFA with out chemical when compared with conventional process. The main problem of community palm oil mill is high FFA content. In the CPO which FFA reducing has to alkaline chemical for neutralization process while microwave heating can be stopped the activity of lipase enzyme and reversed reaction of hydrolysis to produce oil content [14].

Table 2 The qualities of palm spikelet oil after microwave pre-heating

Heating duration (min)	DOBI	PV (mg.kg^{-1})	FFA (%)	TPC (mg.GAE/100 g)
2	2.97	1.97	10.97	20.21
8	3.72	2.63	1.44	18.45
14	3.89	3.28	0.60	16.45
20	3.58	3.60	0.51	16.19
26	3.88	4.35	0.43	14.91

The Two Times Heating Processes

The condition of palm fruitlets after heating by microwave (first process) and hot air (second process)

Table 3 shown the conditions of palm fruitlets after two times heating by microwave (the first process) and hot air (the second process) for treatment premium CPO production. The result showed that the temperature increasing was proportional to the heating duration of microwave and hot air. The optimum heating duration of palm fruitlets was determined to be 3 min of microwave heating and 2.00 hr. of hot air heating. The physical characteristic of fruitlet was slightly soft of mesocarp and white of kernel, and not burning, which get the oil yield and undamaged antioxidant substrate [6]. In first process, sharply increased temperature made to low MC and high OC on short time heating. It also has a positive effect on the quality of oil.

Table 3 The condition of palm fruitlets after double heating by microwave and hot air for treatment premium CPO production

First Process of Microwave Heating Treatment						**Second Process of Hot Air Heating Treatment**					
Heating duration (min)	T (°C)	MC (%)	OC (%)	Condition of the heated fruitlets		Heating duration (hr.)	T (°C)	MC (%)	OC (%)	Condition of the heated fruitlets	
				Mesocarp	Kernel					Mesocarp	Kernel
1	69.82	16.74	76.46	slightly soft	white	1.00	57.08	13.77	75.60	slightly soft	white
2	98.76	11.94	77.20	slightly soft	white	1.50	66.34	9.88	76.38	slightly soft	white
3	105.58	7.43	78.29	slightly soft	white	2.00	70.52	7.69	76.66	slightly soft	white
4	109.04	4.53	78.19	partially dry	slightly brown	2.50	72.84	7.29	77.76	slightly soft	white
5	120.50	1.43	78.83	dry and stiff	completely brown	3.00	78.14	5.53	78.74	slightly soft	white

Table 4 The qualities of crude palm oil after two times heating by microwave (first process) and hot air (second process) at various of heating duration

First Process of Microwave Heating Treatment					**Second Process of Hot Air Heating Treatment**				
Heating duration (min)	DOBI	CC ($mg.kg^{-1}$)	PV ($meq.kg^{-1}$)	FFA (%)	Heating duration (hr.)	DOBI	CC ($mg.kg^{-1}$)	PV ($meq.kg^{-1}$)	FFA (%)
1	4.15	444.90	15.21	0.47	1.00	3.66	487.04	5.58	0.48
2	4.14	458.58	15.11	0.36	1.50	3.71	457.36	5.80	0.48
3	4.80	544.22	9.24	0.29	2.00	4.42	521.17	5.86	0.51
4	3.96	521.36	8.37	0.27	2.50	5.09	509.06	7.35	0.60
5	3.73	531.89	6.50	0.26	3.00	4.49	521.35	7.05	0.87
Limit	>4.00	500-700	<10.00	<1.00	Limit	>4.00	500-700	<10.00	<1.00

Note: Limit – the trending specifications limit of premium crude palm oil (CPO)

The qualities of CPO after microwave and hot air processes shown in Table 4. The results from the first process presented the premium CPO at 3 min of heating duration. This condition gave 4.80 of DOBI, 544.22 $mg.kg^{-1}$ of CC, 9.24 $meq.kg^{-1}$ of PV, and 0.29% of FFA which the results were supported high potential of microwave technology for premium CPO production. Atter 3 min of heating duration the temperature on palm fruit was more than 100°C to indicate that destruction of the physical structure, oil cell rupture, of the mesocarp [14], [15]. In antioxidants of CPO had reported that the hexane extraction mechanism gave the high concentrations of vitamin E and carotene from mesocarp fiber [6] that is antioxidant to encourage protecting the oil from oxidation reaction [8]. Corresponding, total phenolic contents indicated that the oil has antioxidants. From experiment found that the value of TPC and DPPH has similar trending.

The result of TPC and antioxidative activity by DPPH method for first and second processes shown in Table 5. The both processes had slightly decreased TPC and DPPH when heating duration was increased. Oxidation reduction in the oil was cause of reducing of TPC and DPPH. The excess of high temperature and long heating duration could reflect the deterioration in the CPO. Decreased level of antioxidant indicated that the oil was less protected against oxidation which the CPO was deteriorated [8]. Although, the both processes provided similar antioxidative values but hot air heating consumed long time for premium CPO production. Thus, the first process by was the optimum process more than the second process.

Table 5 Total phenolic content and anti-oxidative activity by DPPH method of the CPO

First Process of Microwave Heating Treatment		
Heating duration (min)	TPC (mg.GAE/100 g)	DPPH (µg Trolox/g CPO)
1	15.17	22.3
2	12.55	21.6
3	12.23	20.0
4	12.40	19.5
5	12.92	18.8
Second Process of Hot Air Heating Treatment		
Heating duration (hr.)	TPC (mg.GAE/100 g)	DPPH (µg Trolox/g CPO)
1.00	14.93	22.5
1.50	13.26	21.6
2.00	13.05	20.8
2.50	12.91	17.4
3.00	11.11	16.9

CONCLUSIONS

Microwave had high potential for premium CPO production. The optimum conditions were 14 min for spikelet pretreatment followed to 2 min for drying of palm fruit by microwave. The important point of oil palm pretreatment by microwave was shot operated time for protection of oil deterioration. From all result of experiment were subported as the microwave technology was enveronmental friendly process and can improve the oil quilities.

ACKNOWLEDGMENTS

This research was supported by National Research Council of Thailand (NRCT), under contract no. N41A640264, Thailand Institute of Nuclear Technology (TINT), under Thailand Science Research and Innovation (TSRI), Sang Arun Palm Oil Limited Partnership, Center of Excellence-Oil Palm, Kasetsart University, Department of Chemistry, Faculty of Science, and Faculty of Agriculture, Kasetsart University.

REFERENCES

[1] Kushairi A., Loh S. K., Azman I., Meilina O. A., Zainal Bidin M. N. I., Razmah G., Shamala S., and Parveez G. K. A., Oil palm economic performance in Malaysia and R&D progress in 2017. J. Oil Palm Res., Vol. 30, 2018, pp. 163-195.

[2] Statista. Vegetable oils: Global consumption by oil type. http://www.statista.com/statistics/ 263937/vegetable-oil-global-consumption/, accessed on 1 Nov., 2019.

[3] Krungsri, Industry Outlook 2020-2022: Palm Oil Industry, https://www.krungsri.com/en/research/ industry/industry-outlook/agriculture/sugar-(1)/IO/io-oil-palm-20-th on 30 May., 2022.

[4] Tapanwong M., Rayakorn N. and Vittaya P., Effect of combination microwave and oven drying on the chemical properties of different ripeness crude palm oil. International Journal of GEOMATE, Vol. 18, Issue 67, 2020, pp. 27-32.

[5] Olie, J.J. and Tjeng, T.D., The Extraction of Palm Oil. The Incorporated Society of Planters, Kuala Lumpur, 1974, pp. 29–35.

[6] Cheng S.F., Mohd N. L. and Chuah C.H., Microwave pretreatment: A clean and dry method for palm oil production, Industrial Crops and Products, Vol. 34, 2011, pp. 967-971.

[7] Umudee I., Chongcheawchamnan M., Kaitweerasakul M., and Tongurai C., Sterilization of Oil Palm Fresh Fruit Using Microwave Technique. International Journal of Chemical Engineering and Applications, Vol. 4, Issue 3, 2013, pp.111-113.

[8] Hadi N.A., Han N.M., Majid R.A. and Met C.R. C., The effect of microwave treatment and delayed harvesting on oil palm fruitlets oil quality, J Oil Palm Res, 2021; https://doi.org/10.21894/jopr.2021.0015.

[9] Chow M.C. and Ma A.N., Processing of fresh palm fruits using microwaves, J. Microw. Power EE, Vol. 40, Issue 3, 2007, pp. 165–173.

[10] Kandiah S., Basiron Y., Suki A., Taha R. M., Hwa T. Y. and Sulong M. Continuous sterilization: The new paradigm for modernising palm oil milling. J. Oil Palm Res., Special Issue, 2006, pp. 144-152.

[11] Wolfe K., Wu X., and Liu R.H., Antioxidant Activity of Apple Peels. J ARG Food chem and Food Chemistry, Vol. 51, 2003, pp.609-614.

[12] Yingngam B., Supaka N. and Rungseevijitprapa W. Optimization of process conditions for phenolics extraction from Cratoxylum formosum ssp. formosum leaves using response surface methodology. J Food Sci Technol 2013; 10.1007/s13197-013-1030-y.

[13] Chooklin S., Rehbenmood K., Bunmak J. and Chingsong W. Characterization of Anti-Oxidative Cassava Starch Based Film Supplemented with Anacardium occidentale L. Leaf Extract. Walailak J Sci & Tech, Vol. 14, Issue 12, 2017, pp. 981-995.

[14] Nokkeaw R., development of community crude palm oil mill without steam utilization and method development for percentage oil analysis in fresh fruit bunch for rapid analysis. Thesis of Graduate School, Kasetsart University, 2017.

[15] Chang J.S.L., Law M.C., Chan Y.S., and Leo C.P., Effects of microwave heating on oil palm mesocarp, Chemical Engineering Transactions, Vol. 45, 2015, pp. 1633-1.

8th Int. Conf. on Structure, Engineering & Environment (SEE), Mie, Japan, Nov.10-12, 2022, ISBN: 978-4-909106094 C3051

TUNGSTEN, COPPER, MANGANESE, ZINC, IRON AND ARSENIC CONCENTRATIONS OF PLANTS IN KIWADA MINE

Daiki Yamamoto[1] and Hiroyuki Ii[2]
[1]Graduate School of Systems Engineering, Wakayama University, Japan ;
[2]Faculty of Systems Engineering, Wakayama University, Japan

ABSTRACT

Athyrium yokoscense (a special kind of fern) and *Arabis gemmifera* (a kind of Brassicaceae) are known as hyperaccumulators that contain specific heavy metals. However, only a few studies have confirmed the hyperaccumulator status of other plants. The hyperaccumulator of tungsten (W) was the focus of this study. W has similar chemical properties to molybdenum (Mo). Mo is necessary for plant protein synthesis and nitrogen metabolism, and Mo is recognized as an essential trace element. On the other hand, it remains to be elucidated whether W has such a function. Here quantitative analysis was undertaken to determine the concentration of heavy metals in plants growing in three areas of Kiwada mine that is considered with heavy metals. The deposit at the Kiwada mine is a skarn deposit which contained W formed by alternating limestone in an olistostrome. The main W-bearing mineral is scheelite (CaWO4) and chalcopyrite ($CuFeS_2$), pyrrhotite ($Fe_{1-x}S$) and arsenopyrite (FeAsS) are also present. One of the study areas was near the mine entrance adit, and the other was a place where the excavated ore deposits were stockpiled. Pine, *cyrtomium* and *pteris cretica* (another kind of fern), etc. were found. As a result, it was found that multiple plants contained W over 100 ppm, most of which were concentrated in the roots. These plants are not common but are found in various parts of Japan. Together, these results provide new insight into our understanding into tolerance for heavy metal in plants.

Keywords: Hyperaccumulator, Heavy metals, Tungsten, Fern

INTRODUCTION

By the 1860s, De Saussure, von Sacks, and Knop had shown that C, H, O, N, P, S, K, Ca, Mg, and Fe were essential for plant growth. C, H, O, N, P, S, K, Ca, Mg, and Fe are essential for plant growth. Subsequently, 17 essential elements for plant growth were listed by 1987 [1]. Since heavy metals and other soil contaminants are absorbed together during the absorption process, plants in general cannot grow in areas with high concentrations of soil contaminants. However, some plants prefer to grow in areas with high concentrations of contaminants, especially heavy metals, and absorb and accumulate heavy metals at high levels. These plants are called mine plants or metal-loving plants in Japanese.

Tungsten (W) is a rare metal that exists in the environment in the form of WO_4^{2-} (tungstate ion), an element with very similar chemical properties to molybdenum (Mo). However, while Mo is a trace essential element for plants involved in nitrate reduction, W has not been recognized as essential, and therefore, there are few examples of analysis of W in plants and soil. The reason for the low concentration of W in plants growing in soil is assumed to be that the solubility of W-containing components in soil is low and the supply of W is insufficient compared to that of Mo. On the other hand, hydroponic experiments comparing the absorption of Mo and W using Italian grass showed that the plants absorbed significantly higher concentrations of Mo and W than normal plants growing in soil, and that the higher the concentration in the culture medium, the greater the amount absorbed. Based on these results, it can be predicted that W will be absorbed by plants in the same way as Mo if the supply of W is sufficient [2]. If this is the case, it is possible that wild plants also absorb W in soils with high W concentrations.

The Kiwada Mine, located in Futashika, Iwakuni City, Yamaguchi Prefecture, has long been known as a mineral deposit area, where small mines were established to extract tin (Sn) and copper (Cu) during the Edo period. Since the Meiji period (1868-1912), the area has been known as a tungsten production area due to the discovery of a large amount of ash heavy ore. The Fujigatani Mine is located southwest of the Kiwada Mine, and the Kuga Mine is located northwest of the Kiwada Mine, and ash feldspar was the main ore for both mines [3]. All the mines are now closed, but some of the waste rock containing ash heavy ore has been left in some areas, and it is possible that a large amount of W is contained in the soil.

The purpose of this study is to investigate plants growing naturally in the Kiwada Mine and to measure the concentration of heavy metals, including W, in the collected plants. In addition, we examine whether

there are plants that absorb and accumulate high concentrations of W, and discuss the differences in heavy metal concentrations among plant sites and sampling locations.

METHODS

About The Kiwada Mine

The geology of the Nishiki River basin consists of the Triassic Kuga County Formation and the Late Cretaceous granitoids that intrude the Kuga County Formation. The Kuga County Formation consists of mudstone, chert and sandstone, and has narrow lenticular limestone. The deposits are composed of massive skarn deposits and quartz veins, which are alternated with limestone, and both of them are operated by ash heavy rocks. The number of ore bodies is large, and based on past open-pit mining sites, more than 30 ore bodies are estimated to have existed. The main ore bodies are represented by the Hontei, Suehiro, Mabo, and the 10th ore bodies of the 5th, 8th, and Choei Ants, etc [3].

The term skarn is derived from a mining term used for vein stones composed of coarse-grained calcium-rich silicate minerals from iron mines in the Persberg area of Sweden. Skarn occurs in association with metamorphic and igneous rocks, but it is sometimes enriched in useful elements to the extent that it can be used as a mineral resource, and is called a skarn deposit.

The type of skarn deposit is related to various geological factors, the most significant of which is the oxidation degree of the igneous rocks involved. Based on the amount of magnetite or magnetic susceptibility contained in the granitoids, they are classified into two types: oxidizing magnetite-series and reducing ilmenite-series. On the other hand, based on differences in the source rock, they are divided into I-type and S-type granitoids. When sedimentary rocks containing coal are involved, the rocks become reductive granitoids. When magnetite or I-type granitoids are involved lead, zine, copper, iron, molybdenum, and silver are present, whereas tin and fluorine are present when ilmenite or S-type granitoids are involved. Tungsten is associated with both types of granitoids. Tungsten occurs as ash heavy rocks and is divided into oxidized and reduced forms depending on the type of mineral accompanying it, the letter being associated with ilmenitic granitoids.

Among the W skarns, the oxidized type is composed of glauconite skarn with a low monoclinopyroxene to porphyroxene, with a high monoclinopyroxene to porphyroxene ratio, and tin and fluorine. The Kiwada Mine corresponds to the reduced type, in which the deposit develops in layers or lenses between limestone and sandy-muddy rocks, and is poor in sulfide minerals, with ash heavy rocks sometimes accompanied by quarts and white mica [4].

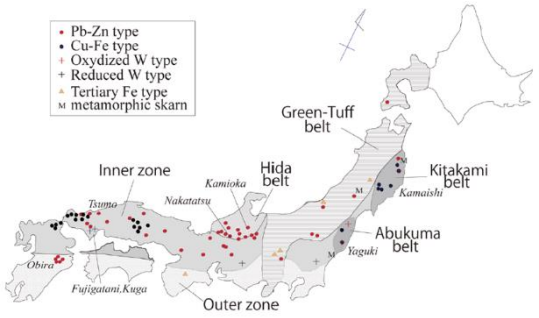

Fig .1 Distribution of skarn deposits in Japan [4]

Outline Of The Study Site

The locations of plant collections in this study are shown in the figure below. Point (1) is Choei Adit and point (2) is the work hut. Point (3) is the ore storage.

Fig .2 Location of Kiwada mine

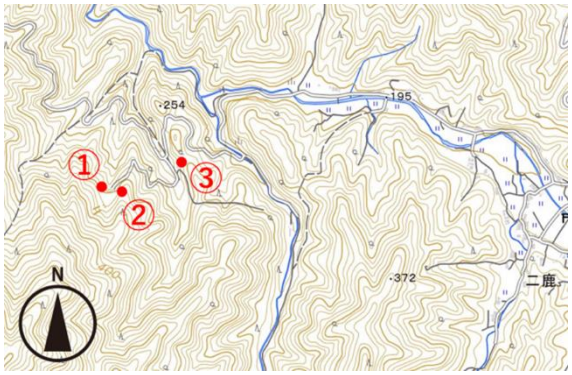

Fig .3 Location of sampling points in Kiwada mine

Figure 4 is a photograph of the entrance to the Choei Adit at point (1). The Choei Adit is one of the mine entrances dug during mining. The ore storage at point (3) refers to a pile of mined ore that has been accumulated in a specific location and discarded as waste. In these rock piles, ash heavy rocks consisting of $CaWO_4$ were found in abundance.

Fig .4 Photograph of the entrance to the Choei Adit at point (1)

Fig .5 Photograph of the ore storage at point (3)

Analysis Method

After pretreatment, the collected plants are measured for heavy metal concentrations in the plants using an ICP optical emission spectrometer.

Pretreatment consists of cleaning the plants and preparing samples. First, the collected plants are separated into root, leaf, and stem parts as much as possible. The soil is washed because it contains a large amount of heavy metals, which can cause large errors in the measurement results. After washing with tap water, an ultrasonic cleaner was used. To use the machine, the sample to be cleaned is placed in a container, soaked in water, and then placed in the machine. Most of the stains are removed in about 20 minutes, but heavily soiled specimens, such as roots, need to be washed again. After the dirt is removed, the specimens are placed in the dryer for one or two days to dry.

A solution sample of heavy metals extracted from plants is prepared for ICP emission spectrometry. First, dried plants are placed in a screw tube and concentrated nitric acid is added. Nitric acid has the effect of oxidatively decomposing organic matter in the sample and extracting heavy metals. After approximately two weeks of standing, the heavy metals in the plants are extracted and a yellow solution is obtained. Fine impurities remain in the screw tube, so these are removed using a filter and syringe.

The analysis was performed using an ICP optical emission spectrometer to measure the concentration of heavy metals in the prepared samples. The heavy metals measured were tungsten (W), copper (Cu), manganese (Mn), zinc (Zn), iron (Fe) and arsenic (As).

From the above steps, the concentration of heavy metals is measured. Since the concentration measured is the concentration in the sample solution, it must be converted to the concentration of heavy metals in the dried plant sample using the following equation

$$a\ (mg/kg) = \frac{b\ (mg/kg) \times c(g)}{d\ (g)} \quad (1)$$

a Heavy metal concentrations in plant samples
b Concentration of solution
c Weight of solution
d Dry weight of sample

RESULTS

In this study, the concentration of six elements were measured: tungsten (W), copper (Cu), manganese (Mn), zinc (Zn), iron (Fe) and arsenic (As). The concentrations of each heavy metal detected are shown in the graphs for each sampling point and site.

Table 1 Collected plants and sampling point

Numbers	Collected plants	Sampling point
A	*Pteris cretica*	①
B	*Cyrtomium fortune*	①
C	*Rubus buergeri*	①
D	*Rubus buergeri*	③
E	*Cyrtomium fortune*	③
F	*Arachniodes standishii*	②
G	*Pinus densiflora*	②

Measurement Results Of W

Figure 6 and Fig 7 show the concentration of W in the dried samples of each plant. The average concentrations in A per site were 6.089 mg/kg for leaves, 2.083 mg/kg for stems and 57.192 mg/kg for

roots. The average concentrations in B per site were 7.531 mg/kg for leaves, 2.442 mg/kg for stems and 136.979 mg/kg for roots. The average concentrations in C per site were 40.119 mg/kg for leaves, 7.818 mg/kg for stems and 49.692 mg/kg for roots. The average concentrations in D per site were 35.27 mg/kg for leaves, 4.102 mg/kg for stems and 237.552 mg/kg for roots. The average concentrations in E per site were 231.29 mg/kg for leaves, 61.317 mg/kg for stems and 1114.655 mg/kg for roots. The average concentrations in F per site were 9.815 mg/kg for leaves, 3.91 mg/kg for stems and 21.595 mg/kg for roots. The average concentrations in G per site were 2.554 mg/kg for leaves and 3.779 mg/kg for stems.

Roots in the plants contain a large amount of W, and among them, E showed W concentrations of more than 800 mg/kg. On the other hand, some plants, such as F, showed almost no W detected even in the roots.

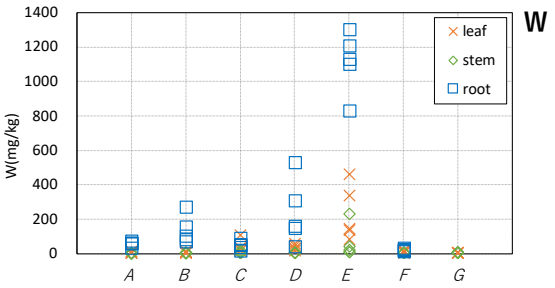

Fig .6 Measurement results for W

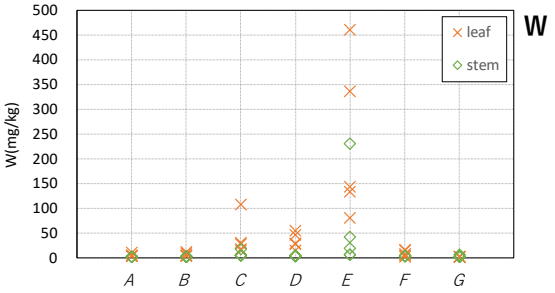

Fig .7 Measurement results for W

Measurement Results Of Cu

Figure 8 shows the concentration of Cu in dried samples from each plant. The average concentrations in A per site were 6.282 mg/kg for leaves, 5.103 mg/kg for stems and 221.925 mg/kg for roots. The average concentrations in B per site were 7.359 mg/kg for leaves, 5.321 mg/kg for stems and 109.236 mg/kg for roots. The average concentrations in C per site were 15.384 mg/kg for leaves, 13.006 mg/kg for stems and 84.858 mg/kg for roots. The average concentrations in D per site were 13.367 mg/kg for leaves, 12.623 mg/kg for stems and 172.653 mg/kg for roots. The average concentrations in E per site were 37.746 mg/kg for leaves, 14.787 mg/kg for stems and 2349.335 mg/kg for roots. The average concentrations in F per site were 9.41 mg/kg for leaves, 4.842 mg/kg for stems and 74.521 mg/kg for roots. The average concentrations in G per site were 3.176 mg/kg for leaves and 6.767 mg/kg for stems.

Cu concentrations in the roots were high, especially in the roots of E. Leaves and stems contained little Cu.

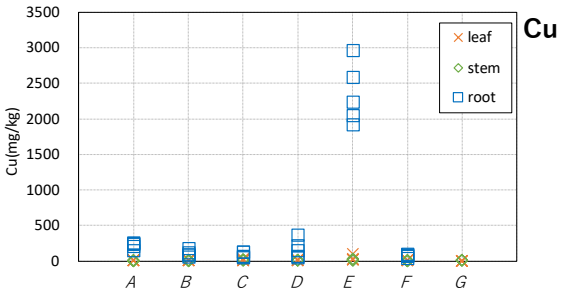

Fig .8 Measurement results for Cu

Measurement Result Of Mn

Figure 9 shows the concentration of Mn in dried samples from each plant. The average concentrations in A per site were 32.755 mg/kg for leaves, 6.358mg/kg for stems and 135.9 mg/kg for roots. The average concentrations in B per site were 59.008 mg/kg for leaves, 18.639 mg/kg for stems and 198.932 mg/kg for roots. The average concentrations in C per site were 154.829 mg/kg for leaves, 51.985 mg/kg for stems and 84.501 mg/kg for roots. The average concentrations in D per site were 497.188 mg/kg for leaves, 35.664 mg/kg for stems and 80.385 mg/kg for roots. The average concentrations in E per site were 52.031 mg/kg for leaves, 22.631 mg/kg for stems and 190.311 mg/kg for roots. The average concentrations in F per site were 53.884 mg/kg for leaves, 17.046 mg/kg for stems and 260.649 mg/kg for roots. The average concentrations in G per site were 114.689 mg/kg for leaves and 40.354 mg/kg for stems.

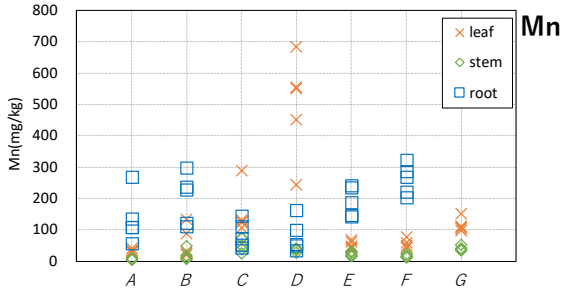

Fig .9 Measurement results of Mn

Measurement Result Of Zn

Figure 10 shows the concentration of Zn in dried samples from each plant. The average concentrations in A per site were 39.326 mg/kg for leaves, 11.965 mg/kg for stems and 74.883 mg/kg for roots. The average concentrations in B per site were 31.816 mg/kg for leaves, 22.317 mg/kg for stems and 66.405 mg/kg for roots. The average concentrations in C per site were 26.167 mg/kg for leaves, 46.706 mg/kg for stems and 132.19 mg/kg for roots. The average concentrations in D per site were 22.929 mg/kg for leaves, 27.452 mg/kg for stems and 153.176 mg/kg for roots. The average concentrations in E per site were 77.237 mg/kg for leaves, 24.035 mg/kg for stems and 282.881 mg/kg for roots. The average concentrations in F per site were 91.786 mg/kg for leaves, 77.17 mg/kg for stems and 90.622 mg/kg for roots. The average concentrations in G per site were 32.871 mg/kg for leaves and 30.847 mg/kg for stems.

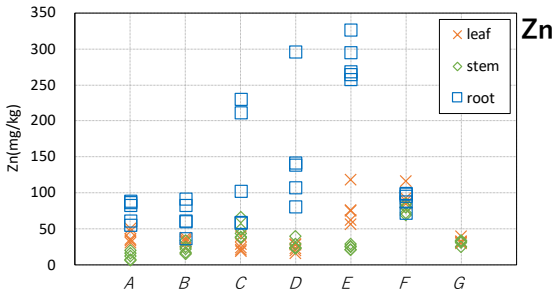

Fig. 10 Measurement results of Zn

Measurement Results Of Fe

Figure 11 shows the concentration of Fe in dried samples from each plant. The average concentrations in A per site were 178.702 mg/kg for leaves, 48.97 mg/kg for stems and 1856.047 mg/kg for roots. The average concentrations in B per site were 133.107 mg/kg for leaves, 20.378 mg/kg for stems and 3691.684 mg/kg for roots. The average concentrations in C per site were 377.678 mg/kg for leaves, 74.636 mg/kg for stems and 572.191 mg/kg for roots. The average concentrations in D per site were 151.567 mg/kg for leaves, 32.182 mg/kg for stems and 1114.103 mg/kg for roots. The average concentrations in E per site were 580.856 mg/kg for leaves, 102.535 mg/kg for stems and 6879.96 mg/kg for roots. The average concentrations in F per site were 199.745 mg/kg for leaves, 28.985 mg/kg for stems and 1150.652 mg/kg for roots. The average concentrations in G per site were 33.735 mg/kg for leaves and 56.949 mg/kg for stems.

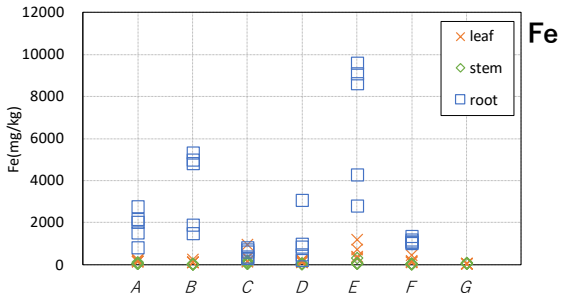

Fig .11 Measurement results of Fe

Measurement Results Of As

Figure 12 shows the concentration of As in dried samples from each plant. The average concentrations in A per site were 67.533 mg/kg for leaves, 130.625 mg/kg for stems and 47.512 mg/kg for roots. The average concentrations in B per site were 6.605 mg/kg for leaves, 1.323 mg/kg for stems and 33.131 mg/kg for roots. The average concentrations in C per site were 1.086 mg/kg for leaves, 0 mg/kg for stems and 11.668 mg/kg for roots. The average concentrations in D per site were 0 mg/kg for leaves, 0 mg/kg for stems and 13.174 mg/kg for roots. The average concentrations in E per site were 3.488 mg/kg for leaves, 0.304 mg/kg for stems and 140.611 mg/kg for roots. The average concentrations in F per site were 0 mg/kg for leaves, 0 mg/kg for stems and 0.724 mg/kg for roots. The average concentrations in G per site were 0 mg/kg for leaves and 0 mg/kg for stems.

Leaves and stems of A contained 40~225 mg/kg As, while them of other plants contained almost no As.

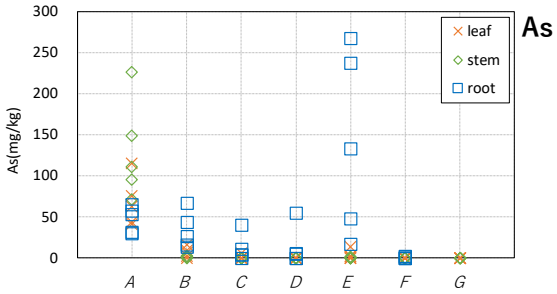

Fig. 12 Measurement results of As

DISCUSSION

Differences In Heavy Metal Concentrations In Different Parts Of The Body

Comparing the heavy metal elements in the collected plants by site, the concentrations of tungsten (W), copper (Cu), iron (Fe) and manganese (Mn) were higher in the roots of all plants. The higher concentrations of Cu, Fe and Mn in roots are thought

to be due to the fact that only the necessary amounts are transported to the leaves during the absorption process, and excess heavy metals are accumulated in the roots. W and As, which are not considered essential elements, were found almost exclusively in the roots. It is thought that the accumulation and adsorption of these elements in the roots during growth may prevent them rom being taken into the body. In addition, Comparing the graphs of heavy metal concentrations in each plant, it can be seen that the heavy metal concentrations of W and Cu have a similar concentration distribution.

Differences In Heavy Metal Concentrations Between Sampling Sites

A comparison of heavy metal concentrations in plants from the Choei Adit and the ore storage shows that W and Cu tend to be more abundant in plants from the ore storage than from the Choei Adit. The ores mined in the Choei Adit were mainly dumped in the ore storage area, with ash feldspar contains calcium (Ca) and tungsten (W), and bress ores contain copper (Cu) and iron (Fe). Therefore, heavy metals are thought to have been leached from these rocks by rainfall and other factors, causing the concentrations of W and Cu to increase at Point (3).

CONCLUSIONS

In this study, heavy metal concentrations in plants collected from the Choei Adit and ore storage areas of Kiwada mine were alalyzed. As a result, it was found that *cyrtomium fortune* contained a large amount of tungsten (W), most of which accumulated in the roots. Interesting results were also obtained, with high concentrations of arsenic (As) detected in *Pteris cretica*. The reason for the significantly higher W concentration in roots then in stems and leaves may be that W is easily precipitated through hydrolysis and polymerization, and W precipitated on the root surface and W absorbed in the root interior are mixed. However, it is possible that W absorbed from the roots of *cyrtomium foutune* may be accumulated in the leaves and stems.

To clarify this fact, it is necessary to investigate whether W adheres to the root surface or permeates the inside of the roots. To this end, it is necessary to expand the study area at the Kiwada mine and also to investigate plants native to the surrounding tungsten mines and W-skarn mines.

As was only found in the leaves and stems of *petris cretica* of Choei Adit. Sakae S. et al.'s study [6] showed that this plant has an accumulation potential for As with the results of the present analysis.

ACKNOWLEDGMENTS

I would like to express my sincere gratitude to Associate Professor Masanobu Taniguchi of graduate school of Systems Engineering, Wakayama University, who took time out of his busy schedule to give me great advice and guidance in the course of this research.

A would like to express my sincere gratitude to the members of the laboratory for their constant guidance and cooperation in laboratory analysis and data processing.

We would like to express our gratitude to all of you for your cooperation.

REFERENCES

[1] Mori T., Mae T., Yoneyama T., Bunseido Publisher, 2001.
[2] Yamada H., Nishimura K., Hattori K., Takahashi E., Absorption of molybdenum and tungsten by Italian grass, Japanese Journal of Soil Science and Fertilizer, Vol.60, No.5, 1989, pp.463-465.
[3] Nagahara S., Geological Deposit and Exploration of Kiwada Mine, Yamaguchi Prefecture, Mining Geology, Vol.28, No.152, 1978, pp.373-384.
[4] Etuo U., Takanori N., Approach to skarn Deposit, Geochemistry, Vol.52, No.4, 2018, pp.149-169.
[5] Shigeyuki M., Hoikusya, Shida no Zukan (illustrated Book of fern), 1986.
[6] Sakae S., Yusuke Y., Kana D., Shigeyoshi W., Accumulation of arsenic in soils by Pteris cretica, Abstracts of the Annual Meeting of the Geological Society of Japan, 2007, pp.615-615.

8th Int. Conf. on Structure, Engineering & Environment (SEE), Mie, Japan, Nov.10-12, 2022, ISBN: 978-4-909106094 C3051

DIFFERENCES IN PLANTS HEAVY METAL CONCENTRATIONS BY REGION

Takuya Ueda[1] and Hiroyuki Ii[2]
Faculty of System Engineering, Wakayama University, Japan

ABSTRACT

This study describes the accumulation of heavy metals in plants. Research is underway on plants that are found to be specific for growing in contaminated soil and accumulating heavy metals at high levels. In this study, the concentrations of heavy metals in plants sampled at Tada Silver Mine in Hyogo prefecture, central Japan were measured in order to clarify the relation between heavy metals concentration and parts of plants. Tada Silver Mine is closed and produced Ag, Zn, Pb, and Cu. There were 5 sites surveyed at the Tada Silver Mine, and the plants growing were *Arabis gemmifera*, *Fallopia japonica*, and *Blechnum niponicum*. The collected plants were pretreated, and the concentration of heavy metal genus plants were measured using ICP emission spectroscopy analysis. As a result, the concentrations of leaves for Zn were 6000 to 13000mg/kg for *Arabis gemmifera*, 100 to 200mg/kg for *Fallopia japonica*, and 100 to 200mg/kg for *Blechnum niponicum*. The concentrations of roots for Pb were 300 to 1100mg/kg for *Blechnum niponicum*, 0to 10mg/kg for *Fallopia japonica*, and 0 to 10mg/kg for *Arabis gemmifera*.

Keyword: Arabis gemmifera, Blechnum niponicum, heavy metal, soil

INTRODUCTION

Plants absorb various inorganic substances present in the soil from their roots and live as nutrients in them. In the process, contaminants in the soil, including heavy metals, are absorbed together, so ordinary plants cannot grow in places with high soil pollutant concentrations [1]. However, some plants prefer to grow in places where there are many pollutants, especially metals, and absorb and accumulate pollutants at high levels [2]. An example is the fern plant *Pteris vittata*, which has been found to accumulate arsenic concentrations 10,000 times higher than other plants [3]. Such plants are called heavy metal accumulation plants and have been focused on from the viewpoint of phytoremediation which uses plants to improve soil contamination, and research and experiments are still being conducted Today [4],[5].

Since the growth conditions of plants differ depending on the environment such as soil and temperature, it was thought that changes in the number of heavy metals in plants occur depending on regional differences. Therefore, I investigated two locations, the Tada Silver Mine in Inagawa Town, Hyogo Prefecture, and the Mino Waterfall in Mino City, Osaka Prefecture, and aimed to verify whether there was a difference in the heavy metal concentration of plants due to changes in the area. Tada Silver Mine is famous as a copper and silver mine with a long history that has been mined since the Nara period and lasted until 1973 [6]. Since ores such as zinc sphalerite, blue lead ore, and chalcopyrite have been found at this survey site, it is thought that zinc, lead, and copper is contaminated [7]. Mino Falls is near where the mine where copper was mined, and it is thought that copper contamination is occurring [8].

APPROACH

Sites② ~ ⑤ of the Tada Mine are contaminated with a lot of heavy metals left in the soil, so plants may be accumulating heavy metals. In addition, in order to clarify the specificity of numerical values, plants at point① of the non-contaminated zone were also collected at the same time and compared. The survey date for Tada Mine is May 22, 2022. There were a total of five types of plants, including *Fallopia japonica*, *Arabis gemmifera*, and *Blechnum niponicum* in the contaminated area, and *Dicranopteris dichotoma* growing naturally in the non-polluted zone. Since we were able to collect *Blechnum niponicum* at three locations, we will pay attention to the change in the concentration of heavy metals due to the difference between each point. Since the ores discovered this time are two types of ore, linarite, and chalcopyrite, and since ores such as bornite, galena, and sphalerite also exist in the Tada Silver Mine, it is presumed that the soil is contaminated with Cu (copper), Pb (lead), and Zn (zinc) [2],[6].

The survey date for Mino Falls is May 25, 2022. At Mino Falls, two kinds of plants were collected: *Arabis gemmifera* and *Athrium yokoscense*. Since *Arabis gemmifera* grew naturally in both the Tada

Mine and Mino Falls, we will conduct a comparative study by region based on the results of the analysis of both.

Table 1 Survey points and details

Site	Detail	Plant Name
Tada Mine	① Non-filthy Dyeing place	*Dicranopteris dichotoma*
Tada Mine	② Smelting and refining traces	*Arabis gemmifera, Fallopia japonica*
Tada Mine	③ Veins along	*Blechnum niponicum*
Tada Mine	④ Aoki Mabu	*Blechnum niponicum*
Tada Mine	⑤ Ore dumping site	*Blechnum niponicum*
Mino Waterfall	⑥ Mino Waterfall	*Arabis gemmifera, Athriumyokoscense*

The collected plants were divided into roots, stems, and leaves and washed to remove the soil adhering to the sample. The cleaning method was a combination of the use of an ultrasonic cleaner and a method of washing directly by hand. After washing, put in the dryer for a week. The dried sample was weighed with an electronic balance, put in a screw tube, concentrated sulfuric acid was added, and the weight was measured. Nitric acid is suitable for the extraction of heavy metals because it oxidizes and decomposes organic matter in the specimen. Thereafter, it was allowed for a week to confirm that the sample had turned light yellow, and then the solids in the solution were removed using a syringe and filter.

In the analysis, it was measured using ICP-AES. ICP emission spectroscopy measures are based on the following principles. First, when plasma energy is applied to the sample, the atoms of the elements contained in the sample absorb the energy and are excited. The excited atom then emits light (spectral lines) when returning to a lower energy level. Since light at this time is specific to the element, it can be analyzed by measuring the wavelength and amount of light. The elements measured in this study are Zn (zinc), Ni (nickel), Cu (copper), Co (cobalt), As (arsenic), Mn (manganese), Cr (chromium), Ca (calcium), Mg (magnesium), Pb (lead), Ag (silver), Cd (cadmium), Al (aluminum), Ba (barium), Bi (bismuth), Li (lithium), Mo (molybdenum), Sb (antimony) , Se (selenium), Sn (tin), Sr (strontium), Th (thorium), U (uranium), V (vanadium).

In this analysis, since the heavy metal concentration of the solution of the sample is measured, Equation (1) was used to obtain the heavy metal concentration of the plant.

$$X = S * \frac{(P+N)}{P} \quad (1)$$

X: Heavy metal concentration in plants(mg/kg)
S: concentration in solution (mg/kg)
P: dry weight of plant (g)
N: weight of nitric acid (g)

RESULTS AND DISCUSSIONS

Specific values were shown from among the heavy metal concentrations detected by ICP emission spectroscopic analysis and graphed for each plant. The X-axis lists the names of the plants and the number of points collected, and the Y-axis indicates the concentration of each heavy metal.

Figure. 1 shows the heavy metal content of Zn in plants. Because Zn is a trace essential element of plants, it was also included in a small amount of *Dicranopteris dichotoma* in non-contaminated zones. The specific value was shown in *Arabis gemmifera*, which contained about 6,000 ~ 13,000 mg/kg in the leaf and showed the highest concentration. Also, when looking at the amount of Zn contained in the Tada Mine and the *Arabis gemmifera* of Mino Falls, the leaves showed the same value, but the stems and roots contained an overwhelming amount of *Arabis gemmifera* of Mino Falls.

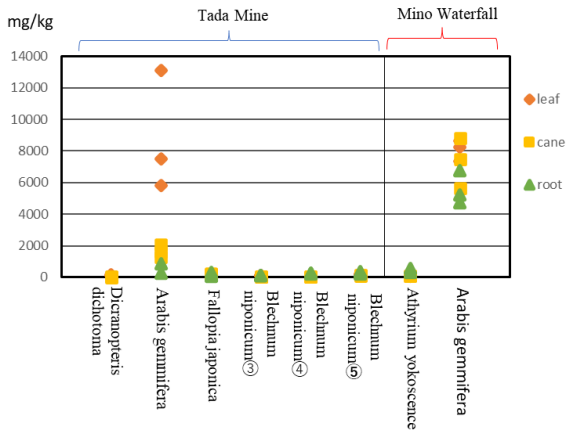

Fig. 1 Zn concentration in plants

Figure. 2 shows the number of heavy metals in Cd in plants. Because CDs are toxic heavy metals that can be harmful even in small quantities of accumulation, they were not included in the non-contaminated areas of *Dicranopteris dichotoma* and *Blechnum niponicum*. However, *Arabis gemmifera*, which grows naturally in the Tada Mine, accumulated a high concentration of 1000 ~ 2000 mg/kg. Furthermore, it is noteworthy that the same species of

Arabis gemmifera also showed different results at the Tada Mine and Mino Falls. Despite accumulating a lot of CDs at the Tada Mine, the *Arabis gemmifera* at Mino Falls contained almost no Cd.

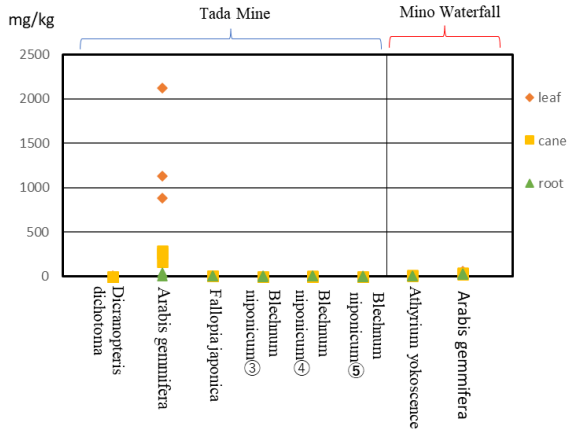

Fig. 2 Cd concentration in plants

Figure. 3 shows the number of heavy metals in Cu in plants. Since Cu is a trace essential element of plants, it was also slightly contained in the *Dicranopteris dichotoma* of the non-contaminated zone. However, plants other than *Dicranopteris dichotoma* showed a large accumulation of heavy metals at the roots of 200 mg/kg~1000 mg/kg. As with the Cd concentration of Fig.2, there was a large difference in the amount of accumulation of Tada Mine and *Arabis gemmifera* at Mino Falls in Cu. In addition, when comparing the Tada mine points③, points④, and points⑤, the *Blechnum niponicum* at point⑤ showed a high concentration, and even within the same mine, large differences in the number of heavy metals were observed depending on the location.

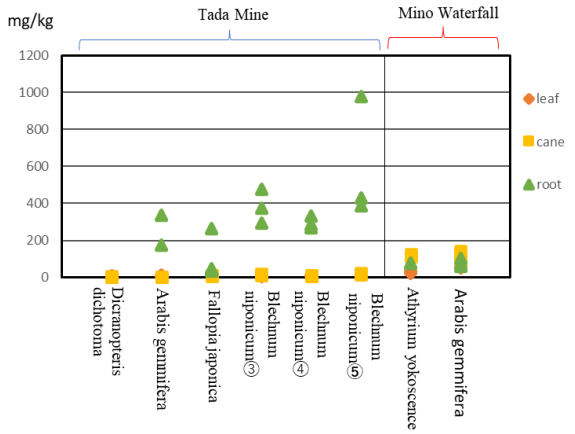

Fig. 3 Cu concentration in plants

Figure. 4 shows the number of heavy metals in Pb in plants. Since Pb is hardly contained in the non-polluted zone, the *Dicranopteris dichotoma* had almost no lead accumulation, but high concentrations were accumulated in the squirrel native to points ③, ④, and ⑤. Further, when compared at points ③, ④, and ⑤, it was found that a large amount of lead was accumulated in the Aoki Mabu at point ④.

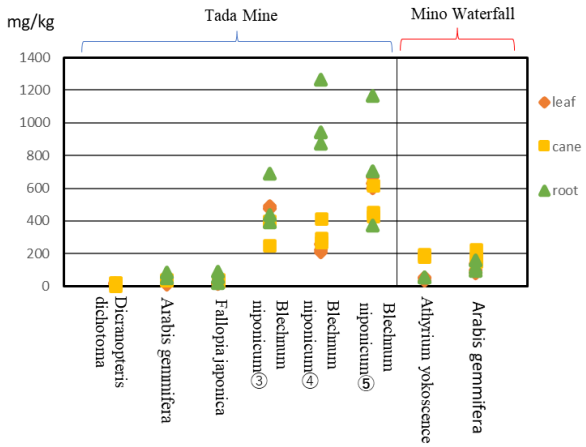

Fig. 4 Pb concentration in plants

Figure. 5 indicates the number of heavy metals in the plant Fe. The plant that showed the highest value was *Athyrium yokoscense* native to Mino Falls, accumulating 3,000 to 4,500 mg/kg at the roots. Also, when viewed as a whole, they tended to accumulate large amounts of Fe in the roots, and the leaves and stems contained almost no Fe.

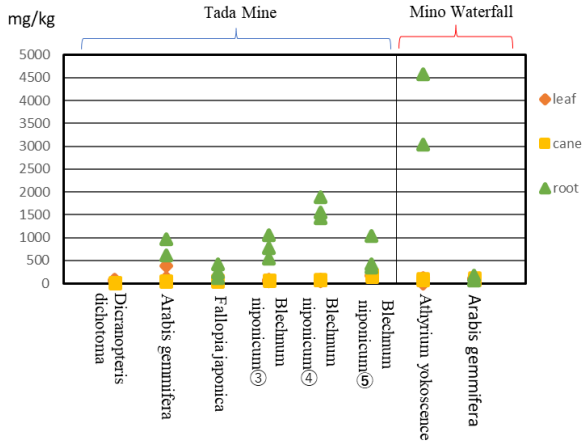

Fig. 5 Fe concentration in plants

If we focus on each part of the leaf, stem, and root, we can see that the place where it accumulates differs depending on the heavy metal. Specifically, *Arabis gemmifera* tends to have a large amount of accumulation in the leaves of Zn and Cd, but Cu and Fe have a large amount of accumulation in the roots. From this, it can be seen that *Arabis gemmifera* is resistant to heavy metals of Zn and Cd and can perform photosynthetic activities even when heavy metals are accumulated in large amounts in leaves. In

addition, when focusing on Pb, a large amount of accumulation is seen in the sea beetle, and high concentrations are shown in all leaves, stems, and roots. So, it was found that the sea lily has Pb tolerance and can grow while accumulating Pb on the leaves, stems, and roots.

In this section, we will focus on the differences in the heavy metal concentrations of plants by region and location. First, when we focused on the *Arabis gemmifera*, which grows naturally in the Tada Mine and Mino Falls, there was not much difference in the concentration of Zn and Pb, and there was no major difference. However, heavy metals from Cd, Cu, and Fe were accumulated at high levels at the Tada Mine but were rarely contained at Mino Falls. If I were to guess why there was a big difference in the number of heavy metals due to regional differences, I think it was because there was a difference in the soil contamination situation. As mentioned in the survey summary, the Tada Mine has strong soil contamination due to the discovery of Pb, Zn, and Cu ores, and as a result, it is thought that it has had a significant impact on plants. Since many Cd are derived from Zn ore, it is thought that a large amount of accumulation was seen in *Arabis gemmifera* for the same reason as before. Copper mining was carried out nearby at Mino Falls, but in this study, there is a high possibility that the survey was conducted in a place with weak contamination of Cu, and it is thought that *Arabis gemmifera* of Mino Waterfall did not accumulate much Cd due to this factor.

Next, when we focused on the *Blechnum niponicum*, it was found that it accumulated a large amount of Pb. Looking at the difference in the number of heavy metals at each point, the heavy metal concentration was about 600 g / kg higher than that along the vein at point③ in the Aoki walk at point ④. It was presumed that Aoki Mabu was the site where Pb ore was mined, so high numbers were indicated, and it was found that the heavy metal concentration of plants also changes depending on the soil contamination situation.

CONCLUSIONS

In this study, we investigated the number of heavy metals in plants native to the Tada Mine and Mino Falls and investigated what kind of plants dominantly contain heavy metals, and whether there are changes in the amount of heavy metal accumulation due to regional differences.

Arabis gemmifera, which grows naturally in the Tada Mine, had a large accumulation of heavy metals of Zn, Cu, Cd, and Fe, while *Arabis gemmifera*, which grows naturally in Mino Falls, had a large amount of Zn accumulation, and not much heavy metals of Cu, Cd, and Fe. From this, it was found that even if it is the same plant, the amount of heavy metal accumulated changes due to differences in the environment such as soil. In this survey, since the soil conditions of the Tada Mine and Mino Falls are very different, it is thought that the heavy metal concentration of plants depends on the soil contamination situation.

As a future task, since there are individual differences in plants and the results of this analysis are not necessarily correct, it is necessary to test the average value to investigate the difference in the accumulation of heavy metal content depending on the individual difference, and to investigate the influence on plants by investigating the soil contamination situation.

ACKNOWLEDGMENTS

In advancing this research, I would like to express my sincere gratitude to my supervisor, Professor Hiroyuki Ii of the Graduate School of System Engineering, Wakayama University, who gave me tremendous advice and guidance during his busy schedule. I would also like to express my heartfelt gratitude to Associate Professor Masanobu Taniguchi for his guidance and encouragement during his busy schedule.

I would like to express my sincere gratitude to everyone in the laboratory for their constant guidance and cooperation in in-room analysis, data processing, etc. I would like to express my gratitude to everyone who has cooperated with me.

REFERENCES

[1] Poisonous Plants - Why Do Plants Store Heavy Metals? - (2007 Vol. 26, No. 6) | National Institute for Environmental Studies News, Vol. 26| National Institute for Environmental Studies (nies.go.jp) https://www.nies.go.jp/kanko/news/26/26-6/26-6-03.html

[2] Takayasu Kitagawa : Analysis of heavy metals in Athyrium yokoscense at Tada Silver Mine, Hyogo Prefecture, Journal of Plant Geography and Taxonomy (2005) p161-165

[3] Obata, Kan, Miyauti, Endo: Basic research on the absorption and removal of soil arsenic by Pteris vittate, Technical Research Presentation of the Tohoku Branch of the Japan Society of Civil Engineers（2012）VII-29

[4] What is phytoremediation| World Social Good Ideas Magazine | IDEAS FOR GOOD https://ideasforgood.jp/glossary/phytoremediation/

[5] Yoshida, Akiyoshi, Fujihara : The Current Situation and Challenges of Phytoremediation, Taisei Construction Center Bulletin No. 38（2005）p.06-1～06-4

[6] Tada Silver and Copper Mine - Inagawa Town Sightseeing Guide to Everything (jimdofree.com) https://inagawa-kankou.jimdofree.com
[7] Ore deposits by origin (hydrothermal deposits: vein deposits): Academic Materials Exhibition Hall, Faculty of Engineering, Yamaguchi University (Yamaguchi-u.ac.jp) http://www.msoc.eng.yamaguchi-u.ac.jp/collection/origin_23.php
[8] Hirao Mine - Ruins Search Map (haikyo.info) https://haikyo.info/s/1333.html

8th Int. Conf. on Structure, Engineering & Environment (SEE), Mie, Japan, Nov.10-12, 2022, ISBN: 978-4-909106094 C3051

A STUDY ON APPLICATION POSSIBILITY OF WOODEN BIOMASS COMBUSTION ASH MODIFIED BY FLOTATION METHOD AS CONCRETE ADMIXTURE

Shilun Liu[1], Koji Takasu[1], Hidehiro Koyamada[1], and Hiroki Suyama[1]
Dept. of Architecture, Faculty of Environmental Engineering, The University of Kitakyushu, 1-1 Hibikino Wakamatsu, Kitakyushu, Fukuoka 8080135, Japan

ABSTRACT

In response to global warming, there has been a growing call for alternative energy sources, and in recent years there has been growing interest in Wooden Biomass power generation. With the popularity of Wooden Biomass power generation, the Wood Biomass Combustion Ash generated by power generation is also on the rise, but there is no good method for the treatment of Wood Biomass Combustion Ash, and it still needs to be treated by landfill. In order to verify whether wood biomass combustion ash can be used as an additive for concrete in buildings, six kinds of ash from different power plants, BC-a, BC-b, BC-c, BCC-a, BCC-b and BCC-c, are modified by the flotation method, and the feasibility of using modified wood biomass combustion ash as an additive for concrete is discussed by studying its physical properties, SEM, particle size distribution, chemical composition, mineral composition and other properties. The results show that wooden biomass combustion ash removes unburned carbon and improves the particle shape through the flotation method. As an additive of concrete, it obtains the fluidity meeting the requirements of JIS, and the activity index is also equivalent to the value specified by JIS I. From the above results, modified wood biomass combustion ash is highly likely to be used as concrete additive.

Keywords: Flotation method, woody biomass combustion ash, flow ratio, chemical composition, XRD/Rietveld method

1.INTRODUCTION

Currently, Japan's draft pledge to reduce greenhouse gas emissions under the Paris Agreement aims to reduce energy-derived carbon dioxide (CO2) emissions by 26 percent by 2030 compared to 2013 levels. The policy aims to reduce the amount of electricity generated from fossil fuels such as coal in the energy mix to meet targets, with plans to close coal-fired power plants.[1)] Renewable energy has been on the rise in recent years due to the closure of thermal power plants. Examples of renewable energy include solar, hydro, wind, geothermal and biomass power generation. In particular, annual power generation from biomass is expected to double by 2030.[2) 3)] At the same time, the burning of woody biomass fuels produces approximately 0.5% to 12% of woody biomass combustion ash (hereafter referred to as WBCA) from the facility.[4)] If WBCA is not used effectively, it is classified as industrial waste under the provisions of the Waste Disposal and Public Cleaning Act.[5)] However, in 2013, a notice from the Ministry of the Environment stated that "incinerator ash that is actually used effectively and is judged to be unnecessary is not classified as industrial waste.[6)] In recent years, research has been conducted on the effective utilization of various substances such as fertilizer raw materials and building materials.[7) 8)]

Solid woody biomass fuels include wood chips, pellets, bark, and construction waste, and have various properties such as moisture content, ash content, and calorific value. Furthermore, some of the ashes from burning them have a very high loss on ignition, which is believed to adversely affect the flow properties of concrete when it is assumed to be used as an admixture to concrete. Therefore, it is necessary to modify WBCA using the flotation method developed by Takasu et al.[9)] Flotation method is a conventional technology mainly used for coal preparation, ore beneficiation, and deinking of wastepaper. is a method of collecting from the bottom[10)] Compared with other modification methods such as heating modification[11)] and electrostatic belt type[12)], the advantage of this method is that the heavy metals contained in FA can be removed by the stirring work of pretreatment and the microbubbles of flotation method.[13)] Therefore, it is better to use flotation method to modify WBCA containing a large amount of heavy metals. However, it is not clear whether WBCA modified by flotation method can be used as an admixture of concrete. And little is known about the properties of woody biomass fuels as concrete burnt ash mixtures. Therefore, in this study, the flotation method was used to modify the special burnt ash, the properties of the raw ash and the modified ash were clarified, and the possibility of using them as admixtures was investigated.

In order to verify whether wood biomass combustion ash can be used as an additive for concrete in buildings, six kinds of ash from different power plants, BC-a, BC-b, BC-c, BCC-a, BCC-b and BCC-c, are modified by the flotation method, and the feasibility of using modified wood biomass combustion ash as an additive for concrete is discussed by studying its physical properties, SEM, particle size distribution, chemical composition, mineral composition and other properties.

2.EXPERIMENTAL OUTLINE

2.1The Materials

Three types of woody biomass fuels BC-a, BC-b and BC-c, which are woody biomass fly ash, were used. The ash obtained by reforming it by flotation are called MBC-b and MBC-c, respectively. BC-a hardens immediately after immersion in water and cannot be modified by flotation method. For comparison, JIS II certified fly ash (hereinafter referred to as FA) is called FA-R and used. In addition, the results of burning ash of woody biomass fuel and coal and its modified ash BCC-a, MBCC-a, BCC-b and MBCC-b used in our previous study are shown in the following figure.

2.2Experimental items and methods

As a pretreatment for flotation, wood biomass fly ash, water and kerosene were added and stirred with a high-speed stirring mixer. Table 1 shows the conditions of the pretreatment. After that, pine oil was added, and the flotation method was carried out for 30 minutes.

The experimental items are density, moisture, specific surface area, loss on ignition, carbon content measured by differential thermogravimetric analysis, flow value ratio, activity index, BET specific surface area, methylene blue adsorption, SEM image, particle size distribution, chemical composition, mineral composition.

Density, moisture, specific surface area, loss on ignition, flow rate ratio, activity index was carried out in accordance with JIS A 6201 "Fly ash for concrete". The carbon content by differential thermogravimetric analysis was measured according to the "Concrete Test Analysis Handbook" of the Japan Society of Concrete Engineering. Carbon content is defined as the value obtained by adjusting the supply of oxygen and nitrogen and subtracting the results in the nitrogen environment from the results in the air environment.The BET specific surface area was measured by the BET method using a specific surface area and pore distribution measuring apparatus (Microtrac Co., Ltd.: BELSORP MINI II). Methylene blue adsorption is based on JCAS I-61 "Test Method for Methylene Blue Adsorption in Fly Ash." The particle size distribution was measured using a laser diffraction/scattering type particle size distribution measuring apparatus. The chemical constituents were identified using a fluorescence X-ray analyzer (RIGAKU: ZSX101e). SEM images were observed with a field emission scanning electron microscope (FE-SEM). The mineral composition was measured by the XRD/Rietveld method using a fully automatic horizontal type multifunctional X-ray diffractometer (manufactured by RIGAKU), and analyzed using analysis software PDXL2 (manufactured by Rigaku).

Table 1 Pre-mixing conditions

Symbol	Raw Fly ash [kg]	Stirring time [min]	Water addition amount [%]	Kerosene addition amount [%]	Pine oil addition amount [%]
MBCC-a	2.0	3.0	30.0	5.0	0.5
MBCC-b					
MBC-b				1.0	0.1
MBC-c		5.0		5.0	0.5

3.RESULT AND DISCUSSION

3.1 Physical properties of each Fly ash

Table 2 shows the physical properties of each fly ash. Focusing on the loss on ignition, the raw ash of woody biomass fly ash other than BC-b does not meet the JIS standard. BC-c does not meet the JIS standard even after modification, but the carbon content is significantly reduced. From this, it is considered that MBC-c has other substances with loss on ignition. The specific surface area of all fly ashes is of comparable quality to JIS II.

3.2 SEM image

Photo 1 shows the SEM images of each ash. For the 500x image, it was confirmed that the FA-R particles were nearly spherical, while the woody biomass burning ash particles had a distorted shape and that the shape and size varied by ash species. Furthermore, when the raw Fly ash and the modified Fly ash are compared, it can be confirmed that the modified ash has a significantly smaller particle size. It is believed that this is because flotation and its pre-stirring have such an effect. Furthermore, for the 5000x image, the modified fly ash particles have a cleaner surface than the original fly ash particles. However, even with the reforming of woody biomass combustion ash, the original particle shape is distorted, Therefore, it is difficult to make it into a state with many spherical particles like FA-R, and it is unlikely to obtain the same fluidity as FA-R when used as an admixture for concrete. A large amount of unburned carbon was confirmed in BC-a with the highest adsorption of methylene blue (red part in

Table 2 Physical properties of fly ash

Types of fly ash	density [g/cm^3]	LOI [%]	specific surface area [cm^2/g]	humidity [%]	BETspecific surface area [m^2/g]	methylene blue adsorption [mg/g]	carbon content [%]	flow ratio [%]	activity index [%]		
									7days	28days	91days
BCC-a	2.22	11.70	3720	0.21	13.1	0.85	-	89.05	76.6	82.6	112.9
MBCC-a	2.38	3.27	4780	0.23	2.7	0.28	-	100.78	74.2	92.6	94.1
BCC-b	2.06	18.79	2230	3.02	16.7	0.72	-	70.24	65.5	72.4	89.1
MBCC-b	2.27	4.94	3940	0.11	7.3	0.66	-	98.90	64.3	100.2	107.6
BC-a	2.30	36.50	3050	0.22	5.2	1.44	-				
BC-b	2.50	3.89	3350	0.29	2.1	-	-	97.43	90.5	100.9	-
MBC-b	2.58	2.79	6890	0.66	4.8	-	-	98.90	91.9	104.5	-
BC-c	2.29	17.24	2940	1.51	57.5	1.45	10.07	70.60	85.0	88.7	-
MBC-c	2.45	9.89	3090	0.21	10.0	1.20	1.96	88.29	91.7	103.7	-
FA-R	2.29	2.70	3060	0.12	1.6	0.10	1.36	111.85	75.5	83.1	110.6

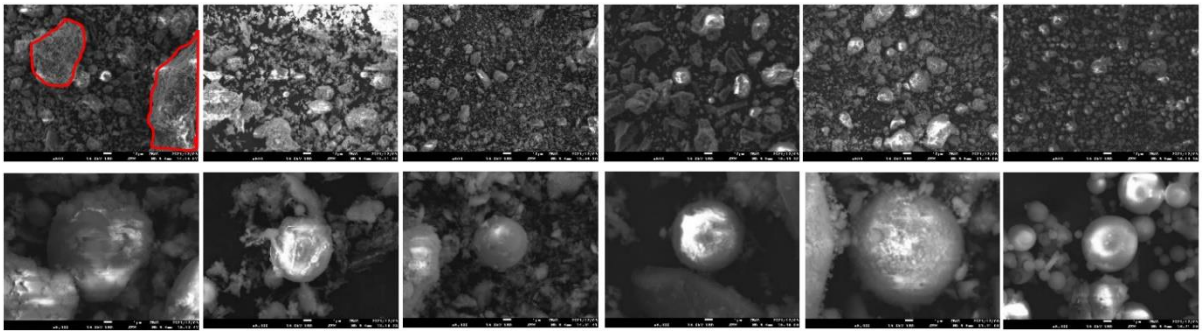

Photo 1 SEM image (top: 500x, bottom: 5000x)

Photo 1.

3.3 Particle size distribution

Figure 1 shows the particle size distribution of each ash. In contrast to FA-R, which has no 100-1000 micron particles, woody biomass combustion ash contains all of it. With the modified BC-b and BC-c, the proportion of coarse particles decreased and the proportion of fine particles increased. It is believed that this is because the flotation process removes unburned carbon causing coarse particles and cleans the particle surface.In addition, the proportion of particles of MBC-b smaller than 10 μm is higher than that of FA-R, and previous studies reported that FA with a higher amount of fine particles tends to have a higher activity index, so the activity index of WBC-b is higher than that of FA-R .

3.4 chemical composition

Figure 2 shows the chemical composition of each ash. The Si content in the special fired ash does not meet the JIS standard whether it has been modified or not. The Ca content of BC-a and BC-b is higher than that of Si and Al, which is significantly different from that of FA-R. In general, SiO2 and Al2O3 in FA are known to be involved in pozzolanic reactions, so BC-a, BC-b, and MBC-b are expected to have lower pozzolanic reactivity than FA-R. Previous studies reported that the proportion of K in woody biomass combustion ash was higher than that of FA, but since K was not present at all in BC-a and BC-b, the chemical composition of fly ash was different when the types of woody biomass fuels were different.

3.5 Mineral composition

Figure 3 shows the mineral composition of each ash by the Rietveld method. The main minerals of FA are quartz, mullite and magnetite. It was confirmed that the proportion of these minerals in the total woody biomass combustion ash was greater than that of FA-R. In addition, woody biomass combustion ash other than BC-b and MBC-b has a higher crystalline phase ratio than FA-R. Since the crystalline phase is a substance that is easily crystallized when water is added, it can be said that the crystallization ratio in woody biomass combustion ash increases when water is added. Judging from the results of loss on ignition in previous studies, it is believed that this is the reason for the increase in the amount of weight loss material after adding water to woody biomass combustion ash. Furthermore, BC-a has no glass (amorphous phase) and is all crystalline, showing significantly different results from the other ashes. It is believed that this is the reason why BC-a solidifies immediately after being immersed in water at the time of flotation. Therefore, if the raw ash has a large amount of crystalline phases, it cannot be upgraded by flotation. It is known that the reaction rate of FA increases with

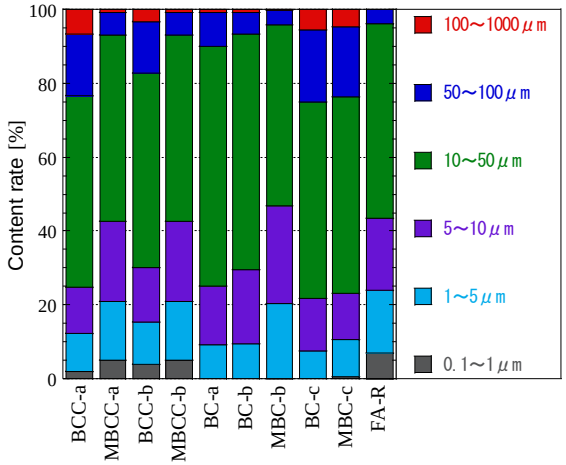

Fig.1 Particle size distribution

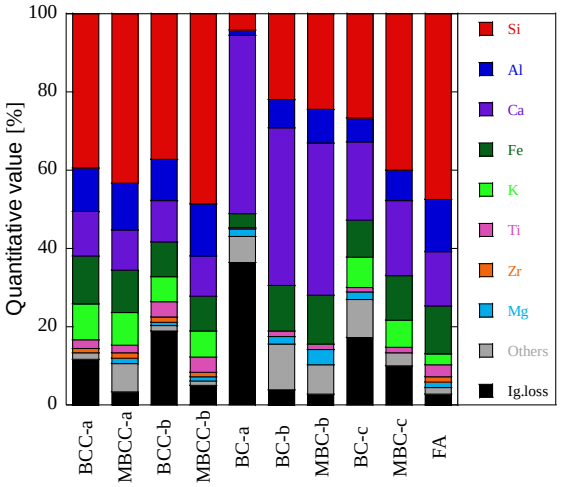

Fig.2 chemical components

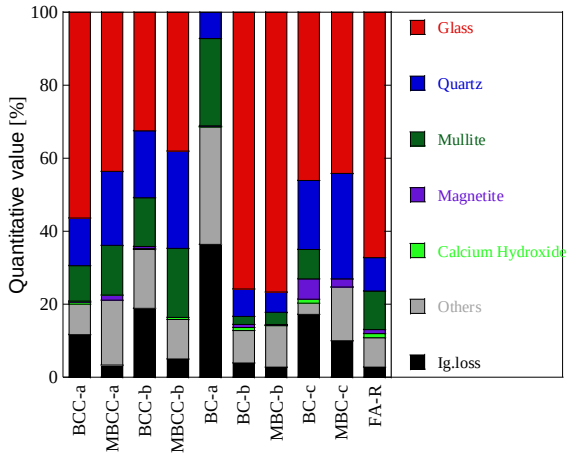

Fig.3 Mineral composition

the amount of glass. Since the amount of glass in BC-b and MBC-b is larger than that in FA-R, the reaction rate is high and the activity index may be higher than that in FA-R.

3.6 Flow ratio and activity index

Figure 4 shows the flow value ratio for each ash type. Although the fluidity change of BC-b is difficult to confirm by modification, BC-c can be improved to a level comparable to JIS type III by modification. Since the particle size distribution of BC-c did not change due to the modification and the carbon content changed significantly, it is considered that the change in particle shape and the reduction in carbon content have a great influence on the fluidity. Figure 5 shows the relationship between the flow value ratio and each item. Since the unburned carbon of FA is said to adversely affect the fluidity of concrete, a correlation between the flow value ratio and the amount of methylene blue adsorption was predicted, but a sufficient correlation was not obtained in this study. However, its coefficient of determination with LOI is 0.96, which is a very high value, indicating that the flow-value ratio of woody biomass combustion ash can be evaluated by LOI. Figure 6 shows the activity index of each ash. The woody biomass fly ash values were very high at 7 days of age. Since woody biomass fly ash contains a large amount of Ca, it is possible to generate a large amount of aluminate. Therefore, the activity index is very high initially. Since all woody biomass fly ash showed values equivalent to JIS class I at 28 days, it is likely that significant amounts of chlorophyll were also produced.

Figure 7 shows the correlation of the 28-day-old activity index with each item. Originally relevant is the loss on ignition, but its coefficient of determination is as low as 0.6. Although not shown due to space limitations, we also investigated the relevance of other items. However, no particular correlation has been demonstrated. The reason for this is thought to be that the chemical and mineral composition of woody biomass combustion ash varies by type, But in the future we will analyze the reaction rate and CH amount of the cement slurry mixed with woody biomass combustion ash, and plan to study the water and reaction changes in detail.

4.CONCLUSION

In this study, woody biomass fly ash was modified by flotation method to clarify the properties of raw ash and modified ash, and to explore the possibility of using it as a concrete admixture.

Flotation is not suitable for woody biomass fly ash containing a large amount of crystalline phase because it hardens due to increased crystallization when water is added. The wood biomass fly ash was upgraded by flotation method to remove unburned carbon and improve particle morphology. When the modified fly ash was used as an admixture, the fluidity equivalent to the JIS standard was obtained, indicating that the fluidity could be evaluated by the

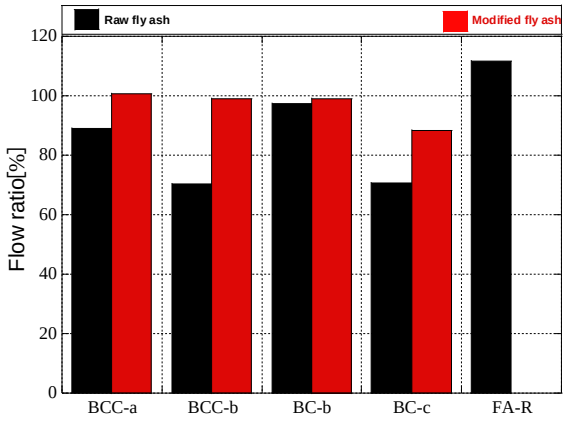

Fig.4 Flow ratio

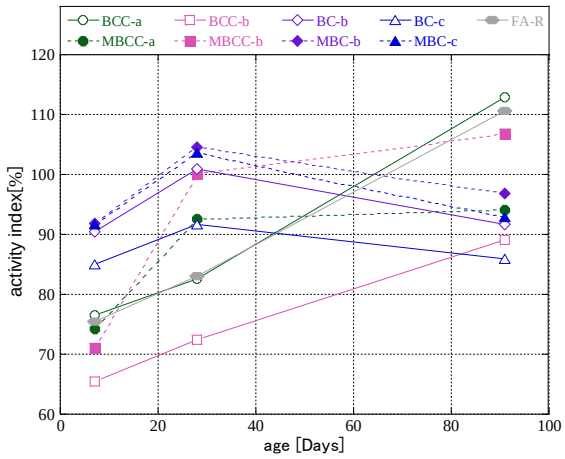

Fig.5 activity index

loss on ignition of woody biomass combustion ash. In addition, the activity kinetic index of the modified fly ash showed a value equivalent to JIS type I. Therefore, it can be said that there is a high possibility that the modified woody biomass fly ash can be used as an admixture

ACKNOWLEDGMENTS

The authors acknowledge the assistance in this work provided by Eiji Mikura and Yuxin Wang. This work was supported by Environment Research and Technology Development Fund, Environmental Restoration and Conservation Agency of Japan (ERCA) (JPMEER F20213G03).

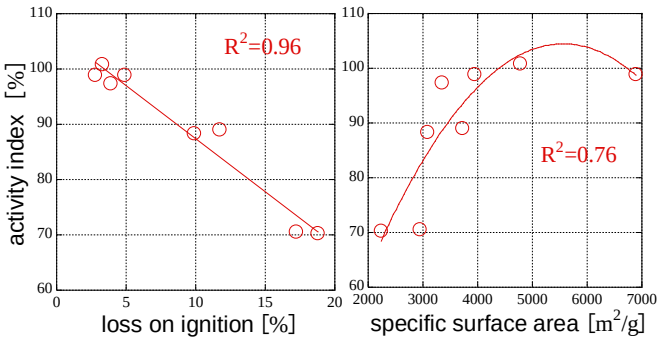

Fig.5 The relationship between the flow ratio and each item

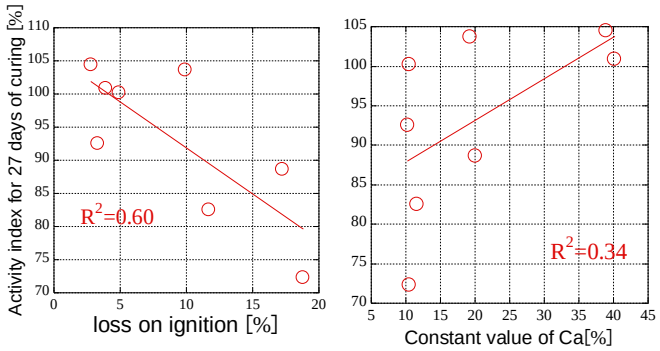

Fig.6 The relationship between the 28 days activity index and each item

REFERENCES

[1] https://www.meti.go.jp/shingikai/enecho/denryoku_gas/denryoku_gas/pdf/026_03_00.pdf%E3%80%80%EF%BC%88%E9%96%B2%E8%A6%A7%E6%97%A5%EF%BC%9A2021.
[2] https://www.isep.or.jp/archives/library/13188
[3] http://www.env.go.jp/earth/ondanka/ghg/mat01_indc.pdf
[4] https://www.enecho.meti.go.jp/statistics/total_energy/results.html#headline7%EF%BC%88%E9%96%B2%E8%A6%A7%E6%97%A5%EF%BC%9A2021
[5] https://www.jwba.or.jp/explanation/heat/%EF%BC%88%E9%96%B2%E8%A6%A7%E6%97%A52021%E5%B9%B410
[6] https://elaws.egov.go.jp/document/lawid=345AC0000000137
[7] http://www.env.go.jp/recycle/waste/reg_ref/no_1306282.pdf%EF%BC%88%E9%96%B2%E8%A6%A7%E6%97%A5%EF%BC%9A2021
[8] Yuki Nojima: Outline of Revision of the Fertilizer Control Law and Fertilizer Use of Woody Biomass Combustion Ash, Journal of the Energy Society of Japan, Enerumikusu, Vol. 100, No. 1, pp.74-80, 2021u
[9] Akihiro Maekawa et al. 4 people: Basic research on various properties of hardened mortar for

mixed woody biomass incinerators, Journal of the Society for Recycling of Waste Resources, Vol. 29, pp.209-210, 2018

[10] Koji Takanashi et al. 2: Characteristics of unburned carbon in concrete by flotation and using fly ash slurry, Architectural Society of Japan Papers on Structures, Vol. 73, No. 1, pp331-pp334, 2014

[11] Lee Sohwa et al. 3: Retrofit of coal ash by wind power generation processing pulverizing system equipped with firing process, Annual Journal of Concrete Engineering, Vol. 29, No. 1, pp. 183-188, 2007Tadashi Misawa: New Supplemental Classification/Classification, C

[12] Etsuro Sakai et al 3: Properties of Fly Ash Removal of Unburned Carbon with Electrostatic Belt Classifier, Cement/Concrete Paper, Vol. 73, Issue 1, Pages 65-70, 2019

[13] Yusuke Sakai and 3 others: Adjustment of fly ash particle size and removal of heavy metal components by a continuous processing system, Steel, Vol. 103, No. 3, pp. 166-173, 2017

8th Int. Conf. on Structure, Engineering & Environment (SEE), Mie, Japan, Nov.10-12, 2022, ISBN: 978-4-909106094 C3051

EXAMINING WATER ENVIRONMENT DATA FOR AN ARTIFICIAL INTELLIGENCE EVALUATION MODEL

Shengping Zhang[1] and Jie Qi[2]
[1]Faculty of Urban Science, Meijo University, Japan.
[2]School of International Studies, Utsunomiya University, Japan.

ABSTRACT

The objective of this study is to discover the most effective water environment improvement measures for the 109 most important watersheds of Japan, which are well-known Class-A watersheds under the jurisdiction of the Japanese government. An artificial intelligence (AI) model has been created by applying Deep Learning technologies, and watershed information from 109 watersheds has been collected as teacher data to train the AI model. This study aims to find the best way to present the water environment data to an artificial intelligence model. In order to provide the most reliable water quality estimations, three different ways of water environment data presentation have been examined. It has been identified that presenting the raw environment data to the AI model as teacher data is the best way for building an AI model. This study concludes by pointing out that preprocessing data will cause information loss of teacher data and will also add biased information into teacher data. Therefore, using raw data without preprocessing as teacher data will help build a more reliable AI model. It is hoped that this study will contribute to establishing a more reliable river environment planning and management methodology.

Keywords: Water Environment Evaluation, Artificial Intelligence (AI) Model, Teacher Data, Data Preprocessing

INTRODUCTION

Artificial intelligence (AI) model has been widely applied to water environment evaluation and planning [1], [2]. The reason why an AI model has been chosen is its powerful capability of processing various types of water environment data such as numerical data, categorical data, image data. It does not require any specific categorizations while presetting data to AI model [3], [4].

This powerful capability of AI models, however, has raised a critical question: as the teacher data required for AI model training, what is the best way to present water environment data to an AI model? A typical water quality index BOD (Biochemical Oxygen Demand) usually can be recorded and represented at least in three different ways: 1) BOD is mostly mentioned in the raw numerical data form that has the unit *mg/l*; 2) BOD is also quite frequently represented by its class according to the water Environment Quality Standards (EQSs) such as Class AA, Class A, etc.; 3) BOD is the categorical yes/no answer to the question whether the administrational water environment management goal has been achieved. The numerical raw data form is the most basic form of BOD data, and the other two forms are the preprocessed results. The most common preprocessing includes filtering and converting, and both EQSs and administrational water environment management goals are served here as a filter. An AI model is capable of dealing with each form of water environment data with or without preprocessing mentioned above.

The ultimate goal of this study is to find the best way to present water environment data to an AI model in order to create a more reliable water environment evaluation AI model.

ARTIFICIAL INTELLIGENCE MODEL

An artificial intelligence model, specifically a neural network model has been adopted to compose a water environment evaluation method for evaluation or prediction problems due to the suitability of neural network models [4], [5].

Structure of Neural Network [5]

A neural network is a network system constructed artificially by idealizing the neurons (nerve cells), and consists of a number of nodes and lines that are called *units* and *connections* (or *links*) respectively. Based on the differences in network structures, neural networks generally are classified into two types: layered networks and interconnected networks. It has been shown that a layered network is suitable for evaluation/prediction problems due to its abilities in learning (self-organization) and parallel processing of information.

A typical layered neural network, which has a layer of input units at the top, a layer of output units at the bottom, and a number of hidden layers between

the input layer and the output layer. Connections exist only between the units in the adjacent layers and connections within a layer or from higher to lower layers are forbidden.

Modelling a Neural Network

For the sake of simplicity, a neural network can be considered as a unit consisting of three layers: let the unit numbers of the input layer, hidden layer and output layer be N, M and 1, respectively. When an input $\{I_i,\ i = 1,2,\cdots,\ N\}$ is given to the units of the input layer, the inputs and outputs of the hidden layer units as well as the output layer units are represented as follows.

$$Y_j = f(X_j),\ \ j = 1,2,\cdots,M \tag{1}$$

$$X_j = \sum_{i=1}^{N} w_{ij} I_i + \theta_i \quad ,\quad j = 1,2,\cdots,M \tag{2}$$

$$O = f(Z) \tag{3}$$

$$Z = \sum_{j=1}^{M} w_j Y_j + \theta \tag{4}$$

Where Y_j : output from the unit j of the hidden layer.
X_j : input the unit j of the hidden layer.
$f(\cdot)$: unit output function.
w_{ij}: connection weight between the input layer unit i and hidden layer unit j.
θ_j : threshold value of the hidden layer unit j
O : output from the output layer unit.
Z : input to the output layer unit.
w_j: connection weight between the hidden layer unit j and the output layer unit.
Θ : threshold value of the hidden layer unit j

For the unit output function $f(\cdot)$, some expressions have been proposed. The following Sigmoid function has been applied frequently. However, it is not necessarily the best one in terms of learning efficiency. A testing process for different output functions is strongly suggested. In this studied this Sigmoid function has been finally adopted after careful tests.

$$f(x) = \frac{1}{1 + e^{-x}} \tag{5}$$

Theoretically, the neural network model expressed by Eqs. (1) through (5) is able to approximate any non-linear relationship between inputs and outputs with any degree of accuracy by using enough hidden layer units and setting connection weights and thresholds to be appropriate through proper learning processes [6]. The potential of this model has been verified with similar problem to this study [3,], [4].

Learning Process of Neural Network Model

For a neural network model, the process of setting the connection weights unit thresholds is called *learning*. The term *learning* here means the self-organization process through which the neural network model automatically adjusts all the parameters (i.e. all the connections and thresholds) to the appropriate values, when a series of samples of input-output data (called teacher data or teacher signals) are shown to the model. If we consider the information processing in a neural network model as a transformation of input data to output data, then model learning can be considered to be a process through which the neural network model gradually becomes capable of imitating the transforming patterns represented by the teacher data.

A lot of learning algorithms have been proposed, and among them the Error Back Propagation Algorithm is the most widely used and most successful algorithm. The following is the summary of the Error Back Propagation Algorithm [7].

Suppose T sets of teacher data are given.

$$\left\{I_1^{(t)}, I_2^{(t)}, \cdots, I_N^{(t)}, O^{(t)};\ t = 1,2,\cdots,T\right\} \tag{6}$$

Notice that the teacher data consists of two parts: the input part $\left\{I_1^{(t)}, I_2^{(t)}, \cdots, I_N^{(t)};\ t = 1,2,\cdots,T\right\}$ and the output part $\left\{O^{(t)};\ t = 1,2,\cdots,T\right\}$.

Now consider an initial value

$$w_{ij}^{[k]}, w_j^{[k]}, \theta_j^{[k]}, \theta^{[k]} \ ,\ k = 0 \tag{7}$$

for each of the connection weights and threshold values, respectively. Notice that the superscript [k] indicates the number of learning iterations and [k=0] means the initial values for all the parameters directly preceding the start of the learning process. Then the outputs corresponding to the inputs of the teacher data $\left\{I_1^{(t)}, I_2^{(t)}, \cdots, I_N^{(t)};\ t = 1,2,\cdots,T\right\}$ can be obtained from Eq. (1) ~ Eq. (5). Let these outputs be $\left\{U^{[k](t)};\ t = 1,2,\cdots,\ T\ and\ k = 0\right\}$. Clearly, $\left\{U^{[k](t)};\ t = 1,2,\cdots,\ T\ and\ k = 0\right\}$ are different from the outputs of the teacher data $\left\{O^{(t)};\ t = 1,2,\cdots,T\right\}$, and an error function can be defined with the two different kinds of outputs as follows.

$$R^{[k]} = \sum_{t=1}^{T} \left(O^{(t)} - U^{[k](t)}\right)^2,\ \ k = 0 \tag{8}$$

Obviously, $R^{[k]}$ is a function of connection

weights and threshold values because $\{U^{[k](t)};\ t = 1, 2, \cdots,\ T\ and\ k = 0\}$ are calculated after all $w_{ij}^{[k]}$, $w_j^{[k]}, \theta_j^{[k]}\ and\ \theta^{[k]}$ are given.

The Error Back Propagation Algorithm makes use of the connection weights and threshold values that minimize the above error function $R^{[k]}$. Usually a non-linear programming method is required to solve the optimization problem along with an iteration process in order to obtain the optimal (but possibly suboptimal) connection weights and threshold values. The final iteration procedures derived from a non-linear programming method known as the Method of Gradient Descent are as follows.

$$w_j^{[k+1]} = w_j^{[k]} - \eta \cdot \sum_{t=1}^{T} \left(\delta^{[k](t)} \cdot Y_j^{[k](t)}\right) \tag{9}$$

$$\theta^{[k+1]} = \theta^{[k]} - \eta \cdot \sum_{t=1}^{T} \delta^{[k](t)} \tag{10}$$

$$w_{ij}^{[k+1]} = w_{ij}^{[k]} - \eta \cdot \sum_{t=1}^{T} \left(\delta^{[k](t)} \cdot w_j^{[k+1]} \cdot \gamma_j^{[k](t)} \cdot I_i^{(t)}\right) \tag{11}$$

$$\theta_j^{[k+1]} = \theta_j^{[k]} - \eta \cdot \sum_{t=1}^{T} \left(\delta^{[k](t)} \cdot w_j^{[k+1]} \cdot \gamma_j^{[k](t)}\right) \tag{12}$$

where the superscript [k] indicates the number of learning iterations as mentioned earlier, and η is a small positive number that indicates the step size of the Method of Gradient Descent for optimization iteration process. The other variables which occurred in the final learning procedures are defined as follows.

$$\delta^{[k](t)} = (O^{(t)} - U^{[k](t)}) \cdot O^{(t)} \cdot (1 - O^{(t)}) \tag{13}$$

$$\gamma_j^{[k](t)} = Y_j^{[k](t)} \cdot \left(1 - Y_j^{[k](t)}\right) \tag{14}$$

In order to avoid the overfitting (or over-learning) problem, a criterion is usually required to make a judgement when the iterative learning process should be terminated. In this study the learning process will be stopped when the Mean Relative Error (MRE) of the outputs is less than a specified relative error expectation for prediction/evaluation results, which is a common treatment for a learning process of teacher data with random errors (i.e. white noise). Needless to say, this error expectation should be set according to the required accuracy of the problem which is being dealt with.

ENVIRONMENT DATA PRESENTATIONS

Teacher Data

In order to apply the neural network model proposed above to a water environment evaluation problem, the model has to be trained appropriately through a deep learning process by using water-environment-related data.

In this study, the data obtained from the water quality survey conducted for the 109 Class-A rivers of Japan are used for the deep learning process [8]. The data are stored in an open source database that is maintained by Ministry of Land, Infrastructure, Transport and Tourism of Japan.

After a careful data verification process, only 104 rivers out of 109 Class-A rivers are chosen to be included in the teacher data set for deep learning because there are quite a few of data missing for the other 5 rivers. For each river the data includes 58 water environment items as shown in Table 1. The data records used in this study are from 1998 to 2018 with a duration of 21 years long.

The 58 environment items are divided into two parts to form a teacher data set, ***evaluation goal variables*** and ***explanation variables***. The evaluation goal variables include the five environment items that are used to define The Water Environment Standards for Rivers as shown in Table 2 [9], which are pH, BOD, SS, DO and Total coliform. All the environment items are used to explain how the achievement of water environment standards are impacted.

Presenting the Teacher Data

In this study, the evaluation goal variables of the teacher data have been presented to the environment evaluation AI model in the following three different ways in order to identify the best way of teacher data presentation by comparison.

The most basic way is to present the raw data of water quality directly to AI model. All the five environment items, pH, BOD, SS, DO and Total Coliform are presented as continuous numerical raw data to AI model as teacher data.

The second way is to present the achievement degree of water Environment Quality Standards to the AI model instead of the raw water quality data. The achievement of EQDs has been scored with an effort to make the final scores for different standard classes that are corresponding to different water use purposes a uniform distribution, which is expected to maximize the score distance between different standard classes. The results are shown in Table 3.

The third way is to present AI model with the categorical yes/no data whether administrational water environment management goal has been achieved for each water quality item.

Needless to say, the explanation variables of the teacher data are presented as raw data without any pre-processing in spite of the very basic and reasonable question whether this is the best way to present the explanation variables to AL models is remained to be answered, which is beyond the research purpose of this study though.

Table 1 Water environment items of teacher data

Category (Number of Items)	Water Environment Item	
Time of Sampling (4)	Year	Month
	Day	Hour
River/Flow Conditions (17)	Place of Sampling	Weather
	Water Level	Quantity of Flow
	Total Water Depth	Water Depth of Sampling
	Temperature	Water Temperature
	Vertical Visibility	Horizontal Visibility
	Water Smell	
	Time of Low Tide of Sampling Day	
	Time of High Tide of Sampling Day	
	Visual Appearance:	
	Water Color	Flow Strength
	Turbidity (Muddiness)	Floating Waste/Garbage
Watershed Conditions (7)	Length of Main Stream	Catchment Area
	Catchment Population	Number of Tributaries
	Annual Average Stream Flow	Number of Dams
	Number of Hydraulic Power Plants	
Water Quality Indexes For The Living Environment (10)	pH	BOD
	COD	SS
	DO	Saturation Degree of DO
	Total Coliform	
	The Amount of N-Hexane Extract (Oil)	
	Total Nitrogen	Total Phosphorus
Water Quality Indexes About Human Health (9)	Cadmium	Cyanogen
	Lead	Hexavalent Chromium
	Arsenic	Total Mercury
	Alkyl Mercury	PCB
	Dichloromethane	
Water Quality Index For Inflow Of Domestic Wastewater (1)	Ammonium Nitrogen	
Others (10)	Chromaticity	Turbidity
	Evaporation Residues	Total Hardness
	Potassium Permanganate Consumption	
	Sodium	Iron
	Manganese	Aluminum
	Residual Chlorine	
(7 categories in total)	(58 items in total)	

Table 2 Water environment quality standards for rivers [9]

Item Class	Water Use	Standard Value				
		Hydrogen-ion Concentration (pH)	Biochemical Oxygen Demand (BOD)	Suspended Solids (SS)	Dissolved Oxygen (DO)	Total Coliform
AA	Water supply class 1, conservation of natural environment and uses listed in A-E	6.5≤pH≤8.5	≤1 ㎎/L	≤25 ㎎/L	≥7.5 ㎎/L	≤50MPN/100mL
A	Water supply class 2, fishery class 1, bathing and uses listed in B-E	6.5≤pH≤8.5	≤2 ㎎/L	≤25 ㎎/L	≥7.5 ㎎/L	≤1000MPN/100mL
B	Water supply class 3, fishery class 2, and uses listed in C-E	6.5≤pH≤8.5	≤3 ㎎/L	≤25 ㎎/L	≥5.0 ㎎/L	≤5000MPN/100mL
C	Fishery class 3, industrial water class 1, and uses listed in D-E	6.5≤pH≤8.5	≤5 ㎎/L	≤50 ㎎/L	≥5.0 ㎎/L	-
D	Industrial water class 2, agriculture water, and uses listed in E	6.0≤pH≤8.5	≤8 ㎎/L	≤100 ㎎/L	≥2.0 ㎎/L	-
E	Industrial water class 3 and conservation of environment	6.0≤pH≤8.5	≤10 ㎎/L	Floating matter such as garbage should not been observed	≥2.0 ㎎/L	-

Table 3 Scoring of achievement degree of EQSs

Water quality class ranked with EQSs for conservation of the living environment	Score
AA	0.9
A with indexes ranked in AA	0.8
A	0.7
B with indexes ranked in A or higher	0.6
B	0.5
C	0.4
D	0.3
E	0.2
Below E	0.1

Training of Neural Network Model

As we explained previously, the neural network model has been trained (put under a learning process) with the collected teacher data. The training process is based on the learning procedures but it is still a process of trial and error because there are still many details that remain undecided, such as a suitable step size of optimization, a suitable output function, an efficient order to present the teacher data to the neural network model, and a proper initial network size (layers and units in each layers). The learning process was stopped after the trained neural network model is able to reproduce the entire teacher data with an acceptable error, which was set in this study to be below 2% in mean relative error.

COMPARISON OF DATA PRESENTATIONS

In order to identify which of the three presentation ways of the teacher data helps construct a better AI model, this study have compared the estimation results of administrational environment management goal achievement by the Al models with the observation results for the year of 2019 (including four season results), which is right after the teacher data duration 1998-2018. The administrational environment management goal achievement has been chosen as the comparison item because it is a common output that three trained AI models can generate.

Indexes for Comparison

The following three well-established statistical evaluation indexes for comparing the presentation ways of teacher data have been defined based on the comparison results of the AI model estimation and observation as shown in Table 4 [10].

$$\text{Accuracy} = \frac{Hits(A)+Hits(U)}{Hits(A)+False(A)+False(U)+Hits(U)} \quad (15)$$

$$\text{Threat Score(A)} = \frac{Hits(A)}{Hits(A)+False(A)+False(U)} \quad (16)$$

$$\text{Threat Score(U)} = \frac{Hits(U)}{Hits(U)+False(A)+False(U)} \quad (17)$$

Table 4 Comparison of administrational management goal achievement results

Estimation results by AI Model	Observation results	
	Achieved	Unachieved
Achieved	Hits(A)	False(A)
Unachieved	False(U)	Hits(U)

Accuracy is the most common index to compare different models. The threat Score is used to measure how well each model is able to hit the target (achieved or unachieved). Threat score(A) usually is used when the achievement rate is emphasized, and Thread Score(U) is used when the un-achievement rate is emphasized. All the three indexes are defined between 0 to 1, and 1 means an ideal estimation.

Comparison Result Discussions

As shown in Table 5, the three different data presentation ways have been compared based on the three indexes defined above for year 2019, which is right after the teacher data duration.

Table 5 Estimation results of administrational management goal achievement during 2019

Way of data presentation	Accuracy	Threat Score (A)	Threat Score (U)
Raw data of water quality	96.88%	96.22%	84.71%
Water EQSs Class score	92.55%	90.96%	70.19%
Management goal achievement	97.12%	96.57%	84.62%

From Table 5 demonstrates that scoring the teacher data according to the water EQSs class generated the worst estimation results of the three different ways of teacher data presentation. A reasonable explanation about this result is that both the water EQSs and the scoring process are either subjective or arbitrary, which means they have basically been decided for human conveniences or calculational purposes without any considerations of the water quality evolution processes. These possibly-biased human pre-processing added to the teacher data have clearly damaged the reliability of the original raw teacher data.

The above hypothesis is also consistent with the fact that the AI model with the raw data as teacher data generated the best water quality estimation in terms of threat score (U). this is because the raw data without any pre-processing, just as expected, include

all the original information about the hidden water quality natural evolution processes.

As a matter of fact, the categorical teacher data of the administrational management goal achievements help AI model generate even better water quality estimation results in terms of both accuracy and threat score(A) than the AI model trained with raw data does. The reasonable explanation is that the outputs of the AI model trained with the administrational management goal achievements, are exactly the results that are used in comparison indexes. Considering the fact that the differences in the comparison indexes between the two models are small enough to be ignored although the AI model trained with the raw data even has not been given any information on the administrational management goal achievements, it is reasonable and fair enough to justify the hypothesis that the AI model trained with the raw data is more reliable than the other models trained with different teacher data in terms of producing accurate water quality estimations. Simply, raw data without any preprocessing are the best teacher data.

CONCLUSIONS

With the purpose to built a reliable artificial intelligence model for water environment evaluation and planning, this study examined different ways in which teacher data are presented to an AI model for its training process or learning.

Artificial intelligence models are so comprehensive and powerful that they are capable to deal with various kinds of teacher data such as numerical data, categorical data and image data. Data pre-processing techniques allows model-builders convert data types so that the well-trained AI model can server the model-builder's purpose better.

This study has examined three different water environment data types (or three different ways of teacher data presentation) as teacher data for AI model training, and water quality estimation results. In order to identify what kind of teacher data help build a better AI model in terms of accuracy of water quality estimation, the well-trained models have been compared with observation results.

The results have shown that the raw water quality data without any pre-processing generated a better AI model than the other two teacher data types with pre-processing. Furthermore, the teacher data preprocessed slightly with a simple criterion about whether the administrational environment management goals have been achieved, generated an even better final model than the heavily-preprocessed teacher data based on the complicated water EQSs for rivers.

Based on the above results, a hypothesis can be formed: preprocessing raw data will possibly cause information loss of the teacher data or add biased information into the teacher data, while raw data without preprocessing will serve as the best teacher data, and help build a more reliable AI model. Needless to say, this hypothesis remains to be further examined.

Moreover, this hypothesis does not deny any necessary teacher data preprocessing if the preprocessing serves the research purpose very well. For example, if the only purpose of building an AI model is to answer the question whether administrational water environment management goal will be achieved, preprocessing water quality data into a categorical yes/no data still can provide a quite satisfied answer.

Further research will focus on applications of the well-trained AI model, such as identifying the most influential water environment factors/items as well as the most effective water environment improvement measures for each river of the 104 Class-A rivers that contribute to the teacher data. These researches all together are expected to contribute to establish a more reliable river environment planning and management methodology.

REFERENCES

[1] Hagihara Y. and Hagihara K. ed., Planning of Urban Water and Green Space, Kyoto University Press, 2010.

[2] Urban Science Study Group, ed., Introduction of Urban Science, Soseisya Publisher, 2020, pp.35-50.

[3] Zhang S. P. and Kido Y., A Study on the Environment Evaluation method for Aise River and the Effectiveness of River Environment Improvement Measures, Urban Science Studies, No. 21, 2016, pp. 45-56.

[4] Zhang S.P. and Qi Jie, Evaluating Habitability of Water Environments for Fireflies with an Artificial Intelligence Model, International Journal of GEOMATE, April, 2020, Vol.18, Issue 68, pp. 87 – 93.

[5] IPA, WHITE PAPER Artificial Intelligence 2019, Kadokawa Publisher, 2018.

[6] Asou H., The Information Processing by Neural Network Models, Sangyo Publisher, 1988. pp. 125-132.

[7] Rumelhart D. E., Hinton G. E., and Williams R. J., Learning Representations by Back-propagating Errors, Nature, Vol. 323, No. 9, 1986, pp. 533-536.

[8] Ministry of Land, Infrastructure, Transport and Tourism of Japan, Water Information System, http://www1.river.go.jp/ (an Online Open Source Database).

[9] Ministry of Environment of Japan, Environmental White Paper, 2020.

[10] Scharfer J. T., The Critical Success Index as an Indicator of Warning Skill, Weather Forecasting, No.5, 1990, pp.570-575.

8th Int. Conf. on Structure, Engineering & Environment (SEE), Mie, Japan, Nov.10-12, 2022, ISBN: 978-4-909106094 C3051

FEASIBILITY OF USING BAUXITE RESIDUE STABILIZED WITH CEMENT KILN DUST FOR GEOETCHNICAL APPLICATIONS

Mohamed Farid Abbas [1,2] and Sultan Abdulaziz Almuaythir [1]
[1]College of Engineering, Prince Sattam Bin Abdulaziz University, Saudi Arabia; [2] Soil Mechanics and Geotechnical Engineering Research Institute, Housing and Building National Research Center (HBRC), Egypt

ABSTRACT

Bauxite residue (BR) is an industrial waste generated during the processing of bauxite into alumina using the Bayer process. For every ton of alumina produced, approximately 1 to 1.5 tons of red mud are also produced. Due to this high level of production and the material's high alkalinity, it can pose a significant environmental hazard. Given the high cost of storage and its high level of toxicity inflicted on this material, it is of a paramount importance to examine the probable approaches for recycling this residue and use it as construction material. This study examines the feasibility of using Cement Bypass Dust (CKD) for BR stabilization. Geotechnical properties were examined, including compaction parameters, volume change, and unconfined compressive strength for a different mixture containing different doses of CKD. Oedometer testing indicated optimum content of the CKD for swell potential as 2.5 %. Unconfined compressive strength testing indicated that UCS increased with adding CKD and curing period and addition of 7.5% of CKD increased the undrained stability by almost three times, indicating its effectiveness.

Keywords: Bauxite residue, Cement Bypass Dust, Stabilization, Volume Change, Unconfined Compressive Strength

INTRODUCTION

Bauxite residue (BR), or termed as red mud, is a waste material generated by the alumina industry via the Bayer process. Bauxite residue (BR) is generally considered hazardous waste due to the high level of alkalinity and contains heavy metals. It can cause environmental pollution due to its highly alkaline nature by dry or liquid red mud [1]. It contains major oxide elements such as Fe_2O_3, Al_2O_3, SiO_2, TiO_2, K_2O, and CaO with some trace elements. The best way to avoid the hazard of BR is to reuse it for engineering applications such as building materials and road constructions.

There are several attractive applications for BR such as; use in iron [2], [3] and titanium recovery [4], [5], component in cement and concrete manufacture [6]–[8], construction material [9], soil stabilization and road construction [10],[11]. Over the years, extensive research has been carried out to improve deficient soils. The two most used stabilizers for BR are cement and lime. Researchers [12], [13] reported that stabilizing this residue with cement or lime admixture is effective but very costly.

The cement kiln dust (CKD) material is a substance produced from cement manufacture known as a bypass that comes in the form of dust. The dust is a particulate mixture of partially calcined and unreacted raw feed, clinker dust, and ash, enriched with alkali sulfates, halides, and other volatiles. Several factors influence the chemical and physical properties of CKD. The dust from each plant can vary significantly in chemical, mineralogical, and physical composition since plant operations differ considerably in raw feed, type of operation, dust collection facility, and type of fuel used [14]. The physical characteristic of CKD materials is highly alkaline with pH between 12 to 14 and the gradation ranging from 0.03 to 0.30 mm. The specific gravity and the surface area for the materials are 2.6 to 2.8 g/cm^3 and 4600 to 14000 cm^2/g, respectively [15]-[17].

Some studies investigated the use of CKD in stabilization of soils [18]-[23] and recommended its use for enhancing the geotechnical properties and as alternative for other costly stabilizer such as cement and lime.

Stabilizing BR with the CKD has received little attention in the literature. For example, no specific studies are available in the literature regarding the suitability of red mud stabilized with cement kiln dust to be used in civil engineering applications

The present research work is related to studying the suitability of stabilizing BR with CKD for geotechnical engineering applications. Several CKD doses is examined and their impact on main geotechnical engineering characteristics is determined.

MATERIALS

In this section, brief description for studied BR and CKD and their chemical compositions are listed.

Bauxite residue (BR)

The bauxite residue (BR) used in the current study was collected from a big storage area located in Ras Al Khair Industrial City, Dammam, Saudi Arabia, related to Ma'aden Aluminium Company. The collected samples were obtained as a dry powder and distinguished by their red color. The chemical composition of collected BR samples is provided in Table 1 as percent by dry mass weight. The results indicate high percentages of aluminum, iron, and silica oxides (Al2O3, Fe2O3, and SiO2, respectively).

Table 1 Chemical composition of bauxite residue percent by weight of dry mass

Mineral	Al2O3	Fe2O3	SiO2	TiO2
%	25.5	18.8	18.8	6.6
Mineral	CaO	P2O5	ZrO2	Loss on Ignition
%	6.0	0.4	0.3	10.3

Cement bypass dust (CKD)

In the current study, the cement bypass dust was used to stabilize the BR to be used as a construction material. Current CKD is a by-product of Yamama cement plant in Riyadh, Saudi Arabia. Table 2 summarizes the average chemical composition of CKD, showing a massive percentage of calcium oxide as well as high percentages of silica and aluminum oxides.

Table 2 Chemical composition of cement bypass dust percent by weight of dry mass

Mineral	CaO	SiO2	Al2O3	K2O
%	67.47	14.37	4.21	2.54
Mineral	Fe2O3	SO3	Cr	Loss on Ignition
%	2.50	2.13	0.42	3.79

METHODS

To study the feasibility of using CKD as a stabilizer of BR, three percentages of CKD by weight (2.5, 5.0, and 7.0 %) were used. In accordance with ASTM D698 (2000), standard compaction tests were executed to determine the compaction characteristics of the selected mixtures. Fig. 1 shows the standard compaction test results for untreated and treated BR. As CKD% increases, the maximum dry density decreases, and optimum moisture content increases, which is comparable with previous research either for the use of CKD or other stabilizers.

As it is well known that the characterization of any geotechnical material is based on its deformation and stability properties, the current experimental program involves oedometer (OED) and unconfined compressive (UCS) tests. Both testing groups were divided into subgroups based on the CKD% added. Oedometer and UCS tests were also executed for different curing periods (1, 7, 14, and 28 days). The actual curing period may slightly differ according to the availability of utilized devices and working days. Each tested sample has been labeled to infer the CKD% added and actual curing period.

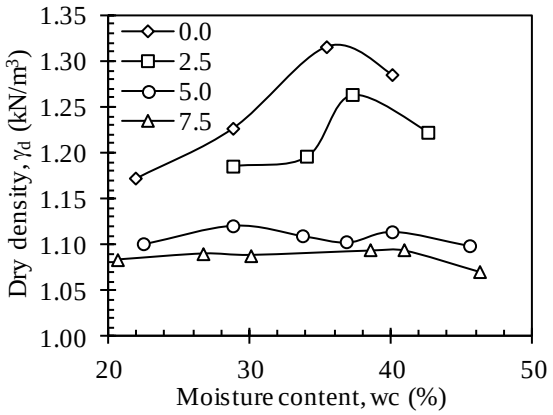

Fig. 1 Standard compaction tests for examined CKD %

In order to prepare OED specimens, dry BR was mixed with respective CKD% and optimum moisture content and thoroughly mixed. After that, the mixture was compacted in an oedometer ring to the desired dry density (i.e., maximum dry density at selected CKD%), wrapped in thin plastic wrap, and cured to the respected curing period in a wet-desiccator. The same is adopted for UCS specimens, except the compacted specimen is dismantled after compaction instead of left in the compaction ring.

OED testing was adopted with respect to ASTM D4546-03 (2003), method B. Once the cured specimen was installed in the oedometer device, seating stress was applied (7 kPa comparable to the stress applied to subgrades) and left for five minutes. After that, the specimen was inundated, and deformation due to wetting was recorded for 24 hours. The final wetting strain was labeled as wetting potential (e_w). Then, the tested specimen was loaded in increments with a load increment ratio (LIR=1) up to maximum stress of 1600 kPa, subsequently unloaded in increments to 25 kPa.

Regarding UCS testing, the strain rate is selected as 0.25%/min. to ensure the undrained condition and avoid moisture evaporation from cured specimens.

RESULTS AND ANALYSIS

In this section, the results and analysis of the experimental program is depicted.

Oedometer testing, OED

Table 3 shows that untreated BR specimens showed a small swell (e_w=1.24%) under token stress applied (7 kPa), which is considered low expansivity soil. However, for some construction projects, such as roads on the subgrade, it is desired to remove any swell potential that might occur during wetting periods. Fig. 2 shows that wetting strain (e_w) reduces with an increase of CKD%. As well, the effectiveness of the curing period is more in the case of CKD%=2.5%. Fig. 3 depicts the impact of CKD% on swell reduction. CKD%=2.5% is almost sufficient to remove the swell potential related to wetting.

Table 3 Summary of oedometer testing results

ID	Wetting strain, ε_w (%)	Compr. Index, Cc	Swell index , Cs	Swell reduct. (%)
CKD_0	1.24	0.08	0.03	0.00
CKD_2.5_1d	0.18	0.09	0.02	85
CKD_2.5_8d	0.11	0.08	0.02	91
CKD_2.5_14d	0.07	0.08	0.02	94
CKD_2.5_28d	0.06	0.09	0.02	95
CKD_5.0_1d	0.05	0.19	0.02	96
CKD_5.0_10d	0.02	0.21	0.02	98
CKD_5.0_17d	-0.01	0.26	0.02	101
CKD_5.0_31d	0.02	0.22	0.02	98
CKD_7.5_1d	0.04	0.30	0.02	97
CKD_7.5_9d	0.00	0.30	0.03	100
CKD_7.5_16d	-0.01	0.28	0.02	101

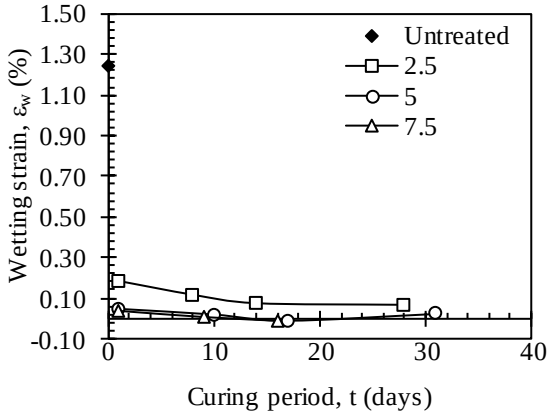

Fig. 2 Variation of wetting strain with curing time for examined CKD %

The key variables in estimating consolidation settlement are compression and swell indices (Cc and Cs, respectively). The compression index (Cc) for the untreated specimen is equal to 0.08, almost equal to that related to CKD%=2.5% for all cured periods, see Table 3. Fig. 4 shows that Cc is not affected by the curing period for CKD%=2.5%, while it is varied for other CKD%. Moreover, Cc is increased with an increase in the added CKD%. On the other hand, Fig. 5 shows that swell index (Cs) is not affected by either CKD% or the curing period and can be considered a constant material.

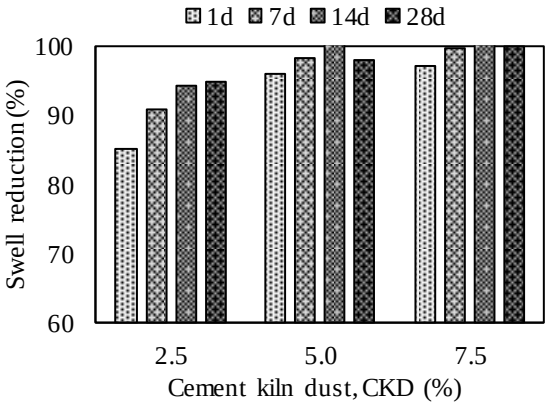

Fig. 3 Swell reduction versus CKD %

It can be concluded that CKD%=2.5% is the optimum value for deformation characteristics of treated BR, where it succeeded in removing the swell potential and maintaining the small Cc value for untreated BR.

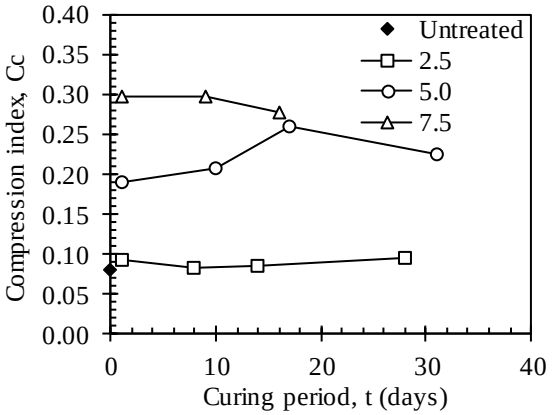

Fig. 4 Variation of compression index with curing time for examined CKD %

Unconfined compressive strength, UCS

The unconfined compressive strength is a key variable for estimating the undrained shear strength of fine-grained soils. The obtained results (see Table 4 and Figure 6) reveal that CKD addition effectively improves BR stability.

As well, UCS of treated specimens increased with curing time. Fig. 7 shows the improvement percentage due to the addition of CKD and shows that

adding 7.5% of CKD increases the undrained stability by almost three times, indicating its effectiveness.

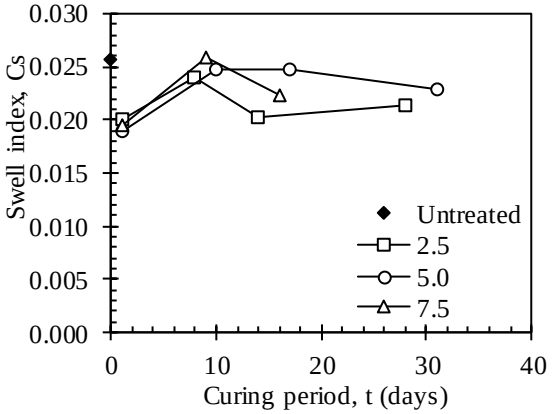

Fig. 5 Variation of the swell index with curing time for examined CKD %

Table 4 Summary of unconfined compressive testing results

ID	Uncon. Compr. Strength, UCS (kN/m^2)	Strength Increase (%)
CKD_0	194.2	0.0
CKD_2.5_1d	347.9	79.1
CKD_2.5_8d	452.1	132.8
CKD_2.5_14d	451.8	132.6
CKD_2.5_28d	454.9	134.2
CKD_5.0_1d	334.0	72.0
CKD_5.0_10d	395.4	103.6
CKD_5.0_17d	403.8	107.9
CKD_5.0_31d	457.8	135.8
CKD_7.5_1d	489.8	152.2
CKD_7.5_9d	592.2	204.9
CKD_7.5_16d	721.9	271.7
CKD_7.5_28d	752.7	287.6

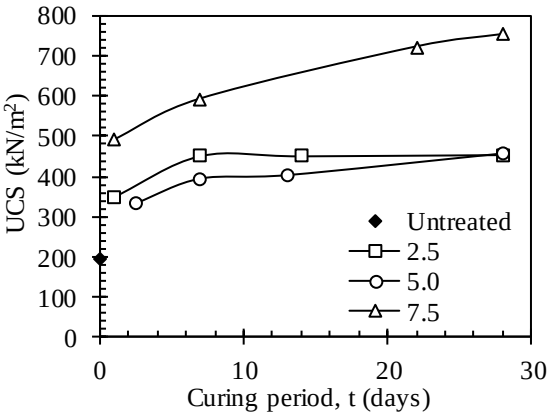

Fig. 6 Variation of unconfined compressive with curing time for examined CKD %

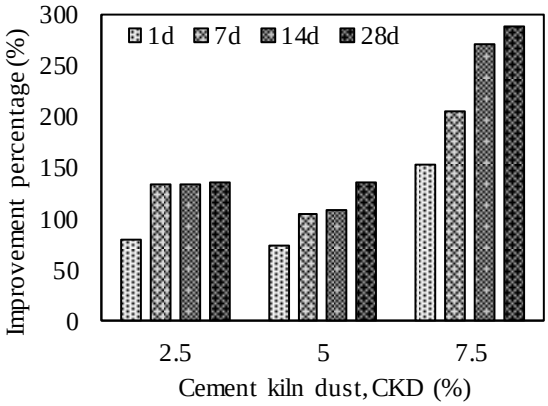

Fig. 7 Unconfined compressive improvement versus CKD %

CONCLUSIONS

During the processing of bauxite into alumina, bauxite residue (BR) is generated as industrial waste. Bauxite residue (BR) can pose a significant environmental hazard due to its high level of production and its high alkalinity. The current study examined the feasibility of recycling this residue and using it as construction material using cement kiln dust (CKD) which is an industrial waste material during cement production. In this regard, this research is of paramount importance for recycling two environmental hazard waste materials used in construction. The compaction parameters, volume change, and unconfined compressive strength were examined for a different mixture containing different doses of CKD.

Oedometer testing revealed that adding 2.5% of CKD is sufficient to remove any swell potential of BR besides maintaining a small compression index Cc, so it is selected as the optimum dose for volume change remediation.

Unconfined compressive strength testing showed that UCS increased with adding CKD and curing period. The addition of 7.5% of CKD increased the undrained stability by almost three times, indicating its effectiveness.

ACKNOWLEDGMENTS

The authors extend their appreciation to the Deputyship for Research & Innovation, Ministry of Education in Saudi Arabia for funding this research work through the project number (IF-PSAU-2021/01/19009).

REFERENCES

[1] Liu, W., Yang, J., & Xiao, B., Applications of Bayer red mud for ion recovery and building material production from alumosilicate residues;

J. Hazardous Materials, Vol. 161, Issue 1, 2009, pp. 474-478.

[2] Paramguru R.K., Rath P.C., Misra V.N., Trends in red mud utilization—a review. Miner. Proc. Extr. Metall. Rev. Vol. 26, Issue 1, 2005, pp. 1–29

[3] Guanzhou Q, Liu Y, Jiang T, Hu Y (1995) Trends in red mud utilization—a review.. J Central South Univ Technol 2(2):27–31.

[4] Erçağ, E., and Apak, R., Furnace smelting and extractive metallurgy of red mud: Recovery of TiO2, Al2O3 and pig iron. Journal of Chemical Technology & Biotechnology, Vol. 70, Issue 3, 1999, pp. 241-246.

[5] Alkan, G., Schier, C., Gronen, L., Stopić, S., and Friedrich, B., A Mineralogical Assessment on Residues after Acidic Leaching of Bauxite Residue (Red Mud) for Titanium Recovery. Open Access Journal, Vol. 7, 2017, 458.

[6] Tsakiridis, P.E., Agatzini-Leonardou, S., and Oustadakis, P., Red mud addition in the raw meal for the production of Portland cement clinker. Journal of hazardous materials, Vol. 116, Issue 1-2, 2004, pp. 103-10.

[7] Pontikes Y. and Angelopoulos G., Bauxite residue in cement and cementitious applications: current status and a possible way forward. Resour Conserv Recycl Vol., 73, 2013, pp. 53–63.

[8] Singh, M., Upadhayay, S.N., and Prasad, P.M., Preparation of special cements from red mud. Waste Management, Vol. 16, 1996, pp. 665-670.

[9] Klauber, C., Gräfe, M., and Power, G.P., Bauxite residue issues: II. options for residue utilization. Hydrometallurgy, Vol. 108, Issue 1, 2011, pp. 11-32.

[10] Biswas, W.K., and Cooling, D., Sustainability Assessment of Red Sand as a Substitute for Virgin Sand and Crushed Limestone. Journal of Industrial Ecology, Vol. 17, Issue 5, 2013, pp. 756–762.

[11] Mukiza, E., Zhang, L., Liu, X., & Zhang, N., Utilization of red mud in road base and subgrade materials: A review. Resources, Conservation and Recycling. Vol. 141, 2019, pp. 187–199.

[12] Osinubi, K.J. Lime modification of black cotton soils. Spectr J, Vol. 2, Issue 1, 1995, pp.112–122.

[13] Balogun, L.A. Effect of sand and salt additives on some geotechnical properties of lime stabilized black cotton soil. Niger Eng. Vol. 26, Issue 2, 1991, pp. 15–24.

[14] Wayne S. Adaska, Donald H. Taubert., Beneficial Uses of Cement Kiln Dust, IEEE/PCA 50th Cement Industry Technical Conference, Miami, FL, 2008, pp. 19-22.

[15] Khater, G. A., Use of bypass cement dust for production of glass ceramic materials. Advances in applied ceramics, Vol. 105, Issue 2, 2006, pp. 107-111.

[16] Marku, J., Dumi, I., Lico, E., Dilo, T., and Cakaj, O., The characterization and the utilization of cement kiln dust (CKD) as partial replacement of Portland cement in mortar and concrete production. Zaštita materijala, Vol. 53, 2012, pp. 334-344.

[17] Siddique, R., and Mehta, A., Effect of carbon nanotubes on properties of cement mortars. Construction and Building Materials, Vol. 50, 2014, pp. 116-129.

[18] Miller G.A., Azad S., Influence of soil type on stabilization with cement kiln dust. J Constr Build Mater, Vol. 14, Issue 2, 2000, pp. 89‑97.

[19] Hossain K.M.A., Mol L., Some engineering properties of stabilized clayey soils incorporating natural pozzolans and industrial wastes. J Constr Build Mater, Vol. 25, Issue 8, 2011, pp. 3495–3501.

[20] Ismaiel H.A.H., Cement kiln dust chemical stabilization of expansive soil exposed at El-Kawther Quarter, Sohag Region, Egypt. Int J Geosci, Vol. 4, Issue 10, 2013, pp. 1416–1424.

[21] Salahudeen, A.B., Eberemu, A.O., and Osinubi, K.J., Assessment of Cement Kiln Dust-Treated Expansive Soil for the Construction of Flexible Pavements. Geotechnical and Geological Engineering, Vol. 32, 2014, pp. 923-931.

[22] Ismail A.I.M. and Belal Z.L., Use of cement kiln dust on the engineering modification of soil materials, Nile Delta, Egypt. J Geotech Geol Eng, Vol. 34, 2016, pp. 463–469.

[23] Ogila, W.A., Effectiveness of fresh cement kiln dust as a soil stabilizer and stabilization mechanism of high swelling clays. Environmental Earth Sciences, Vol. 80, 2021, 1-24.

[24] ASTM D698, Standard test methods for laboratory compaction characteristics of soil using standard effort (12,400 ft-lbf/ft3 (600 kN-m/m3)). ASTM International, 2000, West Conshohocken, PA, USA.

[25] ASTM D4546-03, Standard test methods for one-dimensional swell or settlement potential of cohesive soils. ASTM International, 2003, West Conshohocken, PA, USA.

8th Int. Conf. on Structure, Engineering & Environment (SEE), Mie, Japan, Nov.10-12, 2022, ISBN: 978-4-909106094 C3051

MODELING ADSORPTION OF HEXAVALENT CHROMIUM USING A LOW-COST JORDANIAN OLIVE STONE WASTE ADSORBENT

Aymen Awad

Middle East University (MEU) – Civil Engineering Department - Amman - 11831 - Jordan,
aawad@meu.edu.jo

ABSTRACT

Heavy metals are very toxic metals found in water and wastewater. Heavy metals are nonbiodegradable metals, accumulated in human bodies damaging human health. Many researchers tried to treat and purified water, wastewater and industrial wastewater having these contaminates by using adsorption techniques. They focused on low cost natural materials produced from agricultural waste. Olive stone waste (OSW) one of these materials which is generated in Mediterranean countries such as Jordan. Jordan produced thousands of tons of this natural waste. Olive stone waste (OSW) was used as natural adsorbent to remove the Cr (IV) ions from industrial liquid solutions. The optimal conditions for removal processes were determined previously by sets of experiments. The contact time was 360 minutes, pH was 2.7, the adsorbent dosage was 4 g /L and the temperature was 25ºC. Results of adsorption mechanism data analysis for different Cr(IV) initial concentrations of 0.3, 2.7, 4.5, 9, 18 and 60 mg/l removed by (OSW) adsorbent fitted the Freundlich adsorption isotherm R^2 = 1, and near very closed to pseudo second-order adsorption kinetics also R^2 = 0.998. The adsorption of Cr (VI) was found to be concentration dependent. Olive stone waste indicates highly removal efficiency toward removing hexavalent chromium from liquid industrial wastewater.

Keywords: Hexavalent Chromium, Adsorption, Olive Stone Waste, pseudo second-order adsorption kinetics Model.

INTRODUCTION

Water pollution is a major and essential problem encountered everywhere [1]. Jordan is considered as one of the poorest countries in water. Water scarcity in Jordan is reflected by the water shortage problems and elaborates the main challenges that face the country throughout the recent and future years [2]. Water is very important and essential for human being and societies live. Water and environment are affected by contaminates from different sources especially industrial wastewater which harm the natural sources [3]. Many sources of industrial pollutions affect the water and environment such as of batteries manufacturing, electroplating processes, machining processes, textile dyeing industry and as a biocide addition in cooling waters [4]. Heavy metals are very toxic for environment and pollute water and wastewater with small quantities and low concentrations [5,6]. However, these heavy metals are non-biodegradable and therefore accumulated in the creatures' bodies and in environment systems [7]. One of the most heavy metals contaminates and has significant environmental concern is chromium metals (Cr) [8]. Cr exists in nature in different oxidation number varying from -2 to +6 such as (CrO_4^{-2}) called chromate or ($Cr_2O_7^{-2}$) called dichromate [5]. The most toxic chromium compounds toward the environmental system are the the hexavalent chromium and the trivalent chromium [9]. These compounds are existed in different water and wastewaters sources especially industrial. Consequently, Cr(IV) effluents are discharged to the water bodies and environmental systems from different industries such as electroplating processes and materials dyeing industries…etc., [10,4]. Many attempts were done to treat water and wastewater which have hexavalent chromium contaminants using different techniques. The common used methods and processes for treatment Cr (VI) from liquid solutions are summarized in the following techniques; chemical reduction, coagulations and filtrations, precipitations, ion exchange, reverse osmosis (RO) and adsorption by using active carbon [11,6]. For a different reasons and disadvantages, these methods and techniques are described as expensive, having toxicities, generate harmful byproducts and produce high quantities of residuals during and after treatment time [12]. As a result, scientists and researchers focused on findings new low cost materials used as biosorbents for removal of heavy metals contaminants in the form of ions in aqueous solutions [13].

In the Mediterranean countries, the olive tree is a fundamental crop, there are more than 12 million hectares of this crop (95% of the world's cultivated olive area) [14]. One of the new solid waste byproduct and recently generated as agricultural waste is olive stone waste [15]. The most point

source of this industrial biowaste is the olive oil industry. This industry also is dominated in the Mediterranean Sea countries such as Jordan, Syria, Lebanon and Palestine. Therefore, industries in these countries produce huge quantities of wastewater polluted with olive stone materials and consequently need to be treated for discharging or reuse. Olive waste is considered a low-cost adsorbent, natural materials, such as agricultural and industrial biowaste and have been studied by many researchers [16,17]. Park and others in 2007 investigated the organic materials used as biosorbents which are made of natural biomaterials. Olive stone waste was processed to produce activated carbon chemically by using phosphoric acid (H3PO4) to use as biosorbent [6]. The activated carbon of olive stone waste is considered effective adsorbent because of its high adsorption surface area, its deep microspores and heterogeneous surface functional groups [15].

Adsorption is the most and common method to remove contaminants from aqueous solutions [18,17]. The most effective and widely spread adsorbent is activated carbon, but with a high cost, which convinced researchers and scientists to search for low-cost effective natural adsorbents, recent studies and investigations were focused on natural lignocellulosic waste materials and other agricultural residuals [20,21].

Cr(VI) removal using biosorbents was done and approved that it taken place through the combination of adsorption and reduction mechanisms [27]. Today, regulations are more restricted in applying the effluent standards of pollutant's discharging to environment [23, 24]. Olive stone wastes (biosorbent) can be utilized to make activated carbon; such material is found to be effective for the removal of toxic metals such as aluminum or arsenic from wastewater [25].

Adsorption isotherms represents the properties and equilibrium data which reveal the mechanisms how the pollutants removed by adsorbent materials [10,26]. Langmuir model, Freundlich model, Temkin, and Dubinin-Radushkevich isotherms are the usual used models and equations to test the olive stone waste – hexavalent chromium metals contaminants system [10, 27].

Even though there are many ecological benefits could be achieved when using the natural waste as source of energy or a raw source for manufacturing of active carbon. Therefore it is good for environment to use such biowaste as adsorbent for removal of industrial waste such as heavy metals [23]. Consequently, different studies and many investigations have indicated that the biosorbent made from olive stone wastes could be used to eradicate industrial pollutants such as phenols [28, 29]. Different investigations also approved that olive stone waste is effective adsorbent could be used to remove heavy metals contaminants like Cd(II), Pb(II), Ni(II) and done by the following researchers [30,31,32, 33].

Many researchers approved that the adsorption technology is favorable and good for removal of industrial contaminants such as heavy metals because of its high efficiency, low cost of treatment and low residual production. Again solid residual of olive mill products (SROOMP) was employed potentially by many researches as adsorbent to treat wastewater containing several heavy metals in trace concentration, namely Cr(III), Ni(II), Pb(II), Cd (II) and Zn(II) and the results indicated that significant removal was undertaken [34].

RESEARCH SIGNIFICANCE.

This study was investigated the adsorption of hexavalent chromium metal ions by olive stone waste used as adsorbent. Batch system experiments were used for Cr(IV) adsorption investigations with respect to different initial metal concentrations versus contact time. Equilibrium isotherms studies were studied by using Langmuir model, Freundlich model, Tempkin model, and Dubinin-Radushkevich model isotherms and kinetics for Cr(VI) removal [35].

MATERIALS.

Preparation of adsorbent.

Olive stone waste was collected from different sites in Jordan (Olive extraction oil plants and factories). Firstly; OSW was mixed together, dried, washed with distilled water, and then socked in diluted phosphoric acid H3PO4 for two hours. Secondly; the washed stone was dried and crushed to particle size and sieved between 300 – 800 microns. Thirdly; the homogenous OSW was treated thermally at 104 o C for 3 hours to eliminate the excess acid and evaporate the VOC in the adsorbent [37].

Preparation of Cr (VI) solution.

A standard hexavalent chromium solution of 3000 mg/l concentration was prepared using the desired amount of solid chromium trioxide $Cr_2O_7^{-2}$ ($K_2Cr_2O_7$) dissolved in 250 ml of distilled water. Cr(IV) solutions with the adsorbent amount of 4 g/l were taken in conical flasks and shaken on an electrical bench shaker for time of 360 minutes at 25^{o}C and pH of 2.7.

METHODOLOGY.

Different experiments were done firstly to fix the parameters of pH, adsorbent dosage, mixing or contact time affecting adsorption rate. For the purposes of adsorption isotherms and removal kinetics investigations a tests group upon initial concentrations testing were done. Therefore testing procedures were constructed by taking different initial metal concentrations of Cr(IV) solutions as follows: 0.3, 2.7, 4.5, 9, 18 and 60 mg/l. Stock solution was used to prepare the required initial concentrations by a prober dilution factor for each concentration needed. Testing continued upon each sample with initial concentration (C_i) until the concentration of the residual metal after adsorption was approximately fixed at a point which represents the equilibrium concentration (C_e) of sorbent [Cr(IV)]. During testing the drop in concentration with time was recorded. At the end of each experiment the equilibrium concentration of Cr (VI) was estimated calorimetrically by diphenyl carbazide test method and directly measured with spectrophotometer type of DR 5000 HACH-USA manufacturer.). To estimate the percentage removal of chromium from aqueous solution the following equation was used [20]: -

$$\text{Removal of chromium} = \frac{(\text{C initial} - \text{C final})}{\text{C initial}} \times 100$$

EQUIPMENT.

The experiments of this part of the study were done in 250 ml conical flasks and then mixed at a constant speed of 150 rpm at pH of 2.7 and the five different initial concentrations of the salt's solutions and adsorbent dosage of 4 g/L at ambient temperature (approximately 25°C).

Collected samples during testing were analyzed for the determination of the concentrations of the remaining Cr(VI) by using a spectrophotometer DR5000 Hach, USA. The adsorbent was weighted each time by digital balance (Mettler AE200, USA made), 200 grams capacity ± 0.1 mg accuracy.

RESULTS.

Experiments were carried out at temperature (298 K). Equilibrium adsorption isotherms generated at equilibrium states. Adsorption isotherms are calculated from the results of batch experiments studies at different initial concentrations as shown in (Tables 1 and 2) and (Fig.1) [35,26,27]. These isotherms represent the adsorption capacity of the adsorbent in terms of metal uptake (milligrams of adsorbate per grams of adsorbent) and could be fitted to suitable correlation (Adsorption Model) [27,37]. There are different forms of mathematical models describing the adsorption isotherms, based on physical bases or empirical hypothesizes to represent data achieved experimentally. In this research four models were used to fit the experimental equilibrium data to find out which one is suitable for description the removal process. Langmuir, Freundlich, Temkin and Dubinin–Radushkevich adsorption isotherm models were used to fit the data [38].

Removal percentage versus initial concentration of Cr (VI).

The results of adsorption experiments of Cr (VI) at different initial concentrations ranging from 0.3-60 ppm received at the best value of acidity value of 2.7, the adsorbent dosage was (4g/L), while the stirring time was elapsed to (360 min) and the mixing speed was 150 rpm. Table (1) represents the results of Cr(VI) initial concentrations effects on adsorption of the metals in batch reactor. (Fig.1) shows the removal efficiency of Cr(VI) metal ions removed by the adsorbent (OSW) at 0.3, 2.7, 4.5, 9, 18, and 60 mg/l of Cr(IV) initial concentrations versus time. It is obvious that the percentage removal is increased when the adsorbate concentration is decreased and ranged from 80 percent up to 96 percent. This may be probably due to site limitations on the surface of the adsorbent which can cause a low removal percentage at high concentrations.

Table 1 Effects of initial concentrations of metal ions in a batch reactor using olive stone waste adsorbent @ pH of 2.7 for Cr(VI) solutions. [Processes' temperature is 25 ± 1°C, adsorbent dose of 4 g/L, mixing speed is 150 rpm, and solutions volumes of 0.25 liter]

Time (Min)	Concentration of Hexavalent chromium (mg/l).					
0	0.30	2.70	4.50	9.0	18.0	60
2	0.04	0.46	1.00	3.5	4.4	18
4	0.03	0.32	0.90	2.1	2.4	16
8	0.03	0.25	0.46	1.0	2.3	14
90	0.02	0.23	0.43	0.9	2.2	13
180	0.01	0.21	0.41	0.8	2.1	12
270	0.01	0.15	0.32	0.8	2.1	12
360	0.01	0.15	0.32	0.8	2.1	12

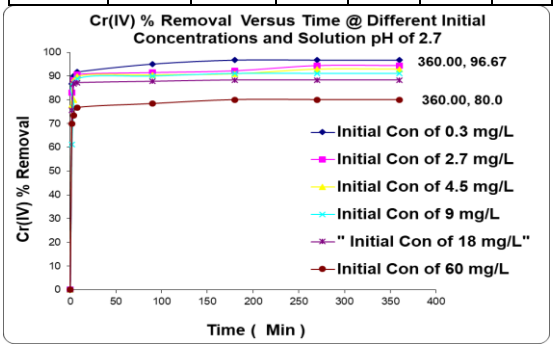

Fig. 1 Removal efficiency of Cr(VI) metal ions removed by olive stone waste at different initial concentrations versus time at an initial pH's of 2.7

DISCUSSION OF RESULTS.

Adsorption Isotherms Models.

The results of the adsorption experiments at equilibrium states were tabulated in in (Table 2). Table 2 shows the calculated parameters for plotting of the liner forms of the adsorption models.
Table 2 Adsorption Isotherm parameters for Langmuir, Freundlich, Temkin and Dubinin–Radushkevich models [38].

Co mg/l	x/ms mg/g)	log (X/M)	log (Ce)	ln Ce
0.3	0.003	-2.602	-2.000	-4.605
2.7	0.038	-1.426	-0.824	-1.897
4.5	0.080	-1.097	-0.495	-1.139
9.0	0.200	-0.699	-0.097	-0.223
18.0	0.525	-0.280	0.322	0.742
60.0	3.000	0.477	1.079	2.485

Co mg/l	Ce (mg/l)	Qe mg/g	Ce/qe l/g	X mg
0.3	0.01	0.073	0.138	0.003
2.7	0.15	0.638	0.235	0.038
4.5	0.32	1.045	0.306	0.080
9.0	0.80	2.050	0.390	0.200
18.0	2.10	3.975	0.528	0.525
60.0	12.00	12.000	1.000	3.000

Co mg/l	ln qe	ε	ε^2	RL
0.3	-2.624	11200	1.3E+08	0.935
2.7	-0.450	4930	2.4E+07	0.616
4.5	0.044	3430	1.2E+07	0.490
9.0	0.718	1960	3.9E+06	0.325
18.0	1.380	944	8.9E+05	0.194
60.0	2.485	194	3.8E+04	0.067

Langmuir Isotherm.

Usually to describe the removal mechanism of liquid molecules by solid material the Langmuir Isotherm is used to test for applicability, Irving Langmuir in 1916 set the model to test the adsorption of gas by adsorbents under certain pressure [39]. The adsorption behavior by using Irving Langmuir model was found to describe the monolayer removal mechanism between liquid phase and solid in case of homogenous sites on adsorbent surface. The model describes the adsorption process quantitatively, monolayer with the same energy value of adsorption onto the outer surface of adsorbent and no other adsorption types [40]. Fig. 2 illustrates the layers of adsorbate attached to the adsorbent [41].

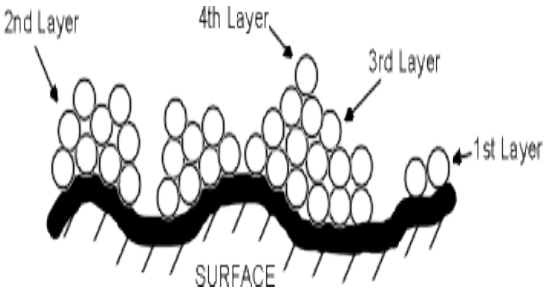

Fig. 2 Adsorption layers of liquids on solid adsorbents [41].

According to the assumptions mentioned, the Langmuir isotherm model is defined by following equation:

$$q_e = \frac{Q_{max} K_L C_e}{1 + K_L C_e} \quad \text{..... (1)}$$

The linear form of the Langmuir isotherm model is:

$$\frac{C_e}{q_e} = \frac{C_e}{q_{max}} + \frac{1}{q_{max} K_L} \text{ ..... (2)}$$

where the amount of adsorbent removed by adsorbent is q_e (mg/grams) and C_e is the concentration of adsorbate at equilibrium in mg/L, q_{max} represents the maximum adsorbent capacity as one layer on the adsorbent surface in (mg/g) and the adsorption isotherm constant is K_L in (L/mg).

The plotting of ($\frac{C_e}{q_e}$) and (C_e) of "Eq. (2)" will give a linear relationship from which q_{max} and K_L can be determined from the slope and intercept of the plotting, respectively, as seen in Fig. 3. "Eq (3)" gives the value of separation factor R_L which describes the Langmuir isotherm process [42]:-

$$R_L = \frac{1}{1 + K_L C_o} \text{ ..... (3)}$$

where C_O is the initial concentration of the adsorbate [Cr(IV)] and RL is the separation factor of the adsorption process, which is unfavorable for value of > 1, linear for value of 1 and strong and irreversible for value = 0. The results are tabulated in Table 1. R_L values indicated that the process of removal are closed to pure adsorption.

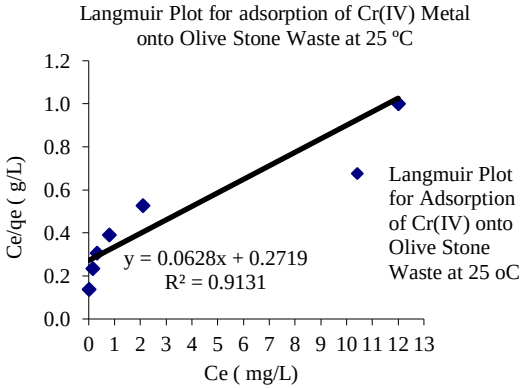

Fig.3 Langmuir Adsorption Isotherm Model

Freundlich Adsorption Isotherm.

The heterogeneous adsorbent surface in the case of multilayer adsorption process is assumed wherever the Freundlich isotherm model is used to fit the experimental data [43,44]. Freundlich explained the behavior of adsorbed molecules on the adsorbent surface and the data are fitted with the following empirical linear form equation:-

$$\log(q_e) = \log K_f + {}^{1}/_{n}\, log C_e \ldots\ldots (4)$$

Where q_e represents the metals uptake (mg/g), K_f is the Freundlich constant, Ce is the equilibrium concentration of adsorbate in (mg/l) and n is the linearity constant describing the adsorption process with respect to adsorbate concentration [44]. Plotting results for n values say that if n = 1 then the process of adsorption is linear adsorption process , if n is less than 1 the process is with chemical reaction but if n is higher than 1 a physical mechanism is included in the adsorption process is attained. As a conclusion if 0 < 1/n < 1 then the situation is favorable and it is cooperative when 1/n > 1 [45,46]. Fitting of the data is illustrated in Fig. 4, with a correlation coefficient R^2 of 1 and the value of the adsorption relation constant n equals 1 which mean that the adsorption is liner process.

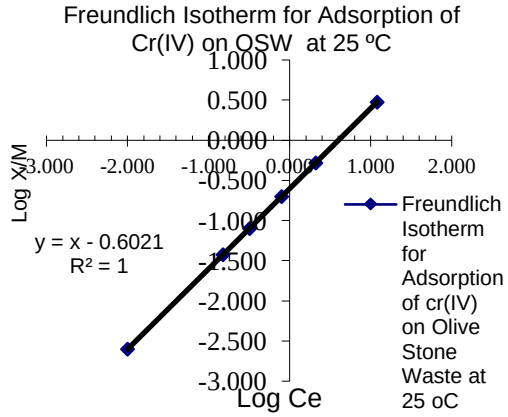

Fig. 4 Freundlich Adsorption Isotherm Model

Pseudo Second- Order Adsorption Isotherm.

This adsorption kinetic model can be expressed in liner form as follows [47, 35]:

$$\left(\frac{t}{q_t}\right) = \frac{1}{h} + \frac{1}{q_e}(t) \quad \ldots\ldots\ldots\ldots \textbf{(5)}$$

The plot of the term (t/q_t) versus time as shown in "Eq. (5)", should give a linear relation. The constants and parameters of the model q_e and k_2 can be determined from the line slope and intercept of the fitted line, respectively.

If the initial adsorption rate, h (mg/g·min) is:

$$h = k_2 q_e^{\,2} \quad \ldots\ldots\ldots\ldots \textbf{(6)}$$

The constant k_2 is refers to the rate constant of the model (pseudo second-order adsorption model) (g/mg·min). At boundary conditions of t = 0 to t = t and q_t = 0 to $q_t = q_t$ the data fitted as shown in Fig. 5. The generated straight line of the fitted data of [t/q_t] versus [t] shows a good agreement of measured data with the kinetic model form for all initial chromium concentrations. The results also indicated that the sorption of Cr(IV) removal behaves as pseudo second-order adsorption kinetics. It developed good correlation coefficient discussed the fittingness of as pseudo second-order adsorption model. (Table 3) lists the calculated constants and parameters obtained from the isotherm models. The correlation coefficient for pseudo second-order kinetic model obtained is 0.999.

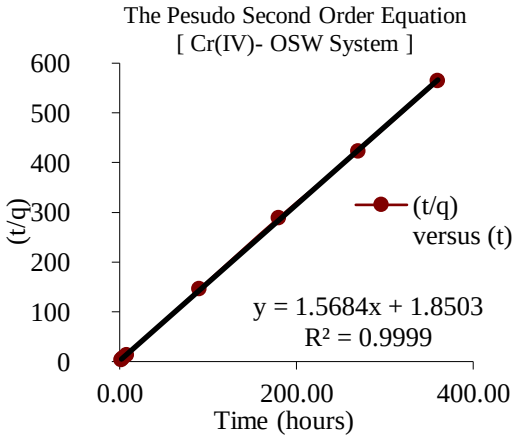

Fig. 5 Pseudo second-order adsorption Model.

Trend revealed that sorption capacity of olive stone waste increase by decreasing the initial

concentration of metal ion. This is due to the fact that in case of low concentration of metal ion solution there are more adsorbent sites available for metal ions to adsorb on it.

Table 3 Adsorption isotherms parameters of Langmuir, Freundlich, Pseudo second-order, Tempkin and Dubinin–Radushkevich isotherm of hexavalent chromium Cr(IV) adsorption onto olive stone waste (OSW).

MODEL	Slope		Constants	
Langmuir	**0.063**	**$=1/q_m$**	**q_m**	**15.92**
Freundlich	**1.000**	**= 1/n**	**n**	**1.00**
Pseudo-second-order	**1.568**	**= 1/h**	**h**	**0.64**
Tempkin	**1.532**	**$=B_T$**	**B_T**	**1.53**
Dubinin–Radushkevich	**-3.0E+08**	**$=-K_{DR}$**	**K_{DR}**	**3E+08**

MODEL	Intercept		Constants	
Langmuir	**0.272**	**= KL*qm**	**kL =**	**0.231**
Freundlich	**-0.602**	**= ln(Kf)**	**Kf =**	**0.548**
Pseudo second - order	**1.850**	**= 1/qe**	**qe=**	**0.541**
Tempkin	**4.481**	**= BTLn(Af)**	**Af =**	**18.642**
Dubinin–Radushkevich	**1.144**	**= Ln(Q_0)**	**Q_o=**	**3.140**

MODEL	R^2
Langmuir	0.913
Freundlich	1.000
Pseudo second - order	0.999
Tempkin	0.685
Dubinin–Radushkevich	0.790

Tempkin Adsorption Isotherm

The process of adsorption of adsorbate by adsorbent in this isotherm is presented by a factor called equilibrium binding constant Af (L/g). This factor is related to the amount of energy that required for the adsorbent to adsorb the pollutant molecules measured in J/mol [48]. The model is set by the following Equation of the nonlinear form [49]: -

$$q_e = \frac{RT}{b_T} Ln(A_T C_e) \ldots\ldots\ldots\ldots\ldots (7)$$

The linear form is given in the following formula:

$$q_e = B_T\, Ln\,(A_T) + B_T Ln(\,C_e) \ldots (8)$$

Where $B_T = \frac{RT}{b_T}$

A_T is the isotherm equilibrium binding constant (L/g); while b_T is the Tempkin isotherm constant; R, the universal gas constant and equals 8.314 J/mol/K; T, is the temperature of the process usually at a temperature of 298 K; B, is a constant related to the heat of sorption in (J/mol). The constants were determined from the slope and intercept of the model fitting by plotting the metal uptake q_e against ln C_e as shown in Fig. 6.

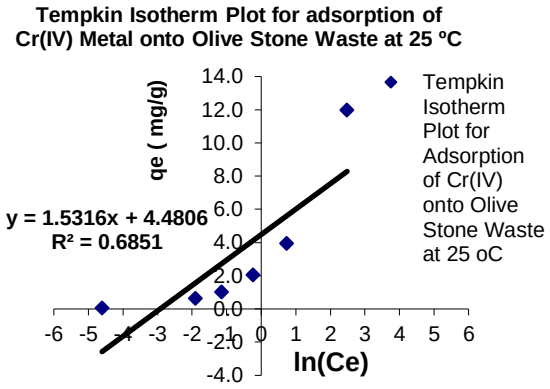

Fig.6 Tempkin adsorption isotherm Model

The plot slope and intercept are taken to calculated the constant and binding energy and they are found to be equal to the, A_T = 18.642 L/µmol, B_T = 1.532 J/mol, where B_T refers to amount of heat for sorption which is indicating a physical adsorption process and the R^2 = 0.6851. Therefore, results of fitting said that this process of removal is not comply with this model with its hypothesis which means that just small amount of energy is needed to achieve the removal of contaminants from solution and this will support the removal by another adsorption model.

The Dubinin-Radushkevich (D-R) Isotherm

This isotherm model depends on temperature and a factor called adsorption potential constant (ε) which considers the energy required for adsorption according to the adsorbent micropore size on the surface of adsorbent and the liner form of the model is represented by the following equation [50]: -

$$Ln(q_e) = Ln(Q_0) - K_{DR}\varepsilon^2 \ldots\ldots (9)$$

Dubinin-Radushkevich (D-R) model presents the required mean free energy for desorption of each molecule from its space site on the adsorbent surface and can be calculated by the following formula [51]:

$$E = \frac{1}{\sqrt{2K_{DR}}} \ldots\ldots\ldots\ldots\ldots (10)$$

The parameter ε can be calculated from the following formula [52]:-

$$\varepsilon = RT\ Ln\left(1 + \frac{1}{C_e}\right) \ldots\ldots\ldots (11)$$

where q_e refers to metal uptake at equilibrium conditions in (mg/g); Q_o related to the theoretical isotherm saturation capacity in (mg/g); K_{DR} is the constant called Dubinin–Radushkevich isotherm constant in (mol^2J^{-2}); ε is the adsorption potential constant; R is the gas constant (8.314 J/mol/K), T is the absolute temperature (K) and C_e adsorbate equilibrium concentration (mg/L). Experimental data were fitted according to Dubinin-Radushkevich (D-R) model where $Ln(q_e)$ versus ε^2 as shown in Fig. 7.

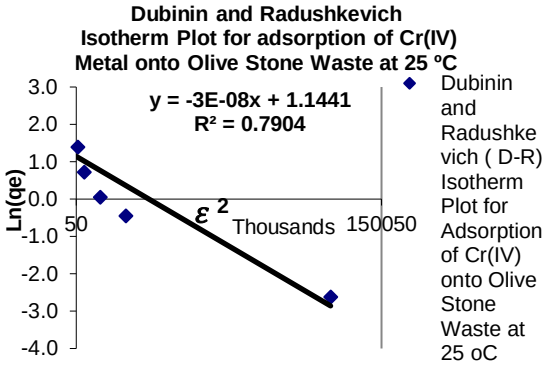

Fig.7 Dubinin–Radushkevich Adsorption Isotherm Model

The slope of fitted data in Fig. 7 corroding to this model is ($-3.0X10^{-8}$), which represents the value of ($-K_{DR}$) and consequently (K_{DR}) equals to ($3X10^{-8}$ mol^2J^{-2}) ; the intercept of the fitted line is 1.1441 which equals to (LnQ_o) then Q_o is calculated and equals to 3.140 mg adsorbed / g of adsorbent used , R^2 = 0.79 . The results achieved depend on this model again confirmed that the process of removal is independent on energy or temperature to certain limits. The value of mean free energy for desorption E = 4082 Joule / mole and this is very large value.

CONCLUSIONS

This research approved that a low-cost Jordanian's olive stone waste could be used as a natural adsorbent to remove the toxic Cr(VI) from aqueous solution and it may be an alternative to more costly materials. This adsorbent has good sorption efficiency reaches value of 96.67 % for the removal efficiency of chromium from aqueous solutions at low initial concentration of 0.3 mg/L and it decreases up to 80 % when the initial concentration of adsorbate increases to 60 mg/L. Olive stone waste has potential to be a good natural resource material for effective removal of chromium (VI) of low concentration from wastewater and may be used for other contaminants to remove. Freundlich adsorption isotherm model agrees very well with experimental data and the mechanism of removal for the adsorption of Cr(IV) onto OSW for different initial Cr(IV) concentrations.

ACKNOWLEDGMENTS

The author would like to express his gratitude to the support extended to him throughout and for the all types of supports and grants to cover the works of this research by Middle East University – Amman (MEU).

REFERENCES

[1] Eman Alabbad*, 2020. "Removal of Direct Yellow 50 from Aqueous Solutions Using Chitosan-ISO-Vanillin Derivatives Chelating Polymers". Research Square, December 21st, 2020, DOI: https://doi.org/10.21203/rs.3.rs-129329/v1.

[2] O. ODEH, 2019. "Water Shortage in Jordan ". International Journal of Engineering and Management Sciences (IJEMS) Vol. 4. (2019).

[3] Crini G and Lichtfouse E, 2019. "Advantages and disadvantages of techniques used for wastewater treatment". Environ 256, Chem Lett. 2019; 17:145-55.

[4] Bai, R.S. and Abraham, T.E., 2001. "Biosorption of chromium (VI) from aqueous solution by Rhizopus nigricans". Bioresource Technology". 2001; 79(1) 73-81.

[5] Seng, H. and Wang, Y.T., 1994." Biological reduction of chromium by E. coli." Journal of Environmental Engineering1994; 120(4) 560-572.

[6] Thouraya Bohli, Abdelmottaleb Ouederni, Nuria Fiol, Isabel Villaescusa., 2015. "Evaluation of an activated carbon from olive stones used as an adsorbent for heavy metal removal from aqueous phases". C. R. Chimie 18 (2015) 88–99, www.sciencedirect.com.

[7] Raji, F. and Pakizeh, M., 2013. "Study of Hg(II) Species Removal from Aqueous Solution Using Hybrid ZnCl2- MCM-41 Adsorbent," Applied Surface Science, Vol. 282, pp. 415_424 (2013). doi: 10.1016/j.apsusc.2013.05.145.

[8] N. Gandhi, D. Sirisha and K.B. Chandra Sekhar. (2013). "Adsorption Studies of Chromium by Using Low Cost Adsorbents". Our Nature (2013), 11(1): 11-16.

[9] Ismael Acosta-Rodríguez, Juan F. Cárdenas-González, María de Guadalupe Moctezuma-Zárate and Víctor M. Martínez-Juárez. 2013. "Removal of Hexavalent Chromium from Solutions and Contaminated Sites by Different Natural Biomasses", 2013, http://dx.doi.org/10.5772/56152.

[10] Aymen Awad, 2014." Adsorption of Hexavalent Chromium Cr(VI) by Using Local Jordanian Sand (LJS) and Iron Dust-Sand Mixed Adsorbents". Jordan Journal of Earth and Environmental Sciences – JJEES - Volume 6, Number 1, September, 2014-ISSN 1995-6681- Pages 9- 14.

[11] Park, D., Yung, Y.S. and Park, J.M., 2004. "Reduction of Hexavalent chromium with the brown seaweed Ecklonia Biomass". Environmental Science Technology 2004; 38(18), 4860-4864.

[12] Sahin, Y. and Öztürk, A., 2004. "Biosorption of chromium (VI) ions from aqueous solution by the bacterium Bacillus thuringiensis". Process Biochemistry 2004; 40 (5), 1895-1901.

[13] Volesky, B. and Holan. Z.R., 1995. "Biosorption of heavy metals". Biotechnology Progress 1995; 11, 235-250.

[14] Rugini, E., Baldoni, L., Muleo, R., Sebastiani, L., Eds., 2016." The Olive Tree Genome". Springer: Cham, Switzerland, 2016; pp. 1–12, ISBN 978-3-319-48887-5.

[15] Thouraya Bohli, Nuria Fiol, Isabel Villaescusa and Abdelmottaleb Ouederni. 2013. "Adsorption on Activated Carbon from Olive Stones: Kinetics and Equilibrium of Phenol Removal from Aqueous Solution". J Chem Eng Process Technol 2013, 4:6 http://dx.doi.org/10.4172/2157-7048.1000165.

[16] Susan E. Bailey, Trudy J.Olin b, R. Mark Bricka b, Dean Adriana., 1999. "A review of potentially low-cost sorbents for heavy metals". Water Research - Volume 33, Issue 11, August 1999, Pages 2469-2479. https://doi.org/10.1016/S0043-1354(98)00475-8.

[17] Fu, F. and Wang, Q. (2011). "Removal of Heavy Metal Ions from Wastewaters: A Review". Journal of Environmental Management, 92, 407-418.

[18] Bansal M, Singh D, Garg VK (2009). "A comparative study for the removal of hexavalent chromium from aqueous solution by agriculture wastes' carbons". J Hazard Mater 171:83–92. doi: 10.1016/j.jhazmat.2009.05.124.

[19] Gupta S, Babu BV (2009). "Removal of toxic metal Cr(VI) from aqueous solutions using sawdust as adsorbent: Equilibrium, kinetics and regeneration studies". Chem Eng J 150:352–365. doi: 10.1016/j.cej.2009.01.013.

[20] Gupta VK, Carrott PJM, Ribeiro-Carrott MML, Suhas (2009). " Lowcost adsorbents: growing approach to wastewater treatment—a review". Crit Rev Environ Sci Tec 39:783–842. doi:10.1080/ 10643380801977610.

[21] Mohan D, Rajput S, Singh VK, Steele PH, Pittman CU (2011). "Modeling and evaluation of chromium remediation from water using low cost bio-char, a green adsorbent". J Hazard Mater 188:319–333. doi:10.1016/j.jhazmat.2011.01.127.

[22] Park D., Lim S.-R., Yun Y.-S. and Park J.M. (2007). "Reliable Evidences that the Removal Mechanism of Hexavalent Chromium by Natural Biomaterials is Adsorption-Coupled Reduction". Chemosphere, 70, 298-305.

[23] Leopoldo M. N., Saloua B.D.A., Gassan H., Catherine F., Salvador R., José A. G., and Javier O, 2010. "Adsorption of iron on crude olive stones". 2010 Elsevier B.V. www.elsevier.com/locate/indcrop. 32 (2010) 467–471.

[24] Rodriguez, G., Lama, A., Rodriguez, R., Jimenez, A., Guillen, R., Fernandez-Bolanos, J., 2008. "Olive stone an attractive source of bioactive and valuable compounds: review". Bioresour. Technol. 99, 5261–5269.

[25] Clara, Piccirillo. (2011). "Use of Olive Stones for Various Technological Applications". Mar 19, 2011.

[26] J. S. Piccin, G. L. Dotto and L. A. A. Pinto, 2011. "Adsorption Isotherms and Thermochemical Data of Fd&C Red N° 40 Binding by Chitosan". Federal University of Rio Grande, Brazil, January 15, 2011.

[27] Crini, G. and Badot, P. M., 2008. "Application of chitosan, a natural amino polysaccharide, for dye removal from aqueous solutions by adsorption processes using batch studies: A review of recent literature". Polymer Science, 33, No. 4, 399-447 (2008).

[28] Stasinakis, A.S., Elia, I., Petalas, A.V., Halvadakis, C.P., 2008. "Removal of total phenols from olive-mill wastewater using an agricultural by-product, olive pomace". J. Hazard. Mater. 160, 408–413.

[29] Akar, T., Tosun, I., Kaynak, Z., Ozkara, E., Yeni, O., Sahin, E.N., Akar, S.T., 2009. "An attractive agro-industrial by-product in environmental cleanup: bye biosorption potential of untreated olive pomace". J. Hazard. Mater. 166, 1217–1225.

[30] Gharaibeh, S.H., Moore, S.V., Buch, A., 1998. "Effluent treatment of industrial wastewater using processed solid residue of olive mill products and commercial activated carbon". J. Chem. Technol. Biotechnol. 71, 291–298.

[31] Pagnanelli, F., Toro, L., Veglio, F., 2002. "Olive mill solid residues as heavy metal sorbent material: a preliminary study". Waste

Manag. 22, 901–907.
[32] Blázquez, G., Hernáinz, F., Calero, M., Ruiz-Núnez, L.F., 2005. "Removal of cadmium ˜ ions with olive stones: the effect of some parameters". Process Biochem. 40, 2649–2654.
[33] Fiol, N., Villaescusa, I., Martinez, M., Miralles, N., Poch, J., Serarols, J., 2006. "Sorption of Pb(II), Ni(II), Cu(II), and Cd(II) from aqueous solution by olive stone waste". Sep. Purif. Technol. 50, 132–140.
[34] Demirbas, A., Erhan, M.K., Elif, Senturkb. and Tuncay, Ozkana. 2004. "Adsorption kinetics for the removal of chromium (VI) from aqueous solutions on the activated carbons prepared from agricultural wastes". Gebze Institute of Technology, 41400 Gebze, Turkey.
[35] Mohamed Al-Meshragi, Hesham G. Ibrahim, and Mohamed M Aboabboud. 2008. "Equilibrium and Kinetics of Chromium Adsorption on Cement Kiln Dust". World Congress on Engineering and Computer Science 2008, WCECS 2008, San Francisco, USA.
[36] Blázquez, G., Calero, M., Ronda, A., Tenorio, G., Martín-Lara, M.A., 2014. "Study of kinetics in the biosorption of lead onto native and chemically treated olive stone". Journal of Industrial and Engineering Chemistry 20, 2754-2760.
[37] Wong, Y. C., Szeto, Y. S., Cheung, W. H. and McKay, G., 2004. "Adsorption of Acid dyes on chitosan–Equilibrium isotherm analyses". Process Biochemistry, 39, No.6, 695-704.
[38] Fulbert Togue Kamga, (2019). "Modeling adsorption mechanism of paraquat onto Ayous (Triplochiton scleroxylon) wood sawdust". Applied Water Science (2019) 9:1, https://doi.org/10.1007/s13201-018-0879-3.
[39] Langmuir, I. (1918). "The adsorption of gases on plane surfaces of glass, mica and platinum". Journal of the American Chemical Society, 40(9), 1361-1403.
[40] Alok Mittal, Lisha Kurup, Jyoti Mittal, 2006. "Freundlich and Langmuir adsorption isotherms and kinetics for the removal of Tartrazine from aqueous solutions using hen feathers ". Maulana Azad National Institute of Technology, Bhopal, 462 007 MP, India.
[41] Maryanti, R., Nandiyanto, A. B. D., Manullang, T. I. B., & Hufad, A. (2020). Adsorption of Dye on Carbon Microparticles: Physicochemical Properties during Adsorption, Adsorption Isotherm and Education for Students with Special Needs. Sains Malaysiana, 49(12), 2949-2960.
[42] Webber TN, Chakravarti RK (1974). "Pore and solid diffusion models for fixed bed adsorbers". J Am Inst Chem Eng 20:228–238.
[43] Chaleshtori AAN, Meghadddam FM, Sadeghi MM, Rahimi RR, Hemati S, Ahmadi AA (2017). "Removal of Acid Red 18 (Azo-Dye) from aqueous solution by adsorption onto activated charcoal prepared from almond shell". J Environ Sci Manag 20:9–16.
[44] Dada, A.O., Olalekan, A.P., Olatunya, A.M., and Dada, O. J. I. J. C. (2012). "Langmuir, Freundlich, Temkin and Dubinin–Radushkevich isotherms studies of equilibrium sorption of Zn2+ unto phosphoric acid modified rice husk". IOSR Journal of Applied Chemistry, 3(1), 38-45.
[45] Voudrias E, Fytianos F, Bozani E (2002)."Sorption description isotherms of dyes from aqueous solutions and waste waters with different sorbent materials". Glob Nest Int J4:75–83.
[46] Mohan S, Karthikeyan J (1997). "Removal of lignin and tannin color from aqueous solution by adsorption on to activated carbon solution by adsorption on to activated charcoal". Environ Pollut, 97:183–187.
[47] Y.S.Ho and G.McKay, 2000. "The kinetics of sorption of divalent metal ions onto sphagnum moss peat". Water research, Volume 34, Issue 3, 15 Feb. 2000, Pages 735-742
[48] Ofarmaja AE (2008). "Kinetic study and adsorption mechanism of methylene blue and methyl violet onto Mansonia (Mansonia altissima) wood sawdust". Chem Eng J 143:85–95.
[49] Tempkin MI, Pyzhev V (1940). "Kinetics of ammonia synthesis on promoted iron catalyst". Acta Phys Chim USSR 12:327–356.
[50] Gunay A, Arslankaya E, Tosun I (2007). "Lead removal from aqueous solution by natural and pretreated clinoptilolite: adsorption equilibrium and kinetics". J Hazard Mater 146:362–371.
[51] Dubinin MM (1960). "The potential theory of adsorption of gases and vapors for adsorbents with energetically non-uniform surface. Chem Rev 60:235–266.

8th Int. Conf. on Structure, Engineering & Environment (SEE), Mie, Japan, Nov.10-12, 2022, ISBN: 978-4-909106094 C3051

EFFECT OF LANDCOVER CHANGE ON LAND SURFACE TEMPERATURE IN THE URBANIZED AREA

Agus Suharyanto
[1]Faculty of Engineering, Universitas Brawijaya, Indonesia; [2,3] Company, Country

ABSTRACT

Changes in land cover affect various things, one of them being land surface temperature. This is because each type of land cover has its characteristics of absorption and reflectance of solar radiation. Solar radiation that is absorbed by objects on the earth's surface will be re-emitted into the air and will warm the earth's surface together with the radiation reflected by these objects. If the type of land cover on the earth's surface changes, the temperature of the earth's surface will also change. This phenomenon is the theme of this research. Changes in land cover and changes in land surface temperature were analyzed from remote sensing satellite imagery. The satellite image processing method has been applied in the analysis. Land cover analysis using an unsupervised classification method with iso cluster analysis is applied in this study. Land surface temperature analysis used the LST method. The research locations are Malang and Surabaya Cities. The results showed that the land covered with vegetation had the lowest land surface temperature. Meanwhile, land covered by soil, asphalt, concrete, zinc roof, and galvanized roof tile has a higher land surface temperature, respectively. In other words, land that reflects a lot of solar radiation will increase the surface temperature of the land, and land cover that absorbs a lot of solar radiation will reduce the surface temperature of the land. The results of the research indicate that changes in land cover will affect changes in land surface temperature.

Keywords: Land cover, Land surface temperature, Solar radiation, Image analysis, Unsupervised classification

INTRODUCTION

The landcover or landuse (LULC) changes are very fast and dynamic in the urbanized area. This phenomenon will be affected by many environmental characteristics such as surface runoff discharge, traffic volume, and land surface temperature (LST) [1]. To minimize the effect, it is necessary to monitor the LULC changes. One of the effective and efficient methods to monitor it is by using satellite remote sensing data [2], [3]. The remote sensing data can be scanned with a wide area at the same time, in digital format, and available in data series from many years before.

The LULC can be analyzed using satellite remote sensing data. One of the LULC characteristics can be represented by Normalized Vegetation Difference Index (NDVI) [4], [5]. The value of NDVI is from 0 to 1, and 0 is indicated that the land is not covered by vegetation, and 1 is indicated that the land covered by vegetation is 100% [6], [7]. Each type of land cover has its characteristic of solar radiation reflection and emission. The reflected and emitted solar energy will affect the air temperature surrounding each landcover type and is named LST [8]. Based on this characteristic it can be predicted that the land covered by the object which has high reflection and emission characteristics will produce high LST. In opposite, the land covered by the object which has low reflection and emission characteristics will produce low LST. For example, the high reflection and emission objects are concrete, zinc roof, and galvanized roof tile. For low reflection and emission objects are vegetation, water, and wetted soil. Consequently, if the LULC is changed the LST will be changed too.

The research areas are Malang and Surabaya Cities, Indonesia, which are the first and second largest cities of East Java Province. The satellite imageries generated from Landsat scanned with sensor OLI and collected in 2015 and 2020 were used in this research. The LULC in both cities changed very fast, especially in the 2000 year. The LULC changes will analyze using the NDVI method and air temperature will analyze using the LST method [9], [10]. To confirm the NDVI values, the classification of LULC will analyze using unsupervised classification method images using isoclass [11].

Based on the analysis result it can be estimated that the LST will change according to LULC changes. The second estimation is the level of NDVI values will follow the types of LULC in the certain area.

RESEARCH AREA

The research areas are Malang and Surabaya Cities, Indonesia. These cities are located in East Java Province. Malang City located in a hilly area with an elevation is about 500 m from MSL (Mean Sea Level). The population is 843.810 souls [12]. Surabaya City

is located in the north area of East Java Province in the flat area. The elevation is about 0 to 10 m from MSL and in the coastal area. The population is 2.87 million souls (BPS Surabaya City, 2021). Two cities were chosen as research areas because those cities are located under different topographic conditions and both cities have the same fast urban development. The city of Malang represents the mountainous area and the city of Surabaya represents the coastal area. The location of the research areas can be shown in Fig. 1.

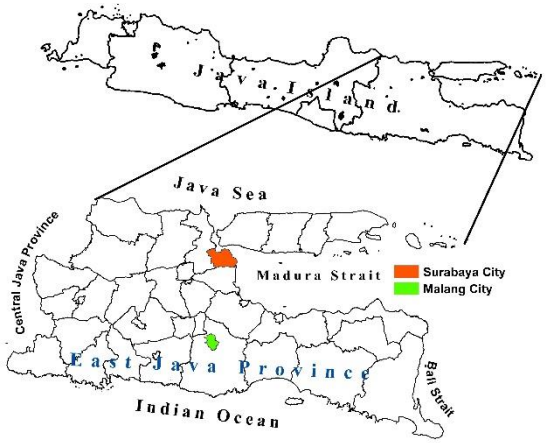

Fig.1 Research area.

MATERIALS AND METHODS

The main material used in this research is satellite imagery. The digital image of the Landsat satellite with sensor OLI was used in this research. The imageries covered of research areas in 2015 and 2020 were collected. The satellite imagery in path/row 118/65 covered Surabaya City and path/row 118/66 covered Malang City. The imageries with a cloud cover of less than 20% were selected. In summary, the selected imageries used in this research are shown in Table 1.

Table 1 Satellite imageries used in this research

Path/Row	Date	City	Seasons
118/65	5	Surabaya	Dry
	6	Surabaya	Dry
118/66	8	Malang	Dry
		Malang	Dry

Landcover Analysis

The landcover of the research area is analyzed using the iso cluster unsupervised classification method. First, the imagery will be classified into 15 landcover categories. By comparing the classified landcover image and high-resolution images such as a quick bird or Google images in the same area, the landcover categories will reclassify from 15 to 5 categories. The five landcover categories are forest, shrub and brush, open land, an agricultural area, and built-up area. This method was proposed, because easy to do and the accuracy is good [13], [14]. The final check of the landcover classification result will be done by comparing the image and the ground survey data. If the comparison result agrees, then the landcover classification process is finished. But if the comparison does not agree, then the image will reclassify from the beginning step.

NDVI Analysis

NDVI is the image representing the level condition of land which are covered by vegetation. The value of NDVI is from 0 to 1. Zero means the land is not covered by vegetation and one means the land is almost 100% covered by vegetation. NDVI value is equal to a band near-infrared minus band red divided by band infrared plus band red as shown in Eq. (1) [15]. For Landsat 8 OLI, the infrared band representing by band 5, and the red band is represented by band 4.

$$NDVI\ \frac{NIR - Rd}{NIR + Rd} \tag{1}$$

where *NIR* is the near-infrared band and *Rd* is the red band.

LST Analysis

The temperature of the land surface is derived from the thermal band of Landsat imagery. For Landsat 8 OLI the thermal band are bands 10 and 11. The LST is analyzed by using Eq. (2) until Eq. (6) [16].

$$TOA = L_\lambda = M_L . C_{cal} + A_L \tag{2}$$

$$TC = \frac{K_2}{\ln\left(\frac{K_1}{L_\lambda} + 1\right)} - 273.15 \tag{3}$$

$$PV = \left(\frac{NDVI - NDVI_{\min}}{NDVI_{\max} - NDVI_{\min}}\right)^2 \tag{4}$$

$$E = 0.004 . PV + 0.986 \tag{5}$$

$$LST = \frac{TC}{\left\{1 + \left[\left(\lambda . TC \middle/ \rho\right) Ln\ E\right]\right\}} \tag{6}$$

Here M_L is the radiance multiplicative scaling factor (Radiance_Mult_Band_10 or 11) obtained from the MTL file on the Landsat data, and A_L is the radiance

additive scaling factor (Radiance_Add_Band_10 or 11) obtained from the MTL file on the Landsat data, and C_{cal} is the digital value of Band 10 or 11. K_1 and K_2 are the band-specific thermal conversion constants taken from the metadata of the imagery file. The number 273.15 is the conversion factor for the temperature unit from Kelvin to Celsius. The λ is the digital number of Band 10 (λ is the wavelength of emitted radiance = 10.8 µm for Landsat TIRS Band 10), ρ = 14,380 ($\rho = h \times c/\sigma$ (1.438×10^{-2} mK)), TC is the brightness temperature, σ is the Boltzmann constant (1.38×10^{-23} J/K), h is the Planck constant (6.626×10^{-34} Js), c is the velocity of light (2.998×10^{8} m/s), and E is the land surface emissivity or error correction.

UHI Analysis

Analysis of the relationship between LST, NDVI, and LULC should ideally be carried out at each pixel in all research locations. Based on the statistical approach, the analysis will be done by the sampling method. The sample must depict pixels that are located in the suburbs to the city center. These pixels will be obtained from a line that runs from the suburb area through the city center and ends in the suburb area again. This line namely the urban heat island line (UHI). The relationship between LST, NDVI, and LULC will be analyzed by comparing the pixel values on the UHI line and the landcover at the same position collected by the ground survey. From the result of the comparison, it will be possible to obtain a relationship between the types of landcover with the NDVI and LST values.

In the same way, as described above, the Landsat imageries scanned on 2015 and 2020 will be analyzed. By comparing the analysis results from 2015 and 2020 imageries, landcover, NDVI, and LST changes can be known well. Thus the effect of LULC change on LST will be analyzed and become the main theme of this research. In principle, the research method for carrying out this research can be seen in the flow diagram chart shown in Fig. 2.

RESULTS AND DISCUSSIONS

The collected satellite imageries were analyzed using image processing software to generate the LULC, NDVI, and LST imageries. For example, the 2020 LULC, NDVI, and LST imageries of Malang City were shown in Fig. 3, 4, and 5, respectively. Six landcover categories can be classified i.e. forest, shrub and brush, agricultural land, open land, built area, and swamp area. From Fig. 4 it can be seen that the lowest NDVI is indicated as wet open land and the highest NDVI is indicated as forest landcover. This relationship was verified by high-resolution satellite imagery as shown in Fig. 6. The same case is shown in Fig. 5. The highest temperature is reflected and

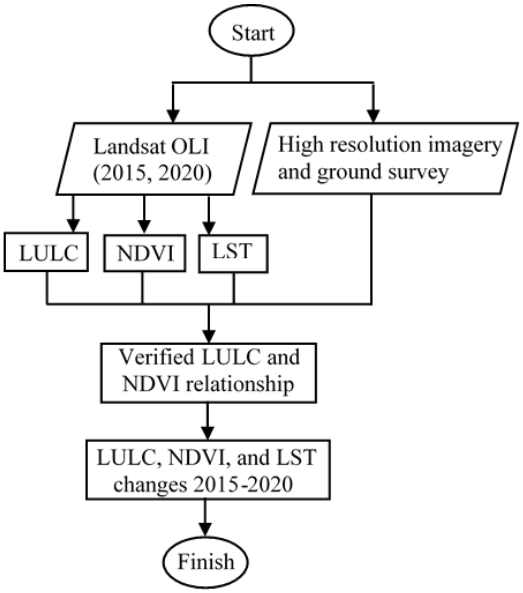

Fig.2 Flow diagram of research methods

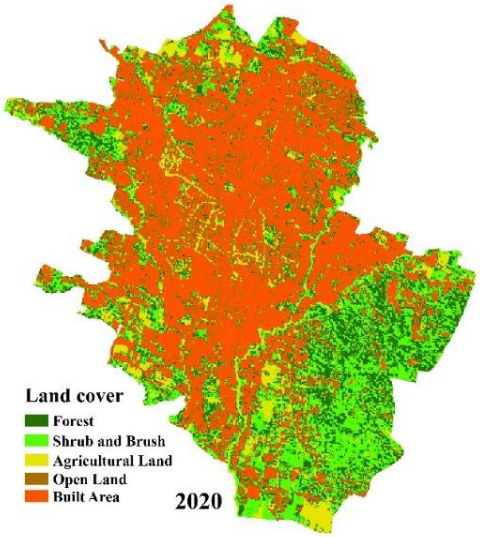

Fig. 3 LULC of Malang City in 2020

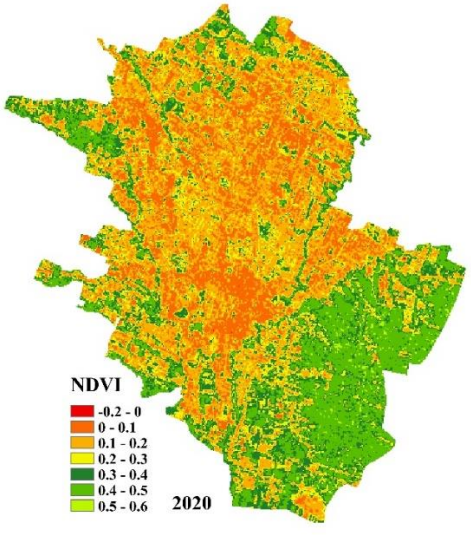

Fig. 4 NDVI of Malang City in 2020

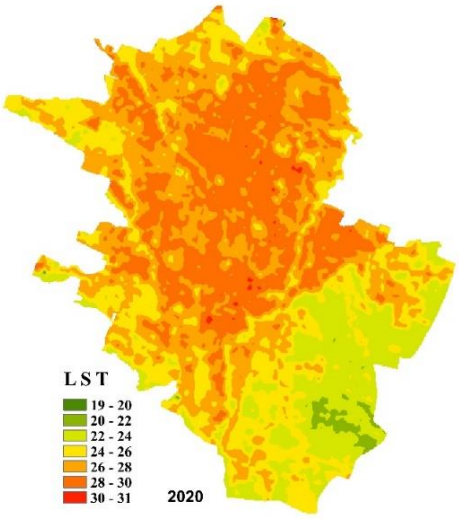

Fig. 5 LST of Malang City in 2020

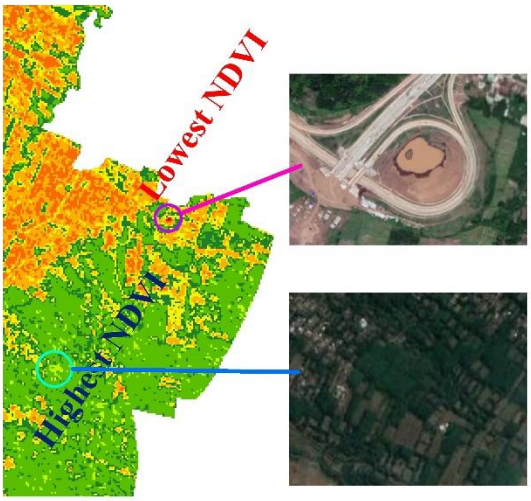

Fig. 6 Verification of NDVI and LULC

Fig. 7 Verification of LST and LULC

emitted by the roof of the factory and the lowest temperature is on open land. This relationship was verified by high-resolution satellite imagery as shown in Fig. 7. This verification process was done also for imageries covered Malang City scanned in 2015 and Surabaya City scanned in 2015 and 2020.

After the relationship between LULC, NDVI, and LST was verified, the LULC changes from 2015 to 2020 were analyzed. The LULC change in Malang and Surabaya Cities from 2015 to 2020 is shown in Table 2. Both cities showed that built area is increased and the others landcover were decreased. The landcover imageries of Surabaya city scanned in 2015 and 2020 are shown in Fig. 8. From this figure it can be seen that the built area represented in red in 2020 looks larger than the 2015 image. To analyze the effect of landcover change on land surface temperature, the landcover will be represented by NDVI. The landcover will not be categorized as landcover types but will categorize as NDVI values.

Table 2 LULC Changes Malang and Surabaya Cities

City	Landcover categories	Area (Ha.) 2015	2020
Malang	Forest	1,554.9	1,621.4
	Shrub and brush	1,808.7	1,933.7
	Agricultural land	1,570.2	988.1
	Open land	420,3	741.1
	Built area	5,636.9	5,706.4
Surabaya	Shrub and brush	6,637.7	3,466.2
	Agricultural land	6,095.2	0
	Open land	2,048.7	1,649.5
	Built area	15,760.2	21,551.4
	Water	2,306.7	6,180.3

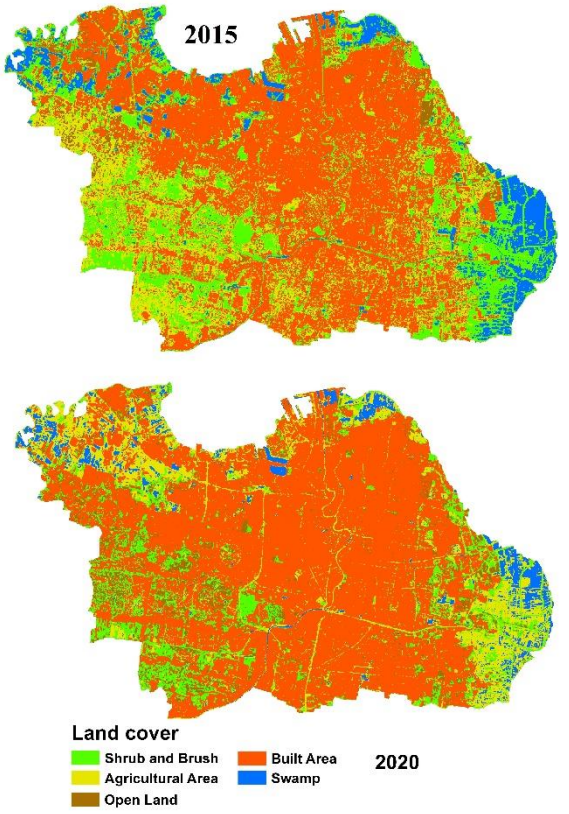

Fig. 8 LULC of Surabaya City in 2015 and 2020.

The values of NDVI are from -1 to +1. The values -1 to 0 indicated that land is not covered by vegetation. The value +1 indicated that land is covered 100% by vegetation. The NDVI value between 0 – 1 indicated the percentage of vegetation covered in the land. For example, if NDVI is equal to 0.25 it means that the land is covered by about 25% of the vegetation.

The NDVI changes in Malang and Surabaya Cities from 2015 to 2020 are shown in Table 3. This table indicated that the lowest, average, and highest NDVI decreased from 2015 to 2020. For LST, the temperature changes of Malang and Surabaya Cities from 2015 to 2020 are shown in Table 4. From this table, it can be concluded that the lowest, average, and highest LSTs increased from 2015 to 2020. Based on Table 3 and Table 4 it is seen that when NDVI goes down, LST goes up. This phenomenon indicates that the land surface that is covered with a lot of vegetation will reduce LST. This is because the land surface that is covered by a lot of vegetation will absorb a lot and slightly reflect solar radiation.

Table 3 NDVI of Malang and Surabaya Cities

City	Year	NDVI		
		Min	Ave	Max
Malang	2015	-0.01	0.23	0.59
	2020	-0.21	0.24	0.59
Surabaya	2015	-0.15	0.14	0.52
	2020	-0.15	0.15	0.55

Table 4 LST of Malang and Surabaya Cities

City	Year	LST		
		Min	Ave	Max
Malang	2015	16.00	26.05	32.12
	2020	18.50	26.41	31.10
Surabaya	2015	18.21	26.96	33.33
	2020	21.00	28.16	34.07

To analyze the relationship between NDVI and LST, it is necessary to draw a graph showing the relationship pixel by pixel from NDVI and LST data. Due to a large number of pixels in one research area, the NDVI and LST data are generated from the UHI line. The relationship between NDVI and LST of Malang and Surabaya Cities is shown in Fig. 9 and Fig. 10. From these figures it can be concluded that NDVI is inversely proportional to LST. When the value NDVI decreases, the LST value increases.

CONCLUSIONS

The landcover, NDVI, and LST of Malang and Surabaya Cities were analyzed using Landsat OLI data scanned in 2015 and 2020. The imageries data were scanned during the dry season. The analyzed result shows that the NDVI is well represented in the

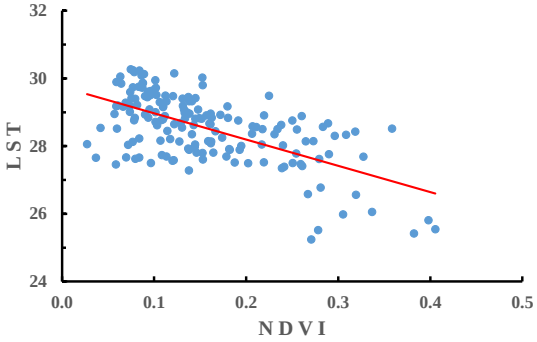

Fig. 9 NDVI vs LST of Malang City 2015

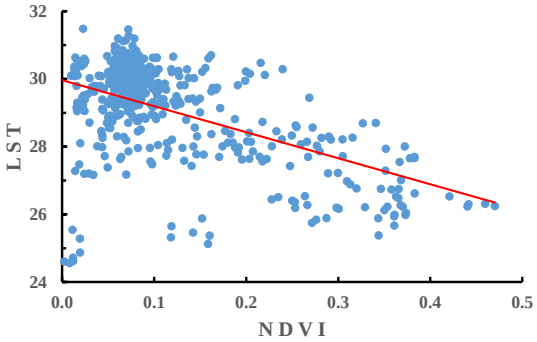

Fig. 10 NDVI vs LST of Surabaya City 2020

condition of land surface covered by vegetation. With a value between 0-1, the higher NDVI indicated that the land surface has a higher land surface covered by vegetation. The minus NDVI indicated that land has not been covered by vegetation such as open land, water, sand, wetted open land, and bare land.

The land cover type and NDVI condition is closed related to the land surface temperature. The analysis result shows that the land cover which has a high reflectance material to solar radiation will have a high LST. Finally, from this research, it can be concluded that NDVI is inversely proportional to LST. An increase in NDVI will have the effect of decreasing LST and conversely, a decrease in NDVI will increase NDVI. This phenomenon is shown by the change in LST of Malang and Surabaya Cities from 2015 to 2020 caused by changes in NDVI. Therefore, changing land cover from vegetation to non-vegetation will increase LST. This phenomenon almost occurred in urban areas due to dynamic development such as Malang and Surabaya Cities Indonesia.

ACKNOWLEDGMENTS

This research is partially funded by the Associate Professor Doctoral Research Grant (Hibah Penelitian Doktor Lektor Kepala), Faculty of Engineering Universitas Brawijaya in the 2022 fiscal year. The

authors also thank Dinas Pengairan Provinsi Jawa Timur for providing the temperature data. Finally, the authors are indebted to the USGS server (https://earthexplorer.usgs.gov/).

REFERENCES

[1] Putra T. H. A., Istijono B., Aprisal, Rusman B., and Ophiyandri T. The Dynamics of Land Cover Change and Casual Factors in the Kuranji Watershed. International Journal of Geomate, Vol.21, Issue 84, 2021, pp.69 - 75. DOI: https://doi.org/10.21660/2021.84.GX126

[2] Fonji S . F. and Taff G. N., Using Satellite Data to Monitor Land-use Land-cover Change in North-eastern Latvia. Springer Plus Vol. 3, Issue 61, 2014. doi: 10.1186/2193-1801-3-61

[3] Mohajane M., Essahlaoui A., Oudija F., El-Hafyani M., El-Hmaidi A., El-Quali A., Randazzo G., and Teodoro A. C., Land Use/Land Cove (LULC) Using Landsat Data Series (MSS, TM, ETM+, and OLI) in Azrou Forest in the Central Middle Atlas of Morocco. Environment, 5, 131, 2018. doi:10.3390/environments5120131

[4] Wibowo A., Yusoff M. M., Adura T. A., and Shidiq I. P. A. Urban Heat Hazard Threat on University Campus (University of Indonesia and University of Malaya). International Journal of Geomate, Vol.19, Issue 76, 2020, pp. 141 - 148. DOI: https://doi.org/10.21660/2020.76. 95107

[5] Sahebjalal E. and Dashtekian K., Analysis of land use-land covers changes using normalized difference vegetation index (NDVI) differencing and classification methods. African Journal of Agricultural Research, Vol. 8, Issue 37, 2013, pp. 4614 - 4622. DOI:10.5897/AJAR11.1825

[6] Aburas M. M., Abdullah S., H., Ramli M. F., and Ash'aari H. Measuring Land Cover Change in Seremban, Malysia Using NDVI Index. International Conference on Environmental Forensics, Conference proceedings, in Procedia Environmental Sciences, Vol. 30, 2015, pp. 238 - 243.

[7] Zhao L., Zhang P., Ma X., and Pan Z. Land Cover Information Extraction Based on Daily NDVI Time Series and Multiclassifier Combination. Mathematical Problems in Engineering, Vol. 2017. https://doi.org/10.1155/2017/6824051

[8] Hussain S., Lu L., Mubeen M., Nasim W., Karuppannan S., Fahad S., Tariq A., Mousa B. G., Mumtaz F., and Aslam M. Spatiotemporal Variation in Land Use Land Cover in the Response to Local Climate Change Using Multispectral Remote Sensing Data. Land, Vol. 11, 2022, pp. 595. https://doi.org/10.3390/land11050595.

[9] Mwangi P. W., Karanja F. N., Kamau P. K., Analysis of the Relationship between Land Surface Temperature and Vegetation and Built-Up Indices in Upper-Hill, Nairobi. Journal of Geoscience and Environment Protection, Vol. 6, 2018, 6, pp. 1-16. http://www.scirp.org/journal/gep

[10] Guha S. and Govil H., Land Surface Temperature and Normalized Difference Vegetation Index Relationship: a Seasonal Study on a Tropical City. SN Applied Science, Vol. 2, 2020, pp. 1661. https://doi.org/10.1007/s42452-020-03458-8

[11] Solórzano J. V., Mas, J. F., Gao, Y., and Gallardo-Cruz, J.A. Land Use Land Covver Classification with U-Net: Advantages of Combining Sentinel-1 and Sentinel-2 Imagery. Remote Sensing, Vol. 13, 2021, pp. 3600. https://doi.org/10.3390/rs13183600

[12] BPS Malang Municipality, Malang Municipality in Figures, 2021. https://malangkota.bps.go.id/publication/2021/02/26/4ccb213f9a2a7ba007bff7c4/kota-malang-dalam-angka-2021.html

[13] Rwanga S. S., and Ndambuki J. M. Accuracy Assessment of Land Use/Land Cover Classification Using Remote Sensing and GIS, International Journal of Geosciences, Vol. 8, 2017, pp. 611 - 622. http://www.scirp.org/journal/ijg

[14] Pande C. B., Moharir K. N., and Khadri S. F. R. Assessment of Land-use and Land-cover Changes in Pangari Watershed Area (MS), India, Based on the Remote Sensing and GIS Techniques. Applied Water Science, Vol. 11, Issue 96, 2021. https://doi.org/10.1007/s13201-021-01425-1

[15] Wright C. K., De-Beurs K. M, Henebry G. M. Combined analysis of land cover change and NDVI trends in the Northern Eurasian grain belt, Front Earth Sci, Vol. 6, Issue 2, 2012, pp. 177 – 187. https://doi.org/10.1007/s11707-012-0327-x.

[16] Guilherme A. P., Biudes M. S., Mota D. dos S., De Musis C. R. Relationship between soil cover type and surface temperature. Sociedade & Natureza, Vol. 32, 2020, pp. 539 - 550. DOI: 10.14393/SN-v32-2020-47462

8th Int. Conf. on Structure, Engineering & Environment (SEE), Mie, Japan, Nov.10-12, 2022, ISBN: 978-4-909106094 C3051

POLICIES AND PLANS FOR OPEN SPACE MANAGEMENT IN PARTNERSHIP IN POST-INDUSTRIAL LANDSCAPES

Tomoko Miyagawa[1], Clare Olver[2], Noriko Otsuka[3], and Hirokazu Abe[4]
[1]Faculty of Systems Engineering, Wakayama University, Japan; [2] The Mersey Forest, the UK;
[3]ILS Research gGmbH, Germany; [4] Cyber Media Centre, Osaka University, Japan

ABSTRACT

Post-industrial landscapes have transformed through environmental regeneration, creating open spaces with public access. To maintain quality in the long term, working in a partnership with voluntary, community, public and private organisations may be necessary. This paper examines policies and plans for open space management through community forestry activities in the post-industrial landscapes of St. Helens in the UK, where the Council has been updating masterplans for green infrastructure. The study methods used here are literature reviews and interviews. This study undertook the two case studies of action plans and one of the strategic sites from the plan which are included within the masterplans for green infrastructure planning within St. Helens. Findings suggest that policies and updated plans can be tools for maintaining sufficient standards of open spaces in restored post-industrial landscapes and to be well used by the community. However, this needs to be in tandem with partnerships working towards long-term management by securing resources for open spaces.

Keywords: Community Forestry Activities; Environmental Regeneration; Green Infrastructure; long-term management

INTRODUCTION

Environmental regeneration, through community forestry activities by public, private, and community sector organisations, has been led by the Mersey Forest Partnership in the northwest of the UK since the 1990s. The Mersey Forest is one of England's Community Forests which have been transforming the landscapes and communities in and around our largest towns and cities [1]. Through its partnership approach environmental regeneration and landscaping in post-industrial landscapes have created new open spaces, that are publicly accessible and require long-term management and continual enhancement. Environmental regeneration becomes particularly important for managing and improving the quality of post-industrial landscapes, as it has been suggested that 'even more importantly some specific pollutant problems remain and will intensify' [2]. Therefore, it is important to consider 'the cumulative impacts of change' of newly created large areas of publicly accessible open spaces by incremental planting and by gaining public access to small parcels of former derelict and other lands' [3]. Accessibility matters particularly for the public, because 'access to nearby nature that allows practical engagement' can lead to improve 'in the challenging settings of socially deprived urban areas' [4]. Simultaneously, examining the policies that support and ensure long-term management can also be necessary [5].

Long-term management can be a key issue in engaging communities in green infrastructure planning, that is, having the potential to reduce public money to be spent, while participation can bring a sense of ownership and inclusion of the local community [6]. Although Green Infrastrucuture planning initially aims to respond the needs of neighbouring communities by increasing the amount of green space for local benefits, such planning focus tends to be shifted in practice. This is because some stakeholders put more priorities on economic benefits (e.g. increasing property values and place re-branding to attract new residents, business growth and investment, [7]) than solving social and environmental issues in local neighbourhoods [8]. Moreover, it has become evident that there are gaps in place-making and place-keeping, various understandings of concepts among users, practitioners, and policy makers due to 'its complexity and the wide implications', and a well-established system for evaluating quality open space in the long term [9]. Thus, long-term management is particularly important given that post-industrial landscapes contribute through their green infrastructure in terms of restoring ecology and improving the health and quality of life of neighbouring communities [10]- [11].

To secure costs and time for sustainable management, long-term management matters for its 'functionality and community appeal' [12]. The UK government's policy document 'The 25 Year Plan for the Environment' recognises the pivotal role of public, private, and philanthropic funding to protect and

enhance the environment, including its role in developing and managing the Northern Forest, a new landscape-scale tree planting project [13]. In the case of the Mersey Forest, 'community forestry approaches have been achieved through a partnership, of over twenty years, with landowners and local partners led by the Mersey Forest team, which has secured resources for long-term management. Working in partnership enables a diverse network of people and groups to share expertise and diversify activities [14]. In case of the Northwest of England, since 2004, the Mersey Forest team has led and helped moderate policy making with the new agenda of green infrastructure [1], [15]. In terms of benefits in building community cohesion, it may also be important to work in partnership to regenerate damaged landscapes arising from contamination or dereliction, to empower the local community with enthusiasm [3].

The ultimate aim of this paper is to discuss key factors which have contributed to a better partnership working in environmental regeneration by reviewing local planning policies and presenting concrete examples from two case studies in which the Mersey forest has been involved over the last 20 years.

Study Methods

This paper examines policies and plans supporting the roles that the Mersey Forest Partnership can play in the management of open space in post-industrial landscapes, focusing on St. Helens, located within the Liverpool City Region. With an area of approximately 13,900 hectares [16] and a population of 180,585 in 2019 [17], St. Helens developed rapidly during the Industrial Revolution through coal mining and glass making which left a legacy of damaged landscapes in post-industrial sites [16], [18]. The St. Helens Council has experience in planning and revitalising post-industrial landscapes since the 1980s [5], [19]. Post-industrial landscapes in St. Helens have been transformed into a variety of open spaces, with further opportunities as many operational landfill sites have planning permission for open space post closure. Further, the restoration requires a certain time frame, some for around ten years or more. To maintain the quality of open spaces at sufficient standards, while simultaneously being well-used by the community, it may be necessary to consider planning policies that support and ensure long-term management [5].

Thus, relevant literature was identified using search engine platforms such as Google Scholar, with keywords including 'environmental regeneration', 'local planning policies', 'St Helens', 'long-term management', and 'open space'. The St. Helens Council has adopted planning documents as follows: Core Strategy Local Plan (adopted October 2012), Saved Policies of the 1998 Unitary Development Plan, Joint Merseyside and Halton Waste Local Plan (adopted July 2013) and the Bold Forest Park Area Action Plan (adopted July 2017). This study examined the two case studies of Bold Forest Park and Colliers Moss Common using relevant maps and revising planning documents including statutory and non-statutory plans regarding open space management policies in St. Helens focusing on post-industrial landscapes in St. Helens. Firstly, Bold Forest Park is a priority area identified in local statutory plans to promote better quality of open spaces for community assets. The second case study is Colliers Moss Common which demonstrates the importance of securing resources for continuous management, and was introduced as a best practice in creating community open space and nature conservation in England [19]. This research also incorporated interviews with representatives from the Mersey Forest team, and a local authority officer from the planning department of St. Helens Council to find out the main issues for long-term management. The interviews were held in August, 2018, and were approximately one hour each.

OPEN SPACE MANAGEMENT POLICIES IN ST. HELENS

The St. Helens Council has undertaken open space management through overall policies for the protection of such spaces and promotion of green infrastructure for 'health, recreation, tourism, and biodiversity', as well as to support economic viability and to act against climate change [18]. Over the past 25 years, the Council has been working closely with the Mersey Forest team to create a network of community woodlands. In terms of protecting open space, the designation of statutory registered sites and the Green Belt have been implemented to secure land for creating and maintaining green space for a long time. According to the local plans adopted in St. Helens, the overall policies are relevant to open space management. To promote an area-wide strategy for green infrastructure at the regional level, the Council has been working with the Mersey Forest Team to enhance existing and newly created networks of community woodlands.

Protection of Open Space and Promoting Green Infrastructure

Open spaces within urban areas are under pressure from housing developers; thus, a sufficiently robust policy framework is necessary. The St. Helens Council has a policy of not permitting development that would lead to the loss of existing open space of specific value, or where the development adversely affects the amenity of open space or a Green Belt [16]. Protection of open spaces is promoted in terms of multi-functionality, for example, recreation, amenity

to provide quality public open spaces, conservation of nature, and creation of culture and education [16]. Open spaces can be connected by strategic networks of greenways [18] including privately-owned land with 'major linear features', such as 'river valleys, canal systems and disused railway lines' (Fig.1). In fact, the St. Helens Council sought to promote more public access and to develop its network of linear greenways [16]. The St. Helens Council has been active in promoting the value of green infrastructure to local communities, to increase additional open spaces and to seek 'positive uses' by protecting, managing, and enhancing with detailed policies [18].

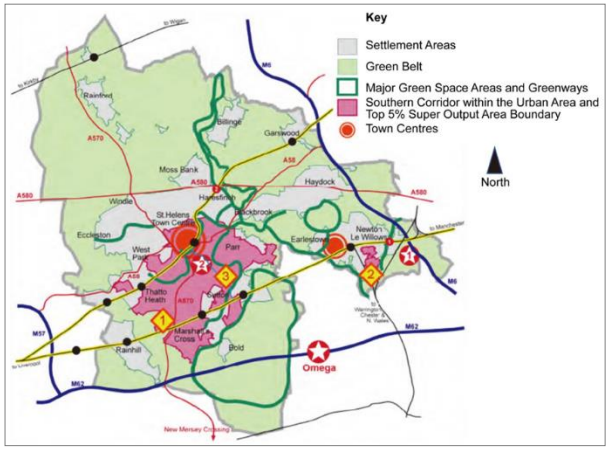

Fig. 1 Map of case study areas with some amendments [18]

St. Helens Council also recognises derelict land as an 'existing or potential value of open space'. According to a survey of open space in 1990, approximately 505 hectares of land were classified as vacant or derelict, and they have the potential to provide functions as open spaces [16]. St. Helens Council has been ensuring the transformation of derelict land into open spaces such as woodlands or grasslands with increased biodiversity; therefore, the improvement of access by local communities and management for conservation of biodiversity are the future tasks and priorities [18]. One approach for transforming vacant or derelict land into open spaces in St. Helens was the near-decade-long Wasteland to Woodland programme.

The Mersey Forest

St. Helens Council was a founding local authority partner in the Mersey Forest Partnership in 1994. Since then, over 3,750 hectares of new habitat and woodland has been created, with the aim of increasing up to 8,000 hectares in the long term [18]. The St. Helens Council supports the delivery of the Mersey Forest Plan through policies within its adopted local plans and through the promotion of additional areas for further development of the community forest. The Mersey Forest Plan is a long term and strategic guide to the work of the Forest and its partners. It is recognised in the National Planning Policy Framework as a material consideration in preparing development plans and deciding planning applications. The Council has played an important role in transforming vacant and derelict land into woodlands, such as the Wasteland to Woodland programme which recognised the potential and character of the southern and eastern areas of the borough [16]. The Mersey Forest Partnership has promoted the benefits of regenerating post-industrial landscapes in terms of 'health, recreation, tourism and biodiversity' as well as reducing negative impacts of climate change, through policies and activities, such as indicative woodland cover targets, and partnership working to support community forestry activities [1], [18]. A partnership between public and private landowners, local authority officers, government organisations, and the community was coordinated by the Mersey Forest which played a key role in transforming the post-industrial sites into green open spaces.

Wasteland to Woodland

The Wasteland to Woodland programme ran from 1989 to 1998 [20]. It created at least 300 hectares of new habitat and woodlands in St. Helens [18] through large-scale tree planting on parcels of derelict land, including previous colliery sites. Much of the land was privately owned with no public access; therefore, the project aimed to address the importance of large-scale environmental regeneration for economic benefits, and attracting investment. It also aimed at meeting the needs of the community through accessible woodlands close to the urban population where possible [20].

The strong partnership programme was led by a steering group comprising representatives from public and private landowners, local authority officers, and government organisations, and was coordinated by environmental charity, the Groundwork Trust. The individual projects became known by the names of the former collieries and transformed into publicly accessible woodlands, such as Sutton Manor, Clock Face, Colliers Moss Common (formerly called Bold Moss Common), and Lyme & Wood Pits (Fig.2) [18]. These sites consisted of spoil heaps, making up around 75 percent of the project area of 330 ha in total [20], and have been included in the plan for Town in the Forest and Bold Forest Park. These have contributed to transforming the southern part of St. Helens into the area addressing both economic and environmental regeneration (Fig.3-4) [21]-[22].

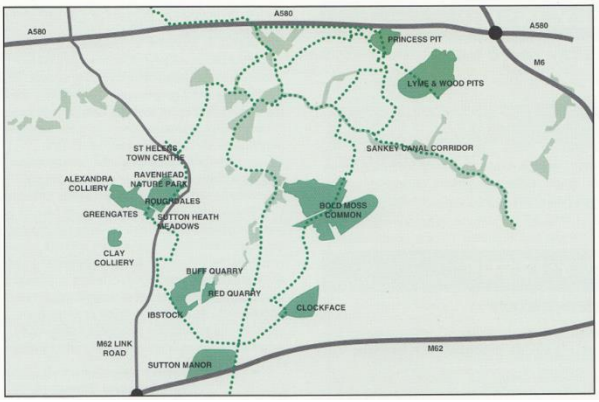

Fig. 2 Map of former collieries sites [20]

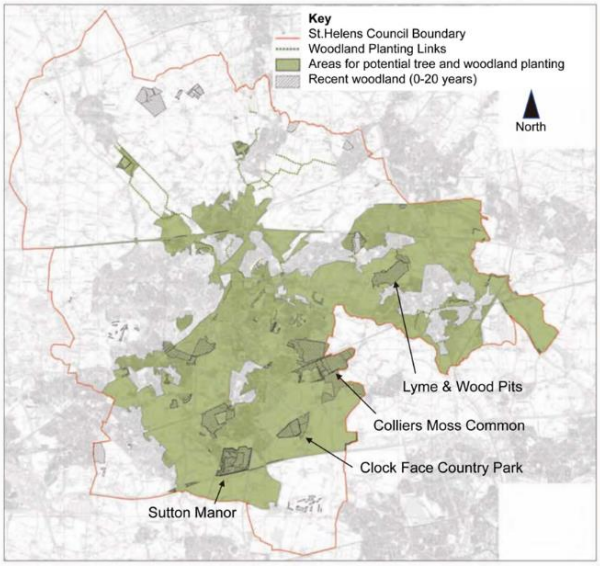

Fig. 3 Map of the area for tree planting with some amendments [21]

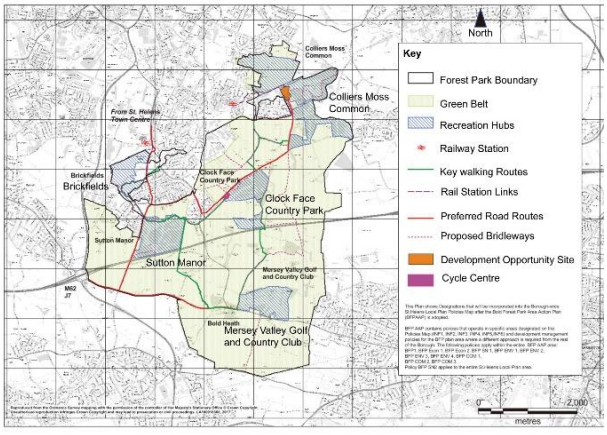

Fig. 4 Map of the Bold Forest Park with some amendments [22]

Town in the Forest

While newly planted mature woodlands can have a positive impact in regenerating and enhancing an area [1], [21]; they can be opportunistic. Over one-third of all the woodlands in St. Helens is recently regenerated and these newly planted trees require substantial time to grow to maturity [21]. To support and guide this landscape transformation, a woodland strategy was published by St. Helens Council in 2006: "Town in the Forest" to guide the creation of a network and enhancement of woodlands. The plan identified sites for developing woodlands which would contribute to and enhance the landscape character of the area, with diversity and distinctiveness [21]. The plan aimed to promote greening and developing linear forests in urban areas, particularly in the urban fringe through renewal processes and connecting green infrastructure to community woodlands, so that the regenerated area could also potentially contribute to the rural economy [18]. This not only could create direct employment but also to provide a healthy working environment in leafy settings to attract inward investment, and contribute to increasing property values [21]. Therefore, improving the image of the area for economic benefits was suggested through environmental regeneration [21].

The plan of St. Helens Town in the Forest Strategic Vision Document analysed the area in terms of transport network, nature conservation, education, recreation, and regeneration opportunities. It identified the sites, including Sutton Manor, Clock Face, Colliers Moss Common (formerly Bold Moss Common), and Lyme and Wood Pits as recent woodlands created within the past 20 years, and also identified areas of potential tree and woodland planting (Fig.3) [21]. The plan suggested that a network between these open spaces be developed to create a woodland framework around the mentioned sites (St. Helens Council, 2006). The Mersey Forest Plan for St. Helens also suggests 20-30% increase in woodland planting on urban fringes, which includes these key sites [1], [21].

Nature Conservation and Site Protection

The St. Helens Council published a Policy for Nature in 1986, defining the importance of wildlife conservation, providing informal space for recreation and education, and improving the image of the borough [16]. Thus, the multi-purpose value of trees, woodlands, and hedgerows will be protected and enhanced by the Council [18]. Statutory site protection, such as local nature reserves, ancient woodlands, local wildlife, and geological sites were adopted to secure the continuity of open spaces and enhance protection of the natural environment. For example, the Northern part of Colliers Moss Common was designated as a local nature reserve, a statutory designation [23]. Sutton Manor, Clock Face, Colliers

Moss Common, and Lyme & Wood Pits were designated as local wildlife sites. This is a non-statutory designation, locally registered within north Merseyside to represent ecological diversity [24]. St. Helens Council addressed the importance of biological, educational, and community interests and value on these sites [16], and therefore developed a masterplan for green infrastructure which is now recognised as one of the main statutory planning policies along with the Core Strategy and the Local Plan.

Green Belt

The Green Belt in St. Helens was designated in 1983 to control urban sprawl, to conserve the countryside, to support urban regeneration, and 'the permanence and protection of Green Belt boundaries', as well as promote the inclusion of land in the Green Belt [16], [25]. The release of the Green Belt for land supply is a sub-regional issue in the Liverpool City Region to be considered in terms of sustainability to minimise the impact on the remaining Green Belt [18].

The Green Belt in St. Helens is located around the urban fringe and extends into the urban area. Around 50% of the borough is categorised as 'rural' (Fig.1) [16]. Most of the land within the Green Belt in St. Helens in the north of the borough is a high-quality agricultural land; however, it also includes seven golf courses; in the south, the Green Belt includes newly created community woodlands on former colliery sites and agricultural lands [18]. Thus, the Green Belt can promote the creation of a network of open spaces with an area-wide environmental policy for conservation.

The next section presents the masterplan for increasing woodlands and two case studies, in St. Helens, which are considered a good practice in creating community open spaces in post-industrial landscapes. First the concept of an action plan of Bold Forest Park will be examines and followed by, an example of a strategic site, Colliers Moss Common from the plan.

CASE STUDY OF STRATEGIC AREAS IN THE SOUTH OF ST. HELENS

Bold Forest Park- A Case Study

Bold Forest Park was recognised as a priority area to increase green infrastructure within the core strategy and local plan in St. Helens [18]. The Bold Forest Park Area Action Plan was adopted in 2017 to regenerate 320 hectares of land with a legacy of raised spoil heaps of the former collieries industry [22]. The vision of the Action Plan was to 'create new economic opportunities through sustainable development' by promoting leisure and tourism and creating networks of open spaces as assets for attracting more local communities [18]. The plan aims to support the local economy by increasing opportunities for recreation [22] by promoting Bold Forest Park as a gateway to the town and as a model case for managing large-scale open spaces of former collieries. The Mersey Forest plan also recognises the area represents potential sites for leisure activities by 'improving tourist infrastructure and creating new visitor attractions' [1].

Most of the area is designated within the Green Belt with five recreation hubs, including Sutton Manor, Clock Face, and Collier Moss Common connected by key walking routes, road links, and proposed bridle ways to enhance its network and improve access. There are two railway stations between Liverpool and Manchester close to Brickfields and Colliers Moss Common, which makes Bold Forest Park easily accessible by train. The M62 motorway transects Forest Park, adjacent to the Griffin Wood and Sutton Manor. The Mersey Forest team is seeking a partnership to find resources to deliver the aspirations of the Area Action Plan that are being developed.

Colliers Moss Common - A Case Study

Collier Moss Common, formerly called Bold Moss Common, is a former mossland complex which was subject to tipping from the former Bold Colliery and Bold Power Station. Owned by the National Coal Board, the site ownership was transferred to the Groundwork Trust St Helens, Sefton, and Knowsley in 1990, who subsequently undertook an ecologically led restoration to create a valuable community asset from derelict land. Restoration was completed in 1994. In 2005, the site was designated by the St Helens Council as a local nature reserve in recognition of the site's ecological and social importance.

The Groundwork Trust for St Helens went into receivership in 2006 and the land was declared bona vacantia, coming under the remit of the Duchy of Lancaster, as owner of last resort with no management of the open space. This led to vandalism, and the site attracted anti-social behaviour. Having unsuccessfully attempted to access government assistance to address the problem, St Helens Council requested that the charity Community Forest Land Trust (CFLT) acquires ownership of the land in order to seek a partnership-led approach to a solution. CFLT took ownership in 2014. It is run by a board of five voluntary trustees and, with no regular funding, must generate income to carry out its activities.

Owing to the ownership of the site, CFLT has facilitated a range of bids for external funding. In total, £213,000 external funds were generated for the improvement of the site from a variety of funding sources. Concurrently, a number of funding bids have been unsuccessful, and clearly demonstrates that open

spaces require continuous management by securing funding, due to the absence of sustainable management plans that can cause anti-social behaviour. It is part of the Collier Moss Common Recreational Hub in the Bold Forest Park Area Action Plan.

DISCUSSIONS

The industrial landscape of St. Helens has been developed for over 250 years [20]. In comparison, policies for open space management and several action plans for transforming post-industrial sites have been undertaken for environmental regeneration in St. Helens over the last 30 years since the 1990's. Environmental regeneration requires extensive time for trees to grow into mature woodlands, due to the complexity of 'greening' process and 'the results are often only partially successful' [26]. Open space management policies in St. Helens are continuously identifying strategic sites, e.g., Sutton Manor, Clock Face, Colliers Moss Common, and Lyme & Wood Pits to promote environmental regeneration with long-term management (Fig.2-4). For example, St. Helens Town in the Forest Strategic Vision Document in 2006 promoted additional planting by identifying existing and new woodland planting to increase the connectivity between woodlands created at different times; therefore, the network of green spaces was a key issue. Sutton Manor, Clock Face, and Colliers Moss Common can be categorised into 'natural and semi-natural sites, including woodlands, grasslands, and former collieries and quarries [27], which play an important role in linking nature and former industrial sites. It can demonstrate activities on sites from former industrial to environmental regeneration to be opened to the communities, by utilising hill-shaped landforms which can become a landmark to the area. Lyme & Wood Pits was a former colliery and a waste disposal site, and is being reclaimed in the process of waste disposal operations, following the restoration and the creation of new access to surrounding neighbourhoods, it has opened as a country park [18]. In terms of the open space assessment based on the Green Flag Award scheme, which sets a management standard for parks and open spaces in England and Wales, the results have shown that Sutton Manor, Clock Face, and Lyme & Wood Pits are undertaking quality of management, while Collier Moss Common needs further improvements in the quality of green open spaces, access, security, facilities, maintenance, and use by different groups of people [27].

This study undertook the two case studies of action plans and one of the strategic sites from the plan which are included within the masterplans for green infrastructure planning within St. Helens. The Bold Forest Park Area Action Plan in 2017 was a statutory planning document with a focus on economic impacts, such as leisure and tourism, through the development of Forest Park as a sub-regional tourist offering located between Liverpool and Manchester. The case of Colliers Moss Common has suggested that continuous management and fundamental condition of the quality of the environment on sites are required for further improvement and enhancement as it became clear from the open space assessment in the previous section. The case studies found an essential role of partnership working as one of the priority issues in sustainable Green Infrastructure planning, and this point has been echoed by a number of previous research [6], [14], [28]- [29]. The case studies also found partnership working with various organaisations can contribute to long-term management by enhancing assets and functions of Green Infrastructure for social, economic, and ecological benefit [28]- [29].

According to an interview given by a former planning officer of St. Helens Council, long-term open space management is an important issue, and it can be challenging to secure resources [9], [30]-[34]. Collaboration of experts with specific skill sets is important, and the same planning officer interviewed maintains that the quality of open space matters, if open space is not well-managed, 'it can cause problems and bring no benefits to the community'. In terms of collaboration, it may be necessary to look after landscaping former landfills, which requires the involvement of experts in waste and mineral management, ground maintenance, as well as the planning department. The quality of open space can only be ensured when such partnerships are in place, based on a long-term strategic maintenance plan.

In St. Helens, The Mersey Forest has been leading the partnership in applying for funding and undertaking projects, while the St. Helens Council has updated relevant plans for green infrastructure planning. Therefore, partnership plays a key role in collaborating with a wide range of people to deliver the plan and undertake long-term management. It requires securing regular funding to maintain open spaces, which has been an issue. The UK government policy, the 25 Year Plan for the Environment, recognises the significance of securing a mixture of public and private funding and financing with various partners for long-term management [13]. This point has been evident in the two case studies, and constant efforts made by the Mersey Forest and St. Helens Council in securing resources for maintenance and improvement are the key ingredients for providing neighbouring communities with high-quality open spaces in post-industrial landscapes.

CONCLUSIONS

In St. Helens, through environmental regeneration, networks of publicly accessible open

spaces have been developed supported by policies for their long-term management. Over the past decade, green infrastructure masterplans have been revised and published by St. Helens Council alongside the area-wide Mersey Forest Plan. In terms of the delivery of these plans, the Mersey Forest Partnership has and continues to secure resources from public and private landowners, local authorities, charities, government organisations, and the community. It is also highlighted in the adopted local plans, as well as The Mersey Forest Plan which identifies priority areas for planting more trees, as a recommendation to enhance community forestry activities. In response to local planning policies and to address local issues, action plans have been created and updated to meet the needs of the area and the community in accordance with the progress of environmental regeneration for further enhancement. Key restoration and community woodland projects on former collieries represent a variety of open spaces, and demonstrate that post-industrial landscapes can be a driver for recreation development and community engagement. In conclusion, to promote long term open space management, policies and updated plans can be a basis for introducing planning tools to maintain sufficient standards in restored post-industrial landscapes and to be well used by the community. However, these policies and action plans need to work alongside delivery by partnerships, to facilitate securing resources for long term management of open spaces to improve and maintain environmental regeneration.

ACKNOWLEDGMENTS

The authors would like to express their gratitude for the financial support provided by the Japan Society for the Promotion of Science (17K06705, 18K18602). The authors would also like to thank the Development Plans Section, St. Helens Council, and Northwest of England Groundwork Trust for providing information.

REFERENCES

[1] The Mersey Forest, More from trees, The Mersey Forest Plan. 2014. https://www.merseyforest.org.uk/about/plan/

[2] Freer-Smith, P., Environmental Change and the Sustainability of European Forests. Journal of Sustainable Forestry, Vol. 24, No.2-3, 2007, pp. 165-187.

[3] Roe, M., Exploring future cultural landscapes. In: New cultural landscapes, M. Roe & K. Taylor, Ed. Routledge, 2014, pp.241-269.

[4] Brook, I., The Importance of Nature, Green Spaces, and Gardens in Human Well-Being. Ethics, Place and Environment, A Journal of Philosophy & Geography, Vol.13, No.3, 2010, pp.295-312.

[5] Miyagawa, T., Olver, C., Otsuka, N. & Abe, H., Environmental regeneration and management in partnership in the Northwest of England. International Journal of GEOMATE, Vol.16, Issue 54, 2019, pp.9-15.

[6] Wilker J., Rusche, K., & Rymsa-Fitschen, C., Improving Participation in Green Infrastructure Planning. Planning Practice and Research, Vol.31, No.3, 2016, pp.229-249.

[7] Forest Research, Benefits of green infrastructure. 2010.

[8] Horwood, K., The Development of Green Infrastructure Policy in the North West Region of the UK 2005–2010. Planning Practice and Research, Vol.35, No.1, 2020, pp.1-17.

[9] Dempsey, N. & Burton, M., Defining place-keeping: The long-term management of public spaces. Urban Forestry & Urban Greening, Vol.11, No.1, 2011, pp.11-20.

[10] Williamson, K.S., Growing with Green Infrastructure. Heritage Conservancy, 2003, pp.1-20.

[11] Handley, J., Pauleit, S. & Gill, S., Landscape, sustainability and the city. In: Landscape and Sustainability, J. F. Benson & M. Roe, Ed. Routledge, 2007, pp.167-195.

[12] Davies, C., Old culture and damaged landscapes: The new cultural landscapes of post-industrial sites in Britain. In: New cultural landscapes, M. Roe & K. Taylor, Ed. Routledge, 2014, pp.41-58.

[13] HM Government., A Green Future: Our 25 Year Plan to improve the Environment. 2018. https://www.gov.uk/government/publications/25-year-environment-plan

[14] Miyagawa T., Olver C., Otsuka N., Kurose T. & Abe H., Lessons and achievements from the Mersey Forest by networking partnership for twenty years. International Journal of GEOMATE, Vol.15, Issue 48, 2018, pp.48-54.

[15] Mell, I., What Future for Green Infrastructure Planning? Evaluating the Changing Environment for Green Infrastructure Planning Following the Revocation of Regional Planning Policy in England. Planning Practice and Research, Vol.35, No.1, 2020, pp.229-249.

[16] St. Helens Council., St. Helens Unitary Development Plan (Originally Adopted by St. Helens Metropolitan Borough Council on 2nd July 1998), 1998. https://www.sthelens.gov.uk/planning-building-control/planning-policy/unitary-development-plan/

[17] St. Helens Council, info4St.Helens website. 2019. https://info4.sthelens.gov.uk/

[18] St.Helens Council., St. Helens Core Strategy. 2012.https://www.sthelens.gov.uk/media/3385/sthelens-local-plan-core-strategy-october-2012.pdf

[19] Ling, C., Handley, J. & Rodwell, J.,

Restructuring the post-industrial landscape: A multifunctional approach. Landscape Research, Vo.32, No.3, 2007, pp.285-309.

[20] Groundwork St Helens, Knowsley & Sefton., Wasteland to Woodland. 1998.

[21] St. Helens Council, St. Helens Town in the Forest Strategic Vision Document. Gillespies, 2006.

[22] St. Helens Council, St. Helens Council, Bold Forest Park Area Action Plan. 2017. https://www.sthelens.gov.uk/planning-building-control/planning-policy/area-action-plans/

[23] Natural England, Designated Sites View. Undated. https://designatedsites.naturalengland.org.uk/SiteSearch.aspx

[24] St. Helens Council, Local Wildlife Sites. Undated. t https://www.sthelens.gov.uk/planning-building-control/natural-built-and-historic-environment/local-wildlife-sites/

[25] St. Helens Council, Green Belt Review December 2018, A Balanced Plan for A Better Future. 2018. https://www.sthelens.gov.uk/media/9432/green-belt-review-2018.pdf

[26] Moffat, A.J., Chapter 21: Green infrastructure and regeneration of brownfield land. In: Handbook on Green Infrastructure, D. Sinnett, N. Smith & S. Burgess, Ed. 2015, pp.395–413.

[27] St. Helens Council, St. Helens Council Open Space Assessment Report. Knight, Kavanagh & Page, 2016.

[28] Mell, I., Can green infrastructure promote urban sustainability? Proceedings of the Institution of Civil Engineers -Engineering Sustainability, Vol. 162, No.1, 2009, pp.23-34.

[29] Lennon, M. & Scott, M., Delivering ecosystems services via spatial planning: reviewing the possibilities and implications of a green infrastructure approach. Town Planning Review, Vol.85, No.5, 2014, pp.563–587.

[30] Thompson, C.W., Urban open space in the 21st century. Landscape and Urban Planning, Vol.60, No.2, 2002, pp.59-72.

[31] Konijnendijk, C.C., A decade of urban forestry in Europe. Forest Policy and Economics, Vol.5, No.2, 2003, pp.173-186.

[32] Reeves, N., The Condition of Public Urban Parks and Greenspace in Britain. Water and Environment Journal, Vol.14, 2007, pp.157-163.

[33] Dempsy, N. & Smith, H. Understanding place-keeping of open space. In: N. Dempsy, H. Smith, & M. Burton, Ed. Place-Keeping Open Space Management in Practice, Routledge, 2014.

[34] Pediaditi, K., Doick, K.J., and Moffat, A.J., Monitoring and evaluation practice for brownfield, regeneration to greenspace initiatives: A meta-evaluation of assessment and monitoring tools. Landscape and Urban Planning, Vol.97, No.1, 2010, pp.22-36.

8th Int. Conf. on Structure, Engineering & Environment (SEE), Mie, Japan, Nov.10-12, 2022, ISBN: 978-4-909106094 C3051

SURVEY ON RESIDENTS' AWARENESS TO BUILD THE SYSTEM OF RESIDENTS'-PATTICIPATION MONITORING FOR SLOPE DISASTER PREVENTION USING THE TILT SENSORS

Zhijun Tang[1], Yoshikazu Miyamoto [2], Shusuke Oji [3] and Hisashi Fujitani [4]
Zhijun Tang [1] in Yamanashi University and Chuo Kaihatsu Corporation, Japan
Yoshikazu Miyamoto [2] in Chuo Kaihatsu Corporation, Japan
Shusuke Oji [3] in Chuo Kaihatsu Corporation, Japan
Hisashi Fujitani [4] in Chuo Kaihatsu Corporation, Japan

ABSTRACT

In recent years, due to the effects of climate change, slope disasters have been occurring frequently and causing severe damage in many places across the globe. In order to reduce the damage of slope disasters, it is important for residents to understand hazards of the slope disaster correctly and protect themselves.

In this paper, we attempt to evaluate risks of slope disasters in local residential area and analyze resident's opinions which gathered trough a workshop with residents about resident's participation slope disaster monitoring using tilt sensor for prevention of slope disaster.

As a result, an overview of the evaluation items for high-risk slopes and their contents was clarified, which had been tacit knowledge, and the structure of local residents' concerns about slopes and their expectations for monitoring by utilizing tilt sensors to take evacuation action.

Keywords: Evacuation, Residents' awareness survey, Slope disaster, Tilt sensor, Monitoring

INTRODUCTION

In recent years, due to the effects of climate change, slope disasters have been occurring frequently and causing severe damage in many places across the globe. In order to reduce the damage of slope disasters, it is important for residents to understand hazards of the slope disaster correctly and protect themselves.

In Japan, there are about 2.7 million dwelling units in contact with the sediment-related disaster warning area, and even if the warning information is transmitted, the damage caused by the delay in escape is constant [1].

There are various factors such as the tendency not to receive warning information as one's own matter, the tendency to avoid evacuation, and the problem of the normalcy bias [2]-[3].

As an aid to solving such problems, by installing an IOT tilt sensor [4], we will directly notify the relevant residents of the warning alarm of sediment-related disasters and encourage the residents to take evacuation actions to protect themselves. The purpose is to verify whether it is possible to build a connection mechanism.

Therefore, after consulting with local residents in Fukuchiyama City, Kyoto prefecture, Japan, where had suffered landslides in the past, to make them aware of the actual slope hazards, we proposed a "slope monitoring system by resident participation using IOT tilt sensors" in which the residents themselves monitor the slopes.

A field survey was conducted in the sediment-related disaster warning area from a geological expert's viewpoints, and high-risk slopes were selected.

A workshop was held for local stakeholders to select houses that should be evacuated to install IOT tilt sensors [4] on selected slopes at high risk of slope failure. In that workshop, the characteristics of the tilt sensors, control thresholds, and lead time for evacuation were explained to the residents to foster their awareness. And then, discussion was held with residents with regard to resident's concern to the slopes and their expectations for monitoring by utilizing tilt sensors to take evacuation action.

In this paper, we attempt to evaluate risks of slope disasters in local residential area and analyze resident's opinions which gathered trough a workshop with residents about resident's participation slope disaster monitoring using tilt sensor for prevention of slope disaster.

ARAKI DISTRICT, FUKUCHIYAMA CITY, KYOTO PREFECTURE

The Araki district of Fukuchiyama City, Kyoto Prefecture, is located in the middle reaches of the Haze River on the east side of the city of Fukuchiyama. The number of households in the district is 67, the population is 157, and the population of elderly people aged 70 and over is 42, as in [5].

As shown in Fig. 1, almost the entire area of the main part of the area is designated as a sediment-related disaster warning area, and part of it is designated as a sediment-related disaster special warning area. There are three evacuation centers in the Araki area: Araki Public Hall at the foot of the mountain, Momijigaoka Hospital, and Toei Junior High School.

In the heavy rains in August 2016, moist air flowed into the stagnant fronts in the Kinki region, and local heavy rains hit the Kinki region and Hokuriku.In Fukuchiyama City, the 24-hour rainfall on the 16th to 17th exceeded 300 mm. In addition, the Yura River temporarily exceeded the flood risk level, and many inland floods and landslides occurred. Evacuation advisories were issued to about 80,000 people throughout Fukuchiyama City, and the Ground Self-Defense Force was dispatched to help. Furthermore, due to this heavy rain, the JR Fukuchiyama Line and the San-In Line were cut off, and the social impact became extremely large. In the Araki district, sediment-related disasters occurred in seven places, such as the collapse of the mountain behind a private house. After that disaster, the voluntary disaster prevention organization by the Araki Neighborhood Association, with the cooperation of the Fukuchiyama City government and Kyoto University, set up its own "evacuation switch" that defines the criteria for residents to start evacuating using landslide potential information and soil rainfall index. [6].

Issues surrounding evacuation information and evacuation behavior

There is multiple awareness of the problem that evacuation information is not directly linked to the evacuation behavior of residents in previous studies on evacuation.

In a study by Takenouchi et al., taking the case of heavy rainfall in northern Kyushu in 2017, they are paying attention to the fact that there are criteria for judgment the area is unique, such as the situation of streams flowing through the district, the inundation situation of houses beside it, and the inundation situation of small bridges in the neighborhood, etc. [7].

From this study, it can be seen that in addition to evacuation information, "external information / situations" such as loud voices, voices of people close to us, behaviors of people around us, and inundating conditions have an effect on evacuation.

On the other hand, Yamori et al.'S research focuses on the inside of the person who received "external information / situation". Disaster information such as disaster prevention weather information and evacuation information are "advanced" and "complex", but residents want to know more about whether they are still okay or really dangerous than detailed evacuation information. This is information that leads to the next action as in [8].

When setting the "evacuation switch" for information that turns on / off the switch inside the person that leads to the next action, not only the disaster prevention weather information provided by the specialized agency, but also the local residents themselves. It is important to utilize a wide range of information such as phenomena that local residents can observe and cases of historical disasters.

Yamori et al. also argues that diversification and double tracking of information that contributes to "switches" is more important than the sophistication of disaster prevention weather information itself when looking at disaster prevention and mitigation in the coming decades.

Based on the above discussion, this paper considers evacuation switches in slope hazards that can be added to the currently applied landslide potential information and soil rainfall indices. Groundwater level and soil moisture content cannot be confirmed without the installation of measuring equipment, and these data in cloud uncertainty because they are indirect methods of observing slope failure potential. In addition, it is dangerous to confirm flooding, inflow water from slopes, and falling pebbles on site. For these reasons, this paper study whether alerts from IOT tilt sensor which measure slope degree directly can be used as evacuation switches.

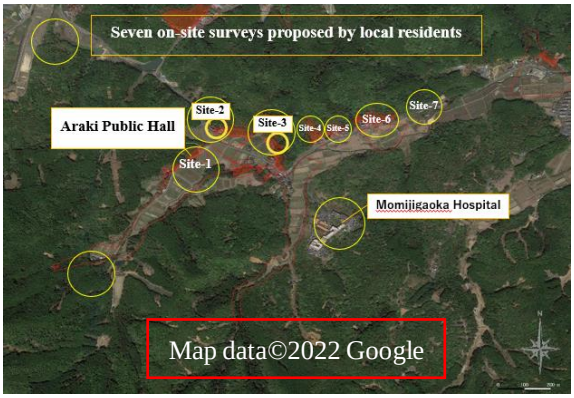

Fig. 1 Araki district, Fukuchiyama City, Kyoto Prefecture (Site 2 and 3 where tilt sensors are installed)

METHOD OF SELECTING SITES FOR TRIAL MONITORING

The selection of sites for trial monitoring was conducted at candidate sites in the Araki area. Seven sites proposed by local residents were inspected together with t them to evaluate the degree of risk of disaster on the slopes. Although there are no established methods for evaluating slope hazard, so, the following six items were identified based on the results of the inspection. Slopes with relatively high levels of each of these six items were evaluated on a three-point scale, and slopes with relatively high levels of each of these items were evaluated as having high risk. As a result, the slopes at Sites 2 and 3 were selected for trial monitoring. (As shown in Table 1 and Fig.1).

Table 1 Evaluation sites for trial monitoring

Evaluation Items	Site						
	1	2	3	4	5	6	7
(a)Slopes with no exposed base rock and collapsible surface soil	△	◎	◎	-	◎	△	△
(b) Evidence of past collapse or cracks	-	◎	○	-	-	◎	◎
(c)Relatively tight slope	◎	◎	◎	◎	○	◎	○
(d)Possibility of collapsed sediment reaching houses, etc	○	◎	◎	△	◎	△	-
(e)Facing a public building	◎	-	-	-	◎	-	-
(f)The degree of damage is assumed to be above a certain scale	○	◎	◎	△	◎	△	○

Note: ◎ : much applicable ○ : applicable
△ : a few applicable - : not applicable

(A) Slopes with no exposed base rock and collapsible surface soil

Talus deposit are present on the slope, or surface soils formed by weathering of base rock or other processes [9]. If the surface soil is not sufficiently covered with forest vegetation, it is considered to be particularly led to collapse [10]. If there are an exposed of hard basement rock on the slope, it is unlikely to collapse except by landslides.

(B) Evidence of past collapse or cracks

If there are traces of collapse or cracks in or near a part of the slope, it is likely to collapse easily. On the other hand, if the entire slope has collapsed in the past and no surface soil is present, the risk of more collapse may be low.

(C) Relatively tight slope

Natural slopes are more easily to collapse if the slope is relatively tight (greater than about 30°). However, even if the slope is relatively tight, the slope is not easily to collapse if there is no collapsible surface soil.

(D) Possibility of collapsed sediment reaching houses, etc.

The risk is high if there is a possibility that sediment from a slope that is expected to collapse will reach houses and other structures that are to be preserved. Even if collapsible surface soil is distributed, it will be not a disaster if it is expected that it will not reach houses and other structures.

(E) Facing a public building

If the conservation target to be damaged in the event of slope failure is a public building such as a shelter, community center, government office, or facility requiring nursing care, the damage may be larger and the risk of disaster is considered higher.

(F) The degree of damage is assumed to be above a certain scale

If the slope collapses, the risk of disaster is considered significant if the damage is expected to be above a certain scale, such as when sediment reaches multiple houses, roads, or other public facilities, or when there is a possibility of causing further damage.

These evaluation items and scales are based on the tacit knowledge of experts and have not yet been established. So, we will attempt this evaluation method to many slopes for establishing from now on.

After selecting the location, we will hold on-site discussions with the house owner (also the landowner of the slope), listen to the situation of past slope disasters, and install a tilt sensor in consideration of the microtopography of the slope, and we examined the position where it to be.

Then, at the position where there is a possibility of collapse, two tilt sensors are installed at site 2 and three at site 3, and started trial monitoring.

WORKSHOP

A workshop on slope disaster evacuation using tilt sensors was held at Araki Public Hall with local

residents, Fukuchiyama City government, and Professor Yamori of Kyoto University.

In the workshop, local residents were made aware of the characteristics and dangers of slopes, the handling of tilt sensors, control thresholds, and evacuation lead times were explained to them. Afterwards, discussions were held on concerns about slopes and expectations for tilt sensors. (As shown in Fig.2).

Local residents' anxiety and concern about heavy rain / sediment disaster

Anxieties and concerns about heavy rains / slope disaster are deep-rooted, especially among local residents.

From the workshop, the opinions on the anxieties and concerns of the local residents regarding heavy rain / sediment disaster were analyzed using the co-occurrence network of text mining analysis.

Fig. 2 Workshop in Araki district.

Analysis method

By performing co-occurrence network analysis, it is possible to visualize word-to-word connections (co-occurrence relationships). The circles in the figure represent the extracted words. The size of the circle indicates the frequency of appearance of words, the higher frequency of appearance, the larger circle. In this paper, we used subgraph detection, which automatically detects and groups words that are relatively strongly connected. The lines in the figure represent the strength of the co-occurrence relationship. The darkness of the line indicates the strength of the co-occurrence relationship, the stronger connection, the darker color of line.

In addition, the Euclidean distance coefficient ("similarity" for words similar to distance) is used on the line representing the co-occurrence relationship. The Euclidean distance coefficient shows the relationship between similarity and distance,

Similar = High similarity = Close distance (small)

Dissimilarity = low similarity = strong characteristics because it is far away (large) [11]-[12].

Analysis results

As a result of morphological analysis of the 9's answers obtained in the workshop, 220 total words and 88 different words were extracted. Figure 3 is a diagram showing the co-occurrence network with a minimum number of occurrences of 2 for the remarks of local residents in the workshop.

The content of the remarks obtained in the workshop is divided into groups by automatically detecting words that are relatively strongly connected to each other, and the results are shown by color coding.

A total of five words were extracted as the answers characteristic of the golden system: "slope," "collapse," "heavy rain," "road," and "scary."

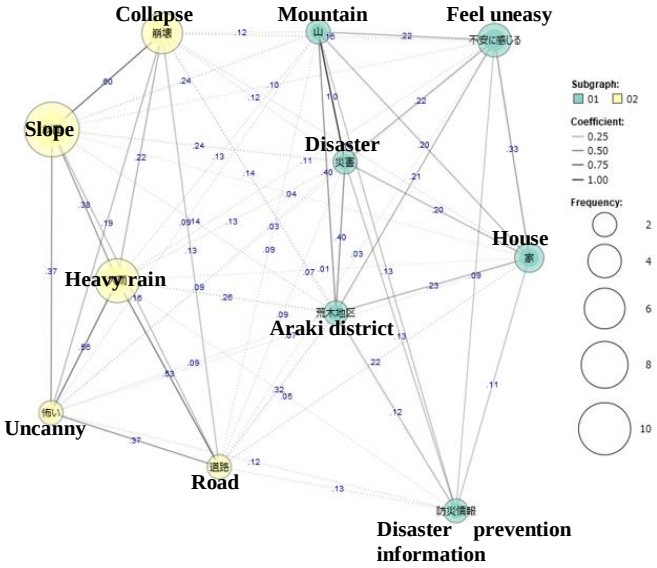

Fig. 3 Results of co-occurrence network analysis.

As the answers characteristic of the light blue system, a total of 6 words were extracted: "Araki district," "disaster," "mountain," "feeling uneasy," "house," and "disaster prevention information."

This is a visualization of the co-occurrence relationship between the yellow system and the light blue system, and the difference in viewpoint depending on the degree of similarity and distance.

In this study, the following four points were clarified as a result of the co-occurrence network analysis of text mining about the anxieties and concerns of the local residents regarding heavy rain / sediment disasters at the workshop conducted for the local residents in the Araki area. (As shown in Fig.3).

(a) Regarding Workshop, the content of the remarks automatically detects words that are relatively yellow connected to each other and divides

them into golden and light blue groups, and the representatives of the words are "heavy rain," "slope," "collapse," and "feel uneasy".

(b) Regarding Workshop, it was recognized that the network of words characteristic of the light blue system has a coefficient of 1.0 for "mountain" and "disaster", and darker line, indicating a strong connection between "mountain" and "disaster.

It was recognized that the network of words characteristic of the yellow system has a coefficient of 0.60 for "slope" and "collapse", and thicker line, the stronger the degree of co-occurrence. It indicates a heavy correlation between "slope" and "collapse".

(c) The connection between "slope," "collapse," "road," and " uncanny" was also observed around "heavy rainfall." It is thought that heavy rain, specific objects such as slope collapse and roads, and the fear of these objects are perceived as a strong relationship.

(d)Focusing on the relationship between the light blue colors, a network of "Araki District" and "disaster," "mountain," "anxiety," "house," and "disaster prevention information" can be seen. This is thought to represent the relationship between the Araki district's elements for disaster anxiety and disaster prevention.

Factors of expectations and expected utilities by local residents

From the workshop conducted in the Araki district, the opinions of local residents regarding their expectations of tilt sensors are shown in a structured diagram (as shown in Fig. 4). This structural diagram visualizes the local residents' statements by breaking them down into their constituent elements and connecting of their statements with arrow lines considering their context. As a result, the statements can be categorized into "factors of expectations" and "expected utilities.

In this diagram, the expected elements of the tilt sensor are: (a) the information can be received by a cellular phone, (b) the risk can be visualized, (c) the information on specific site can be checked, and (d) the information is about a nearby slope. In these elements, (a) and (b) are factors of expectations for the characteristics of the system provided by the tilt sensor. In addition, (c) and (d) are considered to be the reason for the expectation of being able to obtain information on the behavior of the slope itself where the tilt sensor is installed, compared to disaster information issued for a wide area, such as disaster potential information and landslide warning information.

These factors lead to the expectation of utility: (a) → (e) evacuation can be planned, (b) and (c) → (f) to serve as the basis for evacuation decisions, and (d) → (g) early evacuation can be taken into consideration. In other words, slope monitoring with tilt sensors is expected to increase the utilities for evacuation planning, early evacuation, and evacuation decisions by local residents. On the other hand, there is also an opinion that "(i) It will be a reference for deciding when to return home". It is expected to be valuable information for making a decision to return home from the evacuation center.

These factors of expectations and expected utilities by residents should be fully considered in developing a system for participatory slope monitoring.

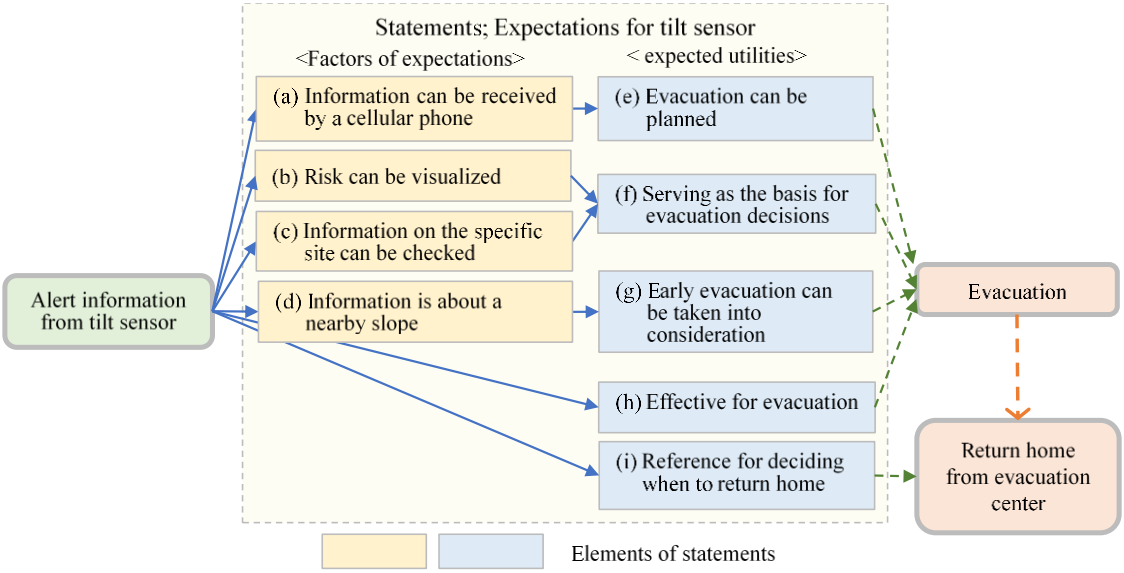

Fig.4 The Structure on factors of expectations and expected utilities by local residents

CONCLUSIONS

In this paper, the overview of the evaluation items for high-risk slopes and their contents was clarified, which had been tacit knowledge, and the structure of local residents' concerns about heavy rain, disaster, slopes and others. In addition, it obtained that the structure of resident's expectations for monitoring by utilizing tilt sensors to take evacuation action.

There are many slope / sediment disaster risk areas due to heavy rain, and it can be said that the risk of slope disaster is high topographically. In fact, it is inevitable that slope disasters caused by heavy rain will occur almost every year. The roles of self-help, mutual assistance, and public assistance are also very important in order to reduce the damage caused by slope disasters. Among them, the basic one is self-help, and by acquiring knowledge about slope disasters, understanding disasters correctly, thinking about what to prepare for, it is important to protect yourself by preparing for a disaster. In order to encourage such self-help efforts, we would like to develop the monitoring system using the IOT tilt sensors with the participation of local residents and provide them with assistance so that they can take appropriate evacuation actions.

ACKNOWLEDGMENTS

We would like to thank the residents of the Fukuchiyama Araki area, Professor Yamori of Kyoto University, and the Fukuchiyama City Crisis Management Office for their great cooperation in this study. We would like to express our deepest gratitude here.

REFERENCES

[1] Yamori.K, Disaster risk sense in Japan and gaming approach to risk communication. International Journal of Mass Emergencies and Disasters, Vol.25 ,2007, pp. 101-131.

[2] Sugiman, T., and Misumi, J., of a new evacuation method for emergencies , Control of collective beha.Development vior by emergent small groups. Journal of Applied Psychology, No.73, 1988, pp. 3-10.

[3] Satoru KIKUCHI , How to recognize cognitive biases in risk perception in case of disasters. Journal of the Japan Landslide Society. Vol.55, No.6, pp.286.201

[4] Uchimura, T., Towhata. I., Wang, L., Nishie S., Yamaguchi, H., Seko, I. and Qiao, J.-P. ,Precaution and early warning of surface failure of slopes by using tilt sensors, Soils and Foundations, Vol.55, No.5 , 2015 , pp. 1086-1099.

[5] National Survey of Japan: https://www.stat.go.jp/.2020.

[6] Japan Meteorological Agency "Weather Cases that Caused Disasters Heavy Rains from Fronts August 15, 2014-August 20, 2014 (Preliminary Report)", August 21, 2014.

[7] Katsuya Yamori,and Kensuke Takenouchi, Setting My Switch For Early evacuation ,2017 Northern Kyushu Heavy Rain Disaster Survey Report,Kyoto University Disaster Prevention Research Institute,2018,pp.99-102.

[8] Katsuya Yamori, Swing, FACP Model.Evacuation Switch Rethinking , Evacuation from Heavy Rain Disasters, Science of Fire and Disaster Prevention, No.134, 2018, pp.7-11.

[9] Kazuya Akiyama , Road earthwork-cutting earthwork / slope stabilization work guideline , Maruzen Publishing Co., Ltd, 2009, pp.14.

[10] Tomoyuki Iida, Knowledge of shallow landslide and deep-seated landslide for technicians , Kashima Publishing Association, 2012, pp. 35.

[11] Koichi Higuchi, Quantitative Analysis of Text-type Data-Differentiation and Integration of Two Approaches, Theory and Method ,No.19(1), 2004, pp101-115.

[12] Lin, C.W. ROUGE., a package for automatic evaluation of summaries. Proceedings of the ACL-04 Workshop Text Summarization Branches Out, Naoki Masuda and Norio Konno, Complex Network Addendum (PDF version), Modern Science, 2004, pp74-81.

8th Int. Conf. on Structure, Engineering & Environment (SEE),
Mie, Japan, Nov.10-12, 2022, ISBN: 978-4-909106094 C3051

CONCRETE BEHAVIOR USING RECYCLED WASTEWATER

Khaled Mohamed Nabil I. Elsayed [1], Gerald Benjamin Felipe Guico [2] and Rabee Rustum[3]
[1,2]Department of Civil Engineering, Heriot-Watt University, United Arab Emirates

ABSTRACT

Concrete is one of the world's most essential and most widely used civil engineering applications, making it the reason to continue the need for development by implementing a more sustainable and less environmentally damaging approach. Water is one of the fundamental pillars in its manufacture and its acquisition of the required mechanical and physical properties through the applicable mixing ratios. So far, tap water is mainly used in this process, whether in the preparation of components, mixing or even after hardening during the curing treatment process. However, this may become a burden in the future due to the continuing increasing scarcity of fresh water, which is only less than 3% of the total water on earth, where regions are suffering due to population growth, climatic changes and poor management of water systems. This paper deals with the use of treated wastewater (recycled water) as an alternative in the concrete industry during the mixing and curing treatment phase by testing the extent of this effect on the mechanical properties of concrete, such as compressive, flexural, and tensile strength from a general perspective. The results show a significant improvement in the compressive strength observed according to the cubes crushing test, reaching 33% after seven days, 70% after 14 days, 56% after 21 days, and the endurance tensile strength test improved by 4% after 28 days.

Keywords: Tertiary Treated Wastewater, Concrete, Tap Water, Mechanical properties.

INTRODUCTION

The construction sector is blamed for being the largest natural resources consumer [7]. Concrete is the most widely used in this industry which is a product of gathered materials mixed as cement, sand, gravel, and with the presence of fresh water. Unfortunately, it is considered one of the largest fresh water-consuming during its different process stages. Practically, one m^3 of concrete requires about 150 litres of fresh water, increasing to 500 litres if counting the washing materials, curing, transportation losses and equipment preparation [11]. It is nearly one trillion m^3 annually reserved for concrete production [12]. It accounts for around 9% of the extraction of fresh water for industrial use, accounting for up to 1.7% of the total extraction of freshwater [1].

Undoubtedly, the stress of global population growth, urbanisation, industrialisation, climate change, poor management of water systems, surface and groundwater contamination, and global warming are the most effective challenging environmental freshwater scarcity [1, 12, 5]. The concrete industry, in general, is not environmentally acting friendly; it is responsible for the emission of more than 1.4 billion tons of CO_2 through the cement process production only, which is equal to 7% of the CO_2 from worldwide production. In addition to the high energy requirement and the excessive use of freshwater in its production processes are not attuned with the sustainability development [13].

Sustainable solutions shall take place in the concrete manufacturing field, as it is strongly needed. The aims were to minimise the freshwater use in the concrete industry, eliminate the continued expanding need for it, and be reserved for drinking purposes only [13]. The freshwater was targeted to be replaced by another alternative that can utilise its functionality in concrete manufacturing. Many types of disposed water were suggested to be investigated by the researchers, for example, treated and untreated wastewater (WW), fertiliser factory WW, textile factory WW, sugar factory WW, service station WW (preliminary, secondary, and tertiary treated) WW, salty water, oily water, stone slurry WW, sludge WW, car wash station WW, and many other types [11].

From the above short list of different water types, the treated wastewater types are the most convenient, sustainably achievable, and globally can be afforded both technically and financially. Moreover, many researchers had achieved progression in studying the differences in mechanically and physically on the concrete when using fresh, tap or potable water compared with wastewater, and it was found to be almost similar or having near properties which promote the idea of replacement in the near future [17].

In this study, an investigation was attempted to focus on the use of the tertiary recycled wastewater as a replacement for the tap water in the concrete mixing and curing stages by studying its impact on mechanical properties as compressive, tensile, and flexural strength and one of the physical properties as workability.

MATERIAL AND METHODOLOGY

Concrete Component

Concrete consists of 3 main components: cement with a sharing rate of 12%, the water of 8%, and aggregate, whether coarse or fine, with a sharing rate of 80% from the mixer [3].

Cement

An ordinary Portland cement of CEMI type and 42.5N class was used under the BS-EN-197-1:2011 speciation. [20]

Water

Tap water: Normal tap water that is distributed by the DEWA authority (Dubai Electric and Water Authority) [19].

Tertiary Treated Wastewater: Obtained from Jebel Ali sewage treatment plant located south of Dubai emirate [18].

Table 1 water quality test comparison between tap water and recycled wastewater

Parameter	Symbol	Unit	Water type	
			Tap Water	Recycled WW
Total suspended solids	TSS	mg/l	4	50
Total dissolved solids	TDS	mg/l	100 to 450	1500
PH	PH	---	7.9 to 8.5	6 to 9
Turbidity	-	NTU	<5.0	75
Biochemical Oxygen demand	BOD	mg/l	0	50
Chemical Oxygen demand	COD	---	0	100
Fecal Coliform bacteria	-	cells/ 100ml	null	1000
Total Coliform	-	MPN/ 100ml	null	1000

Aggregates

Fine: Black sand graded of medium size from (0.4mm to 2mm)

Coarse: two sizes, 10 mm and 20 mm

Concrete Mixing Design

The Concrete mix design used in experiments is proportional between its components (1 cement: 1.5 fine aggregates: 3 coarse aggregates) mixed by a water-cement ratio of 0.5 to produce a concrete characteristic compressive strength of 40 N/mm^{2,} which is known as concrete grade M40.

Table 2 Concrete mixing design ratios and quantity

Material	Cement	Aggregates			Tap Water / Recycled WW
		Fine	Coarse		
			20 mm	10 mm	
Ratio	1	1.5	2	1	0.5
Quantity (kg/m^3)	436.4	654.6	872.7	436.4	218.2

Concrete Testing Preparations.

Physical properties

Workability (slump test): Metallic mold with a cone shape filled with concrete in layers and rod taped 25 times each, then mold pulled up, leaving the concrete to deformity under the influence of its gravity flow.

Mechanical properties

Testing machines:

1. Compressive strength test (concrete cubes crushing test).
2. Tensile strength test.
3. Flexural strength test (beam test).

Concrete Specimens' Preparation

The testing replaced fresh or tap water with treated or recycled wastewater. Both types of water were used interchangeably in the two stages, and so the first testing option was to use only tap water in the mixing and the curing stages. It was denoted by (control specimen or MC), while the second testing option was to keep the tap water in the mixing, whereas the curing with recycled wastewater was denoted by (MC1) specimen. The third testing option comes by replacing the tap water with recycled wastewater; as for the curing stage, tap water is used (MC2), and then the fourth and last testing option is using recycled wastewater in both stages of mixing and curing (MC3) Figure 1.

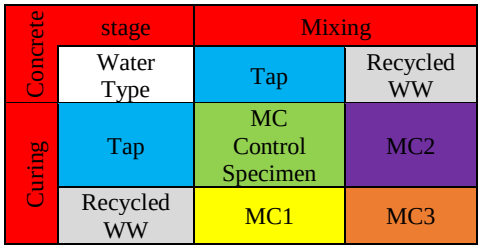

Fig. 1 Shows the arrangement of using the two types of water interchangeably in the mixing and curing stages.

The recycled water used was the output of the tertiary wastewater treatment. The concrete mixtures were arranged to produce a total of 16 concrete specimens classified into 12 concrete cubes of 150 mm length, two concrete cylinders of 150 mm diameter and 300 mm height, in addition to 2 concrete beams with dimensions of 100 mm for width and height and 500 mm for length.

The 12 concrete cubes were conducted to test the concrete compressive strength behaviour. Tests were performed at the ages of 7, 14, and 21 days, with four cubes every time after drying from the curing stage, four cubes that comply with four different water combination options covering the two mixing stages and curing. At the same time, the two concrete cylinders were conducted for the concrete tensile strength that was tested at the age of 28 days using two different water options, which were either fully mixed and cured by tap water or by recycled wastewater. And finally, the two concrete beams were conducted to test the concrete flexural tensile strength behaviour and were tested at 28 days with the same two different water options in the previous test.

RESULTS AND DISCUSSION

Workability (Slump Test)

It was observed that the concrete control specimen produced by mixing the components with tap water had a higher value than that of recycled tertiary treated wastewater. The control specimen slump was 65 mm in height while the recycled wastewater was 46 mm, reflecting a 29% decrease from that in the control specimen values.

In fact, the recycled tertiary treated wastewater contains dissolved solid particles that have a high absorption property that decrease the water content quality. That leads to a lowering of the slump value as agreed with [7,9,10,14], in other words, the existence of high content of fine particles in the recycled wastewater reduces the effective W/C ratio in the mix, and therefore the workability goes down. However, it is still in the acceptance range.

According to the findings of [9], the slump was decreased by 25% when using tertiary treated wastewater, giving a difference of only 4% away from our values, while a decrease of 50% in the case of using secondary treated wastewater.

Compressive Strength Test (Concrete Cubes Crushing Test)

Tests were maintained over time intervals up to 21days; each seven days, four different cubes were required to obtain their compressive strength value.

At seven days interval

The results were compared with the control specimen and were found to be higher when tap water mixing and recycled wastewater in curing (MC1) were used, as it got 24.62 MPa. In comparison, the control specimen got 18.5 MPa, which is 33.1% higher than the control specimen. The other two specimens got lower values as the specimen using recycled wastewater in mixing and tap water in curing (MC2) got 16.66 MPa with low as 8.9 % from the control specimen value. Also, the specimen using recycled wastewater in both stages of mixing and curing (MC3) got 10.99 MPa, as low as 40.4% from the control specimen value.

That was contrary to [2, 3, 7, 8] findings, in which the concrete with treated wastewater exhibited a greater compressive strength than the concrete with tap water. The reason that may arise for lowering the strength of the concrete early age when using recycled treated wastewater in concrete mixing is that it may contain an organic matter that lower the PH, which deteriorates the concrete [11].

At 14 days interval

It was observed that all the results were significantly higher than the control specimen, where it was found that the specimen made by using recycled wastewater in mixing and tap water in curing (MC2) had 37.3 MPa. In comparison, the control specimen got 22 MPa only, which reflects a 69.5% higher than the control specimen got. Also, the other two specimens got higher values as the specimen made using recycled wastewater in both stages of mixing and curing (MC3) got 35.31 MPa with a higher of 60.5 % from the control specimen value. In contrast, the specimen made using tap water in mixing and recycled wastewater in curing (MC1) got 27.46 MPa, a 24.8% increase from the control specimen value.

That was also agreed by [2 and 3] findings that the increase of compressive strength in the concrete mixed with treated wastewater is most significant during the early concrete ages of 7, 14 and 28 days.

At 21 days interval

It was also observed that all the results were significantly higher compared with the control specimen, where it was found that the specimen made by using recycled wastewater in mixing and tap water in curing (MC2) had got 40.5 MPa. In

comparison, the control specimen got 25.9 MPa only, which reflects a 56.4% higher than the control specimen. Also, the other two specimens got higher values as the specimen made using recycled wastewater in both stages of mixing and curing (MC3) got 38.13 MPa reflecting 47.2% higher from the control specimen value. In contrast, the specimen made using tap water in mixing, and recycled wastewater in curing (MC1) got 29.24 MPa with 12.9% increase than the control specimen value.

The [3] found that when the concrete is both mixed and cured using treated wastewater, an increase of 17% in compressive strength is obtained, according to this experiment, an increase of 47.2% was found when the concrete was both mixed and cured with the treated wastewater (MC3).

Results commentary

When comparing the result curves between the different mixing and curing combinations, the curves expressing the combinations using the tap water in mixing as MC and MC1 have very similar patterns as both grew linearly and almost turned into parallel lines. Also, throughout the time intervals, the increase in concrete strength was almost gradually and small. In comparison, the other two curves present the use of recycled wastewater mixing combination as MC2 and MC3 were having nonlinear behaviour. They began lower than those mixed with tap water in strength values as in the seven days test, then significantly increased at the 14 days test and became higher than the tap water mixing curves, then continuing to slightly increase at a rate nearly matching with that in the tap water mixing curves values. Also, MC2 gains more strength as values rather than MC3, but practically, the MC3 gains more strength, since the start was significantly low compared to MC2, as it gained 23.84 MPa more during the period of testing from the 7 to 21 days. MC3 gains a higher value of 27.14 MPa for the same period, which confirms the advantage of using recycled wastewater in curing, figure 2.

Building codes like ACI [21] permit the use of non-potable water in concrete mixing to provide at least 90% of the strength gained by potable water specimen values on both seven and 28-days time testing [3]. By applying the ACI code to the result, it was found that the two used mixing combinations that use non-potable water (MC2) and (MC3) were 90.05% and 59.40%, respectively, for the 7-day test, which means one of them passes (MC2), and the other is failed (MC3). However, the experimental values went higher than those made using potable water (MC and MC1) at 14 and 21 days. Although there is no testing was conducted during the 28 days, it was obvious that the mixing using the non-potable water (MC2 and MC3) values would be higher than the potable water (MC and MC1) values, if not at least equal to them, figure 3.

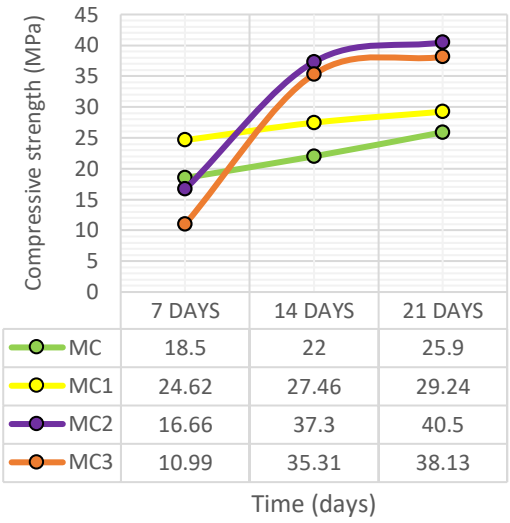

Fig. 2 Chart shows the compressive strength values for all concrete mixing combinations (MC, MC1, MC2, and MC3) for 7, 14, and 21 days periods.

An explanation that might approach the reason for gaining more compressive strength in specimens mixed with recycled wastewater has been illustrated by [4], which mentions that the pore-filling provided by the deposition of dissolved and suspended solids existing in the recycled water was responsible for the strength increasing and may have a relative meaning when curing using the recycled wastewater as the efficiency of cement hydration increased under the pore filling effect. In other words, it is the pore-clogging that exists by settling of dissolved solid particles reducing the porosity, and then it enhances the strength [16]. Even though the concrete mix water was tap water, it may be the reason why the compressive strength differences were found between the results for specimen mixing by tap water and that cured by tap water MC and by recycled water MC1. The differences between control specimen MC and MC1 reached 33% extra in strength at day 7, then reduced to 24.8% at day 14, and finally reached 12.9% extra at day 21, Eventually, the 2 curves of MC and MC1 are likely to meet at day 28, figure 2.

On the contrary, the findings of [6] concerning a study of sharing different proportions between the tap water to treated domestic wastewater of ratios (0,50,75 and 100%) using cylinder concrete

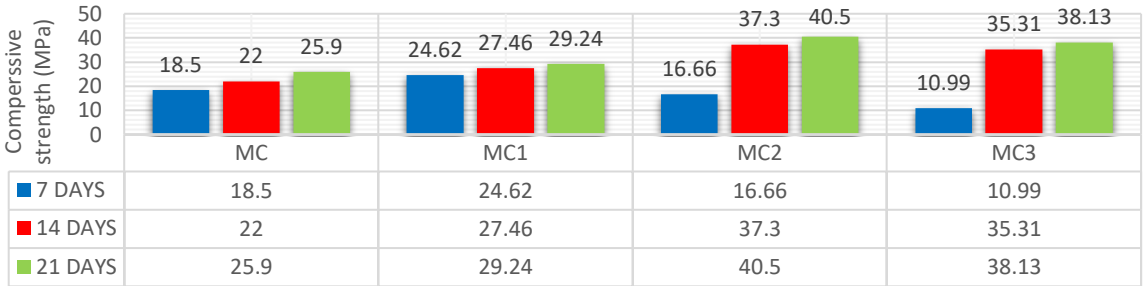

	MC	MC1	MC2	MC3
7 DAYS	18.5	24.62	16.66	10.99
14 DAYS	22	27.46	37.3	35.31
21 DAYS	25.9	29.24	40.5	38.13

Fig. 3 Shows the compressive strength values for all concrete mixing combinations (MC, MC1, MC2, and MC3) for 7, 14, and 21 days period

specimens tested at the age of 28 days. Results revealed that the specimens with a sharing ratio of 50% and 75% of treated wastewater have no significant differences from that of tap water. In comparison, the 100% of treated wastewater share gains a 17.7% increment in compressive strength.

Tensile Strength Test (Splitting Cylinder Test)

Tensile strength test was done at the 28 days of concrete age for two cylinders, one of them was the control specimen, and the other was selected based on the superior results obtained from the compressive strength test at day 21 and using the same corresponding concrete combination for water in mixing and curing, as it was the use of the recycled wastewater in mixing and tap water in curing (MC2). As a result, a slight increase in the results were observed compared with the control specimen, as it got a tensile strength of 2.93 MPa to 2.83 MPa for the control specimen, representing a 4.2% relative increment.

Similarly, [5] found that the tensile strengths of the concrete specimens with 50% wastewater sharing gained a higher value than the control mix. Some researchers pointed out that the reduction or increase in the tensile strength was related to the level of organic matter content in the water, particularly the existence of the BOD and COD values [11].

Flexural Strength Test (Beam Test)

A flexural strength test was done at day 28 of concrete age for two beams. One of them was the control specimen, and the other was selected based on the superior results obtained from the compressive strength test at the 21 days of age and using the same corresponding concrete combination for water in mixing and curing as it was selected previously in the tensile strength test, it was made using the recycled wastewater in mixing and tap water in curing (MC2). A decrease in the results was observed compared with the control specimen, as it got strength of 3.8 MPa to 4.2 MPa for the control specimen, representing an 8 % relative decrement.

According to [9], using secondary and tertiary treated wastewater in concrete mix reduced the flexural strength of the concrete at its early age, then slowly increased its strength at the later stage, as it was found to be 7.71% at 28 days and further decreased at its later ages of 90 days by 25.73%. In comparison with this experiment, the figures were so close in values in which MC2 reveals a decrease in the strength of 8% at 21 days.

Despite the compressive and tensile strength testing results for the MC2 specimen, which were relatively high in comparison with the control specimen MC results, the flexural strength result was less, which proves that there is no relationship between the compressive strength and flexural strength, nevertheless it was noticed that the use of the recycled treated wastewater in concrete mixing effects the concrete bonding strength between the cement pastry and aggregate [11], similarly, what revealed by [9] that the main contributor for flexural strength reduction was the tertiary treated wastewater that has a high alkalinity content formed a layer in the interfacial transition zone between the cement paste and aggregates.

CONCLUSION

It was noticed that to get the excellent benefit of using the recycled wastewater in mixing and curing concrete is to choose the water-cement ratio that enhances the workability, which is reduced by the large content of suspended and dissolved solid particles that absorbs the water in the mixer. Nevertheless, these dissolved solids play a significant enrollment in filing the pores initiated and reducing the porosity in the produced concrete during the mixing stage, which increases its strength

in the early developing ages. Besides, it has the same effect when using the recycled wastewater in the curing stage, where the more suspended and dissolved solid particles and larger curing time helps the concrete to block the remaining pores due to percolation into and filing it, which eventually increases the concrete strength.

The main achievement pursued by the experiment are as follows:

1- The possibility of replacing the tap water with recycled tertiary treated wastewater in concrete manufacturing.
2- Concrete performed using recycled tertiary wastewater has such a close performance mechanically and physically characteristic properties relative to that performed using tap water.
3- Using the recycled tertiary wastewater in the concrete curing stage has an advanced gaining strength similar to tap water use.
4- Using recycled tertiary wastewater in concrete is a great achievement toward sustainability in generally preserving freshwater and concrete manufacturing.

REFERENCES

[1] Farid H, Mansoor MS, Adnan S, Shah R, Khan NM, Muhammad R, et al. Impact Analysis of Water Quality on the Development of Construction Materials. 2019;1–13.
[2] Al-ghusain I, Terro MJ. Use of treated wastewater for concrete mixing in Kuwait. 2003;30(1).
[3] Engineering E. Use of biologically treated domestic wastewater in concrete. 2012;39:97–111.
[4] Swami D, Sarkar K, Bhattacharjee B. Use of treated domestic effluent as mixing water for concrete : Effect on strength and water penetration at 28 days. 2015;(November).
[5] Concrete S. Procedia Engineering Effect of using wastewater on the Properties of High Strength Concrete. 2011;14:370–6.
[6] Paper P. Practical Paper Water reuse in the production of non-reinforced concrete elements : An alternative for decentralised wastewater management Natalia Cangussu Duarte , Ana Elitha dos Santos Amaral , Bianca Graziella Lento Araujo Gomes , Gustavo Henrique Siqu. 2019;596–600.
[7] Testing B, Implementation F. Domestic Wastewater Reuse in Concrete Using. 2016;i.
[8] Askariyeh AH. International Journal of Waste Investigating the Possibility of Using Recycled Industrial Wastewater Instead of Potable Water in Concrete Mixture. 2019;9(1):1–5.
[9] Meena K, Luhar S. Author' s Accepted Manuscript Effect of wastewater on properties of concrete. J Build Eng [Internet]. 2018; Available from: https://doi.org/10.1016/j.jobe.2018.10.003
[10] Haezah A, Muhammad B, Ismail M, Abdul-majid Z. Characteristics of treated ef fl uents and their potential applications for producing concrete. 2012;110:27–32.
[11] Ali B, Kurda R, Brito J De. applied sciences A Review on the Performance of Concrete Containing Non-Potable Water. 2021;
[12] Sheikh M, Asadollahfardi G, Fazlolah S, Jafari S. The difference in chloride ion diffusion coefficient of concrete made with drinking water and wastewater. Vol. 231. Elsevier Ltd; 2020.
[13] June J, Politecnica U, Silva M, Naik TR. Sustainable Use of Resources – Recycling of Sewage Treatment Plant Water in Concrete. 2010;
[14] Al-joulani N. Effect of Waste Water Type on Concrete Properties. International Journal of Applied Engineering Research. 2015;10(0973-4562):39865-70.
[15] Miller SA, Horvath A, Monteiro PJM. resources worldwide. 2018;1(January):69–76.
[16] Sorkor K, Miretu TM. Curing of concrete with wastewater and curing compounds : Effect on strength and water absorption. 2014;(October).
[17] Arooj MF, Haseeb F, Butt AI, Irfan-ul- M. A sustainable approach to reuse of treated domestic wastewater in construction incorporating admixtures. 2020;
[18] Trakhees.ae. [cited 2022 Jun 13]. Available from: https://www.trakhees.ae/en/ehs/env/Documents/Guidelines/Guideline%20ID-EN-G02,%20Water%20Environment,%20Rev.%2000,%20Jan18.pdf, p.4-5
[19] Gov.ae. [cited 2022 Jun 13]. Available from: https://www.dewa.gov.ae/~/media/Files/Customer/Sustainability%20Reports/DEWA%20Sustainability%20Report%202020.ashx , p. 65
[20] EN 197-1 TS. Cement- Part 1: Composition, specifications and conformity criteria for common cements. Turkish Stand. 2002;(November 2011).
[21] ACI Committee 318, American Concrete Institute. Building code requirements for structural concrete (ACI 318-19) : Farmington Hills, Mi: American Concrete Institute; 2019.

8th Int. Conf. on Structure, Engineering & Environment (SEE), Mie, Japan, Nov.10-12, 2022, ISBN: 978-4-909106094 C3051

LOW-COST TECHNOLOGY FOR HERITAGE BUILDINGS DOCUMENTATION

Yohannes Firzal [1]✉, Reni Suryanita [2], M. Arief Al Husaini [3], Nangkula Utaberta [4]
[1, 3] Architecture of Universitas Riau, Pekanbaru, Indonesia
[2] Civil Engineering of Universitas Riau, Pekanbaru, Indonesia
[4] Universiti Tun Hussein Onn, Johor, Malaysia

ABSTRACT

Architectural heritage documentation becomes a serious concern in the learning method which mostly relies on two-dimensional drawing, sketch, observation and recording, and photos of objects. Not only consume time in collecting data and processing, but this conventional method also has other issues related to data accuracy and final results. To overcome these matters, digital documentation methods such as Close-Range Photogrammetry with Ultra-Light UAV are assumed to break-through methods for the problems of time efficiencies and accuracy of results. This digital documentation method is more reliable with the flexibility of multi-platform outputs that allow the final result of the process to adapt to variations in demand.

Keywords: Close-Range Photogrammetry, Ultra-Light UAV, Accuracy, Digital Documentation

INTRODUCTION

Learning architectural documentation demands a level of precaution and proper technical methods. Education in universities is mostly still teaching architectural documentation methods starting with two-dimensional (2D) manual drawing techniques such as sketches, direct observations, direct notes, and taking photos of objects as complements (Fig. 1). However, this conventional architectural documentation method has several limitations related to the processing time of data collection and processing with a good level of accuracy.

By relying on conventional methods, the process of documenting field data is a time consume and requires more operators. This takes longer as more types of documentation methods are applied to produce a good level of data accuracy. In terms of the level of data accuracy, conventional field data documentation methods are strongly influenced by various other technical matters such as the location of the height of the object being observed, the size of the object that is too large, and or the position of the object that is difficult to reach. Moreover, the conventional method of documentation has its own complexity when processing field data. Field data obtained manually in 2D form is then converted into digital data with the help of graphic design software. In this digitization conversion process, vector tracing and interpretation techniques are modified into the plane and three-dimensional (3D) shapes.

The conventional methods become a significant problem in learning architectural heritage documentation for college students because it requires a long and tiring process. Moreover, it will take a much longer time for the iteration process has to occur. From another perspective, students are also required not only to understand and be able to quickly and accurately document the process but also to be able to apply the latest techniques and equipment. In this context, architectural documentation is the starting point in heritage building studies, which is then further defined and specified by technology.

Thus, this paper investigates how digitalizing methods through low-cost technology can overcome the issues related to the time-consuming processing of heritage building documentation, mainly when applied to architectural studies.

Fig. 1 Architectural Documentation by Conventional Technique with Students

DIGITIZING IN ARCHITECTURAL DOCUMENTATION STUDIES

Architectural heritage documentation has developed along with the development of digital technology which is proven to be able to bridge the issue of data retrieval time with a good level of data

accuracy and can speed up data [1]. One of the latest technological leaps in the documentation is known as the Close-Range Photogrammetry (CRP) method. Broadly speaking, the CRP method is part of photogrammetry which is defined as a digital image processing method in orthoimages and mosaics which were initially used more in the field of archaeology [2]. Over the time, photogrammetry began to be recognized as an alternative solution for low-cost but effective documentation in image processing [3] compared to other modern methods [4]. Photogrammetry has also been applied in various disciplines [5] such as geoscience [6], structural investigation [7], cultural heritage documentation [8] [9], building inspections [10], architectural heritage [11], and architectural representations [12].

The CRP method in architectural heritage documentation is mostly a modified form of aerial photogrammetry to a simpler and more flexible form to use [13]. In this context, the CRP method can be effective and efficient in the digital image processing of field data. In its application, the CRP method requires general equipment such as a metric camera, personal computers, photogrammetry software, and scale bars [14]. Furthermore, the CRP method is also recognized as a non-intrusive documentation technique to produce digital 3D models, so it is more suitable for students to use in learning architectural heritage documentation.

Close-Range Photogrammetry converts serial digital images into point clouds with photogrammetry software. As a digital form since the beginning of the process, photogrammetric virtual models have been generated accurately and shortened the analysis process time [15]. Therefore, the CRP method can be more effective in processing and analyzing data at a low cost [16]. The CRP in this context is not to change the role of an architectural researcher, but rather as a means to help overcome architectural obstacles [17].

INSTRUMENT AND DATA COLLECTION TECHNIQUE

Instruments in collecting field data have used an Ultra-Light Unmanned Aerial Vehicle (UAV). The UAV used in this research is the DJI Phantom Mavic Mini 2-12MP 3-axis motorized gimbal Ultra Clear 4K/30 fps drone which is equipped with a 35 mm camera lens. Meanwhile, to process field data to produce cloud images using the Agisoft Metashape Professional 64-bit photogrammetry software.

Collecting field data has been conducted through two technical steps. The first step is to capture still images from various angles using the Ultra-Light UAV cameras. This step is called the fieldwork phase which aims to collect quality and geometric information from the image such as position, size, contrast, filtering, and shape [18]. This first step relies more on the skills of the operator operating the device in the field [13]. The second step is compiling the image by applying photogrammetry software to produce cloud data and dense textures. The software then consecutive interprets the semantic information of the image [19]. This computational phase is executed sequentially in the software workflow to get the 3D image at the end of the process.

The research unit on architectural heritage documentation is a study on two objects of traditional wooden construction buildings; mosques and traditional houses (Fig. 2). Both building objects still have intact and complete construction elements, so they are appropriate as objects of documentation for students.

Fig. 2 Wooden Construction Buildings as the research unit objects

FINDING AND DISCUSSION

Field data acquisition has been collected by the camera of an Ultra-Light UAV. In its working principle, the image capture procedure with the camera is giving more flexible in its movement (Fig. 3). The UAV can easily arrange to move vertically and horizontally. However, operating a UAV is also demanding on the pilot's ability to pay attention to the captured image of the environment around the recorded object so as not to result in excessive loading of image quality.

Image acquisition of objects by the camera is still paying attention to the suitability of the characteristics of the software that has been used to process the images. In this context, the collected images must be ensured that the overlap between the images is at least 60%. Thus, data processing software will quickly determine the order and location of each existing image. By using photogrammetry software, the image preparation workflow is following the process template.

Fig. 3 Image Acquisition Process by Ultra-Light UAV with Students

Image preparation with software is arranged through a series of fixed work sequences according to the workflow of the software (Fig. 4). At each stage of the workflow, the software will display a dialogue box confirming how the parameters will be used. Thus, researchers can still control every step of the process and take necessary action if an error occurs in the process of compiling this image.

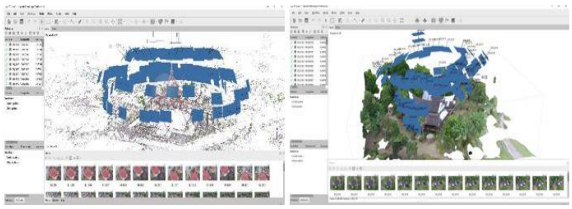

Fig. 4 The Arrangement t of the Images in Photogrammetry Software

The series of processes in photogrammetry software can produce various outputs and depths. The workflow runs sequentially starting from aligned images, dense cloud, mesh, texture, tiled models, DEM, and ortho-mosaic. The view of the process can also set the height and material properties of the object being analyzed (Fig. 5). The use of photogrammetry software also provides more flexibility. This is because the analysis process can determine the multi-platform output to be targeted. Not only produce corrected images and exterior shapes in 3D format, but the photogrammetry software is also externally flexible to link with other/multi-platform software.

However, the use of photogrammetry software also demands several things besides the ability. Time-consuming is still a matter that is of concern to researchers in the analysis process. The level and quality of the output produced will be directly proportional to the time required for the rendering process. The higher and more detailed, the more time it will take.

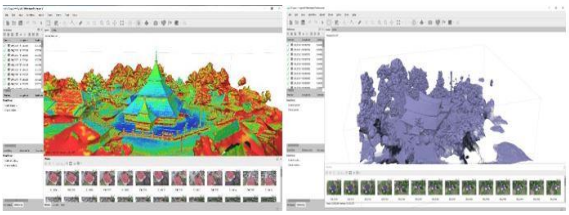

Fig. 5 Various Outputs and Depths of the Object Properties

CONCLUSION

A study using the adapted Close-Range Photogrammetry method has proven to be able to overcome gaps in problems related to architectural heritage documentation, especially for documenting traditional wooden buildings. The application of the CRP method can also answer the need for fast and accurate documentation methods in digital format. When compared with conventional documentation methods, the CRP method is found to be more reliable with the flexibility of multi-platform output. However, the CRP method requires mastery of other basic techniques that support such as the ability to operate an UAV and to run the software.

ACKNOWLEDGMENT

The research team would like to thank the LPPM Universitas Riau and ADB AKSI Project for providing financial support through the International Collaboration Research Scheme in 2021.

REFERENCES

[1] A. Baik and A. Alitany, “From architectural photogrammetry toward digital architectural heritage education,” in *International Archives of the Photogrammetry, Remote Sensing and Spatial Information Sciences - ISPRS Archives*, May 2018, vol. 42, no. 2, pp. 49–54, doi: 10.5194/isprs-archives-XLII-2-49-2018.

[2] M. Hemmleb and A. Wiedemann, “Digital Rectification And Generation Of Orthoimages In Architectural Photogrammetry,” in *IAPRS*, 1997, vol. XXXII, pp. 261–267, [Online]. Available: https://www.researchgate.net/publication/2354891.

[3] P. Grussenmeyer and O. Al Khalil, “From metric image archives to point cloud reconstruction: Case study of the great mosque of aleppo in Syria,” in *International Archives of the Photogrammetry, Remote Sensing and Spatial Information Sciences - ISPRS Archives*, Aug. 2017, vol. 42, no. 2W5, pp. 295–301, doi: 10.5194/isprs-archives-XLII-2-W5-295-2017.

[4] S. G. Barsanti, F. Remondino, and D. Visintini, “3D Surveying And Modeling of Archaelogical Sites,” in *ISPRS Annals of the Photogrammetry, Remote Sensing and Spatial Information Sciences, Volume II-5/W1, 2013 XXIV International CIPA Symposium, 2 – 6 September 2013, Strasbourg, France*, 2013, pp. 145–150.

[5] M. Yakar, H. M. Yilmaz, Saadet Armagan Gülec, and Mustafa Korumaz, “Advantage of digital close range photogrammetry in drawing of muqarnas in architecture,” *Inf. Technol. J.*, vol. 8, no. 2, pp. 202–207, 2009, doi: 10.3923/itj.2009.202.207.

[6] M. J. Westoby, J. Brasington, N. F. Glasser, M. J. Hambrey, and J. M. Reynolds, “‘Structure-from-Motion’ photogrammetry: A low-cost, effective tool for geoscience applications,” *Geomorphology*, vol. 179, pp. 300–314, Dec.

2012, doi: 10.1016/j.geomorph.2012.08.021.

[7] J. Han, K. Hong, and S. Kim, "Application of a Photogrammetric System for Monitoring Civil Engineering Structures," 2012.

[8] F. Remondino, "Heritage recording and 3D modeling with photogrammetry and 3D scanning," *Remote Sens.*, vol. 3, no. 6, pp. 1104–1138, Jun. 2011, doi: 10.3390/rs3061104.

[9] M. Morita and G. Bilmes, "Applications of low-cost 3D imaging techniques for the documentation of heritage objects," *Opt. Pura y Apl.*, vol. 51, no. 2, pp. 1–11, 2018, doi: 10.7149/OPA.51.2.50026.

[10] A. Murtiyoso, F. Remondino, E. Rupnik, F. Nex, and P. Grussenmeyer, "Oblique aerial photography tool for building inspection and damage assessment," in *International Archives of the Photogrammetry, Remote Sensing and Spatial Information Sciences - ISPRS Archives*, 2014, vol. 40, no. 1, pp. 309–313, doi: 10.5194/isprsarchives-XL-1-309-2014.

[11] Z. Sun and Y. Zhang, "Using drones and 3D modeling to survey Tibetan architectural heritage: A case study with the multi-door stupa," *Sustain.*, vol. 10, no. 7, Jun. 2018, doi: 10.3390/su10072259.

[12] M. A. Núñez Andrés and F. Buill Pozuelo, "Evolution of the architectural and heritage representation," *Landsc. Urban Plan.*, vol. 91, no. 2, pp. 105–112, Jun. 2009, doi: 10.1016/j.landurbplan.2008.12.006.

[13] P. Grussenmeyer, K. Hanke, and A. Streilein, "Architectural photogrammetry," in *Digital Photogrammetry*, 2002, pp. 300–339.

[14] A. Murtiyoso and D. Suwardhi, "Teknik Pencocokan Citra dalam Fotogrametri untuk Dokumentasi Cagar Budaya Indonesia Banana Biodiversity and Biogeography Big Data View project DBAT-The Damped Bundle Adjustment Toolbox in Matlab View project," in *Bunga Rampai Forum Peneliti Muda Indonesia 2017*, 2017.

[15] G. Wojciechowska and J. Luczak, "Use of close-range photogrammetry and UAV in documentation of architecture monuments," in *E3S Web of Conferences*, Dec. 2018, vol. 71, doi: 10.1051/e3sconf/20187100017.

[16] E. Alby, P. Grussenmeyer, J.-P. Perrin, E. Alby, P. Grussenmeyer, and J.-P. Perrin, "Integration of Close-Range Photogrammetric Surveys in the Design Proccess of Architectural Projects 'New perspectives to save Cultural Heritage,'" in *XIXth CIPA International Symposium, Oct 2003, Antalya, Turkey*, 2003, pp. 46–51, [Online]. Available: https://halshs.archives-ouvertes.fr/halshs-00263999.

[17] A. Murtiyoso and P. Grussenmeyer, "Virtual disassembling of historical edifices: Experiments and assessments of an automatic approach for classifying multi-scalar point clouds into architectural elements," *Sensors (Switzerland)*, vol. 20, no. 8, Apr. 2020, doi: 10.3390/s20082161.

[18] L. Carnevali, E. Ippoliti, F. Lanfranchi, S. Menconero, M. Russo, and V. Russo, "Close-range MINI-UAVS photogrammetry for architecture survey," in *International Archives of the Photogrammetry, Remote Sensing and Spatial Information Sciences - ISPRS Archives*, May 2018, vol. 42, no. 2, pp. 217–224, doi: 10.5194/isprs-archives-XLII-2-217-2018.

[19] A. Wiedemann, "From Analogue To Digital Close-Range Photogrammetry," 1998. [Online]. Available: https://www.researchgate.net/publication/2332200.

8th Int. Conf. on Structure, Engineering & Environment (SEE), Mie, Japan, Nov.10-12, 2022, ISBN: 978-4-909106094 C3051

APPLICATION OF DESIGN FOR MANUFACTURING AND ASSEMBLY ON TEMPORARY SHELTERS IN THE PHILIPPINES

Cheryl Lyne C. Roxas[1], Orlean G. Dela Cruz[2], Rhem Leoric C. Dela Cruz[3], John Paul Q. De Pedro[3], Jonathan R. Dungca[1], Bernardo A. Lejano[1] and Jason Maximino C. Ongpeng[1]
[1] Faculty, De La Salle University, Philippines; [2] Faculty, Polytechnic University of the Philippines, Philippines; [3]Research Assistant, De La Salle University, Philippines

ABSTRACT

The Philippines has experienced several tropical cyclones over the years. The most destructive disaster recorded in Philippine history was Typhoon Yolanda (Haiyan) in 2013, affecting 14 million people and deaths of at least 6,000. The number of internally displaced persons (IDP) has increased because of disasters from natural hazards. One of the challenges that people face during these times is the lack of durable and easy to build housing. As part of the disaster rehabilitation and recovery plan, a safe and durable house to protect people from the aggressive environment and ensure privacy to cope with emotional and mental health problems is essential in a disaster-prone country like the Philippines. Towards this end, the Design for Manufacturing and Assembly (DfMA) methodology was explored using sustainable materials like steel – cold-formed steel as main structural components and screw piles for the foundation, on a previously designed shelter for the IDPs of Typhoon Yolanda. The application of the proposed scheme has shown slight effect on project completion time but significant benefit in terms of cost efficiency.

Keywords: DfMA, Temporary Shelter, Disaster, Philippines

INTRODUCTION

Annually, shelters in the Philippines are damaged by climate-related disasters, from tropical storms, flooding, earthquakes, and volcanic eruptions. On the average, 300 shelters are affected by these catastrophes each year [1]. In 2013, Super Typhoon Yolanda (International Name: Haiyan) took the lives of about 6300 people and destroyed almost 1.14 million houses upon its landfall in Eastern Visayas [2]. In a more recent event, Typhoon Odette (International Name: Rai) has wreaked havoc on December 16, 2021, in Southern Leyte and Caraga Region, affecting 9,800 families (approximately 40,300 IDPs), which as of March 2, 2022, are still displaced and currently staying in the evacuation centers or residence of their relatives [3].

To address the housing concerns of displaced families, temporary shelters must be constructed; and, as such, guidelines for constructing these shelters have been developed. Considering the technical factors, it is suggested that the temporary shelters should be easy to erect and dismantled [4], has no complexities in their design since design complexities may cause delays in the timely construction of the shelter [5], could withstand and protect the inhabitants from subsequent calamities [6], and must be built from economical materials that are environmentally friendly, easy to manufacture and construct, and recyclable [7]. Several shelters have already been designed to match these guidelines. However, the developed designs also came with potential issues, which, in general, involve construction methodologies, site execution, and complexities due to numerous specifications [5] that would consume construction time.

To alleviate the potential issues stipulated in previous shelter designs, this paper explores the application of the Design for Manufacturing and Assembly (DfMA) to the temporary shelters developed in the Philippines. Previous studies have also applied DfMA in construction such as the construction of a light wall in 4-story houses [8], modules of cable-stayed towers [9], and student dormitory modules [10]. DfMA improves design by considering the downstream processes of manufacturing and assembly [11] that can reduce assembly and manufacturing costs and improvement in quality of work and production time through simplification of the system [12]. To further explore the advantages of applying DfMA, this paper utilizes cold-formed steel (CFS) for the shelter framing system and screw piles serving as its foundation. The selection of CFS as a structural material for the frame is supported by its benefits: reduced cost of materials and implementation, reduced structural elements, less maintenance, and suitability for prefabrication [13]. As for the screw piles, related studies established that they are easy to install with the use of minimal equipment and manpower, and reusable to other sites [14]. The usage of these materials is similar with another shelter scheme used in Vietnam from the

IFRC Eight Designs [15], but without DfMA application.

METHODOLOGY

For this research, a case study was developed in collaboration with a local steel contractor which specializes in the manufacturing and assembly of CFS sections and the installation of screw piles as foundation. The case study covers the application of DfMA using CFS and screw piles on a selected shelter previously designed and constructed in the Philippines.

Selection of Shelter for DfMA

In this research, DfMA methodology using CFS and screw piles was applied to address the concerns in a previous temporary shelter design in the Philippines. The researchers chose a Philippine 2011 shelter from the International Federation of Red Cross and Red Crescent Societies' Ten Designs for Post Disaster Shelter [5]. In overview, the shelter is constructed using reinforced concrete columns and foundations, masonry and timber walls, and timber roof framing with a dimension of 4.0mx5.0m (Fig. 1). Based on the front elevation (Fig. 2), it has a gable roof with a braced column height of 2.40m. This shelter took 12 days to be built, and it has an anticipated lifespan of 5 years. Its performance analysis against hazards indicates the possibility of failure in resisting wind loads even at the reduced level, and non-compliance with the structural code requirements for seismic loads indicating that it could only withstand seismic events at a reduced load level [5]. The other IFRC documented shelter for the Philippines was a timber shelter and it was already found to be structurally adequate; and, therefore, was not selected for this study.

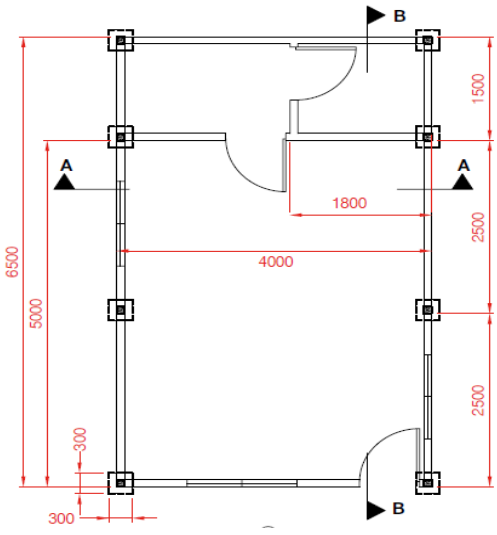

Fig. 1 IFRC Philippine shelter 2013 plan [5]

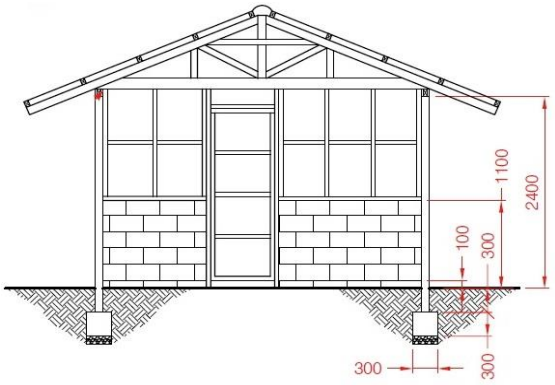

Fig. 2 IFRC Philippine shelter 2013 elevation [5]

Initial Design of the Structural System

Design of CFS Frame

The selected shelter was prepared with an initial CFS framing and screw pile as foundation complying with the design load requirements set by the National Structural Code of the Philippines (NSCP) requirements. The initial CFS frame was designed using the software STAAD in accordance with American Iron and Steel Institute (AISI) standards and imported to Vertex BD, a Building Information Modelling (BIM) software that facilitated the DfMA phase. For the design, the selected shelter was assumed to be situated in a hypothetical location in San Gerardo Subdivision, Tacloban City, Leyte. The wind and seismic parameters shown in Tables 1 and 2, respectively, were used in the design of the frame in STAAD.

Table 1 Wind Load Parameters

Parameter	Input Values
Wind Speed	290 kPh
Exposure Category	Exposure C

Table 2 Seismic Load Parameters

Parameter	Input Values
Soil Profile Type	S_D
Near Source Factors	Na = 1.0, Nv = 1.0
Seismic Zone Factor	0.40
Response Modification Factor, R	4.50 (Intermediate Moment Frame)

Design of Screw Piles

For the shallow screw piles in cohesionless soils, the cylindrical shear method was used for the design using the equations suggested by Nasr (2004) [16] for piles under compression, and Mitsch and Clemence (1985) [17] for tension/uplift.

Shown in Table 3 are the soil parameters used in the design of the screw piles. The soil parameters are site specific and were obtained from an available soil investigation report that generally assumes the parameters of a very dense sand of the selected site.

Table 3 Soil parameters

Parameter	Values
Internal Friction Angle, φ	35°
Effective Unit Weight, γ'	10.19 kN/m^3
Breakout Factor, Fq	10

Design Assessment Using DfMA Criteria

The scope of the research is limited to the application of DfMA as a design process and its consequent effect on the material cost and approximated theoretical time of installation of the prototype shelter with CFS and screw pile. In the design phase, DfMA criteria were utilized to optimize the production of the prototype. The following criteria are as follows: (a) minimization of the number of parts, (b) ease of handling, (c) ease of insertion of parts, (d) standardized parts, (e) design for current process capabilities, and (f) maintain margin for alternative design and assembly processes [11].

Usage of Building Information Modelling (BIM)

Upon application of the DfMA criteria, design output was imported to Vertex BD for creation of the shop drawings of the CFS framing and connections which were the basis of the material cost estimate and theoretical time of completion for assembly. After which, the obtained values were compared to the values of the original IFRC temporary shelter scheme. The original scheme was designated as IFRC and the new scheme applying DfMA with CFS and screw piles was designated as CFS.

DATA AND ANALYSIS

Structural Design Results

STAAD models shown in Fig. 3 for the trusses and Fig. 4 for the frame show that the CFS sizes were designed according to the code specifications of AISI for CFS sections which assure the adequacy of its resistance against the wind and seismic loads. Since the structure is relatively lightweight, the governing load is the wind; thus, the sections, in majority, were designed against the wind. Furthermore, due to wind, the governing support reaction used in the design of the screw pile is an uplift force of 14 kN. The designed specification of the screw piles as shown in Fig. 5 mitigates the issue of the IFRC foundation of a possible uplift occurring during typhoons.

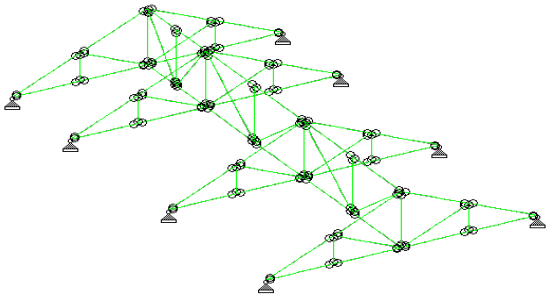

Fig. 3 Trusses STAAD model

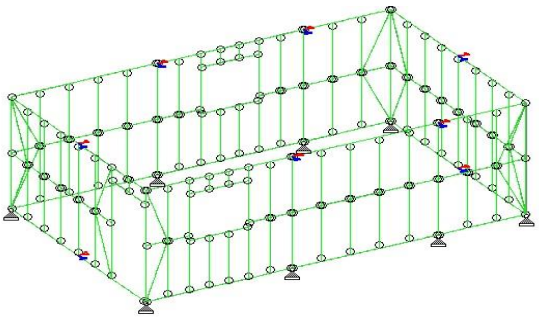

Fig. 4 CFS Frame STAAD model

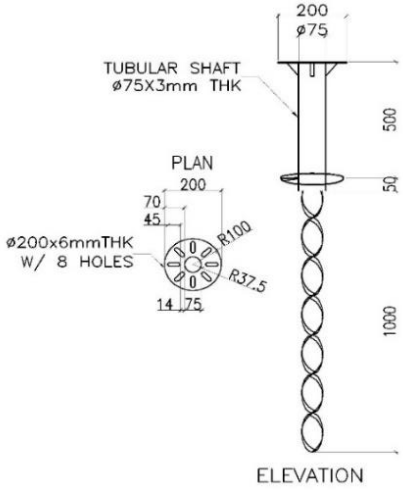

Fig. 5 Screw pile design specification

Application of DfMA

Following the results of the structural design, the criteria for DfMA were applied through the importation of the STAAD file to Vertex BD.

Minimization of the number of parts

The number of parts was already trimmed down to the required number of members based on structural requirements. Hence, the number of parts is already optimized. No further reduction of members is necessary as all parts are deemed essential.

Design for ease in handling

The Vertex BD output was readily imported to the roll forming machine that would automatically manufacture the CFS sections according to the cutting list. Hence, this process eases the flat-pack packaging of the CFS. The sections were relatively light such that handling each section would require two persons only. Assembly is guided by the designations marked by the Vertex BD for each member of a panel. Shop drawings from Vertex BD include the specification of each member designation shown in Table 4 and its respective designation on the parts of the truss shown in Fig. 6.

Table 4 Vertex BD truss parts specifications

Mark	Qty	Size	Use	Length (mm)
5	1	DH140-50-1.40	Jack	1193
3	1	DH140-50-1.40	Web	1117
6	1	DH140-50-1.40	Web	1117
2	1	DH140-50-1.40	Web	643
7	1	DH140-50-1.40	Web	643
4	1	U140-50-1.40	Bottom Chord	4259
8	1	U140-50-1.40	Top Chord	2949
1	1	U140-50-1.40	Top Chord	2941

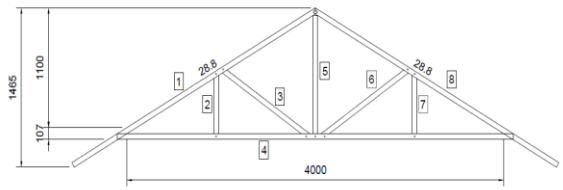

Fig. 6 Vertex BD truss part designation

Design for ease in insertion and connections

Self-drilling screws are used for each connection. Each intersection would only require a single screw, as reflected in the shop drawings, and a dimple was already provided for each screw connection during the manufacturing process to lessen the amount of time spent in the fastening of members, as shown in Fig. 7. The location of these screws is also indicated in the shop drawings created in the Vertex BD. These self-drilling screws possess relatively high strength, and their installation would only require a screw gun for fastening.

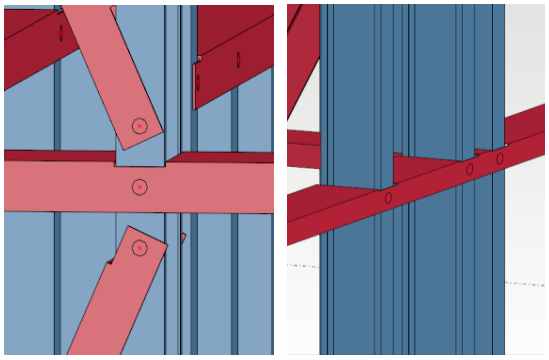

Fig. 7 Single screw connections of CFS frame

Standardized parts

CFS components will be fabricated only by a single local manufacturer. Moreover, all of the parts of the frame were set to be constructed at the same length, size, and configuration. All frame connections were also standardized as single screw connection. From Tables 5 and 6, the quantity take-off of the standardized parts is shown, adding up to 129 parts.

Table 5 CFS frame parts

Size	Use	Length (mm)	Quantity (pcs)
DH140-50-1.40	Stud	2392.00	41.00
DH140-50-1.40	Stud	292.00	8.00
DH140-50-1.40	Stud	1092.00	5.00
U140-50-1.40	Header	1135.00	1.00
U140-50-1.40	Header	1345.00	2.00
U140-50-1.40	Sill	1345.00	2.00
U140-50-1.40	Diagonal Brace	1188.00	8.00
U140-50-2.50	Top Track	4000.00	2.00
U140-50-2.50	Bottom Track	4000.00	2.00
U140-50-2.50	Top Track	6212.00	2.00
U140-50-2.50	Bottom Track	6212.00	2.00
U140-50-1.40	Noggin	2905.00	1.00
U140-50-1.40	Noggin	1832.00	1.00
U140-50-1.40	Noggin	3995.00	1.00
U140-50-1.40	Noggin	476.00	1.00
U77-32-0.80	Top Track	3696.00	1.00
U77-32-0.80	Bottom Track	2696.00	1.00
U77-32-0.80	Noggin	2702.00	1.00
U77-32-0.80	Header	1031.00	1.00
U77-32-0.80	Top Track	1487.40	1.00
U77-32-0.80	Bottom Track	493.10	1.00
U77-32-0.80	Noggin	493.80	1.00
U77-32-0.80	Header	1023.00	1.00
U77-32-0.80	Header	1031.00	1.00

Table 6 CFS truss parts

Size	Use	Length (mm)	Qty (pcs)
DH140-50-1.40	Top Chord	2252.80	4.00
DH140-50-1.40	Bottom Chord	4258.60	4.00
DH140-50-1.40	Web	1116.80	4.00
DH140-50-1.40	Web	643.30	4.00
DH140-50-1.40	Web	1193.00	4.00
U100-50-1.40	Top Chord	2224.40	2.00
U100-50-1.40	Bottom Chord	2224.40	2.00
U100-50-1.40	Web	1175.00	6.00
U100-50-1.40	Diagonal Brace	1501.00	4.00
U100-50-1.40	Top Chord	1463.10	1.00
U100-50-1.40	Bottom Chord	1463.00	1.00
U100-50-1.40	Web	1172.00	3.00
U100-50-1.40	Diagonal Brace	1294.00	2.00

Design for current process capabilities

A local CFS manufacturer was consulted regarding the application of the DfMA parameters for the frames. As such their current practices been embedded in the application of DfMA.

Margin for alternative design and assembly process

Exploration of modularization and 3D volumetric packaging options are suggested for future assemblies, as well as assessing the impact of adopting these methodologies.

Project Completion Time

The original IFRC shelter was recorded to be constructed in 12 days. Based on the Gantt Chart shown in Fig. 8, the total number of days for construction was reduced to 11 days by applying the new scheme involving CFS and screw piles, saving only 1 day in the construction period. In the chart, manufacturing and delivery must be included in the scheduling since the CFS and screw piles specifications are not commercially available and are to be fabricated according to the design specifications, which, in the process, consumed 2 days of the overall schedule. Thus, if the CFS and screw piles are readily available, the construction period would only take 9 days to complete.

Project Cost

Using the quantities provided by the IFRC in the original scheme and the present unit costs of materials, the present estimated cost for the original IFRC increases by 98.99% in overall project cost when replaced with the CFS scheme as shown in Fig. 9. Material cost is the primary contributor to the increase since the CFS scheme uses steel, a material known for expensive cost that escalates every year.

Work Description	Duration (days)	DAY 1	2	3	4	5	6	7	8	9	10	11
Foundation Works												
Manufacturing of Screw Piles	2											
Delivery of Screw Piles	1											
Installation of Screw Piles	1											
Framing System												
Manufacturing of CFS sections	2											
Delivery of CFS sections	1											
Assembly and Installation of CFS	2											
Roof Framing												
Trusses assembly and installation	2											
Purlins Installation	1											
Roofing Sheet Installation	1											
Partitions												
Exterior Walls Installation	3											
Interior Drywalls Installation	2											
Hardwares												
Hinges Installation	1											
Doors Installation	1											
Windows Installation	1											
Utilities Installation	1											

Fig. 8 CFS Gantt chart

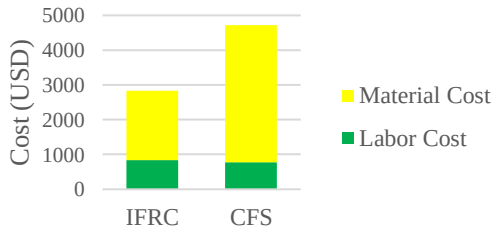

Fig. 9 Estimated project cost of IFRC and CFS

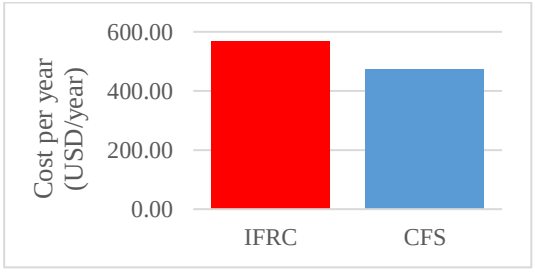

Fig. 10 Cost per year of IFRC and CFS shelters

However, to appropriately assess the efficiency of using the CFS scheme, the anticipated lifespan of each scheme must be taken into consideration. The IFRC frame only has an anticipated lifespan of 5 years, whereas the CFS frame may last up to 30 years in lifespan [18]. On the other hand, Eurocode has set temporary structures to have a design life of 10 years [19] which will be the anticipated lifespan that will be taken into consideration for the CFS since it will definitely be able to last the 10-year requirement due to its adequacy in design and documented anticipated service life. Therefore, to properly assess the cost efficiency of the two schemes, it would be appropriate to distribute the estimated cost over the indicative

service life of both schemes which are 5 and 10 years for IFRC and CFS, respectively. As reflected in Fig. 10, the IFRC incurs a higher annual cost at 567.75 USD per year compared to the CFS which only costs 472.75 USD per year which shows more favorable cost efficiency by saving about 20.10% yearly costs.

CONCLUSION

This paper shows the process and advantages of applying DfMA using CFS and screw piles in temporary shelters that could be utilized in the Philippines after a disaster. DfMA considers the manufacturing and assembly of the designed CFS sections in the design which in turn would facilitate the ease in construction process, cost and completion. While the effect of using the proposed scheme to the completion time of the shelter was insignificant due to addition of the manufacturing and delivery period of the parts, it was shown that the cost efficiency of using the proposed scheme is more favorable than the original scheme followed in constructing the shelter.

ACKNOWLEDGMENTS

This project is funded by the Department of Science and Technology (DOST) through the Science for Change Program (S4CP) – Collaborative Research and Development to Leverage Philippine Economy (CRADLE) and monitored by DOST - Philippine Council for Industry, Energy, and Emerging Technology Research and Development (PCIEERD) with Project No. 8739. The authors would like to acknowledge DOST, PCIEERD, De La Salle University and Accutech Steel and Services, Inc. for their support on this paper.

REFERENCES

[1] Department of Human Settlements and Urban Development - Philippines and The World Bank. Post-Disaster Shelter Recovery Policy Framework: Building a Responsive System to Support Resilient and Equitable Recovery in the Philippines. 2021.

[2] United Nations Office for the Coordination of Humanitarian Affairs (OCHA) Philippines: Destructive Tropical Cyclones from 2006 – 2016. March Issue, 2017.

[3] United Nations High Commissioner for Refugees (UNCHR). Safeguarding the rights of the Vulnerable: Ensuring solutions for the internally displaced population due to Super Typhoon Rai in Caraga Region and Southern Leyte province. Thematic Bulletin Issue No. 1. 2022.

[4] Bashawari, A., Garrity, S. and Moodley, K. An Overview of Design Relief Shelters. 4th International Conference on Building Resilience, Salford Quays, United Kingdom. 2014.

[5] IFRC/RCS 2013. Post-disaster shelter: Ten designs. Geneva: International Federation of Red Cross and Red Crescent Societies. 2013.

[6] Camp Coordination/Camp Management 2010. Collective Center Guidelines. United Nations High Commissioner for Refugees and International Organization for Migration. 2010.

[7] Sever, S. M. & Altun, M. C. Design of a post disaster temporary shelter unit. ITU Journal of Faculty of Architecture, Vol. 6, 2009, pp. 58-74.

[8] Gerth, R., Boqvist, A., Bjelkemyr, M., & Lindberg, B. Design for construction: Utilizing production experiences indevelopment. Construction Management and Economics, Vol. 31, Issue No. 2, 2013. pp. 135–150.

[9] Peterseim, J. H., White, S., & Hellwig, U. Novel solar tower structure to lower plant cost and construction risk. AIP Conference Proceedings, Volume 1734, Issue No. 1, 2016.

[10] Ramaji, I. J., Memari, A. M., & Messner, J. I. Product-oriented information delivery framework for multistory modular building projects. Journal of Computing in Civil Engineering, Vol. 31, Issue No.4, 2017.

[11] Boothroyd, G. Assembly automation and product design. CRC Press, 2005.

[12] Lu, W., Tan T., Xu, J., Wang, J., Chen, K., Gao, S. and Xue, F..Design for manufacture and assembly (DfMA) in construction: the old and the new, Architectural Engineering and Design Management, Vol. 17, Nos. 1-2, 2021 pp. 77-91.

[13] Alemdar, F. and Al Gaadi, F.M.A. Experimental Study of Earthquake Simulator for 3D Cold-Formed Steel Frame Structure. Latin American Journal of Solids and Structures, Vol. 19, 2022.

[14] Zhang, D.J.Y. “Predicting Capacity of Helical Screw Piles in Alberta Soils”. MS Thesis, Department of Civil and Environmental Engineering, University of Alberta. 1999.

[15] IFRC/RCS 2011. Post-disaster shelter – Eight designs. Geneva: International Federation of Red Cross and Red Crescent Societies. 2011.

[16] Nasr, M.H., 2004. Large capacity screw piles. In: Proceedings of the International Conference: Future Vision and Challenges for Urban Development. Cairo, Egypt, 20–22 December, pp. 1–15.

[17] Mitsch, M.P., Clemence, S.P., 1985. The uplift capacity of helix anchors in sand. In: Uplift Behaviour of Anchor Foundations in Soil. American Society of Civil Engineers, New York, pp. 26–47.

[18] Lu, W. Chapter 12: Sustainable applications of cold-formed steel structures: connections and joints. Recent Trends in Cold Formed Steel Structure. Woodhead Publishing. 2016. p.245

[19] European Committee for Standardization. Eurocode BS EN 1990:2002 +A1:2005. 2010.

8th Int. Conf. on Structure, Engineering & Environment (SEE), Mie, Japan, Nov.10-12, 2022, ISBN: 978-4-909106094 C3051

DETECTION OF GEOGRAPHIC FRACTURE-FAULT STRUCTURES USING DEEP LEARNING MODEL WITH STEPWISE ELIMINATION METHOD FROM HIGH RESOLUTION SATELLITE IMAGERY IN DJIBOUTI

Denis Pastory Rubanga[1], Sergio Azael May Cuevas[1], Yessy Arvelyna[2] and Sawahiko Shimada[1]
[1]Faculty of Regional Environment Science, Tokyo University of Agriculture, Japan; [2] Remote Sensing Technology Center of Japan, Japan

ABSTRACT

In the arid lands of Eastern African Djibouti, underground water is essential for supporting the livelihood of humans and livestock animals since no permanent surface water exists. Several attempts have been made to estimate the groundwater flow in the regions to delineate the accessibility of the water resources. However, accurate groundwater simulation is hindered sometimes by the existence of the geological fault and fractures, which influence the groundwater cycling systems in terms of the flow direction change, linkage or damming functions. This study uses deep learning techniques in fracture-fault detection in the target area within Ali Faren sub-catchment of Ambouli Wadi, Djibouti. We used WorldView-3 (WV-3) , high-spatial resolution Earth imaging multispectral satellite image of eight bands as input in training deep convolutional neural network (Deep-CNN) model using wadi streamline derived from AW3D-DEM as labels. The fracture-fault structures were extracted by stepwise elimination method using the geological characteristics. We further validated the results using fault distribution from relief images derived from adaptive gradient filter applied on ortho-rectified PALSAR-1 RTI and PALSAR-2 Global Mosaic (herein PALSAR-1/2) image data. The result showed that fracture-fault lines were detected using multi-input images in the deep CNN model. The proposed Deep-CNN model will be applied to other catchments in Djibouti to help in groundwater flow model simulations and eventually help locate the potential area for groundwater resources in the entire country of Djibouti.

Keywords: Fracture-fault, High-resolution satellite, Deep-learning, Stepwise elimination method

INTRODUCTION

Djibouti covers a land area of 23,200 km^2, located on the north side of the Horn of Africa. The country is characterized with fracture-fault lines due to its geology setting that consist of ancient sedimentary lands from Mesozoic age (secondary era). Fracture-fault structure systems such as the Ali Sabieh horst (ca, 27 to 23 Ma) from Djibouti city south into the north of the Aysha horst in Ethiopia. The fracture-fault systems within borders of this horst are composed by rhyolitic lavas on the East (ca, 25 to 19 Ma) and in the west side (14 Ma to 10 Ma) and covered mainly by basaltic flows, such as the Dalha series (ca, 9 to 4 Ma), Somalis basalt (ca, 7 to 3 Ma) in the east side. In the central region, Tadjourah basalts (3 Ma to 1 Ma). In the Asal rift zone, Tadjourah region (central of Djibouti), the lavas from magmatic episode of Fieale volcano (ca, 300 to 65 ka) in current elevation contour lines, form the topography and geology of the rift zone. Fracture-faults volcanic aquifers have been analyzed as the main water resources in Djibouti, shown by the pumping test data which consist of major basaltic series [1]. The geochemical and isotopic surveys in the southwest of Djibouti show a common evolutionary pattern of groundwater, i.e. a recharge from wadi-rivers flown into the alluvium layer, then, circulated downward into the basalt sub-surface layer through major faults, and mixed with a more geochemically evolved groundwater [2]. Djibouti with a semi-arid and arid type of weather, is characterized by low rainfall of about 130 mm/year, whereby 83% evaporates to the air and 6% flows on the ground surface, 5.5% penetrates sub-surface and 5% into sub-ground, forming the renewable ground water resources estimated as 300 Mm^3/year [3].

In the current work to estimate the groundwater flow in the regions to delineate the accessibility of the water resources, GETFLOWS (a General purpose terrestrial fluid-flow simulator) is used based on previous works of [3] and [4], to simulate both surface and subsurface systems (forming the underground water reserve). A component of GETFLOWS subsurface water simulation includes stream formation that are purely based on hydrodynamic principles governed by recharge, topography, hydraulic conductivity, and flow parameters. Since evolutionary patterns of groundwater as recharge of wadi streams are majorly circulated through fracture-

fault systems, poor fracture-fault delineation using GETLFOWS greatly impacts underground water simulation, therefore, it is necessary to clearly delineate the fracture-fault distribution in any locality to support locating an area with high possibility of groundwater resources. However, the success of such work require data which apparently is limited.

In this study, we propose a Deep-CNN [5] approach that relies on easily accessible satellite derived datasets that could help calibrate and evaluate GETFLOWS hydrologic models for an ungauged catchment area. Deep-CNN approach is used for fracture-fault detection based on WV-3 [6], PALSAR-2 [7], 5 m resolution DEM (ALOS World 3D level 1 DSM) [8] and slope derived from DEM in training a multi-input Deep-CNN model using wadi streamline derived from AW3D-DEM as fracture-fault labels of target area as shown in Fig. 1.

The use of deep learning techniques in geological feature settings has widely been used, such as automatic extraction of seismic landslides in large areas with complex environment in earthquake areas [9] [10]. [11] used object-oriented classification technique to segment homogeneous images using high-resolution multi-spectral data. Other works have used U-NET models in image classification [12]. However, the application of deep learning on surface geological structures such as fracture- fault is limited.

STUDY AREA

Study Area Data

In this study, we used WorldView-3 (WV-3) the latest in a constellation of commercial high-spatial resolution Earth imaging satellites developed by DigitalGlobe Inc (Longmont, Colorado, USA). [8] High-spatial images collected between 12th May 2018 and 5th April 2021 with 0% cloud cover between N.W Latitude 11.55372100 and Longitude 42.77572500, 8-band multispectral image (red, red edge, coastal, blue, green, yellow, near-IR1, and near-IR2) 400 nm – 1040 nm of 1.2-m spatial resolution, and 5-m spatial resolution AW3D DEM (ALOS World 3D level 1 DSM). The original DEM resolution of 5-m was downscaled to same resolution as the PALSAR-2 images. Using ESRI's ArcGIS Pro v 2.7 (ESRI 2021), we created the slope images derived from the DEM and PALSAR-2, that were stacked together to create a composite of 11-band raster image. The PALSAR-2 Global Mosaic data is a seamless global SAR image created by mosaicking the SAR image in backscattering coefficients measured by PALSAR-2 with 25-m resolution. Since PALSAR-2 are filled with speckle noise due to the interference during signal transmission, the adaptive filter Enhanced Lee Filter was applied to reduce speckle noise on the image [13], [14]. Fracture-fault labels as wadi streamline were derived from AW3D-DEM of the target area. The coverage of the created composite layer included the target Ali Faren catchment. (Fig. 1)

Labeling the Training Data

To train the Deep-CNN model on a generated multi-band raster image, a group of labeled raster cells of the 11-multi-band, which can indicate the characteristics of fracture-fault, must be used to train the model. We obtained the fracture-fault label by using ArcGIS Pro software, applying the buffer method of 50 m resulting into a polygon shape as shown in Fig. 1. The derived polygon shape files were used as Region of Interest (ROI) in ENVI Deep Learning in creating training labels [15], [16].

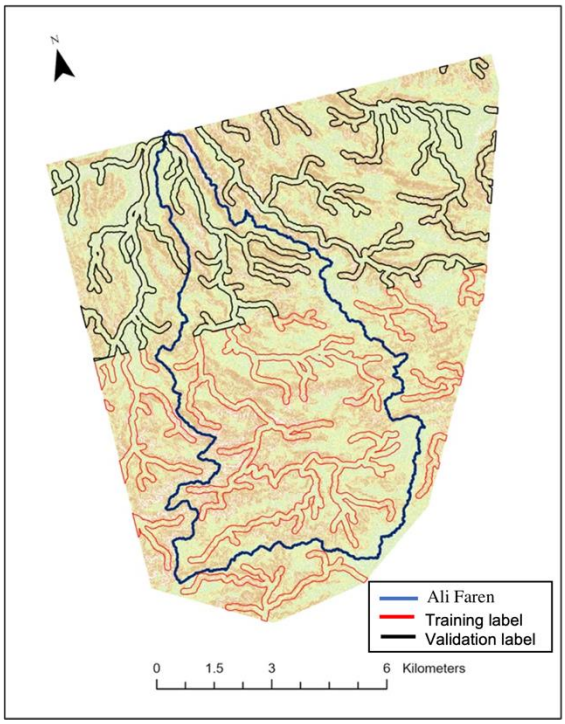

Fig. 1 Stacked 11-band raster image showing Ali Faren water catchment in blue polygon, wadi streamline polygons of training (red) and validation (black) data for training Deep-CNN model

DEEP-CNN TRAINING AND RESULTS

ENVINet5 (built in ENVI version 5.6, and ENVI Deep Learning version 1.2) is used to train the Deep-CNN model on the multi-band raster image. The ENVINet5 architecture shown in Fig. 3 is a mask-based encoder-decoder fully convolutional network with 5 levels and 23 convolutional layers. Its architecture is based on U-Net [17] with some modifications on layers of convolution and the size of

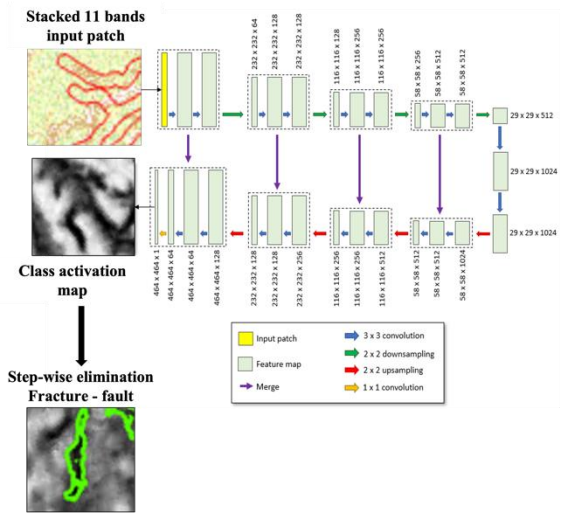

Fig. 2 ENVINet5 architecture.
Source; Harris Geospatial Solution (2021) [16]

input and output. The input of ENVINet5 is a patch with fracture-fault polygon sampled from the 11-band multi-input raster images. Training raster is used to train the initialization model. Model training is to expose training raster to the model. The model learns to convert the spectral and spatial information in the training raster into a class activation map, a probability map, highlighting the target to be extracted as shown in Fig. 5.

ENVINet5 refers to the binary cross-entropy loss function with the weighted map used by U-Net

$$E = \sum_{x \in \Omega} \omega(x) \log\left(p_{l(x)}(x) \right), \tag{1}$$

where $p_{l(x)}(x)$ is the softmax loss function; $l : \Omega \rightarrow \{1,\cdots,K\}$ is the label value of the pixel and $\omega:\Omega\varepsilon R$ is the weight of the pixel that gives a higher weight to the pixel close to the boundary point in the raster image[18].

The number of patches per epoch determines the amount of training. The settings are lower for small datasets and higher for large datasets. The number of patches per epoch is set to 414 and number of patches per image set to 32. The number of patches per batch system is automatically set to 1. The rest of the parameters ENVI automatically determines the appropriate values. To prevent overfitting, data augmentation is used. Data augmentation is a technique commonly used with deep learning to supplement the original training data. By having more information to extract from the training data, the trainer and classifier can more effectively learn the appearance of features of interest. During each epoch, ENVI creates a new training dataset with a randomly assigned angle per training example. Likewise, it creates a new training dataset with a randomly assigned scale factor per training example.

In traditional Deep-CNN training, an epoch represents the period in which all data sets are passed into the training model. However, it is different in the ENVI Deep Learning Module, which intelligently extracts patches from the training raster, so high-brightness characteristic pixel areas are more often encountered than low-brightness regions at the beginning of training. At the end of the training, all areas look more uniform. Because there is bias determination in patch extraction, an epoch in ENVI deep learning refers to the number of patches trained before bias decision adjustment.

To get a better model, multiple epochs are needed to fully train the model. The number of epochs and the number of patches per epoch depend on the diversity of feature sets to be learned, which has no exact value. In general, enough epochs are needed to adjust the weight to ensure smooth progress. We set number of epochs to 50.

Model training were run on a Windows 10 Pro Operating System Intel (R) Core 9TM i9-990K CPU processor clocking 3.6GHz and with a NVIDIA GeForce RTX 2080i GPU. The training time of the model is 50 min. The curves of training accuracy, training loss, training precision and training recall are shown in Fig. 3.

RESULTS AND DISCUSSION

Training and evaluation result

The training curve showing accuracy, loss, precision, and recall is shown in Fig 3. Similarly, results of validation of the raster images showing validation accuracy, validation loss, validation precision and validation recall curves are shown in Fig. 4.

ENVI generates a model based on the lowest point of the validation loss value, that is, the epoch with the best match between the classifier and the validation data. The lowest loss value of the trained model is 0.0393, accuracy is 0.9604, precision is 0.8438, recall is 0.9582 and F1 is 0.8997. Validation of data yielded a loss 0.03391556, accuracy of 0.9684, precision of 0.9124, recall of 0.9701 and F1 of 0.8997

Image classification

To classify other raster images for fracture-faults using the trained model, class activation map raster represented in Fig. 5 was generated. The class activation map shows each pixel in the grayscale image roughly represented as probability of belonging to the fracture-fault, and the threshold ranges from 0 to 1. The black area in the class activated grayscale image represents the area with high probability, which means it is identified as a

fracture-fault. The result identified by the trained model is a fracture-fault probability map; the larger the values in this probability map, the more confident the identified fracture-fault.

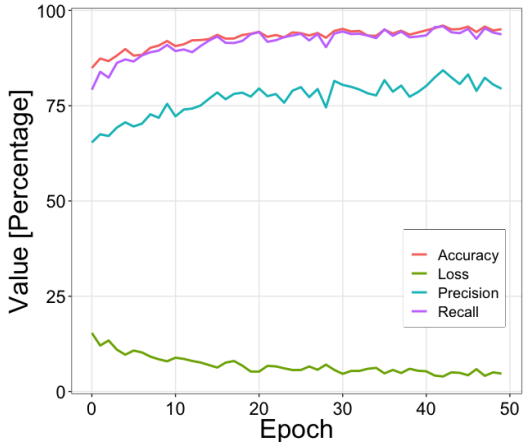

Fig. 3 Showing Training curve for accuracy, loss, precision, recall of the experiment

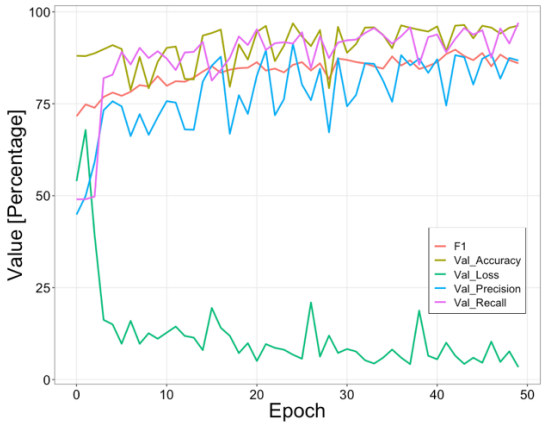

Fig. 4 Validation curves for accuracy, loss, precision, recall and F1

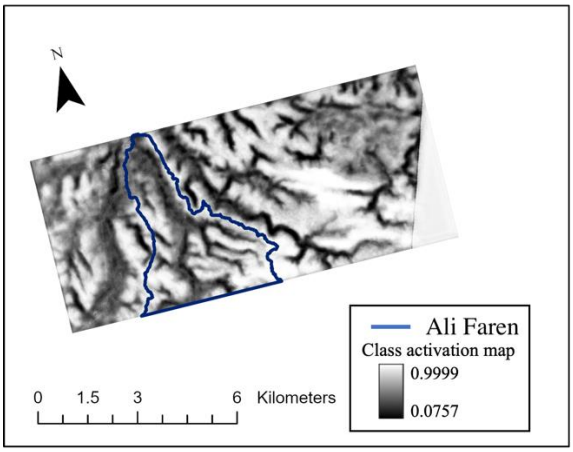

Fig. 5 Image class activation raster of selected validation area. In blue: Ali Faren watershed.

Step-wise elimination in fracture-fault classification

Fracture-fault classification from the classified image based on activation map is not a straightforward approach. To identify the real fracture-fault a stepwise elimination approach was used to identify the fracture-fault from the wadi streamlines class activation map since the result of the activation map are a mixture of wadi streamline and fault fracture.

Using the stepwise elimination, we set conditions based on geological characteristics of fracture-fault. Fracture-fault will not winded as much as wadi. Wadis will not go beyond their watershed regions and some parts of the fracture-faults might be used as wadi. Fracture-fault shapes as defined in geological maps also tend to be straight.

The predefined assumption of the stepwise elimination considered setting threshold to the class activation maps. With the set threshold of class value of given pixel values of greater than or equal to the threshold value, the polygon will be designated as the fracture-fault feature class within the polygon.

Through trial and error, the appropriate threshold used was between 0.0588 and 0.8409 for a mixture of wadi and fracture-fault polygons. The best threshold for fracture-fault activation were between 0.186343 to 0.499941. We further eliminated the classified raster based on the prior defined activation map, result of the final fracture-fault are shown in Fig. 6 and Fig. 7.

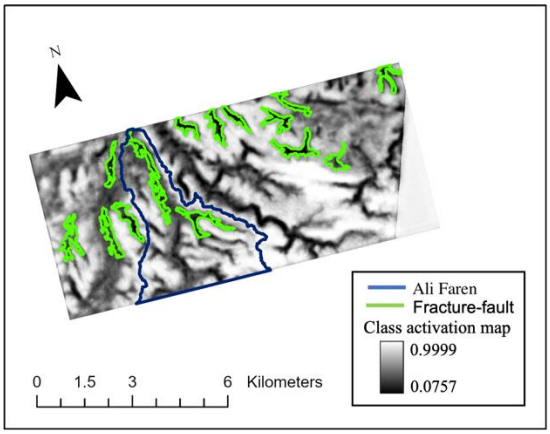

Fig. 6 Image class activation raster showing fracture-fault (green) after stepwise elimination

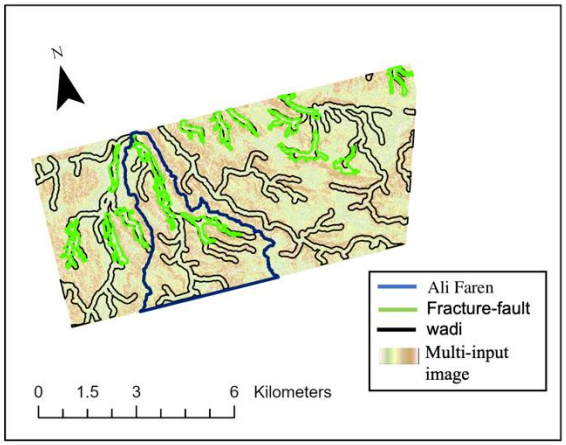

Fig. 7 Fracture-fault as seen on a wadi after step-wise elimination

CONCLUSIONS

In this study, we used Deep-CNN technique in detection on fracture-fault structures in Ali Faren catchment in Djibouti. Our solution evaluated the possibility of fracture-fault structure detection from high resolution satellite data, DEM, Slope and PALSAR-2 data. Further, determination of fracture-faults is not straightforward, so we applied a stepwise technique to the Deep-CNN generated class activation map containing both wadi and fracture-fault features to attain only fracture-fault structures.

The result showed that using multi-layer 11-data in deep-CNN model, fracture-fault lines were detected as evaluated using explained evaluation metrics such as accuracy, precision, and recall. The proposed Deep-CNN model results could be applied to other catchments in Djibouti to help in groundwater flow model simulations and eventually help locate the potential area for groundwater resources in the entire Djibouti.

Future research of this work will focus on evaluating the developed deep-CNN models and its application in wider areas within Djibouti, and on the implementation of approaches based on other deep learning architecture, such as Feature engineering of most appropriate parameter, that includes several multispectral bands as inputs. The intended goal would be to use the most appropriate models and limited multispectral bands in developing a deep-CNN model to be used in other water catchments in Djibouti and eventually integrating fracture-faults detected results from deep learning models in groundwater flow model simulation.

ACKNOWLEDGMENTS

This study was supported by Japan Science and Technology Agency (JST) and Japan International Cooperation Agency (JICA) under the project of Science and Technology Research Partnership for Sustainable Development (SATREPS GRANT NUMBER: JPMJSA1802) SATREPS (Science and Technology Research Partnership for Sustainable Development). This study acknowledge the copyright Notice for ALOS PALSAR RTC:© NASA 2006-2007, Includes Material © JAXA, METI [2006-2007]. The PALSAR-2 Global Mosaic data have been provided by the Japan Aerospace Exploration Agency.

REFERENCES

[1] Razack, M., Jalludin, M., & Houmed-Gaba, A. (2019). Simulation of climate change impact on a coastal aquifer under arid climate. The Tadjourah Aquifer (Republic of Djibouti, Horn of Africa). *Water*, *11*(11), 2347

[2] Awaleh, M.O, Baudron, P., Soubaneh, Y.D., Boschetti T., Hoch, F.B., Egueh, N.M., Mohamed, J., Dabar, O.A., Dufresne, J.M., Cassani, J. 2017. “Recharge, groundwater flow pattern and contamination processes in an arid volcanic area: Insights from isotopic and geochemical tracers (Bara aquifer system, Republic of Djibouti)”, Journal of Geochemical Exploration 175, pp. 82-98.

[3] Fadoumo A. Malow, Sawahiko Shimada, Aurelien Hazart, Event-based Rainfall-runoff Simulations using GETFLOWS for Kourtimalei Catchment in Djibouti, International Journal of Environmental and Rural Development, 2017, Volume 8, Issue 1, Pages 169-176.

[4] Tosaka,H., Mori, K., Tada., Tawara, Y. and Yamashita,K 2010. A general-purpose terrestrial fluids/heat flow simulator for catchment system management. In IAHR International Groundwater Symposium

[5] LeCun, Yann, Yoshua Bengio, and Geoffrey Hinton. "Deep learning." *nature* 521.7553 (2015): 436-444.

[6] WordlView-3 Specifications. Available online: https://earth.esa.int/eogateway/missions/worldview-3 (accessed on 24 January 2022).

[7] JAXA, Global PALSAR-2/PALSAR/JERS-1 Mosaic and Forest/Non-Forest Map (FNF) Daset Description, https://www.eorc.jaxa.jp/ALOS/en/palsar_fnf/DatasetDescription_PALSAR2_Mosaic_FNF_revI.pdf

[8] DigitalGlobe. 2021. WorldView-3 datasheet. https://www.digitalglobe.com/sites/default/files/DG_WorldView3_DS_forWeb_0.pdf

[9] Prakash, N.; Manconi, A.; Loew, S. Mapping landslides on EO data: Performance of deep learning models vs. traditional machine learning models. *Remote Sens.* 2020, *12*, 346. 12.

[10] Liu, P.; Wei, Y.; Wang, Q.; Chen, Y.; Xie, J. Research on post-earthquake landslide extraction

algorithm based on improved U-Net model. *Remote Sens.* 2020, *12*, 894.

[11] Wu, J.; Shi, Y.; Wang, W. Fault Imaging of Seismic Data Based on a Modified U-Net with Dilated Convolution. Appl. Sci. 2022, 12, 2451. https://doi.org/10.3390/ app12052451

[12] Lin, L., Zhong, Z., Cai, Z., Sun, A. Y., & Li, C. (2022). Automatic Geological Fault Identification from Seismic Data Using 2.5 D Channel Attention U-net. *Geophysics*, *87*(4), 1-58

[13] Kulkarni, S., Kedar, M. and Rege, P.P., 2018, April. Comparison of Different Speckle Noise Reduction Filters for RISAT-1 SAR Imagery. In *2018 international conference on communication and signal processing (ICCSP)* (pp. 0537-0541). IEEE.

[14] Jiang, Z., Pan, W.D. and Shen, H., 2020. Spatially and spectrally concatenated neural networks for efficient lossless compression of hyperspectral imagery. *Journal of Imaging*, *6*(6), p.38.

[15] Fetai, B., Račič, M. and Lisec, A., 2021. Deep Learning for Detection of Visible Land Boundaries from UAV Imagery. *Remote Sensing*, *13*(11), p.2077.

[16] Exelis Visual Information Solutions. ENVI Deep Learning—Training Background. Available online: https://www.l3harrisgeospatial.com/docs/ BackgroundTrainDeepLearningModels.html (accessed on 9 May 2021).

[17] Subraja, N. and Venkatasekhar, D., 2022, April. Satellite Image Segmentation using Modified U-Net Convolutional Networks. In *2022 International Conference on Sustainable Computing and Data Communication Systems (ICSCDS)* (pp. 1706-1713). IEEE.

[18] Zhang, P.; Xu, C.; Ma, S.; Shao, X.; Tian, Y.; Wen, B. Automatic Extraction of Seismic Landslides in Large Areas with Complex Environments Based on Deep Learning: An Example of the 2018 Iburi Earthquake, Japan. Remote Sens. 2020, 12, 3992. https://doi.org/10.3390/rs12233992

8th Int. Conf. on Structure, Engineering & Environment (SEE), Mie, Japan, Nov.10-12, 2022, ISBN: 978-4-909106094 C3051

SPATIAL ANALYSIS ON THE WIN OF CANDIDATE NUMBER 2 IN THE 2020 DEPOK CITY ELECTION

Imam Budi Hartono [1] , Chotib [2]
[1,2,] Development Studies Study Program Urban, School of Strategic and Global Studies, University of Indonesia, Indonesia

ABSTRACT

Depok City is one of the the city that embraces system democracy, since 1999 expansion, system election head area in Depok City has been carried out by democracy. Of all many elections that have been taking place in Depok City, the Depok City Local Election for the 2021-2024 period was one of the sufficient interesting Local Election processes, because there are two strong candidates from the previous power holder with different partner. This research aims to spatially analyze the victory of pair number 2 in the 2020 Depok City election. Spatial analysis of the research use LISA Moran's and spatial regression using Geoda software. The results of the analysis show that there is no spatial dependence of the factors that affect the winning of the pair number 2. The distribution of votes for pair number 2 has 31 sound bases and 30 bases for pairs number 1 and 2 in neutral villages, namely Grogol and Curug. Based on picture Moran's Scatterplot picture on value : 0.163. This show existence trend formation cluster spatial between nearby village.

Keywords: Depok 2020 Pilkada, Geoda, Couple No. 2, Regression Spatial

INTRODUCTION

Geography political is a branch of humans geography, which learns connection Among behavior politics and physical features. This means that behavior political residents are explained by their attachment on the physique characteristics the environment in which the community man that live (Hayati , 2007). From all many elections that have been taking place in Depok City, the Depok City Pilkada for the 2021-2024 period is one of the interesting Election process, because there are two candidates from previous period who had strong holder power with different partner. Based on temporary survey results, Idris Imam was potential to become the winner and it turns out the became the winner. The Idris – Imam pair got 415,699 votes in the 2020 election defeated Pradi – Aviva couple which gained 333,304.

For this reason, it is necessary to do a regression to show that the use of the absolute number of votes as the dependent variable is better than using a basic and non-basic. And the next, just use regression analysis with data on the absolute number of votes 02. The purpose of this research is to test classical regression analysis (OLS) and spatial regression of votes for pair 02 in the 2020 Depok Regional Head Election. In addition, this research also simulates 02 votes based on the model. formed, either by classical regression or spatial regression.

RESEARCH METHODS

According to Jaya (2016) in Lloyd (2010) Spatial data is all everything related to earthiness room characterized by geographical attributes like location coordinate and others that the Geographical Information System (GIS) has role important in studies spatial. GeoDa software was introduced first time by Luc Anselin 2002 .

The spatial effect spatial is divided into two parts: spatial dependency and spatial heterogeneity. Dependency spatial occurred because of the existence dependence on regional data, while heterogeneity spatial occurred because of the existence difference among one region to another. Panel data linear regression model containing interaction between spatial units will have variable dependent spatial lag or spatial process in common mistakes called the spatial lag model (SAR) and the spatial error model (SEM), (Elhorst , 2010). The Spatial lag (SAR) model shows influence variable independent on space j with respect to variable dependent room I (Hasna, 2013). One of the statistical tests to find out existence dependencies spatial is by doing selection early regression using the Lagrange Multiplier (LM) test to detect existence dependencies spatial by more Specific that is between LM (lag), LM (error) or models both of them are usually called the Spatial Autoregressive Moving Average (SARMA), in testing this determine choice best model Among spatial lag or spatial error.

This research used regression spatial and quantitative method by testing autocorrelation spatial with Moran's scatterplot method, and LISA by using secondary data in the form of amount population/ district, total valid votes per candidate couple, mapping Depok City Administration. According to Chotib (2019), Moran's I as in the equation:

$$Z = \frac{I - E(I)}{\sqrt{V(I)}} \quad (1)$$

According to opan (2019) spatial error or spatial moving average is a model that considers interaction correlation error between regions. Spatial errors can be described instability. The spatial error equation is as follows :

$$y = \alpha + \lambda W\varepsilon + Xi\beta + \varepsilon \quad (2)$$

Description :
α : Constant
y : Variabel dependent
$\boldsymbol{Xi}$: Variabel independent i
β : Vektor coefficient independent variable (k × 1) which has free from error effect.
λ : The coefficient of moving average that accommodates the effect of the error from the interacting neighboring region by spatial
ε : Vector error term where $\varepsilon \sim N(0, \sigma\ 2\ I)$.

This research used two types of variable, independent variable and tied variable. According to Asmarani (2018), free variable that influenced bound variable, where free variable is a control from bound variable bound, while bound variable is variables that are influenced by free variables. Bound Variable used in research is the amounts of votes couple number 2 (Idris – Imam) on election head Depok City area in 2020. Meanwhile free variable used in research is a number of influencing factors, there are voters in Depok City in 2020 including density residents, non-moslem residents, novice resident, formal residents, and High school education level and above residents. The regression modeling used is classical regression (OLS) and spatial error regression.

ANALYSIS RESULTS

a. Descriptive Analysis

Data processing is carried out to integrate using SPSS and Geoda software.

Table 1 Summary of Statistics

	Y	X_1	X_2	X_3	X_4	X_5
N	63	63	63	63	63	63
Mean	6603,21	10175,67	0,06	0,15	0,06	0,48
Median	5514,00	8983,00	0,05	0,16	0,05	0,49
Std. Dev	3276,33	5179,40	0,03	0,01	0,03	0,06
Min	2143	2587	0,02	0,14	0,03	0,33
Max	17651	24582	0,18	0,19	0,27	0,65
Sum	416002	641067	4,00	10,05	3,84	30,32

Source : Analysis Results , 2022

Description :
Y : Voice Number 2 (people)
X_1 : Population Density (people/km2)
X_2 : Pro Non Muslim (%)
X_3 : Beginner Pro (%)
X_4 : Pro Formal Workers (%)
X_5 : Pro high school and above (%)

Based on the descriptive analyze test, from 63 villages the results are as following :

1. Vote number 2 has a minimum value is 2,143 people and a maximum is 17,651 people with an average of 6,603.21 people and a median of 5,514 people, with a standard deviation of 3276,33.
2. The population density has a minimum value of 2,587 people/km^2 and a maximum of 24,582 people/km^2 with an average of 10,175.67 people/km^2 and a median of 8,983.00 people/km^2 with a standard deviation of 5,179.40 people/km^2.
3. Non moslem voters have a minimum value of 2% and a maximum of 18% with an average of 6.3%, median of 5% and standard deviation of 3.3%;
4. Beginner voters have minimum value 14%, maximum is at numbered 19% with an average of 15.9%, a median of 16% and a standard deviation of 1.03%;
5. Formal workers voters have 3% minimum value , maximum numbered 27% with an average of 6.1%, a median of 5% and a standard deviation of 3.54%;
6. High school graduates and above have minimum value 33%, maximum numbered 65% with an average of 48.13%, median 49 % and standard deviation 6.98%.

Based on the results of 2020 general election, for couples number 2 Idris - Imam, has election base in 31 urban villages, 30 non-basic areas and 2 urban villages which has neutral character, 2 villages that had neutral character are Grogol Village and Curug Village, Cimanggis Sub District. As described in distribution as follows :

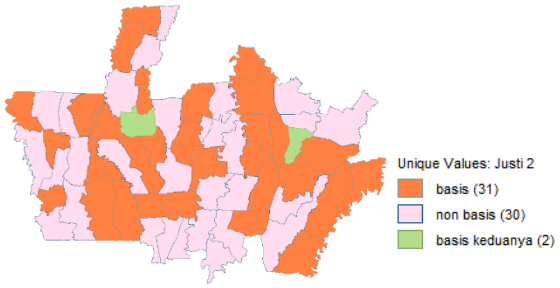

Fig. 1 Distribution Region Spatial Votes
Source : Analysis Results, 2022

By using percentage of votes number 2, the author did the scatter area selector mapping, the Type of the map to be chosen must present different visualizations and each maps gives different conclusion to either high or low location numbers. Highest and most value are generally depicted with darker colors.

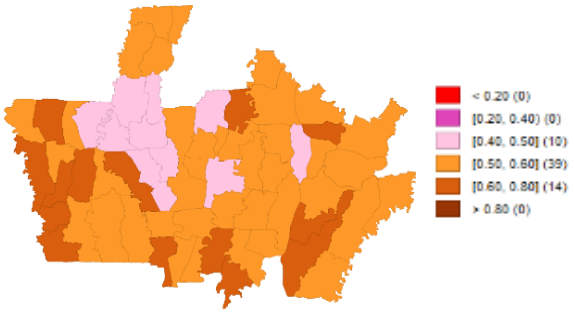

Fig. 2 Distribution Spatial Custom Break
Source : Analysis Results , 2022

Based on *custom break map* above, the percentage of couple number 2 is divided to 3 categories including :

1. Category 40% to 50% of the votes, in 10 urban villages ,
2. Category 50% to 60% of the votes , in 39 urban villages .
3. Category 60% to 80% of the votes, in 14 urban villages.

Depok City was dominated by 02 votes, ranging from 50% to above 80%. Only a few regions have a 02 vote percentage of less than 50%.

b. Analysis Autocorrelation Spatial Voter

Analysis autocorrelation spatial covers testing and visualization statistics Moran's I global (test for clustering) and local (test for clusters). Global test visualized with using a Moran scatter plot (Hawkins et al., 1999). Autocorrelation can be seen from Moran's Index and local autocorrelation could seen from Local Indicators of Spatial (LISA).

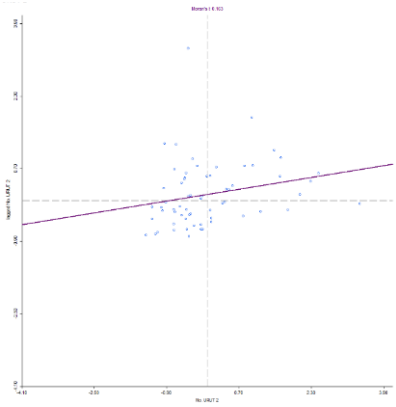

Fig. 3 Moran's Scatterplot Voice Number 2
Source : Analysis Results Geoda , 2022

Based on picture Moran's Scatterplot picture on value : 0.163. This indicates trend formation existence cluster spatial between nearby villages by mapping LISA Cluster Map.

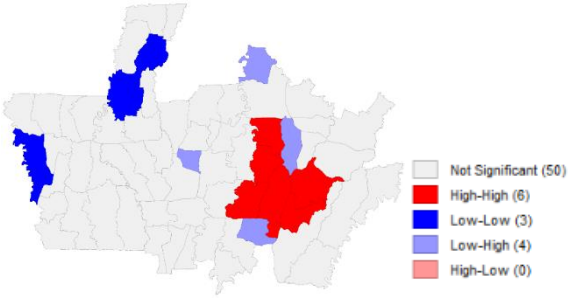

Fig. 4 Lisa Cluster Map Voice Number 2
Source : Analysis Results processed Geoda , 2022

In the figure 4, the voters of couple number 2 are not equal, each region has been colored to signify spatial effect on each region by using (LISA) method, that tested autocorrelation locally. In the mapping there are 3 colors showing existence indication spatial based on density area/location.

Quadrant I *High – High* (HH) consists of over 6 villages with percentage 9.52%, Quadrant I *High – High* (HH) consists of over 6 villages with percentage 9.52%, Quadrant II *Low – High* (LH) consists of over 6 villages with percentage 6.34%, Quadrant III *Low – Low* (LL) consists of over 3 wards with percentage 4.76%, Quadrant IV *High – Low* (HL) consists of over 0 wards with percentage 0%, No Significant there are 50 villages with percentage of 79%. Based on pictures and tables above, as example Pasir Gunung Selatan Village is in quadrant II Low – High means has very different significant value 0.001 with area surroundings (marked with color very dark green), however from aspect voice including 0.60 – 0.80% of the vote. While nearby village has above 80%, that means votes in Pasir Gunung Selatan Village correlates with votes of nearby village that is Pondok Cina Village (with spatial effects) which is low and insignificant, while Pasir Gunung Selatan Village has high score.

c. Regression Analysis

The research evaluated how far the specification regression classic is, which is well-known in criminology literature, and strong for explicit spatial effect consideration (Anselin et al., 2006). The results showed the classical regression on the votes of pair number 2 as follows :

Table 2 Correlation Test Results Inter OLS Regression Variable

Var	Coef	Sta. Error	t-Sta	Prob
Const	829,24500	247,45400	3,35111	0,00143**
X_1	-0,06370	0,02498	-2,55015	0,01348**
X_2	-0,30775	0,11798	-2,60858	0,01159**
X_3	1,04154	0,15581	6,68467	0,00000**
X_4	-0,25319	0,14223	-1,78013	0,08039

X_5	0,16285	0,06000	2,71427	0,00877**

Coefficient estimated significance at * p≤0.1; ** p≤0.05; *** p≤0.01
Source : Analysis Results Author , 2022

Based on results regression R-squared value of 0.953536 or 95%. And the Adjusted R-squared is 0.949460. From result above regression indicated that there is four correlated variables tall with significant numbers of 0.005 or <= 0.05 or = 0.1 as variable Density (X_1), Non Moslem Voters (X_2), Beginners Voters(X_3) and Voters with high school education graduates (X_5), background and above < 0.05. Based on the results of classic regression classic above, the equation obtained regression is as follows :

$Y = 829.245 - 0.0637029x_1 - 0.307754x_2 + 1.04154x_3 – 0.253191x_4 + 0.162846x_5$

The model indicated that :

1. Characteristics of number 2 voters was not at high density (x_1), because if it had 1% increase in high density it would decrease 0.06 votes.
2. Characteristics of number 2 voters was not non-Moslem (x_2), because if had 1% increase in non – Moslem voters, it would decrease 0.30 votes .
3. Characteristics of number 2 voters was beginner voters (x_3), because if it had 1% increase in beginner voters, it would increase 1.04 votes.
4. Characteristics of number 2 voters was not formally educated (x_4), because if it had 1% increase in Formal educated voters it would decrease 0.25 votes.
5. Characteristics of number 2 voters had high school background and above (x_5), because if it had 1% increase, it would increase 0.16 vote.

Classic regression election was chosen as early step, conducted by using the Large Multiplier (LM) test to find out spatial dependencies influence (autocorrelation) so that at the end spatial regression model could be formed properly or more specific. The level of significance of the model at = 0.05 or = 0.1. Based on The results of the LM test on the OLS regression model, spatial test dependency results as follows :

Table 3 Spatial Output Econometrics

DIAGNOSTICS FOR SPATIAL DEPENDENCE FOR WEIGHT MATRIX : Batas_Kelurahan_Polygon_10022022 (row-standardized weights)			
test	mi/df	value	prob
Moran's I (error)	0,19	2,87	0,00403 **
Lagrange Multiplier (lag)	1	0,04	0,82610
Robust lm (lag)	1	0,18	0,66933
Lagrange Multiplier (error)	1	5,24	0,02199 **
Robust lm (error)	1	5,38	0,02036 **
Lagrange Multiplier (sarma)	2	5,42	0,06623

Coefficient estimated significance at * p≤0.1; ** p≤0.05; *** p≤0.01
Source : Analysis Results Author , 2022

Result of the above table shows that the Moran I test has significant results or LM value (lag) > = 0.05 with value 0.00403 . P value on test this more small from level real 5%, it can be concluded that there is spatial lag influence on this model. Based on LM error test results > = 0.05 or = 0.1. P-value in testing this level value exceeds 5%, it can be concluded that there is spatial error influence in the model. Because the Lagrange Multiplier (Lag) is smaller than the Lagrange Multiplier (Error)/SEM, and the robustness value shows that the error model is more significant than the lag model.

Table 4 Spatial Output Lagrange Multiplier (Error)

Var	Coef	Sta. Error	Z-Value	Prob
Const	825.048	262.678	3.14091	0.00168**
X_1	-0.0562797	0.0234015	-2.40496	0.01617**
X_2	-0.377924	0.102054	-3.70317	0.00021**
X_3	0.860177	0.146466	5.87289	0.00000**
X_4	-0.323263	0.134929	-2.39581	0.01658**
X_5	0.231911	0.053911	4.30173	0.00002**
Lambda	0.431663	0.143378	3.01067	0.00261**

Coefficient estimated significance at * p≤0.1; ** p≤0.05; *** p≤0.01
Source : Analysis Results Author , 2022

Based on the results of spatial error regression abovef, the equation obtained regression is as follows:

$Y = 825.048 + 0.431663 - 0.0562797X_1 - 0.377924X_2 + 0.860177X_3 - 0.332263X_4 + 0.231911X_5$

that model indicated that k increase 1 unit variable besides variable independent used in models in nearby something output will raise 0.431663 votes in the village (meaning there is other variables that comes from the surrounding area). Increasing of 1 inhabitant /km^2 density population will decrease 0.06 votes for couple number 2. 1 inhabitant would increase non moslem population will decrease 0.40 votes for couple number 2. 1 inhabitant would increase beginner population will raise 0.86 votes for couple number 2. Increase 1 inhabitant of formal residents will decrease 0.32 votes for couple number 2. Increase 1 inhabitant with high school background will raise 0.23 votes couple number 2.

Processing results with regression model spatial error and OLS between variable free to achievements voice couple number 2 presented in table 5 :

Table 5 Estimation Coefficient Regression Spatial Errors and OLS

VARIABEL	SPASIAL EROR	OLS
Density	-0.0562797 (0.0234015) **	-0,06370 (0,02498)**
Non Moslem	-0.377924 (0.102054) ***	-0.307754 (0.11798) **

Beginner	0.860177	1,04154
	(0.146466)***	(0,15581)***
formal	-0.323263	-0,25319
	(0.134929)**	(0,14223)*
High School and Upper	0.231911	0,16285
	(0.053911)***	(0,06000)**
Lambda	0.431663	
	(0.143378)**	
constant	825.048	829,24500
	(262.678)**	(247,45400)**

Coefficient estimated significance at * p≤0.1; ** p≤0.05; *** p≤0.01
Source : Analysis Results Author , 2022

The results of the simulation analysis using the Classical OLS Regression Model and the Spatial Error Regression Model produce a slightly different estimate of the number of votes 02. The two estimation simulations are presented in Figure 5 which shows a higher similarity in the Classical OLS Regression Model than the Spatial Error Regression Model. It seems that the Classical Regression Model is more appropriate to use for estimating vote acquisition than the use of the Spatial Error Model, although there is a spatial effect on the vote acquisition of 02. The result showed that connection existence between regions that can affect achievements voice couple number 2 is already taken into account in the spatial model.

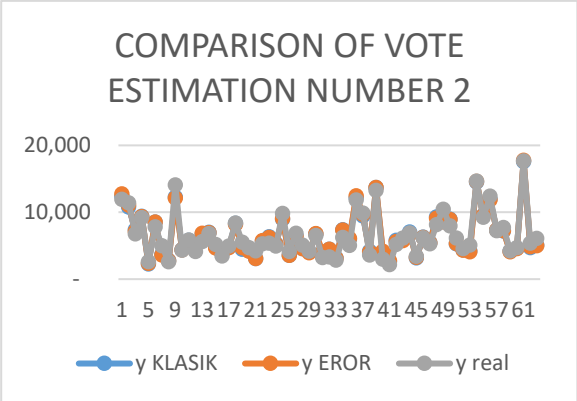

Figure 5. Comparison Estimate Voice
Source : Analysis Results Author , 2022

Based on picture on conclusion for estimation voice should use equality regression classic (OLS) versus with use regression spatial error, with Y OLS value of 416,002 and Y Real 416,002 while Y Error worth 415,333. From this calculation, it appears that the Classical Regression Model is closer to reality than the calculation results using the Spatial Error Regression Model. To prove again that the classical OLS model is closer to the real results, it can be tried using the estimated value of each kelurahan.

CONCLUSION

Based on the modeling and mapping of voters for serial number 2 as follows:

1. The distribution of votes for pair number 2 has 31 sound bases and 30 bases for pair number 1 and 2 in neutral villages, namely Grogol and Curug. And by using the percentage of votes for pair number 2 is in 3 categories including: the 40% to 50% category in 10 urban villages, the 50% to 60% category in 39 villages and the 60% to 80% category in 14 villages.
2. If using spatial autocorrelation analysis, the value of the Moran's Index and local autocorrelation can be seen from the Local Indicator of Spatial (LISA). III Low – Low, 0 village is in Quadrant IV High – Low, and there are 50 villages that are not significant.
3. The results of the comparison between the spatial regression model (error model) and OLS show that the OLS regression model is more appropriate to be used in analyzing the factors that affect the votes of pair number 2. Islam, novice voters, voters who have formal jobs, and voters with an educational background of high school and above. For estimation voice should use equality regression classic (OLS) versus with use regression spatial error , with Y OLS value of 416,002 and Y Real 416,002 while Y Error worth 415,333.

REFERENCES

[1] Alam, Moh Zainul. (2019). East Java economic growth modeling with a spatial panel econometric approach. Journal of trunojoyo: Economics and Development studies.

[2] Andriaty, Purri. (2004). Influence Economic Agglomeration and Factors Production to the GRDP of the Regency /City on the Island Java : Comparison 2001 and 2002 (Spatial Analysis econometrics). Depok : Postgraduate Thesis Faculty of Economics s and Business University of Indonesia.

[3] Anselin, Luc. (2005). Exploring Spatial Data with GeoDA : A Workbook. Center for Spatially Integrated Social Science.

[4] Anselin, L., Lozano, L., & Koschinsky, J. (2006). Rate transformations and smoothing. Urbana-Champaign: patial Analysis Laboratory Department of Geography University of Illinois.

[5] Application Spatial For Development. (2019). Department Geography Faculty Mathematics and Science Knowledge nature . University of Indonesia. ISBN: 978-623-92282-1-7.

[6] Annur Muhammad Firman. (2019). Analysis of Human Development Index Factors in Landak District Using the Spatial Regression Model. Riemann Research of Mathematics and

Mathematics Education. Volume 1, No. 1, October 2019, p. 44-54.

[7] Baltagi H. Badi & Long Liu. (2012). Testing for Spatial Lag and Spatial Error Dependence Using Doble Length Artificial Regressions. Stat Papers(2014)55: 477-486.

[8] Fauzi, Fatkhurokhman. (2016). The Best Spatial Regression Model for the Central Java Province Human Development Index.

[9] Hamdan, Opan Fauzan. (2019). Ratio of Educators, Ratio of Health Workers, and Human Development Achievements in Analysis Spatial. Depok: Master of Economics and Population Thesis Faculty of Economics and Business, University of Indonesia.

[10] Jaya, et al. (2016). Optimization Geoda In Modeling And Mapping Diseases in Bandung City.

[11] Lloyd, C. (2010). Spatial data analysis. New York: OXFORD University Press.

[12] LeSage, James P. (1999). The Theory and Practice of Spatial Econometrics. ResearchGate.

[13] Mills, Terence C & Patterson, Kerry. (2009). Palgrove Handbook of Econometrics Science. New York:Springer .

[14] Nugroho, Aditya Harin . (2014). Spatial Economics and Policy Analysis : Crime Property Polda Metro Jaya. Depok: Thesis Department Economics , Faculty of Economics and Business, University of Indonesia.

[15] Novriandi Purba, Ongki. (2016). Modeling Growth economy North Sumatra Province with approach econometrics spatial panel data. Journal science and art ITS Vol.5 No.2.

[16] Prahutama, Alan. (2014). Analysis of the 2013 Central Java Governor Election (Pilgub) Victory With Spatial Autocorrelation. Statistics, Vol. 2, No. 1, May 2014.

[17] Tobler, W. (1979). Cellular geography. In Philosophy in geography, eds. S. Gale and G. Olsson, pp.379-86, Dodrech: Reidel.

8th Int. Conf. on Structure, Engineering & Environment (SEE), Mie, Japan, Nov.10-12, 2022, ISBN: 978-4-909106094 C3051

EVALUATION OF GEOGRAPHICAL CHARACTERISTICS OF FARMLANDS LOCATION IN DJIBOUTI USING GIS

Ayako Sekiyama[1], Towa Goto[2], Takumi Sato[3] and Sawahiko Shimada[1]
[1]Faculty of Regional Environment Science, [2]System Quest Inc, Japan, [3]CAC Corp, Japan.

ABSTRACT

Djibouti is in Northeast Africa and is a severely arid region with annual precipitation of less than 200 mm. The government of Djibouti is promoting an agro-pastoralist system to improve self-sufficiency, and it is necessary to establish new agricultural land. In order to make this goal, it is needed to understand the current location characteristics of farmlands and the potential of water resources in Djibouti. In this study, the location and area of farmlands in 2010 and 2020 were first investigated using Google Earth and satellite image called ALOS AVNIR-2. Next, wadis were created from a digital elevation model "AW3-DEM" using GIS software. The amount of accumulated water inflow into the wadis was calculated, and the wadis were classified into three classes: large, medium, and small. Using these data, the relationship between topographic characteristics, such as altitude and slope where farmland is located, and wadi as water resources, was analyzed. As results, it was found that most of the farmlands were distributed in areas with an altitude of less than 200 m and a slope of less than five degrees. Regarding the distance between farmlands and wadis, it was shown that in the last decade the distribution has increased in areas further away from large wadis. Farmlands in Djibouti were established to be more concentrated in areas that are flat and close to densely populated areas.

Keywords: ALOS World 3D, Digital elevation Model, Hydrology Modeling, Wadi

INTRODUCTION

Djibouti, located in the "Horn of Africa" in the northeast of the African continent, is situated at the northern end of the Rift Valley land area under a desert climate (Fig.1). Annual precipitation of Djibouti is less than 200 mm which is a severe arid condition. Most of the country is a desert surface covered with basalt. There are no flowing rivers, so only shallow groundwater from the Wadi area is available for agriculture, livestock, and domestic use. Population is 974,000 as at 2019 [1]. In Djibouti, less than 1% of the population is engaged in agriculture and about 25% is involved in the pastoral husbandry, including nomadic pastoralism. Nomad people is 25% of the population, half of nomad is in southern region of Djibouti. Pastoralism is only traditional and non-commercial. The share of agricultural production is less than 5% of GDP, and the food self-sufficiency rate is only 13% in terms of production value. The food self-sufficiency rate is only about 13% in terms of production value. However, drought caused by recent climate change has resulted in a shortage of pasture grasses. The nomadic life has become more difficult, and many nomads are currently in need of additional income, such as Gulf labor. To improve this situation, the Djibouti government has developed the Primary Industries Development Plan 2010-2020 (PDDSP), which is designed to help rural nomads augment their alternative income sources through agriculture. Farming operations conducted by farmers in Djibouti are mainly based on irrigation systems using shallow groundwater from the Wadi. Therefore, geographic proximity to the Wadi is an essential location for agriculture in Djibouti. An agricultural example in Djibouti is the successful agropastoral and sustainable farming of vegetables, orchards, and livestock using shallow groundwater. In addition to these successful examples, analysis of the relationship between location, water resource environment, and farming conditions in many farmlands operating in Djibouti is necessary to achieve the Ministry of Agriculture's goal of "designing new agricultural lands". However, in the rural areas of Djibouti, the use of land is allowed by the customary system, and the procedures for acquiring farmlands to the public organization are not carried out. Therefore, it is not possible to obtain statistical information on the location, size, and status of farming operations used as farmlands. In order to build new farmlands, fundamental information is required on the current situation of the area and the location of farmlands all over Djibouti. It has also been reported that the distribution of precipitation period varies with altitude in Djibouti. Furthermore, altitude and slope factors are also important from the aspects of farmland establishment design and farming operations. The objective of this study is to extract from satellite imagery, to clarify the geographical characteristics of their location environment using GIS, and to evaluate their agricultural potential throughout Djibouti.

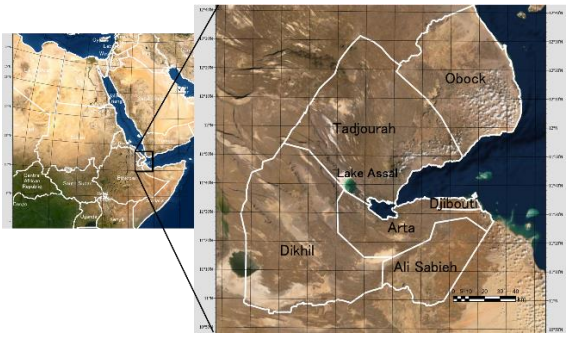

Fig. 1 Location of Djibouti (six province) in Africa.

METHODOLOGIES

Data Collection of farmland sites in Djibouti

Many farmlands in rural Djibouti are surrounded by stone walls to protect crops from grazing livestock and hot winds. Farmlands were extracted from satellite image data by visually identifying these fences as boundaries. ALOS AVNIR-2 imagery was used to produce plantation polygon data for Djibouti in 2010. The spatial resolution of AVNIR-2 imagery was pan-sharpened to 2.5 m using ALOS panchromatic imagery, as AVNIR-2 has a spatial resolution of 10 m, which is insufficient for visual interpretation of farmlands. Satellite imagery taken between 6th October 2006 and 5th January 2011 was used, although most areas in Djibouti were taken in 2010.

Google Earth Pro was used for the 2018 polygon data of farmland. Most areas were taken between 2018 and 2020, but some areas include imagery taken in 2016.

The number of farmlands across Djibouti that could be visually determined from Google Earth Pro was 670, with a total area of 1090 ha. Compared to 2010, the number of farmlands and the area of farmlands increased. Compared to the other provinces, more farmlands were distributed in the three southern provinces, which accounted for about 80% of the total area. The density of farmlands in the eastern part of Alta and the south-western region of Dhikil showed the same trend in 2010 and 2020, and this trend was even stronger in 2020. This farmland polygon data preparation has been described in detail in previous studies [2],[3].

Digital Elevation Model

Satellite remote sensing by earth observation satellites is effective for understanding wadi and watersheds distributed over a wide area. One of the advantages of satellite remote sensing is that wide areas can be observed periodically, which may be useful in the study area. Many studies have reported the use of satellite remote sensing to extract watersheds and wadis in arid regions [4], [5].

In this study, a high-resolution DEM called AW3D (ALOS World 3D) with a spatial resolution of 5 m, produced using satellite imagery taken by ALOS PRISM, was used (Fig.2). The altitude of the Lake in central Djibouti is -176 m, and the altitude of the mountainous area on the border between Ethiopia and Eritrea at the northern edge is about 2,020 m. The country has an undulating terrain. The slope distribution was calculated from this DEM as geographical data for evaluating the location environment (Fig.3). Relatively low slope throughout Djibouti but appears to be steep in many areas in Tadjourah Province.

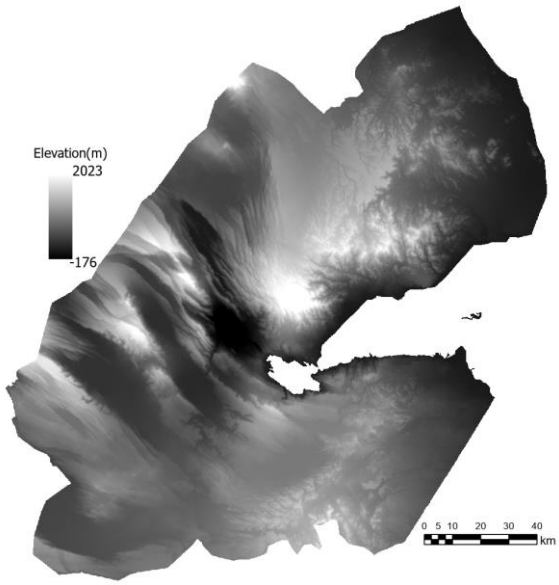

Fig. 2 DEM (AW3D) in all of Djibouti

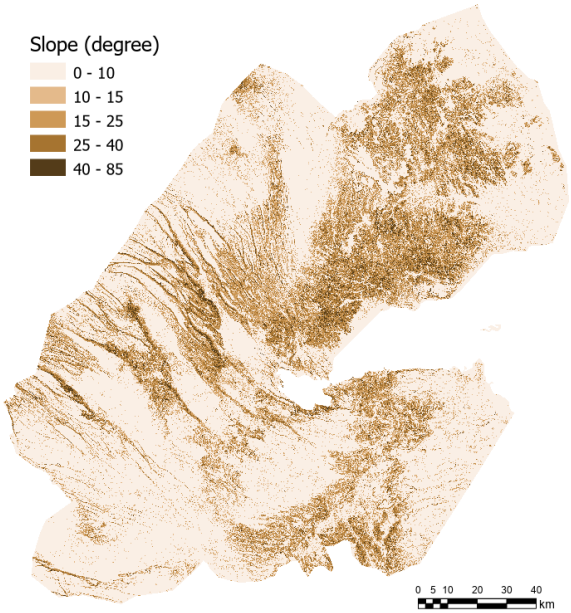

Fig. 3 Slope distribution from DEM in Djibouti.

Hydrological Modeling

Wadi means river or valley in Arabic. Generally, wadis only receive running water during heavy

rainfall, and usually have only a dry sand and gravel covered riverbed. In Djibouti, which depends on rainfall and is not able to store water, people use the shallow groundwater in wadis for their livelihoods and for agricultural purposes. A river model (wadi channel) was calculated from the slope direction and accumulated flow data using hydrological analysis in ArcGIS Pro. The accumulated flow data were then used to classify the threshold values for the number of accumulated pixels (one pixel = 5 m) into three classes: more than ten thousand pixels, more than one million pixels and more than three million pixels. The wadi channels for each class were calculated and defined as small, medium and large wadi classes, respectively. The distribution of Wadi streams in each class is shown in Figure 4. The small and medium wadi classes are approximately equally distributed throughout Djibouti (Fig.4a, Fig. 4b). The large wadi class was less distributed in the southern part of Tadjoura province, which is at a relatively high altitude (Fig.4c).

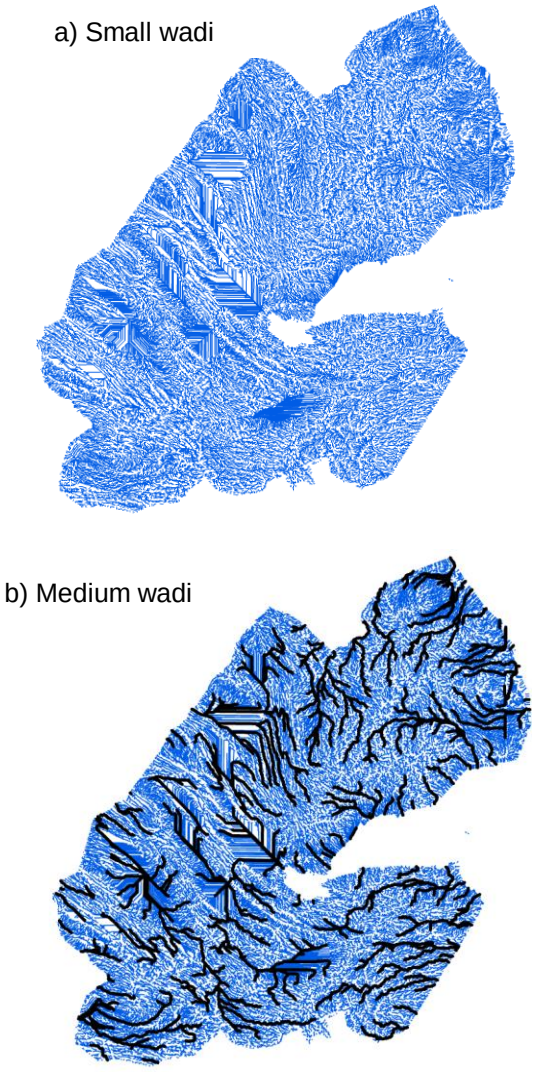

Fig.4 Wadi channel distribution in each class. Medium and large wadi class lines are indicated by bold lines. a) Small wadi (Accumulated flow pixels less than ten thousand), b) Medium wadi (less than one million), c) Large wadi (less than three million)

RESULTS AND DISCUSSIONS

Change of farmland area in Djibouti

The area of farms in each province in 2010 and 2020 is shown in Table 1. Data on the location of wells was used from the surveys conducted by FAO in 2017. Between 2010 and 2020, the number of farmlands throughout Djibouti has twice and their area has increased by about 1.6 times. In 2010, the number of farmlands in Dhikil Province increased from 354.3 ha (147 sites) to 388.2 ha (211 sites), accounting for about half of the total area of farmlands in Djibouti. In 2020, the proportion of the area of farmlands in Djibouti and nearby Arta, which includes the capital Djibouti City, and, additionally, in Ali Sabieh and Tajurah provinces, increased. These provinces are relatively well resourced in terms of water quality and water resources, such as wells.

Figure 5 shows the distribution of farmlands in 2010 and 2020. The number of farmlands in 2020 appears to have increased, mainly in areas where farmlands existed in 2010 throughout Djibouti. The expansion of farmlands, particularly in the densely populated surroundings of Djibouti City, which faces the Gulf of Aden, has been significant. There was no tendency for new farms to be established in 2020 in areas where no farms existed in 2010. Therefore, geographical factors may have prevented the establishment of new farms from the initial potential.

Table 1 Farmland area and water resource information of each Province in 2010 and 2020.

Province name	Area (ha) in 2010	Area (ha) in 2020	Area increasing rate (%)	Number of well (FAO, 2017)
Djibouti	41.1	47.1	115	208
Arta	130.1	294.5	226	412
Ali-sabieh	78.2	193.9	248	324
Dikhil	354.3	388.2	110	337
Tadjourah	68.2	145.8	214	523
Obock	15.4	20.6	134	285
Total	687.3	1090.1	159	2089

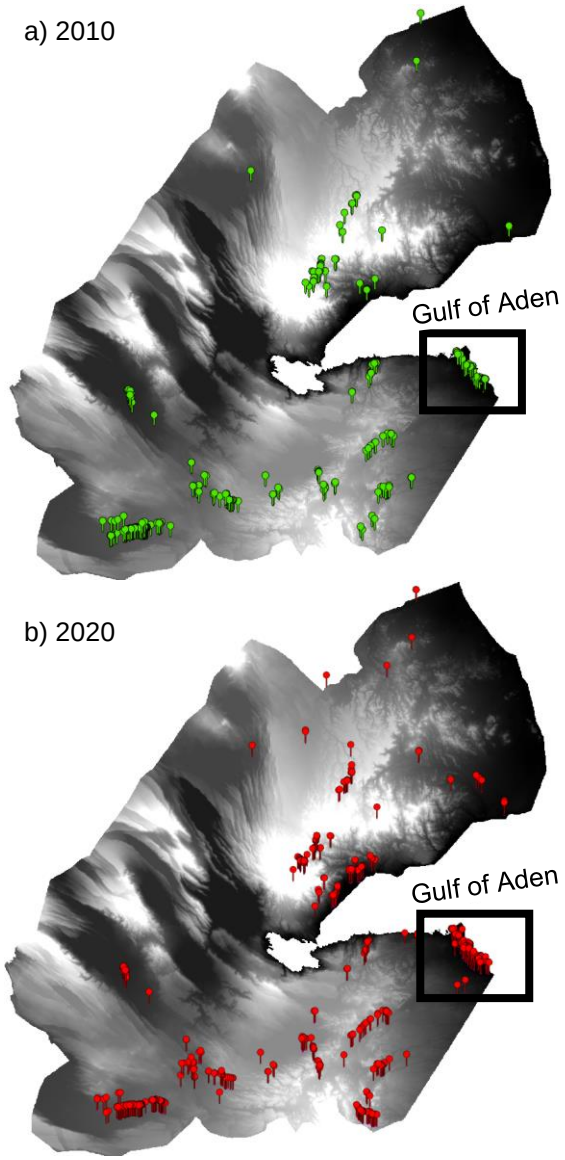

Fig.5 Farmland distribution in 2010 and 2020. Symbols in the figure show the location of the farmland.

Geographical characteristics of farmland in Djibouti

The area of farmland by altitude class was calculated for 2010 and 2020. The results showed that in 2010 the maximum was between 200 m and 400 m, while in 2020 the maximum was below 200 m, as shown in Figure 6. It is considered that during this period, farmlands were expanded to lower altitude areas below 200 m. Most of the farmlands are located in lowland areas at altitudes below 400 m, although some farmlands have expanded in the area between 400 m and 800 m in 2020.

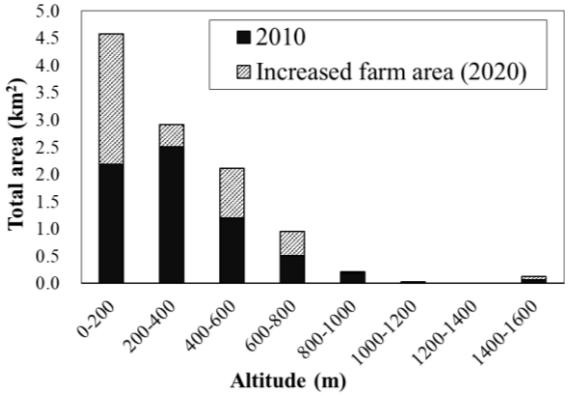

Fig.6 Altitude distribution of farmland in 2010 and 2020.

Next, the area by slope class was calculated for the years 2010 and 2020 as well. The results show that in both periods, as shown in Figure 7, farmlands were located in areas with slopes of five degrees or below. It was therefore assumed that the establishment of farmlands was restricted to areas with slopes of five degrees or below.

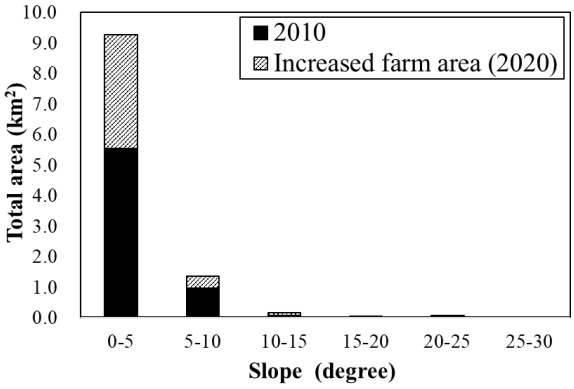

Fig.7 Slope distribution of farmland in 2010 and 2020.

From the above, it is considered appropriate to establish farmlands in low and flat areas, but there is potential for establishing farmlands at relatively high altitudes if the slope degree is gently.

Finally Geographical proximity was further investigated by calculating the Euclidean distance between the farmlands and each wadi. In 2010 and 2020, areas with geographical proximity of 100 m from small wadis were selected as farmlands (Fig. 8). For medium and large wadis, the distance between wadi and farmland was more significant in 2020 than in 2010, and the difference is more pronounced for large wadis. Therefore, it can be considered that in the last decade, farmlands have been established in areas far distance from the large wadis.

The above results indicate that the location characteristics of the farmlands are low altitude and relatively flat areas. It was also found that in the last decade, farmlands have been established at a further distance from large wadis.

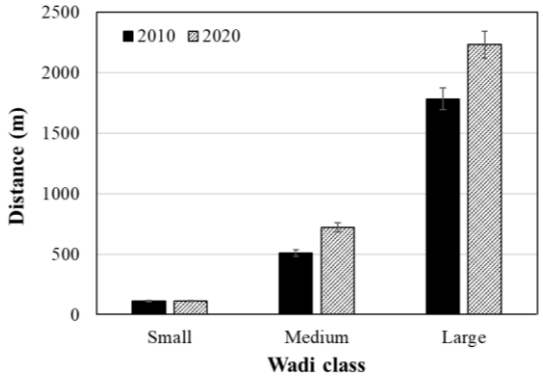

Fig.8 Average distance from farmland to wadi in each wadi class.

CONCLUSIONS

In this study, the geographical characteristics of farmlands in 2010 and 2020 were analyzed. Altitude, slope and distance of farmland from wadis were investigated. Wadis were analysed and classified into three classes - large, medium and small - according to the accumulated inflow of water. The results of the analysis were as follows.

- Farmlands were distributed in areas with an altitude of less than 200 m and a slope of less than five degrees.
- Regarding the distance between farmlands and wadis, it was shown that in the last decade the distribution has increased in areas further away from large wadis.
- It was found that farmlands are increasingly being established in areas that satisfy the above conditions.

ACKNOWLEDGMENTS

This research was supported by Science and Technology Research Partnership for Sustainable Development (SATREPS), Japan Science and Technology Agency (JST) / Japan International Cooperation Agency (JICA).

REFERENCES

[1] United Nations. https://population.un.org/wpp/Download/Standard/Population/ (Last access,4th Jul. 2022)

[2] T. Sato. Farm extraction using deep learning with satellite imagery in Djibouti. Tokyo University of Agriculture, 2020, Master thesis.

[3] T. Sato, A. Sekiyama, S. Saito and S. Shimada. Applicability of Farmlands Detection in Djibouti from Satellite Imagery using Deep Learning. International Journal of Arid Land Studies. 2022, In press.

[4] C. Kessar, Y. Benkesmia, B. Blissag, L. Wahib Kébir. Delineation of groundwater potential zones in Wadi Saida Watershed of NW-Algeria using remote sensing, geographic information system-based AHP techniques and geostatistical analysis. Journal of Groundwater Science and Engineering. Vol. 9, Issue 1, 2021.pp.45-64.

[5] M. Abdekareem, N. Al-Arifi, F. Abdalla, A. Mansour and F. El-Baz. Fusion of Remote Sensing Data Using GIS-Based AHP-Weighted Overlay Techniques for Groundwater Sustainability in Arid Regions. International Journal of sustainability. Vol. 14, Issue 13, 2022. 7871; https://doi.org/10.3390/su14137871

8th Int. Conf. on Structure, Engineering & Environment (SEE), Mie, Japan, Nov.10-12, 2022, ISBN: 978-4-909106094 C3051

ENVIRONMENTAL IMPACTS ASSESSMENT OF REAL ESTATE PROJECT AT PALLABI EASTERN HOUSING AREA IN DHAKA CITY, BANGLADESH

*Md. Mahabub Alam[1], Md. Soybur Rahman[2], Alex Otieno Owino[3], Abd Elmageed Atef [3], Md. Yachin Islam[3] and Zakaria Hossain[3]

[1]Department of Environmental Science, State University of Bangladesh, Bangladesh
[2]Department of Environmental Science, Bangladesh Agricultural University, Bangladesh
[3]Department of Environmental Science and Technology, Mie University, Japan

ABSTRACT

Dhaka is the capital city of Bangladesh. A lot of people migrate every day. For their survival, the housing sector is flourishing day by day. The demand impacts the supplies. A number of people are doing housing business to support the situation. Still, on the contrary, they are grabbing a lot of green fields or water bodies from private properties evacuating the owners. One of the ill examples is considered as Pallabi Eastern Housing 2nd Phase Project. The study is to find the socio-economic status of the land owners and local inhabitants who are evicted from their land for the project. According to the primary observation and information collected from different sources, approximately 350 families are relocated. Of the 45 relocated people placed under survey from the questionnaire survey by snowball sampling, it was found that most people were displaced from their original location through the involuntary procedure. The income level, housing condition, and utility facilities are worse off than before the resettlement. They are unaware of taking action against the developer for the deprivation in the land price. The study discovered different aspects that clarified how land developers exploited the local people. The four different actors, namely land developers, local musclemen, local officials, and local people, were identified who actively played various roles in this relocation procedure. A few scopes are identified to rehabilitate the victims to recover from their present situation. Government should adequately care about the reallocated people to compensate at the current rate considering the long period of suffering. There is scope for more intensive study on the topic.

Keywords: Housing sector, Socio-economic, Developer, Land, Government

1. INTRODUCTION

Bangladesh is a densely populated country. About 25 percent of the population (35 million people) live in urban areas. The urbanization process is linked with economic development and contributes to the national economy. Urbanization and rapid urban change may be a negative sign of development, provided urban problems arise due to improper management and unplanned growth[1]. The increasing number of high rise commercial buildings is making the area a high class slum, causing problems such as dampness, shadow, disruption of airflow, turbulence of airflow, etc.[2]. Land developers are converting low-lying areas as well as agricultural land.

Consequently, land development companies have a dominant force in the land market and significantly impact land development and planning. Thus it is crucial to have a clear understanding of the relocation process in the urban fringe of Dhaka city due to private land development projects. This research also tried to explore the socio-economic impact of relocation on the locally affected people[3].

Bangladesh is a developing country. Dhaka is its capital city and the center of all main activities of the country, providing civic utilities. The real estate and housing sector of Dhaka City illustrates the scenario of the real estate and housing situation of Bangladesh. The establishment of the real estate market in Bangladesh is hundred years old, but now it has matured significantly another form of profit earning campaign initiated by the developers is the transformation of residential plots as well as flats into commercial and business utilization which in turn putting pressure on the infrastructure, services, road network and creating greater environmental impacts of Real Estate Projects in Dhaka City[4]. Although the plots of (EHL) Residential Area were primarily allocated for residential buildings with a maximum height limitation of 6 stories, most of the single houses are turning into high-rise residential cum commercial apartments. In most cases, they do not follow the setback rules and in other instances, violate the height restriction rules too. As a result, the increasing numbers of high rise commercial buildings are making the area a high class slum which in turn is causing the problems such as dampness, shadow, disruption of airflow,

turbulence of airflow, etc. [5].

The main objective of this research is to study the environmental impact of Eastern Housing Limited in Dhaka city. This research intends to focus on the local people's relocation process and assess the relocated people's present and previous socio-economic status. No work has been yet done on the relocation of local people because of private land development projects.

2. METHODOLOGY

2.1 Location of The Study

The study area is the Real Estate Project of Eastern Housing Pallabi 2nd phase, Mirpur, a thana of Dhaka city, Bangladesh. It is bounded by Pallabi Thana to the north, Mohammadpur Thana to the south, Kafrul to the east, and Savar Upazila to the west.

Map 1: Eastern Housing Pallabi 2nd phase, Mirpur

2.2 Data Collection

Data were collected from both primary and secondary sources to fulfill the research objectives. According to an 80% confidence level and confidence interval of 5, at least 50 questionnaires needed to be surveyed. This research used snowball sampling for the questionnaire survey. Snowball sampling is also called network or chain sampling. Residents of adjacent land development projects were the main introducing section for snowball sampling, and data were randomly collected from the field level. Secondary data included relevant literature related to this research topic, including published and unpublished thesis papers, study reports, journals, books, newspaper magazines, research publications, seminar papers, ordinance/policy, etc. Information on housing projects was collected from RAJUK, REHAB, offices of land developers, and advertisements published in media and websites. The Internet was another informative source of secondary data used in this report.

2.3 Data Analysis

After getting data from the field survey, the existing documents were analyzed using MS Excel. To the best of his knowledge, the researcher avoided plagiarism and maintained high ethical standards in preparing this research paper.

3 RESULTS AND DISCUSSION

Every day, many people migrate to Dhaka City for their livelihood. As a result, real estate activities are increasing day by day. This study was conducted to identify the environmental problem due to real estate projects in Dhaka City. The results of this study have been presented and discussed under the following headings.

3.1 Problem of outside labor in Real estate Project

Data indicates that due to outside labor in the Real estate Project relocated people suffering 30(67%) respondents and not suffering 15(33%) respondents. Problems with outside labor strongly relate to the improvement of real estate activities. Maximum relocating people suffering with outside labour issues in real estate project in Dhaka city[6].

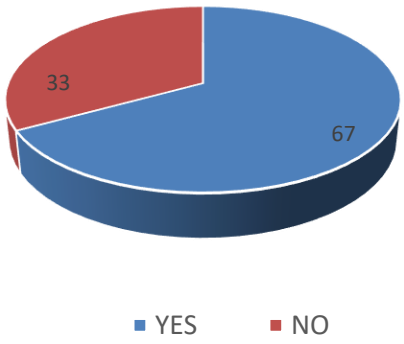

Fig. 1: Cause of Environmental Problem for real Estate project

3.2 Impact of Real Estate project in Land Value

Survey indicates that due to real estate project land value increased 30 (67%) respondent and deceased 14 (31%) and not changed 01 (2%) respondent confirmed the status. It is clear that continuous constructing building has significant effect on the price of land. Land price become more than twice within 20 years due to real estate activities [7].

Table 1: Increased or decreased of Land Value for Real Estate project

Chain Land Value	Frequency	Present (%)
Increased	30	67
Decreased	14	31
Unchanged	1	2
Total	45	100

3.3 Cause of Environmental Problems for Real Estate Projects

The survey indicates that environmental impact is there due to real estate projects. Problem 33 (77%) respondent and No Problem 12 (23%) respondent Confirm. It can be said that the environmental problem has increased due to real estate projects. Developing activities increase violations of human rights, natural or human-made disasters, and other social problems [8].

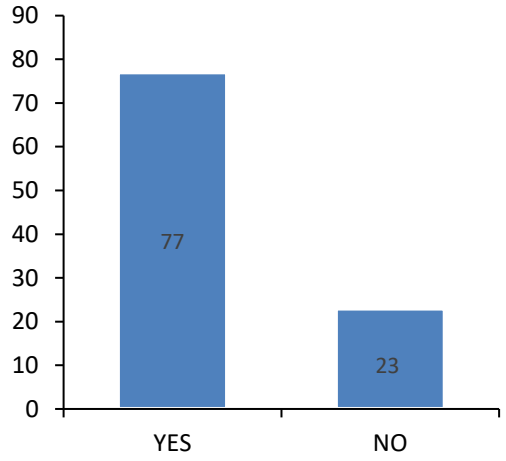

Fig. 2: Cause of Environmental Problems for real Estate project

3.4 Socio-economic Impact on Real Estate Project

Data indicates that Socio economics impact for Real Estate project is happened 38 (84%) respondent and No impact to 07 (16%) respondent. The result clearly shows that almost all people suffer socially and financially from real estate projects. Land is the primary source of livelihood for many living in the fringe areas. The poorest are often forced into temporary settlements in urban fringe land. The urban fringe poor depend to a greater extent on access to natural resources than wealthier, urban-based groups [9].

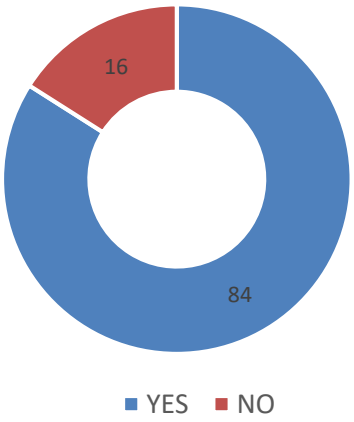

Fig. 3: Socio-economic impacts for Real Estate project

3.5 Compensated from Real Estate Company for relocated people

Data indicate that Compensated from Real Estate Company for relocated people is given totally 7(16%) respondent, No Compensated 13 (24%) and same Compensated given 25 (59%) respondent confirm. Real Estate Companies partially compensate the majority of relocating people. Less than one-fourth of people don't get compensation from Real Estate Companies. It is a major challenge for the City Development Authority (RAJUK) to manage the urban spatial growth and to meet the growing population's demand with its limited resource and maximum real estate company trying to provide compensation for relocating people[10].

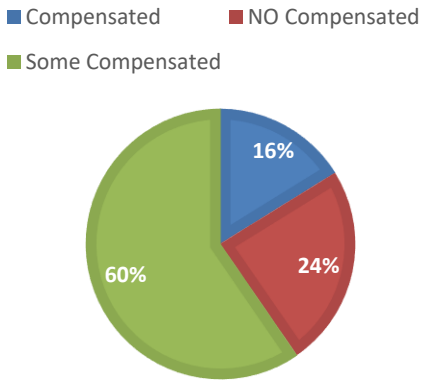

Fig.4: Compensated from Real Estate Company for relocated people

4. CONCLUSIONS

Local people relocation is a complex issue. This study has unfolded the procedure of local people relocation in Dhaka City. Land developers with the help of local musclemen and local officials, used many techniques to buy land from local people. Both voluntary and involuntary procedures were used for relocation. About 500 households relocated because of the Eastern Housing limited land project. Though this research outcome clearly shows that maximum local people were displaced from their original location through the involuntary procedure. This research also identified the socio-economic condition of relocated people. The study shows that the overall socio-economic conditions of local people are inferior compared with previous locations, which ultimately supported social researchers' opinion about the negative effect of relocation. This study briefly recommends some broad steps to consider for relocation issues. Good governance is a prime consideration for fringe area development. National Policy on Resettlement and Rehabilitation should be implemented as soon as possible to protect the land right of local people.

ACKNOWLEDGMENTS

At first, all praises belong to Almighty Allah, the cherisher and sustainer of the world, who allowed me to conduct this study. I express my gratitude to Khan Ferdousour Rahaman, Associate Professor & Head, Department of Environmental Science, State University of Bangladesh, for his kind consideration of designing the approaches and methodologies and his time-to-time suggestions, advice, and untiring efforts for the efficient preparation of this paper. My special thanks to my friend Md. Aminul Islam, Ebrahim Khalil, and the Shanto Mariam University of Creative Technology students for providing me with their valuable time and Energy for my data collection at the field level.

REFERENCES

[1] Haial, G., "Rapidly Growing African Cities Need to Adopt Smart Growth Policies to Solve Urban Development Concerns," Urban Forum, 2008.

[2] Seraj, A.N., Climate Change Adaptation assessment: A Case Study of the Eastern Fringe of Dhaka, Bangladesh, MSc Thesis, Department of Urban Management and Development, Netherland, 2004.

[3] Tawhid, S., "Health Implications of Involuntary Resettlement and Rehabilitation in Developmental Projects in India", Society for Health Education and Learning Packages, Vol.01, New Delhi, India, 2010

[4] Mahmud, Md. Akter., "Corruption in Plan Permission Process in RAJUK: A Study of Violations and Proposals," Transparency International Bangladesh, Dhaka, 2007.

[5] Arku, G., "Rapidly Growing African Cities Need to Adopt Smart Growth Policies to Solve Urban Development Concerns," Urban Forum, 2009.

[6] Arman, M. S. B., and Alam, P. D. R., "Sustainability of Development Trends in the Urban Fringe: A Case Study on North-Eastern Dhaka City," Protibesh, Volume 12, Issue 2 pp. 55-67 Dhaka, Bangladesh, 2018.

[7] Kabir, I., "Wetlands of Dhaka Metro Area: A study from social, Economic & Institutional perspectives," A HDevelopment Publishing House, Dhaka, Bangladesh. 2019.

[8] Lobo, L., and Kumar, S., "Land Acquisition, Displacement and Resettlement in Gujrat: 1947-2004," SAGE publication, Delhi, India, 2009.

[9] Clark, D. A. L., "Environmental Challenges to Urban Planning: Fringe areas, Ecological Footprints and Climate Change. Key Challenges in the Process of Urbanization in Ho Chi Minh City," Governance, Socio-Economic, and Environmental Issues, Vietnam, 2009.

[10] Masum,"Urban Fringe Management and Role Of Good Governance: Integrating Stakeholders in Land Management Process," in 7th FIG Regional Conference, Hanoi, Vietnam, 19-22 October 2009.

8th Int. Conf. on Structure, Engineering & Environment (SEE), Mie, Japan, Nov.10-12, 2022, ISBN: 978-4-909106094 C3051

SEASONAL VARIATION OF RESIDENTIAL INDOOR AIR QUALITY IN MYMENSINGH CITY, BANGLADESH

Md. Soybur Rahman[1], Md. Mahabub Alam[2], Alex Otieno Owino[3], Abd Elmageed Atef[3], Md. Yachin Islam[3] and Zakaria Hossain[3]

[1]Department of Environmental Science, Bangladesh Agricultural University, Bangladesh
[2]Department of Environmental Science, State University of Bangladesh, Bangladesh
[3]Department of Environmental Science and Technology, Mie University, Japan

ABSTRACT

Indoor concentrations of PM2.5, PM10, TVOC, and CO_2 were measured in winter and summer in 90 naturally ventilated houses in three locations in Mymensingh city. Average indoor concentrations of PM2.5, PM10, TVOC, and CO_2 for all households in winter were (121.68 ± 50.28) μg/m^3, (137.91 ± 57.69) μg/m^3, (0.820 ± 8.0894) μg/m^3, (660.31±130.12) ppm. Summer average indoor concentrations were PM2.5 (86.753 ± 35.44) μg/m^3, PM10 (103.55 ± 38.90) μg/m^3, TVOC (0.387 ± 0.0762) μg/m^3, CO_2 (581, 73 ± 78.50) ppm, and the results showed PM10 and PM2.5 experienced large seasonal variations, with air quality declining especially in winter. Average indoor PM2.5 concentrations in Akua, Maskanda, and Town Hall were 70.96 μg/m^3, 70.475 μg/m^3, 95.85 μg/m^3 in summer, and 130 μg/m^3, 70.51 μg/m^3, and 129.625 μg/m^3, respectively in winter. The average PM10 concentrations in summer in the surveyed houses were 86.3612 μg/m^3 in Akua, 78.77 μg/m^3 in Maskanda, 128.077 μg/m^3 in Town Hall, and 159.41 μg/m^3, and 71, 78 μg/m^3,170.225 μg/m^3 in winter respectively. The average indoor CO_2 concentrations of the studied dwellings were 569.86 ppm (Akua), 547.1ppm (Maskanda), and 574.891ppm (Town Hall), respectively, during summer and 649.602 ppm, 629.133ppm, and, 724.76 ppm during the winter season. This investigation found that the indoor PM10 and PM2.5 concentrations were notably higher than the WHO guidelines in all selected dwellings throughout the two sample periods. In contrast, TVOC and CO_2 values were not exceeding the WHO guideline. Indoor pollutant concentrations were strongly dependent on ambient concentrations due to increased ventilation rates in summer, with indoor sources influencing indoor concentrations in winter due to increased human activity and poor ventilation.

Keywords: Indoor air, PM2.5, PM10, CO_2, TVOC, Summer, Winter

INTRODUCTION

Indoor air quality (IAQ) is a fundamental issue that is receiving increasing attention in both developed and developing countries as people spend almost 90% of their time indoors and a higher proportion of household expenditure[1]. Sensitive groups such as the elderly and children may be indoors all day and be at greater risk due to their exposure to many indoor air pollutants from various indoor and outdoor sources[2]. Indoor air quality (IAQ) is strongly influenced by many factors, including indoor emission sources, building characteristics (including design and ventilation), and outdoor air quality. Most indoor air pollutants can cause respiratory and cardiovascular problems. The severity of their effects depends on their toxicity, concentration, duration of exposure, and the health of the people exposed to them [3].

Particulate matter (PM) is an essential air pollutant associated with indoor and outdoor health effects[4]. PM comprises particles that were penetrated from outdoor sources and those generated indoors. Particles generated inside buildings can be released directly from indoor sources, known as elemental PM, or from chemical reactions of gaseous precursors. For example, particles with aerodynamic diameters below 10 μm, known as PM10, can be separated into coarse particles of 2.5-10 μm in diameter (PM2.5-10). A small fraction of fine particles with aerodynamic diameters greater than 2.5 micrometers (PM2.5) often contain toxic substances that can penetrate deep into the lungs[5]. Thus, fine particles increase morbidity and mortality from respiratory and cardiovascular diseases[6]. Sources of ambient particulate matter generation in urban environments include vehicle emissions, industrial processes, construction activities, road dust from brake wear and tire washing, particulate reactivation, and road transport[7].

Carbon dioxide (CO_2) is mainly produced by combustion and human metabolism. As a result, CO_2 concentrations are higher in indoor residential environments than in outdoor environments[8]. Recent trends in building design, including improving air tightness and reducing building

ventilation rates to save energy and mitigate climate change, can reduce indoor air quality and increase CO_2 emissions[9]. Indoor CO_2 concentrations indicate whether the rate of outdoor air entering a room is sufficient to dilute indoor air pollutants [10]. Recent trends in building design, including improving air tightness and reducing building ventilation rates to save energy and mitigate climate change, can reduce indoor air quality and increase CO_2 emissions[11][12]. Indoor CO_2 concentrations indicate whether the rate of outdoor air entering a room is sufficient to dilute indoor air pollutants [13]. There are different classifications of Total Volatile Organic Compounds (TVOC). The most common definition is that of the World Health Organization (WHO), which characterizes the volatility (or boiling point) of organic compounds to identify volatile organic compounds (VOCs) and semi-volatile organic compounds (VOC). It is generally related to the molecular length of the carbon skeleton. The sum of all VOCs is called total volatile organic compounds (TVOCs). VOCs are ubiquitous both outdoors and indoors. Depending on the design and use, the room may simultaneously be contaminated with different organic compounds. The World Health Organization (WHO) presents guidelines on protecting public health from the risks posed by certain chemicals commonly found in indoor air[14]. IAQ data are generally scarce in Mymensingh city, and the problem is less understood. There is currently a lack of research studies in Mymensingh to investigate IAQ in urban homes. Therefore, the current work aims to estimate seasonal variations in the quality of indoor air in a number of residential dwellings of Mymensingh during the winter and summer seasons.

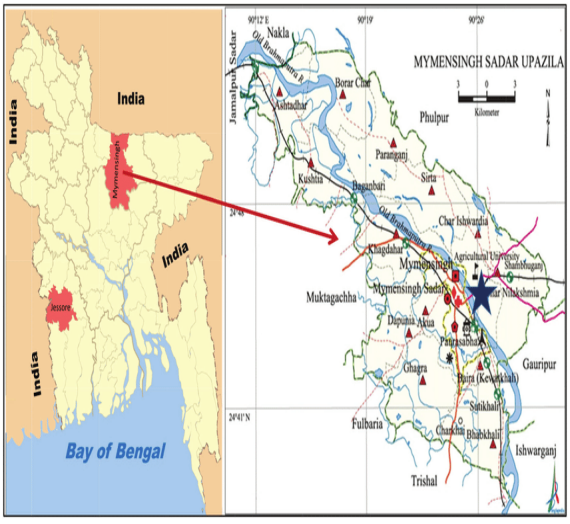

Fig. 1 Location of the sudy

METHODOLOGY

Location of the study area

The present study was conducted in several locations in Mymensingh city, Bangladesh. Mymensingh is located on the bank of the Brahmaputra River, about 120 km north of the national capital Dhaka; it is a major financial center and educational hub of north-central Bangladesh.

Sample collection

Indoor air samples of PM10, PM2.5, TVOC, and CO_2 were taken from 90 houses located in a dense urban and commercial residential area. Air sampling was carried out in two measurement periods

1. Winter (January to February/2022) and
2. Summer (June to July/2022).

Sampling sites were all private apartments situated at different distances from high-traffic routes. A typical architectural design of residential buildings in the city providing living rooms with balconies is an essential source of natural ventilation. Outdoor air samples were taken just outside the living area. Indoor and outdoor air measurements of PM10, PM2.5, TVOC, and CO_2 were taken, followed by calculating the average values. This included the condition and age of the building, the ventilation pattern, the size of the living area, the number of occupants, the number of smokers, the frequency of cleaning and cooking, and any potential factors.

Indoor and outdoor temperature, RH, and CO_2 levels were monitored simultaneously using portable Q-Trak monitors (BENTECH GM8802). Indoor and outdoor concentrations of PM10 and PM2.5 and Total Organic Carbon (TVOC) were measured simultaneously in each home using Lighthouse Handheld 3016 IAQ.

BENTECH GM8802

Handheld 3016 IAQ

Data analysis

All descriptive statistics and statistical analyzes of the data were performed using the Statistical Package for the Social Sciences (SPSS) for Windows (version 20.0, SPSS, Inc., NY, USA).

RESULTS AND DISCUSSION

The mean indoor and outdoor levels of measured air pollutants (PM10, PM2.5, CO_2, and TVOC) for all households in the three study areas in the two sampling periods under investigation are shown.

PM2.5

Daily mean PM2.5 concentrations measured at all residential sites in Mymensingh were relatively high, varying from 55 to 186 µg/ m^3. Outdoor PM2.5 concentrations measured outside the studied apartment reached as high as 60 to 172 µg/m^3.PM2.5 concentrations in three study areas showed remarkable variation in summer and winter except for the Maskanda area in indoor and outdoor air. Many studies across different countries have surveyed, identified, and quantified PM in residential areas in the United States, reporting an average concentration of 10.8 µg/m^3. Birmingham, UK, found a value of 7.9 µg/m^3. Concentrations of PM2.5 display winter maxima concluded that indoor and outdoor PM2.5 levels increased from rural to urban to roadside environments[15].

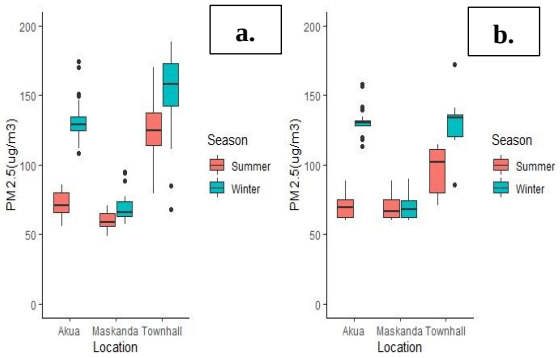

Fig.1: Box plots for indoor (a) and outdoor (b) PM2.5 concentrations in the selected areas of Mymensingh city [Lines across each box indicate the median value, box edges represent the 25th and 75th percentiles, and values outside this percentile range are shown as black dots].

PM10

Daily mean PM10 concentrations measured at all residential sites in Mymensingh were relatively high, varying from 65 to 215 µg/ m^3. Outdoor PM10 concentrations measured outside the studied apartment reached as high as 70 to 165 µg/m^3. The average indoor PM10 concentrations of examined houses were 86.3612 µg/m^3 for Akua, 78.77 µg/m^3 for Maskanda, and 128.077 µg/m^3 for Town Hall, respectively in summer season and 159.41 µg/m^3, 71.78 µg/m^3, 170.225 µg/m^3 in the winter season. The average outdoor PM10 concentrations of examined houses were 73.95µg/m^3 for Akua, 82.8066 µg/m^3 for Maskanda, and 127.27µg/m^3 Town Hall, respectively, in the summer season and 147.35µg/m^3, 82.805 µg/m^3, 138.092 µg/m^3 in the winter season.

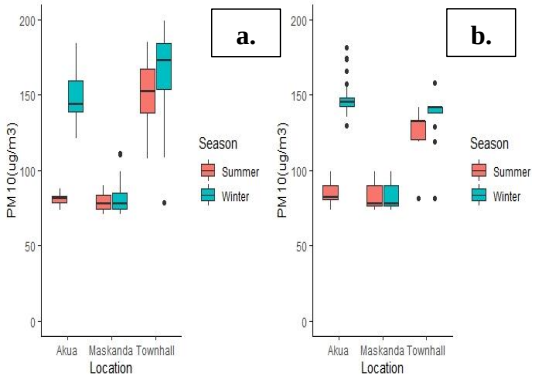

Fig.1 Box plots for indoor (a) and outdoor (b) PM10 concentrations in the selected areas of Mymensingh city [Lines across each box indicate the median value, box edges represent the 25th and 75th percentiles, and values outside this percentile range are shown as black dots].

Carbon dioxide (CO_2)

The average indoor CO_2 concentration of examined houses was 569.86 ppm (Akua), 547.16 ppm (Maskanda), and 574.891 ppm (Town Hall), respectively, in the summer season and 649.602 ppm, 629.133 ppm, 724.76 ppm in the winter season. The average outdoor CO_2 concentrations of examined houses were 495.03 ppm (Akua), 494.954 ppm (Maskanda), and 636.4 ± 110.61 ppm (Town Hall), respectively, in the summer season and 553.99 ppm, 568.51 ppm, 633.4 ppm in the winter season.

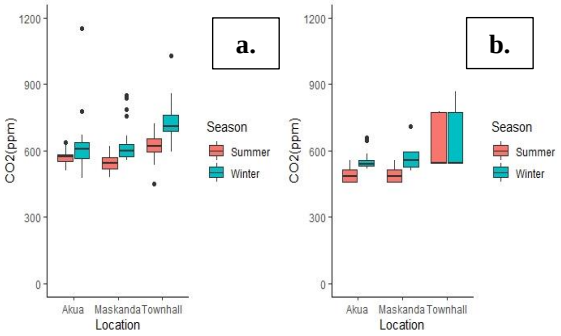

Fig.3 Box plots for indoor (a) and outdoor (b) CO_2 concentrations in the selected areas of Mymensingh city [Lines across each box indicate the median value, box edges represent the 25th and 75th percentiles, and values outside this percentile range are shown as black dots].

Total Volatile Organic Compound (TVOC)

100% TVOC concentrations in all selected houses were below 0.6 µg/m3. TVOC concentration of 0.3 mg/m3 is considered a low TVOC concentration value; values between 0.3 µg/m^3 and 0.5 µg/m^3 are acceptable (Airmax IOT blog, 2020). TVOC concentrations in the Akua region showed the most significant variation between summer and winter due to the different types of lifestyles, building structures, people's behaviors, and mixed cultures in the residential area of Akua. The study area of Muskanda is a sparsely populated, rural city with less variability in indoor TVOC, and indoor TVOC concentrations were lower in winter than in summer (Figure 4.3.4.1). After all, the Town hall Hall is where cultural events, trade fairs, political meetings, events, and performances occur, and it was higher than the two study locations. Formaldehyde and TVOC emissions from dry and wet building materials. We found that temperature and relative humidity significantly affected emissions, with formaldehyde emissions being much higher in summer than in winter [16].

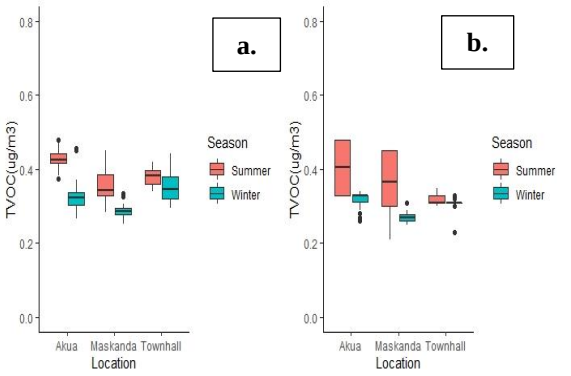

Fig.4 Box plots for indoor (a) and outdoor (b) TVOC concentrations in the selected areas of Mymensingh city [Lines across each box indicate the median value, box edges represent the 25th and 75th percentiles, and values outside this percentile range are shown as black dots].

Indoor/outdoor ratios

Indoor concentrations were compared with those outdoors using I/O ratios. I/O ratios obtained for each residence in the 90 houses are presented in Fig. 5. The average I/O ratios for all sample sites throughout the summer season were 1.13 with a range of 0.74–1.39, and median: 1.13 for CO_2; 1.12 with a range of 0.79–3.37 and median: 0.94) for PM10, 0.94 with range 0.57–1.59 and median: 0.96 for PM2.5, and 1.09 with range 1.01–1.47 and median: 1.12 for TVOC during the summer season. During the winter season, the average I/O ratios at all sample sites were 0.96 with a range of 0.79–1.58 and median: 1.1 for CO_2, 1.05 with a range of 0.86–1.42 and median: 1.01 for PM10, 0.981 with a range of 0.71–1.48 and median: 0.98 for PM2.5 and 1.31 with a range of 0.86–1.49 and median: 0.98 for TVOC.

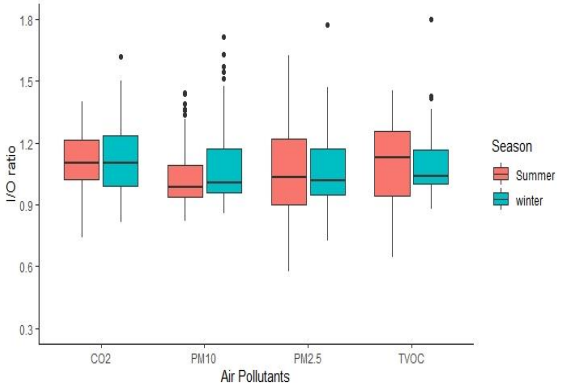

Fig.5 Box plots for indoor-outdoor ratios of air quality in the study area [Lines across each box indicate the median value, box edges represent the 25th and 75th percentiles, and values outside this percentile range are shown as black dots].

Toxicity Potential (TP) for PM2.5 and PM10

Toxicity Potential (TP) = $\mathbf{Cp}/\mathbf{Sp}$

Where Cp is the observed concentration of the pollutants and Sp is the usual recommendation value of 25 µg/m3 for PM2.5 and 50 µg/m3 for PM10 (WHO 2006).

Table 1 TP PM10 and TP PM2.5 values in the three selected areas throughout the winter and summer seasons.

Pollutants	TP
PM2.5	4.52
PM10	3.01

A TP value of more than 1 suggests a possible health risk of the specified pollutant in a given location. Table 1 exhibits TP PM10 and TP PM2.5 values throughout the winter and summer seasons in the three selected areas where TP values are more than one, suggesting a possible health issue [17].

CONCLUSIONS

Indoor and outdoor concentrations of PM10, PM2.5, TVOC, and CO_2 were measured simultaneously in 90 naturally ventilated urban homes (25 homes were supplied with AC) at three selected study sites in

Mymensingh city during the winter and summer season. This study revealed that the indoor PM10 and PM2.5 concentrations were noticeably higher than the WHO guidelines in all selected homes during the two sampling periods. For indoor TVOC and CO_2 levels, none of the values exceeded the WHO guideline and the ANSI/ ASHRAE Standard 62.1, respectively, even though both TVOC and CO_2 were very suitable for indoor air quality. The toxicity potential of particulate matter was 3 to 4 times higher, causing concern that particulate matter exposure can lead to multiple adverse health effects. The winter season had a higher PM2.5 concentration within the houses than in the summer. However, the average PM2.5 concentration inside different places (balcony, kitchen, living room) of homes was remarkably similar in each season. PM2.5 and PM10 concentrations in the three study areas showed remarkable variation in summer and winter except for the Maskanda area in indoor and outdoor air. Finally, the total volume of indoor air quality in the study area was satisfying for the indoor environment. According to the air quality index, particulate matter concentrations were unhealthy, and TVOC and CO_2 concentrations were fine.

ACKNOWLEDGMENTS

The author feels glad to pay his heartiest respect, most profound gratitude, and cordial thanks to all course teachers of the Department of Environmental Science, Bangladesh Agricultural University, Mymensingh, and others who directly or indirectly helped complete this paper by giving valuable advice, suggestions, and co-operation.

REFERENCES

[1] Odeh, I., and T. Hussein. (2016). Activity pattern of urban adult students in an eastern Mediterranean society. Int.J. Environ. Res. Public Health 13 (10):960–65.

[2] Gabriel, M.F., Felgueiras, F., Batista, R., Ribeiro, C., Ramos, E., Mourão, Z. and de Oliveira Fernandes, E. (2020). Indoor environmental quality in households of families with infant twins under 1 year of age living in Porto. Environmental Research, 198 :110477.

[3] Maynard, R. L. (2019). Health effects of indoor air pollution. In Indoor air pollution, ed. R. E. Hester and R. M. Harrison. London, UK: Royal Society of Chemistry. 196–218.

[4] Franck, U., O. Harbarth, S. Röder, U. Schlink, M. Borte, U. Diez, U. Krämer, and I. Lehmann. (2011). Respiratory effects of indoor particles in young children are size dependent. Sci. Total Environ. 409 (9):1621–31.

[5] Ghio, A. J., M. S. Carraway, and M. C. Madden. (2012). Composition of air pollution particles and oxidative stress in cells, tissues and living systems. J. Toxicol. Environ. Health B 15 (1):1–21.

[6] Cincinelli, A., and T. Martellini. (2017). Indoor air quality and health. Int. J. Environ. Res. Public Health 14-1286.

[7] Charron, A., and R. M. Harrison. (2005). Fine (PM2.5) and coarse (PM2.5-10) particulate matter on a heavily trafficked London highway: Sources and processes. Environ. Sci. Technol. 39 (20):7768–76.

[8] Fisk, W. J. (2017). The ventilation problem in schools: Literature review. Indoor Air 27 (6):1039–51.

[9] Papachristos, G. (2015). Household electricity consumption and CO2 emissions in the Netherlands: A model-based analysis. Energy Build. 86:403–14.

[10] Gall, E., T. Cheung, I. Luhung, S. Schiavon, and W. Nazaroff. (2016). Real-time monitoring of personal exposures to carbon dioxide. Build. Environ. 104:59–67.

[11] Papachristos, G. (2015). Household electricity consumption and CO2 emissions in the Netherlands: A model-based analysis. Energy Build. 86:403–14.

[12] Shrubsole, C., I. G. Hamilton, N. Zimmermann, G. Papachristos, T. Broyd, E. Burman, D. Mumovic, Y. Zhu, B. Lin, and M. Davies. (2019). Bridging the gap: The need for a systems thinking approach in understanding and addressing energy and environmental performance in buildings. Indoor Built. Environ. 28 (1):100–17.

[13] Gall, E., T. Cheung, I. Luhung, S. Schiavon, and W. Nazaroff. (2016). Real-time monitoring of personal exposures to carbon dioxide. Build. Environ. 104:59–67.

[14] Meyer c. 2021.Overview of TVOC and Indoor Air Quality Environmental Protection Agency, Acute Exposure Guideline Levels for Airborne Chemicals.

[15] Mohamed F. Yassin, Bothaina E.Y. Al-Thaqeb, Eman A.E. Al-Mutiri. (2012). Assessment of indoor PM2.5 in different residential environments.56:65-85.

[16] Chan, A. T. (2002). Indoor-outdoor relationships of particulate matter and nitrogen oxides under different outdoor meteorological conditions. Atmos. Environ. 36 (9):1543–51.

[17] Chamseddine, A., Alameddine, I., Hatzopoulou, M., & El-Fadel, M. (2019). Seasonal variation of air quality in hospitals with indoor–outdoor correlations. Building and Environment, 148: 689–700.

Next SEE Conference will be merged with GEOMATE Conference

- The "International Journal of GEOMATE" is a Scientific Journal of the GEOMATE International Society that encompasses a broad area in Geotechnique, Construction Materials and Environment.
- The key objective of this journal is to promote interdisciplinary research from various regions of the globe.
- The editorial board of the journal is comprised of extensively qualified researchers, academicians, scientists from Japan and other countries of the world.
- It is peer-reviewed Journal that is published quarterly till 2015 and now monthly. All articles published in this journal are available online.
- Contributors may download the manuscript preparation template for submitting paper or contact to the Editors-in-Chief

[editor@geomatejournal.com]